

High Frequency Asymptotics of Electromagnetic Field on a Strongly Elongated Spheroid

I. V. Andronov

University of St. Petersburg, Russia

Abstract— In this paper the creeping waves on a strongly elongated spheroid are considered. The high frequency asymptotics of such waves is derived in the form of inverse Mellin transform of Whittaker functions. Numerical analysis of the poles of the integrand allows to study the effect of large transverse curvature on the attenuation of creeping waves.

1. INTRODUCTION

The process of high frequency diffraction on a strongly elongated body has its specifics being in the necessity to take into account the three dimensional character of the problem. The large transverse curvature ρ_t may cause significant decrease of creeping waves attenuation. Though many results for creeping waves on strongly elongated bodies are known (see e.g., [2]) there is still no satisfactory agreement between numerical results and asymptotic theory. In particular this may be caused by variation of transverse curvature along the geodesics which was not properly taken into account in the previous analysis.

In this paper we consider the problem of plane electromagnetic wave diffraction by an elongated spheroid. The main large parameter of the problem is $k\rho$ where k is the wavenumber and ρ is radius of curvature. To characterize the elongation we introduce another large parameter ρ/ρ_t , where ρ_t is the radius of curvature in perpendicular cross-section. From previous results [1] it is known that specific reconstruction of the usual asymptotics happens when $\rho/\rho_t = O((k\rho)^{2/3})$. We consider this case and introduce scaled radius of transverse curvature

$$\kappa = 2m^2 \frac{\rho_t}{\rho} = O(1), \quad m = \left(\frac{k\rho}{2} \right)^{1/3}.$$

It is well known [3] that spheroidal coordinate system allows variables separation in Helmholtz equation. We assume that the surface of the elongated body locally coincides with the surface of a spheroid with appropriate parameters. If this spheroid is strongly elongated some kind of scaling can be used to simplify the spheroidal equation. This simplification allows the large parameter of the problem to be excluded from the equations. Resolution of these simplified scaled equations gives the high frequency asymptotics of acoustic field on a strongly elongated body.

We derive such an asymptotics. First we introduce spheroidal coordinates and extract rapidly oscillating factor. Then we stretch coordinates and by collecting higher order terms derive the parabolic equation. We separate variables and get the formula for the field in the form of an integral containing unknown amplitude. Substituting this representation into the boundary condition allows an integral equation for this amplitude to be derived. Then we solve this integral equation and substitute the amplitude in the integral representation. Further simplifications use the properties of special functions that are involved in the integral.

2. PARABOLIC EQUATION

Introduce spheroidal coordinates (ξ, σ, φ) by the formulae [3]

$$z = p\xi\sigma, \quad r = p\sqrt{\xi^2 - 1}\sqrt{1 - \sigma^2},$$

where p is a parameter which will be chosen later and (r, φ, z) are the cylindrical coordinates. The coordinate ξ is the radial coordinate ($1 \leq \xi$) and σ is angular coordinate ($-1 \leq \sigma \leq 1$).

In the new variables Maxwell equations take the form

$$\begin{aligned} \sigma h_\varphi E_\varphi - \varphi h_\sigma E_\sigma &= -ikh_\sigma h_\varphi H_\xi, & \sigma h_\varphi H_\varphi - \varphi h_\sigma H_\sigma &= ikh_\sigma h_\varphi E_\xi, \\ \varphi h_\xi E_\xi - \xi h_\varphi E_\varphi &= -ikh_\varphi h_\xi H_\sigma, & \varphi h_\xi H_\xi - \xi h_\varphi H_\varphi &= ikh_\varphi h_\xi E_\sigma, \\ \xi h_\sigma E_\sigma - \sigma h_\xi E_\xi &= -ikh_\xi h_\sigma H_\varphi, & \xi h_\sigma H_\sigma - \sigma h_\xi H_\xi &= ikh_\xi h_\sigma E_\varphi, \end{aligned}$$

where h_ξ , h_σ and h_φ are metric coefficients

$$h_\xi = p\sqrt{\frac{\xi^2 - \sigma^2}{\xi^2 - 1}}, \quad h_\sigma = p\sqrt{\frac{\xi^2 - \sigma^2}{1 - \sigma^2}}, \quad h_\varphi = p\sqrt{\xi^2 - 1}\sqrt{1 - \sigma^2}.$$

We assume that all the components of the electromagnetic field depend on the angle φ via the factor $e^{i\ell\varphi}$.

Further from the first, the second, the fourth and the fifth equations we express E_ξ , E_σ , H_ξ and H_σ via E_φ and H_φ . Substituting these expressions into equations number 3 and number 6 yields the system of differential equations for E_φ and H_φ . We exploit the symmetry of these two equations and by setting

$$E_\varphi = P + Q, \quad H_\varphi = -iP + iQ$$

separate the system into two independent differential equations for P and Q .

We extract quick oscillating factor

$$\exp(ikp\xi_0\sigma),$$

introduce scaled coordinates

$$kp = m^2\sqrt{2\kappa} \quad \left(p = \frac{\rho}{m}\sqrt{\frac{\kappa}{2}} \right), \quad \xi_0 = 1 + \frac{\kappa}{4}m^{-2},$$

$$\xi = 1 + \frac{\nu}{4}m^{-2}, \quad \nu = 2m^2\frac{\rho t + n}{\rho}$$

and sort the terms by the powers of large parameter m . Thus in the leading order of m^3 we get

$$\nu^2 P\nu^2 + P\nu + i\frac{\sqrt{2\kappa}}{4}(1 - \sigma^2)P\sigma + \frac{1}{8} \left(\kappa\nu - \kappa^2(1 - \sigma^2) - \frac{2(1 - \ell)^2}{\nu} \right) P = 0, \quad (1)$$

$$\nu^2 Q\nu^2 + Q\nu + i\frac{\sqrt{2\kappa}}{4}(1 - \sigma^2)Q\sigma + \frac{1}{8} \left(\kappa\nu - \kappa^2(1 - \sigma^2) - \frac{2(1 + \ell)^2}{\nu} \right) Q = 0. \quad (2)$$

These equations should be completed with the boundary conditions. For the case of perfect conductor we require on the surface $E_\varphi = 0$ and $E_\sigma = 0$. This gives the system of boundary conditions

$$\begin{cases} P + Q = 0, \\ 2\kappa P\nu - 2\kappa Q\nu + P - Q = 0. \end{cases} \quad (3)$$

3. INTEGRAL REPRESENTATION

By variables separation we can write the solution corresponding to the diffraction of plane electromagnetic wave

$$E_x^{(i)} = e^{ikz}, \quad E_y^{(i)} = E_z^{(i)} = 0, \quad H_y^{(i)} = e^{ikz}, \quad H_x^{(i)} = H_z^{(i)} = 0.$$

in the form

$$E_\varphi = \cos(\varphi) \frac{\exp(ikp\xi_0\sigma - i(\kappa/2)^{3/2}\sigma)}{\sqrt{\nu}\sqrt{1 - \sigma^2}} \int_{C-i\infty}^{C+i\infty} I(\mu) \quad (4)$$

$$\times \left(\frac{1 + \sigma}{1 - \sigma} \right)^{-\mu} \left(M_\mu^0 \left(-i\sqrt{\frac{\kappa}{2}}\nu \right) + A(\mu)W_\mu^0 \left(-i\sqrt{\frac{\kappa}{2}}\nu \right) + B(\mu)W_\mu^1 \left(-i\sqrt{\frac{\kappa}{2}}\nu \right) \right) d\mu, \quad (5)$$

$$H_\varphi = \sin(\varphi) \frac{\exp(ikp\xi_0\sigma - i(\kappa/2)^{3/2}\sigma)}{\sqrt{\nu}\sqrt{1 - \sigma^2}} \int_{C-i\infty}^{C+i\infty} I(\mu) \quad (6)$$

$$\times \left(\frac{1 + \sigma}{1 - \sigma} \right)^{-\mu} \left(M_\mu^0 \left(-i\sqrt{\frac{\kappa}{2}}\nu \right) + A(\mu)W_\mu^0 \left(-i\sqrt{\frac{\kappa}{2}}\nu \right) - B(\mu)W_\mu^1 \left(-i\sqrt{\frac{\kappa}{2}}\nu \right) \right) d\mu. \quad (7)$$

Here C is some constant, $I(\mu)$, $A(\mu)$ and $B(\mu)$ are the amplitudes, $M_\mu^\alpha(x)$ and $W_\mu^\alpha(x)$ are the standard solutions of Whittaker equation

$$\frac{d^2 f(x)}{dx^2} + \left(-\frac{1}{4} + \frac{\mu}{x} + \frac{1 - 4\alpha^2}{4x^2} \right) f(x) = 0.$$

The terms containing $M_\mu^0()$ in the integral representations (4), (5) express the incident wave and other terms correspond to the reflected electromagnetic field.

We first find the amplitude $I(\mu)$ such that on the surface the first term coincides with the incident field, that is

$$\frac{\exp(-i(\kappa/2)^{3/2}\sigma)}{\sqrt{\kappa}\sqrt{1-\sigma^2}} \int_{C-i\infty}^{C+i\infty} I(\mu) \left(\frac{1+\sigma}{1-\sigma} \right)^{-\mu} M_\mu^0 \left(-i\sqrt{\frac{\kappa}{2}}\kappa \right) d\mu = 1.$$

The integral in the left-hand side of this integral equation is the inverse Mellin transform. Using direct transform and integral representation [4, formula 9.221] for Whittaker function $M_\mu^0(x)$ yields

$$I(\mu) = \frac{e^{-i\pi/4} 2^{1/4}}{2\pi} \frac{1}{\kappa^{1/4}} \Gamma\left(\frac{1}{2} - \mu\right) \Gamma\left(\frac{1}{2} + \mu\right).$$

The amplitudes $A(\mu)$ and $B(\mu)$ in representations (4), (5) should be found such that the boundary conditions (3) are satisfied. These conditions yield the system of linear algebraic equations wherefrom

$$A(\mu) = -\frac{W_\mu^1 \left(-i\frac{\kappa^{3/2}}{\sqrt{2}} \right) \widehat{M}_\mu^0 \left(-i\frac{\kappa^{3/2}}{\sqrt{2}} \right) + M_\mu^0 \left(-i\frac{\kappa^{3/2}}{\sqrt{2}} \right) \widehat{W}_\mu^1 \left(-i\frac{\kappa^{3/2}}{\sqrt{2}} \right)}{W_\mu^0 \left(-i\frac{\kappa^{3/2}}{\sqrt{2}} \right) \widehat{W}_\mu^1 \left(-i\frac{\kappa^{3/2}}{\sqrt{2}} \right) + \widehat{W}_\mu^0 \left(-i\frac{\kappa^{3/2}}{\sqrt{2}} \right) W_\mu^1 \left(-i\frac{\kappa^{3/2}}{\sqrt{2}} \right)}, \quad (8)$$

$$B(\mu) = \frac{W_\mu^0 \left(-i\frac{\kappa^{3/2}}{\sqrt{2}} \right) \widehat{M}_\mu^0 \left(-i\frac{\kappa^{3/2}}{\sqrt{2}} \right) - M_\mu^0 \left(-i\frac{\kappa^{3/2}}{\sqrt{2}} \right) \widehat{W}_\mu^0 \left(-i\frac{\kappa^{3/2}}{\sqrt{2}} \right)}{W_\mu^0 \left(-i\frac{\kappa^{3/2}}{\sqrt{2}} \right) \widehat{W}_\mu^1 \left(-i\frac{\kappa^{3/2}}{\sqrt{2}} \right) + \widehat{W}_\mu^0 \left(-i\frac{\kappa^{3/2}}{\sqrt{2}} \right) W_\mu^1 \left(-i\frac{\kappa^{3/2}}{\sqrt{2}} \right)}. \quad (9)$$

Here we introduced functions

$$\begin{aligned} \widehat{W}_\mu^\alpha \left(-i\frac{\kappa^{3/2}}{\sqrt{2}} \right) &= \left(\mu + i(\kappa/2)^{3/2} \right) W_\mu^\alpha \left(-i\frac{\kappa^{3/2}}{\sqrt{2}} \right) + W_{\mu+1}^\alpha \left(-i\frac{\kappa^{3/2}}{\sqrt{2}} \right), \\ \widehat{M}_\mu^0 \left(-i\frac{\kappa^{3/2}}{\sqrt{2}} \right) &= \left(\mu + i(\kappa/2)^{3/2} \right) M_\mu^0 \left(-i\frac{\kappa^{3/2}}{\sqrt{2}} \right) + M_{\mu+1}^0 \left(-i\frac{\kappa^{3/2}}{\sqrt{2}} \right). \end{aligned}$$

4. DISPERSION EQUATION AND NUMERICAL RESULTS

Equating to zero the denominator of the amplitudes (6), (7) yields the dispersion equation for the electromagnetic creeping waves

$$W_\mu^0 W_{\mu+1}^1 + W_\mu^1 W_{\mu+1}^0 + 2 \left(\mu + i(\kappa/2)^{3/2} \right) W_\mu^0 W_\mu^1 = 0. \quad (10)$$

Calculation of the residue shows that creeping waves attenuation is given by the exponential

$$\exp \left(-\frac{2\text{Re}(\mu)}{\rho\rho_t} s \right).$$

Comparing it to the usual creeping waves asymptotics allows the attenuation parameter to be introduced $\xi = 2^{3/2}\kappa^{-1/2}\text{Re}(\mu)$.

Solutions of this dispersion equation and the attenuation parameters ξ are presented in Table 1. We see that for large values of κ the attenuation is close to the usual attenuation of TE and TM creeping waves given by the imaginary part of the first zero of Airy function $w_1()$ for TE wave or its derivative for TM case. When the transverse curvature increases the attenuation of TE creeping

Table 1: Solution of dispersion equation and electromagnetic creeping wave attenuation.

	TE wave		TM wave		without torsion	
	μ	ξ	μ	ξ	μ	ξ
0.10	1.502-0.029 i	13.441	0.499-0.000 i	4.467	0.000-3.982 i	0.000
0.25	1.521-0.104 i	8.608	0.492-0.001 i	2.784	0.007-1.105 i	0.041
0.50	1.575-0.241 i	6.303	0.454-0.032 i	1.817	0.097-0.590 i	0.391
1.00	1.705-0.518 i	4.823	0.412-0.218 i	1.166	0.241-0.533 i	0.682
2.00	1.352-0.889 i	2.704	0.464-0.674 i	0.929	0.403-0.834 i	0.807
3.00	1.514-1.471 i	2.473	0.543-1.179 i	0.887	0.513-1.280 i	0.839
4.00	1.667-2.099 i	2.357	0.619-1.739 i	0.876	0.602-1.810 i	0.852
5.00	1.809-2.773 i	2.288	0.690-2.354 i	0.873	0.679-2.407 i	0.859
6.00	1.942-3.495 i	2.242	0.755-3.020 i	0.872	0.748-3.062 i	0.864
7.00	2.068-4.261 i	2.210	0.815-3.736 i	0.872	0.810-3.770 i	0.867
8.00	2.186-5.070 i	2.186	0.872-4.498 i	0.872	0.868-4.526 i	0.869
9.00	2.299-5.920 i	2.168	0.926-5.304 i	0.873	0.923-5.328 i	0.870
10.00	2.407-6.809 i	2.153	0.977-6.152 i	0.874	0.974-6.173 i	0.872
∞		2.025		0.882		0.882

wave also increases, but the attenuation parameter of TM creeping wave first decreases and reaches its minimum at $\kappa \approx 6$. But with further increase of transverse curvature attenuation increases again and for $\kappa < 3$ becomes greater than in the usual case of nonelongated body.

It seems that large transverse curvature decreases the attenuation, but large torsion increases it. If we neglect torsion and exclude Whittaker functions with the upper index equal to one, we get instead of (8) another equation

$$W_{\mu+1}^0 + \left(\mu + i(\kappa/2)^{3/2}\right) W_{\mu}^0 = 0.$$

Solutions of this equation and the attenuation parameters corresponding to it are presented in the last columns of Table 1. We see very low attenuated wave.

By putting $\nu = \kappa$ in formula (5) one obtains the principal order term of the asymptotic formula for the transverse magnetic field on the surface of a strongly elongated body

$$H_{\varphi} = A \left(\frac{z}{\sqrt{\rho\rho_t}}; k\rho_t \sqrt{\frac{\rho_t}{\rho}} \right) \sin \phi,$$

where

$$A(\sigma; a) = \frac{2e^{-3i\pi/4} \sqrt{a} e^{-ia\sigma/2}}{\pi \sqrt{1-\sigma^2}} \int_{-i\infty}^{+i\infty} \left(\frac{1-\sigma}{1+\sigma} \right)^{\mu} \Gamma \left(\frac{1}{2} + \mu \right) \times \frac{W_{\mu}^1(-ia)}{W_{\mu}^0(-ia)W_{\mu+1}^1(-ia) + W_{\mu+1}^0(-ia)W_{\mu}^1(-ia) + (2\mu - ia)W_{\mu}^0(-ia)W_{\mu}^1(-ia)} d\mu. \quad (11)$$

The effect of transverse curvature is characterized by the parameter $a = k\rho_t^{3/2} \rho^{-1/2}$ which is of order $O(1)$ for a strongly elongated body.

Figures show the absolute value of the transverse magnetic component on different elongated spheroids. Solid curves are computed by the method of moments by M. Duruflé (Institut de Mathématiques de Bordeaux, France), the results computed by the asymptotic formula (9) are presented in dashed lines. Oscillations of solid curves are due to the interference of right-going waves with waves that are reflected from the right end of the spheroid. These back going waves are not taken into account in the asymptotic formula.

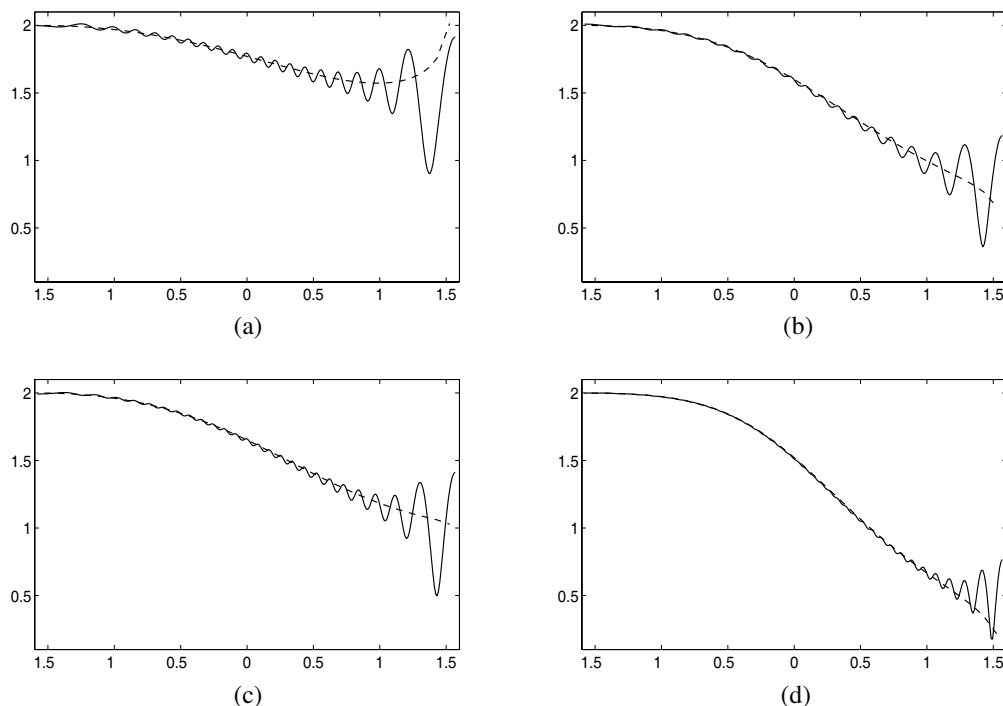


Figure 1: Magnetic field at $f = 1$ GHz on spheroids with semi-axes (a) 0.3125 m and 1.397 m, (b) 0.5 m and 1.25 m, (c) 0.5 m and 1.767 m, (d) 1.0 m and 2.5 m.

5. CONCLUDING REMARKS

The presented above asymptotic formulae were derived in the supposition that the body is strongly elongated. This allowed to exclude some terms in the equation which prevent from variables separation. If the body is not strongly elongated these terms can not be excluded and as the result separation of variables is possible only for scalar waves and in the case of electromagnetic field which does not depend on the angle φ . In that cases separation of variables leads to an equation for spheroidal functions and this equation contains the large parameter.

We see good agreement of the asymptotic formula for the transverse magnetic field with the result obtained by the method of moments.

ACKNOWLEDGMENT

The research is supported by CEA/DAM contract.

REFERENCES

1. Andronov, I. V. and D. Bouche, "Asymptotic of creeping waves on a strongly prolate body," *Ann. Télécommun.*, Vol. 49, No. 3–4, 205–210, 1994.
2. Molinet, F., I. V. Andronov, and D. Bouche, *Asymptotic and Hybrid Methods in Electromagnetics*, IEE Electromagnetic Waves, Series 51, The IEE, London, 2005.
3. Komarov, I. V., L. I. Ponomarev, and S. Y. Slavyanov, "Spheroidal and coulomb spheroidal functions," 319, Moscow, 1976 [in Russian].
4. Gradshteyn, I. S. and I. M. Ryzhik, "Tables of integrals, sums, series and infinite products," 1100, Moscow, 1963 [in Russian].

Electromagnetic Creeping Waves and Their Degeneration

I. V. Andronov¹ and D. Bouche²

¹University of St. Petersburg, Russia

²CEA-DAM-DIF, F 91297 Arpaçon, France

Abstract— In this paper, the creeping waves asymptotics is analyzed and different types of its degeneration are identified. This may be geometrical degeneration on caustics of geodesics or in focal points. The other types of degenerations are caused by the impedance that approaches to critical values. We present and compare the solutions and effects obtained in these different cases of degeneration.

1. INTRODUCTION

Creeping waves describe high frequency field on the shadowed side of a smooth convex object. It is convenient to describe creeping waves in geodesic coordinates (s, a, n) , where s denotes the arc-length measured along an arbitrary geodesics, a is the second surface coordinate orthogonal to s (the equation $a = \text{const}$ specifies the geodesics) and n is the normal to the surface. In the boundary layer near the surface the stretched normal $\nu = 2m^2n/\rho$ is used, here $m = (k\rho/2)^{1/3}$ is the asymptotic parameter, k is the wave number, ρ is the radius of curvature of the geodesics. In the general case, there are two types of electromagnetic creeping waves, one is transverse electric (TE), the other is transverse magnetic (TM). In TE wave the electric field is directed mainly along transverse (a) coordinate and in TM wave the magnetic field is directed along a coordinate. In the principal order these components of the creeping wave fields are described by formulae [1]

$$E_a, H_a = A_{E,H}(a) \exp \left(iks + i \left(\frac{k}{2} \right)^{1/3} \int_{s^\circ(a)}^s \frac{\xi_{E,H}}{\rho^{2/3}} ds \right) \frac{1}{\rho^{1/6}} \frac{1}{\sqrt{h}} \frac{1}{\sqrt{Q_{E,H}}} w_1(\xi_{E,H} - \nu). \quad (1)$$

Here $A_{E,H}$ are the amplitudes defined by the incident field, h is the divergence of the geodesics pencil on the surface, $Q_{E,H} = (w_1'(\xi_{E,H}))^2 - \xi_{E,H} w_1^2(\xi_{E,H})$ characterizes the energy flux, $w_1()$ is Airy function, $\xi_{E,H}$ are the attenuation parameters of the electric and magnetic creeping waves and are defined from the equations

$$w_1'(\xi_{E,H}) = iq_{E,H} w_1(\xi_{E,h}), \quad q_E = \frac{m}{Z}, \quad q_H = mZ, \quad (2)$$

where Z is the impedance in the boundary condition

$$\mathbf{E}_t = Z \mathbf{e}_n \times \mathbf{H}$$

specifying relation between the tangential component of electric field \mathbf{E}_t and the magnetic field \mathbf{H} on the surface.

It is worth noting that the asymptotic parameter m is retained in the dispersion Equation (2), which results in the uniformity of the asymptotic Formula (1) with respect to the value of the impedance, in particular in the case of perfectly conducting surface when $Z = 0$ the Equation (2) are reduced to

$$w_1(\xi_E) = 0, \quad w_1'(\xi_H) = 0.$$

Similar to that limiting case the Equation (2) have infinite number of solutions, that is in a general case there are infinitely many TE creeping wave and infinitely many TM creeping waves.

2. CAUSTICS OF CREEPING WAVES

Though the Formulae (1) describe the creeping waves asymptotics in the general case, there are many cases of degeneration which invalidate that asymptotics. Some of these degenerations appear due to geometrical characteristics of the surface (caustics and focal points on the surface).

In this section, we consider the case of a caustic. On the envelope, or caustic C of creeping rays, the term $h^{-1/2}$ in the asymptotics (1) for creeping wave amplitude diverges. In the vicinity of C ,

one uses coordinates (s', t, n) , where s' is the curvilinear abscissa along C , t is the geodesic distance from C (n is as previously the distance to the surface). For the magnetic creeping wave, we choose the ansatz [2]

$$H = \exp\left(iks' + k^{1/3}p(s', t)\right) \sum_{j=0}^N H_j k^{-j/3},$$

where H_j are functions of stretched variables ν and μ

$$\mu = \left(\frac{2k^2}{\rho_g}\right)^{1/3} t.$$

Here ρ_g is the radius of curvature of the caustics C in the plane tangential to the surface (it is finite because caustics is not a geodesics of the surface). Performing the analysis in the boundary layer, we get

$$H_0^t = A(s', t) v(-\mu) w_1(\xi - \nu) \quad (3)$$

and show that $p(s', t) = (p_o + p_i)/2$, where p_o and p_i are respectively the phase for the outgoing (i.e., receding from C) and the ingoing creeping waves. The caustic of creeping waves problem therefore decouples into the usual creeping wave problem, which determines the normal dependency $w_1(\xi - \nu)$ and a 2D caustic problem which determines the binormal dependency $v(-\mu)$. As for the 2D caustic problem, the amplitude $A(s', t)$ is determined by matching to the creeping waves solution.

3. FOCAL POINT

Another case of geometrical factors degeneration may be observed for on axis illumination of an axisymmetric object [3]. In this case, a focal point of creeping waves appears. It is convenient to introduce polar geodesic coordinate system (l, φ, n) , l geodesic distance from focal point, φ polar angle, n is the normal. If the incident creeping wave is given by the Formula (1) with $h \approx l$, the binormal component of the creeping wave field H_φ (or E_φ) in a vicinity of the focal point is given by the formula

$$H_\varphi \approx e^{-i\pi/4} \sqrt{2\pi k} A J_1'(kl) w_1(\xi - \nu). \quad (4)$$

The amplitude is found by matching to the creeping waves solution. We see the effect of field amplification by the factor \sqrt{k} .

4. DEGENERATION DUE TO THE IMPEDANCE

Other types of degeneration may be caused by the impedance that characterizes the surface. The case when the attenuation parameters of two creeping waves of one polarization coincide is studied in [4]. This happens when q_E or q_H approach to one of critical values given by the equation

$$w_1'(-q^2) = iq w_1(-q^2).$$

First three solutions are $q_1 = 0.571998 - 1.6340228i$, $q_2 = 0.853350 - 1.9610989i$, $q_3 = 1.038404 - 2.2021337i$. For that values of q the Equation (2) has double solution $\xi = -q_\ell^2$ and the term $Q^{-1/2}$ in the asymptotics (1) corresponding to two creeping waves with such attenuation parameter diverges. The behaviour of attenuation parameters in a vicinity of their critical values is presented on Figure 1.

A special resonant solution is derived in a boundary layer of length $k^{-2/9}$ where the fields of two creeping waves can not be distinguished [4]

$$U = \exp\left(iks + i\left(\frac{k}{2}\right)^{1/3} \frac{-q_\ell^2}{\rho_0^{2/3}} (s - s_0)\right) (\alpha W_1(\sigma) + \beta W_2(\sigma)), \quad (5)$$

$$\sigma = k^{2/3} \left(\frac{-2^{1/3} i q_\ell}{\rho_0^{4/3}} \left(\frac{Z'_0}{Z_0} + \frac{1}{3} \frac{\rho'_0}{\rho_0}\right)\right)^{1/3} (s - s_0).$$

Here U stands for the tangential component of the electric field if two TE waves degenerate, or for the tangential component of magnetic field in the case of TM waves degeneration, the lower index zero denotes that the values are taken in the point of degeneration and prime stands for

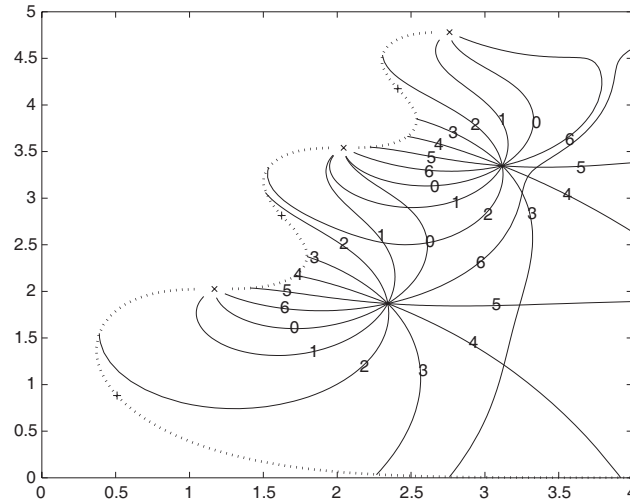


Figure 1: Curves $\xi(q_\ell + e^{i2\pi j/7}\mathbb{R}_+)$ on the complex plane (curves are marked with the index j). Dotted line separates impedances corresponding to absorbing surfaces from those of radiating surfaces. Zeros of w_1 are denoted by symbols \times and zeros of w'_1 by plusses (+).

the derivative by s . The functions W_1 and W_2 are the Airy functions that are defined by their asymptotics

$$W_{1,2}(\sigma) \sim \sigma^{-1/4} \exp\left(\pm \frac{2}{3}\sigma^{3/2}\right), \quad s - s_0 \rightarrow -\infty.$$

The sign plus in the exponential is taken for W_1 and minus for W_2 . The functions W_1 and W_2 can be expressed via w_1 and w_2 , but as σ can be arbitrary complex there are too many subcases and we do not present these formulae.

The solution (5) is matched to the usual creeping waves asymptotics which defines the values of the coefficients α and β and allows to describe the effect of creeping wave passing through the line of degeneration. If the attenuation parameter of the incident creeping wave has the asymptotics $\xi(q_\ell + \delta) \sim -q_\ell^2 + \sqrt{2i\delta}$, $\delta \rightarrow 0$, then

$$\alpha = ae^{-i\pi/6}, \quad \beta = 0,$$

$$a = \frac{k^{1/18} A_0}{2^{2/9} \rho_0^{5/18} (q'(s_0))^{1/6} w_1(-q_\ell^2)} \exp\left(i \left(\frac{k}{2}\right)^{1/3} \int_{s_0}^{s_0} \frac{\xi ds}{\rho^{2/3}}\right).$$

If the attenuation parameter of the incident creeping wave has the asymptotics $\xi(q_\ell + \delta) \sim -q_\ell^2 - \sqrt{2i\delta}$, $\delta \rightarrow 0$, then

$$\alpha = 0, \quad \beta = ae^{i\pi/3}.$$

We see some similarity with the case of a caustic. However the amplification is of order $O(k^{1/18})$. After passing the domain of degeneration the asymptotics (5) matches to one or two creeping waves. The effect is as follows, the incident creeping wave with lower attenuation produces two creeping waves after passing the degeneration point, while the incident creeping wave with higher attenuation transforms to the creeping wave with lower attenuation.

5. INTERACTION OF CREEPING WAVES

Another case of degeneration caused by the impedance is the case of $Z = 1$. In this case, all the creeping waves of one type coincide with the corresponding creeping waves of the other type. This case was partly studied in [5]. In more details the asymptotic analysis of this case will be presented at this Symposium [6]. Therefore we do not present the formulae here. Though no difficulties are seen in the asymptotics (1) in that case, one can discover that if the geodesics have torsion, no next order terms exist. That is the degeneration takes place at the first order correction to (1). The zone of degeneration is of the length of order $O(k^{-1/6})$. In that zone, the effect of torsion appears more significant than in the usual nondegenerated case.

Table 1: Effects of degeneration.

type of degeneration	caustics	focal point	$Q = 0$	$Z = 1$
diverging term in (1)	$h^{-1/2}$	$h^{-1/2}$	$Q^{-1/2}$	next order term
size of the domain	$k^{-2/3}$	k^{-1}	$k^{-2/9}$	$k^{-1/6}$
asymptotic parameter	$k^{-1/3}$	$k^{-1/3}$	$k^{-1/9}$	$k^{-1/6}$
amplification	$k^{1/6}$	$k^{1/2}$	$k^{1/18}$	no
number of degenerating waves	all	all	2	all
interaction of waves	no	no	2 waves	all waves in pairs
dimension of the problem	3D	3D axisymmetric	2D	3D
influence of torsion	no	—	no	crucial

6. CONCLUSION, COMPARISON OF THE EFFECTS

Analysis of the asymptotics derived for the above cases of degeneration allows to identify similarity and the difference in the electromagnetic effects that take place in the domains of degeneration where the usual asymptotics of creeping waves fail. The summary of the effects is presented in Table 1.

REFERENCES

1. Molinet, F., I. Andronov, and D. Bouche, “Asymptotic and hybrid methods in electromagnetics,” *IEE Electromagnetic waves series 51*, London, 2005.
2. Bouche, D., *J. Acoust.*, Vol. 5, 507, 1992.
3. Bouche, D., “Champ à la surface d’un objet axisymétrique conducteur au voisinage d’un point focal de rayons rampants,” *Ann. Télécommun.*, Vol. 47, No. 9–10, 413–420, 1992.
4. Andronov, I. V. and D. P. Bouche, “Degeneration of electromagnetic creeping waves in a vicinity of critical values of anisotropic impedance,” *IEEE Transactions on Antennas and Propagation*, Vol. 56, No. 7, 1984–1992, 2008.
5. Andronov, I. V. and D. P. Bouche, “Asymptotics of creeping waves in a degenerated case of matrix impedance,” *Progress In Electromagnetics Research*, PIER 59, 215–230, 2006.
6. Zaika, D. Y., I. V. Andronov, and M. V. Perel, “The interaction of creeping waves on a smooth anisotropic impedance surface,” *26th PIERS Abstracts*, Moscow, August 15–19, 2009.

The Interaction of Creeping Waves on a Smooth Anisotropic Impedance Surface

D. Yu. Zaika¹, M. V. Perel^{1,2}, and I. V. Andronov¹

¹St. Petersburg University, Russia

²Ioffe Institute, Russia

Abstract— Creeping waves on an anisotropic impedance surface are studied. The zone with impedance degeneration is identified. In this zone, a singularity in the first order correction of the creeping waves asymptotics appears. A special resonant asymptotics is constructed and matched to creeping waves outside the zone of degeneration. The effect of TM mode generation by an incident TE creeping wave is discovered and analysed.

1. INTRODUCTION

Analysis of the creeping waves field is important for antenna coupling and other applications. Creeping waves can be conveniently presented in surface geodesic coordinate system (s, a, n) , where s is the arc-length measured along the geodesics in the family, a is the second surface coordinate orthogonal to s and n is the normal to the surface. The asymptotic decomposition for the field of a creeping wave have the following form [1]

$$\exp\left(iks + ik^{1/3}p(s, a)\right) \sum_{j=0}^{\infty} U_j\left(s, a, k^{2/3}n\right) k^{-j/3}. \quad (1)$$

By simple manipulation with Maxwell equations it is possible to reduce the problem for the creeping waves computation to the analysis of only two components of electromagnetic vectors, usually transverse electric E^a and transverse magnetic H^a components. On an impedance surface with the boundary condition

$$E_t = \begin{pmatrix} Z_1 & 0 \\ 0 & Z_2 \end{pmatrix} e_n \times H$$

there exist two infinite series of creeping waves. The creeping waves of TM type have $E_0^a = 0$ and creeping waves of TE type have $H_0^a = 0$. The attenuation of creeping waves is described by the function $p(s, a)$ in the exponential factor,

$$p = \frac{1}{2^{1/3}} \int_{s_0(a)}^s \frac{\xi(s, a)}{\rho^{2/3}(s, a)} ds,$$

where ρ is the radius of curvature of the geodesics, $s_0(a)$ is defined by the variant of the excitation and ξ is the attenuation parameter defined from the equation

$$\dot{w}_1(\xi) = iq w_1(\xi),$$

with $q = (k\rho/2)^{1/3}Z_2$ for TM waves and $q = (k\rho/2)^{1/3}/Z_1$ for TE waves.

On a general surface, the system of geodesics has caustics with several cusp points or focuses. In a vicinity of such singularities, the asymptotic expansion (1) can not be used and other special ansatz should be introduced. Other domains where (1) is not valid appear due to the impedance matrix degenerations [2, 3]. One of such degenerations is studied in this paper.

Suppose that at some line \mathcal{L} the impedances $1/Z_1$ and Z_2 coincide. Then the attenuation parameters of TE creeping waves and of TM creeping waves coincide on \mathcal{L} . As it is shown in [2] and will be shown below, on a surface with nonzero torsion τ , this causes divergence of the first order correction U_1 and spoils the asymptotic expansion.

The paper is organized as follows, first we briefly derive the creeping wave asymptotics in the domain where $1/Z_1$ and Z_2 are significantly different. We present the principal order term and the diverging part of the first order correction. Analysis of the asymptotic procedure allows

the structure of the diverging component to be found and by this to determine the width of the resonant domain near the line \mathcal{L} where the decomposition (1) loses its asymptotic character. Then we introduce stretched coordinate and using the technique of [4–6] derive resonant solution. Finally, by matching this resonant solution to the creeping waves asymptotics outside the resonant domain we study the effect of creeping wave incidence on the line \mathcal{L} .

2. ADIABATIC APPROXIMATION

Introduce two-component vector $\Psi = (\Psi_1, \Psi_2)^T$, such that

$$hE^a = \exp\{iks\} \left(\Psi_1 + O\left(\varepsilon^{2/3}\right) \right), \quad hH^a = \exp\{iks\} \left(\Psi_2 + O\left(\varepsilon^{2/3}\right) \right),$$

where $h = h(s, a)$ is the divergence of the geodesics on the surface of the body. The Maxwell equations in coordinates (s, a, ℓ) , $\ell = k^{2/3}n$ can be rewritten in the matrix form sorted by increasing orders of small parameter $\varepsilon = k^{-1}$

$$\left[\mathbf{L} + i\varepsilon^{1/3}\mathbf{H} + \dots \right] \Psi = -i\varepsilon^{1/3} \frac{\partial \Psi}{\partial s}, \quad \varepsilon \ll 1. \quad (2)$$

Boundary conditions read

$$\mathbf{B}\Psi = \varepsilon^{2/3}\mathbf{J} \frac{\partial \Psi}{\partial a} + \dots, \quad \ell = 0, \quad (3)$$

where

$$\begin{aligned} \mathbf{L} &= \frac{1}{2} \frac{\partial^2}{\partial \ell^2} + \frac{1}{\rho} \ell, & \mathbf{H} &= \begin{pmatrix} h'_s/2h & -\tau \\ \tau & h'_s/2h \end{pmatrix}, \\ \mathbf{B} &= \frac{\partial}{\partial \ell} + i\mathbf{Z}, & \mathbf{Z} &= \begin{pmatrix} 1/Z_1 & 0 \\ 0 & Z_2 \end{pmatrix}, & \mathbf{J} &= \begin{pmatrix} 0 & 1/h \\ -1/h & 0 \end{pmatrix}. \end{aligned}$$

We seek the solution in the form

$$\Psi = \exp\left\{ ik^{1/3}p(s, a) \right\} \Phi(s, a, \ell), \quad \Phi = \sum_{k=0}^{\infty} \varepsilon^{k/3} \Phi^{(k)}. \quad (4)$$

By standard asymptotic technique, we get a recurrent system of boundary-value problems which allows the components of the series (4) to be determined. For the components $\Phi_1^{(k)}$, $\Phi_2^{(k)}$, we have

$$\begin{aligned} \left(\frac{\partial^2}{\partial \nu^2} + \nu - \xi \right) \Phi_1^{(k)} &= F_1^{(k)}(\nu), & \left(\frac{\partial^2}{\partial \nu^2} + \nu - \xi \right) \Phi_2^{(k)} &= F_2^{(k)}(\nu), \\ \left(\frac{\partial}{\partial \nu} + iq_1 \right) \Phi_1^{(k)} &= G_1^{(k)}, \quad \nu = 0, & \left(\frac{\partial}{\partial \nu} + iq_2 \right) \Phi_2^{(k)} &= G_2^{(k)}, \quad \nu = 0. \end{aligned} \quad (5)$$

We introduced here the notations: $\xi = 2^{1/3}\rho^{2/3}\partial p/\partial s$, $\nu = (2/\rho)^{1/3}\ell$, $q_1 = (\rho/2)^{1/3}(1/Z_1)$, and $q_2 = (\rho/2)^{1/3}Z_2$. We assume that $1/Z_1 \neq Z_2$, then $q_1 \neq q_2$.

The problems for the leading terms are homogeneous, $F_j^{(0)}(\nu) = 0$, $G_j^{(0)} = 0$, $j = 1, 2$. Thus we have two independent problems for the Airy equation, radiation and the boundary conditions. For TE creeping waves, we find

$$\Phi_1^{(0)} = A_1^{(0)}(s, a)w_1(\xi - \nu), \quad \Phi_2^{(0)} = 0.$$

where the eigenvalue $\xi = \xi_E$ is one of the roots of the equation $\dot{w}_1(\xi_E) = iq_1w_1(\xi_E)$. We assume that ξ_E is not an eigenvalue of the second problem. The amplitude $A_0(s, a)$ can be found when considering the next order problems.

The first order corrections $\Phi_1^{(1)}$, $\Phi_2^{(1)}$ satisfy Equation (5) with the right-hand sides

$$\begin{aligned} F_1^{(1)}(\nu) &= -i2^{1/3}\rho^{2/3} \left[w_1(\xi_E - \nu) \frac{\partial A_1^{(0)}}{\partial s} + w_1(\xi_E - \nu) \left(\ln \sqrt{h} \right)'_s A_1^{(0)} + \frac{\partial w_1(\xi_E - \nu)}{\partial s} A_1^{(0)} \right], \quad G_1^{(1)} = 0, \\ F_2^{(1)}(\nu) &= -i2^{1/3}\rho^{2/3}\tau w_1(\xi_E - \nu)A_1^{(0)}, \quad G_2^{(1)} = -i(\rho/2)^{1/3}(1/h)p'_a w_1(\xi_E)A_1^{(0)}. \end{aligned}$$

The problem for $\Phi_1^{(1)}$ is solvable if the condition

$$\frac{\partial A_1^{(0)}}{\partial s} + \left(\frac{\partial}{\partial s} \ln \left(\sqrt{\xi_E + q_1^2} w_1(\xi_E) \rho^{1/6} \sqrt{h} \right) \right) A_1^{(0)} = 0$$

is satisfied. This condition yields

$$A_1^{(0)}(s, a) = C(a) \frac{\rho^{-1/6}}{\sqrt{\xi_E + q_1^2}} \frac{1}{w_1(\xi_E)} \frac{1}{\sqrt{h}}.$$

Now we can obtain the leading order of the expansion:

$$\Psi_{\text{TE}} = C(a) \frac{\rho^{-1/6}}{\sqrt{\xi_E + q_1^2}} \frac{w_1(\xi_E - \nu)}{w_1(\xi_E)} \frac{1}{\sqrt{h}} \exp \left\{ ik^{1/3} p_E(s, a) \right\} \begin{pmatrix} 1 \\ 0 \end{pmatrix} + O(\varepsilon^{1/3}), \quad (6)$$

$$p_E(s, a) = \int_{s(a)}^s \frac{\xi_E}{2^{1/3} \rho^{2/3}} dt. \quad (7)$$

Here, we introduce the subscript TE to distinguish modes with different polarizations. Similarly, if we choose $\xi = \xi_H$, which is the root of equation $\dot{w}_1(\xi) = iq_2 w_1(\xi)$, we obtain solution of another polarization:

$$\Psi_{\text{TM}} = C(a) \frac{\rho^{-1/6}}{\sqrt{\xi_H + q_2^2}} \frac{w_1(\xi_H - \nu)}{w_1(\xi_H)} \frac{1}{\sqrt{h}} \exp \left\{ ik^{1/3} p_H(s, a) \right\} \begin{pmatrix} 0 \\ 1 \end{pmatrix} + O(\varepsilon^{1/3}), \quad (8)$$

$$p_H(s, a) = \int_{s(a)}^s \frac{\xi_H}{2^{1/3} \rho^{2/3}} dt. \quad (9)$$

We continue resolving the recurrent system. The solution of the problem for $\Phi_2^{(1)}$ is not unique. It contains solution of the homogeneous Airy equation $w_1(\xi - \nu)$ with an arbitrary at this step amplitude $A_1^{(1)}$

$$\Phi_1^{(1)} = A_1^{(1)}(s, a) w_1(\xi_E - \nu) + \tilde{\Phi}_1^{(1)}(s, a, \nu).$$

The component $\Phi_2^{(1)}$ is defined uniquely. Separating the term with a singularity at $q_1 = q_2$, we have

$$\Phi_2^{(1)} = A_2^{(1)}(s, a) w_1(\xi_E - \nu) + \tilde{\Phi}_2^{(1)}(s, a, \nu),$$

$$A_2^{(1)}(s, a) = \frac{1}{q_2 - q_1} \left(-i2^{1/3} \rho^{2/3} (\xi_E + q_1^2) \right) T A_1^{(0)}, \quad T(s, a) = \tau + \frac{1/h}{2^{2/3} \rho^{1/3}} \frac{1}{\xi_E + q_1^2} (p_E)'_a.$$

3. SOLUTION ON THE BOUNDARY OF THE ADIABATIC ZONE

Let the condition $q_1 = q_2 = q^0$ be satisfied on the curve $s = s^0(a)$. One can check that the singularities in the higher-order terms for Φ_2 are accumulated in the following function

$$\Phi_2 = \sum_{m=1}^{\infty} \varepsilon^{m/3} \left[\frac{d_m(s, a)}{(q_2 - q_1)^{2m-1}} w_1(\xi_E - \nu) + \dots \right],$$

$$d_m = -A_1^{(0)} T \left(-i2^{1/3} \rho^{2/3} (\xi_E + q_1^2) \right)^m (-1)^m (2m-3)!! (q_2' - q_1')^{m-1}.$$

Hence the series loses its asymptotic character if $|s - s^0(a)| \ll \varepsilon^{1/6}$. The width of the zone where the adiabatic solution is not applicable is of the order $\varepsilon^{1/6}$. This suggests to introduce a stretched coordinate $\sigma = \varepsilon^{-1/6} (s - s^0(a))$.

For further matching, it is useful to find the solution on the boundary of the adiabatic zone. By using the Taylor expansion, we get

$$\Psi_{\text{TE}}(s^0 + \varepsilon^{1/6} \sigma, a, \ell) = \exp \left\{ ik^{1/3} p_E^0 + ik^{1/6} (p_E)'_s \sigma + i(p_E)''_{ss} \sigma^2 / 2 \right\} \times \left[\left(A_1^{(0)} \right)^0 w_1(\xi^0 - \nu^0) \begin{pmatrix} 1 \\ 0 \end{pmatrix} \right. \\ \left. + \varepsilon^{1/6} \left(T^0 \left(A_1^{(0)} \right)^0 \dots S w_1(\xi^0 - \nu^0) \right) \right] + O(\varepsilon^{1/3}), \quad (10)$$

where we use the notation $f^0(a) = f(s^0(a), a)$ for any f ,

$$S = \frac{1}{2\alpha\sigma} \sum_{m=1}^{\infty} \frac{(2m-1)!!}{(-2\alpha\sigma^2)^m}, \quad \alpha = \frac{1}{2} ((p_H)_{ss}^0 - (p_E)_{ss}^0). \quad (11)$$

We use denote by dots in (10), the terms that do not influence the result of matching with resonant solution in the leading order term.

4. RESONANT EXPANSION

In a vicinity of the curve $s = s^0(a)$, we introduce scaled coordinate σ and represent the operators of the problem (2) by Taylor series in powers of σ :

$$\begin{aligned} \mathbf{L} &= \mathbf{L}^0 + \varepsilon^{1/6} \mathbf{L}^{(1)} \sigma + \varepsilon^{2/6} \mathbf{L}^{(2)} \sigma^2 / 2 + \dots, & \mathbf{H} &= \mathbf{H}^0 + \dots \\ \mathbf{B} &= \mathbf{B}^0 + \varepsilon^{1/6} \mathbf{B}^{(1)} \sigma + \varepsilon^{2/6} \mathbf{B}^{(2)} \sigma^2 / 2 + \dots, & \mathbf{J} &= \mathbf{J}^0 + \dots \end{aligned}$$

We search the asymptotic expansion of the solution as

$$\psi = \exp \left\{ ik^{1/3} p_E^0 + ik^{1/6} (p_E)_s^0 \sigma + i(p_E)_{ss}^0 \sigma^2 / 2 \right\} \phi(\sigma, a, \ell). \quad (12)$$

Then the system (2) and boundary condition (3) read:

$$\begin{aligned} (\mathbf{L}^0 - (p_E)_s^0) \phi &= -\varepsilon^{1/6} \left[i \frac{\partial}{\partial \sigma} + (\mathbf{L}^{(1)} - (p_E)_{ss}^0) \sigma \right] \phi - \varepsilon^{2/6} \left[i \mathbf{H}^0 + \mathbf{L}^{(2)} \sigma^2 / 2 \right] \phi + \dots, \\ \mathbf{B}^0 \phi &= -\varepsilon^{1/6} \mathbf{B}^{(1)} \sigma \phi + \varepsilon^{2/6} \left[-\mathbf{B}^{(2)} \sigma^2 / 2 + i(p_E)_a^0 \mathbf{J}^0 \right] \phi + \dots, \quad \ell = 0. \end{aligned}$$

We substitute the series $\phi = \sum_{k=0}^{\infty} \varepsilon^{k/6} \phi^{(k)}$ in the equations and boundary conditions and obtain a recurrent system. The equations of each approximation split into two problems (5). A special feature of that problems is that $q_1 = q_2$. Eigenvalues of both problems coincide. At the leading order, both problems are homogeneous and have nontrivial solutions. Without loss of generality we restrict our derivations to the case of the following solution

$$\phi_1^{(0)} = a_1^{(0)}(\sigma, a) w_1(\xi^0 - \nu), \quad \phi_2^{(0)} = 0.$$

The condition of the solvability of the next order approximation is satisfied automatically if $a_1^{(0)}$ does not depend on σ . The first order correction has the form

$$\phi_1^{(1)} = a_1^{(1)}(\sigma, a) w_1(\xi^0 - \nu) + \tilde{\Phi}_1^{(1)}, \quad \phi_2^{(1)} = a_2^{(1)}(\sigma, a) w_1(\xi^0 - \nu).$$

Here $\tilde{\Phi}_1^{(1)}$ is known, $a_1(\sigma, a)$, $d_1(\sigma, a)$ will be found from the condition of solvability of the next order approximation. The equation for d_1 takes the form

$$\frac{\partial a_2^{(1)}}{\partial \sigma} - 2i\alpha\sigma a_2^{(1)} = -T^0 a_1^{(0)}.$$

Its solution can be expressed in terms of the probability integral:

$$a_2^{(1)}(\sigma, a) = -T^0 a_1^{(0)} e^{i\alpha\sigma^2} \int_0^{\sigma} e^{-iat^2} dt + a_2^{(1)}(0, a) e^{i\alpha\sigma^2},$$

where $a_2^{(1)}(0, a)$ will be found by matching with adiabatic expansion, α and T are defined in (11).

5. MATCHING OF THE INNER AND OUTER EXPANSIONS

We have found that the resonant expansion is determined by the formula (12), where ϕ reads

$$\phi(\sigma, a, \ell) = a_1^{(0)} w_1(\xi^0 - \nu^0) \begin{pmatrix} 1 \\ 0 \end{pmatrix} + \varepsilon^{1/6} \begin{pmatrix} a_1^{(1)}(\sigma, a) w_1(\xi^0 - \nu) + \tilde{\Phi}_1^{(1)} \\ a_2^{(1)}(\sigma, a) w_1(\xi^0 - \nu) \end{pmatrix} + O(\varepsilon^{1/3}).$$

The outer expansion has been found as follows

$$\Phi(s^0 + \varepsilon^{1/6}\sigma, a, \ell) = (A_1^{(0)})^0 w_1(\xi^0 - \nu^0) \begin{pmatrix} 1 \\ 0 \end{pmatrix} + \varepsilon^{1/6} \left(T^0 (A_1^{(0)})^0 \overset{\dots}{S} w_1(\xi^0 - \nu^0) \right) + O(\varepsilon^{1/3}).$$

One can check that the adiabatic and resonant zones have an intersection. We match solutions in this common areas and establish that a new mode is born there. The most important for the description of the new mode is matching $a_2^{(1)}$ and $T^0(A_1^{(0)})^0 S$. The appearance of the new mode is governed by the Stokes phenomenon for the probability integral. The asymptotics of this integral at large negative and large positive σ is different. Under the assumption that $\arg \alpha \in [-\pi/2, \pi/2)$ it contains one term at negative σ and two terms at positive σ . One term is matched to the incoming from minus infinity mode and defines $a_1^{(0)} = (A_1^{(0)})^0$, two terms are matched to the same mode and a newborn mode which appears in the approximation of order $\varepsilon^{1/6}$. Then the effect of creeping wave passing through the resonant zone up to the order of $\varepsilon^{1/3}$ can be described as follows

$$\begin{aligned} \psi &\rightarrow \Psi_{\text{TE}}, \quad \sigma \rightarrow -\infty, \\ \psi &\rightarrow \Psi_{\text{TE}} - \varepsilon^{1/6} T^0 \sqrt{\frac{2\pi}{((p_H)_{ss}^0 - (p_E)_{ss}^0)}} \exp\left\{ ik^{1/3} (p_E^0 - p_H^0) \right\} \Psi_{\text{TM}}, \quad \sigma \rightarrow +\infty. \end{aligned}$$

6. CONCLUSIONS

We have considered the propagation of the electromagnetic creeping waves on a convex anisotropic impedance surface. We are interested in a special case of the dependence of impedance along the path of mode propagation. The propagation parameters of each pair of creeping waves with different polarizations as functions of the distance along the path have a point of intersection. This point which is called the degeneracy point is responsible for modes interaction. We assume that one TE mode approaches the point of the degeneration and have found that adiabatic approach fails near this point because all the higher-order terms have singular terms near it. We have analyzed the singularity, introduced a new stretched coordinate near it. We have constructed the resonant asymptotics near this point and have found that the probability integral describes the modes interaction. We have established that TM modes appears as the result of degeneration in the $\varepsilon^{1/6}$ order of approximation and we have found the excitation factor.

REFERENCES

1. Molinet, F., I. Andronov, and D. Bouche, "Asymptotic and hybrid methods in electromagnetics," *IEE Electromagnetic Waves Series*, London, 2005.
2. Andronov, I. V. and D. Bouche, "Asymptotics of creeping waves in a degenerated case of matrix impedance," *Progress In Electromagnetics Research*, PIER 59, 215–230, 2006.
3. Andronov, I. V. and D. Bouche, "On the degeneration of creeping waves in a vicinity of critical values of the impedance," *Wave Motion*, Vol. 45, 400–411, 2008.
4. Perel, M. V., J. D. Kaplunov, and G. A. Rogerson, "An asymptotic theory for internal reflection in weakly inhomogeneous elastic waveguides," *Wave Motion*, Vol. 41, 95–108, 2005.
5. Perel, M. V., I. V. Fialkovsky, and A. P. Kiselev, "Resonance interaction of bending and shear modes in a nonuniform Timoshenko beam," *Journal of Mathematical Sciences*, Vol. 111, 3775–3790, 2002.
6. Perel, M. V., "Overexcitation of modes in an anisotropic earth-ionosphere waveguide on transequatorial paths in the presence of two close degeneracy points," *Izvestiya Vysshikh Uchebnykh Zavedenii, Radiofizika*, Vol. 33, No. 11, 1208–1216, 1990.

“Complex Source”: Singularities in Real Space

A. M. Tagirdzhanov¹, A. S. Blagovestchenskii¹, and A. P. Kiselev²

¹Physical Faculty, St. Petersburg State University, Russia

²St. Petersburg Department, Steklov Mathematical Institute, Russia

Abstract— We consider the complexified Green function for the 3D Helmholtz operator, introduced by Izmet’shev and Deschamps as an exact solution showing asymptotically the Gaussian-beam paraxial behavior. We perform an accurate calculation showing that the aforementioned complexified solution satisfies a certain inhomogeneous Helmholtz equation, with the source localized on a 2D surface that depends on definition of a branch cut in the complexified distance. The matter is that the square root has a jump at a branch cut. We discuss several choices of branch cuts and describe the corresponding field sources.

1. INTRODUCTION

The complexified Green function for the 3D Helmholtz operator

$$\Delta + k^2 = \partial^2/\partial x^2 + \partial^2/\partial y^2 + \partial^2/\partial z^2 + k^2$$

in free space is

$$G_* = \exp(ikR_*)/R_*. \quad (1)$$

Here,

$$R_* = \sqrt{\rho^2 + (z - ia)^2}, \quad \rho = \sqrt{x^2 + y^2}, \quad (2)$$

with $a > 0$ a free constant, is a complexified distance. The function (1) was introduced in [1, 2] as an exact solution of the Helmholtz equation showing a Gaussian beam behavior [3] near the z -axis and is referred to as “Gaussian beam beyond paraxial approximation” or “complex source function”. However, researchers mainly fail to notice that the homogeneous Helmholtz equation $(\Delta + k^2)G_* = 0$ is never satisfied in the full 3D space because of jumps of G_* due to branching of R_* , and the true equation has thus the form

$$(\Delta + k^2)G_* = F \quad (3)$$

with the field source F being a generalized function. Kaiser [4, 5] recently discussed the right hand side of (3) in complex space. It was mentioned in [5] that the generalized function F , whose support is a 2D manifold with boundary, is non-zero in real 3D space. The boundary is the same for all the branch cuts: it is a circle

$$\mathcal{C} = \{z = 0, \rho = a\}. \quad (4)$$

Here, we perform an accurate calculation showing that the correct equation in real space has the same form, with F being a generalized function dependent on the exact definition of the square root. The matter is that the root in (2) has jumps at branch cuts. We discuss here two choices of branch cuts and describe the corresponding generalized functions F . The calculation is based on standard techniques of generalized functions [7].

2. CHOICE OF THE BRANCH CUT ALONG THE POSITIVE REAL AXIS

Define the complex plane of the radicand in (2) as

$$s = \rho^2 + z^2 - a^2 - 2iaz. \quad (5)$$

To make R_* single-valued, choose now the cut

$$\{\Re s \geq 0, \Im s = 0\} \quad (6)$$

and let R_* be real and positive on the lower side of the cut (6). Evidently, R_* takes different values on the sides of the branch cut, and $R_* \rightarrow \pm\sqrt{\rho^2 - a^2}$ as $z \rightarrow \pm 0$. Therefore, G_* has a jump on

$$\mathcal{S} = \{\rho \geq a, z = 0\}$$

and thus \mathcal{S} is the support of F (i.e., $F \equiv 0$ outside of \mathcal{S}). In the simple case of $\rho > a$, an elementary calculation shows that

$$F = (\Delta + k^2)G_* = [G_*]_{z=0} \delta'(z) + \left[\frac{\partial G_*}{\partial z} \right]_{z=0} \delta(z), \quad \rho > a, \tag{7}$$

where $[G_*]_{z=0} = G_*|_{z \rightarrow +0} - G_*|_{z \rightarrow -0}$ is a jump of G_* on \mathcal{S} and

$$[G_*]_{z=0} = 2 \frac{\cos k\sqrt{\rho^2 - a^2}}{\sqrt{\rho^2 - a^2}}, \quad \left[\frac{\partial G_*}{\partial z} \right]_{z=0} = 2ika \frac{\sin k\sqrt{\rho^2 - a^2}}{\rho^2 - a^2} + 2ia \frac{\cos k\sqrt{\rho^2 - a^2}}{(\rho^2 - a^2)^{\frac{3}{2}}}.$$

As seen, the above description of F fails as $\rho \rightarrow a$. We present the result for $\rho \geq 0$. A more sophisticated calculation provides the following definition of the generalized function F via its action on an arbitrary smooth test function $f = f(\rho, z, \varphi)$ [7]

$$(F, f) = \int_a^\infty \int_0^{2\pi} \rho d\rho d\varphi \left(2ika \frac{\sin k\sqrt{\rho^2 - a^2}}{\rho^2 - a^2} f(\rho, 0, \varphi) - 2 \frac{\cos(k\sqrt{\rho^2 - a^2})}{\sqrt{\rho^2 - a^2}} \frac{\partial f}{\partial z}(\rho, 0, \varphi) \right) + 2ai \int_a^\infty \int_0^{2\pi} \rho d\rho d\varphi \frac{(f(\rho, 0, \varphi) \cos k\sqrt{\rho^2 - a^2} - f(a, 0, \varphi))}{(\rho^2 - a^2)^{\frac{3}{2}}},$$

where φ is the polar angle. It can be seen that, for $\rho > a$, the above expression reduces to (7).

Consider now the behavior of the wavefield generated by the above source F in the paraxial area, where $\rho \ll |z - ia|$, $k\rho^4 \ll |z - ia|^3$. We easily obtain the asymptotic expression

$$G_* \approx \frac{\exp ik(z - ia)}{z - ia} \exp\left(\frac{ikz\rho^2}{2(z^2 + a^2)}\right) \exp\left(-\frac{ka\rho^2}{2(z^2 + a^2)}\right), \tag{8}$$

which describes a wave beam propagating in the direction of the z -axis¹. This differs from the standard expression for the Gaussian beam [3, 6] by the factor $\exp(ka)$. We observe that the Gaussian beam is not a solution of the wave equation in the source free space, but is generated by the field source F described above.

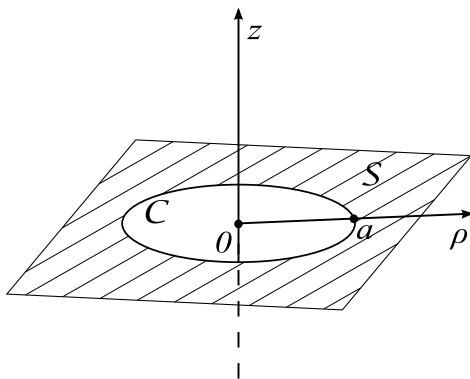


Figure 1: The support of F for the branch cut chosen in accordance with (6).

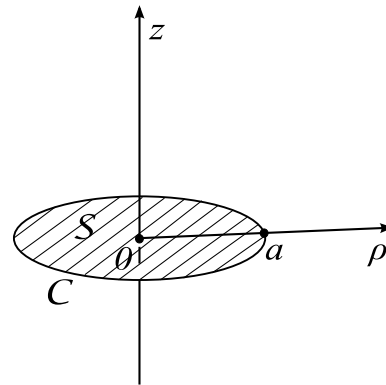


Figure 2: The support of F for the branch cut chosen in accordance with (9).

3. ANOTHER CHOICE OF THE BRANCH CUT

Now we consider another choice of the branch cut. We fix R_* real and positive on $\{\Re s > 0, \Im s = 0\}$ and choose the branch cut to be

$$\{\Re s \leq 0, \Im s = 0\}. \tag{9}$$

¹We understand the time-dependence of the form $\exp(-i\omega t)$

On the lower side of the branch cut (9), $\Im R_* > 0$. Then we obtain F in (3) with a support

$$\mathcal{S} = \{\rho \leq a, z = 0\}.$$

Calculation now provides the following description of the generalized function F

$$\begin{aligned} (F, f) = & \int_0^a \int_0^{2\pi} \rho d\rho d\varphi \left(2ika \frac{\sin k\sqrt{\rho^2 - a^2}}{\rho^2 - a^2} f(\rho, 0, \varphi) - 2 \frac{\cos(k\sqrt{\rho^2 - a^2})}{\sqrt{\rho^2 - a^2}} \frac{\partial f}{\partial z}(\rho, 0, \varphi) \right) \\ & + 2ai \int_0^a \int_0^{2\pi} \rho d\rho d\varphi \frac{\left(f(\rho, 0, \varphi) \cos k\sqrt{\rho^2 - a^2} - f(a, 0, \varphi) \right)}{(\rho^2 - a^2)^{\frac{3}{2}}}. \end{aligned} \quad (10)$$

In this case, analysis shows that the paraxial asymptotic wavefield is strongly different from (8) and is emitted from the field source in both directions $\pm z$.

4. CONCLUSION

We are planning to discuss elsewhere some other choices of the square root in (1) and to describe the arising field sources and the corresponding wavefields for the Helmholtz equation and also for the wave equation in 2D and 3D.

REFERENCES

1. Izmet'sev, A. A., "One parameter wave beams in free space," *Radiophys. Quant. Electron.*, Vol. 13, No. 9, 1062–1068, 1970.
2. Deschamps, G. A., "Gaussian beam as a bundle of complex rays," *Electron. Lett.*, Vol. 7, No. 23, 684–685, 1971.
3. Kogelnik, H. and T. Li, "Laser beams and resonators," *Proceedings of IEEE*, Vol. 54, 1321–1329, 1966.
4. Kaiser, G., "Complex-distance potential theory, wave equations, and physical wavelets," *Math. Methods Appl. Sci.*, Vol. 25, 1577–1588, 2002.
5. Kaiser, G., "Physical wavelets and their sources: Real physics in complex spacetime," *J. Phys. A: Math. Gen.*, Vol. 36, No. 30, R291–R338, 2003.
6. Kiselev, A. P., "Localized light waves: Paraxial and exact solutions of the wave equation (a review)," *Optics and Spectroscopy*, Vol. 102, No. 4, 603–622, 2007.
7. Gel'fand, I. M. and G. E. Shilov, *Generalized Functions. Vol. I: Properties and Operations*, Academic Press, New York, 1964.

Developing Sample Holders for Measuring Shielding Effectiveness of Thin Layers on Compound Semiconductor Substrates

A. Fehér¹, Sz. Nagy¹, and I. Mojzes²

¹Department of Telecommunications, Széchenyi István University
H-9026 Győr, Egyetem tér 1, Hungary

²Department of Electronics Technology, Budapest University of Technology and Economics
H-1111, Budapest, Goldmann Gy. tér 3., Hungary

Abstract— Ohmic contacts can be formed, if thin metallic layers grown on compound semiconductor substrates are heat treated. The type of the arising contact depends on the composition of the materials and the growing and thermal treating circumstances. If the layers are thin enough, fractal-like topology of the metallic clusters can also occur. The systems can be studied by scanning electron microscopy or atomic force microscopy and the images can be analyzed by various topology determining algorithms. These values can characterize the metal-semiconductor contact. Also, resistance and other electromagnetic properties are needed for a proper description.

In the present work sample holders and measuring setups for determining the shielding effectiveness or the reflectivity of such small scale, thin, planar samples are tested. The measured data are compared to finite element model results using a commercial program package for electromagnetic calculations materials with well known electromagnetic properties. The irregular shape, the small size and the mechanical rigidity of the samples makes the measurements complicated. In the models high cylindrical symmetry is used with surprisingly good accordance. The frequency range is rather large, 9 kHz to 6 GHz, which is not covered by the current standards of shielding effectiveness measurements. The sample holders originate from those of the standards with much smaller size and specially modified flanges and fixing. The measured data is shape and size independent up to a certain level.

1. INTRODUCTION

Because of the increasing need for computational power and the continuous development of the manufacturers, the size of the elements on a semiconductor slice and the line thickness in these devices reaches the mesoscopic scale soon. In these nanometer scaled objects the quantummechanical effects tend to overwhelm the bulk properties, thus new characteristics arise. The new phenomena also appear in the contacts to these semiconductor devices. The Ohmic contacts are generated by thermal treating of thin metallic layers on the desired spots. Because of the small size of the devices to be contacted, the metallic layer has to be rather thin, and as the thickness of these layers decrease, the heat treating causes interesting behavior of the metallic film. Scanning electron microscopy (SEM) and atomic force microscopy (AFM) shows, that on compound semiconductor surfaces the 50 nm to 100 nm thick metallic films transform into an island-like structure, and the arisen islands have often fractal topology [1–3]. The structure of these systems can be characterized by their fractal dimension as well as by their localization type based on structural entropy calculations [4, 5]. Mostly, the DC resistivity of the resulting structure is measured for determining whether the contact is of Ohmic type. Since a lot of the circuits operate in the microwave domain, the radio frequency behavior should be analyzed, as well.

2. SHIELDING EFFECTIVENESS MEASUREMENTS

Shielding effectiveness and dielectric permittivity characterizes the microwave behavior of the material rather well. However, the standards and the usually applied methods are not suitable for the above mentioned samples. The standards for measuring shielding effectiveness are based on two setups. For measurements according to IEEE-STD-299, a shielded enclosure with a proper sized window is needed, and the sample should be fastened into the window frame. Two antennas in both sides of the sample measure shielding effectiveness. The size of the necessary sample is about 1 m in diameter, which is impossible to be produced even from clean semiconductor.

The other usual measurement setup consists of an enlarged coaxial line, cut in two halves and flanged, measured by a network analyzer. The sample is to be fastened between the two flanges of the sample holder, as it can be seen in Fig. 1.

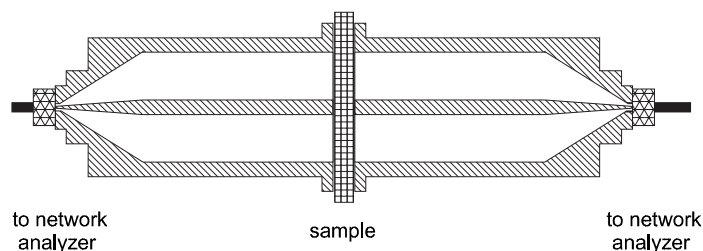


Figure 1: Sample holder with specimen for standard ASTM D4935-99. The device is air-filled, the required sample diameter is 133 mm the inner electrode diameter is 33 mm. The center rod is usually elastic for the safe contact.

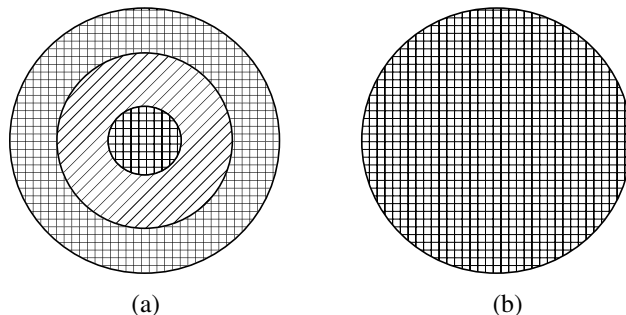


Figure 2: (a) Reference and (b) specimen for standard ASTM D4935-99. The sample is a full circle with 133 mm diameter, while the reference covers only the electrodes, it consists of a circle of diameter 33 mm, and a ring.

The size of the sample is not very large, and the coaxial line could be scaled to suitable size, thus this setup seems to be more satisfactory for testing the compound semiconductor based thin metallic films. Variations of the scaled sample holder for special purposes, like testing nano-designed materials [6], shielding textiles [7, 8], or carbon nanotube films [9] appeared recently in the literature. The setup, however has some drawbacks. First, for the standard measurement a reference is also needed according to Fig. 2.

The reference is a circle covering the inner rod of the sample holder and a ring for covering the flanges. If a substrate is necessary for the specimen, it has to be a full circle in case of the reference, too. In our case the first problem would be to produce circular substrate, since although semiconductor slices are produced in almost cylindrical shape, their size is not proper and they break by their crystal planes, thus the substrates are usually slices of circles, squares or trapezoids. It is also complicated to grow ring-like structures of the metallic layer, moreover, it is not guaranteed that the reference and the sample will have the same fractal structure. This is why we have chosen the so called “air reference” method [6] with a model calculation background. The second problem is the elasticity of the inner rods. The surface of the semiconductor slices are very precisely plane, but they are rather thin and break easily, thus we have chosen to have non-elastic inner electrode, polished to the plane of the flanges. Our sample holder is not air- but Teflon-filled resulting in a high stability of the inner rod and a good planar surface for the sample to lie upon. Scratching of the layers could also be avoided by this setup.

3. CALCULATIONS

The shielding effectiveness is defined as

$$SE = 20 \lg \left(\frac{E_{\text{ref}}}{E_{\text{load}}} \right), \quad (1)$$

where E_{ref} is the electrical field strength with the reference inserted into the holder whereas E_{load} with the specimen.

The sample holder consists of two Teflon-filled coaxial line pieces with rather large flanges on the contact surfaces. The other end of the device is a standard N-type mother connector. The

characteristic impedance of the coaxial line is

$$Z_0 = \frac{60}{\varepsilon_0} \ln \frac{D}{d}, \quad (2)$$

with ε_0 being the relative permittivity of the filling material ($\varepsilon_{\text{Teflon}} = 2.02$, D the diameter of the outer electrode and d that of the inner rod. In our case, the diameters are $d = 2.04$ mm, $D = 11$ mm, the characteristic impedance is 50Ω . The sample holder can operate up to the frequency, where the higher order modes appear [10], i.e., until

$$f_c = \frac{1}{\pi \varepsilon} \frac{2c}{d + D} \quad (3)$$

with c being the velocity of light. For the above described sample holder this cutoff frequency is ≈ 7.3 GHz.

For simulation the RF toolbox of the finite element program package COMSOL Multiphysics were applied. The high cylindrical symmetry of the sample holder was used, resulting in the sample being cylindrical, too. As a test, a Silicon specimen was tested with relative dielectric constant $\varepsilon_{\text{Si}} = 11.7$ for the whole frequency band. In order to model the large flanges, a ring of air was put around the sample with proper metallic or inter-dielectrics boundary conditions. In Fig. 3 the electric and magnetic field norms are summarized for 1 GHz frequency with coaxial excitation of the device at its left end.

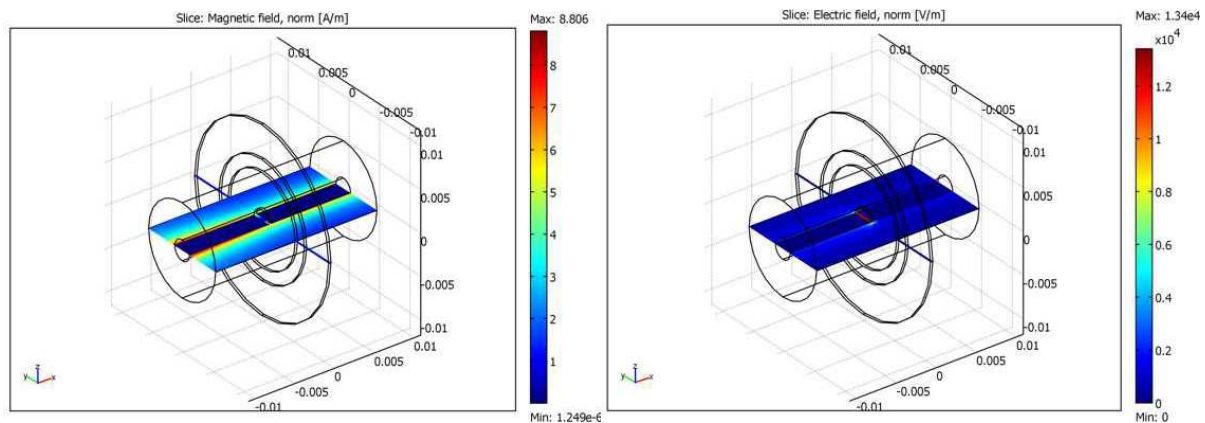


Figure 3: The cross-section color plot of the norm of the magnetic and electric fields in the sample and sample holder at 1 GHz frequency.

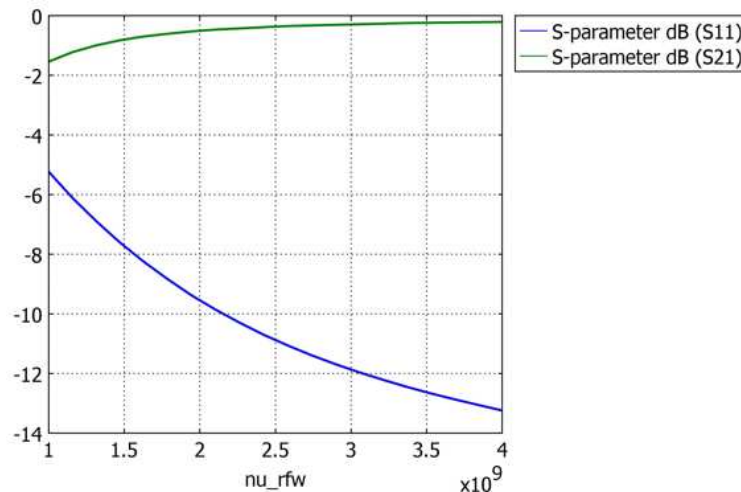


Figure 4: The parameters S_{11} , S_{21} simulated with the model in Fig. 3 with 1 mW exciting power, coaxial port.

Clearly, the electromagnetic field concentrates at the center of the sample. Similar results appeared in all the studied frequencies, the energy density between the flanges was zero, or very small. This results in the suggestion, that the shape of the sample is indifferent as long as it covers the high energy density central region of the sample holder.

The parameters S_{11} and S_{21} were calculated for the 1 GHz to 4 GHz region of frequency, and plotted in Fig. 4. S_{21} has an increasing saturating type of behavior as the frequency grows, whereas S_{11} decreases.

4. MEASUREMENTS

The measurements were carried out in the Radio Frequency Test Laboratory of the Széchenyi István University in Győr, Hungary. A network analyzer by R&S was used with a frequency range 9 kHz to 6 GHz. The sample holder without load gave the parameter S_{11} , S_{21} , S_{12} and S_{22} results summarized in Fig. 5

It can be seen, that the parameters S_{21} and S_{12} start to deviate from their ideal 0 dB level at 4 GHz, much lower than the expected cutoff frequency. However, in the 9 kHz to 4 GHz domain, the sample holder behaves very well.

The 300 μm Silicon slice specimens had irregular shapes, all covering the whole surface of the teflon filling and the inner rod, with varying coverage of the flanges. The measured data for one specific trapezoidal sample are summarized in Fig. 6. Similar, almost shape-independent results came from other shaped pieces.

Clearly, resonances appear around 1 GHz and 4 GHz. The parameter S_{11} differs from the numerically modeled values, while that of the parameter S_{21} is rather similar to the calculated line. Considering, that the model is oversimplified, the second result is surprisingly good. The high reflectivity can be the result of the insufficient coupling between the sample holder and the measuring instrument. The square shape of the specimen holder can cause extra loss.

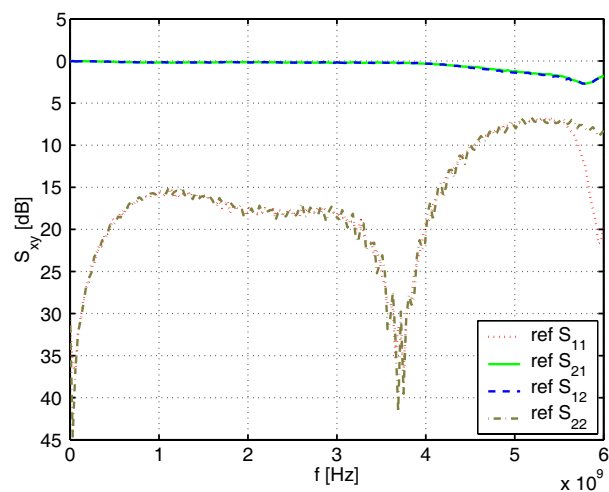


Figure 5: The parameters S_{11} , S_{21} , S_{12} and S_{22} measured on the sample holder without load.

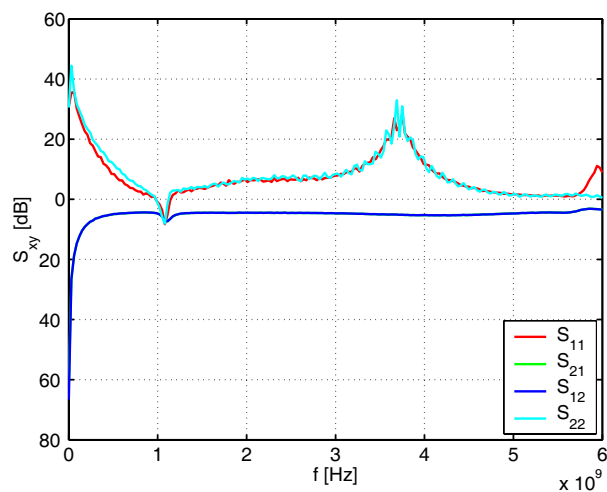


Figure 6: The parameters S_{11} , S_{21} , S_{12} and S_{22} measured on the sample holder with a trapezoidal load.

5. CONCLUSION

A coaxial line based sample holder for thin, small, rigid, irregularly shaped planar samples is studied both by numerical simulations and by measurements. The numerical study showed, that due to the large flanges of the specimen holder the non central regions of the sample does not affect the main results, which was also proven by network analyzer measurements. Comparing numerical and measured data can result in shielding effectiveness and dielectric constant determination methods without reference sample.

ACKNOWLEDGMENT

This work was supported by the Bolyai János Research Fellowship of the Hungarian Academy of Sciences.

REFERENCES

1. Dávid, L., L. Dobos, B. Kovács, I. Mojzes, and B. Pécz, “Fractal character of in situ heat treated metal-compound semiconductor contacts,” *J. Mater. Sci: Mater. Electron*, Vol. 17, No. 4, 321–324, 2006.
2. Mojzes, I., Cs. Dominkonics, G. Harsányi, Sz. Nagy, J. Pipek, and L. Dobos, “Heat treatment parameters effecting the fractal dimensions of AuGe metallization on GaAs,” *Appl. Phys. Lett.*, Vol. 91, No. 7, article No. 073107, 2007.
3. Schuszter, M., L. Dobos, K. A. Nemcu, Sz. Nagy, and I. Mojzes, “Analysis of morphology changes of heat treated metallization of compound semiconductors by the fast wavelet-transform based on B-spline,” *J. Optoelectron. Adv. Mat.*, Vol. 9, No. 7, 2241–2244, 2007.
4. Pipek, J. and I. Varga, “Universal classification scheme for the spatial localization properties of one-particle states in finite d-dimensional systems,” *Phys. Rev. A*, Vol. 46, 3148–3164, 1992.
5. Pipek, J. and I. Varga, “Scaling behavior of energy functionals of highly complex distributions,” *Int. J. Quantum Chem.*, Vol. 70, 125–131, 1998.
6. Vasquez, H., L. Espinoza, K. Lozano, H. Foltz, and Sh. Yang, “Simple device for electromagnetic interference Shielding effectiveness measurement,” *EMC IEEE EMC Society Newsletter*, Vol. 220, 62–68, 2009.
7. Bula, K., J. Koprowska, and J. Janukiewicz, “Application of cathode sputtering for obtaining ultra-thin metallic coatings on textile products,” *Fibers and Textiles in Eastern Europe*, Vol. 14, No. 5, 75–79, 2006.
8. Więckowski, T. W. and J. M. Janukiewicz, “Methods for evaluating the shielding effectiveness of textiles,” *Fibers and Textiles in Eastern Europe*, Vol. 14, No. 5, 18–22, 2006.
9. Xu, H., S. M. Anlage, L. Hu, and G. Gruner, “Microwave shielding of transparent and conducting single-walled carbon nanotube films,” *App. Phys. Lett.*, Vol. 90, article No. 183119, 2007.
10. ASTM Standard Designation D 4935-99, “Standard test method for measuring the electromagnetic shielding effectiveness of planar materials,” 1999.

Cross-linked Transmission Line Based Planar TLM-net with Effective Dispersion of 4th Order

S. A. Ivanov¹, B. V. Sestorovsky², and A. N. Bogolyubov¹

¹Moscow State University, Moscow, Russia

²Lavochkin Association, Moscow, Russia

Abstract— Hereby the technique of optimization of dispersion of classical planar TLM net [1, 2] is suggested. This technique is based on partial elimination of spatial anisotropy and frequency dispersion which is expressed in the dependence of phase velocity and intrinsic impedance of plane net wave on frequency and direction of propagation. As a result of this optimization the planar TLM net with amplitude-phase dispersion independent of the direction of propagation at 2nd order of accuracy and simultaneously with amplitude-phase dispersion of the 4th order of accuracy at some shifted frequency was constructed.

1. INTRODUCTION

This paper is devoted to optimization of dispersion of classical planar TLM (Transmission Line Matrix) net [1, 2], proposed by P. B. Johns in 1971 for solution 2-dimensional scattering problems of electrodynamics. As a rule numerical dispersion is defined as the dependence of phase velocity of plane net wave propagated in regular TLM net on frequency and direction of propagation. Another type of numerical dispersion is also applied in this paper — the dependence of intrinsic impedance of plane net wave on frequency and direction of propagation. We shall call the first type “phase numerical dispersion” and the second type — “amplitude one”.

The numerical dispersion of regular TLM nets is the one of significant factors affecting solution accuracy; that’s why its investigation and constructing of optimized nets with improved dispersion is reflected in the great amount of papers. We shall note that numerical dispersion of regular nets is a common phenomenon existing not only in TLM method. For example the analogous phenomenon exists in FDTD [3] method.

Technique proposed in this paper is based on partial elimination of spatial anisotropy and frequency dispersion of classical planar TLM net.

The idea of this procedure is composed of integrating of two classical TLM nets turned against each other by 45° into one whole net and its further optimization. The optimization of the resulting net consists of two steps. The first step is the optimization of the spatial dispersion. For this purpose parameters of the integrated net are selected in such a way that amplitude-phase dispersion not to be dependant on the direction of propagation at the 2nd order of accuracy. The second step is the optimization of frequency dispersion of the resulting net. This optimization is based on the procedures of correction of phase velocity and intrinsic impedance of plane net wave. The procedure of phase velocity correction is based on the following considerations. Let’s propose that stationary processes in TLM net at some frequency ω_0 have to be researched. If we excite the net on some easily determined effective frequency ω_{eff} then the phase velocity of plane net wave will be equal to light velocity with the 2nd order of accuracy. The using of this procedure became possible due to preliminary optimization of anisotropy of TLM net and that allowed to decrease the phase dispersion up to the 4th order of accuracy. The procedure of intrinsic impedance correction resolves to the correction of internal impedance of exciting circuits.

2. CONSTRUCTING OF THE NET BEING OPTIMIZED

Elementary cell of classical TLM net is depicted on Fig. 1.

This cell is formed by four transmission lines with time delay Δt and intrinsic admittance $Y_0/2$. During the cell uniting intrinsic admittances are added. Intrinsic admittances of transmission lines in infinite net Fig. 2 formed by cells Fig. 1 are equal to Y_0 .

Phase numerical dispersion equation of net Fig. 2 is stated below:

$$2 \cos \omega_0 \Delta t = \cos k_x d + \cos k_y d \quad (1)$$

where

$$(k_x, k_y) = k_n \mathbf{n} = \mathbf{k}_n \quad (2)$$

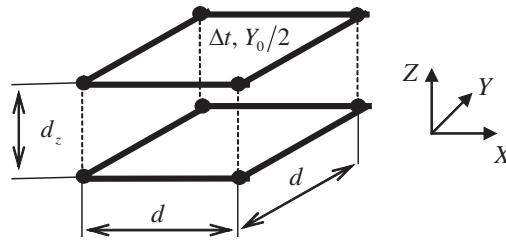


Figure 1: Elementary cell of classical TLM net.

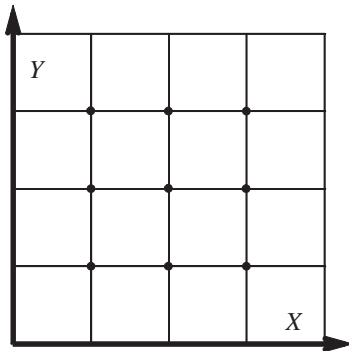


Figure 2: Infinite TLM net formed by cells Fig. 1 (top view).

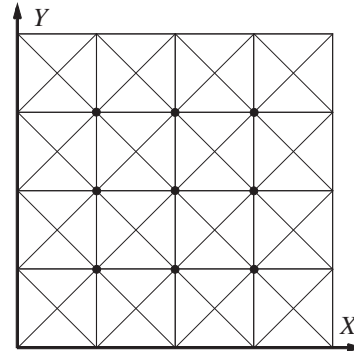


Figure 3: Infinite TLM net obtained by uniting two TLM nets turned against each other by 45° (top view).

where d is elementary cell length along axes X and Y , ω_0 is frequency, k_n is net wave number, $\mathbf{n} = (\cos \alpha, \sin \alpha)$ is direction of wave propagation. Approximate analysis of dispersion Equation (1) leads to the following relationship for net wave number k_n :

$$k_n = k_0 \left(1 + \frac{\cos^2 2\alpha}{48} k_0^2 d^2 \right) + O(d^4) \tag{3}$$

where $k_0 = 2\pi/\lambda_0 = \omega_0/c$ is wave number in free space, λ_0 is wave length in free space, c is light velocity in vacuum.

Relationship (3) shows that phase velocity of plane net waves depends on direction of propagation at second order of accuracy. Besides there is no parameter regulating this dependence. This missing parameter can be obtained by uniting two TLM nets turned against each other by 45° into one whole net. It may be done in various ways. This paper represents the way of uniting as in Fig. 3.

The net Fig. 3 consists of horizontal and vertical transmission lines with intrinsic admittances Y_1 and diagonal ones with intrinsic admittances Y_2 . Transmission lines are joined in points depicted as circles. Type of line junction is parallel node.

3. SOLVING ALGORITHM DEVELOPMENT

We shall construct solving algorithm in terms of voltages in net nodes. Let's introduce Cartesian coordinate system and enumerate TLM net nodes Fig. 3 by index (p, q) along X and Y axes accordingly. Each node of TLM net Fig. 3 is parallel one by the construction of the net. The following identities are true for n-ports parallel node:

$$O_i + \Pi_i = U, \quad \text{where} \quad U = \frac{2}{Y} \sum_{i=1}^n Y_i \Pi_i = \frac{2}{Y} \sum_{i=1}^n Y_i O_i, \quad Y = \sum_{i=1}^n Y_i \tag{4}$$

where U is voltage in the node, Π_i is incoming impulse for port i , O_i is outgoing impulse for port i , Y_i is intrinsic admittance of port i . Taking into account that incoming impulses are outgoing

ones for neighboring nodes, we shall get relationship for voltages in neighboring nodes:

$$U^{(p,q,n+1)} = C_1 \left(U^{(p-1,q,n)} + U^{(p,q-1,n)} + U^{(p+1,q,n)} + U^{(p,q+1,n)} \right) + C_2 \left(U^{(p-1,q-1,n)} + U^{(p+1,q-1,n)} + U^{(p+1,q+1,n)} + U^{(p-1,q+1,n)} \right) - U^{(p,q,n-1)} \quad (5)$$

where $U^{(p,q,n)}$ is voltage in node with indexes (p, q) at time point $t_n = n\Delta t$,

$$C_1 = \frac{Y_1}{2Y_1 + 2Y_2}, \quad C_2 = \frac{Y_2}{2Y_1 + 2Y_2} \quad (6)$$

Thus to find the voltage in node at time point t_{n+1} it is necessary to know voltages in neighboring nodes at time point t_n and voltage in the same node at time point t_{n-1} . This algorithm require storing of 2 parameters per one node and using 8–10 operations for one time step per one node.

4. OPTIMIZATION OF PHASE NUMERICAL DISPERSION

Optimization of phase numerical dispersion is realized in two steps. The first step is decreasing of anisotropy of net Fig. 3. The second one is correction of frequency dispersion.

Let's derive phase numerical dispersion equation. We shall propose that for each time point and for each node of the net Fig. 3 the following relationships for voltages are fulfilled:

$$U^{(p,q,n)} = U_0 \cos(\mathbf{k}_n \mathbf{r}_{p,q} - \omega_0 t_n + \phi) \quad (7)$$

where U_0 is wave magnitude, ϕ is wave phase, $U^{(p,q,n)}$ is voltage in node with indexes (p, q) at time point $t_n = n\Delta t$, $\mathbf{r}_{p,q} = (pd, qd)$ is radius-vector of node with indexes (p, q) . Putting (7) in (5) we shall obtain phase numerical dispersion equation:

$$\cos \omega_0 \Delta t = C_1 (\cos k_x d + \cos k_y d) + 2C_2 \cos k_x d \cdot \cos k_y d \quad (8)$$

Dispersion Equation (8) establishes implicit dependence $k_n(k_0, \alpha)$. Analysis of (8) shows that under fulfillment of conditions

$$\Delta t = \frac{d}{c} \sqrt{0.6}, \quad Y_1 = 4Y_2, \quad (9)$$

where $c = \omega_0/k_0$ is light velocity in vacuum, this dependence is the following:

$$k_n = k_0 \left(1 + \frac{1}{60} k_0^2 d^2 + O(d^4) \right) \quad (10)$$

i.e., velocity of plane net waves is equal to light velocity in vacuum within the accuracy of first-order members and does not depend on angle in second order of accuracy.

Optimization of frequency dispersion was carried out taking into account the following things. Let's propose that device at some frequency ω_{eff} have to be researched. If we excite the net at shifted frequency

$$\omega_0 = \omega_{eff} \left(1 - \frac{1}{60} \frac{\omega_{eff}^2 d^2}{c^2} + a \frac{\omega_{eff}^4 d^4}{c^4} + O(d^6) \right) \quad (11)$$

where a is unknown factor, we shall obtain that on the shifted frequency ω_0 net wave number k_n found from (8) depends on effective wave number $k_{eff} = \omega_{eff}/c$ in the following way:

$$k_n = k_{eff} \left(1 + \left(a + 10^{-3} + \frac{\cos^2 2\alpha}{1440} \right) k_{eff}^4 d^4 \right) + O(d^6) \quad (12)$$

If $a = -10^{-3}$ approximate relationship for net wave number is the following:

$$k_n = k_{eff} \left(1 + \frac{\cos^2 2\alpha}{1440} k_{eff}^4 d^4 \right) + O(d^6) \quad (13)$$

If we compare last relationship with dispersion Equation (3) we shall conclude that phase numerical dispersion in the new net is less in $k_{eff}^2 d^2/30$ times then phase numerical dispersion in the original net. When $d/\lambda_0 = 1/20$ then phase numerical dispersion in the new net is less in 304 times, when $d/\lambda_0 = 1/10$ — in 76 times.

5. OPTIMIZATION OF MAGNITUDE NUMERICAL DISPERSION

The main problem of definition of magnitude numerical dispersion (in this case of intrinsic impedance of plane net wave) consists in the solution of the following problem: how to determine magnetic field in TLM net if there is just one operand — electric field (voltage) in the node used in solving algorithm? There is a doubt in appropriateness of application of universal method — definition of magnetic field in TLM net arising from the voltage in neighboring nodes; as in this case locality and simultaneousness of determination magnetic field is broken and this can not be satisfied while research of plane net wave. We can acknowledge acceptable such a definition where the magnetic field is determined in the same space and time points as the electric field (i.e., in nodes of TLM net and in the time points $t_n = n\Delta t$).

Such definition can be given with the help of the circuit Fig. 4. Half infinite TLM net is depicted at this figure; this net is constructed in the following way. The infinite TLM net Fig. 3 at section $x = pd$ is cut in halves. In this connection intrinsic admittance of transmission lines at this section will decay in two times. The right half of the net is deleted; in its place the nodes of the net are loaded with admittances Y_x .

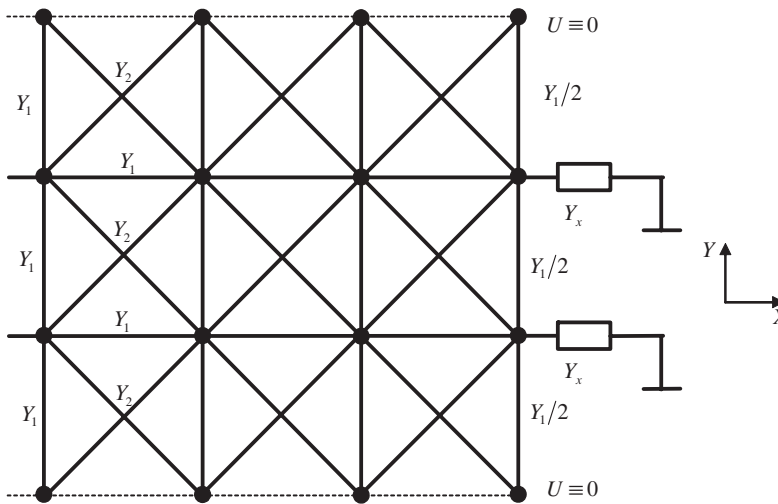


Figure 4: TLM circuit aimed for determination of intrinsic admittance of plane net wave.

If admittances fitted in such a way that plane net wave being propagated from left to right (i.e., with wave number $\mathbf{k}_n = (k_x, k_y)$ where $k_x > 0$) will be absorbed by them without reflections then we can say that for such TLM net magnetic field H_y in nodes will be described with the help of relationship

$$H_y = -Y_x U / d_z \quad (14)$$

where U is voltage in nodes, d_z is the size of elementary cell along the axis Z . The full magnetic field can be defined in the following way:

$$\mathbf{H} = (H_x, H_y) = U d_z^{-1} (-Y_y, Y_x) \quad (15)$$

where Y_y is determined from the circuit analogous to Fig. 4. Intrinsic admittance of plane net wave can be defined according to (15) in the following way:

$$\mathbf{Y}_n = (Y_x, Y_y) \quad (16)$$

Physical meaning of admittance (16) consists of the following: if phase of plane net wave is propagated in direction of wave number \mathbf{k}_n then the energy is propagated in direction \mathbf{Y}_n which may not coincide with direction \mathbf{k}_n . That's why intrinsic admittance of plane net wave is involuntarily determined as vector one.

While suppressing intermediate manipulations which were held according to model described in [4] we shall mention relationship for intrinsic admittance of plane net wave:

$$\mathbf{Y}_n = \frac{1}{\sin \omega_0 \Delta t} (Y_1 \sin k_x d + 2Y_2 \cos k_y d \cdot \sin k_x d, Y_1 \sin k_y d + 2Y_2 \cos k_x d \cdot \sin k_y d) \quad (17)$$

Magnitude numerical dispersion is determined by $\mathbf{n} - \mathbf{Y}_n/Y_0$ where Y_0 is intrinsic admittance of vacuum. Relationship (17) analysis shows that with satisfaction of the requirement

$$Y_1 = \frac{2}{\sqrt{15}}Y_0, \quad Y_1 = 4Y_2, \quad (18)$$

which can be realized simultaneously with condition (9); magnetic numerical dispersion will be described by relationship

$$\mathbf{n} - \mathbf{Y}_n/Y_0 = -0.05\mathbf{n} k_0^2 d^2 + \mathbf{O}(d^4) \quad (19)$$

i.e., it will be small quantity of 2nd order and will not depend on angle in the same order. Frequency dispersion correction of intrinsic admittance \mathbf{Y}_n can be carried out by postprocessing [3] or with the help of perfect exciting circuits [4].

6. CONCLUSIONS

The technique of optimization of numerical dispersion of TLM net [1,2] suggested in the paper allows to construct TLM net having amplitude-phase numerical dispersion independent of the direction of propagation at 2nd order of accuracy and simultaneously having amplitude-phase numerical dispersion of the 4th order of accuracy at some shifted frequency. The advantages of the constructed net are the large time step (larger than original net has) and high efficiency computational algorithm which need to store two parameters per one node and take 8–10 operations per one node and one time step. This technique can be easily generalized in case of taking into account dielectrics and also three dimensional nets.

ACKNOWLEDGMENT

This work was carried out with support of RFBR, project No. 06-01-00146.

REFERENCES

1. Johns, P. B. and R. L. Beurle, "Numerical solution of 2-dimensional scattering problems using a transmission-line matrix," *Proc. Inst. Elec. Eng.*, Vol. 118, 1203–1208, Sept. 1971.
2. Sestroretsky, B. V., "Opportunities of direct numerical solving of boundary value problems based on the method of impedance analogue of electromagnetic space (IAES)," *Problems of Radioelectronics, Ser. "General Problems of Radioelectronics"*, Vol. 2, 113–128, 1976.
3. Juntunen J. S. and T. D. Tsiboukis, "Reduction of numerical dispersion in fdtd method through artificial anisotropy," *IEEE Trans. on MTT*, Vol. 48, No. 4, April 2000.
4. Klimov K. N., B. V. Sestroretsky, V. A. Vershkov, S. V. Soldatov, T. V. Kamishev, and V. A. Ruchenkov, *Electrodynamical Analysis of Two-dimensional Inhomogeneous Media and Plasma*, MAKS Press, Moscow, 2005.

A Low Phase-noise Low-power PLL in 0.13- μm CMOS for Low Voltage Application

Q. Guo, H. F. Zhou, W. W. Cheng, Y. Han, X. X. Han, and X. Liang

Department of Information Science and Electronic Engineering
Zhejiang University, Hangzhou, Zhejiang 310027, China

Abstract— A low voltage, low power phase-locked loop (PLL) using a standard 0.13- μm CMOS 1P8M process is presented. The voltage-controlled oscillator (VCO) can operate from a 0.5 V supply while the phase-frequency detector (PFD), charge pump (CP) and the divider use 0.8 V supply. The dc power consumption of the PLL is only 2.5 mW. Due to the use of the wideband nulling of flicker noise up conversion technique, the worst phase noise of the whole tuning range is -122.5 dBc/Hz at 1 MHz frequency offset and the phase noise displays little dependence on the frequency tuning.

1. INTRODUCTION

Due to the continuous growth of personal wireless communications, it demands low-cost low-power solutions in the design of wireless systems. To reduce the power consumption of the system, power supply reduction has been a popular method, especially for digital circuits where voltage scaling has been pushed beyond the subthreshold voltage. However, in analog and RF circuits, voltage scaling cannot be sustained mainly due to noise. This is especially true for VCOs in wired and wireless communication systems for which high carrier power is necessary to lower the phase noise. This paper proposed an LC VCO which can operate from a 0.5 V supply while the other blocks of the PLL use 0.8 V supply voltage. The tuning range of the VCO is 2.32 GHz \sim 2.51 GHz. And during the whole output frequency range, the phase noise only changes 1.2 dB, it displays little dependence on the frequency tuning. The dc power consumption of the PLL is only 2.5 mW. It will be implemented in a standard 0.13 μm CMOS process.

2. CIRCUIT DESIGN

2.1. VCO Design

Figure 1 shows the block diagram of the proposed PLL. In the PLL design, one of the most challenging tasks is to realize a high performance VCO with a reduced supply voltage and power consumption. While there are several VCO topologies, in order to operate at an ultra-low supply voltage, a differential NMOS-only topology is adopted for VCO because it reduces the voltage headroom and provides higher output swing for low supply voltage. We realize the elimination of flicker noise through the construction shown in Fig. 2 [1]. Removing the tail current source and using two tail inductors instead of the tail current source can raise the tail impedance at the oscillation frequency and its harmonics at the output node and also lower the voltage headroom. An inductor and varactors in series with passive metal-isolator-metal capacitors are used to make a clean control voltage as shown in Fig. 2. It only suppresses the high frequency signal and has no effect on dc voltage [2].

2.2. PFD, CP and Loop Filter Design

The PFD is implemented by modified precharge [3] topology since it can operate from a 0.8 V supply (Fig. 3). However till now, all the papers concerning it said that it had a dead zone around

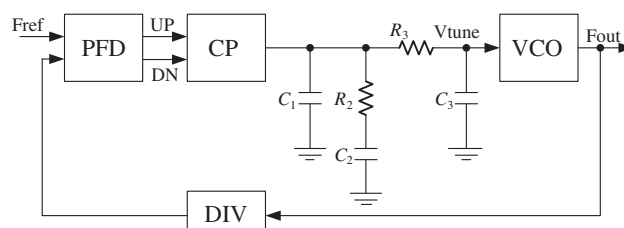


Figure 1: The block diagram of the phase-locked loop.

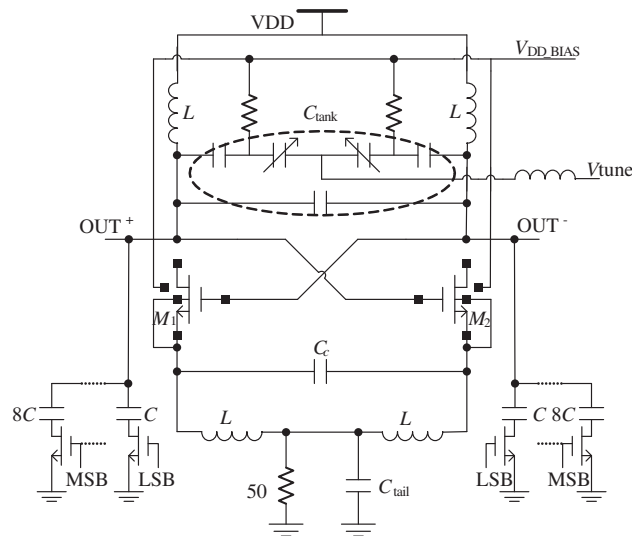


Figure 2: Circuit diagram of prototype VCO.

zero phase error. Through carefully analysis of the construct of the pt-PFD, we find that the dead zone can be remove by suitably designing the size of the transistors. The maximum operation frequency is defined as the shortest period with the correct UP and DN signals together with the inputs having the same frequency plus 90° phase difference [4]. Using this comparison criterion, the operation frequency for the proposed PFD is obtained greater than 200 MHz.

The proposed charge pump is shown in Fig. 4. With the reduced supply voltage, stacking transistor stages should be prevented. Thus, the switches at the gate terminals of M_2 and M_3 are utilized to control the functionality of charging or discharging the loop filter. The controlled voltage is connected to the gate terminals of M_5 and M_6 establishing a negative feedback to suppress the mismatch [5].

For the desirable output characteristics, a third-order loop filter is employed. The third order loop filter is useful in filtering spurs or noise caused by the PLL that at an offset frequency of ten times the loop bandwidth or greater. The phase margin relates to the stability of the PLL. This parameter is typically chosen between 40 and 55 degrees. Simulations show that a phase margin of about 45 degrees yields the optimal lock time. Higher phase margins may decrease peaking response of the loop filter at the expense of degrading the lock time [6].

2.3. Divider Design

A divided-by 128/129 dual-modulus prescaler circuitry using the traditional transmission gate flip-flop (TGFF), is shown in Fig. 5. This D flip-flop circuit use three stage 6T MOS. The speed is limited by divide-by 4/5 prescaler circuit [7]. Based on 0.13 μm CMOS technology with the supply voltage of 0.8 V, the prescaler circuit in gray area of Fig. 5 can run at 4 GHz with 0.71 mW power consumption. The asynchronous $\div N$, where N is 32 in this $\div 128/129$ prescaler, consists of one true-single-phase-clock (TSPC) FF [8]. It is simple and can work well at high frequencies.

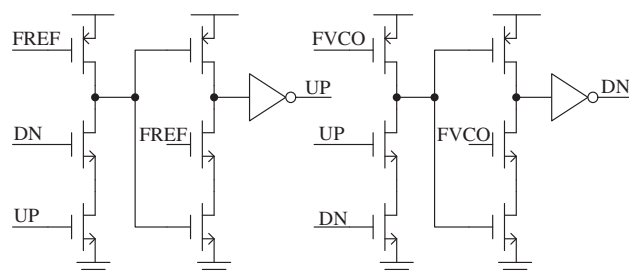


Figure 3: Schematic of precharge type PFD.

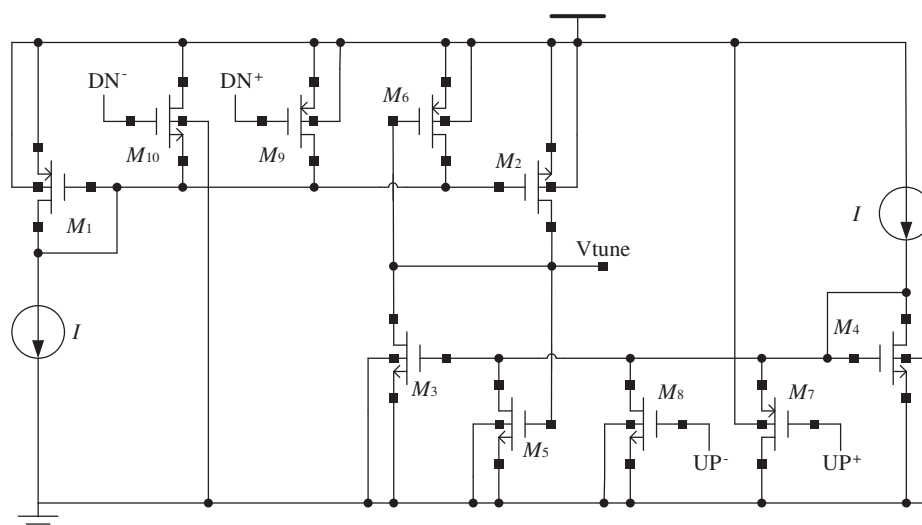


Figure 4: The proposed charge pump topology.

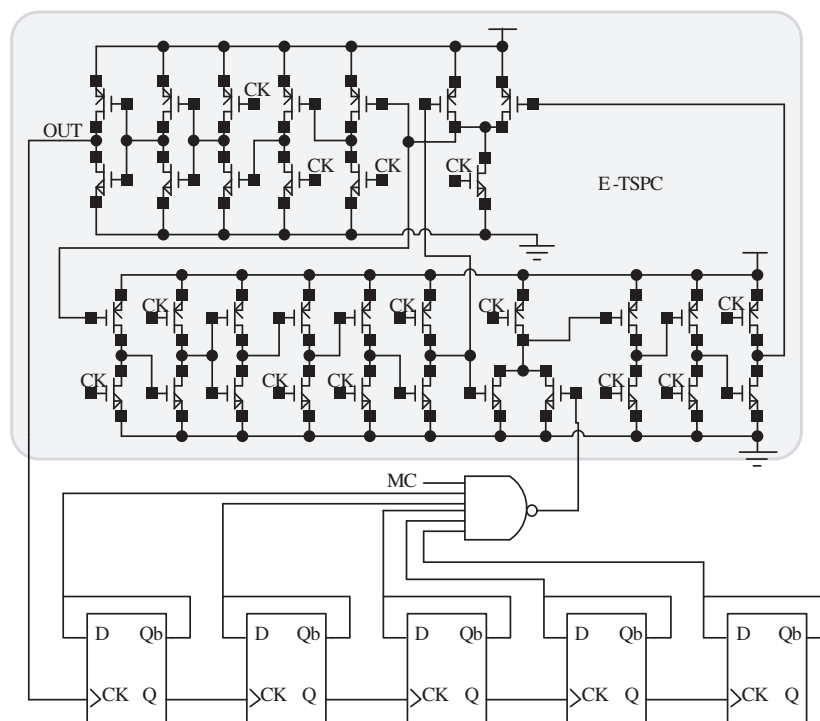


Figure 5: Schematic of the divide-by 128/129 dual-modulus prescaler.

3. SIMULATION RESULTS

The simulation results presented are for a standard 0.13- μm CMOS 1P8M technology. Fig. 6 shows the current variations against the output voltage variations of the charge pump circuit. For the proposed charge pump, the sourcing/sinking current matching is nearly perfect. By a combining discrete and continuous tuning [9], a family of overlapping tuning curves which guarantee continuous frequency coverage over the tuning range, as shown in Fig. 7. This VCO is tunable over 170 MHz with a sensitivity of about 25 MHz/V. The Fig. 8 shows the phase noise at 1 MHz offset along the whole frequency tuning range and the phase noise displays little dependence on the frequency tuning. With a reference frequency of 18.75 MHz, the output frequency of the loop locked at 2.4 GHz is shown in Fig. 9 and the settling time of the proposed PLL is less than 30 μs . The power consumption is 1.3 mW for the VCO, 1.2 mW for the other blocks of the PLL. The performance of the proposed PLL is summarized in Table 1.

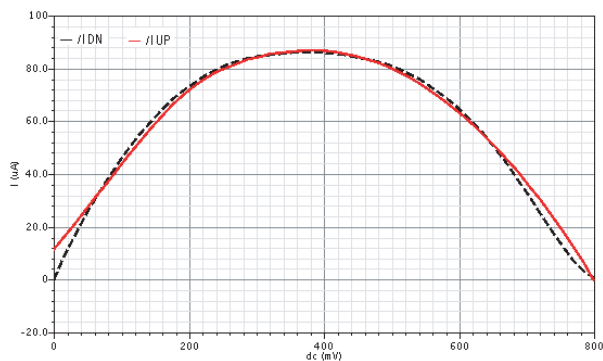


Figure 6: Charge pump current matching characteristic.

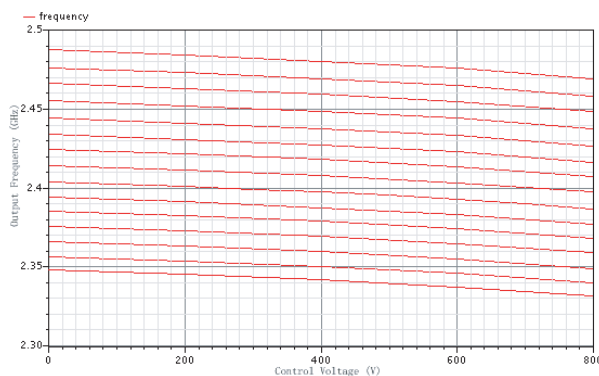


Figure 7: Tuning characteristics of the proposed VCO.

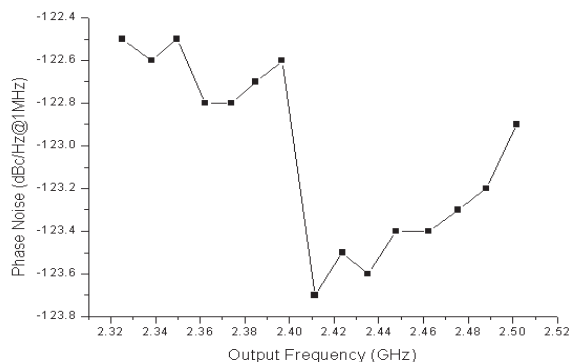


Figure 8: Phase noise for the VCO at 1 MHz offset frequency.

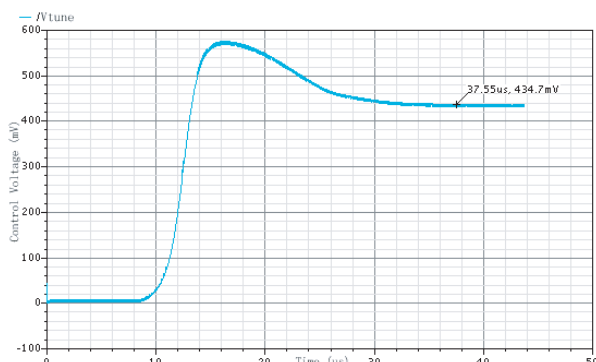


Figure 9: Settling time of the proposed PLL.

Table 1: Performance summary of the PLL.

Technology	0.13- μ m CMOS
VCO Supply Voltage	0.5 V
PFD & CP & DIV Supply Voltage	0.8 V
DC Power	2.5 mW
VCO Tuning	2.32~2.51 GHz
VCO PN@1 MHz (the worst)	-122.5 dBc/Hz
Loop Bandwidth	<200 kHz
Settling Time	<30 μ s

4. CONCLUSION

Using a standard 0.13 μ m CMOS technology, a low phase noise, low power PLL is presented in this paper for low voltage application. With the novel techniques involved in the building blocks, significant performance improvement in terms of phase noise and output swing is achieved.

ACKNOWLEDGMENT

The author would like to thank Semiconductor Manufacturing International Corporation (SMIC) for chip fabrication and technical support.

REFERENCES

1. Ismail, A. and A. A. Abidi, "CMOS differential LC oscillator with suppressed up converted flicker noise," *Proc. of Int. Solid-State Circuits Conference, ISSCC*, 98–99, San Francisco, USA, Feb. 2003.
2. Zhou, H. F., Y. Han, S. R. Dong, et al., "An ultra-low-voltage high-performance VCO in

- 0.13 μm CMOS,” *Journal of Electromagnetic Waves and Applications*, Vol. 22, No. 17/18, 2417–2426, 2008.
3. Lee, G. B., P. K. Chan, and L. Siek, “A CMOS phase frequency detector for charge pump phase-locked loop,” *Circuits and Systems, 42nd Midwest Symposium*, Vol. 2, 601–604, Aug. 1999.
 4. Razavi, B., *Monolithic Phase-Locked Loops and Clock Recovery Circuits: Theory and Design*, Wiley-IEEE Press, Apr. 1996.
 5. Hsieh, H. H., C. T. Lu, and L. H. Lu, “A 0.5-V 1.9-GHz low-power phase-locked loop in 0.18- μm CMOS,” *20th Symposium on VLSI Circuits*, 164–165, Kyoto, Japan, Jun. 2007.
 6. Jau, T. S., W. B. Yang, and Y. L. Lo, “A new dynamic floating input D flip-flop (DFIDFF) for high speed and ultra low voltage divided-by 4/5 prescaler,” *13th IEEE International Conference on Electronics, Circuits and Systems*, 902–905, Nice, France, Dec. 2006.
 7. Navarro, J. and W. V. Noije, “A 1.6-GHz dual modulus prescaler using the extended true-single-phase-clock CMOS circuit technique (E-TSPC),” *IEEE J. Solid-State Circuits*, Vol. 34, 97–102, 1999.
 8. Yuan, J. and C. Svensson, “High-speed CMOS circuit technique,” *IEEE J. Solid-State Circuits*, Vol. 24, 62–70, Feb. 1989.
 9. Hegazi, E. and A. A. Abidi, “A 17-mW transmitter and frequency synthesizer for 900 MHz GSM fully integrated in 0.35- μm CMOS,” *IEEE J. Solid-State Circuits*, Vol. 38, No. 5, 782–792, 2003.

A Concurrent Triple-band CMOS LNA Design for 4G Applications

Yohan Jang, Nackgyun Seong, and Jaehoon Choi

Division of Electrical and Computer Engineering, Hanyang University
17 Haengdang-dong, Seongdong-gu, Seoul 133-791, Korea

Abstract— In this paper, a concurrent triple-band low noise amplifier (LNA), which operates at 698 MHz–800 MHz 1920 MHz–2170 MHz and 2300 MHz–2400 MHz is designed for Long Term Evolution (LTE), WCDMA/HSDPA and WiBro services. The circuit is designed with TSMC 0.18 μm RF CMOS process. The main topology of the proposed LNA is cascode architecture with source degeneration. In order to obtain necessary gains for this frequency bands, a series LC circuit is added in parallel with the parallel LC tank of a single-band LNA. The proposed LNA has voltage gains of 17.9 dB and 18.7 dB, and noise figures (NF) of 2.3 dB and 3.1 dB at 749 MHz and 2160 MHz, respectively while dissipating 7 mA from a 1.8 V supply voltage.

1. INTRODUCTION

To satisfy the ever growing demand for various mobile services, the communication technology has been changed rapidly. Especially, to provide high quality multimedia services to increasing mobile users, it is inevitable to develop new technologies for high data rate, interoperability among different communication protocols and services, user friendliness and high security [1]. The fourth generation (4G) wireless systems are under development to satisfy such demands by adopting various advanced technologies. CMOS technology will be one of key technologies not only to provide the high performance but also to reduce the manufacturing cost [2]. In this paper, a concurrent triple-band CMOS LNA for LTE, WCDMA/HSDPA, and WiBro bands is proposed.

2. LNA CIRCUIT DESIGN

Recently, there has been growing demand for providing multiple services with a single mobile terminal. For this purpose, multi-band wireless receivers have been introduced recently [3–5]. For a conventional LNA, passive networks are used to create the wideband transconductance characteristic of an active device in order to obtain necessary gain and impedance matching at the desired frequency band. In addition, LNAs are required to have high gain, low noise, high linearity, and low power consumption properties. In this paper, we proposed a concurrent triple-band CMOS LNA using a Cadence SpectreRF [6] with TSMC 0.18 μm RF CMOS process.

2.1. Cascode-based Dual-resonance Input Matching Configuration

Figures 1(a) and 1(b) show the input stage and small-signal equivalent circuit model of the proposed triple-band LNA. The proposed LNA design is based on a single-stage inductively degenerated common-source cascode amplifier topology which has major advantages such as high power gain, wide bandwidth, and high reverse isolation [7]. To achieve the input impedance matching to 50 Ω characteristic impedance of the proposed LNA, the series inductance L_g , capacitance C_{ex} parasitic capacitance C_{gs} and inductance L_s are used [8].

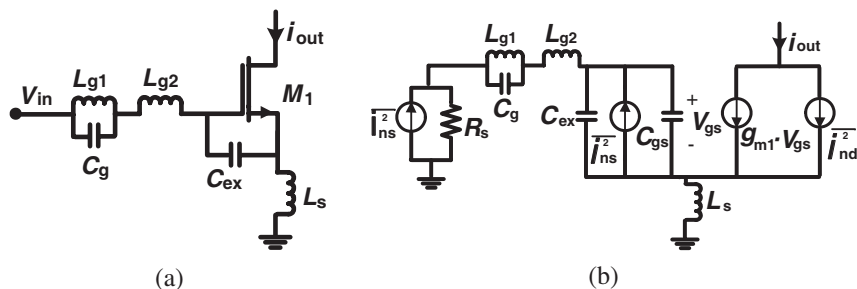


Figure 1: (a) Input stage of the proposed triple-band LNA, (b) small-signal equivalent circuit of the proposed concurrent triple-band CMOS LNA.

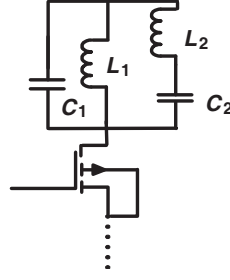


Figure 2: Output stage of the proposed triple-band LNA.

According to the small signal equivalent circuit shown in Figure 1(b), the input impedance of the proposed LNA, Z_{in} can be written as

$$Z_{in} = \frac{sL_{g1}}{1 - \omega^2 L_{g1} C_g} + s(L_{g2} + L_s) + \frac{1}{s(C_{gs} + C_{ex})} + \frac{g_{m1}}{(C_{gs} + C_{ex})} L_s \quad (1)$$

This input impedance must satisfy the following conditions at two resonate frequencies;

$$\text{Re}(Z_{in}) = \frac{g_{m1}}{(C_{gs} + C_{ex})} L_s = 50\Omega, \quad (2)$$

$$\text{Im}(Z_{in}) = \frac{sL_{g1}}{1 - \omega^2 L_{g1} C_g} + s(L_{g2} + L_s) + \frac{1}{s(C_{gs} + C_{ex})} = 0 \quad (3)$$

In Equation (2), inductance L_s should be chosen to match the real part of the input impedance to the characteristic impedance. To satisfy the condition given by Equation (3) at two resonance frequencies, L_s , L_{g1} , L_{g2} , C_g and C_{gs} need to be adjusted accordingly. In addition, the capacitance C_{ex} is added to enhance the specified frequency bandwidth performance at low frequency such as LTE band. The overall performance of the proposed LNA is greatly dependent upon the input matching method.

2.2. Output Matching Configuration

To obtain the necessary gain and to achieve impedance matching at required frequency bands, a series LC branch in parallel with a parallel LC tank is added at the output stage shown in Figure 2.

The two LC circuits (one series and one parallel) shown in Figure 2 generate the rejection band and in turn, this property can be used to enhance the image rejection of the receiver [9]. The values of inductors and capacitors are listed in Table 1.

Table 1: Circuit parameter values.

L_1	L_2	C_1	C_2
8.1 nH	9.9 nH	0.7 pF	0.6 pF

2.3. LNA Design Approach

Figure 3 shows the schematic diagram of the proposed concurrent triple-band CMOS LNA. To provide good circuit performance, the transistor width and the bias current need to be optimized. The choice of input transistor (M_1) size is depending on the transconductance and current consumption requirements. The optimum width of gate and bias voltage (V_g) are $160\ \mu\text{m}/0.18\ \mu\text{m}$ and $0.7\ \text{V}$, respectively. Transistor M_2 is used to improve the isolation between the input and output and its characteristic has the substantial effect on the overall noise performance of LNA [10]. Its width is $80\ \mu\text{m}/0.18\ \mu\text{m}$. The output buffer composed of M_3 and M_4 is added for output matching purpose.

3. SIMULATION RESULTS

This section presents the simulation results of a current triple-dual band CMOS LNA which operates at 698 MHz–800 MHz, 1920 MHz–2170 MHz, and 2300 MHz–2400 MHz. The design is based on the cascode topology with source degeneration scheme shown in Figure 2. It is implemented with TSMC

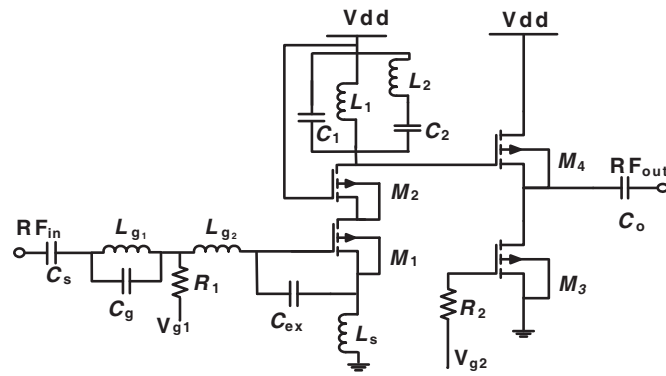


Figure 3: The schematic diagram of the proposed concurrent triple-band CMOS LNA.

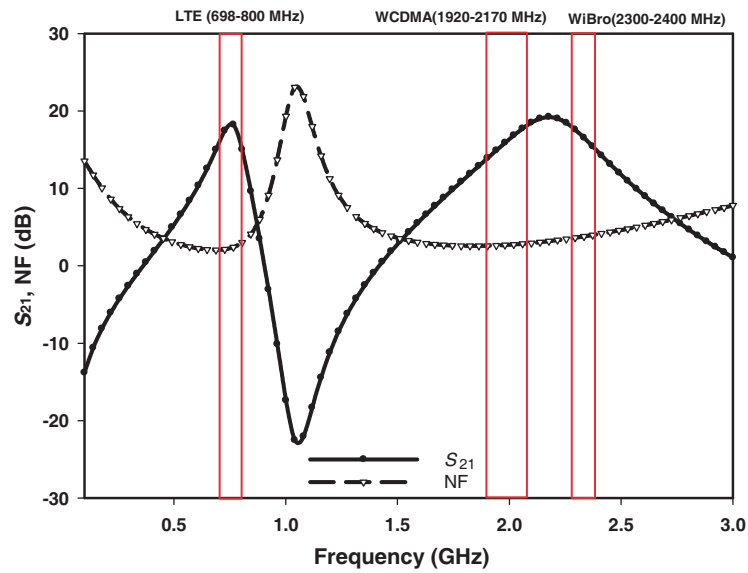


Figure 4: Simulated S_{21} and NF of the triple-band CMOS LNA.

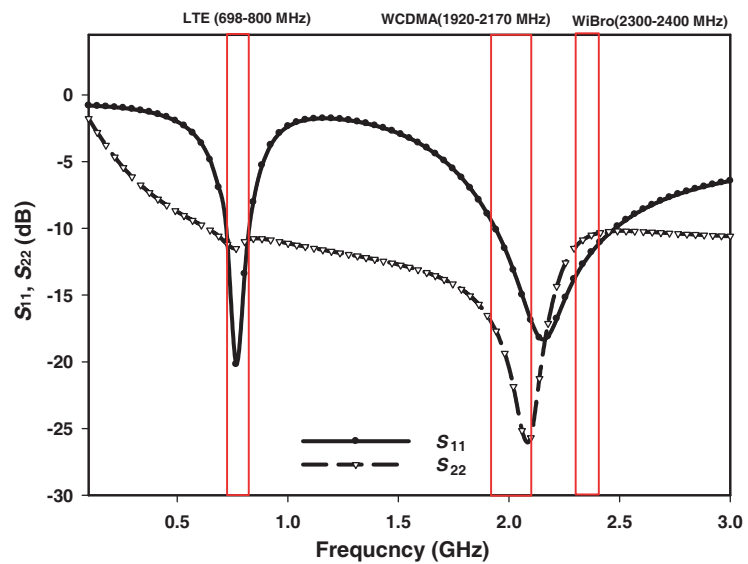


Figure 5: Simulated S_{11} and S_{22} of the triple-band CMOS LNA.

0.18 μm RF CMOS process using Cadence SpectreRF. The input parallel resonator is made by using a 0.7 pF capacitance and a 9.7 nH inductance. Figure 4 shows the simulated voltage gain and noise figure of the proposed concurrent triple-band CMOS LNA. The designed LNA has voltage gains of 15 dB–18.2 dB and 14.2 dB–19.1 dB, and noise figures (NF) of 2.1 dB–2.9 dB and 2.5 dB–4.1 dB at 698 MHz–800 MHz and 1920 MHz–2400 MHz, respectively. Especially, the proposed LNA provides high gain and wideband characteristic at a higher frequency band covering WCDMA/HSDPA and WiBro services. As shown in Figure 5, 10 dB return loss bandwidths for both input and output ports are large enough to cover the required frequency bands. The proposed LNA drains 7 mA from a 1.8 V supply voltage.

4. CONCLUSION

The proposed triple-band CMOS LNA for 4G application is suggested in this paper. The proposed LNA is implemented by 0.18 μm RF CMOS technology and utilized cascode topology with source degeneration. In order to obtain the necessary triple-band gain, a series LC circuit is added in parallel with the parallel LC tank of a single-band LNA. To satisfy the bandwidth requirement parallel LC tank and capacitance C_{ex} are used at input stage and two LC circuits (one series and one parallel) are added at output stage. The proposed concurrent triple-band CMOS LNA could be a good candidate for 4G mobile systems.

ACKNOWLEDGMENT

This research was supported by the Ministry of Knowledge Economy, Korea, under the Information Technology Research Center support program supervised by the Institute of Information Technology Advancement.

REFERENCES

1. Jamil, M., S. P. Shaikh, M. Shahzad, and Q. Awais, "4G: The future mobile technology," *IEEE Region 10 Conference TENCON 2008*, Hyderabad, India, November 2008.
2. Amor, M. B., A. Fakhfakh, H. Mnif, and M. Loulou, "Dual band CMOS LNA design with current reuse topology," *International Conference on Design and Test of Integrated Systems in Nanoscale Technology*, 57–61, Tunis, Tunisia, September 2006.
3. Wu, S. and B. Razavi, "A 900-MHz/1.8-GHz CMOS receiver for dual-band applications," *IEEE Journal of Solid-state Circuits*, Vol. 33, No. 12, 2178–2185, 1998.
4. Fong, K. L., "Dual-band high-linearity variable-gain low noise amplifiers for wireless applications," *IEEE International Solid-state Circuits Conference*, Digest of Technical Papers 13.3, 1999.
5. Ryyanen, J., K. Kivekas, and J. Jussila, "A dual-band RF front-end for WCDMA and GSM applications," *IEEE Journal of Solid-state Circuits*, Vol. 36, No. 8, 1198–1204, 2001.
6. "Spectre circuit simulator," *Cadence Design Systems Inc.*, www.cadence.com.
7. Mohan, S. S., M. M. Hershenson, S. P. Boyd, and T. H. Lee, "Bandwidth extension in CMOS with optimized on-chip inductors," *IEEE Journal of Solid State Circuits*, Vol. 35, No. 3, 346–355, March 2000.
8. Amor, M. B., S. Douss, A. Fakhfakh, and M. Loulou, "Optimized design of a dual band low noise amplifier for the third generation of wireless system," *SSD'05*, Sousse, Tunisia, March 2005.
9. Hashemi, H. and A. Hajimiri, "Concurrent dual-band CMOS low noise amplifiers and receiver architectures," *VLSI Circuits Symp. Dig.*, 247–250, June 2001.
10. Bevilacqua, A. and A. M. Niknejad, "An ultrawideband CMOS low noise amplifier for 3.1–10.6 GHz wireless receivers," *IEEE Journal of Solid State Circuits*, Vol. 39, No. 12, 2259–2268, December 2004.

Design of Metallic Cylindrical Waveguide Bandpass Filters Using Genetic Algorithm Optimization

R. Thabet and M. L. Riabi

Laboratory of Electromagnetism and Telecommunications, University of Constantine, Algeria

Abstract— This paper presents a general algorithm for the characterization and the optimization of coupled-cavity band-pass filters in metallic cylindrical waveguides using the Mode-Matching Method coupled to the Genetic Algorithm. The step discontinuities of the studied structures are treated and the S parameters are determinate to obtain the various frequency responses. Higher order mode interactions between waveguide uniaxial discontinuities are rigorously considered in the design procedure and a study on the convergence of modes is presented for the optimization of computational time. The genetic algorithm introduced is intended to evolve optimal structures parameters required to yield better performances in pass-band and satisfy specifications for the optimized filters.

1. INTRODUCTION

In this paper, the objective will be to optimize the choice of the parameters defining the geometrical dimensions of the proposed microwave structures in order to obtain best performances together with minimizing structures size and weight.

The mode-matching method [1–4], associated with the generalized scattering matrix technique, has been applied for the design of coupled cavity band-pass filters in metallic cylindrical waveguides. The characterization of the whole structure is carried out by computing the generalized scattering matrix of each discontinuity, then, cascading the different matrix taking in consideration the length between them. Finite iris thickness and interaction effects of dominant and higher order modes between the discontinuities are rigorously considered in the design procedure. Furthermore, a study on the convergence of modes is made for computational time optimization.

The application of electromagnetic theory to scattering problems requires, in the majority of the cases, the use of optimization. For this goal, several studies using various optimization techniques are used. In our work, we propose to use the genetic algorithm synthesis procedure [5, 6]. The genetic algorithms (GAs), which are global optimization techniques, use the stochastic random choice to search through a coding of a parameter space. They are based on the concept of the genetic evolution of the species which simulates natural selection and reproduction. GAs are applied to a variety of electromagnetic problems such as the design of broadband microwave absorbers [7], the synthesis of antenna array [8], filters design [9]...

2. THEORY

2.1. Description

We present the study of cylindrical waveguide filters coupled by thick circular irises (Fig. 1).

The design of the conventional band-pass filters is based on a common approach described in [10]. The Cohn's synthesis method together with Levy's large-aperture design formulas extended to the design of circular waveguide irises in coupled-resonator waveguide filters [11] and which includes the McDonald's thick aperture theory, are applied in the case of rectangular waveguide

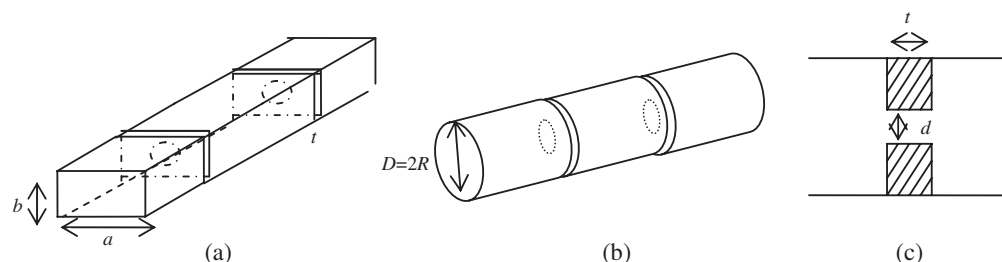


Figure 1: (a) Rectangular cavity coupled by circular irises using in narrow-band filter design, (b) circular cavity coupled by circular irises, (c) circular iris of thickness t and diameter d .

filter. Large circular irises and finite wall thickness may be treated by correction factors. This approximate treatment results in a designed pass-band filters which need to be improved to satisfy design specifications. The geometrical dimensions (Lengths of resonators and radii of irises) of the resulting filters are used as initial values for the design optimization.

2.2. Design Constraints

Our aim is to define filters with better selectivity and lower insertion losses. The possibility of minimizing the weight and the overall size of the filter is also considered. The variables including in the GA process are the geometrical dimensions (lengths of resonators and diameters of irises) of the filter. To avoid unreasonable geometrical parameters, it is necessary to fix the limits of the search interval used in the optimization process for both lengths and diameters.

2.2.1. Limits on the Lengths of the Resonators

They are chosen to be at $\pm 0.01 \text{Leng}(j)$ for rectangular resonators and $\pm 0.03 \text{leng}(j)$ for circular resonators; $\text{Leng}(j)$ are determinate by the synthesis method such as:

$$\text{Leng}(j) = \theta(j) \frac{\lambda_g}{2\pi} \quad (1)$$

where

$$\theta(j) = \pi - \frac{1}{2} [\tan^{-1}(2x(j)) + \tan^{-1}(2x(j+1))] \quad (2)$$

$\text{Leng}(j)$ is the length of the j th resonator and λ_g is the guide wavelength of fundamental mode relating to the center frequency, $x(j)$ is given by:

$$\begin{aligned} x(j) &= \frac{4\pi M(j)}{ab\lambda_g} && \text{for rectangular waveguide} \\ x(j) &= \frac{16M(j)}{0.955D^2\lambda_g} && \text{for circular waveguide} \end{aligned} \quad (3)$$

and it represents the normalized reactance of the j th iris and $M(j)$ is the magnetic polarizability [10].

2.2.2. Limits on the Diameters of the Irises

In the case of rectangular waveguide filter, Equation (4) defines the magnetic polarizability in terms of the diameter for the j th iris, such as:

$$M(j) = c_0 c_1 c_2 d(j)^3 / 6 \quad (4)$$

where c_0 , c_1 , c_2 are correction factors (in terms of the iris diameter) used for large irises; more details are given in [11]. Equation (4) results in a function of the j th iris diameter and will be solved by the secant method. The solution of the equation for each iris gives the corrected diameter. For application in the GA algorithm, the limits on the diameters are chosen to be at $\pm 0.01d(j)$.

For the circular waveguide filter, the magnetic polarizability is defined by [10]:

$$M(j) = d(j)^3 / 6 \quad (5)$$

Approximate corrections on the thickness and size are made for thick and larges irises ($t/d > 0.1$) and compensated polarizabilities are calculated such as [10]:

$$M_c(j) = M(j) \left[1 - \left(\frac{1.7d(j)}{\lambda_0} \right)^2 \right] \cdot 10^{\frac{1.6t}{d(j)}} \sqrt{1 - \left(\frac{1.7d(j)}{\lambda_0} \right)^2} \quad (6)$$

Corrected values of diameters or $d_c(j)$ are defined using (5) and (6). In this case, limits on the diameters are at $\pm 0.05d_c(j)$.

2.3. Genetic Algorithm Application

The GA performs an inherently parallel search on M individuals or chromosomes. Each chromosome represents the coding of a data set which corresponds to a potential solution of the problem. The algorithm starts by generating an initial population of random potential solutions. The generation of a new population from the preceding one is carried out in three phases: Evaluation where the fitness function is estimated for all the chromosomes in the current population, based on certain characteristics which are desired in the solution. Next, the selection is applied and the GA selects the individuals that optimize best the fitness function. At each generation, the best solution is chosen as elite individual and is directly copied into the population of the next generation. The reproduction by crossover and mutation is then performed on the selected parents to generate two children that replace their parents in the new population. Mutation is carried out by randomly changing one or more genes (variables) of the created offspring. The crossover is a fundamental operator in the GA, it is performed with a probability p_c ($= 0.7$ – 0.8). Mutation is performed with a probability p_m ($= 0.06$ – 0.08); it is used to add a certain diversity to the population. According to the evolutionary theory, the new generation will be more adapted to the problem than the preceding one. The evolution optimization process is reiterated until satisfaction of a given halting criterion or if a total number of generations is reached. The best individual (corresponding to the lower fitness) in the population is taken as the final answer.

2.3.1. Fitness Function

In order to evaluate the frequency response of the filter, the scattering parameters are calculated by the mode-matching method and the fitness function, which is a function to minimize, is defined by:

$$F = \sum_{i=1}^N w_i f_i \quad \text{where} \quad f_i = \sqrt{|S_{21\text{desired}} - S_{21\text{calculated}}|} \quad (7)$$

for the fundamental mode at the i th sampling point and the w_i is the corresponding weighting value. N represents the number of sampling points.

3. NUMERICAL RESOLUTION AND DISCUSSION

The first example of studied filters is a three-resonator rectangular waveguide narrow-band filter coupled by circular irises. Starting with a design specification, the geometrical dimensions of the filter have been computed by the synthesis method. The calculated dimensions do not satisfy the design specification and an optimization process will be necessary to improve filter performances. Fig. 2 shows the result of optimization for the considered filter. It is designed for a pass-band at about 15.04 GHz and a relative band wide of 0.0013. The irises are inserted in a WR62 rectangular waveguide ($15.8 \text{ mm} \times 7.9 \text{ mm}$) and they have a thickness equal to 0.218 mm. The excitation at the input waveguide is realized by the TE_{10} fundamental mode. The dimensions of the filter are given in Table 1. The plotted curve is the frequency response of the TE_{10} fundamental mode in pass-band. Our results are compared to those of reference [12]. The optimized filter performances show improved pass-band performance, improved selectivity and better rejection quality in the stop-band. The return losses are larger than 21.23 dB in the pass band.

A rigorous study on the convergence of the obtained results is made for the optimization of computational time. The number of modes taken into account for the field theory modeling of the

Table 1: Dimensions (in mm) of the optimized rectangular three-resonator filter.

		Ref. [12]	Optimized by GA
Radius of the irises	R_1	2.577	2.5598
	R_2	1.142	1.1454
	R_3	1.125	1.1456
	R_4	2.592	2.5848
Lengths of the resonators	L_1	12.499	12.4916
	L_2	12.819	12.8334
	L_3	12.461	12.4807

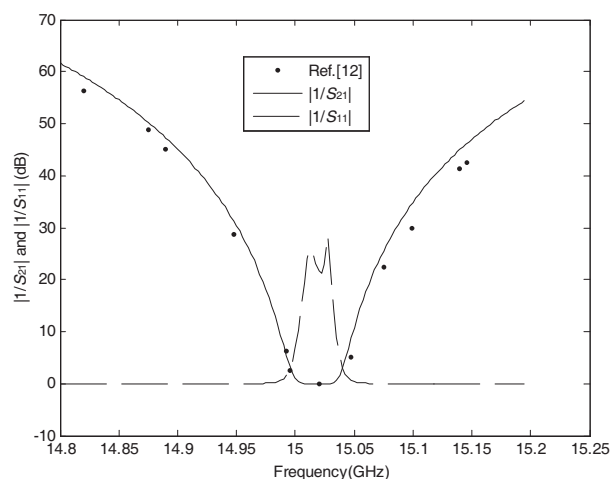


Figure 2: Frequency response of a three-resonator rectangular waveguide narrow-band filter coupled by circular irises.

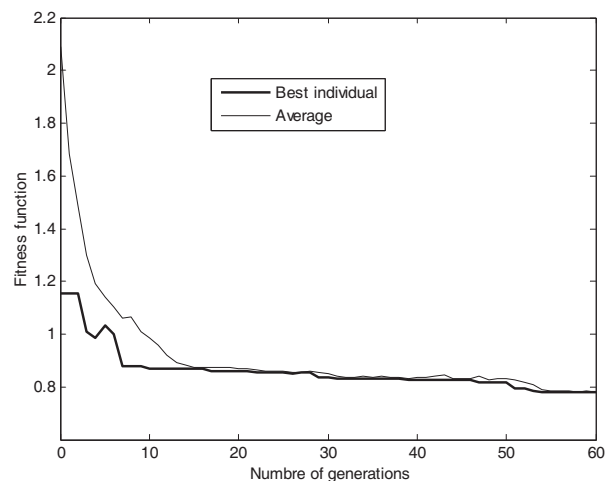


Figure 3: Evolution of fitness function (30 individuals/generation) for the best individual and the average of fitness function.

proposed filter is for TE_{mn} and $TM_{m'n'}$ up to $m = 24$, $n = 12$, $m' = 8$, and $n' = 6$ in the resonator sections and $m = 5$, $n = 12$, $m' = 5$, and $n' = 5$ in the circular iris sections.

Figure 3 shows the progress of the fitness value for the most adapted individual in the population (thick line) and the progress of the average of the fitness values (thin line) as a function of the number of generations. Geometrical parameters were coded using natural binary coding. Each chromosome contains a number of genes corresponding to the number of geometrical parameters of the structure to optimize. The result was achieved with less than 1800 evaluations (30 individuals in the population and 60 generations) of the fitness function. Note that the individuals in the population tend to identify with the better one.

The second example of filters treated in this work is a three-resonator circular waveguide filter coupled by circular irises working in Ku band (the housing waveguide is of radius $R = 6.965$ mm). The thickness of the irises is 0.192 mm. The TE_{11} mode is the incident mode. In the case of junction between two axially circular waveguides, the electromagnetic field at the discontinuities is described only by TE_{1r} and TM_{1r} modes with $r = 1, 2 \dots$ [4]. The convergence of the results is obtained using $r = 25$. The frequency response for the TE_{11} fundamental mode and the corresponding dimensions are given in Fig. 4 and Table 2. Comparison is made with results of reference [13]. The curves show improved characteristic in pass band. The return losses are larger than 22.29 dB in pass band, a slight improvement of the rejection quality in stop-band is observed in Fig. 4(b) and

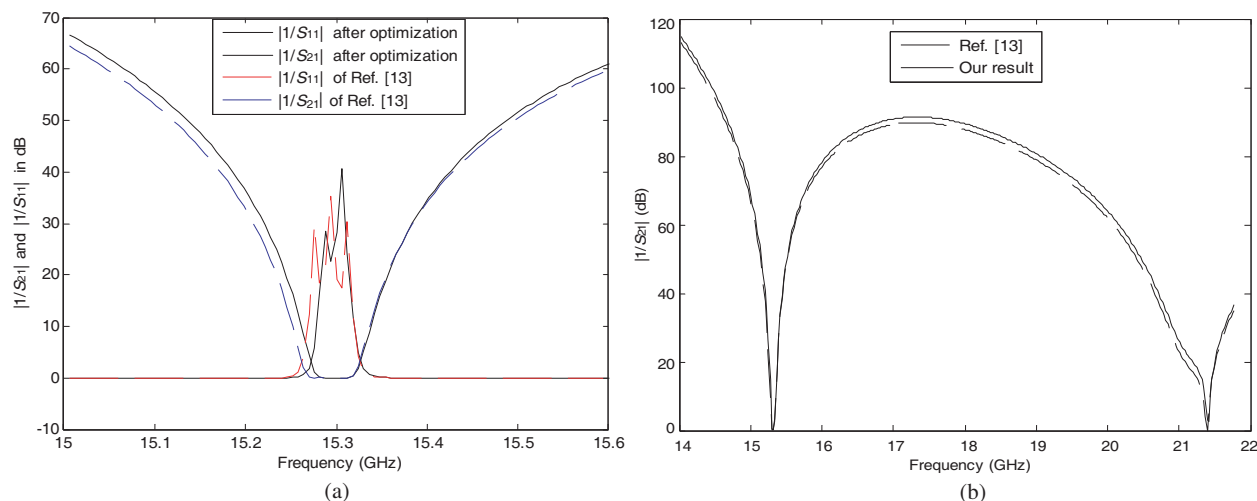


Figure 4: Frequency response of a three-resonator circular waveguide filter coupled by circular irises. The corresponding dimensions are given in Table 2.

Table 2: Dimensions (in mm) of the optimized circular three-resonator filter.

		Ref. [13]	Optimized by GA
Radius of the irises	R_1	3.1	3.1173
	R_2	1.695	1.6383
	R_3	1.695	1.6383
	R_4	3.1	3.1173
Lengths of the resonators	L_1	16.599	16.5713
	L_2	17.219	17.2192
	L_3	16.599	16.5713

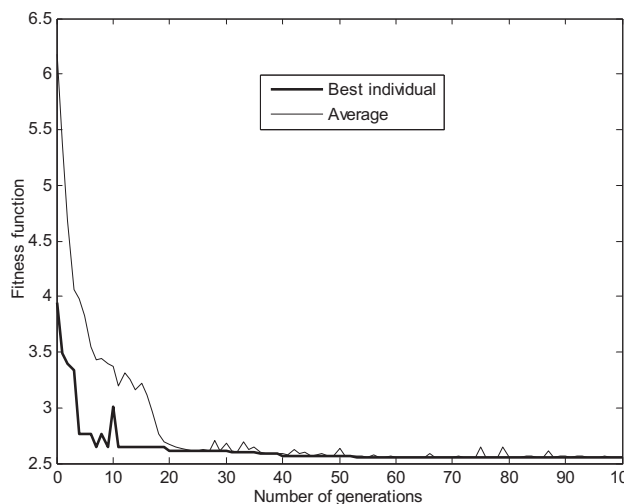


Figure 5: Evolution of fitness function (14 individuals/generation) for the best individual and the average of fitness function.

a slight decrease in the overall length of the filter is obtained. Fig. 5 represents the variation of fitness function versus number of generations for the best individual in the population (thick line) and for the average of the fitness values (thin line). The population includes 14 individuals, so each generation required up to 14 evaluations of the fitness function which corresponds to evaluating (7).

4. CONCLUSION

General optimization algorithms for the design of rectangular and circular waveguide band-pass filters coupled by circular irises have been presented by employing the mode matching method in conjunction with the genetic algorithm. The theory, which includes the finite iris thickness, the higher order mode interactions between step discontinuities, is rigorously treated to design the proposed filters.

The selection of the most relevant geometrical parameters allows an improvement of the performances. The study has combined advantageously the efficiency of the mode-matching method with the flexibility of GA and the ability of the optimization process is confirmed.

REFERENCES

1. Wexler, A., "Solution of waveguide discontinuities by modal analysis," *IEEE Trans. Microwave Theory Tech.*, Vol. 15, No. 9, 508–517, September 1967.
2. Wade, J. D. and R. H. Macphie, "Scattering at circular-to-rectangular waveguide junctions," *IEEE Trans. Microwave Theory Tech.*, Vol. 34, No. 11, 1085–1091, November 1986.
3. Gesell, G. A. and I. R. Ciric, "Recurrence modal analysis for multiples waveguide discontinuities and its application to circular structures," *IEEE Trans. Microwave Theory Tech.*, Vol. 41, 484–490, 1993.
4. Sabatier, C., "Etude des discontinuités en guide circulaire à l'aide de l'analyse modale. Application aux cornets," *Proc. JINA '88*, 432–436, 1988.

5. Goldberg, D. E., *Algorithmes Génétiques: Exploration, Optimisation et Apprentissage Automatique*, Addison-Wesley, S.A., France, June 1994.
6. Rahmet-Samii, Y. and E. Michielssen, *Electromagnetic Optimization by Genetic Algorithms*, Wiley, New York, 1999.
7. Michielssen, E., J. Sajer, S. Ranjithan, and R. Mittra, “Design of lightweight, broad-band microwave absorbers using genetic algorithms,” *IEEE Trans. Microwave Theory Tech.*, Vol. 41, 1024–1031, June/July 1993.
8. Allard, R. J., D. H. Werner, and P. L. Werner, “Radiation pattern synthesis for arrays of conformal antennas mounted on arbitrarily shaped three-dimensional platforms using genetic algorithms,” *IEEE Trans. Antennas Propagat.*, Vol. 51, 1054–1062, 2003.
9. Lai, M. I. and S. K. Jeng, “Compact microstrip dual-band bandpass filters design using genetic-algorithm techniques,” *IEEE Trans. Microwave Theory Tech.*, Vol. 54, No. 1, 160–168, January 2006.
10. Matthei, G. L., L. Young, and E. M. T. Jones, *Microwave Filters, Impedance-Matching Networks and Coupling Structures*, Artech House, Norwood, MA, 1980.
11. Jennings, A. and R. L. Gray, “Extension of Levy’s large-aperture design formulas to the design of circular irises in coupled-resonator waveguide filters,” *IEEE Trans. Microwave Theory Tech.*, Vol. 32, No. 11, 1489–1493, November 1984.
12. Papziner, U. and F. Arndt, “Field theoretical computer-aided design of rectangular and circular iris coupled rectangular or circular waveguide cavity filters,” *IEEE Trans. Microwave Theory Tech.*, Vol. 41, No. 3, 462–471, March 1993.
13. Belmeugenai, M., M. L. Riabi, and M. Kadi, “Accurate modeling of transformers and filters in circular and rectangular waveguides,” *OHD2003 Proceeding*, 9, Calais, France, September 3–5, 2003.

General Design of Compact T-shaped Line Filter with Ultra-wide Stopband

Y. Z. Zhu^{1,2}, X. J. Zhang¹, and G. Y. Fang¹

¹Institute of Electronics, Chinese Academy of Sciences, China

²Graduate University of Chinese Academy of Sciences, China

Abstract— In this paper, the series quarter-wavelength line in conventional filters are replaced by open-stub T-shaped lines, resulting to ultra-wide stop band. Generalization of this compact open-stub T-shaped transmission structure is presented. Filters with this structure have ultra stopband as well as a smooth passband and a steep transition band. The design equations for generating the parameters of the T-shaped lines are derived. Furthermore, this structure can also reduce the size of conventional filter. A hairpin bandpass filter with center frequency at 2.5 GHz is designed with the proposed structure. The simulation show good characteristics. Its 35 dB stopband reaches 10.6 GHz. The results show that the strong restriction band can be as high as the fourth order harmonic frequency with compact layout and good passband.

1. INTRODUCTION

Filters are crucial components in microwave and millimeter-wave circuits. However, filters always suffer from the interference of its spurious passbands, which are normally at its second or third harmonic resonant frequencies. Several techniques have been proposed to restrict its spurious passband. For example, stepped-impedance resonators are used to shift the second harmonic passband to higher frequency [1] and changes of the input and output tapping could have extra transmission zeros in the stopband [2]. Furthermore, the EBG/DGS-based filter has over 20-dB restriction at the second harmonic [3, 4]. The shunt quarter-wave-length open stubs were introduced to produce transmission zeros at the stopband [5]. Filters in corrugated and wiggly line have over 30 dB suppression at the harmonic band [6, 7]. Another method to restrict harmonics is to using asymmetric parallel-coupled units [8]. However, these methods are still accompanied by complicated design or process limitation. Additionally, some of them would also affect the insertion loss in the passband and increase the overall circuit size.

In this paper, we substitute the equivalent open-stub T-shaped lines for the series quarter-wavelength connecting lines in filter form, realizing the integrating bandstop filters into the conventional bandstop or bandpass filter. In this way, the proposed filters have compact size and ultra-wide stopband, which is as high as triple or quadruple fundamental frequency. Similar methods has been reported by several thesis academically [9–11]. However, there is no design equation for the equivalent lines in [9] and its design is a simple pleonastic tentative procedure. In [10], the design equations are only given for a special case (all line are of the same characteristic impedance). In [11], the lengths of used open-stub are fixed at quarter-wavelength, which only restrain the second harmonic band and the higher spurious passband cannot be restricted.

This paper presents the generalization of the compact open-stub T-shaped transmission structure. By substituting the generalized T-shaped transmission lines for the series transmission line of conventional filters, we could get a bandpass or lowpass filter with ultra stopband as well as a smooth passband and a steep transition band. The design equations for generating the parameters of the equivalent open-stub T-shaped lines are derived by building transmission-line model. Based on this model, the equivalent T-shaped lines show good passband characteristics in the fundamental resonant band and sharp band-rejection characteristics in the harmonic frequency band. Furthermore, this open-stub T-shaped transmission structure can also reduce the size of conventional filter. A hairpin bandpass filter with center frequency at 2.5 GHz and 400 MHz bandwidth is designed with the proposed structure. The electromagnetic simulation show good characteristics. The insertion loss is less than 1.4 dB and the VSWR is less than 1.4 in the passband. The 40 dB stopband reaches 8.16 GHz and 35 dB stopband reaches 10.6 GHz. Its size is 23.4% less than the conventional hairpin bandpass filter. The results show that the strong restriction band can be as high as the fourth order harmonic frequency with compact structure and good passband.

2. DESIGN OF FILTER WITH ULTRA-WIDE STOPBAND

A conventional 6-order microstrip hairpin bandpass filter is shown in Figure 1. It is built in a microwave substrate whose relative permittivity ϵ_r is 2.55 and thickness is 20 mil. Its central frequency is 2.5 GHz and 3 dB bandwidth is 400 MHz. Its input and output ports are designed to be 50 ohm line. Its size is 21.93 mm \times 56.72 mm. The detailed designer procedure of this hairpin filter are presented in classic microstrip filter literature. The characteristics of it are shown in Figure 4. Here we pay attention to its stopband instead of its passband. If we define that the stopband where S_{21} is greater than -35 dB is spurious bands, the figure denotes that there are three spurious bands which exist from 4.89 GHz to 5.36 GHz, from 7.42 GHz to 7.64 GHz and from 9.10 GHz to 10.52 GHz. The three spurious bands are respectively corresponding the first, second and third fundamental frequency. This will have great influence to the noise that lie in these spurious bands.

In order to restrict the spurious bands in the stopband without increase the overall filter size, we substitute the open-stub T-shaped lines for the series transmission line. The substitutional sketch is shown in Figure 2(a). The open-stub T-shaped lines has great attenuation in its resonant frequency but has small insertion loss within other frequency band. If we set its resonant frequency to be the spurious frequency point, it can be a good choice of harmonic suppression. As the spurious bands are relatively discrete in frequency band, only one or two substitution is not enough. We replace all the six series transmission line with six open-stub T-shaped lines. After substitution, the transformative 6-order microstrip hairpin bandpass filter is shown as Figure 3. Its input and output ports are also designed to be 50 ohm line. Its size is only 19.67 mm \times 43.47 mm, which is 23.4% less than the conventional hairpin bandpass filter. The length of open stubs is to control the restricted position at frequency. Thus these six open-stub T-shaped lines produce several transmission zero points in the stopband, which restrict spurious bands.

The transmitted and reflected characteristics of the transformative T-shaped line hairpin filter is also described in Figure 4. From this figure we can see, the characteristic of passband is almost not affected by the substitution while the stopband is greatly optimized. Here we pay attention to its stopband instead of its passband. The insertion loss of passband only falls with 0.2 dB and the reflection loss only increase with less than 4 dB. The VSWR in the passband is still less than 1.4 after substitution. At the same time, the 40 dB stopband reaches 8.16 GHz and the 35 dB stopband reaches 10.8 GHz. The first, second and third harmonic spurious bands are all be suppressed. The results show that we get a compact bandpass hairpin filter with ultra stopband as well as a good passband and a steep transition band. Its stopband can be as high as the fourth order harmonic frequency.

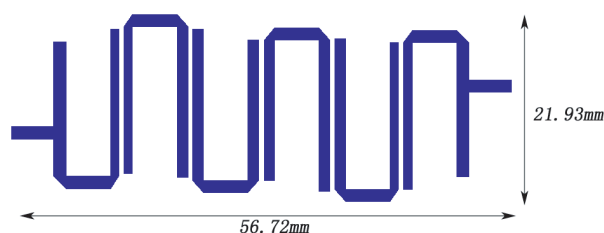


Figure 1: Conventional 6-order microstrip hairpin bandpass filter.

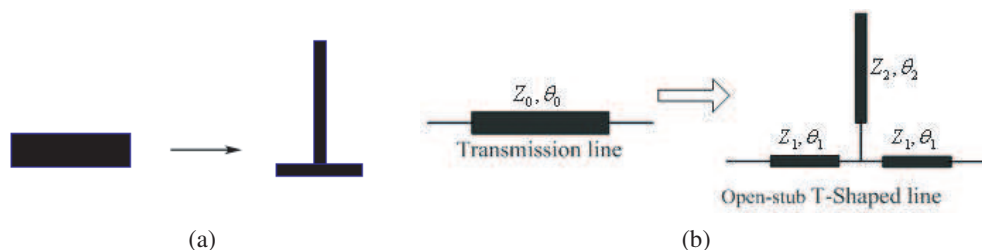


Figure 2: Series transmission line is replaced by open-stub T-shaped. (a) Sketch, (b) equivalent transmission model.

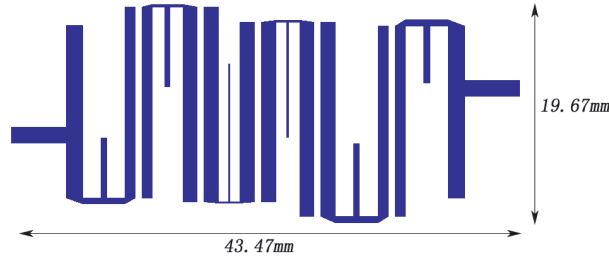


Figure 3: T-shaped line 6-order microstrip hairpin bandpass filter after substitution.

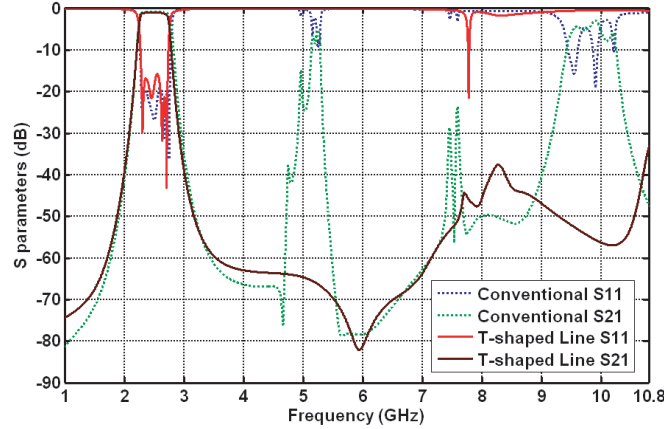


Figure 4: Characteristics of conventional and T-shaped line hairpin bandpass filter.

3. ANALYSE OF THE T-SHAPED LINE AND ITS DESIGN PARAMETERS

The normal transmission line and the T-shaped line are contrasted in Figure 2(b). Suppose the characteristic impedance of transmission line is Z_0 and its electrical length is θ_0 . The characteristic impedance of the connected line and open stub of T-shaped line are respectively Z_1 and Z_2 , and their electrical length are respectively θ_1 and θ_2 .

The $ABCD$ matrix of the normal transmission line is

$$M_0 = \begin{bmatrix} \cos \theta_0 & jZ_0 \sin \theta_0 \\ \frac{j \sin \theta_0}{Z_0} & \cos \theta_0 \end{bmatrix}. \quad (1)$$

The open stub T-shaped line consisted of two side connected lines and one open stubs. If the discontinuity of T shaped line and the open end effect of open stub are ignored, their $ABCD$ matrix are respectively

$$M_1 = \begin{bmatrix} \cos \theta_1 & jZ_1 \sin \theta_1 \\ \frac{j \sin \theta_1}{Z_1} & \cos \theta_1 \end{bmatrix}, \quad M_2 = \begin{bmatrix} 1 & 0 \\ \frac{j \tan \theta_2}{Z_2} & 1 \end{bmatrix}. \quad (2)$$

Considering the cascading of these two network, the equivalent $ABCD$ matrix of open stub T-shaped line can be expressed as

$$M_T = M_1 M_2 M_1 \quad (3)$$

If we substitute the open-stub T-shaped lines for the series transmission line, the following equation must hold true,

$$M_T = M_0 \quad (4)$$

With (1)–(5), we can get

$$Z_1 = \cot \theta_1 \cdot \frac{1 - \cos \theta_0}{\sin \theta_0} \cdot Z_0, \quad Z_2 = \tan \theta_2 \cdot \frac{\cos^2 \theta_1}{\cos 2\theta_1 - \cos \theta_0} \cdot \frac{1 - \cos \theta_0}{\sin \theta_0} \cdot Z_0 \quad (5)$$

Equation (5) is the design relation between the normal transmission line and the open stub T-shaped line. We analyze these two equations in this section:

- (i). The open stubs is to suppress harmonic frequency. The order which suppressed harmonic frequency n is determined by $\theta_2 : \theta_2 = 90^\circ/n$.
- (ii). In substituting, Z_0 , θ_0 and the suppressed harmonic order n is known, Z_1 , Z_2 and θ_1 is to be designed. Therefore there are infinite groups solutions that satisfy (5). Considering the realization of microstrip line (line width should be greater than 0.1 mm and so on), only part of them is reasonable. We can choose suitable value for θ_1 , then Z_1 and Z_2 can be determined.
- (iii). From (5), only $\cos 2\theta_1 - \cos \theta_0 > 0$ makes Z_2 positive. Thus the range of θ_1 can be limited within $0 < \theta_1 < \theta_0/2$. This also denotes that the physical length of the open stub T-shaped line is less than that of the normal transmission line, which insure the compactness of the transformative filter.
- (iv). When $\theta_1 = \theta_0/2$, $Z_1 = Z_0$ and $Z_2 \rightarrow \infty$. The input impedance of open stubs is also run to ∞ , which is equivalent to open circuit. Actually this is the normal transmission line regressively.

4. CONCLUSION

The generalized open stub T-shaped transmission lines is presented to replace the series transmission line of conventional filters in this paper. By this way, we could integrate bandstop characteristics into conventional filter and thus get a bandpass or lowpass filter with ultra stopband as well as a smooth passband and a steep transition band. Moreover, this open-stub T-shaped transmission structure can also make filters more compact. Over 35 dB harmonic frequency suppress and 23.4% size deduction have been achieved. Strong restriction band can be as high as the fourth order harmonic frequency with good passband. The open stub T-shpaed line will have great potential in current microwave and millimeter-wave applications.

REFERENCES

1. Hsieh, L. H. and K. Chang, "Compact, broad-stopband elliptic-function lowpass filters using microstrip stepped impedance hairpin resonators," *IEEE MTT-S International Microwave Symposium*, 1775–1778, Philadelphia, USA, June 2003.
2. Kuo, J. T. and E. Shih, "Microstrip stepped impedance resonator bandpass filter with an extended optimal rejection bandwidth," *IEEE Trans. Microw. Theory Tech.*, Vol. 51, No. 5, 1554–1559, 2003.
3. Kong, Y. W. and S. T. Chew, "EBG-based dual mode resonator filter," *IEEE Microw. Wireless Compon. Lett.*, Vol. 14, No. 3, 124–126, 2004.
4. Ahn, D., J. S. Park, C. S. Kim, Y. Qian, and T. Itoh, "A design of lowpass filter using the novel microstrip defected ground structure," *IEEE Trans. Microw. Theory Tech.*, Vol. 49, No. 1, 86–93, 2001.
5. Zhu, L. and W. Menzel, "Compact microstrip bandpass filter with two transmissstion zeros using a stub-tapped half-wavelength line resonator," *IEEE Microw. Wireless Compon. Lett.*, Vol. 13, No. 1, 16–18, 2003.
6. Kuo, J. T., W. H. Hsu, and W. T. Huang, "Parallel coupled microstrip filters with suppression of harmonic response," *IEEE Microw. Wireless Compon. Lett.*, Vol. 12, No. 10, 383–385, 2002.
7. Lopetegi, C., M. Laso, J. Hernandez, M. Bacaicoa, D. Benito, M. Garde, M. Sorolla, and M. Guglielmi, "New microstrip 'wiggly-line' filters with spurious passband suppression," *IEEE Trans. Microw. Theory Tech.*, Vol. 49, No. 9, 1593–1598, 2001.
8. Gao, J. and L. Zhu, "Investigation on asymmetric parallel-coupled CPW for $\lambda/4$ bandpass filters with broad rejection band," *IEICE Electron. Express*, Vol. 1, No. 11, 1–6, 2004.
9. Quendo, C., E. Rius, C. Person, and M. Ney, "Integration of optimized low-pass filters in a bandpass filter for out-of-band improvement," *IEEE Trans. Microw. Theory Tech.*, Vol. 49, No. 12, 2376–2383, 2001.
10. Manchec, A., C. Quendo, E. Rius, C. Person, and J.-F. Favennec, "Synthesis of dual behavior resonator (DBR) filters with integrated low-pass structures for spurious responses suppression," *IEEE Microw. Wireless Compon. Lett.*, Vol. 16, No. 1, 4–6, January 2006.
11. Tu, W. H. and K. Chang, "Compact second harmonic-suppressed bandstop and bandpass filters using open stubs," *IEEE Trans. Microw. Theory Tech.*, Vol. 54, No. 6, 2497–2502, June 2006.

Simulation of Transmission Characteristics in Columnar of Different Radius Using Magnetic/Metal Materials

Keiko Masuda and Masatoshi Sano

Department of Electrical Engineering, Faculty of Engineering, Tokyo University of Science
1–3 Kagurazaka Shinjyuku-ku, Tokyo 162-8601, Japan

Abstract— The characteristics were analyzed on the three type's structure of the transmission line. The length of transmission line was 6 mm in columnar elements at frequency between 40 GHz from 10 GHz. Type 1 line was the column structure of a single radius. When the radius of the column structure was changed from 150 μm to 5 μm , the bandwidth narrowed from 11.2 GHz to 8 GHz. The frequency of attenuation pole was approximately 24.5 GHz irrespective of radius size. Type 2 line was structure to change a part of the transmission line into the line of small radius. When the length of the line of the small radius was changed from 0 mm to 3 mm, the bandwidth has changed between from 10 GHz to 7.8 GHz. The frequency of attenuation pole has changed between from 21.8 GHz to 24.6 GHz according to the length of the line of the small radius. Type 3 line was structure to exchange the magnetic material into the metal in part of small radius of Type 2. The frequency of attenuation pole was approximately 9 GHz irrespective of the length size. When the length of the line of the small radius was changed from 0 mm to 3 mm, the attenuation pole has changed between from 20.2 GHz to 24.6 GHz. The model designed by using the magnetic material was able to be constant the bandwidth, and to move the attenuation pole in the large range.

1. INTRODUCTION

The circuits are operated in high density at the high frequencies [1, 2]. It is necessary to think the transmission characteristics when designing a circuit at the high frequency.

The transmission characteristics in the high frequency have to examine the idea of the skin effect [3]. It is known that the current flows only to the surface at the high frequency, and the transmission line is handled almost like the thin line. This effect depends on electrical conductivity and relative permeability. The analysis is done by using the electromagnetic field simulator.

The transmission line is designed by varying the length, the radius and the material. The transmission characteristics are analyzed for three type's structure of models. The first type line is the column structure of a single radius. The second type line is structure to change a part of the transmission line into the line of small radius. The thread type line is structure to exchange the magnetic material into the metal in part of the line of small radius. The analytical frequency range was from 10 GHz to 40 GHz.

2. SIMULATION MODEL

The transmission line was designed by varying the radius, the length and the material. The transmission characteristics are analyzed for three type structure of models. The range of the simulation frequency was from 10 GHz to 40 GHz.

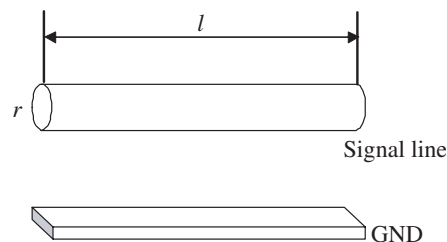


Figure 1: Model of Type 1 line.

2.1. Structure with Single Radius (Type 1 Line)

Type 1 line is shown in Figure 1. Type 1 line was the column structure of a single radius size. The length of the transmission line l was 6 mm, and the radius r made between from 5 μm to 150 μm . The analysis details in Type 1 line is shown in the Table 1. The electrical conductivity σ was 5×10^7 S/m, the relative permeability μ_r was 1.

Table 1: Type 1 line.

Length [mm]	Radius [μm]	Electrical conductivity [S/m]	Permeability
$l = 6$	$r = 5 \sim 150$	5×10^7	1

2.2. Structure with Different Radius (Type 2 Line)

The model is shown in Figure 2. Type 2 line was structure to change a part of the transmission line into small radius. The length of the total of l_1 and l_2 was as same as length of Type 1 line. The radius of the l_1 was r_1 , and the radius of the l_2 was r_2 . The analysis details in Type 2 line is shown in the Table 2. The length of l_2 took the value between from 0 mm to 3 mm, the radius (r_2) was 10 μm . The length of the l_1 took the value $6 - l_2$ [mm], the radius (r_1) was 100 μm .

Table 2: Type 2 line.

	Length [mm]	Radius [μm]	Electrical conductivity [S/m]	Permeability
Part 1	$l = 6 - l_2$	$r_1 = 100$	5×10^7	1
Part 2	$l_2 = 0 \sim 3$	$r_2 = 10$	5×10^7	1

2.3. Structure with Magnetic Material (Type 3 Line)

Type 3 line is shown in Figure 3. Type 3 line was structure to exchange the magnetic material into the metal in part of l_2 in Type 2 line. The analysis defines in Type 3 line is shown in the Table 3. The l_2 used the material to consider the magnetic metal. The electrical conductivity σ of Part 2 was 1×10^7 S/m, the relative permeability μ_r of Part 2 was 600 [4].

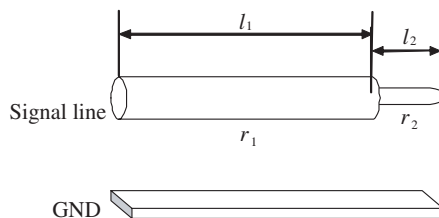


Figure 2: Model of Type 2 line.

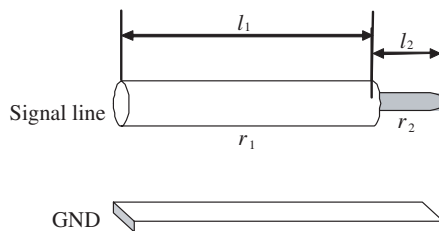


Figure 3: Model of Type 3 line.

3. RESULT

3.1. Structure with Single Radius (Type 1 Line)

Figure 4 shows transmission characteristics, $|S_{11}|$ and $|S_{21}|$. The transmission characteristic of Type 1 line had transmission characteristics like BPF.

Table 3: Type 3 Line.

	Length [mm]	Radius [μm]	Electrical conductivity [S/m]	Permeability
Part 1	$l = 6 - l_2$	$r_1 = 100$	5×10^7	1
Part 2	$l_2 = 0 \sim 3$	$r_2 = 10$	1×10^7	600

$|D_{|s_{11}|}|$ and $|D_{|s_{21}|}|$ referred to the difference between the maximum values and the minimum values. Figure 5 shows $|D_{|s_{11}|}|$ and $|D_{|s_{21}|}|$.

$|D_{|s_{11}|}|$ was about 18 dB of the similar value at each radius.

$|D_{|s_{21}|}|$ in the line with $r = 5 \mu\text{m}$ was 8.4 dB and $|D_{|s_{21}|}|$ with $150 \mu\text{m}$ was 2.9 dB. The difference in $|D_{|s_{21}|}|$ was 5.5 dB.

Figure 6 shows the bandwidth (the width of the frequency of having fallen by -3 dB from the maximum value).

Figure 7 shows attenuation pole (the frequency of the minimum value).

The bandwidth narrowed from 11.2 GHz to 8 GHz as radius decreases from $150 \mu\text{m}$ to $5 \mu\text{m}$. The frequency of attenuation pole was approximately 24.5 GHz irrespective of radius size.

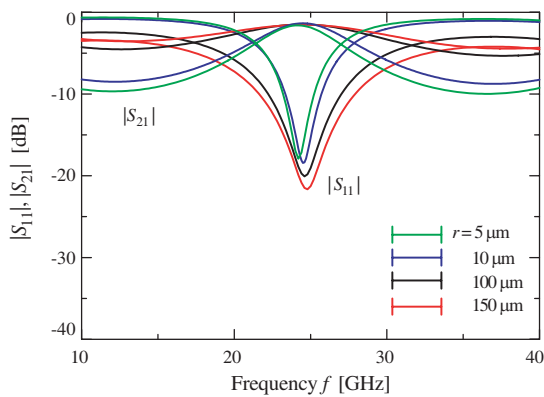


Figure 4: Transmission characteristic, $|S_{11}|$ and $|S_{21}|$.

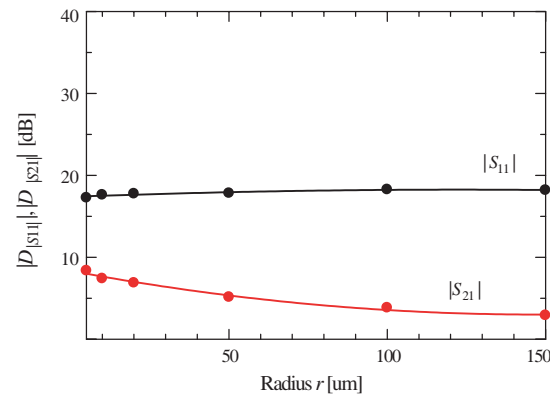


Figure 5: Value of $|D_{|s_{11}|}|$ and $|D_{|s_{21}|}|$.

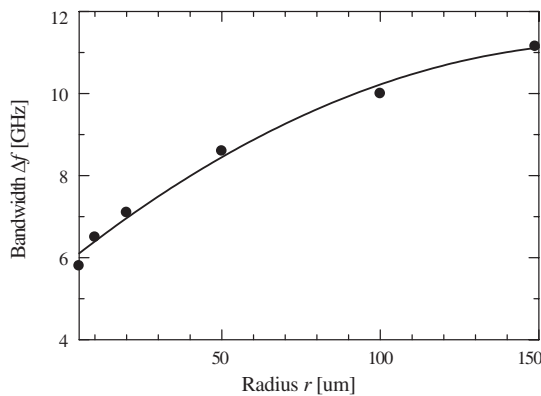


Figure 6: Dependence on the radius in the bandwidth.

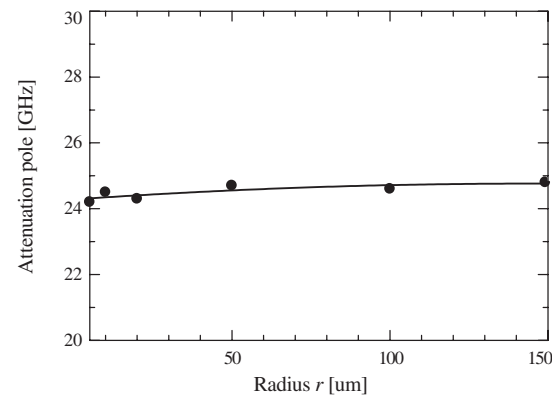


Figure 7: Relationship between radius and attenuation pole.

3.2. Structure with Different Radius (Type 2 Line)

Figure 8 shows transmission characteristics of $|S_{11}|$ and $|S_{21}|$. Figure 9 shows $|D_{|s_{11}|}|$ and $|D_{|s_{21}|}|$.

The value of $|D_{|s_{11}|}|$ had had the maximum value 34.6 dB at the length of $l_2 = 1.5$ mm. The minimum value of $|D_{|s_{11}|}|$ was 8.8 dB at length of $l_2 = 3$ mm.

The value of $|D_{|s_{21}|}|$ increased or decreased between 3.8 dB and 7.1 dB. The value of $|D_{|s_{21}|}|$ was smaller than the value of $|D_{|s_{11}|}|$.

Figure 10 shows the bandwidth. Figure 11 shows the attenuation pole.

When the length of l_2 became from 0 mm to 2.5 mm, the bandwidth became small from 10 GHz to 7.8 GHz. The attenuation poles changed like the quadratic function from 0 mm to 3 mm. The lowest frequency was 21.8 GHz at $l_2 = 1.5$ mm. The attenuation pole has changed between from 21.8 GHz to 24.6 GHz according to the length of the l_2 .

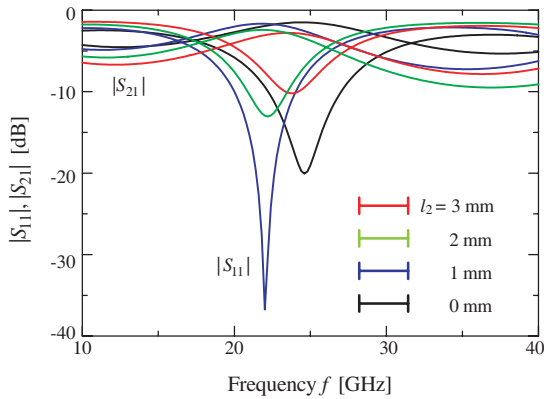


Figure 8: Transmission characteristic, $|S_{11}|$ and $|S_{21}|$.

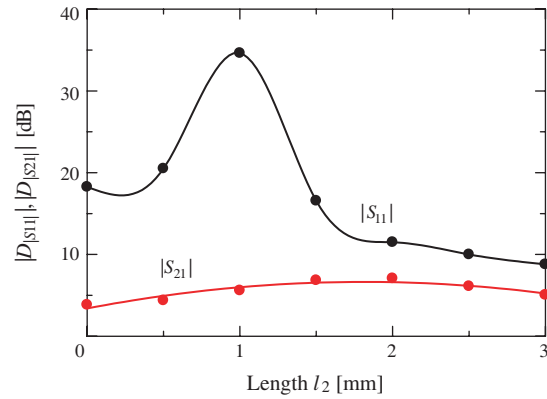


Figure 9: Value of $|D_{|s_{11}|}|$ and $|D_{|s_{21}|}|$.

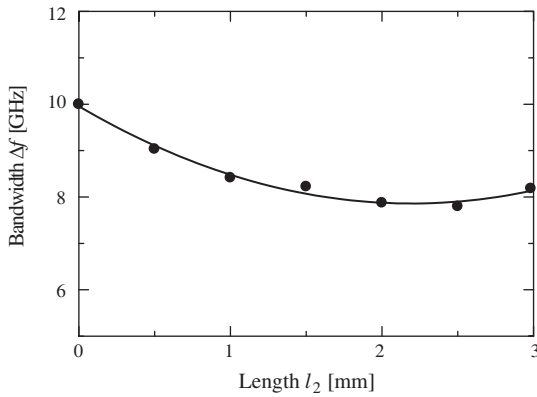


Figure 10: Dependence on the length in the bandwidth.

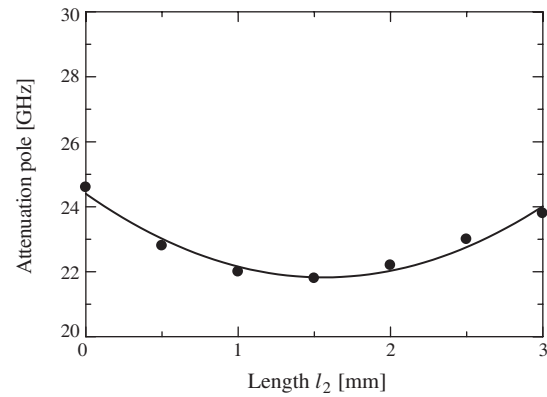


Figure 11: Relationship between length and attenuation pole.

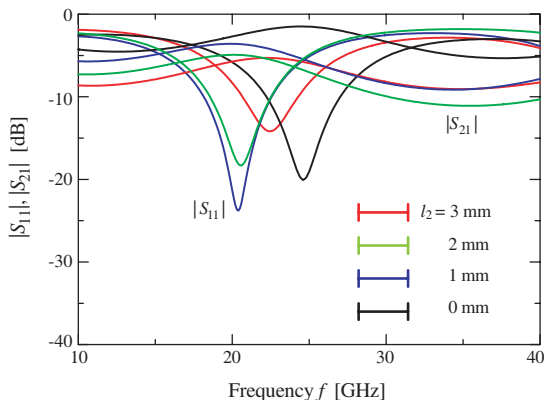


Figure 12: Transmission characteristic, $|S_{11}|$ and $|S_{21}|$.

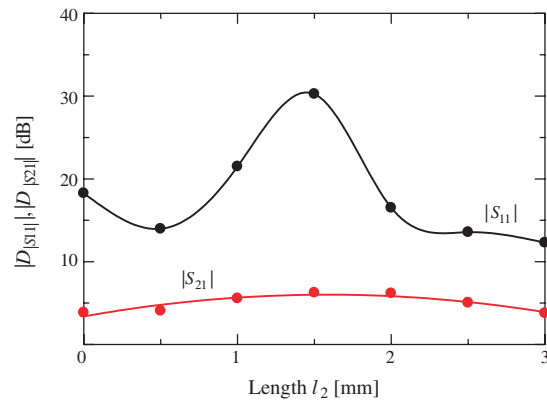


Figure 13: Value of $|D_{|s_{11}|}|$ and $|D_{|s_{21}|}|$.

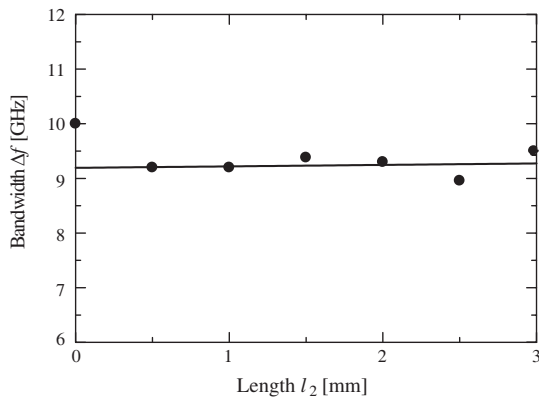


Figure 14: Dependence on the length in the bandwidth.

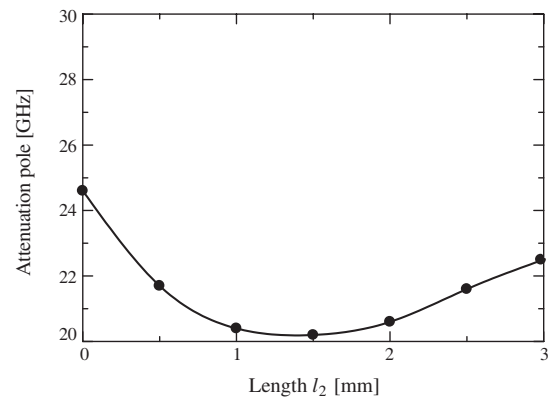


Figure 15: Relationship between length and attenuation pole.

3.3. Structure with Magnetic Material (Type 3 Line)

Figure 12 shows transmission characteristics, $|S_{11}|$ and $|S_{21}|$. Figure 13 shows $|D_{|s11|}|$ and $|D_{|s21|}|$.

The value of $|D_{|s11|}|$ had had the maximum value 30.2 dB at the length of $l_2 = 1.5$ mm. The minimum value of $|D_{|s11|}|$ was 12.3 dB at length of $l_2 = 3$ mm.

The value of $|D_{|s21|}|$ increased or decreased between 3.8 dB and 6.2 dB. The value of $|D_{|s21|}|$ was smaller than the value of $|D_{|s11|}|$.

Figure 14 shows the bandwidth. Figure 15 shows the attenuation pole.

When the length of l_2 was 0.5 mm or more, the bandwidths were the similar value about 9.2 GHz. The lowest frequency was 20.2 GHz at $l_2 = 1.5$ mm. When the length of l_2 was changed from 0 mm to 3 mm, the attenuation pole has changed between from 20.2 GHz to 24.6 GHz.

4. CONCLUSION

The characteristics were analyzed on the three type's structure of the transmission line.

The transmission line of Type 1 was the column with a single radius. When the radius of the column structure was changed from 150 μm to 50 μm , the bandwidth narrowed from 11.2 GHz to 8 GHz. The frequency of attenuation pole was approximately 24.5 GHz irrespective of radius size.

The transmission line of Type 2 was structure to change a part of Type 1 line into the column of small radius. When the length of the column line of the small radius was changed from 0 mm to 3 mm, the bandwidth has changed between from 7.8 GHz to 10 GHz. The frequency of attenuation pole has changed between from 21.8 GHz to 24.6 GHz according to the length of the small radius.

The transmission line of Type 3 was structure to exchange the magnetic material into the metal in part of small radius of Type 2 line. The frequency of attenuation pole was approximately 9 GHz irrespective of the length size in line of the small radius. When the length of line of the small radius was changed from 0 mm to 3 mm, the attenuation pole has changed between from 20.2 GHz to 24.6 GHz. The model designed by using the magnetic material was able to be constant the bandwidth, and to move the attenuation pole in the large range.

REFERENCES

1. Hong, S. and K. Chang, "Stub-tuned microstrip bandpass filters for millimeter-wave diplexer," *IEEE Microwave and Wireless Components Letters*, Vol. 15, No. 9, 582–584, 2005.
2. Wang, H., L. Zhu, and W. Menzel, "Ultra-wideband bandpass filter with hybrid microstrip/CPW structure," *IEEE Microwave and Wireless Components Letters*, Vol. 15, No. 12, 844–846, 2005.
3. He, J., N. S. Nahman, and S. M. Riad, "A causal skin-effect model of microstrip lines," *IEEE MTT-S Digest*, Vol. OF-2-6, 1993.
4. Bozorth, R. M., *Ferromagnetism*, IEEE Press, 1951.

Reservation Based Call Admission Control in Wireless Communication

Malay Ranjan Tripathy¹, Ashish Sharma², and Rachid Talhi³

¹Department of Electronics and Communication Engineering
Jind Institute of Engineering and Technology
Panipat Road, Jind 126102, India

²Department of Information Technology, Maharaja Agrasen Institute of Technology
Rohini Sector 22, Delhi 110086, India

³University of Tours and CNRS-UMR 6115, Orleans 45071, France

Abstract— This work presents reservation based call admission control algorithms and a comparative study on them. Guard Channel Schemes fall under call admission control strategies for 2G Systems. The basic Guard Channel Allocation algorithm is bound to have certain limitations. Approximation Method Guard Channel Scheme provides an edge over the basic algorithm. 3G cellular networks is highly influenced by common channel interference in the air interface. Interference Based Channel Assignment Schemes deal with this to increase the system capacity.

1. INTRODUCTION

Call admission control is a key element in the provision of guaranteed quality of service in wireless networks. It is a technique to provide QoS in a network by restricting the access to network resources. Simply stated, it is a mechanism that accepts a new call request provided there are adequate free resources to meet the QoS requirements of the new call request without violating the committed QoS of already accepted calls. Dropping a call in progress is more annoying than blocking a new call request. Hence handoff calls are typically given higher priority. There are two categories of Call Admission Control (CAC) schemes in cellular networks:

- 1) Deterministic CAC
- 2) Stochastic CAC

The CAC schemes, which are investigated in this paper, fall in the stochastic category.

- Channel borrowing scheme — In this when a cell has utilized all its assigned resources it borrows from the neighboring cell. However, this introduces a problem of channel locking [5] according to which the number of cells, which could not reuse it, increases.
- Queuing scheme — This also had a limitation of waiting time i.e., if the waiting time becomes more then the dropping probability again increases [3].
- Reservation scheme — In this policy, a set of channels called the guard channels are permanently reserved for handoff calls. In this, we could have static as well as dynamic reservation. A static reservation typically results in poor resource utilization. To deal with this problem, several dynamic reservation schemes were proposed in which the optimal number of guard channels is adjusted dynamically based on the observed traffic load and dropping rate in a control time window ([3, 4]).

2. CALL ADMISSION CONTROL ALGORITHMS

Algorithm 1: Guard Channel Allocation for HAP (High Altitude Platform) Networks

Aim: *This CAC scheme gives preferential treatment to high priority calls, such as handoff calls, by pre-reserving the channel guards known (Guard Channel in terms of bandwidth). An approximation method is proposed to calculate the channel guards, which keep the dropping probability of hand-off calls under predefined threshold while approaching the maximum bandwidth reservation. The algorithm takes into account the general operating scenario of HAP networks.*

In a particular network, guard channel is the bandwidth that is reserved for every traffic class thereby giving priority to handoff calls as compared to new calls. Here by reserving guard channel, we prevent the acceptance of new calls and leave available resource for handoff calls when the resource utilization is high. In our approach, we consider HAP, which could be airships or solar powered airplanes operating at 20 km above ground. To support communication between adjacent

platforms; each HAP should have a *Switching Device* and *Inter Platform Links*. IPL extends the system coverage area and reduces the need for terrestrial infrastructure. Arrival and departure of new calls is considered as single event while handoffs occur in batches. For the a mobile wireless network consisting of new calls, handoff calls and QoS considerations, the most widely used CAC scheme is Guard Channel scheme that was proposed in mid 80's. A mobile system (HAP network) may have several traffic classes and each traffic class will have separate Guard channel (G_i). They have minimum bandwidth guaranteed to it (b_i) and the total bandwidth reserved at any time (t) could be $\sum n_i(t)b_i$. Thus the algorithm to handle calls for such network:

Algorithm [1]: If incoming call is new call then it will be checked whether *the bandwidth requirement of the call is less* than then the available bandwidth in the traffic class. If it is, then the call will be accepted else it *would be rejected*. The available bandwidth is calculated by, $G_i - \sum n_i(t)b_i$.

If incoming call is handoff call then again it will be checked whether *the bandwidth required by handoff call difference is less then the available bandwidth*. If yes then call will be accepted else it will be rejected.

Algorithm 2: Approximation Method Guard Channel Scheme

Aim: The above approach was based on multi dimensional Markov Chain approach had disadvantages such as complicated process, CPU time consuming, large domain of G. Hence, we moved towards approximation method. This method was based on Transformation approach.

In this, we have transformed from multidimensional approach to single dimension.

The transformation rules ([2]) are,

Parameters	From	To
Minimum bandwidth requirement	b_j	b_i
Holding time	$1/\mu_j$	$1/\mu_i$
Arrival rate for new calls	α_j	$\alpha_{ji} = (b_j\mu_i/b_i\mu_j) * \alpha_j$
Arrival rate for handoff calls	$\alpha^H m_j$	$\alpha_{ji}^H = (b_j\mu_i / (b_i\mu_j + \mu^H)) * \alpha^H m_j$

Further calculations gives the dropping probability, which is:

$$P_i^d(H) = \sum_{j=1}^{C/b_i} p_i(j, H) P_i^d(j) \quad (1)$$

In this approach, we take ' H_i ' channel guard that specifies the number of channels. After every transformation we use binary search algorithm to find the optimal guard channel out of the array of guard channels.

Algorithm: We define a function here ([1]),

Function Binary Search Guard (begin, end)

Here we require $\text{begin} \leq \text{end}$. If $\text{begin} = \text{end}$, i.e., there is one guard channel then we check whether the $P^d(H) \leq d$ (threshold dropping probability). If yes then we return to begin else we quit. If $\text{begin} < \text{end}$, then we divide the ascending order sorted array in the exactly two halves. If the dropping probability of the guard channel at the middle of the array is less then the threshold probability then we further search for the optimal guard channel in the later half else we would have searched in the former half of the array. This search continues until $P_i^d(H) == d$.

At this, we get the optimal channel guard and return H i.e., the channel guard which when multiplied with minimum bandwidth of the class gives the *optimal guard channel*.

Algorithm 3: Interference based Channel Assignment Algorithm

Aim: This CAC scheme gives preferential treatment to high priority calls, such as handoff calls, by pre-reserving a certain amount of channel margin against the interference effect. It is called the interference guard margin (IGM) scheme.

Guard channel allocation schemes are not applicable to 3G WCDMA systems where system capacity is limited by maximum tolerable interference in the system. Thus, an interference based channel assignment scheme is used. The dynamic call admission control scheme proposed in [2] is based on prior reservation of a certain amount of IGM (interference guard margin) for high priority calls. The resource reservation estimation module residing in the base station dynamically adjusts IGM. This scheme uses load curve to estimate the load an interference increase. Load curve makes it possible to consider different interference increments introduced by heterogeneous traffic with various service rates (i.e., the data rate).

The capacity of a CDMA system is limited by the total interference the system can tolerate. Such a system is referred to as the interference-limit system. Each additional active mobile user will increase the overall level of interference. Call blocking occurs when the overall interference level reaches a certain level above the background noise. The system capacity depends on system parameters as well as the amount of the interference increment that each active mobile user brings in.

Interference increment due to user I ,

$$\Delta I_i = \frac{\Delta \rho_i \cdot I_{\text{total}}}{(1 - \rho)} \quad (2)$$

where $\Delta \rho_i$ = load factor increment due to user I , I_{total} = total received power at base station, ρ = total load factor (i.e., $\sum \Delta \rho_i$).

A certain amount of interference-based guard margin (IGM) is pre-reserved for the use of high priority calls. For a new call to be admitted, the total interference level should not exceed the upper bound of the interference with threshold I_{th} that the system can tolerate. In addition to the constraint of I_{th} , a lower priority call should comply with the augmented constraint I'_{th} .

$\text{IGM} = I_{\text{th}} - I'_{\text{th}}$. Before admitting a new or handoff call, j , in a cell, this dynamic resource reservation estimation scheme estimates the interference guard margin IGM based on a weighted sum of estimated minimum interference-increments according to the traffic profile for each neighboring active calls.

$\text{IGM} = \alpha \sum \omega_i \cdot I_{\text{min},I}$ where α = an empirical factor which capture the facts of either some calls are terminated before they can arrive or calls in current cell left and release the resource, ω_i = weighting factor for each call is a function of the mobility of user I , M_i , and the distance from user I to base station, d_i . The value of ω_i is $\omega_i \propto (M_i/d_i)$.

The algorithm [2] uses IGM in the following manner:

If Incoming calls are new calls and are non-rate adaptive and If $(I_{\text{current}} + \Delta I_i) < (I_{\text{th}} - \text{IGM}_{\text{new}})$, call is admitted with rate R_i . If calls are rate adaptive and if $(I_{\text{current}} + \Delta I_{\text{max},I}) < (I_{\text{th}} - \text{IGM}_{\text{new}})$, call is admitted with rate $R_{\text{max},i}$. Else if $(I_{\text{current}} + \Delta I_{\text{max},I}) < (I_{\text{th}} - \text{IGM}_{\text{new}})$, call is admitted with rate $R_{\text{max},i}$. If none of these conditions are met the call is discarded. The same procedure is followed for handoff calls using the IGM for handoff calls.

3. COMPARITIVE ANALYSIS

COMPARISON FACTORS	ALGORITHM NAME		
	GUARD CHANNEL CALL ADMISSION POLICY	GUARD CHANNEL APPROXIMATION (TRANSFORMATION)	INTERFERENCE BASED CHANNEL ALLOCATION
Application Area	2G technologies (e.g. TDMA/FDMA)	2G technologies	3G technologies (e.g., WCDMA)
Approach Used	Based on multidimensional Markov Chain [1]	Transformation of multidimensional Markov channel into single dimensional Markov channel [1, 7]	Interference-based guard margin (IGM) is prereserved for the use of high priority calls. IGM is dynamically adjusted by the RRE module [2].
Constraints to be Handled	Hard Constraints	Hard Constraints	Soft Constraints
Efficiency	Finding optimal G is very complicated process that requiring heavy CPU-time consuming due to the large multi-dimensional Markov chain and large domain of	If we considered the estimation of simulation is the actual value of the optimal channel guard, then the comparison shows that most of the model estimation has absolute error within 0:05 and	Higher system utilization for traffic with the rate-adaptive capability than that without the rate-adaptive capability under heavy traffic loads [2].

	G. In order to have simple method to approximate optimal solution, we use the transformation approach [1, 6].	the remaining part just exceeds the 0:05 but not much. Hence, we say that approximation method is fairly accurate [1].	The system can provide calls with a degraded service in terms of lower bandwidth when the system is congested, thus increasing the overall system utilization.
Goal of the Algorithm	To have proper call admission policy and the calls are accepted if and only if it full fills the criteria of guard channel of its corresponding class. To give more priority to the hand-off calls	To overcome the disadvantages of the earlier approach and to find the optimal G in such a way that the bandwidth reservation is maximum and the P^d is less than the threshold dropping probability. It must also ensure that it is meeting all the requirements of QOS.	To investigate the QoS performance in terms of the objective function J (in terms of the weighted sum of the rejection probability for each class within each service attribute). The performance of the non-priority scheme, the fixed guard margin scheme as well as the dynamic IGM scheme with the associated resource reservation estimation module were compared [2].
Qos	In this case there are several traffic classes each with different guard channel, minimum bandwidth etc. This is based on multi dimensional markov channel approach. Hence, maintaining QOS in this case is quite difficult [1].	The optimal set of guard channels G is the one that gives maximum reserved bandwidth while its dropping probability is under the dropping threshold. The optimal G calculated by the simulation and the model approximation is approximately the same [1].	Fixed and dynamic IGM schemes outperform the non-priority scheme in the overall objective function J . Significantly reduces the handoff dropping probability without much increase in the new call blocking probability, under light as well as heavy traffic load conditions [2].
Suggested Enhancements	To reduce the CPU time consumption and find the optimal G faster.	To find Optimal G there is no specific formula. Even at the time of finding the efficiency we had to try out different simulations. We could thus find a stable formula for it. This is applicable to 2G technologies however by bringing further changes we should try to make it applicable for higher generation technologies also.	Multi-user detection (MUD) technique and the soft handoff scheme to achieve better QoS support.

4. CONCLUSION

In this paper, a comparative study on reservation based call admission control is carried out. Guard channel call admission scheme is for 2G technologies but has limitations. This is based on multi dimensional Markov channel approach. Hence, maintaining QOS in this case is quite difficult. The other Guard channel approximation scheme is also for 2G technologies. It shows hard constraint. However, it has improvements in comparison to earlier scheme in 2G segments. Interference based channel allocation scheme is better than others. It has soft constraint. It is used for 3G technologies. Interference-based guard margin (IGM) is pre-reserved for the use of high priority calls. It shows higher system utilization for traffic with the rate-adaptive capability. The system can provide calls with a degraded service in terms of lower bandwidth when the system is congested, thus increasing the overall system utilization.

REFERENCES

1. Luong, D. D., A. P. M. Tran, and T. V. Do, “Guard channel CAC algorithm for high altitude platform (HAP) networks,” *HET-NETs-2006*, UK, 22/1–22/10, Sep. 11–13, 2006.
2. Chen, H., S. Kumar, and C. C. J. Kuo, “Dynamic call admission control and resource reservation with interference guard margin (IGM) for CDMA systems,” *IEEE Wireless Communication and Networking*, Vol. 3, No. 20, 1568–1572, 2003.
3. Ghaderi, M. and R. Boutaba, “Call admission control in mobile cellular networks: A comprehensive survey,” *Wireless Communications and Mobile Computing*, Vol. 6, No. 1, 69–93, 2005.
4. Katzela, I. and M. Naghshineh, “Channel assignment schemes for cellular mobile telecommunication systems: A comprehensive survey,” *IEEE Personal Communication Magazine*, 10–29, Jun. 1996.
5. Olivré, A., “Call admission control,” Chapter 3, a dissertation submitted to the University of Dublin.
6. Poisson Process — Wikipedia, the free encyclopedia, http://en.wikipedia.org/wiki/Poisson_process.
7. http://www.dartmouth.edu/~chance/teaching_aids/books_articles/probability_book/Chapter-11.pdf for Markov Chain.

3D Discrete Wavelet Transform VLSI Architecture for Image Processing

Malay Ranjan Tripathy¹, Kapil Sachdeva¹, and Rachid Talhi²

¹Department of Electronics and Communication Engineering
Jind Institute of Engineering and Technology, Jind, Haryana, India

²University of Tours and CNRS-UMR 6115, Orleans 45071, France

Abstract— In this paper, we propose an improved version of lifting based 3D Discrete Wavelet Transform (DWT) VLSI architecture which uses bi-orthogonal 9/7 filter processing. This is implemented in FPGA by using VHDL codes. The lifting based DWT architecture has the advantage of lower computational complexities transforming signals with extension and regular data flow. This is suitable for VLSI implementation. It uses a cascade combination of three 1-D wavelet transform along with a set of in-chip memory buffers between the stages. These units are simulated, synthesized and optimized for Spartan-II FPGA chips using Active-HDL Version 7.2 design tools. The timing analysis tools of this (Active-HDL), reports the frequency above 100 MHz and ensures 100% hardware utilization.

1. INTRODUCTION

Recent advances in medical imaging and telecommunication systems require efficient speed, resolution and real-time memory optimization with maximum hardware utilization [1–3]. The 3D Discrete Wavelet Transform (DWT) is widely used method for these medical imaging systems because of perfect reconstruction property. DWT can decompose the signals into different sub bands with both time and frequency information and facilitate to arrive at high compression ratio. DWT architecture, in general, reduces the memory requirements and increases the speed of communication by breaking up the image into the blocks.

Recently, a methodology for implementing lifting based DWT has been proposed because of lifting based DWT has many advantages over convolution based one [4–6]. The lifting structure largely reduces the number of multiplication and accumulation where filter bank architectures can take advantage of many low power constant multiplication algorithms. FPGA is used in general in these systems due to low cost and high computing speed with reprogrammable property [3].

In this paper, we present a brief description of 3D DWT, lifting scheme and filter coefficients in Section 2. Section 3 discusses architecture of 3D DWT processor and outlines the results. Finally, brief summaries are given in Section 4 to conclude the paper.

2. 3D DISCRETE WAVELET TRANSFORM

2.1. 3D Discrete Wavelet Transform

The 3D DWT can be considered as a combination of three 1D DWT in the x , y and z directions, as shown in Fig. 1. The preliminary work in the DWT processor design is to build 1D DWT modules, which are composed of high-pass and low-pass filters that perform a convolution of filter coefficients and input pixels. After a one-level of 3D discrete wavelet transform, the volume of image is decomposed into HHH, HHL, HLH, HLL, LHH, LHL, LLH and LLL signals as shown in the Fig. 1 [3].

2.2. Lifting Scheme

The basic idea behind the lifting scheme is very simple; try to use the correlation in the data to remove redundancy [4, 5]. First split the data into two sets (split phase) i.e., odd samples and even samples as shown in Fig. 2. Because of the assumed smoothness of the data, we predict that the odd samples have a value that is closely related to their neighboring even samples. We use N even samples to predict the value of a neighboring odd value (predict phase). With a good prediction method, the chance is high that the original odd sample is in the same range as its prediction. We calculate the difference between the odd sample and its prediction and replace the odd sample with this difference. As long as the signal is highly correlated, the newly calculated odd samples will be on the average smaller than the original one and can be represented with fewer bits. The odd half of the signal is now transformed. To transform the other half, we will have to apply the predict step on the even half as well. Because the even half is merely a sub-sampled version of the

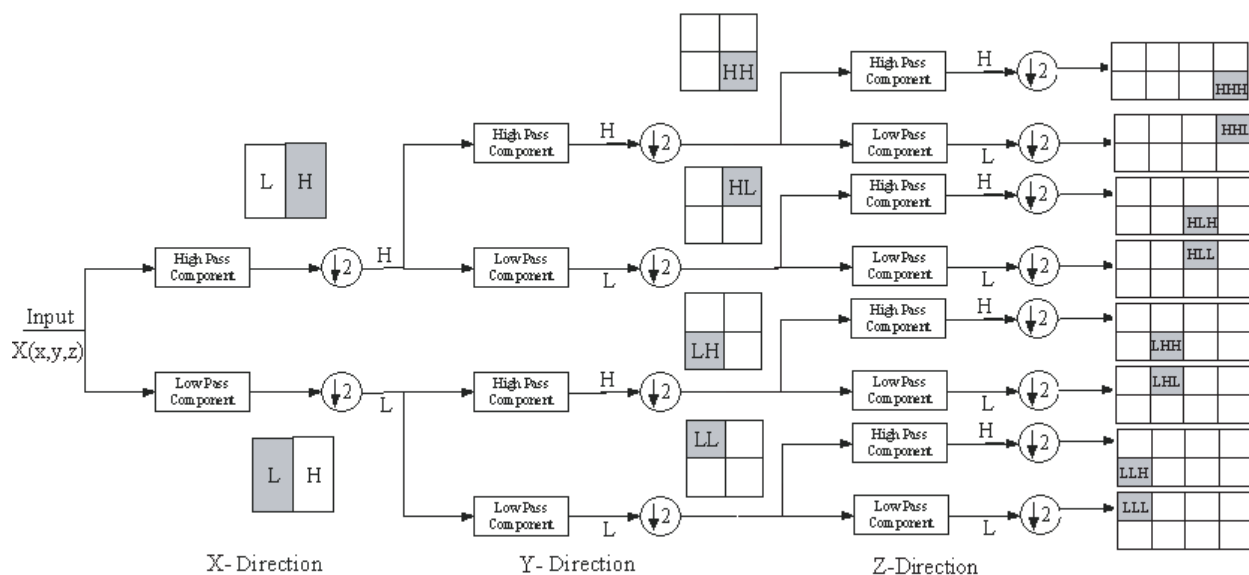


Figure 1: One-level 3D DWT structure.

original signal, it has lost some properties that we might want to preserve. In case of images we would like to keep the intensity (mean of the samples) constant throughout different levels. The third step (update phase) updates the even samples using the newly calculated odd samples such that the desired property is preserved. Now the circle is round and we can move to the next level. We apply these three steps repeatedly on the even samples and transform each time half of the even samples, until all samples are transformed.

2.3. Rationalization of Filter Coefficients

As already stated lifting scheme is one of the most efficient algorithms for the implementation of discrete wavelet transform. But one of the major shortcomings with this scheme is that the lifting coefficients obtained for the implementation of bi-orthogonal 9/7 wavelet transformation are irrational numbers [7, 8]. Hence the direct irrational coefficient implementation requires lot of hardware resources and the processing time at the cost of slight improvement in the compression performance. On the other hand, lower precision in filter coefficients results in smaller and faster hardware at the cost of compression performance. In addition to this rationalization also determines other critical hardware properties such as throughput and power consumption. Hence it is suggested that they should be optimally rationalized without much affecting the compression performance.

Table 1 shows the irrational and approximated rational counterpart for 9/7 filter which are considered as a very good alternative to irrational coefficients. When these coefficients are applied to image coding, the compression performance is almost same as that of irrationalized filter coefficient implementation, while the computational complexity is reduced remarkably.

The heart of 3-D DWT implementation is designing of 1-D processor which is clearly elaborated in Fig. 4. The different lifting coefficients can be easily obtained for Daubechies 9/7 filter by factorization of poly phase matrix. Fig. 3 shows the implementation of 9/7 lifting scheme. This figure is direct implementation of Fig. 2 for the required scheme. When the signal passes through various steps, it is split into three separate one dimensional transforms, the high pass component

Table 1: Irrational and rational lifting coefficients for 9/7 wavelet transform.

	Irrational value	Rational value
α	-1.5861343420...	-3/2
β	-0.0529801185...	-1/16
γ	0.8828110755...	4/5
δ	0.4435068520...	15/32
ζ	1.1496043988...	$4\sqrt{2}/5$

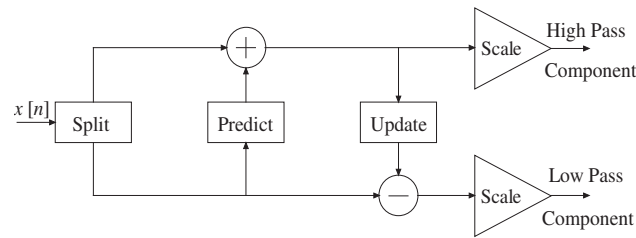


Figure 2: The lifting scheme: Split, predict, update and scale phases.

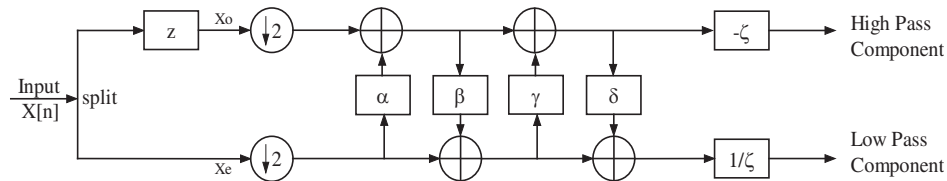


Figure 3: 1-D lifting scheme of daubechies 9/7 for forward wavelet DWT.

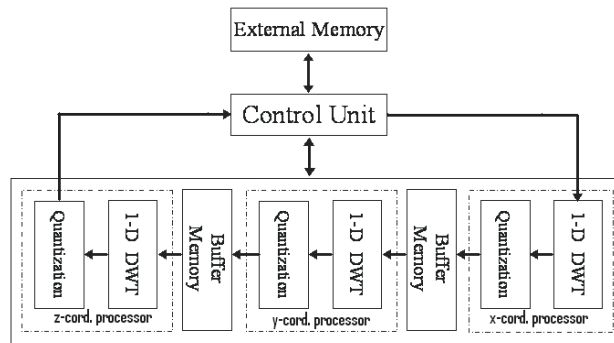


Figure 4: 3-D DWT processor architecture.

(HHH) and a low pass component (LLL). Because of sub sampling the total number of transformed coefficients is same as that of original one. These transformed coefficients are then processed by x -coordinate Processor, which have the same architecture as that of y and z -processor, to complete 3-D transformation.

The bi-orthogonal 9/7 wavelet can be implemented as four lifting steps followed by scaling; requires that the following equations be implemented in hardware.

$$x_1[2n+1] \leftarrow x[2n+1] + \alpha \{x[2n] + x[2n+2]\} \quad (1)$$

$$x_2[2n] \leftarrow x[2n] + \beta \{x_1[2n+1] + x_1[2n-1]\} \quad (2)$$

$$x_3[2n+1] \leftarrow x_1[2n+1] + \gamma \{x_2[2n] + x_2[2n+2]\} \quad (3)$$

$$x_4[2n] \leftarrow x_2[2n] + \delta \{x_3[2n+1] + x_3[2n-1]\} \quad (4)$$

$$x_5[2n+1] \leftarrow 1/\zeta \{x_3[2n+1]\} \quad (5)$$

$$x_6[2n] \leftarrow \zeta \{x_4[2n]\} \quad (6)$$

The original data to be filtered is denoted by $x[n]$; and the 1-D DWT outputs are the detail coefficients $x_5[n]$ and approximation coefficients $x_6[n]$. The lifting step coefficients α , β , γ and δ and scaling coefficient ζ are constants given by Table 1. The above equations are implemented on VHDL to obtain the coefficients $x_5[n]$ and $x_6[n]$. These coefficients correspond to H and L respectively. Now these coefficients are passed through the 1-D processor 3 times. Where, z -coordinate processor gives the final output as the eight subsets of original image as shown in Fig. 1. These coefficients are then stored in external memory in the form of binary file. For the multiple level of decomposition this binary file can be invoked iteratively to obtain further sublevels.

3. RESULTS AND DISCUSSION

The proposed 3-D DWT algorithm based on 9/7 Daubechies filter using lifting scheme is designed and implemented using Active-HDL Version 7.2 design tools. The entire code is written in VHDL and compilation of code is done on same simulator. The whole code is developed using structural based design to tailor the hardware utilization and delay at each step.

In case of 1-D DWT, one pixel per clock cycle is taken as input. As soon as five pixels are taken as input, the x -coordinate processor (shown in Fig. 4) starts working. Although total nine pixels are required for generation of coefficient set (i.e., one high pass and one low pass) but because of applied boundary extension, the x -coordinate processor starts processing after five clock cycles. In this case, because of boundary extension, the left hand side extended (two pixel) data is same as that of right hand side. Hence only five pixels are needed to start the computation. The results of 1-D DWT are presented in Fig. 5 for clear elaboration. Fig. 6 shows quantized output of the processor which can be verified along with these waveforms (shown in Fig. 5). Both the high pass and low pass components are quantized in such a way that output is only eight bit wide.

This will help in easier cascading of the y -coordinate processor and z -coordinate processor. Fig. 5 and Fig. 6 clearly show the different outputs generated by 1-D processor which are in accordance with Equations (1)–(6). The different waveforms have their names written against it.

3-D DWT is simple extension of 1-D DWT. The input data in case of 1-D DWT (x -coordinate processor), picked from image file is in binary format. Once it generates the output set of coefficients it stores the result into buffer memory. After the sufficient number of coefficients are collected the y -coordinate processor starts working and it stores its results again in another buffer memory. The similar process is also followed in the case of z -coordinate processor. The output of z -coordinate processor is the final coefficient set (i.e., high pass and low pass coefficient set).

The overall memory requirement is of the order of N where N is number of pixels present in one column. This is because in the output file one line is written at a time and hence we have to collect all the coefficients in one column, which will become row when transposed, and store it in the output binary file at a time.

The other modules which we have implemented in VHDL are different adders and shifters which are basic building blocks of multipliers. The different multipliers implemented are α , β , γ , δ , ζ and $1/\zeta$ multipliers. All these codes are synthesizable individually and they are implemented via shift-add operation. The multipliers are implemented using structural design approach. These all multiplier blocks are cascaded together to obtain the overall 1-D DWT implementation. The size of input that the each multiplier accepts, and the output it generates is different for each multiplier. This size is decided according to the architecture requirement.

In the whole implementation of multiplier modules, 2's compliment is used as standard for data

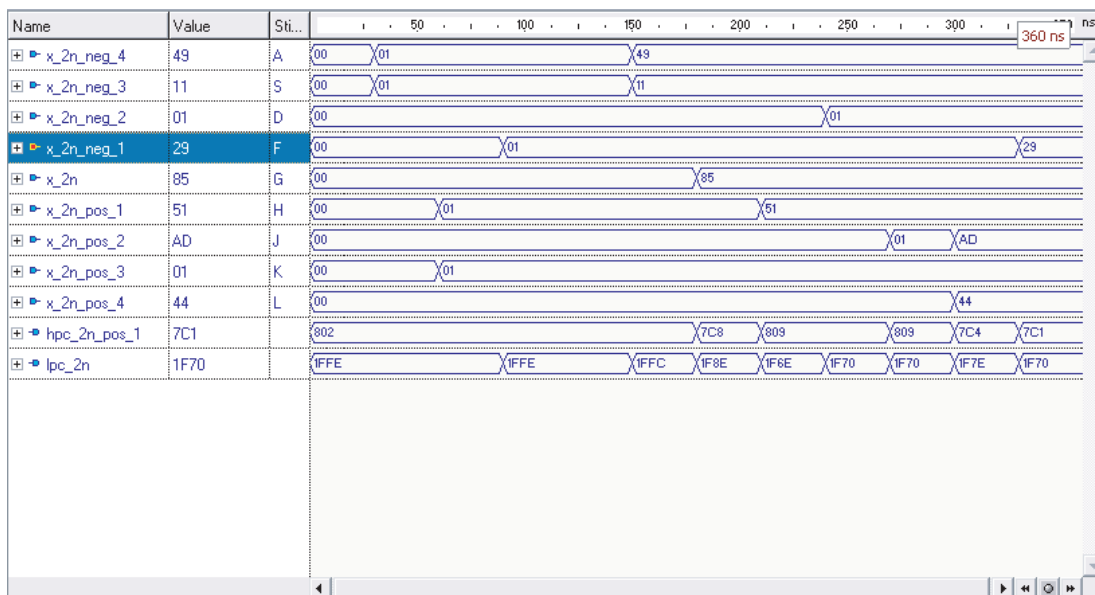


Figure 5: Waveform for 1-D DWT.

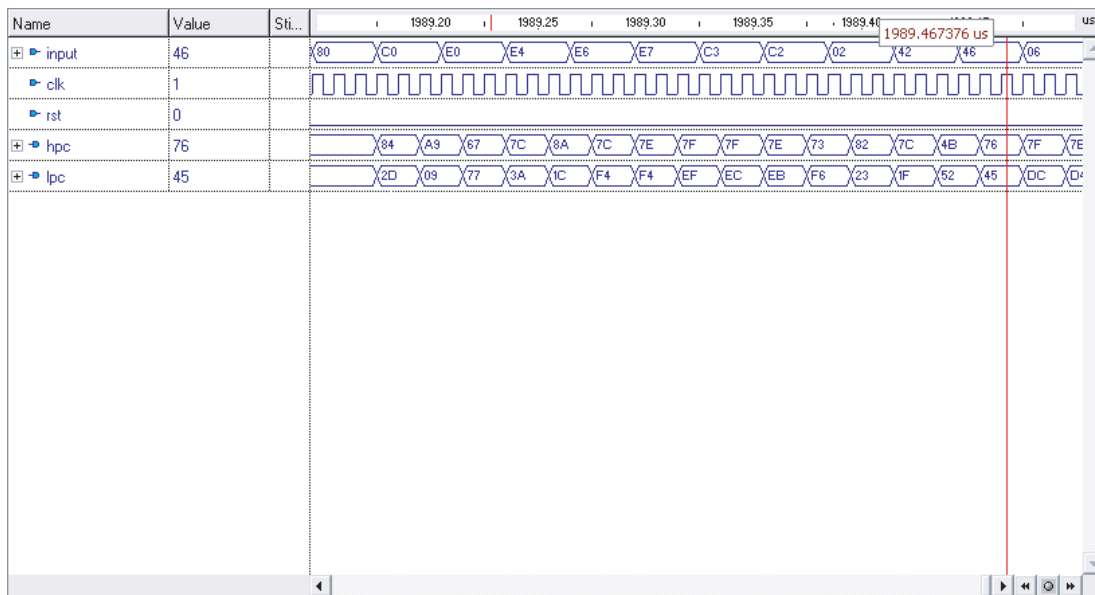


Figure 6: Waveform for 1-D DWT quantization.

representation and multiplication. Wherever it is required to divide the negative number, the number is first converted into positive number, divided, and again converted back into the negative number. This approach is adopted because it requires minimal hardware (since we have to take 2's complement only for two times, one for converting negative number into positive number and other for converting it back into negative number after division) as compared to other implementations.

Proposed 9/7 lifting scheme utilizes only 42% of the total resources available of the Spartan-II chip (50 K). The chip used for the implementation is XC2S50TQ144-5. The memory requirement for this kind of architecture and data flow is only N (i.e., the length of the column required for the storage of the DWT coefficients) for the input image size of $N \times N \times N$. The maximum clock frequency reported by the timing analysis tool is more than 100 MHz.

4. CONCLUSION

In conclusion, the proposed lifting based 3D DWT architecture can save hardware cost while being capable of high throughput. This 3D DWT processor makes it possible to map sub filters onto one Xilinx FPGA. Such a high speed processing ability is expected to offer potential for real-time 3D imaging.

REFERENCES

1. Daubechies, I., "Ten lectures on wavelets," *SIAM*, Philadelphia, 1992.
2. Mallat, S. G., "A theory for multiresolution signal decomposition: The wavelet representation," *IEEE Transactions on Pattern Analysis and Machine Intelligence*, Vol. 11, No. 7, 674–693, July 1989.
3. Jiang, R. M. and D. Crookes, "FPGA implementation of 3D discrete wavelet transform for real-time medical imaging," *ECCTD*, 519–522, August 2007.
4. Sweldens, W., "The lifting scheme: A custom-design construction of biorthogonal wavelets," *Applied and Computational Harmonic Analysis*, Vol. 3, No. 2, 186–200, Article No. 15, April 1996.
5. Daubechies, I. and W. Sweldens, "Factoring wavelet transforms into lifting steps," *Journal of Fourier Analysis and Applications*, Vol. 4, No. 3, 247–269, 1998.
6. Sweldens, W., "The lifting scheme: A construction of second generation wavelets," *SIAM Journal on Mathematical Analysis*, Vol. 29, No. 2, 511–546, March 1998.
7. Spiliotopoulos, V., N. D. Zervas, C. E. Androulidakis, G. Anagnostopoulos, and S. Theoharis, "Quantizing the 9/7 daubechies filters coefficients for 2D DWT VLSI implementations," *Digital Signal Processing*, Vol. 1, 227–231, 2002.
8. Xiong, C., S. Zheng, J. Tian, and J. Liu, "The improved lifting scheme and novel reconfigurable vlsi architecture for the 5/3 and 9/7 wavelet filters," *ICCCAS*, Vol. 2, 728–732, June 2004.

Effective Refractive Index Approximation and Surface Plasmon Resonance Modes of Metal Nanoparticle Chains and Arrays

Ergun Simsek

Department of Electrical and Electronics Engineering, Bahcesehir University, Istanbul, Turkey

Abstract— The discrete-dipole approximation method is implemented with an effective refractive index approximation to obtain surface plasmon resonance modes of metal nanoparticle chains and arrays in a multilayered medium. This fully retarded theoretical model includes the effects of retardation, radiative damping and dynamic depolarization due to the finite size of the nanoparticles. The use of diagonal terms of dyadic Green's functions and different polarizability coefficients along the semi-axes of ellipsoidal nanoparticles provide the complete set of resonance modes. Numerical results show a reasonable agreement with experiment results.

1. INTRODUCTION

Surface Plasmons (SPs), which are simply electromagnetic waves that propagate along a conductor-dielectric interface, are quite attractive to a wide spectrum of engineers and scientists due to their potential in developing new types of optical antennas, photonic devices and sensors. Their importance comes from the fact that when periodically located, metal nanoparticles (MNPs) can lead to giant electromagnetic field enhancement and sub-wavelength lateral mode confinement.

A very important design parameter of an optical waveguide with sub-wavelength lateral mode confinement is the dispersion relation. In this direction, many researchers have studied dispersion relation of SP resonance (SPR) modes of MNP chains experimentally in the last decade [1–5]. In the mean time novel theoretical models have been developed to analyze such systems. One very commonly used theoretical model is the discrete dipole approximation (DDA) [2, 3, 6, 7]. DDA is a simple yet effective method but requires a homogeneous background that is not the case most of the time for real MNP applications, e.g., MNPs fabricated on top of indium tin oxide (ITO) coated-glass slides [1–5] creating a three-layer media (air/ITO/glass). In such structures, background can be assumed to be a multilayered environment and DDA can be still helpful given it is implemented via layered-media Green's functions (LMGFs). However, the evaluation of these computationally expensive LMGFs is a bottleneck for many researchers due to their mathematical complexity. Some researchers have tried to overcome this problem by the help of image theory (IT) [2, 7]. Experimental results support the validity of the theoretical model but it is not clear that how IT can be implemented for structures with more than two layers, especially for the case where the width of the layer (on which NPs are aligned) is less than the half of the height of the NPs.

In this work, we adopt a simple effective refractive index (ERI) approximation to overcome the above complexity issues regarding the SPR modes of metal NP chains and arrays embedded in a multilayered structure. We first applied this approximation to one dimensional (1D) periodically located NP chains. Numerical studies show that ERI results are very close to the ones obtained experimentally. Then, we applied this approximation onto two dimensional (2D) periodically located MNP arrays by extending the theory developed by Weber and Ford for the 1D case [6]. The results of this novel 2D DDA implementation show a reasonable agreement with the experiment results.

2. EFFECTIVE INDEX APPROXIMATION

In [1], Crozier et al. studies SPR modes of gold nanoparticle chains fabricated on ITO-coated glass slides. They successfully support their experimental observations by the help of numerical results obtained with a finite-difference time-domain solver, which can handle an inhomogeneous background. In that work, they also compare experimentally obtained SPR modes against numerically calculated ones based on DDA. They apply DDA technique twice: first they assume point dipoles exist in air, second they assume point dipoles exist in glass. Interestingly, experimentally obtained dispersion results lay in between those two sets of simulation results. Same research group studies the effect of ITO layer's thickness numerically in [4] and they conclude that 15 to 30 nm ITO layer causes a red shift in resonance frequencies but maintain similar characteristic in dispersion. Inspired by these experimental studies, in this work we adopt a simple ERI model for multilayered backgrounds. We assume that a multilayered background can be replaced with a homogeneous

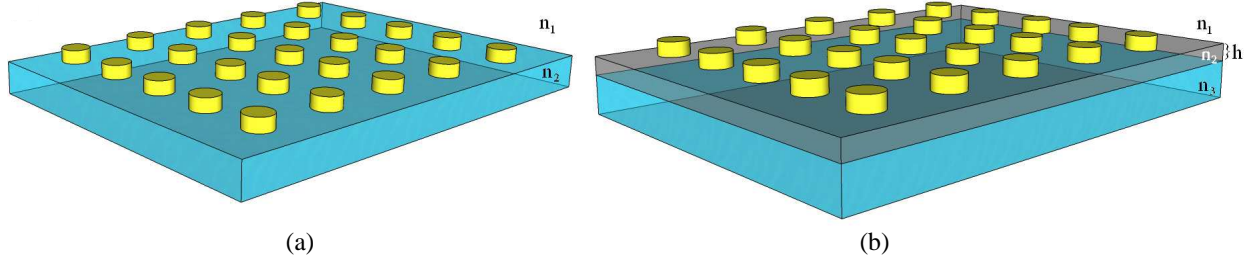


Figure 1: (a) NPs, depicted as yellow cylinders, in a two layer medium: upper layer is air; lower layer is glass, which has a thickness of several wavelengths. n_1 and n_2 are refractive indices of upper and lower layers, respectively. (b) NPs in a three layer medium, where the height of the mid-layer is h . n_1 , n_2 , and n_3 are refractive indices of upper, middle, and lower layers, respectively.

medium whose refractive index, $n_{effective}$, depends on wavelength and each layer's refractive index, and hence we can obtain SPR modes as if MNPs are located in a homogenous medium.

We can briefly describe our ERI model as follows. If we deal with a half-space problem, depicted as Figure 1(a), we simply take the average of refractive indices of two neighboring layers. If the number of layer is more than two, ERI depends on the ratio of the width of the mid-layers to the wavelength (λ). For example, if the height of the mid-layer, h , of a three-layer background, shown as Figure 1(b), is much less than the wavelength, electric field does not propagate long enough in the mid-layer to be effected and transmitted field does not differ significantly than the one in Figure 1(a), assuming $n_1^{(a)} = n_1^{(b)}$ and $n_2^{(a)} = n_3^{(b)}$. On the other hand, if h is much larger than the wavelength, the effect of the bottom layer should be negligible. As a result of this wavelength-layer thickness dependency, the following equation is used to calculate the ERI of a three-layer medium

$$n_{effective} = \begin{cases} \frac{1}{2} \left[n_1 + n_2 \frac{h}{\lambda} + \left(1 - \frac{h}{\lambda} \right) n_3 \right], & (h \leq \lambda), \\ \frac{n_1 + n_2}{2}, & (h \geq \lambda). \end{cases} \quad (1)$$

It should be noted that Equation (1) simplifies into the two-layer case, when (a) h is equal to zero (b) $n_2 = n_3$ or $n_1 = n_2$. If the number of layer is more than 3, a similar methodology can be followed for each additional layer.

3. SURFACE PLASMON RESONANCE MODES

For the SPR modes of MNP chains, we follow the procedure described in [6] implemented with the ERI approximation and a comparative study is provided in Section 4. For the SPR modes of MNP arrays, we develop a novel 2D DDA method as follows.

It is known that SPR modes occur when the dipole moment of a single oscillating particle becomes equal to the induced moment. Here induced moment is defined by the sum of each surrounding particle's polarizability coefficient times the total electric field created by those surrounding oscillating dipoles. This can be written as

$$1 - \alpha_x \sum_{all} G_{xx}(x, y, z|x', y', z') = 0 \quad \text{Longitudinal mode (L)} \quad (2a)$$

$$1 - \alpha_y \sum_{all} G_{yy}(x, y, z|x', y', z') = 0 \quad \text{Transverse-1 Mode (T}_1\text{)} \quad (2b)$$

$$1 - \alpha_z \sum_{all} G_{zz}(x, y, z|x', y', z') = 0 \quad \text{Transverse-2 Mode (T}_2\text{)} \quad (2c)$$

where $G_{\xi\varphi}(x, y, z|x', y', z')$ is the Dyadic Green's function which describes the ξ -component of the electric field at (x, y, z) due to an oscillating point dipole located at (x', y', z') directing φ -axis, where ξ and φ are either x , y , or z ; α_φ defines the relative polarizability along φ -axis. For a finite number of particles, the above equations can be expressed in a matrix form, \mathbf{S} , as similar to the one dimensional case [6]. If we have $N \times M$ nanoparticle, \mathbf{S} is an $NM \times NM$ matrix and the frequency

values where determinant of \mathbf{S} is equal to zero define the SP resonant modes. In order to find the complex zeros determinant of \mathbf{S} , we calculate the determinant of \mathbf{S} on a complex radial frequency (ω) domain. The details of this complex root search will be explained at the conference.

4. NUMERICAL RESULTS

Even though we compared dozens of experiment result sets existing in the literature with the developed method, here we only provide two of them for the sake of brevity. For both, the experimental values for the optical constants of gold are used [8], rather than the Drude model to avoid the concerns about the selection of the appropriate values for plasmon and relaxation frequencies. For the simulations, the numbers of MNPs in the chain and array are equal to 20 and 400 (20×20), respectively.

4.1. One Dimensional Chain of Gold Nanoparticles

Experiment Setup: Gold NP chains are fabricated by e-beam lithography on ITO-coated glass slides [1]. The diameter and height of gold disks are 92 nm and 55 nm, respectively. Inter-particle spacing is 140 nm along the length of the chain. The thickness of ITO-coating is 20 nm. The refractive indices of ITO and air are assumed to be 1.45 and 1, respectively. The glass is assumed to be a borosilicate glass Schott BK7 (n_{BK7} changes between 1.53 and 1.51) and the ERI procedure described above is followed on the complex ω domain.

Figure 2 shows both experimental [1] and numerical results obtained via this method for the longitudinal and transverse resonant modes. Even though numerical results do not perfectly agree with the experimental results -the maximum error between them is 2.34 percent-, they still provide much closer results than the numerical results given in [1] where they use either refractive index of 1 or 1.51. The second transverse mode (T_2), depicted as the red line, agrees well with the experimental result, see [1] for details. Note that T_2 mode also interacts strongly with the light line same as the T_1 mode.

4.2. Two Dimensional Array of Gold Nanoparticles: $d_x = d_y$

Experimental Setup: Gold NP arrays are fabricated on ITO-coated glass slides with inter-particle spacing varying from 520 to 640 nm [5]. To minimize the contrast between the layers, the medium above the glass substrate is chosen to be water. The cylindrical gold disks are 180 nm in diameter and 40 nm thick. The red points in Figure 3 show resonance peak positions of the measured extinction cross section spectra as a function of grating constant. For numerical simulation, disks are approximated as ellipsoidal with semi-axes of 90, 90, and 20 nm. The refractive index of water is changes between 1.3441 and 1.326 based on the wavelength and the glass is assumed to be a borosilicate glass Schott BK7. In Figure 3, blue solid line shows the resonant modes obtained with the 2D DDA method. Numerical results do not perfectly agree with experimental results but still

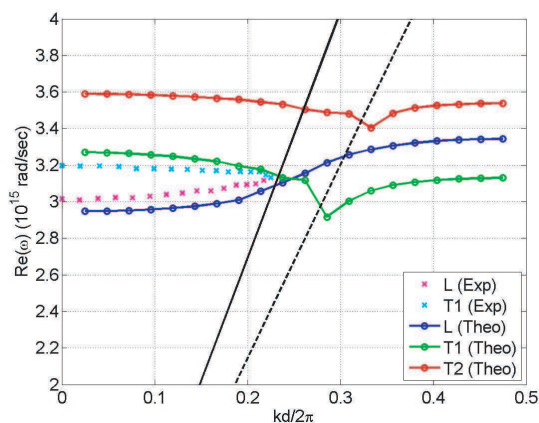


Figure 2: SP dispersion relationship of metal nanoparticle chains: experiment (dots) vs. theory (lines). Black solid and dashed lines depict the light line in air and effective medium, respectively.

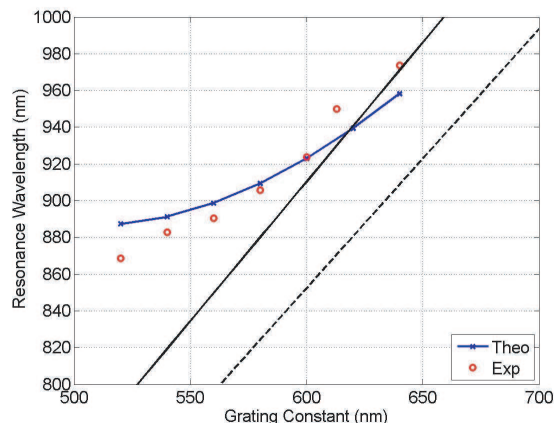


Figure 3: SPR modes of metal nanoparticle arrays: experiment (red dots) vs. theory (blue line) for $d_x = d_y = (520, 540, 560, 580, 600, 620, 640)$ nm. Black dashed and solid lines depict first grating order in glass and effective medium, respectively.

provide a very good estimation: the maximum error between them is 2.25 percent. Note that there are two SPR modes due to different polarization vectors along the vertical (corresponds to T_2 mode) and horizontal axes (corresponds to L and T_1 modes, which are equivalent in this case, since interparticle spacing and semi-axes along the x and y axes are equal to each other: $d_x = d_y$ and $a = b$). Since T_2 mode occurs at wavelengths shorter than 800 nm, we do not see this mode in the figure.

5. CONCLUSIONS

Surface plasmon resonance modes of metal nanoparticle chains and arrays in a multilayered medium are approximately calculated using discrete dipole approximation method which is implemented with an effective refractive index approximation. This approximate method includes the effects of retardation, radiative damping and dynamic depolarization due to the finite size of the nanoparticles. Numerical results show that discrete dipole with effective refractive index approximation can provide a good estimate of the complete set of surface plasmon resonance modes in a multilayered medium, which might be very useful at the pre-experimental stage.

REFERENCES

1. Crozier, K., E. Togan, E. Simsek, and Y. Tang, "Experimental measurement of the dispersion relations of the surface plasmon modes of metal nanoparticle chains," *Opt. Express*, Vol. 15, 17482–17493, 2007.
2. Koenderink, A. F. and A. Polman, "Complex response and polariton-like dispersion splitting in periodic metal nanoparticle chains," *Phys. Rev. B*, Vol. 74, 033402-1-4, 2006.
3. Koenderink, A. F., R. D. Waele, J. C. Prangsma, and A. Polman, "Experimental evidence for large dynamic effects on the plasmon dispersion of sub-wavelength metal nanoparticle waveguides," *Phys. Rev. B*, Vol. 76, 201403, 1–4 Rapid Communication, 2007.
4. Yang, T. and K. B. Crozier, "Dispersion and extinction of surface plasmons in an array of gold nanoparticle chains: Influence of the air/glass interface," *Optics Express*, Vol. 16, 8570, 2008.
5. Chu, Y., E. Schonbrun, T. Yang, and K. B. Crozier, "Experimental observation of narrow surface plasmon resonances in gold nanoparticle arrays," *Appl. Physics Lett.*, Vol. 93, 181108–181111, 2008.
6. Weber, W. H. and G. W. Ford, "Propagation of optical excitations by dipolar interactions in metal nanoparticle chains," *Phys. Rev. B*, Vol. 70, 125429, 2004.
7. Noguez, C., "Surface plasmons on metal nanoparticles: The influence of shape and physical environment," *J. Phys. Chem. C*, Vol. 111, 3806–3819, 2007.
8. Rakic, A. D., A. B. Djuricic, J. M. Elazar, and M. L. Majewski, "Optical properties of metallic films for vertical-cavity optoelectronic devices," *Appl. Opt.*, Vol. 37, 5271–5283, 1998.

An All Optical Switch Based on Nonlinear Photonic Crystal Microcavities

N. Nozhat, A. Taher Rahmati, and N. Granpayeh

Faculty of Electrical Engineering, K. N. Toosi University of Technology, Tehran, Iran

Abstract— In this paper, the performance of an all optical switch based on two dimensional (2-D) nonlinear photonic crystal (PC) microcavities has been demonstrated. We have used an effective numerical method based on the finite-difference time-domain (FDTD) method. It has been shown that by increasing the input signal power the refractive indices of the rods besides the waveguide are changed, due to the nonlinear Kerr effect. Therefore, the resonant frequency of the cavity shifts to a lower value, compared to that of the linear case. The performance of the switch in linear and nonlinear states for various radii of the microcavity and different distances from the waveguide have been simulated and analyzed. The distributions of the electromagnetic fields have been illustrated. The nonlinear resonant frequency of the cavity and the refractive index variations of the rods due to the Kerr nonlinearity have been derived.

1. INTRODUCTION

Recently, photonic crystals, either two or three dimensional periodic structures, have attracted many researchers' attentions. These structures have a photonic band gap (PBG), the range of frequency that the light cannot be propagated in them. Because of their attractive properties, some optical communication devices incorporating photonic crystals, such as thresholdless laser diodes (LDs), low-loss and sharp bend waveguides, endlessly single mode fibers and Mach-Zehnder interferometers have been proposed and fabricated [1–6]. Among various devices, channel add-drop filters, which select one wavelength from the input spectrum and leaving the others, have been applicable to wavelength division multiplexing (WDM) systems. In recent years, some all optical switches based on linear photonic crystals have been proposed and fabricated. For example, tunability of the photonic band-gap (PBG) has been obtained by modulating the PC's refractive index by electro-optic or thermo-optic effect [7–9].

Also, nonlinear photonic crystals have remarkable properties for using in the all optical information processing. For example, the bistability of the nonlinear PCs have been utilized to design optical switches, transistors, logical gates, and optical memories [10–12]. Therefore, the other useful approach for ultra-fast switching is to use nonlinear photonic crystals.

In this paper, the performance of a switch in linear and nonlinear states for various radii of the microcavity and different distances from the waveguide have been simulated and analyzed by the FDTD method. The distributions of the electromagnetic fields have been demonstrated. The nonlinear resonant frequency of the cavity and the refractive index variations of the rods due to the Kerr nonlinearity have been derived.

2. NUMERICAL RESULTS AND DISCUSSION

The proposed structure, as shown in Fig. 1, consists of one waveguide and one resonant microcavity adjacent to it. The structure composed of a 15×15 square lattice of AlGaAs rods with linear refractive index of $n_0 = 3.4$ and nonlinear-index coefficient of $n_2 = 1.5 \times 10^{-17} \text{ m}^2/\text{W}$ at 1550 nm wavelength. The rods are located in air with radii of $r = 0.2a$, where a is the lattice constant. The structure has a large bandgap for transverse magnetic (TM) fields between frequencies of $0.29(c/a)$ and $0.42(c/a)$, where c is the speed of light in vacuum.

In the linear state, when the frequency of the input signal is the same as the resonant frequency of the cavity, that is $f = 0.3816(c/a)$, the input lightwave couples to the cavity and there is no output power at port 2, as demonstrated in Fig. 2(a). By increasing the power of the input signal, the refractive indices of the rods and the resonant frequency of the cavity change, because of the nonlinearity of the rods. So, the input lightwave transmits through the waveguide, without coupling to the cavity, and there is an output power at port 2, as shown in Fig. 2(b). The normalized nonlinear frequency is 0.38.

Since the defect involves removing dielectric material of the crystal, the effective refractive index of the cavity decreases and the mode moves towards the higher edge of the gap [13, 14].

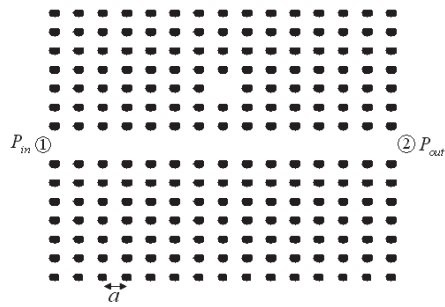


Figure 1: Schematic of proposed nonlinear photonic crystal switch with one waveguide and one cavity besides it.

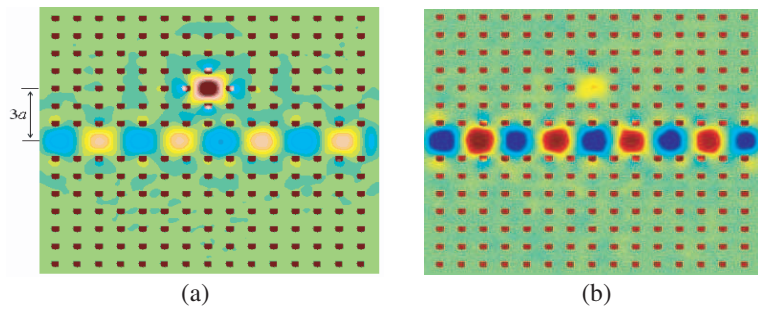


Figure 2: Electric field distribution of the photonic crystal switch at normalized resonant frequency of 0.3816 in (a) linear and (b) nonlinear states.

In linear state, by increasing the refractive index of all rods of the structure to 3.54, similar to nonlinear state, the incident light cannot couple to the cavity at $f = 0.3816(c/a)$. This has simulated the effect of the refractive index variations of the rods by the Kerr nonlinearity.

We have also investigated the effect of variation of the radius and the distance of the microcavity from the waveguide to the resonant frequency of the switch.

If the cavity distance from the waveguide is decreased to $2a$, the resonant frequency increases to $f = 0.3832(c/a)$, which is due to the slight decrease in the effective refractive index of the cavity. Also, the coupling loss increases [12]. The transmittance spectrum of the structure in drop state is shown in Fig. 3. So, when we have launched a sinusoidal wave with frequency of $f = 0.3832(c/a)$ to port 1 of the waveguide, there is no output power at port 2.

By increasing the input power, the resonant frequency of the cavity decreases to $f = 0.382(c/a)$, due to the Kerr nonlinear effect; so the input power transmits through the waveguide and exits from port 2. In this situation, the amount of increase in the refractive index of the rods is 0.1.

The normalized resonant frequencies of the cavity in linear and nonlinear states for cavity distances of $3a$ and $2a$, have been demonstrated in Fig. 4. In both cases, the resonant frequencies in the nonlinear states have been shifted to lower frequencies.

Now instead of removing one rod, the radius of it is increased, which result in decreasing of the resonant frequency. By increasing the rod radius, its effective refractive index of it increases and hence the resonant frequency decreases. Therefore, the microcavity resonant frequency can be tuned by modifying the size the cavity [4].

For the cavity rod radius of $r = 0.1a$, the linear resonant frequency of the cavity is $f = 0.3286(c/a)$. When we increase the input power, the photonic crystal shows its nonlinearity and the resonant frequency of the cavity decreases to $f = 0.3272(c/a)$. Also, by increasing the refractive index of the rods to 3.6 in linear state, we can see the similar results of nonlinearity.

The normalized frequencies of the cavity with $r = 0.1a$ in linear and nonlinear states have been depicted in Fig. 5.

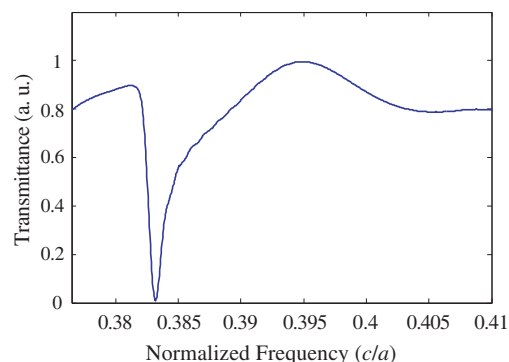


Figure 3: Transmittance spectrum of the photonic crystal switch at normalized frequency of 0.3832. The microcavity distance from the waveguide is $2a$.

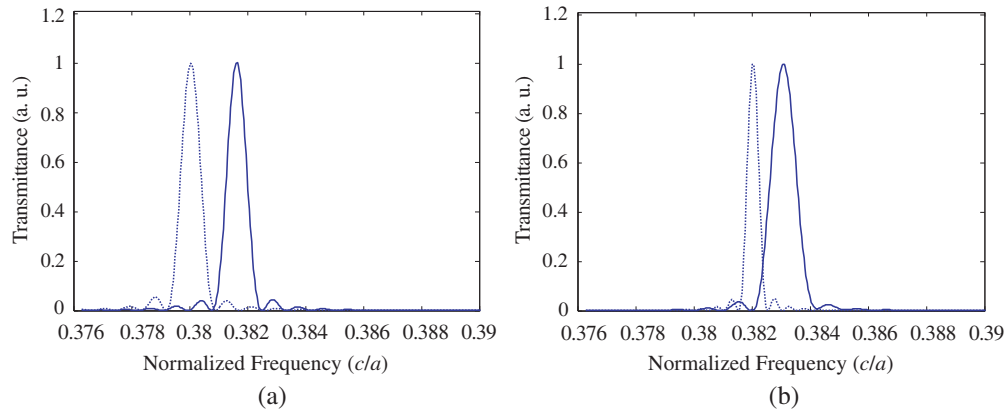


Figure 4: Spectrum of the resonant frequency of the microcavity at the distances of (a) $3a$ and (b) $2a$ from the waveguide. The solid and dashed lines show the resonant frequency in linear and nonlinear states, respectively.

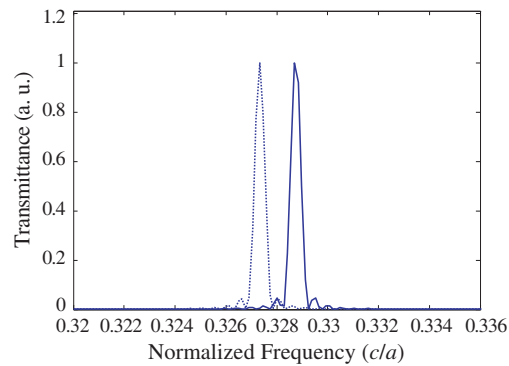


Figure 5: Spectrum of the resonant frequency of the microcavity with $r = 0.1a$ and $2a$ distance from the waveguide. The solid and dashed lines show the resonant frequency in linear and nonlinear states, respectively.

3. CONCLUSION

In this paper, the performance of a nonlinear photonic crystal switch has been investigated. The linear and nonlinear resonant frequencies of the microcavity for various radii of the cavity and different distances from the waveguide have been calculated. It has been shown that if the input lightwave signal frequency is the same as the resonant frequency of the cavity, there is no power at port 2. By increasing the input signal power the resonant frequency of the cavity changes, due to the Kerr nonlinear effect and hence the wave transmits through the waveguide and exits from port 2. For every case, the nonlinear resonant frequency of the cavity has been obtained. The refractive index variations of the rods due to the Kerr nonlinearity have been calculated.

REFERENCES

1. Adar, R., C. H. Henry, C. Dragone, R. C. Kistler, and M. A. Milbrodt, "Broad-band array multiplexers made with silica waveguides on silicon," *IEEE J. Lightwave Technol.*, Vol. 11, No. 2, 212–219, 1993.
2. Haus, H. A. and Y. Lai, "Narrow-band optical channel-dropping filter," *IEEE J. Lightwave Technol.*, Vol. 10, No. 1, 57–62, 1992.
3. Little, B. E., S. T. Chu, H. A. Haus, J. Foresi, and J.-P. Laine, "Microring resonator channel dropping filters," *IEEE J. Lightwave Technol.*, Vol. 15, No. 6, 998–1005, 1997.
4. Imada, M., S. Noda, A. Chutinan, M. Mochizuki, and T. Tanaka, "Channel drop filter using a single defect in a 2-D photonic crystal slab waveguide," *IEEE J. Lightwave Technol.*, Vol. 20, No. 5, 873–878, 2002.
5. Song, B. S., T. Asano, Y. Akahane, Y. Tanaka, and S. Noda, "Multichannel add/drop filter based on in-plane hetero photonic crystals," *IEEE J. Lightwave Technol.*, Vol. 13, No. 3, 1449–1455, 2005.

6. Ren, H., C. Jiang, W. Hu, M. Gao, and J. Wang, “Design and analysis of two-dimensional photonic crystals channel filter,” *Opt. Commun.*, Vol. 266, 342–348, 2006.
7. Fan, S., P. R. Villeneuve, and J. D. Joannopoulos, “Channel drop filters in photonic crystals,” *Opt. Express*, Vol. 3, No. 1, 4–11, 1998.
8. Scrymgeour, D., N. Malkova, S. Kim, and V. Gopalan, “Electro-optic control of the superprism effect in photonic crystals,” *Appl. Phys. Lett.*, Vol. 82, No. 19, 3176–3178, 2003.
9. Yoshino, K., Y. Shimoda, Y. Kawagishi, K. Nakayama, and M. Ozaki, “Temperature tuning of the stop band in transmission spectra of liquid-crystal infiltrated synthetic opal as tunable photonic crystal,” *Appl. Phys. Lett.*, Vol. 75, No. 7, 932–934, 1999.
10. Xu-Hong, C., L. Xu-Sheng, and L. Sheng, “Significant enhancement of unidirectional transmission in asymmetrically confined photonic crystal defect pairs,” *Chin. Phys. Lett.*, Vol. 25, No. 6, 2085–2088, 2008.
11. Bravo-Abad, J., A. Podriguez, P. Bermel, S. G. Johnson, J. D. Joannopoulos, and M. Soljacic, “Enhanced nonlinear optics in photonic-crystal microcavities,” *Opt. Express*, Vol. 15, No. 24, 16161–16176, 2007.
12. Nicolae, C. P., B. Mayank, and M. O. Richard, “All-optical tunability of a nonlinear photonic crystal channel drop filter,” *Opt. Express*, Vol. 12, No. 8, 1605–1610, 2004.
13. Nozhat, N. and N. Granpayeh, “Analysis and simulation of a channel add-drop filter composed of two dimensional photonic crystal,” *Proc. of Asia Optical Fiber Communication & Optoelectronic Exposition & Conference (IEEE/AOE)*, 534–536, Shanghai, China, Oct. 2007.
14. Villeneuve, P. R., S. Fan, and J. D. Joannopoulos, “Microcavities in photonic crystals: Mode symmetry, tunability, and coupling efficiency,” *Phys. Rev. B*, Vol. 54, No. 11, 7837–7842, 1996.

Homogenization of Dissipative Photonic Crystals

Lyudmila Gumen¹, Jesús Arriaga², and Arkadii Krokhin³

¹Universidad Popular Autónoma del Estado de Puebla, Mexico

²Instituto de Física, Universidad Autónoma de Puebla, Mexico

³University of North Texas, USA

Abstract— We consider propagation of the H - and E -modes in a periodic arrangement of dissipative dielectric cylinders. Using the plane-wave expansion method, we derive analytical formulas for the imaginary part of the low-frequency effective dielectric constants. The formula for the anti-Hermitian part of the effective dielectric tensor is valid for arbitrary Bravais lattice and arbitrary filling fractions.

1. INTRODUCTION

Propagation of electromagnetic wave in any matter is accompanied by dissipation of electromagnetic energy. For a monochromatic wave, $E \propto \exp(-i\omega t)$, the rate of dissipation in a unit volume $Q = \frac{\omega \varepsilon''}{4\pi} |E|^2$ is determined by the imaginary part of dielectric constant ε'' . Sometimes strong absorption is desirable, e.g. in the case of so-called perfect absorber [1] or metallic photonic crystal, which enables modification of thermal emission [2]. However, as a rule, absorption and dissipation strongly reduce the efficiency of optical devices. Dissipation in photonic crystals containing metallic components sets the limit for the efficiency, bandwidth, resolution, etc of photonic-crystal-based devices. It is the most negative but inevitable factor for operation of a perfect lens of left-handed metamaterial [3]. In all these cases it is very desirable to reduce the level of dissipation. To evaluate the energy losses in photonic crystals one needs to calculate the imaginary part of the effective dielectric constant ε'' . Although there are some phenomenological formulas for these quantities in a style of Drude model, a ‘microscopic’ theory is still lacking.

The microscopic approach takes into account periodicity of the structure, i.e., the type of Bravais lattice and also the distribution of the dissipative material in the unit cell. The speed of light in a photonic crystal, as well as the level of dissipation, are functions of the frequency ω . In general case these characteristics can be calculated only numerically for a given ω and for a given structure. However, if the wavelength λ exceeds much the structure period a , the inhomogeneous periodic structure can be replaced by a homogeneous effective medium. Being homogeneous, this effective medium turns out to be anisotropic, in the case of low-symmetric unit cell. Then the effective dielectric constant depends on the direction of the Bloch vector $\mathbf{n} = \mathbf{k}/k$. This dependence is obtained from Fresnel ellipsoid. In general case all three principal dielectric constants are different that corresponds to biaxial anisotropy. If two of them are equal, then the corresponding effective medium is birefringent (uniaxial anisotropy). For dissipative medium the tensor of effective dielectric tensor has hermitian and anti-hermitian part, $\hat{\varepsilon}_{eff} = \hat{\varepsilon}' + i\hat{\varepsilon}''$. In what follows we calculate the anti-hermitian part $\hat{\varepsilon}''$ for a photonic crystal of long cylinders. The hermitian part $\hat{\varepsilon}'$ was calculated in Refs. [4, 5], using the method of expansion over plane waves.

2. PERTURBATION THEORY IN THE LIMIT OF WEAK DISSIPATION

We consider a 2D periodic structure of dielectric cylinders with their axes parallel to z . The background material is an isotropic dielectric with permittivity $\varepsilon_b = \varepsilon'_b + i\varepsilon''_b$ and the cylinders are characterized by $\varepsilon_a = \varepsilon'_a + i\varepsilon''_a$. Dissipation of energy leads to exponential decay of the wave. The decay length must exceed the wavelength in order for the wave to be a propagating one. This means that, as a whole, the effective medium exhibits weak dissipation. In terms of the effective dielectric parameters this condition can be written as follows,

$$\varepsilon''(\mathbf{n}) \ll \varepsilon'(\mathbf{n}). \quad (1)$$

According to this inequality, the dissipation can be considered as small perturbation. Within the allowed frequency zones this perturbation leads to slow decay of the wave. Near the band edges it gives rise to smoothing of the bands and to finite values of the density of states within photonic band gaps. The latter effect was considered in Ref. [6] and it was shown that for a photonic crystal

of cylinders the density of states does not vanish in the band gap but it decays away from the band edge at ω_c as $(\omega - \omega_c)^{-1}$.

At low frequencies the dispersion relation for electromagnetic wave propagating in a periodic medium is linear, $\omega = kc/\sqrt{\varepsilon'}$. This relation defines the real part of the effective dielectric constant. In the limit of weak dissipation Eq. (1) the real part ε' can be calculated using the plane wave expansion [4, 5]. The details of these calculations can be found in Ref. [5]. For the E -mode (electric field is parallel to the cylinders) ε' is independent on the direction of propagation in the x - y plane and is given by the volume-weighted dielectric constant

$$\varepsilon'_E = \bar{\varepsilon}' = f\varepsilon'_a + (1 - f)\varepsilon'_b, \quad (2)$$

where f is the filling fraction of the cylinders in the unit cell.

For the H -mode (magnetic field is parallel to the cylinders) the effective dielectric constant is expressed through the Fourier components of the inverse dielectric function, $\eta'(\mathbf{r}) = 1/\varepsilon'(\mathbf{r})$,

$$\varepsilon'_H(\mathbf{n}) = \left\{ \bar{\eta}' - \sum_{\mathbf{G}, \mathbf{G}' \neq 0} \mathbf{n} \cdot \mathbf{G} \mathbf{n} \cdot \mathbf{G}' \eta'(\mathbf{G}) \eta'(-\mathbf{G}') [\mathbf{G} \cdot \mathbf{G}' \eta'(\mathbf{G} - \mathbf{G}')]^{-1} \right\}^{-1}. \quad (3)$$

Here $[\dots]^{-1}$ implies matrix inversion in \mathbf{G} -space excluding the point $\mathbf{G} = \mathbf{G}' = 0$, while $\{\dots\}^{-1}$ means “reciprocal”. The Fourier components of the periodic functions $\varepsilon'(\mathbf{r})$ and $\eta'(\mathbf{r})$ are defined as follows,

$$\begin{aligned} \varepsilon'(\mathbf{r}) &= \sum_{\mathbf{G}} \varepsilon'(\mathbf{G}) \exp(i\mathbf{G} \cdot \mathbf{r}), & \eta'(\mathbf{r}) &= \sum_{\mathbf{G}} \eta'(\mathbf{G}) \exp(i\mathbf{G} \cdot \mathbf{r}), \\ \varepsilon'(\mathbf{G}) &= \frac{1}{A_c} \int_{A_c} \varepsilon'(\mathbf{r}) \exp(-i\mathbf{G} \cdot \mathbf{r}) d\mathbf{r}, & \eta'(\mathbf{G}) &= \frac{1}{A_c} \int_{A_c} \eta'(\mathbf{r}) \exp(-i\mathbf{G} \cdot \mathbf{r}) d\mathbf{r}. \end{aligned} \quad (4)$$

The summation runs over the reciprocal-lattice vectors \mathbf{G} and the integration runs over the unit cell area A_c , $\bar{\eta}' = f/\varepsilon'_a + (1 - f)/\varepsilon'_b$. As it was demonstrated in Ref. [7] that Eq. (3) provides good convergence, even for high dielectric contrast between the constituents. Eq. (3) defines a rotated ellipse in the x - y plane [5]. The semi-axes of this ellipse give two principal values of the tensor $\hat{\varepsilon}'$. The third principal value is given by Eq. (2).

Equations (2) and (3) is zero-approximation result in our calculation of the imaginary part of the effective dielectric constant. Without dissipation the eigenvalue problem for the band structure of the photonic crystal is hermitian, i.e., all the eigenfrequencies $\omega_n(\mathbf{k})$ are real. Dissipation gives rise to small imaginary part, $\omega_n(\mathbf{k}) = \omega'_n(\mathbf{k}) - i\omega''_n(\mathbf{k})$. At low frequencies in the first allowed zone ($n = 1$), where the dispersion is linear, $\omega' - i\omega'' = kc/\sqrt{\varepsilon' + i\varepsilon''}$ the following formula is valid

$$\frac{\varepsilon''(\mathbf{n})}{\varepsilon'(\mathbf{n})} \approx 2 \frac{\omega''(\mathbf{n})}{\omega'(\mathbf{n})}. \quad (5)$$

Thus, the imaginary part of the effective dielectric constant can be calculated is the anti-hermitian correction $\omega''(\mathbf{k})$ is known. The latter can be obtained from the eigenvalue problem using a standard perturbation theory for hermitian operators. We give here the final formula for $\omega''_n(\mathbf{k})$ obtained in the linear approximation over dissipation [6],

$$\frac{\omega''_n(\mathbf{n})}{\omega'_n(\mathbf{n})} = \frac{1}{2(\eta'_a - \eta'_b)} \left[\eta''_a - \eta''_b - (\eta''_a \eta'_b - \eta''_b \eta'_a) \frac{c^2}{\omega_n'^2} \sum_{\mathbf{G}} |\mathbf{k} + \mathbf{G}|^2 |\mathbf{h}(\mathbf{G})|^2 \right]. \quad (6)$$

Here, $\eta'_a = 1/\varepsilon'_a$, $\eta'_b = 1/\varepsilon'_b$, $\eta''_a = \varepsilon''_a/\varepsilon_a'^2$, and $\eta''_b = \varepsilon''_b/\varepsilon_b'^2$. The Fourier components $\mathbf{h}(\mathbf{G})$ of magnetic field

$$\mathbf{H}(\mathbf{r}) = \sum_{\mathbf{G}} \mathbf{h}(\mathbf{G}) \exp[i(\mathbf{k} + \mathbf{G}) \cdot \mathbf{r}] \quad (7)$$

are obtained from the solution of the following eigenvalue problem

$$\left(\frac{\omega^2}{c^2} - \bar{\eta}' |\mathbf{k} + \mathbf{G}|^2 \right) \mathbf{h}(\mathbf{G}) = - \sum_{\mathbf{G}' \neq \mathbf{G}} \eta'(\mathbf{G} - \mathbf{G}') (\mathbf{k} + \mathbf{G}) \times [(\mathbf{k} + \mathbf{G}') \times \mathbf{h}(\mathbf{G}')]. \quad (8)$$

Since the right-hand-side of Eq. (6) is linear over η''_a and η''_b , the dissipation is omitted in the eigenvalue problem Eq. (8).

3. LOW-FREQUENCY LIMIT

In the limit $\omega, k \rightarrow 0$ Eq. (6) is strongly simplified. Since the second term in square brackets contains ω^2 in the denominator, the numerator must be expanded over k , keeping the terms $\sim k^2$.

$$\sum_{\mathbf{G}} |\mathbf{k} + \mathbf{G}|^2 |\mathbf{h}(\mathbf{G})|^2 \approx k^2 + \sum_{\mathbf{G} \neq 0} |\mathbf{G}|^2 |\mathbf{h}(\mathbf{G})|^2. \quad (9)$$

It follows from Eq. (8) that all the Fourier harmonics $\mathbf{h}(\mathbf{G})$ vanish in the low-frequency limit, $\mathbf{h}(\mathbf{G} \neq 0) \sim k$, as it should be for a homogenized medium. The only non-vanishing term is $\mathbf{h}(\mathbf{G} = 0) = 1 - \alpha k^2$. According to Eq. (7) this term defines a plane wave, $\mathbf{H}(\mathbf{r}) \sim \exp(i\mathbf{k} \cdot \mathbf{r})$.

Calculations of the sum in Eq. (6) in the low-frequency limit are performed separately for the H - and E -mode. Omitting all the mathematical details, we give the final result for the dissipative part of the effective dielectric constant.

H -mode

$$\frac{\varepsilon''_H(\mathbf{n})}{\varepsilon'_H(\mathbf{n})} = \frac{\eta''_a - \eta''_b}{\eta'_a - \eta'_b} - \frac{\eta''_a \eta'_b - \eta''_b \eta'_a}{\eta'_a - \eta'_b} \varepsilon'_H(\mathbf{n}) (1 + n_i n_k B_{ik}), \quad i, k = x, y. \quad (10)$$

Here the real part $\varepsilon'_H(\mathbf{n})$ is given by Eq. (3) [4, 5] and the tensor B_{ik} is defined as follows

$$B_{ik} = \sum_{\mathbf{G}} G^2 Z_i(\mathbf{G}) Z_k^*(\mathbf{G}), \quad (11)$$

where

$$\mathbf{Z}_i(\mathbf{G}) = \sum_{\mathbf{G}'} \mathbf{G}' \eta(\mathbf{G}') [\mathbf{G} \cdot \mathbf{G}' \eta(\mathbf{G} - \mathbf{G}')]^{-1}. \quad (12)$$

In general case, the dependence of the real and imaginary part on the direction of propagation \mathbf{n} is different. It means that the direction of the highest optical density may be different from the direction of the highest dissipation. In the limit of $\varepsilon'_a \rightarrow \varepsilon'_b$ the numerator and denominator in Eq. (10) vanish. The limit $\frac{0}{0}$ can be easily calculated, giving an obvious result, $\varepsilon''_H = \overline{\varepsilon''} = f\varepsilon''_a + (1-f)\varepsilon''_b$.

E -mode

$$\frac{\varepsilon''_E}{\varepsilon'_E} = \frac{\eta''_a - \eta''_b}{\eta'_a - \eta'_b} - \frac{\eta''_a \eta'_b - \eta''_b \eta'_a}{\eta'_a - \eta'_b} \varepsilon'_E \left[1 + \overline{\eta}^2 (\overline{\varepsilon^2} - \overline{\varepsilon^2}) \right]. \quad (13)$$

Here $\overline{\varepsilon^2} = f/\varepsilon_a^2 + (1-f)/\varepsilon_b^2$.

In the limit $\varepsilon'_a \rightarrow \varepsilon'_b$ Eq. (13) (as well as Eq. (10)) gives $\varepsilon''_E \rightarrow \overline{\varepsilon''}$. For the E -mode the real, Eq. (2), and the imaginary, Eq. (13), part of the effective dielectric constant turn out to be independent on the direction of propagation \mathbf{n} . This symmetry comes from the fact that the lines of the electric field do not cross the interface between the material a and material b . Unlike this, for the H -mode there is a refraction of the lines at the interface, therefore the effective dielectric constant in general case changes with \mathbf{n} . Only if the unit cell possesses a third- or higher-order rotational axis z , then the second-rank tensor in Eq. (11) is reduced to a scalar, and the dissipation becomes isotropic.

Equations (10) and (13) are the linear corrections to the effective-medium theory results (2) and (3), respectively. They define the decay rate of the eigenmodes in 2D photonic crystal.

4. CONCLUSION

We calculated the imaginary part of the dielectric function for a dissipative photonic crystal of infinite cylinders in the long-wavelength limit, $\omega, k \rightarrow 0$. The obtained analytical results are valid for weakly dissipative media, when the decay length of the propagating modes exceeds the wavelength. Applications of the obtained formulas to metallodielectric photonic crystal and the corresponding numerical results will be published elsewhere.

ACKNOWLEDGMENT

Supported by the US Department of Energy, grant # DE-FG02-06ER46312.

REFERENCES

1. Landy, N. I., S. Sajuyigbe, J. Mock, D. Smith, and W. Padilla, “Perfect metamaterial absorber,” *Phys. Rev. Lett.*, Vol. 100, 207402, 2008.
2. Han, S., A. Stein, and D. Norris, “Tailoring self-assembled metallic photonic crystals for modified thermal emission,” *Phys. Rev. Lett.*, Vol. 99, 053906, 2007.
3. Pendry, J. B. and D. R. Smith, “Reversing light with negative refraction,” *Phys. Today*, Vol. 57, 37, 2004.
4. Halevi, P., A. A. Krokhin, and J. Arriaga, “Photonic crystal optics and homogenization of 2D periodic composites,” *Phys. Rev. Lett.*, Vol. 82, 719, 1999.
5. Krokhin, A. A., P. Halevi, and J. Arriaga, “The long-wavelength limit (homogenization) for two-dimensional photonic crystals,” *Phys. Rev. B*, Vol. 65, 15208, 2002.
6. Krokhin, A. A. and P. Halevi, “Influence of weak dissipation on the photonic band structure of periodic composites,” *Phys. Rev. B*, Vol. 53, 1205, 1996.
7. Arriaga, J., A. A. Krokhin, and P. Halevi, “Effective dielectric constant of 2D photonic crystals with high dielectric contrast,” *Phys. E*, Vol. 17, 436–439, 2003.

Invariant Embedding Method in the Problem of 3D Photonic Crystal Modeling

V. L. Kuznetsov and A. S. Rudkovskiy

Moscow State Technical University of Civil Aviation, Russia

Abstract— In our work, rather new approach in modeling effects of interaction electromagnetic field and photonic crystal (PC) is being developed. It is based on invariant embedding method. The embedding equations for reflection and transition matrix coefficients of Lin & Fleming photonic crystal were got and results of numerical calculations for some values of structure parameters were shown.

1. INTRODUCTION

Some methods of solving problem of electromagnetic field and periodical 3D structure interaction are developing now. These are composition of Watson dispersion operators method (T-matrix technique) [1], embedding method [2] and method of transfer-matrixes [3]. In our work, approach based on application of the invariant embedding method is being developed. This approach allows reducing Helmholtz equation for electromagnetic field in complex periodical structure to Cauchy's problem. Embedding equations were created using new variables-reflection and transition operators that satisfy the principle of dynamic causality.

This article covers the problem of Lin & Fleming photonic crystal (PC) creating. This PC consists of dielectric cylinders stack (Fig. 1).

Under such geometry in space specters of transferred and reflected fields (like in any 3D PC), there are all possible specters of plane waves with wave vectors $\vec{k}_n^p = \{k_z, \vec{q}_0 + \vec{\kappa}_x \cdot n + \vec{\kappa}_y \cdot p\}$, $n, p \in Z$. Here, $\vec{\kappa}_x, \vec{\kappa}_y$ — Basis vectors of PC reciprocal lattice, \vec{q}_0 — Projection of \vec{k}_0 — Wave vector of field that interacts with PC. The difference of our model from general case of 3D PC consist in is that considerable part of embedding equations simplifies to easy integrating equations and it appreciably reduce the number of calculations.

2. PROBLEM DIFINITION

Periodical structure of Lin & Fleming PC (Fig. 1) consist of layers that formed by right-angled timbers with inductive capacity ε , width d_x for odd number of layers and d_y — for others. Period of structure along correspond axes define Λ_x and Λ_y , accordingly. Monochromic plane wave fall from above on the structure. This plane wave has defined polarization and wave vector $\vec{k} = (q_{mx}, q_{py}, k_z)$, where q_{mx} and q_{py} can be calculated from equation: $q_{mx} = q_{0x} + \frac{2\pi}{\Lambda_x} \cdot m$, $m \in Z$, $q_{0x} < \frac{2\pi}{\Lambda_x}$.

It is necessary to define matrix coefficients of reflection ${}_{\alpha\beta}R_{nm}^{sp}(h)$ and transition ${}_{\alpha\beta}T_{nm}^{sp}(h)$ as PC height (h) functions. Parameter β characterizes polarization of falling wave and α — Polarization of (n, s) — Component of space specter of diffracted field.

To solve this problem we use embedding method [2, 4] with variable thickness has an embedding parameter [5, 6].

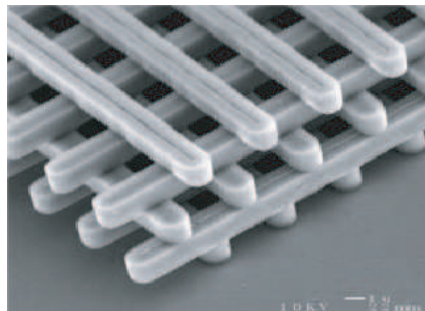


Figure 1: Schematic view of Lin & Fleming PC.

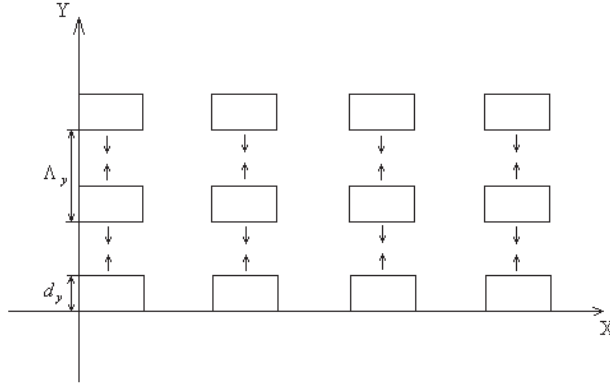


Figure 2: Transition from general case of 3D PC to Lin & Fleming architecture.

3. MATHEMATICAL MODEL OF LIN & FLEMING PC

3.1. General Case of 3D Pc. Transition to Lin & Fleming Architecture

Every separate layer of Lin & Fleming relatively simple but their mutual position requires taking into account all the features of field and PC interaction that occur in 3D PC models.

In this case, it is simpler to consider general case of 3D PC and after that realize a transition to Lin & Fleming architecture by ($d_y \rightarrow \Lambda_y$) as it is shown on Fig. 2.

In accordance with ideology of invariant embedding method [5, 6] mark out thin (elementary) layer of PC that limited by two planes $z = const$ and $z + \Delta z = const$. Thickness of elementary layer Δz is small and Born approximation can be used when dispersion of field is describing:

$$\vec{E}(\vec{r}) = \vec{E}_0(\vec{r}) + \int_{\Delta\Omega} d\vec{r}' \hat{\Gamma}(\vec{r}, \vec{r}') [(\tilde{\varepsilon}(\vec{r}') - 1) k^2 \vec{E}_{in}(\vec{r}')], \quad (1)$$

Here, $\hat{\Gamma}$ — Green's function, $\Delta\Omega$ — Part of space where elementary layer situated and $\vec{E}_0(\vec{r})$ — General solution of Helmholtz equation that satisfies edge conditions for elementary layer. $\vec{E}(\vec{r})$ and $\vec{E}_0(\vec{r})$ — Fields outside the elementary layer, $\vec{E}_{in}(\vec{r})$ — Field inside elementary layer and it can be defined by following formula:

$$\vec{E}_{in}(\vec{r}) = \begin{cases} \hat{A} \vec{E}_0(\vec{r}) & ??? \quad \vec{r} \in \Delta\Omega' \\ \vec{E}_0(\vec{r}) & ??? \quad \vec{r} \notin \Delta\Omega' \end{cases} \quad (2)$$

Here $\Delta\Omega'$ — Part of elementary layer space $\Delta\Omega$ that characterized $\tilde{\varepsilon}(\vec{r}) = \varepsilon$ and $\hat{A} = diag\{1, 1, 1/\varepsilon\}$.

In (\vec{q}, z) — Presentation (Oz axis directed out along the normal to upper plane of PC), Equation (1) can be presented in the following view:

$$\vec{E}^\pm(\vec{q}, z \pm \Delta z) = \vec{E}^\pm(\vec{q}, z) e^{ik_z \Delta z} + \sum_m \hat{\Gamma}^\pm(\vec{q}, \pm 0) \hat{A} \frac{4(\varepsilon - 1) k_0^2 \cdot \vec{E}_m}{\Lambda_x(q_{mx} - q_x) \Lambda_y(q_{py} - q_y)} \times \sin\left(\frac{d_x}{2} (q_{mx} - q_x)\right) \sin\left(\frac{d_y}{2} (q_{py} - q_y)\right) \sum_{j=-\infty}^{+\infty} \delta\left(q_x - q_{mx} - \frac{2\pi}{\Lambda_x} j\right) \sum_{k=-\infty}^{+\infty} \delta\left(q_y - q_{py} - \frac{2\pi}{\Lambda_y} k\right) \cdot \Delta z \quad (3)$$

Sign “+” corresponds plane waves that extend along Oz , sign “-” corresponds plane waves that extend in opposite direction, \vec{q} — Projection of plane wave \vec{k} on upper plane of PC. In such presentation, Green's function has the following view:

$$\hat{\Gamma}_{\alpha\beta}^\pm(q, +0) = \frac{i}{2 \cdot k^2} \cdot \frac{k^2 \delta_{\alpha\beta} - k_\alpha \cdot k_\beta}{k_z} \quad (4)$$

Here $\delta_{\alpha\beta}$ — Kronecker symbol (α and β possesses the values x, y, z)

In (3), δ — Functions define only directions where diffracted field extended. Making the transition from (3) in difference equation to differential equation for angular specter amplitudes of diffracted field we get the following system of differential equations:

$$\begin{aligned} \pm \frac{\vec{E}_n^{s\pm}(z)}{dz} &= ik_z(n, s) \cdot \vec{E}_n^{s\pm}(z) + \sum_m \hat{\Gamma}_{nm}^{sp\pm} \cdot \frac{(\varepsilon - 1)k_0^2 \cdot \widehat{A} \cdot \left(\vec{E}_m^{p\pm}(z) + \vec{E}_m^{p\mp}(z) \right)}{\pi^2(n - m)(s - p)} \\ &\times \sin\left(\frac{\pi d_x(n - m)}{\Lambda_x}\right) \sin\left(\frac{\pi d_y(s - p)}{\Lambda_y}\right) \end{aligned} \quad (5)$$

In accordance with Lin & Fleming architecture PC consists of layers with timbers that oriented along axes OX or OY . Let's consider layer with timbers oriented along OY (results for another version of orientation can be defined similarly). The equation for it can be got from (5) by $d_y \rightarrow \Lambda_y$. One can see that in all cases except $s \neq p$, the second summand in (5) is equal to 0 and electromagnetic field extends without interaction with PC. In case $s = p$ use obvious relationship in right part of (5):

$$\lim_{d_y \rightarrow \Lambda_y} \sin\left[\frac{\pi \cdot d_y}{\Lambda_y}(s - p)\right] / (s - p) = \pi$$

The relationship between diffracted — $\vec{E}_n^{s\pm}$ and initial — $\vec{E}_m^{p\pm}$ fields can be defined using reflection and transition coefficients of elementary layer:

$$\vec{E}_n^{s\pm} = \hat{t}_{nm}^{sp\pm} \cdot \vec{E}_m^{p\pm}, \quad \vec{E}_n^{s\pm} = \hat{r}_{nm}^{sp\pm} \cdot \vec{E}_m^{p\mp} \quad (6)$$

It's easy to see that equations for these coefficients have the following view:

$$\hat{t}_{nm}^{sp\pm} = \vec{I} \cdot \delta_{nm} \cdot \delta_{sp} + I \cdot ik_z(n, s) \cdot \Delta z + \sum_m \Gamma_{nm}^{sp\pm} \cdot \delta_{sp} \cdot \frac{(\varepsilon - 1)k_0^2 \widehat{A}}{\pi(n - m)} \sin\left(\frac{\pi d(n - m)}{\Lambda}\right) \cdot \Delta z \quad (7)$$

$$\hat{r}_{nm}^{sp\pm} = \sum_m \Gamma_{nm}^{sp\pm} \cdot \delta_{sp} \cdot \frac{(\varepsilon - 1)k_0^2 \widehat{A}}{\pi(n - m)} \sin\left(\frac{\pi d(n - m)}{\Lambda}\right) \cdot \Delta z \quad (8)$$

In (7) and (8), elements proportional Δz describes interaction of wave field with elementary layer. Designate them as τ and ρ respectively. Using new designations (5) can be presented in the following view:

$$\pm \frac{d\vec{E}_n^{s\pm}(z)}{dz} = \sum_m \hat{t}_{nm}^{sp\pm}(z) \cdot \vec{E}_m^{p\pm}(z) + \sum_m \hat{r}_{nm}^{sp\pm}(z) \cdot \vec{E}_m^{p\mp}(z) \quad (9)$$

3.2. Transition to Polarization Bases of Spectral Components of Initial and Diffracted Fields

Matrixes that appear in (9) are multiindex and it makes calculations very complex during solving the embedding equations. In this case, it is better to present the polarization of field spectral components in polarization basis of vertical and horizontal polarized waves, i.e., present vectors \vec{E}^{\pm} in the following view $\vec{E}^{\pm} \rightarrow (\vec{E}_h^{\pm}, \vec{E}_v^{\pm})^T$, where \vec{E}_h^{\pm} and \vec{E}_v^{\pm} — Horizontal and vertical components of field spectral mode.

To realize such a transition it's necessary to present Green's function as block matrix. Each component of such matrix describes transformation of some plane wave with certain polarization (horizontal or vertical) to another mode with certain polarization:

$$\hat{\Gamma}^{\pm} \rightarrow \begin{pmatrix} \hat{\Gamma}_{hh}^{\pm} & \hat{\Gamma}_{hv}^{\pm} \\ \hat{\Gamma}_{vh}^{\pm} & \hat{\Gamma}_{vv}^{\pm} \end{pmatrix}$$

The view of matrixes for reflection and transition coefficients can be appreciably simplified if for each component of space specter the field would be presented in basis of horizontally and vertically polarized waves. To do this it's enough to use the following rotation matrix:

$$U_n^{s\pm} = \begin{pmatrix} \cos \theta_n^s \cdot \cos \alpha_n^s & \cos \theta_n^s \cdot \sin \alpha_n^s & \pm \sin \theta_n^s \\ -\sin \alpha_n^s & \cos \alpha_n^s & 0 \\ \mp \sin \theta_n^s \cdot \cos \alpha_n^s & \mp \sin \theta_n^s \cdot \sin \alpha_n^s & \cos \theta_n^s \end{pmatrix}, \quad (10)$$

Here angles φ_n^s and θ_n^s should be calculated for each (n, s) — Component of diffracted waves space specter, and full rotation matrix has view of block matrix $U^\pm = \|U_n^{s\pm}\|$ with blocks $U_n^{s\pm}$, where “+” correspond to reflected fields, and “−” — Transitioned fields.

In new presentation, Equation (9) have the following view:

$$\begin{aligned} \pm \frac{d}{dz} \begin{pmatrix} E_{nh}^{s\pm} \\ E_{nv}^{s\pm} \end{pmatrix} &= \sum_m \begin{bmatrix} \hat{U}_n^{s\pm} \cdot [\hat{\rho}_{nm}^{sp}] \cdot (U_m^{p\mp})^{-1} & \hat{U}_n^{s\pm} \cdot [\hat{\rho}_{nm}^{sp}] \cdot (U_m^{p\mp})^{-1} \\ \hat{U}_n^{s\pm} \cdot [\hat{\rho}_{nm}^{sp}] \cdot (U_m^{p\mp})^{-1} & \hat{U}_n^{s\pm} \cdot [\hat{\rho}_{nm}^{sp}] \cdot (U_m^{p\mp})^{-1} \end{bmatrix}^\pm \cdot \begin{pmatrix} E_{mh}^{p\mp} \\ E_{mv}^{p\mp} \end{pmatrix} \\ &+ \sum_m \begin{bmatrix} \hat{U}_n^{s\pm} \cdot [\hat{\tau}_{nm}^{sp}] \cdot (U_m^{p\pm})^{-1} & \hat{U}_n^{s\pm} \cdot [\hat{\tau}_{nm}^{sp}] \cdot (U_m^{p\pm})^{-1} \\ \hat{U}_n^{s\pm} \cdot [\hat{\tau}_{nm}^{sp}] \cdot (U_m^{p\pm})^{-1} & \hat{U}_n^{s\pm} \cdot [\hat{\tau}_{nm}^{sp}] \cdot (U_m^{p\pm})^{-1} \end{bmatrix}^\pm \cdot \begin{pmatrix} E_{mh}^{p\pm} \\ E_{mv}^{p\pm} \end{pmatrix} \end{aligned} \quad (11)$$

3.3. Embedding Equations for Lin & Fleming PC

The exfoliation method is used to get embedding equations. In this case, let's differentiate equation $E^+(z) = \hat{R}(z) \cdot E^-(z)$ that describes relationship between initial and reflected field. After that it's necessary to exclude fields' derivatives using (11) and one can get Riccati equation for reflection matrix coefficient \hat{R} :

$$\frac{d\hat{R}_{nm}^{sp-}}{dz} + \hat{R}_{nk}^{sp-} \cdot (\hat{\rho}_{kl}^{sr+}) \cdot R_{lm}^{rp-} + \hat{R}_{nk}^{sq-} \cdot (\hat{\tau}_{km}^{qp+}) + (\hat{\tau}_{nk}^{sr-}) \cdot R_{km}^{rp-} + \rho_{nm}^{sp-} = \hat{0} \quad (12)$$

The equation for transition matrix coefficient \hat{T} can be got similarly:

$$\frac{d\hat{T}_{nm}^{sp+}}{dz} = \hat{\tau}_{nk}^{sl+} \cdot \hat{T}_{km}^{lp+} + R_{nk}^{sl+} \cdot (\hat{\rho}_{kl}^{lq+}) \cdot T_{lm}^{qp+} \quad (13)$$

From (12), (13) taking into account (7), (8), one can see that during calculations of elementary layer under condition $s \neq p$ the embedding equations simplifies appreciably:

$$\frac{d\hat{R}_{nm}^{sp-}}{dz} + \hat{R}_{nm}^{sp-} \cdot ik_z(m, p) + ik_z(n, s) \cdot R_{nm}^{sp-} = \hat{0} \quad (14)$$

$$\frac{d\hat{T}_{nm}^{sp+}}{dz} = ik_z(n, s) \cdot \hat{T}_{nm}^{sp+} \quad (15)$$

These equations have simple analytical solutions and don't require much time during calculations. During calculations with number of modes N for 3D PC, it's necessary to solve N^4 Equations (12) and (13), but for PC with Lin & Fleming architecture — Only N^2 . This difference shows advantage PC with Lin & Fleming architecture beside 3D PC.

It's necessary to equip differential Equations (12)–(15) with simple boundary conditions:

$$\hat{R}_{nm}^{sp-}(0) = \hat{0} \quad \text{and} \quad \hat{T}_{nm}^{sp+} = \delta_{nm} \cdot \delta_{sp}, \quad (16)$$

(16) together with (12)–(15) forms mathematical model for PC with Lin & Fleming architecture.

4. RESULTS OF NUMERICAL CALCULATIONS

The described above mathematical model was tested with Pointing's theorem. The results of the tests match to theoretical result with 10^{-6} accuracy. The number of modes in calculations was chosen like that group of homogeneous modes was surrounded with “layer” that consists of 3 or 4 heterogeneous modes. The dependence of field energy stream transitioned through the PC as function of λ/Λ ratio in case of horizontal (a) and vertical (b) polarization is shown on Fig. 3 (where λ — Wave length and Λ — Period of crystal structure). The dependence of reflection (a) and transition (b) elements absolute value on central mode as function of dimensionless thickness h/λ ratio in case of horizontal polarization is shown on Fig. 4.

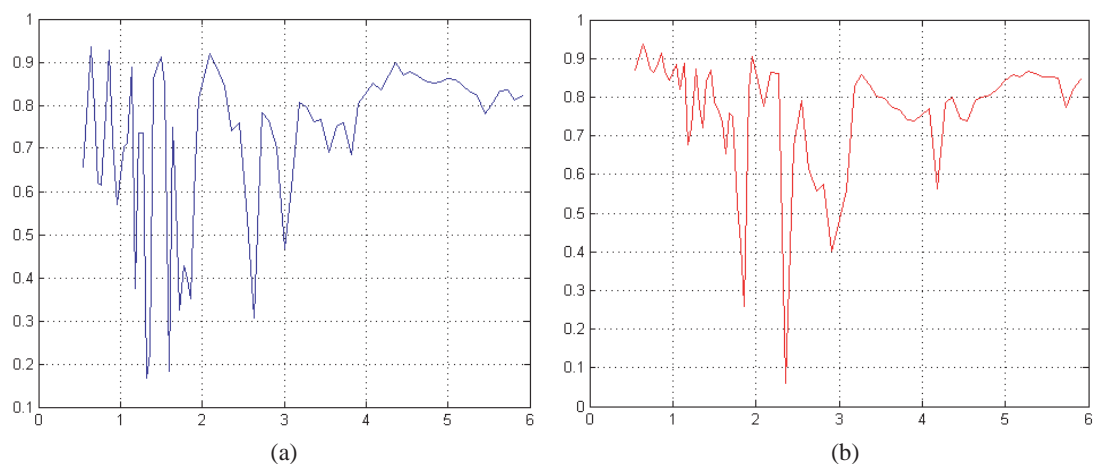


Figure 3: (a) Horizontal polarization, (b) vertical polarization.

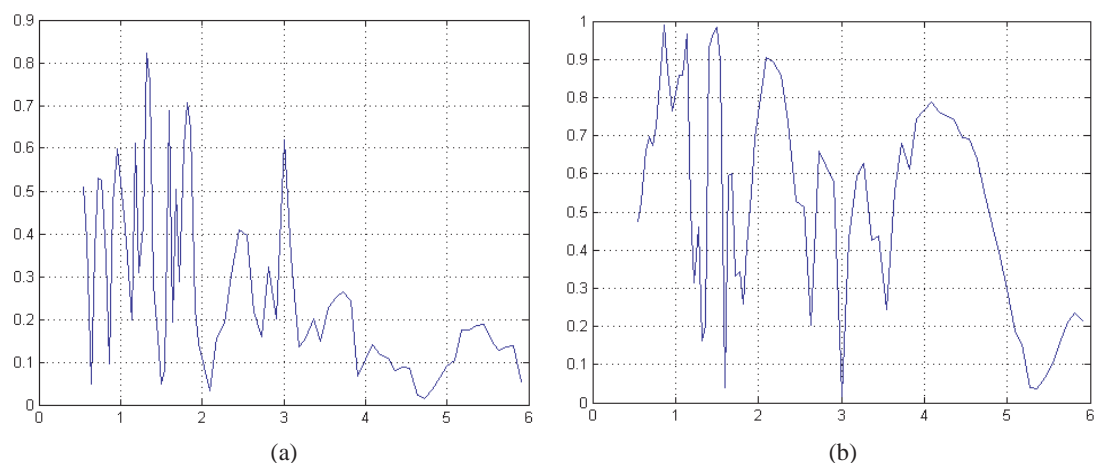


Figure 4: (a) Reflection element, (b) transition element.

REFERENCES

1. Goldberger, M. L. and K. M. Watson, *Collision Theory*, New York, 1964.
2. Bellman, R. and G. M. Wing, *An Introduction to Invariant Imbedding*, Wiley Intersc., New York, 1975.
3. Barnes, C., and J. B. Pendry, "Multiple scattering of waves in random media: A transfer matrix approach," *Proc. R. Soc. Lond. A*, Vol. 437, 185, 1991.
4. Klyatskin, V. I., *The Imbedding Method in the Theory of Wave Propagation*, Nauka, Moscow, 1986 (in Russian).
5. Barabanenkov, Yu. N., V. L. Kouznetsov, and M. Yu. Barabanenkov, "Transfer relations for electromagnetic wave scattering from periodic dielectric one-dimensional interface: TE polarization," *Progress In Electromagnetics Research*, PIER 24, 39–75, 1999.
6. Barabanenkov, Yu. N. and V. L. Kouznetsov, *Radiotekhnika I Elektronika*, Vol. 44, No. 6, 659, 1999 (in Russian).

Simulation of an Ultrashort 2D Photonic Crystal Switch Based on Nonlinear Directional Coupler

A. Taher Rahmati and N. Granpayeh

Faculty of Electrical Engineering, K. N. Toosi University of Technology, Tehran, Iran

Abstract— In this paper, we have simulated the nonlinear photonic crystal directional coupler by the finite difference time domain method. Refractive index of the rods of the central row of the coupler is changed by input signal power due to nonlinear Kerr effect; therefore, input signal beam can be controlled so as to be exchanged between two output ports. Optimized radius and physical length are chosen to increase the coupling efficiency and also reduce the coupling length in linear and nonlinear states of the device.

1. INTRODUCTION

Several photonic crystal (PC) structures have been intensely studied in recent years, because of their micro-scale dimensions and ability to prevent the propagation of some modes. Optical properties of these periodical structures have led them to be employed in different telecommunication devices. Photonic crystal waveguides can be achieved by removing one row of rods, and the directional coupler is produced by setting two waveguides close to each other [1]. Directional couplers execute different functions in conventional optical devices, including power splitting and combining [2] and wavelength-selective coupling [3]. Switching [1] and wavelength multiplexing or demultiplexing [4] can also be achieved by incorporating the nonlinear properties of the material or other control elements of the structure.

Photonic crystal waveguide properties are very sensitive to small variations in arrangement or refractive index of the PC [5, 6]. This sensitivity makes them perfect for switching applications made by directional couplers [7]. Electro-optic and nonlinear refractive index modulations in optical switches are some methods of tuning the coupling length to permit or prevent coupling between waveguides. Different PC directional couplers have been designed to improve the coupling efficiency and coupling length [7, 9].

In this paper, we have analyzed a nonlinear photonic crystal directional coupler by the finite difference time domain method (FDTD). Linear and nonlinear optical properties are changed by variation of the radius, material and refractive index of the central row rods and the input optical power.

2. DESCRIPTION OF THE STRUCTURE

Directional couplers can be obtained by removing two parallel rows of a photonic crystal structure. Our proposed PC directional coupler is composed of input, coupling and output regions in a triangular lattice as, shown in Fig. 1. The coupling region is important in switching performance. Each isolated waveguide supports only a single mode, but by setting two waveguides close to each other, the modes in the waveguides interact to create supermodes and split in two odd and even modes, according to their symmetry with respect to the plane between the guides. Thus the input power will couple to the other waveguide and exchange between them periodically.

The coupling length is the distance over which the phase difference between two modes is 180° , and depends on the difference between propagation constants of the odd and even modes

$$L_c = \frac{\pi}{|\beta_{\text{odd}} - \beta_{\text{even}}|}. \quad (1)$$

Therefore, by increasing difference between propagation constants, the coupling length is reduced. Variations of radius (r_c) and refractive index of the central row rods cause shifting in even mode propagation constant in dispersion diagram [10] and thus changing the coupling length. According to this property of the structure, the power can be guided to the other waveguide and the coupler act as an optical switch, but the switching efficiency and the coupling physical length must be optimized.

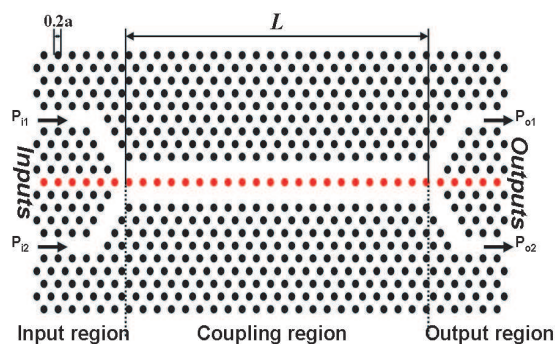


Figure 1: Schematic view of the proposed directional coupler switch. It consists of three regions of input, coupling and output. Total length of the coupling region is L .

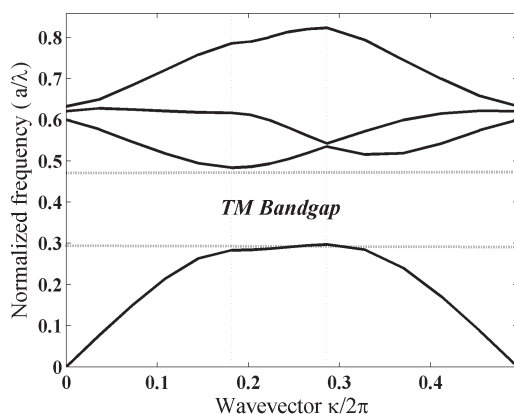


Figure 2: Band diagram for TM polarization in a triangular lattice of AlGaAs rods ($\epsilon = 11.56$) in air substrate.

3. SWITCHING PERFORMANCE

In our proposed switch design, as demonstrated in Fig. 1, the radii of the rods are $r = 0.2a$, where a is the lattice constant. The rods are made of AlGaAs with dielectric constant of $\epsilon = 11.56$ and nonlinear index coefficient of $n_2 = 1.5 \times 10^{-17} \text{m}^2/\text{W}$ at wavelength of $1.55 \mu\text{m}$ [6]. The band gap of this structure is calculated by plane wave expansion (PWE) method. As shown in Fig. 2, the TM band gap of the structure is in the range of $0.3034 \leq a/\lambda \leq 0.4833$, where λ denotes the optical wavelength in free space.

To obtain the switching performance of the device, third order nonlinear coefficient of the dielectric material can be employed to modulate the refractive index by launching high input power. The physical coupling length is chosen such that in the certain frequency, in linear regime the input light is guided in the upper waveguide and in nonlinear regime, due to the launched high input power, is coupled to the lower port.

As depicted in Fig. 3, by changing r_c , the switching frequency is also shifted and approximately in a constant coupling length, increasing r_c causing to decrease the frequency. When the switching frequency is constant, coupling length increases by decreasing r_c [1].

Selecting the proper frequency is so important to have the shortest coupling length, the maximum power output ratio and the minimum reflected power. To select frequency at which the switch works in bar state, a Gaussian beam is launched into the upper input and is sampled in the output ports. The Fourier transform of the output lightwave signals show the certain frequency peaks in which the switch works in bar or cross states. When $r = r_c$, normalized frequency is 0.3697 and coupling length is $4a$.

For better performance and efficiency of such devices, ratio of the output and input powers is an important factor. In linear regime with low input power and nonlinear regime with high input power, the ratio of the output power and reflected power for different r_c were derived by FDTD, the result of which are shown in Fig. 4.

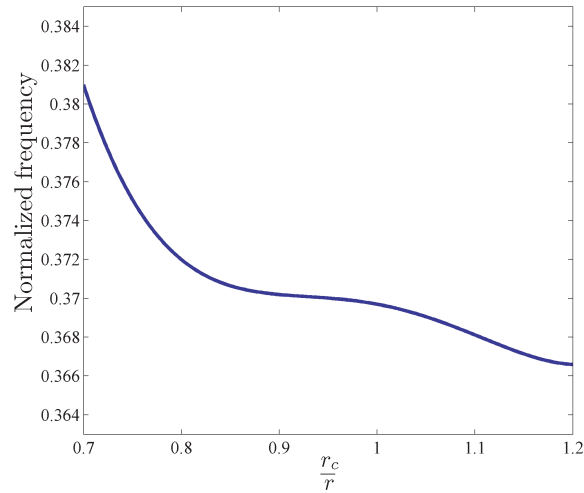


Figure 3: Normalized frequency of switching as a function of r_c/r . Normalized frequency range is from 0.3666 to 0.3810. The frequencies are selected in the range of TM band gap in which a single mode from upper input is coupled to the upper output.

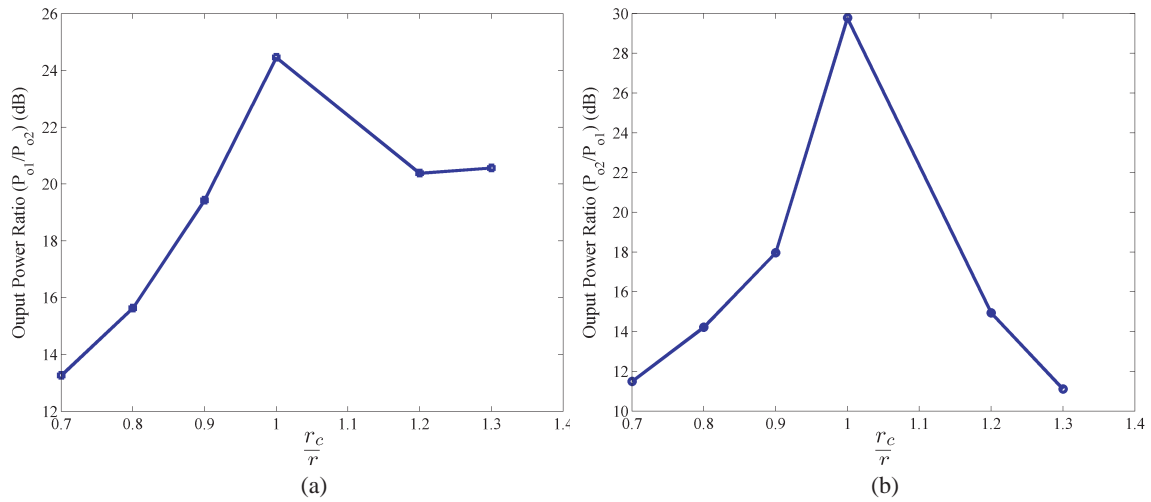


Figure 4: Output power ratio in (a) linear (b) nonlinear states.

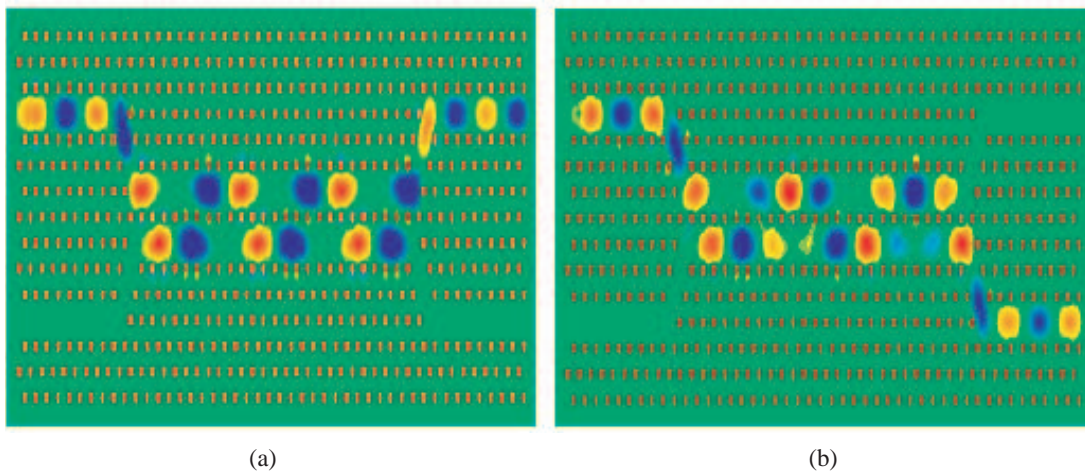


Figure 5: Electric field distribution of the coupler for $r_c = r$ in linear (a) and nonlinear (b) states.

As depicted in Fig. 4, the maximum output power ratio is achieved when r_c is equal to r . The output power ratio in linear and nonlinear states are reduced, when r_c is more or less than r , so it is clear that the optimized value for r_c is r . Although, increasing propagation constant difference of the odd and even modes with decreasing central row rods radius may result in a shorter coupling length [1], but it reduces the switching efficiency. The process can be repeated for the reflected power, until the appropriate r_c can be obtained.

In nonlinear state, when $r_c = r$, power required for switching is 1.55 W and it is 18% lower than the state in which $r_c = 0.7r$. Due to this result, there must be a tradeoff between coupling length, output power ratio and also required power in nonlinear regime.

In Fig. 5, the field distributions for $r_c = r$ in linear and nonlinear regimes are demonstrated. The coupling lengths in both cases are the same, but the lightwave frequencies are different. The lightwave power in linear state is guided to the upper waveguide and in the nonlinear regime is switched to the lower output.

4. CONCLUSION

In this paper, a switch based on nonlinear photonic crystal directional coupler with nonlinear central rods has been proposed. The coupling length, efficiency and performance of the switch in linear (low input power) and nonlinear (high input power) for different radii of the rods of the central row in hexagonal lattice have been analyzed and simulated. The results show that decreasing the radius of the nonlinear central rods up to the radius of the structure rod, causing to increase the output power ratio in nonlinear and linear regime and also decrease the power required for nonlinear state.

ACKNOWLEDGMENT

The authors wish to thank Iran Telecommunication Research Center for the financial support of this project.

REFERENCES

1. Martinez, A., F. Cuesta, and J. Marti, "Ultrashort 2-D photonic crystal directional couplers," *IEEE Photon. Technol. Lett.*, Vol. 15, No. 5, 694–696, 2003.
2. Wang, Y., "Nonlinear optical limiter and digital optical switch by cascaded nonlinear couplers: Analysis," *IEEE J. Lightwave Technol.*, Vol. 17, No. 2, 292–297, 1999.
3. Ferreras, A., F. Rodriguez, E. Gomez-Salas, J. L. De Miguel, and F. Hernandez-Gil, "Useful formulas for multimode interference power splitter/combiner design," *IEEE Photon. Technol. Lett.*, Vol. 5, No. 10, 1224–1227, 1993.
4. Roy, J. N., "Mach-Zehnder interferometer-based tree architecture for all-optical logic and arithmetic operations," *Optik*, in Press, 2009.
5. Maksymov, I. S., L. F. Marsal, and J. Pallares, "An FDTD analysis of nonlinear photonic crystal waveguides," *Opt. and Quantum Electron.*, Vol. 38, No. 1, 149–160, 2006.
6. Zhou, H., X. Jiang, T. Yu, J. Yang, and M. Wang, "Two-mode-interference switching in photonic crystal waveguides," *Int. Symp. on Biophotonics, Nanophotonics and Metamaterials*, 332–334, China, 2006.
7. Qu, Y., H. Ren, and C. Jiang, "A novel design of 2-D photonic crystal directional coupler with high extinction ratio and short coupling length," *IEEE Quantum Electron.*, Vol. 43, No. 11, 974–981, 2007.
8. Fan, S., P. R. Villeneuve, and J. D. Joannopoulos, "Channel drop tunneling through localized states," *Phys. Rev. Lett.*, Vol. 80, No. 5, 960–963, 1998.
9. Yamamoto, N., T. Ogawa, and K. Komori, "Photonic crystal directional coupler switch with small switching length and wide bandwidth," *Opt. Express*, Vol. 14, No. 3, 1223–1229, 2006.
10. Cuesta-Soto, F., A. Martinez, B. Garcia-Banos, and J. Marti, "Numerical analysis of all-optical switching based on a 2-D nonlinear photonic crystal directional coupler," *IEEE Selec. Top. in Quantum Electron.*, Vol. 10, No. 5, 1101–1106, 2004.

Processing Time of Photon Generation

Tibor Bercei

Budapest University of Technology and Economics, Hungary

Abstract— The paper presents a simple new approach providing results on some properties of photon generation like its processing time, energy density, etc. The main goal of the investigation is to establish some basic relationships. Based on the results of the present approach a relationship is obtained between the processing time and energy: the processing time is inversely proportional to the inherent energy in the specific process.

1. INTRODUCTION

Processing time is an important characteristic of every process in physics. A question can be arisen: is the processing time an inherent property of the material? In this paper that very generic question is investigated in details. For that purpose the photon generation is used as a good example.

The photon generation has always been a very interesting phenomenon. It has already been discussed in many excellent papers. So far the best explanations come from quantum physics. Spontaneous emission can be calculated very accurately using quantum electrodynamics [1, 2]. This way, statistical results are obtained, because the process is taken statistical. By other words, it is possible to calculate probabilities of large numbers of interactions.

The aim of this paper is to find understanding and explanations for the behavior and characteristics of photon generation based on a simple approach. The transition of an electron from an upper energy level to a lower level and the accompanying photon emission can be assumed as an instantaneous process. That is utilized in this paper because currently a single photon emission is already feasible for performing experiments [3].

The main goal of the investigation is to establish some basic relationships for the process of photon generation. Its properties can be described more easily if we consider the generation of photons in a semiconductor material. In this paper that method is used. The derived relationships are in good conformity with the well-known properties of photon generation, however, they provide some new results as well.

2. PHOTON GENERATION PROCESS

We consider the photon generation in a direct band gap semiconductor material based on its well-known process [4, 5]. According to that when an electron is in the conductance band, it is at a stable energy level, consequently there is no radiation. When the electron transits from the conductance band to the valence band a photon can be emitted. Then, when the electron is in the valence band it is again at a stable energy level, there is no radiation. Accordingly, radiation can occur during the time interval, when the electron gets from the conductance band to the valence band. The time interval of this transition is equal to the processing time of photon generation.

The question arises: can the transition time be an immediate energy change without taking any time, or does it take some time although a very short time? We can get the answer to this question by considering that the generated photon has a specific frequency. On that basis we propose an approach to estimate the time interval of electron transition which is equal to the processing time of photon generation.

In a direct band gap semiconductor material, there is an energy difference between the conductance band and the valence band, called band gap energy. The energy of the radiated photon is equal to the band gap energy. The frequency, f_{ph} of the photon is given by the well-known equation [6, 7]:

$$f_{ph} = \frac{E_b}{h} \quad (1)$$

where E_b is the band gap energy, and h is the Planck constant.

When we try to estimate the processing time of photon generation we can use Eq. (1) as a basis. This equation tells us that the photon has a specific frequency and this frequency is dependent only on the band gap energy [5, 6].

3. PROCESSING TIME

The question is the following: is the radiating transition of the electron from one energy level to another one an immediate process in time or does it need some time? In the first case the transition process could be described by a Dirac delta function in time [8]. That means the generated photon should have infinite number of frequencies which is not in agreement with the experimental results or by other words it is not a realistic approach. Therefore the second assumption is more likely, i.e., the transition of the electron from the conductance band to the valence band takes some time, although this time is extremely short. That extremely short transition time is the duration of photon generation or by other words the processing time of photon generation.

How can we estimate the processing time? A photon can be represented by an extremely short electromagnetic wave at a frequency given by Eq. (1). Therefore, we suggest an assumption taking the half period of the photon frequency as its generation time. In that case the Fourier expansion of a time function representing the photon generation with the duration of the processing time provides a fundamental frequency for the wave representation of the photon which is equal to the photon frequency f_{ph} given by Eq. (1). Therefore, taking the half period of the photon frequency as its generation time seems to be a good estimation:

$$\tau_{ph} = \frac{T_{ph}}{2} \quad (2)$$

Here τ_{ph} is the processing time of photon generation and T_{ph} is the period time of photon frequency: $T_{ph} = 1/f_{ph}$. In that case the energy is concentrated into the half period of the photon frequency. In the following that assumption is used.

The next question is as follows: is the generation time constant or is it dependent on some effect? The answer is: the generation time is not constant, it is dependent on the band gap energy. From Eqs. (1) and (2):

$$\tau_{ph} = \frac{h}{2E_b} \quad (3)$$

If the band gap energy is higher the generation time is shorter, or by other words the radiated energy pulse or burst is shorter.

4. UNCERTAINTY PRINCIPLE

We use now the uncertainty principle for estimating the processing time in a different way. Based on Eq. (1) there is a relation between the period time T_{ph} of the photon frequency and the band gap energy E_b generating the photon:

$$T_{ph} = \frac{h}{E_b} \quad (4)$$

When we want to determine the processing time we have to consider the Heisenberg uncertainty principle [9]. Accordingly, we get:

$$\Delta t \Delta E \geq \frac{\hbar}{2}. \quad (5)$$

Here Δt is the change in time due to the ΔE change in the energy and $\hbar = h/2\pi$ where h is the Planck constant. In our case:

$$\Delta E = E_c - E_v = E_b \quad (6)$$

E_c is the energy level of the electron in the conductance band and E_v is the energy level of the electron in the valence band. Their difference is the band gap energy E_b .

Further on, Δt is the time elapsed from the start of the process up to the end of the process, or by other words Δt is the processing time, i.e., the duration of photon generation:

$$\Delta t = \tau_{ph} \quad (7)$$

Based on Eqs. (3), (5), (6) and (7) we can write:

$$\tau_{ph} = \frac{h}{2E_b} \geq \frac{h}{4\pi E_b} \quad (8)$$

Consequently, the estimation for the duration of photon generation which is $T_{ph}/2$ is in conformity with the Heisenberg uncertainty principle [9].

We presented an approach to estimate the duration of photon generation. Although we consider the photon having a specific generation time and energy it cannot be separated into smaller parts because the photon has been generated by a single or unique energy transition of the electron in an atom [10].

5. ENERGY DENSITY

Based on Eq. (1) the energy of the photon is proportional to the band gap energy. Therefore, a higher frequency photon carries higher energy. However, the question arises: what is the energy density of photon generation?

The energy density of a process (ρ) can be defined as the ratio of the energy involved in the process (ΔE) and the processing time (Δt):

$$\rho = \frac{\Delta E}{\Delta t} \quad (9)$$

Therefore, in the case of photon generation the energy density is:

$$\rho_{ph} = \frac{E_b}{\tau_{ph}} = \frac{2E_b^2}{h} \quad (10)$$

The energy density of photon generation is proportional to the square of the band gap energy.

By considering the relation between the generation time and the band gap energy it can be concluded: when the band gap energy is higher the duration of photon generation is shorter, therefore the energy density is even higher. By other words the energy density is higher at higher frequencies due to the higher energy and also due to the shorter generation time. This way the ratio of the photon energy densities at different frequencies is proportional to the square of the ratio of their band gap energies (or their frequencies):

$$\frac{\rho_{ph2}(f_2)}{\rho_{ph1}(f_1)} = \left(\frac{E_{b2}}{E_{b1}}\right)^2 = \left(\frac{f_2}{f_1}\right)^2 \quad (11)$$

The indices 1 and 2 refer to quantities at two different photon frequencies.

This quadratic equation holds when photons are generated in a direct band gap semiconductor material. That statement does not depend on the estimated value of the generation time because the same approach is used at every photon frequency. It is worth mentioning that similar results have been obtained by Planck for black body radiation [11] showing not a linear but a faster increase in the spectral energy density with enhancing frequency of radiation.

6. ENERGY DISTRIBUTION

The photon can be represented by an electromagnetic energy burst. That burst is described by its electric field component A_{ph} which is created during the processing time of photon generation.

Based on that the time function of the electric field component is written as:

$$A_{ph}(t) = 0, \quad \text{if } t < 0 \quad (12)$$

$$A_{ph}(t) = A_0 \sin(\omega_{ph}t), \quad \text{if } 0 \leq t \leq \frac{T_{ph}}{2} \quad (13)$$

$$A_{ph}(t) = 0, \quad \text{if } t > \frac{T_{ph}}{2} \quad (14)$$

where $T_{ph}/2$ is the half period time of the sinusoidal time function of the electric field component at the photon angular frequency ω_{ph} or by other words the processing time of photon generation.

This way for the distribution of the photon energy we get:

$$S_{ph}(t) = 0, \quad \text{if } t < 0 \quad (15)$$

$$S_{ph}(t) = K A_0^2 \sin^2(\omega_{ph}t), \quad \text{if } 0 \leq t \leq \frac{T_{ph}}{2} \quad (16)$$

$$S_{ph}(t) = 0, \quad \text{if } t > \frac{T_{ph}}{2} \quad (17)$$

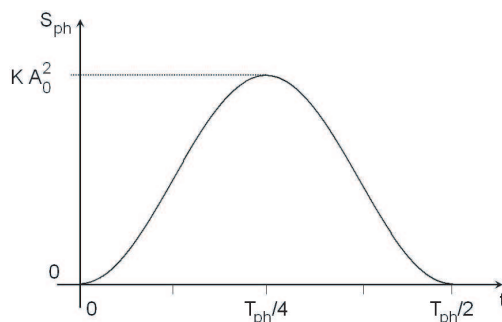


Figure 1: Time function of the photon energy distribution.

Here K is a coefficient analog to the characteristic impedance of the free space.

The distribution of the photon energy given by Eqs. (15), (16) and (17) is plotted in Fig. 1. This relationship shows a smooth energy transition from zero to maximum and then back to zero in the time period from 0 to $T_{ph}/2$.

The total energy E_{ph} of the photon in this representation is obtained by taking the integral of Eq. (16) from $t = 0$ to $t = T_{ph}/2$:

$$E_{ph} = \int_0^{T_{ph}/2} S_{ph}(t) dt = K A_0^2 \int_0^{T_{ph}/2} \sin^2(\omega_{ph} t) dt = K A_0^2 T_{ph}/4 \quad (18)$$

That energy is equal to the band gap energy:

$$E_{ph} = K A_0^2 T_{ph}/4 = E_b \quad (19)$$

In this equation we get a relationship between the band gap energy and the amplitude of the electric field component representing a photon.

7. PROCESSING TIME AND ENERGY RELATIONSHIP

As the processing time or duration of photon generation is inversely proportional to its frequency and its frequency is directly proportional to the band gap energy — see Eq. (3) — we can state: the generation time is inversely proportional to the band gap energy.

Furthermore, it can be stated for a general case: the processing time is inversely proportional to the energy utilized for performing a specific process. Here it is assumed that the other parameters of the process, e.g., electric charge, mass, temperature, material, etc. are unchanged.

Based on the previous statements a more general rule can be suggested: the processing time is inversely proportional to the energy involved in the process. That creates connection between time and energy. Furthermore we can state: time is an inherent property of nature.

8. LENGTH OF OPTICAL PULSES

The generation of an optical pulse is a crucial task in many applications. There is a trend to generate shorter and shorter pulses. The question arises: is there a lower limitation on the pulse length. The answer is: yes, the processing time of the photon generation has to present a limitation. It can be assumed that the half of the processing time is a good estimation as the lower limit for generating an optical pulse. The reason is that the time difference between the half power points of Fig. 1 is equal to the half of the processing time of photon generation.

For example if we take $1 \mu\text{m}$ wavelength, its frequency is 3×10^{14} and thus the half of the processing time at this frequency is $0.83 \times 10^{-15} = 0.83 \text{ fs}$ which is assumed to be the lower limit for the length of an optical pulse at that wavelength. As the processing time of a photon is dependent on its frequency, the pulse length can be shorter if we generate the pulse at a higher frequency (or at a shorter wavelength).

9. PASSING TIME

What is the meaning of the phrase “passing time” or “time is passing”? We can state: time is passing as changes occur in the state of the material, like changes in its energy level, location, motion, composition, etc. To perform such a change, some energy is needed. If the inherent energy

of a specific physical process which is utilized to carry out the change in the state of material is higher, the change is carried out in a shorter time.

We also can say: processing time is the consequence of the utilized (or delivered) energy in a process changing the state of the material. Naturally, the utilization (or delivery) of energy is dependent on external conditions as well, therefore, the same conditions are assumed for the relationship between time and energy.

The relationship between energy and time can be extended to many other physical processes. Further on, it can be seen: time is a phenomenon inherent in physical processes because there is a direct connection between time and energy involved in a specific physical process. This relation gives connection between energy and time.

As another consequence of this relationship we can state: due to the quantized property of energy, time is also quantized. Therefore, a quantum of time belongs to a quantum of energy or by other words the quantum of time is dependent on the quantum of energy involved in a process in nature.

The relationship between energy and time is now applied for a material having relativistic speed, or by other words for a material moving with a velocity approaching the speed of light. In that case the mass of the material is increased and therefore the utilization or delivery (emission) of the same amount of energy will occur during a longer interval of time. By other words at relativistic speed, time is slowed down, the same action needs longer time. That is in complete agreement with the relativity theory.

10. CONCLUSIONS

In this paper a simple new approach has been presented which gives results on some properties of electron-photon interactions like the processing time, energy density and on the relationship between the processing time and the utilized energy. That relationship can be extended to other processes in photonics stating as a general rule that the processing time is inversely proportional to the inherent energy in the specific process.

REFERENCES

1. Yariv, A., *Quantum Electronics*, third edition, John Wiley, New York, 1989.
2. Bohr, N., *Quantum Theory and Measurement*, 9–49, Editors: J. A. Wheeler, W. H. Zurek, Princeton University Press, Princeton, NJ, 1984.
3. Jacques, V., E. Wu, F. Grosshans, F. Treussart, P. Grangier, A. Aspect, and J.-F. Roch, “Experimental realization of Wheeler’s delayed-choice Gedanken experiment,” *Science*, Vol. 315, No. 5814, 966–968, February 16, 2007.
4. Saleh, B. E. A. and M. C. Teich, *Fundamentals of Photonics*, John Wiley, New York, 1991.
5. Sze, S. M., *Physics of Semiconductor Devices*, 2nd Edition, John Wiley, New York, 1981.
6. Einstein, A., “Zur Quantentheorie der Strahlung (On the quantum theory of radiation),” *Physikalische Zeitschrift*, Vol. 18, 121–128, 1917.
7. Stachel, J., editor, *The Collected Papers of Albert Einstein*, University Press, Princeton, 1989.
8. Dirac, P. A. M., *Quantum Mechanics*, Oxford, London, 1970.
9. Heisenberg, W., *The Physical Principles of Quantum Theory*, 1930.
10. Bohr, N., *Nature*, Vol. 121, 580, 1928.
11. Burkhardt, C. E. and J. J. Leventhal, *Topics in Atomic Physics*, Springer, 2006.

Bit Error Rates for Focused General-type Beams

Serap Altay Arpali and Yahya Baykal

Electronic and Communication Engineering Department, Çankaya University, Öğretmenler
Cad. No. 14, Yüzüncüyıl 06530, Balgat, Ankara, Turkey

Abstract— Using the scintillation index of general beam formulation, bit error rate (BER) is investigated for focused Gaussian, cos-Gaussian, cosh-Gaussian and annular beams in weak atmospheric turbulence. We have employed our previously derived formulation of the scintillation index of these beams by Rytov method. Rytov method scintillation theory is known to yield accurate results for focused beams on horizontal paths under certain regions. Therefore we find the scintillation indices of the mentioned beams for the valid region. Using the log-normal distributed intensity, BER values versus signal-to-noise ratio (SNR) are calculated for Gaussian, cos-Gaussian, cosh-Gaussian and annular beams. In our study, the focal lengths (radius of curvature) of all the mentioned focused beams are equal to the propagation distance. The improvement of BER is observed for variations of propagation length, source size and wavelength of operation. Based on these parameters, BER values of Gaussian, cos-Gaussian, cosh-Gaussian and annular beams are compared. BER values we found for the focused Gaussian, cos-Gaussian, cosh-Gaussian and annular beams decrease with increasing source sizes. Likewise, BER values of focused Gaussian, cos-Gaussian, cosh-Gaussian and annular beams decrease with increasing wavelength. The focused annular beam attains the lowest BER value for small source sizes and long propagation distances. Moreover, BER for focused beams is compared with their collimated counterparts. We observe that focused beams have lower BER values than the collimated beams on horizontal paths. Our formulation can easily be extended to cover corresponding higher order beams, however in this paper we concentrate mainly on the zero order beams.

1. INTRODUCTION

In atmospheric optical communication systems, turbulence causes intensity fluctuations in the received signal. This effect reduces the performance of optical communication systems. One of the important performance criteria of atmospheric optical communication links is BER, which is related to the intensity fluctuations. BER of optical beam was studied by Andrews et al. [1]. Recently, BER of the Gaussian beam has been extensively examined [2, 3]. In our previous study, we investigated BER for collimated general beams in weak atmospheric turbulence [4]. In this study we analyze the BER for focused Gaussian, cos-Gaussian, cosh-Gaussian and annular beams in weak atmospheric turbulence versus SNR variations. Theoretical and experimental studies of performance analysis of focused beams generally center around the scintillation index [5]. Scintillation index of focused general-type beams was investigated by our group [6]. In this study, for the BER calculation, we used the scintillation index of higher order general beam formula developed earlier [7].

2. BIT ERROR RATE

For the BER calculation, we use the on-off keying (OOK) modulation in binary direct detection receivers. In the weak atmospheric turbulence, the average BER which is based on the log-normal probability density function associated with the intensity fluctuations, is given as [1]:

$$\langle \text{BER} \rangle = \frac{1}{2\sqrt{2\pi\sigma_I^2}} \int_0^\infty \frac{1}{u} \exp \left\{ -\frac{[\ln(u) + \frac{1}{2}\sigma_I^2]^2}{2\sigma_I^2} \right\} \text{erfc} \left(\frac{\langle \text{SNR} \rangle u}{2\sqrt{2}} \right) du, \quad u > 0, \quad (1)$$

where $u = s/\langle i_s \rangle$ is the normalized signal with unit mean, $\text{erfc}(x)$ is the complementary error function, σ_I^2 is the scintillation index and the mean signal to noise ratio $\langle \text{SNR} \rangle$ in atmospheric turbulence is defined by

$$\langle \text{SNR} \rangle = \frac{\text{SNR}_0}{\sqrt{\frac{P_{SO}}{\langle P_S \rangle} + \sigma_i^2 \text{SNR}_0^2}}. \quad (2)$$

Here P_{SO} is the signal power in the absence of atmospheric turbulence, $\langle P_S \rangle$ is the averaged power of the received signal propagating in atmosphere. For a point detector, the powers P_{SO} and $\langle P_S \rangle$ become the on-axis counterparts and σ_I^2 becomes the on-axis scintillation index. SNR_0 is the signal to noise ratio in the absence of atmospheric turbulence and is defined by the ratio of the detector signal current i_s to the standard deviation of the detector noise σ_N .

3. RESULTS AND DISCUSSION

Using Eq. (1), we plot $\langle \text{BER} \rangle$ versus $\langle \text{SNR} \rangle$ for the focused Gaussian, cos-Gaussian, cosh-Gaussian and annular beams in weak atmospheric turbulence. For the numerical calculation of σ_I^2 in Eq. (1), scintillation index formula in Ref. [7] is utilized. In Ref. [7], scintillation index formula is derived in weak atmospheric turbulence using the Rytov method and is evaluated at the on-axis position, hence $\langle \text{BER} \rangle$ is calculated at the on-axis point. Since Rytov method scintillation theory is known to yield accurate results for focused beams on horizontal paths under certain regions, we find the scintillation indices of the mentioned beams for the valid region [5]. $\langle \text{BER} \rangle$ variations of the focused Gaussian, cos-Gaussian, cosh-Gaussian and annular beams are observed versus the propagation length, source size and the wavelength. The necessary steps to derive the scintillation indices of these beams are provided in Ref. [7]. In the case of our beams, scintillation index, which is derived using Rytov method, satisfy $\sigma_I^2 < 1$ for the given propagation parameters [1]. In our plots, for the scintillation index values, structure constant C_n^2 is taken as $10^{-14} \text{ m}^{-2/3}$, focal lengths (radius of curvature) of all the mentioned focused beams are equal to the propagation distance $F = L$, for all the beams, the source sizes are taken to be equal $\alpha_s = \alpha_{s1} = \alpha_{s2}$, except the annular beam source sizes. In Figs. 1(a), 1(b), 3(a) and 3(b), displacement parameters are taken as $V_x = 50 \text{ m}^{-1}$ and $V_x = 50i \text{ m}^{-1}$ for cos-Gaussian and cosh-Gaussian beams, respectively. For the focused zero order beam types in all figures, orders of the beams are equal to zero, i.e., $n = 0$ and $m = 0$.

Figure 1(a) shows $\langle \text{BER} \rangle$ variation versus $\langle \text{SNR} \rangle$ for the focused Gaussian, cos-Gaussian, cosh-Gaussian and annular beams. In this figure, the propagation length, source size and wavelength of operation values are taken as $L = 2.5 \text{ km}$, $\alpha_s = 1 \text{ cm}$ and $\lambda = 1.55 \mu\text{m}$, respectively. It is seen that focused annular beam has the lowest $\langle \text{BER} \rangle$ value.

In Fig. 1(b), we only increase the propagation distance to $L = 3 \text{ km}$ to examine the effect of the propagation length. Like in Fig. 1(a), in Fig. 1(b), focused annular beam has also the lowest $\langle \text{BER} \rangle$ value. On the other hand, comparing Fig. 1(a) and Fig. 1(b), it is seen that $\langle \text{BER} \rangle$ increases as the propagation length increases.

In Figs. 2(a) and 2(b), displacement parameters are arranged for cos-Gaussian beam as $V_x = 1/\alpha_s$ and purely imaginary for cosh-Gaussian beam. Source sizes for Figs. 2(a) and 2(b) are taken as $\alpha_s = 1 \text{ cm}$ and $\alpha_s = 1.5 \text{ cm}$, respectively. In both figures, the other parameters are given as $\lambda = 1.55 \mu\text{m}$ and $L = 2.5 \text{ km}$. When Figs. 2(a) and 2(b) are compared, $\langle \text{BER} \rangle$ values of the focused beams decrease with increasing source sizes. From Fig. 2(a), we observe that $\langle \text{BER} \rangle$ of focused cosh-Gaussian beam is the smallest for the given parameters. In Fig. 2(b), focused cosh-Gaussian beam attains the lowest $\langle \text{BER} \rangle$ and annular beam has almost the same $\langle \text{BER} \rangle$.

Wavelength variation of the mentioned focused beams is examined in Fig. 3(a) in which we take $\lambda = 0.85 \mu\text{m}$, $L = 2.5 \text{ km}$ and $\alpha_s = 1 \text{ cm}$. According to Fig. 3(a), focused annular beam reaches the best system performance. It is detected from Figs. 1(a) and 3(a) that, $\langle \text{BER} \rangle$ values of the focused beams increase with decreasing wavelength for the given parameters.

Figure 3(b) displays the $\langle \text{BER} \rangle$ variation versus the $\langle \text{SNR} \rangle$ for the collimated Gaussian, cos-

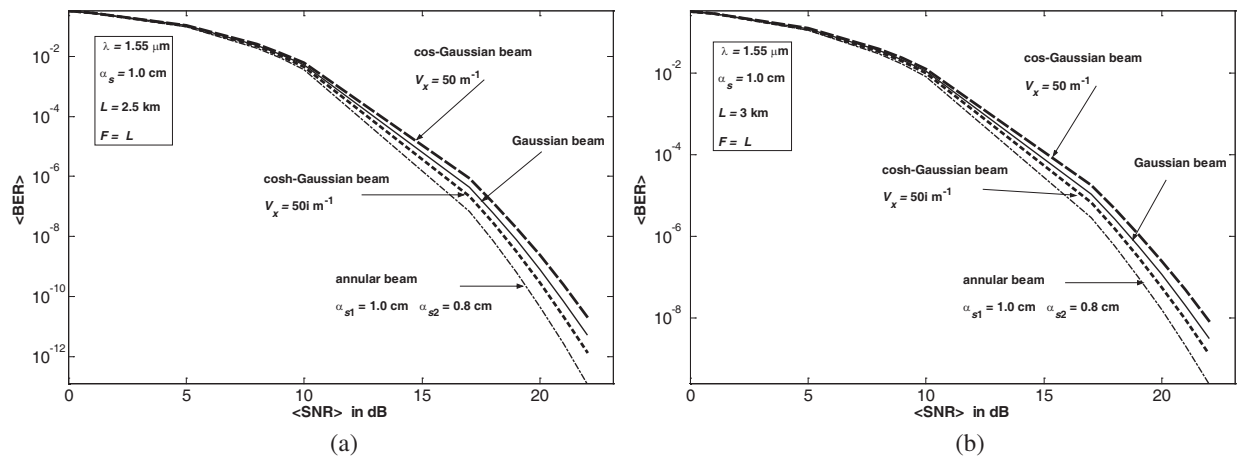


Figure 1: $\langle \text{BER} \rangle$ of focused Gaussian, cos-Gaussian, cosh-Gaussian and annular beams versus $\langle \text{SNR} \rangle$ at the propagation length of (a) $L = 2.5 \text{ km}$ and (b) $L = 3 \text{ km}$.

Gaussian, cosh-Gaussian and annular beams. In this figure, in order to compare with the focused counterparts, we investigated the $\langle \text{BER} \rangle$ of the collimated beams having focal length $F = \infty$, propagation length $L = 2.5$ km, source size $\alpha_s = 1$ cm and wavelength of operation $\lambda = 1.55$ μm . Based on Fig. 1(a) and Fig. 3(b), we note that the focused beams have lower BER values than the collimated beams.

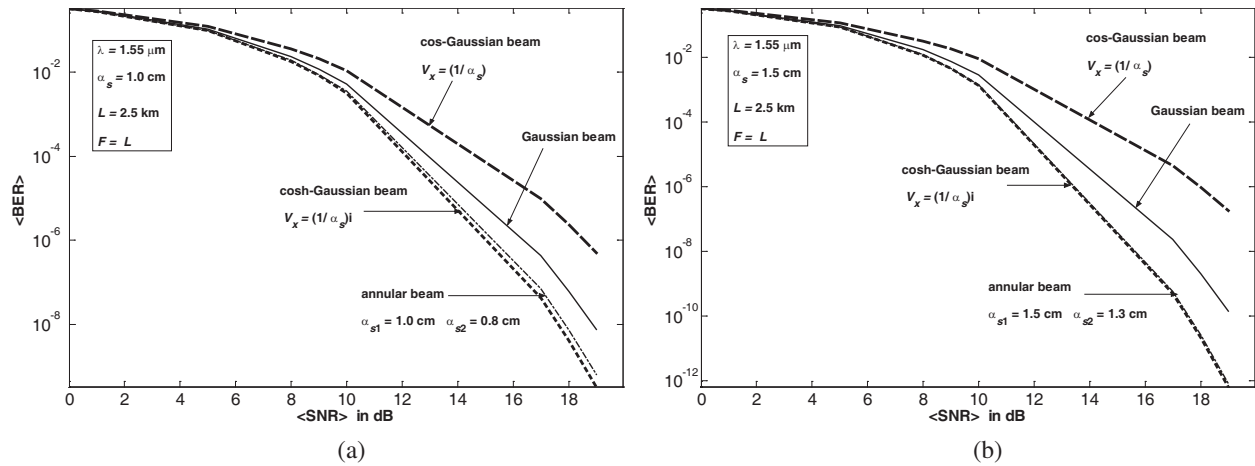


Figure 2: $\langle \text{BER} \rangle$ of focused Gaussian, cos-Gaussian, cosh-Gaussian and annular beams versus $\langle \text{SNR} \rangle$ at the source size of (a) $\alpha_s = 1$ cm and (b) $\alpha_s = 1.5$ cm.

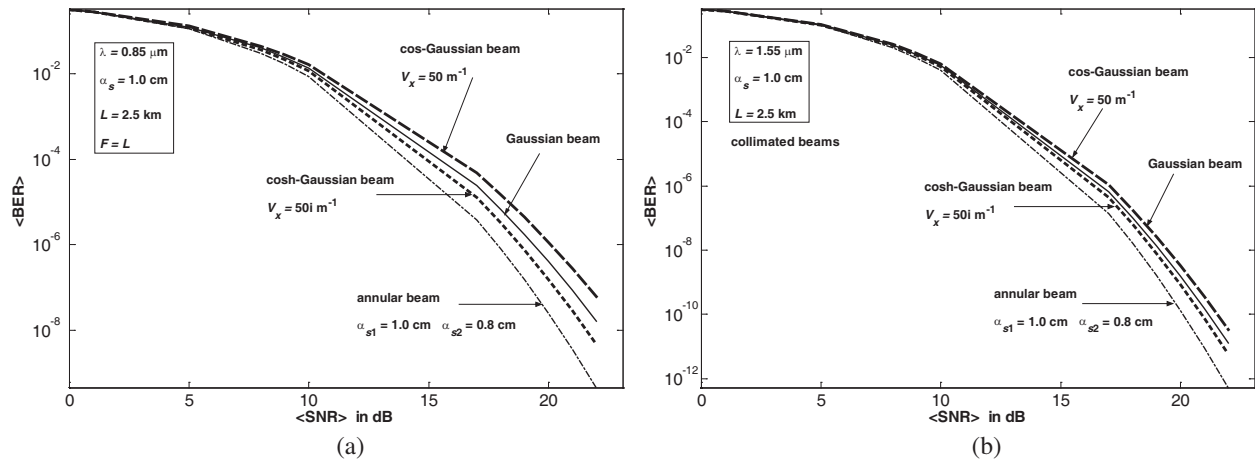


Figure 3: (a) $\langle \text{BER} \rangle$ of focused Gaussian, cos-Gaussian, cosh-Gaussian and annular beams versus $\langle \text{SNR} \rangle$ at $L = 2.5$ km, $\alpha_s = 1$ cm and $\lambda = 0.8$ μm . (b) $\langle \text{BER} \rangle$ of collimated Gaussian, cos-Gaussian, cosh-Gaussian and annular beams versus $\langle \text{SNR} \rangle$ at $L = 2.5$ km, $\alpha_s = 1$ cm and $\lambda = 1.55$ μm .

4. CONCLUSIONS

We have examined the average BER of focused Gaussian, cos-Gaussian, cosh-Gaussian and annular beams in direct detection optical receivers. For this purpose, based on on-off keying modulation, average BER versus average SNR is calculated for the mentioned focused beams in weak atmospheric turbulence. Using the formulation for the scintillation index of general beam, BER characteristics of focused Gaussian, cos-Gaussian, cosh-Gaussian and annular beams are investigated and compared with respect to the propagation length, source size and wavelength of operation. We observed that if the displacement parameters of the beams are fixed, focused annular beam improves the system performance more than the other focused beams for long propagation distances and at small source sizes. As expected, BER values of these beams increase with extended link length. To investigate the source size effect on system performance, we set the displacement parameters of cos-Gaussian and cosh-Gaussian beams to be the inverse of the respective source sizes. The graphical outputs show that BER values of all the mentioned beams decrease with growing source sizes. When

examined versus the wavelength, it is seen that BER values of the focused beams increase with decreasing wavelength. Additionally, BER of the collimated counterparts of these beams are also analyzed and it is observed that the focused beams improve the system performance more than the collimated beams.

REFERENCES

1. Andrews, L. C., R. L. Phillips, and C. Y. Hopen, *Laser Beam Scintillation with Applications*, SPIE, Washington, 2001.
2. Ricklin, J. C. and F. M. Davidson, "Atmospheric optical communication with a Gaussian Schell beam," *J. Opt. Am. A*, Vol. 20, No. 5, 856–866, 2003.
3. Korotkova O., L. C. Andrews, and R. L Philips, "Model for a partially coherent Gaussian beam in atmospheric turbulence with application in Lasercom," *Opt. Eng.*, Vol. 43, No. 2, 330–341, 2004.
4. Arpali, S. A., H. T. Eyyuboğlu, and Y. Baykal, "Bit error rates for general beams," *Appl. Opt.*, Vol. 47, No. 32, 5971–5975, 2008.
5. Baker G. J., "Gaussian beam weak scintillation: Low-order turbulence effects and applicability of the Rytov method," *J. Opt. Am. A*, Vol. 23, No. 2, 395–417, 2006.
6. Baykal, Y. and H. T. Eyyuboğlu, "Intensity fluctuations of focused general-type beams in atmospheric optics links," *Proceedings of SPIE*, 660320-1–660320-8, Florence, Italy, 2007.
7. Arpali, S. A., H. T. Eyyuboğlu, and Y. Baykal, "Scintillation index of higher order cos-Gaussian, cosh-Gaussian and annular beams," *J. Mod. Opt.*, Vol. 55, No. 2, 227–229, 2008.

Analytic Estimate for the Mass of the Photon

A. H. J. Fleming

Biophotonics Research Institute, Melbourne, Australia

Abstract— Regardless of considerable speculation that a non-zero photon mass might not allow gauge invariance or would break the symmetry of the Lagrangian formulations of the various quantum field theories, an analytic expression has been derived for the mass of the photon. Self-field theory was recently used to investigate the role of the photon as the binding energy inside the hydrogen atom where it yielded deterministic eigensolutions to the Maxwell-Lorentz equations. This is a mathematically distinct method to the Lagrangian-based quantum field theories such as quantum electrodynamics. Fundamentally self-field theory obtains an expression for Planck's constant $\hbar = \frac{q^2}{4\pi\epsilon_0 v_e}$ as the energy per cycle of the principal eigenstate thus providing the analytic origin of the various quantum theories. Based on a composite photon, an analytic expression for photon mass is also obtained $m_\gamma c^2 = \frac{\hbar\omega_\gamma v_e}{4c}$, where ω_γ is an integer photon transition frequency within each cycle that can be estimated via the experimentally and theoretically determined g-Landé factor for the electron, that is found to be compatible with the fine-structure constant $\alpha = \frac{v_e}{c} = \frac{4m_\gamma c^2}{\hbar\omega_\gamma}$, where $\omega_\gamma = 54$ and $m_\gamma = 0.396 \times 10^{-55}$ kg (0.221×10^{-19} eV). This value of the mass of the photon is commensurate with current estimates for the photon's upper limit. Thus the photon can be viewed both as a composite particle and a wave resolving its long-standing enigmatic dual nature. Also, the relativistic nature of the photon is understood via the two electromagnetic spinors describing its self fields where its internal motions are involved in the Lorentz transformations. In regards gauge and symmetry, it is noted there are two photons of conjugate spin involved. The photon's composite structure leads to the concept of photon chemistry where various bosons can be understood as compounds of sub-photon particles, similar to atomic compounds. The various gluons can be understood as composites of three sub-photon particles.

1. INTRODUCTION

Since the early days of the quantum field theories (QFTs) namely in the years leading up to World War II when quantum electrodynamics (QED) evolved, symmetry has been connected with the structures of the matrices associated with the various Lagrangian formulations. Real eigenvalues require symmetry or skew symmetry of the interaction matrices resulting from the numerical implementation of the particular QFT. At the same time gauge calibration of the metric $g \rightarrow e^{2\lambda}g$ produces a transformation $A \rightarrow A - d\lambda$ of the potentials. Thus the photon, the quantum of electromagnetic (EM) energy, has been assumed to be massless. During this same period, no other option for a mathematical description of the electron within the atom has been available. For the QFTs, gauge invariance is assumed to imply a massless photon, likewise for the neutrino, and other gauge bosons, otherwise spontaneous symmetry breaking would be observed. Jackson discussing the experimental limit on the inverse square law of electrostatics concluded that the photon mass can be assumed to be zero throughout the classical range of distances and deep into the quantum domain as well. The Particle Data Group lists the best estimates on the upper limit of the photon mass giving the current limit as $< 2 \times 10^{-16}$ eV by Lakes who measured the torque on a toroid Cavendish balance and obtained the limit via the Maxwell-Proca equations.

Recently experimental and theoretical findings have arisen to challenge the zero mass assumption. The neutrino, a member of the lepton family of particles, was found to have a finite, non-zero mass. The SuperKamiokande experiment in Japan put the mass at about 0.1 eV compared with the rest mass of the electron 0.511 MeV. In the experiment muon and tau neutrinos resulted in asymmetric oscillations that depend on the existence of differing non-zero neutrino masses. Theoretically the self-fields of single particles were studied in 1903–4 by Abraham and Lorentz. They modeled the electron as a charged spherical surface of finite radius and found inconsistencies with classical EM theory as the radius went to zero. In 2005 the self-fields of pairs of particles were understood as a mutual phenomenon. The singularity problem at the charge points, similar to that afflicting the QFTs, was solved by using periodic motions that avoid the charge points. The assumption is made that at equilibrium the two particles rotate never residing at their own centres of rotation. The Self-Field Theory (SFT) model for the EM field as a moving stream of photons provides an analysis of the hydrogen atom and yields an analytic derivation of Planck's number

\hbar . The bi-spinorial function for each particle provides a physically plausible interpretation of relativity. The ‘beads on a string’ stream-like EM field modifies the field laws at the atomic level that must now be measured between centres of rotation rather than between charge points. The atomic self-field motions are obtained as closed-form expression using the Maxwell-Lorentz (ML) equations. Depending on permittivity, permeability, energy density, spin of the particles, particle mass ratio, and composition of the bosons, SFT has application across a wide range of physics domains from the photon upwards. SFT involves a concept termed photon chemistry that reveals how fields and particles interact. In 2007 SFT was used to study the binding energy of the hydrogen atom. A single period of the electron and the proton inside the hydrogen atom was investigated. This revealed the presence of two new quantum numbers linked to the photon states within the atom. This photonic mechanism promises to extend current predictive mathematics within chemical interactions such as the way water binds to molecules within both the weather cycle and the cell cycle. As shown below, the electron-proton cycle can also be used to obtain an analytic estimate of the photon mass by balancing Planck’s energy with the energy of the photons within each cycle. Gauge is maintained if the photons transiting between electron and proton are of conjugate spin. In SFT terms the system is stable and periodic if a synchronous double rotation is maintained by the electric- and magnetic-fields where both the orbital and cyclotron separations between electron and proton differ in phase by π . On their own such synchronous orbits are unstable, but together they can form stable dynamic equilibria. Using a modified form of 6 ML equations dynamic equilibria may also exist for strong nuclear regions involving triple rotations where gluons are known to have mass and the motions of the quarks differ in phase by $2\pi/3$.

2. SELF-FIELD THEORY

The particles and EM fields that control the motions of charged particles satisfy the ML equations. For application to atomic physics, regions where particle-field interactions occur are assumed isotropic and homogeneous and the constitutive parameters, ε_0 and μ_0 the permittivity and permeability of free-space, are scalars. Where discrete particles carrying units of elementary charge q of opposite polarity are studied, in the absence of nebular regions of charge and current density, the Maxwell-Lorentz equations are written

$$\nabla \cdot \vec{E} = \frac{q}{v_q} \quad (1a)$$

$$\nabla \cdot \vec{H} = 0 \quad (1b)$$

$$\nabla \times \vec{E} + \mu_0 \frac{\partial \vec{H}}{\partial t} = 0 \quad (1c)$$

$$\nabla \times \vec{H} - \varepsilon_0 \frac{\partial \vec{E}}{\partial t} = \frac{\pi}{s_q} q \vec{v} \quad (1d)$$

The Lorentz equation for the field-forces acting on the particles is written

$$\vec{F} = q\vec{E} + q\vec{v} \times \vec{B} \quad (1e)$$

The constitutive equations in free-space are

$$\vec{B} = \mu_0 \vec{H} \quad (1f)$$

$$\vec{D} = \varepsilon_0 \vec{E}. \quad (1g)$$

The relationship between the speed of light and the ratio of the fields

$$c = (\varepsilon_0 \mu_0)^{-1/2} \quad (1h)$$

$$dU = \rho dV = \frac{1}{2} \left(\varepsilon_0 \vec{E} \cdot \vec{E} + \mu_0 \vec{H} \cdot \vec{H} \right) dV \quad (1i)$$

The atomic energy density per volume (1i) depends upon the E - and H -fields in the atomic region. (1a)–(1d) are termed the EM field equations. In these equations, v is the particle velocity, m is its mass. It is assumed that the volume of integration v_q over which the charge density is evaluated, and the area the charge circulates normal to its motion s_q , are calculated during

successive periods over which the internal motions of the atom take place. At this stage, the periodic motions are not assumed circular, regular, or constant. The area parameters need retrospective examination to check any solutions that are uncovered for a particle's motion. In distinction to quantum theory, charge- and mass-points are non-singular, as a particle does not reside at the charge-point due to the assumed bi-spinorial motions. The simplest application is to assume the proton is of infinite mass and hence the problem resolved down to the Bohr model. The motion of the electron forms an EM self-field solution, its position is a sum of two spinors $\sigma_o(r_o, \omega_o)$ and $\sigma_c(r_c, \omega_c)$: where r_o and r_c are orbital and cyclotron radii and ω_o and ω_c are orbital and cyclotron angular velocities.

$$r(r_o, \omega_o, r_c, \omega_c) = r_o e^{j\omega_o t} + r_c e^{j\omega_c t} \quad (1c)$$

In Equation (2), only discrete eigenvalues of r_o , r_c , ω_o and ω_c are allowed. After suitable algebraic manipulation, the system may be recast in terms of the energies in diagonal matrix form. The Principal mode ($\lambda = 1$) of the resulting eigenvalue system of equations can be written as

$$\begin{bmatrix} 1 & 0 \\ 0 & 1 \end{bmatrix} \begin{bmatrix} V \\ T \end{bmatrix} = \begin{bmatrix} \hbar\omega \\ \hbar\omega \end{bmatrix} \quad (1d)$$

In (3), $V = V_o = \frac{1}{4\pi\epsilon_o} \frac{q}{r_o} = V_c = \frac{1}{4\pi\epsilon_o} \frac{q}{r_c}$, and $T = T_o = T_c = 1/2m_e v_o^2 = T_c = 1/2m_e v_c^2$ are orbital and cyclotron components of the potential and kinetic energies. In the principal mode $\omega = |\omega_o| = |\omega_c|$ and $r = |r_o| = |r_c|$ where the orbital and cyclotron velocities are also equal $v_o = \omega_o r_o = v_c = \omega_c r_c$. From inspection (3) can be seen to contain the elements needed to rewrite the Schrödinger equation for the hydrogen atom in SFT form. Note also that the right hand side of (3) contains a variable herein termed Planck's 'number' that empirically agrees with the known value of Planck's constant to an accuracy of 7 significant figures. The value of Planck's number \hbar comes from $\hbar\omega = \frac{q^2}{8\pi^2\epsilon_o}$ so $\hbar = \frac{q^2}{4\pi\epsilon_o v_o} = \frac{q^2}{4\pi\epsilon_o v_c}$ can be calculated from the solution of (3) that agrees with similar accuracy to the Bohr radius and the known resonant frequency of the hydrogen atom. To see the relationship between Planck's number and velocity, let $\hbar = \frac{E_o}{\nu_o} = \frac{q^2}{4\pi\epsilon_o r_o} \frac{1}{\nu_o} = \frac{q^2}{4\pi\epsilon_o v_o}$ where ν_o is the electron frequency and E_o is the E -field potential energy. By involving the effect of the magnetic field upon the electron the solution forms an extension of Bohr's theory. As it stands (3) contains four variables yielding the deterministic motion of the electron given by (2). This agrees with the four quantum numbers known via quantum mechanics.

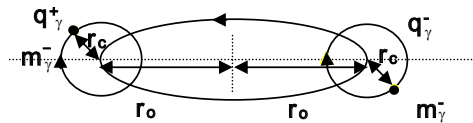


Figure 1: Photon sub-structure consists of two particles, the eplectron, and the phroton, of equal mass.

3. PHOTON MASS

If the intrinsic energy of the system changes from that of free-space ϵ_o and μ_o (as in (1f), (1g), and (1i)) the EM fields within the atom can change thus altering the atomic and molecular binding structures. In effect this means that the radial and spin states of the two photons (one for the electric- the other for the magnetic-field) involved in the binding energy can adapt (in equal fashion to each other for the Principal mode) to the energy change where the photons themselves are assumed to have a composite structure. Now the system has six variables including the electric and magnetic fields in response to the ambient energy conditions. The two extra variables give a range of variation orthogonal to the phase diagrams of atoms. A typical phase diagram shows only a solid line separating the various phases into solid, liquid, or gas indicating a very narrow range of energies between these common phases. SFT indicates a small range of binding structures that depend on the intrinsic energy of the system.

The photons are assumed to transit between electron and proton via a series of resonant elastic collisions. The phase length during transit $\pi/2$ maintains the periodicity of the atom providing a method for analytically comparing the energy of the photon with that of the electron $m_\gamma c^2 = \frac{\hbar\omega_\gamma v_e}{4c}$, where ω_γ is the integer collision frequency of the photon. This collision-based form of periodic

motion by the electron illustrates the non-classical nature of SFT. Assuming a polygonal motion circumscribes a circle representing the Bohr mageton, the photon collision frequency is estimated as 54 to several places of significance from the known value of the Landé g-factor. Thus m_γ evaluates to 0.396×10^{-55} kg (0.221×10^{-19} eV). The analytic expression for the photon mass is compatible with the expression for the fine-structure constant $\alpha = \frac{v_e}{c} = \frac{4m_\gamma c^2}{\hbar\omega_\gamma}$. The numerical value for m_γ is compatible with the experimental estimates for photon mass listed by the Particle Data Group.

REFERENCES

1. Miller, A. I., *Early Quantum Electrodynamics, A Source Book*, Cambridge U. Press, Cambridge, U.K., 1995.
2. Fukuda, Y., et al., “(Super-Kamiokande Collaboration) Evidence for oscillation of atmospheric neutrinos,” *Phys. Rev. Lett.*, Vol. 81, 1562–1567, 1998.
3. Jackson, J. D., *Classical Electrodynamics*, 3rd Edition, John Wiley & Sons, New York, NY, 1999.
4. Caso, C., et al., (Particle Data Group), *European Physical Journal*, Vol. C3, 1, 1998.
5. Yahgjian, A. D., *Relativistic Dynamics of a Charged Sphere, Updating the Lorentz-Abraham Model*, 2nd edition, Lect. Notes Phys., m11, Springer, New York, 2005.
6. Fleming, A. H. J., “Electromagnetic self-field theory and its application to the hydrogen atom,” *Physics Essays*, Vol. 18, No. 3, 265–285, 2005.
7. Fleming, A. H. J., “Self-field theory, analytic spectroscopy of the ordinary photon,” *Proc. 2nd EHE Intl. Conf.*, 18–23, Wroclaw, Poland, 2007.
8. Bertrand, J., “Théorème relatif au mouvement d’un point attiré vers un centre fixe,” *C. R. Acad. Sci.*, Vol. 77, 849–853, 1873.

Ionization-induced Dynamics of Laser-matter Interaction in a Tightly Focused Laser Pulse

E. S. Efimenko and A. V. Kim

Institute of Applied Physics, Russian Academy of Sciences, Nizhny Novgorod, Russia

Abstract— We study the laser-matter interaction via optical-field-ionization of a medium in a focused ultrashort laser pulse by means of the finite-difference-time-domain (FDTD) modeling of the Maxwell equations. A new and unanticipated regime of the interaction with a tightly focused laser beam when small-scaled plasma structures can be generated and strongly influence the field distribution, energy deposition and scattering characteristics is presented. We also show that plasma-field dynamics significantly depends on the focusing angle of the laser pulse and the pulse spectrum as well.

1. INTRODUCTION

The physics of laser-matter interaction where optical-field ionized plasmas are generated has been studied for many years. This topic is of great interest owing to the unique properties of such plasmas and the fact that they suit many important applications, such as x-ray lasers [1–3], attosecond [4, 5] and terahertz [6, 7] pulse generation. However, the importance of this topic is not only due to their applications but is also related to the fundamental issue that ionization nonlinearity plays an important role in determining the dynamical evolution of the system. This follows from the rapid ionization of atoms that strongly modifies the index of refraction, even on a time scale less than the optical period [4, 5, 8]. This effect leads to a number of interesting nonlinear phenomena such as ionization instabilities [9, 10], frequency up-conversion and pulse self-compression [11–14], high-order harmonics generation in a linearly polarized light [15], and long plasma channel guiding [16–18]. Recently, the growing attention was given to the field of the so-called “extreme light” [19, 20] where extreme light parameters for laser-matter interactions, such as very high intensities and/or very short pulse durations, can be realized. For example, tight focusing optics is used in up-to-date experiments to make refractive index modifications in a small volume for waveguide writing in dielectric media [21, 22] and for relativistic laser-plasma interactions in a λ^3 -regime [23]. Additional stimulus nowadays comes also from the expected extremely high intensities approaching the Schwinger limit when direct field-induced ionization of vacuum through pair production can occur [24, 25].

In the present paper we study different regimes of laser-matter interaction, when rapid ionization of a medium strongly modifies the index of refraction. Particular attention is given to the case when the generated plasma density is higher than critical one. We discovered a new and unanticipated regime of interaction at the angles of laser beam focusing exceeding a critical one, when small-scaled plasma structures can be generated in the focal region and strongly influence field distribution, energy deposition and scattering characteristics as well. We also show that the critical angle notably depends on gas density and pulse spectrum.

2. BASIC EQUATIONS

Let us start our consideration of the laser-matter interaction via optical-field-ionization of a medium by direct modeling of the Maxwell equations. This approach allows us to consider self-consistent ionization dynamics in a tightly focused laser beam, including few-optical-cycle pulses, outside the parabolic approximation. In this case, the density of the generated plasma and free-electron current density are governed by the equations [6, 7, 10, 26]

$$\frac{\partial \mathbf{J}}{\partial t} = \frac{e^2 N_e}{m} \mathbf{E}, \quad \frac{\partial N_e}{\partial t} = w(|\mathbf{E}|)(N_m - N_e), \quad (1)$$

$$w(|\mathbf{E}|) = 4\omega_a \left(\frac{I_a}{I_h}\right)^{5/2} \frac{E_a}{|\mathbf{E}|} \exp\left[-\frac{2}{3}\left(\frac{I_a}{I_h}\right)^{3/2} \frac{E_a}{|\mathbf{E}|}\right], \quad (2)$$

where N_e is the electron density, N_m is the initial atom density, I_a and I_h are the ionization potential of the atom under consideration and hydrogen, respectively, $\omega_a = me^2/h^3 = 4.16 \times 10^{16} \text{ s}^{-1}$ is the

atom frequency, $E_a = m^2 e^5 / h^4 = 5.1 \times 10^9$ V/cm is the field strength at the Bohr radius, and e and m are the electron charge and mass, respectively. We also neglected both the linear and nonlinear polarization of the neutrals, assuming that the laser frequency is far from atom resonances and laser power is less than the critical one for self-focusing. Since for ultrashort laser pulses the dominant ionization process is tunnel ionization [4, 5, 8], here we have also neglected the electron collisions, including avalanche ionization and electron-ion recombinations. The ionization achieves saturation when the electron density is equal to the density of neutrals. The Maxwell equations together with Eqs. (1) and (2) were simultaneously solved by the finite difference time domain method (FDTD) [27]. We also used absorbing boundary conditions by the method of perfect matched layers [28]. The developed numerical code is two-dimensional (x, z) in space and allows simulating both TE- and TM-polarized modes. The normalizations of our calculations are selected to model the propagation of electromagnetic radiation in the form of a spatio-temporal pulse with central frequency in vacuum $\lambda_o = 0.8 \mu\text{m}$. We simulate an incident linearly polarized pulse whose spatio-temporal distribution at the boundary has the function $\mathbf{E}(t, x) = \mathcal{E}(t, x)g(x)\mathbf{e}_y$ (TE-mode, x the transverse coordinate, z the coordinate along the propagation direction):

$$\begin{aligned} \mathcal{E}(t, x) = & \frac{A_o}{4} \{1 - \tanh[-\alpha(t - t_o - t_d(x))]\} \times \{1 - \tanh[\alpha(t - 3t_o - t_d(x) - t_p)]\} \\ & \times \sin \left\{ \frac{2\pi}{T} [t - t_o - t_d(x)] \right\}, \end{aligned} \quad (3)$$

where t_o is the rise time of the pulse related to the parameter α by $t_o = \alpha/2.276$, t_p is the length of the parts of pulse having an envelope larger than $0.99 \cdot A_o$, $t_d(x)$ is the inhomogeneous delay applied along the transversal direction of the beam centered at $x = x_o$ in order to create focusing of the beam at distance l_f :

$$t_d(x) = -\frac{l_f}{c} \left[\sqrt{1 + \frac{(x - x_o)^2}{l_f^2}} - 1 \right] \quad (4)$$

For realistic simulations, we used pulses with the following parameters: $t_p = 0.3$ fs, $t_o = 50$ fs referred to as 100-fs Gaussain-like laser pulse, $t_p = 0.3$ fs, $t_o = 25$ fs referred to as 50-fs Gaussain-like laser pulse and $t_p = 0.3$ fs, $t_o = 12.5$ fs referred to as 25-fs Gaussain-like laser pulse. The spatial beam is selected to be Gaussian with a half width equal to w_o : $g(x) = \exp[-(x - x_o)^2/(2w_o^2)]$. The half width of the beam w_o was changed between 10 and 30 μm . The amplitude was taken to be comparable to the characteristic atomic field. We focus the laser pulse in a slab of hydrogen with neutral gas density N_g in the range from 0.1 to $10N_{cr}$. Focusing angle expressed as $\theta = \arctan(w_o/l_f)$ was changed from 0.1 to 0.78. In this paper we focus attention on plasma dynamics, especially in the case of large focusing angles.

3. RESULTS OF NUMERICAL EXPERIMENT

We start our consideration from the case of low gas densities, specifically, $0.1N_{cr}$. In Fig. 1(a), maximum plasma density achieved during pulse propagation in the gas with $N_g = 0.1N_{cr}$ is depicted versus focusing angle θ for Gaussian-like laser pulse with 25 fs (solid line), 50 fs (dashed line) and 100 fs duration (dash-dotted line), a theoretical prediction for the maximum density obtained by using the quasioptical approach, $N_{\max} \approx N_{cr}\theta^2$, is also shown in the picture. A similar dependence for $N_g = 10N_{cr}$ is given in Fig. 1(b) and will be discussed later.

The first point we want to emphasize is that for low gas densities the maximum plasma density for different pulse durations is nearly the same throughout the focusing angles range used in numerical simulation. The difference for the angles in the interval from 0.15 to 0.26 does not exceed 10% at maximum ($0.01N_{cr}$ in absolute value) and its further growth for higher angles is suppressed by the ionization saturation effect. It is worthy of notice that maximum plasma density value outdoes the quasioptical model by factor of 1.3–1.5 even for low angles. For the majority of angles plasma distribution is smooth, but for large focusing angles ($\theta = 0.68$ – 0.78) plasma irregularities can be observed at the intermediate stage (see Figs. 2(a) and 2(b)). We theoretically identify these structures as an unsuspected effect caused by the laser field inhomogeneities under conditions of tight focusing. As is shown in Ref. [29], by solving the Helmholtz equation in vacuum for the case of monochromatic Gaussian laser beam focusing, visible modulations up to 30% can arise in the focal region as a result of the interference effect at tight focusing of a laser wave into a small volume. These intensity modulations usually may be rather small, but due to the sharp dependence of the

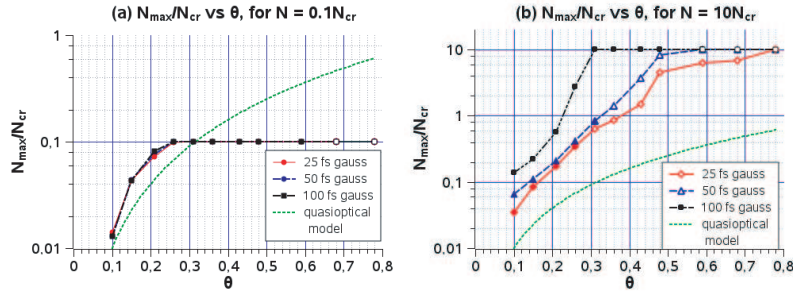


Figure 1: N_{max}/N_{cr} versus focusing angle θ for neutral gas density (a) $0.1 N_{cr}$, (b) $10 N_{cr}$ and different pulse duration: solid line — 25 fs, dashed line — 50 fs, dash-dotted line — 100 fs. Color-filled dots correspond to smooth plasma distribution, hollow — to the case when plasma inhomogeneities are formed at transient stage of pulse dynamics.

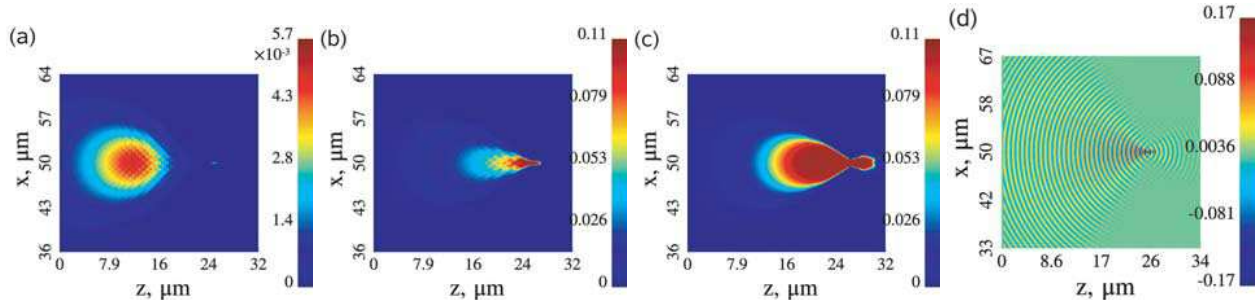


Figure 2: Electron density dynamics (a-c) and electric field distribution (d) for 100 fs Gaussian-like laser pulse focused at $\theta = 0.78$ in gas with $N_{gas} = 0.1 N_{cr}$. Propagation direction from left to right. (a) electron density snapshot for $t = 116$ fs; (b) electron density snapshot for $t = 133$ fs; (c) electron density snapshot for $t = 159$ fs; (d) electric field snapshot for $t = 133$ fs.

ionization rate on field intensity, given by Eq. (2), they may be strongly enhanced through the generation of huge field-induced density perturbations. We estimate the lower angle boundary for this effect as $\theta_{Helmholtz} \simeq 0.4$. In the case of low gas densities, such plasma inhomogeneities at the transient stage of pulse dynamics do not affect significantly further spatio-temporal electron density evolution, and final plasma distribution is smooth (see Fig. 2(c)). This can be explained by ionization saturation and/or relatively low electron density growth rate which is limited by the gas density. Similar plasma structures at the transient stage of plasma dynamics are observed for all the studied pulse durations at large focusing angles, although spectrum broadening for a shorter pulse can lead to smearing of plasma structures. Field dynamics is also affected by plasma formation (see Fig. 2(d)), but only slightly.

Considering the case of high gas density we reveal several important effects which lead to significant modification of the field-plasma dynamics in comparison with the low density case. Firstly, enhanced defocusing nonlinearity due to high plasma density produced during pulse propagation limits field amplitude at the early stage of evolution inhibiting further ionization process. This together with high neutrals density increases characteristic focusing angles for which saturation is observed. Secondly, high electron density growth rate makes the system more sensitive to small field perturbations and leads to shortening of characteristic temporal and spatial scales. The latter imposes a strict limitation on spatio-temporal steps of numerical scheme and demands significant computational resources to model propagation of a tightly focused laser pulse in condensed media or high density gas with $N_g \geq 10 \div 20 N_{cr}$. Finally, strong reflection from overdense plasma complicates plasma-field dynamics and makes it less predictable.

It is clearly seen from Fig. 1(b) that maximum electron density value depends on pulse duration in contrast with the low density case. Increased plasma growth rate leads to plasma formation with rather high electron densities at the early stage of pulse dynamics, when defocusing nonlinearity is insufficient to compensate the focusing of the laser beam, so that the remaining part of the laser pulse where field intensity is sufficient to ionize gas will have strongly nonlinear, even chaotic dynamics.

For a 100 fs laser pulse plasma, distribution at the early stage mimics vacuum field distribution (see Fig. 3(a)) similar to the case of low densities (see Fig. 2(a)), but now the electron density

in inhomogeneities quickly exceeds a critical value (see Fig. 3(b)) and microstructured plasma distribution is finally formed, even with a cavity in the inner part (see Fig. 3(c)) which can trap up to 12 % of the initial pulse energy. At the later stages, plasma-field interaction leads to complicated field dynamics when the pulse splits in a number of flows and is mainly back reflected from dense plasma distribution (see Fig. 3(d)). The minimum angle for such small-scaled structure formation in case of 100 fs pulse is 0.5, which is close to the boundary found by employing the Helmholtz equation analysis.

In case of shorter pulses we have observed a similar effect for large focusing angles. Next we present plasma-field dynamics for 25 fs Gaussian-like laser pulse focused at $\theta = 0.78$ in gas with $N_{gas} = 10N_{cr}$. A broader spectrum in comparison with 100 fs pulse leads to diffusion of well-structured field distribution and, therefore, to smearing of plasma structures (see Fig. 4(a)), which at the early stage follows vacuum field distribution. At the later stages a strongly-coupled regime of field-plasma interaction leads to the formation of small-scaled irregular plasma structures (see Fig. 4(b) and 4(c)), which are not so overdense and let significant part of pulse penetrate through the interaction region (see Fig. 4(d)).

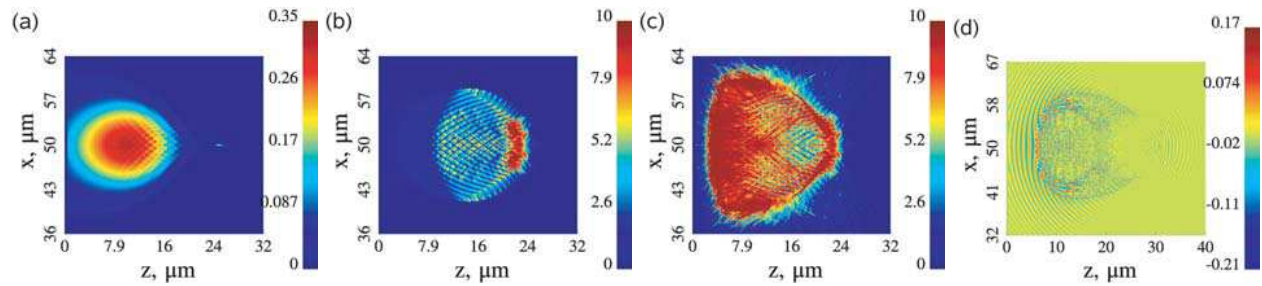


Figure 3: Electron density dynamics (a-c) and electric field distribution (d) for 100 fs Gaussian-like laser pulse focused at $\theta = 0.78$ in gas with $N_{gas} = 10N_{cr}$. Propagation direction from left to right. (a) Electron density snapshot for $t = 116$ fs; (b) electron density snapshot for $t = 141$ fs; (c) final plasma distribution; (d) electric field snapshot for $t = 133$ fs.

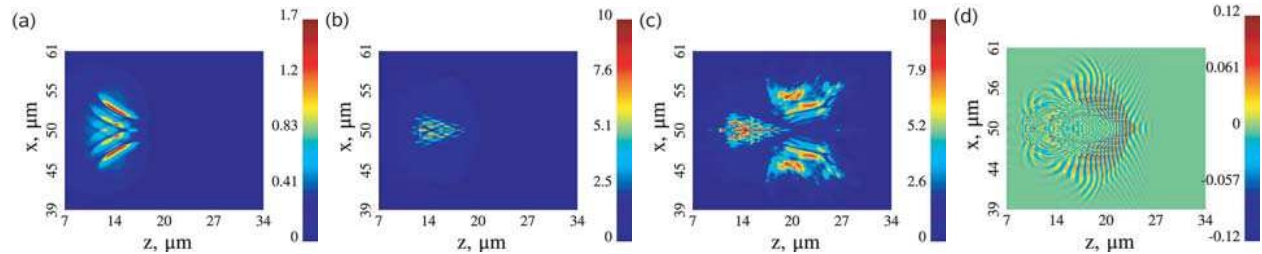


Figure 4: Electron density dynamics (a-c) and electric field distribution (d) for 25 fs Gaussian-like laser pulse focused at $\theta = 0.78$ in gas with $N_{gas} = 10N_{cr}$. Propagation direction from left to right. (a) Electron density snapshot for 75 fs; (b) electron density snapshot for 83 fs; (c) final plasma distribution; (d) electric field snapshot for $t = 91$ fs.

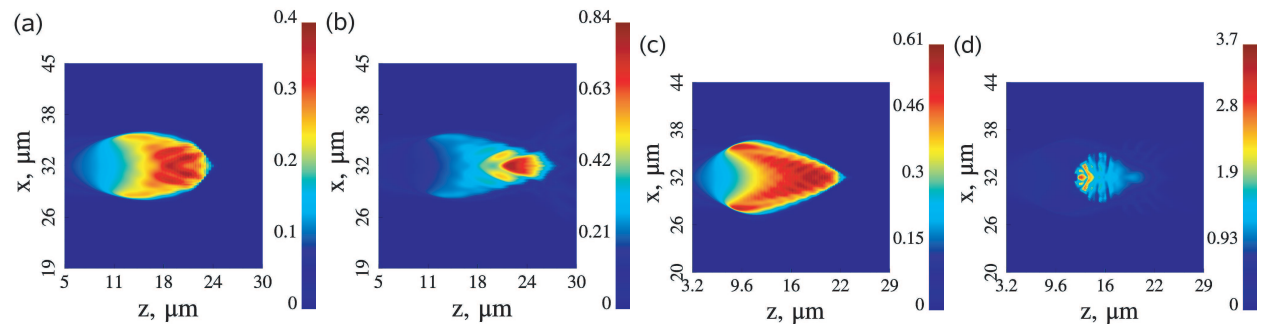


Figure 5: Electron density dynamics for 25 fs Gaussian-like pulse focused at $\theta = 0.36$ (a,b) and 50 fs Gaussian-like laser pulse focused at $\theta = 0.43$ (c,d) in gas with $N_{gas} = 10N_{cr}$. Propagation direction from left to right. Electron density snapshot for (a) $t = 91$ fs, $\theta = 0.36$; (b) $t = 200$ fs, $\theta = 0.36$; (c) $t = 99$ fs, $\theta = 0.43$; (d) $t = 200$ fs, $\theta = 0.43$.

Another important effect is that the boundary angle depends on pulse duration (see Fig. 1(b)) and can be below the value determined from the Helmholtz equation analysis ($\theta_{Helmholtz} \simeq 0.4$). We explain this by the fact that each spectral component has its own focusing length and focal size. A superposition of all spectral components in case of a short pulse can give slight field inhomogeneities near focal plane at a transient stage which, being enforced by sharp ionization rate dependence on field amplitude, may lead to formation of plasma inhomogeneities. While a 100 fs pulse has a relatively narrow spectrum and is unsusceptible to this effect, even for 50 fs and shorter pulses this mechanism plays a key role in laser-matter interaction at intermediate focusing angles and can lead to formation of irregular plasma distribution when the pulse vanishes (see Fig. 5).

4. CONCLUSION

We have shown that at tight focusing of laser beams, a new regime of field-induced plasma generation is realized where plasma density is microstructured and these small-scaled plasma structures may play a key role in the laser-matter interactions. Such structures may be observed at the transient stage for both under- and overdense plasmas. It should be noted that for high density gas, plasma density in these structures can greatly exceed the critical value. This regime of interaction is realized for focusing angles exceeding the critical value and this is completely different compared with the traditional quasioptical approach corresponding to the relatively small angles of beam focusing, where the generated plasma structures are smooth on a laser wavelength scale. The interaction regime and critical focusing angle notably depend on neutrals gas density and laser pulse duration.

REFERENCES

1. Amendt, P., D. C. Eder, and S. C. Wilks, *Phys. Rev. Lett.*, Vol. 66, 2589, 1991.
2. Nagata, Y., et al., *Phys. Rev. Lett.*, Vol. 71, 3774, 1993.
3. Lemoff, B. E., et al., *Phys. Rev. Lett.*, Vol. 74, 1574, 1995.
4. Brabec, T. and F. Krausz, *Rev. Mod. Phys.*, Vol. 72, 545, 2000.
5. Baltuška, A., et al., *Nature*, Vol. 421, 611, London, 2003.
6. Dai, J., X. Xie, and X.-C. Zhang, *Phys. Rev. Lett.*, Vol. 97, 103903, 2006.
7. Gildenburg, V. B. and N. V. Vvedenskii, *Phys. Rev. Lett.*, Vol. 98, 245002, 2007.
8. Popov, V. S., *Physics-Uspexhi*, Vol. 47, 855, 2004.
9. Lontano, M., et al., *Physica Scripta*, Vol. 63, 141, 1996.
10. Antonsen, Jr., T. M. and Z. Bian, *Phys. Rev. Lett.*, Vol. 82, 3617, 1999.
11. Yablonovich, E., *Phys. Rev. A*, Vol. 10, 1888, 1974.
12. Wood, W. M., G. B. Fogth, and M. C. Downer, *Opt. Lett.*, Vol. 13, 984, 1988.
13. Gildenburg, V. B., A. V. Kim, and A. M. Sergeev, *JETP Lett.*, Vol. 51, 104, 1990.
14. Kim, A. V., et al., *Phys. Rev.*, Vol. 42, R2493, 1990.
15. Brunel, F., *JOSA B*, Vol. 7, 521, 1990.
16. Braun, A., et al., *Opt. Lett.*, Vol. 20, 73, 1995.
17. Anderson, D., et al., *Phys. Rev. E*, Vol. 52, 4564, 1995.
18. Sergeev, A. M., et al., *Laser Part Beams*, Vol. 17, 129, 1999.
19. Mourou, G. A., T. Tajima, and S. V. Bulanov, *Rev. Mod. Phys.*, Vol. 78, 309, 2006.
20. Wegener, M., *Extreme Nonlinear Optics*, Springer-Verlag, Berlin, 2005.
21. Nolte, S., et al., *Appl. Phys. A*, Vol. 77, 109, 2003.
22. Bhardwaj, V. R., et al., *J. Appl. Phys.*, Vol. 97, 083102, 2005.
23. Naumova, N. M., et al., *Phys. Rev. Lett.*, Vol. 92, 063902, 2004.
24. Tajima, T. and G. Mourou, *Phys. Rev. ST-AB*, Vol. 5, 031301, 2002.
25. Bulanov, S. S., N. B. Narozhny, V. D. Mur, and V. S. Popov, *JETP*, Vol. 102, 9, 2006.
26. Gildenburg, V. B., V. I. Pozdnjakova, and I. A. Shereshevskii, *Phys. Lett. A*, Vol. 203, 214, 1995.
27. Yee, S., *IEEE. Trans. Antennas*, Vol. 14, 302, 1966.
28. Berenger, J. P., *J. Comput. Phys.*, Vol. 144, 185, 1994.
29. Efimenko, E. S., A. V. Kim, and M. Quiroga-Teixeiro, *Phys. Rev. Lett.*, Vol. 102, 015002, 2009.

Excitation and Propagation of Whistler Waves in a Magnetoplasma Containing Density and Magnetic-field Nonuniformities

P. V. Bakharev¹, A. V. Kudrin¹, and T. M. Zaboronkova²

¹University of Nizhny Novgorod, Russia

²Technical University of Nizhny Novgorod, Russia

Abstract— Excitation and propagation of whistler-mode waves in a magnetoplasma containing cylindrically symmetric nonuniformities of plasma density or external static magnetic field are studied. Using a rigorous solution for the total source-excited field comprising both the discrete and continuous parts of the spatial spectrum of waves, the radiation resistance of a loop antenna in the presence of such structures is determined. Conditions are found under which the radiation resistance of the loop antenna located in a weakly nonuniform plasma-density depletion or magnetic-field enhancement can be notably greater than that in a homogeneous magnetoplasma whose parameters coincide with those near the nonuniformity axis.

1. INTRODUCTION

Whistler-mode waves guided by cylindrical density enhancements in a magnetoplasma have received much careful study and there are many accounts of them (see, e.g., [1] and references therein). However, there exists very little theory of the phenomena related to the source-excited whistler waves in the guiding structures located in an unbounded background magnetoplasma and formed by density depletions or nonuniformities of an external static magnetic field. Earlier studies of the whistler wave guidance by such plasma structures employed various approximate approaches such as the geometrical optics or the WKB approximation [2, 3]. In the present work, the full-wave approach is used to analyze the features of excitation and propagation of whistler waves in a magnetoplasma containing the above-mentioned cylindrical structures in the case where their radii are comparable to or less than typical wavelengths of the guided modes.

2. FORMULATION OF THE PROBLEM

We consider a cold unbounded collisionless magnetoplasma containing a cylindrical nonuniformity in which either the plasma density or external static magnetic field is a function of radial distance from the nonuniformity axis. This axis is taken as the z axis of a cylindrical coordinate system (ρ, ϕ, z) . Parallel to this axis is an external static magnetic field $\vec{B}_0 = B_0 \hat{z}_0$. The plasma is assumed to be described by the cold-plasma dielectric tensor ε whose nonzero elements are written as follows: $\varepsilon_{\rho\rho} = \varepsilon_{\phi\phi} = \varepsilon_0 \varepsilon$, $\varepsilon_{\rho\phi} = -\varepsilon_{\phi\rho} = -i\varepsilon_0 g$, and $\varepsilon_{zz} = \varepsilon_0 \eta$, where ε_0 is the permittivity of free space. General expressions for the quantities ε , g , and η are determined by the medium parameters and are given elsewhere [1].

It is assumed that the frequency ω belongs to the whistler range

$$\omega_{\text{LH}} \ll \omega < \omega_{\text{H}} \ll \omega_{\text{p}}, \quad (1)$$

where ω_{LH} is the lower hybrid frequency, ω_{H} is the electron gyrofrequency, and ω_{p} is the electron plasma frequency.

We take the following models of cylindrical nonuniformities in a magnetoplasma. The first one is a density duct in a uniform static magnetic field. In this case, the plasma density N is a constant, \tilde{N} , in the inner core $\rho < a_0$, a constant, N_a , in the outer region $\rho > a_1$, and varies smoothly from \tilde{N} to N_a within the duct wall $a_0 < \rho < a_1$ by the law

$$N(\rho) = \left\{ \tilde{N} + N_a + \left(\tilde{N} - N_a \right) \sin \left[\pi(a - \rho) / (a_1 - a_0) \right] \right\} / 2, \quad (2)$$

where $a = (a_0 + a_1)/2$. The second kind of nonuniformity to be considered is a magnetic-flux tube in a plasma of constant density. In this case, the external magnetic field B_0 takes constant values \tilde{B}_0 and B_a in the regions $\rho < a_0$ and $\rho > a_1$, respectively, and varies in the interval $a_0 < \rho < a_1$ according to the law that can be obtained from (2) by making the replacements $\tilde{N} \rightarrow \tilde{B}_0$, $N_a \rightarrow B_a$, and $N(\rho) \rightarrow B_0(\rho)$.

The electromagnetic field is excited by a ring electric current whose density (with the $\exp(i\omega t)$ time dependence dropped) is given by

$$\vec{J}(\rho, z) = \hat{\phi}_0 I_0 \delta(\rho - b) \delta(z), \quad (3)$$

which corresponds to a circular loop antenna commonly used in appropriate experiments. Here, δ is the Dirac function, b is the loop radius, and I_0 is the total antenna current.

Our main task is to study the efficiency of excitation of guided and unguided waves which are radiated from source (3) located in a density duct or magnetic-flux tube. To do this, we should obtain the solution of the Maxwell equations in the presence of a cylindrical nonuniformity in the plasma.

3. FIELD EXPANSION IN THE PRESENCE OF A CYLINDRICAL NONUNIFORMITY

Due to the azimuthal symmetry of the problem, the solution of the source-free Maxwell equations can be sought in terms of the modal fields

$$\begin{bmatrix} \vec{E}_{s,\alpha}(\vec{r}, q) \\ \vec{B}_{s,\alpha}(\vec{r}, q) \end{bmatrix} = \begin{bmatrix} \vec{E}_{s,\alpha}(\rho, q) \\ \vec{B}_{s,\alpha}(\rho, q) \end{bmatrix} \exp(-ik_0 p_{s,\alpha}(q)z), \quad (4)$$

where q is the transverse wave number in the ambient magnetoplasma ($\rho > a_1$), normalized to the free-space wave number $k_0 = \omega/c$; the function $p_{s,\alpha}(q)$ describes the dependence of p , the axial wave number normalized to k_0 , on the transverse wave number q for the “ordinary” ($\alpha = o$) and “extraordinary” ($\alpha = e$) characteristic waves of the ambient uniform plasma; the subscript s denotes the wave propagation direction ($s = -$ and $s = +$ designate waves propagating in the negative and positive directions of the z axis, respectively); and $\vec{E}_{s,\alpha}(\rho, q)$ and $\vec{B}_{s,\alpha}(\rho, q)$ are the vector wave functions describing the radial distribution of the field of a mode corresponding to the transverse wave number q and the indices s and α . The functions $p_{s,\alpha}(q)$ obey the relation $p_{+,\alpha}(q) \equiv p_\alpha(q) = -p_{-,\alpha}(q)$, where $p_\alpha(q)$ is written as

$$p_\alpha(q) = \left[\varepsilon_a - \frac{1}{2} \left(1 + \frac{\varepsilon_a}{\eta_a} \right) q^2 + \chi_\alpha R_p(q) \right]^{1/2}, \quad R_p(q) = \left[\frac{1}{4} \left(1 - \frac{\varepsilon_a}{\eta_a} \right)^2 q^4 - \frac{g_a^2}{\eta_a} q^2 + g_a^2 \right]^{1/2}. \quad (5)$$

Here, ε_a , g_a , and η_a denote the quantities ε , g , and η , respectively, in the outer region, and $\chi_o = -\chi_e = -1$. It is assumed that $\text{Re } R_p(q) > 0$ and $\text{Im } p_\alpha(q) < 0$. Note that the functions $\vec{E}_{s,\alpha}(\rho, q)$ and $\vec{B}_{s,\alpha}(\rho, q)$ can be expressed in terms of two scalar functions $E_{\phi; s,\alpha}(\rho, q)$ and $B_{\phi; s,\alpha}(\rho, q)$.

Following work [1], it can be shown that in the considered case, a complete set of normal modes over which the total field can be expanded comprises the discrete spectrum of transversely localized eigenmodes, which are guided by the plasma nonuniformity, and the continuous spectrum of unguided modes that are necessary to describe the radiation field.

The unguided modes correspond to positive real values of q . In the uniform outer region ($\rho > a_1$), the fields of the continuous-spectrum modes are written as follows:

$$\begin{aligned} E_{\phi; s,\alpha}(\rho, q) &= i \left[\sum_{k=1}^2 C_{s,\alpha}^{(k)}(q) H_1^{(k)}(k_0 q \rho) + D_{s,\alpha}(q) H_1^{(2)}(k_0 q \alpha \rho) \right], \\ B_{\phi; s,\alpha}(\rho, q) &= -c^{-1} \left[\sum_{k=1}^2 C_{s,\alpha}^{(k)}(q) n_{s,\alpha}^{(1)} H_1^{(k)}(k_0 q \rho) + D_{s,\alpha}(q) n_{s,\alpha}^{(2)} H_1^{(2)}(k_0 q \alpha \rho) \right]. \end{aligned} \quad (6)$$

Here, $H_1^{(1,2)}$ are Hankel functions of the first and second kinds, $C_{s,\alpha}^{(1,2)}$ and $D_{s,\alpha}$ are coefficients to be determined, and

$$\begin{aligned} n_{s,\alpha}^{(1,2)}(q) &= -\varepsilon_a \left[\left(q_\alpha^{(1,2)} \right)^2 + p_\alpha^2(q) + \frac{g_a^2}{\varepsilon_a} - \varepsilon_a \right] (p_{s,\alpha}(q) g_a)^{-1}, \\ q_\alpha^{(1)} &= q, \quad q_\alpha^{(2)} = q_\alpha(q) = \left[\varepsilon_a - p_\alpha^2(q) - \frac{g_a}{\varepsilon_a} \left(g_a - \frac{\eta_a p_{s,\alpha}(q)}{n_{s,\alpha}^{(1)}(q)} \right) \right]^{1/2}, \end{aligned} \quad (7)$$

where it is assumed that $\text{Im } q_\alpha(q) < 0$.

In the nonuniform part of the cylindrical structure, the fields of unguided modes cannot be expressed in terms of known functions, and the field equations must be solved numerically. There are four independent solutions for the field in the region $\rho < a_1$, of which two solutions, hereafter denoted as $\tilde{E}_{\phi; s,\alpha}^{(1)}(\rho, q)$, $\tilde{B}_{\phi; s,\alpha}^{(1)}(\rho, q)$ and $\tilde{E}_{\phi; s,\alpha}^{(2)}(\rho, q)$, $\tilde{B}_{\phi; s,\alpha}^{(2)}(\rho, q)$, are regular at $\rho = 0$. Then the solution for the field in the region $\rho < a_1$ is written as

$$E_{\phi; s, \alpha}(\rho, q) = i \sum_{k=1}^2 A_{s, \alpha}^{(k)}(q) \tilde{E}_{\phi; s, \alpha}^{(k)}(\rho, q), \quad B_{\phi; s, \alpha}(\rho, q) = -c^{-1} \sum_{k=1}^2 A_{s, \alpha}^{(k)}(q) \tilde{B}_{\phi; s, \alpha}^{(k)}(\rho, q), \quad (8)$$

where $A_{s, \alpha}^{(1,2)}$ are coefficients to be determined. It is evident that in the uniform inner core ($\rho < a_0$), the particular solutions $\tilde{E}_{\phi; s, \alpha}^{(k)}(\rho, q)$ and $\tilde{B}_{\phi; s, \alpha}^{(k)}(\rho, q)$ reduce to cylindrical functions (see [1] for more details). Knowing the values of these functions and their derivatives at $\rho = a_0$, one can easily find the functions $\tilde{E}_{\phi; s, \alpha}^{(k)}(\rho, q)$ and $\tilde{B}_{\phi; s, \alpha}^{(k)}(\rho, q)$ in the nonuniform region $a_0 < \rho < a_1$ by numerically solving the wave equations for each q . Such a procedure automatically ensures the continuity of the tangential field components at $\rho = a_0$. Next, satisfying the continuity conditions for the tangential field components at $\rho = a_1$, we arrive at the system of linear equations for unknown coefficients $A_{s, \alpha}^{(1,2)}$, $C_{s, \alpha}^{(1,2)}$, and $D_{s, \alpha}$. This system can be represented in matrix form as $\mathbf{S} \cdot \vec{G} = C_{s, \alpha}^{(1)} \vec{F}$, where the elements of the column vector \vec{G} are given by the expressions $G_{1,2} = A_{s, \alpha}^{(1,2)}$, $G_3 = C_{s, \alpha}^{(2)}$, and $G_4 = D_{s, \alpha}$. The elements of the matrix \mathbf{S} and the components of the column vector \vec{F} , which are not written here for brevity, are expressed in an obvious manner via particular field solutions entering the representations of the tangential fields on both sides of the interface $\rho = a_1$. The above-mentioned matrix equation gives four linear relationships for five coefficients $A_{s, \alpha}^{(1,2)}$, $C_{s, \alpha}^{(1,2)}$, and $D_{s, \alpha}$, so that one of these coefficients can be taken arbitrary [1]. For numerical calculations, it is most convenient to put $C_{s, \alpha}^{(1)} = \det \|\mathbf{S}\|$ and then determine the remaining coefficients.

The transversely localized eigenmodes (also called the discrete-spectrum modes) guided by the cylindrical nonuniformity correspond to discrete complex quantities q_n ($n = 0, 1, 2, \dots$). It turns out that these quantities are zeros of the coefficient $C_{s, \alpha}^{(1)}$ and have the negative imaginary part (i.e., $\text{Im } q_n < 0$). The substitution of q_n into $p_{s, \alpha}(q)$ yields the axial wave numbers $p_{s, n}$ of the eigenmodes. It is adopted that $p_{\pm, n} = \pm p_n$. For shortening the writing, we represent the fields of the discrete-spectrum modes in the form

$$\begin{bmatrix} \vec{E}_{s, n}(\vec{r}) \\ \vec{B}_{s, n}(\vec{r}) \end{bmatrix} = \begin{bmatrix} \vec{E}_{s, n}(\rho) \\ \vec{B}_{s, n}(\rho) \end{bmatrix} \exp(-ik_0 p_{s, n} z), \quad (9)$$

where $\vec{E}_{s, n}(\rho) = \vec{E}_{s, \alpha}(\rho, q_n)$ and $\vec{B}_{s, n}(\rho) = \vec{B}_{s, \alpha}(\rho, q_n)$.

With allowance for the performed analysis, the field excited by an axisymmetric source in the presence of a cylindrical nonuniformity is given by the following expansion over the discrete- and continuous-spectrum modes outside the source region:

$$\begin{bmatrix} \vec{E}(\vec{r}) \\ \vec{B}(\vec{r}) \end{bmatrix} = \sum_n a_{s, n} \begin{bmatrix} \vec{E}_{s, n}(\vec{r}) \\ \vec{B}_{s, n}(\vec{r}) \end{bmatrix} + \sum_{\alpha} \int_0^{\infty} a_{s, \alpha}(q) \begin{bmatrix} \vec{E}_{s, \alpha}(\vec{r}, q) \\ \vec{B}_{s, \alpha}(\vec{r}, q) \end{bmatrix} dq, \quad (10)$$

where $a_{s, n}$ and $a_{s, \alpha}$ are the excitation coefficients of the respective modes. In expansion (10), one should put $s = +$ for $z > 0$ and $s = -$ for $z < 0$. Next, following the well-known technique developed for finding the excitation coefficients of modes of open waveguides [1], we can obtain for source (3)

$$a_{\pm, n} = I_0 2\pi b N_n^{-1} E_{\phi; \mp, n}^{(T)}(b), \quad a_{\pm, \alpha}(q) = I_0 2\pi b N_{\alpha}^{-1}(q) E_{\phi; \mp, \alpha}^{(T)}(b, q). \quad (11)$$

Here, the superscript (T) denotes fields taken in a medium described by the transposed dielectric tensor ϵ^T , and the normalization quantities N_n and $N_{\alpha}(q)$ for modes are given by

$$N_n = \frac{2\pi}{\mu_0} \int_0^{\infty} \left[\vec{E}_{+, n}(\rho) \times \vec{B}_{-, n}^{(T)}(\rho) - \vec{E}_{-, n}^{(T)}(\rho) \times \vec{B}_{+, n}(\rho) \right] \cdot \hat{z}_0 \rho d\rho, \quad (12)$$

$$N_{\alpha}(q) = -\frac{16\pi}{Z_0 k_0^2} \left(\frac{dp_{\alpha}(q)}{dq} \right)^{-1} \left[1 + \eta_a^{-1} \left(n_{+, \alpha}^{(1)} \right)^2 \right] C_{+, \alpha}^{(1)}(q) C_{+, \alpha}^{(2)}(q),$$

where μ_0 and Z_0 are the permeability and wave impedance of free space, respectively.

The total radiation resistance of the loop antenna with current (3) is written as

$$R_{\Sigma} = 2P_{\Sigma}/|I_0|^2 = \sum_n R_n + R_{cs}, \quad (13)$$

where P_{Σ} is the total radiated power and

$$R_n = -2\pi b \text{Re} (I_0^{-1} a_{s, n} E_{\phi; s, n}(b)), \quad R_{cs} = -2\pi b \text{Re} \int_0^{\infty} I_0^{-1} a_{s, e}(q) E_{\phi; s, e}(b, q) dq. \quad (14)$$

The quantities R_n and R_{cs} are the partial radiation resistances corresponding to the discrete- and continuous-spectrum modes, respectively. We emphasize that the ‘‘ordinary’’ wave, which is evanescent in range (1), does not contribute to the radiation.

4. NUMERICAL RESULTS

An examination shows that in range (1), volume eigenmodes can exist only in ducts with decreased density or tubes with enhanced static magnetic field. The normalized axial wave numbers of such modes lie in the range $2\tilde{\varepsilon}^{1/2} < p < 2\varepsilon_a^{1/2}$. Hereafter, the tilde quantities refer to the inner region of the cylindrical nonuniformity. In addition, such structures can guide no more than one eigenmode of surface type with the axial wave number $p < 2\tilde{\varepsilon}^{1/2}$. However, the surface modes are of little interest since they are excited inefficiently by source (3). As an example, Figs. 1 and 2 show the field components of the lower-order volume eigenmode (guided mode whose axial wave number p is minimum) with the azimuthal index $m = 0$ for a duct with decreased plasma density and a tube with enhanced static magnetic field, respectively. Note that the values of dimensionless parameters chosen for numerical calculations are appropriate to conditions typical of the corresponding modeling laboratory experiments (see [1, 4] and references therein). Similarity of the field distributions in the figures is indicative of the fact that the features of eigenmodes on the guiding structures of both types are almost identical.

Figure 3 shows the results of numerical computations of the total radiation resistance R_Σ of the loop antenna with current (3) as a function of the antenna radius b in the presence of a density depletion duct and the analogous dependences of the partial radiation resistances R_n for the volume eigenmodes. For comparison, Fig. 3(a) also shows the total radiation resistance of the same antenna immersed in a homogeneous magnetoplasma whose density coincides with that in the inner region of the duct. We can infer from Fig. 3 that for the chosen parameters, the radiation resistance of the loop antenna located in a weakly nonuniform density depletion can be several times greater than the radiation resistance of the same source immersed in a homogeneous plasma with the corresponding density. Note that in the considered case, the surface eigenmode and the continuous-spectrum

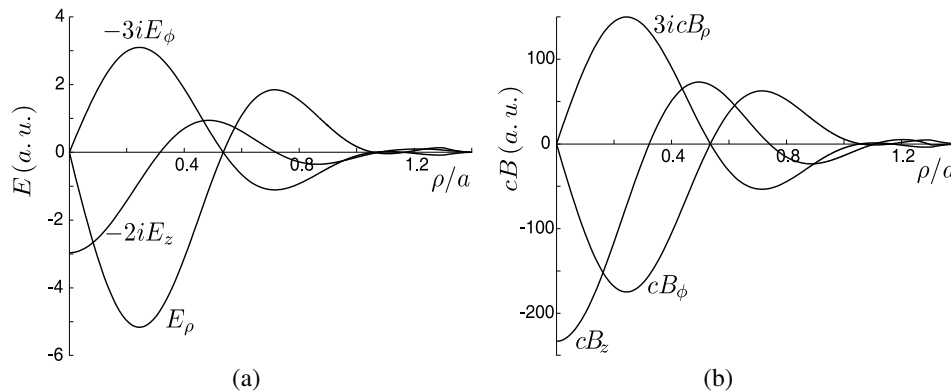


Figure 1: Field components of the lower-order axisymmetric volume eigenmode as functions of ρ for a density depletion duct if $\omega/\omega_H = 0.3$, $\tilde{\omega}_p/\omega_p = 0.82$, $\omega_p/\omega_H = 29.3$, $\omega_H a/c = 0.42$, $a_0/a = 0.8$, and $a_1/a = 1.2$. The quantities ω_p and ω_H refer to the plasma of the outer region.

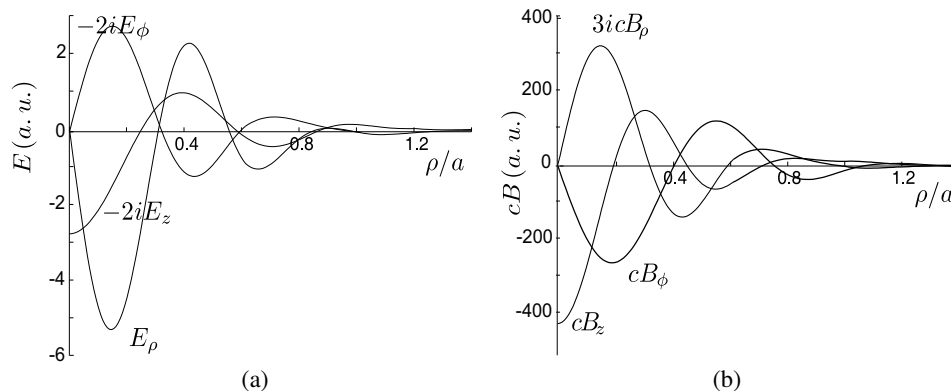


Figure 2: Field components of the lower-order axisymmetric volume eigenmode as functions of ρ for a tube with enhanced static magnetic field if $\omega/\omega_H = 0.24$, $\omega_H/\tilde{\omega}_H = 0.82$, $\omega_p/\tilde{\omega}_H = 29.3$, $\tilde{\omega}_H a/c = 0.42$, $a_0/a = 0.8$, and $a_1/a = 1.2$. The same notations as in Fig. 1.

modes give the very small contribution to R_Σ . It turns out that the contribution of the continuous-spectrum modes to the total radiation resistance is negligible if $\tilde{\omega}_p b/c > 1$. Thus, the maxima of R_Σ in our case are determined by the maxima of R_n for the dominant volume modes. With increasing duct radius a , the number of guided modes accordingly increases, the maxima of R_Σ become smoothed, and the gain in the total radiation resistance no longer takes place.

We do not present the numerical results for the radiation resistance of the loop antenna in a tube with enhanced static magnetic field for the parameters used in Fig. 2 since the dependences of R_Σ and R_n on b in this case turn out to be similar to those presented in Fig. 3.

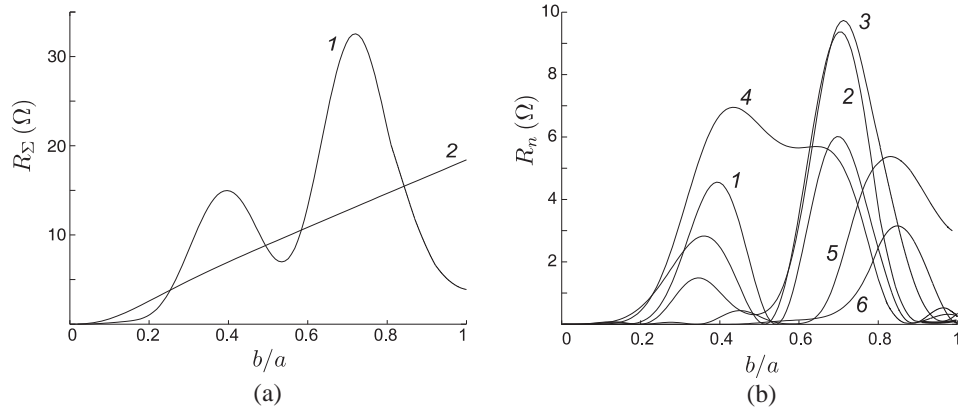


Figure 3: (a) Total radiation resistance of the loop antenna as a function of its radius b in the cases where the antenna is located in a density depletion duct with the above-described density profile (curve 1) and in a homogeneous magnetoplasma whose density coincides with that in the inner region of the duct (curve 2). (b) Partial radiation resistances for the eigenmodes as functions of the loop radius b (the curves are labeled in order of increasing axial wave numbers of the eigenmodes). The same values of parameters as in Fig. 1.

5. CONCLUSION

The features of excitation and propagation of whistler-mode waves in a magnetoplasma containing weakly nonuniform guiding structures in the form of either a duct with decreased density or tube with enhanced static magnetic field have been found to be similar in the whistler frequency range. It has been established that under certain conditions, the radiation resistance of the loop antenna in such plasma structures can be notably greater than that in a homogeneous magnetoplasma whose parameters coincide with those near the nonuniformity axis.

ACKNOWLEDGMENT

This work was supported by the Russian Foundation for Basic Research (project No. 09-02-00164-a) and the Ministry of Education and Science of the Russian Federation (project No. 2.1.1/1167).

REFERENCES

1. Kondrat'ev, I. G., A. V. Kudrin, and T. M. Zaboronkova, *Electrodynamics of Density Ducts in Magnetized Plasmas*, Gordon and Breach, Amsterdam, 1999.
2. Karpman, V. I. and R. N. Kaufman, "Whistler wave propagation in density ducts," *J. Plasma Phys.*, Vol. 27, No. 2, 225–238, 1982.
3. Kaufman, R. N., "Whistler propagation in magnetic tubes," *Radiophys. Quantum Electron.*, Vol. 29, No. 7, 579–585, 1986.
4. Zaboronkova, T. M., A. V. Kostrov, A. V. Kudrin, S. V. Tikhonov, A. V. Tronin, and A. A. Shaikin, "Channeling of waves in the whistler frequency range within nonuniform plasma structures," *Sov. Phys. JETP*, Vol. 75, No. 4, 625–632, 1992.

Resonant Transmission through Dense Plasmas via Amplification of Evanescent Mode

N. Sternberg¹ and A. I. Smolyakov²

¹Department of Mathematics and Computer Science, Clark University, Worcester, MA, USA

²Department of Physics and Engineering Physics, University of Saskatchewan, Saskatoon, Canada

Abstract— A study of electromagnetic wave propagation in a dense plasma layer when the plasma frequency is higher than the wave frequency is presented. Under such conditions, the wave amplitude is usually exponentially attenuated due to collisionless skin effect. It is shown that absolute, 100%, transparency can be achieved through resonant excitation of evanescent modes by a diffraction grating placed into vacuum preceding the plasma layer.

1. INTRODUCTION

The behavior of surface modes is the subject of much current research. Surface modes are (exponentially) localized eigen-modes which exist at the interfaces of two regions with opposite signs of the dielectric constants. A closely related field is the study of propagation of the electromagnetic radiation in metamaterials, which are materials with negative dielectric permittivity ϵ and negative permeability μ . The increased interest in surface modes has been driven by the tremendous potential to guide and manipulate electromagnetic radiation at the subwavelength scales below the diffraction limit in composite devices involving metallic nanostructures. The electromagnetic waves in these devices take the form of surface waves (Surface Plasmons) supported by free electrons in the metal and localized at the metal-dielectric interfaces [1–5].

Inside a dense region, electromagnetic wave energy is carried by evanescent modes. The general solution inside a medium of negative permittivity is a sum of two exponential functions, one that decays and the other one that grows with the distance. The corresponding component of the time averaged Poynting vector may become finite when the growing and decaying evanescent modes are superimposed with a finite phase shift. The condition of the absolute transparency is equivalent to the resonant condition for the excitation of the surface plasma mode. At resonance, the Poynting flux inside the slab becomes equal to that of the incident radiation, and the opaque plasma slab becomes absolutely transparent [6].

One can find in the literature studies of various media that allow signal transmission via amplification of evanescent waves through surface modes. General conditions for resonant signal transmission via a two-layer structure were studied in [7, 8], and a three-layer structure was considered in [9, 10]. In [8] a two-layer structure consisting of a layer of rarified plasma with $0 < \epsilon_1 < 1$ of width a_1 and a layer of dense plasma with $\epsilon_2 < 0$ of width a_2 was considered, and it was shown that total signal transmission is achieved if the effective dielectric constant of the total structure is zero, i.e., $\bar{\epsilon} \equiv \epsilon_1 a_1 + \epsilon_2 a_2 = 0$. The three layer structure considered in [10] consisted of a dense plasma layer nested between two layers of rarified plasma. It was shown in [10] that in contrast to a two-layer structure, resonant signal transmission for such three-layer model can be achieved by choosing the width of each boundary layer comparable in size with the width of the dense plasma. Furthermore, the bandwidth of the transmitted wave is much larger than in the two-layer structure. In [11, 12], resonant transmission of an electromagnetic wave through a dense plasma layer was achieved by placing a diffraction grating into the vacuum layer on each side of the plasma.

In the present paper, we study resonant signal transmission through surface modes and possible applications to the problem of communication interruption with an aircraft surrounded by a dense plasma layer (the black-out problem) [13–15]. In that application, the model with two diffraction gratings is not useful, because one cannot place a diffraction grating on the exterior side of the plasma layer. The question is whether resonant transmission can be achieved by using only one diffraction grating (along the side of the aircraft) which precedes the dense plasma layer. This paper is an attempt to answer this question. Using a model for the diffraction grating similar to the one in [11, 12] for plasma parameters relevant to hypersonic flights [13], we show that by choosing appropriate parameters for the diffraction grating, resonant transmission of electromagnetic waves through a dense plasma layer is possible even if only one diffraction grating is being used.

2. GENERAL EQUATIONS AND BOUNDARY CONDITIONS FOR THE DIFFRACTION GRATING

We consider the propagation of electromagnetic radiation through a multi-layer structure as depicted in Fig. 1. A dense plasma layer is nested between two semi-infinite vacuum (air) layers. An electromagnetic wave is incident from a semi-infinite vacuum (air) region on the left. The transmitted wave propagates into a semi-infinite vacuum (air) region on the right. In general, there are incident and reflected waves on the left, but there is no reflected wave on the right. When a dense plasma layer is present within the structure, the reflection coefficient is large, and most of the radiation is reflected due to the skin effect screening. The question is whether by placing a diffraction grating into the vacuum region to the left of the dense plasma (at $z = 0$) it is possible to create conditions when the reflection is low and most of the radiation is transmitted through the structure.

We consider a p -polarized normal incident wave: $\mathbf{H} = (H_x, 0, 0)$, and $\mathbf{E} = (0, E_y, E_z)$. The wave equation for a non-homogenous (in y and in z) medium is then

$$\varepsilon \frac{\partial}{\partial y} \left(\frac{1}{\varepsilon} \frac{\partial H_x}{\partial y} \right) + \varepsilon \frac{\partial}{\partial z} \left(\frac{1}{\varepsilon} \frac{\partial H_x}{\partial z} \right) + \frac{\omega^2}{c^2} \varepsilon H_x = 0 \quad (1)$$

The dependence in the y direction is always periodic $H_x \sim \exp(ik_y y)$, with k_y real. We assume that the permittivity ε is defined by a step-function such that $\varepsilon = 1$ in the vacuum layer and $\varepsilon = \varepsilon_p < 0$ in the dense plasma layer. At the plasma-vacuum interfaces one finds from (1) the boundary conditions

$$[H_x]_{-}^{+} = 0 \quad \text{and} \quad \left[\frac{1}{\varepsilon} \frac{dH_x}{dz} \right]_{-}^{+} = 0 \quad (2)$$

where, “+” and “-” indicate the corresponding limits from the right and left at the plasma-vacuum interface.

To model the diffraction grating interface, we use an equation similar to the one in [11, 12]:

$$\frac{d^2}{dz^2} H_x - k_y^2 H_x + \frac{\omega^2}{c^2} \varepsilon H_x + \frac{\omega^2}{c^2} h_g \varepsilon_g \alpha \cos(qy) \delta(z) H_x = 0 \quad (3)$$

where q is a wave vector of the grating, α is a modulation parameter, h_g is the grating thickness, and ε_g is the grating dielectric constant. Note that due to the delta function, Equation (3) is used only in the neighborhood of the grating and produces the following boundary conditions:

$$[H_x]_{-}^{+} = 0 \quad \text{and} \quad \left[\frac{dH_x}{dz} \right]_{-}^{+} = -\frac{k_g \alpha}{2} (e^{iqy} + e^{-iqy}) H_x|_{z=0} \quad (4)$$

where $k_g = \varepsilon_g h_g \omega^2 / c^2$, and “+” and “-” indicate the corresponding limits from the right and left at the diffraction grating.

The role of the diffraction grating is to generate the sideband harmonics so that the total solution (neglecting higher harmonics) is of the form

$$H_x = H_0 e^{ik_y y} + H_+ e^{i(k_y + q)y} + H_- e^{i(k_y - q)y} \quad (5)$$

where H_0 is the amplitude of the principal harmonics (the same as the incident wave), and H_+ and H_- are the amplitude of the sidebands. We will consider here only a normal incidence wave, thus, $H_+ = H_-$, and it is sufficient to consider only H_0 and H_+ . Note that H_0 and H_+ are corresponding solutions of (1) and, in each layer, they can be represented as

$$H_0 = A (\exp(\gamma z) + \Gamma \exp(-\gamma z)) \quad \text{and} \quad H_+ = A^+ (\exp(\gamma^+ z) + \Gamma^+ \exp(-\gamma^+ z)) \quad (6)$$

for appropriate γ and γ^+ and corresponding A , A^+ , Γ , Γ^+ . In the vacuum regions, the incidence wave is propagating and $\gamma = ik_0$, $k_0 = \omega/c$, while the sideband are evanescent with $\gamma^+ = -\gamma_v^+$, where $\gamma_v^+ = \sqrt{q^2 - k_0^2}$, $q > k_0$. In the dense plasma layer, the incidence wave is evanescent with $\gamma = -\gamma_p$, with $\gamma_p = \sqrt{-\varepsilon_p} \omega/c$, and so are the sidebands with $\gamma^+ = -\gamma_p^+$, with $\gamma_p^+ = \sqrt{q^2 - \varepsilon_p \omega^2 / c^2}$.

3. WAVE IMPEDANCE AND TRANSPARENCY

To study our model, we will use the impedance matching technique described in [10]. The local wave impedance is defined by

$$Z = -\frac{E_y}{H_x} = -\frac{i}{\omega\epsilon_0\epsilon} \frac{1}{H} \frac{\partial H_x}{\partial z} \quad (7)$$

In the semi-infinite vacuum region $z < 0$, the incidence wave is propagating and its impedance, according to (6) and (7) is

$$Z_3(z) = Z_0 \frac{(\exp(ik_0z) - \Gamma_3 \exp(-ik_0z))}{(\exp(ik_0z) + \Gamma_3 \exp(-ik_0z))} \quad (8)$$

where $Z_0 = k_0/(\omega\epsilon_0)$ is the vacuum characteristic impedance. The sideband is evanescent with $\Gamma_3^+ = 0$ and its impedance is

$$Z_3^+(z) = -\frac{i\gamma_v^+}{\omega\epsilon_0} \quad (9)$$

In the vacuum region, $0 < z < a$, the corresponding impedances for the incidence wave and the sideband are

$$Z_2(z) = Z_0 \frac{\exp(ik_0z) - \Gamma_2 \exp(-ik_0z)}{\exp(ik_0z) + \Gamma_2 \exp(-ik_0z)} \quad \text{and} \quad Z_2^+(z) = Z_0^+ \frac{\exp(-\gamma_v^+z) - \Gamma_2^+ \exp(\gamma_v^+z)}{\exp(-\gamma_v^+z) + \Gamma_2^+ \exp(\gamma_v^+z)} \quad (10)$$

where $Z_0^+ = i\gamma_v^+ / (\omega\epsilon_0)$ is the characteristic impedance of the vacuum region for the sidebands. In the plasma region, $a < z < d = a + l$, the corresponding impedances are

$$Z_p(z) = Z_{ch} \frac{\exp(-\gamma_pz) - \Gamma_p \exp(\gamma_pz)}{\exp(-\gamma_pz) + \Gamma_p \exp(\gamma_pz)} \quad \text{and} \quad Z_p^+(z) = Z_{ch}^+ \frac{\exp(-\gamma_p^+z) - \Gamma_p^+ \exp(\gamma_p^+z)}{\exp(-\gamma_p^+z) + \Gamma_p^+ \exp(\gamma_p^+z)} \quad (11)$$

where $Z_{ch} = i\gamma_p / (\omega\epsilon_0\epsilon_p)$ and $Z_{ch}^+ = i\gamma_p^+ / (\omega\epsilon_0\epsilon_p)$. In the last semi-infinite vacuum region, $z > d = a + l$, the impedances of the transmitted propagating wave and of the corresponding sideband are

$$Z_1(z) = Z_0 \quad \text{and} \quad Z_1^+(z) = Z_0^+ \quad (12)$$

The quantity of primary interest is the reflection coefficient which is determined by the expression

$$\Gamma_3 = \frac{Z_0 - Z_3(0)}{Z_0 + Z_3(0)} \quad (13)$$

If $\Gamma = 0$ then there is a 100% wave transmission. Thus, the transparency condition is

$$Z_3(0) = Z_0 \quad (14)$$

4. MATCHING CONDITIONS AND RESONANCE

At the plasma-vacuum boundaries, the impedance is continuous. Hence,

$$Z_p(d) = Z_1(d) = Z_0 \quad Z_p^+(d) = Z_1^+(d) = Z_0^+ \quad Z_p(a) = Z_2(a) \quad Z_p^+(a) = Z_2^+(a) \quad (15)$$

The matching condition at the diffraction grating follows from (4) and yields:

$$Z_3(0) = Z_2(0) - \frac{k_g^2 \alpha^2}{2\omega^2 \epsilon_0^2 (Z_3^+(0) - Z_2^+(0))} \quad (16)$$

According to (14), resonance is achieved when

$$Z_3(0) = Z_0 = \text{Re}(Z_2(0)) \quad (17)$$

and

$$i\text{Im}(Z_2(0)) - \frac{\alpha^2 k_g^2}{2\omega^2 \epsilon_0^2 (Z_3^+(0) - Z_2^+(0))} = 0 \quad (18)$$

Equation (17) holds if

$$L_p^2 - \frac{L_v^2 L_p^2}{\epsilon_p} - 2 \frac{L_v L_p}{\sqrt{-\epsilon_p}} = 0 \quad (19)$$

where $L_p = \tanh(\gamma_p l)$, $L_v = \tan(k_0 a)$. From Equation (19), we find L_v , which yields the width of the vacuum layer a needed for resonant transmission to take place:

$$a = \frac{1}{k_0} \tan^{-1}(L_v) \quad (20)$$

Note that, using the equations from the previous section, we find

$$Z_3^+(0) - Z_2^+(0) = -Z_0^+ \frac{(1 + L_v^+)(2 + L_p^+(K + 1/K))}{1 + L_p^+/K + L_v^+ + L_p^+ L_v^+ K} \quad (21)$$

where $K = Z_{ch}^+/Z_0^+$, $L_v^+ = \tanh(\gamma_v^+ a)$ and $L_p^+ = \tanh(\gamma_p^+ l)$. On the other hand, from (18)

$$Z_3^+(0) - Z_2^+(0) = -i \frac{\alpha^2 k_g^2}{2\omega^2 \epsilon_0^2 \text{Im}(Z_2^0)} \quad (22)$$

and we obtain the dispersion relation

$$\gamma_v^+(1 + L_v^+) \frac{2 + L_p^+(K + 1/K)}{1 + L_p^+/K + L_v^+ + L_p^+ L_v^+ K} = \frac{\alpha^2 k_g^2}{2\omega \epsilon_0 \text{Im}(Z_2^0)} \quad (23)$$

Our computations have shown that for an appropriate choice of parameters k_g and α , resonant transmission of electromagnetic waves is possible. In fact, if k_g and α are chosen so that $q \in (21.27, 21.284) \cup (21.39, \infty)$, the right-hand side of (23) is positive, and resonant transmission will always take place. This is illustrated in Fig. 2 which shows the dependence of the reflection coefficient on the diffraction wave vector q for $\alpha^2 k_g^2 = 4000$, $l = 0.02$ m and $\epsilon_p = -35$. Resonant transmission takes place at about $q = 21.6$.

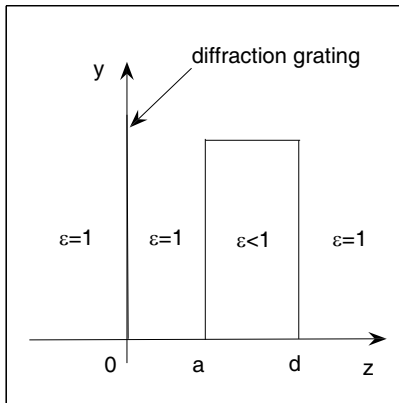


Figure 1: Plasma layer and a diffraction grating.

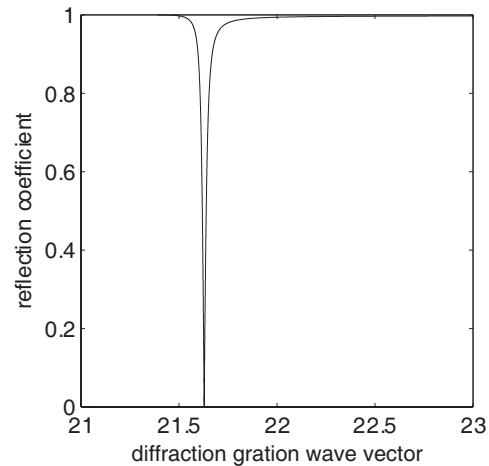


Figure 2: Reflection coefficient versus diffraction wave vector.

5. CONCLUSION

Anomalously high transmission of electromagnetic radiation through a dense plasma layer has been observed in experiments and numerical simulations. In those observations, electromagnetic wave transmission resulted from resonant amplification of evanescent waves by surface modes at the plasma boundary. In particular, in [11, 12], resonant transmission through dense plasma was achieved by placing the plasma layer between two diffraction gratings. In some applications, however, it is not possible to create such symmetric configuration. For example, to investigate the

communication black-out problem during hypersonic flight, one could put the diffraction grating along the side of the aircraft, but not at the exterior side of the plasma layer. It is therefore important to understand whether resonant transmission can be achieved by placing the diffraction grating only on one side of the plasma layer. This is the configuration we have considered in the present paper. Using an equation for the diffraction grating similar to the one in [11, 12], we were able to demonstrate that for an appropriate choice of parameters, resonant transmission of electromagnetic waves through a dense plasma layer is possible even if only one diffraction grating is used. In our investigation, we neglected the effects of dissipation caused by electron-atom collisions and/or by electron thermal motion [16, 17]. Those effects could be especially detrimental for the narrow resonances situation. On the other hand, electron thermal motion effects could lead to the appearance of new resonant modes and additional transparency regimes [8]. All those questions go beyond the scope of this paper and are left for future studies.

ACKNOWLEDGMENT

This work was supported in part by AFOSR Award #FA9550-07-1-0415 and NSERC Canada. The authors wish to thank Yu. Bliokh and V. Godyak for helpful discussions.

REFERENCES

1. Alu, A. and N. Engheta, *IEEE Antennas and Wireless Propagation Letters*, Vol. 4, 417–420, 2005.
2. Hooper, I. R., T. W. Preist, and J. R. Sambles, “Making tunnel barriers (including metals) transparent,” *Physical Review Letters*, Vol. 97, No. 5, 053902, 2006.
3. Pendry, J. B., “Negative refraction makes a perfect lens,” *Physical Review Letters*, Vol. 85, No. 18, 3966–3969, 2000.
4. Tomita, S., T. Yokoyama, H. Yanagi, B. Wood, J. B. Pendry, M. Fujii, and S. Hayashi, “Resonant photon tunneling via surface plasmon polaritons through one-dimensional metal-dielectric metamaterials,” *Optics Express*, Vol. 16, No. 13, 9942–9950, 2008.
5. Wegener, M., G. Dolling, and S. Linden, “Plasmonics — backward waves moving forward,” *Nature Materials*, Vol. 6, No. 7, 475–476, 2007.
6. Fourkal, E., I. Velchev, C.-M. Ma, and A. Smolyakov, “Resonant transparency of materials with negative permittivity,” *Phys. Letters A*, Vol. 361, 277–282, 2007.
7. Alù, A. and N. Engheta, “Pairing an ϵ -negative slab with a μ -negative slab: Resonance, tunneling and transparency,” *IEEE Trans. Antennas and Propagation*, Vol. 51, No. 10, 2558, 2003.
8. Fourkal, E., I. Velchev, C.-M. Ma, and A. Smolyakov, “Evanescent wave interference and total transparency of warm high-density plasma slab,” *Phys. Plasmas*, Vol. 13, 092113, 2006.
9. Dragila, R., B. Lutherdavies, and S. Vukovic, “High transparency of classically opaque metallic films,” *Phys. Rev. Letters*, Vol. 55, 1117, 1985.
10. Sternberg, N. and A. Smolyakov, “Resonant transmission of electromagnetic waves in multi-layer dense plasma structures,” *IEEE Trans. Plasma Sci.*, 2009.
11. Bliokh, Yu. P., J. Felsteiner, and Y. Slutsker, “Total absorption of electromagnetic waves by an overdense plasma,” *Phys. Rev. Lettes*, Vol. 95, 165003, 2005.
12. Bliokh, Yu. P., “Plasmon mechanism of light transmission through a metal film or a plasma layer,” *Optics Commun.*, Vol. 259, 436, 2006.
13. Josyula, E. and W. Bailey, “Governing equations for weakly ionized plasma flowfields of aerospace vehicles,” *J. of Spacecraft and Rockets*, Vol. 60, No. 6, 845, 2003.
14. White, M. and S. Sherer, “High-order simulation of communication through a weakly ionized plasma for reentry vehicles,” *44th AIAA Aerospace Science Meeting and Exhibit*, Reno, Nevada, January 2006.
15. Nazarenko, S. V., A. C. Newell, and V. E. Zakharov, “Communication through plasma sheath via Raman (three-wave) scattering process,” *Phys. Plasmas*, Vol. 1, 9, 1994.
16. Lieberman, M. and V. Godyak, “From Fermi acceleration to collisionless discharge heating,” *IEEE Trans. Plasma Sci.*, Vol. 26, No. 3, 955–986, 1998.
17. Godyak, V., “Hot plasma effects in gas discharge plasma,” *Phys. Plasmas*, Vol. 12, 055501, 2005.

Comparison of Uniform and Discontinuity Dielectric Profile in THz Radiation Field

P. Zobdeh¹, S. Mahmoodi¹, and D. Sardari²

¹Department of Physics, Qom Branch, Islamic Azad University, Qom, Iran

²Science and Research Campus, Islamic Azad University, Tehran, Iran

Abstract— Optical rectification, photoconductive antenna, Quantum cascade intersubband, Varactor Frequency Doublers are the various methods to generate THz radiation. Recently THz emission is generated by electron bunches bending in a magnetic field, traversing a refractive index. In high intense femtosecond laser interaction with plasma, THz emission was observed when well collimated, ultra short *MeV* electron bunch is accelerated due to the transverse wave breaking. The plasma-vacuum boundary already acts as the sharp dielectric discontinuity. In this work, we have presented the effect of linear plasma dielectric discontinuity in terahertz emission. It can be predicted that: The THz radiation by propagation of electrons through a discontinuity dielectric can be more intensified than conventional laser-based THz source. This could be used for design and optimize powered THz source instead of optical rectification or the photoconductive antenna sources.

1. INTRODUCTION

THz radiation is interested over the last decade. Various schemes are presented to generate THz radiation such as optical rectification, photoconductive antenna, Quantum cascade intersubband, Varactor Frequency Doublers and est. Using the femtosecond laser pulses with electro-optic crystals and semiconductors through optical rectification is a direct way to make THz by [1, 2]. Recently THz emission is generated by electron bunches bending in a magnetic field, traversing a refractive index [3]. In high intense femtosecond laser interaction with plasma, a well collimated, ultra short *MeV* electron bunch is obtained due to the transverse wave breaking [4–6]. In the last decade, the generation of laser pulses in the multi-terawatt (or even pettawatt) power range is possible with compact chirped-pulse amplification (CPA) systems and the extreme light infrastructure (ELI) will be able to generate intensities in the range of $10^{25} - 10^{26}$ W/cm² [7]. In CPA table-top lasers, the laser intensities increased up to $I = 10^{22}$ W/cm², and electric field strengths of more than 10^{14} V/m were obtained [8]. Particles can be accelerated in these high gradient fields and used for various applications, including transmutation of cheap and hazardous materials of long-living radioactive wastes to valuable radioisotopes [9]. The extremely high electric field makes the laser wakefield acceleration method attractive for the development of a new generation of accelerators [10]. In the laser wakefield scheme, the ponderomotive force associated in the front and the rear sides of a short laser pulse expels the plasma electrons from the regions where the laser field is the most intense [11]. The induced charge separation between the electrons and the ions gives rise to a space charge field and a plasma wave [12]. Large amplitude plasma waves are generated by this ponderomotive force in the laser wake field accelerator (LWFA). The ponderomotive force F_p is given by $F_p \approx -\nabla a^2$, where a is the laser pulse envelope. The acceleration gradient resulting from the charge displacement is reported to be about 100 GV/cm when plasma density is 10^{18} cm⁻³ [13].

The plasma-vacuum boundary already acts as the emitting dielectric discontinuity. The generation of electromagnetic pulses from plasma channels induced by femtosecond light strings is presented [14, 15]. The sub-Thz pulses emitted by the filamentary structure from an intense femtosecond laser pulse were detected [16, 17]. In this work, we have presented the effect of linear plasma dielectric discontinuity in terahertz emission.

2. ELECTROMAGNETIC PULSE (EMP) RADIATION

During the high intense femtosecond laser interaction with plasma, plasma channel by multiphoton ionization was reported experimentally. Observation of these channel attain dipole moments which subsequently oscillate at the plasma frequency and radiate [16]. The generated EMP propagates radially away from the plasma channel. To obtain an approximate solution for EMP due to the oscillation electron plasma, the longitudinal current was considered. Maxwell equation wave can be

solved along with this longitudinal current and finally by using the Green's function for the wave equation and it can be obtained as [14]

$$E_{rad}(r, t) = \frac{e\mu_0 N_e(t) r_0^2}{4} \int_{-\infty}^{\infty} dz \frac{\ddot{\xi} \left(t - \sqrt{r^2 + z^2}/c \right)}{\sqrt{r^2 + z^2}}, \quad (1)$$

where $N_e(t)$ is the density on the fact that it decays on a time slowly in comparison of plasma oscillation. Eq. (1) shows radiation field is strongly related to plasma density (that prescribes the dielectric function).

3. DIELECTRIC FUNCTION EFFECT IN PLASMA

The dielectric function in plasma can be approximated by $\varepsilon(\omega) = 1 - \omega_p^2/\omega^2$ that ω is the laser angular frequency, and ω_p is the plasma frequency. It can be seen that the plasma-vacuum interface has indeed a strong dielectric discontinuity for laser frequencies $\omega \leq \omega_p$, in laser plasma interaction. This produces the coherent terahertz emission. In this work, we have considered the laser interaction with under dense plasma. We have modeled linear plasma density profile and obtained longitudinal and transverse fields numerically. Figure 1 shows a prediction for emission spectra of terahertz radiation in both homogeneous and discontinuity dielectric. Results show the emission amplitude increases transversely for discontinuity dielectric.

4. NUMERICAL STUDIES AND DISCUSSIONS

We have provided an numerical investigation of the electromagnetic fields in plasma during the propagation of laser in a collisionless, unmagnetized and nonisothermal plasma. In this analyze, we assume that a steepened density profile is produced by leading the expanded plasma. By using the fourth-order Runge-Kutta integration, electric field profiles for different steepened scale lengths is obtained. For underdense plasma region we suppose the density is a linear function of position, and the wave equation is [18]:

$$\frac{d^2 E_x}{dz^2} + \frac{\omega^2}{c^2} \left(1 - \frac{4\pi e^2}{m\omega^2} e^{-e^2 E_x^2 / m\omega^2 T_e} \left(n_0 + \frac{n_{cr}}{L} Z \right) \right) E_x = 0 \quad (2)$$

Electrical field is obtained from the Eq. (2) numerically by using fourth-order Runge-Kutta integration. We show the plots of the electric and magnetic field profiles versus Z for above density profile (steepened profile) and compare it with the uniform density profile in the next section.

An s -polarized laser pulse with wavelength $\lambda_l = 800$ nm and 50 fs duration is focused on the interface with a spot size less than $6 \mu\text{m}$ diameter. Laser intensity is assumed about $I = 1.0 \times 10^{17}$ (Wcm^{-2}). The electromagnetic fields distribution is sinusoidal standing wave versus z in the plasma.

Electromagnetic fields for these steepened profile and homogeneous (uniform) density profile are plotted in Figures 2 and 3. Result shows, the electric field reaches to more than wavebreaking limit (about 100 Gv/m) for the steepened density profile, which is enough for nonrelativistic wave breaking.

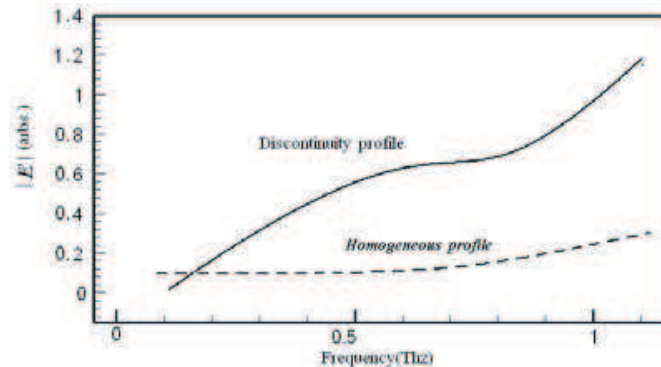


Figure 1: THz Emission spectra prediction for uniform and discontinuity profile.

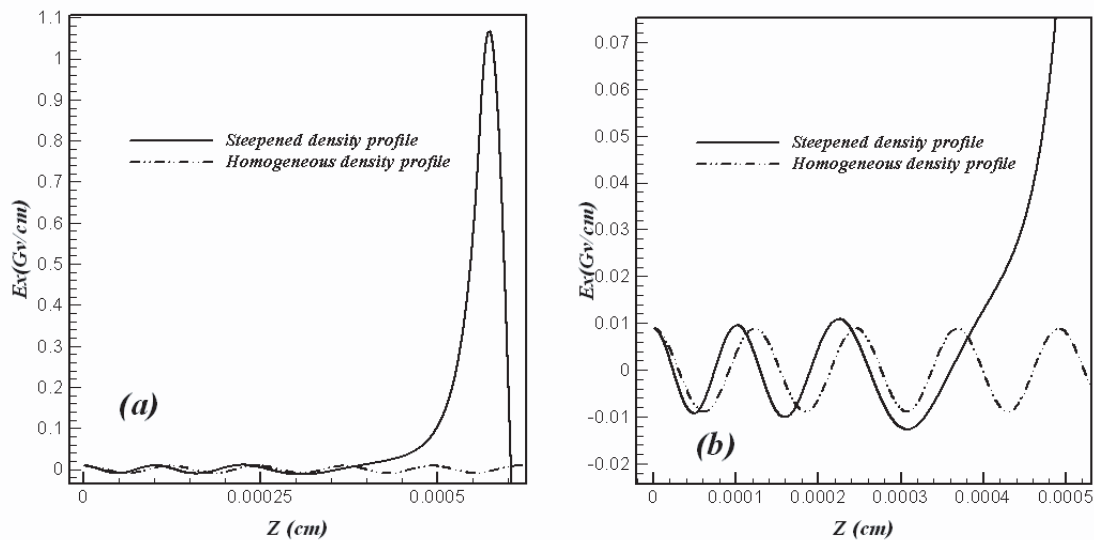


Figure 2: Electric field (E_x) for steepened (solid curve, steepened length) and homogeneous (dash-dotted curve, density profile).

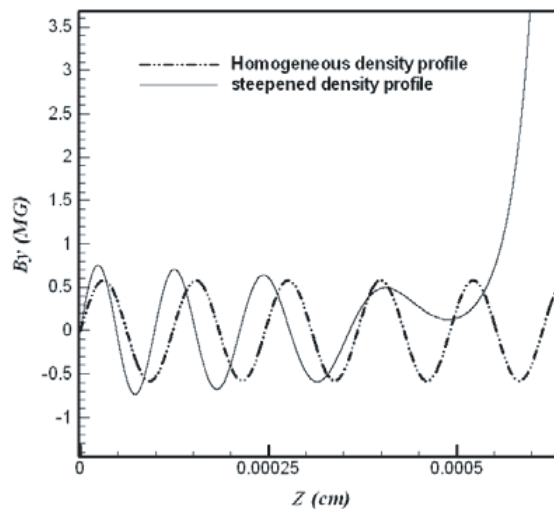


Figure 3: Magnetic field (B_y) for steepened (solid curve, steepened length) and homogeneous (dash-dotted curve) density profile.

5. CONCLUSION

The electrons generated by high intense laser-plasma interaction are over millions electrons at femtosecond duration. Electron-ion system starts to oscillate longitudinally at the plasma frequency and generates an EMP propagating radially away from plasma channel. In this work, A comparison of steepened density profile and a homogeneous density profile presented. Finally, a new injection method based on self trapping of background plasma electrons was obtained with using the steepened density profile when the wavebreaking occurred. It can be obtained the emitted THz radiation by propagation of laser through a discontinuity dielectric can be more intensified than conventional laser-based THz source. This could be used for design and optimize powered THz source instead of optical rectification or the photoconductive antenna sources.

REFERENCES

1. Melo, A. M., J. L. S. Lima, R. S. Oliveira, and A. S. B. Sombra, "Photonic time division multiplexing using ultrashort picoseconds pulses in terahertz optical asymmetric demultiplexer," *Optical Communications*, Vol. 205, 299–312, 2002.

2. Saedikia, D. and R. R. Mansour, “A submilliwatt terahertz high-temperature superconductive photomixer array source: Analysis and design,” *IEEE. Trans. Appl. Supercon.*, Vol. 15, No. 3, 3868–3873, 2005.
3. Leemans, W. P., J. Van Tilborg, J. Faure, C. G. R. Geddes, C. T’oth, C. B. Schroeder, E. Esarey, G. Fubiani, and G. Dugan, “Terahertz radiation from laser accelerated electron bunches,” *Phys. Plasmas*, Vol. 11, No. 5, 2899, 2004.
4. Zobdeh, P., R. Sadighi-Bonabi, H. Afarideh, E. Yazdani, and R. R. Nasirabad, “Using the steepened plasma profile and wave breaking threshold in laser-plasma interaction,” *Phys. Plasmas*, Vol. 48, No. 8, 555–560, 2008.
5. Zobdeh, P., R. Sadighi-Bonabi, and H. Afarideh, “New ellipsoid cavity model in the high intense laser-plasma interaction,” *Plasma Devices and Operations*, Vol. 16, No. 2, 105–114, 2008.
6. Sadighi-Bonabi, R., H. A. Navid, and P. Zobdeh, *Laser & Particle Beam*, Vol. 27, No. 2, 223–231, Cambridge University Press, 2009.
7. Gerestener, E., “Physicists are planning lasers powerful enough to rip apart the fabric of space and time,” *Nature*, Vol. 446, 16–18, 2007.
8. Umstadter, D., “Relativistic laser-plasma interactions,” *J. Phys. D: Appl. Phys.*, Vol. 36, R151–R165, 2003.
9. Sadighi-Bonabi, R. and O. Kokabee, “Evaluation of transmutation of $^{137}\text{Cs}(\gamma, n)^{136}\text{Cs}$ using ultra-intense laser in solid targets,” *Chin. Phys. Lett.*, Vol. 6, 1434–1436, 2006.
10. Geddes, C., et al., “Laser guiding at relativistic intensities and wakefield particle acceleration in plasma channels,” *SciDAC Meeting*, 2004.
11. Malka, V., et al., “Staged concept of laser-plasma acceleration toward multi-GeV electron beams,” *Phys. Rev. Spe. Top. — Acce, and Beams*, Vol. 9, 091301-1-10, 2006.
12. Robson, L., et al., “Scaling of proton acceleration driven by petawatt-laser — Plasma interactions,” *Nature Phys.*, Vol. 3, 58–62, 2007.
13. Hemker, R. G., et al., “Computer simulations of a single-laser double-gas-jet wakefield accelerator concept,” *Phys. Rev. ST Accel. Beams*, Vol. 5, 041301-1-8, 2002.
14. Cheng, C.-C., E. M. Wright, and J. V. Meloney, “Generation of electromagnetic pulses from plasma channels induced by femtosecond light strings,” *Physical Review Letters*, Vol. 87, No. 21, 213001:1–4, 2001.
15. Gennady, S., I. Kaganovich, and E. Startsev, “Comment on generation of electromagnetic pulses from plasma channels induced by femtosecond light strings,” *Physical Review Letters*, Vol. 89, No. 13, 139301-1, 2002.
16. Proulx, A., A. Talebpour, S. Petit, and S. L. Chin, “Fast pulsed electric field created from the self-generated filament of a femtosecond Ti: Sapphire laser pulse in air,” *Optical Communications*, Vol. 174, 305–309, 2000.
17. Tzortzakis, S., G. Mechain, G. Patalano, B. Andre, B. Prade, M. Franco, A. Mysyrowicz, J.-M. Munier, M. Gheudin, G. Beaudin, and P. Encrenaz, “Coherent subterahertz radiation from femosecond infrared filaments in air,” *Opt. Lett.*, Vol. 27, No. 21, 1944–1946, 2002.
18. Zobdeh, P., R. Sadighi-Bonabi, H. Afarideh, E. Yazdani, and R. R. Nasirabad, “Using the steepened plasma profile and wave breaking threshold in laser-plasma interaction,” *Phys. Plasma*, Vol. 48, No. 8, 555–560, 2008.

Using the High Intense Laser Interaction with Plasma for Generation of Clean Electron Beam

P. Zobdeh¹ and R. Sadighi-Bonabi²

¹Department of Physics, Qom Branch, Islamic Azad University, Qom, Iran

²Department of Physics, Sharif University of Technology, 11365-9567, Tehran, Iran

Abstract— In this work, we have presented a clean electron beam generation in theory and experimental parts. Theoretical part describes a new ellipsoid model and develops bubble accelerator. Required conditions for producing of this cavity are obtained in this section and the electron trajectory is analyzed. We have shown the quality of the electron beam is improved in contrast to other methods such as that using periodic plasma wake field, spherical cavity regime and plasma channel guided acceleration. The trajectory of the electron motion can be described as hyperbola, parabola or ellipsoid path. It is influenced by the position and energy of the electrons and the electrostatic potential of the cavity. The best matched laser focusing point above the nozzle gas is found to obtain a stable ellipsoid bubble experimentally.

1. INTRODUCTION

The intensity of laser beam could be increased up to $I = 10^{22}$ W/cm² by chirped pulse amplification technique in the new generation of table-top lasers. A high gradient electric field more than 10^{14} V/m is generated by the interaction of this high intense laser beam with plasma gas [1]. The key issue in realizing an advanced compact accelerator based on laser driven plasma acceleration is the generation of a monoenergetic electron beam [2, 3]. In the high gradient generated fields, electrons can be accelerated. Producing the mono-energetic electron beam with maximum electron beam energies up to the 200 MeV has reported with large Boltzmann-type or power-law distributions [4]. Although the generated electrons distributions in some cases were quasi-monoenergetic at energies up to 20 MeV from low density electrons [1, tajima], but at high electron energies from electrons densities up to 10^{20} cm⁻³ the reported electrons spectrum were more combined distributions of quasi-monoenergetic and Boltzmann-type [5]. Under proper conditions, a very efficient “bubble” regime can be realized. Recent investigation of the bubble regime has demonstrated the generation of high-quality electron bunches with energies as high as 1 GeV, with relatively small energy spread, and emittance approaching that of a conventional accelerator [6–8].

Although in previous works the generation of well collimated ultra short MeV electron bunches in this regime was described by sphere cavity model, but the cavity shape is not exactly sphere, and some deviations between shadowgraphs, PIC simulation and analytical calculation results, are reported because of the spherical estimation for cavity shape [9–12]. The field inside of this cavity and energy spectrum for relativistic trapped electrons is evaluated in this work, and appropriate condition of forming ellipsoid cavity is discussed.

Based on this advanced model, in the experimental part of this work, we have focused 20 TW maximum power and 30 fs laser pulse duration in the best matched point at 1 mm above the He gas jet nozzle to obtain a stable ellipsoid bubble. In suitable arranged condition almost pure quasi monoenergetic electron beam at electron energy of 39 MeV was generated. In stable ellipsoidal bubble formation the record electron gain of 0.15 electrons per stradian at electron densities above 10^{20} was achieved. These conditions and achievements are discussed.

2. CAVITY FORMING AND ELECTRON TRAJECTORY

By considering the electron dynamic equations, internal electromagnetic fields and ponderomotive force of the laser propagation we obtain:

$$\ddot{r}\hat{r} = \left(\ddot{r} - r\dot{\theta}^2\right)\hat{r} + \frac{1}{r}\frac{d}{dt}\left(r^2\dot{\theta}\right)\hat{\theta} = \frac{1}{\mu}\left(\frac{-eQ_i}{4\pi\epsilon_0 r^2}\hat{r} + E_P\hat{\theta}\right), \quad (1)$$

that E_p , μ , r , \dot{r} , θ , $\dot{\theta}$, Q_i , e , and ϵ_0 are ponderomotive force, electron mass with approximately laser group velocity, radial component, derivative of radial component, tangential component, derivative of tangential component, average ion charge in the cavity, electron charge, and cavity dielectric constant, respectively.

Finally, we have obtain

$$r(\theta) = \frac{\alpha}{1 + \varepsilon \cos \theta}, \tag{2}$$

where α and ε are constant. Similar considerations and derivations may also be found in classical dynamics of particles and systems [12].

From Eq. (2) follows, that the electron trajectory is a hyperbola if $\varepsilon > 1$, a parabola if $\varepsilon = 1$, an ellipse if $0 < \varepsilon < 1$, and a circle if $\varepsilon = 0$. This is shown in Fig. 1.

3. ELECTROSTATIC POTENTIAL IN A PLASMA ELLIPSOID CAVITY

We have considered an electrically neutral bulk plasma ellipsoid cavity. The electrostatic potential inside a uniformly charged ellipsoid is calculated [13,15] that satisfies the Poisson equation. We have obtained the normalized potential at the generated cavity boundary as

$$\varphi(x, y, z) = 1 + \varphi_0 \left[1 - (x/a_e)^2 - (y/b_e)^2 - (z/c_e)^2 \right], \tag{3}$$

where in this equation

$$\varphi_0 = \frac{3a_e b_e c_e c_{cavity}}{2\varepsilon_0 [(a_e b_e)^2 + (a_e c_e)^2 + (b_e c_e)^2]}, \tag{4}$$

and $2a_e$, $2b_e$, and $2c_e$ are axes of cavity ellipsoid and c_{cavity} is the electrical capacity of the plasma in vacuum and ε_0 is the cavity dielectric constant.

If we assume $a_e b_e c_e = R^3$, for spheroid ellipsoid ($a_e > b_e = c_e$), we will have

$$\varphi(x, y, z) = 1 + \left(\frac{3a_e^2}{(2a_e^2 + b_e^2)} \right) \cdot \left[1 - (x/a_e)^2 - (y/b_e)^2 - (z/c_e)^2 \right], \tag{5}$$

To calculate the fields for cavity (that is moving in plasma with the relativistic velocity $v_0 \approx 1$ along x -axis), we have written the Maxwell equations in terms of potentials by using the convenient gauge $A_x = -\varphi$ as [14], with spherical symmetry and the wake field potential will obtain as

$$\Phi = 1 - \left[\frac{3}{\frac{4}{a_e^2} + \frac{4}{b_e^2} + \frac{4}{c_e^2}} \cdot \left(1 - \frac{\zeta^2}{a_e^2} - \frac{y^2}{b_e^2} - \frac{z^2}{c_e^2} \right) \right], \tag{6}$$

The energy of electrons in an ellipsoid cavity can be derived using the Hamiltonian formulation. The one dimensional Hamiltonian of a charged particle in an electromagnetic field is

$$H = \sqrt{1 + (p_c + A)^2 + a^2} - v_0 p_c - \varphi, \tag{7}$$

where, p_c is the particle canonical momentum and φ is the scalar potential.

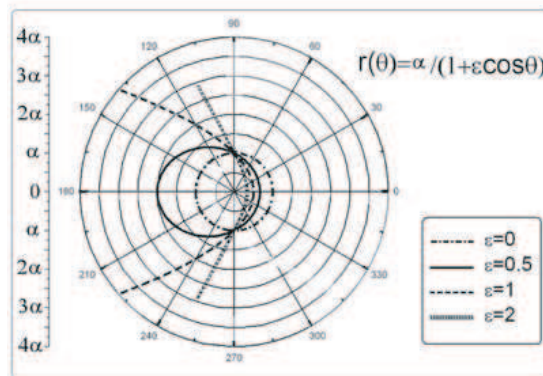


Figure 1: The trajectory of the electron motion in ellipsoid model.

With solving the Hamiltonian equation, the maximum energy of the accelerated peaks at the cavity center

$$\gamma_{\max} = 2\gamma_0^2 + 2\gamma_0^2\Phi_0 \left(1 - \frac{\zeta^2}{a_e^2}\right), \quad (8)$$

By substituting the $\Phi_0 = \frac{3}{\frac{4}{a_e^2} + \frac{4}{b_e^2} + \frac{4}{c_e^2}}$ in Eq. (8) for cavity center, we obtain:

$$\gamma_{\max} = 2\gamma_0^2 + \frac{3\gamma_0^2}{\frac{2}{a_e^2} + \frac{2}{b_e^2} + \frac{2}{c_e^2}}, \quad (9)$$

That for elongation case when ($a_e > b_e = c_e$):

$$\gamma_{\max} = 2\gamma_0^2 + \frac{3\gamma_0^2 b_e^2}{4}, \quad (10)$$

We have found cavity elongation in laser propagation direction is not effective on electron energy and for other directions; the elongations are small and can be neglected. Initial condition to obtained ellipsoid cavity is defined by laser-plasma parameters. In conclusion, it can be considered the electrons of the bunch have equal energy and the ellipsoid cavity holds the electron bunch in quasi-monoenergetic situation better than previous spherical models. In spherical model, energy of the accelerated electrons peak is given by [14]

$$\gamma_{\max} \approx \frac{1}{2}\gamma_0^2 R^2, \quad (11)$$

In this equation, R is radius of spherical bubble and γ_0 is defined by $\gamma_0 = (1 - v_0)^{-1/2}$ that v_0 is the laser pulse group velocity [14]. As the Eq. (11) shows electron bunch energy strongly is related to the transverse radius of cavity and during the laser propagation because of transverse elongation of cavity the energy peak spectrum will spread but in ellipsoid model, Eq. (10) shows the longitudinal elongation (a_e) is not effective on energy spectrum of electron bunch. The result electron beam in ellipsoid model will be quasi-monoenergetic.

4. QUASI-MONOENERGETIC ELECTRON RESULT

In order to generate a laser acceleration wake field, a 20 TW, 30 fs laser pulse based on the Ti-Sapphire CPA laser system has focused onto a supersonic He gas jet with a $f/5$ off-axis gold-coated parabolic mirror. The scheme of the experimental setup is shown in Fig. 2.

The focal spot size and the focusing location at different positions from the beginning of the gas jet are measured by using a charged coupled device (CCD) camera with a microscope objective lens. We obtained quasi-monoenergetic electrons one can obtain high energy electrons with narrower energy distribution by better and precise focusing. When we moved further along the laser beam,

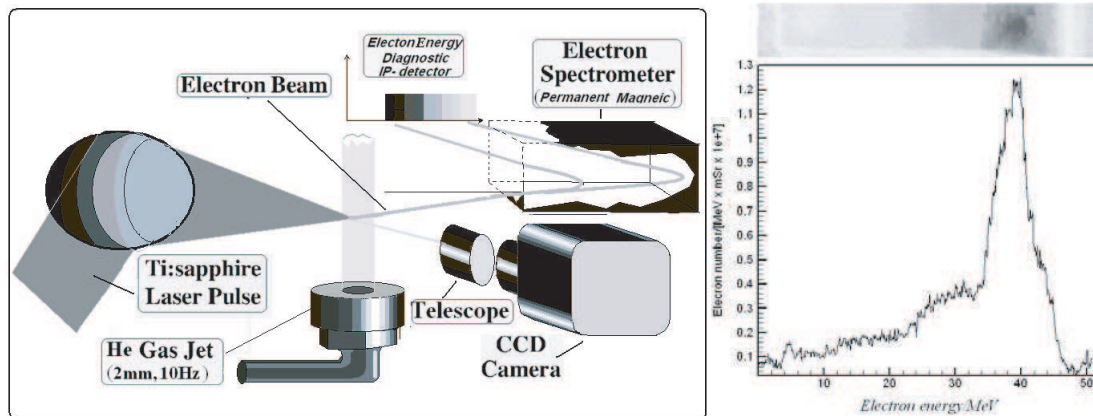


Figure 2: Clean electron beam generation, observation of quasi-monoenergetic electron beam.

the profile of the electrons changed more to the quasi-Maxwellian shapes. Under the conditions of this experiment (focusing radius of 5.5 μm), points less than 600 μm showed 100% distribution of electron energy.

5. CONCLUSION

Instead of periodic plasma wave, it is possible to have a cavity behind the laser pulse. By increasing the intensity of laser pulse the wave-breaking is observed that can be the initial point for other acceleration regimes as cavity. Previous cavity models such as the spherical model show some deviations in comparison with experimental and PIC results [14]. The presented work demonstrates an analytical calculation of the new elliptical model that shows the electron trajectory can be formed as a hyperbola, parabola or ellipse, and there are initial and final conditions for the ellipsoid cavity formation. A dense bunch of relativistic electrons with monoenergetic spectrum is self-generated, and the fields depend linearly on the coordinates. We have shown that the cavity elongation has not affected the maximum electron energy, so the quality of the electron beam is improved.

Finally, based on our experiments and calculations we conclude that in a defined density profile, only defined points can produce mono-energetic electrons beam and by using the higher power lasers it is possible to obtain larger focal spots with intensities larger than the critical relativistic intensities and it can be observed bigger bubbles for trapping more electrons.

REFERENCES

1. Umstadter, D., "Relativistic laser-plasma interactions," *J. Phys. D: Appl. Phys.*, Vol. 36, R151–R165, 2003.
2. Miura, E., et al., "Demonstration of quasi-monoenergetic electron-beam generation in laser-driven plasma acceleration," *Appl. Phys. Lett.*, Vol. 86, 251501, 2005.
3. Umstadter, D. J., "Relativistic laser-plasma interactions," *Phys. D*, Vol. 36, R151, 2003.
4. Malka V., et al., "Electron acceleration by a wake field forced by an intense ultrashort laser pulse," *Science*, Vol. 298, 1596, 2002.
5. Faure, J., et al., "A laser-plasma accelerator producing monoenergetic electron beams," *Nature*, Vol. 431, 541, 2004.
6. Pukhov, A. and J. Meyer-ter Vehn, "Laser wake field acceleration: The highly non-linear broken-wave regime," *Appl. Phys. B — Laser Opt.*, Vol. 74, 355–361, 2002.
7. Kostyukov, I., et al., "Phenomenological theory of laser-plasma interaction in "bubble" regime," *Phys. of Plasmas*, Vol. 11, No. 11, 5256, 2004.
8. Gordienko, S. and A. Pukhov, "Scalings for ultrarelativistic laser plasmas and quasi-monoenergetic electrons," *Phys. of Plasmas*, Vol. 12, No. 4, 043109-1-11, 2005.
9. Zobdeh, P., R. Sadighi-Bonabi, H. Afarideh, E. Yazdani, and R. Rezaei NasirabadAbad, "Using the steepened plasma profile and wave breaking threshold in laser-plasma interaction," *Contrib. Plasma Phys.*, Vol. 48, No. 8, 555–560, 2008.
10. Zobdeh, P., R. Sadighi-Bonabi, and H. Afarideh, "New ellipsoid cavity model in the high intense laser-plasma interaction," *Plasma Devices and Operations*, Vol. 16, No. 2, 105–114, 2008.
11. Sadighi-Bonabi, R., H. A. Navid, and P. Zobdeh, "Observation of quasi mono-energetic electron bunches in the new ellipsoid cavity model," *Laser & Particle Beam*, Vol. 27, No. 2, 2009 (in print).
12. Marion, J. B. and S. T. Thornton, *Classical Dynamics of Particles and Systems*, 3rd Edition, H. B. Jovanovich Pub., New York, 1998.
13. Amusia, M. Ya. and Y. Korniyushin, "Application of the nuclear liquid drop model to atomic and molecular physics problems," *Contemp. Phys.*, Vol. 41, 219–229, 2000.
14. Pukhov, A., et al., "The bubble regime of laser-plasma acceleration: Monoenergetic electrons and the scalability," *Plasma Phys. Control. Fusion*, Vol. 46, B179, 2004.
15. Sadighi-Bonabi, R., S. Rahmatallahpor, H. Navid, E. Lotfi, P. Zobdeh, Z. Reiazie, M. Bostandoust, and M. Mohamadian, "Energy evaluation of mono-energetic electron beam produced by ellipsoid cavity model in the bubble regime," *Contrib. Plasma Phys.*, Vol. 49, No. 1–2, 49–54, 2009.

Scattering by an Infinite Elliptic Metallic Cylinder Coated by a Circular Dielectric One

G. P. Zouros and J. A. Roumeliotis

School of Electrical and Computer Engineering
National Technical University of Athens, Greece

Abstract— The scattering of an electromagnetic plane wave by an infinite elliptic metallic cylinder, coated by a circular dielectric one is treated. The electromagnetic field is expressed in terms of both elliptical and circular-cylindrical wave functions, connected with one another by well-known expansion formulas. When the solution is specialized to small values of the eccentricity $h = c/a$, ($h \ll 1$), where $2c$ is the interfocal distance of the elliptic conductor and $2a$ the length of its major axis, analytical expressions of the form $S(h) = S(0)[1 + g^{(2)}h^2 + g^{(4)}h^4 + \mathcal{O}(h^6)]$ are obtained for the scattered field and the various scattering cross-sections. Both polarizations are considered for normal incidence. Numerical results are given for various values of the parameters.

1. INTRODUCTION

Scattering from composite bodies can be used for the detection of their internal structure i.e., the existence of nonsymmetries, inhomogeneities and also in diagnostic methodologies in biological tissues. The shapes of the boundaries severely limit the possibility for analytical solution of such problems. Various mathematical and numerical techniques are used for complicated geometries. Such geometries including one or more elliptic cylinders are treated, among others, in [1–11].

In the present work, the scattering of an electromagnetic plane wave by an infinite circular dielectric cylinder containing a coaxial elliptic metallic cylinder is treated. The geometry of the scatterer is shown in Fig. 1. The interfocal distance of the elliptic cylinder is $2c$, while $2a$ and $2a'$ are the lengths of its major and minor axes, respectively. The radius of the circular dielectric cylinder is b . The present geometry is a perturbation of the coaxial circular one with radii a and b . All the materials are lossless. Both polarizations are considered for normal incidence.

Using expansion formulas between elliptical and circular cylindrical wave functions [12, 13] and satisfying the boundary conditions we conclude, after some manipulation, to two infinite sets of linear nonhomogeneous equations for the electromagnetic field in Region II.

For general values of $h = c/a$ these sets can be solved only numerically, by truncation, but for $h \ll 1$ an analytical solution is possible. After lengthy, but straightforward calculations, analytical expressions of the form $S(h) = S(0)[1 + g^{(2)}h^2 + g^{(4)}h^4 + \mathcal{O}(h^6)]$ are obtained for the scattered field and the scattering cross-sections. The expansion coefficients $g^{(2)}$ and $g^{(4)}$ are given by exact, closed-form expressions, independently of h , while $S(0)$ corresponds to the coaxial circular problem ($h = 0$). The main advantage of this expression is that it is valid for each small value of h , “free” of Mathieu functions, while all numerical techniques should repeat the calculation, from the beginning, for each different h small or large. So, once $g^{(2)}$ and $g^{(4)}$ are known, $S(h)$ is immediately evaluated by quick “back-of-the-envelope” calculations, for each small h .

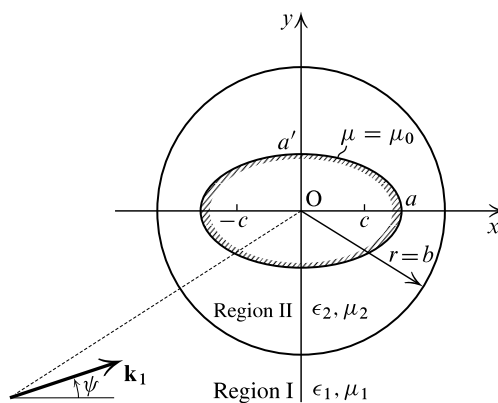


Figure 1: The geometry of the scatterer.

The terms omitted in our solution are of the order of h^6 and higher. So the restriction $h \ll 1$ is not so severe as it may appear at first. Independent numerical solution of this same problem shows that the errors in the approximate analytical results of this paper remain low enough, even for values of h up to 0.7 or higher (maximum possible $h = 1.0$ corresponding to a metallic strip).

Apart from the mathematical interest of its solution, the circular-elliptical combination of the present problem may increase or decrease the scattering cross sections, as compared to the ones of the concentric circular geometry.

The E -wave polarization is examined in Section 2 and the H -wave polarization is examined in Section 3. Finally, in Section 4 numerical results are given for various values of the parameters.

2. E-WAVE POLARIZATION

2.1. Solution of the Problem

The incident plane wave impinging normally on the z axis, has the form [13]

$$E_z^i = e^{-jk_1 r \cos(\varphi - \psi)} = \sum_{n=0}^{\infty} \varepsilon_n j^{-n} J_n(k_1 r) \cos[n(\varphi - \psi)] \quad (1)$$

where r, φ are the polar coordinates with respect to xOy , ψ defines the direction of incidence with respect to Ox , J_n is the cylindrical Bessel function of the first kind, $\varepsilon_0 = 1$, $\varepsilon_n = 2$, ($n \geq 1$) is the Neumann factor and k_1 is the wavenumber in Region I. The time dependence $\exp(j\omega t)$ is suppressed throughout.

The scattered field is expressed as

$$E_z^s = \sum_{n=0}^{\infty} H_n(k_1 r) [P_n \cos(n\varphi) + Q_n \sin(n\varphi)] \quad (2)$$

where $H_n(k_1 r)$ is the Hankel function of the second kind with the upperscript (2) omitted for simplicity.

The field in Region II, satisfying the boundary condition $E_z^{II} = 0$ at the elliptical boundary $\mu = \mu_0$, has the expression [3]

$$E_z^{II} = \sum_{i=0}^{\infty} \{ A_i [J e_i(h', \cosh \mu) N e_i(h', \cosh \mu_0) - J e_i(h', \cosh \mu_0) N e_i(h', \cosh \mu)] S e_i(h', \cos \theta) \\ + B_i [J o_i(h', \cosh \mu) N o_i(h', \cosh \mu_0) - J o_i(h', \cosh \mu_0) N o_i(h', \cosh \mu)] S o_i(h', \cos \theta) \} \quad (3)$$

where $h' = k_2 c$.

In (3), μ, θ are the transverse elliptical cylindrical coordinates with respect to xOy , $J e_i(J o_i)$ and $N e_i(N o_i)$ are the even (odd) radial Mathieu functions of the first and second kind, respectively, while $S e_i(S o_i)$ are the even (odd) angular Mathieu functions [12].

To satisfy the boundary conditions at $r = b$ we use the expansion formulas connecting the Mathieu functions with the coaxial circular cylindrical ones [13] in steps similar with those in [5, 14]. These boundary conditions are

$$E_z^{II} = E_z^i + E_z^s, \quad \mu_2^{-1} \partial E_z^{II} / \partial r = \mu_1^{-1} \partial (E_z^i + E_z^s) / \partial r \quad (4)$$

By satisfying them we express P_n and Q_n in terms of A_i 's and B_i 's

$$P_n = \frac{\sqrt{\pi/2}}{H_n(x_1)} \sum_{i=0}^{\infty} A_i j^{n-i} B_n^e(h', i) [N e_i(h', \cosh \mu_0) J_n(x_2) - J e_i(h', \cosh \mu_0) N_n(x_2)] \\ - \varepsilon_n j^{-n} \frac{J_n(x_1)}{H_n(x_1)} \cos(n\psi), \quad n \geq 0 \quad (5)$$

$$Q_n = \frac{\sqrt{\pi/2}}{H_n(x_1)} \sum_{i=1}^{\infty} B_i j^{n-i} B_n^o(h', i) [N o_i(h', \cosh \mu_0) J_n(x_2) - J o_i(h', \cosh \mu_0) N_n(x_2)] \\ - 2j^{-n} \frac{J_n(x_1)}{H_n(x_1)} \sin(n\psi), \quad n \geq 1 \quad (6)$$

where N_n is the cylindrical Bessel function of the second kind (Neumann function) and we finally obtain the following two infinite sets of linear nonhomogeneous equations for the expansion coefficients A_i and B_i

$$\sum_{i=0}^{\infty} a_{mi} A_i = K_m, \quad m \geq 0 \quad (7)$$

$$\sum_{i=1}^{\infty} b_{mi} B_i = K'_m, \quad m \geq 1 \quad (8)$$

where

$$a_{mi} = \sqrt{\frac{\pi}{2}} j^{m-i} B_m^e(h', i) \left\{ \sqrt{\frac{\mu_1}{\mu_2}} [N e_i(h', \cosh \mu_0) J'_m(x_2) - J e_i(h', \cosh \mu_0) N'_m(x_2)] - \sqrt{\frac{\epsilon_1}{\epsilon_2}} [N e_i(h', \cosh \mu_0) J_m(x_2) - J e_i(h', \cosh \mu_0) N_m(x_2)] \frac{H'_m(x_1)}{H_m(x_1)} \right\} \quad (9)$$

$$b_{mi} = \sqrt{\frac{\pi}{2}} j^{m-i} B_m^o(h', i) \left\{ \sqrt{\frac{\mu_1}{\mu_2}} [N o_i(h', \cosh \mu_0) J'_m(x_2) - J o_i(h', \cosh \mu_0) N'_m(x_2)] - \sqrt{\frac{\epsilon_1}{\epsilon_2}} [N o_i(h', \cosh \mu_0) J_m(x_2) - J o_i(h', \cosh \mu_0) N_m(x_2)] \frac{H'_m(x_1)}{H_m(x_1)} \right\} \quad (10)$$

$$K_m = \sqrt{\frac{\epsilon_1}{\epsilon_2}} \epsilon_m j^{-m} \left[J'_m(x_1) - J_m(x_1) \frac{H'_m(x_1)}{H_m(x_1)} \right] \cos(m\psi), \quad K'_m = K_m \tan(m\psi) \quad (11)$$

and m, i are both even or odd. In (9)–(11), we have used the substitutions $x_1 = k_1 b$ and $x_2 = k_2 b$.

For general values of h' the sets (7) and (8) can be solved only numerically by truncation, a complicated task due to the calculation of the Mathieu functions for each different h' . However, for small h' an analytical, closed-form solution can be obtained. Instead of h' the eccentricity $h = c/a$ ($h' = k_2 a h$) is used, as well as Maclaurin series expansions in powers of h^2 [15] for each function of h ($\ll 1$) appearing in the process. After lengthy, but straightforward calculations, one can find expansions of the form

$$a_{mm} = C_{mm}^{(0)} + C_{mm}^{(2)} h^2 + C_{mm}^{(4)} h^4 + \mathcal{O}(h^6), \quad a_{m,m\pm 2} = C_{m,m\pm 2}^{(2)} h^2 + C_{m,m\pm 2}^{(4)} h^4 + \mathcal{O}(h^6), \quad (12)$$

$$a_{m,m\pm 4} = C_{m,m\pm 4}^{(4)} h^4 + \mathcal{O}(h^6)$$

$$b_{mm} = D_{mm}^{(0)} + D_{mm}^{(2)} h^2 + D_{mm}^{(4)} h^4 + \mathcal{O}(h^6), \quad b_{m,m\pm 2} = D_{m,m\pm 2}^{(2)} h^2 + D_{m,m\pm 2}^{(4)} h^4 + \mathcal{O}(h^6),$$

$$b_{m,m\pm 4} = D_{m,m\pm 4}^{(4)} h^4 + \mathcal{O}(h^6) \quad (13)$$

The set (7) takes the following form, up to the order h^4 :

$$a_{m,m-4} A_{m-4} + a_{m,m-2} A_{m-2} + a_{mm} A_m + a_{m,m+2} A_{m+2} + a_{m,m+4} A_{m+4} = K_m, \quad m=0, 1, 2, \dots \quad (14)$$

A similar expression holds also for the set (8), with $m = 1, 2, 3, \dots$. As it is evident from (3) the subscripts of A 's (and B 's) are always nonnegative. In the opposite case A 's (and B 's) are equal to zero and so disappear. The same is valid also for the corresponding a 's (and b 's). Each of the sets (7) and (8) separates into two distinct subsets, one with m even and the other with m odd.

A 's are obtained from the solution of the set (14) by Cramer's rule, using Formulas (27)–(29) from [16] for the determinant Δ of a 's in (14) and for the determinant Δ_n originating from Δ after the substitution of its n th column by the column of K 's. Using the expansions (12) and (13) we obtain

$$A_n = \frac{\Delta_n}{\Delta} = A_n^{(0)} + A_n^{(2)} h^2 + A_n^{(4)} h^4 + \mathcal{O}(h^6), \quad n \geq 0 \quad (15)$$

Similarly B_n is given by an expansion analogous to (15).

2.2. The Scattered Far Field

By using the asymptotic expansion for the Hankel function in (2), we obtain the scattered far field expression and next the back scattering or radar (σ_b), forward (σ_f) and total (Q_t) scattering cross sections [3]

$$k_1\sigma_b = 4|G(\psi + \pi)|^2, \quad k_1\sigma_f = 4|G(\psi)|^2, \quad k_1Q_t = 4|P_0|^2 + 2\sum_{n=1}^{\infty} (|P_n|^2 + |Q_n|^2) \quad (16)$$

where

$$G(\varphi) = \sum_{n=0}^{\infty} j^n [P_n \cos(n\varphi) + Q_n \sin(n\varphi)] \quad (17)$$

The coefficients P_n and Q_n are given in (5) and (6). If we substitute there the expansions of the various quantities for small h , we obtain

$$P_n = P_n^{(0)} + P_n^{(2)}h^2 + P_n^{(4)}h^4 + \mathcal{O}(h^6), \quad Q_n = Q_n^{(0)} + Q_n^{(2)}h^2 + Q_n^{(4)}h^4 + \mathcal{O}(h^6) \quad (18)$$

Analogous expansions are obtained for $G(\varphi)$, $\sigma(\varphi)$ and Q_t . So, $G^{(\ell)}(\varphi)$, $\ell = 0, 2, 4$ is obtained from (17), by simply using $P_n^{(\ell)}$ and $Q_n^{(\ell)}$ in place of P_n and Q_n respectively, while

$$\begin{aligned} |G(\varphi)|^2 &= G(\varphi)G^*(\varphi) = \left|G^{(0)}(\varphi)\right|^2 + 2\text{Re} \left[G^{(0)*}(\varphi)G^{(2)}(\varphi) \right] h^2 \\ &\quad + \left\{ 2\text{Re} \left[G^{(0)*}(\varphi)G^{(4)}(\varphi) \right] + \left|G^{(2)}(\varphi)\right|^2 \right\} h^4 + \mathcal{O}(h^6) \end{aligned} \quad (19)$$

with Re representing the real part and the asterisk denoting the complex conjugate.

Using next expansions analogous to (19) for $|P_n|^2$, $n \geq 0$ and $|Q_n|^2$, $n \geq 1$, we find from (16) that

$$k_1Q_t = k_1Q_t^{(0)} + k_1Q_t^{(2)}h^2 + k_1Q_t^{(4)}h^4 + \mathcal{O}(h^6) \quad (20)$$

Eq. (20) can be set in the form

$$k_1Q_t = k_1Q_t^{(0)} \left[1 + g_Q^{(2)}h^2 + g_Q^{(4)}h^4 + \mathcal{O}(h^6) \right], \quad g_Q^{(\ell)} = Q_t^{(\ell)}/Q_t^{(0)}, \quad \ell = 2, 4 \quad (21)$$

A similar expression holds also for $k_1\sigma_b$ and $k_1\sigma_f$, namely,

$$k_1\sigma = k_1\sigma^{(0)} \left[1 + g_\sigma^{(2)}h^2 + g_\sigma^{(4)}h^4 + \mathcal{O}(h^6) \right], \quad g_\sigma^{(\ell)} = \sigma^{(\ell)}/\sigma^{(0)}, \quad \ell = 2, 4 \quad (22)$$

In (21) and (22) $Q_t^{(0)}$ and $\sigma^{(0)}$ correspond to the coaxial circular geometry.

The correctness of our results was checked by the forward scattering theorem [17]

$$k_1Q_t^{(\ell)} = -4\text{Re} \left[G^{(\ell)}(\psi) \right], \quad \ell = 0, 2, 4 \quad (23)$$

which was verified to a very good accuracy for various values of the parameters.

3. H-WAVE POLARIZATION

The incident wave H_z^i and the scattered wave H_z^s are again given by Eqs. (1) and (2), respectively. The field in Region II, satisfying the boundary condition $\partial H_z^{II}/\partial\mu = 0$ at $\mu = \mu_0$ is the same as (3), with the only difference that $J_{e_i}(h', \cosh \mu_0)$ and $N_{e_i}(h', \cosh \mu_0)$ are now replaced by their derivatives with respect to μ at $\mu = \mu_0$. In (4), E_z , μ_1 , μ_2 should be replaced by H_z , ϵ_1 , ϵ_2 , respectively.

Following steps identical with the ones for the E -wave polarization we obtain again Eqs. (5)–(23) with the aforementioned changes.

4. NUMERICAL RESULTS AND DISCUSSION

In Figs. 2(a)–4(a), the scattering cross-sections are plotted versus ψ , for the E -wave polarization. The same is done in Figs. 2(b)–4(b) for H -wave polarization. In each figure the corresponding scattering cross-section for $h = 0$ (coaxial circular cylinders with radii a and b) is also plotted. The results are symmetric about $\psi = 90^\circ$.

From Figs. 2(a)–4(a) the higher sensitivity of σ_b to the change of ψ is evident, as compared to that of σ_f and Q_t , in the case of E -wave. It is also evident, from all figures, that the deviation of the scatterer examined here from the coaxial circular one, by making the inner metallic cylinder elliptic, increases or decreases the scattering cross-sections, depending on the values of the parameters. Inversely, this may be useful for the detection of a shape perturbation in the inner cylinder.

The results of Figs. 2(a)–4(b) were verified, to a high degree of accuracy, by comparing to

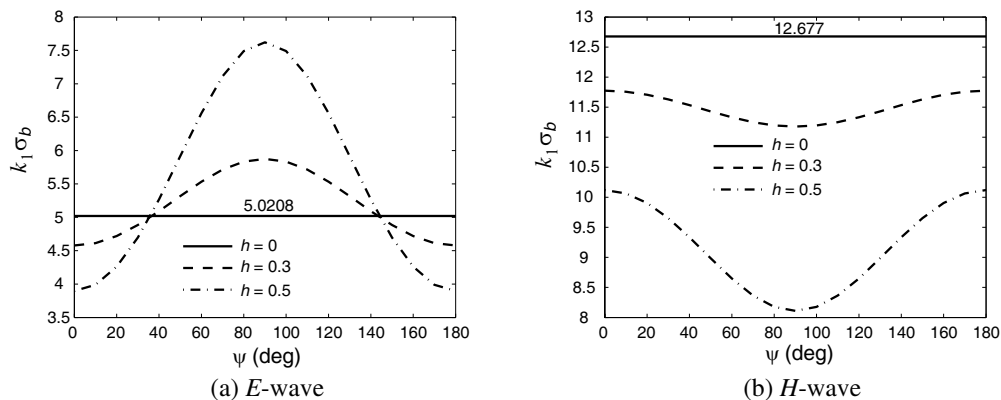


Figure 2: Back scattering cross sections for $\epsilon_2/\epsilon_1 = 2.54$, $\mu_2/\mu_1 = 1$, $a/b = 0.4$ and $k_1b = \pi$.

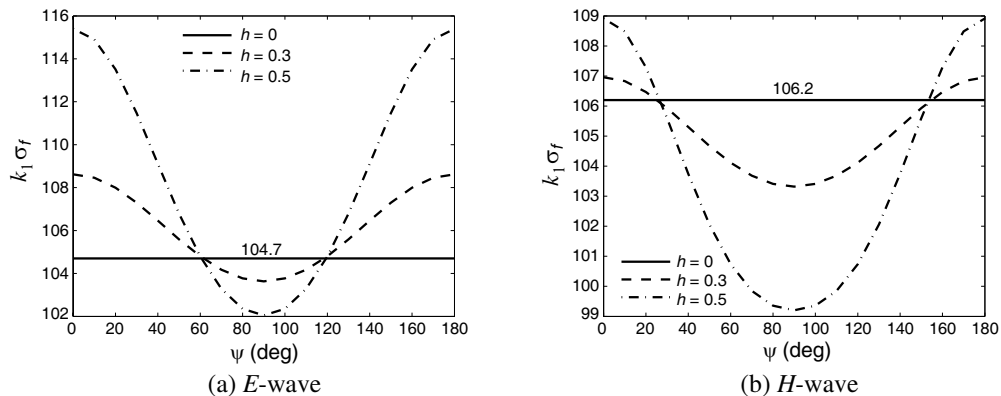


Figure 3: Forward scattering cross sections for $\epsilon_2/\epsilon_1 = 2.54$, $\mu_2/\mu_1 = 1$, $a/b = 0.4$ and $k_1b = \pi$.

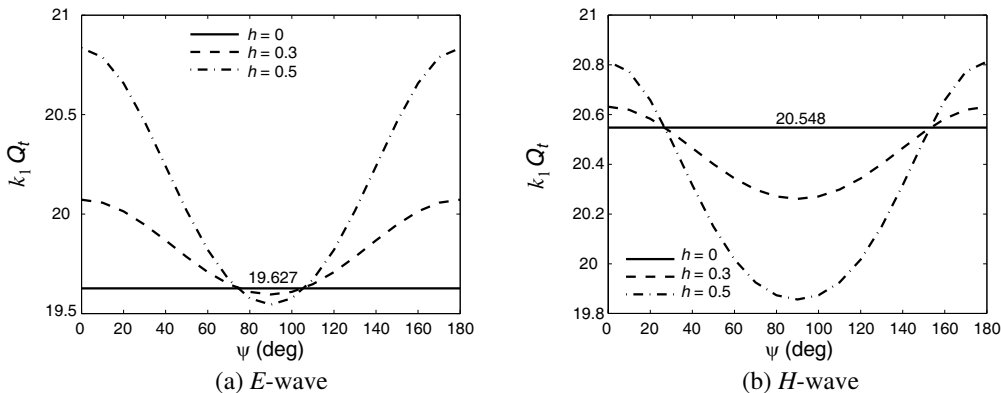


Figure 4: Total scattering cross sections for $\epsilon_2/\epsilon_1 = 2.54$, $\mu_2/\mu_1 = 1$, $a/b = 0.4$ and $k_1b = \pi$.

independent results obtained from the numerical solution of the same problem, by truncating the sets (7) and (8).

It should be noticed finally that we have verified the various plotted results given in [17] in every case, for all the values of the parameters used there.

REFERENCES

1. Nicolet, A., F. Zolla, and S. Guenneau, "Finite-element analysis of cylindrical invisibility cloaks of elliptical cross section," *IEEE Trans. Magnetism*, Vol. 44, 1150–1153, Jun. 2008.
2. Caorsi, S. and M. Pastorino, "Scattering by multilayer isorefractive elliptic cylinders," *IEEE Trans. Antennas Propag.*, Vol. 52, 189–196, Jan. 2004.
3. Roumeliotis, J. A. and S. P. Savaidis, "Scattering by an infinite circular dielectric cylinder coating eccentrically an elliptic metallic one," *IEEE Trans. Antennas Propag.*, Vol. 44, 757–763, May 1996.
4. Savaidis, S. P. and J. A. Roumeliotis, "Scattering by an infinite circular dielectric cylinder coating eccentrically an elliptic dielectric cylinder," *IEEE Trans. Antennas Propag.*, Vol. 52, 1180–1185, May 2004.
5. Savaidis, S. P. and J. A. Roumeliotis, "Scattering by an infinite elliptic dielectric cylinder coating eccentrically a circular metallic or dielectric cylinder," *IEEE Trans. Microwave Theory Tech.*, Vol. 45, 1792–1800, Oct. 1997.
6. Hamid, A. K. and M. I. Hussein, "Electromagnetic scattering by a lossy dielectric-coated elliptic cylinder," *Canadian Journal of Physics*, Vol. 81, 771–778, May 2003.
7. Sebak, A. R., "Scattering from dielectric-coated impedance elliptic cylinder," *IEEE Trans. Antennas Propag.*, Vol. 48, 1574–1580, Oct. 2000.
8. Sebak, A. R., H. A. Ragheb, and L. Shafai, "Plane wave scattering by dielectric elliptic cylinder coated with nonconfocal dielectric," *Radio Science*, Vol. 29, 1393–1401, Nov.–Dec. 1994.
9. Kim, C. S. and C. Yeh, "Scattering of an obliquely incident wave by a multilayered elliptical lossy dielectric cylinder," *Radio Science*, Vol. 26, 1165–1176, Sept.–Oct. 1991.
10. Richmond, J. H., "Scattering by a conducting elliptic cylinder with dielectric coating," *Radio Science*, Vol. 23, 1061–1066, Nov.–Dec. 1988.
11. Ragheb, H. A. and L. Shafai, "Electromagnetic scattering from a dielectric-coated elliptic cylinder," *Canadian Journal of Physics*, Vol. 66, 1115–1122, Dec. 1988.
12. Morse, P. M. and H. Feshbach, *Methods of Theoretical Physics*, New York, McGraw-Hill, 1953.
13. Stratton, J. A., *Electromagnetic Theory*, New York, McGraw-Hill, 1941.
14. Roumeliotis, J. A. and S. P. Savaidis, "Cutoff frequencies of eccentric circular-elliptic metallic waveguides," *IEEE Trans. Microwave Theory Tech.*, Vol. 42, 2128–2138, Nov. 1994.
15. Kokkorakis, G. C. and J. A. Roumeliotis, "Power series expansions for Mathieu functions with small arguments," *Mathematics of Computation*, Vol. 70, No. 235, 1221–1235, 2001.
16. Tsogas, G. D., J. A. Roumeliotis, and S. P. Savaidis, "Scattering by an infinite elliptic metallic cylinder," *Electromagnetics*, Vol. 27, 159–182, 2007.
17. Kakogiannos, N. B. and J. A. Roumeliotis, "Electromagnetic scattering from an infinite elliptic metallic cylinder coated by a circular dielectric one," *IEEE Trans. Microwave Theory Tech.*, Vol. 38, 1660–1666, Nov. 1990.

High Performance Angular Resolution Algorithm for Radar Systems

B. A. Lagovsky

Moscow State Institute of Radio Engineering and Automation, Technical University, Russia

Abstract— This paper describes how the angular resolution of radar systems can be improved in the problems of the target image identification. A comparison of the developed methods is carried out. The boundaries of maximum possible angular resolution of observed objects are defined as functions of the noise level.

1. INTRODUCTION

It is well known that to improve the quality of the target image identification we need to improve the angular resolution. Similar problems are especially important in problems of remote sensing. In particular, it is required to work out the intensity distribution of the echo signal over a surface or volume of the target. For the targets located in a far zone, the angular resolution based on Rayleigh criterion is usually represented as

$$\delta\theta \cong \lambda/d, \quad (1)$$

where d is a size of antenna, λ — wave-length.

The estimation of beamwidth as in (1) has fundamental character. It follows from the uncertainty relation. The magnitude of the angular resolution (1) is introduced artificially, on the basis of the possibility of separate observation of two close located objects. It gives a principal opportunity to increase the angular resolution for processing results of measurements.

2. PROBLEM STATEMENT

At scanning on an angle α we shall receive the signal $U(\alpha)$. As the additional given requirement we shall consider that the angular sizes of a signal source do not exceed $\Omega = [\alpha_1, \alpha_2]$, and thus we have

$$U(\alpha) = \int_{\Omega} f(\alpha - \varphi)I(\varphi)d\varphi, \quad (2)$$

The problem is to reconstruct an angular intensity distribution $I(\alpha)$ of the reflected signal on the basis of the analysis of an output signal $U(\alpha)$ and the known directional pattern $f(\alpha)$. The considered problem relates to inverse ill-posed problems. The numerical solutions of the Eq. (2) became unstable when we try to obtain the angular resolution better then (1).

The basic reason of the origin of instabilities is noise component of a received signal. At the angular resolution as (1) their influence is possible to neglect, but it sharply increases at attempts to receive the greater resolution. The increase in the resolution from above (1) is possible, but up to the certain limit determined, basically, by signal-to-noise ratio.

To improve the solution stability the various procedures of regularization are used. There efficiency depends on forms of the function $f(\alpha)$ and unknown function $I(\alpha)$. Therefore these procedures are not universal and are not always effective.

For this reason the offered algebraic methods of the analysis based on a representation of a signal and desired intensity distribution in a discrete form seem to be encouraging.

Let's consider a linear equidistant antenna array consisting of $2M + 1$ elements with distances d between the next emitters. The directional pattern focused in a direction α' is:

$$f(\alpha - \alpha') = \sum_{n=-M}^M J_n \exp(-ikd(\sin \alpha - \sin \alpha')) \quad (3)$$

where $k = 2\pi/\lambda$, J_n is the amplitude of a current on the emitter n . On substituting (3) into Eq. (2)

a linear integral equation with a degenerate kernel is obtained:

$$U(\alpha) = \sum_{n=-M}^M J_n \exp(-ikdn \sin \alpha) \int_{\Omega} \exp(ikdn \sin \alpha') I(\alpha') d\alpha' = \sum_{n=-M}^M J_n \exp(-ikdn \sin \alpha) a_n,$$

$$a_n = \int_{\Omega} \exp(ikdn \sin \alpha') I(\alpha') d\alpha' \quad (4)$$

The solution of Eq. (4) is usually expressed with the help of eigenfunctions. The number of eigenfunctions of the given Hermitian kernel is finite. The eigenvalues of such integral operator are real.

Let's introduce the scalar product of functions u, v as

$$(u, v) = \int_{\Omega} \overline{u(\alpha)} v(\alpha) d\alpha$$

Then the eigenfunctions of the kernel (3), belonging to different eigenvalues, are orthogonal. The eigenfunctions (3) represent $2M + 1$ sums

$$\psi_m(\alpha) = \lambda_m \sum_{n=-M}^M c_n^m \exp(-ikdn \sin \alpha), \quad m = 0, 1, \dots, 2M, \quad (5)$$

where λ_m are the eigenvalues of the kernel (3). Factors c_n^m are the coordinates of the eigenvectors c^m of a matrix A with elements:

$$a_{pq} = J_p J_q \int_{\alpha_1}^{\alpha_2} \exp(-ik(p-q)\alpha) d\alpha, \quad p, q = 0, 1, \dots, 2M, \quad (6)$$

for small angles α_1, α_2 . Then the solution of the integral Eq. (4) is reduced to the solution of the system of linear equations:

$$\left(A - \frac{1}{\lambda} E \right) C = 0, \quad (7)$$

where E is the identity matrix, and C is an eigenvector, corresponding to the eigenvalue λ^{-1} .

As a result, the solution of the integral Eq. (2) can be submitted as a superposition of eigenfunctions:

$$I(\alpha) = \sum_{m=1}^{2M+1} \lambda_m(\psi_m, U) \psi_m(\alpha) + \varphi(\alpha) \quad (8)$$

where $\varphi(\alpha)$ is an arbitrary function, orthogonal to all eigenfunctions $\psi_m(\alpha)$. Setting the distribution of amplitudes of currents on the emitters J_n as the elements of the vector c^m , we shall receive a signal U^m from a direction $\alpha = 0$ as

$$U^m(0) = \int_{\Omega} \psi_m(\alpha) \sum_{n=1}^{2M+1} \lambda_n(U, \psi_n) \psi_n(\alpha) d\alpha = \lambda_m(U, \psi_m)$$

The stability of (7) is estimated with the help of the condition number K as:

$$\frac{\|\delta I\|}{\|I\|} \leq K \frac{\|\delta U\|}{\|U\|}, \quad K \leq |\lambda|_{\max} / |\lambda|_{\min}. \quad (9)$$

where $\|A\|$ is the norm of the linear operator A ; δI and δU — inaccuracies of I and U , $|\lambda|_{\max}$ and $|\lambda|_{\min}$ the greatest and least, in the module, eigenvalue of matrix A , respectively.

The numerical evaluations demonstrate that it happens at N_{\max} significantly less than $2M + 1$. In this case, it is impossible to consider the representation of the required intensity based on expansion of several first eigenfunctions in (8) as the best solution, than in the expansion in other systems of orthogonal functions.

The condition number K for various systems of orthogonal functions differ. It indicates the potential to obtain a greater resolution at a successful choice of a system of orthogonal functions.

3. MAIN RESULTS AND EXAMPLES

Various systems of orthogonal functions $S_j(\alpha)$, $j = 1, 2 \dots N$ on Ω are considered. Their use allows to take into account preliminary information on the distribution $I(\alpha)$ and to increase the angular resolution.

For many problems the most convenient choice appears to be step functions. The required angular distribution $I(\alpha)$ can be represented as a decomposition on final system of functions $S_j(\alpha)$ with unknowns factors b_j :

$$I(\alpha) = \sum_{j=1}^N b_j S_j(\alpha) + \eta(\alpha), \quad (10)$$

where $\eta(\alpha)$ is an arbitrary function, orthogonal to all $S_j(\alpha)$. Considering without loss of generality $J_n = 1$, instead of Eq. (4) we have

$$U(\alpha) = \sum_{j=1}^N \sum_{n=-M}^M b_n a_{jn} \exp(-ikdn \sin \alpha), \quad a_{jn} = (\exp(-ikdn \sin \alpha'), S_j(\alpha)) \quad (11)$$

From Eq. (11), having multiplied both parts with the complex conjugate function on $\overline{S_j(\alpha)}$, after integration we obtain the system of linear equations

$$(S_j, U) = \sum_{n=-M}^M b_n a_{nj} \overline{a_{jn}}, \quad j = 1, 2 \dots N. \quad \text{or } U^s = A\bar{A}B \quad (12)$$

Solving Eq. (12), we find b_j , and, hence, using (10), required angular distribution $I(\alpha)$.

3.1. Simple Algorithms

The numerical characteristics of the increase of the angular resolution and its limits were investigated. The improvement of the resolution was estimated in comparison with the beamwidth (1).

An antenna array system of size $30d/\lambda$ with uniform excitation $J_n = 1$ was considered. The angular distribution of the reflected signal was set by a function identically equal to zero outside of the zone Ω and as continuous complex function within the domain.

The representation $I(\alpha)$ as superposition of step function means, that the true distribution $I(\alpha)$ is replaced by an average distribution on each step $\Delta\alpha$.

The system of Eq. (12) is solved at the beginning for two-step approximation of the function $I(\alpha)$, i.e., when the observation zone is separated into two sectors. If we manage to obtain a solution, then the observation zone is separated into 3 or 4 sectors and the system of Eq. (12) is solved once again, and so on up to the collapse of the solution.

The most simple of the considered methods is based on representation of a signal $U(\alpha)$ in a discrete form. In this case instead of a continuous $U(\alpha)$ we have a vector of complex values U with N elements. Then, instead of the integral Eq. (2), according to Eq. (11), we have system of the linear equations:

$$U = FB, \quad (13)$$

where B is the vector with factors b_j and F is a matrix with elements:

$$F_{ij} = \int_{\Omega} f(\alpha_i - \alpha) S_j(\alpha) d\alpha \quad (14)$$

$i, j = 1, 2 \dots, N$, i — number of receiving beam; j — number of step function from the chosen system.

In Figure 1, the results of restitution of the target with the minimal achieved step are given. 1 — initial angular distribution of intensity, 2 — restored image with the given step $\Delta\alpha$. The step on $\theta_{0.5}$ is expressed in normalized beamwidth unities and is equal to $1/8 \theta_{0.5}$. On the horizontal axis numbers of points of supervision m inside area $\theta_{0.5}$ are marked. Numbers on the vertical axis, characterize the amplitude of radiation of a discrete element of the target at number m , i.e., $I(m)$ in relative units, i.e., after normalization on the maximum value of intensity. The effective resolution has increased in 8 times in comparison with Rayleigh criterion (1). The solution of the problem based on the of eigenfunctions (5) yields much the worst results.

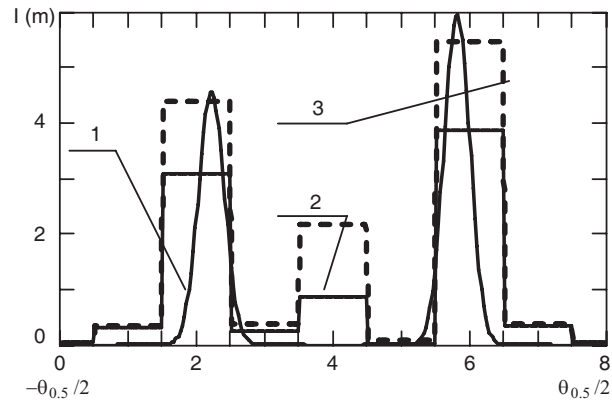


Figure 1: The example of $\theta_{0.5}/8$ resolution. Step functions are used.

3.2. Influence of Noise

The influence of noise level on the effective resolution was investigated on mathematical model. The maximum value of the signal-to-noise ratio at which the image of the target yet does not undergo appreciable changes using the algorithm based on Rademakher functions, we denoted as R . Absolute value of R is very small, and was used as a unit of measure of stability.

In a Figure 1 are shown a variant of the restored image at the presence of a noise — at an average level $100R$ — 2. The reduction of number of restored points of the image allows to receive images of the worse quality, but at the greater noise level — up to $10^{3\div 4}R$. At a level $10^5 R$ it becomes impossible to find a satisfactory solution to the system of Eq. (12) using the described algorithms. However, more complex algorithms described below, demanding a much greater time for signal processing, successfully allow solving the problem at a noise level — up to $10^{6\div 7}R$.

For improving the resolution twice it is necessary to increase the signal-to-noise ratio by one order.

3.3. Complex Algorithms

Having replaced in Eq. (2) the required distribution of intensity of the reflected signal by its expansion on orthogonal functions $S_n(\alpha)$ and having multiplied both parts of the obtained expression by the function $S_m(\alpha)$, after integration we obtain:

$$\int_{\Omega} U(\alpha') S_n(\alpha') d\alpha' = \sum_{m=1}^M b_m \int_{\Omega} S_n(\alpha') \int_{\Omega} f(\alpha' - \alpha) S_m(\alpha) d\alpha d\alpha'$$

$$V_n = \int_{\Omega} U(\alpha') S_n(\alpha') d\alpha' \quad g_{m,n} = \int_{\Omega} S_n(\alpha) \int_{\Omega} f(\alpha' - \alpha) S_m(\alpha') d\alpha' d\alpha \quad (15)$$

for $m, n = 1 \dots N$, as well as for the above mentioned methods, we obtain a system of the linear equations

$$V = GB, \quad (16)$$

where V is a vector with elements v_n , G is a matrix with elements $g_{m,n}$.

At integration $U(\alpha)$ the role of stochastic noise in the received signal is reduced. So the integration is a regularizing factor for the solving inverse problems.

The further magnification of the resolution is possible on the basis of more complicate measurements and algorithms of processing of the obtained information.

Let signal reception and radiation carried out by two independent scanning beams $f_r(\alpha)$ and $f_e(\beta)$. Then the received signal is a convolution integral from two variables α and β :

$$U(\alpha, \beta) = \int_{\Omega} f_e(\alpha - \alpha') f_r(\beta - \alpha') I(\alpha') d\alpha' \quad (17)$$

The measurements (2) are then included in (17). One of the most perspective methods of processing Eq. (17) is preliminary integration on an angle of scanning

$$\begin{aligned}
 V(\alpha) &= \int_{\Omega} U(\alpha, \beta) d\beta = \int_{\Omega} f_e(\alpha' - \alpha) I(\alpha') \int_{\Omega} f_r(\alpha' - \beta) d\beta d\alpha' \\
 &= \int_{\Omega} f_e(\alpha' - \alpha) \phi(\alpha') I(\alpha') d\alpha' = \int_{\Omega} F(\alpha' - \alpha) I(\alpha') d\alpha', \\
 \phi(\alpha') &= \int_{\Omega} f_r(\alpha' - \beta) d\beta, \quad F(\alpha' - \alpha) = f_e(\alpha' - \alpha) \phi(\alpha')
 \end{aligned} \tag{18}$$

The integrated Eq. (18) formally coincides with Eq. (2) by replacing $f(\alpha - \alpha')$ with $F(\alpha - \alpha')$. Hence, processing of the received signals can be carried out with the help of all methods stated above.

The condition numbers for different algorithms from number of resolved points are given in Figure 2. The condition numbers are normalized on value of the maximum number. The values of condition numbers are given for the Rademakher functions — 1, eigenfunctions of the kernel — 2, the Walsh functions — 3, and the Formulas (18) — 4.

The method of double integration (18) potentially yields the best results, but requires much greater time for signal processing.

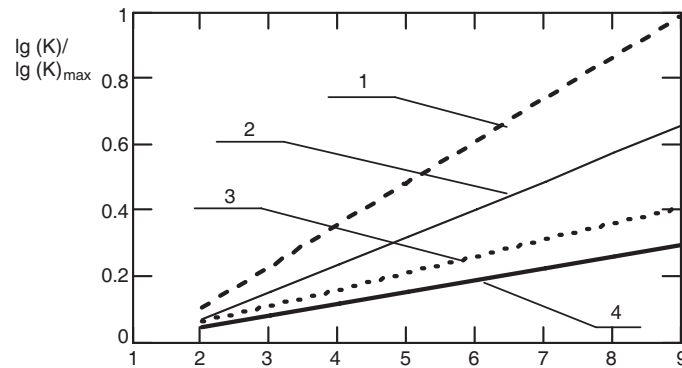


Figure 2: Condition numbers for different algorithms.

4. CONCLUSION

Algebraic methods of image restoration with improved angular resolution are developed. As a whole, these algebraic methods allow to increase the effective angular resolution by 2–6 times when using simple algorithms and by 6–10 when using composite specialized algorithms. It is shown, that the quality of image restoration first of all depends on condition numbers of the relevant matrices. At close values of condition numbers the quality of the images is determined by a successful choice of system of orthogonal functions for the searched target. Systems of orthogonal functions which should be used for restoration of various types of targets are described. The limitations of increase of the angular resolution are found depending on the signal-to-noise ratio.

Algorithm for the Determination of Targets Coordinates in Structure of the Multiple Target with the Increased Effective Resolution

B. A. Lagovsky

Moscow State Institute of Radio Engineering and Automation (Technical University), Russia

Abstract— The approximate numerical solutions of some inverse problems of electrodynamics allow to increase angular resolution of radar-tracking systems and systems of remote sensing. The method of imagery of point targets in the multiple targets is developed. It is not complicated for practical realization in a real-time operation mode. A comparison of the efficiency known and the developed method is carried out. The results of numerical experiments on mathematical model are set out.

1. INTRODUCTION

The locked-on signal is connected with angular distribution of amplitude of the reflected signal by Fredholm integral equation of the first order:

$$U(\alpha) = \int_{\Omega} f(\alpha - x)I(x)dx, \quad (1)$$

where $f(\alpha)$ — is the directional pattern of antenna system, Ω is the angular sizes of a signal source. It is required to restore the angular distribution of amplitude of the signal reflected from the target $I(\alpha)$ on the basis of numerical processing with the greatest possible angular resolution.

The angular resolution based on Rayleigh criterion is represented as

$$\delta\theta \cong \lambda/d, \quad (2)$$

where d is a size of antenna, λ — wave-length.

Digital processing of the locked-on signals on special algorithms allows to increase accuracy of measurement of angular coordinates and angular resolution of measuring systems. In Articles [1–6] a number of methods of signal processing, allowing to raise effective angular resolution is described. Their efficiency depends on forms of the function $f(\alpha)$ and unknown function $I(\alpha)$. These methods are not universal and not always allow to improve noticeably the angular resolution. Besides they are rather complicated for image restoration in a real time mode. The minimal signal-to-noise ratio necessary for them is equal 20–25 dB.

The developed method allows to take into account a priori information about function $I(\alpha)$ and to increase the effective resolution in comparison with Eq. (2) at essentially smaller values of a signal-to-noise ratio than known methods.

2. PROBLEM STATEMENT

At scanning on an angle α we shall receive the signal $U(\alpha)$:

$$U(\alpha) = \int_{\Omega} f(\alpha - \varphi)I(\varphi)d\varphi, \quad (3)$$

The problem is to restore an angular intensity distribution $I(\alpha)$ of the reflected signal on the basis of the analysis of an output signal $U(\alpha)$ and the known directional pattern $f(\alpha)$. The considered problem relates to inverse ill-posed problems.

Let's show, that the satisfactory approached decisions can be received at essential lower a signal-to-noise ratio if more full to use the preliminary information on characteristics of the targets.

In many problems of radio navigation and a radio location, the angular sizes of the investigated targets there is much less than the width of the directional pattern. We use this additional clause as priory information at the decision of an inverse problem (1).

Let in the radar view on one of angular coordinates α there are M objects with the negligible small angular sizes. Then angular position of the target with number m can be described by means of delta-function in the form of $\delta(\alpha - \alpha_m^0)$.

In this case Eq. (1) will be transformed to:

$$U(\alpha) = \sum_{m=1}^M A_m f(\alpha - \alpha_m^0) \quad (4)$$

where A_m — the amplitude of the signal reflected by the target with the number m .

The search problem is to find with possible greater resolution: — the number of targets M , — their angular positions α_m^0 and the amplitudes of the reflected signal from each of targets A_m .

The offered method of the approximate solution Eq. (1) consists in sizing the factors C_m and α_m , providing minimal mean-square deviation the values of the sum:

$$\sum_{n=1}^M C_m f(\alpha - \alpha_m)$$

from the value $U(\alpha)$, i.e., the minimization of the functional:

$$\delta^2 = \int_{\varphi_1}^{\varphi_2} \left| U(\alpha) - \sum_{m=1}^M C_m f(\alpha - \alpha_m) \right|^2 d\alpha \quad (5)$$

where $\Omega = [\varphi_1, \varphi_2]$.

Thus, the parametrization of an inverse problem (1) is carried out, and it is reduced to minimum search of multi variable function.

3. MAIN RESULTS

The solution of a problem (4) is realized on the assumption of additional normalization requirement:

$$\int_{\varphi_1}^{\varphi_2} |U(\alpha)|^2 d\alpha = \int_{\varphi_1}^{\varphi_2} \left| \sum_{m=1}^M C_m f(\alpha - \alpha_m) \right|^2 d\alpha \quad (6)$$

which from the physical point of view provides equality received at scanning and computed by means of Eq. (3) signal power. From the mathematical point of view Eq. (5) increases stability of the computational solution and improves the convergence of iterative process.

The direct computational minimum search of the functional (4) on heterogeneous variables C_m and α_m leads to a multiextremal problem and does not guarantee reception global minimum. The solution of a problem (4), (5) is carried out on the basis of iterative process. In the beginning, the angular size of area Ω it is estimated, whether the tipe of $U(\alpha)$ can be provided by one point target. If not, the approached location of two point targets is set. Further, initial locations α_m are fixed and the values C_m , providing a minimum of the functional (4), (5), are under investigation.

The decision of last problem for any number of the point targets is analytically. If we differentiate Eqs. (4), (5) on all C_m , we shall receive a system of the linear equations:

$$\int_{\varphi_1}^{\varphi_2} U(\alpha) f(\alpha - \alpha_j) d\alpha = (\lambda + 1) \sum_{m=1}^M C_m \int_{\varphi_1}^{\varphi_2} f(\alpha - \alpha_j) f(\alpha - \alpha_m) d\alpha \quad j = 1, 2, \dots, M \quad (7)$$

on conditions that

$$\sum_{m,j=1}^M C_m C_j \int_{\varphi_1}^{\varphi_2} f(\alpha - \alpha_j) f(\alpha - \alpha_m) d\alpha = P \quad (8)$$

where λ — uncertain Lagrangian coefficients, P — the known power of the locked-on signal at scanning.

Having introduced a vector of factors C , elements of matrix F and vector V :

$$F_{m,j} = \int_{\varphi_1}^{\varphi_2} f(\alpha - \alpha_j) f(\alpha - \alpha_m) d\alpha \quad V_j = \int_{\varphi_1}^{\varphi_2} U(\alpha) f(\alpha - \alpha_j) d\alpha \quad (9)$$

we can represent the Eqs. (6)–(8) in the matrix form:

$$V = (\lambda + 1)FC. \quad (10)$$

From Eqs. (6)–(9) we find λ and the amplitudes of the reflected signals:

$$\lambda + 1 = \sqrt{\frac{V^T F^{-1} V}{P}} \quad C = \frac{1}{\lambda + 1} F^{-1} V \quad (11)$$

At a following stage of the decision the found vector C is fixed and new values α_m are numerically searched, providing a minimum Eqs. (4), (5). Further, the found values α_m are used as a new initial approximation search of new values of elements of vector C according to (8)–(10), etc. Iterative process appears quickly converging and stops after achievement of the set relative accuracy in 1% through 3–4 iterations for the group targets consisting of two point targets and through 6–10 iterations for three point targets.

4. EXAMPLES

The increase of effective resolution and its dependence on a signal-to-noise ratio were investigated. The linear antenna array with a length $37d/\lambda$ was investigated. The effective resolution was estimated in comparison with a beamwidth $\theta_{0.5} = 2^\circ$. Search of a location of targets was realized at a consecutive increase in the number of separate targets in structure of the group target. Each found decision was characterized by the value of the mean-square error in the form of (4).

Results of numerical researches on model have shown, that the value δ_M^2 sharply decreases at coincidence of true number of the targets and number M in (4): in 100 times at a small noise level and in 10 times at a significant level. It allows to find number of objects in the group target for sure.

In Figure 1, the results of restoration of the group target are shown at a high noise level $-q = 2 \cdot 10^{-1}$. The target represented two pin-point targets with angular distance $0.15\theta_{0.5}$. 1 — the locked-on signal; 2 — angular position and amplitudes of the located targets; 3 — the restored targets.

The decision well describes the angular position of the targets, the found amplitudes appear are very close to real too. The effective angular resolution run up to $1/6\theta_{0.5}$, i.e., has increased in 6.7 times in comparison with Rayleigh criterion. At a signal-to-noise ratio q greater then $4 \cdot 10^{-1}$ the quality of the decision becomes unacceptable. The results of the restoration of a group target consisting of three pinpoint targets are shown in Figure 2. 1 — the locked-on signal; 2 — the located targets; 3 — the restored targets.

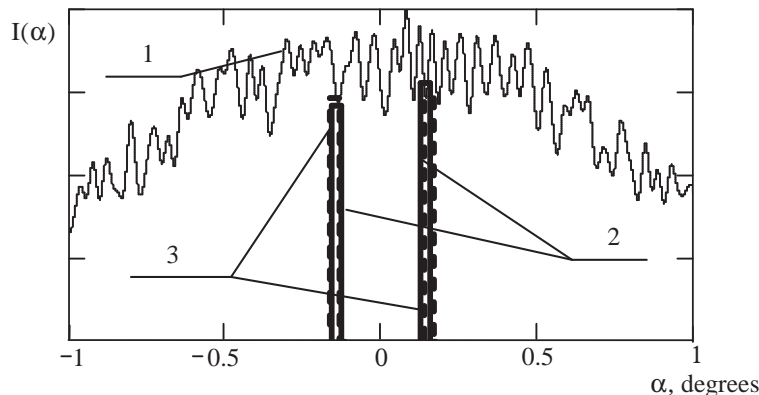


Figure 1: Image restoration of a group target at a high noise level.

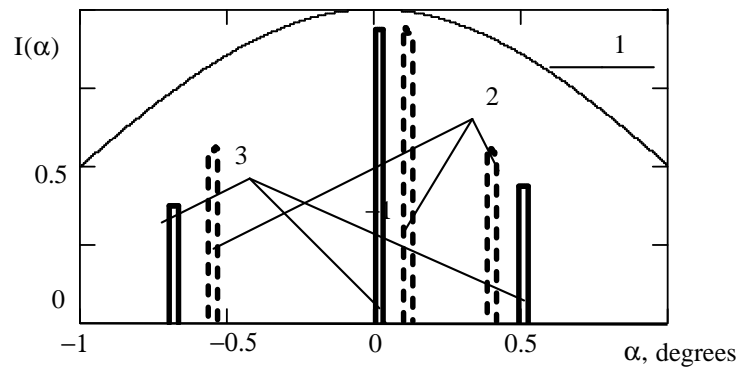


Figure 2: Image restoration of a group target consisting of three point targets.

As in advance the number of the targets was not known, search of the decision in the beginning was accomplished in the assumption of presence of two pin-point targets, and then of three. Each decision was characterized by the value of the mean-square error (4). Quality of restoration of the image of three targets appears a little bit worse, than of two, but still remains good.

5. CONCLUSION

The developed signal processing method allows to restore an angular intensity distribution of the group target and to increase an angular resolution in comparison with Rayleigh criterion in 2–5 times. The minimal signal-to-noise ratio necessary for it is equal 10–15 dB. It is essentially smaller value, than for known methods. The developed method allows to restore radar-tracking images of the group target consisting of unknown quantity of the separate targets.

REFERENCES

1. Oliver, C. J., "Synthetic-aperture radar imaging, review article," *J. Phys. D: Appl. Phys.*, No. 22, 871–890, 1989.
2. Radoi, E. and A. Quinquis, "A new method for estimating the number of harmonic components in noise with application in high resolution radar," *EURASIP Journal on Applied Signal Processing*, No. 8, 1177–1188, 2004.
3. Weixing, S., F. Dagang, Y. Zhenglong, and L. Zhan, "Super-resolution for real radar aperture," *Sci. and Technol. Natur. Sci.*, J. Nanjing Univ., Vol. 24, No. 4, 289–295, 2000.
4. Changyin, S. and B. Zheng, "Super-resolution algorithm for instantaneous ISAR imaging," *Electron. Lett.*, Vol. 36, No. 3, 253–255, 2000.
5. Odendaal, J. W., E. Barnard, and C. W. Pistorius, "Two-dimensional super resolution radar imaging using the MUSIC algorithm," *IEEE Trans. on Antennas and Propagation*, Vol. 42, No. 10, 1386–1391, 1994.
6. Nickel, U. R., "Aspects of implementing super-resolution methods into phased array radar," *AEU: Int. J. Electron, and Commun.*, Vol. 53, No. 6, 315–323, 1999.

Simulation of Scattered Fields from Rotating Cylinder in 2D: Under Illumination of TE and TM Gaussian Pulses

Mingtsu Ho

Department of Electronic Engineering, WuFeng Institute of Technology, Taiwan

Abstract— The computational results of the scattered EM fields from a rotating circular cylinder of infinite length were demonstrated in this paper. Maxwell's equations were numerically solved through the application of the method of characteristics (MOC) combined with a newly developed numerical technique, passing center swing back grids (PCSBG's). PCSBG is proposed as a treatment for the difficulty of grid deformation when objects of interest undergo rotational motion and originated from the fact that by MOC all field quantities are defined at the cell centroid. The explanation of the PCSBG technique is included as well. There are two types of excitations, transverse magnetic (TM) and transverse electric (TE) Gaussian EM pulses. Since a rotating circular cylinder, even with a relativistic angular velocity does not cause any relativistic effects, and in order to display the cylinder is rotating and scattering EM fields at the same time, the circular cylinder was equally split into an even number of slices which are one perfect reflector and one non-reflector by turns. The vortex structure observed in the field distribution over the domain is the evidence supporting the feasibility of the combination of MOC and PCSBG on solving the EM scattering problem by rotating circular cylinder.

1. INTRODUCTION

Since the early 1970s a large amount of researchers' attentions have been drawn to the study of the EM scattering problems by moving objects. Several publications dealt with the derivation of the theoretical expressions for the EM fields reflected from uniformly moving perfect planes [1–4] while some with that from linearly vibrating objects [5, 6]. Efforts made on the numerical simulation of the scattered EM fields from perfect planes that are moving and vibrating [1, 5, 6]. J. Van Bladel focused on the analytical studies of EM scattering by rotating bodies [7]. The studies of the return signal from helicopter's blades published in the very early 2000s revealed the fact that it may provide important information in communication area [8].

In reference [1] Harfoush et al. applied the finite-difference time-domain (FDTD) technique for the numerical results analysis on electromagnetic wave scattering from moving surfaces. In order to calculate the magnetic field and electric field immediately next to the moving surface, both Faraday's and Ampere's laws were employed whenever the boundary moves away from the mesh node. Recently, the reflected EM fields from constantly travelling and/or vibrating perfect plane were numerically simulated using MOC in cooperation with the relativistic EM field boundary conditions. It was observed that the reflected fields were modulated in both phase and amplitude and that the resultant spectra bear Doppler shifts as signatures of the moving reflectors. The followings were pointed out in references 15 through 17. Because the boundary is traveling, grid cells may be eliminated little by little from the grid system if the boundary is straight on with the incident fields. On the other hand, grid cells may be gradually brought into the grid system when the boundary is trailed by the incident fields.

However, numerical simulation of the EM scattering problems by rotating objects encounters dilemma when grid cells suffer from unrecoverable distortion. It is the objective of this paper to introduce a new technique for the resolution of the grid distortion problem, then to prove its practicability by providing the computational results of EM scattered fields by rotating objects. The origin of proposing PCSBG is based on the fact that MOC positions all field components at the cell centroid. This is quite different from the most popular FDTD technique where the electric field components form the edges of the cube, and the magnetic field components form the normals to the faces of the cube, or standard Cartesian Yee cell. When using MOC numerically solving Maxwell equations, one takes all metric terms of grid cell into account. That is, every change in the geometric shape of each grid cell due to the movement of object has to be carefully updated and formulated in the numerical procedure. In fact, it takes few minor modifications to adapt the existing MOC code for problems with moving objects.

2. NUMERICAL METHODS AND GRID SYSTEM

It is clear that the success of numerically solving EM scattering problems by rotating objects relies on the resolution of the cell distortion difficulty. The proposal of PCSBG is to aid MOC to resolve the cell distortion due to the rotating objects while MOC positions all field components in the center of grid cell. On the basis of the following provisions, the combination of PCSGB and MOC promises a feasibility of numerically solving Maxwell equations featured with rotating objects. First, the object of interest has simple or symmetric geometry for complex structures can not be solved analytically or numerically. Second, every change in the cell geometry can be precisely updated during the process. Third, the distorted grid cells can be recovered from deformation.

A modified body-conforming O-type grid is employed in the present modeling for the cylinder has a circular cross-section as shown in Figure 1. Grid cells are concentric and in the shape of trapezoid. The grid number is doubled from zone to zone. It is to ensure that the number of grid for the shortest wavelength component of interest is adequate and that the numerical accuracy is maintained. For simplicity, only four zones are shown. The solid cylinder is placed at the center. There is a single layer of cells immediately next to the cylinder defined as swing back grids.

Two sets of diagrams given in Figure 2 are to illustrate the idea of PCSBG in two different coordinate systems, Cartesian and curvilinear. A simplified version of the modified O-grid with only two layers of grid cells is shown for clear demonstration. The solid cylinder is located at the center and rotates clockwise. Grid cells next to the cylinder are defined as swing back grids which will be deformed by the rotating cylinder. Note that the two letters N and K are two grid indices for the swing back grids and the cylinder, respectively. Assuming the situation in Figure 2(a) is the initial state, depicted in Figures 2(b) and 2(c) are the swing back grids being twisted by cylinder. Note that in Figure 2(c) grid point on the cylinder side is about half-way of the grid cell and will pass the centroid by one more move. At this particular moment, all grid lines swing back

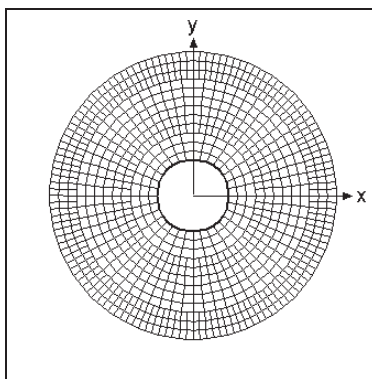


Figure 1: Modified O-type grid in the Cartesian system.

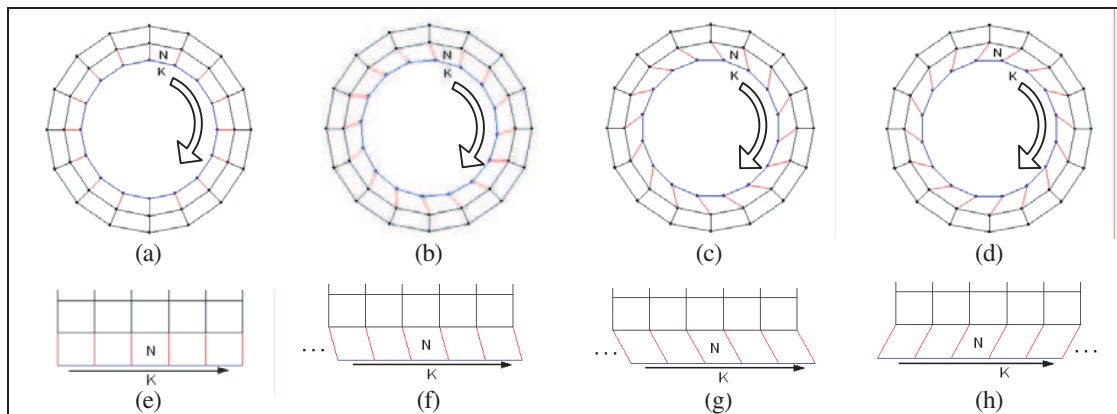


Figure 2: Idea of passing center swing back grids (PCSBG) is diagrammed in Cartesian (a)–(d) and curvilinear (e)–(h) systems. (a), (e) rotation is initiated, (b), (f) cells are distorted, (c), (g) grid points are about to pass the centroid, (d), (h) grid lines swing back with one cell off.

as in Figure 2(d) where the two cell indices are differed by a cell. Same scenario is described in curvilinear system as in Figures 2(e) through 2(h). During the process, the following are observed. The normal vector of the cell face on the cylinder side of each swing back grid changes direction as cylinder rotates. All grid lines of the swing back grids are tilted. These variants are taken into account by MOC solving for the field variables. Finally, the area of each swing back grid stays constant and causes no modification on the numerical time step.

3. THE PROBLEM

In the two-dimensional numerical model, the rotating cylinder is 0.1 m in radius and placed at the center. The computational domain is measured one meter from the cylinder and composed of five zones of concentric cells. The cell number around each zone ranges from 144 to 2304. The size of grid cell (in mm) is as follows: 6.2 in radial direction and 2.8 to 5.7 for the other two sides. The illuminating sources are Gaussian EM pulses either transverse electric (TE) or transverse magnetic (TM). For a two dimensional model the TE mode EM pulse has three field components (B_x , B_y , D_z) while TM has (B_z , D_x , D_y). Both EM pulses are truncated at 100 dB cut-off level and have a pulse width of 200 ps. The schematic drawing of the problem is given in Figure 3. Each Gaussian pulse then ends up with a span of about 1.92 ns. The incident EM pulse propagates in the positive- x direction and illuminates on the rotating cylinder.

Since a rotating circular solid cylinder made of perfect conductor yields no relativistic effects, further assumption was made for clear exhibiting the cylinder is rotating and scattering EM fields simultaneously. The circular cylinder may be evenly divided into an even number of slices such that the cylinder is composed of perfectly electric conducting (PEC) slices and non-PEC slices in turns as in Figure 4. There is a convenient time basis in defining the frequency of the rotating cylinder, the Gaussian pulse span 1.92 ns. By taking it as the period of rotation, one simply specifies the number of turns and then defines the angular velocity of every point on the cylinder surface. For a cylinder with a radius of 10 centimeters makes one complete turn in 1.92 ns, the resultant angular velocity is about 1.09 times of the speed of light.

Because cylinder used in the numerical model is made of two different materials, three types of boundary conditions (BCs) are needed respectively on PEC, non-PEC, and the most outer boundary. The implement of BCs on the truncated computational domain boundary is straightforward

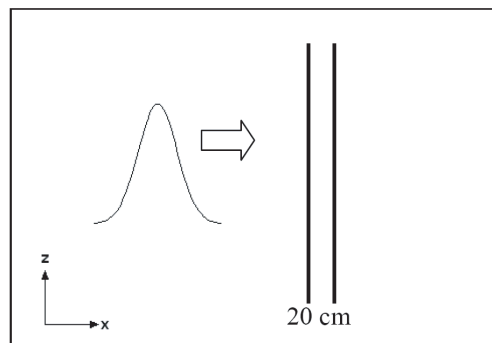


Figure 3: Schematic drawing of the problem.

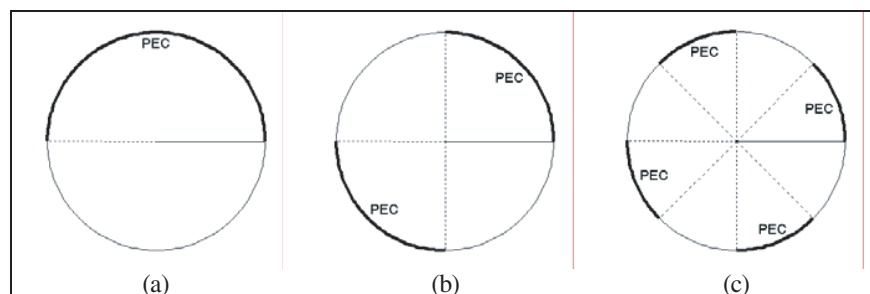


Figure 4: Cylinder is divided into (a) two halves, (b) four quarters, (c) eight pieces. They are PEC and non-PEC alternatively.

which ensures no reflection of EM fields from this artificial border. On the PEC surface, the physics requires that there exist no tangential electric components and that there no penetration of the electric and magnetic fields into the cylinder:

$$\hat{n} \times \vec{D} = 0, \quad (1)$$

$$\hat{n} \cdot \vec{D} = 0, \quad (2)$$

$$\hat{n} \cdot \vec{B} = 0, \quad (3)$$

where \vec{D} and \vec{B} are the electric and magnetic flux density and \hat{n} is the normal vector of the grid on cylinder surface. The unknown field variables can be solved through the aid of the characteristic variable (CV) boundary conditions as given in the following section. On the other hand, all field components are set to be zero in magnitude on the non-PEC surface.

In MOC, CVs are defined as the product of the field variable vector and the eigenvector matrix. By definition each CV is associated with one eigenvalue indicating speed and direction that which propagates across the cell face. Note that all CVs have to be updated every time step. For a EM pulse of TM mode the CV is

$$CV^{TM} = \hat{n} \times \vec{B} + \eta_o \vec{D}, \quad (4)$$

and TE

$$CV^{TE} = \frac{\vec{B}}{\eta_o} - \hat{n} \times \vec{D} \quad (5)$$

here η_o is the characteristic impedance of free space. By definition, these two CVs are used to approximate those at the boundary by taking \vec{D} and \vec{B} from the adjacent cell. By combining above equations, one can obtain all field quantities on the cylinder's surface.

4. NUMERICAL RESULTS

For a solid circular cylinder made of perfect conductor, whether or not it is rotating, the scattered EM fields exhibit alike behaviors, since every point on the cylinder surface has its normal vector perpendicular to the instantaneous velocity. Four different field distributions are given in Figure 5 depicting the scattered EM fields both of TE and TM incident pulses from a stationary solid circular cylinder. These sever as comparison reference patterns. Note that the incident pulse propagates straight in the course despite the grid cells are concentric and that backgrounds are shown in different colors they are zero in magnitude. Another set of four field distributions are plotted in Figure 6 where the cylinder is divided into two halves and rotates two cycles during the pulse duration. Comparing to the previous set, one finds some details reveal results of the interaction between the incident EM pulse and the split rotating cylinder.

The cylinder was further divided into more slices for the purpose of clear illustration of the numerical results. Figure 7 shows a four-slice rotating cylinder yields more apparent evidence that the cylinder rotates and scatters EM fields. Figures 8 and 9 demonstrate field distributions from an eight-slice cylinder rotating at two different frequencies. It is observed that the more pieces the cylinder is sliced into or the faster the cylinder rotates the finer vortex structure the scattered fields formed. It is also shown that the combination of MOC with PCSBG can resolve the grid distortion difficulty.

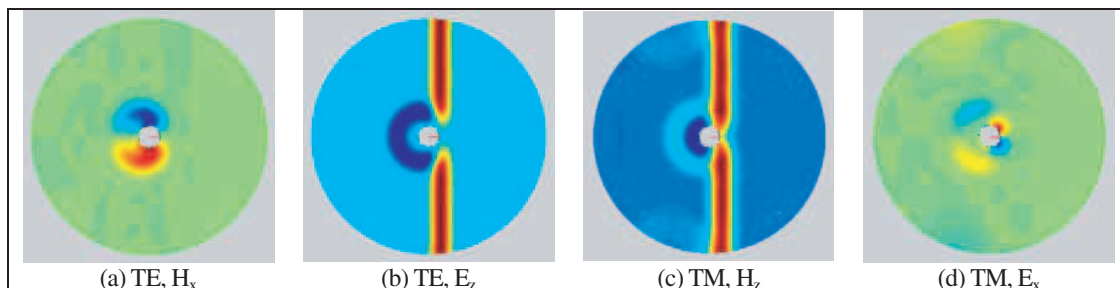


Figure 5: Field distributions: stationary solid circular cylinder. (Background: zero, red: positive, blue: negative).

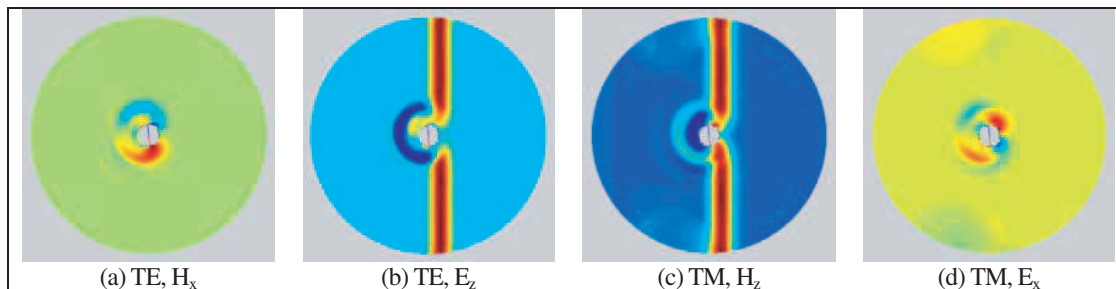


Figure 6: Field distributions: two slices rotate two cycles. (Background: zero, red: positive, blue: negative).

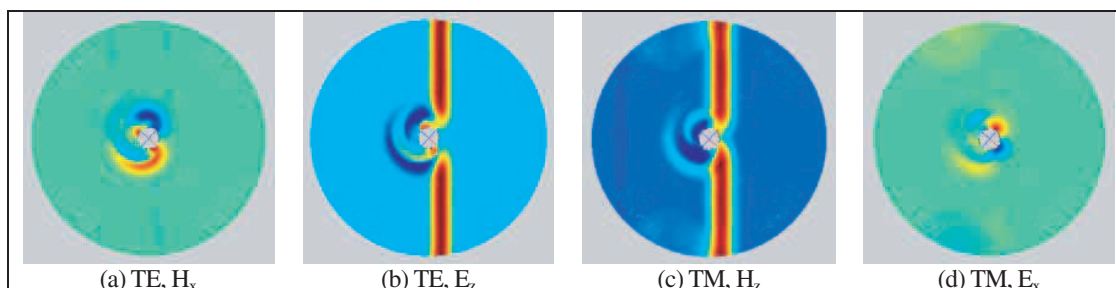


Figure 7: Field distributions: four slices rotate one cycle. (Background: zero, red: positive, blue: negative).

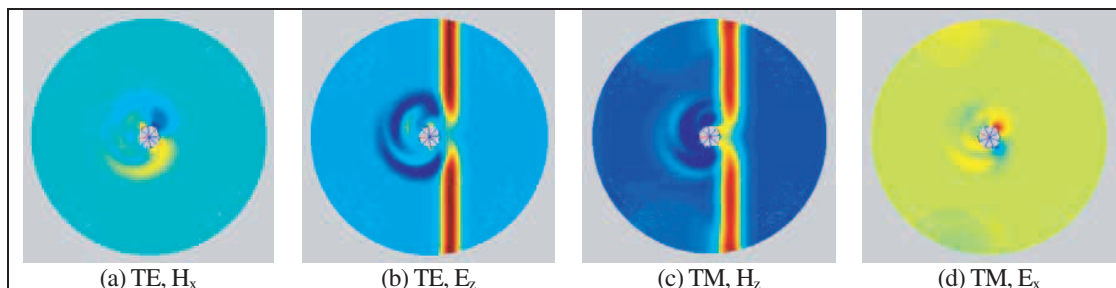


Figure 8: Field distributions: eight slices rotate one half cycles. (Background: zero, red: positive, blue: negative).

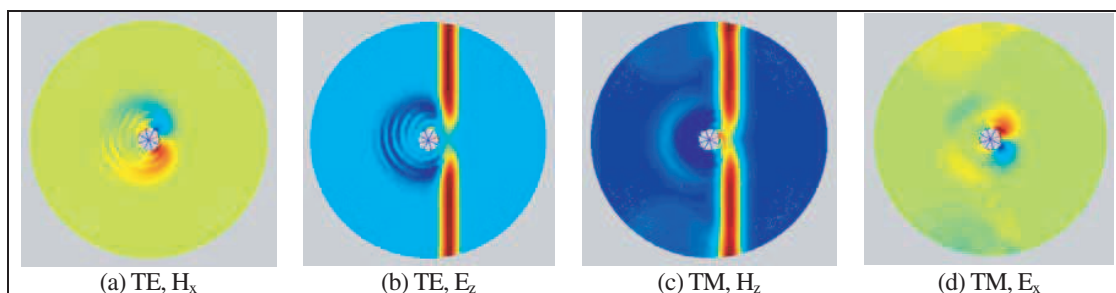


Figure 9: Field distributions: eight slices rotate two cycles. (Background: zero, red: positive, blue: negative).

5. CONCLUSION

In this paper the author applied the MOC/PCSBG technique to the numerical simulation of the scattered electric fields from a rotating cylinder and demonstrated field distributions for several situations where the cylinder is divided into different number of slices and rotating at various frequencies. The PCSBG approach was clearly explained. The grid distortion dilemma can be resolved by the combination of MOC and PCSBG. Field distribution patterns with vortex structures are the evidence that the cylinder is rotating and scattering EM fields simultaneously. The future

work will apply MOC/ PCSBG to the prediction of the scattered EM fields by rotating objects where the relativistic effects can not be neglected.

REFERENCES

1. Harfoush, F., A. Taflove, and G. Kriegsmann, "A numerical technique for analyzing electromagnetic wave scattering from moving surfaces in one and two dimensions," *IEEE Transactions on Antennas Propagation*, Vol. 37, 55–63, 1989.
2. De Cupis, P., P. Burghignoli, G. Gerosa, and M. Marziale, "Electromagnetic wave scattering by a perfectly conducting wedge in uniform translational motion," *Journal of Electromagnetic Waves and Applications*, Vol. 16, No. 8, 345–364, 2002.
3. Ciarkowski, A., "Electromagnetic pulse diffraction by a moving half-plane," *Progress In Electromagnetics Research*, PIER 64, 53–67, 2006.
4. Censor, D., "Free-space relativistic low-frequency scattering by moving objects," *Progress In Electromagnetics Research*, PIER 72, 195–214, 2007.
5. Ho, M., "One-dimensional simulation of reflected EM pulses from objects vibrating at different frequencies," *Progress In Electromagnetics Research*, PIER 53, 239–248, 2005.
6. Ho, M., "Scattering of EM waves by vibrating perfect surfaces simulation using relativistic boundary conditions," *Journal of Electromagnetic Waves and Applications*, Vol. 20, No. 4, 425–433, 2006.
7. Van Bladel, J., "Electromagnetic fields in the presence of rotating bodies," *Proceedings of the IEEE*, Vol. 64, No. 3, 301–318, 1976.
8. Zhang, Y., A. Hoorfar, V. Mancuso, J. Nachamkin, and M. G. Amin, "Characteristics of the rotating blade channel for FH/FM communication systems," *Sixth International Symposium on Signal Processing and Its Applications*, Vol. 2, 493–496, 2001.

Analysis of Current Propagation on Single Conductor Line Using Point Charges and Propagating Line Currents

T. Sokooshi, T. Hisakado, U. Paoletti, and O. Wada
Department of Electrical Engineering, Kyoto University, Japan

Abstract— The purpose of this paper is to clarify the mechanism of common mode propagation which has no explicit return path. In order to simplify the problem, we consider a single conductor line, which also has no explicit return path. First, we define point charges and propagating line currents as fundamental elements of the proposed model. Using the elements, we analytically derive the electric field. If we put together some elements, the proposed model can represent conductors of complex shape. Second, we analyze the current propagation on a single cylindrical perfect conductor line which is bending at a right angle and confirm the reflection and transmission phenomena. Finally, we consider the validation of the proposed model. A kind of transmission line model that could represent the current propagation on a single conductor line with few elements is highly desirable. We ascertain that this model can represent the current propagation with a small number of elements. It indicates that the proposed method is a valid model for the current propagation on a single conductor line.

1. INTRODUCTION

The common mode radiation is an important cause of EMI problem. In the case of two conductor transmission lines, the common mode has no explicit return path, whereas the differential mode has the return path. A. Sommerfeld originally studied the modes on the single conductor lines using Hankel function [1], and G. Goubau analyzed the surface waves in detail [2]. Recently, the single conductor line has attracted considerable attention also for power line communication and terahertz transmission [3]. However, it is difficult to analyze the current propagation on the single conductor line with the existing circuit theories, because the voltage cannot be defined explicitly. We propose a simple model for analyzing the current propagation on the single conductor line.

2. POINT CHARGES AND PROPAGATING LINE CURRENTS

2.1. The Definition of Propagating Line Currents including Forward and Backward Waves

First of all, we consider a finite length line on z -axis shown in Fig. 1 and call this a line element. We assume that a current $I_n^f(t)$ is applied to $z = z_n$ and propagates with a velocity of light c in the positive direction, and assume that the current is removed at $z = z_{n+1}$. From the conservation law of the electric charge, a line charge density $\lambda_n^f(t) = \frac{I_n^f(t)}{c}$ is also applied to $z = z_n$ and removed at $z = z_{n+1}$. $I_n^f(t)$ and $\lambda_n^f(t)$ are defined by

$$I_n^f(z, t) \equiv I_n^f \left(t - \frac{z}{c} \right) \{ H(z - z_n) - H(z - z_{n+1}) \}, \quad (1)$$

$$\lambda_n^f(z, t) \equiv \frac{I_n^f \left(t - \frac{z}{c} \right)}{c} \{ H(z - z_n) - H(z - z_{n+1}) \}. \quad (2)$$

The law of the charge conservation is satisfied except at the start and end of the line element. As the same as $I_n^f(t)$ and $\lambda_n^f(t)$, we also assume that the current $I_n^b(t)$ and line charge density $\lambda_n^b(t)$ are applied to $z = z_{n+1}$ and removed at $z = z_n$. $I_n^b(t)$ and $\lambda_n^b(t)$ propagate in the negative direction

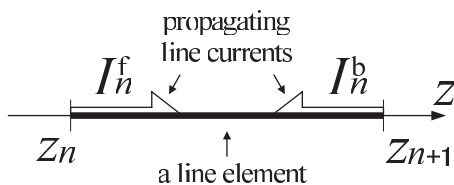


Figure 1: Propagating line currents.

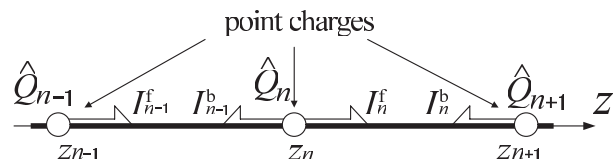


Figure 2: Point charges.

and are defined by

$$I_n^b(z, t) \equiv I_n^b \left(t + \frac{z - z_{n+1}}{c} \right) \{H(z - z_{n+1}) - H(z - z_n)\}, \quad (3)$$

$$\lambda_n^b(z, t) \equiv \frac{I_n^b \left(t + \frac{z - z_{n+1}}{c} \right)}{c} \{H(z - z_{n+1}) - H(z - z_n)\}. \quad (4)$$

We describe both $I(t)$ and $\lambda(t)$ as propagating line current.

2.2. The Definition of Point Charges

Next, we connect some line elements and consider a connection point between the $(n - 1)$ th and the n th line elements shown in Fig. 2. In order to satisfy the conservation law of the electric charge on the boundary of the line elements, we assume that the charge $\hat{Q}_n(t)$ is accumulated at $z = z_n$. We describe $\hat{Q}_n(t)$ as point charge and it is defined by

$$\hat{Q}_n(t) = \int_0^t \left\{ I_{n-1}^f \left(t' - \frac{|z_{n+1} - z_n|}{c} \right) + I_n^b \left(t' - \frac{|z_n - z_{n+1}|}{c} \right) - I_n^f(t') - I_{n-1}^b(t') \right\} dt'. \quad (5)$$

Putting together these elements, we can represent the current propagation on the complex object.

3. THE ELECTRIC FIELD DERIVED FROM POINT CHARGES AND PROPAGATING LINE CURRENTS

We derive the electric fields on a point $P(r, z)$ produced by the elements. The length of the line element is l . The z -component of the electric field \tilde{E}_{zn} and the r -component of the electric field \tilde{E}_{rn} shown in Fig. 3 are produced by $I_n^f(t)$ and $I_n^b(t)$, and are described by

$$\tilde{E}_{zn}(r, z, t) = \frac{-1}{4\pi\epsilon_0 c} \left[\left\{ \frac{I_n^f \left(t - \frac{R_n}{c} \right)}{R_n} - \frac{I_n^f \left(t - \frac{l+R_{n+1}}{c} \right)}{R_{n+1}} \right\} - \left\{ \frac{I_n^b \left(t - \frac{R_{n+1}}{c} \right)}{R_{n+1}} - \frac{I_n^b \left(t - \frac{l+R_n}{c} \right)}{R_n} \right\} \right], \quad (6)$$

$$\tilde{E}_{rn}(r, z, t) = \frac{-1}{4\pi\epsilon_0 c} \left[\left\{ -\frac{R_n + (z - z_n)}{r} \frac{I_n^f \left(t - \frac{R_n}{c} \right)}{R_n} + \frac{R_{n+1} + (z - z_{n+1})}{r} \frac{I_n^f \left(t - \frac{l+R_{n+1}}{c} \right)}{R_{n+1}} \right\} - \left\{ -\frac{R_{n+1} + (z - z_{n+1})}{r} \frac{I_n^b \left(t - \frac{R_{n+1}}{c} \right)}{R_{n+1}} + \frac{R_n + (z - z_n)}{r} \frac{I_n^b \left(t - \frac{l+R_n}{c} \right)}{R_n} \right\} \right], \quad (7)$$

$$R_n = \sqrt{r^2 + (z - z_n)^2}. \quad (8)$$

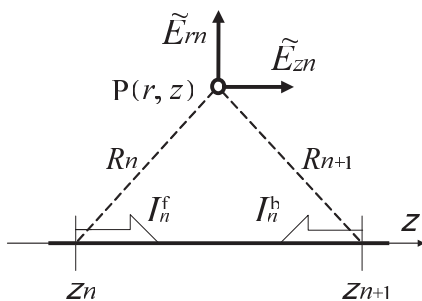


Figure 3: \tilde{E}_{zn} and \tilde{E}_{rn} produced by $I_n^f(t)$ and $I_n^b(t)$.

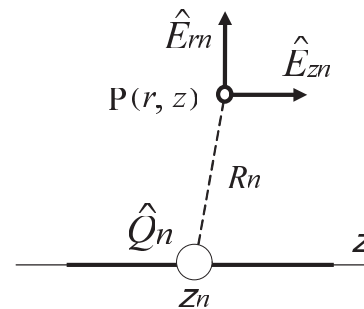


Figure 4: \tilde{E}_{zn} and \tilde{E}_{rn} produced by $\hat{Q}_n(t)$.

The electric fields \hat{E}_{zn} and \hat{E}_{rn} produced by $\hat{Q}_n(t)$ shown in Fig. 4 are described by

$$\hat{E}_{zn}(r, z, t) = \frac{-1}{4\pi\epsilon_0} \frac{\partial}{\partial z} \int_0^t \left\{ \frac{I_{n-1}^f(t' - \frac{l+R_n}{c})}{R_n} + \frac{I_n^b(t' - \frac{l+R_n}{c})}{R_n} - \frac{I_n^f(t' - \frac{R_n}{c})}{R_n} - \frac{I_{n-1}^b(t' - \frac{R_n}{c})}{R_n} \right\} dt', \quad (9)$$

$$\hat{E}_{rn}(r, z, t) = \frac{-1}{4\pi\epsilon_0} \frac{\partial}{\partial r} \int_0^t \left\{ \frac{I_{n-1}^f(t' - \frac{l+R_n}{c})}{R_n} + \frac{I_n^b(t' - \frac{l+R_n}{c})}{R_n} - \frac{I_n^f(t' - \frac{R_n}{c})}{R_n} - \frac{I_{n-1}^b(t' - \frac{R_n}{c})}{R_n} \right\} dt'. \quad (10)$$

In order to easily handle the time delay, we use the Laplace transform in Eq. (6) to Eq. (10). In the complex frequency domain, these equations are represented by

$$\tilde{E}_{zn}(r, z, s) = \frac{-1}{4\pi\epsilon_0 c} \left\{ \frac{I_n^f(s)e^{-R_n s}}{R_n} - \frac{I_n^f(s)e^{-(l+R_{n+1})s}}{R_{n+1}} - \frac{I_n^b(s)e^{-R_{n+1}s}}{R_{n+1}} + \frac{I_{n+1}^b(s)e^{-(l+R_n)s}}{R_n} \right\}, \quad (11)$$

$$\begin{aligned} \tilde{E}_{rn}(s) = \frac{-1}{4\pi\epsilon_0 c} \left[I_n^f(s) \left\{ -\frac{R_n + (z - z_n)e^{-R_n s}}{r} \frac{1}{R_n} + \frac{R_{n+1} + (z - z_{n+1})e^{-R_{n+1}s}}{r} \frac{1}{R_{n+1}} \right\} \right. \\ \left. - I_n^b(s) \left\{ -\frac{R_{n+1} + (z - z_{n+1})e^{-R_{n+1}s}}{r} \frac{1}{R_{n+1}} + \frac{R_n + (z - z_n)e^{-R_n s}}{r} \frac{1}{R_n} \right\} \right], \quad (12) \end{aligned}$$

$$\hat{E}_{rn}(r, z, s) = \frac{-1}{4\pi\epsilon_0 c} \left\{ \frac{I_{n-1}^f(s)e^{-ls}}{s} + \frac{I_n^b(s)e^{-ls}}{s} - \frac{I_n^f(s)}{s} - \frac{I_{n-1}^b(s)}{s} \right\} \frac{\partial}{\partial r} \left(\frac{e^{-R_n s}}{R_n} \right), \quad (13)$$

$$\hat{E}_{zn}(r, z, s) = \frac{-1}{4\pi\epsilon_0 c} \left\{ \frac{I_{n-1}^f(s)e^{-ls}}{s} + \frac{I_n^b(s)e^{-ls}}{s} - \frac{I_n^f(s)}{s} - \frac{I_{n-1}^b(s)}{s} \right\} \frac{\partial}{\partial z} \left(\frac{e^{-R_n s}}{R_n} \right), \quad (14)$$

$$\frac{\partial}{\partial z} \left(\frac{e^{-R_n s}}{R_n} \right) = -\frac{(1 + R_n s)(z - z_n)}{R_n^3} e^{-R_n s}, \quad (15)$$

$$\frac{\partial}{\partial r} \left(\frac{e^{-R_n s}}{R_n} \right) = -\frac{(1 + R_n s)r}{R_n^3} e^{-R_n s}. \quad (16)$$

Equations (11) to (14) are analytical representation of the electric field produced by the point charges and propagating line currents.

4. ANALYSIS OF A SINGLE CONDUCTOR LINE USING POINT CHARGES AND PROPAGATING LINE CURRENTS

We analyze the current propagation on a single cylindrical perfect conductor line bending at the center shown in Fig. 5. The inner length of the conductor line is L and the radius is a . We assume that currents propagate on the surface of the conductor line. We model a cylindrical conductor element using N_ϕ line elements shown in Fig. 6 and describe it as conductor cell. The length of

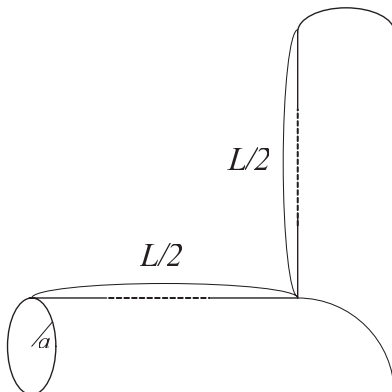


Figure 5: A conductor line bending at the center.

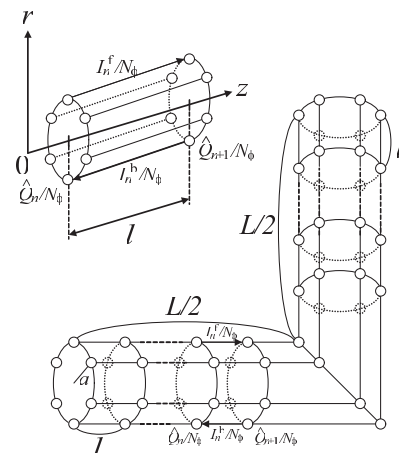


Figure 6: The model of the conductor line using the elements.

the conductor cell is l and the current which propagates on the conductor cell is divided equally into N_ϕ line elements in the ϕ direction. Therefore, each propagating line current is $I_n^f(t)/N_\phi$ and $I_n^b(t)/N_\phi$. Then, we model the conductor line using N_L conductor cells shown in Fig. 6. The current propagating on the conductor line is modeled by $2N_L$ propagating line currents I_n^f, I_n^b ($n = 0, 1, \dots, N_L - 1$). As a source of the currents, we give $I_0^f(s)$ and fix $I_0^b(s) = 0$. We use the boundary condition that the tangent components of the electric fields are equal to 0. Applying the inversion of Laplace transform on the currents, we obtain the waveform of the currents in the time domain [4].

5. SIMULATION RESULTS

We set $L = 60$ mm and $a = 0.2$ mm and add a step current on the edge, that is, $I_0^f(s) = \frac{1}{s}$. The maximum frequency used in the inversion of Laplace transform is 320 GHz.

The propagations of the current and charge are shown in Fig. 7 and Fig. 8. The currents and charges are given by

$$I_n(t) = I_n^f(t) - I_n^b\left(t - \frac{l}{c}\right), \quad (17)$$

$$Q_n(t) = \left\{ I_n^f(t) + I_n^b\left(t - \frac{l}{c}\right) \right\} l/c + \hat{Q}_{n+1}(t). \quad (18)$$

Figure 7 indicates that the reflection and transmission current are generated at the bending point. Meanwhile, Fig. 8 shows that the charges are accumulated at the bending point. We speculate that the charges at the bending point produce both the reflection and transmission currents. A kind of transmission line model that could represent the current propagation on a single conductor line with a few elements is highly desirable. We decreased the number of N_ϕ and N_L . N_ϕ dependence of the current propagation at $t = 150$ ps are shown in Fig. 9. There is few difference in the current propagation when N_ϕ is larger than 4. This result corresponds to the

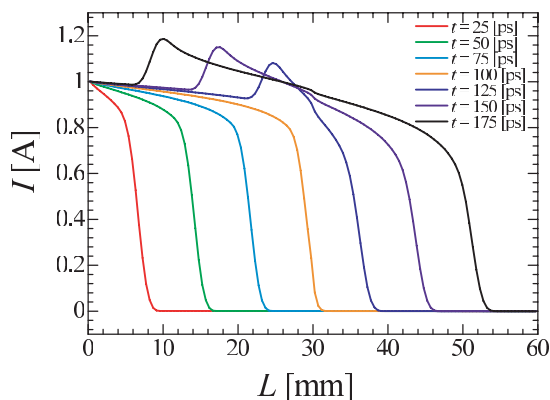


Figure 7: Current propagation.

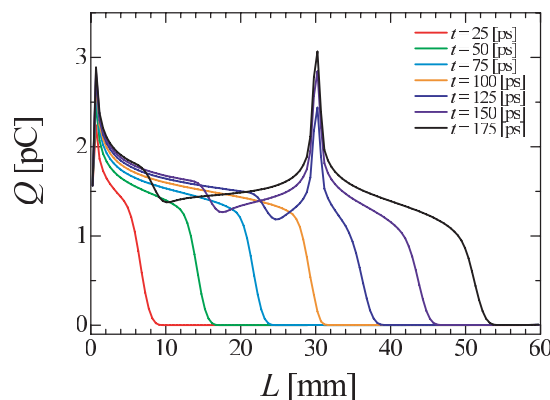


Figure 8: Charge propagation.

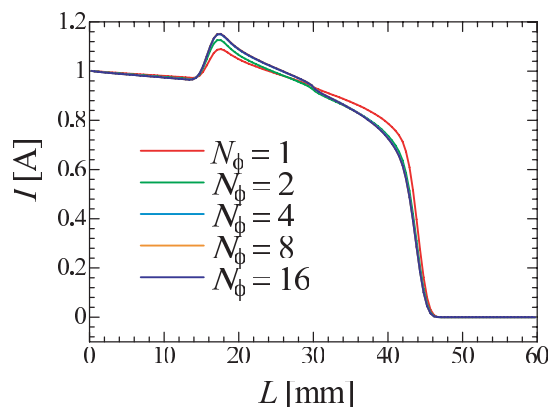


Figure 9: The current waveform depending on the number of N_ϕ at $t = 150$ ps.

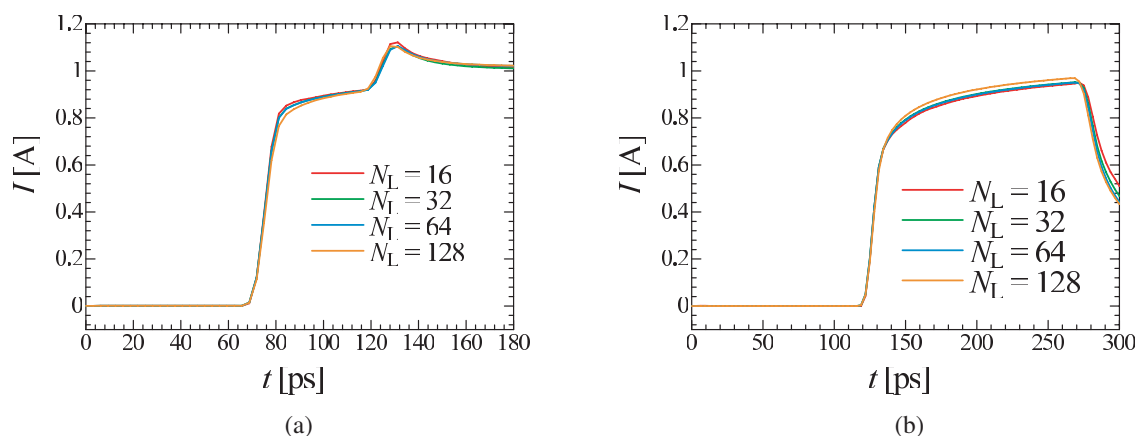


Figure 10: The current waveform depending on the number of N_L . (a) $L = 22.5$ mm, (b) $L = 37.5$ mm.

fact that it is difficult to approximate a circular cylindrical conductor with $N_\phi \leq 2$. The current waveforms at $L = 22.5$ mm and $L = 37.5$ mm in the time domain are shown in Fig. 10(a) and Fig. 10(b). We observed a reflection current waveform near $t = 125$ ps in Fig. 10(a). It indicates that the waveform of the current does not depend strongly on the number of N_L .

The wavelength of the maximum frequency using in the inversion of Laplace transform is 0.9375 mm. Compared with this, the case $N_L = 16$ the length of each conductor cell is 3.75 mm. It indicates that the proposed method could analyze the current propagation by means of the elements whose length is longer than a minimum wavelength of the frequency using in the inversion of Laplace transform. This is because the elements include the propagating line currents which is valid for a model of Maxwell's equation.

6. CONCLUSION

This paper proposed a model that could represent current propagation on a single conductor line with point charges and propagating line currents. We analytically derived the electric fields produced by the elements. In addition, we also clarified that the proposed method could analyze the current propagation on a single conductor line. We use the elements whose lengths are longer than the minimum wavelength of the frequency in the simulation. It indicates that the proposed model with propagating line currents is valid for a model of Maxwell's equations.

REFERENCES

1. Sommerfeld, A., *Electrodynamics*, Academic Press, New York, 1964.
2. Goubau, G., "Surface waves and their application to transmission lines," *Journal of Applied Physics*, Vol. 21, 1119–1128, 1950.
3. Akalin, T., A. Treizebre, and B. Bocquet, "Single-wire transmission lines at terahertz frequencies," *IEEE Transactions on Microwave Theory and Techniques*, Vol. 54, No. 6, 1064–1076, June 2006.
4. Hisakado, T. and K. Yoshimura, "Analysis of common mode propagation based on single conductor line," *Progress In Electromagnetics Research Symposium*, Tokyo, Japan, August 2–5, 2006.

Ferromagnetic Microwires Composite Metamaterials with Tuneable Microwave Electromagnetic Parameters

M. Ipatov¹, V. Zhukova¹, L. V. Panina², and A. Zhukov¹

¹Dpto. de Física de Materiales, Fac. Químicas, Universidad del País Vasco
San Sebastián 20009, Spain

²School of Computing, Communications and Electronics, University of Plymouth
Plymouth, PL4 8AA, United Kingdom

Abstract— The effect of the external magnetic field on microwave response from composites containing CoFeSiBCr amorphous wires has been demonstrated by measuring S-parameters in free space in the frequency band of 0.9–17GHz. Two types of composites made of lattices of continuous and short-cut wires are considered to employ different types of spectra of the dielectric function (plasmonic and resonant). In both cases, the application of the field increases the dielectric losses owing to increase in the wire impedance. The observed changes in the reflection/transmission spectra are more than 10% in a certain lower frequency range. The results are analyzed in terms of the effective permittivity.

1. INTRODUCTION

Composites with embedded metallic wires may demonstrate a strong dispersion of the effective permittivity ε_{ef} in the microwave range [1–4]. The use of ferromagnetic wires makes it possible to sensitively tune this dispersion by changing the magnetic structure of the wire with external magnetic, mechanical or thermal stimuli. The possibility to control or monitor the electromagnetic parameters (and therefore scattering and absorption) of composite metamaterials is of great interest for large-scale applications such as remote non-destructive testing, structural health monitoring, tuneable coatings and absorbers. The magnetic tunability of microwave response was reported in a number of works for different types of wire media demonstrating that underlying physics is related with the magnetoimpedance (MI) effect in wires [5–7]. In this work, we consider two types of magnetic wire composites (see Fig. 1): arrays of continuous wires and of short-cut wires made of CoFeSiBCr glass coated amorphous wires showing large MI [8]. We demonstrate that in the both cases the application of a magnetic field to the whole composite strongly increases the dielectric losses, which affects the reflection/transmission spectra.

2. EFFECTIVE PERMITTIVITY OF WIRE MEDIA.

Composites containing long parallel wires as shown in Fig.1a may support very low frequency plasmons and can be characterised by plasma-like dispersion of ε_{ef} [1, 2] with a negative value of the real part of the permittivity below the characteristic plasma frequency, f_p :

$$\varepsilon_{ef}^2 = 1 - \frac{\omega_p^2}{\omega^2(1 + i\gamma)}, \quad \omega_p = 2\pi f_p, \quad f_P^2 = \frac{c^2}{2\pi b^2 \ln(b/a)} \quad (1)$$

Here, γ is the relaxation parameter and c is the velocity of light. For wire radius a in the micron range and spacing b between them of about 1 cm the characteristic plasma frequency is about 4 GHz. A number of experimental studies confirmed a negative permittivity in the GHz region for wire media. In some works, the relaxation is ignored which could be justified in the case of a very

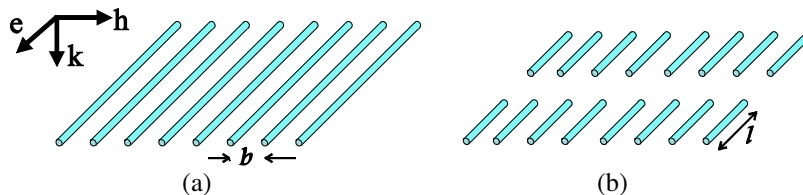


Figure 1: Sketch of the wire composites.

strong skin effect. We have demonstrated that in general γ is defined by the wire surface impedance ζ_{zz} :

$$\gamma = \frac{c\zeta_{zz}}{\omega a \ln(b/a)} \quad (2)$$

For magnetic wires, this parameter may change greatly when an external magnetic field is applied as a result of the MI effect. Then, the permittivity spectra will depend on the external magnetic field as demonstrated in Fig. 2(a).

The composites with short-cut wire inclusions as shown in Fig. 1(b) are characterized by a resonance type of the ε_{eff} as the wires behave as dipole antennas with the resonance at half wave length condition: $f_R = c/2l\sqrt{\varepsilon_d}$, where ε_d is the permittivity of the supporting matrix. If the interaction between the wires is neglected, the effective permittivity is composed of the averaged dipole polarization χ and may be expressed analytically for an important case of not very strong skin effect [7]:

$$\varepsilon_{eff} = \varepsilon + 4\pi p\chi, \quad \chi = \frac{1}{2\pi \ln(l/a)(\tilde{k}a)^2} \left(\frac{2}{\tilde{k}l} \tan(\tilde{k}l/2) - 1 \right), \quad (3)$$

$$\tilde{k} = k \left(1 + \frac{i c \zeta_{zz}}{\omega a \ln(l/a)} \right)^{1/2}, \quad k = \omega \sqrt{\varepsilon}/c \quad (4)$$

Here p is the wire volume concentration and, \tilde{k} is the renormalized wave number. Comparing Equations (2) and (4) it is seen, that in both cases the dependence on the wire surface impedance occurs in a similar way, controlling the dielectric losses in the case of a moderate skin effect. The permittivity spectra for short-cut wire composites are given in Fig. 2(b). It is seen that applying a magnetic field which increases the wire impedance suppresses the resonance behavior due to increased losses.

Amorphous ferromagnetic microwires with negative magnetostriction having a circumferential anisotropy are characterized by large change in impedance when subjected to an axial magnetic field which rotates the magnetisation away from the circular direction. This effect remains essential even at GHz frequencies. This makes them very promising for engineering artificial dielectrics with tuneable microwave properties. As the wire impedance depends on the dc magnetisation (via the ac permeability) it is expected that any physical effect (magnetic field, mechanical stress, temperature) that results in change in the magnetic structure (whilst the ac permeability remains high) will affect the dispersion of the effective permittivity.

3. EXPERIMENTAL

The microwave properties of wire composites were investigated by free space methods requiring large samples. $\text{Co}_{66}\text{Fe}_{3.5}\text{B}_{16}\text{Si}_{11}\text{Cr}_{3.5}$ glass coated amorphous wires with radius of $20\ \mu\text{m}$ were glued in paper to form wire-lattices of $50 \times 50\ \text{cm}^2$ with separation b of 10 mm, as shown in Fig. 1(a). After measurements, such wire-lattice was sequentially cut in stripes of 40, 20 and 10 mm wide

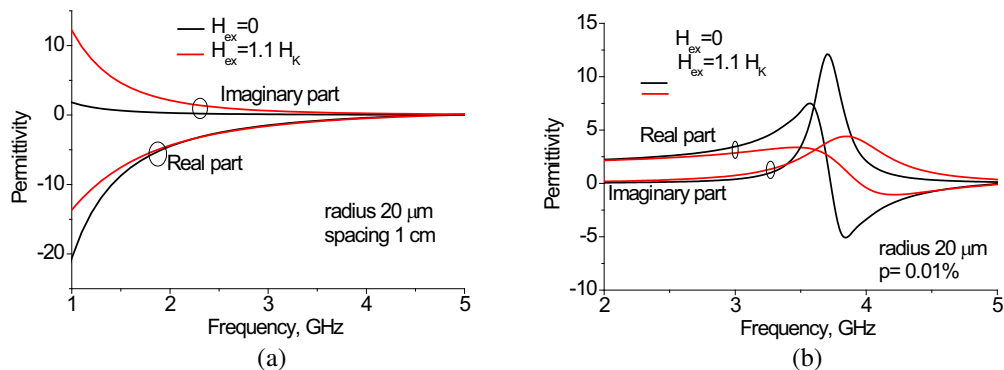


Figure 2: Effective permittivity spectra in composites depicted in Figs. 1(a), (b), respectively, with the external field as a parameter. Modelling is performed for wires with a circumferential anisotropy (anisotropy field $H_k = 500\ \text{A/m}$). The other parameters are: resistivity $130\ \mu\Omega\text{cm}$, magnetisation 0.05 T, wire radius $20\ \mu\text{m}$. For (a), $b = 1\ \text{cm}$. For (b), $l = 4\ \text{cm}$, $p = 0.01\%$.

to form the composites with short dipole wires as depicted in Fig. 1(b). The S -parameters were measured in the frequency range of 0.9–17 GHz in the presence of external field ranging up to 3000 A/m applied through a plane coil with turns perpendicular to the electrical field in the incident wave. The effective permittivity spectra were deduced from S -parameters with the help of Reflection/Transmission Epsilon Fast Model. The magnetic properties of wires were defined from measurements of dc magnetisation loops and MI in the frequency range up to 500 MHz.

4. RESULTS AND DISCUSSION

The results on dc magnetisation loops (not shown here) have confirmed that the wires possess a circumferential anisotropy with the effective anisotropy field of about 400 A/m. The impedance plots vs. field seen in Fig. 3 have two symmetrical peaks which is typical of circumferential anisotropy and indicate the impedance change ratio up to 300% at 500 MHz.

Figure 4 shows the spectra of the reflection R , transmission T , and the effective permittivity ϵ_{ef} for long-wire composites with the field H_{ex} as a parameter. The relative change in R and T is about 10% at lower frequencies while the phase of transmission shifts about 40 degrees at 1 GHz with the change of the field. The permittivity spectra deduced from R and T plots are consistent with the theoretical plots seen in Fig. 2(a). The effective thickness was taken equal to the lattice period of 1 cm. The imaginary part of the permittivity increases with the field due to the increase in the wire impedance resulting in decrease in the transmission amplitude (although the reflection amplitude also decreases).

Figure 5 shows the spectra for cut-wire composites with different wire length of 40, 20 and 10 mm and with the field as a parameter. The transmission spectra have a deep minimum near a resonance

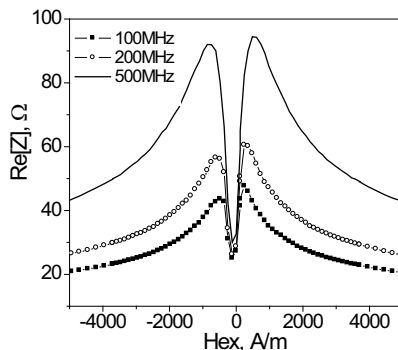


Figure 3: Wire impedance vs. field for different frequencies.

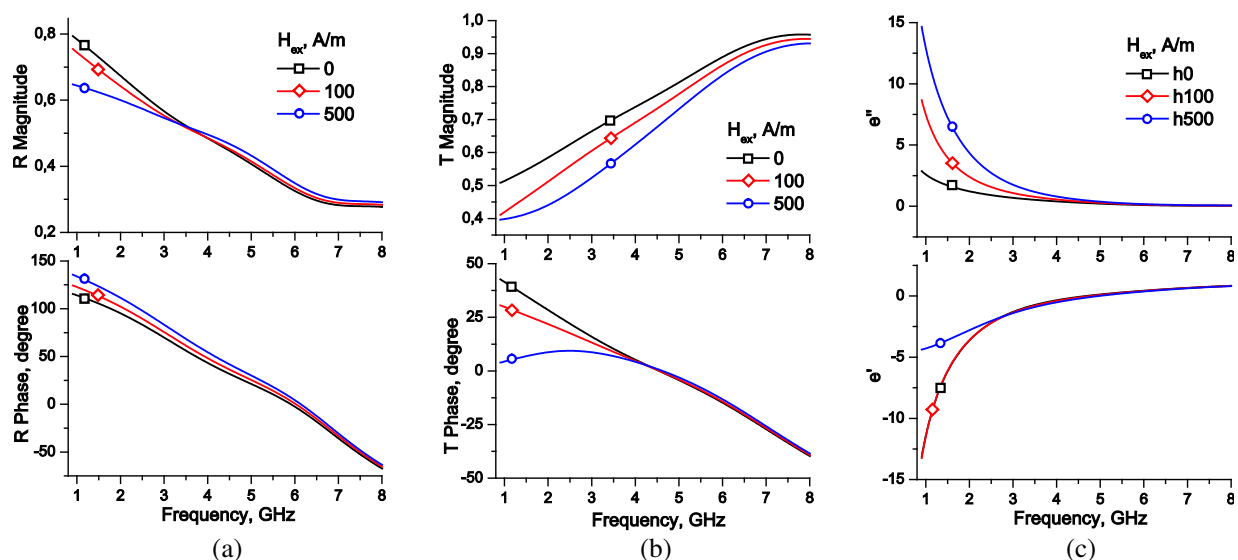


Figure 4: Spectra of R , T and ϵ_{ef} for composites with long wires with H_{ex} as a parameter ($H_{ex} = 0, 100, 500$ A/m).

demonstrating a stop filter behaviour. The magnitude of this minimum depends strongly on the field for longer wires with lower resonance frequency. For shorter wires with the dispersion at a higher frequency band the field dependence is not noticeable since the wire ac permeability is nearly unity and the impedance becomes insensitive to the magnetic properties. The resonance frequency corresponds to that for wires in the medium with the permittivity of unity. For comparison of two composites, the effective thickness to calculate the effective permittivity was taken 1 cm, however, this may be questionable since even a thin layer of the supporting matrix may change the resonance frequency.

The phase of the transmitted wave shows a reversal near a resonance frequency which sensitively shifts with the field.

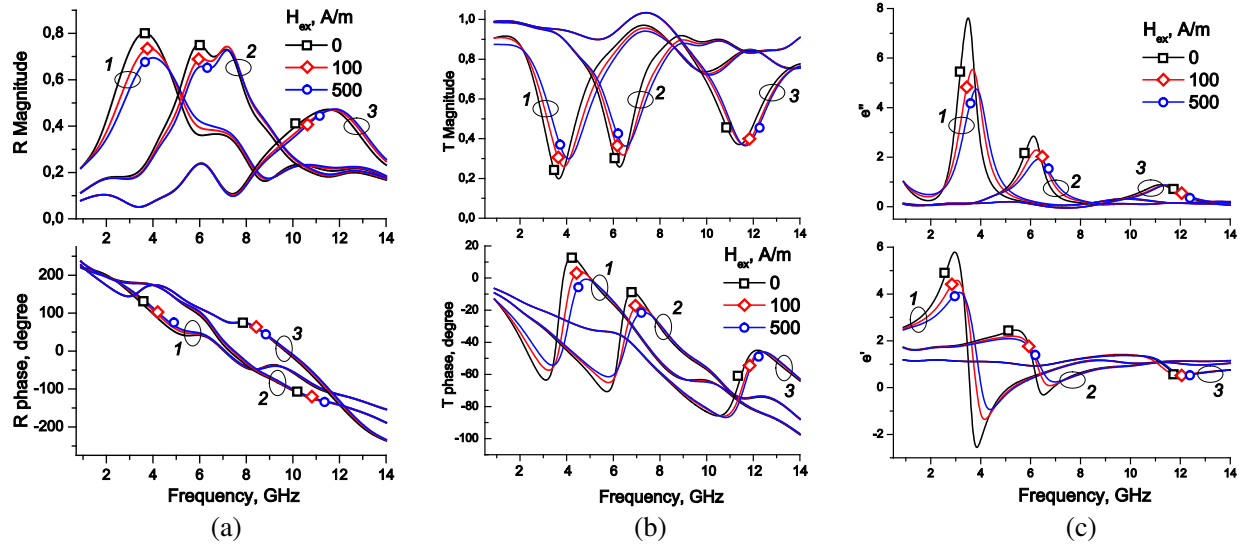


Figure 5: Spectra of R , T and ϵ_{ef} of composites with cut wires of length 40 (1), 20 (2) and 10 (3) mm with the field as a parameter.

Table 1: Experimental data for short-wire composite (T_{\min} is a minimum of transmission at resonance, ϵ''_{\max} is a maximum of imaginary part of permittivity, Δf_{anom} is a width of the region with anomalous dispersion, $H_1 = 0$ A/m, $H_2 = 500$ A/m).

l , mm	f_r , GHz (H_1)	f_r , GHz (H_2)	T_{\min} (H_1)	T_{\min} (H_2)	ϵ''_{\max} (H_1)	ϵ''_{\max} (H_2)	Δf_{anom} , GHz (H_1)
40	3.65	4.08	0.20	0.30	7.62	4.75	3.12–4.23
20	6.27	6.51	0.26	0.36	2.85	1.92	5.74–6.83
10	11.40	11.66	0.37	0.36	0.89	0.88	10.5–12.2

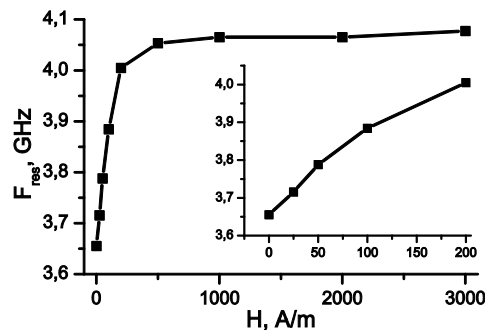


Figure 6: Dependence of the resonance frequency f_r on the external magnetic field for composite with 40 mm long wires.

Table 1 summarizes some experimental data of practical interest for the short-wire composites obtained from the transmission measurements. These results are consistent with the theoretical analysis.

Figure 6 shows the dependence of the resonance frequency f_r on magnetic field for composite with 40 mm inclusions. The similar form has the minimum of transmission magnitude T_{\min} that is a result of a dumping increasing with magnetic field.

5. CONCLUSIONS

Here we report novel results on the magnetic field effect on the dielectric response in composites with arrays of parallel magnetic wires, continuous and short-cut, in the frequency region of 0.9–17 GHz utilising free-space measurement method and analysis in terms of the effective permittivity depending on the wire surface impedance. Both the real and imaginary parts of ε_{ef} show strong variations with increasing the field owing to the field dependence of the wire impedance which controls the losses in the dielectric response. Long-wire composite has a plasmonic type dispersion of ε_{ef} with negative values of its real part below the plasma frequency which is in the GHz range for wire spacing of about 1 cm and wire diameter of few microns. The presence of the external magnetic field suppresses low-frequency plasmons increasing the value of the real part of the permittivity. In the case of cut-wire composites, it is confirmed that their effective permittivity has a resonance type dispersion due to the dipole resonance in wires at half wavelength condition. The application of the field broadens the resonance and shifts it towards the higher frequencies. Therefore, both types of wire composites possess a strong dependence of the effective permittivity on the external magnetic field and are suitable for large scale applications as tuneable microwave materials.

REFERENCES

1. Rotman, W., "Plasma simulation by artificial dielectrics and parallel plate media," *IRE Trans. Antennas Propagat.*, Vol. 10, 82–95, 1962.
2. Pendry, J. B., A. J. Holden, W. J. Stewart, and I. Youngs, "Extremely low frequency plasmons in metallic mesostructures," *Phys. Rev. Lett.*, Vol. 76, No. 25, 4773–4776, 1996.
3. Lagarkov, A. N. and A. K. Sarychev, "Electromagnetic properties of composites containing elongated conducting inclusions," *Phys. Rev. B*, Vol. 53, 6318, 1996.
4. Liu, L., S. M. Matitsine, Y. B. Gan, and K. N. Rozanov, "Effective permittivity of planar composites with randomly or periodically distributed conducting fibers," *J. Appl. Phys.*, Vol. 98, 63512, 2005.
5. Reynet, O., A.-L. Adent, S. Deprot, O. Acher, and M. Latrach, "Effect of the magnetic properties of the inclusions on the high-frequency dielectric response of diluted composites," *Phys. Rev. B*, Vol. 66, 94412, 2002.
6. Makhnovskiy, D. P. and L. V. Panina, "Field dependent permittivity of composite materials containing ferromagnetic wires," *J. Appl. Phys.*, Vol. 93, 4120, 2003.
7. Makhnovskiy, D. P., L. V. Panina, C. Garcia, A. P. Zhukov, and J. Gonzalez, "Experimental demonstration of tunable scattering spectra at microwave frequencies in composite media containing CoFeCrSiB glass-coated amorphous ferromagnetic wires and comparison with theory," *Phys. Rev. B*, Vol. 74, 064205-1–064205-11, 2006.
8. Zhukova, V., M. Ipatov, A. Zhukov, J. Gonzalez, and J. M. Blanco, "GMI effect in ultra-thin glass-coated Co-rich amorphous wires," *Sens. Actuators B-Chemical*, Vol. 126, 318–323, 2007.
9. Sandacci, S. I., D. P. Makhnovskiy, and L. V. Panina, "Valve-like behavior of the magnetoimpedance in the GHz range," *J. Magn. Magn. Mat.*, 272–276, 1855, 2004.

Measurement of Tunable Permeability and Permittivity of Microwires Composites at Microwave Frequency

L. Liu, S. Matitsine, C. B. Tang, and L. B. Kong

Temasek Laboratories, National University of Singapore, 117508, Singapore

Abstract— Polymeric composites filled with glass-coated ferromagnetic microwires were fabricated with molding method. Tunable magnetic permeability of composites with regularly distributed microwires was measured with coaxial line method from 50 MHz to 3 GHz. Tunable dielectric permeability of composites with extremely low concentration of randomly distributed microwires was measured with free space setup from 4 GHz to 18 GHz. Potential applications of such microwire composites include smart materials or remote sensing.

1. INTRODUCTION

Composites with glass-coated ferromagnetic microwire inclusions attract great interest recently due to their high magnetic permeability and loss from MHz to GHz frequency, as well as the negative permeability at ferromagnetic resonance frequency. Since the conductive microwires are coated with a layer of glass which blocks the current flow from contacting microwires, composites with microwire inclusions are expected to have lower effective permittivity value than these with bare conductive wires. Such feature makes glass-coated ferromagnetic microwires a suitable candidate for many applications, such as EM shielding materials, high attenuation materials and double negative meta-materials, etc.

Casting (Taylor-Ulitovsky) method was used to fabricate glass-coated microwires with different components and structures of metallic nucleus for decades [1, 2]. Microwires consist of an inner metallic nucleus covered by a Pyrex-like coating. The composition of alloy and process parameters (includes casting rate and cooling rate) determine the microstructure and geometrical characteristics, as well as static and dynamic magnetic behaviour [1]. Microwires with core diameter of 0.8 to 30 μm and the glass coating thickness of 2 to 15 μm have been produced. This method can control and adjust the geometrical parameters during fabrication, also produce microwires with repeatable properties at mass production [1]. High frequency permeability of composite with parallel amorphous microwire was investigated by coaxial line and the method for thin film measurement [3, 4]. Co-based wires exhibit a lower coercive force than Fe-based wires which is attributed to their different domain structures. Permeability values at 10 MHz were significantly higher for Co-based wires than for the Fe-based materials [3]. It is found that the permeability of Co-based wire composites depends not only on the composition but also on the dimensional characteristics, such as metallic core diameter and glass-cover thickness [5]. The complex permittivity and permeability of composites filled with regular and short-cut chaotic Fe-based microwire were measured with Q-meter and coaxial line method from 1 MHz to 10 GHz. However, the permeability of randomly distributed wire composite is close to 1 which can be explained by the high coercive force of Fe-based wires [6]. Composites with regularly or randomly distributed CoFeNiSiB ferromagnetic microwires were fabricated and characterized by us [7]. Permeability of such composites were investigated with impedance and coaxial line methods from 1 MHz to 10 GHz. High magnetic permeability and loss were obtained from composites with low volume fraction of microwires, which can be explained by materials and shape anisotropy. The reflectivity of microwire composite to incident wave calculated from measured permeability and permittivity shows potential for high attenuation applications. Negative magnetic permeability found between 0.5 to 5 GHz may also be employed to fabricate metamaterials with negative refraction index [7].

Except for high magnetic properties at high frequency, amorphous microwires have also found applications such as remote sensing, non-destructive testing, and control of mechanical stress inside of implants. Among them, tunable electromagnetic properties such as tunable permittivity and permeability of composites with extremely low concentration of microwires have attracted more attention recently [8, 9]. The main mechanism of turning mechanism can be explained through magneto-impedance effect and the changing of surface impedance tensor [10]. The theoretical analysis was based on the asymptotic-series-expansion method of solving the Maxwell equations for a ferromagnetic wire with an AC permeability tensor of a general form associated with magnetization rotation. The magnetic structure-dependent impedance tensor was calculated for any frequency

and external magnetic field, and was not restricted to the case when only strong skin effect is present. This approach provided a rigorous quantitative analysis of magneto-impedance characteristics in wires, depending on the type of magnetic anisotropy, the magnitude of DC bias current, and an excitation method [10]. However, only few measurement method and results are available at current moment for the tunable properties of microwire composites at microwave frequency.

The first objective is to set up the measurement facilities for the tunable electromagnetic properties, such as tunable permittivity and permeability. Due to the limitation of fixtures, coaxial line method and free space method are developed for low and high frequency measurement. The second purpose is to measure the tunable EM properties of microwire composites, with both regular and random distributions.

2. EXPERIMENT

CoFeNiSiB amorphous ferromagnetic microwire was provided by Microfir Tehnologii Industriale which was wounded on bobbins. The inner diameter is about 5 microns and outer diameters of the microwire provided are about 10 microns. The geometry and dimension of microwire were examined with JEOL JSM-6340F field emission scanning electronic microscope (SEM) as given in Figure 1.

For measurement of tunable permeability in parallel direction of microwires, the microwire of 130 mm in length was cut from the bobbin and wound on a pin with 3 mm in diameter. Then it was put into a mold with 7 mm in diameter before filled up with silicone (Sin-Etsu 1800 T). The estimated volume fraction of microwire is 8%. 0.05 wt% of microwire with length of 5 mm and 10 mm individually were put into silicone matrix to prepare sheet sample for free space measurement. The size of sample is 20 cm by 20 cm by 1 mm. The mould was then cured in an oven at 70°C for 24 hours.

APC-7 coaxial transmission line fixture and Agilent N5230A vector network analyzer were employed to measure the tunable permeability. The inner diameter of samples for permeability measurement is 3 mm, outer diameter is 7 mm and the thickness is about 2 mm. The coaxial line fixture

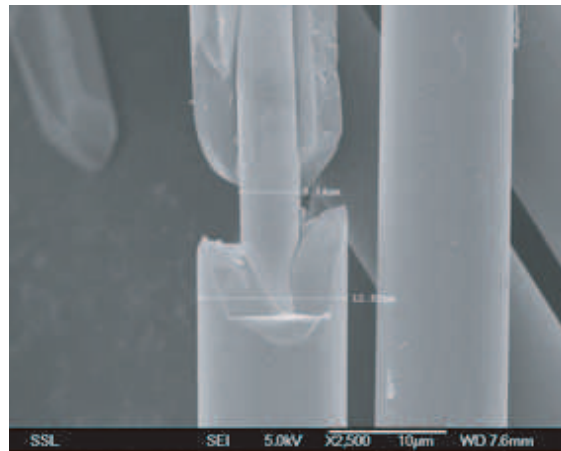


Figure 1: SEM image of microwires.

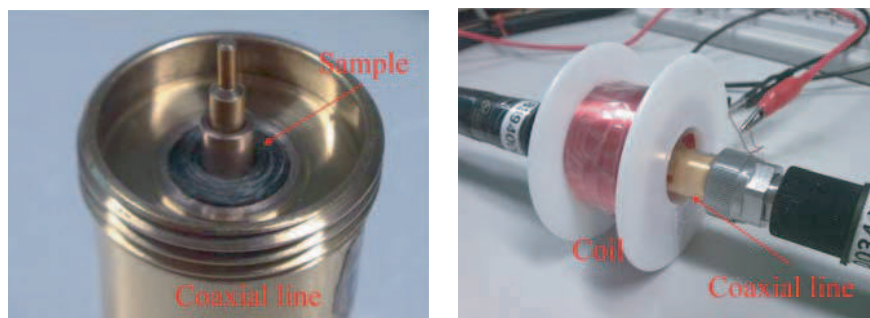


Figure 2: Coaxial line fixture with bias magnetic field from coil.

loaded with a piece of toroidal shape of sample is shown in Figure 2. A coil with 900 turns of 0.8 mm enameled copper wire was used to provide the tunable magnetic bias field. The whole coaxial line with toroidal sample was inserted into the coil as shown in Figure 2. The bias magnetic field inside the bobbin was measured with Gauss meter (GM07, HIRST Magnetic Instrument Ltd).

Free space setup was developed in Temasek laboratories. Figure 3 is the free space setup to measure transmission/reflection coefficient from 4 GHz to 18 GHz. Agilent vector network analyzer N5230A was used as microwave signal source as well as amplitude and phase analyzer. Measurement fixture includes a mini-anechoic chamber with pyramid radar absorbers to reduce the reflection from the environment, and a pair of high gain broadband transmitter and receiver antennas, DP240 from FLANN microwave with working frequency from 2 GHz to 18 GHz. The Gain of the horns is from 5 dB to 18 dB and the 3 dB beamwidth is from 10° to 60° . The feature of this free space setup is that a piece of high performance absorber with a 15 cm hole was employed to suppress the fringing wave of the sample under test. Two pieces of magnets have been used to provide bias magnetic field to the rubber sheet sample under test. The two rare earth permanent magnets can provide quite large magnetic field on their surface. However, due to the large sample size (20 cm by 20 cm), the bias field measured by Gauss meter at the center of the sample is about 20 Gauss.

3. RESULTS AND DISCUSSIONS

Figure 4(a) plots the measured unbiased and biased magnetic permeability from 50 MHz to 3GHz of composite with 8% regularly distributed microwires. Both permeability real and imaginary parts decrease dramatically under bias magnetic field. The biggest change is within 50 MHz to 1 GHz. When frequency is more than a few GHz, the tunability is not observable. The reason could be the magneto-impedance and skin effect of the magnetic microwire. When the diameter is much larger than the skin depth, the permeability and tunability is not significant anymore. Figure 4(b) plots the dependence of the permeability on the bias magnetic field from 0 G to 200 G. More than 50% of tunability of permeability can be achieved by bias magnetic field of 200 G, which is considered as small magnetic field. More investigation will be carried out to find out microwire with better tunability under even smaller bias.

Tunable permittivity was measured with free space measurement as shown in Figure 5. It is found that both real and imaginary permittivity are increased dramatically (50 ~ 100% over the

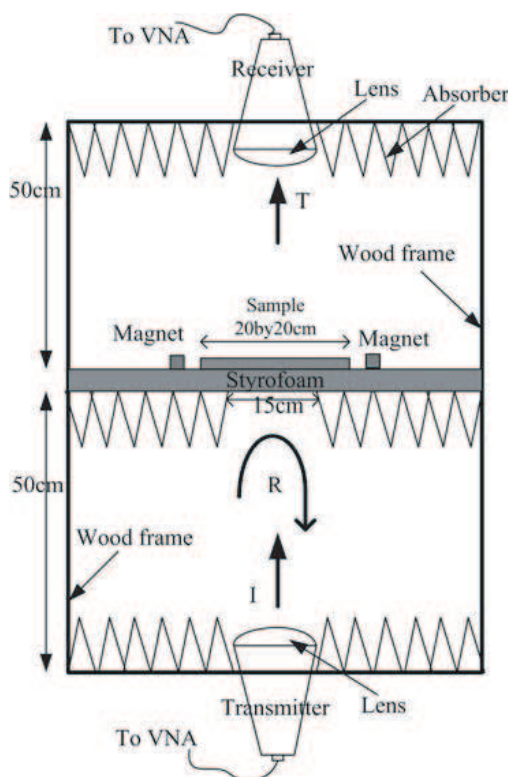


Figure 3: Free space system with bias magnetic field from permanent magnet.

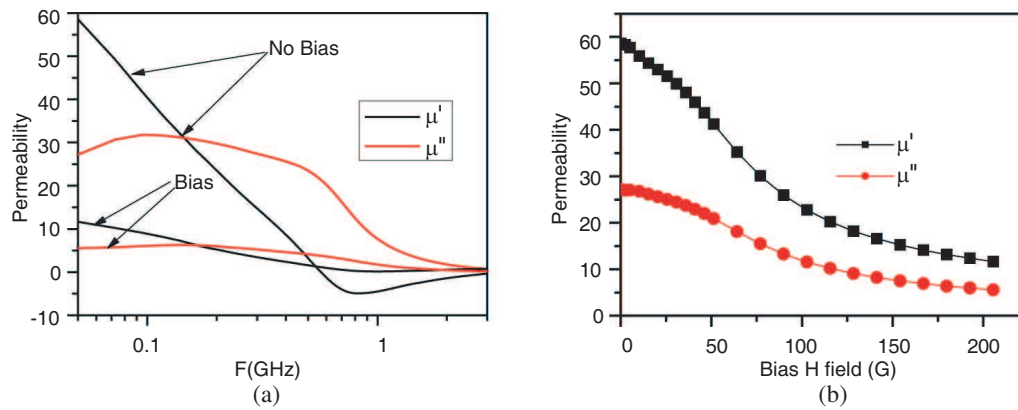


Figure 4: Measured tunable permeability with coaxial line from (a) 50 MHz to 3 GHz, (b) from 0 G to 200 G @ 50 MHz.

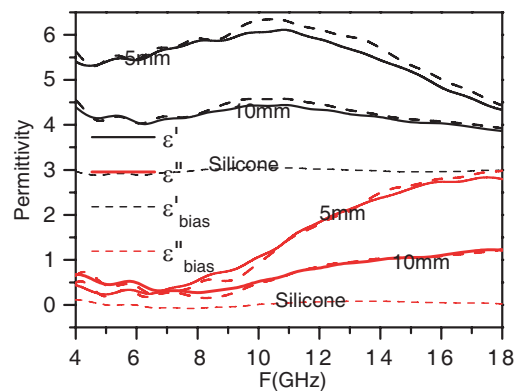


Figure 5: Tunable permittivity of microwire composites measured with free space method.

frequency band) as compared with pure silicone sample without any microwire inclusion. It could be very useful to make materials with high permittivity at microwave frequency with extremely low concentration of microwires. Sample with 5 mm microwires has higher permittivity than that with 10 mm microwires. Tunable permittivity of rubber sheet with microwires of different length was also measured. The results are shown in Figure 5 (dash lines). Small tunability (about 5% at resonant frequency) could be found. The tunability can be caused by the small bias magnetic field (around 20 G) generated by the magnet. If larger bias field (is available for free space setup, the tunability might be larger [8]). Therefore, other fixtures, such as strip line or waveguide, should be used for the measurement of tunable permittivity with bias magnetic field. Due to the smaller sample size, larger bias magnetic field could be easily generated.

4. CONCLUSIONS

Tunable magnetic permeability and dielectric permittivity of composites with regularly or randomly distributed microwires were measured with coaxial line method from 50 MHz to 3 GHz and free space method from 4 GHz to 18 GHz. Significant tunable permeability was found from microwire composite at MHz frequency. Slight tunable permittivity was found from the microwire composites at GHz frequency. The possible reason could be due to the inaccessibility of higher bias magnetic field for free space setup. The potential applications of such kind of microwire composites include smart materials or sensors. The focus of the investigation in the future will be on the theoretical understanding and modeling of the tunable dielectric and magnetic properties, and optimizing of the tunable properties for various applications.

ACKNOWLEDGMENT

The authors appreciate Dr K. N. Rozanov (ITAE, Moscow, Russia) for the fruitful discussion, Dr D. Maknovskiy (Uni. of Plymouth, UK) and Dr V. Larin (MFIT Ltd, Moldova) for the useful information and discussion. The research was supported by Defense Science and Technology Agency (DSTA), Singapore, under project POD0103671.

REFERENCES

1. Larin, V. S., A. V. Torcunov, A. Zhukov, J. Gonzalez, M. Vazquez, and L. Panina, "Preparation and properties of glass-coated microwires," *JMMM*, Vol. 249, 39, 2002.
2. Notonenk, A. N., E. Sorkine, A. Rubshtein, V. S. Larin, and V. Manov, "High frequency properties of glass-coated microwires," *J. of Appl. Phys.*, Vol. 83, No. 11, 6587, 1998.
3. Acher, O., P. M. Jacquart, and C. Boscher, "Investigation of high frequency permeability of thin amorphous wire," *IEEE Trans. on Magnetics*, Vol. 30, No. 6, 4542, 1994.
4. Jacquart, P. M. and O. Acher, "Permeability measurement on Composites made of oriented metallic wires from 0.1 to 18 GHz," *IEEE Trans. on MTT*, Vol. 44, No. 11, 2116, 1996.
5. Dprot, S., A. L. Adenot, F. Bertin, and O. Acher, "Frequency response engineering of CoFeNiBSi microwires in the gigahertz range," *JMMM*, Vol. 242–245, 247, 2002.
6. Starostenko, S. N., K. N. Rozanov, and A. V. Osipov, "Microwave properties of composites with glass coated amorphous magnetic microwires," *JMMM*, Vol. 298, 56, 2006.
7. Liu, L., L. B. Kong, G. Q. Lin, S. Matitsine, and C. R. Deng, "Microwave permeability of ferromagnetic microwires composites/metamaterials and potential applications," *IEEE Trans. on Magnetics*, Vol. 44, No. 11, 2008.
8. Makhnovskiy, D. P. and L. V. Panina, "Field dependent permittivity of composite materials containing ferromagnetic wires," *J. Appl. Phys.*, Vol. 93, No. 7, 4120, 2003.
9. Columbus, F., *Progress in Ferromagnetism Research*, Nova Science Publisher, USA, 2004.
10. Makhnovskiy, D. P., L. V. Panina, and D. J. Mapps, "Field-dependent surface impedance tensor in amorphous wires with two types of magnetic anisotropy: Helical and circumferential," *Phys. Rev. B*, Vol. 63, 144424, 2001.

Electromagnetic Wave Diffraction on Array of Complex-shaped Metal Elements Placed on Ferromagnetic Substrate

S. L. Prosvirnin¹ and V. A. Dmitriev²

¹Institute of Radio Astronomy, Ukraine

²Federal University of Para, Brasil

Abstract— Full wave numerical study of electromagnetic wave reflection from and transmission through an array of thin, perfect conducting, planar strip complex-shaped elements placed on a magnetized ferrite substrate is carried out. Our results show, that the absorption level and the frequency band of the structure, when the ferromagnetic resonance and a metal element resonance are close in frequency, are larger than the corresponding characteristics of the ferrite layer without metal elements. A significant enhancement of the Faraday rotation is also observed in the vicinity of the metal element resonances. Both right-handed and left-handed circular polarized incident waves interact effectively with a metal array placed on ferrite substrate unlike the known resonant interaction when only one kind (right- or left-handed) of circular polarized waves interacts with the ferrite slab without metal elements.

1. INTRODUCTION

Periodic arrays of planar complex-shaped metal elements placed on a dielectric substrate are used as frequency selective surfaces (FSS), polarizers, absorbers, etc. It is well known that ferrite materials in a magnetic biasing field are described by a permeability tensor. Combining resonance responses of metal arrays and ferromagnetic characteristics of the ferrite substrate, one can expect to find new functional features of such structures.

An important peculiarity of the metal array-ferrite structures is the possibility of controlling their properties by a dc magnetic field. Significant change of transmission, reflection and absorption characteristics can be obtained as a result of such control.

It was shown in paper [1], that the frequency shift of resonance response of FSS with metal crosses on a ferrite substrate depends significantly on biasing magnetic field. But the presented in paper [1] results are concerned only with transmitted power, and the ferrite material of the substrate was considered to be lossless. Besides, the investigated frequency range was rather far from the ferromagnetic resonance where the possibilities of controlling are not very wide. Thus, the electromagnetic properties of such structures were not analyzed yet in detail.

The effects of interaction of electromagnetic waves with the suggested planar metamaterial can be described conveniently in terms of a scattering matrix. Symmetry of the problem which depends on the symmetry of the ferrite substrate, of the metal elements and of a dc magnetic field and its orientation, stipulates some restrictions on the operators entering the scattering matrix. Using the theory of magnetic groups we give some examples of such restrictions.

In our paper, we present also some results of numerical study of electromagnetic wave reflection from and transmission through an array of rosette-shaped elements placed on a magnetized ferrite substrate. The choice of complex-shaped elements gives us an opportunity to produce a symmetrical array having small sizes of elementary cell as compared with wavelength but nevertheless manifesting resonance properties.

2. SYMMETRY ANALYSIS

In Fig. 1, we show some possible geometries of metamaterials composed of a ferrite substrate magnetized in the direction normal to it and of metal elements in the form of a rosette, case (a), and crosses, cases (b) and (c). In case (b), the crosses are placed only on one side of the ferrite substrate, and they are on both sides of the substrate in case (c).

The resulting magnetic group of symmetry of the problems depends on the symmetry of the ferrite substrate, of the metallic elements and of a dc magnetic field and its orientation. This symmetry can be defined using Curie's principle of symmetry superposition [2]. The symmetry defines some restrictions on the elements (more exactly, operators because the reflection is not specular) of the scattering matrix.

The scattering matrix \bar{S} relates the tangential components of the electric fields of the scattered and incident waves in the planes 1–1 and 2–2 (see Fig. 1(a)) as follows: $(E_{x1}^s, E_{y1}^s, E_{x2}^s, E_{y2}^s)^T =$

$\bar{S} \cdot (E_{x1}^i, E_{y1}^i, E_{x2}^i, E_{y2}^i)^T$. Notice that the tangential components of an incident wave are defined by the angle of incidence. Using the theory of magnetic groups [2] we have determined the restrictions on the matrix elements. In Table 1, the magnetic groups of symmetry (in Schoenflies notations [2]) and the number of their elements, the calculated scattering matrices and the number of independent parameters of the matrices for the metamaterials in Fig. 1 are presented.

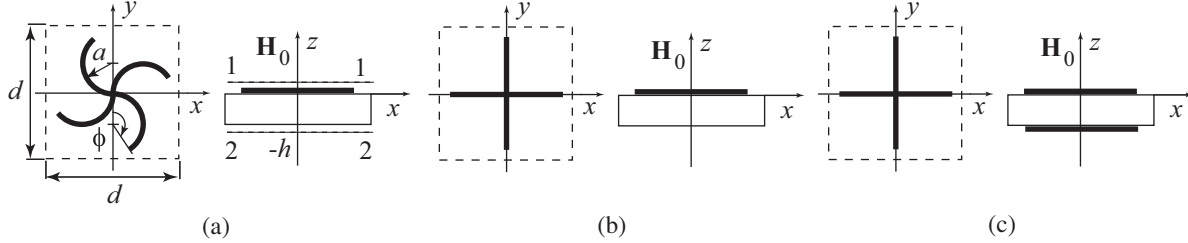


Figure 1: Examples of FSSs: (a) one-sided rosette; (b) one-sided cross; (c) two-sided cross.

Table 1: Symmetry description of the metamaterials shown in Fig. 1.

Characteristic	case (a)	case (b)	case (c)
Magnetic group of symmetry	C_4	$C_{4v}(C_4)$	$D_{4h}(C_{4h})$
Number of group elements	4	8	16
Scattering matrix	$\begin{pmatrix} S_{11} & S_{12} & S_{13} & S_{14} \\ -S_{12} & S_{11} & -S_{14} & S_{13} \\ S_{31} & S_{32} & S_{33} & S_{34} \\ -S_{32} & S_{31} & -S_{34} & S_{33} \end{pmatrix}$	$\begin{pmatrix} S_{11} & S_{12} & S_{13} & S_{14} \\ -S_{12} & S_{11} & -S_{14} & S_{13} \\ S_{13} & S_{14} & S_{33} & S_{34} \\ -S_{14} & S_{13} & -S_{34} & S_{33} \end{pmatrix}$	$\begin{pmatrix} S_{11} & S_{12} & S_{13} & S_{14} \\ -S_{12} & S_{11} & -S_{14} & S_{13} \\ S_{13} & S_{14} & S_{11} & S_{12} \\ -S_{14} & S_{13} & -S_{12} & S_{11} \end{pmatrix}$
Number of independent matrix elements	8	6	4

Our method of calculation is based on the commutation relations for the scattering matrix \bar{S} and the 4×4 matrix representation \bar{R} of the symmetry elements (in fact, among the elements of the groups, we can use only the so-called generators). These commutation relations are $\bar{R} \cdot \bar{S} = \bar{S} \cdot \bar{R}$, $\bar{R} \cdot \bar{S} = \bar{S}^T \cdot \bar{R}$ for unitary and antiunitary elements of the corresponding magnetic group, respectively.

3. DERIVATION OF ANALYTICAL EXPRESSION FOR THE TRANSFER MATRIX OF A FERROMAGNETIC LAYER

The fields, intensities, and polarization characteristics of the electromagnetic waves diffracted by the array of rosette-shaped elements were calculated by the full wave method described in [3]. Notice that earlier the method of [3] was applied to structures with nonmagnetic isotropic substrates. This approach is based on the method of moments for solution of vector integral equation for surface currents induced by the electromagnetic field on the array elements. The equation was derived with boundary conditions that assume a zero value for the tangential component of the electric field on metal strips. In our calculations, we used the Fourier transformations of fields and surface current distributions.

The main original part of our present work is the analytical expression obtained for the transfer matrix of normally magnetized ferromagnetic layer for the case of *arbitrary* orientation of wave vector of propagated or evanescent wave. This simplifies greatly the following numerical calculations.

We use common expressions for permittivity and permeability of z -axis biased ferrite taking

into account the magnetic losses [4]

$$\varepsilon_f = \varepsilon_0 \varepsilon, \quad \hat{\mu}_f = \mu_0 \begin{bmatrix} \mu & i\beta & 0 \\ -i\beta & \mu & 0 \\ 0 & 0 & 1 \end{bmatrix} \quad (1)$$

where

$$\begin{aligned} \mu &= 1 + \chi' - i\chi'', & \beta &= K' - iK'', \\ \chi' &= \omega_0 \omega_m [\omega_0^2 - \omega^2(1 - \alpha^2)] D^{-1}, & \chi'' &= \omega \omega_m \alpha [\omega_0^2 + \omega^2(1 + \alpha^2)] D^{-1}, \\ K' &= \omega \omega_m [\omega_0^2 - \omega^2(1 + \alpha^2)] D^{-1}, & K'' &= 2\omega^2 \omega_0 \omega_m \alpha D^{-1}, & D &= [\omega_0^2 - \omega^2(1 + \alpha^2)]^2 + 4\omega_0^2 \omega^2 \alpha^2, \end{aligned}$$

and typical ferrite parameters in the microwave region are $\varepsilon = 10$, $\alpha = 0.05$, $\omega_m/2\pi = 5.6$ GHz, $\omega_0/2\pi = 4$ GHz. The frequency dependencies of the permeability parameters are presented in Fig. 2. The values of $\text{Im}\mu$ and $\text{Im}\beta$ are so close to each other that their graphs coincide in the figure.

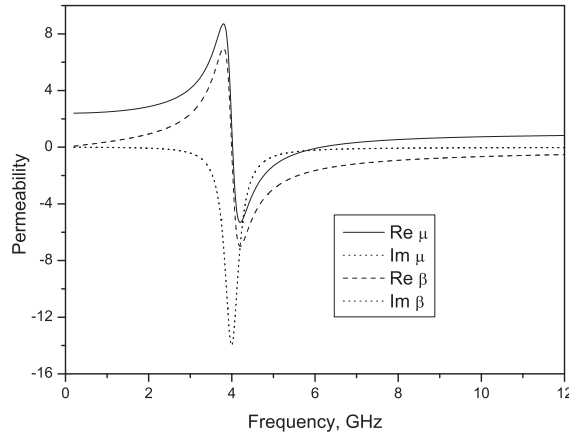


Figure 2: Frequency dependencies of permeability parameters of z -axis biased ferrite substrate. Graphs of $\text{Im}\mu$ and $\text{Im}\beta$ are so close that they do not distinguish in the figure.

Solutions of the Maxwell equations

$$\nabla \times \mathcal{E}(\mathbf{r}) = -ikZ_0 \hat{\mu}_f \mathcal{H}(\mathbf{r}), \quad \nabla \times \mathcal{H}(\mathbf{r}) = ikZ_0^{-1} \varepsilon_f \mathcal{E}(\mathbf{r}) \quad (2)$$

can be sought in the form

$$\mathcal{E}(\mathbf{r}) = \exp(-ik_x x - ik_y y) \mathbf{E}(z), \quad \mathcal{H}(\mathbf{r}) = \exp(-ik_x x - ik_y y) \mathbf{H}(z) \quad (3)$$

where $k = \omega \sqrt{\varepsilon_0 \mu_0}$, $Z_0 = \sqrt{\mu_0 / \varepsilon_0}$.

It is easy to derive the equation

$$\frac{d}{dz} \bar{F}(z) = \bar{M} \cdot \bar{F}(z) \quad (4)$$

for the 4-vector $\bar{F}(z) = (E_x, E_y, H_x, H_y)^T$ which presents the tangential components of the fields, by using Equations (2) and expressions (3).

Next, we assume that the vector $\bar{F}(z)$ is known in the plane $z = z_0$ and look for an analytical solution of the Cauchy problem for Equation (4) in the form

$$\bar{F}(z) = \bar{T}(z, z_0) \cdot \bar{F}(z_0). \quad (5)$$

The 4×4 -matrix $\bar{T}(z, z_0)$ is a transfer matrix for the magnetized ferrite homogeneous layer. The analytic expressions of the matrix elements are unwieldy formulas derived by using of a computer software for analytic transformations. The small paper volume does not allow us present here these expressions.

4. ANALYSIS OF NUMERICAL RESULTS

The numerical results presented below relate to the rosettes in Fig. 1(a). The width of metal strips of elements is assumed to be narrow as compared with their stretched length and with the wavelength. The sizes of the array elements are chosen in such a way that their first low-frequency resonances to be near of the ferromagnetic resonance frequency. The rosettes are arranged in square cell arrays with the period $d = 15$ mm. The width of the infinitely thin perfectly conducting strips of the rosettes is assumed to be 0.8 mm, the radius $a = 5$ mm, and the bending angle $\phi = 120^\circ$. The magnetized ferrite substrate with above mentioned relative permittivity and permeability parameters has the thickness $h = 1.5$ mm.

We present here a comparison of transmission, reflection, absorption, and polarization properties of the array placed on the magnetized ferrite substrate and of the ferrite slab without array. It is assumed below that a plane electromagnetic wave is incident from the space region $z > 0$.

As it is well known, the eigenwaves of unbounded ferrite medium with longitudinal magnetization are right-handed and left-handed circular polarized (RCP and LCP) waves. Thus normally incident RCP or LCP wave does not change its polarization when transmitted through ferrite slab or through ferrite with an infinitely thin array with 4-fold rotational symmetry. But the polarization of RCP or LCP wave changes to opposite at the reflection.

In Fig. 3 and Fig. 4 we present frequency dependencies of absolute values of the transmission T and reflection R coefficients and also the absorption defined as $(1 - |T|^2 - |R|^2)$ for the ferrite slab with the array structure in the case of circular polarized incident waves. A ferromagnetic resonance may be observed only for RCP wave incidence on the slab and for both RCP and LCP wave incidence on the array. Notice that we use here the optical definition of right-handed and left-handed circular polarization, i.e., electric field rotates respectively clockwise and anticlockwise for observation opposite to the wave propagation direction.

There are resonances of transmission and reflection observed in the same frequencies for the RCP and LCP incident wave due to resonance properties of elements of array. A level of the array absorption and the width of frequency band of large absorption are approximately the same for both kinds of circular polarization of the incident wave (see Fig. 4). The radical difference of the slab and the array properties may be seen for the LCP incident wave. Ferromagnetic resonance of the slab does not appear for the LCP wave. An explanation for the significant absorption of the ferrite layer with array is excitation of complex electromagnetic field of evanescent waves inside the substrate.

A polarization state of the electromagnetic wave transmitted through the ferromagnetic slab or the array structure may be characterized by angles of azimuth and ellipticity (see Fig. 5). We present frequency dependencies for rotation and ellipticity of electromagnetic field transmitted through the ferrite slab and the array placed on the ferrite substrate. It is assumed that normally incident wave has linear polarization along x -axis. We found an enhancement of the rotation of electric field and change the sign of rotation in the vicinity of the resonances of the array metal elements.

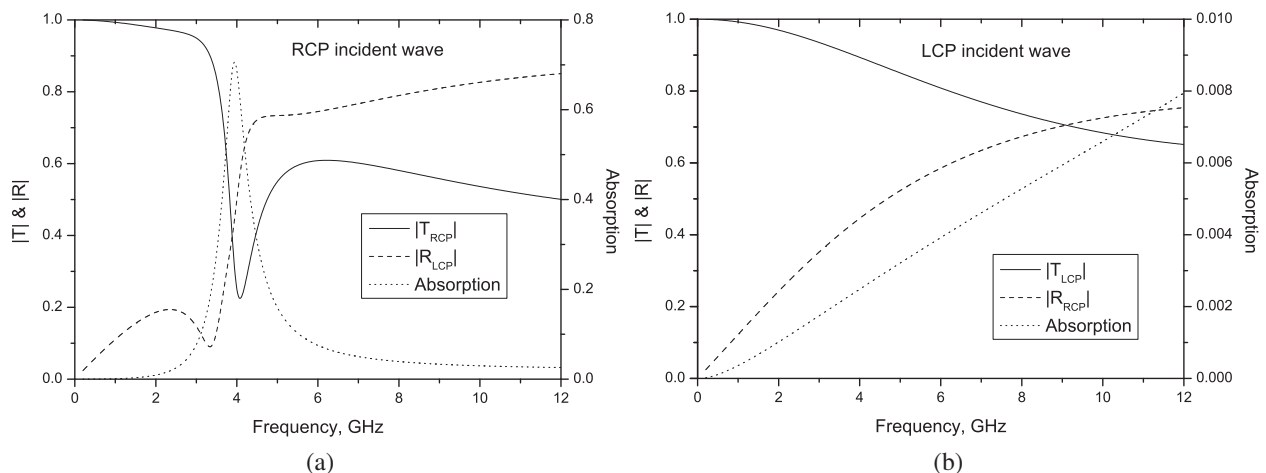


Figure 3: Frequency dependence of transmission and reflection coefficients and relative absorption power of magnetized ferrite slab for RCP (a) and LCP (b) normally incident waves.

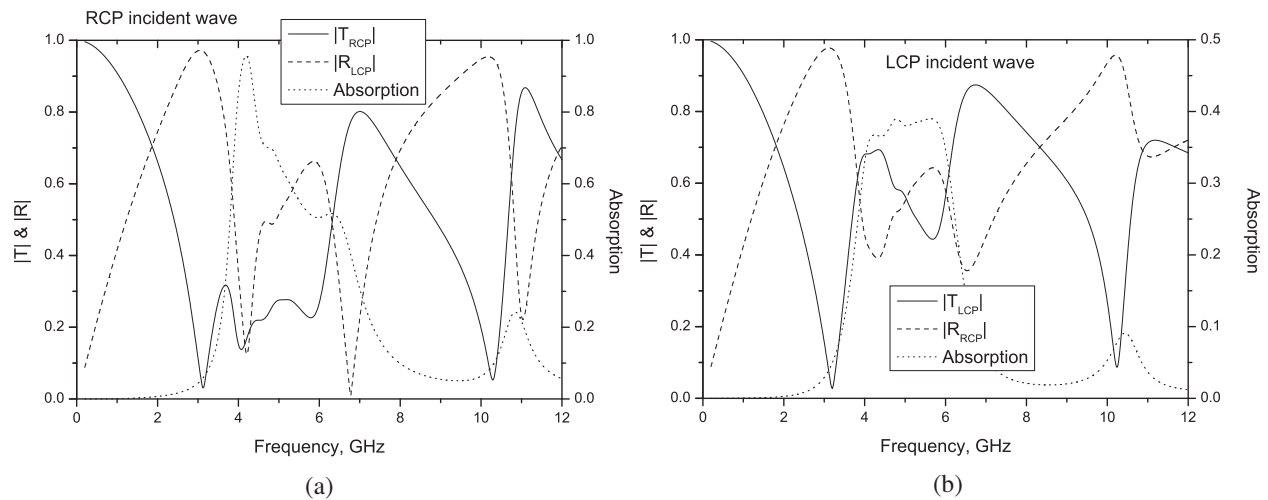


Figure 4: Frequency dependence of transmission and reflection coefficients and relative absorption power for the array of rosette-shaped elements placed on magnetized ferrite slab for RCP (a) and LCP (b) normally incident wave.

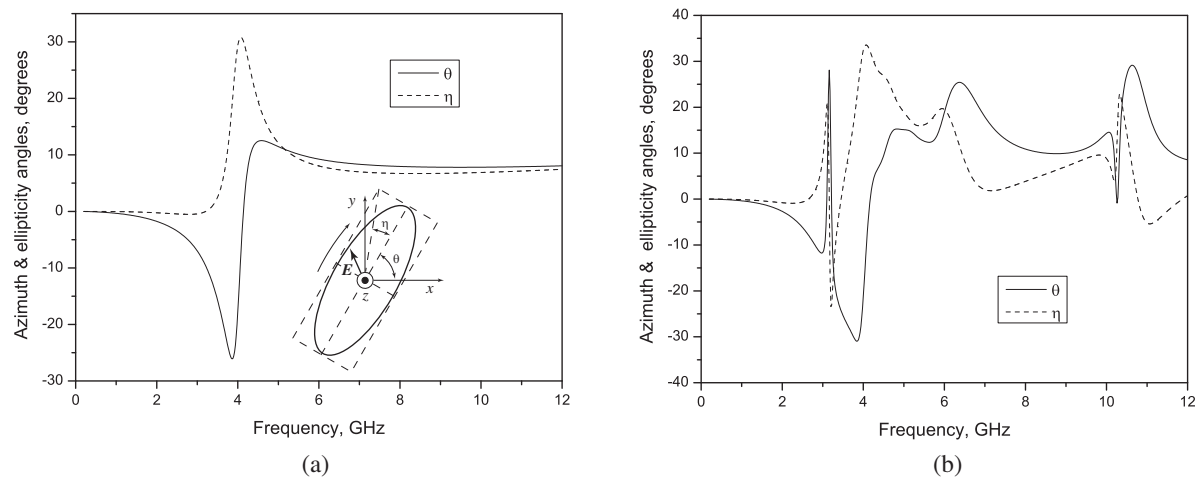


Figure 5: Frequency dependencies of azimuth and ellipticity angles of electromagnetic wave transmitted through the magnetized ferrite slab (a) and the array placed on magnetized ferrite substrate (b). A normally incident wave has x -axis linear polarized electric field. A definition of polarization angles is shown in an insert of figure (a). In the definition a wave propagation direction is assumed coincide with z -axis in the insert. The polarization parameter θ is the azimuth of polarization, and η is the ellipticity angle. The positive and negative sign of η corresponds to right-handed polarization (i.e., \mathbf{E} rotates clockwise as it is shown by arrow) and left-handed polarization for observation opposite to a wave propagation direction.

5. CONCLUSION

Our results show that the absorption level and the frequency band of the discussed structure of rosette-shaped elements, when the ferromagnetic resonance and a metal element resonance approximately coincide, are larger than the corresponding parameters of the ferrite substrate without metal elements. We also observe a significant enhancement of the Faraday rotation. This effect is observed when the ferromagnetic resonance is close to the metal element resonance and also when these resonances are far from each other. The sign of rotation changes with a small variation of frequency in the vicinity of resonance. Both RCP and LCP incident waves interact with the array placed on ferrite substrate in contrast to the case of ferrite slab without metal elements.

ACKNOWLEDGMENT

The authors would like to acknowledge the financial support of the Brazilian agency CNPq, and National Academy of Sciences of Ukraine (Grant No. 1-02-a).

REFERENCES

1. Li, G. Y., Y. C. Chan, T. S. Mok, and J. C. Vardaxoglou, “Analysis of frequency-selective surfaces on a biased ferrite substrate,” *Int. J. Electronics*, Vol. 78, No. 6, 1159–1175, 1995.
2. Barybin, A. A. and V. A. Dmitriev, *Modern Electrodynamics and Coupled-mode Theory: Application to Guided-wave Optics*, Rinton Press, Princeton, New Jersey, 2002.
3. Prosvirnin, S. L., “Transformation of polarization when waves are reflected by a microstrip array made of complex-shaped elements,” *J. of Communications Technology and Electronics*, Vol. 44, No. 6, 635–640, 1999.
4. Collin, R. E., *Foundations for Microwave Engineering*, Wiley-Interscience, New York, 1992.

Passive Microwave Mobile System for Atmospheric Boundary Layer Temperature Profilers and Total Water Vapour Content

E. N. Kadyrov¹, V. V. Folomeyev¹, E. A. Miller¹
A. V. Troicky², and E. A. Vorobeva²

¹Central Aerological Observatory, Russian Federation

²Radiophysical Research Institute, Russian Federation

Abstract— This paper presents a new mobile microwave system for continuous measurements of atmospheric boundary layer thermodynamics. The main parts of the system are scanning 5 mm radiometer for atmospheric boundary layer temperature profile measurements, dual channel microwave radiometer for total water vapor content measurements, GPS receiver, meteorological station and data system. Mobile system was successfully tested in September 2008 in the field expedition at mountains region.

1. INTRODUCTION

Permanent data about thermodynamic characteristics of atmospheric boundary layer (ABL) are necessary for a long range of investigations and applications, they are investigation of urban heat island, analysis of emissions of different gases in air, exploration of solar eclipse in atmosphere effect, perfection of short-range forecasts, prognosis of air-pollution spreading, danger meteorological occurrences prognosis and high-frequency propagation prognosis [1–3]. Since 1994 for continuous measurements of temperature profiles in ABL meteorological temperature profiler MTP-5 is widely used [1, 4]. Experience of applying MTP-5 showed that often required mobility of measurements, especially for urban heat island investigation, features of mountain thermal conditions [1]. Therefore in 2005–2006 was developed and produced mobile system for exploration temperature profiles in ABL which was used in both large cities and field scientific expeditions [1, 3]. New version of the microwave mobile system was created and tested in 2008 on the basis of off-highway car UAZ “Patriot” (Fig. 1). Basic difference of new mobile system is a presence of the channel for measurement of total water vapor content and using new direct-gain radiometer in the temperature profiler.



Figure 1: Mobile microwave system installed on UAZ “Patriot”.

2. SYSTEM DESCRIPTION AND RESULTS OF TESTS

The mobile microwave radiometric system for investigations of thermodynamic characteristics includes a microwave temperature profiler installed in box protected from vibration and dust influence, two-channel microwave radiometer for measurements of total vapor content, navigation GPS

receiver, meteo-station, commutator, meteo-shell and a data receiving system based on mobile PC. Structural chart showed at the Fig. 2.

The meteorological temperature profiler MTP-5 used for measurements of temperature profiles of ABL [1–4]. The meteorological temperature profiler consists of scanning device, antenna system, microwave radiometer, analog-digital converter and control of scanning device board. Direct-gain microwave receiver is used in the temperature profiler. Rejection from superheterodyne scheme construction has allowed to increase sensitivity and to improve stability. This makes radiometer more reliable. Structural chart of temperature profiler showed at the Fig. 3. MTP-5 controlled from PC through analog-digital converter and control of scanning device board. Scanning process goes through 12 angles from horizon to zenith ($0-90^\circ$). Antenna system consists of dual-mode horn feed fixed at a radiometer cabinet and rotating parabolic deflector.

Microwave radiometer consists of front waveguide made from thin-walled rust-resisting pipe which also serve as crossover from circular waveguide to rectangular waveguide. Front waveguide operates as thermo-coupling too. In a temperature-controlled unit located modulator (M), rectifying cell (RC), three high-frequency amplifiers (HAF) which assembled on basis CHA2159 chip, microwave filter, square detector (SqD), low-frequency amplifier (LFA), synchronous detector (SyncD), reference voltage generator (RVG).

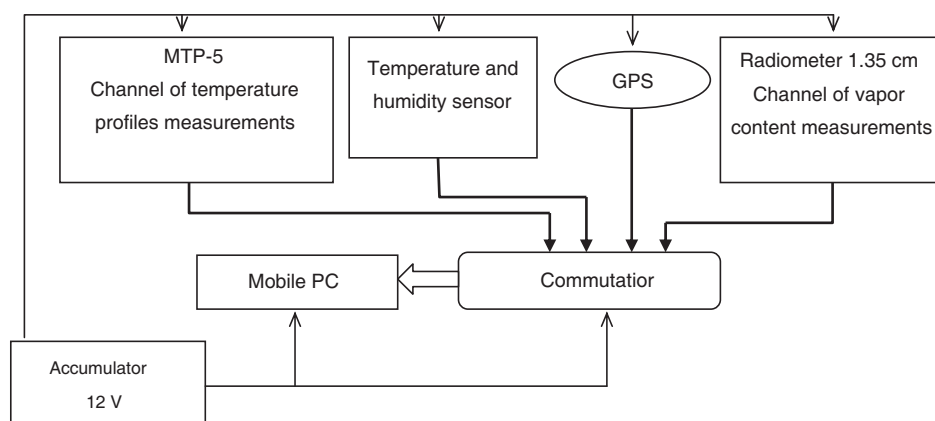


Figure 2: General structural chart of mobile microwave radiometric system.

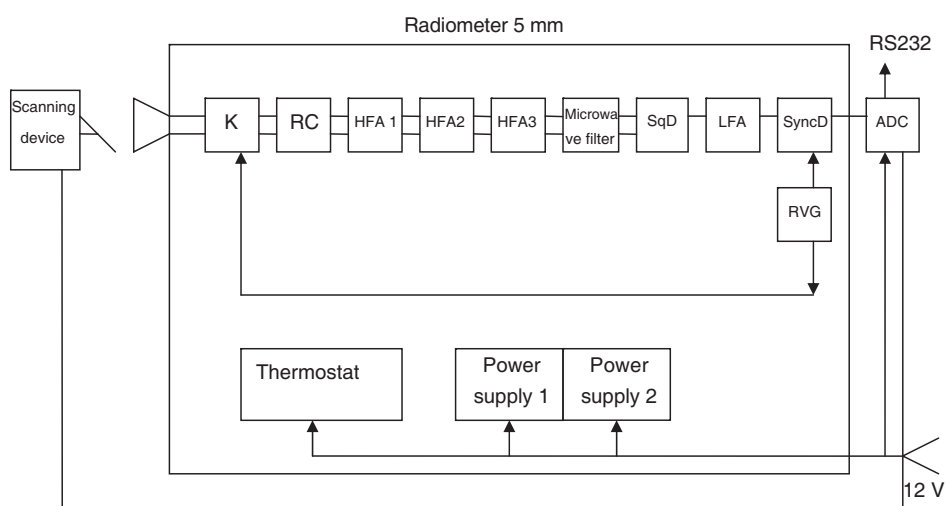


Figure 3: General structural chart of meteorological temperature profiler MTP-5.

Whole system placed in shell and powered from stabilized power supply by 12–15 Volt.

Microwave temperature profiler provides measurements of temperature in a range 0–600 meters with a step 50 meters every 5 minutes with inaccuracy $0.2-0.7^\circ\text{C}$ twenty-four hours a day almost in any conditions.

Instrument for measurements of total vapor content in atmosphere constructed on a basis of 1.35 cm range radiometer. Channel for measurements of integral water content consist of receiving horn antenna, thermo-coupling, broadband circulator which used for dividing receiving channels by frequencies, filter 1 to $f \sim 22253$ MHz (Δf -400 MHz), filter 2 to $f \sim 25$ GHz (Δf -600–800 MHz), modulator, broadband circulator $\mathcal{N}_0. 2$, wideband high-frequency amplifier, square detector with low-frequency amplifier and two synchronous detectors. Output of synchronous detector 1 give voltage v_1 analogical to receiver antenna temperature on frequency f_1 , output of synchronous detector 2 have voltage v_2 which analogical to temperature on frequency f_2 . Integral water content of atmosphere will proportional to difference of voltages $\Delta v = v_1 - v_2$. Utilization of this scheme allows to improve accuracy of measurements of total vapor content in atmosphere and to simplify calibration process. Comparisons with radiosondes showed that radiometer provides measurements of total vapor content with inaccuracy 0.2 g/cm^2 .

Creation of movable system for investigations of thermodynamic parameters of atmosphere solves problem of moving all system to different locations for measurements. For accurate navigation and for height monitoring system includes GPS-receiver. In a record mode location data writing into measurements data files simplifying data processing. Temperature and humidity sensors included in the system for monitoring of surface layer parameters and also for MTP-5 profiler calibration.

Mobile microwave system was successfully tested in the expedition to Karachay-Cherkess Republic, Stavropol Krai in an area of Kislovodk city and also in a mountains on different heights.

3. CONCLUSION

In a range of modern meteorological devices appeared new distant system for monitoring thermodynamic characteristics of atmospheric boundary layer. Utilization of this system can be useful both for fundamental investigations of atmosphere and surface layer interaction and for carrying out a range of applied works.

REFERENCES

1. Kadygrov, E. N., G. N. Shur, and A. S. Viazankin, "Investigation of atmospheric boundary layer temperature, turbulence, and wind parameters on the basis of passive microwave remote sensing," *Radio Science*, Vol. 38, No. 3, 8048, Mar. 12, 2003.
2. Kadygrov, E. N. and D. R. Pick, "The potential for temperature retrieval from an angular-scanning single-channel microwave radiometer and some comparisons with in situ observations," *Meteorological Applications*, Vol. 5, No. 4, 393–404, 1998.
3. Westwater, E. R., Y. Han, V. G. Irisov, V. Levskiy, E. N. Kadygrov, and A. S. Viazankin, "Remote sensing of boundary layer temperature profiles by a scanning 5-mm microwave radiometer and RASS: Comparison experiments," *Journal of Atmosp. and Ocean. Techn.*, Vol. 16, 805–818, Jul. 1999.
4. Troitsky, A. V., K. P. Gaykovich, E. N. Kadygrov, A. S. Kosov, and V. A. Gromov, "Thermal sounding of the atmosphere boundary layer in oxygen absorbtion band center," *IEEE Trans. on Geosciens and Remote Sensing*, Vol. 31, No. 1, 116–120, 1993.

Distance Measurement by Means of a Groove Guide Oscillator

Thomas F. Bechteler¹ and A. Sevinç Aydınlık Bechteler²

¹İzmir University, Turkey

²İzmir Institute of Technology, Turkey

Abstract— In this work, a system for measuring the distance between two metallic plates is presented. A groove guide resonator operating in the X-band with an incorporated Gunn element serves as the distance sensor. According to the distance between the two metallic plates, the resonant frequencies of the groove guide oscillator change. In a first step, the fundamental resonant frequency of the groove guide oscillator at various distances is computed by means of the FDTD (Finite Difference Time Domain) method. In a second step, the resonant frequencies of the realized groove guide oscillator were measured. Although the signal's wavelength is about 30 mm, the resolution of the measurement is in the sub-millimeter level, i.e., about 25 μm . Furthermore, in case of distance variations, even within a short time, the system is able to track distance variations nearly instantaneously. The resonant frequency information is processed using a heterodyne system.

1. INTRODUCTION

By presenting the groove guide as a novel waveguide structure, Tischer [1] initiated many works on the groove guide. EM-modes in the groove guide were given, for instance, in [2]. In [3–5], the groove guide was analytically analyzed, whereas in [6, 7] it was numerically analyzed. Possible coupling structures were investigated in [8, 9]. In this work, a groove guide resonator with an implemented Gunn element is presented. This groove guide oscillator can be used as a contact-less distance sensor. Fig. 1 illustrates two possible applications. First, the groove guide oscillator moves above a metallic surface and measures the distance h to this metallic surface. Second, the groove guide oscillator is mounted at a distance \bar{h} close to a rotating metallic drum. Due to the unbalance of the drum, the distance \bar{h} changes, which is detected by the groove guide oscillator. In both cases, the metallic surfaces serve as the counterpart of the groove guide structure.



Figure 1: Application examples for groove guide oscillator.

2. THE CIRCULAR GROOVE GUIDE OSCILLATOR

Figure 2 shows photographs of the manufactured groove guide oscillator and its closeup. Since the oscillator should operate in the X-band, the groove width, depth and diameter are $w = 15.0$ mm, $d = 5.0$ mm and $D = 60.0$ mm, respectively. The groove guide oscillator consists of a plane plate and a grooved plate, both with the dimensions 200×200 mm², and has been measured at various plate distances h . The diameter of the loop was chosen to be 10 mm, which is the optimum diameter according to the coupling investigations in [9]. The Gunn element as the active element is directly connected to the loop. Therefore, the loop serves for the microwave coupling as well as for the DC bias of the Gunn element.

Figure 3 shows the measurement results for the passive groove guide resonator and the active groove guide oscillator at three plate distances $h = 13.0$ mm, 14.0 mm and $h = 15.0$ mm. The difference between the resonant frequency of the resonator and of the oscillator at a certain plate distance h is due to the reactive part of the Gunn element's impedance.

Figure 4 plots the distance versus frequency data for three cases: First, for the simulated resonator (triangles), second, for the measured passive resonator (circles), and third, for the measured oscillator (stars). The straight lines, connecting the data points, are the interpolated data which serve for the calibration data stored on a computer. The frequency deviation between simulation

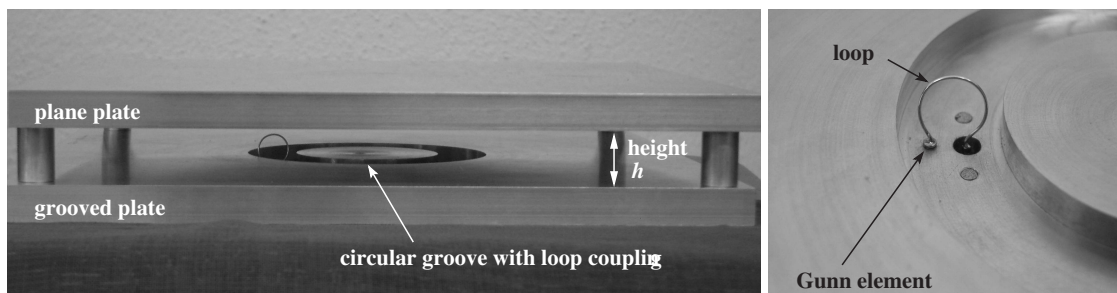


Figure 2: Photograph of groove guide oscillator and closeup of loop coupling.

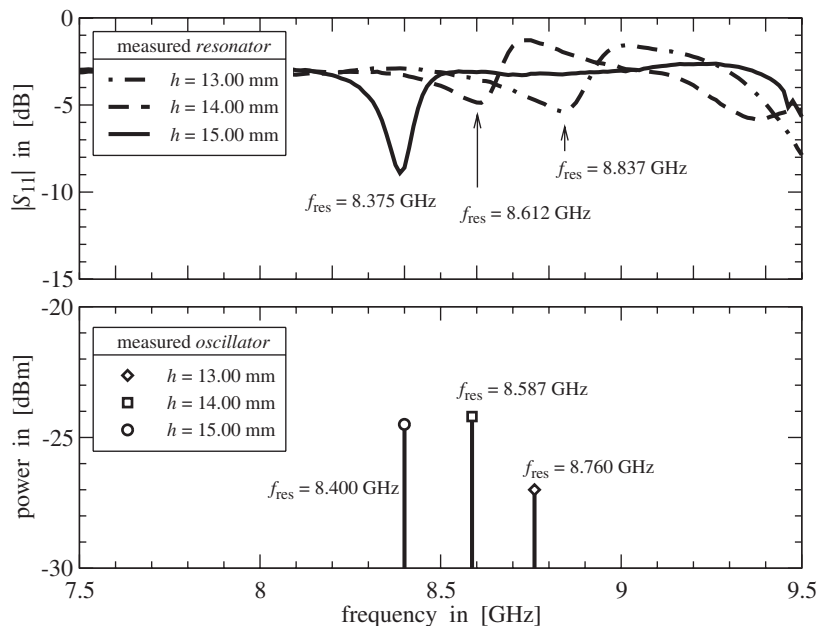


Figure 3: Measurement of the groove guide structure — passive and active.

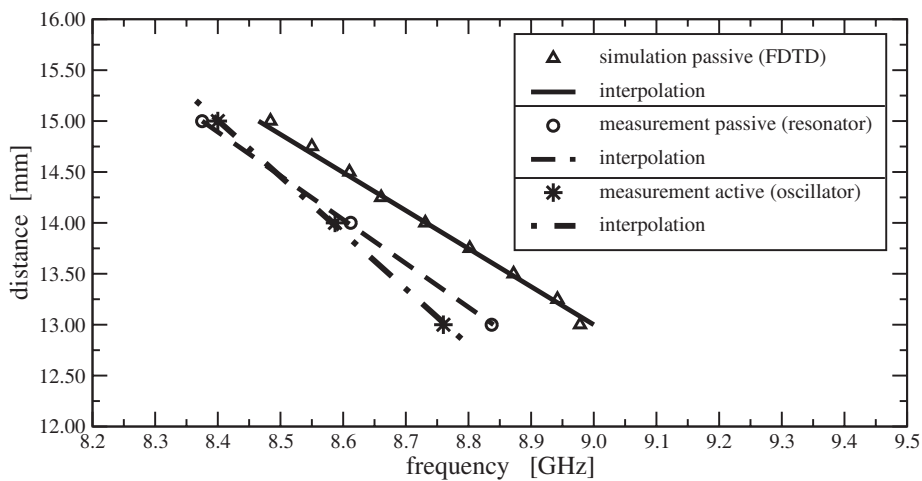


Figure 4: Interpolated distance versus frequency.

and measurement is due to fabrication errors of ± 0.05 mm. The frequency deviation between the measured passive resonator and the measured oscillator is due to the Gunn element, as mentioned before. Considering the interpolation curve for the measured oscillator, the sensitivity is determined

to

$$\frac{\Delta f}{\Delta h} = -181 \text{ MHz/mm.} \quad (1)$$

For instance, when the distance h increases by 0.1 mm, the resonant frequency decreases by 18.1 MHz.

3. THE HETERODYNE SYSTEM

In order to evaluate the groove guide oscillator's resonant frequency, a heterodyne system is realized. The block diagram of the heterodyne system is shown in Fig. 5. The groove guide oscillator is DC biased, and the resonant frequency is mixed down by means of a passive diode mixer. Since the evaluated signal is sinusoidal, no demodulator is required. The intermediate frequency is then directly measured by a frequency counter. The used frequency counter measures up to 2.5 GHz. Unwanted signals with a frequency higher than 2.5 GHz are filtered by an optional low-pass filter. The frequency counter is connected to a computer which contains the calibration data. Hence, the distance h between the two plates can be directly displayed on the computer screen.

The system's measurement accuracy is limited by the following three devices: the groove guide oscillator, the local oscillator and the frequency counter. Both, the stability of the implemented local oscillator (LO) and the accuracy of the frequency counter are better than the frequency stability of the groove guide oscillator. Hence, the measurement accuracy of the whole system is defined by the frequency stability of the groove guide oscillator. Most important is a highly stable DC bias of the Gunn element. The frequency accuracy has been determined to $\Delta f = \pm 5 \text{ MHz}$ which, according to Eq. (1), results in a distance measurement accuracy of $\Delta h = \mp 28 \text{ }\mu\text{m}$.

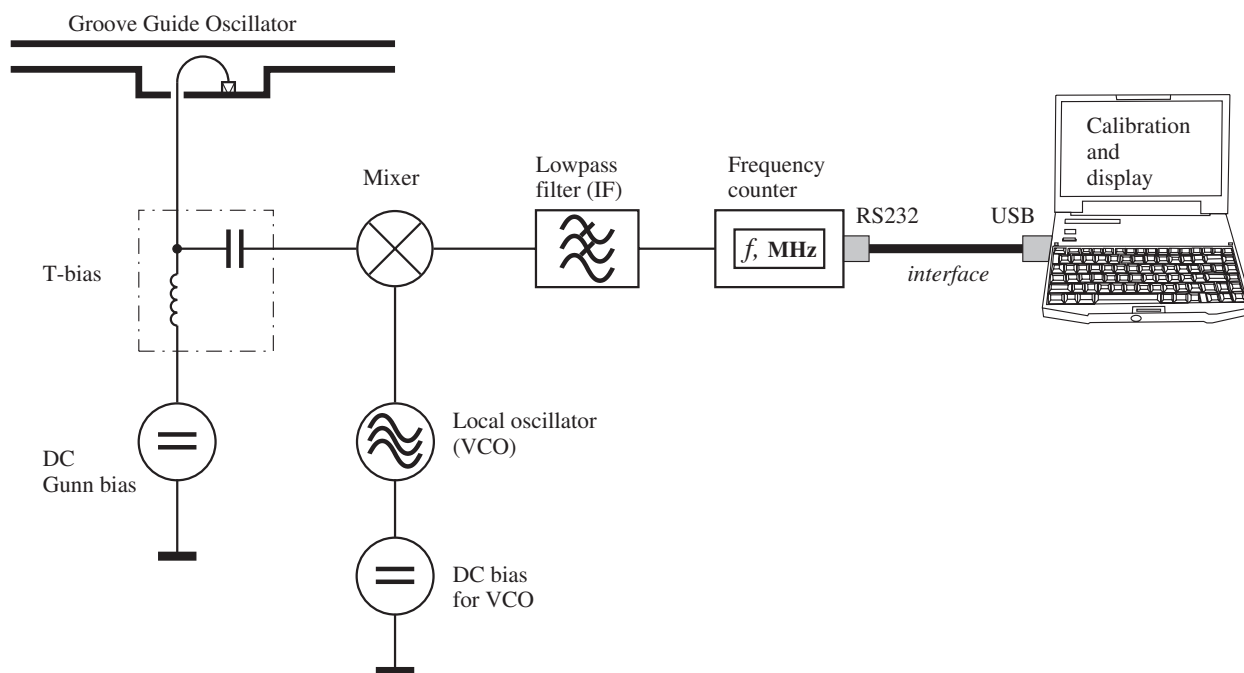


Figure 5: Heterodyne system for distance measurement.

4. CONCLUSION

In this paper, a distance measurement system with a groove guide oscillator as the distance sensor has been presented. A change in the distance between the two plates of the oscillator results in a change of its resonant frequency. This resonant frequency is evaluated by a heterodyne receiver connected to a computer.

Limitations of this system are, on the one hand, the measurement accuracy of about $25 \text{ }\mu\text{m}$, and, on the other hand, the measurement range of a few millimeters. The measurement accuracy is due to the DC bias stability of the Gunn element. Variations of the bias voltage result in variations in the resonant frequency. The measurement range is limited due to the multiple modes propagating in

the groove guide. Considering the frequency difference of about 500 MHz between two neighboring modes results in a measurement range of about 3 mm.

Another application which is under consideration, is the permittivity measurement of dielectric sheets. Such sheets can easily be inserted between the two plates of the groove guide oscillator and change its resonant frequency accordingly.

ACKNOWLEDGMENT

The authors would like to thank the Scientific and Technological Research Council of Turkey TÜBİTAK for the financial support of this project (106E100).

REFERENCES

1. Tischer, F. J., "The groove guide, a low loss waveguide for millimeter waves," *IEEE Trans. on Microwave Theory and Techn.*, Vol. 11, No. 9, 291–296, 1963.
2. Griemsmann, J. W. E., "The groove guide," *The Symposium on Quasi Optics*, 565–578, Polytechnic Institute of Brooklyn, Brooklyn, USA, June 1964.
3. Oliner, A. A. and P. Lampariello, "The dominant mode properties of open groove guide: An improved solution," *IEEE Trans. on Microwave Theory and Techn.*, Vol. 33, No. 9, 755–763, 1985.
4. Fernyhough, M. and D. V. Evans, "Full multimodal analysis of an open rectangular groove waveguide," *IEEE Trans. on Microwave Theory and Techn.*, Vol. 46, No. 1, 97–107, 1998.
5. Vertiy, A. A., S. P. Gavrilov, A. S. Aydınlik, and S. R. Samedov, "Circular groove shaped resonator for millimeter waves," *Int. Journal of Infrared and Millimeter Waves*, Vol. 17, No. 10, 1613–1637, 1996.
6. Bechteler, A. S. A., "Design, simulation and experimentation of a semi-symmetrical groove guide resonator in millimeter wave band," Ph.D. Thesis, İstanbul Technical University, İstanbul, Turkey, July 2003.
7. Bechteler, A. S. A. and L. Sevgi, "Millimeter waveband semisymmetrical groove guide resonators," *IEEE Microwave Magazine*, No. 9, 51–60, 2004.
8. Bechteler, T. F., "Analysis of excitations for a groove guide resonator at 10 GHz by means of the FDTD method," *Int. Journal of Infrared and Millimeter Waves*, Vol. 26, No. 6, 819–830, 2005.
9. Bechteler, T. F., A. Kuştepelı, and S. A. Bechteler, "Design of coupling structures for groove guide resonators," *Microwave and Optical Technology Letters*, Vol. 50, No. 5, 1406–1410, 2008.
10. Bildik, S., "Setup and calibration of a heterodyne receiver for microwave sensors," M.S. Thesis, İzmir Institute of Technology, İzmir, Turkey, July 2008.

Microwave and Millimeter Wave EBG Waveguide Circuits

S. E. Bankov

Institute of Radio Engineering and Electronics of Russian Academy of Science, Russian Federation

Abstract— Novel waveguide circuits for microwave and millimeter wave applications based on electromagnetic bandgap (EBG) structures are presented. The following aspects of the problem are discussed: Fundamentals of compensating sources technique for EBG circuits computer design, numerical analysis of regular waveguides inside bandgap arrays, analysis of waveguide components, experimental investigation of EBG components and devices.

1. INTRODUCTION

Electromagnetic bandgap (EBG) structures are a class of three-dimensional (3-D) periodic objects that prevent the propagation of electromagnetic waves in a specified frequency range for all angles of propagation and all polarization states [1]. These structures have a lot of applications [2]. Among them are structures with defects. A typical defect is a removed from array element which provides a cavity in EBG media that may be used for example as a high-Q resonator. Waveguide in EBG structure may be obtained in the same way as well as waveguide junctions and other elements.

Defects in EBG structures were mostly studied with help of numerical techniques. For example a powerful computational scheme based on a finite-difference time-domain (FDTD) technique is applied in [1] for EM field analysis in various 3-D and 2-D PBG structures.

The focus of this paper is effective analytical-numerical compensating sources technique (CST) based on an EBG structure Green's function and its applications to EBG waveguide circuits analysis. EBG structure sufficiently differs from continuous media and because of it special sources and special Green's function are introduced below. Proposed technique may be extended to 3-D case but only 2-D version is presented below.

2. CST SCHEME

CST scheme consists of two stages. At the first stage basis definitions are formulated and key problems are solved. Among them are:

- solution of a problem of plane wave scattering by a single element of array and presentation of scattered field as a sum of cylindrical harmonics with amplitudes depending on parameters of an incident wave;
- introduction of a compensating source (CS) which is a virtual source that produces field in form of a sum of cylindrical harmonics with fixed amplitudes, every CS is associated with some element of array;
- solution of a problem of regular array excitation by a CS and definition of a special Green's function (SGF) of a regular EBG array that connects vector of amplitudes of cylindrical harmonics produced by every element in array with vector of amplitudes of the CS;
- formulation of a boundary condition for amplitude vector of a defected element.

The second stage is analysis of an EBG structure containing defects that includes:

- substitution of a defected element by a regular element with CS with unknown amplitude vector;
- formulation and solution of a system of linear algebraic equations (SLAE) relatively unknown amplitude vectors of the above CS.

3. COMPENSATING SOURCES AND SPECIAL GREEN'S FUNCTION

A key problem for CST is a plane wave scattering by a two-dimensional cylinder (see Fig. 1) that may have arbitrary cross-section and may be metallic or magneto-dielectric one.

We suppose that scattered by a cylinder field E_{zsc} may be written in the following way:

$$E_{zsc} = \sum U_N(E_{zi}) H_N^{(2)}(k_0 r) e^{-iN\varphi} \quad (1)$$

where U_N — amplitudes depending on incident field E_{zi} , $H_N^{(2)}(x)$ — second type Hankel function of the N -th order, k_0 — free space wave number. Thus one may conclude that a total field inside array may be presented as a set of cylindrical harmonics excited by all elements of the array. CS produces field in the analogous way:

$$E_{zs} = \sum V_{sN} H_N^{(2)}(k_0 r) e^{-iN\varphi}, \quad (2)$$

SGF connects vector $\mathbf{V}_{p,q}$ of CS's amplitudes \mathbf{V}_{sN} with vector $\mathbf{U}_{n,m}$ of amplitudes U_N produced by an element which position in the array is characterized by indexes n, m (n corresponds to x coordinate and m to y coordinate, see Fig. 2). CS corresponds to the element with indexes p, q . Relation between $\mathbf{U}_{n,m}$ and $\mathbf{V}_{p,q}$ may be found with help of discrete Fourier transform analogously to free space Green's function:

$$\mathbf{U}_{n,m} = \mathbf{G}(n - p, m - q) \mathbf{V}_{p,q}, \quad (3)$$

where $\mathbf{G}(n - p, m - q)$ is SGF of regular array.

Boundary condition for widely used defect-removed from array element requires absence of scattered by such element field. It is absent if

$$\mathbf{U}_{n,m} = 0. \quad (4)$$

4. ANALYSIS OF EBG STRUCTURES WITH DEFECTS

Now let us consider as an example the simplest element-resonator, which is formed by one element with indexes 0,0 removed from regular array (see Fig. 3). In accordance with CST we should temporarily suppose that the array does not contain removed elements but CS with unknown amplitude vector \mathbf{V} is inserted in the element with indexes 0,0. Then applying relation (3) and substituting it in formula (4) one may obtain SLAE: $\mathbf{G}(0,0)\mathbf{V} = 0$. The SLAE has a non-trivial solution if determinant of matrix $\mathbf{G}(0,0)$ is equal to zero. Solving the equation $\det(\mathbf{G}(0,0)) = 0$ relatively frequency f one may find complex resonance frequencies of the resonator.

A special case is analysis of waveguide multi-port junctions that have semi-infinite waveguides as output ports. Direct application of scheme described above gives SLAE of an infinite order that is not suitable for numerical solution. Infinite SLAE reduction is based on the preliminary study of waveguide eigen modes. Knowledge of eigen waves allows one to describe fields in reference plane located enough far from junction as a sum of incident wave with known amplitude and reflected wave with unknown amplitude. It excludes semi-infinite waveguide from analysis and reduces SLAE order to a finite one.

Described in Sections 3 and 4 approach was realized as a computer program intended for design and investigation of a wide range of EBG elements. An important for numerical investigation step is a choice of a class of EBG structures. At microwaves good perspectives have EBG structures formed inside parallel plate waveguide (PPW) shown in Fig. 4. They may be fabricated in different ways in particularly as a printed circuit board [2]. Designed computer program allows one to analyze structures formed by cylinders with axial symmetry. In this paper will be presented numerical results obtained for metal and dielectric cylinders.

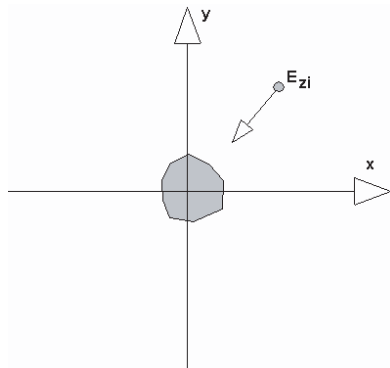


Figure 1. Array element.

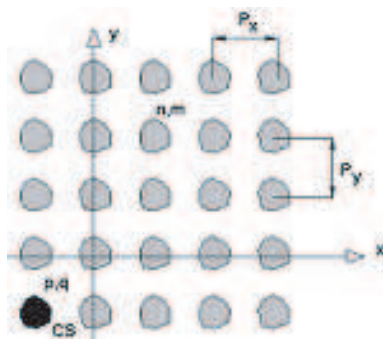


Figure 2. Array excitation.

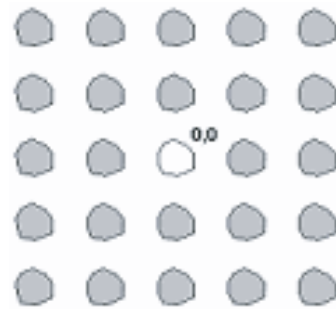


Figure 3. EBG resonator.

5. UNIFORM ARRAYS

Potential characteristics of EBG devices strongly depend on electromagnetic properties of basis structures: uniform arrays and infinite waveguides. We will consider in this section eigen modes of uniform arrays.

Zone structure is the most interesting for future investigation characteristic of a uniform array. The array in operating frequency range has only evanescent modes that may be characterized by attenuation factor α_e . Typical frequency dependencies of parameter $\alpha_e P$ (P — array period, the array has square grid) are shown in Figs. 5(a) and (b) that correspond to metal and dielectric cylinders.

In case of metal cylinders stop band (frequency range in which $\alpha_e \neq 0$) has only upper margin. Array is non-transparent up to zero frequency. Curves 1–3 in Fig. 5(a) are calculated for cylinders with radius $R = 0.75, 1, 1.5$ (all dimensions here and below are presented in millimeters). Stop bands for arrays of dielectric cylinders with $\varepsilon = 10$ and $R = 1, 1.5, 2$ (curves 1–3) are shown in Fig. 5(b). It is seen from these two pictures that dielectric cylinders provide much more narrow stop band than metal one.

6. REGULAR WAVEGUIDES AND COUPLED WAVEGUIDES

Regular waveguide formed by an infinite column (row) deleted from array is shown in Fig. 4. Investigation of its dominant eigen mode includes calculations of retardation factor U ($U = \beta/k$, β — propagation constant), attenuation factor α , operating frequency range $K = 2(f_{\max} - f_{\min}) / (f_{\max} + f_{\min})$, where f_{\max} and f_{\min} are maximal and minimal frequencies of the range.

Cutoff frequency of the dominant wave defines frequency f_{\min} . Cutoff frequency of a uniform array eigen mode defines f_{\max} (the array becomes transparent at $f > f_{\max}$). Dependence of parameter K on normalized to array period diameter of metal cylinder d is shown in Fig. 6. The same parameter of a standard waveguide is equal to 0.66. It is seen that EBG waveguide operating frequency range may be even greater than range of standard waveguide. Theoretical frequency dependence of retardation factor and experimental points are shown in Fig. 7. Calculated and measured results are in a good agreement.

Theoretical dependence of attenuation factor (curve 1) on frequency with experimental points are presented in Fig. 8. For comparison standard waveguide (23×10 mm) attenuation factor (curve 2) is also shown in Fig. 8. Results shown in Figs. 7 and 8 were calculated for cylinders with diameter $D = 5$ and array period $P = 12.5$.

System of coupled waveguides consisting of two waveguides is shown in Fig. 10(a). The system is characterized by two eigen modes: odd and even with retardation factors U_o, U_e . Coupling coefficient $C = (U_o - U_e)k/2$ also describes coupled waveguides. Theoretical dependence of coefficient C on frequency f and experimental points obtained for waveguides with $D = 5$ and $P = 12.5$ are shown in Fig. 9.

7. MULTIPORT DEVICES

Directional coupler (DC) and several power dividers were designed and optimized for applications in microwave range. They are shown in Figs. 10 and 12. The main part of DC is a section of coupled waveguides (see Fig. 10). Odd and even modes interference produces energy transmission from port 1 to port 3 as it is shown in Fig. 11. Isolation and return loss of the DC are less than -20 dB.

The following dividers were investigated and optimized: linear power divider, T-type divider and

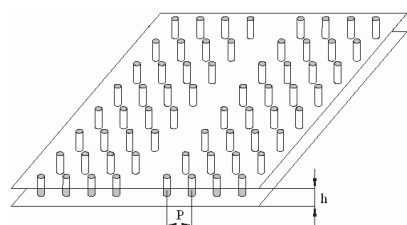


Figure 4. EBG structure in PPW.

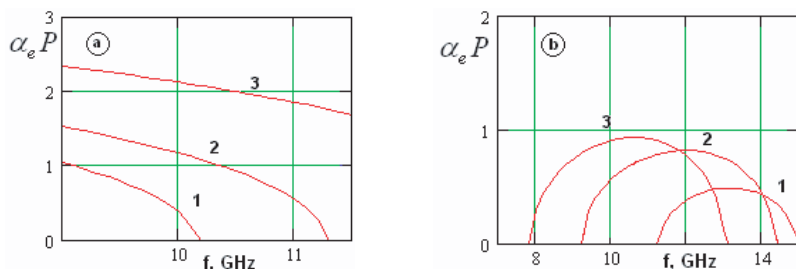


Figure 5. Attenuation factor of uniform array waves.

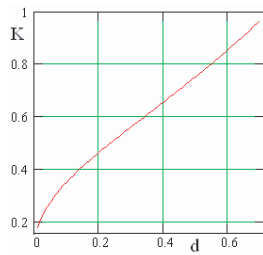


Figure 6. Waveguide operating frequency range.

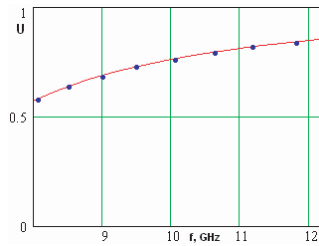


Figure 7. Retardation factor.

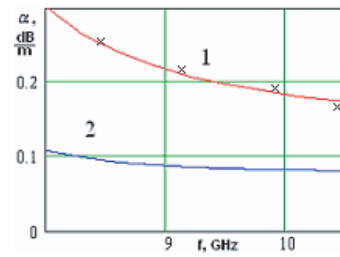


Figure 8. Attenuation factor.

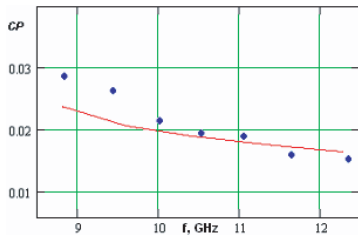


Figure 9. Coupling coefficient.

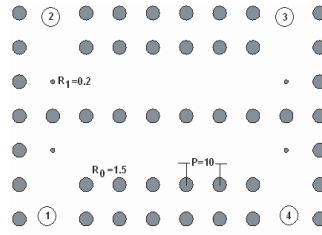


Figure 10. Directional coupler.

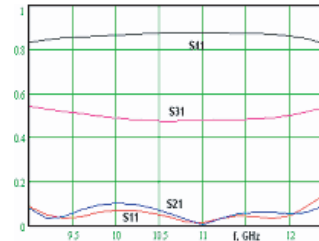


Figure 11. Coupler S -parameters.

four-port divider (shown in Figs. 12(a)–(c)). Corresponding dependencies of their S -parameters are presented in Figs. 13(a)–(c). T-type divider has compact dimensions and demonstrates good matching in wide frequency range and thus it may be used as an element of multi-channel feeding circuits for antenna arrays. Four-port divider may be considered as an example of such more complicated circuit that contains three T-type dividers. Its design is more complicated problem than in case of conventional waveguide divider because walls separating EBG waveguides are partially transparent and produce undesirable inter-channel coupling. Due to it four-port divider is not a simple combination of two-port dividers (see Fig. 12(c)).

8. INTERLAYER CONNECTORS

All presented above devices have planar structure. Multi-layer circuits present additional opportunities. Waves in such circuits propagate from one layer to another through so-called interlayer connectors. Two types of connectors were considered: forward and backward. Backward connector is shown in Fig. 14. Both connectors include coupling slot and two semi-infinite waveguides. Connector bandwidth strongly depends on PPW height h . The best results were obtained for $h = 5$. They are shown in Fig. 15. Curves 1,2 correspond to forward (backward) connectors with the following parameters: $w = 2(3)$, $L = 29(24)$, $c = 6.5(4)$, parameters t , P , D are same in both cases — $t = 1$, $P = 12.5$, $D = 5$.

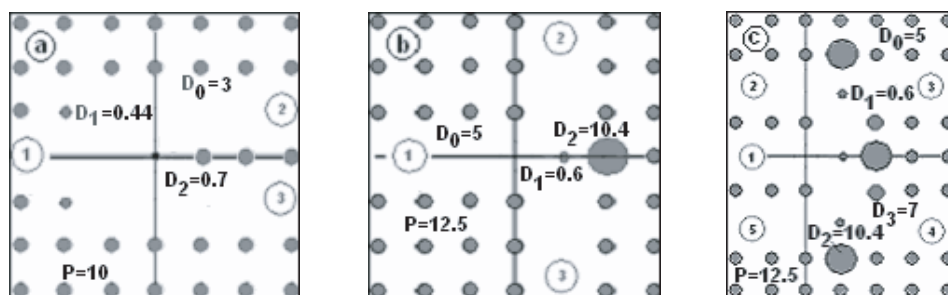


Figure 12. Power dividers.

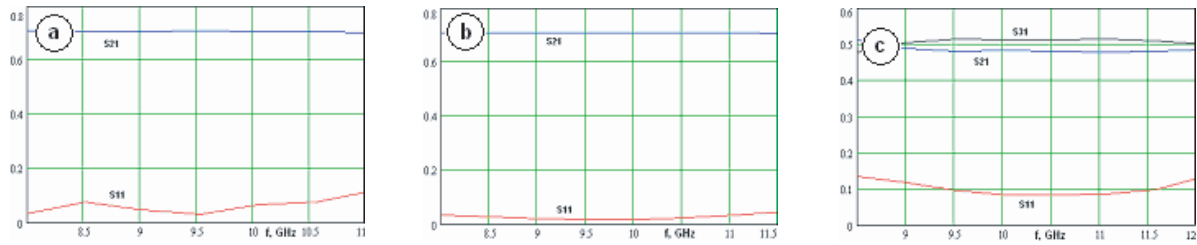
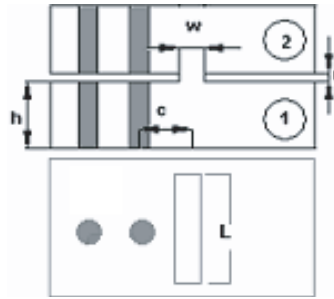
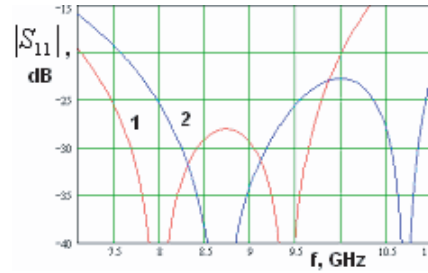
Figure 13. S -parameters of power dividers.

Figure 14. Interlayer connectors.

Figure 15. Connectors S -parameters.

ACKNOWLEDGMENT

Presented work was supported by Russian Foundation of Fundamental Researches, grant 08-08-12200-ofi.

REFERENCES

1. Mosallaei, H. and Y. Rahmat-Samii, "Periodic bandgap and effective dielectric materials in electromagnetics," *IEEE Trans. AP*, Vol. 51, No. 3, 549–563, 2003.
2. Simpson, J. J., A. Taflove, J. A. Mix, and H. Heck, *IEEE Microwave and Wireless Comp. Lett.*, Vol. 14, No. 7, 356, 2004.

Phased-array Antenna Ferroelectric Phase Shifter for a Higher Microwave Power Level

O. G. Vendik¹, A. N. Vasiliev¹, M. D. Parnes²,
A. E. Nikitenko², and R. G. Shifman³

¹St. Petersburg Electrotechnical University, Russia

²Resonance Ltd., St. Petersburg, Russia

³Svetlana-EP, St. Petersburg, Russia

Abstract— The mass production of the phased-array antenna needs in the phase shifters with the following substantial characteristics: 1) Small power in the biasing networks, 2) Relatively high microwave power, 3) Low production cost. This problem can be solved by using thin film ferroelectric tunable capacitors. The basic components of the transmission type phase shifter are reflection type phase shifters in a combination with a branch line hybrid junction. The reflection type phase shifter is formed as a parallel junction of ferroelectric tunable capacitors and of an inductive component. Analysis shows that, if the maximum biasing voltage is 200 V, the amplitude of the microwave voltage across the tunable capacitors can reach 20 V or 50 V for different design versions without essential cross modulation. That provides 1 W or 10 W in pulse for each reflection type phase shifter. The duration of the phase distribution rearrangement is estimated as nanosecond time interval. Thereafter, a small capacitance of the tunable capacitors provides a small recharge current. A leakage current of the ferroelectric capacitors is smaller than 10^{-9} A. The information about industrial production of microwave ferroelectric devices of low cost is now available.

Methods of modeling and design of the ferroelectric components and systems have been developed. The phase shifters have been designed for phased-array antennas, smart antennas, and other communication and radar applications.

Results of the simulation and experimental investigation of the phase shifter based on (Ba,Sr)TiO₃ films at the frequency 3.7 GHz are discussed.

1. INTRODUCTION

The phase shifters for phased-array antennas were being studied many years and some theoretical and experimental results have been reported [1–3]. The possibility to obtain an electrically steering of the radiation pattern of such an antenna is currently under investigation [4, 5]. The characteristic features of the ferroelectric films oriented for application at microwave devices have been carefully studied [6, 7]. The realization of industrial production of low cost ferroelectric phase shifter has been reported [8].

The goal of this paper is to present an experimental realization of a ferroelectric phase shifter designed for application in the case of a higher microwave power. The following characteristic features of the ferroelectric phase shifter intended for operation under a higher microwave power should be proclaimed [8, 9]:

- 1) The *dc* biasing voltage applied to control the capacitances must be much higher than the microwave voltage across the capacitor. The reasonable value of the *dc* biasing voltage is 200 V.
- 2) The reflection type phase shifter is used as basic components of a transmission type phase shifter. The reflection type phase shifters are combined with branch line hybrid junctions. The reflection type phase shifter should be formed as a parallel junction of ferroelectric tunable capacitor and an inductive component.
- 3) Each active component should be formed by two ferroelectric tunable capacitors, which are connected in parallel with respect to the microwave voltage and in series with respect to the *dc* biasing voltage. Such a scheme provides sufficient decreasing of a modulation of the total capacitance of two capacitors by the microwave voltage and eliminating the cross modulation of the signals.

Design arrangement of the phase shifter discussed is based on (Ba,Sr)TiO₃ films included in a thin film interdigital capacitors.

2. SIMULATION OF THE PHASE SHIFTER

In Fig. 1, the scheme of the phase shifter is shown.

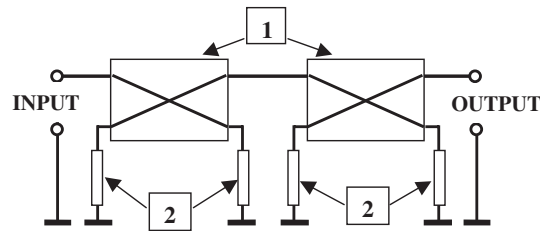


Figure 1: The scheme of the phase shifter 1) Hybrid junctions, 2) Single reflection type phase shifters.

The typical quadrature hybrids are used. The simplest version of the reflection type phase shifter is formed as a parallel junction of a tuneable capacitor and an inductor. The scheme of such a phase shifter is shown in Fig. 2.

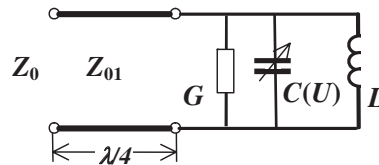


Figure 2: The scheme of the reflection type phase shifter. The quarter wave length transformer is used to provide the required tuneable phase shift in the case of given value of the tuneable capacitance.

Impedance of the parallel contour (Fig. 2) is determined as a function of controlling parameter $q(U)$ and frequency:

$$Z(f, q(U)) = \frac{1}{\left[iX_0 \cdot \frac{f}{f_0} \right]^{-1} + \left[-iX_0 \cdot \frac{f_0}{f} \cdot \frac{2q(U)}{n+1} \cdot \left(1 + i \cdot \frac{\tan \delta}{q(U)} \right) \right]^{-1}}. \quad (1)$$

Here f_0 — is the resonance frequency. That corresponds to:

$$L = \frac{X_0}{2\pi f_0}; \quad C_0 = \frac{1}{2\pi f_0 X_0}. \quad (2)$$

Parameter n is the tunability of the capacitor. We suppose that $n = 2$.

The controlling parameter can be presented as follows:

$$q(U) = \frac{C(0)}{C(U)}. \quad (3)$$

The reflection coefficient from the reflection type phase shifter is

$$\Gamma(f, q(U)) = \frac{Z_1(f, q(U)) - Z_{00}}{Z_1(f, q(U)) + Z_{00}}, \quad (4)$$

where in accordance with nomination in Fig. 2

$$Z_{00} = \frac{Z_{01}^2}{Z_0}. \quad (5)$$

The phase shift and the dissipation of the reflected wave are determined as follows:

$$\varphi(f, q(U)) = \frac{180}{\pi} \cdot \arg(\Gamma(f, q(U))); \quad L(f, q(U)) = 20 \cdot \log(|\Gamma(f, q(U))|). \quad (6)$$

Microwave voltage across the tuneable capacitor is determined by the power of the incident wave P_{incid} and the reflection coefficient from the reflection type phase shifter

$$U_C(f, q(U)) = \sqrt{2Z_0 P_{\text{incid}}} \cdot |1 + \Gamma(f, q(U))|, \quad (7)$$

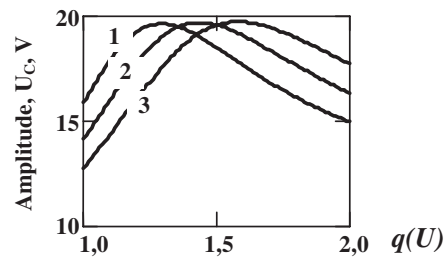


Figure 3: Microwave voltage across the tuneable capacitor in the case $P_{\text{incid}} = 1 \text{ W}$, $Z_0 = 50 \text{ Ohm}$ for different frequencies 1) 3.6, 2) 3.8, 3) 4.0 GHz.

It was shown [4], that the tuneable phase shift from a reflection type phase shifter can reach 360° , but as the phase shift is near 360° , incident power is fully dissipated. Thus to have a reasonable efficiency of the phase shifter the value of the tuneable phase shift of one reflection type phase shifter was selected to be 180° .

3. EXPERIMENTAL REALIZATION OF THE REFLECTION TYPE PHASE SHIFTER

In Fig. 4, the photo of design of the reflection type phase shifter is shown.

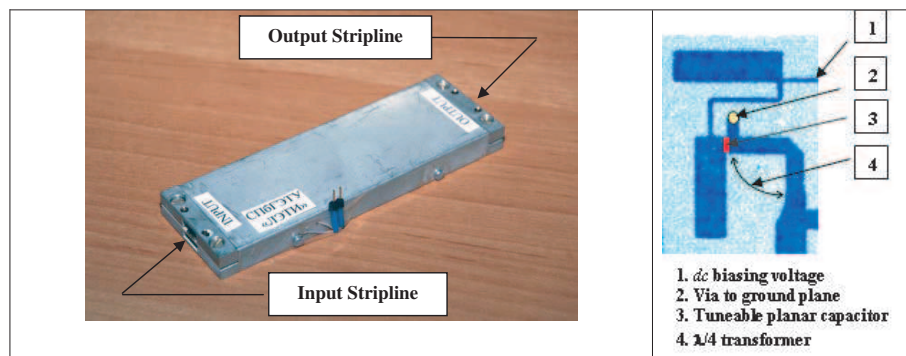


Figure 4: Design of the phase shifter.

The design shown in Fig. 4 corresponds to the scheme of Fig. 1. At the right part of the picture, the design of a single reflection type phase shifter is shown. The via to ground plane and a short stub form the inductor, which is included in parallel with the tuneable planar capacitor. The quarter wave length sections of wide transmission lines serve as a short circuit of the tuneable planar capacitor to the ground plane and as a short circuit in the dc - RF filter in the line of dc biasing voltage.

The tuneable planar capacitor is formed as an interdigital capacitor based on $(\text{Ba,Sr})\text{TiO}_3$ film of thickness $0.6 \mu\text{m}$ on alumina substrate.

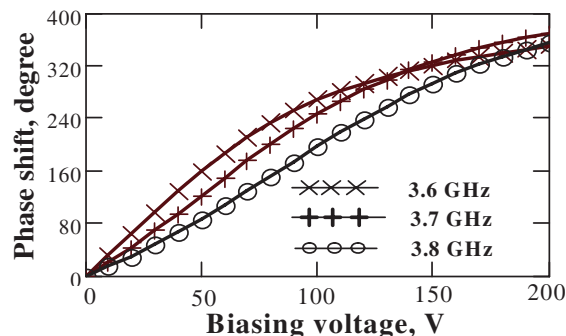


Figure 5: Phase shift of the transmission type phase shifter as a function of the biasing voltage for different frequencies.

As a background of the whole construction the thin copper foil-clad dielectric substrate is used. The dielectric permittivity of the main substrate is $\epsilon_S = 2.8$.

In Figs. 5–7, the result of an experimental investigation of the transmission type phase shifter is shown.

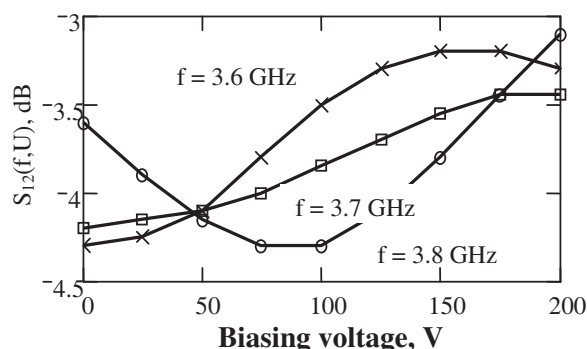


Figure 6: Insertion loss of the transmission type phase shifter as a function of the biasing voltage for different frequencies.

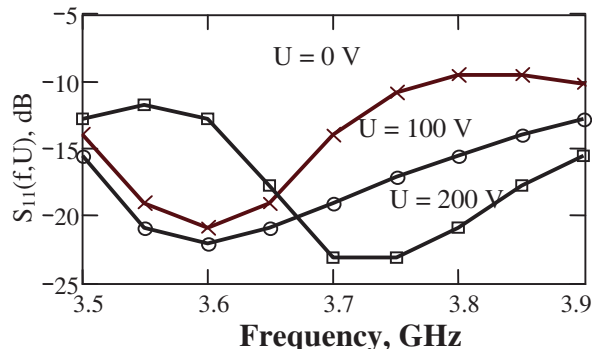


Figure 7: Return loss of the transmission type phase shifter for different value of the biasing voltage.

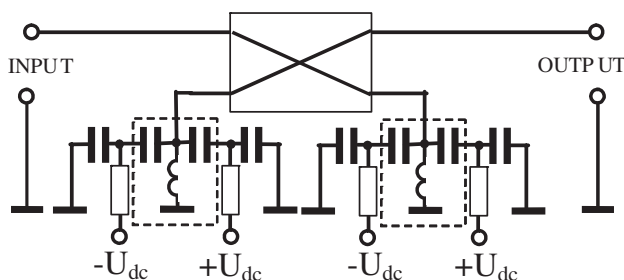


Figure 8: A section of a transmission type phase shifter with modified reflection type phase shifters.

4. DISCUSSION

Manufacturing of the phase shifter based on ferroelectric interdigital planar tunable capacitors and a thin copper foil-clad dielectric substrate is promising for the realization of a low cost phase-array antenna. However one has to pay an attention to the high insertion loss of such a phase shifter. Such a problem was discussed a couple of year ago in connection with a ferroelectric reflection type phase shifter [3]. It was shown that two main contributing losses in the ferroelectric phase shifter should be distinguished: the loss in the tunable capacitor and the loss in the associated circuitry (metallization and substrate). At the level of modern technology, the values of these two kinds of losses are quite comparable. It was proclaimed [3] that one may anticipate that the real figure-of-merit of a ferroelectric tunable phase shifter can reach the value -200 deg/dB . In the phase shifter realized in this work we have the figure-of-merit -90 deg/dB . Sufficient contribution to the insertion is given by the quarter wave length sections of wide transmission lines serving as a short circuit to the tunable planar capacitor to the ground plane and as a short circuit in the dc - RF filter in the line of dc biasing voltage. These quarter wave length sections could be replaced by blocking capacitors in combination with via junctions. Unfortunately the high quality microwave blocking capacitors for 200 V operational voltage are rather expensive. That is in contradiction with the main idea to design a low cost phase-array antenna. As we know from the industrial practice, such a problem can be solved in the process of developing mass production.

As it is shown in the Section 2 of this paper, the 1 Watt of the microwave power, which incidents to a single reflection type phase shifter, provides 20 Volt amplitude of microwave voltage across the tunable capacitor. The 20 Volt amplitude is 10% of the maximum of the biasing voltage. The simple simulation shows that in this case the modulation of the capacitance of a tunable capacitor by the microwave voltage is about 1%. Such value of modulation is acceptable. One may consider a modified version of a reflection type phase shifter (Fig. 8) [9]. In this case two tunable capacitors

are included in parallel with respect to the microwave voltage and in series with respect to the dc biasing voltage. In such a version of a reflection type phase shifter, the 50 Volt amplitude or 25% of the maximum of the biasing voltage provides of 1% modulation of the capacitance of a tuneable capacitor. That corresponds to 10 Watt of the controlled microwave power.

5. CONCLUSION

The design of the transmission type phase presented in this paper can be considered as preparatory period of an industrial mass production. The estimation of the microwave power for two versions of a reflection type phase shifter section has shown that microwave power can reach value of 1 W or 10 W. The experimental investigation of operation of the phase shifter under the higher microwave power will be soon reported.

REFERENCES

1. Romanofsky, R., J. Bernhard, G. Washington, F. VanKeuls, F. Miranda, and C. Cannedy, "K-band phased array antenna based on $Ba_{0.60}Sr_{0.40}TiO_3$ thin film phase shifters," *IEEE Trans. MTT*, Vol. 48, No. 12, 2504–2510, Dec. 2000.
2. Sherman, V., K. Astafiev, N. Setter, A. Tagantsev, O. Vendik, I. Vendik, S. Hoffmann-Eifert, and R. Waser, "Digital reflection-type phase shifter based on a ferroelectric planar capacitor," *IEEE Microwave and Wireless Components Letters*, Vol. 11, No. 10, 407–409, Oct. 2001.
3. Vendik, O. G., "Insertion loss in reflection-type microwave phase shifter based on ferroelectric tunable capacitor," *IEEE Trans. MTT*, Vol. 55, No. 2, 425–429, Feb. 2007.
4. Vendik, O. G. and M. Parnes, "A phase shifter with one tunable component for a reflectarray antenna," *IEEE Antennas and Propagation Magazine*, Vol. 50, No. 4, 53–65, Aug. 2008.
5. Romanofsky, R., "Array phase shifters: Theory and technology," *NASA/TM*, 214906, Glenn Research Center, Cleveland, Ohio, USA, 2007.
6. Tagantsev, A. K., V. O Sherman, K. F. Astafiev, J. Venkatesh, and N. Setter, "Ferroelectric materials for microwave tunable applications," *Journal of Electroceramics*, Vol. 11, 5–63, 2003.
7. Vendik, O. G. and S. P. Zubko, "Modeling microwave dielectric characteristics of thin ferroelectric films for tunable planar structures," *Integrated Ferroelectrics*, Vol. 34, No. 1–4, Pt. 5, 215–226, 2001.
8. nGimat Co, "A low cost analog phase shifter product family for military, commercial and public safety applications," *Microwave Journal*, Vol. 49, No. 3, 152, Mar. 2006.
9. Vendik, O. G., "Ferroelectrics find thier "niche" between tuneable microwave divices," *Solid Stata Physics [Fizika Tverdogo Tela*, St. Petersburg], Vol. 51, No. 7, 1441–1445, 2009.

Optimum Design of Low Pass Filters for General LC Network Configurations by the Method of Least Squares

H. Oraizi and M. S. Esfahlan

Department of Electrical Engineering, Iran University of Science and Technology
Tehran 1684613114, Iran

Abstract— There are several classic methods for the design of low pass, high pass, band pass and band stop filters, such as Butterworth, Chebyshev, elliptic, k-constant, m-derived and insertion loss methods. We present here a design procedure based on the method of least squares using the insertion loss, which also incorporates the impedance matching of the load to source impedances in desired frequency bands. By this method we can design low pass filters with arbitrary LC configuration.

1. INTRODUCTION

Filters are commonly designed by the Butterworth, Chebyshev, elliptic, k-constant and m-derived methods [1, 2]. Each one of these design methods has its own advantages and has specific circuit configurations and frequency response characteristics. The order of filters should be altered to achieve the specified frequency response. However, it is quite possible to achieve the desired performance by lower order filter circuits than those required by the common configuration and design methods.

The proposed method of filter design based on the method of least square will achieve the specified frequency response by the construction of an error function using the insertion losses (in the pass, transition and stop bands) [3]. The error function is minimized with respect to the values of lumped inductance (L) and capacitance (C) and its minimization of the error function may be performed by any optimization method, but we use the combination of genetic algorithm (GA) [4, 5], and conjugate gradient method (CG).

Referring to the two-port network in Fig. 1, where the source voltage E_S with internal impedance Z_S is connected to the input port and the load impedance is connected to the output port. Since the filter is a cascade of reactive elements, the overall $ABCD$ matrix of the filter circuit may be obtained as the product of $ABCD$ matrices of the circuit blocks. As shown in Fig. 1, the input voltage and currents are related to those at the output port by following equation:

$$\begin{bmatrix} V_1 \\ I_1 \end{bmatrix} = \begin{bmatrix} A & B \\ C & D \end{bmatrix} \begin{bmatrix} V_2 \\ I_2 \end{bmatrix} \quad (1)$$

The source voltage using $V_2 = Z_L I_2$ is:

$$E_S = Z_S I_1 + V_1 = [Z_S(CZ_L + D) + (AZ_L + B)] I_2 \quad (2)$$

where $Z_S = R_S + jX_S$ and $Z_L = R_L + jX_L$.

The available power P_{avs} is the highest power, which the source delivers to the input of two port network under the condition on its input impedance $Z_{in} = Z_S^*$. Then

$$P_{avs} = \frac{|E_S|^2}{8R_S} \quad (3)$$

The input power to the load impedance is:

$$P_L = \frac{1}{2} R_L |I_2|^2 \quad (4)$$

Therefore, the power loss ratio is:

$$P_{LR} = \frac{P_{avs}}{P_L} = \frac{|AZ_L + B + CZ_S Z_L + DZ_S|^2}{4R_S R_L} \quad (5)$$

Since the transmission coefficient is [3]:

$$S_{21} = \frac{2\sqrt{R_S R_L}}{AZ_L + B + CZ_S Z_L + DZ_S} \tag{6}$$

The power loss ratio would be equal to:

$$P_{LR} = \frac{1}{|S_{21}|^2} \tag{7}$$

2. DESIGN PROCEDURE AND VALIDATION OF THE METHOD

For the filter design, several parameters are specified, such as the frequency bandwidth of the pass band, transition band, cut-off band, the value of ripple voltages in the pass band and cut-off band attenuation.

Now, we construct an error function according to the frequency response in the pass band, transition band and stop band as shown in Fig. 2. Therefore, the filter frequency response should pass through the white area in Fig. 2 and avoid the dashed regions. The error function is taken as the sum of the following partial errors.

$$ER_P = \sum_{k=1}^{K_P} \frac{1}{2} \left[1 - \text{sign} \left(\left| S_{21}^k \right|_{\text{dB}} - L_{Ar} \right) \right] \left(\left| S_{21}^k \right|_{\text{dB}} - L_{Ar} \right)^2$$

$$ER_T = \sum_{k=K_P+1}^{K_T} \frac{1}{2} \left[1 + \text{sign} \left(\left| S_{21}^k \right|_{\text{dB}} - L_{At} \right) \right] \left(\left| S_{21}^k \right|_{\text{dB}} - L_{At} \right)^2$$

$$L_{At} = L_{As}(f_i - f_p)/(f_s - f_p)$$

$$ER_S = \sum_{k=K_T+1}^{K_S} \frac{1}{2} \left[1 + \text{sign} \left(\left| S_{21}^k \right|_{\text{dB}} - L_{As} \right) \right] \left(\left| S_{21}^k \right|_{\text{dB}} - L_{As} \right)^2$$
(8)

where L_{Ar} is the ripple amplitude in the pass band, L_{As} is the minimum allowable losses in the stop band and $\text{sign}(x)$ is defined as follows:

$$\text{sign}(x) = \begin{cases} -1 & x < 0 \\ 1 & x \geq 0 \end{cases} \tag{9}$$

The total error is

$$\text{Error} = W_P \times ER_P + W_T \times ER_T + W_S \times ER_S \tag{10}$$

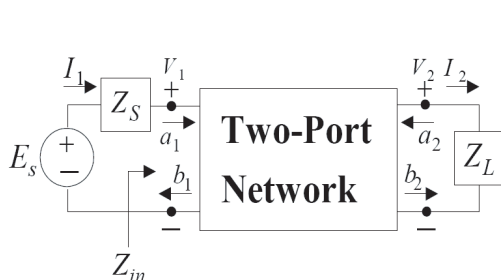


Figure 1: Schematic diagram of a two port network.

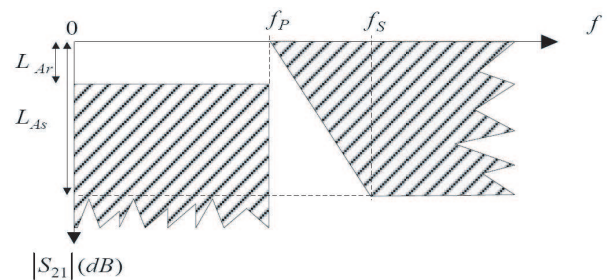


Figure 2: Diagram of design specifications.

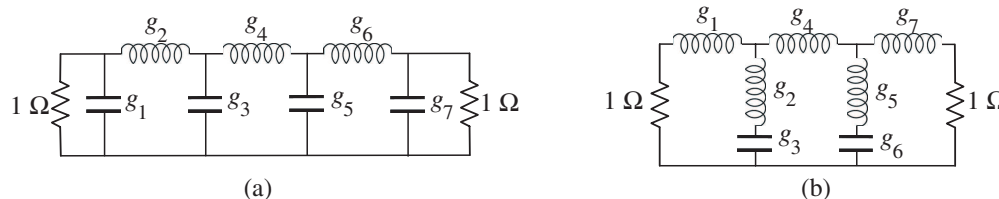


Figure 3: Low pass prototype filter for (a) Chebyshev function; (b) elliptic function.

where W_P , W_T and W_S are weighting factors.

Now we present several MLS design examples for the low pass filters and compare them with the common design procedures. First, we present filter designs with the configurations and specifications available in the literature as in Fig. 3(a) for a Chebyshev function and Fig. 3(b) for an

Table 1: Element values for Chebyshev and elliptic functions low pass prototype filter $R_S = R_L = 1 \Omega$, $\omega_p = 1 \text{ rad/sec}$, $\omega_S = 1.6129 \text{ rad/sec}$, $L_{Ar} = 0.1 \text{ dB}$.

		L_{As}	g_1	g_2	g_3	g_4	g_5	g_6	g_7	Error
Chebyshev	Literature [1]	41.9 dB	1.1812	1.4228	2.0967	1.5734	2.0967	1.4228	1.1812	—
	Designed by MLS		1.115	1.4429	2.055	1.5749	2.14	1.4046	1.245	3.59E-21
			1.21	1.3955	2.11	1.5797	2.07	1.4575	1.14	0
			1.165	1.4541	2.07	1.5720	2.125	1.3945	1.195	0
elliptic	Literature[1]	47.6 dB	1.0481	0.1244	1.2416	1.6843	0.354	1.0031	0.8692	—
	Designed by MLS		1.0385	0.1237	1.245	1.6903	0.3558	1.0000	0.8721	2.00E-16
			1.0816	0.1281	1.22	1.6952	0.3478	1.015	0.8535	5.28E-06
			1.0669	0.1273	1.235	1.6907	0.3494	1.01	0.8680	2.26E-06

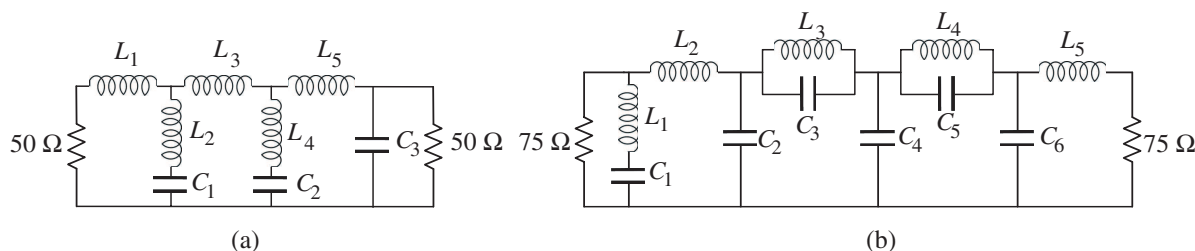


Figure 4: Design by the method of least squares.

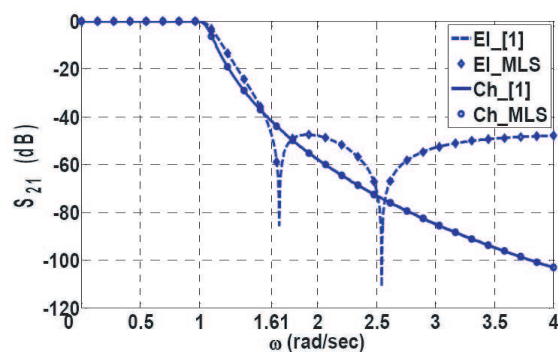


Figure 5: Frequency responses of Chebyshev and elliptic filter and their corresponding designs by the method of least squares.

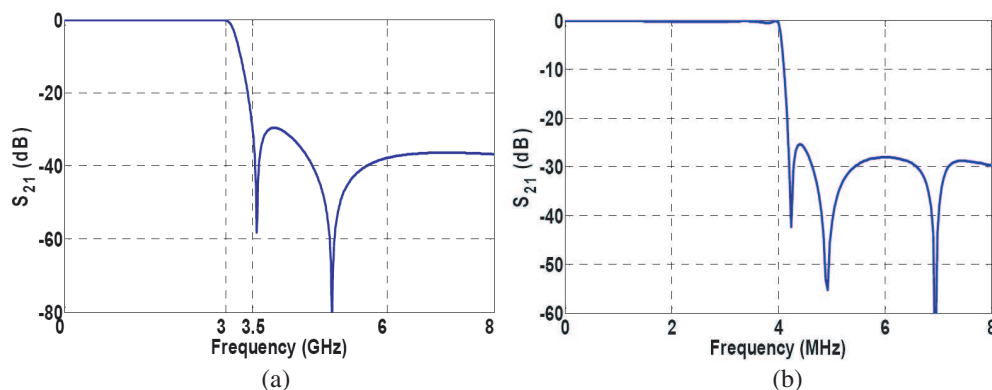


Figure 6: Filter design by the method of least squares for circuit configuration in Figs. 4(a) and (b) respectively.

elliptic function [1]. Filters with the same specifications are designed three times by MLS. The values of design parameters as g_i for Fig. 3 configurations are given in Table 1.

The frequency responses as $|S_{21}|$ of the filters are drawn in Fig. 5 and in the legend of this figure, Ch_[1] denotes Chebyshev filter configuration and El_[1] denotes elliptic filter configuration as given in reference [1]. MLS denotes for first design of Table 1 by the method of least squares.

Another filter designs are performed by MLS for the circuits in Fig. 5. Their frequency responses are drawn in Fig. 6 and the values of their reactive elements are given in Table 2 and Table 3.

Table 2: Element values for a designed (MLS) low pass filter $R_S = R_L = 50 \Omega$, $f_p = 3 \text{ GHz}$, $f_s = 3.5 \text{ GHz}$.

L_{Ar}	L_{As}	L_1 (nH)	L_2 (nH)	C_1 (pF)	L_3 (nH)	L_4 (nH)	C_2 (pF)	L_5 (nH)	C_3 (pF)
0.1 dB	30 dB	1.568	0.8294	1.23	2.8615	2.267	0.8701	2.7519	1.12

Table 3: Element values for a designed (MLS) low pass filter $R_S = R_L = 75$, $f_p = 4 \text{ MHz}$, $f_s = 4.2 \text{ MHz}$.

L_{Ar}	L_{As}	L_1 (μH)	C_1 (nF)	L_2 (μH)	C_2 (nF)	L_3 (μH)	C_3 (nF)	C_4 (nF)	L_4 (μH)	C_5 (nF)	C_6 (nF)	L_5 (μH)
0.3 dB	25 dB	3.4925	0.3007	2.9459	0.1205	1.5402	0.3403	0.5620	1.4344	0.9852	0.4621	4.5577

3. CONCLUSION

By the method of least squares, it is possible to design any filter having general network configuration for any specified frequency performance. Several filter designs were performed for general specifications of ripple amplitudes in the pass band, slope of frequency response in the transition band and attenuation in the stop band. The proposed filter design may also incorporate impedance matching of the source and load impedances, which may lead to simpler and smaller network realizations.

ACKNOWLEDGMENT

This paper was in part supported by Iran Telecommunication Research Center.

REFERENCES

1. Hong, J. S. and M. J. Lancaster, *Microstrip Filter for RF/Microwave Applications*, Wiley, New York, 2001.
2. Pozar, D. M., *Microwave Engineering*, 3rd Edition, Wiley, New York, 2004.
3. Frickey, D. A., "Conversion between S , Z , Y , h , $ABCD$, and T parameters which are valid for complex source and load impedances," *IEEE Trans. on MTT*, Vol. 42, 205–211, 1994.
4. Haupt, R. L. and S. E. Haupt, *Practical Genetic Algorithms*, 2nd Edition, John Wiley & Sons Inc., 2004.
5. Melanie, M., *An Introduction to Genetic Algorithms*, MIT Press, 1999.

Experimental Study on Super-resolution Techniques for High-speed UWB Radar Imaging of Human Bodies

T. Sakamoto, H. Taki, and T. Sato

Graduate School of Informatics, Kyoto University
Yoshida-Honmachi, Sakyo-ku, Kyoto 606-8501, Japan

Abstract— UWB (Ultra Wide-Band) radar systems are used in a variety of applications. The UWB radar imaging algorithm SEABED (Shape Estimation Algorithm based on BST and Extraction of Directly scattered waves) is a method that can be used in real-time operation, although it requires high-resolution data. Although the resolution of radar is basically restricted by its bandwidth, super-resolution techniques can be used to overcome the conventional resolution limit. In this paper, we investigate super-resolution techniques for UWB radar experimental data.

1. INTRODUCTION

UWB radar systems are used in a variety of applications including land-mine detection, driving assistance and robotics. The fast UWB radar imaging algorithm SEABED [1], is, however, the only method that can be used in applications demanding real-time operation, such as security surveillance systems. The SEABED algorithm is based on a reversible transform IBST (Inverse Boundary Scattering Transform) between the target shape and a time delay observed at multiple locations. Because the IBST is very sensitive to the resolution of the time delay, it is imperative that high-resolution data be obtained to estimate various parts of the human-body. Although the resolution of radar is basically restricted by its bandwidth, super-resolution techniques have been applied to GPR (Ground Penetrating Radar) to enhance the conventional resolution limit [2]. In this paper, we investigate experimentally super-resolution techniques for UWB radar data using a pig's anterior abdominal wall as a model of the human body. The results show that the super-resolution techniques are indeed capable of improving the UWB radar performance.

2. SEABED ALGORITHM

We assume a mono-static radar system, in which an omni-directional antenna is scanned along a straight line. UWB pulses are transmitted at fixed intervals and received by the antenna. The received data is converted from analog to digital and stored in memory. We estimate target shapes using the obtained data. We define a real space in which targets and the antenna are located. We express the 2-dimensional real space with the parameters (x, y) . Both x and y are normalized by λ , which is the center wavelength of the transmitted pulse in air. We assume $y > 0$ for simplicity. The antenna is scanned along the x -axis in r -space. We define $s(X, Y)$ as the received waveform after applying a matched filter at the antenna location $(x, y) = (X, 0)$. Here, we define Y with time t and the speed of the radiowave c as $Y = ct/(2\lambda)$. We define a data space expressed by (X, Y) .

In previous work, we developed a fast radar imaging algorithm, SEABED, based on a BST (Boundary Scattering Transform) [3–6]. The algorithm uses a reversible transform, BST, between target shapes and pulse delays. The BST is expressed as

$$X = x + ydy/dx, \quad (1)$$

$$Y = y\sqrt{1 + (dy/dx)^2}, \quad (2)$$

where (X, Y) is a point on a quasi-wavefront, and (x, y) is a point on the target boundary [7]. The inverse transform of the BST is given by

$$x = X - YdY/dX, \quad (3)$$

$$y = Y\sqrt{1 - (dY/dX)^2}, \quad (4)$$

where we assume $|dY/dX| \leq 1$. This condition is required because y should be a real number. First, quasiwavefronts are extracted from the received signals $s(X, Y)$ in the SEABED algorithm. Quasi-wavefronts are extracted to satisfy the conditions $ds(X, Y)/dY = 0$ and $|dY/dX| \leq 1$. Finally, we apply the IBST to the quasiwavefronts, and obtain the final image. The extraction

of quasi-wavefronts is critical to obtaining high-quality images with this algorithm. However, the quasi-wavefronts cannot be accurately estimated if multiple echoes are closely located in the received signal. Therefore, high-resolution techniques are indispensable to apply the SEABED algorithm in actual environments.

3. FREQUENCY-DOMAIN HIGH-RESOLUTION METHOD

The MUSIC (Multiple Signal Classification) algorithm [8] is often used as a high-resolution imaging method for multiple signals based on the eigen-decomposition of correlation matrices. Suppose $g(t)$ is a transmitted signal and $G(\omega)$ is its Fourier transform, where ω is an angular frequency. Suppose $f_0(t)$ is a received signal and $F_0(\omega)$ is its Fourier transform. To retrieve the propagation transfer function, we apply the inverse filter to $F_0(\omega)$ as $F(\omega) = F_0(\omega)/G(\omega)$. Furthermore, suppose a vector \mathbf{x} is defined as

$$\mathbf{x} = [F(\omega_1), F(\omega_2), \dots, F(\omega_M)]^T, \quad (5)$$

where T denotes the transposition operator of a matrix. Let us introduce a correlation matrix $R_{xx} = E[\mathbf{x}\mathbf{x}^H]$, where E is the expectation operator, and H denotes the Hermite operator. Suppose R_{xx} has eigenvalues $\lambda_1 \geq \lambda_2 \geq \dots \geq \lambda_M$ and corresponding eigenvectors e_1, e_2, \dots, e_M . Suppose $\lambda_n \simeq 0$ for $n \geq L + 1$, then the space spanned by e_n for $n \geq L + 1$ is called a noise subspace. The MUSIC algorithm uses the characteristic that the transfer function (or Green's function) \mathbf{x}_{true} for the actual delay is orthogonal to the noise subspace as $\mathbf{x}_{true}^H \lambda_n = 0$ for $n \geq L + 1$. Hence, a high-resolution signal $f_{MUSIC}(t)$ can be obtained as

$$f_{MUSIC}(t) = \frac{\mathbf{x}_0(t)^H \mathbf{x}_0(t)}{\sum_{n=L+1}^M |\mathbf{x}_0(t)^H \lambda_n|}, \quad (6)$$

where $\mathbf{x}_0(t)$ is the transfer function assuming an echo with a time delay t .

The actual parameter settings for the MUSIC algorithm for our UWB radar experiment are described below. The MUSIC algorithm is applied in the frequency domain to enhance the resolution for the UWB radar signals as in [2]. First, we select $2M - 1$ frequency-domain data samples with S/N (signal-to-noise ratio) larger than -20 dB, where the maximum power density is 0 dB, and $M = 70$ is empirically chosen. Next, a frequency smoothing technique is applied to resolve correlated interferences, where $M \times M$ covariance matrices are averaged M times. Then, an eigenvalue decomposition is applied and a MUSIC spectrum is produced for each antenna location assuming a 2-dimensional signal subspace.

4. EXPERIMENTAL INVESTIGATION

Figure 1 shows the experimental UWB radar site in an anechoic chamber. The system includes a short pulse generator, a pair of omni-directional wideband planar patch antennas, and a wideband oscilloscope. The transmitted pulse, with a classical range resolution of about 50 mm, has a center frequency of 3.7 GHz and bandwidth of 3.0 GHz. In this figure, a 20-mm thick mortar board is set as a target. The distance between the antenna pair and the mortar board is set to 118 mm.

The pulse is transmitted, received by the oscilloscope, converted from analog to digital, and stored in memory. After subtracting the direct wave from the transmitted antenna to the receiving antenna, we obtain the echoes caused by the upper and lower boundaries of the mortar board shown in Figure 2.

A conventional Wiener filter technique is applied to this signal to enhance the resolution

$$F_W(\omega) = F_0(\omega)G^*(\omega) / \{\eta + (1 - \eta)|G(\omega)|^2\}, \quad (7)$$

where $0 \leq \eta \leq 1$ is a parameter that depends on the S/N of the signal. Note that the optimal parameter η cannot be determined here because multiple echoes contained in the signal $f(t)$ have different S/N values. Figure 3 shows the output of the Wiener filter for various η applied to the experimental signal from the mortar board, where $\eta = 0$ and $\eta = 1$ correspond to the lower and upper signals, respectively. Although two echoes are seen in this figure, other undesired components are observed as well. Figure 4 shows the signals processed by the MUSIC algorithm, the Wiener filter and the matched filter. Here, an appropriate $\eta = 0.3$ for the Wiener filter is chosen based on the signals in Figure 3. The output of the matched filter, which has the lowest resolution, cannot resolve the two echoes, whereas the other techniques can resolve them. The resolution of

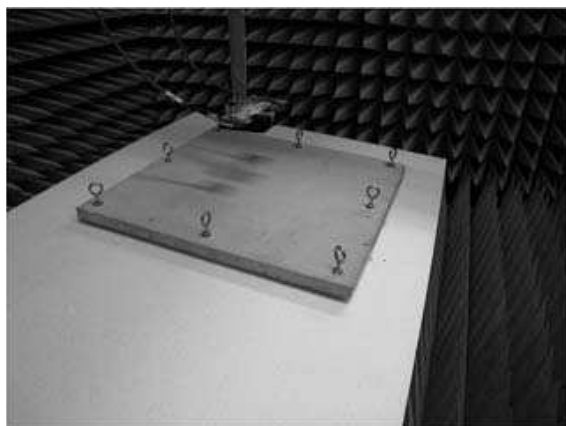


Figure 1: Experimental site for UWB radar with a mortar board.

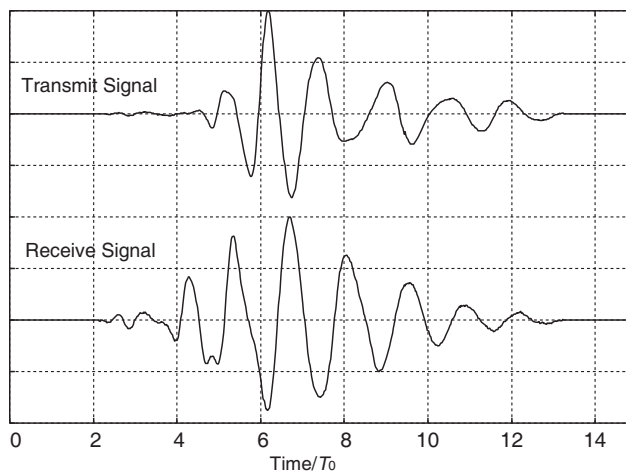


Figure 2: Transmitted and received signals with a mortar board.

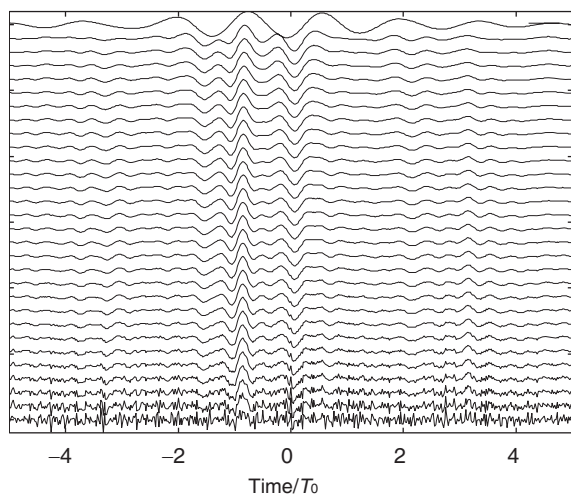


Figure 3: High-resolution signal with Wiener filters with various parameters.

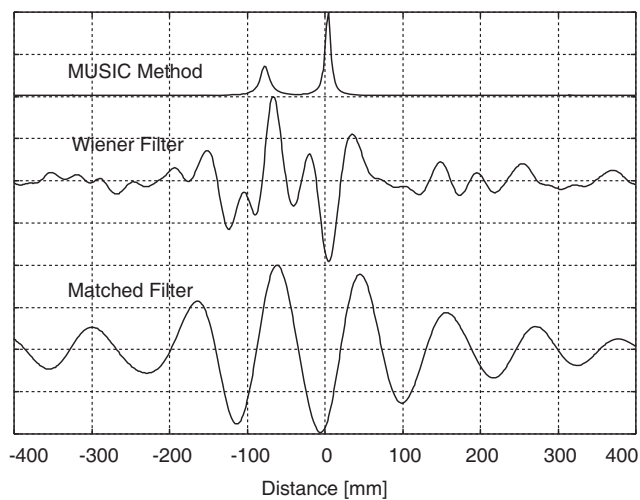


Figure 4: Signals processed by MUSIC algorithm, Wiener filter, and matched filter.



Figure 5: Experimental site for UWB radar with an anterior abdominal wall.

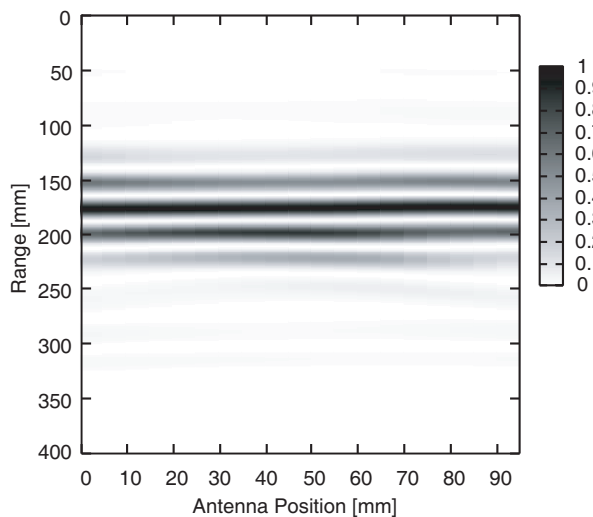


Figure 6: Image of the surface of an abdominal wall with the matched filter.

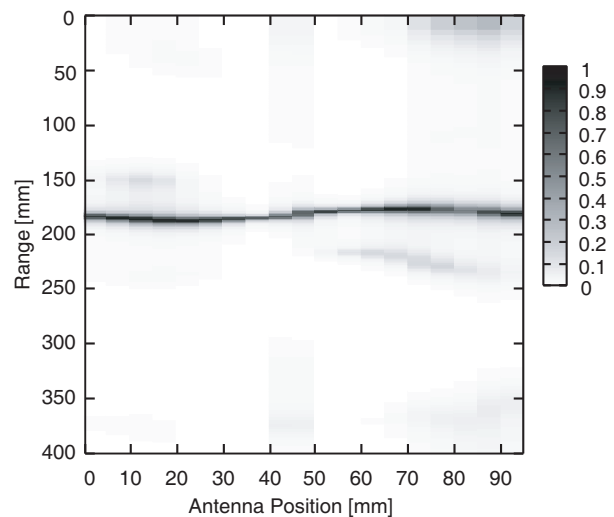


Figure 7: Super-resolution image of the surface of an abdominal wall.

the MUSIC algorithm is much higher than the Wiener filter. Here, the actual number of targets $L = 2$ is given to the MUSIC algorithm. We also set $L = 3$ and 4 to see the output signal and confirm that the image is still clear with a high resolution property, which means that the setting of L does not have much effect on the results.

The relative permittivity of the mortar board is estimated as 4.8 by another measurement. Thus, the equivalent thickness of the board in the UWB radar experiment is calculated as $\sqrt{4.8} \times 2 \times 20 \text{ mm} = 87.6 \text{ mm}$. The equivalent thickness estimated from the MUSIC spectrum in Figure 4 is 82.1 mm which has an error of 5.5 mm or 6.3% of the actual thickness.

Figure 5 shows an experimental setup with part of pig's body as a target. As seen in the figure, the pair of antennas is positioned above the pig's anterior abdominal wall. The two antennas are scanned in a straight line and the received signal is recorded every 5 mm. The pig's anterior abdominal wall is used here as a realistic model of a human body, which is an important study for an attractive application to surveillance and security systems. Figure 6 shows the image obtained by a conventional matched filter. We do not see the detail of the surface fluctuation of the target due to its low resolution property. Figure 7 shows the image estimated with the MUSIC algorithm, in which a clear target boundary is visible with a high resolution of about 10 mm. This is 5 times higher than the classical resolution of 50 mm. This super-resolution technique can be employed in conjunction with the SEABED algorithm to obtain a detailed structure of the human body.

5. CONCLUSION

In this paper, we investigated experimentally super-resolution techniques for UWB radar data using a mortar board and a pig's anterior abdominal wall as a model of the human body. The results showed that the super-resolution techniques work well to improve the UWB radar performance. The results indicate that it is possible to obtain a high-resolution image within a short time by using a super-resolution technique together with the SEABED algorithm. The investigation of low-computational, high-resolution techniques should be an important future study.

REFERENCES

1. Sakamoto, T., "A fast algorithm for 3-dimensional imaging with UWB pulse radar systems," *IEICE Trans. Commun.*, Vol. E90-B, No. 3, 636–644, Mar. 2007.
2. Le Bastard, C., V. Baltazart, Y. Wang, and J. Saillard, "Thin-pavement thickness estimation using GPR with high-resolution and superresolution methods," *IEEE Trans. on Geosc. & Remote Sensing*, Vol. 45, No. 8, 2511–2519, 2007.
3. Sakamoto, T. and T. Sato, "Fast imaging of a target in inhomogeneous media for pulse radar systems," *Proc. 2004 IEEE International Geoscience and Remote Sensing Symposium*, Vol. 3, 2070–2073, Sep. 2004.

4. Sakamoto, T. and T. Sato, "A fast algorithm of 3-dimensional imaging for pulse radar systems," *Proc. 2004 IEEE AP-S International Symposium and USNC/URSI National Radio Science Meeting*, Vol. 2, 2099–2102, Jun. 2004.
5. Sakamoto, T. and T. Sato, "A phase compensation algorithm for high-resolution pulse radar systems," *IEICE Trans. Commun.*, Vol. E87-B, No. 11, 3314–3321, Nov. 2004.
6. Sakamoto, T. and T. Sato, "A phase compensation algorithm for high-resolution pulse radar systems," *Proc. 2004 International Symposium on Antennas and Propagation*, 585–588, Aug. 2004.
7. Sakamoto, T. and T. Sato, "A target shape estimation algorithm for pulse radar systems based on boundary scattering transform," *IEICE Trans. Commun.*, Vol. E87-B, No. 5, 1357–1365, May 2004.
8. Schmidt, R. O., "Multiple emitter location and signal parameter estimation," *Proc. RADC Spectral Est. Workshop*, 243–258, 1979.

Novel Mathematical Model for the Analysis of Flat Substrate Imperfections

A. Baryshev

Moscow Lomonosov State University, Moscow, Russia

Abstract— A novel mathematical model for the analysis of flat substrate imperfections has been proposed. The model has been applied to compare pit and bump far-field patterns in the case of scalar boundary-value problem. The solution of the problem has been constructed on the basis of Discrete Sources Method (DSM).

1. INTRODUCTION

Substrate imperfections analysis based on light scattering measurements associated with the presence of shallow pit or bump on the substrate surface have been a subject of interest in last decades. Especially in the field of semiconductor manufacturing where the detection and identification of imperfections arising at different stages of the manufacturing process seems to be one of the most important problem now. Direct analysis methods often fail for several reasons. For instance, the defects analysis based on the Discrete Sources Method (DSM) [1] fails because of the difficulties associated with the disposition of the discrete sources which are multipoles of high order inside very shallow pit or bump under consideration. In this presentation, we would like to suggest a novel mathematical model for the analysis of flat substrate imperfections. According to that model we can consider shallow pit or bump as a part of more extensional obstacle.

2. METHOD OUTLINES

For the simplicity we shall consider scalar problem. Let us consider R^3 space which is divided by a plane surface $\Xi(z = 0)$ into two half-spaces $D_1(z > 0)$ and $D_2(z < 0)$. Let us introduce a Cartesian coordinate system $Oxyz$, by selecting its origin at the plane Ξ and axis Oz to be directed into the domain D_1 . Let us denote the inner area of the axisymmetric particle as D_i and let us suppose that its position with respect to the plane Ξ is specified by the position of the point C which is the middle of the particle's major semi-axis (see Fig. 1). Let u_0 be the incident plane wave propagating in D_1 under an angle $\pi - \theta_1$ with respect to axis Oz . First let us solve the scattering problem for the external excitation u_0 on the plane Ξ and construct the external excitation field $u_\zeta^0(\zeta = 1, 2)$, which is a superposition of the incident and reflected waves in D_1 and refracted plane wave in D_2 . Then mathematical formulation of the scattering problem can be formulated in the following form

$$\left\{ \begin{array}{l} \Delta u_e + k_e^2(M)u_e = 0, \quad M \in D_e; \quad \Delta u_i + k_i^2 u_i = 0, \quad M \in D_i \\ u_i - u_e = u_\zeta^0; \quad \frac{\partial u_i}{\partial n} - \frac{\partial u_e}{\partial n} = \frac{\partial u_\zeta^0}{\partial n}, \quad P \in \partial D_i; \quad [u_e] = 0; \quad \left[\frac{\partial u_e}{\partial n} \right] = 0, \quad P \in \Xi \\ \frac{\partial u_1}{\partial r} + jk_1 u_1 = o(r^{-1}), \quad r \rightarrow \infty, \quad z > 0; \quad u_2 = o(\exp\{|\text{Im}k_2|z\}), \quad z \rightarrow -\infty, \quad D_2 \end{array} \right. \quad (1)$$

Here $D_e = D_1 \cup D_2$; $k_e^2(M) = \begin{cases} k_1^2, & M \in D_1 \\ k_2^2, & M \in D_2 \end{cases}$; $u_\zeta^0 = \begin{cases} u_1^0, & P \in \partial D_i^1 \\ u_2^0, & P \in \partial D_i^2 \end{cases}$; $\partial D_i = \partial D_i^1 \cup \partial D_i^2$. $[\]$ is the jump of a variable across the surface; u_e is the scattered field in the corresponding region D_1 or D_2 ; u_i is the total field inside the particle; u_1^0 is the total field of the incident and reflected waves in D_1 ; u_2^0 is the field of the wave that passed into D_2 . We also assume $\text{Im}(k_2^2) < 0$; $\text{Im}(k_{1,i}) \leq 0$ (time dependence is supposed to be $\exp\{j\omega t\}$), $\partial D_i \subset C^2$. Then the above boundary-value problem is uniquely solvable [2].

The DSM is based on the conception of an approximate solution when we represent $u_{e,i}$ as a finite linear combination of electric dipoles, deposited on some auxiliary surfaces $S_{e,i}$ located inside D_i , which satisfy Helmholtz equations in $D_{1,2,i}$, infinity conditions and transmission conditions at the plane interface Ξ . Thus the solution of the boundary-value scattering problem (1) is reduced to an approximation of the field of external excitation at the particle surface only. That is

$$u_i - u_e = u_\zeta^0; \quad \partial u_i - \partial u_e = \partial u_\zeta^0, \quad P \in \partial D_i \quad (2)$$

where $\partial := \partial/\partial n$.

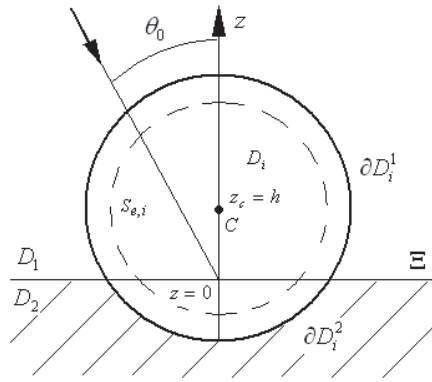


Figure 1.

We chose some auxiliary rotation surfaces $S_{e,i}$ as shown in Fig. 1. Let the sets of points satisfy the condition $\{\overline{M_n^{e,i}}\}_{n=1}^{\infty} = S_{e,i}$. Then the approximate solution can be represented by finite linear combinations

$$u_i^N(M) = \sum_{n=1}^{N_i} p_n^i \chi_n^i(M) = \sum_{n=1}^{N_i} p_n^i \sin(k_i R_{MM_n}) / R_{MM_n}; \quad u_e^N(M) = \sum_{n=1}^{N_e} p_n^e G_n(M) \quad (3)$$

where $N_{e,i}$ is the number of sources located on the auxiliary surfaces $S_{e,i}$ correspondingly. p_n^e and p_n^i are the unknown sources amplitudes, representing scattered and total field in corresponding domains D_e and D_i . p_n^e and p_n^i are to be determined from the transmission conditions (2). Representation for the scattered field u_e in $D_{1,2}$ is constructed on the basis of Green function $G_e(M, M_0)$ of the following boundary-value problem

$$\begin{cases} \Delta G_e + k_e^2 G_e = -4\pi\delta(M, M_0), & M_0 \in D_e, \quad [\partial G_e] = [G_e] = 0 \text{ on } \Xi \\ \text{radiation conditions in } D_1; \quad \text{attenuation conditions in } D_2 \end{cases}$$

$G_n(M) = G_e(M, M_n)$ is the Green function of the half-space, which has the Sommerfeld integral representation

$$G_n(M) = G_e(M, M_n) = \int_0^{\infty} J_0(\lambda r) v(\lambda, z, z_n) \lambda d\lambda$$

where $r^2 = (x - x_n)^2 + (y - y_n)^2$. $J_0(\lambda r)$ is a cylinder Bessel function, and (x_n, y_n, z_n) are the Cartesian coordinates of the point M_n . The spectral function $v(\lambda, z, z_n)$ ensures the validity of the transmission conditions $[\partial u_e] = 0$, $[u_e] = 0$ on the interface Ξ . The exact expression for the spectral function can be found in [3].

In paper [3], it is shown that for any degree of immersion of the particle into the substrate D_2 under the following conditions $\partial D_i \subset C^2$; $\text{Im}(k_2^2) < 0$; $\text{Im}(k_{1,i}) \leq 0$ and under the corresponding conditions for S_i system of functions underlying the representation of the approximate solution (3) is complete and closed in space $H^0 = L_2(\partial D_i) \times L_2(\partial D_i)$. It was also proved that the approximate solution constructed on the basis of DSM converges to the exact solution of the boundary-value problem (1).

3. NUMERICAL SCHEME

As it was mentioned above, the approximate solution constructed on the basis of DSM satisfies the boundary conditions of the scattering problem (1). So, the determination of the unknown amplitudes of discrete sources $\{p_n^e\}_{n=1}^{N_e} \{p_n^i\}_{n=1}^{N_i}$ is to be performed from the fitting of the boundary conditions (2) in $L_2(\partial D_i)$ norm [4]. To do this, we need an expression for the external exciting field u_ζ^0 . We consider a plane wave u_0 , propagating from D_1 in ZX -plane under the angle $\pi - \theta_1$ with respect to OZ axis. Then an expression of the external exciting field depends on degree of the immersion of the particle into the substrate D_2 and has the following form:

$$u_\zeta^0 = \begin{cases} u_1^0, & z \geq 0 \\ u_2^0, & z \leq 0 \end{cases} = \begin{cases} \exp(-jk_1(x \sin \theta_1 - z \cos \theta_1)) + R \cdot \exp(-jk_1(x \sin \theta_1 + z \cos \theta_1)), & z \geq 0 \\ T \cdot \exp(-jk_2(x \sin \theta_2 - z \cos \theta_2)), & z \leq 0 \end{cases}$$

$R = \frac{k_2 \cos \theta_2 - k_1 \cos \theta_1}{k_2 \cos \theta_2 + k_1 \cos \theta_1}$ $T = \frac{2k_1 \cos \theta_1}{k_2 \cos \theta_2 + k_1 \cos \theta_1}$ are reflection and refraction coefficients. θ_2 is the angle under which the wave u_0 passes into D_2 . Angles θ_1 and θ_2 satisfy the Snell law $\sin \theta_2 = (k_1/k_2) \sin \theta_1$. If $|k_1| > |k_2|$ there may arise a case $|\sin \theta_2| > 1$, when θ_1 varies from 0 to $\pi/2$. That is taken into account by choosing a corresponding branch of cosine in such a way that transmitted into D_2 wave decays in D_2 . That leads to an expression $\cos \theta_2 = -j(\sin^2 \theta_1 - 1)^{1/2}$ for any $\theta_2 \in [0, \pi/2]$.

Various schemes for the amplitude determination can be applied. It has been established that stable results can be obtained by using pseudo-inversion of an over-determined system of linear equations obtained by following the generalized point-matching technique [2]. Select a set of matching points on the particle $\{P_l\}_{l=1}^L \in \partial D_i$, homogeneously covering the surface. Then the linear system to be used for determining the discrete sources amplitudes is found from matching the boundary conditions (2) at the set $\{P_l\}_{l=1}^L$. This procedure leads to an over determined matrix having dimension $2L \times 2(N_e + N_i)$ and the discrete sources amplitudes are evaluated by a pseudo-inversion technique. This approach enables an estimation of the error in the solution from the surface residual in $L_2(\partial D_i)$ norm.

After DS amplitudes have been determined the far-field pattern $F_\zeta(\theta, \varphi)$ in both half-spaces can be computed as

$$u_e^N = \frac{\exp(-jk_\zeta r)}{r} F_\zeta^N(\theta, \varphi) + o(r^{-1}), \quad r = |M| \rightarrow \infty, \quad \theta, \varphi \in \Omega, \quad \zeta = 1, 2$$

Using the asymptotic approach [4] for evaluation of the Weyl-Sommerfeld integrals we obtain the following expressions for far-field pattern

$$F_1^N(\theta, \varphi) = \sum_{n=1}^{N_e} e^{jk_1 \sin \theta (x_n \cos \varphi + y_n \sin \varphi)} \begin{cases} \exp(jk_1 z_n \cos \theta) + \frac{\eta_1 - \eta_2}{\eta_1 + \eta_2} \exp(-jk_1 z_n \cos \theta), & z_n \geq 0 \\ \frac{2\eta_1}{\eta_1 + \eta_2} \exp(\eta_2 z_n), & z_n \leq 0 \end{cases}$$

$$\eta_1 = jk_1 |\cos \theta|; \quad \eta_2 = \sqrt{(k_1 \sin \theta)^2 - k_2^2}; \quad \theta \in [0; \pi/2], \quad \varphi \in [0, 2\pi]$$

$$F_2^N(\theta, \varphi) = \sum_{n=1}^{N_e} e^{jk_2 \sin \theta (x_n \cos \varphi + y_n \sin \varphi)} \begin{cases} \frac{2\eta_2}{\eta_1 + \eta_2} \exp(-\eta_1 z_n), & z_n \geq 0 \\ \exp(jk_2 z_n \cos \theta) + \frac{\eta_2 - \eta_1}{\eta_1 + \eta_2} \exp(jk_2 z_n |\cos \theta|), & z_n \leq 0 \end{cases}$$

$$\eta_2 = jk_2 |\cos \theta|; \quad \eta_1 = \sqrt{(k_2 \sin \theta)^2 - k_1^2}; \quad \theta \in [\pi/2; \pi], \quad \varphi \in [0, 2\pi]$$

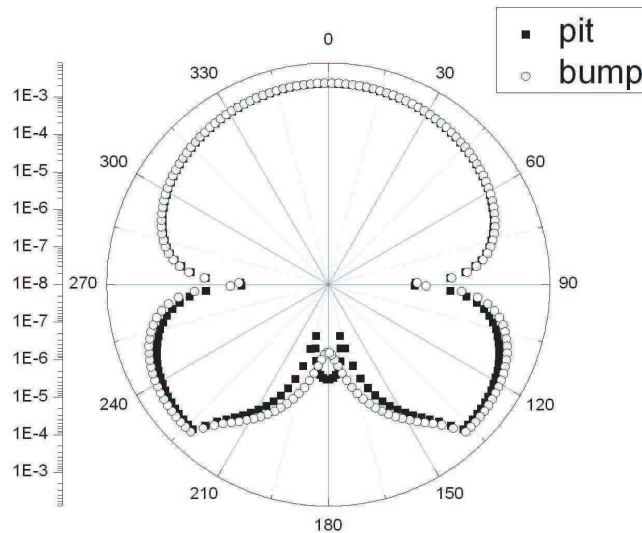


Figure 2.

4. RESULTS

The model of the particle immersed into the substrate can be used for investigating pits and bumps on the substrate surface. That can be done by using the “fictitious particle” method. For example for investigating or modeling a pit in the substrate D_2 , we can choose the wave number of the immersed into the substrate particle in such a way that it slightly (for example in the eight significant number) differs from the wave number of the half-space D_1 . A bump on the substrate D_2 can be investigated or modeled in a similar way by immersing the particle into the substrate and choosing its wave number in such a way that it slightly differs from the wave number of the substrate D_2 . It is assumed that in both cases z -coordinate of the centre of the major axis of the particle differs in the following manner $-d/2 < z_C < d/2$.

We consider a spherical particle with radius $r_l = 1$. The incident plane wave propagates from the half-space D_1 under the angle $\theta = 0$ with respect to OZ axis. The bold arrow in the figure denotes the direction of the incident wave.

In the Fig. 2, we can see logarithmical far-field pattern for pit and bump in the substrate in the whole space. The pit has the following parameters: $k_1 = 1$, $k_i = 1.00000001$, $k_2 = 1.5$, $z_c = 0.95$. And the bump has the following: $k_1 = 1$, $k_i = 1.50000001$, $k_2 = 1.5$, $z_c = -0.95$. In both cases the residual is less than 2%.

5. CONCLUSION

A novel mathematical model for the analysis of flat substrate imperfections has been developed in this paper. The basic numerical results will be presented during the conference. This work was supported by Russian Foundation for Basic Research (RFBR grant No. 09-01-00318-a).

REFERENCES

1. Eremin, Yu. A. and A. G. Sveshnikov, “Computer technology for analysis of scattering problems based on discrete sources method,” *Comput. Maths. Math. Phys.*, Vol. 40, No. 12, 1769–1783, 2000.
2. Doicu, A., Yu. A. Eremin, and T. Wriedt, *Acoustic and Electromagnetic Scattering Analysis Using Discrete Sources*, Academic Press, New York, 2000.
3. Baryshev, A. V. and Yu. A. Eremin, “Justification of an integro-functional method for diffraction problems in the presence of a half-space,” *Differential Equations*, Vol. 44, No. 9, 1281–1288, 2008.
4. Eremin, Yu. A., N. V. Orlov, and A. G. Sveshnikov, “Models of electromagnetic scattering problems based on discrete sources methods,” *Generalized Multipole Techniques for Electromagnetic and Light Scattering*, 39–79, Edited by T. Wriedt. Elsevier Science, Amsterdam, 1999.

A Scheme to Analyze Scattering from an Iris on an Infinite Waveguide Structure Using the Conjugate Gradient Method

H. Belhadj and T. Aguli

Sys'Com Lab, National Engineering School of Tunis, Tunisia

Abstract— An efficient iterative method to solve electromagnetic scattering problem, modeled by the method of generalized equivalent circuit, is developed on this paper. This method adopt a new implementation of the conjugate gradient algorithm to solve an equation with the impedance operator to determinate the current density. This method has been applied to a fractal iris structure. Results obtained are conformed to theory and to the ones finding by the moment method with a significant gain on the computational time and on computer storage.

1. INTRODUCTION

Various numerical methods were used to solve scattering problem. One of the most interesting and relevant method is the iterative Conjugate Gradient (CG) one. The greatest advantage of this method is that convergence is guaranteed under all conditions and after a finite number of iterations. It has also the advantage of iterative methods that round-off errors do not propagate and are limited to the last iteration.

In many electromagnetic applications, the conjugate gradient method is combined with the Fast Fourier Transform (FFT) technique for an efficient computation and resolution of an integrodifferential equation to determinate the unknown current density [1–5]. Sarkar on [3] has proved that for a problem of complexity N , the computational time required using the CGFFT method is reduced to $4N(1 + \log_2 N)$, comparing to the Method of Moment (MoM) [6], where it is proportional to N^3 .

The basic approach of this paper consists on solving an electromagnetic scattering problem modeled by the Method of Generalized Equivalent Circuit (MGEC) [7, 8], and to apply the CG method to solve the impedance operator's equation resulted. This new implementation provides a gain on computational time and storage comparing to the previous mentioned methods.

In Section 2, we present the problem to treat. The MGEC method was applied to the structure and the electromagnetic equation to solve has been deduced. Section 3 presents the details of the implementation of the conjugate gradient algorithm to solve scattering from a fractal iris structure on an infinite waveguide.

Section 4 deals with experimental results. The current density evaluated by the CG method has been determined, and the errors behavior of this method has been plotted. The last section draws conclusions and suggests future work.

2. GENERALIZED EQUIVALENT CIRCUIT TO MODEL SCATTERING PROBLEM

We consider the structure given on Figure 1. That is a fractal structure of the Cantor iris of the second order. We have introduced into the waveguide windows formed by zero thickness obstacles with edges parallel to the electric field (TE₁₀-mode in rectangular guide).

The Method of Generalized Equivalent Circuit is applied to this structure in order to determine the electromagnetic equation. In fact, this method translates relation between electric and current fields into equivalent circuit as shown in Figure 2.

The excitation E_0 is the fundamental mode TE₁₀ in rectangular waveguide. An electric current J is then generated on the metallic surface. This method allows us to identify the relation between the electric field and the current using the impedance operator. In fact, when we apply the laws of tension and current, we can deduct the following equation:

$$E = E_0 + \hat{Z}J \quad (1)$$

where E denotes the total electric field; E_0 is the excitation field, J is the unknown current density vector and \hat{Z} is the impedance operator.

In this work, we have first identified the modes existed in this type of guide structure, in order to determinate the mode function expression [10]. Since the geometry is uniform in the y direction, there is no variance along the y axis. Only the modes TE _{n 0} are propagating.

We remind that E_0 is the TE₁₀-mode propagating in a rectangular waveguide;

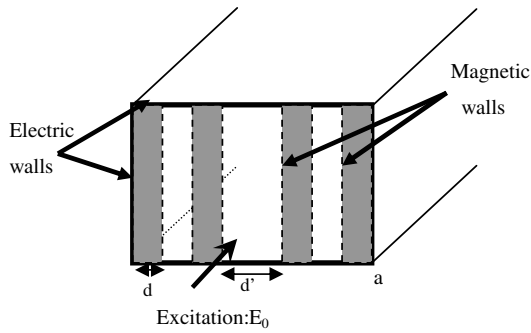


Figure 1: Cross sectional view of the structure.

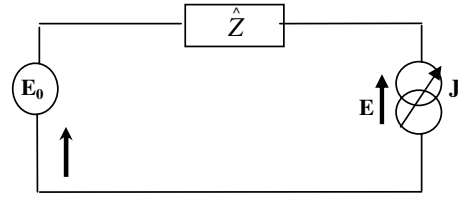


Figure 2: The corresponding equivalent circuit.

$$E_0 = \sqrt{\frac{2}{a}} \sin\left(\frac{\pi}{a}x\right) \quad (2)$$

It is known that the impedance operator is given by

$$\hat{Z} = \sum_n |f_n\rangle z_n \langle f_n| \quad (3)$$

where z_n denotes the mode impedance.

We know that the total electric field is null on the metallic surface, and there is no current distribution above the dielectric. Therefore, we can write the Equation (1) on the metallic surface as:

$$\hat{Z}J = -E_0 \quad (4)$$

We have obtained an equation with the impedance operator, where the unknown is the current distribution. We will see in the following how we can solve such type of equation by the conjugate gradient method.

3. APPLICATION OF THE CG ITERATIVE METHOD

The well known conjugate gradient method [2] proceeds by generating successive approximations to the solution, and search directions used in updating iterates and residuals.

In our case, in order to impose the boundaries conditions, we need to introduce the Heaviside operator defined as

$$\hat{H}_m = \begin{cases} 1 & \text{on the metal} \\ 0 & \text{outside} \end{cases}$$

since the Equation (4) to solve is only valid on the metallic surface.

Then, we compute the initial residual and direction vectors, and we give an initial guess of the unknown current. We have chosen: $J_0 = 0$; $r_0 = \hat{H}_m * E_0$, and $p_0 = r_0$.

The residual at the k^{th} iteration is given by

$$r_k = \hat{Z}J_k + E_0 \quad (5)$$

The unknown vectors J_k are updated in each iteration as following:

$$J_{k+1} = J_k + \alpha_k p_k \quad (6)$$

where p_k is the direction vector and α_k is the scalar coefficient.

The impedance operator is described on the mode basis, it is a discrete operator applied on the spectral domain. We remind that we have a one dimensional problem. If we apply the impedance operator on J we obtain:

$$\hat{Z}J(x) = \sum_n |f_n\rangle z_n \langle f_n, J(x)\rangle \quad (7)$$

To transform the continuous function $J(x)$, the discrete function is formed by sampling the original one at equally spaced point. We have a one-dimensional problem, so meshing is used only on the x axis direction.

The x -axis is divided into N equivalent segments and the current is assumed to be constant over each segment. If we decompose J on the mode basis, we obtain

$$J(x) = \sum_n a_n f_n(x) \quad (8)$$

J is described on the spatial domain and Z on the spectral one so we need to use the FFT principle. We have discrete the entire domain, we can write:

$$\langle f_n(x), J(x) \rangle = \sum_i f_n(x_i) J(x_i) \Delta x_i = a_n \quad (9)$$

Δx_i is the uniform distance between x_i and x_{i+1} , it is equal to a/N , we note on the following Δ . So we have

$$\hat{Z}J(x_i) = \sum_n a_n z_n |f_n(x_i)\rangle = \sum_n \left(\sum_i f_n(x_i) J(x_i) \Delta \right) z_n f_n(x_i) \quad (10)$$

then, we will use the Equation (10), in fact, the product $A * p$ (in the CG algorithm) will be replaced by $Z * p$ as:

$$\hat{Z} * p(x_i) = \sum_n \left(\sum_i f_n(x_i) p(x_i) \Delta x \right) z_n f_n(x_i) \quad (11)$$

On literature we find two type of the arrested test criterion used on the convergence of the CG algorithm. The first one is the residual error given by:

$$Err_k = \frac{\|r_k\|}{\|E_0\|} < \varepsilon \quad (12)$$

The second critter is the relative error given by:

$$err = \frac{\|J_{k+1} - J_k\|}{\|J_k\|} < \varepsilon \quad (13)$$

This criterion has the inconvenient that it can be satisfied and the solution is not well approached. On the next section, we study the behavior of these criterions.

4. NUMERICAL RESULTS

We consider the structure shown in Figure 1, the guide dimensions used are: $a = 22.9$ mm, $b = 10.2$ mm, $d = a/9$ and $d' = a/3$, we discrete the x domain into 128 samples. The CG algorithm is then implemented in order to determinate the current J . We have two types of convergence, one is related to the error criterion and the second is the mode convergence. In fact we said that convergence is achieved when the residual and relative error are less than $\varepsilon = 10^{-2}$, and when the current values are not changing as a function of the mode number.

We present on Figure 3 the errors behavior as a function of iteration number, and we plot on Figure 4 the current distribution evaluated by the CG method for a fractal iris structure, as a function of the mode number.

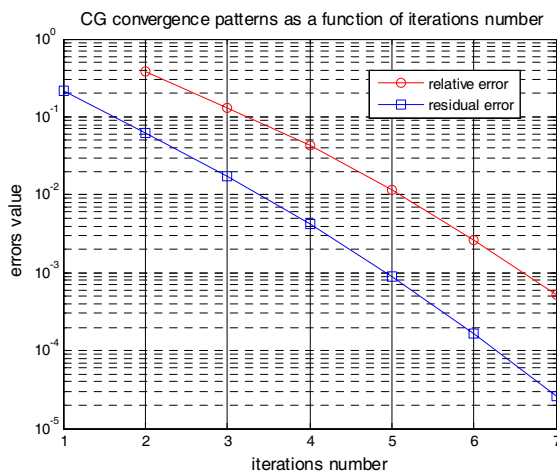


Figure 3: The errors behavior of the CG algorithm.

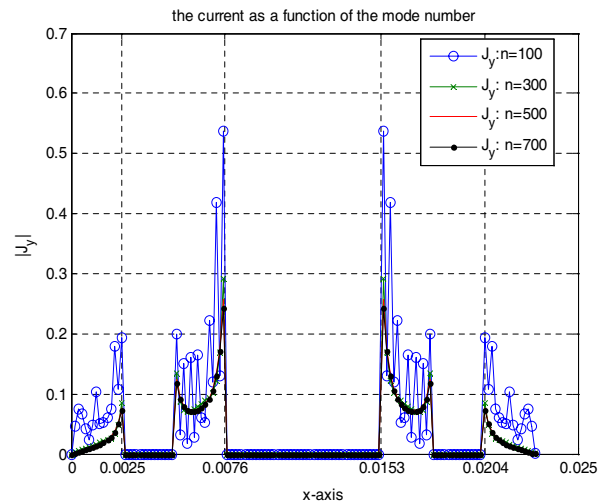


Figure 4: The current density evaluated by the CGM.

Figure 3 show that if we select the error tolerance equal to 10^{-2} , convergence is obtained in four iterations, for a problem with 128 unknowns. In this case convergence is obtained in few seconds.

Figure 4 draws the current behavior obtained before and at convergence. In fact, this figure proved that for $n = 100$, we are not in convergence although the relative and residual error criterion was satisfied. This shows that the mode number convergence is an indispensable criterion to stop the iterative process of our algorithm. So, we deduct that convergence is obtained for $n = 500$, when we have no variance on the current values.

Result obtained in Figure 4 is conformed to theory with respect to the boundary conditions. In fact the tangential current component is null on the dielectric and is maximum on the magnetic wall and minimum on the electric one. For $x = a/3$ and $x = 2a/3$, for example, we have a magnetic wall, the tangential current is then maximum. For $x = 0$ and $x = a$, we have the electric walls (the guide walls), so J is minimum which is shown in Figure 4. Also results obtained are conformed to those finding by the TMWLAB software which is developed to provide results obtained using the MoM [9].

5. CONCLUSIONS

The conjugate gradient method has been developed and exposed on this work to solve electromagnetic scattering problem. This method have been used to determinate the electromagnetic unknown current. Convergence is achieved in four iterations and in few seconds for a problem with 128 unknowns, with a residual error less than 10^{-2} . The current and the errors behaviors have been determined using this method and have been plotted. Results obtained were conformed to those finding by the moment method with respect to boundary conditions.

Simulation studies have indicated that this method can exhibit very favorable performance and hold to a computational time gain and on computer storage, comparing to the MoM method.

The primary area of future work is to validate this method for two and three dimensional structures.

REFERENCES

1. Barkeshli, K. and J. L. Volakis, "Applications of the conjugate gradient FFT method to radiation and scattering," *Progress In Electromagnetic Research*, PIER 5, 199–239, 1991.
2. Peterson, A. F., S. L. Ray, C. H. Chan, and R. Mittra, "Numerical implementation of the conjugate gradient method and the CGFFT for electromagnetic scattering," *Progress In Electromagnetic Research*, PIER 5, 241–300, 1991.
3. Sarkar, T. K., E. Arvas, and S. M. Rao, "Application of FFT and the conjugate gradient method for the solution of electromagnetic radiation from electrically large and small conducting bodies," *IEEE Trans. Antennas Propagat.*, Vol. 34, No. 5, 635–640, 1986.
4. Barkeshli, K. and J. L. Volakis, "Improving the convergence rate of the conjugate gradient FFT using subdomain basis functions," *IEEE Trans. Antennas Propagat.*, Vol. 37, No. 7, 893–900, 1989.
5. Peterson, A. F and R. Mittra, "Convergence of the conjugate gradient method when applied to matrix equations representing electromagnetic scattering problems," *IEEE Trans. Antennas Propagat.*, Vol. 34, 1447–1454, 1986.
6. Harrington, R. F., "Field computation by moment methods," *IEEE Press Series on Electromagnetic Waves*, Syracuse University, 1993.
7. Baudrand, H., "Representation by equivalent circuit of the integrals methods in microwave passive elements," *IEEE*, 1359–1364, 1990.
8. Aguilí, T., "Modélisation des composantes SFH planaires par la methode des circuits equivalents généralisée," Thesis manuscript, National Engineering School of Tunis, Tunisia, 2000.
9. Ben Salah, T. and T. Aguilí, "Software implementation of a new multi-scale method for fractal shaped structure's diffraction analysis," *Progress In Electromagnetics Research Symposium*, Cambridge, 2008.
10. Markuwitz, N., *Waveguide Handbook*, Wiley-Interscience, New York, 1986.

Interaction of Infrared Electromagnetic Pulses in Resonant Layered Structures with n -GaAs Semiconductor Film

V. Grimalsky, S. Koshevaya, J. Escobedo-A., and M. Tecpoyotl-T.
 CIICAp, Autonomous University of State Morelos (UAEM)
 Cuernavaca, ZP 62209, Mor., Mexico

Abstract— Interaction of infrared electromagnetic (EM) waves in layered structures with n -GaAs film is investigated theoretically. An oblique incidence of EM wave is considered, when the total internal reflection and resonant transmission occur. This structure modulates effectively the infrared EM wave. The modulation mechanism is due to electron transfer from the upper valley to the higher ones in a strong bias electric field. An interaction of strong incident infrared EM pulses with this structure is also considered in the case of absence of a bias electric field. Both nonlinear switching of short pulses and modulation instability of long strong pulses take place there.

1. INTRODUCTION

Last time, the multilayer structures are widely investigated in nonlinear optics [1–3]. The layered structures with semiconductor layers are of a great interest because they give a possibility to control effective refraction indices due to changing the electron concentration [3, 5]. The semiconductors with multi-valley structure of conduction band, like n -GaAs, possess electron nonlinearity in millimeter, THz wave ranges, and in the infrared range. Therefore, to investigate an interaction of infrared waves in layered structures with semiconductor films, it is rather better to use simpler structures with a few layers [5, 6], because a fabrication of multilayer structures is difficult, and the dissipation of infrared waves is high.

A simple resonant structure is formed by three layers with relative dielectric permittivities ε_1 , ε_2 , ε_1 , see Fig. 1. The surrounding medium has a dielectric permittivity ε_4 . It is assumed that the following inequalities are satisfied: $\varepsilon_1 < \varepsilon_4 < \varepsilon_2$. In the case of the oblique incidence of an infrared wave, when the total internal reflection at interfaces occurs, such a structure behaves as a double barrier one for an incident electromagnetic (EM) wave and a phenomenon of resonant transmission at a set of frequencies can be observed [6]. If the layer 2 is n -GaAs, then there is a possibility to change the effective dielectric permittivity in the infrared range by means of redistribution of electrons between the valleys, because of an essential difference of effective masses and collision frequencies of electrons in lower (Γ) and upper (L, X) valleys [7].

The present report is devoted to investigations of the linear and nonlinear interaction of infrared pulses in double barrier structures with n -GaAs films. High effective modulation of pulses by applying a bias electric field is demonstrated. In the case of an incidence of short powerful pulses, a possibility of the auto switching and the modulation instability in specified frequency ranges and angles of incidence has been demonstrated.

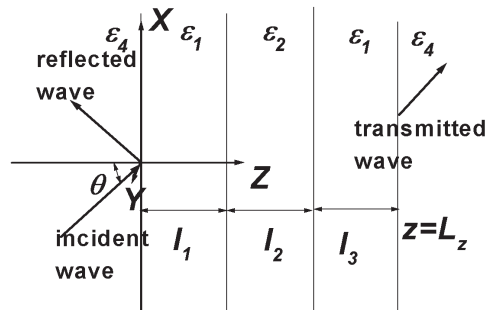


Figure 1: The double barrier resonant structure. The media 1, 4 are dielectrics, the layer 2 is n -GaAs.

2. BASIC EQUATIONS

Consider an interaction of infrared pulses with the structure presented in Fig. 1. This structure is uniform in y direction. The electric field of the wave is polarized along the axis OY (s -polarization). The pulse includes many periods of oscillations, and the nonlinearity is assumed as moderate. The media 1 and 4 are linear, whereas the nonlinearity in the semiconductor layer is taken into account.

The basic equation for the electric field $E \equiv E_y$ of EM wave in the layered structure is:

$$\left(\frac{\partial^2}{\partial x^2} + \frac{\partial^2}{\partial z^2} \right) E = \frac{1}{c^2} \frac{\partial^2}{\partial t^2} ((\varepsilon(z) + \Delta\varepsilon)E), \quad (1)$$

where $\varepsilon(z)$ is the lattice part of the dielectric permittivity, $\Delta\varepsilon$ is its part due to conduction electrons in n -GaAs film. Because $\Delta\varepsilon$ depends on the intensity of the EM wave, Eq. (1) is nonlinear. The value of $\Delta\varepsilon$ can be modulated by a bias electric field too.

We seek a solution of Eq. (1) as:

$$E = A(z, t) \times \exp(i(\omega t - k_x x)) + c.c. \quad (2)$$

Here $A(z, t)$ is a wave amplitude, ω is the carrier frequency; $k_x = (\omega/c)(\varepsilon_4)^{1/2} \sin \theta$ is the x -component of the wave vector of the wave; $\theta \neq 0$ is the incidence angle. The following condition should be satisfied: $|\partial A/\partial t| \ll \omega|A|$, thus, a slow variation of $A(z, t)$ on time t only is assumed [8]. After substitution of (2) into Eq. (1), one can obtain the following equation for $A(z, t)$:

$$\frac{\partial A}{\partial t} + \frac{i\omega}{2} \left(1 + \frac{\Delta\varepsilon'}{\varepsilon(z)} \right) A - \frac{\omega \cdot \Delta\varepsilon''}{2\varepsilon(z)} A - \frac{ik_x c^2}{2\omega\varepsilon(z)} A + \frac{ic^2}{2\omega\varepsilon(z)} \frac{\partial^2 A}{\partial z^2} = 0. \quad (3)$$

Here $\Delta\varepsilon(z, \omega) = \Delta\varepsilon' + i\Delta\varepsilon''$. The imaginary part $\Delta\varepsilon''$ leads to some additional dissipation of the wave.

Equation (3) should be added by boundary conditions at $z = 0$ and $z = L_z$. The amplitude $F(t)$ of the incident wave is given at $z = 0$: $E_{inc}(z = 0, t) = (1/2)F(t) \times \exp(i\omega t) + c.c.$ At $z = L_z$, only the outgoing wave is present. From the conditions of continuity of tangential components of electric (E_y) and magnetic (H_x) fields, the following boundary conditions have been derived:

$$\frac{i}{k_{z4}} \frac{\partial A}{\partial z} + A = F(t) \text{ at } z = 0; \quad \frac{i}{k_{z4}} \frac{\partial A}{\partial z} - A = 0 \text{ at } z = L_z \quad (4)$$

Here $k_{z4} = (\omega/c)(\varepsilon_4)^{1/2} \cos \theta$.

The balance equations for electron concentrations $n_{1,2}$, velocities $V_{1,2}$, and average energies $W_{1,2}$ for electrons in Γ valley (Index 1) and L ones (Index 2), added by the Poisson equation, are used [7]. Below, the equations for Γ valley are given, because the heavy electrons in L valleys can be considered as immobile:

$$\begin{aligned} \frac{\partial n_1}{\partial t} + \text{div} \left(n_1 \vec{V}_1 \right) &= -n_1 \nu_{n12}(W_1) + n_2 \nu_{n21}(W_2) \equiv - \left(\frac{\partial n_2}{\partial t} + \text{div} \left(n_2 \vec{V}_2 \right) \right); \\ \frac{\partial \vec{V}_1}{\partial t} + \left(\vec{V}_1 \nabla \right) \vec{V}_1 &= \frac{e\vec{E}}{m_1^*} - \frac{1}{n_1 m_1^*} \nabla (n_1 T_1) - (\nu_{p1}(W_1) + \nu_{n12}(W_1)) \vec{V}_1; \\ \frac{\partial W_1}{\partial t} + \left(\vec{V}_1 \nabla \right) W_1 &= e\vec{E} \vec{V}_1 - \frac{1}{n_1} \nabla \left(n_1 \vec{V}_1 T_1 - \kappa_1 \nabla T_1 \right) - \nu_{w1}(W_1) (W_1 - W_{10}) \\ &\quad + \frac{W_{12}(W_1)}{n_1} (-n_1 \nu_{n12}(W_1) + n_2 \nu_{n21}(W_2)); \\ \varepsilon_0 \varepsilon_2 \text{div} \vec{E} &= e(n_1 + n_2 - n_0) \end{aligned} \quad (5)$$

Here $\varepsilon_0 \approx 8.86 \times 10^{-12}$ F/m is the electric constant, ν_{p1} , ν_{w1} are momentum and energy relaxation rates, ν_{n12} , ν_{n21} are intervalley transfer rates ($1 \rightarrow \Gamma$, $2 \rightarrow L$); $T_{1,2} = (2/3)(W_{1,2} - m_{1,2}^* V_{1,2}^2/2)$ are electron temperatures in energetic units; $m_{1,2}^*$ are effective masses in the valleys. The function $W_{12}(W_1)$ determines the electron energy transfer between the valleys [7]. The used parameters of n -GaAs have been taken from [7, 9].

The electron velocity has the parts both at the high frequency of an incident EM wave ($\sim 10^{14} \text{s}^{-1}$) and at the lower frequency range ($< 10^{12} \text{s}^{-1}$), whereas the electron concentration and the average electron energy do not include high frequency parts. The equations at the lower frequency range in Γ valley are:

$$\begin{aligned} \frac{\partial n_1}{\partial t} &= -n_1 \nu_{n12}(W_1) + n_2 \nu_{n21}(W_2); \quad n_1 + n_2 = n_0 = \text{const}; \\ \frac{\partial W_1}{\partial t} &= Q - \nu_{w1}(W_1)(W_1 - W_{10}) + \frac{W_{12}(W_1)}{n_1} \frac{\partial n_1}{\partial t}; \quad W_2 = \text{const}; \\ Q &\equiv e \langle V_{1y} E_y \rangle = \frac{e^2 |A|^2 \nu_p(W_1)}{2m_1^* [\omega^2 + \nu_p(W_1)^2]}; \quad \vec{V}_{1,2} \approx 0, \quad \vec{E} = 0 \end{aligned} \quad (6)$$

Here $\nu_p \equiv \nu_{p1} + \nu_{n12}$. The function Q is the heating power for the electrons due to infrared EM field.

The high frequency part of the electron velocity $V_1 \equiv V_{1y}$ is:

$$V_1 = e / (2m_1^* (i\omega + \nu_p)) A \times \exp(i\omega t) + c.c. \quad (7)$$

The expression for the part of the effective dielectric permittivity due to electrons in n -GaAs is:

$$\Delta \varepsilon = -\frac{\omega_p^2}{\omega(\omega - i\nu_p)} = -\frac{\omega_p^2}{\omega^2 + \nu_p^2} - i \frac{\omega_p^2 \nu_p}{\omega(\omega^2 + \nu_p^2)} \quad (8)$$

Here $\omega_p = (e^2 n_1 / m_1^* \varepsilon_0)^{1/2}$ is the electron plasma frequency. It depends essentially on the electron concentration in Γ valley n_1 , which can be changed both by a bias electric field or a strong infrared wave.

The principal mechanism of changing effective dielectric permittivity at high frequencies is the modulation of the electron concentration in Γ valley. In the case of small amplitudes of the incident EM wave, it is possible to modulate the electron concentration by applying the bias electric field in x or y directions. The EM field of a high amplitude leads to the heating of the electron gas. This heating results in both the electron transfer to the upper (L) valleys and also to increase of collision frequency ν_p in the Γ valley.

3. RESULTS OF SIMULATIONS

The Eqs. (3) and (6) have been solved by finite differences. The lattice dielectric permittivities of layers are: $\varepsilon_1 = 2$, $\varepsilon_2 = 6.25$, $\varepsilon_4 = 4$. The thicknesses of layers are of about 1 ... 8 μm . The lattice dissipation has been taken into account as the imagine parts of dielectric permittivities $\varepsilon_1'' = -10^{-4}$, $\varepsilon_2'' = -10^{-3}$.

A typical dependence of the transmission coefficient $T = |A(t, z = L_z)/A_0|^2$ on a frequency ω for the resonant structure is presented in Fig. 2. The value of the electron concentration is

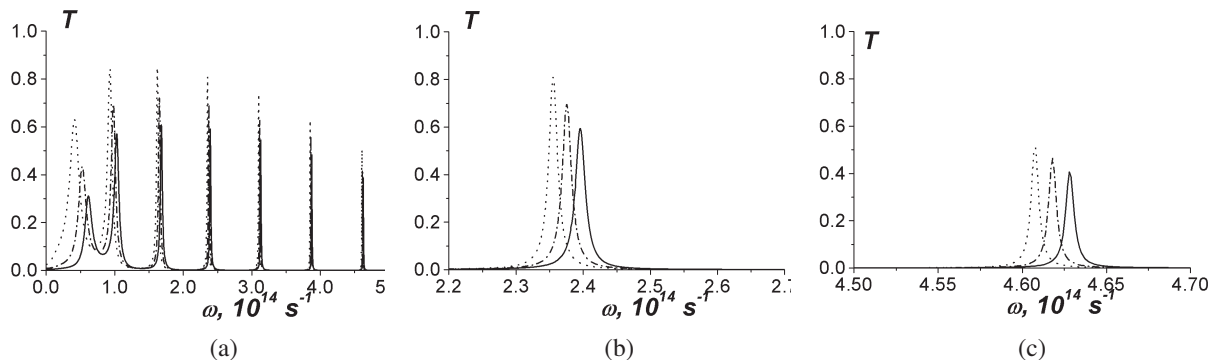


Figure 2: Dependence of the transmission coefficient T on the infrared frequency ω . The thicknesses of layers are: $l_1 = l_2 = l_3 = 6 \mu\text{m}$, the incidence angle of the wave is $\theta = 45^\circ$. Part (a) is a general view, parts (b), (c) are detailed representations.

$n_0 = n_1 = 3 \times 10^{17} \text{ cm}^{-3}$. This dependence consists of a series of sharp peaks of a resonant transparency. The most interesting results can be obtained when the carrier frequency ω of incident pulses is in the vicinity of a resonant transmission frequency.

Initially we have investigated a modulation of a continuous EM wave in the infrared range by applying the bias electric field to *n*-GaAs layer, see Fig. 2. To obtain 50% transfer of electrons into the upper valleys, it is necessary to apply the bias electric field $\sim 5 \text{ kV/cm}$ [7]. A bias electric field leads to a redistribution of electrons between the valleys, so $n_2 \sim n_1$ within the *n*-GaAs film. The incident wave amplitudes are assumed as small here.

In Fig. 2, the transmission coefficients are presented in the case of the absence of a bias electric field (all the electrons are within the Γ valley, the solid line) and in the presence of it ($n_1 = 2 \times 10^{17} \text{ cm}^{-3}$, $n_2 = 1 \times 10^{17} \text{ cm}^{-3}$, dash-dot line; $n_1 = 1 \times 10^{17} \text{ cm}^{-3}$, $n_2 = 2 \times 10^{17} \text{ cm}^{-3}$, dot line). At the frequencies $\omega = 2.395 \times 10^{14} \text{ s}^{-1}$, $3.132 \times 10^{14} \text{ s}^{-1}$, $3.877 \times 10^{14} \text{ s}^{-1}$ an effective modulation is $\approx 95\%$, when the ratio of electron population of the valleys is $n_2/n_1 = 2$.

More interesting results have been obtained when the pulses of high input amplitudes interact with the structure without a bias electric field. Various dynamic nonlinear phenomena take place there. Auto switching of the short pulses and the modulation instability of long pulses can occur. An incident pulse is rectangular-like $F(t) = A_0 \times \exp(-((t - t_1)/t_0)^6)$, where A_0 is a maximum amplitude. The value $A_0 = 10$ corresponds to the intensity of the EM wave $\approx 10 \text{ MW/cm}^2$. In Fig. 3, the incident and transmitted pulses are given. The incident pulses are short, the durations are 5 ... 50 ps. At low input amplitudes, the reflection of the pulse is weak there. At higher amplitudes, the reflection increases and the shape of transmitted pulse changes, when compared with the linear case. The nonlinear increase of transparency (switching from reflection to transmission) also can take place.

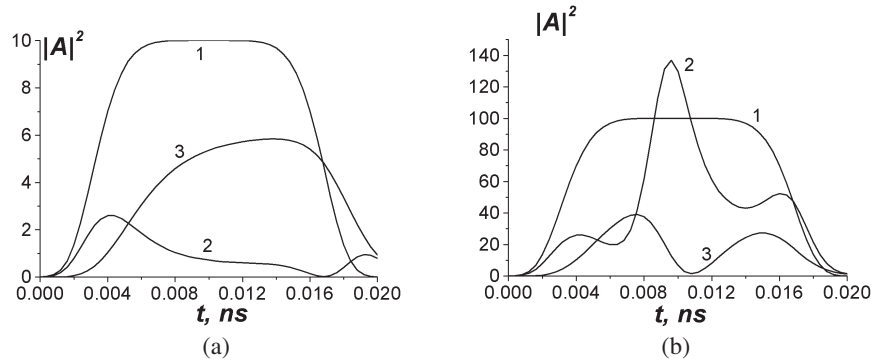


Figure 3: Switching of linear (part (a)) and nonlinear (part (b)) short pulses. The thicknesses of the layers are $l_1 = l_2 = l_3 = 6 \mu\text{m}$, the incidence angle is $\theta = 45^\circ$, the carrier frequency is $\omega = 2.395 \times 10^{14} \text{ s}^{-1}$. Part (a) is for $A_0^2 = 10$, part (b) is for $A_0^2 = 100$. Curve 1 is the input pulse, 2 is reflected wave, 3 is transmitted one.

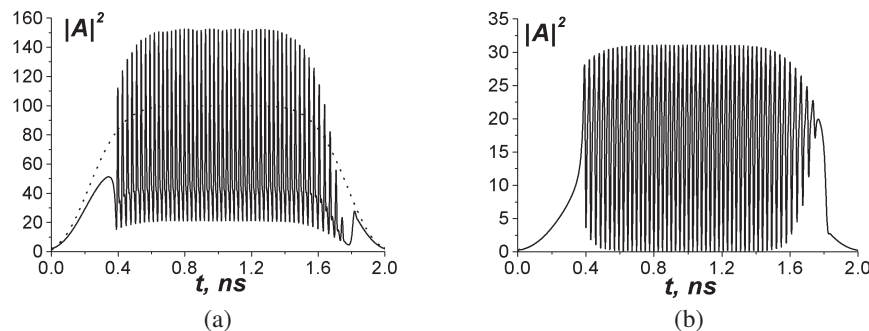


Figure 4: Modulation instability of a long pulse. The thicknesses of layers are $l_1 = l_2 = l_3 = 6 \mu\text{m}$, a carrier frequency is $\omega = 4.6225 \times 10^{14} \text{ s}^{-1}$; the incidence angle is $\theta = 45^\circ$. Part (a) is incident (dot line) pulse and reflected (solid line) wave; part (b) is transmitted wave.

The most interesting phenomenon is an occurrence of the modulation instability of long input pulses. The modulation instability takes place in the vicinity of the higher resonant transmission frequencies, where the peaks of transparency are narrow, see Fig. 2(c). To produce the modulation instability, the amplitude of the incident pulse should be higher than some threshold value (the intensity is of about 5 MW/cm^2). The higher frequency transmission zones should be chosen. In Fig. 4, a typical dynamics of the modulation instability is presented. The carrier frequency is $\omega = 4.6225 \times 10^{14} \text{ s}^{-1}$.

4. CONCLUSION

The interaction of linear and nonlinear infrared EM waves with layered structures in the case of the oblique incidence is considered. The total internal reflection and the resonant transparency can be observed there. The structures that include n -GaAs layers can be used as effective modulators in the infrared range. A mechanism of the modulation and nonlinearity is the redistribution of electrons between the lower (Γ) and upper (L) valleys within the semiconductor. The redistribution occurs both by a bias electric field and a field of strong infrared pulse. When the amplitude of an incident pulse is enough high, the auto switching of the short pulses takes place. In the case of long pulses, the occurrence of the modulation instability of strong pulses has been demonstrated, when the carrier frequency is chosen in a vicinity of higher frequency transparency regions.

ACKNOWLEDGMENT

This work was supported by CONACyT, Mexico (Project 48955).

REFERENCES

1. Dutta Gupta, S., "Nonlinear optics of stratified media," *Progress in Optics*, Elsevier, Amsterdam, Vol. 38, 1998.
2. Kivshar, Y. S. and G. P. Agrawal, *Optical Solitons: From Fibers to Photonic Crystals*, Academic Press, San Diego, CA, 2003.
3. Slusher, R. E. and B. J. Eggleton, *Nonlinear Photonic Crystals, Springer Series in Photonics*, Vol. 10, Springer, Berlin, 2003.
4. Escobedo-Alatorre, J., J. Sanchez-Mondragon, M. Torres-Cisneros, et al., "A device approach to propagation in nonlinear photonic crystal," *Optical Materials*, Vol. 27, No. 11, 1260–1265, 2005.
5. Shkerdin, G. N. and A. I. Voronko, "Peculiarities of the nonlinear reflection of the far infrared radiation from a structure with high doped GaAs layer," *Photonics and Optoelectronics*, Vol. 1, No. 4, 193–200, 1993.
6. Shvartsburg, A. B., "Tunneling of electromagnetic waves," *Phys. Usp.*, Vol. 50, No. 1, 37–52, 2007.
7. Tomizawa, K., *Numerical Simulation of Submicron Semiconductor Devices*, Artech House, London, 1993.
8. Scalora, M. and M. E. Crenshaw, "A beam propagation method that handles reflections," *Opt. Commun.*, Vol. 108, No. 1, 191–196, 1994.
9. "New semiconductor materials. characteristics and properties," <http://www.ioffe.ru/SVA/NSM/>.

Photo-induced Modification of Refractive Index in Compounds

$\text{As}_x\text{S}_{1-x}$

A. Popescu, D. Savastru, and S. Micloș

National Institute of R&D for Optoelectronics INOE-2000

409 Atomiștilor Str., Magurele, Ilfov 077125, Romania

Abstract— Non-crystalline chalcogenide compounds have a large domain of glass formation, good optical transparency including middle IR, consistent large value of refractive index (2.4–3.3). The films of $\text{As}_x\text{S}_{1-x}$ with thickness of 0.5–3.0 μm and different composition were obtained by vacuum thermal evaporation. The refractive index for thin films was calculated from transmission spectra $T(\lambda)$ of films measured in spectral range of 300–2000 nm and the transmission spectra of pure oxide glass substrate. The transmission spectra of films modified by argon laser irradiance were measured and the modification of refractive index was calculated. The permanent modification value of Δn is 0.05.

1. INTRODUCTION

Refractive index and absorption coefficient modifications were studied for thin films of chalcogenide compounds obtained by thermal vaporization.

As_2S_3 film is irradiated by an Argon laser, emitting on 0.48 μm . As a result of illumination with an intensity of 20–40 mW/cm^2 , photostructural modifications arise in material manifesting by increase of the absorption coefficient at photon energies around the fundamental absorption edge. Modifications also arise in the range of the weak absorption but these may be put in evidence by special methods, for instance investigating the light propagation through planar optical waveguides. The refractive index was measured in the spectral range 0.6–1.0 μm . The dispersion curves are displayed in Fig. 1 for a 60 s exposure. From the displayed results it can be noticed that the illumination of the film with photons having the energy of quanta $h\omega > E_g$ (for As_2S_3 , $E_g = 2.4 \text{ eV}$) produces essential changes of the refractive index in all the spectral band. But in the region of the shorter wavelength the variation of the refractive index $\Delta n = 0.07$ is larger than in the spectral range of larger wavelengths ($\lambda = 1.0 \mu\text{m}$), where it increases with 0.04. In the spectral range of 0.85 μm an increase of the refractive index is noticed. This fact may be determined by a higher density of the energetic levels. Being placed deeply in the band gap ($\sim E_g/2$), population of these energy levels will have a larger life time. Thus the modifications induced by laser irradiation will persist for a larger time.

The character of the modifications of the refractive index differs in dynamics in different portions of the spectrum. The results presented in Fig. 2 indicate a rapid increase of the refractive index at the wavelength of 0.65 μm , further taking place the saturation. In the spectral segment of larger wavelength $\lambda = 1.0 \mu\text{m}$ a tergiversation can be noticed and only after 50–60 s the refractive index begins to increase.

Also in these materials the measurements made with a profilometer revealed that the thickness of the film diminished as result of illumination. The decreases are about $\Delta h/h \sim 5 \cdot 10^{-2}$.

2. THE STUDY OF WEAK OPTICAL ABSORPTION IN AMORPHOUS As_2S_3 FILMS

The investigation of the energy levels spectrum in amorphous materials is made different methods. One of them is the method of optical absorption. Concluding results using this method were obtained studying band-to-band absorption, that manifests by the dependence $(h\omega - E_g)^n$ of the absorption coefficient α on the photons energy and also in the domain of Urbach absorption, that is characterized by an exponential dependence of the optical absorption coefficient $\alpha \sim \exp(h\omega/E_1)$. The parameter E_1 characterize the extent of the states placed in the band gap. For the most amorphous materials the value of the energy E_1 lays in the interval 0.05–0.08 eV and it is a reproducible amount for the given material, depending weakly of the conditions of the preparation.

At energies lower than Urbach absorption threshold ($\alpha \sim 1 \text{ cm}^{-1}$) in non-crystalline materials a weak optical absorption may be identified. Spectral dependence $\alpha = f(h\omega)$ in this domain may be also approximated to an exponential, but the exponential parameter differs much from the Urbach domain.

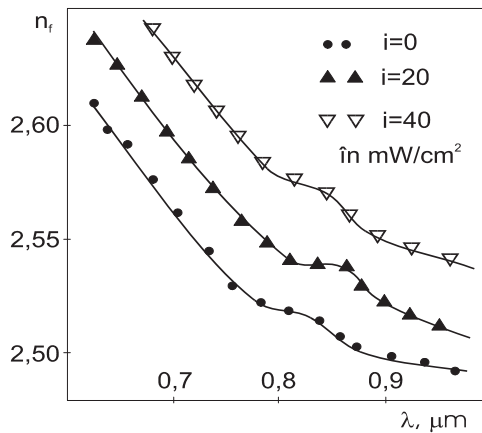


Figure 1: Spectral dependence of the refractive index of the As_2S_3 amorphous films.

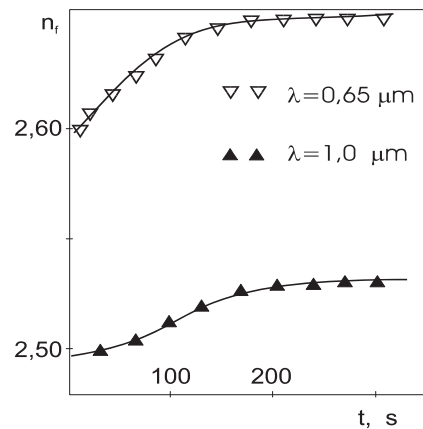


Figure 2: Refractive index modifications dynamics in As_2S_3 films.

The measurements of the weak absorption spectrum [1] revealed a strong dependence of the spectrum on the technological conditions in which the material was obtained and on the presence of the impurities. The exponential parameter for this domain is 0.3 eV for As_2S_3 .

Taking into account these peculiarities of the weak optical absorption in non-crystalline materials it is important to know the absorption spectrum for thin films. The accomplishment of these measurements for films thinner than $5 \mu\text{m}$ presents considerable difficulties. The methods based on the measurement of the optical transmission have a low sensitivity because for films the product αd is in the range of 10^{-4} . The weak optical absorption spectrum in thin films was studied first in the paper [2], using the method of light propagation in As_2S_3 films made as planar waveguides.

Coupling the light in the guide as well the extraction of the light is accomplished using rutile prisms. As light source is used a halogen Xenon lamp. Monochromatic light is obtained using MDR24 monochromator. In order to provide a good coupling of the light into the guide a collimation system composed of two cylindrical lenses was used. The obtained results for two positions of the prisms are adjusted with data got for the wavelength $0.63 \mu\text{m}$ using a He-Ne laser. The spectral dependence of the optical absorption in As_2S_3 thin films is displayed in Fig. 3.

The Urbah part of the spectrum (B) corresponds exactly with the published results for bulk and fiber materials. At the same time the characteristic parameters for part C essentially differ of the absorption in bulk and fibers. The spectral dependence may be approximated by the formula $\alpha = 3.5 \cdot 10^{-2} \exp(h\nu/0.5) \text{ cm}^{-1}$, so the exponential parameter for films is 0.5 eV.

At illumination of the film with Argon laser radiation, having the wavelength of $0.51 \mu\text{m}$ and the intensity 20 mW/cm^2 , during 5 min the absorption spectrum shifts towards the red part of the spectrum with 0.15 eV. Also, the Fig. 3 reveals a considerable increase of the optical losses in domain C, because the light scattering following the clusters forming.

Starting from the exponential distribution of the states in the band gap Wood and Tauc [4] deduced the expression of optical absorption coefficient, which is proportional to the total concentration of the localized states. Basing on this model and using the experimental data they estimated the concentration of the localized energetic levels in bulk materials in the range $10^{16} - 10^{17} \text{ cm}^{-3}$.

Analyzing the data in Fig. 3 on the basis of the model [4] the states concentration in As_2S_3 films may be estimated in the range $10^{18} - 10^{19} \text{ cm}^{-3}$. Thus it was found that the concentration of the localized states in films is with two magnitude orders higher than in bulk samples. A second characteristic element consists in the difference of the exponential parameter, that characterizes the speed of the diminishment of the concentration of the energetic levels towards the center of the band gap. For films resulted 0.5 eV, that differs much from the value 0.3 eV characteristic for bulk materials and optical fibers made of As_2S_3 .

3. MODIFICATIONS INDUCED BY CO_2 LASER RADIATION TREATMENT

The action of CO_2 CW laser radiation on amorphous As-S compounds was studied using 1–2 μm -thick films obtained by thermal evaporation on a BK7 glass substrate.

CO_2 laser radiation (wavelength $10.6 \mu\text{m}$) is focused by a Germanium lens up to a $100 \mu\text{m}$ diameter spot and it is perpendicular to the film surface. The glass substrate with the deposited

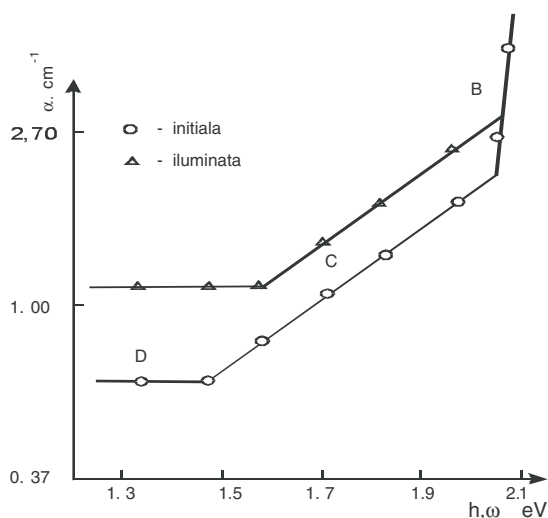


Figure 3: Dependence of optical absorption coefficient in As_2S_3 amorphous films on photon energy.

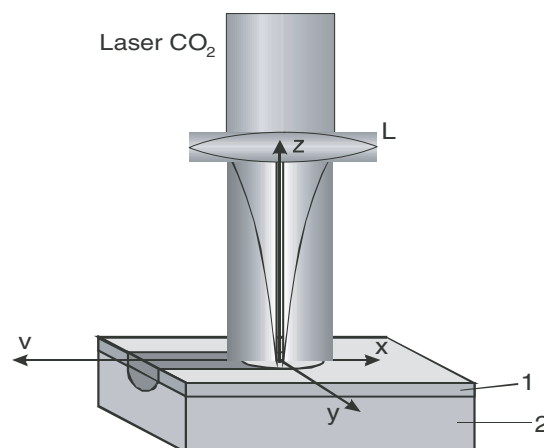


Figure 4: Achievement of the light channel in planar wave guides by laser annealing using CO_2 CW laser radiation.

film is mounted on a translation mechanism that moves at constant speed between 0.75 and 4 mm/s. Using filters the laser power may be attenuated in the range 50–300 mW. Experimental layout is schematically displayed in Fig. 4.

In order to compute the conditions of the laser annealing with CO_2 laser radiation it is necessary to solve the heat diffusion equation for a heat source Q that is shifting with the speed v . The heat amount emitted by a source having a Gaussian distribution in section, that moves towards direction x with the speed v can be computed from the equation:

$$Q = (1 - R) \cdot \frac{P}{2\pi a^2} \cdot \alpha \exp(\alpha z) \cdot \exp\left[-\frac{(x - vt)^2 + y^2}{2a^2}\right]$$

where P is the laser power; R is the coefficient of optical reflection on the structure surface. Positive direction of the z -axis is outward the material, considered a semi-infinite medium.

The absorption coefficient of the glass for the wavelength $10.6 \mu\text{m}$ is $\alpha = 5 \cdot 10^3 \text{ cm}^{-1}$. Thus the laser radiation penetrates till a depth that is much less than the estimated depth of the thermal front, which is about $100 \mu\text{m}$. It may be considered that the heat emits uniformly in a layer with a thickness $d = 1/\alpha$. The thickness of the As-S film is much lower than the depth at which the thermal front propagates and may be neglected. Therefore, in the equation of the thermal diffusion it will be applied the thermal diffusion coefficients ($6.4 \cdot 10^{-3} \text{ cm}^2/\text{s}$) and the specific thermal capacity ($0.71 \cdot 10^3 \text{ J/kg}\cdot\text{K}$) for the glass used as substrate. On these conditions the equation may be integrated using the approximations of Cline and Antony [5].

The modifications of the optical parameters of As_2S_3 and As_2S_5 amorphous films, exposed to laser annealing, were examined using an interferometric transmission microscope of Mach-Zender

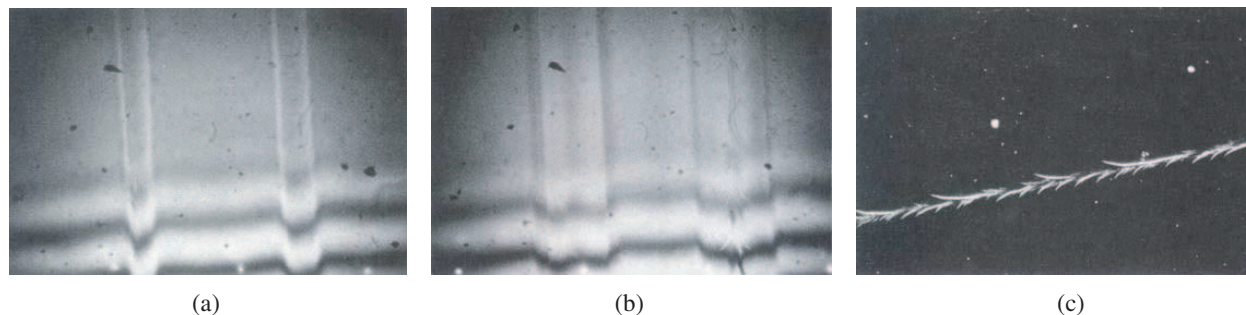


Figure 5: Interferograms of the modification of the optical path in As_2S_5 films: (a) Power: 100 mW. Left — 1.5 mm/s, right — 1 mm/s, (b) Power: 210 mW speed 4 mm/s, left — after eight consecutive scans, (c) needle-form structure.

type in order to get quantitative measurements. For As_2S_3 the interferograms are displayed in Fig. 5. In the areas scanned by the CO_2 laser beam the interference lines shift toward the direction perpendicular to the movement direction.

Researches on laser annealing on As_2S_5 films showed that the modification of the optical path is backward as for As_2S_3 films. For high scan speeds (4 mm/s) in the middle of the channel there are forming spatial structures resembling to needle crystals (dendrites) (Fig. 5(c)). These structures have a periodic character.

4. CONCLUSIONS

Multiple scanning of the channel with the same beam re-melts the micro crystals and leads to restauration of the amorphous state. The profilometric measurements determined a considerable increase of the film thickness, up to 20%, followed by a diminishment of the refractive index. That is why the As_2S_5 compounds does not allow the light propagation in the channels achieved by the given method.

The considerable modifications of the characteristics of this material may be explained as a result of some important changes in structure. According to the data of the authors [6] (p. 94), maintaining the amorphous compound As_2S_5 at the temperature of 190°C leads to dissociation of the structural tetrahedral units S-As-S into chain-form $\text{AsS}_{3/2}$ and $\text{SS}_{2/2}$ structural units. A similar situation appears when heating the films by laser beams.

REFERENCES

1. Kanamari, T. and Y. Terunuma, *J. of Lightwave Technology*, Vol. 2, No. 5, 607–613, 1984.
2. Popescu, A., et al., “Weak absorption tails in As_2S_3 thin films,” *Paper Abstracts of National Physics Conference*, 91, Iasi, 1992.
3. Andriesh, A. M., S. D. Shutov, E. P. Kolomeiko, and I. N. Lerman, “Fizicheskie svoistva slozhnyh poluprovodnikov,” *Sbornik*, Kishinev, 187–191, 1973.
4. Kolomiets, B. T., S. K. Pavlov, and T. F. Mazets, “Amorfnye poluprovodniki-80,” *Elektroopticheskiï Effect v Stekloobraznom As_2S_3 . Materialy Mezhdunarodnoi Konferentsii*, Kishinev, 238–240, 1980.
5. Cline, H. E. and T. R. Antony, “Heat treating and molting material with a scanning laser or electron beam,” *J. Appl. Phys.*, Vol. 48, 3895, 1977.
6. Borisova, Z. U., “Halkogenidnye poluprovodnikovye stekla,” Leningrad, 1983.

Temperature Dependence of Piezoelectric Potential Phonon Scattering Properties of ZnO Of the Quantum — Qusi Two Dimensional System under Two Directional Circularly Polarized Oscillating Fields

Su-Ho Lee², Joung-Young Sug¹, Jun-Yong Choi¹, Ji Ho Park¹,
Gi-Dong Oh³, and Geon Sa-Gong²

¹Electronic and Electrical Engineering School, Kyungpook National University
Daegu 702-701, Korea

²Department of the Electrical Engineering, Dong-A University
Pusan 604-714, South Korea

³Research Institute of Myoung-Bo Electronic Company
Pusan 604-714, South Korea

Abstract— We investigated theoretically the quantum cyclotron resonance transition properties of ZnO in quasi 2-dimensional Landau splitting system, based on quantum transport theory. We apply the quantum transport theory to the system in the electrons confined by a square well potential. We investigate the optical quantum transition line shapes of ZnO relating with the absorption power and the quantum transition line widths of ZnO relating with the scattering effect in the electron-piezoelectric potential phonon interacting system under a circularly polarized oscillatory external fields. The half-widths $\gamma(T)_{total}$ of ZnO in external field wavelength 295 μm increase as the temperatures increase. Through the analysis of this work, we found the increasing properties of QTLW and QTLS with the temperature. We also found the dominant scattering processes are the phonon emission transition process and inter level transition process.

1. INTRODUCTION

It is well known that ZnO is the piezoelectric potential phonon interaction scattering effect active. The reason why we are mostly interested in these materials The wide band-gap semiconductors, including ZnO AlN, InN, and their ternary compounds, have great potential for applications in high-power and optoelectronic devices in the blue and the ultraviolet regions. Than, the investigation of quantum optical transition properties of this materials is very important, So, in this research, we investigated the quantum optical transition properties of ZnO, in qusi 2-Dinensinal Landau splitting system, based on quantum transport theory.

There are many theories regarding the quantum transport problems in various methodologies [1–17], among them we use the projected Liouville equation method with in the equilibrium average projection scheme (EAPS) [13]. The merit of using EAPS is that the quantum response function and the scattering factor formula can be obtained in a onestep process by expanding the quantum transport theory. In the previous work [14], we applied the EAPS theory in Ge and Si, since there are abundant experimental date [15]. We compared our results of numerical calculations of the EAPS theory [14] with existing experimental data [15] and showed a good agreement between them. This indicated that the EAPS theory is useful in analyzing many-body systems. The analysis of the temperature and the magnetic field dependence of the QTLW is very difficult in other theories or experiment, because the absorption power in the various external field wavelengths is required to be calculated or observed. The QTR theory within EAPS is advantageous in this respect as it allows the QTLW to be directly obtained through EAPS, in the various external field wavelengths. In short calculation of the absorption power is not required to obtain the QTLW if EAPS is introduced [11]. But, the previous work [14] restricted for non-confining potential systems with the extremely weak coupling (EWC) approximation.

Low-dimensional electron systems are very important and useful for the study of quantum many-body effects. Experimental realization of the quasi-two dimensional quantumwell structures has raised a lot of interest in the quantum transport properties of electrons in confining potential systems. The properties of the electrons are determined by interactions between electrons and scatterers. If an electromagnetic wave enters a system, the electrons make the optical transition between energy states formed in a quantum well, which is influenced by the interactions. Therefore, the study of the transitions provides information not only on electronic structures but also

on carrier scattering mechanisms in condensed matters. The optical power absorption spectrum of the transitions measured in experiments is directly related to the electric conductivity tensor, and the spectrum's linewidth to its line-shape function. Hence, it is important to obtain an explicit expression of the line-shape function for a given confining potential system on the basis of a theoretical formulation. Recently, we suggested a more precise procedure of expanding and application of EAPS in Low-dimensional electron systems with the moderately weak coupling (MWC) approximation in Refs. [15–17]. In the MWC scheme, the distribution components can provide an adequate explanation of the quantum transition processes [15–17]. In a previous work [14], the intermediate states of quantum transition processes do not appear.

In this work, we investigate the optical Quantum Transition Line Shapes (QTLSs) of ZnO which show the absorption power and the Quantum Transition Line Widths (QTLWs) of ZnO, which show the scattering effect in the electron-piezoelectric potential phonon interacting system under circularly polarized oscillatory external fields. With the numerical calculation, we analyzed the temperature dependences of the QTLW and QTLS in various cases. In order to analyze the quantum transition, we compare the magnetic field dependencies of the QTLW and the QTLS on four transition processes, namely, the intra-level transition process, the the inter-level transition process, the phonon emission transition process and the phonon absorption transition process.

2. THE ABSORPTION POWER FORMULA AND THE SCATTERING FACTOR FUNCTION

When a static magnetic field $\vec{B} = B_z \hat{z}$ is applied to an electron system, the single electron energy state is quantized to the Landau levels. We select a system of electrons confined in an infinite square well potential (SQWP) between $z = 0$ and $z = L_z$ in the z -direction. We use the eigenvalue and eigenstate of Ref. [10] of the square well potential system. We suppose that an oscillatory electric field $E(t) = E_0 \exp(i\omega t)$ is applied along the z -axis, which gives the absorption power delivered to the system as $P(\omega) = (E_0^2/2)\text{Re}\{\sigma(\omega)\}$, where “Re” denotes the real component and $\sigma(\omega)$ is the optical conductivity tensor which is the coefficient of the current formula. Here the absorption power represents the optical QTLS and the scattering factor function represents the optical QTLW. We consider the electron-phonon interacting system and then we have the Hamiltonian of the system as

$$H_s = H_e + H_P + V = \sum_{\beta} \langle \beta | h_0 | \beta \rangle a_{\beta}^{\dagger} a_{\beta} + \sum_q \hbar \omega_q b_q^{\dagger} b_q + \sum_q \sum_{\alpha, \mu} C_{\alpha, \mu}(q) a_q^{\dagger} a_{\mu} (b_q + b_{-q}^{\dagger}). \quad (1)$$

Here H_e is the electron Hamiltonian, h_0 is a single-electron Hamiltonian, H_P is the phonon Hamiltonian and V is the electron-phonon (or impurity) interaction Hamiltonian. The $b_1(b_2^{\dagger})$ are the annihilation operator (creation operator) of boson particle, and \vec{q} is phonon (or impurity) wave vector. The interaction Hamiltonian of electron-phonon interacting system is $V \equiv \sum_q \sum_{\alpha, \mu} C_{\alpha, \mu}(q) a_{\alpha}^{\dagger} a_{\mu} (b_q + b_{-q}^{\dagger})$ where the coupling matrix element of electron-phonon interaction

$C_{\alpha, \mu}(q)$ is $C_{\alpha, \mu}(q) \equiv V_q \langle \alpha | \exp(i\vec{q} \cdot \vec{r}) | \mu \rangle$, \vec{r} is the position vector of electron and V_q is coupling coefficient of the materials and the corresponding Liouville operator L_s are given by $L_s X \equiv [H_s, X]$ for an arbitrary operator X . For the optical quantum transition system under a right circularly polarized external field current, we replace the current with $J_k \equiv J^-$ and $J_l \equiv J^+$ for the current system under an oscillating external field of frequency ω . The many-electron current operators J^- and J^+ are defined $J^- \equiv \tilde{g}_{(sys)} \sum_{\beta} \sqrt{N_{\beta}} a_{\beta}^{\dagger} a_{\beta+1}$ and $J^+ \equiv \tilde{g}_{(sys)} \sum_{\beta} \sqrt{(N_{\beta} + 1)} a_{\beta+1}^{\dagger} a_{\beta}$ with

$\tilde{g}_{(sys)} \equiv (-ie\hbar/m_e^*) \sqrt{1/l_0^2}$. $\tilde{g}_{(sys)}$ can be changed for other systems and external fields. Here $l_0 = \sqrt{\hbar/eB}$ is the radius of cyclotron motion, $\omega_c = eB/m_e^*$ is the cyclotron frequency, m_e^* is the effective mass of electron.

Recently, we suggested a more precise procedure of expanding and application of EAPS with the moderately weak coupling (MWC) approximation in Refs. [15–17]. Using the properties of the projection operator and the conventional series expansion of the propagator, we obtained a right circularly polarized external field current $J^R(\omega)$ and the scattering factor $\Xi_{kl}^{(R)}(\omega)$ in a simple form by using a weak interacting system approximation in pair interacting system as

$$J^R(\omega) = \left[\frac{-(i/\hbar) \Lambda_{kl}^{(R)}}{\omega - A_{kl}^{(R)} + \Xi_{kl}^{(R)}(\omega)} \right] E(\omega), \quad (2a)$$

where $\Lambda_{kl}^{(R)} = -\left\{\left(\frac{i}{\omega}\right) \sum_{\alpha} j_{\alpha+1,\alpha}^{+} j_{\alpha,\alpha+1}^{+} (f_{\alpha+1} - f_{\alpha})\right\}$, $A_{kl}^{(R)} = i\omega_c$.

We can easily obtain the ohmic left circular current under a left circularly polarized external field (LCF) from the response formula with the EAPS, while recent research on the response formula was restricted to the ohmic right circular current under a right circular polarized external field. For the left circular polarized external field system, we replace r_k to $J_k \equiv J^+$, $L_l'X$ with $L_l'X \equiv (-i/\omega)[J^-, X]$, and $J_l \equiv J^-$. We obtain the ohmic left circular current from the response formula as follow;

$$J^L(\omega) = \left[\frac{-(i/\hbar)\Lambda_{kl}^{(L)}}{\omega - A_{kl}^{(L)} + \Xi_{kl}^{(L)}(\omega)} \right] E(\omega), \quad (2b)$$

where $\Lambda_{kl}^{(L)} = -\left[\left(\frac{i}{\omega}\right) \sum_{\alpha} j_{\alpha+1,\alpha}^{+} j_{\alpha,\alpha+1}^{+} (f_{\alpha} - f_{\alpha+1})\right]$ and $A_{kl}^{(L)} = -i\omega_c$.

Using the properties of the projection operator and the conventional series expansion of the propagator $G_k^q(\omega_l)$ [15–17], we obtain the scattering factor as a simple form with a weak interaction system approximation in a pair interaction system, as

$$\Xi_{kl}^{(R)}(\omega_l) \equiv \frac{i}{\hbar\Lambda_{kl}^{(R)}} \langle L'_+ L_v G_d L_v J^- \rangle_B, \quad (3a)$$

$$\Xi_{kl}^{(L)}(\omega_l) \equiv \frac{i}{\hbar\Lambda_{kl}^{(L)}} \langle L'_- L_v G_d L_v J^+ \rangle_B, \quad (3b)$$

where the diagonal propagator is $G_d = 1/(\hbar\omega - L_d)$. Here, we used the Ref. [11], $Tr^{(e)}\{J_k L_1 L_2 \dots L_n L' \rho_s\} = (-1)^{n+1} \langle L' L_n \dots L_2 L_1 J_k \rangle$, and the $\langle \dots \rangle$ means the ensemble average of the electron states and background particle state. The scattering factor function, $\Xi_{kl}(\omega_l)$, is expressed in a complex form like $\Xi_{kl}(\omega_l) \equiv i\Delta_{\text{total}} + \gamma_{\text{total}}(\omega)$ with $\Delta_{\text{total}} \equiv \text{Im}\Xi_{kl}(\omega_l)$, giving a line shift of a response-type formula, and $\gamma_{\text{total}}(\omega) \equiv \text{Re}\Xi_{kl}(\omega)$ giving the half-width of the response-type formula. In most cases, the imaginary part of the scattering factor, Δ_{total} , is negligible in a real system because of its small value. With in the continuous approximation [14] in a right circularly polarized external field, the absorption power formula (or the QTLS formula) is obtained finally as

$$P^{(R)}(\omega) \propto \left(\frac{e^2 \omega_c^2}{\pi^2 \hbar \omega} \right) \left[\frac{\gamma_{\text{total}}^{(R)}(\omega_c) \sum_{N_{\alpha}} \int_{-\infty}^{\infty} dk_{z\alpha} (N_{\alpha} + 1) (f_{\alpha} - f_{\alpha+1})}{(\omega - \omega_c)^2 + \left(\gamma_{\text{total}}^{(R)}(\omega_c)\right)^2} \right], \quad (4)$$

where the scattering factor function (or QTLW) is given by

$$\gamma_{\text{total}}^{(R)}(\omega) \equiv \text{Re}\Xi_{kl}^{(R)}(\omega) \equiv \sum_{\mp} \sum_{N_{\alpha}=0} \sum_{N_{\beta}=0} \gamma_{\alpha,\beta}^{(R)\mp} = \left(\frac{\Omega}{4\pi\hbar^2 v_s} \right) \frac{\sum_{\mp} \sum_{N_{\alpha}=0} \sum_{N_{\beta}=0} \int_{-\infty}^{\infty} dk_{z\alpha} \int_{-\infty}^{\infty} dq_z Y_{\alpha,\beta}^{(R)\mp}}{\sum_{N_{\alpha}=0} \int_{-\infty}^{\infty} dk_{z\alpha} (N_{\alpha} + 1) (f_{\alpha+1} - f_{\alpha})}. \quad (5)$$

Likewise, for the left circularly polarized external field, we obtained the absorption power formula (or the QTLS formula) as

$$P^{(L)}(\omega) \propto \left(\frac{e^2 \omega_c^2}{\pi^2 \hbar \omega} \right) \left[\frac{\gamma_{\text{total}}^{(L)}(\omega_c) \sum_{N_{\alpha}} \int_{-\infty}^{\infty} dk_{z\alpha} (N_{\alpha} + 1) (f_{\alpha+1} - f_{\alpha})}{(\omega - \omega_c)^2 + \left(\gamma_{\text{total}}^{(L)}(\omega_c)\right)^2} \right], \quad (6)$$

where the scattering factor function (or QTLW) is given by

$$\gamma_{\text{total}}^{(L)}(\omega) \equiv \text{Re}\Xi_{kl}^{(L)}(\omega) \equiv \sum_{\mp} \sum_{N_{\alpha}=0} \sum_{N_{\beta}=0} \gamma_{\alpha,\beta}^{(L)\mp} = \left(\frac{\Omega}{4\pi\hbar^2 v_s} \right) \frac{\sum_{\mp} \sum_{N_{\alpha}=0} \sum_{N_{\beta}=0} \int_{-\infty}^{\infty} dk_{z\alpha} \int_{-\infty}^{\infty} dq_z Y_{\alpha,\beta}^{(L)\mp}}{\sum_{N_{\alpha}=0} \int_{-\infty}^{\infty} dk_{z\alpha} (N_{\alpha} + 1) (f_{\alpha+1} - f_{\alpha})}. \quad (7)$$

The integrand-factor $Y_{\alpha,\beta}^{(L)\mp}$ and $Y_{\alpha,\beta}^{(R)\mp}$ has a complicated form, recently, we suggested the final derivation of the integrand of the scattering factor in Refs. [15–17]. We use the result equations from (18) to (23) in Ref. [17].

3. THE ANALYSIS AND SUMMARY

Through the numerical calculation of the theoretical result of QTLS and of the QTLW, we analyze absorption power and line widths of ZnO. We use the material constant of Table 1. In order to analyze the quantum transition process, we denote the total QTLW as $\gamma_{\text{total}} \equiv \gamma_{\text{em}} + \gamma_{\text{ab}}$, where $\gamma_{\text{intra}} \equiv \gamma_{0,0}^+ + \gamma_{0,0}^-$, $\gamma_{\text{interl}} \equiv \gamma_{0,1}^+ + \gamma_{1,0}^+ + \gamma_{0,1}^- + \gamma_{1,0}^-$, $\gamma_{\text{em}} \equiv \gamma_{0,0}^+ + \gamma_{0,1}^+ + \gamma_{1,0}^+$ and $\gamma_{\text{ab}} \equiv \gamma_{0,0}^- + \gamma_{0,1}^- + \gamma_{1,0}^-$ are the QTLW of the intra level transition, the inter level transition, the total phonon emission and absorption transition process, respectively.

Table 1: Material constant of ZnO.

Symbol	Contents	Value	Symbol	Contents	Value
m^*	Effective mass of electron	$0.28m_0$	\bar{K}	Electromechanical constant	$6 \times 10^{-2} \text{ m/s}$
\bar{m}	Effective mass of hole	$0.59m_0$	\bar{v}_s	Speed of sound	4300.5 m/s
ρ	Mass density	4090 kg/m^3	$\bar{\varepsilon}_s$	Energy gap	1.219 eV
κ	Characteristic constant	$17.88 \times 10^{-4} \text{ eV/K}$	L_z	Length of well of z direction	$50 \times 10^{-9} \text{ m}$
ξ	Characteristic constant	204			

In Fig. 1(a), the temperature dependence $\gamma(T)$ of QTLW is plotted. As shown in Fig. 1(a), $\gamma(T)$ increase as temperatures increase for the external field wavelengths, $\lambda = 190, 295, 394, 513$ and $720 \mu\text{m}$. This result implies that the scattering effect of phonons enlarges with the increasing temperatures in ZnO. The results explain that the scattering effect caused by a thermal lattice vibration in the electron- optical phonon interacting system increases with temperatures. In Fig. 1(b), the temperature dependence of the QTLW, $\gamma(T)_{\text{total}}$, $\gamma(T)_{\text{em}}$ and $\gamma(T)_{\text{ab}}$ of ZnO for external field wavelength $\lambda = 295 \mu\text{m}$ is shown. The QTLWs, $\gamma(T)_{\text{total}}$, $\gamma(T)_{\text{em}}$ and $\gamma(T)_{\text{ab}}$ increase as the temperatures increase. The result implies that the phonon emission transition process prevails against the phonon absorption transition process because the $\gamma(T)_{\text{em}}$ is closer to $\gamma(T)_{\text{total}}$. Even though we cannot separate experimentally the scattering effects of the phonon emission and absorption transition, the analysis of the relation between the total scattering effect and the scattering effect of two processes represents the thermal characteristic of the scattering effect of the system. The contributions of two processes can be appeared differently in various cases in various systems. In this work, our results reveal that values of QTLW are $\gamma(T)_{\text{interl}} < \gamma(T)_{\text{intra}} < \gamma(T)_{\text{total}}$ and $\gamma(T)_{\text{ab}} < \gamma(T)_{\text{em}} < \gamma(T)_{\text{total}}$.

Figure 2(a) represents the magnetic field dependence of the absorption power $P(B)$ of the QTLS of ZnO for the external field wavelength $\lambda = 295 \mu\text{m}$ at several temperatures, $T = 50, 70, 80, 90$ and 120 K . In order to compare the line of QTLS in the same graph, we plot the value of $P_{nr}(B) = \alpha P(B)$ here $\alpha \equiv (T/10)P_S(B)$. The $P_S(B)$ is the maximum value at $T = 30$. As seen

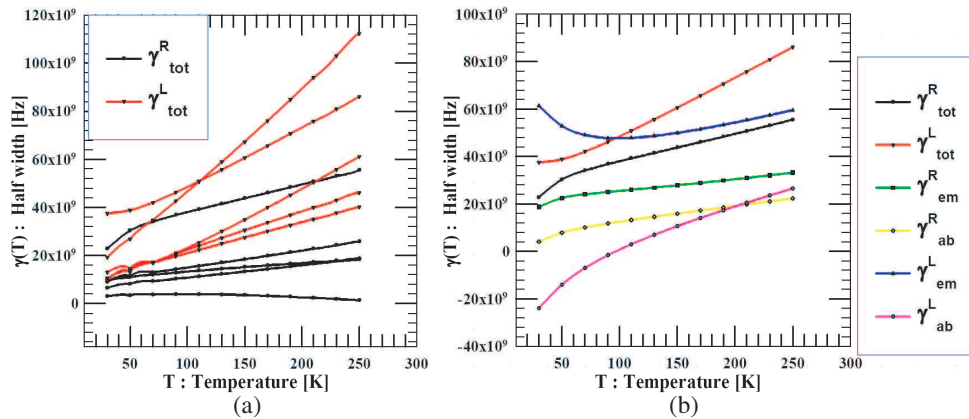


Figure 1: (a) The temperature dependence of QTLW, $\gamma(T)$ with $\lambda = 190, 295, 394, 513$ and $720 \mu\text{m}$ (from the top line to the bottom line), (b) comparisons of the temperature dependence of QTLW, $\gamma(B)_{\text{total}}$, $\gamma(B)_{\text{em}}$ and $\gamma(B)_{\text{ab}}$ with $\lambda = 190, 295, 394, 513$ and $720 \mu\text{m}$.

in Fig. 2(a), $P(B)$ increases as the temperature increases. Also the linewidth increases with the increasing temperatures. The results explain the resonant phenomena in the electron-piezoelectric potential interacting system because the collision effect of phonons due to the thermal lattice vibration is expected to become larger with increasing temperatures. The results indicate that the QTR of EAPS is a useful method to explain the resonant phenomena based on the quantum transition and scattering effect in a microscopic view. In the Fig. 2(b), we can read the magnetic-field dependence of the maximum absorption power. The Fig. 2(c) shows the relative frequency dependence of the absorption power (QTLS), $P(\Delta\omega)$ of ZnO, with $\lambda = 190, 295, 394, 513$ and $720 \mu\text{m}$ at $T = 50 \text{ K}$. The broadening effects near the resonance peaks for various external fields appeared.

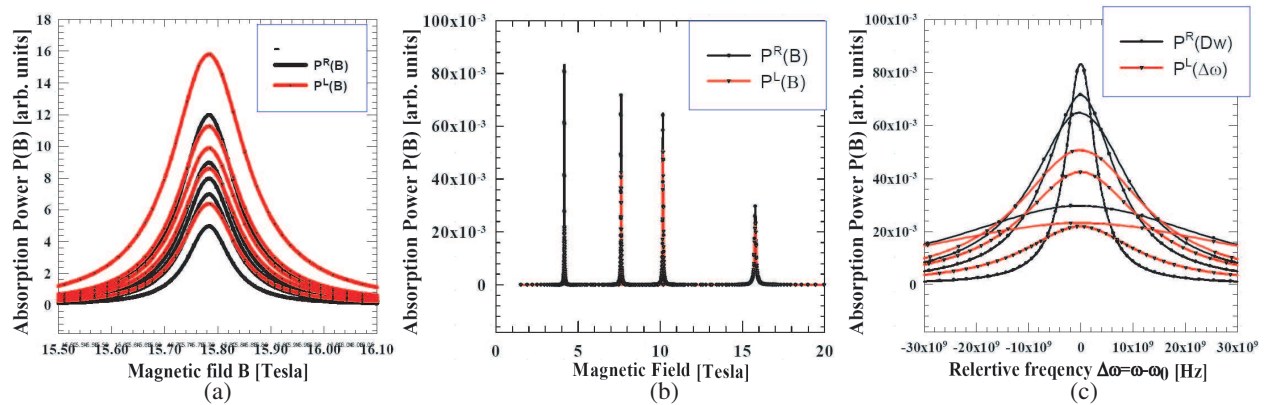


Figure 2: (a) The magnetic field dependence of the relative absorption power, $P_r(B)$ of ZnO with $\lambda = 295 \mu\text{m}$, at $T = 50, 70, 80, 90$ and 120 K (from the bottom line to the top line), (b) the magnetic field dependence of the absorption power, $P_r(B)$ of ZnO with $\lambda = 190, 295, 394, 513$ and $720 \mu\text{m}$ (from the right to the left), (c) the relative frequency ($\Delta\omega$) dependence of (QTLS), $P(\Delta\omega)$ of ZnO, with $\lambda = 190, 295, 394, 513$ and $720 \mu\text{m}$ (from the top line to bottom) the at $T = 50 \text{ K}$.

4. CONCLUSION

In a summary, it should be emphasized that our EAPS theory makes the analysis of quantum transition processes in the various circumstances much easier than other theories, since less steps are involved in the calculation. We also found the dominant scattering processes are the phonon emission transition process and inter level transition process. We also shown the reasonable resonating pictures of QTLS. The results of this work will help to analyze numerically the scattering mechanisms in the electron-piezoelectric potential interacting materials

REFERENCES

1. Ting, C. S., S. C. Ying, and J. J. Quinn, "Theory of cyclotron resonance of interacting electrons in a semiconducting surface inversion layer," *Phys. Rev. B*, Vol. 16, 5394, 1977.
2. Wu, X., F. M. Peeters, and J. T. Devreese, "Theory of the cyclotron resonance spectrum of a polaron in two dimensions," *Phys. Rev. B*, Vol. 34, 8800, 1986.
3. Grigolini P. and G. P. Parravidini, "Phonon thermal baths: A treatment in terms of reduced models," *Phys. Rev. B*, Vol. 125, 5180, 1982.
4. Barker, J. R., "Quantum transport theory of high-field conduction in semiconductors," *J. Phys. C*, Vol. 6, 2633, 1973.
5. Kubo, R., "General theory and simple applications to magnetic and conduction problems," *J. Phys. Soc. Jpn.*, Vol. 12, 570, 1957.
6. Mori, H., "Transport, collective motion, and brownian motion," *Progr. Theor. Phys.*, Vol. 33, 423, 1965.
7. Nagano, K., T. Karasudani, and H. Okamoto, "Reduced equations of motion for generalized fluxes and forces in the continued-fraction expansion," *Progr. Theor. Phys.*, Vol. 63, 1904, 1980.
8. Zwanzig, R., "Ensemble method in the theory of irreversibility," *J. Chm. Phys.*, Vol. 33, 1338, 1960.

9. Zwanzig, R., "Theoretical basis for the Rouse-Zimm model in polymer solution dynamics," *J. Chm. Phys.*, Vol. 60, 2717, 1960.
10. Kenkre, V. M., "Integrodifferential equation for response theory," *Phys. Rev. A*, Vol. 4, 2327, 1971.
11. Kenkre, V. M., "Theory of electrical resistivity," *Phys. Rev. A*, Vol. 6, 769, 1972.
12. Sug, J. Y. and S. D. Choi, "Quantum transport theory based on the equilibrium density projection technique," *Phys. Rev. E*, Vol. 55, 314, 1997.
13. Sug, J. Y. and S. D. Choi, "Quantum transition processes in deformation potential interacting systems using the equilibrium density projection technique," *Phys. Rev. B*, Vol. 64, 235210, 2001.
14. Kobori, H., T. Ohyama, and E. Otsuka, "Line-width of quantum limit cyclotron resonance. I. Phonon scatterings in Ge, Si, CdS and InSb," *J. Phys. Soc. Jpn.*, Vol. 59, 2141, 1989.
15. Sug, J. Y., S. H. Lee, and J. J. Kim, "The magnetic field dependence of the deformation potential materials in the square well confinement potential," *Cent. Eur. J. Phys.*, Vol. 6, No. 4, 812, 2008.
16. Sug, J. Y., S. H. Lee, J. Y. Choi, G. Sa-Gong, and J. J. Kim, "Magnetic properties of optical quantum transition line shapes and line widths of electron-piezoelectric potential phonon interacting materials under circularly oscillating fields," *J. Appl. Phys. Jpn.*, Vol. 47, 7757, 2008.
17. Sug, J. Y., S. H. Lee, and J. Y. Choi, "Scattering factor functions of quasi two dimensional quantum transition systems based on the projected liouville equation," *J. Kor. Phys. Soc.*, Vol. 4, 1403, 2009.

Magnetic Field Dependence of Electron Phonon Scattering Properties of ZnS of the Quantum — Qusi Two Dimensional System

Joung-Young Sug¹, Su-Ho Lee², Jun-Yong Choi¹, Ji Ho Park¹,
Cheol-Hwan Kim³, and Geon Sa-Gong²

¹Electronic and Electrical Engineering School, Kyungpook National University
Daegu 702-701, Korea

²Department of the Electrical Engineering, Dong-A University
Pusan 604-714, South Korea

³Research Institute of Myoung-Bo Electronic Company
Pusan 604-714, South Korea

Abstract— We investigated theoretically the quantum optical transition properties of ZnS, in quasi 2-Dimensional Landau splitting system, based on quantum transport theory. We apply the Quantum Transport theory (QTR) to the system in the confinement of electrons by square well confinement potential under circularly polarized oscillating field. We use the projected Liouville equation method with Equilibrium Average Projection Scheme (EAPS). In order to analyze the quantum transition, we compare the magnetic field dependencies of the QTLW and the QTLS on two transition processes, namely, the phonon emission transition process and the phonon absorption transition process. Through the analysis of this work, we found the increasing properties of QTLW and QTLS with magnetic fields. We also found the dominant scattering processes are the phonon emission transition process.

1. INTRODUCTION

It is well known that ZnS is the piezoelectric potential phonon interaction scattering effect active. The reason why we are mostly interested in these materials The wide band-gap semiconductors, including ZnO, AlN, InN, and their ternary compounds, have great potential for applications in high-power and optoelectronic devices in the blue and the ultraviolet regions. Then, the investigation of quantum optical transition properties of this materials is very important, So, in this research, we investigated the quantum optical transition properties of ZnS, in quasi 2-Dimensional Landau splitting system, based on quantum transport theory.

There are many theories regarding the quantum transport problems in various methodologies [1–18], among them we use the projected Liouville equation method with in the equilibrium average projection scheme (EAPS) [13]. The merit of using EAPS is that the quantum response function and the scattering factor formula can be obtained in a onestep process by expanding the quantum transport theory. In the previous work [14], we applied the EAPS theory in Ge and Si, since there are abundant experimental data [15]. We compared our results of numerical calculations of the EAPS theory [14] with existing experimental data [15] and showed a good agreement between them. This indicated that the EAPS theory is useful in analyzing many-body systems. The analysis of the temperature and the magnetic field dependence of the QTLW is very difficult in other theories or experiment, because the absorption power in the various external field wavelengths is required to be calculated or observed. The QTR theory within EAPS is advantageous in this respect as it allows the QTLW to be directly obtained through EAPS, in the various external field wavelengths. In short calculation of the absorption power is not required to obtain the QTLW if EAPS is introduced [13]. But, the previous work [15] restricted for non-confining potential systems with the extremely weak coupling (EWC) approximation. Recently, we suggested a more precise procedure of expanding and application of EAPS in Low-dimensional electron systems with the moderately weak coupling (MWC) approximation in Refs. [16–18]. In the MWC scheme, the distribution components can provide an adequate explanation of the quantum transition processes [16–18]. In a previous work [14], the intermediate states of quantum transition processes do not appear.

In this work, we investigate the optical Quantum Transition Line Shapes (QTLWs) of ZnS which show the absorption power and the Quantum Transition Line Widths (QTLWs) of ZnS, which show the scattering effect in the electron-piezoelectric potential phonon interacting system under circularly polarized oscillatory external fields. The analysis of the temperature and the magnetic

field dependence of the QTLW is very difficult in alternative theories or experiment, because the absorption power in the various external field wavelengths is required to be calculated or observed. The QTR theory of EAPS is advantageous in this respect as it allows the QTLW to be directly obtained, through EAPS, in the various external field wavelengths. In short the calculation of the absorption power is not required to obtain the QTLW [13].

With the numerical calculation we analyzed the temperature and the magnetic-field dependences of the QTLW and QTLS in various cases. In order to analyze the quantum transition, we compare the magnetic field dependencies of the QTLW and the QTLS on four transition processes, namely, the intra-level transition process, the inter-level transition process, the phonon emission transition process and the phonon absorption transition process.

2. THE ABSORPTION POWER FORMULA AND THE SCATTERING FACTOR FUNCTION

When a static magnetic field $\vec{B} = B_z \hat{z}$ is applied to an electron system, the single electron energy state is quantized to the Landau levels. We select a system of electrons confined in an infinite square well potential (SQWP) between $z = 0$ and $z = L_z$ in the z -direction. We use the eigenvalue and eigenstate of Ref. [12] of the square well potential system. We suppose that an oscillatory electric field $E(t) = E_0 \exp(i\omega t)$ is applied along the z -axis, which gives the absorption power delivered to the system as $P(\omega) = (E_0^2/2)\text{Re}\{\sigma(\omega)\}$, where “Re” denotes the real component and $\sigma(\omega)$ is the optical conductivity tensor which is the coefficient of the current formula Here the absorption power represents the optical QTLS and the scattering factor function represents the optical QTLW We consider the electron-phonon interacting system and then we have the Hamiltonian of the system as

$$H_s = H_e + H_P + V = \sum_{\beta} \langle \beta | h_0 | \beta \rangle a_{\beta}^{\dagger} a_{\beta} + \sum_q \hbar \omega_q b_q^{\dagger} b_q + \sum_q \sum_{\alpha, \mu} C_{\alpha, \mu}(q) a_q^{\dagger} a_{\mu} (b_q + b_q^{\dagger}). \quad (1)$$

Here H_e is the electron Hamiltonian, h_0 is a single-electron Hamiltonian, H_P is the phonon Hamiltonian and V is the electron-phonon (or impurity) interaction Hamiltonian The $b_1(b_2^{\dagger})$ are the annihilation operator (creation operator) of boson particle, and \vec{q} is phonon (or impurity) wave vector The interaction Hamiltonian of electron-phonon interacting system is $V \equiv \sum_q \sum_{\alpha, \mu} C_{\alpha, \mu}(q) a_{\alpha}^{\dagger} a_{\mu} (b_q + b_q^{\dagger})$

where the coupling matrix element of electron-phonon interaction $C_{\alpha, \mu}(q)$ is $C_{\alpha, \mu}(q) \equiv V_q \langle \alpha | \exp(i\vec{q} \cdot \vec{r}) | \mu \rangle$, \vec{r} is the position vector of electron and V_q is coupling coefficient of the materials and the corresponding Liouville operator L_s are given by $L_s X \equiv [H_s, X]$ for an arbitrary operator X . For the optical quantum transition system under a right circularly polarized external field current, we replace the current with $J_k \equiv J^-$ and $J_l \equiv J^+$ for the current system under an oscillating external field of frequency ω . The many-electron current operators J^- and J^+ are defined $J^- \equiv \tilde{g}_{(sys)} \sum_{\beta} \sqrt{N_{\beta}} a_{\beta}^{\dagger} a_{\beta+1}$ and $J^+ \equiv \tilde{g}_{(sys)} \sum_{\beta} \sqrt{(N_{\beta} + 1)} a_{\beta+1}^{\dagger} a_{\beta}$ with $\tilde{g}_{(sys)} \equiv (-ie\hbar/m_e^*) \sqrt{1/l_0^2}$.

$\tilde{g}_{(sys)}$ can be changed for other systems and external fields. Here $l_0 = \sqrt{\hbar/eB}$ is the radius of cyclotron motion, $\omega_c = eB/m_e^*$ is the cyclotron frequency, m_e^* is the effective mass of electron.

Recently, we suggested a more precise procedure of expanding and application of EAPS with the moderately weak coupling (MWC) approximation in Refs. [16–18]. Using the properties of the projection operator and the conventional series expansion of the propagator, we obtained a right circularly polarized external field current $J^R(\omega)$ and the scattering factor $\Xi_{kl}^{(R)}(\omega)$ in a simple form by using a weak interacting system approximation in pair interacting system as

$$J^R(\omega) = \left[\frac{-(i/\hbar) \Lambda_{kl}^{(R)}}{\omega - A_{kl}^{(R)} + \Xi_{kl}^{(R)}(\omega)} \right] E(\omega), \quad (2)$$

where $\Lambda_{kl}^{(R)} = -\{(\frac{i}{\omega}) \sum_{\alpha} j_{\alpha+1, \alpha}^{\dagger} j_{\alpha, \alpha+1}^{\dagger} (f_{\alpha+1} - f_{\alpha})\}$, $A_{kl}^{(R)} = i\omega_c$.

Using the properties of the projection operator and the conventional series expansion of the propagator $G_k^q(\omega_l)$ [16–18], we obtain the scattering factor as a simple form with a weak interaction system approximation in a pair interaction system, as

$$\Xi_{kl}^{(R)}(\omega_l) \equiv \frac{i}{\hbar \Lambda_{kl}^{(R)}} \langle L'_+ L'_v G_d L'_v J^- \rangle_B, \quad (3)$$

where the diagonal propagator is $G_d = 1/(\hbar\omega - L_d)$. Here, we used the Ref. [13], $Tr^{(e)}\{J_k L_1 L_2 \dots L_n L' \rho_s\} = (-1)^{n+1} \langle L' L_n \dots L_2 L_1 J_k \rangle$, and the $\langle \dots \rangle$ means the ensemble average of the electron states and background particle state. The scattering factor function, $\Xi_{kl}(\omega_l)$, is expressed in a complex form like $\Xi_{kl}(\omega_l) \equiv i\Delta_{\text{total}} + \gamma_{\text{total}}(\omega)$ with $\Delta_{\text{total}} \equiv \text{Im}\Xi_{kl}(\omega_l)$, giving a line shift of a response-type formula, and $\gamma_{\text{total}}(\omega) \equiv \text{Re}\Xi_{kl}(\omega)$ giving the half-width of the response-type formula. In most cases, the imaginary part of the scattering factor, Δ_{total} , is negligible in a real system because of its small value. With in the continuous approximation [16] in a right circularly polarized external field, the absorption power formula (or the QTLS formula) is obtained finally as

$$P^{(R)}(\omega) \propto \left(\frac{e^2 \omega_c^2}{\pi^2 \hbar \omega} \right) \left[\frac{\gamma_{\text{total}}^{(R)}(\omega_c) \sum_{N_\alpha} \int_{-\infty}^{\infty} dk_{z\alpha} (N_\alpha + 1) (f_\alpha - f_{\alpha+1})}{(\omega - \omega_c)^2 + \left(\gamma_{\text{total}}^{(R)}(\omega_c) \right)^2} \right], \quad (4)$$

where the scattering factor function (or QTLW) is given by

$$\gamma_{\text{total}}^{(R)}(\omega) \equiv \text{Re}\Xi_{kl}^{(R)}(\omega) \equiv \sum_{\mp} \sum_{N_\alpha=0} \sum_{N_\beta=0} \gamma_{\alpha,\beta}^{(R)\mp} = \left(\frac{\Omega}{4\pi\hbar^2 v_s} \right) \frac{\sum_{\mp} \sum_{N_\alpha=0} \sum_{N_\beta=0} \int_{-\infty}^{\infty} dk_{z\alpha} \int_{-\infty}^{\infty} dq_z Y_{\alpha,\beta}^{(R)\mp}}{\sum_{N_\alpha=0} \int_{-\infty}^{\infty} dk_{z\alpha} (N_\alpha + 1) (f_{\alpha+1} - f_\alpha)}. \quad (5)$$

The integrand-factor $Y_{\alpha,\beta}^{(R)\mp}$ has a complicated form, recently, we suggested the final derivation of the integrand of the scattering factor in Refs. [16–18]. We use the result equations from (18) to (23) in Ref. [18].

3. THE ANALYSIS AND SUMMARY

Through the numerical calculation of the theoretical result of QTLS and of the QTLW, we analyze absorption power and line widths of ZnS. We use the material constant of the below. In order to analyze the QTLW and the QTLS of ZnS, inserting these constants into Eqs. (4), (5) yields the line shapes from which the line width can be measured. We use the material constant of Refs. [19–21]. We use $m^* = 0.19m_0$ and $\bar{m} = 1.2m_0$ which are the effective masses of ZnS. Here the m_0 is the free-electron mass, $m_0 = 9.1095 \times 10^{-31}$ kg. The other constants of ZnS are $\rho = 409$ kg/m³, $\kappa = 8.58 \times 10^{-4}$ eV/K, $\xi = 235$ K and $|K|^2 = 2.98005 \times 10^{-2}$. The speed of sound v_s shall be replaced by the average value \bar{v}_s of v_{sl} and v_{st} , as $\bar{v}_s = (v_{sl} + v_{st})/2 = 4300.5$ m/s, here v_{sl} is the longitudinal sound velocity and v_{st} is the transverse sound velocity. The energy gap $\varepsilon_g(T)$ replaced by $\tilde{\varepsilon}_g = 3.42$ eV in approximation by noting that the variation against the temperature is very small. We choose $\varepsilon_0 = 8.85419 \times 10^{-12}$ c²/N·m².

In order to analyze the quantum transition process, we denote the total QTLW as $\gamma_{\text{total}} \equiv \gamma_{\text{em}} + \gamma_{\text{ab}}$, where $\gamma_{\text{ab}} \equiv \gamma_{0,0}^- + \gamma_{0,1}^- + \gamma_{1,0}^-$ are the QTLW of the intra level transition, the inter level transition, the total phonon emission and absorption transition process, respectively.

In Fig. 1(a), we plotted the magnetic field dependence of the QTLW, $\gamma(B)$ of ZnS, at $T = 50, 70, 80, 90$ and 120 K. The results indicate that increase as the magnetic field in the temperatures at the low the magnetic field less than $B = 12$ Tesla while decrease as the magnetic field in the temperatures at the high the magnetic field lager than $B = 12$ Tesla. The analysis of the magnetic field dependence of the QTLW seems to be very difficult to do with other theories or experiment because it needs to calculate or observe the absorption power for the various external field wavelengths. The QTR theory of EAPS provides a useful tool to do it because we can directly obtain the QTLW, based on EAPS for the various external field wavelengths. We need not calculate the absorption power to obtain QTLW. In Fig. 2(b), Comparisons of the magnetic field dependence of QTLW, $\gamma(B)_{\text{total}}$, $\gamma(B)_{\text{em}}$ and $\gamma(B)_{\text{ab}}$ of ZnS, at $T = 50, 70, 80, 90$ and 120 K is shown. The QTLWs, $\gamma(B)_{\text{total}}$, $\gamma(B)_{\text{em}}$ and $\gamma(B)_{\text{ab}}$ increase as the magnetic field in all the temperatures at the low the magnetic field less than $B = 12$ Tesla while decrease as all the magnetic field in the temperatures at the high the magnetic field lager than $B = 12$ Tesla. The contributions of two processes can be appeared differently in various cases in various systems. In this work, our results reveal that values of QTLW are $\gamma(B)_{\text{interl}} < \gamma(B)_{\text{intra}} < \gamma(B)_{\text{total}}$ and $\gamma(B)_{\text{ab}} < \gamma(B)_{\text{em}} < \gamma(B)_{\text{total}}$.

In the Fig. 2(a), we can read the magnetic-field dependence of the maximum absorption power. The Fig. 2(b) shows the relative frequency dependence of the absorption power (QTLS), $P(\Delta\omega)$ of ZnS, with $\lambda = 190, 295, 394, 513$ and 720 μm at $T = 50$ K. The analysis of the relative frequency

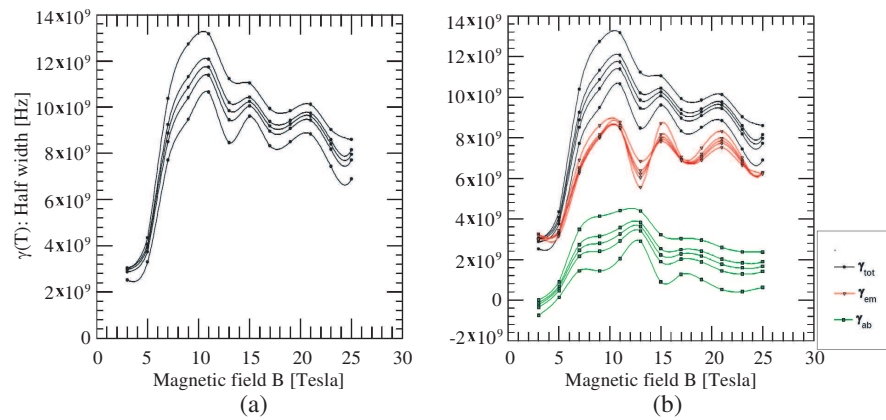


Figure 1: (a) The magnetic field dependence of of QTLW, $\gamma(B)$ of ZnS at $T = 50, 70, 80, 90$ and 120 K (from the bottom line to the top line), (b) comparisons of the magnetic field dependence of QTLW, $\gamma(B)_{\text{total}}$, $\gamma(B)_{\text{em}}$ and $\gamma(B)_{\text{ab}}$ at $T = 50, 70, 80, 90$ and 120 K.

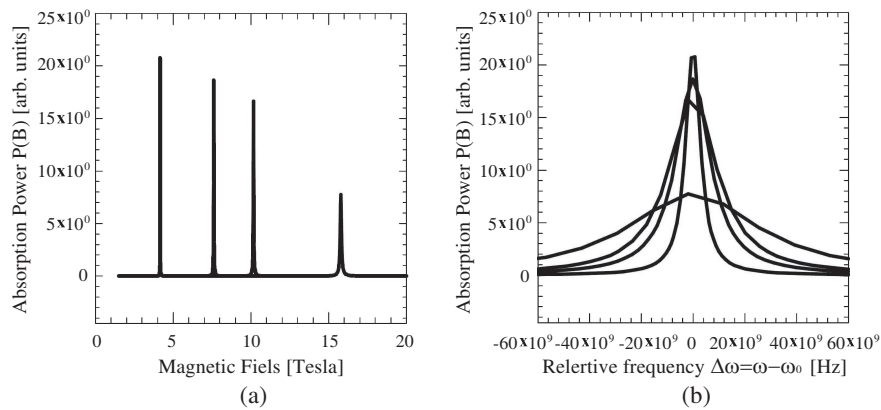


Figure 2: (a) The magnetic field dependence of the absorption power, $P(B)$ of ZnS with $\lambda = 190, 295, 394$ and $720 \mu\text{m}$ (from the right to the left), (b) the relativity frequency ($\Delta\omega$) dependence of (QTLS), $P(\Delta\omega)$ of ZnS, with $\lambda = 190, 295, 394, 513$ and $720 \mu\text{m}$ (from the top line to bottom) the at $T = 50$ K.

dependence of the absorption power (QTLS) represents the magnetic field dependency property of the absorption power given for an external field wavelength and the conditions of the system. The broadening effects near the resonance peaks for various external fields appeared. The results indicate that the QTR of EAPS is a useful method to explain the resonant phenomena based on the quantum transition and scattering effect in a microscopic view.

In a summary, it should be emphasized that our EAPS theory makes the analysis of quantum transition processes in the various circumstances much easier than other theories, since less steps are involved in the calculation. The approach to the analysis of quantum transition processes with ease is the merits of our EAPS theory. Through the analysis of this work, we found the increasing properties of QTLW and QTLS with the temperature and the magnetic fields. We also found the dominant scattering processes are the phonon emission transition process. We also shown the reasonable resonating pictures of QTLS. The results of this work will help to analyze numerically the scattering mechanisms in the electron-piezoelectric potential interacting materials.

ACKNOWLEDGMENT

This research has been supported by the program of the Post Brain Korea 21.

REFERENCES

1. Ting, C. S., S. C. Ying, and J. J. Quinn, "Theory of cyclotron resonance of interacting electrons in a semiconducting surface inversion layer," *Phys. Rev. B*, Vol. 16, 5394, 1977.
2. Wu, X., F. M. Peeters, and J. T. Devreese, "Theory of the cyclotron resonance spectrum of a polaron in two dimensions," *Phys. Rev. B*, Vol. 34, 8800, 1986.

3. Grigolini P. and G. P. Parravidini, "Phonon thermal baths: A treatment in terms of reduced models," *Phys. Rev. B*, Vol. 125, 5180, 1982.
4. Barker, J. R., "Quantum transport theory of high-field conduction in semiconductors," *J. Phys. C*, Vol. 6, 2633, 1973.
5. Kubo, R., "General theory and simple applications to magnetic and conduction problems," *J. Phys. Soc. Jpn.*, Vol. 12, 570, 1957.
6. Mori, H., "Transport, collective motion, and brownian motion," *Progr. Theor. Phys.*, Vol. 33, 423, 1965.
7. Nagano, K., T. Karasudani, and H. Okamoto, "Reduced equations of motion for generalized fluxes and forces in the continued-fraction expansion," *Progr. Theor. Phys.*, Vol. 63, 1904, 1980.
8. Zwanzig, R., "Ensemble method in the theory of irreversibility," *J. Chem. Phys.*, Vol. 33, 1338, 1960.
9. Zwanzig, R., "Theoretical basis for the Rouse-Zimm model in polymer solution dynamics," *J. Chem. Phys.*, Vol. 60, 2717, 1960.
10. Kenkre, V. M., "Integrodifferential equation for response theory," *Phys. Rev. A*, Vol. 4, 2327, 1971.
11. Kenkre, V. M., "Theory of electrical resistivity," *Phys. Rev. A*, Vol. 6, 769, 1972.
12. Jo, S. G., N. L. Kang, Y. J. Cho, S. D. Choi, and J. Kor, "Modeling of the cyclotron transition theory for quasi-two-dimensional electron systems by the isolation-projection technique," *Phys. Soc.*, Vol. 30, 105, 1997.
13. Sug, J. Y. and S. D. Choi, "Quantum transport theory based on the equilibrium density projection technique," *Phys. Rev. E*, Vol. 55, 314, 1997.
14. Sug, J. Y. and S. D. Choi, "Quantum transition processes in deformation potential interacting systems using the equilibrium density projection technique," *Phys. Rev. B*, Vol. 64, 235210, 2001.
15. Kobori, H., T. Ohyama, and E. Otsuka, "Line-width of quantum limit cyclotron resonance. I. Phonon scatterings in Ge, Si, CdS and InSb," *J. Phys. Soc. Jpn.*, Vol. 59, 2141, 1989.
16. Sug, J. Y., S. H. Lee, and J. J. Kim, "The magnetic field dependence of the deformation potential materials in the square well confinement potential," *Cent. Eur. J. Phys.*, Vol. 6, No. 4, 812, 2008.
17. Sug, J. Y., S. H. Lee, J. Y. Choi, G. Sa-Gong, and J. S. Kim, "Magnetic properties of optical quantum transition line shapes and line widths of electron-piezoelectric potential phonon interacting materials under circularly oscillating fields," *J. Appl. Phys. Jpn.*, Vol. 47, 7757, 2008.
18. Sug, J. Y., S. H. Lee, and J. Y. Choi, "Scattering factor functions of quasi two dimensional quantum transition systems based on the projected liouville equation," *J. Kor. Phys. Soc.*, Vol. 54, 1403, 2009.
19. Wolfe, C. M. and G. E. Stillman, *Physical Properties of Semiconductors*, Prentice-Hall, Englewood Cliffs, New Jersey, 1989.
20. Ferry, D. K., *Semiconductors*, Macmillan, New York, 1991.
21. Chung, S. L., *Physics of Optoelectronic Devices*, Wiley, New York, 1995.

Effect of the Hand-hold Position on the EM Interaction of Clamshell-type Handsets and a Human

S. I. Al-Mously¹ and M. M. Abousetta²

¹Department of Electrical and Electronic Engineering, School of Applied Sciences and Engineering Academy of Graduate Studies, Tripoli, Libya

²Department of Electrical and Electronic Engineering, Faculty of Engineering Al-Fateh University, Tripoli, Libya

Abstract— A thorough investigation into the effect of the hand-hold position on the electromagnetic (EM) wave interaction of a clamshell-type cellular handset and a human is presented in this paper. A FDTD-based platform, *SEMCAD-X*, is used to achieve the simulations, where two semi-realistic handset models of different external-antenna attachment positions (left and right-side) are designed with the most parts configuration and operating at different GSM-frequency standards (GSM-900, GSM-1800/DCS, and UMTS/IMT-2000). Moreover, homogeneous and heterogeneous CAD models are used to simulate the user's head, whereas, a homogeneous model with three different tissues is designed to simulate the user's hand-hold. The antenna performance, as well as, the specific absorption rate (SAR) in tissues are both examined for different (42) possible cases, where several antenna/hand positions are considered in simulation.

1. INTRODUCTION

Nowadays, cellular handset manufacturers producing developed types come in a variety of shapes, or forms, such as; bar, clamshell, slider, swivel and flip-type, where most of these types can adopt either external or built-in antennas. For certain frequency, input power, antenna configuration and handset position with respect to user's head, the induced SAR in head-tissues may differ according to handset type.

Measuring the induced SAR in a human head exposed to the handset antenna radiation, most standards, e.g., IEEE-1528 [1], EN 50360 [2] and EN 62209-1 [3], are not considering the use of hand model due to various possible hand-hold positions and the worst case SAR value is obtained without the use of a hand model. However, a hand-hold has a considerable impact on a handset antenna performance which can be altered according to antenna type, antenna position and hand-hold position. Hence, it is precious to predict the EM interaction of a cellular handset and the user's head taking into account different hand-hold positions.

Although over the last fifteen years many authors [4–7] have investigated the interaction between the EM field radiated by the cellular handheld and human head, but nothing has been published yet about the hand effect on the EM interaction of clamshell handset antennas and a human by examining both handset antenna performance and the amount of SAR induced in head, with taking into consideration the positions effect of the hand, antenna and handset with respect to head. Published works on the handset user's hand impact are extensively surveyed in [8].

In this paper, the prediction of the EM wave interaction due to grasping the handset at different positions is based on evaluating the handset antenna performance as well as the SAR and absorbed power in both head and hand tissues using FDTD method, where different antenna positions are examined. A *cheek*-position of the handset with respect to head is considered [1] as the common position used for the clamshell types.

2. FDTD MODELING AND GRID GENERATION

A FDTD-based electromagnetic (EM) solver, *SEMCAD X* by SPEAG — Schmidt & Partner Engineering AG [9], is used for simulating the study cases in this work due to its handling, functionality and features for highly detailed CAD models as well as efficient FDTD solver for simulating advanced applications.

A clamshell cellular handset with different external antenna positions (left and right-side) at different operating frequencies; 900, 1800 and 2025 MHz is hereby designed and simulated with its real parts configuration using *SEMCAD-X*, Figure 1. The handset with the left-side antenna will be referred later as model1, whereas, the handset with the right-side antenna will be referred as model2. The maximum dimensions of the handset model when it is closed are; $50 \times 19 \times 89 \text{ mm}^3$.

The considered handset electromechanical parts are: *antenna*, *antenna cover*, *acoustic parts*, *PCB*, *shields*, *LCD and LCD-holder*, *housing parts*, *keypad and buttons*, *battery and battery contacts*, and *connectors*. The dielectric parameters of the handset materials given in [8] are used. A short-whip antenna top loaded with a small cylinder [8] is suggested as depicted in Figure 2. At 900 MHz the antenna is matched with 17.16 nH lumped element, whereas, at 1800 and 2025 MHz no matching is needed.

A semi-realistic hand model consists of three tissues; skin, muscle and bone [8], is designed with two common different holding positions that will be referred as hand1 and hand2. Hand1 grasping the posterior lower part of the clamshell, whereas, hand2 grasping the posterior upper part of the clamshell base. These proposed hand-holds represent the two possible extreme cases.

The user's head is simulated using both, homogeneous and heterogeneous CAD-models. The homogeneous head model is the SAM phantom available with *SEMCAD-X* and consists of two dielectric materials, shell and liquid. A heterogeneous high-resolution European female head (HR-EFH) [8], available with SPEAGE — Schmidt & Partner Engineering AG [9] is used. This phantom consists of 121 different slices, with slice thicknesses of 1-mm (ear region) and 3 mm and a transverse spatial resolution of 0.2 mm. The following different twenty five tissues are recognized; *air*, *blood vessel*, *bones*, *brain/grey matter*, *brain/white matter*, *cerebellum*, *cerebrospinal fluid*, *ear (cartilage)*, *eye-cornea*, *eye-lens*, *eye-vitreous body*, *fat*, *jaw*, *mastoid cells (bones)*, *mid-brain*, *muscles*, *nasal cavity*, *parotid gland*, *spin*, *skull*, *spinal cord*, *spine*, *thalamus*, *tongue* and *ventricles*.

Head and hand tissues properties are set according to the material properties data given in [8].

To align the simulated handset components to the FDTD grid accurately (in free space) a minimum spatial resolution of $0.5 \times 0.5 \times 0.5 \text{ mm}^3$ and maximum spatial resolution of $5 \times 5 \times 5 \text{ mm}^3$ in the x , y , and z directions are chosen with grading ratio of 1.2. This grid setting is also applied for the handset in hand and the handset in hand proximity to SAM phantom, whereas, for the handset in hand proximity to HR-EFH the same setting but with a maximum spatial resolution of $10 \times 10 \times 10 \text{ mm}^3$ is used instead. This is due to the limited number of FDTD-grid cells that the

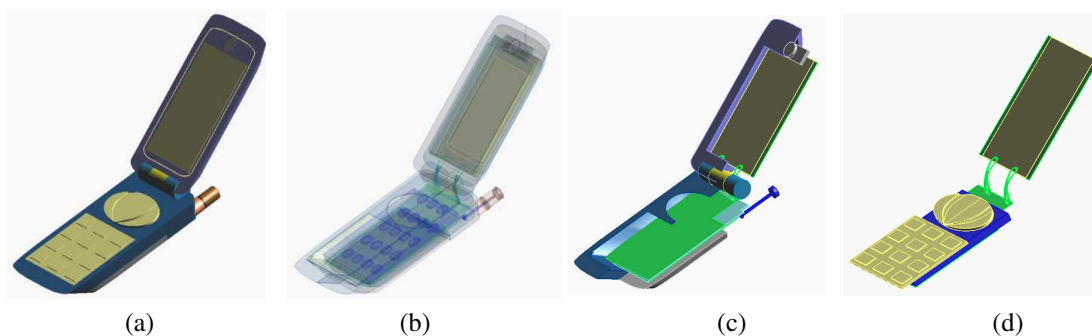


Figure 1: Numerical components structure of the clamshell-type handset model2; (a) A 3D view with all parts, (b) A transparent 3D view, (c) A 3D cut-view of the housing with PCB, antenna, speaker and battery, and (d) A 3D view of PCB, keypad and buttons.

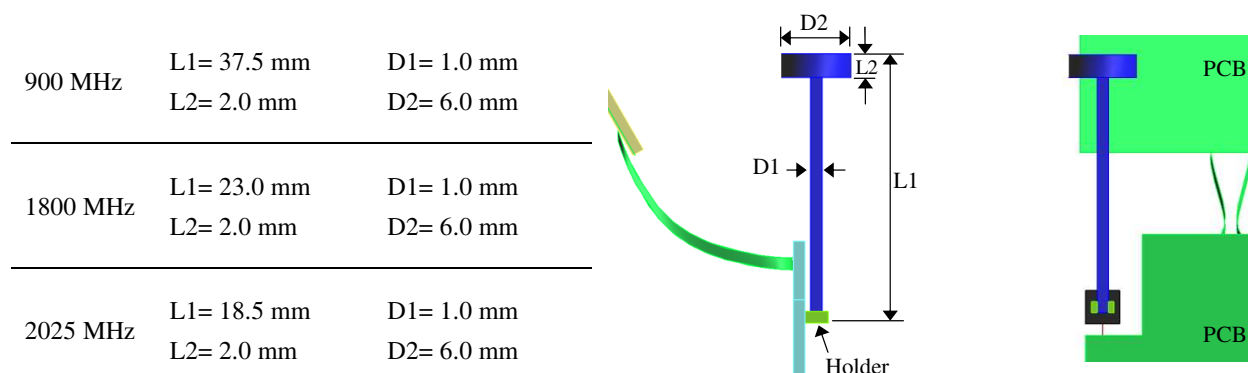


Figure 2: Different views of the proposed loaded short-whip antenna attached to the PCB with its dimensions at the adopted frequencies.

machine can process. A refinement factor of 10 is used for the solid regions, tissues and handset parts. The simulations assume a steady state voltage at the 900, 1800 and 2025 MHz, with a feed point of 50-Ohm voltage source of 0.5 mm gap. A transient excitation of 12 periods is set as guarantee to achieving a steady state. The absorbing boundary conditions (ABC's) are set as U-PML mode with 10 layers thickness [9].

3. RESULTS AND INFERENCES

Table 1 lists the total mesh cells and the antenna total efficiency for the handset simulation in different conditions, whereas, Figure 3 shows the far-field voltage radiation pattern of model1 in different setups at 900 MHz. Table 2 indicates the spatial peak SAR averaged over 1g and 10g in head, radiated power, absorbed power in tissues, dielectric loss, and power budget error (PBE) [8] for the handheld sets model1 and model2 close to head (SAM and HE-EFH) in different conditions.

All simulations are achieved with antenna source power of 0.6, 0.125 and 0.125 W at 900, 1800 and 2025 MHz, respectively. The 0.6 W is for the analogue phones only, whereas, all the digital mobile phones at 900 MHz are operating at 0.25 W. That is because the main aim of the study is to investigate the hand implication on the coupling between human head and cellular phone than the compliance with current exposure regulations. As an example, realistic SAR levels should be obtained by decreasing the reported SAR results of a factor of 2.4, at 900 MHz.

The simulation results show a significant decrease in the handset total efficiency due to the impact of holding the handset proximity to head. The maximum reduction in the antenna total efficiency is obtained at GSM-1800 frequency, about 94.2%, whereas, the maximum difference due to hand position change is obtained at UMTS/IMT-2000 frequency, about 32.1%. Moreover, the results demonstrate a considerable deviation in the values of both SAR and power absorption in head-tissues owing to the hand presence at different positions, where the maximum percent difference in the SAR_{1g} is obtained at UMTS/IMT-2000 frequency, about -61%. The maximum power budget error (PBE) [8] in cases of the HR-EFH presence is 2.43%, whereas, the maximum is 2.64% in the cases of SAM presence. The sliced-distribution of SAR in Figure 4 depicts that the peak SAR occurs in the cheek muscle region, away from the ear tissues.

Table 1: Computational results of the antenna performance parameters of both handset models at 900, 1800 and 2025 MHz for all conditions.

Parameter	Amount of Grid-Cells (Mcells)	Total Efficiency (η_{tot}) %							
		900 MHz		1800 MHz		2025 MHz			
Handset model	Model1	Model2	Model1	Model2	Model1	Model2	Model1	Model2	
No head	free-space	3.70881	3.70881	71.3%	71.3%	88.7%	88.7%	88.7%	88.7%
	in hand1	9.09321	9.08579	56.6%	63.1%	54.4%	61.8%	60.1%	64.9%
	in hand2	8.17021	8.16007	35.4%	50.9%	17.4%	37.5%	18.3%	39.8%
SAM	Hand1	18.0854	18.0736	21.8%	24.7%	26.1%	33.0%	30.9%	37.4%
	Hand2	16.4359	16.4198	11.5%	17.6%	5.15%	18.7%	5.80%	18.2%
HR-EFH	Hand1	23.4686	23.8015	30.3%	33.8%	35.2%	37.5%	42.1%	43.9%
	Hand2	21.3790	21.6749	15.9%	24.5%	8.47%	24.3%	9.98%	25.4%

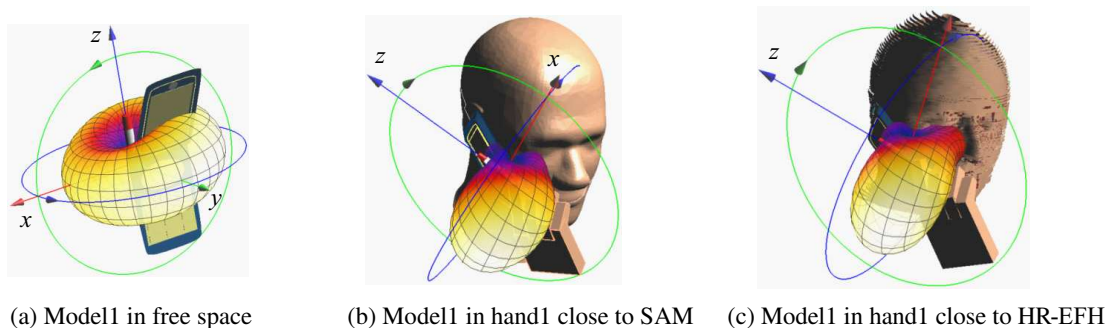
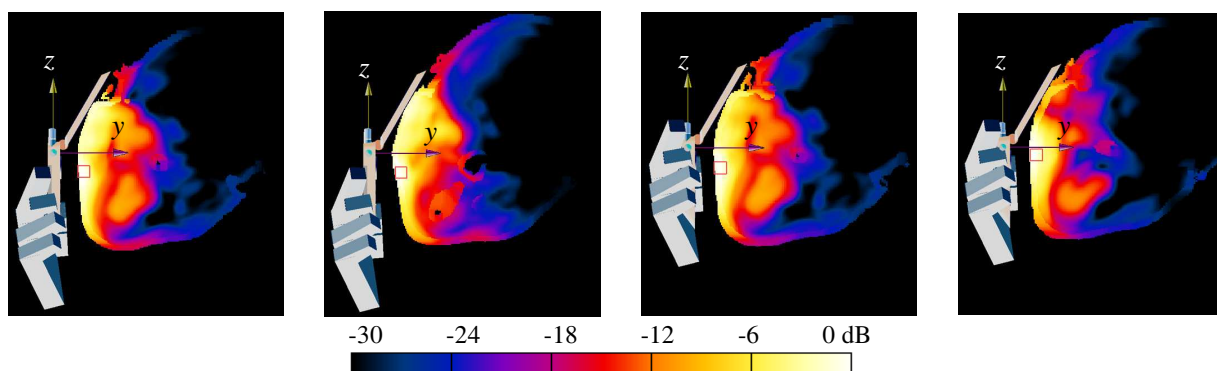


Figure 3: The 3-D far-field voltage radiation patterns of the handset model1 in different setups at 900 MHz.

Table 2: The computed SAR in head, radiated power, absorbed power in tissues, dielectric loss, and PBE for handset models in hand closed to head at different positions operating at different frequencies.

Handset model	Model1				Model2			
	SAM		HR-EFH (adult)		SAM		HR-EFH (adult)	
	Hand1	Hand2	Hand1	Hand2	Hand1	Hand2	Hand1	Hand2
Input power (mW)	600	600	600	600	600	600	600	600
SAR _{1g} in head (W/kg)	1.923	1.557	1.14	0.915	2.16	2.17	1.086	1.02
SAR _{10g} in head (W/kg)	1.410	1.11	1.01	0.80	1.49	1.50	0.94	0.89
Radiated power (mW)	131.06	69.07	182.2	95.41	148.4	106.1	203.0	147.3
Absorbed power in head	220.57	164.06	171.58	136.75	227.36	217.1	176	171.7
Absorbed power in hand	93.78	193.33	110	205.35	75	126.5	90	147.8
Dielectric loss (mW)	148.32	157.9	133.6	147.37	143.16	142.95	128.3	127.3
PBE (%)	1.05	2.61	0.44	2.52	1.01	1.23	0.45	0.98
Input power (mW)	125	125	125	125	125	125	125	125
SAR _{1g} in head (W/kg)	0.625	0.3	0.32	0.15	0.7	0.56	0.29	0.218
SAR _{10g} in head (W/kg)	0.381	0.169	0.180	0.087	0.41	0.32	0.164	0.125
Radiated power (mW)	32.67	6.45	43.93	10.60	41.25	23.36	46.83	30.4
Absorbed power in head	44.53	19.25	28.33	14.53	39.82	29.93	27.52	22.65
Absorbed power in hand	35.92	87.57	32.80	84.34	34.48	61.88	35.63	56.9
Dielectric loss (mW)	10.46	9.37	17.18	13.35	9.20	9.45	14.56	14.53
PBE (%)	1.14	1.88	2.21	1.74	0.20	0.30	0.37	0.42
Input power (mW)	125	125	125	125	125	125	125	125
SAR _{1g} in head (W/kg)	0.72	0.281	0.29	0.117	0.74	0.60	0.316	0.23
SAR _{10g} in head (W/kg)	0.42	0.16	0.18	0.06	0.43	0.34	0.16	0.13
Radiated power (mW)	38.7	7.30	52.64	12.47	46.7	22.78	54.87	31.75
Absorbed power in head	41.65	17.86	28.11	13.15	37.77	30.05	28.54	23.51
Absorbed power in hand	32.3	88.35	24.50	84.17	30.52	61.35	23.06	56.1
Dielectric loss (mW)	9.78	8.67	17.8	12.17	9.68	9.85	17.84	12.17
PBE (%)	2.06	2.26	1.6	2.43	0.26	0.78	0.55	1.18



(a) Peak location in mm
at (- 30.6, 26.0, -6.3)

(b) Peak location in mm
at (26.9, 31.8, -9.2)

(c) Peak location in mm
at (- 32.4, 26.0, -9.2)

(d) Peak location in m
at (2.8, 30.8, -4.6)

Figure 4: Slice distribution of spatial peak SAR over 1 g; (a) Model1 in hand1 close to HR-EFH at 1800 MHz, 0 dB = 0.32 W/kg, (b) Model2 in hand1 close to HR-EFH at 1800 MHz, 0 dB = 0.29 W/kg, (c) Model1 in hand2 close to HR-EFH at 1800 MHz, 0 dB = 0.15 W/kg, and (d) Model2 in hand2 close to HR-EFH at 1800 MHz, 0 dB = 0.218 W/kg.

Although the IEEE-Std. C95.1b-2004 [10] applies the SAR limit for the extremities to the pinnae, and since the used MRI-based head model (HR-EFH) has pressed pinnae; in this paper the pinnae are subject to the same exposure limit, for peak spatial SAR, as the head. It has been observed that there are no substantial differences between the computed SAR values for the head with and without pressed pinnae, where the peak spatial SAR location is not at the pinna or the region around as it occurs due to bar-type handsets [8], instead the peaks shift to the cheek tissues and sometimes even up to the nose.

4. CONCLUSION

This paper investigated the EM coupling between cellular handset and a human. Clamshell type handset with external antenna attached at different positions was taken as a model to determine the various aspects and results as occurring with changing phenomenon of the users hand position in realistic phone handset usage. A considerable impact of the user's hand-hold alteration on both the handset antenna total efficiency and the induced SAR in head is observed. A maximum difference in the antenna total efficacy and a maximum percent difference in the peak spatial SAR_{1g} values due to the hand-hold alteration are both obtained in the UMTS/IMT-2000 frequency.

REFERENCES

1. IEEE Standard-1528, "IEEE recommended practice for determining the peak spatial-average specific absorption rate (SAR) in the human head from wireless communications devices: Measurement techniques," December 2003.
2. Product standard to demonstrate the compliance of mobile phones with the basic restrictions related to human exposure to electromagnetic fields (300 MHz–3 GHz), European Committee for Electrical Standardization (CENELEC), EN 50360, Brussels, 2001.
3. Human exposure to radio frequency fields from hand-held and body-mounted wireless communication devices — Human models, instrumentation, and procedures — Part 1: Procedure to determine the specific absorption rate (SAR) for hand-held devices used in close proximity to the ear (frequency range of 300 MHz to 3 GHz), IEC 62209-1, 2006.
4. Kivekäs, O., J. Ollikainen, T. Lehtiniemi, and P. Vainikainen, "Bandwidth, SAR, and efficiency of internal mobile phone antennas," *IEEE Transactions on Electromagnetic Compatibility*, Vol. 46, No. 1, 71–86, 2004.
5. Watanabe, S.-I., H. Taki, T. Nojima, and O. Fujiwara, "Characteristics of the SAR distributions in a head exposed to electromagnetic fields radiated by a hand-held portable radio," *IEEE Transactions on Microwave Theory and Techniques*, Vol. 44, No. 10, Part 2, 1874–1883, 1996.
6. Graffin, J., N. Rots, and G. F. Pedersen, "Radiations phantom for handheld phones," *Proceedings of the IEEE Vehicular Technology Conference (VTC '00)*, Vol. 2, 853–860, Boston, Mass, USA, September 2000.
7. Su, C.-M., C.-H. Wu, K.-L. Wong, S.-H. Yeh, and C.-L. Tang, "User's hand effects on EMC internal GSM/DCS mobile phone antenna," *Proceedings of the IEEE Antennas and Propagation Society International Symposium (APS '06)*, 2097–2100, Albuquerque, NM, USA, July 2006.
8. Al-Mously, S. I. and, M. M. Abousetta, "Anticipated impact of hand-hold position on the electromagnetic interaction of different antenna types/positions and a human in cellular communications," *International Journal of Antennas and Propagation (IJAP)*, Vol. 2008, Article ID 102759, 22, 2008.
9. SEMCAD X, Reference Manual for the SEMCAD Simulation Platform for Electromagnetic Compatibility, Antenna Design and Dosimetry, SPEAG, <http://www.semcad.com>.
10. IEEE standard for safety levels with respect to human exposure to radio frequency electromagnetic fields, 3 kHz to 300 GHz, Amendment 2: Specific Absorption Rate (SAR) Limits for the Pinna, IEEE Standard C95.1b-2004, December 2004.

Impact of Human Head with Different Originations on the Anticipated SAR in Tissue

S. I. Al-Mously¹ and M. M. Abousetta²

¹Department of Electrical and Electronic Engineering, School of Applied Sciences and Engineering
Academy of Graduate Studies, Tripoli, Libya

²Department of Electrical and Electronics Engineering, Al-Fateh University, Faculty of Engineering
Tripoli, Libya

Abstract— The impact of human head with different originations on the induced SAR owing to the RF emissions of different cellular handset models is intensively investigated in this paper. Four homogeneous head phantoms with normal (non-preserved) ears are designed and used in simulations for evaluating the electromagnetic (EM) wave interaction between handset antennas and human head at 900 and 1800 MHz with radiated power of 0.25 and 0.125 W, respectively. The Difference in heads dimensions due to different origins shows different EM wave interaction with cellular handsets.

1. INTRODUCTION

In numerical dosimetric of SAR induced in cellular-handset user's head, different types of human head models, i.e., homogeneous and heterogeneous, are used by many authors. Usually, the homogeneous head model was presented by the Specific Anthropomorphic Mannequin (SAM) [1–3], whereas, the heterogeneous head model was presented by different MRI-based anatomically correct models of different sexes, ages, resolutions and number of tissues [2–10]. In the previous works [8–10], the effect of human head size due to the age difference was well investigated. Nothing has been published yet about the influence of human head of different originations on the EM interaction between them and cellular handset antennas. In this paper, four homogeneous human-head models with different originations are used to investigate their EM coupling with cellular handsets.

2. NUMERICAL METHOD

A FDTD-based electromagnetic (EM) solver, *SEMCAD X* [11], is used for simulating the study cases in this work due to its handling, functionality and features for highly detailed CAD models, as well as efficient FDTD solver for simulating advanced applications. *SEMCAD-X* is a 3-D full wave simulation environment based on the FDTD method. The FDTD method proposed by Yee in 1966 [12] is a direct solution of Maxwell's curl equations in the time domain. Maxwell's curl equations are discretized using a 2nd order finite-difference approximation both in space and in time in an equidistantly spaced mesh [11].

2.1. Mobile Phone Models

Two semi-realistic handset CAD models, i.e., candy-bar type with external and internal antennas, are designed to operate at 900 and 1800 MHz [3] as follows:

- (a) Handset model-A. This model is a candy-bar type handset with left-side external antenna of a short whip top-loaded with a small cylinder [3].
- (b) Handset model-B. This model is a candy-bar type handset with internal patch antenna positioned at the upper part of the PCB with a shorting pin [3].

The handset electromechanical parts under consideration are; *antenna, antenna cover, PCB, shields, LCD and its holder, housing parts, keypad and buttons, battery and battery contacts, and connectors*. The dielectric parameters of the handset materials given in [3] are used. The antenna radiated power of 0.25 W at 900 MHz and 0.125 W at 1800 MHz, which characterize the digital generation of GSM mobile phone, are used in the simulations of this study. Figure 1 shows the *SEMCAD* models of both handsets.

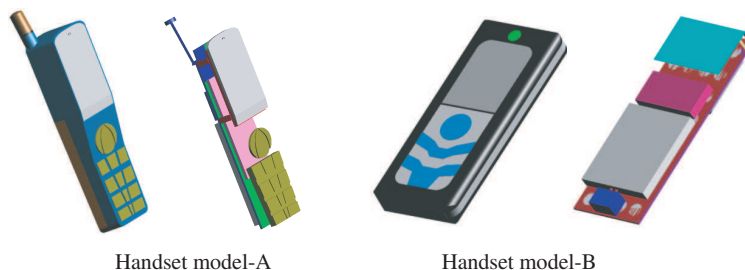


Figure 1: *SEMCAD* representation of the cellular handset model-A and model-B in different views showing different parts.

2.2. Human Head Models

Four homogeneous human-head models of different originations are designed with non-pressed pinnae in accordance with real human head dimensions, named and described as follows:

- (a) *AF-FH*. This is a CAD head-model of thirty years old African female.
- (b) *LA-MH*. This is a CAD head-model of thirty years old Latin American male.
- (c) *Eu-MH*. This is a CAD head-model of thirty years old Western-European male.
- (d) *Eu-OMH*. This is a CAD head-model of sixty years old Eastern-European male.

Each head model is assumed to be made from a single tissue with material properties similar to the SAM liquid properties in order to simulate the head including the pinnae for measuring the peak spatial SAR in compliance with the ICNIRP Guidelines [13]. Figure 2 shows the mobile phone model-B in close proximity to the four head phantoms at *cheek*-position adopted in this paper and described in [14] as the most usual test position of the cellular handset. Figure 3 shows the SAM phantom explaining the dimensions given in Table 1, for comparison, with dimensions of the four head models.

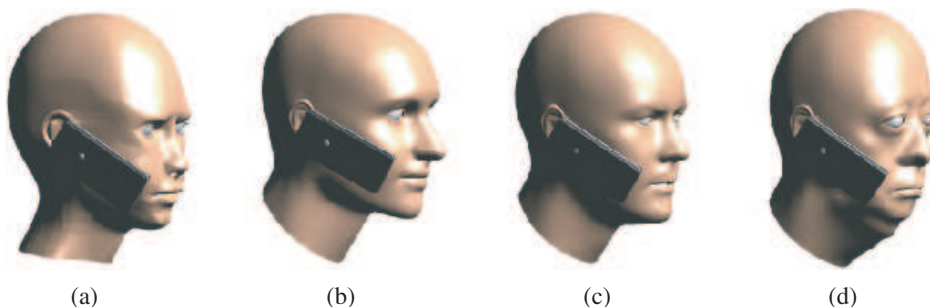


Figure 2: Phone model-B close to (a) *AF-FH*, (b) *LA-MH*, (c) *Eu-MH*, and (d) *Eu-OMH*, at *cheek*-position.

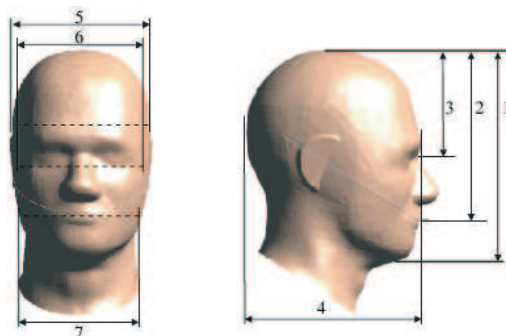


Figure 3: Two-dimensional views (front to left and side to right) of the SAM phantom explaining the dimensions of the various parts of the head.

3. FDTD-GRID GENERATION

To align the simulated mobile phone components to the FDTD grid accurately a minimum spatial resolution of $0.5 \times 0.5 \times 0.5 \text{ mm}^3$ and a maximum spatial resolution of $5 \times 5 \times 5 \text{ mm}^3$ in the x , y , and z directions are chosen for simulating the phone in hand close to head. Depending on the case complexity, a refining factor of (10) with grading ratio of (1.2) is used for the solid regions during the simulations. The simulations assume a steady state voltage at 900 and 1800 MHz, with a feed point of 50-Ohm voltage source of 1-mm physical gap. The absorbing boundary conditions (ABC) are set as U-PML mode with 10 layers thickness, where a minimum level of absorption at the outer boundary is ($\geq 99.9\%$) [12].

4. RESULTS AND INFERENCES

In this paper, the pinna is treated in accordance with ICNIRP Guidelines [13] that apply the same peak spatial SAR limits for the pinna and the head. Table 2 depict the spatial peak SAR_{10g} [13] that induced in head tissues, and power loss in head, antenna total efficiency, and the total isotropic sensitivity (TIS) [3] computed for both handset models at *cheek*-position with respect to head and operating at 900 and 1800 MHz. The mass of the head phantoms are calculated with mass density; $\rho = 1000 \text{ kg/m}^3$. The maximum power budget error (PBE) [3] obtained in all different cases are $\leq 2.5\%$. The deviation (difference between maximum and the minimum) in the induced SAR values of the head phantoms in different conditions, Figure 4, shows that with handset model-B

Table 1: The various parts dimensions of the SAM and the four designed head phantoms.

		SAM	AF-FH	LA-MH	Eu-MH	Eu-OMH
1	Height to the head (mm)	246	234	212	220	230
2	Stoma-Vertex (mm)	210	197	166	167	190
3	Eye-Vertex (mm)	123	124	96	90	107
4	Length of the head (mm)	210	198	202	198	186
5	Head breadth (mm)	162	135	137	147	158
6	Bizygomatic breadth (mm)	150	116	126	130	140
7	Bigonial breadth (mm)	142	108	122	122	136
	Pinna thickness (mm)	11.0	11.1	12.3	11.7	13.0

Table 2: Mass, SAR_{10g} and power loss in head (including pinnae), antenna total efficiency, and total isotropic sensitivity computed for both models-A and B close to head at *cheek*-position and operating at 900 and 1800 MHz with antenna radiated power of 0.25 and 0.125 W, respectively.

			AF-FH	LA-MH	Eu-MH	Eu-OMH
Mass (kg) for Mass density $\rho = 1000 \text{ kg/m}^3$			3.78	3.92	4.27	4.53
SAR_{10g} in Head (W/kg)	Phone Model-A	900 MHz	1.853	1.622	1.649	1.646
		1800 MHz	0.814	1.088	1.101	1.083
	Phone Model-B	900 MHz	2.080	1.720	1.790	1.846
		1800 MHz	0.926	1.277	1.141	1.213
Power Loss in Head (mW)	Phone Model-A	900 MHz	190.8	198.7	193.2	181.6
		1800 MHz	64.12	69.25	69.27	65.41
	Phone Model-B	900 MHz	199.6	201.9	197.2	189.6
		1800 MHz	66.51	69.26	69.74	69.44
Antenna Total Efficiency (η_{tot} %)	Phone Model-A	900 MHz	12.70	14.10	14.20	15.30
		1800 MHz	31.50	31.60	32.50	34.50
	Phone Model-B	900 MHz	15.90	17.50	18.10	19.30
		1800 MHz	40.10	40.70	39.80	41.50
Total Isotropic Sensitivity (TIS) in dBm	Phone Model-A	900 MHz	-97.10	-97.50	-97.60	-97.90
		1800 MHz	-101.0	-101.0	-101.1	-101.4
	Phone Model-B	900 MHz	-98.00	-98.40	-98.60	-98.90
		1800 MH	-102.1	-102.1	-102	-102.2

the deviation in SAR_{10g} due to difference in head origins may reach over 0.36 W/kg at 900 MHz. The origination difference of human shows more impact on the induced SAR in head while exposed to the handset model-B, as compared with model-A. Moreover, the origination difference shows more impact on mobile-B total efficiency at 900 MHz (percent difference = 21.3%) as compared with mobile-A (percent difference = 20.4%). The maximum difference in the TIS due to the impact of human head with different origins is also observed in case of model-B at 900 MHz (0.9 dB). In general, AF-FH phantom shows higher induced SAR_{10g} at 900 MHz and lesser induced SAR_{10g} at 1800, as compared with the other used head phantoms. Also, the AF-FH phantom shows more impact on both mobile phone models at 900 and 1800 MHz, as compared with the other used head phantoms. This is due to the different pinna size and thickness that every adopted head phantom has, Table 1, which make the distance between the antenna source and nearest head tissue of every phantom is different accordingly.

Figure 5 demonstrates the voltage radiation patterns, normalized to 0.125 W antenna radiated power, of both handset models-A and B in close proximity to human head phantoms at *cheek*-positions operating at 1800 MHz. No major impact of heads with different origins is observed on the radiation patterns of both handset models at 900 and 1800 MHz.

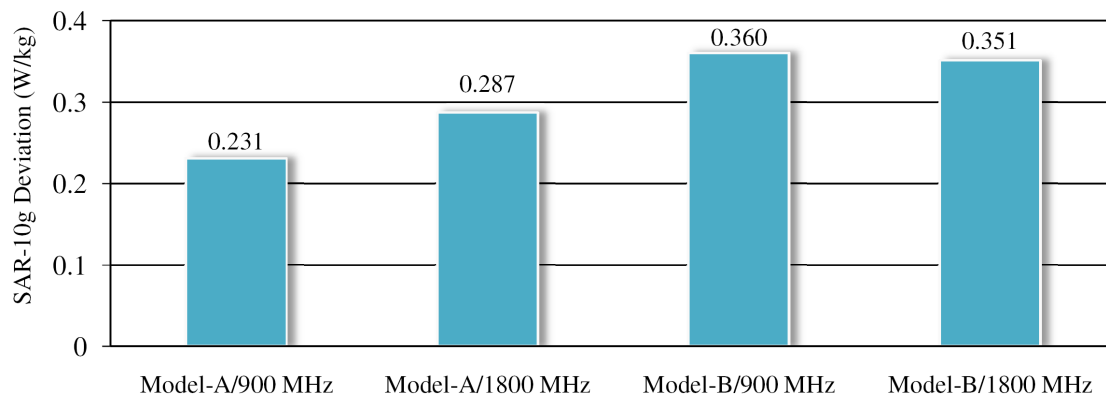


Figure 4: The deviation in the induced SAR_{10g} in head phantoms computed in different conditions.

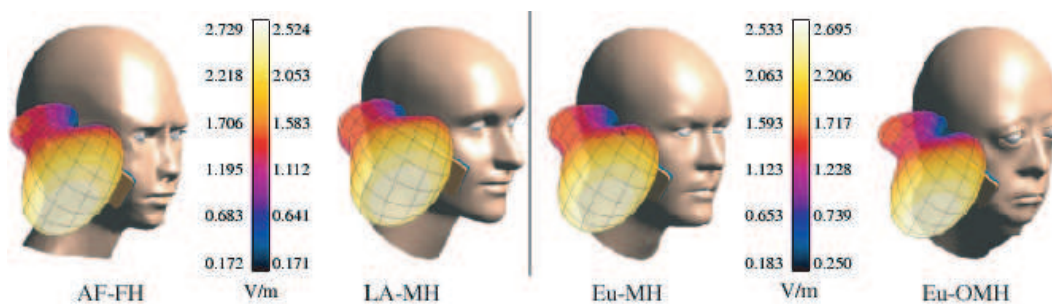


Figure 5: Voltage radiation patterns of handset models-A at *cheek*-position operating at 1800 MHz.

5. CONCLUSION

This paper investigated thoroughly the implication of the human head with different origins on their coupling with different mobile phone models. Both the mobile phone antenna performance and the peak spatial SAR_{10g} induced in head tissues were computed while simulating the EM coupling between two different mobile phone models and four different human head origins with normal pinnae. The SAR induced in head tissues was computed in accordance with the ICNIRP Guidelines. The origin of the head may make a difference in SAR in tissue and a difference in its impact on the mobile phone antenna performance. This is because of the possible difference in pinna size and thickness.

REFERENCES

1. Chavannes, N., R. Tay, N. Nikoloski, and N. Kuster, "Suitability of FDTD-based TCAD tools for RF design of mobile phones," *IEEE Antennas & Propagation Magazine*, Vol. 45, No. 6, 52–66, 2003.
2. Beard, B. B., W. Kainz, T. Onishi, T. Iyama, S. Watanabe, O. Fujiwara, J. Wang, G. Bit-Babik, A. Faraone, J. Wiart, A. Christ, N. Kuster, A. Lee, H. Kroeze, M. Siegbahn, J. Keshvari, H. Abrishamkar, W. Simon, D. Manteuffel, and N. Nikoloski, "Comparisons of computed mobile phone induced SAR in the SAM phantom to that in anatomically correct models of the human head," *IEEE Transactions of Electromagnetic Compatibility*, Vol. 48, No. 2, 397–407, 2006.
3. Al-Mously, S. I. and M. M. Abousetta "Anticipated impact of hand-hold position on the electromagnetic interaction of different antenna types/positions and a human in cellular communications," *International Journal of Antennas and Propagation (IJAP)*, Vol. 2008, 22, Article ID 102759, 2008.
4. Khalatbari, S., D. Sardari, A. A. Mirzaee, and H. A. Sadafi, "Calculating SAR in two models of the human head exposed to mobile phones radiations at 900 and 1800 MHz," *PIERS Online*, Vol. 2, No. 1, 104–109, 2006.
5. Okoniewski, M. and M. Stuchly, "A study of the handset antenna and human body interaction," *IEEE Transaction on Microwave Theory and Techniques*, Vol. 44, No. 10, 1855–1864, 1996.
6. Bernardi, P., M. Cavagnaro, and S. Pisa, "Evaluation of the SAR distribution in the human head for cellular phones used in a partially closed environment," *IEEE Transactions of Electromagnetic Compatibility*, Vol. 38, No. 3, 357–366, 1996.
7. Koulouridis, S. and K. S. Nikita, "Study of the coupling between human head and cellular phone helical antennas," *IEEE Transaction of Electromagnetic Compatibility*, Vol. 46, No. 1, 62–70, 2004.
8. Wang, J. and O. Fujiwara, "Comparison and evaluation of electromagnetic absorption characteristics in realistic human head models of adult and children for 900-MHz mobile telephones," *IEEE Transactions on Microwave Theory and Techniques*, Vol. 51, No. 3, 966–971, 2003.
9. Martinez-Burdalo, M., A. Martin, M. Anguiano, and R. Villar, "Comparison of FDTD-calculated specific absorption rate in adults and children when using a mobile phone at 900 and 1800 MHz," *Physics in Medicine and Biology*, Vol. 49, 345–354, 2004.
10. Lee, H. C., H. Lee, and J. Pack "Human head size and SAR characteristics for handset exposure," *ETRI Journal*, Vol. 24, 176–179, 2002.
11. SEMCAD X, "Reference manual for the SEMCAD simulation platform for electromagnetic compatibility, antenna design and dosimetry," SPEAG — Schmid & Partner Engineering AG, <http://www.semcad.com>.
12. Yee, K. S., "Numerical solution of initial boundary value problems involving Maxwell's equations in isotropic media," *IEEE Transaction on Antennas and Propagation*, Vol. 14, No. 3, 302–307, 1966.
13. ICNIRP (International Commission on Non-Ionizing Radiation Protection) "Guidelines for limiting exposure to time-varying electric, magnetic and electromagnetic fields (Up to 300 GHz)," *Health Phys.*, Vol. 74, 494–522, 1998.
14. Recommended Practice for Determining the Peak Spatial — Average Specific Absorption Rate (SAR) in the Human Head from Wireless Communications Devices — Measurement Techniques, IEEE Standard-1528, December 2003.

Application of New Algorithms of Electrical Impedance Tomography in Biomedicine

T. Kříž, J. Dědková, and E. Gescheidtová

Department of Theoretical and Experimental Electrical Engineering, Brno University of Technology
Kolejní 2906/4, Brno 612 00, Czech Republic

Abstract— This paper describes an usage of new techniques to solve an electrical impedance tomography (EIT) inverse problem in the biomedical engineering. Usually, a set of voltage measurements is acquired from the boundaries of an investigated volume, whilst this is subjected to a sequence of low-frequency current patterns. In principle, measuring both the amplitude and the phase angle of the voltage can result in images of the electric conductivity and permittivity in the interior of a body. It is well known that while the forward problem is well-posed, the inverse problem is nonlinear and highly ill-posed. The recently described methods are based on deterministic or stochastic approach to solve mainly 2D problems. The aim of this paper is to introduce new techniques of reconstruction of EIT images for their using in a biomedicine. New techniques, which make use of combination of well known methods for reconstruction EIT images (Total Variation Method and Tikhonov Regularization Method) and method used for image segmentation. This way enable exactly specify boundaries of an area with a known conductivity. In this paper are used new techniques for a specification of a human tissue, based on the tissue conductivity. Numerical results of the reconstruction based on new methods are presented and compared.

1. INTRODUCTION

The electrical impedance tomography (EIT) is a widely investigated problem with many applications in physical and biological sciences. Geophysical imaging is used for the searching underground conducting fluid plumes near the surface and obtaining information about rock porosities or fracture formations. Another application of EIT is for example in non-destructive testing and identification of material defects like cracks or identification of corrosion in production materials. Medical imaging can be used primarily for the detection of pulmonary emboli, non-invasive monitoring of the heart function and the blood flow, and for the breast cancer detection. The theoretical background of EIT is given in [1]. The principle of EIT is based on the back image reconstruction, which is highly ill-posed inverse problem. The aim is to reconstruct, as accurately and fast as possible, the internal conductivity or permittivity distributions in two or three dimensional models. The optimization necessitates algorithm that impose regularization and some prior information constraint.

2. BASIC PRINCIPLES OF NEW APPROACH

Let suppose an arrangement for EIT back reconstruction due to Figure 1 (left). Further we will consider only the conductivity σ for simplicity. The scalar potential U can be therefore introduced, and so the resulting field is conservative and the continuity equation for the current density can be expressed by the potential U

$$\operatorname{div}(\sigma \operatorname{grad}U) = 0. \quad (1)$$

Equation (1) together with the modified complete electrode model equations are discretized by the finite element method (FEM) in the usual way. Using the FEM we calculate approximate values of electrode voltages for the approximate element conductivity vector σ ($NE \times 1$), NE is the number of finite elements, see Figure 1 (right). Furthermore, we assume the constant approximation of the conductivity σ on each of all elements.

The forward EIT calculation yields an estimation of the electric potential field in the interior of the volume under certain Neumann and Dirichlet boundary conditions. The FEM in two or three dimensions is exploited for the forward problem with current sources. Image reconstruction of EIT is an inverse problem, which is usually presented as minimizing the suitable objective function $\Psi(\sigma)$ relative to σ . To minimize the objective function $\Psi(\sigma)$ we can use a deterministic approach based on the Least Squares method. Due to the ill-posed nature of the problem, regularization has to be used. It is possible to use the standard Tikhonov regularization method (TRM) described in [2] or

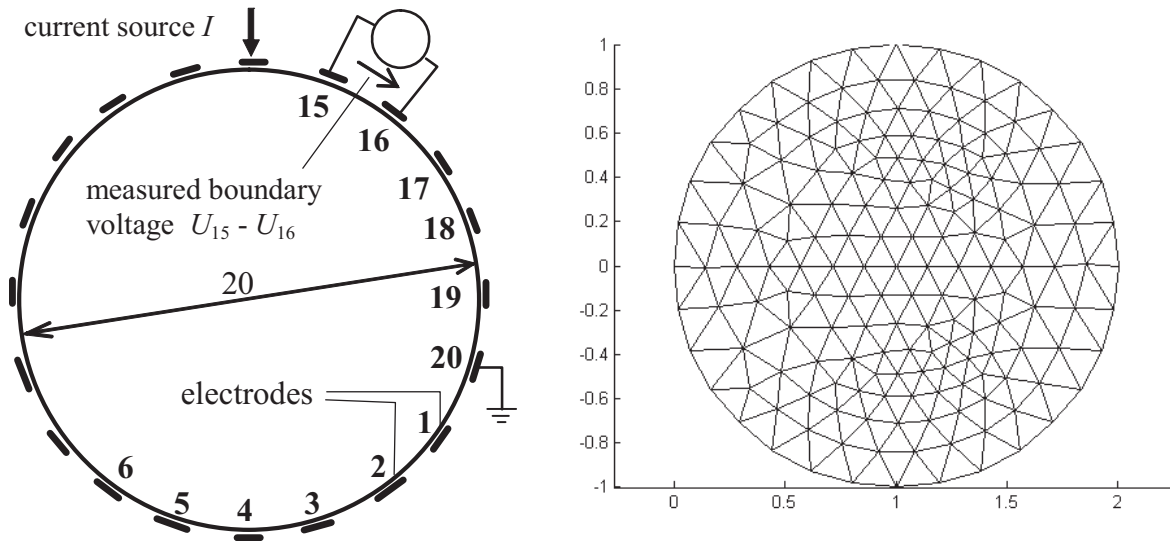


Figure 1: An arrangement for conductivity reconstruction, FEM grid with 300 elements and 167 nodes.

Total Variation method PD-IPM (TVM) described in [2] to solve this inverse EIT problem. Then we have to minimize the objective function $\Psi(\sigma)$, which is described

$$\Psi(\sigma) = \frac{1}{2} \sum \|\mathbf{U}_M - \mathbf{U}_{\text{FEM}}(\sigma)\|^2 + \alpha \|L\sigma\|^2 \quad (2)$$

here σ is the unknown conductivity distribution vector in the object, U_M is the vector of measured voltages on the object boundary, $U_{\text{FEM}}(\sigma)$ is the vector of computed peripheral voltages in respect to σ which can be obtained using the FEM, α is a regularization parameter and L is a regularization matrix connecting adjacent elements of the different conductivities.

To minimize the objective function $\Psi(\sigma)$ we can use also Total variation PD-IPM (TV) described in [2]

$$\Psi(\sigma) = \frac{1}{2} \sum (\mathbf{U}_M - \mathbf{U}_{\text{FEM}}(\sigma))^2 + \alpha \text{TV}_\beta \quad (3)$$

Here, σ is the vector of unknown volume conductivities. \mathbf{U}_M is the vector of measured voltages, \mathbf{U}_{FEM} is the vector iteratively calculated by using the FEM, α is the regularization parameter and regularization term can be described by

$$\text{TV}_\beta = \sum_{\text{all elements}} \int |\text{grad}\sigma| d\Omega = \sum \sqrt{\|\mathbf{R}\sigma\|^2 + \beta} \quad (4)$$

Here \mathbf{R} is a suitable regularization matrix connecting adjacent elements of the different conductivity values and β is a small positive parameter, which represents an influence on the smoothing of $\Psi(\sigma)$.

To obtain the solution of (2) or (3) we applied the Newton-Raphson method. This iterative procedure is commonly used in the EIT inverse problem for its fast convergence and good reconstruction quality. However, it is likely to be trapped in local minima and so additional regularization must be taken into account to obtain the stable solution. The stability of the TRM algorithm is a bit sensitive to the setting of the starting value of conductivity and to an optimal choice of the parameter α provides balance between the accuracy and the stability of the solution. The value of the parameter α can be adaptively changed during this iteration process in both regularization methods. In this way we can obtain the stable solution with required higher accuracy of the reconstruction results. Regularization methods are used to find regions with different conductivities and theirs near surroundings.

The level set method was applied to identifying of the location of the regions with different conductivities. Level set method is used to identify regions with different image or material properties [3–6]. The Level set method (LS) [3–5] is based on the deforming of a function ϕ . Then the border of object is given by the zero level of function ϕ . The evolution equation of the level set

function ϕ in general form, described in [6] is

$$\frac{\partial \phi}{\partial t} + F |\text{grad} \phi| = 0 \quad (5)$$

here ϕ is level set function, F is speed function and t is time step.

The distribution of unknown conductivity can be described in terms of level set function F depending on the position of the point r with respect to the boundary D between regions with different values of a conductivity. During the iteration process based on minimizing the objective function $\Psi(\sigma)$ the boundary D is searched in accordance with the request that the $\sigma(r)$ minimize the $\Psi(\sigma)$

$$\sigma(r) = \begin{cases} \sigma_{\text{int}} \{r : F(r) < 0\} \\ \sigma_{\text{ext}} \{r : F(r) > 0\} \end{cases} \quad D = \{r : F(r) = 0\} \quad (6)$$

To improve the stability and the accuracy of EIT image reconstructions we created a new algorithm based on both of mentioned methods TRM and level set. During this iteration process based on minimizing objective function $\Psi(\sigma)$ the boundary D is searched in accordance with request that the $\sigma(r)$ minimize the $\Psi(\sigma)$, too.

After regions with different conductivities was found and theirs near surroundings. Regularization methods are used to find final value of conductivity.

3. DESCRIPTION OF TASK

The new technique of an image reconstruction EIT is used for a specification of a human tissue based on the different tissue conductivity. The composition of this task is in Figure 2 (left). There is a horizontal cut through human chest. There are defined three regions with different conductivities. There are two blue regions representative lungs, red region representative heart and lighter blue is surroundings tissue. The conductivity of lungs is 0.1 S/m, heart is 0.666 S/m and surroundings tissue 0.333 S/m.

For solving of this task was used the combination of the regularization methods and Level set method for searching of the regions with lungs and heart. The principle of new approach is used one of regularization method to find regions with different conductivities and theirs near surroundings. The level set method was applied to identifying of the location of the regions with different conductivities. There was applied one of the regularization method again on the segmented regions by the level set method to find value of conductivity.

Results of investigated tasks are in Figures 2, 3. Results are for the combination TR-LS-TR methods. There are found regions with different conductivities after the using TR and LS methods Figure 2 (right) and Figure 3 (left). After second use of TR method are found values of regions with different conductivities. The objective function progresses during iteration process for both TR methods are shown in Figure 4.

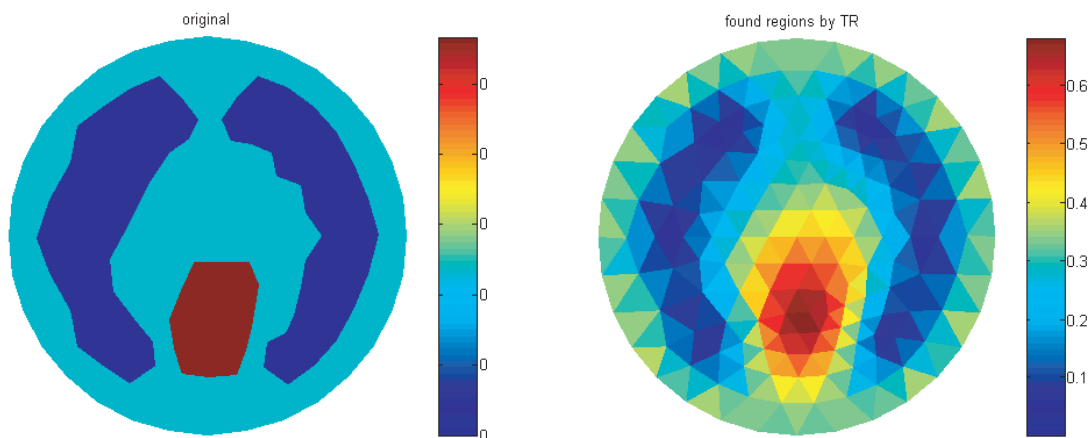


Figure 2: Original distribution of conductivity, conductivity distribution by TR and found regions.

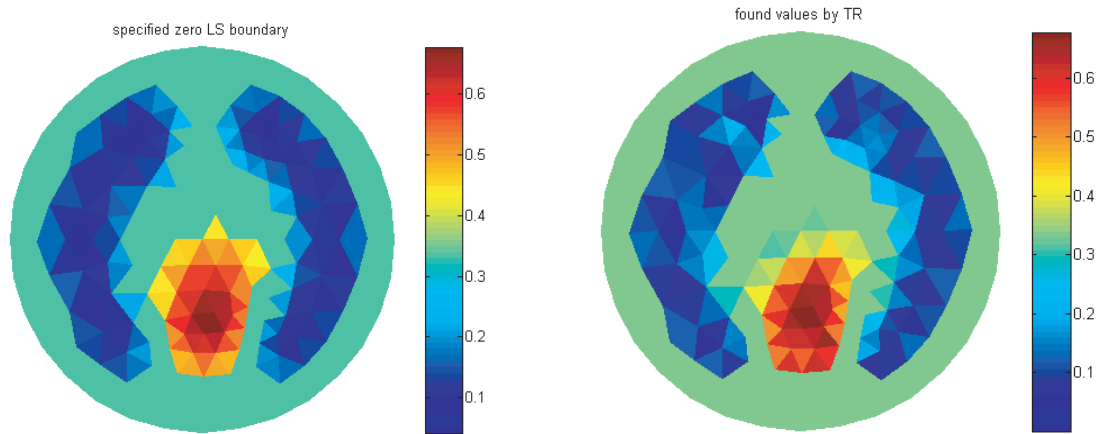


Figure 3: Regions selected by LS method, final distribution of conductivity.

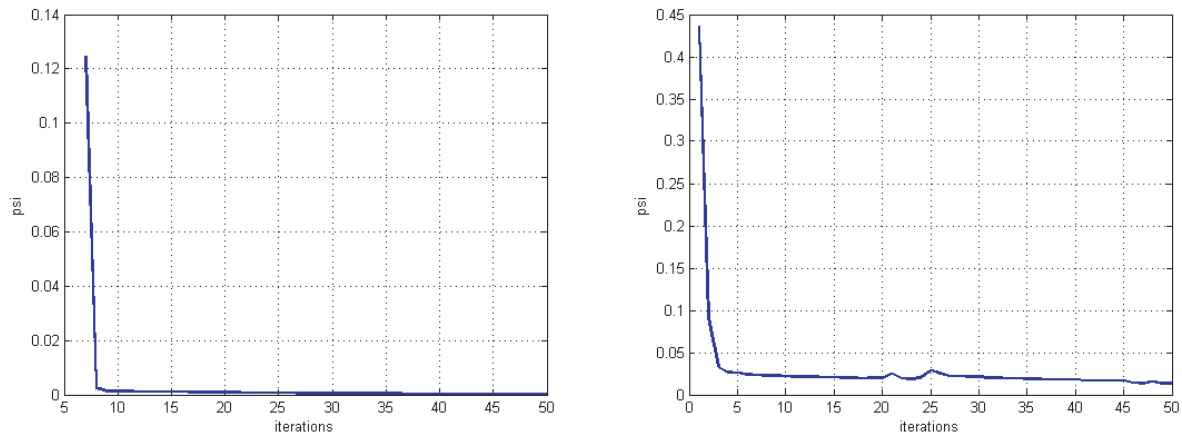


Figure 4: Objective function during first (left) and second (right) use of TR.

4. CONCLUSIONS

This paper describes new algorithms for electrical impedance tomography in biomedicine. There were tested various combinations of regularization methods and Level set method. The good reconstruction results were achieved for the combination of TR-LS-TR methods. Results were compare with results obtained by classical regularization methods. Results and regions with different conductivities obtained by above proposed new approach are more accurate.

ACKNOWLEDGMENT

The research described in the paper was financially supported by the research program MSM 0021630503.

REFERENCES

1. Cheney, M., D. Isaacson, and J. C. Newell, "Electrical impedance tomography," *SIAM Rev.*, Vol. 41, No. 1, 85–101, 1999.
2. Borsic, A., "Regularization methods for imaging from electrical measurement," Ph.D. Thesis, Oxford Brookes University, 2002.
3. Burger, M. A., "level set method for inverse problems," *Inverse Problems*, Vol. 17, 1327–1356, 2001.
4. Sethiah, J. A., *Level Set Methods and Fast Marching Methods*, Cambridge, Cambridge University Press, 1999.
5. Chan, T. and L. Vese, "Active contour without edges," *IEEE Trans. Imag. Proc.*, Vol. 10, 266–277, 2001.
6. Osher, S. and R. Fedkiw, *Level Set Methods and Dynamic Implicit Surfaces*, Springer-Verlag, New York, 2002.

Using Electromagnetic Microwave Field in Treatment of Lumbar Pain

L. Rabenok¹, Noe Oroza Hernandez¹, and Jesús Escobedo Alatorre²

¹IMSS, Plan de Ayala, Cuernavaca, Morelos, Mexico

²CIICAp, Autonomous University of Morelos State (UAEM), Cuernavaca, 62209, Mor., Mexico

Abstract— The authors analyzed the results of a treatment of 28 patients with a lumbar pain. The patients with a lumbar pain underwent a method of treatment using electromagnetic microwaves field (EM). We used a portable apparatus that operates in the millimeter (mm) wave range in 4 regimes. The intensity of EM radiation was 2–10 mW/cm². A peculiarity of the method was an absence of any pharmaceutical medicine. The exposure of the radiation was 10 min. The total course included 7–10 procedures. An application of low intensity EM radiation was started to the biological active points of acupuncture (VG3, VG4, VB30) in the sedative regime (the repetition rate 9–10 Hz) during 10 min. Clinical symptomatology, radiographic findings were analyzed as well. The results were acknowledged to be satisfactory, there were no complications. A pain disappear, movements in vertebral column have improved. We consider the use of low intensity electromagnetic radiation to be effective in the treatment of patients with a lumbar pain.

1. INTRODUCTION

A problem of prophylactics and treatment lumbar pain is actual till now. This is due to a frequent occurrence of such a disease, decreasing an efficiency of a therapy with anti-inflammatory medicines, and also duration of terms of a treatment; in some cases, undesirable consequences may occur [1, 2]. The lumbar region is the source of most of the lower back problems worldwide. In fact 8 out of 10 adults will experience lower back pain at some point in their lives. A few of the causes of lower back pain are:

- Poor overall posture
- Slumped over, flexion of the lower back
- Poor back posture
- Stress and daily work habits
- Riding in a vehicle for hours on end without a break, especially in a vibrating vehicle which is very hard on the lower back
- Lack of flexibility in the hip joint which causes the back to compensate by flexing/bending forward
- Deterioration of general physical fitness
- Overweight
- Lack of endurance in the extensor muscles of the lower back
- If fit, then incorrect lifting techniques being utilized
- Rounded back when lifting or bending forward during a lift
- Failure to flex at the hip and substituting the lower back to make up for the lack of flexibility in the hip joint

Usually treatment of lumbar pain includes: 1) Rest, 2) Anti-Inflammatory Medications, 3) Heat Application, 4) Exercise, 5) Narcotic Pain Medication, 6) Muscle Relaxers, 7) Physical Therapy, 8) Epidural Steroid Injections. Nowadays, the microwave therapy is used in clinical practice very often [2]. Nevertheless, in the literature there are only several notes on an influence of low intensity EM radiation on a process [2, 3]. A critical analysis of the problem of lumbar pain argues for a necessity of searching principally new approaches to a treatment of such a pathology under conditions of outpatient clinics.

The goal of the present investigations is an improvement of results of a treatment of patients with lumbar pain by means of using low intensity microwave EM radiation.

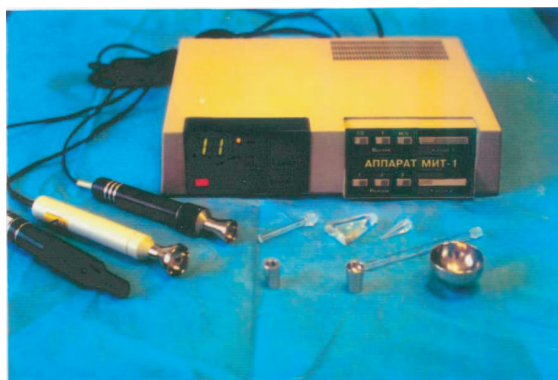


Figure 1: General view of the apparatus MIT-1 KVCH-2.

2. MATERIALS AND METHODS OF TREATMENT

We used the apparatus MIT-1 KVCH-2 (Fig. 1). The portable device MIT-1 KVCH-2 operates with low intensity EM radiation of mm wave range in four frequency bands. The intensity of EM mm wave radiation was $2\text{--}10\text{ mW/cm}^2$. This device was used for a treatment of 28 patients with acute lumbar pain. Those patients formed a group under investigations. A control group included 30 patients, which were treated by ordinary methods. The investigation group and the control one were representative with respect to the age and gender.

The treatment was realized as follows. A peculiarity of the method was an absence of medicines during a treatment by low intensity EM radiation. An exposure of an influence was 10 min. The total course included 7–10 procedures.

An influence of low intensity EM radiation was started to the biological active points of acupuncture (VG3, VG4, VB30) in the sedative regime (the repetition rate 9–10 Hz) during 10 min.

To estimate an efficiency of the proposed method of treatment there were used clinical, radiographic findings, and also static methods of investigations.

The results were acknowledged to be satisfactory, there were no complications. A pain disappear, movements in vertebral column have improved.

3. RESULTS OF INVESTIGATIONS AND DISCUSSION

After 3–4 procedures the pain perceptions diminished, a region of inflammatory tissues diminished too, compared with the patients of the control group. After 3–5 procedures, simultaneously with an essential anesthetic effect, the inflammation of tissues decreased.

We have observed that EM radiation of mm wave range has anesthetic effect which is due to improvements of the blood circulation in the pathological organs. A tranquilizing action to the nervous system is due to an action on the conductivity of nervous pulses. A pain disappear, movements in vertebral column have improved.

An interpretation of the obtained results is given due to the resonant character of the interaction of EM radiation with molecular and cellular structures; thus, an influence of EM radiation is physiological and is directed to the regenerative processes. Namely, the frequencies of $10^9\text{--}10^{12}$ Hz are similar to natural frequencies of oscillations in albuminous molecules, DNA, RNA, oscillations of membranes and other parts of the cells, conformation transitions in enzymes, that creates an opportunity of resonant absorption of microwave EM field [3, 4]. Also, the organism as a whole can have own resonant frequencies: from alive cells up to the man [1].

4. CONCLUSIONS

1. An application of low intensity EM radiation of mm wave range is efficient for a treatment of lumbar pain.
2. When using low intensity EM radiation in the method proposed here, there is no necessity to apply anti-inflammatory medicines.

REFERENCES

1. Sit'ko, S. P., "Conceptual bases for physics of the alive," *Physics of the Alive*, Vol. 6, No. 1, 57–72, 1998.

2. Afoshin, S. A. and M. Y. Gerasimenko, “Low-energy wideband electromagnetic radiation and manual therapy in the treatment of neurological manifestations of spinal osteochondrosis,” *Vopr Kurortol Fizioterapii Lech Fiz Kult*, No, 3, 32–34, May–June 2006.
3. Gasparyan, L., V. Hovanessian, and G. Grigorian, “Medical application of low-intensity lasers and millimetre electromagnetic radiation,” *Trans Black Sea Region Symposium on Applied Electromagnetism*, BISIY_8–BISIY_8, 1996.
4. Pilla, A. A., “Mechanisms and therapeutic applications of time-varying and static magnetic fields,” *Handbook of Biological Effects of Electromagnetic Fields*, 3rd edition, Barnes F., Greenebaum B., editor, CRC Press, 2006 (in press).

Real-time Measurement of Air Ion Spectrum Using Gerdien Tube with Segmented Inner Electrode

Z. Roubal, M. Steinbauer, Z. Szabó, and R. Kubásek

Department of Theoretical and Experimental Electrical Engineering
University of Technology Brno Kolejní, 4, 612 00 Brno, Czech Republic

Abstract— The gerdien tube measurement method is useful to measure spectrum of air ions. When we measurement spectrum of air ions by standard type of the gerdien tube with non-segmented electrode we must change voltage in the time. The disadvantage of this method is impossibility of real-time measurement air ion spectrum because it is very long-time.

When we measurement currents of the segmented inner electrode by the help of two voltage it is possible estimation of the air ions spectrum. This paper deals with a mathematic analyze and numerical modeling of ions trajectories in the gerdien tube with the segmented inner electrode. Show the result estimation air ions spectrum for given ions.

1. INTRODUCTION

The air ions have serious influence on human body. The light negative ions have positive influence, heavy ions and positive ions have negative influence [1, 3]. The objective is to increase the concentration of light air ions in these spaces. Another task is to set up a simulated therapy room, with conditions similar to speleotherapy caves. It sets the requirements for accurate measurement of ion field with good repeatability. That reason is important know air ion spetrum. In the standard type gerdien tube described in [3, 5, 6] is necessary measurement saturation characteristic that we calculation air ion spectrum. This measuring is very long-time. So in the Department of Theoretical and Experimental Electrical Engineering was design new type gerdien tube with segmented inner electrode. The estimation of air ion spectrum in new type we can measurement of currents segmented inner electrode by the help of two voltage value.

2. MEASURING METHOD PRINCIPLE

The principle gerdien tube with segmented electrode is showed in the Figure 1. This gerdien tube has inner electrode divided four segment. Here is r_2 — outer electrode radius, r_1 — inner electrodes radius, from L_1 to L_4 are lengths individual segments of inner electrode. Ions enter to gerdien tube with velocity v_x .

Ion is motion in direction axis x velocity v_x and owing to electric field direction to inner electrode velocity v_y . With a view to electronic field, viscosity air and flowing of air influence fan, is possible derive equation of motion for ion entered to gerdien tube with segmented inner electrode for initial point $A[0, y_0]$

$$y^2 = -2 \cdot x \cdot k \cdot \frac{U_{AK}}{v_x \cdot \ln\left(\frac{r_2}{r_1}\right)} + y_0^2. \quad (1)$$

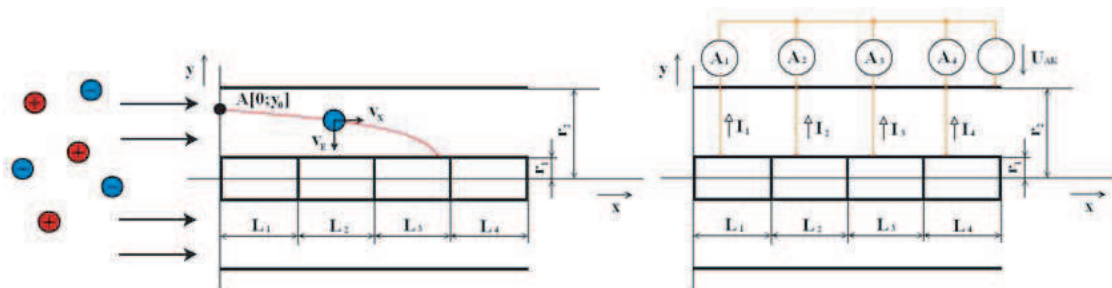


Figure 1: The trajectory air ion in gerdien tube is showed left, the measurement of individual segment currents of inner electrode and applied polarization voltage is showed right.

Here k is mobility air ion, U_{AK} is voltage between outer and inner electrodes. Ion will fall onto one segment of inner electrode according to own mobility and initial position. We will obtain coordinate of point impact when we give $y = r_1$. The segment of inner electrode, whereon ion will fall, will be determined. The ion induces current which is measurement by electrometres from A_1 to A_4 . Polarization voltage U_{AK} produces electric field inside gerdien tube. There are two methods by the help of which is possible to elect measuring interval of air ion spectrum. The first method uses segments of inner electrode the same length and voltage on the segment are different. And the second method uses different lengths of segment inner electrode and voltage on the segment is the same. In Figure 1 is simpler the second method. Whereby Equation (1) is possible determine trajectory of ions for the first method. In the program Matlab was executed universal analyze of ions enter to gerdien tube with segmented inner electrode and for individual mobility $k[\text{m}^2 \cdot \text{V}^{-1} \cdot \text{s}^{-1}]$ and ions concentration $n [\text{ion} \cdot \text{cm}^{-3}]$ was calculated currents of individual segment of inner electrode. The results for $n = 200 \text{ ions} \cdot \text{cm}^{-3}$ and $k = 1.2 \cdot 10^{-4} \text{ m}^2 \cdot \text{V}^{-1} \cdot \text{s}^{-1}$ are in Figure 2, the results for $n=2000 \text{ ions} \cdot \text{cm}^3$ and $k = 2.0 \cdot 10^{-4} \text{ m}^2 \cdot \text{V}^{-1} \cdot \text{s}^{-1}$ are in Figure 3.

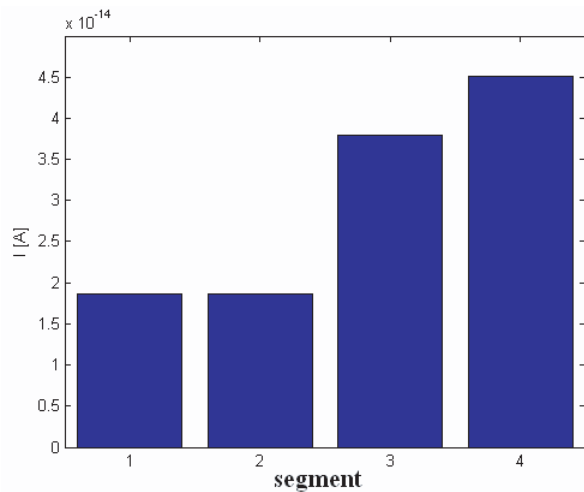


Figure 2: Currents segmented inner electrode $n = 200 \text{ ions} \cdot \text{cm}^{-3}$ and $k = 1.2 \cdot 10^{-4} \text{ m}^2 \cdot \text{V}^{-1} \cdot \text{s}^{-1}$.

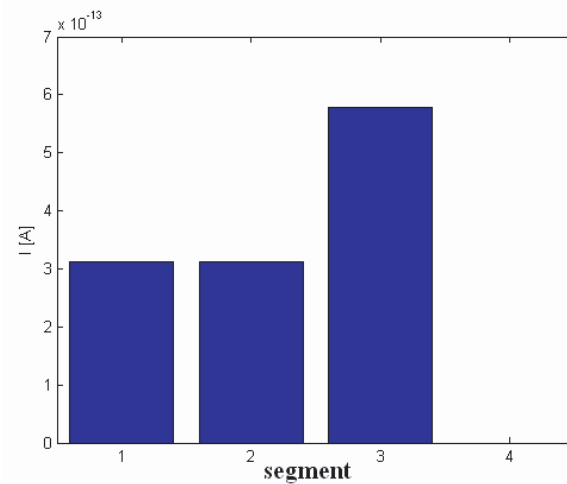


Figure 3: Currents segmented inner electrode $n = 2000 \text{ ions} \cdot \text{cm}^{-3}$ and $k = 2.0 \cdot 10^{-4} \text{ m}^2 \cdot \text{V}^{-1} \cdot \text{s}^{-1}$.

3. ESTIMATION OF THE AIR ION SPECTRUM

The currents of individual electrode are determine by distribution function of charge density $\rho(k)$ and function G gerdien tube with segmented inner electrode. According to [2] give

$$I = \int G\rho(k)dk. \quad (2)$$

The number of ions in interval from k_1 to k_2 relate distribution function of charge density according to

$$n(k_1, k_2) = \frac{\rho(k_1, k_2)}{e} \quad (3)$$

We determine from the Equation (3) currents induced ions in the segments of inner electrode. The ratio function from G_1 to G_4 to volume rate air flow M for individual segment of inner electrode was determined from equation of motion in Matlab for voltage $U_{AK} = 25 \text{ V}$ numerical analyze. The result is in the Figure 3.

For us don't useful result function G_1 to G_4 Function G for individual segment electrode overlape and begin in heavy ions. So as to is advantageous measurement current I_1 až I_n for to two voltage U_1 and U_2 . If we substract suitable this function G , we give for individual segment inner electrode new function G (show in the Figure 3 right) which formulation numbers of ions between two limitation mobility. Using a theorem of the mean integral value, we obtain three mean value concentration air ions. If spectrum doesn't contain too heavy ions, we can estimation four interval from summed

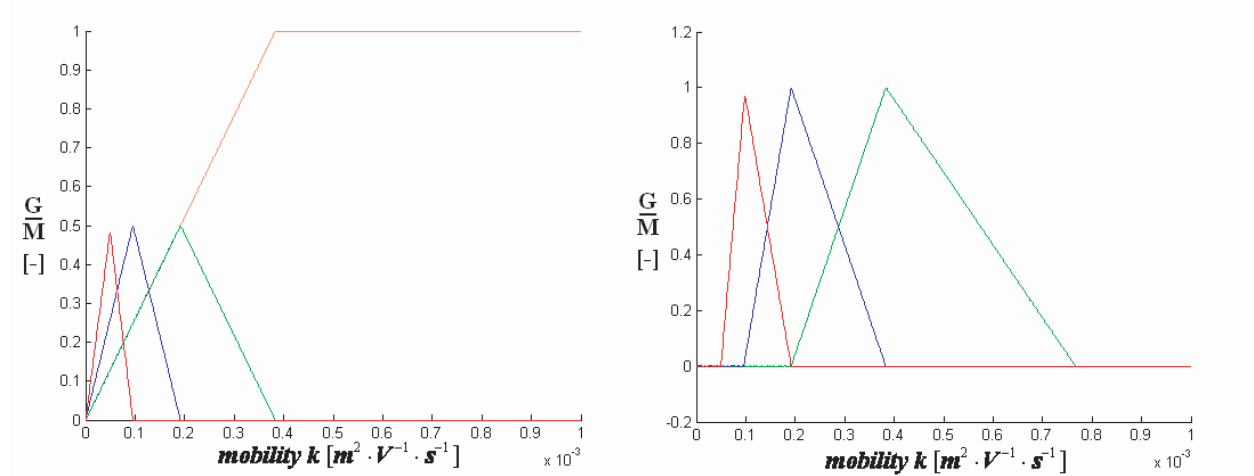


Figure 4: In left is function G_1 až G_4 for $U = 25$ V, in right is result after subtract G function for U_1 and U_2 .

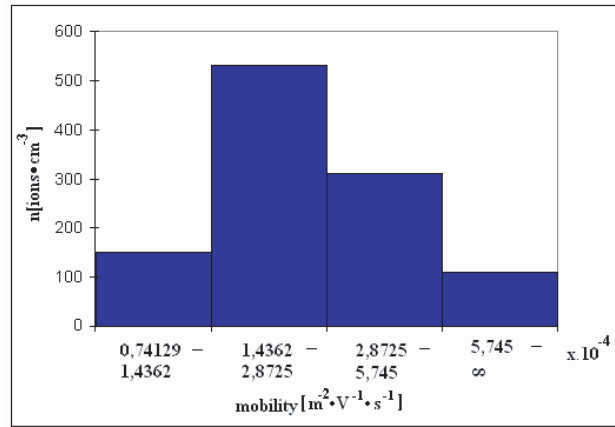


Figure 5: Estimation of the air ion spectrum for gardien tube with segmented inner electrode.

current. For $j = 2$ to number of segmented give

$$C_n = \frac{L_n}{2 \cdot \ln \left(\frac{r_2}{r_1} \right)} \tag{4}$$

$$k_{aj} = \frac{(a + 1) \cdot M}{8\pi \left(\sum_{n=1}^{n=j-1} C_n + C_n \right) U_2}, \tag{5}$$

$$k_{bj} = \frac{(a + 1) \cdot M}{8\pi \sum_{n=1}^{n=j-1} C_n U_2} \tag{6}$$

$$\rho(k_{aj}, k_{bj}) = \frac{aI_j(U_1) - I_j(U_2)}{(a - 1) M} \tag{7}$$

Here is $a = (U_2/U_1)$, k_{an} and k_{bn} are new limit intervals, where is distribution function of charge density, which is determine (7). The number of ions determines Equation (4). The result of estimation air ion spectrum for optimizing lengths segmented inner electrode from L_1 to L_4 are showed in Figure 5. We can estimate number of light ions in measurement interval. The result for group ions $n_1=200$ ions·cm⁻³ and $k_1 = 1.2 \cdot 10^{-4}$ m²·V⁻¹·s⁻¹, $n_2 = 600$ ions·cm⁻³ and $k_2 = 2.3 \cdot 10^{-4}$ m²·V⁻¹·s⁻¹, $n_3 = 200$ ions·cm⁻³ and $k_3 = 4.0 \cdot 10^{-4}$ m²·V⁻¹·s⁻¹, $n_4=100$ ions·cm⁻³ and $k_4 = 8.0 \cdot 10^{-4}$ m²·V⁻¹·s⁻¹ is shower in the Figure 5. The U_1 was 25 V and $a = 2$.

4. ELECTROMETRIC AMPLIFIER

Electrometric amplifier measurement very small current, the measurement is high-impedance type. It is necessary to minimize leak current. INA116 makes it possible to use active shielding (principle schema in the Figure 6). The specific current range for the designed gerdien tube with segmented inner electrode is from 10^{-10} A to 10^{-13} A. There are used four this electrometric amplifier. The design of this electrometric amplifier is in Figure 7.

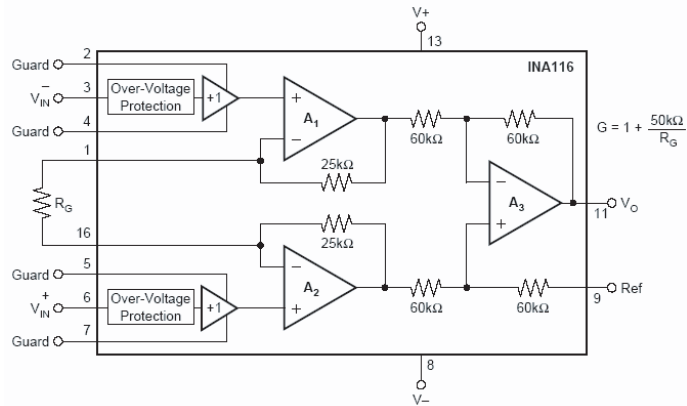


Figure 6: Principle scheme INA116.

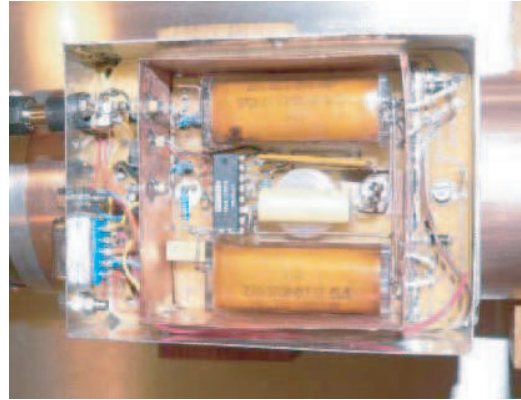


Figure 7: Design Electrometric amplifier.

5. ACTIVE SHIELDING AND ELECTROSTATIC SHIELDING

The gerdien tube with segmented inner electrode uses active shielding for increase of insulating resistance between inner and outer electrode for reason minimize leak current. The feederthrough insulator and inner electrode holder are protected by active shielding.

Electrostatic shielding protects gerdien tube with segmented inner electrode against influence external electric field. For the shielding of magnetic field generated near the fan is used the ferrite potty in a base of inner electrode and the permalloy belt closely under the aspiration condenser case. For suppressing the switched magnetic field from the fan we enclose it in the steel ring.

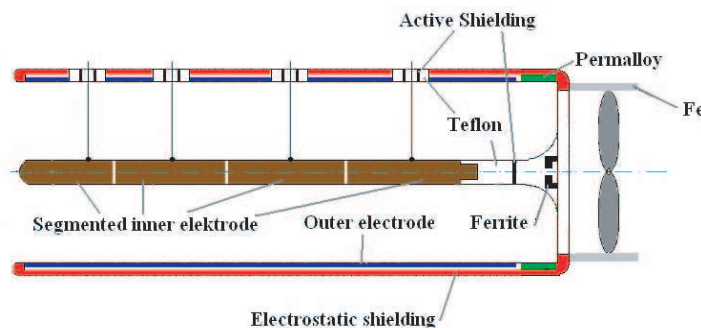


Figure 8: Sketch of the gerdien tube with segmented electrode construction details.

6. CONCLUSIONS

Gerdien tube with segmented inner electrode was designed for minimization leak current. The electrostatic shielding was used, so it is not necessary to locate gerdien tube on conductive plate. Segments length of inner electrode was designed so that air light ion spectrum was divided into four intervals. When we use standard non-segmented inner electrode the number of necessary setting voltage will be higher and measurement of air ion spectrum is slower.

ACKNOWLEDGMENT

The paper was prepared within the framework of VUT Brno of the Czech Republic and with the support of the research plan MSM 0021630516 and grant GAAV No. B208130603.

REFERENCES

1. Mikulka, J., M. Steinbauer, and Z. Szabó, “Application of low-level measurement principles to air ion field characterization,” *The 18th International Conference “Elektromagnetic Disturbances EMD’ 2008” Proceedings*, Vol. 1, No. 2008, 137–140, 2008.
2. Tammet, H. F., *The Aspiration Method for Determination of Atmospheric Ion Spectra*, IPST, Jerusalem, 1970.
3. Israëel, H., *Atmosphärische Elektrizität*, Akademische Verlagsgesellschaft, Lipsko, 1957.
4. Smutný, T., *Vliv Obvodových Prvků na Přesnost Měření Iontových Polí*, *Diplomová Práce*, VUT Brno, 2004.
5. Steinbauer, M., P. Fiala, K. Bartušek, and Z. Szabó, “Experiments with accuracy of air ion field measurement,” *PIERS Proceedings*, 1062–1066, Hangzhou, China, March 24–28, 2008.
6. Fiala, P., K. Bartušek, T. Vojtek, and T. Skoupil, “Accuracy of air ion field measurement,” *PIERS Proceedings*, 578–581, Beijing, China, March 26–30, 2007

Interaction between a Triple Band Handset Antenna and Human Head by Applying Various Head Models

D. Davoodi, P. Saghatoleslami, and M. A. Ebrahimi-Ganjeh
Sadjad Institute of Higher Education, Mashhad, Iran

Abstract—The interaction between human head tissues and handset antennas is a crucial concept in mobile communications. This paper presents a comprehensive study on the performance of a triple band PIFA antenna designed for operating in DCS, PCS and UMTS frequency bands, next to various human head models. Radiation patterns and VSWR of this antenna are computed in free space as well as in the presence of head models. Three different models are investigated: a spherical six layer model, a glass sphere model and a flat phantom. For six layer model and the glass phantom a 82 percent scaled model is also used in order to examine the interactions in presence of a child's head (seven years old). All the simulations are done for three different distances between the antenna and the model (5 mm, 15 mm, 25 mm). The specific absorption rate (SAR) is calculated in the glass sphere model. In addition, radiation efficiencies of the handset antenna is computed in the presence of head. All numerical simulations are performed using the Ansoft HFSS software. For validation of the numerical simulations, the simulated peak 1 g-SAR in the glass sphere model is compared to measured 1 g-SAR.

1. INTRODUCTION

Interaction of handset antennas with human body is a great consideration in cellular communications. The user's body, especially head, influence on the antenna voltage standing wave ratio (VSWR), gain and radiation patterns. Furthermore, thermal effect, when tissues exposed to unlimited electromagnetic energy, can be a serious health hazard. So standard organizations have set exposure limits in terms of the specific absorption rate (SAR) [1, 2].

In this paper, performance of a triple band PIFA (internal) antenna is evaluated in the presence of three various head models. In this study, all radiation characteristics including radiation patterns, radiation efficiency and VSWR are examined. To normalize the output radiated power, the 1-g SAR (W/kg) is calculated and compared to measured values of SAR [3]. All numerical simulations are performed using the Ansoft HFSS v10.

2. POWER ABSORPTION AND SAR

Energy absorption in biological tissues is characterized by Specific Absorption Rate (SAR). SAR is defined as the time derivative of the incremental energy (dW) dissipated in an incremental mass (dm) contained in a volume element (dV) of a given density (ρ) [4, 5].

$$\text{SAR} = \frac{d}{dt} \left(\frac{dW}{dm} \right) = \frac{d}{dt} \left(\frac{dW}{\rho dV} \right) \quad (1)$$

The concept of SAR is meaningful only in the frequency range between approximately 100 kHz and 6 GHz–10 GHz, i.e., where the penetration depth of the electromagnetic energy in the tissue is of the order of 1 cm or more [5].

3. STANDARD HEAD MODELS

Biological tissues could be modeled based on their permittivity and conductivity. The complex permittivity (ε) of a biological tissue is given as:

$$\varepsilon = \varepsilon_0 \varepsilon_r + j \frac{\sigma}{\omega} \quad (2)$$

where, σ (S/m) is the conductivity of tissue in siemens per meter and $\varepsilon_0 = 8854 \times 10^{-12}$ F/m.

3.1. Model 1 (Flat Phantom)

Model 1 is based on liquid phantom used as head model [4]. The size of this phantom is 225 mm by 150 mm and the depth of the liquid material in the shell must be more than 150 mm to minimize the reflections from the upper surface [4]. The thickness of the phantom shell is 2.5 mm.

3.2. Model 2 (Glass Phantom)

Model 2 has a simplified homogeneous spherical head model [3] Diameter of this spherical model is 213 mm with 5 mm thick glass shell. Properties of the head tissue-equivalent dielectric and the glass shell are presented in Table 1 [3, 4] For computation of SAR the head tissue density is assumed to be 1000 kg/m^3 .

3.3. Model 3 (Six Layer Model)

Model 3 consists of 6 layers including skin, FAT, Bone, Dura, CSF and Brain [6]. The radius, mass density and the electric properties of each layer are available in [6, 7].

Figure 1 demonstrates the simulation configuration that will be used for analysis of handset antenna performance in the presence of human head. The position of the antenna with the PCB board is exactly in the middle of the model. ($a = 49 \text{ mm}$)

4. VALIDATION TEST

To verify the validity of numerical simulations we first perform a validation test on the glass phantom and compare its results with published measurement results. This test was performed with a half wave-length dipole antenna at 1900 MHz. Table 2 compares the measured [3] and simulated peak 1-g SAR for three different distances (d) between the radiating dipole and the phantom. The SAR quantity reported in Table 2 is normalized to the output power of 0.5 W. This test indicates that the simulation results are in fine agreement with the measured values.

5. TRIPLE BAND PIFA ANTENNA

A triple band PIFA antenna is simulated according to reference [8]. The radiating element substance is perfect electric conductor (PEC) and it was fed with a 50Ω bent microstrip feed line. As shown in Fig. 2. The FR-4 substrate is simulated with ($\epsilon_r = 4.6$).

6. SIMULATION RESULTS

In this paper, all the simulations performed using Finite Element Method based on Ansoft HFSS v10. In this section, antenna properties mentioned earlier are discussed under various situations.

6.1. VSWR

Figure 3 illustrates the computed VSWR of the PIFA antenna in the frequency ranges of 1700 MHz–2200 MHz for all introduced models. Distance between antenna and head is 5 mm, 15 mm, 25 mm

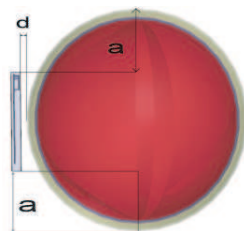


Figure 1: Position of handset and head in numerical simulations.

Table 1: Properties of the flat [4] and spherical [3] head phantoms.

Model	Phantom shell		tissue-equivalent material	
	ϵ_r	σ	ϵ_r	σ
Flat Phantom	4	0	40.0	1.4
Glass Phantom	4	0	45.5	1.31

Table 2: Comparison of measurement [3] and simulation results for peak 1 g-SAR in glass phantom.

D (mm)	Peak 1 g-SAR measured	Peak 1 g-SAR simulated	Error percentage
5	17.45	17.25	1%
15	4.96	4.71	5%
25	1.69	1.54	9%

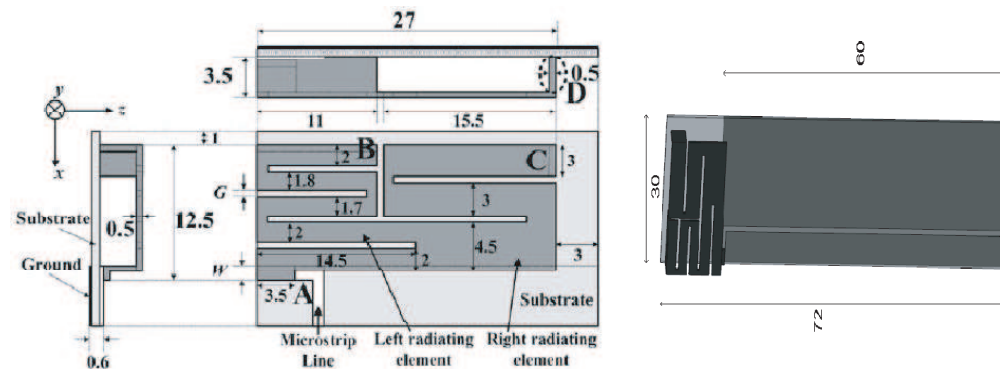


Figure 2: Dimensions of the PIFA antenna and the PCB board [8].

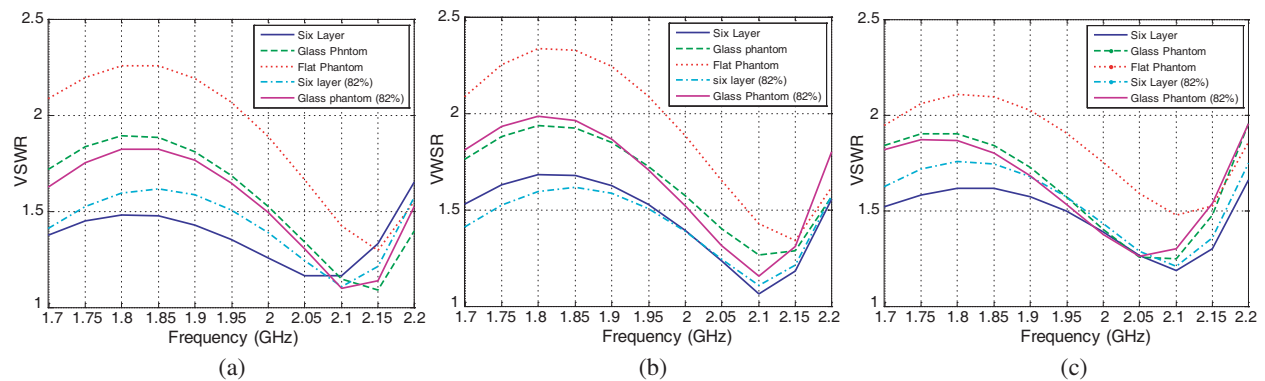


Figure 3: Computed VSWR. (a) 5 mm, (b) 15 mm, (c) 25 mm.

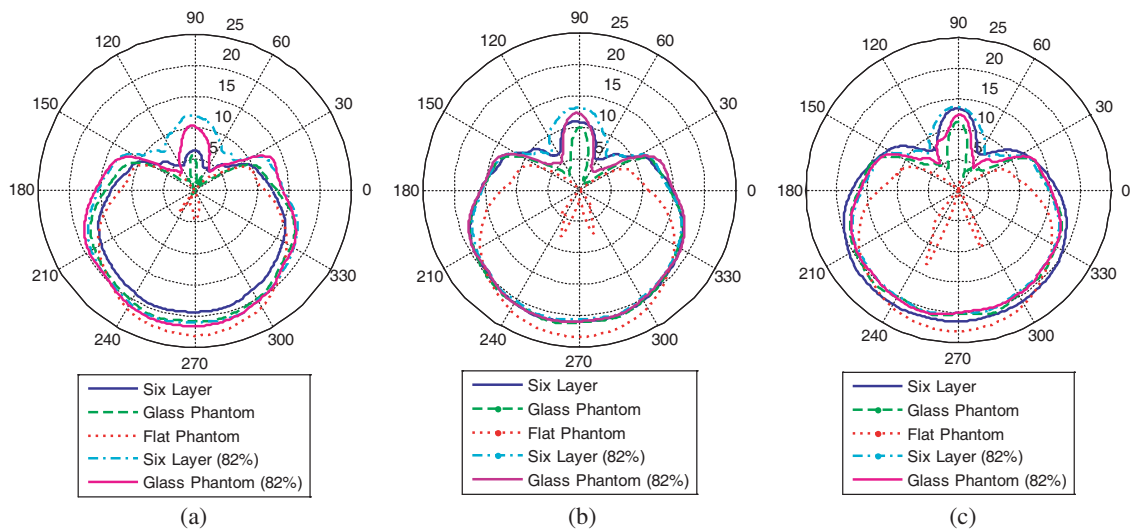


Figure 4: Radiation patterns of the PIFA antenna ($\theta = 90^\circ$). (a) 5 mm, (b) 15 mm, (c) 25 mm.

respectively. This frequency range covers DCS, PCS and UMTS frequency bands.

Figure 3 depicts the variations in the VSWR caused by different models in a constant distance. It could be seen that there is an obvious increment in the VSWR especially in the lower frequencies for the two layer models (Flat, Glass). On the other hand, the variations caused due to the distance (d) are illustrated for each model.

6.2. Radiation Pattern

Figure 4 shows the total-power radiation patterns of the PIFA antenna. Radiation patterns are computed in presence of head models at 1900 MHz. Figures 4(a), 4(b) and 4(c) are corresponding

to radiation at distance $d = 5$ mm, 15 mm, and 25 mm respectively. These radiation patterns are plotted in the azimuth plane ($\theta = 90^\circ$). Fig. 5 shows the radiation patterns for all values of (d) in the zenith plane ($\varphi = 90^\circ$).

In these figures, it could be seen that largest decrement in the radiated power occurs in range between $60^\circ < \varphi < 120^\circ$. The flat phantom demonstrates the largest variation in the radiated power in this particular range. Table 3 presents the value of power reduction in a specific direction due to the presence of head ($\varphi = 90^\circ, \theta = 90^\circ$).

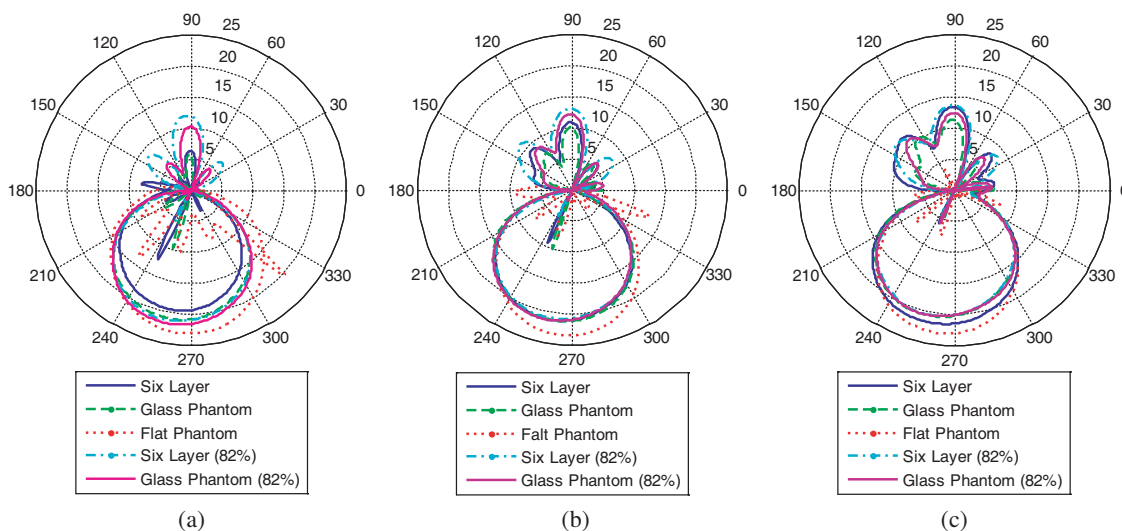


Figure 5: Radiation patterns of the PIFA antenna ($\varphi = 90^\circ$). (a) 5 mm, (b) 15 mm, (c) 25 mm.

Table 3: Variations in the radiated power in the head direction ($\varphi = 90^\circ, \theta = 90^\circ$).

1900 MHz	5 mm	15 mm	25 mm
Six Layer	-16.78 dB	-12.3 dB	-9.74 dB
Glass Phantom	-17.72 dB	-13.13 dB	-11.89
Flat Phantom	-27.61 dB	-24.53 dB	-22.05 dB
Six Layer (82%)	-11.2 dB	-10.06 dB	-9.48 dB
Glass Phantom (82%)	-12.86 dB	-10.96 dB	-10.72 dB

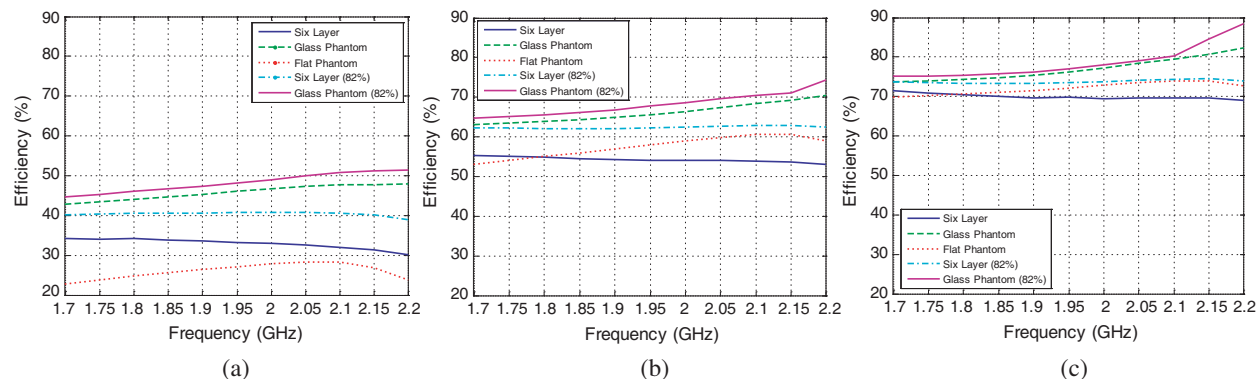


Figure 6: Radiation efficiency of the PIFA antenna. (a) 5 mm, (b) 15 mm, (c) 25 mm.

6.3. Radiation Efficiency

Due to energy absorption in human body, radiated power of a handset antenna is decreased. This decrement of radiated power is characterized by radiation efficiency (η).

$$\eta = \frac{P_{rad}}{P_{in}} = \frac{P_{rad}}{P_{loss} + P_{rad}}$$

where, P_{abs} is the power absorbed within lossy tissues, P_{rad} is the power radiated to the far field.

Figure 6 shows the radiation efficiency of the PIFA antenna in frequency range between 1.7 GHz–2.2 GHz.

This figure indicates that the distance between the antenna and head models play a crucial role in antenna's efficiency. For a handset system increasing the radiation efficiency results in improvement of battery life.

7. CONCLUSION

A comprehensive study has been presented on the performance of a triple band PIFA antenna. VSWR and radiation patterns have been computed in presence of three head models.

Presence of the head has a considerable effect on the radiation efficiency of the handset antenna; this parameter is highly dependable on the distance between the radiating antenna and head model. Power absorption in the models varies between 15%–75%. The radiation pattern in presence of head shows sensible reduction especially in the head direction. For the VSWR concept, simulations indicate that the distance between head and antenna serves an important role in the amount of power delivered to the antenna. For the simulated properties, it could be seen that applying more advanced models shows different results. However this difference was of a small value in comparison with result derived from the effect of various distance between the radiating antenna and a particular model.

REFERENCES

1. ICNIRP (International Commission on Non-Ionizing Radiation), "Guidelines for limiting exposure to time-varying electric, magnetic, and electromagnetic fields (up to 300 GHz)," *Health Physics*, Vol. 74, 494–522, 1988.
2. IEEE Std C95.1(tm)-2005, IEEE standard for safety levels with respect to human exposure to radio frequency electromagnetic fields, 3 kHz to 300 GHz, IEEE, New York, 2005.
3. Yu, Q. and O. P. Gandhi, "An automated SAR measurement system for compliance testing of personal wireless devices," *IEEE Trans. EMC*, Vol. 41, No. 3, 234–244, 1999.
4. IEEE Std 1528TM-2003, IEEE recommended practice for determining the peak spatial-average Specific Absorption Rate (SAR) in the human head from wireless communications devices: Measurement techniques, IEEE, New York, 2003.
5. Adair, E. R. and R. C. Peterson, "Biological effects of radiofrequency/microwave radiation," *IEEE Trans. MTT*, Vol. 50, No. 3, 953–961, 2002.
6. Kim, J. and Y. R. Samii, "Implanted antenna inside a human body: Simulation, design and characterization," *IEEE Trans. MIT*, Vol. 52, No. 8, 1934–1943, 2004.
7. Anderuccatti, D., R. Fossi, and C. Gabriel, "Calculation of the dielectric properties of body tissues," 2002 <http://www.niremf.ifac.cnr.it/tissprop/htmlclie/htmlclie.htm>.
8. Sim, D. U. and S. O. Park, "A triple-band internal antenna: Design and performance in presence of the handset case, battery, and human head," *IEEE Trans. EMC*, Vol. 47, No. 3, Aug. 2005.

Use of Magnetic Resonance to Determine Radial Slices of Plants

K. Bartusek¹, E. Gescheidtova², and Z. Dokoupil¹

¹Institute of Scientific Instruments, Academy of Sciences of the Czech Republic
Kralovopolska 147, Brno 612 00, Czech Republic

²Faculty of Electrical Engineering and Communication, Brno University of Technology
Kolejni 2906/4, Brno 612 00, Czech Republic

Abstract— The paper deals with the measurement of radial slices of plant stalks using magnetic resonance imaging. MR images (26×26 mm, 256×256 pixels, slice thickness 3 mm) of radial slices weighted by spin density, relaxation time T_2 , and proton core density were measured. Current pulse sequences of spin echo (SE) and pulse-gradient-spin echo (PGSE) were used and the images measured were subsequently processed. The images being measured were compared with images obtained by the classical microscopic method of monitoring vascular bundles. The results show that the MR images characterize the location of vascular bundles mainly in younger plants and bring information on the distribution of protons throughout the stalk. An advantage of the MR method is that the plant does not get destructed and that the measurement is simpler.

1. INTRODUCTION

Magnetic resonance (MR) enables studying the motion of liquids in the stalks of plants via radial slices of plants. When classical methods are used, pictures are made of dyed thin radial slices of stalks and the structure of vascular bundles is analyzed. To produce thin slices of stalks is very demanding. Currently there are not many workplaces that publish results of studying via MR imaging the transport of ions through plants. Scheenen [1] describes the design of a microscope for the observation of vascular bundles in plants. MR is a non-destructive examination method but its drawback is lower resolution ($100 \mu\text{m}$) and higher image noise. Its advantage is the possibility of obtaining images weighted by spin density, relaxation times and diffusion. Making use of subsequent image processing, new information can be obtained on the plant structure and motion of liquids through the plant.

2. METHOD

Radial MR images weighted by spin density were obtained using the classical SE sequence with the following parameters: spin echo time $T_E = 11$ ms, repetition time $T_R = 1.5$ s, matrix dimension 256×256 pixels (26×26 mm with a resolution of $100 \mu\text{m}/\text{pixel}$), layer thickness $d = 3$ mm, and without averaging operation. There is a connection between the signal-to-noise ratio and the size of the image being measured. The repetition time is equal to the spin-lattice relaxation time T_1 and the measurement time equals $256 T_R$. To reduce noise in the image, wavelet filtering with optimally chosen functions is used. The classical MR SE pulse sequence is shown in Fig. 1.

Figure 2 gives schematically the lay-out of MR measurement. Plant roots were placed in a container with water and the site around the stalk was sealed with wax. An RF detection coil of saddle shape, 26 mm in diameter, was positioned around the stalk at a distance of 30 mm from the plant roots.

Figure 3 gives a comparison of images obtained by the classical microscopic method with MR images. In MR images clearly delineated areas of increased amounts of proton cores flowing through vascular bundles can be seen. It should be emphasized that, owing to technical reasons, not the same plants were used and that the position of vascular bundles is different.

The samples of scanned vegetables were prepared at Mendel University of Agriculture and Forestry in Brno. The experiments were carried out on an 4.7 T/120 mm MR tomograph system (i.e., 200 MHz for ^1H nuclei) with actively shielded gradient coils ($G_{\text{max}} = 180$ mT/m). The data measured were processed in the MAREVISI and MATLAB programs. Post-acquisition processing of images enhances vascular bundles and various image contrasts.

The relaxation times of the cores being measured characterize mutual bonds among protons and in molecules. Their changes may point to a change in chemical bonds or distances inside or outside the vascular bundle. The measurement was conducted using the SE pulse sequence for two different echo times, $T_E = 11$ ms and 30 ms.

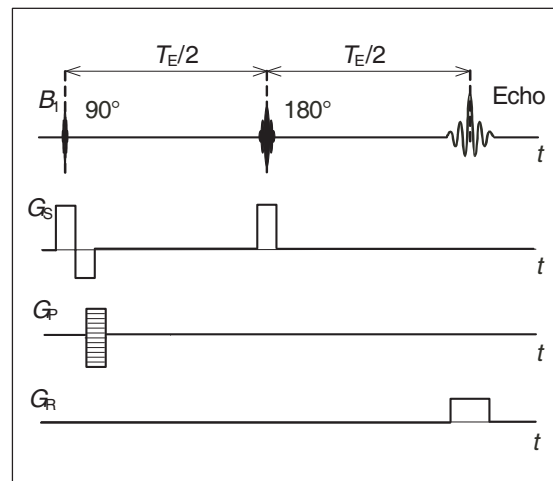


Figure 1: Classical SE pulse sequence.

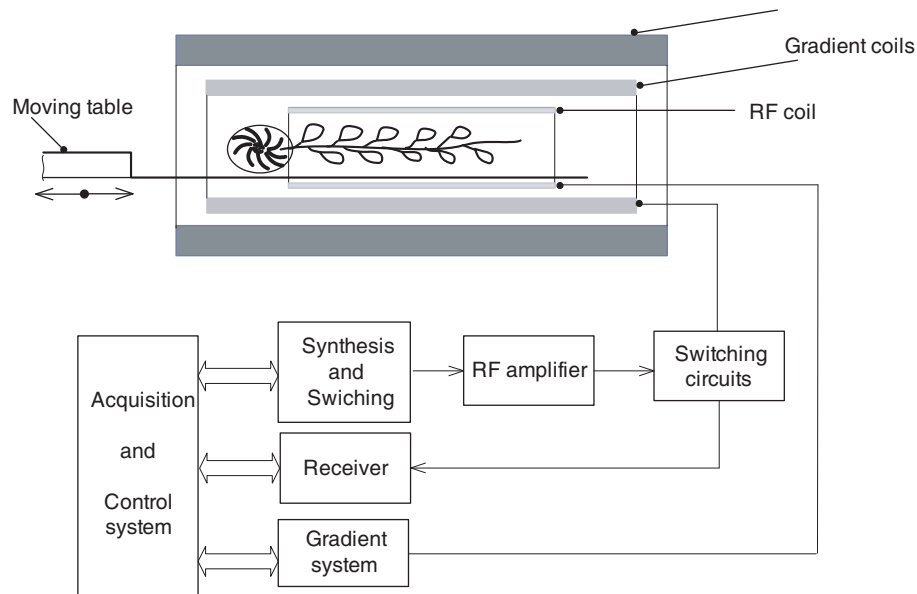


Figure 2: Schematic of MR measurement lay-out.

Relaxation time T_2 is calculated [2] for the images $M_1(x, y)$ and $M_2(x, y)$ measured for different echo times T_{E1} and T_{E2} from the relation

$$T_2 = (T_{E1} - T_{E2}) / \{\ln [M_1(x, y)] - \ln [M_2(x, y)]\} \quad (1)$$

Maize, sunflower and cucumber plants were used in the measurement. The slice being measured was placed 25 mm above the plant root. The MR images weighted by relaxation times T_2 are given in Fig. 4. The vascular bundles show a slight decrease in relaxation time. In the stalk area the relaxation time is the same, namely $T_2 = 145$ ms for maize, $T_2 = 161$ ms for sunflower, and $T_2 = 725$ ms for cucumber. Cucumber has freely bonded in the stalk and its relaxation times are very long.

The diffusion-weighted image makes use of the classical MRI pulse sequence PGSE given in Fig. 5. The principle of measuring in the current spin-echo pulse sequence consists in applying two diffusion gradients of length δ [3]. The first of them is located between two RF pulses and serves to bring the spins out of phase in a defined way while the other gradient is applied after the 180° pulse and serves to bring the spins into phase again. For the whole period of measuring, a static gradient magnetic field G_0 is acting on the spins, which is due to the magnetic susceptibility of the material being measured. The effect of this field on the precision of measuring the diffusion coefficient should be minimized.

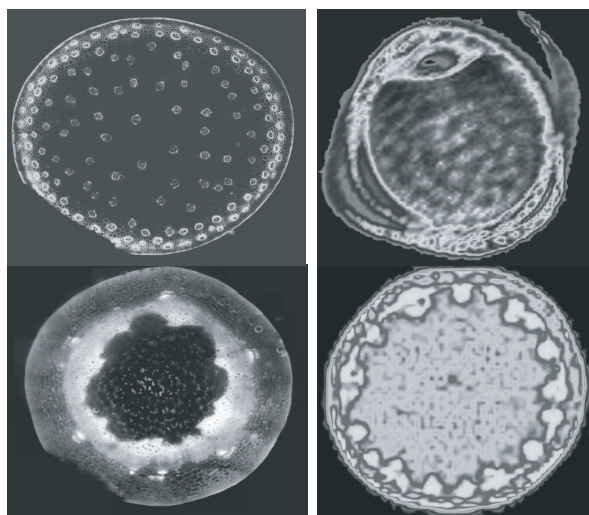


Figure 3: Examples of slices through maize stalk: top left — image obtained by classical method, top right — MR image. Bottom left — classical image of slice through sunflower stalk, bottom right — MR image.

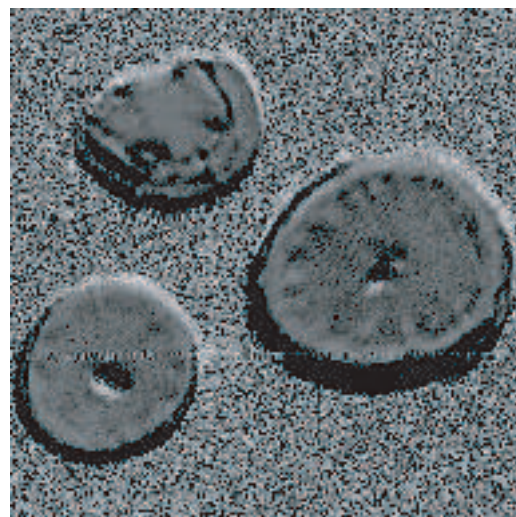


Figure 4: Example of measuring MR images weighted by relaxations T_2 , 25 mm above roots, for sunflower (top left), maize (top right) and cucumber (bottom).

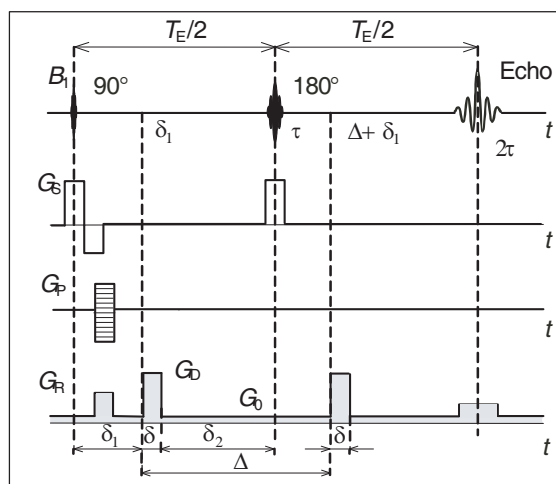


Figure 5: Diffusion-weighted SE sequence.

Simple calculations can be used to compensate for the inhomogeneities of static magnetic field, which are due to the magnetic susceptibility of the substance being measured. Shaped impulses in the measuring sequence extend the diffusion measurement time, which is always limited by relaxation time T_1 of the substance under measurement. To be able to measure diffusion in substances with short relaxation times T_1 , we must reduce the measuring time to a minimum while maintaining sufficient precision of the measurement. The measurement was carried out on the same samples as the measurement of relaxation time T_2 . The measurement parameters are: $\delta = 3$ ms, $\Delta = 20$ ms, $G_D = \pm 171$ mT/m. For the chosen parameters of the pulse sequence the diffusion contrast in the image is given by the relation

$$D = \frac{\ln \left(\frac{M_{G_D} M_{-G_D}}{M_{G_D=0}^2} \right)}{-2\gamma^2 \delta^2 \left(\Delta - \frac{\delta}{3} \right) G_D^2}. \quad (2)$$

The accuracy of the measurement of diffusion coefficients depends on the inaccuracy of the diffusion gradient magnitudes, timing and determination of the spin echo magnitude. The timing error can be neglected in current tomography systems. The accuracy of determining the spin-echo magnitude greatly depends on the signal-to-noise ratio and on the drop in echo magnitude for the

diffusion gradient used. The diffusion coefficient in heterogeneous materials calculated by relation (2) carries an error that is due to the cross term. In this case, the relative error due to the error in measuring the amplitude of NMR signal is given by the relation

$$\delta_D = \frac{4\delta_M}{\ln\left(\frac{M_{G_D}M_{-G_D}}{M_{G_D=0}^2}\right)}. \quad (3)$$

In the case of the measurement described the relative error of diffusion measurement due to noise in MR image was 7.5% at the most. The MR images measured at a height of 25 mm above roots are given in Fig. 6.



Figure 6: Example of measuring diffusion-weighted MR images 25 mm above roots, for sunflower (top left), maize (top right) and cucumber (bottom).

For all the slices of plant stalks the diffusion coefficient magnitude is identical and there is noise in the image, which corresponds with the measuring error. No differences in the magnitude of diffusion in the area of vascular bundles and outside the bundles can be seen. In view of the magnitude of diffusion length (distance by which the cores change their position during measurement), which is $5\ \mu\text{m}$, this could be expected. The diffusion coefficients are: $D = 0.89 \cdot 10^{-9}\ \text{m}^2/\text{s}$ for sunflower, $D = 0.57 \cdot 10^{-9}\ \text{m}^2/\text{s}$ for maize, and $D = 0.63 \cdot 10^{-9}\ \text{m}^2/\text{s}$ for cucumber.

3. CONCLUSIONS

The measurement of vascular bundles of plants via MR imaging shows that in young plants the vascular bundles are differentiated and are clear to see in the images. For MR images weighted by spin density it will be necessary to increase image resolution and measure the plant in several slices at different heights. Images weighted by relaxations and diffusion do not exhibit any differences. It will be necessary to judge whether an ion transport through plant stalk, which is faster than the change due to diffusion, can be measured.

ACKNOWLEDGMENT

This work was supported within the framework of project No. 102/07/0389 of the Grant Agency of the Czech Republic.

REFERENCES

1. Scheenen, T., et al., "Functional imaging of plants: A NMR study of a cucumber plant," *Biophysical Journal*, Vol. 82, 481–492, 2002.
2. Bartusek, K., "Processing of MR images weighted by relaxation time T_2 to increase their contrast resolution," *Measurement Science and Technology*, Vol. 17, No. 4, 727–731, 2006.
3. Bartusek, K. and E. Gescheidtova, "MRI method of diffusion measurement in heterogeneous materials," *Measurement Science and Technology*, Vol. 19, 1–8, 2008.

Finite Size Effect on the Resonant Microwave Absorption of Er^{3+} Doped Ag Nanoparticles

J. M. Vargas¹, W. Iwamoto¹, L. M. Holanda, Jr.¹, P. G. Pagliuso¹,
C. Rettori¹, and S. B. Oseroff²

¹Instituto de Física “Gleb Wataghin”, UNICAMP, Campinas-SP, 13083-970, Brazil

²San Diego State University, San Diego, California 92182, USA

Abstract— The influence of finite sample size effects and structural defects on the ground state of Er^{3+} in diluted Ag:Er alloys is studied. The chosen metallic systems were, nanoparticles (5–10 nm) of the alloy $\text{Ag}_{1-x}\text{Er}_x$ ($x = 0.04$) and the bulk alloy of $\text{Ag}_{1-x}\text{Er}_x$ ($x = 0.001$) which was used as a reference. The Ag:Er alloy nanoparticles were prepared by chemical synthesis that gives an excellent morphological and crystalline homogeneity and the bulk alloy of Ag:Er by a conventional arc-melting. The nanoparticles resonant microwave absorption (Electron Spin Resonance) at X (9.5 GHz)-band of Er^{3+} obtained at low- T (4–20 K) show a T -independent g -value of 6.74(4) and linewidth of 50(5) Oe. However, above $T \approx 20$ K an exponential T -dependence of the linewidth is observed. A preliminary interpretation of these results suggests that: i) the exchange interaction, $J_{fs}\mathbf{S}\cdot\mathbf{s}$, between the Er^{3+} localized magnetic moment and the host's conduction-electrons has been quenched; and ii) at high- T the spin-lattice relaxation is mainly due to the spin-orbit coupling via lattice phonons involving Er^{3+} crystal field excited levels.

1. INTRODUCTION

The study of surface, finite size effects and structural defects in nanoparticles (NPs) is today a subject of growing interest in nanoscience from both, academic and technological point of view [1]. Despite the large number of investigations, still there are many open questions about the surface and size influence on the general properties of metallic NPs. In particular, metallic Ag and Au systems in the nanoscale regime show striking features that are not observed in the bulk counterparts, as in the case of the ferromagnetism reported in Au NPs coated by protective agents as dodecane thiol [2]. Resonant microwave absorption, as Electron Spin Resonance (ESR) of doping rare-earths (RE) ions, is a powerful technique because it may provide information about crystal field (CF) effects, RE ground state, site symmetry, valence of the paramagnetic ions, g -value, fine and hyperfine interaction, in a wide variety of doped magnetic and non-magnetic compounds [3–5]. Moreover, the ESR spectra of the magnetic doping ions allow not only to learn about the doping ion, but also about the properties of the host lattice. In this work, we present an ESR study of the ground state of Er^{3+} diluted in bulk and NPs Ag hosts.

2. SAMPLE PREPARATION & EXPERIMENTAL TECHNIQUES

The bulk dilute alloys of $\text{Ag}_{1-x}\text{Er}_x$ ($x = 0.001\%$) were prepared by arc-melting the amount of elements in the appropriated stoichiometric ratio under inert Ar atmosphere as reported elsewhere [4, 5]. These samples were labeled as bulk. The nanoparticles of dilute alloy of $\text{Ag}_{1-x}\text{Er}_x$ ($x = 0.04\%$) were synthesized by chemical route adapting the procedure described by Tang et al. [6]. Firstly, the Ag-metallic precursor ($\text{C}_{54}\text{H}_{45}\text{NO}_3\text{P}_3\text{Ag}$) was prepared from the stoichiometric amount of silver nitrate (1.1 mmol) and triphenylphosphine (3 mmol), mixed in 10 mL of warm acetonitrile. After heated at 80°C in inert atmosphere for 3 hs a white powder is obtained. Thereafter, 10 mmol of oleyamine and 10 mmol of oleic acid were slowly added to the phenylether solution of Ag-metallic precursor with 0.04 mmol of $\text{Er}(\text{CF}_3\text{COO})_3$. The above mixture was gently heated up to the final temperature of 225°C for 40 min under Ar gas flux. Finally, the solution was cooled down to room- T . The colloidal nanoparticles were washed and centrifuged after adding excess of ethanol. The particles can be easily dispersed in non-polar solvents such as toluene or chloroform. These samples were labeled as NPs. The particle diameters and distribution were measured by Transmission Electron Microscopy (TEM) (300 keV JEM 3010 microscope) at the Brazilian Synchrotron Light Laboratory (LNLS). The X-ray diffraction (XRD) patterns were measured using Synchrotron radiation ($\lambda = 1.78922 \text{ \AA}$) at the beam-line XRD2 (LNLS). The magnetic properties were measured with a SQUID (Quantum Design, MPMS XL) dc -magnetometer. The ESR experiments were carried out in colloidal (NPs in toluene) and bulk (powdered) samples in a Bruker spectrometer at

9.48 GHz (X-band), using appropriate resonators coupled to a T -controller of a helium gas flux system in the range $4.2\text{ K} < T < 300\text{ K}$.

3. RESULTS & DISCUSSION

Figure 1(a) shows a typical low-resolution TEM images of the Ag:Er nanoparticles. A highly homogeneous Lognormal distribution of particles of mean diameter $D_m = 9.0\text{ nm}$ with standard deviation of $\sigma = 0.25$ (see histogram in Fig. 1(c) is obtained. Both, high resolution TEM (HRTEM) and XRD are used to obtain the structural information of the Ag:Er NPs. The HRTEM images show that the internal structure of the particles corresponds to multiple crystalline domains, as it is clearly indicated by the different atomic lattice fringes inside of the particles (see Fig. 1(b)). Fig. 1(d) presents the NPs and bulk XRD patterns intensity as a function of the modulus of the scattering vector, $s = 2 \sin \theta / \lambda = 1/d$ (d is the interplanar distance, θ is one-half of the scattering angle and λ is the incident wavelength). The principal peaks at $s = 0.42$ and 0.48 \AA^{-1} are indexed as (111) and (200)-Ag, respectively. The existence of structural defects, namely, twins and stacking faults, are observed in the XRD pattern where the small peaks at $s = 0.40$ and 0.45 \AA^{-1} may be used as fingerprints for the presence of defects in the particles [7]. We should mention that these peaks are not observed in the Ag:Er bulk sample, where only the principal Ag peaks are observed (see Fig. 1(d)). Using the Scherrer formula [8] we have determined the crystalline size for the NPs (7(1) nm) and bulk ($\approx 100\text{ nm}$) samples, respectively. For the NPs sample this value is in good agreement with the HRTEM images in which the polycrystalline particle structure is observed.

As it is expected for weakly interacting magnetic Er^{3+} ions the T -dependence of the dc -magnetic susceptibility follows a Curie-Weiss law (not shown) in both $\text{Ag}_{1-x}\text{Er}_x$ alloys, bulk and NPs samples, from where the values of $x = 0.001$ and 0.04 were respectively determined.

Figure 2 shows the Er^{3+} X-band ESR spectrum at $T = 4.2\text{ K}$ for both NPs and bulk samples. The differences between both resonances is evident. The spectrum of the bulk sample show the typical Dysonian line-shape (skin depth \ll sample size) [9–10] with a weakly resolved hyperfine splitting of the Er^{3+} resonance, commonly expected for Ag:Er alloys with concentrations of the order of 1000 ppm. The g -value of 6.85(5) is found to be T -independent between 4.2 K and 12 K (see Fig. 3(a)) and the T -dependence of the Er^{3+} resonance intensity follows approximately the Curie-Weiss behavior (inset of Fig. 2, open circles), indicating that the resonance arise from a Γ_7 Kramers

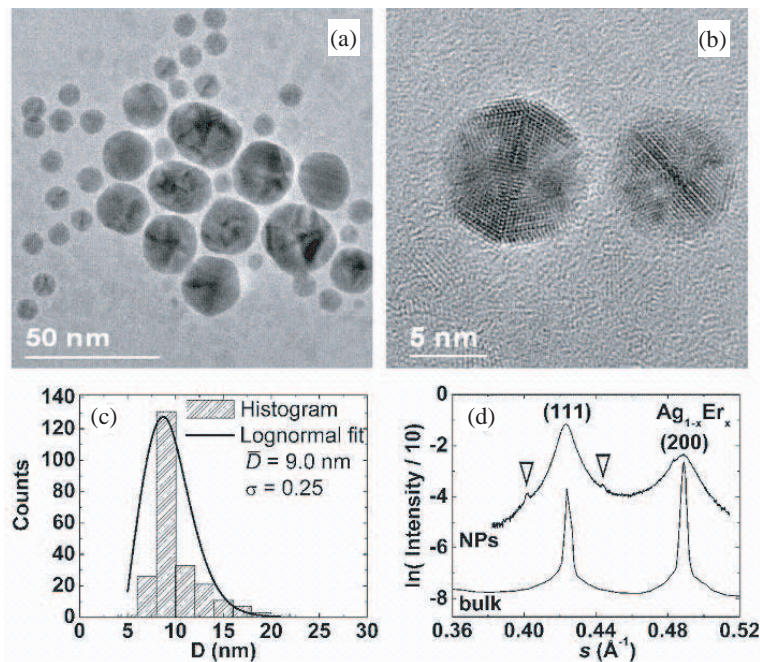


Figure 1: (a) TEM and (b) HRTEM nanoparticles images of the $\text{Ag}_{1-x}\text{Er}_x$ alloy ($x = 0.04$). (c) The particles histogram was obtained by counting more than 200 particles, and the solid line corresponds to the Lognormal fitting. (d) XRD of the Ag bulk and Ag NPs with the indexed Ag-peaks (111) and (200). The triangles indicate the peaks positions associated to the presence of defects in the particles.

doublet ground state of the Er^{3+} cubic CF splitted J -multiplet ($J = 15/2$), in good agreement with previous reported results of Ag:Er alloys [4, 5]. In the counterpart, the Er^{3+} resonance in the NPs shows a Lorentzian line-shape (skin depth \gg sample size) [9–10] with the typical resolved hyperfine structure corresponding to the $^{166}\text{Er}^{3+}$ ($I = 0$) and $^{167}\text{Er}^{3+}$ ($I = 7/2$) isotopes [4, 5]. The short-vertical lines in Fig. 2 indicate the positions of the hyperfine lines corresponding to the $^{167}\text{Er}^{3+}$ isotope hyperfine parameter of $A = 75(5)$ Oe, in good agreement with the value reported for the Ag:Er alloy [4]. The measured g -value was found to be T -independent between 4.2 K and 36 K (see Fig. 3(a)). However, its value of 6.74(4) is close to that reported for Er^{3+} in the insulating ThO_2 host [11]. This g -value leads to a g -shift of $\Delta g = (6.85 - 6.74) \approx 0.11$ between our Ag:Er bulk and NPs samples. This value is about the same of the g -shift usually found for diluted Er^{3+} in non-magnetic metallic hosts and is attributed to the exchange interaction between Er^{3+} and conduction-electrons, $J_{fs}\mathbf{S}\cdot\mathbf{s}$, which seems to be absent in our Ag:Er NPs. The T -dependence of the Er^{3+} resonance intensity follows approximately the Curie-Weiss behavior (inset of Fig. 2, solid circles), indicating that a Γ_7 Kramers doublet is also the Er^{3+} ground state in our Ag:Er NPs.

Figure 3(b) shows the T -dependence of the linewidth, ΔH , at X-band for both samples. These results show that: i) for the bulk sample, between 4.2 K and 12 K ΔH follows a linear T -dependence, $\Delta H = a + bT$ (Korringa-relaxation), with $b = d\Delta H/dT = 7.9(2)$ Oe/K, in agreement with previous reports [5]; ii) for the NPs sample, between 4.2 K and 18 K, the linear T -term (Korringa relaxation) was totally absent; and iii) for the NPs sample above $T \approx 20$ K an exponential increase of ΔH is observed. Assuming that the line broadening results from a phonon spin-lattice relaxation process involving excited CF levels the T -dependence of the linewidth can be written as: [12–13]

$$\Delta H = \Delta H_0 + c\Delta^3 / \exp\left(\frac{\Delta}{k_B T} - 1\right), \quad (1)$$

where ΔH_0 is the residual linewidth ($T \rightarrow 0$), c is a constant, k_B the Boltzmann constant and Δ is the energy separation between the ground and first CF excited state. From the fitting of the experimental ΔH to Eq. (1), we obtain $\Delta H_0 = 50(4)$ Oe, $c = 0.00027(3)$ Oe/K³, and $\Delta = 173(15)$ K. Notice that this Δ value is approximately five times bigger than the reported value of ≈ 35 K for the Ag:Er bulk alloy [5]. Thus, our results indicate that the effective crystal field environment around the Er^{3+} ions is strongly affected by the finite size of the NPs.

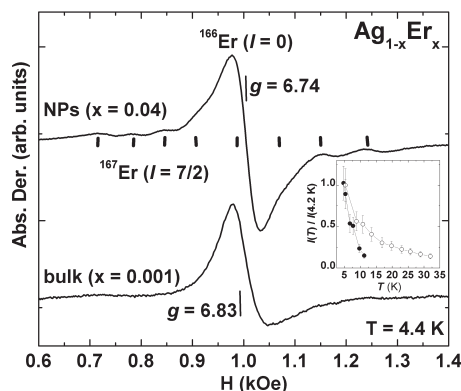


Figure 2: ESR spectra of Er^{3+} in Ag nanoparticles (NPs) and Ag bulk (bulk) of the alloys $\text{Ag}_{1-x}\text{Er}_x$ measured at $T = 4.4$ K (9.48 GHz). The short-vertical lines correspond to the position of the hyperfine lines for the $^{167}\text{Er}^{3+}$ ($I = 7/2$) isotope. Inset show the normalized absorption intensity, $I/I_{(T=4.2\text{ K})}$ as a function of T for the NPs (solid circles) and bulk (open circles) samples.

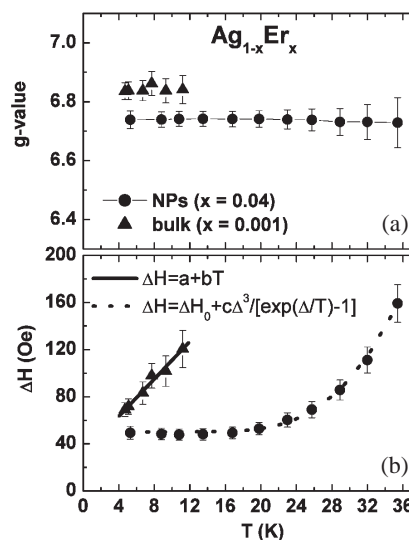


Figure 3: T -dependence of the ESR, (a) g -value and (b) ΔH at X-band for Er^{3+} in Ag nanoparticles (NPs) and Ag bulk (bulk) alloys. The solid line is the fit to linear T -behavior and the dashed line is the fit to Eq. (1), leading to $\Delta \approx 173$ (15) K (see text).

4. CONCLUSION

In summary, in this work we have shown strong experimental evidences for the existence of finite size effects on some of the ground state properties of Er^{3+} ions diluted in Ag host NPs. The local field (absence of g -shift) and spin-lattice relaxation (absence of Korringa-relaxation) due to the Ag conduction-electrons, and the effective crystal field environment were seriously affected. These results suggest that the exchange interaction, $J_{fs}\mathbf{S}\cdot\mathbf{s}$, between the spin, \mathbf{S} , of the Er^{3+} localized $4f$ magnetic moments and the spins of the conduction-electrons, \mathbf{s} , have suffered a serious quenched. Thus, a subtle interplay between the boundary conditions and the crystalline defects, naturally imposed by the finite size of the NPs, may strongly modify the electronic density of state at the Fermi level of the Ag host and, in turn, the static and dynamic properties of the Er^{3+} ground state in these Ag NPs. Besides, the crystalline structure of the Ag:Er NPs was observed to have many defects which may also influence their magnetic properties. Further experiments and theoretical models in other metallic NPs will certainly contribute to clarify if our results may be attributed to the confinement of the host's conduction-electrons leading to the observation of the onset of quantum size effects. Moreover, we believe that above observed features probably make the Ag:Er NPs suitable for potential applications in Ag:Er NPs doped quartz fibers for optical devices.

ACKNOWLEDGMENT

We thank Prof. Daniela Zanchet for the instructive discussions and suggestions. LME/LNLS is acknowledged for the TEM instrument (JEM-3010). LNLS is acknowledge for use of the XRD2 beamline. The work at UNICAMP was supported by FAPESP and CNPq, Brazil.

REFERENCES

1. Murray, C. B., C. R. Kagan, and M. G. Bawendi, "Synthesis and characterization of monodisperse nanocrystals and close-packed nanocrystal assemblies," *Annu. Rev. Mater. Sci.*, Vol. 30, 545, 2000.
2. Hori, H., Y. Yamamoto, T. Ywamoto, T. Miura, T. Teranishi, and M. Miyake, "Diameter dependence of ferromagnetic spin moment in Au nanocrystals," *Phys. Rev. B*, Vol. 69, 174411, 2004.
3. Barnes, S. E., "Theory of electron spin resonance of magnetic ions in metals," *Adv. in Phys.*, Vol. 30, 801, 1981.
4. Chui, R., R. Orbach, and B. L. Gehman, "Hyperfine splitting of a localized moment in a metal," *Phys. Rev. B*, Vol. 2, 2298, 1970.
5. Rettori, C., D. Davidov, and H. M. Kim, "Crystalline-field effects in the EPR of Er in various cubic metals," *Phys. Rev. B*, Vol. 8, 5335, 1973.
6. Tang, Y. and M. Ouyang, *Nature materials*, Vol. 6, 754, 2007.
7. Rocha, T. C. R. and D. Zanchet, *J. Phys. Chem. C*, Vol. 111, 6989, 2007.
8. Cornell, R. M. and U. Schwertmann, *The Iron Oxides: Structure, Properties, Reactions, Occurrence and Uses*, VCH, New York, 1996.
9. Feher, G. and A. F. Kip, "Electron spin resonance absorption in metals. I. Experimental," *Phys. Rev.*, Vol. 98, 337, 1955.
10. Dyson, F. J., "Electron Spin resonance absorption in metals. II. Theory of electron diffusion and the skin effect," *Phys. Rev.*, Vol. 98, 349, 1955.
11. Abraham, A., A. Weeks, G. W. Clark, and C. B. Finch, "Electron spin resonance of rare-earth ions in thorium oxide: Yb^{3+} and Er^{3+} ," *Phys. Rev.*, Vol. 137, A138, 1965.
12. Davidov, D., C. Rettori, A. Dixon, K. Baberschke, E. P. Chock, and R. Orbach, "Crystalline-field effects in the electron-spin resonance of rare earths in the noble metals," *Phys. Rev. B*, Vol. 8, 3563, 1973.
13. Barberis, G. E., D. Davidov, J. P. Donoso, C. Rettori, J. F. Suassuna, and H. D. Dokter, "Electron spin resonance of Nd^{3+} and Gd^{3+} in d-band intermetallic compounds," *Phys. Rev. B*, Vol. 19, 5495, 1979.

Diagnostic Volume Phenomenon in Noninvasive Medical Spectrophotometry and a Simple Theoretical Definition of That

D. A. Rogatkin, L. G. Lapaeva, and E. N. Petritskaya

Moscow Regional Research & Clinical Institute “MONIKI”, RF, Russia

Abstract— The article proposes a strict definition of the notation of “diagnostic volume” (DV) in a modern medical *in vivo* spectrophotometry. Theoretical description of a calculation algorithm to evaluate DV with the use of exact modified one-dimensional Kubelka-Munk approach is proposed as well. In a general case, numeric calculations show that for typical human soft tissues effective DV in the simplest one-dimensional theoretical case is lying in a range of 1–8 mm of a depth of the both scattering and absorbing medium.

1. INTRODUCTION

In recent 10–15 years, a general medical practice has been successfully enriched with some new methods of noninvasive optical diagnostics such as a Laser-Doppler Flowmetry, Laser Fluorescent Diagnostics, Tissues Reflectance Oximetry, etc., which all in totality we now call a *Noninvasive Medical Spectrophotometry* (NMS) [1]. All these methods allow a doctor to evaluate both *in vivo* and more exactly a functional condition of soft tissues, especially to study finenesses of respiratory and blood microcirculation processes in a skin or mucosa [2, 3]. NMS technique is based on a dependence of all photometric properties of biological tissues and liquids (spectral coefficients of absorption, scattering, fluorescence, etc.) on an anatomical and morphological structure of the tissue as well as on a content of various biochemical components (hemoglobin, collagen, fat, water, natural porphyrins, etc.) in it [4, 5]. Regarding a quantitative evaluation of volume concentration of different biochemical substances in tissues by NMS methods, especially while executing comparative (relative) measurements in the pathological area and in a chosen intact (normal) point on patient’s body, it is necessary for the depth of penetration of radiation in the object being researched to be the same every time. At least, during each diagnostic measurement, a doctor needs to have an opportunity to evaluate the effective volume of biological tissue from which the main useful signal arrives into the registration system. Thus, it is necessary to have an opportunity to evaluate the so called “*sampling volume*” or “*diagnostic volume*” (DV) of the object being studied during the experiment. In a case of any functional or physiological changes, caused by the sickness in biological tissues, their DV will be changing as a result of changes of optical properties of blood, changes of the blood fraction in the volume of examination, changes of optical properties of the skin, etc. That is why the evaluation and determination of DV are extremely important in the practice of NMS. Various authors today have under consideration different aspects of DV in NMS [5, 6]. However, up to now the notion of DV has not been strictly determined and widely accepted yet in a modern biomedical optics. So, the goal of our study was: The looking for a convenient theoretical definition and description of the DV term in exact items of light transport and scattering theory what potentially makes it possible to have a simple and uniform theoretical calculation algorithm to evaluate DV in the most of practical cases of NMS.

2. THE MAIN DEFINITION AND A DIAGNOSTIC PROCEDURE

To reach our goal we have defined the notion of DV as [7] “*an effective volume of biological tissue (the medium of propagation of light radiation) in the area being tested, which brings in the registered optical signal at least P_{\min} of power, where P_{\min} is estimated at a 75–95% level of the total power of radiation being registered from the biological tissue (signal evaluation by the level of 0.75 ($P_{0.75}$), the level of 0.95 ($P_{0.95}$), etc.)*”. This definition potentially allows anyone to evaluate DV which is reached in experiments in the strict terms of physic and mathematical models of the classic Radiative Transport Theory (RTT). In general, any *in vivo* conventional diagnostic procedure in NMS (Fig. 1) consists of illumination of a part of biotissue by low-level optical radiation, for example, by low-level laser light radiation, and of receiving of a part of backscattered radiation from the tested biological tissue back by the diagnostic system to analyze. As theoretically, the backscattered flux is described and calculated in frameworks and terms of the RTT, the definition resulted above adheres concept of DV to a registered stream of radiation.

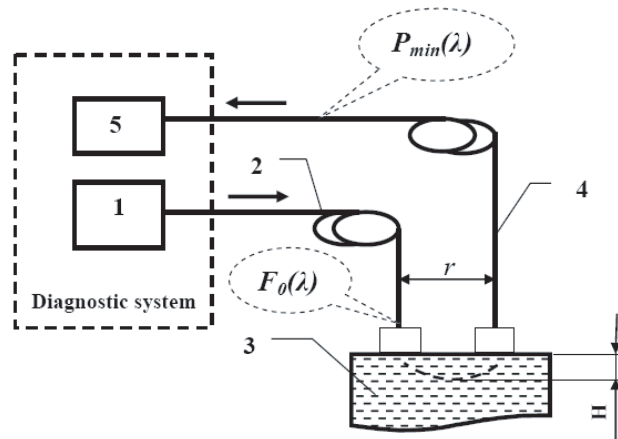


Figure 1: Diagnostic procedure and diagnostic system's setup. 1 — sources of light power; 2 — illumination fiber; 3 — biotissue; 4 — receiving fiber; 5 — photodetectors. $F_0(\lambda)$ — Initial illumination flux as a function of wavelength; $P_{\min}(\lambda)$ — Registered flux as a function of wavelength; H — indicates a depth.

For a purpose of a creation of a first simplified theoretical model, describing DV in NMS, it can be first considered a following simple theoretical problem of one-dimensional ($r = 0$) distribution of optical radiation in a macro-homogeneous turbid medium with multiple scattering. In this our study, we have tried to use the new Modified Exact Kubelka-Munk approach (MEKM) [8–10] in a capacity of the theoretical tool to calculate DV in the one-dimensional (1D) problem. If it is supposed an illumination of biological tissues and a registration of a backscattered flux from the front surface of the biological tissues (see Fig. 1), then the mathematical formulation of the 1D problem is: To determine such an effective depth H (DV in 1D case) of scattering medium with predefined transport optical properties $K = \mu_a$ and $S = \mu_s$ (absorption and scattering in terms of classic Kubelka-Munk model and RTT) from which the backscattered radiation $P_{\min}(H)$, being registered by the NMS device, constitutes a part of $\gamma = 0.9\text{--}0.95$ of the total backscattered radiation $P_{bs}(\infty)$ from the same semi-infinite medium — The medium of a geometrical depth significantly exceeding H , i.e.,

$$P_{\min}(H) = \gamma \cdot P_{bs}(\infty). \quad (1)$$

Calculating a backscattered radiation from the semi-infinite medium with similar known transport optical properties, on the basis of (1), it is easily possible to count up a stream $P_{\min}(H)$ as well as an effective H corresponding $P_{\min}(H)$.

3. SIMPLE THEORETICAL NUMERIC EXAMPLES

In the most simple and explicit case, we suppose a 1D problem ($r = 0$) and a perfect scattering medium with $\mu_a = 0$. For this case under a multiple scattering, it was obtained previously [8, 10]:

$$\mu_s = R\mu_\rho / (1 - R), \quad (2)$$

where: R — A reflection coefficient on the borders of optical heterogeneities, μ_ρ — Transport density of scattering heterogeneities in the medium.

A power of backscattered flux from a depth H of the scattering medium can be determined as [9]:

$$P_{bs}(H) = F_0\mu_s H / (1 + \mu_s H), \quad (3)$$

where: F_0 — is a power of the initial illuminating flux.

Supposing a unit stream of outer radiation ($F_0 = 1$), as it follows from (3) under $H = \infty$:

$$P_{bs}(\infty) = F_0 = 1. \quad (4)$$

So, combining (1)–(4), it is easy to obtain:

$$H = \frac{\gamma}{\mu_s(1 - \gamma)}. \quad (5)$$

As one can see, the effective H values will range 0.16–19 cm for typical $R = 0.02\text{--}0.05$; $\mu_\rho = 50 \dots 1000 \text{ cm}^{-1}$ and, accordingly, $\mu_s \approx 1 \dots 55 \text{ cm}^{-1}$ (typical biological tissues). It is necessary to

note, that for every separate wavelength λ the DV (H in the 1D case) will differ because of the dependence of μ_s on λ .

The presence of absorption in the medium ($\mu_a \neq 0$), evidently, significantly decreases the effective DV. Analogous calculations in the general case of light-scattering medium with absorption not equal to zero can be made with the use of general results of MEKM model [8]. Omitting some intermediate calculation, the final exact equation can be written as:

$$H = \frac{1}{2\alpha} \cdot \ln \left[\frac{\alpha(1 + \gamma)/(1 - \gamma) + \beta_1}{\alpha + \beta_1} \right], \quad (6)$$

where:

$$\alpha = \sqrt{\beta_1^2 - \beta_2^2}; \quad \beta_1 = \omega \cdot \frac{\mu_a - \mu_\rho \ln(1-R) + \mu_\rho \ln \left(1 - \omega + \sqrt{\omega^2 - R^2 e^{-2\mu_a/\mu_\rho}} \right)}{\sqrt{\omega^2 - R^2 e^{-2\mu_a/\mu_\rho}}}$$

$$\beta_2 = R \cdot e^{-\mu_a/\mu_\rho} \cdot \frac{\mu_a - \mu_\rho \ln(1-R) + \mu_\rho \ln \left(1 - \omega + \sqrt{\omega^2 - R^2 e^{-2\mu_a/\mu_\rho}} \right)}{\sqrt{\omega^2 - R^2 e^{-2\mu_a/\mu_\rho}}}; \quad \omega = \frac{1 - (1-2R) \cdot e^{-2\mu_a/\mu_\rho}}{2}.$$

In the case, the numeric calculations for different combination of transport optical properties of tissues are more complex, but with the use of modern personal computer technique are not very difficult yet.

On the graph Fig. 2, curves show some changes in H as a function (6) for different sets of R , μ_a , μ_ρ under $\gamma = 0.95$. As it is seen, here the typical effective values of H turn out to be lying in a range of 1–8 mm for the typical absorbing soft human turbid tissues. It must be additionally noted that for any spatial tasks (2D or 3D when $r \neq 0$) H will differ for different base r of the measurements (see Fig. 1). So, together with DV the base of measurements r becomes one of the main metrological parameters of diagnostic equipment in NMS. To execute reproducible as well as steadily comparable measurements in NMS using different diagnostic equipment, it is necessary to have the same DV and r for them all time.

If transport optical properties of a tested biological tissue are not known *a priori*, the only way out while defining DV is to evaluate DV directly from the results of experiments. Analogous procedure had been developed, for example, in goniophotometry in 1990 [11]. There is in the goniophotometry a so called *far zone* of diffraction. In a real experiment, its value is not known *a priori*, but is very important to evaluate all results of the experiment. So, the special procedure with the use of final numeric results of the experiment was developed to verify whether the condition of the far zone was reached in the experiment or not. In the future something similar is represented

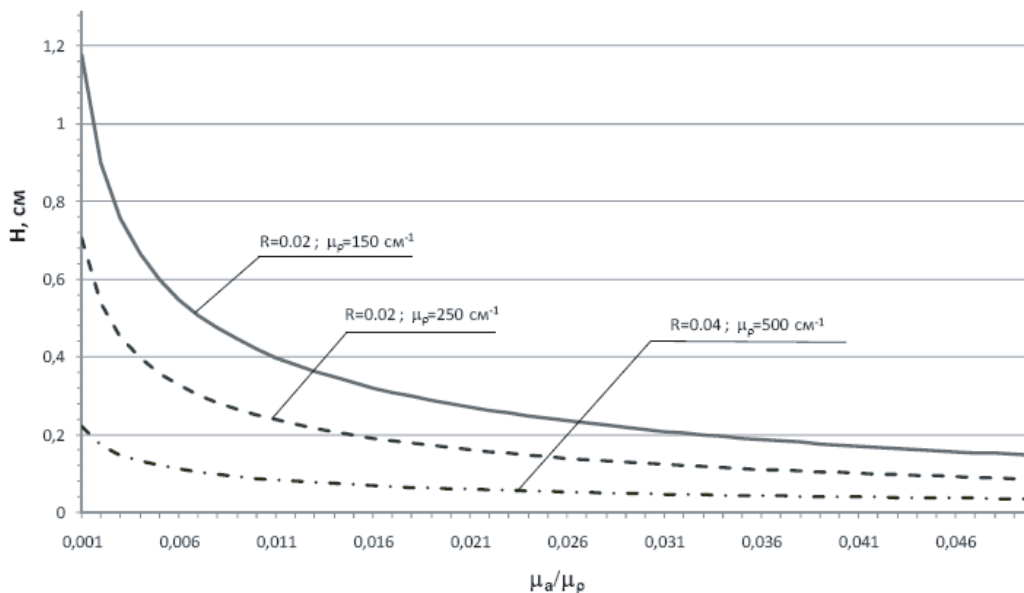


Figure 2: Results of calculations of H as a function (6) for different sets of R , μ_a , μ_ρ under $\gamma = 0.95$.

expedient to be developed for DV in NMS as well. Like it follows from (1)–(5), the decreasing of registered backscattered flux from the tested tissue will inform doctors about corresponding decreasing of DV. So, the less signal is registered the less DV exists in a tissue.

4. CONCLUSION

Today, with the development of noninvasive medical spectrophotometry (NMS), it appears a necessity to evaluate the so called “*diagnostic volume*” (DV) of the human soft tissues being studied during the experiment. Various authors today have under consideration different aspects of DV in NMS. However, up to now, the notion of DV has not been strictly determined and widely accepted yet in a modern biomedical optics. So, the goal of our study was: The looking for a convenient theoretical definition and description of the DV.

To reach our goal, we have defined the notion of DV in the strict terms of Radiation Transport Theory (RTT). This definition basing on a concept of the counting of backscattered radiation potentially allows anyone to evaluate DV which is reached in experiments using the classic RTT theoretical approaches. As theoretically, the backscattered flux is described and calculated in frameworks and terms of the RTT, the definition connects the concept of DV to a magnitude of a stream of radiation registered by a diagnostic system.

Numeric calculations show that for typical human soft tissues effective DV in a simplest 1D theoretical case turn out to be approximately lying in a range of 1–8 mm of a depth of the 1D both scattering and absorbing medium. But if transport optical properties of a tested biological tissue are not known *a priori*, the only way out while defining DV is to evaluate DV directly from the results of the experiments.

ACKNOWLEDGMENT

This study was supported by RFBR grant No. 08-02-00769a.

REFERENCES

1. Rogatkin, D. A. and L. G. Lapaeva, “Prospects for development of noninvasive spectrophotometric medical diagnosis,” *Biomedical Engineering*, Vol. 37, No. 4, 217–222, 2003.
2. Krupatkin, A. I. and V. V. Sidorov, *Laser Doppler Flowmetry of Blood Microcirculation*, Medicina, Moscow, 2005 (in Russian).
3. Tchernyi, V. V., D. A. Rogatkin, R. V. Gorenkov, et. al., “Complex noninvasive spectrophotometry in examination of patients with vibration disease,” *Proc. SPIE*, Vol. 6078, 363–370, 2006.
4. Hoft, K. A., I. Kanter, E. Barbiro-Michaely, and A. Mayevsky, “Classification of tissue pathological state using optical multiparametric monitoring approach,” *Proc. SPIE*, Vol. 7280, 72801K, 2008.
5. Tuchin, V. V., *Handbook of Optical Biomedical Diagnostics*, SPIE Press, Washington, 2002.
6. Tai Dean, C. S., D. A. Hooks, J. D. Harvey, et. al., “Illumination and fluorescence collection volumes for fiber optic probes in tissue,” *Journal of Biomedical Optics*, Vol. 13, No. 3, 034033, 2007.
7. Rogatkin, D. A., L. G. Lapaeva, and O. A. Bychenkov, “Problems of metrological provisions for noninvasive medical spectrophotometric apparatus and systems,” *Proc. of Intern. 7-th Research Conf. MCA-2006 “Measurement, control & informatization”*, 119–122, Barnaul, RF, 2006.
8. Rogatkin, D. A., “A specific feature of the procedure for determination of optical properties of turbid biological tissues and media in calculation for noninvasive medical spectrophotometry,” *Biomedical Engineering*, Vol. 41, No. 2, 59–65, 2007.
9. Lapaeva, L. G. and D. A. Rogatkin, “Improved Kubelka-Munk approach for determination of tissues optical properties in biomedical noninvasive reflectance spectroscopy,” *Proc. SPIE*, Vol. 6536, 65360Z, 2007.
10. Dmitriev, M. A., M. V. Feducova, and D. A. Rogatkin, “On one simple backscattering task of the general light scattering theory,” *Proc. SPIE*, Vol. 5475, 115–122, 2004.
11. Rogatkin, D. A. and V. V. Konyakhin, “Estimating the quality of goniophotometric installations,” *Instruments and Experimental Techniques*, No. 5, 913–915, 1991.

Look at the Spark Cross Size Development in a Sliding Submicrosecond Discharge from the Theory of Ionization Wave Front Propagation

K. K. Trusov

P. N. Lebedev Physical Institute of RAS
Leninsky prospect 53, Moscow 119991, Russia

Abstract— The work is aimed at studying the initiation, development and scaling of multi-channel and quasi-homogeneous pulse high-current sliding discharges in gases, and assumes the analysis of both the separate channel formation and their structure in the discharge gap. In this report the results from experimental measurement of the spark channel widths in sliding multichannel discharge of opposite polarities in Ne, Ar and Xe are presented and discussed. The experiments were performed at submicrosecond discharge pulse duration ($50 \div 200$ ns) and gas pressures of 30 and 100 kPa, with alumina ceramics as the dielectric substrate. The data showed the optical width of the channels at negative voltage supply polarity to be $1.27 \div 1.6$ times greater than that at positive polarity, depending on the gas type and its pressure. The earlier theoretical study by U. Ebert, W. van Saarloos and C. Caroly on the propagation of opposite polarity ionization wave fronts in gases was applied to the experimental results analysis. The registered difference between the widths of opposite polarity channels and the estimations prove our earlier viewpoint of a negligible effect of electron diffusion process (as compared to the electron drift) on the channel cross expansion within the pulse duration studied. From two approaches of the above pointed theory only the “nonlocalized initial conditions” one can reasonably explain: a) The interrelation between the channel optical width and the electron mobility that was revealed in our previous experiments; b) experimental ratios of the widths of negative-to-positive channels; c) comparatively short (≤ 0.5 ns) and approximately equal time intervals of channel cross expansion for the gases and their pressures studied; d) expansion of the negative polarity channels with a velocity not less (but actually exceeding) than the electron drift velocity in the transverse electric field round the spark channel. Numerical solutions of the channel expansion equation specified that the channel expansion velocity is set by both the drift electrons and free electrons generated by a short-range source in a narrow layer ahead of the channel expansion wave front. The depth of the latter layer was estimated to be comparable to the wave front depth and, thus, much less than the channel radius. The most probable source of free electrons round the channel is gas photoionization by the radiation from the channel.

1. INTRODUCTION

In previous works [1, 2] we studied experimentally the development of a multichannel sliding discharge of submicrosecond pulse duration in rare gases Ne, Ar and Xe at pressures of 30 and 100 kPa. The experiments have been made at one polarity (negative) of the voltage supply only, with the alumina ceramics as a dielectric substrate. From the data obtained the interrelation of the optical spark channel width with the mobility of electrons in the gas was revealed [1] and attributed [2] to the radial expansion of channels primary due to the drift of electrons from a thin surface layer of channels in the transverse electric field round the channel. The latter electric field results from the spark channel potential U relative to the conductive plate underlying the dielectric substrate. The above interrelation shows that the parameter

$$\frac{r_0^2 \left[\ln \frac{2h + r_0}{r_0} + 0.5 \right]}{2\mu_e \langle \varepsilon \rangle} \frac{1}{U} \quad (1)$$

is close to a constant (~ 1 ns) for the gases and their pressures studied, where h , $\langle \varepsilon \rangle$ are the thickness and the “effective” permittivity [2] of the dielectric substrate, and r_0 , μ_e are the optical spark channel radius and the mobility of electrons in particular gas correspondingly. Physical meaning of the parameter (1) looks dual [2]. First, it characterizes the time constant of electron density increase in close vicinity to the channel surface. Second, it means the time interval of channel expansion up to the final (observed) optical radius r_0 in the assumption that the radial speed of expansion is equal to the electron drift velocity in the transverse electric field round the

channel. For better understanding of the mechanisms of the channel cross size development and contribution of the electron drift into the process, the experiments at positive polarity of the power supply and a comparison of their results with the previous ones seems to be promising.

Here we report the experimental data on the spark channel radii at both polarities and offer the data analysis based on the theory by U. Ebert, W. Van Saarloos and C. Caroli of the ionization wave front propagation in gases [3].

2. EXPERIMENTAL

All the experiments at both polarities of power supply have been executed on the setup described in [1] and sketched in Fig. 1.

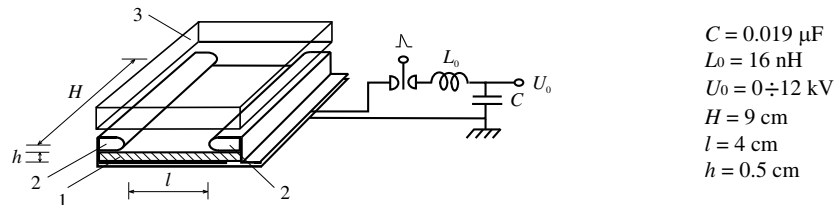


Figure 1: Schematic and parameters of the experimental setup.

Pulse discharge over the surface of the dielectric substrate 1 between strip electrodes 2 was initiated from a capacitive pulse source by commutation of the spark gap. Typical voltage-current pulse duration equaled to $50 \div 200 \text{ ns}$ depending on U_0 and gas pressure. The discharge structure varied from single to multiple sparks and then to quasi-homogeneous gap filling with sparks when U_0 increased beginning from the gap breakdown threshold. Each pulse discharge voltage and current oscilloscope traces, as well as the multi-spark structure of the discharge on the substrate 1, were registered (the latter by photo of the interelectrode gap from top through the transparent glass cover 3). Channel widths were measured at $l/2$ distance from the cathode, typically at $U_0 = 2.5 \div 4.6 \text{ kV}$, the total discharge peak current $I = 0.3 \div 1.0 \text{ kA}$ and current/voltage pulse duration $90 \div 200 \text{ ns}$ depending on the gas type and its pressure. Under particular conditions shown in Table 1, the channels filled $0.3 \div 0.5$ of the gap width H , thus being well separated from each other. The optical radius r_0 defined as the half of the channel full width at half maximum (FWHM) was estimated by photometry of those single pulse channel images exposed to the normal darkness of the photo film, and these original results were then averaged for each gas and pressure independently. Spatial resolution of the photo registration system is not worth than 0.01 cm of the channel width, i.e., 0.005 cm of its radius. The values of r_0 estimated in this way at opposite polarities of U_0 both with the ratios r_0^-/r_0^+ are summarized in Table 1 with the note “*experim.*”, where the upper index indicates the channel polarity. The radii of negative polarity channels (NC) are seen to exceed those of the positive channels (PC) that could specify in degree of contribution of the electron drift over diffusion into the expansion process. At the same time, the ratios r_0^-/r_0^+ look unexpectedly small if one considers the drift and diffusion of electrons only. Thus, other processes contribute, and they are desirable for imagining.

Actually, we determined the optical (radiation) channel radii instead of their electrodynamic ones and, hence, inaccuracy of the plasma channel radius definition and related absolute value of r_0 are present. However, the data in [4–7] for the streamers far from the surfaces showed the radii of both types to be connected with each other and differ less than 2 times. Thus, the optical values of r_0 in Table 1 are informative and admissible for relative comparison.

Briefly summarized, at least the following features of the near-surface spark channels resulted from our earlier and present experiments with three gases need explaining in common: a) The interconnection of r_0^- with μ_e ; b) relatively small values of r_0^-/r_0^+ ratios (Table 1) and their slow dependence on the gas type and pressure; c) approximately equal and small ($\sim 1 \text{ ns}$) estimated time intervals (1) of channel expansion in gases at pressures under consideration; d) expansion of NC at velocities close to that of the electron drift.

3. DISCUSSION

Estimations in [2] for NC showed the transverse electric field round the channel to be screened within a narrow channel surface layer δ so that $r_0/\delta \approx 47 \div 86$. The latter enables one to consider

Table 1: Results of the experimental measurement and calculation of the channel cross expansion features.

Gas type	Ne		Ar		Xe	
Gas pressure, kPa	30	100	30	100	30	100
U_0 , kV	$2.5 \div 3$	$3.8 \div 4$	$4.3 \div 4.6$	$4.3 \div 4.5$	$3.4 \div 3.5$	$4.3 \div 4.6$
I , kA	$0.4 \div 0.6$	$0.4 \div 0.5$	$0.9 \div 1$	$0.6 \div 0.8$	$0.3 \div 0.4$	$0.3 \div 0.4$
$r_0^+ \{ \textit{experim.} \}$, cm	0.107	0.073	0.059	0.035	0.044	0.033
$r_0^- \{ \textit{experim.} \}$, cm	0.165	0.11	0.094	0.047	0.07	0.042
$r_0^- / r_0^+ \{ \textit{experim.} \}$	1.58	1.5	1.6	1.34	1.59	1.27
D	0.08	0.08	0.34	0.34	0.15	0.15
$r_0^- / r_0^+ \{ LIC \}$ at $t = t_{\text{int}}$	23.4	53	5.5	7.9	8.1	12.2
$r_0^- / r_0^{dr} \{ LIC \}$ at $t = t_{\text{int}}$	1.35	1.35	1.4	1.4	1.3	1.26
Λ	0.043	0.016	0.1	0.03	0.07	0.013
$t_{\text{int}} \{ NIC \}$, ns	0.45	0.65	0.65	0.53	0.45	0.43
$r_0^- / r_0^{dr} \{ NIC \}$ at $t = t_{\text{int}}$	1.9	2	1.8	2.1	1.8	2.2
$\Lambda \alpha_0 \delta \{ NIC \}$	0.7	0.75	0.78	0.59	0.85	0.3

the processes within (and in close vicinity to) the surface layer in one-dimensional (i.e., planar) representation by analogy to [3]. Moreover, the ionization wave front propagation theory of [3] seems to be applicable to the transverse expansion of NC and PC in our sliding discharge experiments. Despite the theory was developed for the stationary wave fronts only, it would be admissible to the quasi-stationary fronts, in the first approximation, if temporal-spatial variations of the external electric field near the wave front were “slow” as compared to the temporal-spatial scale of the front formation. Typical wave front formation time results from calculations in [3] to be $\tau_{fr} \approx (10 \div 1000) / \alpha_0 \mu_e E_0$ and, following the approximations of [2] for the parameters involved, does not exceed 10^{-2} ns, and i.e., is much shorter than the estimated channel expansion time of $\approx 1 \div 2$ ns [2]. Also, a typical scale of the radial electric field variation round the channel is $> r$, the instant channel radius [2], and, thus, exceeds δ by $1.5 \div 2$ orders of magnitude. Hence, the latter estimations allow us to take advantages and consider the experimental data following both approaches (of “localized” and “nonlocalized” initial conditions) of the theory [3] in account of combined effect of electron drift and diffusion, as well as the impact gas ionization.

3.1. “Localized Initial Conditions” Approach (LIC)

In this approach, the velocity V^- of the negative wave front in natural units is expressed as

$$V^- = \mu_e |E| + 2\sqrt{D_e \mu_e E \alpha(|E|)}, \quad (2)$$

where E is the local electric field strength ahead of the front; D_e , the electron diffusion factor; $\alpha(|E|)$, the electron impact ionization index that may be approximated as [2]

$$\alpha = \alpha_0 \exp(-\sqrt[3]{|E_0/E|}) \{ \text{Ne} \} \quad \alpha = \alpha_0 \exp(-\sqrt{|E_0/E|}) \{ \text{Ar, Xe} \} \quad (3)$$

based on the data from [8]. On the contrary, the positive wave front velocity V^+ in [3] was found numerically only. Basing on the calculation results in Fig. 4 in [3] one may approximate E -dependence of V^+ as

$$V^+ = \alpha_0 D_e (-A + BE/E_0) \quad (4)$$

where A , B are the constants equal to ≈ 0.077 and ≈ 0.22 , respectively, within the range of dimensionless diffusion constant $0 \leq D \leq 0.35$ [3]. The maximum values of D , estimated on the data from [8] and shown in Table 1 for the gases studied, are just within the noted range and, thus, allow the application of (4). Equations (2)–(4) together with the transverse electric field near the channel surface [2]

$$E(r) = \frac{\langle \varepsilon \rangle U}{r \ln \frac{2h+r}{r}}, \quad (5)$$

give easy solution of equations for NC and PC radial expansion

$$\frac{dr^\pm}{dt} = V^\pm. \quad (6)$$

Time interval of integration t_{int} we have chosen to correspond to the NC expansion from the initial streamer head radius (defined by the condition $|E| = |E_0|$ [9]) to the observed optical value r_0^- . For the comparison with the earlier conclusions of [2], the values of NC radii r_0^{dr} in account of the electron drift only (i.e., the electron diffusion being omitted in (2)) were also found. The calculated ratios r_0^-/r_0^+ and r_0^-/r_0^{dr} with the note “*LIC*” (i.e., the same without the point) are shown in Table 1. Fig. 2 demonstrates an example of these ratios’ development in the interval t_{int} . It is clearly seen that: a) NC expansion velocity exceeds that of electron drift; b) maximum contribution of the electron diffusion into NC expansion process does not exceed 40% of NC final radius that results from r^-/r^{dr} values; c) calculated r_0^-/r_0^+ ratios exceed the experimental ones significantly, and differ in pressure dependence as well. The last discrepancy of r_0^-/r_0^+ ratios makes *LIC* unsuitable for further discussion.

3.2. “Nonlocalized Initial Conditions” Approach (NIC)

According to this approach the wave front velocities of both polarities in natural units are expressed

$$V^\pm = \mu_e |E| \left[\frac{\alpha(|E|)}{\alpha_0 \Lambda} \mp 1 \right] + D_e \alpha_0 \Lambda, \quad (7)$$

where Λ is the dimensionless localization parameter (its analog in natural units being $\alpha_0 \Lambda$), that characterizes the inverse depth of an initial spatial distribution of free electrons in the gas, and the sign selection corresponds to the wave front polarity. Thus, (3), (5), and (7) enable the solution of the expansion Equation (6) in this approach too, and finding of NC and PC radii by known values of Λ and t_{int} . Instead, from the experiments we know NC and PC radii, while Λ and t_{int} being unknown, and thus, the inverse task may be solved. By analogy to *LIC* the time integration continued up to the moment t_{int} at which the calculated radii r^-, r^+ became equal to the observed optical values r_0^-, r_0^+ (and their ratios too!). The values r_0^{dr} and r_0^-/r_0^{dr} were also determined. The calculated results are shown in Table 1 with the note “*NIC*” (i.e., the same without the point), Fig. 3 demonstrates an example of the calculated values development during the interval t_{int} .

Contrary to the *LIC*, the *NIC* estimations show that all the features of the near-surface spark channels enlisted in the last paragraph of Section 2 get evident explanation in common. Here it is sufficient to account the initial electrons ahead of the wave expansion front whose spatial distribution is described by the only dimensionless parameter Λ (or $\Lambda \alpha_0$ in natural units). Despite the estimated values of Λ in Table 1 strongly depend on the gas type and pressure and, thus, Λ may seem non-informative, it gets clear meaning when compared to the front depth δ values presented in [2]. The last line in Table 1 shows dimensionless product of δ and $\Lambda \alpha_0$ in natural units. These product values lead to the drawback: A short-range source (similar in three gases

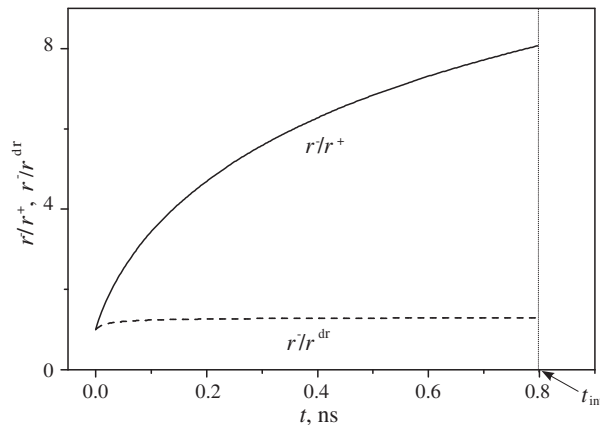


Figure 2: *LIC* computer simulation of the radii ratio time dependence during t_{int} . Xe, 30 kPa, $U = 2$ kV, $\langle \varepsilon \rangle = 4.4$.

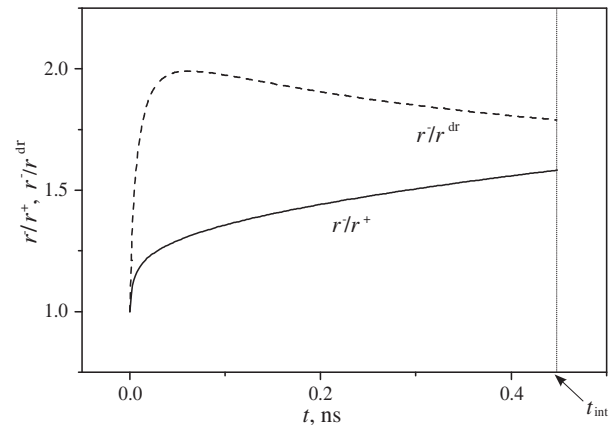


Figure 3: *NIC* computer simulation of the radii ratio time dependence during t_{int} . Xe, 30 kPa, $U = 2$ kV, $\langle \varepsilon \rangle = 4.4$.

studied) generates free electrons in a very thin gas layer (of $1/\Lambda\alpha_0$ depth) ahead of the channel lateral surface. As follows from computer simulations, this source leads to the increase of NC and PC expansion velocity up to 3.4 and 1.4 of electron drift (at the moment t_{int}) correspondingly, while the contribution of electron diffusion is less than 0.14 of the electron drift velocity. Gas photoionization by radiation from the channel looks the most probable source of free electrons.

4. CONCLUSION

Experiments with the sliding discharge of submicrosecond duration (≤ 200 ns) in Ne, Ar and Xe at 30 and 100 kPa of gas pressure showed the spark channel radii to depend on the polarity of supplied voltage, so that NC are $1.6 \div 1.27$ times wider than PC. The dependence together with the earlier revealed interconnection of the NC radius and mobility of electrons in these gases reflects contribution of electron drift into the channel cross expansion process.

The theory of ionization wave front propagation was applied to the data analysis. The approach of “nonlocalized initial conditions” of this theory, which considers the initial free electrons ahead of the wave front along with the electron impact ionization, drift and diffusion of electrons, is capable to reasonably explain in common the features of the near-surface spark channels resulted from our earlier and present observations and enlisted above in the last paragraph of Section 2. A comparison of the experimental results with computer simulations related to this approach indicates that a short range source initiates free electrons in a thin layer round the lateral surface of the channel. These free electrons may increase the NC and PC expansion speed up to 3.4 and 1.4 electron drift velocities, correspondingly, at very small contribution of electron diffusion into the channel expansion velocity. The depth of the thin layer was estimated to be comparable to the expansion wave front depth and, thus, much less than the channel radius. The most probable source of free electrons is gas photoionization by the radiation from the channel.

REFERENCES

1. Trusov, K. K., “Dynamics of multichannel and quasi-homogeneous sliding discharge formation in rare gases,” *J. Phys. D: Appl. Phys.*, Vol. 40, 786–794, 2007.
2. Trusov, K. K., “Effect of the electron drift in a transverse electric field on the width of spark channels in a multichannel sliding discharge,” *Phys. Plas. Rep.*, Vol. 34, 338–348, 2008.
3. Ebert, U., W. Van Saarloos, and C. Caroli, “Propagation and structure of planar streamer fronts,” *Phys. Rev. E*, Vol. 55, 1530–1549, 1997.
4. Stritzke, P., I. Sander, and H. Raether, “Spatial and temporal spectroscopy of a streamer discharge in nitrogen,” *J. Phys. D: Appl. Phys.*, Vol. 10, 2285–2300, 1977.
5. Pancheshnyi, S. V., M. M. Nudnova, and A. Y. Starikovskii, “Development of a cathode-directed streamer discharge in air at different pressures: Experiment and comparison with direct numerical simulation,” *Phys. Rev. E*, Vol. 71, 016407, 2005.
6. Nudnova, M. M. and A. Y. Starikovskii, “Streamer head structure: Role of ionization and photoionization,” *J. Phys. D: Appl. Phys.*, Vol. 41, 234003, 2008.
7. Luque, A., V. Ratushnaya, and U. Ebert, “Positive and negative streamers in ambient air: Modeling evolution and velocities,” *J. Phys. D: Appl. Phys.*, Vol. 41, 234005, 2008.
8. Dutton, J., “A survey of electron swarm data,” *J. Phys. Chem. Ref. Data*, Vol. 4, 577–855, 1975.
9. D’yakonov, M. I. and V. Y. Kachorovskii, “Theory of streamer discharge in semiconductors,” *Zh. Eksp. Teor. Fiz.*, Vol. 94, 321–332, 1988; *Sov. Phys. JETP*, Vol. 67, 1049–1058, 1988.

Modeling of Two-component Plasma Dynamics in Near-wall Region of Charged Probe with Coulomb Collisions

I. A. Kudryavtseva and A. V. Panteleyev

The Moscow Aviation Institute (State Technical University), Russia

Abstract— In the article edge strongly ionized plasma dynamics with charged particle collisions near charged probe without influence of magnetic fields is researched. Three geometric shapes of probe are observed. These are plane, cylinder and sphere. The mathematical model that consists of the Fokker-Planck equation and Poisson equation is formulated. The method of getting solution based on the Monte-Carlo method is developed. The results of modeling are obtained and analyzed.

1. INTRODUCTION

The low-temperature plasma diagnostics is the actual problem because plasma is used in different technical equipment and mechanisms, for example in daylight lamps, electronic devices, plasma mover and etc. Also the plasma is environment for space-system engineering.

One of low-temperature plasma diagnostics methods is the probe diagnostics [1, 2]. These methods are contact methods so the problem of research of edge region near the probe appears. In undisturbed region the potential distribution is getting sufficiently complicated and the function distributions differ from Maxwellian functions.

In this paper the case when the ratio of free length to probe radius of curvature (Knudsen number) is close to 1 is considered. The cases when the Knudsen number tends to infinity (the case of Langmuir probe) or to zero (the case of continuum) are considered in detail [2]. Then it's necessary to take into consideration of collisions between charged particle and neutral atom and Coulomb collisions. In papers [3] the model with collisions between charged particles and neutral atom is considered. In present article the model describing influence of ion-ion collisions and ion-electron collisions on measured parameters of plasma is constructed. It is not researched in detail earlier.

2. THE PROBLEM DEFINITION

The following definition of the probe diagnostics problem is considered. The charged probe is immersed into undisturbed plasma consisting of electrons and single charged ions. Suppose, on the probe surface the condition of ideal absorption is obeyed. Temperatures $T_{i\infty}$, $T_{e\infty}$ and concentrations $n_{i\infty}$, $n_{e\infty}$ of particles in undisturbed plasma are defined. Initial distribution functions are Maxwellian. Particles are moved by the influence of electric field; magnetic field is absent.

It is required to evaluate self-consistent electric field intensity $\bar{E}(\bar{r}, t)$, ion and electron concentrations $n_i(\bar{r}, t)$, $n_e(\bar{r}, t)$ and their current densities $j_i(\bar{r}, t)$, $j_e(\bar{r}, t)$ in case of charged particles collisions influence.

The mathematical model is given by [2, 4]:

$$\frac{\partial f_\alpha(\bar{r}, \bar{v}, t)}{\partial t} + \bar{v} \cdot \frac{\partial f_\alpha(\bar{r}, \bar{v}, t)}{\partial \bar{r}} + \frac{q_\alpha \bar{E}(\bar{r}, t)}{m_\alpha} \cdot \frac{\partial f_\alpha(\bar{r}, \bar{v}, t)}{\partial \bar{v}} = \left(\frac{\partial f_\alpha(\bar{r}, \bar{v}, t)}{\partial t} \right)_c + S_\alpha(\bar{r}, \bar{v}, t), \quad (1)$$

$$\Delta \varphi(\bar{r}, t) = -\frac{e}{\varepsilon_0} (n_i(\bar{r}, t) - n_e(\bar{r}, t)), \quad \bar{E}(\bar{r}, t) = -\nabla \varphi(\bar{r}, t),$$

where the first equation of the system (1) is the Fokker-Planck equation describing transportation and charged particles collision process; the second equation is the Poisson equation describing self-consistent electric field behavior; $f_\alpha(\bar{r}, \bar{v}, t)$ is the distribution function of particles of sort α

($\alpha = i, e$); $S_\alpha(\bar{r}, \bar{v}, t)$ describes particle sources and particle run-offs; $q_\alpha = \begin{cases} -e, & \alpha = e, \\ e, & \alpha = i, \end{cases}$; $\varphi(\bar{r}, t)$

is self-consistent electric field potential. The functional $\left(\frac{\partial f_\alpha(\bar{r}, \bar{v}, t)}{\partial t} \right)_c$ is given by [4]:

$$\frac{1}{\Gamma_\alpha} \left(\frac{\partial f_\alpha}{\partial t} \right)_c = \frac{1}{2} \nabla_v \nabla_v : (f_\alpha \nabla_v \nabla_v g_\alpha) - \nabla_v \cdot (f_\alpha \nabla_v h_\alpha),$$

where $\nabla_v \nabla_v g_\alpha(\bar{r}, \bar{v}, t)$ is second-rank covariant tensor derivative; $(:)$ denotes double summation; $\Gamma_\alpha = \frac{Z_\alpha^4 e^4}{4\pi \varepsilon_0^2 m_\alpha^2} \ln D_\alpha$, $D_\alpha = \frac{12\pi \varepsilon_0 k T_{\alpha\infty}}{Z_\alpha^2 e^2} \left(\frac{\varepsilon_0 k T_{e\infty}}{n_{e\infty} e^2} \right)^{1/2}$, $Z_\alpha = 1$, $\alpha = i, e$,

$$g_\alpha(\bar{r}, \bar{v}, t) = \sum_{b=i,e} \left(\frac{Z_b}{Z_\alpha} \right) \int f_b(\bar{r}, \bar{v}', t) |\bar{v} - \bar{v}'| d\bar{v}', \quad \alpha = i, e,$$

$$h_\alpha(\bar{r}, \bar{v}', t) = \sum_{b=i,e} \frac{m_\alpha + m_b}{m_b} \cdot \left(\frac{Z_b}{Z_\alpha} \right) \int \frac{f_b(\bar{r}, \bar{v}', t)}{|\bar{v} - \bar{v}'|} d\bar{v}', \quad \alpha = i, e$$

Initial and boundary conditions are as follows

$$\begin{aligned} t = 0 : f_\alpha(\bar{r}, \bar{v}, 0) &= f_\alpha^{maksv}, \quad \alpha = i, e, \\ \bar{r} \in \Omega_p : f_\alpha(\bar{r}, \bar{v}, t)|_{\bar{r} \in \Omega_p} &= 0, \quad \alpha = i, e, \\ \varphi(\bar{r}, t)|_{\bar{r} \in \Omega_p} &= \varphi_p, \\ \bar{r} \in \Omega_\infty : f_\alpha(\bar{r}, \bar{v}, t)|_{\bar{r} \in \Omega_\infty} &= f_\alpha^{maksv}, \quad \alpha = i, e, \\ \varphi(\bar{r}, t)|_{\bar{r} \in \Omega_\infty} &= 0, \end{aligned} \quad (2)$$

where $f_\alpha^{maksv} = n_{\alpha\infty} \left(\frac{m_\alpha}{2k\pi T_{\alpha\infty}} \right)^{3/2} \exp\left(-\frac{m_\alpha}{2kT_{\alpha\infty}} |\bar{v} - \bar{v}_\infty|^2\right)$, $\alpha = i, e$; Ω_p , Ω_∞ are sets of particle radius-vectors whose ends belong to plane of plate and disturb region boundary respectively.

3. THE SOLUTION METHOD OF THE PROBLEM

Subject to shapes of probe coordinate systems are used as follows: Cartesian system for plane, cylindrical system for cylinder and spherical system for sphere. The system of Equations (1)–(2) notes in corresponding systems of coordinates according to following hypotheses.

In Cartesian coordinate system phase coordinates are x, y, z, v_x, v_y, v_z . However it's supposed the plane is infinitely large as compared with typical scale of problem. So distribution function of particle depend on only y, v_y, t .

In cylindrical coordinate system phase coordinates are $r, \theta, z, v_r, v_\theta, v_z$, where $r = r(t)$ is radius vector of particle, $\theta = \theta(t)$ is azimuth. In this case the distribution functions and potential are invariant with respect to translation in z-direction, i.e., $\left(\frac{\partial f_\alpha}{\partial z} = 0, \frac{\partial \varphi}{\partial z} = 0\right)$. As a result number of coordinates decrements by two, functional dependence on r, θ, v_r, v_θ remains.

In spherical coordinate system phase coordinate are $r, \psi, \theta, v_r, v_\psi, v_\theta$. The distribution functions and potential are invariant by rotation about Oz-axis, i.e., $\left(\frac{\partial f_\alpha}{\partial \psi} = 0, \frac{\partial \varphi}{\partial \psi} = 0\right)$. As a result number of coordinates decrements by one, functional dependence on $r, \theta, v_r, v_\psi, v_\theta$ remains.

For instance, in cylindrical coordinate system for dimensionless variables the system will have the following appearance:

$$\frac{\partial \hat{f}_\alpha}{\partial \hat{t}} + \sqrt{\delta_\alpha} \left\{ \hat{v}_r \frac{\partial \hat{f}_\alpha}{\partial \hat{r}} + \frac{\hat{v}_\theta}{\hat{r}} \frac{\partial \hat{f}_\alpha}{\partial \hat{\theta}} + \left(\frac{\hat{v}_\theta^2}{\hat{r}} + \frac{z_\alpha \hat{E}_r}{2\varepsilon_\alpha} \right) \frac{\partial \hat{f}_\alpha}{\partial \hat{v}_r} + \left(\frac{z_\alpha \hat{E}_\theta}{2\varepsilon_\alpha} - \frac{\hat{v}_r \hat{v}_\theta}{\hat{r}} \right) \frac{\partial \hat{f}_\alpha}{\partial \hat{v}_\theta} \right\} = \Gamma_\alpha \tilde{K} \hat{f}_\alpha, \quad \alpha = i, e,$$

$$\begin{aligned} \tilde{K} \hat{f}_\alpha &= \frac{1}{2} A_g^\alpha \left\{ \frac{\partial^2}{\partial [\hat{v}_r]^2} \left(\hat{f}_\alpha \frac{\partial^2 \hat{g}_\alpha}{\partial [\hat{v}_r]^2} \right) + \frac{\partial^2}{\partial [\hat{v}_\theta]^2} \left(\hat{f}_\alpha \frac{\partial^2 \hat{g}_\alpha}{\partial [\hat{v}_\theta]^2} \right) + 2 \frac{\partial^2}{\partial \hat{v}_r \partial \hat{v}_\theta} \left(\hat{f}_\alpha \frac{\partial^2 \hat{g}_\alpha}{\partial \hat{v}_r \partial \hat{v}_\theta} \right) \right\} \\ &\quad - A_h^\alpha \left\{ \frac{\partial}{\partial \hat{v}_r} \left(\hat{f}_\alpha \frac{\partial \hat{h}_\alpha}{\partial \hat{v}_r} \right) - \frac{\partial}{\partial \hat{v}_\theta} \left(\hat{f}_\alpha \frac{\partial \hat{h}_\alpha}{\partial \hat{v}_\theta} \right) \right\}, \end{aligned}$$

$$\frac{\partial^2 \hat{\varphi}}{\partial \hat{r}^2} + \frac{1}{\hat{r}} \frac{\partial \hat{\varphi}}{\partial \hat{r}} + \frac{1}{\hat{r}^2} \frac{\partial^2 \hat{\varphi}}{\partial \hat{\theta}^2} = -(\hat{n}_i - \hat{n}_e), \quad \hat{E}_r = -\frac{\partial \hat{\varphi}}{\partial \hat{r}}, \quad \hat{E}_\theta = -\frac{1}{\hat{r}} \frac{\partial \hat{\varphi}}{\partial \hat{\theta}},$$

$$\begin{aligned}
 \hat{t} = 0 : \quad & \hat{f}_\alpha(\hat{r}, \theta, \hat{v}_r \hat{v}_\theta, 0) = \hat{f}_\alpha^{maksv}, \quad \alpha = i, e, \\
 \hat{r} = \hat{r}_p : \quad & \hat{f}_\alpha(\hat{r}_p, \theta, \hat{v}_r \hat{v}_\theta \hat{t}) = 0, \quad \alpha = i, e, \\
 & \hat{\varphi}(\hat{r}_p, \hat{t}) = \hat{\varphi}_p, \\
 \hat{r} = \hat{r}_\infty : \quad & \hat{f}_\alpha(\hat{r}_\infty, \theta, \hat{v}_r \hat{v}_\theta, \hat{t}) = \hat{f}_\alpha^{maksv}, \quad \alpha = i, e, \\
 & \hat{\varphi}(\hat{r}_\infty, \hat{t}) = 0,
 \end{aligned}$$

where $\hat{f}_\alpha^{maksv} = \begin{cases} \frac{1}{\pi} \exp(-\hat{v}_r^2 - \hat{v}_\theta^2), & \alpha = i, \\ \frac{1}{\pi} \exp\left(-\frac{m_i T_{e\infty}}{m_e T_{i\infty}} (\hat{v}_r^2 + \hat{v}_\theta^2)\right), & \alpha = e, \end{cases}$, $\delta_\alpha = \frac{\varepsilon_\alpha}{\mu_\alpha}$, $\varepsilon_\alpha = \frac{T_{\alpha\infty}}{T_{i\infty}}$, $\mu_\alpha = \frac{m_\alpha}{m_i}$, $A_g^\alpha = \frac{M_g^\alpha M_t}{(M_v^\alpha)^4}$, $A_h^\alpha = \frac{M_h^\alpha M_t}{(M_v^\alpha)^2}$, M_g^α , M_h^α are coefficients defined in the way described in [5]. For dimensionless variables following scales were used: Debye radius, the speed of thermal motion of particles, the concentration of particles in undisturbed plasma, potential of charge sharing in Debye sphere, and other derived quantities.

The Monte-Carlo method is applicable for described problem. It is necessary to turn the system (1) containing Fokker-Plank equation into the following system containing stochastic differential equation (Ito equation):

$$d\Psi_\alpha(\hat{t}) = a_\alpha(\hat{t}, \Psi_\alpha(\hat{t})) + \sigma_\alpha(\hat{t}, \Psi_\alpha(\hat{t}))dW(\hat{t}), \quad \alpha = i, e, \quad (3)$$

where $\Psi_\alpha(\hat{t}) = [\hat{r}(\hat{t}) \quad \theta(\hat{t}) \quad \hat{v}_r(\hat{t}) \quad \hat{v}_\theta(\hat{t})]^T$ is state vector, $[\hat{v}_r(0) \quad \hat{v}_\theta(0)]^T \sim \hat{f}_\alpha^{maksv}$, $\alpha = i, e$,

$$a_\alpha(\hat{t}, \Psi_\alpha(\hat{t})) = \left[\sqrt{\delta_\alpha} \hat{v}_r \sqrt{\delta_\alpha} \frac{\hat{v}_\theta}{\hat{r}} \quad A_h^\alpha \frac{\partial \hat{h}_\alpha}{\partial \hat{v}_r} + \sqrt{\delta_\alpha} \left(\frac{\hat{v}_\theta^2}{\hat{r}} + \frac{z_\alpha \hat{E}_r}{2\varepsilon_\alpha} \right) \quad A_h^\alpha \frac{\partial \hat{h}_\alpha}{\partial \hat{v}_\theta} + \sqrt{\delta_\alpha} \left(\frac{z_\alpha \hat{E}_\theta}{\varepsilon_\alpha} - \frac{\hat{v}_r \hat{v}_\theta}{\hat{r}} \right) \right]^T,$$

$\sigma_\alpha(\hat{t}, \Psi_\alpha(\hat{t}))\sigma_\alpha^T(\hat{t}, \Psi_\alpha(\hat{t})) = A_g^\alpha \left\| \frac{\partial^2 \hat{g}_\alpha}{\partial \hat{v}_s \partial \hat{v}_q} \right\|$, $s, q = r, \theta$, $\alpha = i, e$, $W(\hat{t})$ is a standard stochastic Wiener process.

To solve this system it is required to evaluate values of elements \hat{E}_s , $s = r, \theta$ of electric field intensity vector using evaluated previously values of potential $\hat{\varphi}$ and applying numerical differentiation formulas.

Values of potential $\hat{\varphi}$ are obtained from the solution of Poisson equation boundary problem which is suggested to be solved by application of Fourier variables separation method.

Partial derivatives $\frac{\partial \hat{h}_\alpha}{\partial \hat{v}_s}$, $s = r, \theta$, $\frac{\partial^2 \hat{g}_\alpha}{\partial \hat{v}_s \partial \hat{v}_q}$, $s, q = r, \theta$ can be obtained using approximating numerical differentiation formulas based on previously evaluated values of \hat{h}_α and \hat{g}_α . To evaluate values of integrals contained in expressions of \hat{h}_α and \hat{g}_α functions Monte-Carlo method is used.

The solution of Ito Equation is found by Euler stochastic method [5]. The value Ψ_α^k of state vector $\Psi_\alpha(\hat{t})$ is obtained from the solution of Ito equation in discrete moment of time $\hat{t}_k = \hat{t}_0 + kh_\tau$, $k = 0, \dots, N_t$, h_τ is step of integration, N_t is number of time steps. Based on value Ψ_α^k the concentration of particles n_i , n_e and the current densities j_i , j_e to the probe is evaluated by the Monte-Carlo Method.

4. CONCLUSIONS

The program package for the solution of described problem is developed and the computational experiments are performed. While these experiments the initial problem arguments are varied. The initial arguments are the probe potential, the probe radius and particles concentrations in undisturbed plasma. The results for two modes (collisional and non-collisional) are obtained...

When the potential of the probe is negative the probe pushes electrons away. Therefore, positive volume charge forms near the probe which is acknowledged by zero electrons concentrations and non-zero ion concentrations about $\hat{r} = \hat{r}_p$. When particle collisions are considered, the shape of concentration graphics and volume charge changes. Furthermore, the results show that establishment process with collisions proceeds faster. It is noticed also that collisional current density of ions is less than noncollisional one.

REFERENCES

1. Bernstein, I. B. and I. N. Rabinowitz, “Theory of electrostatic probes in low-density plasma,” *Phys. Fluids*, Vol. 2, No. 2, 112–121, 1959.
2. Alekseev, B. V. and V. A. Kotel’nikov, *The Probe Method of Plasma Diagnostics*, Energoatomizdat, Moscow, 1988 (in Russian).
3. Kotel’nikov, M. V. and V. A. Kotel’nikov, *The Mathematical Modeling of Weakly-ionized Collisional Flow Plasma around a Body*, Mir, Moscow, 2007 (in Russian).
4. Montgomery, D. C. and D. A. Tidman, *Plasma Kinetic Theory*, New York, 1964.
5. Kudryavtseva, I. A. and A. V. Panteleyev, “The applying of the Monte-Carlo Method for analysis of two-component plasma behavior with charged particles collisions,” *The Collection of MIREA*, 122–128, 2008 (in Russian).

Metamaterials with Tunable Negative Refractive Index Fabricated from Amorphous Ferromagnetic Microwires: Magnetostatic Interaction between Microwires

A. V. Ivanov¹, A. N. Shalygin^{1,2}, V. Yu. Galkin²,
A. V. Vedyayev¹, and K. N. Rozanov³

¹M. V. Lomonosov Moscow State University, Moscow, Russia

²R & P Vichel (High-frequency Systems), Moscow, Russia

³Institute for Theoretical and Applied Electromagnetics of the RAS, Moscow, Russia

Abstract— For inhomogeneous mediums the optical Magnus effect has been derived. The metamaterials fabricated from amorphous ferromagnet Co-Fe-Cr-B-Si microwires are shown to exhibit a negative refractive index for electromagnetic waves over wide scale of GHz frequencies. Optical properties and optical Magnus effect of such metamaterials are tunable by an external magnetic field, magnetic field from neighbourhood microwires and mechanical stress.

1. INTRODUCTION

For a few recent years, new developments in artificially structured materials giving rise to negative refractive index $n = \sqrt{\varepsilon(\omega) \cdot \mu(\omega)} < 0$ with simultaneously negative real parts of frequency dependent permittivity $\varepsilon(\omega)$ and permeability $\mu(\omega)$ in some frequency ranges have been attracting much attention. These materials are consistent with causality and with the well established properties of group velocity in isotropic media. They are named left-handed mediums or left-handed materials, negative-index mediums, negative phase-velocity mediums (NPVM), backward wave mediums or even double negative media. The nonconflicting possibility of negative phase-velocity was theoretically discussed (see Refs. [1–3]). By now, after invention of first NPVM in microwave range around 7 years ago, the modern NPVM leveled the red edge of a visible spectra [4]. Recently developed NPVM have been paid much attention in journals and press. In *homogeneous NPVM* anomalous effects such as negative refraction, Doppler shift, Cherenkov-Vavilov radiation, light pressure, invisibility effect have been discovered in different frequency ranges. For them the gyrotropic phenomena are possible as well [5–7]. The other polarized electromagnetic effects such as optical Rytov and Magnus effects are given by a circular polarization of propagating waves, $\Xi = \pm$, and ∇n . Are they anomalous in *inhomogeneous NPVM* and is it possible to realize them per se? This paper tries to provide answers to these problems.

2. OPTICAL MAGNUS EFFECT

When a circularly polarized electromagnetic wave propagates in an inhomogeneous medium, the direction of its kinetic momentum does not vary. Then, according to the kinetic momentum conservation law, the ray trajectory becomes twisted, which means the optical Magnus effect. In Ref. [8], the Magnus optical effect has been described as the topological spin transport of photons using Berry phase. In this paper we apply the geometric optics approximation. For propagating electromagnetic wave its forces E and $H \propto \exp\{i(\vec{k} \cdot \vec{r} - \omega \cdot t + \psi(s))\}$, where $\psi(s)$ is a wave phase (eikonal) on the way s . The direction of rays \vec{l}_0 is given by $\nabla\psi = k\vec{l}_0$ ($\nabla\psi \cdot \vec{E} = 0$ and $\nabla\psi \cdot \vec{H} = 0$). Then from Maxwell's equations after very time consuming calculations one can get the ray equation of a circular polarized electromagnetic wave as follows:

$$\frac{\partial \vec{S}}{\partial s} = \vec{l}_0 \times \nabla \ln n \times \vec{S} + \frac{\Xi}{k} \left[\begin{array}{l} \frac{\partial}{\partial s} (\nabla \ln n \times \vec{S}) + \\ \frac{1}{2} \frac{\partial \ln \varepsilon}{\partial s} \nabla \ln \mu \times \vec{S} + \\ \frac{1}{2} \frac{\partial \ln \mu}{\partial s} \cdot \nabla \ln \varepsilon \times \vec{S} \end{array} \right] \quad (1)$$

($\vec{S} = \frac{c(\vec{E}_0 \times \vec{H}_0^* + \vec{E}_0^* \times \vec{H}_0)}{16\pi}$ is the Umov-Poynting vector). As would be expected, Eq. (1) is symmetric with respect to replacement $\varepsilon \Leftrightarrow \mu$.

3. TUNABLE NPVM FROM AMORPHOUS FERROMAGNETIC MICROWIRES

It is difficult to reach tunable gradient inhomogeneity essential for the optical Magnus effect (1) in NPVM formed from artificial nanoresonators or natural materials. At present the glass coated amorphous ferromagnetic microwires are of interest both from fundamental and applied points of view [9–12]. Based on them metamaterials can be constructed [13]. This section is devoted to the ordered system of amorphous ferromagnetic microwires. Let us take microwires with diameter $2a$ which are parallel to z -axis and occupy sites of a square lattice with a lattice constant b in xy -plane. Then consider a linear polarized electromagnetic wave, propagating along y -axis with electric force along z -axis in an external magnetic field $\{0, 0, H_0\}$. The frequency dispersion of

the material had taken into account in non-renormalised permeability tensor $\hat{\mu} = \begin{pmatrix} \mu & -im & 0 \\ im & \mu & 0 \\ 0 & 0 & 1 \end{pmatrix}$,

where $\mu = \frac{\omega_0(\omega_0 + \omega_M) - \omega^2}{\omega_0^2 - \omega^2}$, $\omega_0 = \gamma H_0$, $\omega_M = 4\pi\gamma M$, $m = \frac{\omega\omega_M}{\omega_0^2 - \omega^2}$ ($\gamma = \frac{|e|}{mc}$ -magnetomechanical constant). One can derive the effective permeability of this system [14]:

$$\mu_{eff} = \frac{1}{2} \frac{(\omega_0 + \omega_m)^2 - \omega^2}{\omega_0(\omega_0 + \omega_m) - \omega^2} \left(1 + \sqrt{\left[\frac{\sigma}{\omega\varepsilon} \left(2\pi \frac{a}{b} \right)^2 \right]^2 + 1} \right) \quad (2)$$

Here $\omega_m = \left(2\pi \frac{a}{b} \right)^2 \gamma M$ ($\omega_0 = \gamma H_0 \gg \omega_m$, M is a saturation magnetization of amorphous ferromagnetic with a bulk conductivity σ). The approach developed in Ref. [15] can be extended for the case of ferromagnetic wires. Then the effective permittivity is

$$\varepsilon_{eff} = \varepsilon_0 - \left(\frac{c}{\omega b} \right)^2 \frac{2\pi}{\ln \frac{b}{a} \left(1 + i \frac{c\xi_{zz}}{\omega a \ln \frac{b}{a}} \right)} \quad (3)$$

Here $\xi_{ZZ} = (1 - i) \sqrt{\frac{\omega\mu}{8\pi\sigma}} \left[1 + (1 + i) \frac{\delta}{4a\sqrt{\mu}} \right]$, ($\delta = \frac{c}{\sqrt{2\pi\sigma\omega}}$) (c.f. [9–12] and Leontovich-Schukin boundary condition) is the longitudinal component of a surface impedance tensor for strong skin-effect, $\frac{a\sqrt{\mu}}{\delta} > 1$. In Eq. (3) we work under assumption $b \gg a$ and the transfer to dilute Drude metal occurs due to the decrease of a carrier density and the increase of an effective carrier mass in plasma frequency as in [16].

4. INTERACTION BETWEEN MICROWIRES

For considering system of microwires the interaction between microwires should be taken into account [17]. The model for description of the interaction of a few microwires is the dipole-dipole interaction. In this paper a model where microwires are considered as the dipoles has been predicted. Let us consider a scalar magnetic potential of the cylinder characterized by a radius R and a length L with magnetization along the cylinder:

$$U(\bar{r}) = - \int_V \frac{\nabla' \cdot \bar{M}(r')}{|\bar{r} - \bar{r}'|} d^3r' + \oint \frac{\bar{M}(r')}{|\bar{r} - \bar{r}'|} d\bar{S} \quad (4)$$

Using the expansion of the reverse distance through the Bessel function [18] $\frac{1}{|\bar{r} - \bar{r}'|} = \sum_{m=-\infty}^{\infty} e^{im(\varphi - \varphi')}$

$\int_0^{\infty} d\bar{k} J_m(k\rho) J(k\rho') \cdot e^{-k(z-z')}$ the potential of the wire in cylindrical coordinates have been obtained:

$$U(r) = \pi M_z R^2 \left(\frac{1}{\sqrt{\rho^2 + (z - L)^2}} - \frac{1}{\sqrt{\rho^2 + z^2}} \right), \quad (5)$$

where z — is the cylinder axis, ρ — is the axial radius of the cylindrical coordinates.

It is easy to calculate created magnetic field $\bar{H}(\bar{r}) = -\nabla U(r)$ from (5):

$$\bar{H}(r) = \pi M_z R^2 \left\{ \frac{z - L}{\left(\rho^2 + (z - L)^2 \right)^{\frac{3}{2}}} - \frac{z}{\left(\rho^2 + z^2 \right)^{\frac{3}{2}}} \right\} \quad (6)$$

If we want to take into account all neighboring microwires, we should count such an integral $\bar{H}_{neighboring} = \frac{1}{R'} \int_{2R}^{\infty} \bar{H}(r) d\rho$, where R' — the average distance between microwires, c — concentration of microwires.

5. CONCLUSION

As follows from Eq. (1) in inhomogeneous NPVM the optical Magnus effect is reversed with respect to inhomogeneous normal ones as well as the other light effects in homogeneous NPVM. Since the Umov-Poynting vector $\vec{S} = w \cdot \vec{v}$ (\vec{v} — a group velocity, w — an electromagnetic energy density), the 1st term in square brackets coincides with equation for the Magnus optical effect $\pm \nabla \ln n \times \frac{\vec{v}}{k}$ of Ref. [8]. According to Eq. (1), the linear polarized electromagnetic wave, incident on NPVM, should be split in two circular polarized waves propagating in different ways. For typical magnitudes of amorphous Co-Fe-Cr-B-Si ferromagnets $\sigma \approx 10^{16} \text{ c}^{-1}$, $M = 500 \text{ Gc}$, $\xi_{zz} \approx 10^{-3}$, $\mu = 20$ [9-11] for microwires with $a = 10^{-3} \text{ cm}$, $b = 10^{-1} \text{ cm}$ in dielectric $\varepsilon_0 = 2$ and $H_0 = 10 \text{ Oe}$ we get $n = \sqrt{\varepsilon_{eff}(\omega)} \cdot \sqrt{\mu_{eff}(\omega)} < 0$ in the range of $1.9 \text{ GHz} < \omega < 21.7 \text{ GHz}$. By now the negative value of μ_{eff} , Eq. (2), has been confirmed by experiment [19]. In case of a homogeneous ε_{eff} the inhomogeneity of n can be created by, e.g., gradient $\nabla H_0 = \{\nabla_x H_0, 0, 0\}$. Putting the latter into Eq. (2), according to Eq. (1) one can derive the optical Magnus effect. Created magnetic field from each other microwires has been calculated. Created magnetic field from each other microwires has been taking into account $\omega_0 = \gamma(H_0 + H_{neighboring})$.

ACKNOWLEDGMENT

This work was supported by RFBR (Russian Foundation for Basic Research), Grant 08-02-00830.

REFERENCES

1. Veselago, V. G., “Electrodynamics of materials both permittivity and permeability being negative,” *Uspekhi Fizicheskikh Nauk (in Russian)*, Vol. 92, No. 7, 517–526, 1967.
2. Tretyakov, S. A., *EPFL Latsis Symposium 2005*, 30–35, Lausanne, Switzerland, February–March 2005.
3. Agranovich, V. M. and Y. N. Gartstein, “Spatial dispersion and negative refraction of light,” *Uspekhi Fizicheskikh Nauk (in Russian)*, Vol. 176, No. 10, 1051–1068, 2006.
4. Soukoulis, C. M., S. Linden, and M. Wegener, “Negative refractive index at optical wavelengths,” *Science*, Vol. 315, 47–49, 2007.
5. Lindell, I. V., S. A. Tretyakov, K. I. Nikoshinen, et al., “BW media-media with negative parameters, capable of supporting backward waves,” *Microwave and Opt. Tech Lett.*, Vol. 31, 129–133, 2001.
6. Mackay, T. G. and A. Lakhtakia, “Plane waves with negative phase velocity in Faraday chiral mediums,” *Phys. Rev. E.*, Vol. 69, 026602–026611, 2004.
7. Ivanov, A. V., O. A. Kotelnikova, and V. A. Ivanov, “Gyrotropic left-handed media: Energy flux and circular dichroism,” *JMMM*, Vol. 300, e67–e69, 2006.
8. Bliokh, K. Y. and Y. P. Bliokh, “Optical Magnus effect as a consequence of Berry phase anisotropy,” *JETP Lett.*, Vol. 79, No. 11, 519–522, 2004.
9. Zhukov, A., “Design of the magnetic properties of fe-rich, glass-coated microwires for technical applications,” *Adv. Funct. Mater.*, Vol. 16, No. 5, 675–680, 2006.
10. Makhnovskiy, D. P., L. V. Panina, C. Garcia, et al., “Experimental demonstration of tunable scattering spectra at microwave frequencies in composite media containing CoFeCrSiB grass-coated amorphous ferromagnetic wires and comparison with theory,” *Phys. Rev. B.*, Vol. 74, No. 6, 064205–064216, 2006.
11. Panina, L. V., S. I. Sandacci, and D. P. Makhnovskiy, “Stress effect on magnetoimpedance in amorphous wires at gigahertz frequencies and application to stress-tunable microwave composite materials,” *J. Appl. Phys.*, Vol. 97, No. 1, 013701–013707, 2005.
12. Starostenko, S. N., K. N. Rozanov, and A. V. Osipov, “Microwave properties of composites with glass coated amorphous magnetic microwires,” *JMMM*, Vol. 298, No. 1, 56–64, 2006.
13. Molokanov, V. V., P. P. Umnov, N. V. Kurakova, et al., “The influence of the glassy cover thickness to structure and properties of amorphous low-coercivity cobalt alloy,” *Perspektivnye Materialy (in Russian)*, Vol. 2, 5–14, 2006.

14. Ivanov, A. V., A. N. Shalygin, A. V. Vedyayev, et al., “Optical Magnus effect in metamaterials fabricated from ferromagnetic microwires,” *JETP Letters*, Vol. 85, No. 11, 565–569, 2007.
15. Sarychev, A. K. and V. M. Shalaev, *Electrodynamics of Metamaterials*, World Scientific, 2007.
16. Pendry, J. B., A. J. Holden, W. J. Stewart, et al., “Extremely low frequency plasmons in metallic mesostructures,” *Phys. Rev. Lett.*, Vol. 76, 4773–4776, 1996.
17. Sampaio, L. C., E. H. C. P. Sinnecker, and G. R. C. Cernicchiaro, “Magnetic microwires as macrospins in a long-range dipole-dipole interaction,” *Phys. Rev. B.*, Vol. 61, No. 13, 2000.
18. Smythe, W. R., *Static and Dynamic Electricity*, New York, Toronto, London, 1950.
19. Ivanov, A. V., V. Y. Galkin, V. A. Ivanov, et al., *Solid State Phenomena*, Vol. 152–153, 333, 2009.

Ventilation Efficiency and Carbon Dioxide (CO₂) Concentration

M. N. Halgamuge¹, T. K. Chan², and P. Mendis¹

¹Department of Civil & Environmental Engineering, The University of Melbourne
Parkville, VIC 3010, Australia

²Faculty of Architecture, Building & Planning, The University of Melbourne
Parkville, VIC 3010, Australia

Abstract— In animals metabolic processes, involve complex organic molecules being broken down to simpler molecules, such as carbon dioxide and water. Carbon dioxide waste is removed from the body through respiration. Carbon dioxide content in fresh air is approximately 400 parts per million. In this study, we investigate the relationship between ventilation efficiency and carbon dioxide (CO₂) concentration. Carbon dioxide concentration can give an indication of the indoor air quality in indoor and enclosed environments. It serves as a measure of ventilation efficiency in areas where air-conditioning and mechanical ventilation is provided.

Our survey of various enclosed environments indicate that CO₂ levels may exceed the levels that have been suggested to cause occupants to grow drowsy, get headaches, or function at lower activity levels. Elevated levels of CO₂ are observed in public transport when filled almost to capacity and these concentrations remain for long durations.

1. INTRODUCTION

The most periodic found gases on the earth is carbon dioxide (CO₂) [1]. This produces from natural metabolism of living organisms and combustion processes. We inhale oxygen (O₂) and exhale carbon dioxide. Indoor CO₂ levels in general vary between 400 and 2000 ppm (parts per million) while outdoor CO₂ levels are 350–450 ppm and also heavily industrialized or contaminated areas may occasionally have a CO₂ concentration of up to 800 ppm. Moreover, with very heavy traffic area the levels of outdoor CO₂ are higher [1, 2].

Carbon dioxide levels are a replacement for measuring indoor pollutants. Unusually high indoor carbon dioxide levels may cause occupants to grow drowsy, get headaches, or function at lower activity levels. Prime indoor source of carbon dioxide is human. Indoor carbon dioxide levels indicates of the suitability of outdoor air ventilation relative to indoor occupant density. Indoor carbon dioxide level must be reduced to below 600 ppm to eliminate most indoor air quality complaints [3]. The US National Institute for Occupational Safety and Health (NIOSH) considers that indoor CO₂ concentrations that exceed 1,000 ppm suggest inadequate ventilation. The American Society of Heating, Refrigerating and Air Conditioning Engineers (ASHRAE) recommends that the CO₂ levels not exceed 1,000 ppm within an occupied space [4].

2. METHODOLOGY

Three carbon dioxide sensor nodes were designed measure indoor gas concentrations, store these measurements in memory, and to operate at low battery powered voltages. These sensor nodes will eventually be coupled with wireless radio devices to be deployed as wireless sensor nodes in the near future and must therefore operate for long periods of time with minimum power consumption. The CDM4161 carbon dioxide sensor module from Figaro Engineering Inc., Japan was selected for its high selectivity to CO₂, compact size, low power consumption and maintenance free operation. The sensor detection range of 400 to 4,000 ppm is the concentrations that are of interest in many indoor environments. The sensor output is then connected directly to the analog-digital convertors of an ATmega128 micro-controller. The node is powered from six AA-sized alkaline batteries providing 9.0 V supply voltage and regulated to 5.0 V for both the ATmega128 and sensor module.

The sensor requires a warm-up period of two hours after the module is powered up. By assuming that the baseline level represents fresh air (400 ppm of CO₂), actual CO₂ concentrations are calculated based on the difference between the baseline level and the current sensor output. As a result, accurate readings cannot be expected if an accurate baseline is not provided. If the module is warmed up in an environment where the CO₂ concentration is higher than normal fresh air, the baseline will represent a polluted level. Power to the module should be on at all times. Since the baseline is memorized in a microcomputer, if the power should be cut off, the memory would be

lost and operation would resume from the warm-up process. The module is designed for indoor use and should be protected from exposure to rain, wind, sun and heat radiation.

This preliminary investigation was focused on examining the air quality in three indoor environments: Public spaces, private home, and public transport.

3. RESULTS & DISCUSSION

The three sensor nodes were deployed into two lecture theatres at the university one was a large 250 seat theatre with an older air-conditioning system, and another was a newly refurbished 120 seat theatre with a modern air-conditioning system. Measurements were commenced in the first theatre at 12.00 noon with a class of 100 students for a period of approximately 1 hour and 50 minutes. The sensors were placed at desk height (approximately 800 mm from the floor level) at the front, middle and rear of the theatre. As the lecture theatre was occupied prior to this session, the CO₂ concentration in the theatre was between 500 and 800 ppm at the start of the data collection period. The results indicate that the CO₂ level in the middle of the theatre reduced to 400 ppm after 1 hour, but the levels at the rear and front initially increased to a maximum of 700 and 900 ppm, respectively, before gradually reducing to a steady level of 600 and 800 ppm during the second hour of the session. As the front of the theatre was much lower than the rear, the denser CO₂ was concentrated at the front and remained at a level between 700 and 800 ppm even though the levels at the middle and rear have improved as shown in Figure 1.

Similar measurements in a newly refurbished lecture theatre indicate that the ventilation was adequate for an audience of 30 students as shown in Figure 2. The three sensors were placed in the empty theatre before the commencement of the class, and confirmed that the levels of CO₂ were similar to that of the ambient environment. Carbon dioxide levels increased from 400 to levels between 600 and 800 ppm once the students entered the theatre and remained at these levels throughout the 80 minute session. It can be seen that the ventilation at the rear of the theatre was less efficient with CO₂ concentration at approximately 800 ppm whereas the concentration at the front and middle was only 600 ppm.

In order to examine the levels of carbon dioxide in various public transport modes, a sensor node was carried into a typical tram. The CO₂ sensor was placed near at approximately foot level (approximately 80 mm above the floor level) at the front of the tram. The sensor was brought into the tram when it was almost full with passengers as indicated by a high CO₂ reading of 1150 ppm immediately upon entry as shown in Figure 3. The CO₂ concentrations gradually declined from the peak of 1150 to 600 ppm as passengers alighted from the trains and air exchanged with the exterior through the opening and closing of the doors at each stop. This elevated CO₂ level indicate that although the tram was equipped with a ventilation system, the CO₂ concentration only showed some improvements when more than half the passengers have alighted from the tram.

Similar measurements were carried out in a room located on second floor of a two-storey detached house. The CO₂ measurements were taken from 9:30 pm to 9:00 am in following day to

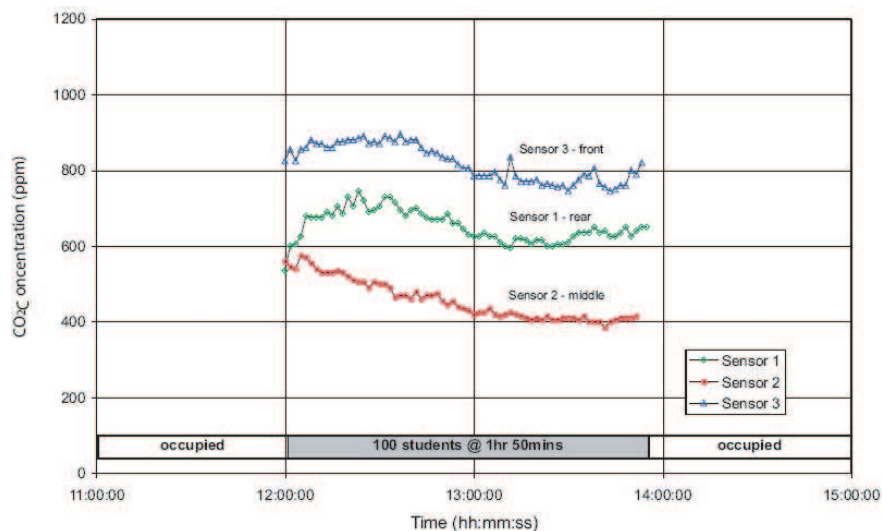


Figure 1: CO₂ concentrations at the faculty of architecture building and planning.

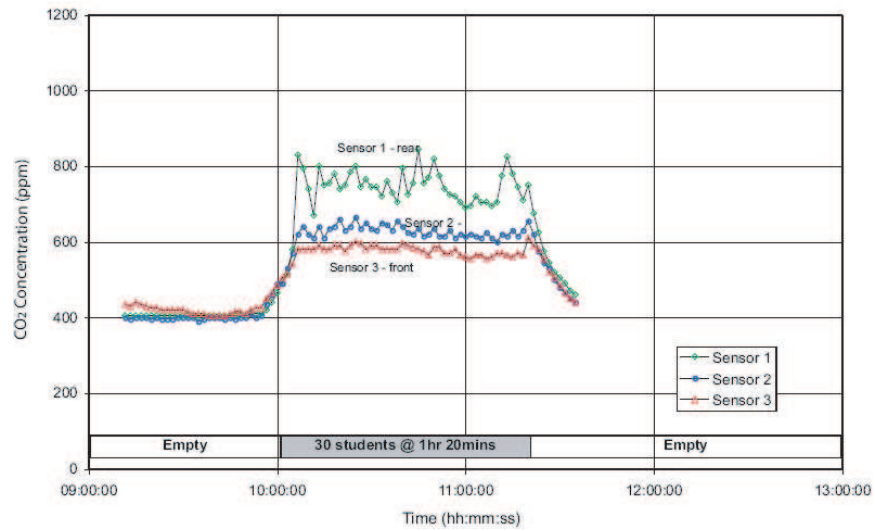


Figure 2: CO₂ concentrations at the engineering faculty.

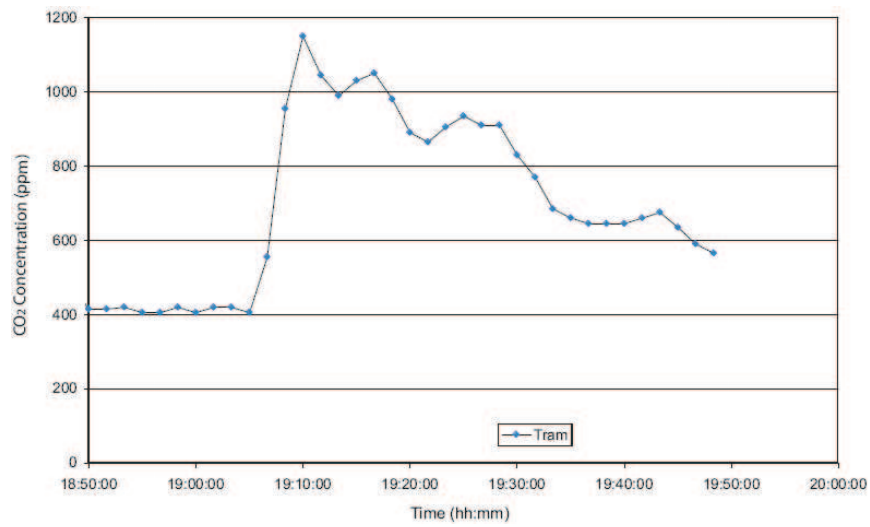


Figure 3: CO₂ concentrations in a typical tram.

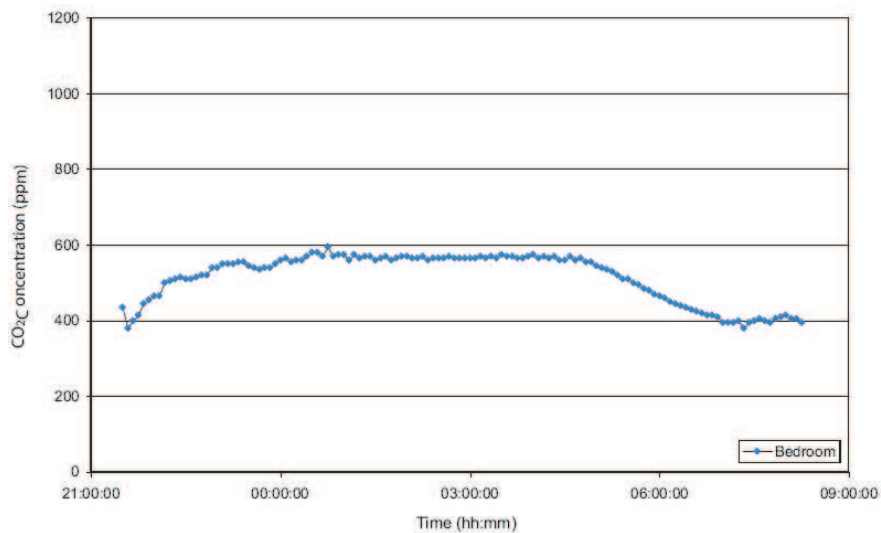


Figure 4: CO₂ concentrations in a room with a single adult occupant.

investigate the efficiency of the natural ventilation system present within the room. This room was not mechanically ventilated or air-conditioned. This room was occupied by a single adult who was sleeping in the room from 9:30 pm until 4:30 am. It is clear that the CO₂ concentration increased immediately at 9:30 pm until it reached a steady state condition at about 11:00 pm as shown in Figure 4. The maximum CO₂ concentration was constant at 580 ppm for the entire duration until 4:30 am when it started to decrease gradually to the ambient level of 400 ppm. This result clearly indicates that CO₂ levels within a room in a house can increase significantly if the windows and door are kept closed.

4. CONCLUSION

The results clearly indicate that the CO₂ concentrations can give an indication of the indoor air quality in these indoor and enclosed environments. It serves as a measure of ventilation efficiency in areas where air-conditioning and mechanical ventilation is provided. This preliminary investigation has shown that in an older lecture theatre, CO₂ levels may exceed the levels that have been suggested to cause occupants to grow drowsy, get headaches, or function at lower activity levels. Similar investigations in public transport have shown that elevated levels of CO₂ are present when the tram is near to capacity and these concentrations remain for long durations.

Although the monitoring of CO₂ in a house has indicated that the concentration has not reached unhealthy levels, it will be worth comparing this result with the effects of forced ventilation. Future work will focus on the deployment of a number of wireless sensor nodes equipped with CO₂, temperature and humidity sensors to investigate a range of air quality parameters in similar spaces and to develop strategies for managing indoor air quality concerns with these novel sensor technologies.

REFERENCES

1. Egeland, A. and H. Martin, "Research & development, production of gas sensors with IR-technique," *SenseAir AB*, No. 10, 1–7, 1993.
2. Barankova, P., K. G. Naydenov, K. G. Melikov, and A. K. Sundell, "Distribution of carbon dioxide produced by people in a room: Part I — Laboratory study," *Book of Abstracts, Roomvent*, Portugal, Sep. 2004.
3. Chou, P. C., C. H. Chiang, Y. H. Li, C. Y. Lee, and K. F. Chang, "Natural ventilation efficiency in a bedroom with a central-pivoting window," *Indoor and Built Environment*, Vol. 17, No. 2, 164–172, 2008.
4. "Indoor environmental quality: Building ventilation," National Institute for Occupational Safety and Health, 2008.

Design and Produce an E -plane Filter in Ka-band

A. Mirtaheri and Z. Mehdipour

K. N. Toosi University, Iran

Abstract— Mode Matching Technique (MMT) will be demonstrated in a resonator waveguide structure as a preliminary element of E -plane filters. The E -plane filter design procedure has been illustrated based on the results of MMT. Validity of this method was confirmed by HFSS software and experimental measurements of the filter designed by it. All responses showed excellent agreement but the MMT method has the advantage of time saving. This method drastically reduces the CPU time for analysis. E -plane filters are introduced as a practical, inexpensive and easy to make among waveguide filters. The stages of the design and produce an E -plane filter in Ka band with 5 resonators is presented. This filter was tuned by Network Analyzer with three screws. The insertion loss in the middle of band width is 0.83 dB.

1. INTRODUCTION

Analysis of waveguide discontinuities, especially H -plane and E -plane, have been the subject of many papers, but in most cases thickness of the E or H plane and interaction between different higher order modes were ignored [1, 2]. So the responses of them had a shift in frequency band. The design method of E -plane filters was described in these papers, too [3]. However, the actual bandwidth of the designed E -plane type filters deviated considerably [4].

In this paper by applying MMT, we could enter the thickness of planes furthermore in all cases we consider the mutual effect between modes. By MMT results, we design an E -plane filter; simulation of this filter by numerical method and by HFSS software has a good agreement. Fabricating and tuning this filter the measurement responses were acceptable and in according to the simulation results. Finally, we claim that designation of E -plane filter in different frequency band could be done in less than 20 minutes with a reliable measure for the inserted plane with this method.

2. RESONATORS SIMULATION

Figure 1(a) shows a resonator waveguide with dimension. This structure is analyzed applying MMT. Initially the structure could be divided into seven regions and for each subregion the relation of electric and magnetic field is written. The first region has been excited with TE_{10} and amplitude of electric field is 1 and number of modes in the other regions is infinity. So the other amplitudes of forward and backward waves in the rest of regions are unknown. The inserted plane with thickness t is a perfect electric conduct. Applying the boundary conditions at the metallic surface and matching the tangential field components some equations are obtained. In order to solve these equations the number of modes should be limited. Therefore, there are N_1 modes in second and fifth regions, N_2 modes in third and sixth regions and M modes in first, fourth and seventh regions. These numbers are to be found applying convergence condition. Simultaneously solving the above equations the unknown coefficient B^I and F^{VII} will be obtained. Since the amplitude of incident wave in first region is 1, the above coefficients are S_{11} , S_{12} respectively. Fig. 1(b) shows these parameters versus frequency. In this figure, the MMT response has been compared with HFSS response. Note that in this example the convergence condition was reached with $N_1 = N_2 = 11$ and $M = 22$, it means that increasing the number of modes in each region have no effect on the responses.

To analyze E -plane filter, it would be sufficient to find the S parameters of the resonators considering their dimensions, and then cascading them with distinct lengths; the total filter S parameters then are obtained.

3. E -PLANE FILTER DESIGN PROCEDURES

An E -plane filter is composed of 2 halves waveguide and an inner plane between these two. Assembling these 2 halves has an all over hole in its length. Measure of two halves is calculated considering the standard waveguide according to frequency band. So the purpose of design is determining the dimensions of the holes on inserted plane. These dimensions has a 0.001 precision which is produced with a lithography method, so we have the ability implementing this precision with low cost such that the cost of inner plane in mass production is almost 5% of the fabrication cost of the halves waveguide. This the superiority of E -plane filters in comparison to other waveguide filters.

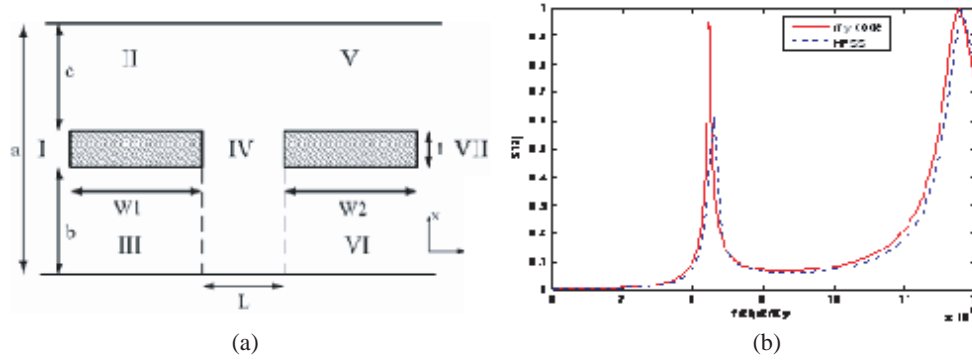


Figure 1: (a) Cross section of resonator with dimension (mm): $a = 22.86, b = c = 10.93, t = 1, L = 2.195, w_1 = 4.195, w_2 = 4.195$, (b) frequency response of resonator with above dimensions.

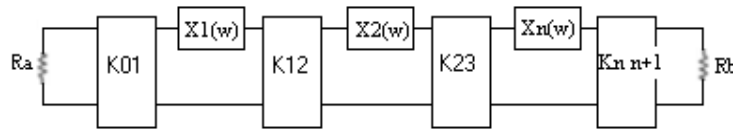


Figure 2: Equivalent circuit for band-pass filter with impedance inverter.

The equivalent circuit shown in Fig. 2 is used for any band pass filter such as waveguides, microstrip circuits and The degree of filter (n), the values X_1, X_2, \dots, X_n and impedance inverter coefficients $K_{01}, K_{12}, \dots, K_{nn+1}$ are calculated taking into consideration the insertion loss of in-band and cut-off-band [5]. To obtain the coefficient X_j in waveguides using a simple length waveguide would be sufficient; Although to implement K_{jj+1} coefficient there are different methods like E -plane, H -plane, and inductive posts. Finding relationships of this coefficient and filter dimensions is our purpose. In H -plane filters, there is a close form. It means that with taking into consideration the H -plane dimensions we calculate the coefficient K_{jj+1} . To determine this equation in E -plane, we have to do as below.

The equivalent circuits of a waveguide resonators which is the preliminary of E -planes filters structure is demonstrated in Fig. 3 and the equation between parameters X_A, X_B, θ is mentioned below:

$$K = \tan \left(\frac{\theta}{2} + \arctan \frac{X_A}{Z_0} \right) \tag{1}$$

$$\theta = -\tan^{-1} \left(\frac{2X_B}{Z_0} + \frac{X_A}{Z_0} \right) - \tan^{-1} \left(\frac{X_A}{Z_0} \right) \tag{2}$$

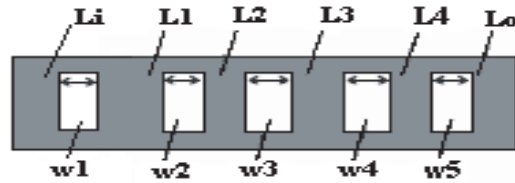
Suppose that T circuit is terminated from both sides with dominant mode wave impedance of Z_{FH} . The relation between structure's scattering parameter $S_{11} = \text{Re}^{j\phi_r}$ and X_A, X_B are as below:

$$\begin{cases} D = \frac{\cos \phi_r + R}{\cos \phi_r - R} \\ E = \frac{-\sin \phi_r}{\cos \phi_r - R} \end{cases} \tag{3}$$

$$\begin{cases} A = E + (E^2 + D)^{1/2} \\ B = E - A \end{cases} \tag{4}$$

$$\begin{cases} X_A = AZ_{FH} \\ X_B = BZ_{FH} \end{cases} \tag{5}$$

Finding the values X_A, X_B using the Equations (1) and (2), parameters K, θ will be distinct. In another word, knowing S_{11} of each resonator coupling coefficient values and equivalent electrical length can be found. Although with resonator dimensions S_{11} coefficient is yielded.

Figure 3: Inserted plane of E -plane filter.

So to design the filter firstly considering its characteristics, coupling coefficient K_{needed} and the essential electrical length θ for each resonator is found. Then starting with initial dimension (length and width) of inner plane the scattering coefficient will be obtained, so by use of above formula the K is found. This value is named $K_{\text{modematch}}$. By comparing $K_{\text{modematch}}$ with K_{needed} , we can check the accuracy of our initial assumptions about the dimension of each septum. It means that if $K_{\text{modematch}}$ is larger than K_{needed} , we will reduce the width of the septum, and vice versa. This process is repeated until the proper K is reached. Finally, the width of each septum will be determined. All calculations is started with the initial value of $t = 0.3$ mm for each septum, and if by changing the width of the septum in permitted range we were unable to find the desired K the reduction of thickness (t) would be an option. In all cases, we have to take into consideration the ability of fabrication and the range of the permitted changes. In order to find the resonator length, after determination the final S_{11} that provided K_{needed} , X_A , X_B , then according to Equation (2), θ will be figured out. The relationship of θ with physical length is described below [6]:

$$\theta_j = \pi - \frac{1}{2} \left[\tan^{-1} \frac{2X_{j-1,j}}{Z_0} + \tan^{-1} \frac{2X_{j,j+1}}{Z_0} \right] \quad j = 1, 2 \dots n \quad (6)$$

$$L_j = \frac{\theta_j \lambda_{g0}}{2\pi} \quad (7)$$

λ_{g0} is the conductance wavelength in center frequency [6].

4. E -PLANE FILTER DESIGN IN KA-BAND

An optimizing computer program was used for design an E -plane filter according to above formulas. A kind of implementation of this program with input and output has been shown. Characteristics of filter (f_1 & f_2 : Start and stop frequency of pass band, f_a & f_b : Start and stop frequency of cut-off band) are chosen according to ETSI standard. WR42 is selected for this case. Dimensions of inserted plane are shown in Fig. 3.

Input

Enter the frequency in f_a (GHz) = **22.132**.

Enter the frequency in f_1 (GHz) = **22.432**.

Enter the frequency in f_2 (Ghz) = **23.030**.

Enter the frequency in f_b (GHz) = **23.330**.

Attenuation in f_a or f_b (dB) = **40**.

LAr is maximum attenuation in bandpass, Enter the LAr (dB) = **0.1**.

Output

Degree of filter = **5**, Thickness of E -plane versus mm (t) = **0.1**.

Wide of each septum versus mm (h) = **1.866 5.682 6.495 6.495 5.682 1.866**.

Length of resonator versus mm (l) = **5.6755 5.673 5.672 5.673 5.6755**.

According to above figure, width of septum i is w_i and length of all septum is 0.42 inch. L_i and L_o should be greater than $\lambda/2$. In this case, $\lambda/2$ is 5 mm, but for high reliability and having more length for tuning screw these lengths have been considered 15 mm. In designated filter, there are two tune screws in these regions.

To make sure of the accuracy of above filter, it should be analyzed with the mentioned method. Therefore the above filter has been simulated with MMT and HFSS. The result has been shown in Fig. 4.

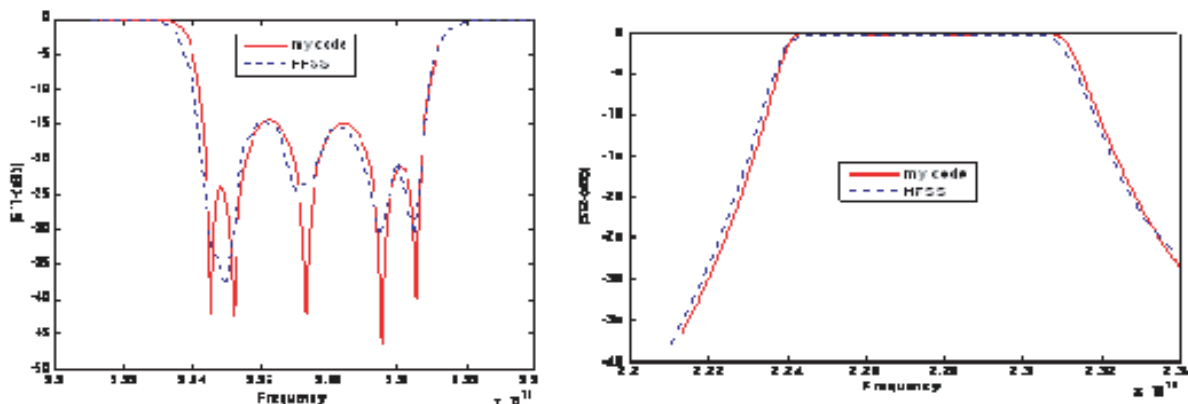


Figure 4: Frequency responses of designated filter.



Figure 5: Connection of filter to directional coupler and detector.

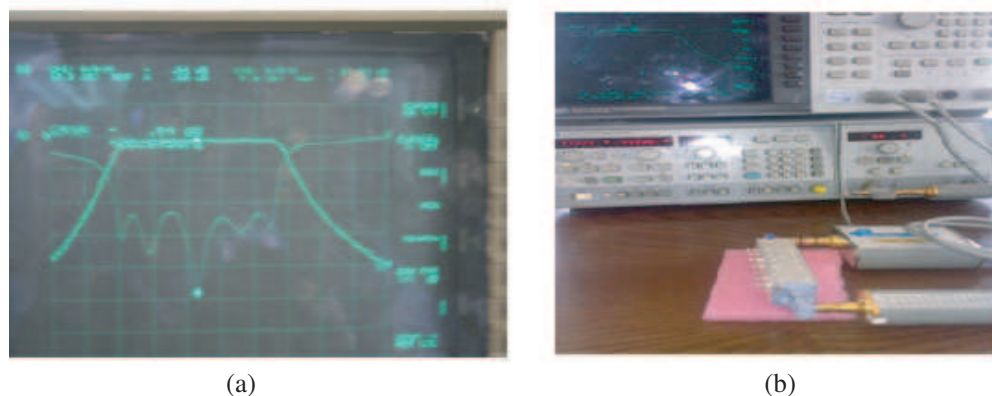


Figure 6: (a) Response of the filter on network page, (b) connection of filter to network analyzer.

5. NUMERICAL RESULTS AND EXPERIMENTS OF DESIGNATED FILTER

All parts are silver plated; this will lead to filter loss reduction and has a great effect on its performance. Placing the tuning screws on the filter body in the middle of each resonator is unavoidable and it has an important role for compensating the tolerance of dimensions. Test and tuning is done by utilizing network analyzer and prior to using the device calibration of it should be done. Fig. 5 shows the fabricated filter with all essential accessories.

This filter is tuned in 30 minutes and its response is shown in Fig. 6(a). Also a scheme of this filter that connected to network analyzer is demonstrated in Fig. 6(b). Parameters of network are as: Start Frequency: 22 GHz, Stop Frequency: 23.5 GHz, Channel one: $|S_{12}|$ -dB with Scale: 10 dB/div and Channel two: $|S_{11}|$ -dB with Scale: 5 dB/div. The insertion and return loss in different frequency is shown in Table 1. Insertion loss average in pass band is about -1 dB and its return loss is about -13 dB.

Table 1: Return and insertion loss in different frequency.

Frequency (GHz)	$ S_{12} $ -dB	$ S_{11} $ -dB
22.330	-1.25	-15
22.432	-1.18	-17.46
22.645	-0.83	-24.13
22.989	-1.26	-11
23.030	-4.5	-5.28
24.5	-43	-0.1

6. CONCLUSIONS

In this paper, a design theory has been described for E -plane metal insert filters. The theory includes higher order mode interaction and finite thickness of the insert plane. A typical E -plane filter in Ka-band was designed and implemented. The measurement responses have a good agreement with simulation curves.

ACKNOWLEDGMENT

It should be appreciated of **Iran Telecommunication Research Center** for financial support of this project.

REFERENCES

1. Shih, Y. C., "Design of waveguide E -plane filters with all metal inserts," *IEEE Trans. MTT*, Vol. 32, No. 7, 695–704, 1984.
2. Bui, L., D. Ball, and T. Itoh, "Broadband millimeter-wave E -plane bandpass filters," *IEEE Trans. MTT*, Vol. 32, No. 12, 1655–1658, 1984.
3. Saad, A. M. K. and K. Schunemann, "Design and performance of fin-line bandpass filters," *Proc. 9th European Micro. Conf.*, 397–401, 1979.
4. Vahldieck, R., J. Bornemann, and F. Arndt, "Optimized waveguide E -plane metal insert filters for millimeter-wave application," *IEEE Trans. MTT*, Vol. 31, No. 1, 65–69, 1983.
5. Marcuvitz, N., *Waveguide Handbook*, McGraw-Hill, New York, 1951.
6. Hounter, I. C., *Theory and Design of Microwave Filters*, IEEE Press Series on Electromagnetic Wave, 49–100, 2001.

Broad Omnidirectional Band of Reflection from Fibonacci One-dimensional Photonic Crystals

N. V. Grushina, P. V. Korolenko, A. Y. Mishin, and A. M. Zotov

Faculty of Physics, M. V. Lomonosov Moscow State University, Moscow 119992, Russia

Abstract— On the basis of numerical simulation the problem of omnidirectional reflection (ODR) of radiation from aperiodic 1D photon crystal has been considered. It is assumed that layers with different refractive indices alternate in a crystal according to the Fibonacci generation scheme. It has been shown that we can considerably broaden spectral range with high refractive index at different incidence angles by increasing in thickness of layers linearly or stepwise. This increase in layer thickness also allows improving phase modulator characteristics.

1. INTRODUCTION

Now in photon crystal optics the great attention is devoted to the study of Fibonacci 1D photon crystals. They represent multilayer systems (MS) with alternating layers of two materials according to the Fibonacci generation scheme. Fibonacci MSs are successfully applied in selective waveguide devices, in impulse compression systems, in frequency converters and optical radiation amplifiers. In some cases in their use it is required to provide ODR of light waves in a certain spectral range, free of dissipative losses.

The possibility of ODR realization in a wide spectral range with regard to Fibonacci MS, was considered in literature on the basis of different approaches [1–6]. We emphasize the approaches, based on application of repeating blocks of alternative layers and on perturbation (sometimes random) of MS. In certain cases such approaches allow expanding considerably a wavelength range in which reflection factor is close to 1. Nevertheless, this problem remains the urgency from the viewpoint of additional possibilities of more effective ODR. These possibilities are substantially connected with the occurrence of new technologies that allow producing qualitative MSs consisted of several hundreds of layers. To design new types of MSs the revision of estimations is required. These estimations are a reference point in the definition of a spectral interval within which one can observe practically total reflection of radiation irrespectively of an incidence angle. In this paper, on the basis of the numerical simulation features of ODR from MS with various parameters and different quantity of layers have been studied. The possibility of improving ODR characteristics by increasing in thickness of layers, has also been considered.

2. REFLECTION PROPERTIES OF FIBONACCI MS

It should be mentioned that in respect to Fibonacci MS there is no problem of effective radiation reflection in narrow frequency intervals. If the central frequencies of these intervals are known, it is not difficult to fabricate a corresponding MS. Figure 1 illustrates the reflection factor distribution from 34 layer MS versus frequency and incidence angle for *s*-polarized radiation. The distributions are plotted in the assumption that layers with refractive indices $N_l = 1.44$ and $N_h = 3.35$ are alternated. Such refractive indices in near infrared region have layers of silicon and silicon oxide. Figure 1(a) is plotted in 3D representation, Figure 1(b) — in 2D. In Figure 1(b) two direct vertical dot-dash lines are drawn. Their positions correspond to the central frequencies of the spectral intervals. Within these spectral intervals reflection factor is high at all incidence angles of radiation.

The first of them is located in the left (in relation to the frequency $\bar{\omega} = 1$) wide band gap, its central frequency is $\bar{\omega} = 0.84$, the second is located in the right wide band gap, its central frequency is $\bar{\omega} = 1.4$ ($\bar{\omega}$ — normalized frequency; $\bar{\omega} = \omega/\omega_0$, where ω — cyclic frequency of radiation, ω_0 — the frequency, at which optical thickness of layers is quarter-wave-length). Along these lines there remains high value of reflection factor. The angular distributions of reflection factor R corresponding to the mentioned values of frequency are shown in Figure 1(c) and (d). From these distributions one can conclude that the best conditions for high reflection at different angles are in the left band gap. The frequency range, in which there is almost 100% reflection irrespectively of incidence angle, is $0.65 < \bar{\omega} < 0.88$ for the left band gap. In the right band gap the frequency range of high reflection sharply decreases. In regard to this band gap almost total reflection can be found only near the frequency $\bar{\omega} = 1.4$ and only at angles of less than $\theta \approx 78^\circ$.

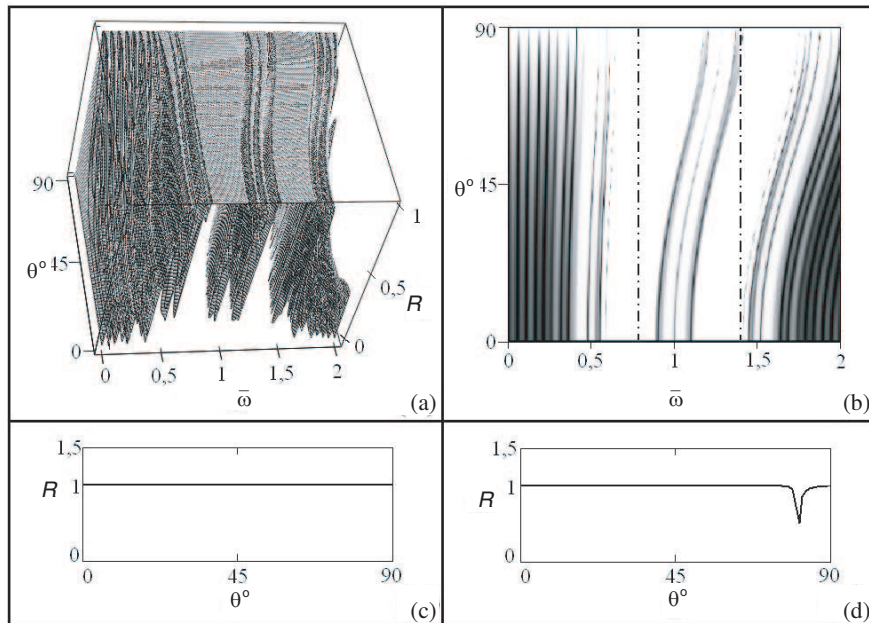


Figure 1: MS reflection factor R versus frequency of radiation $\bar{\omega}$ and incidence angle θ° (s -polarization). (a) 3D; (b) 2D (light zones correspond to high reflection factor); (c) reflection along the left dot-dash line; (d) reflection along the right line.

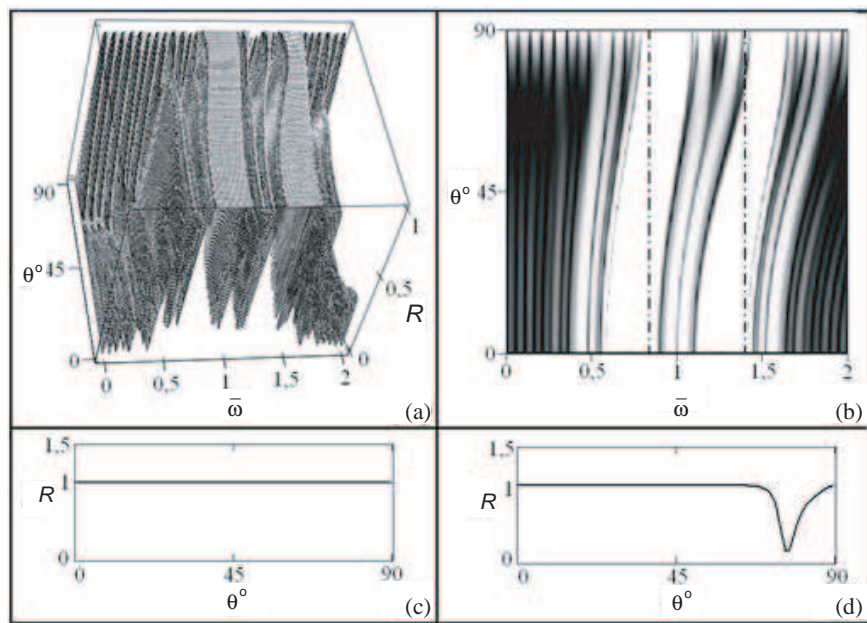


Figure 2: MS reflection factor R versus frequency of radiation $\bar{\omega}$ and incidence angle θ° (p -polarization). The definitions are the same, as well as in Figure 1.

For p -polarized radiation the similar curves are resulted in Figure 2. Here again we see high reflection properties of MS, though weaker. The width of high reflection area in the left band decreases and is equal to $0.8 < \bar{\omega} < 0.87$. In the right band gap high reflection at different angles will be observed only at the frequency $\bar{\omega} = 1.4$, at angles of less than $\theta \approx 68^\circ$.

3. PROPERTIES OF FIBONACCI MS WITH VARYING LAYER THICKNESS

By modifying the MS structure it is possible to expand spectral region of total reflection and to reduce the dependence on refractive indices contrast. In the process of investigation different

modifications have been considered. They are the regular alternation of blocks with a certain sequence of layers, and the introduction of fixed or random perturbation into optical thickness of layers with different refractive indices. All these methods along with advantages have also a number of disadvantages. Numerical simulation has shown that method of spectral range broadening, based on linear or stepwise increase in optical thickness of layers, is the most general and simple from the viewpoint of practical realization [7].

In this case phase incursions in layers are described by the expression

$$\varphi_j = \alpha + k(j - 1), \quad (1)$$

where j — a layer number; α — phase incursion in the first layer. The coefficient k characterizes increase in layer thickness with rising j . It is convenient to set it as

$$k = \left(\frac{\pi}{2} - \alpha\right) \cdot \frac{2}{J}, \quad (2)$$

where J — the total number of layers in MS. From Relations (1) and (2) it is clear that if $\alpha = \pi/2$ phase incursions in layers will be the same and equal to $\pi/2$. By changing α it is possible to find the optimum value of k providing the maximum width of spectral range with the maximum reflection at various incidence angles. The estimations have shown that the best result is reached when $\alpha = \frac{\pi}{2} \cdot 0.65$, irrespective of the total number of layers. At this value of α the trend in layer thickness leads to considerable broadening of a spectral range with high reflection.

For example, for 34 layer MS reflection factor is no less than 0.99 at all incidence angles, when $0.61 < \bar{\omega} < 0.97$. The width of this spectral interval is almost twice as long as the width of that, corresponding to unperturbed system. It is possible to broaden even more spectral interval with high reflection factor by increasing the total number of MS layers. Thus for 89 layer MS the spectral interval will be $0.47 < \bar{\omega} < 1.5$. If we increase the quantity of layers up to 144 the width of the interval will increase further.

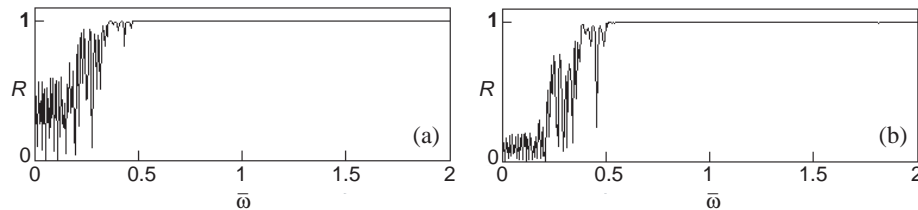


Figure 3: Reflection factor versus frequency at an incidence angle of $\theta = 45^\circ$ for 144 layers. (a) s -polarization; (b) p -polarization.

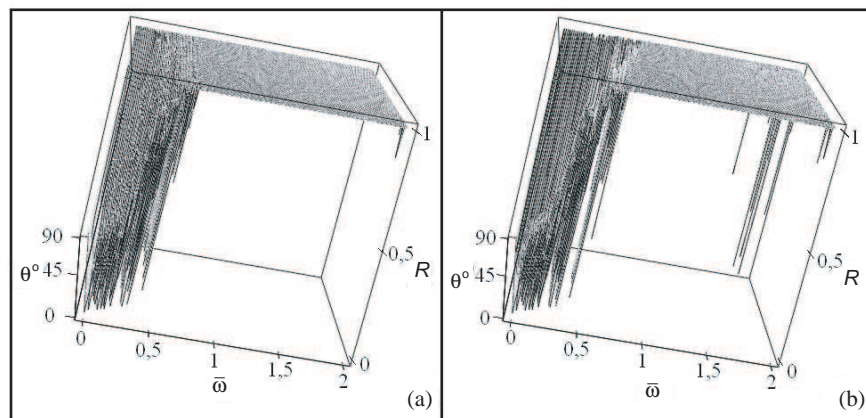


Figure 4: ODR from MS with trend in thickness of layers. (a) s -polarization; (b) p -polarization.

These estimations have been made for s -polarized mode. If incident radiation is p -polarized, the estimations do not undergo radical changes. However in spectral intervals with high reflection there can be separate, rather narrow areas in which reflection factor sharply decreases. This illustrates

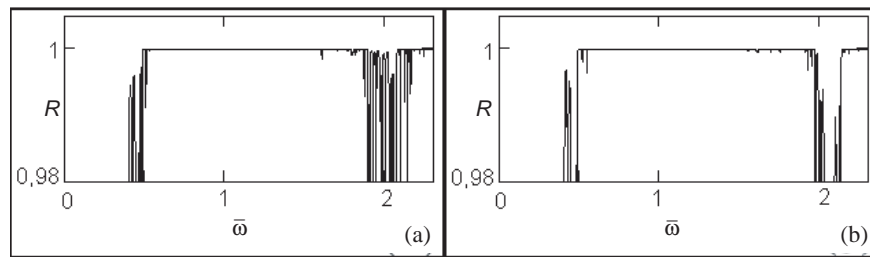


Figure 5: Reflection spectra from 100 layer Fibonacci MS at an incidence angle of $\theta = 30^\circ$. (a) Linear trend; (b) step trend.

Figure 3. The plot in Figure 3(a) characterizes the reflection factor distribution versus frequency for 144 layer MS, for s -polarized mode and incident angle of $\theta = 45^\circ$. Figure 3(b) shows the distribution for p -polarized mode for the same incidence angle. 3D representations of corresponding dependences are resulted in Figure 4.

When carrying out the computations it was discovered that we can replace linear trend in layer thickness with step trend to get ODR. This modification provides practically the same results, but it is much easier realized technically. So, if the MS consists of 100 layers instead of the dependence (1) it is possible to use the following distribution of phase incursions: $\varphi_j = \varphi_{12}$, if $0 < j \leq 25$; $\varphi_j = \varphi_{37}$, if $25 < j \leq 50$; $\varphi_j = \varphi_{62}$, if $50 < j \leq 75$; $\varphi_j = \varphi_{87}$, if $75 < j \leq 100$. This confirms Figure 5 in which reflection spectra for s -polarization are represented at different ways of layer thickness increasing. The suggested way can be applied to other types of MS: periodic and aperiodic.

4. PHASE MODULATION EFFECTS

ODR from Fibonacci MS is closely connected with designing of phase modulators of light beams. The presence in Fibonacci MS transmission spectrum of a great number of narrow band gaps makes these systems a convenient means for phase modulation. The application of Fibonacci MS as phase modulators supposes periodic varying of each layer thickness, as a rule, with the use of acoustic or electro-optical effects. If the variation of phase incursions in layers occurs in band gaps, phase modulation of the reflected radiation will occur practically without changing its intensity.

Nevertheless, the practical realization of certain phase modulator modifications demands imple-

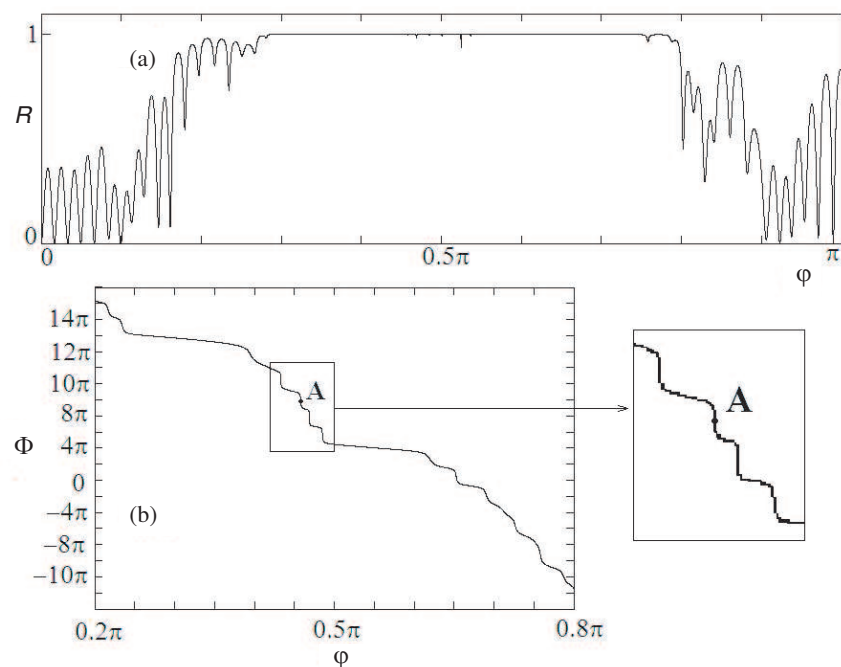


Figure 6: (a) Reflection spectrum from 55 layer MS, (b) the change of reflected wave phase.

mentation of multiparametric optimization. Indeed, the efficiency of phase modulation (estimated by the amplitude of phase changes) will depend on band gap width connected with the total number of layers in MS. The reduction of the band gap width in order to increase in the sensitivity of the modulator can considerably limit a range of possible variations of incidence angles of radiation.

The calculations, with regard to Fibonacci MS consisting of layers with refractive indices $N_h = 2.3$ and $N_l = 1.45$, show that by changing layer thickness by 0.1% the amplitude of phase change $\Delta\Phi$ is approximately equal to 0.036 rad if we use 75 layer MS. The deviation scope of incidence angles (from normal) is limited by $\Delta\alpha = 10^\circ$. If we increase $\Delta\Phi$ twice, this will demand increasing in the total number of layers up to 144 and lead to reduction $\Delta\alpha$ down to 5° .

It is possible to improve radically the properties of light modulators by applying the described above method, connected with increase in layer thickness. In the presence of this trend in spectral range with high reflection, areas with abrupt phase change of reflected signal are formed. Their presence allows increasing considerably the phase modulator sensitivity to variation of parameters of layers in MS.

In Figure 6, reflection spectrum from 55 layer MS with the curve of phase change of reflected wave, is shown for s -polarization (φ -phase incursion in the central layer). It is visible that these areas are in almost total reflection range. Point A corresponds to the steepest curve interval. If we take this point as a working one, a little variation of phase incursion will cause a great change of refracted wave phase. If we will vary the layer thickness by 0.1%, for this working point the variation of reflected signal phase is equal to π .

5. CONCLUSION

Thus, the performed research show that ODR in MS has some peculiarities. They are caused by several band gaps. Spectral intervals with ODR are not wide enough because band gaps are narrow. It is possible to broaden considerably ODR spectral intervals by increasing in thickness of layers linearly or stepwise. MS with increasing layer thickness can be efficiently applied in a phase modulator. The working area of the modulator is located in narrow band gap regions of Fibonacci MS with fixed layer thickness.

ACKNOWLEDGMENT

The work presented in this paper was supported by The Leading Scientific Schools Support Program (project SS-4408.2008.2).

REFERENCES

1. Dong, J. W., P. Han, and H. Z. Wang, "Broad omnidirectional reflection band forming using the combination of Fibonacci quasi-periodic and periodic one-dimensional photonic crystals," *Chinese Physics Letters*, Vol. 20, No. 11, 1963–1965, 2003.
2. Barriuso, A. G., J. J. Monzon, L. L. Sanchez-Soto, and A. Felipe, "Comparing omnidirectional reflection from periodic and quasiperiodic one-dimensional photonic crystals," *Optics Express*, Vol. 13, No. 11, 3913–3917, 2005.
3. Zhang, D., Z. Li, W. Hu, and B. Cheng, "Broadband optical reflector — An application of light localization in one dimension," *Applied Physics Letters*, Vol. 67, No. 17, 2431–2432, 1995.
4. Abdelaziz, K. B., J. Zaghdoudi, M. Kanzari, and B. Rezig, "A broad omnidirectional reflection band obtained from deformed Fibonacci quasi-periodic one dimensional photonic crystals," *Journal of Optics A: Pure and Applied Optics*, Vol. 7, No. 10, 544–549, 2005.
5. Lusk, D. and F. Placido, "Omnidirectional mirror coating design for infrared applications," *Thin Solid Films*, Vol. 492, 226–231, 2005.
6. Jiang, L., G. Zheng, L. Shi, J. Yuan, and X. Li, "Broad omnidirectional reflection design using genetic algorithm," *Optics Communications*, Vol. 281, No. 19, 4882–4888, 2008.
7. Popov, K. V., J. A. Dobrowolski, A. V. Tikhonravov, and B. T. Sullivan, "Broad high-reflection multilayer coating at oblique angles of incidence," *Applied Optics*, Vol. 36, No. 10, 2139–2151, 1997.

Application of Graphical Processors in Signal Processing of MTI Systems

M. A. Ershadi and E. K. Keshmarzi

Department of Electrical Engineering, Sharif University of Technology, Tehran, Iran

Abstract— Moving Target Indicator (MTI) radars are developed and used extensively to detect and follow specific moving targets and eliminate clutters. Processing system in these radars is so massive and complex, since it is supposed to perform a great amount of processing in very short time. Generally these processing are performed on digital signal processors, however DSPs are usually expensive and in some applications they seem to be ineffective. In this paper a cost effective approach is introduced which utilizes Graphics Processing Unit (GPU) to perform MTI radar signal processing computations.

1. INTRODUCTION

Moving Target Indicator radar is a subclass of pulse radar systems which is used to track desirable moving targets and omit unwanted echoes from both stationary objects like lands and mountains, and also undesirable moving background such as seas, clouds and rain that are generally called clutter.

Primitive MTI radar systems utilized analog methods that were able to eliminate only stationary objects. As digital technology introduced in radar systems many other capabilities, such as finding desired objects and removing clutters, were added to these systems. MTI systems must be able to work in a near real time manner. However, complex and time consuming processing steps in these systems is a considerable challenge [1]. Single core processors are not usually able to handle this amount of computations as fast as radars require. Parallel data processing, using DSPs, is usually utilized to accelerate the process. In the case of MTI systems, DSPs with multiple parallel threads must be used to perform high amount of computations. The latter capability makes DSPs so expensive. In addition, these kinds of DSPs are somehow inaccessible due to their military applications. In this paper, graphics hardware is used as a parallel processor instead of DSPs to perform MTI systems computations. Graphics hardware has been utilized in variety of general computing problems for sake of their low price to performance ratio [2]. Implementation of different mathematical algorithms in image and signal [2, 4] processing and physics problems modeling are some applications of graphics hardware's general usage. Although we have proposed using graphics hardware in MTI signal processing for the first time, however some of its main algorithms had already been developed in these hardware.

In Section 2 of the paper basic principles related to MTI systems is discussed, in Section 3 graphics hardware structure is introduced. In Section 4, our method of implementation is given and finally in Section 5 Discussion and conclusion are presented and analyzed.

2. BASIC PRINCIPLES

As had already been mentioned, MTI radar is a kind of pulse radar system. Pulse radar transmits a train of modulated pulses toward targets and receives their echoes. Time interval between consecutive pulses is called Inter-pulse Period (IPP) that is inverse of pulse repetition frequency (PRF). Target's range is determined using time delay between sent and received signals. In addition, target's velocity is calculated by analyzing Doppler shift of the received signal. Generally block diagram for these systems can be presented as Figure 1. As this Figure shows, a coherent oscillator (COHO) is employed both in transmitter and receiver sections. This oscillator maintains a precise phase that is necessary to extract the Doppler shift at the receiver. According to the Figure 1, the first multiplier generates the IF signal which after amplification enters a quadrature demodulator.

Quadrature demodulator generates a pair of perpendicular video signals (Inphase & Quadrature

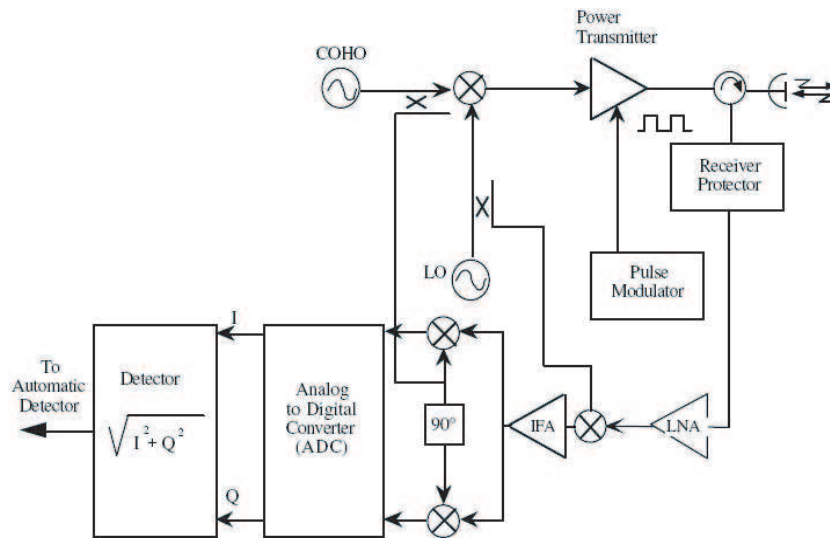


Figure 1: Transmitter/receiver block diagram in pulse radar.

phase) that mathematically can be represented as below:

$$\begin{aligned}
 U_I &= A_d \sin \left[2\pi f_d t - \frac{4\pi f_0 R}{C} \right] \\
 U_Q &= A_d \cos \left[2\pi f_d t - \frac{4\pi f_0 R}{C} \right]
 \end{aligned}
 \tag{1}$$

These two signals are used to extract Doppler shift of the received signal that is directly related to target's velocity by:

$$V = \frac{f_d \lambda}{2}
 \tag{2}$$

where λ is wavelength and f_d is the Doppler shift of the received signal.

In MTI radar systems, further analysis is performed on I and Q video signals to detect desirable moving targets. The basic idea to achieve this goal is to subtract two consecutive cycles of the video signal. If the video signal is echoed from a moving target, then the output of subtractor has sinusoidal variations, otherwise there is little or no variation. This idea can be implemented using Delay Line Canceller shown in Figure 2:

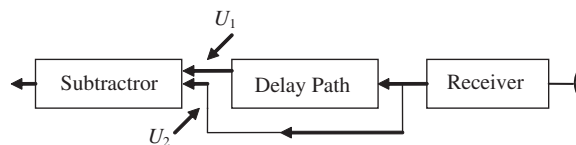


Figure 2: Simple delay line canceller.

In Figure 2, U_1 is similar to U_2 except for having a time delay equal to IPP. Moving target detection can be explained by investigating frequency response of Delay Line Canceller. Power density of clutters is usually concentrated in zero frequency and integer multiples of PRF. Whereas, power density of moving targets is concentrated in the middle of the frequency band. On the other hand, Delay Line Canceller has a band pass frequency response which allows detection of moving targets and rejecting clutters. Figure 3 depicts frequency response for clutter, moving target and Delay Line Canceller. The idea of Delay Line Canceller in modern MTI radars is realized using Doppler Filter Bank which is aggregation of adjacent narrowband filters which have high quality band pass characteristic.

Today, modern MTI systems utilize digital methods providing possibility for doing more processes and increasing system capabilities. Digital Filter Bank is utilized in digital MTI systems. This Filter Bank is mostly FFT Filter Bank which we employed in our work. In this method 2^n

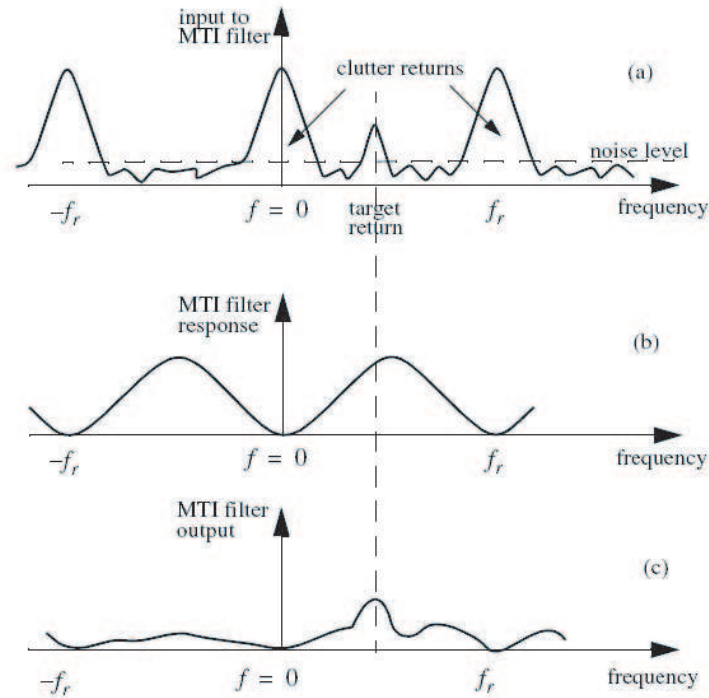


Figure 3: Frequency characteristics for: (a) Input clutter and target, (b) filter bank, (c) filter bank output.

number of consecutive received pulses are stored and their I and Q samples are produced. Algorithm of FFT operates on 2^n samples in the same spatial position of consecutive pulses. Outputs of operation are 2^n frequencies or frequency response of the related positions in spatial space. Therefore a spatial-frequency space is created. In the next step some frequencies corresponding to moving targets are extracted by means of CFAR (Constant False Alarm Method). In CFAR an adaptive threshold is determined for each sample in spatial-frequency space by weight averaging in a square window surrounding that sample. If sample value is greater than the obtained threshold, its related frequency is considered as moving target frequency, otherwise it is rejected.

Beside functions mentioned above, one other necessary function which is performed in MTI radar systems is Pulse Compression. Pulse compression is a technique by which it is possible to provide both appropriate level of transmitted power and also high radar bandwidth for better range resolution. In this technique, high length pulse is generated in radar transmitter to meet transmitted power limit. On the other hand, transmitted signal bandwidth increases using specific kinds of phase or frequency modulation. Using an adaptive filter in the receiver, high length pulse is processed and its bandwidth decreases. One well known method to generate high length pulses with high bandwidth utilizes Barker Code pattern. In this method, a pulse with a length of T is divided into a specified numbers of narrow pulses (equal to Barker Code length) with a length of τ ($\tau \ll T$). Then according to the Barker Code pattern, a phase of 0 or π is assigned to each of narrow pulses. Adaptive filter in receiver correlates received signal by Barker Code to reach a powerful narrow width pulse [1].

3. GPU: GENERAL PURPOSE

The main task for Graphics Processing unit (GPU) is the projection of 3D polygon on a 2D plane. Parallel mechanism, which is employed by GPU to speed up rendering, comprises two types of processors: Vertex Processors (VPs) and Fragment Processors (FPs). In modern GPUs, FPs presents higher performance rather than VPs. So in most general applications, GPUs utilize FPs as computational engine. These applications employ stream programming. In stream programming, data is organized into streams and computations are expressed as a kernel that operates on the streams [2]. Streams in these applications are usually located in the video memories of textures that are able to be fetched into FPs. Kernel is a program that is provided for FPs. The output results can be transferred from video memory to main memory using API such as OpenGL. Vectorization

is necessary to obtain maximum advantages of GPUs, since FPs are structured to process RGBA vector which is an array of 4 elements. Therefore for optimal performance, data should be arranged in 4-element vectors [4].

4. MTI RADAR ON THE GPU

Programs to be implemented on GPUs must be compatible with GPUs architecture. Besides, amount and frequency of data communication between CPU and GPU must be minimized to approach the maximum performance.

To accelerate computation rate, the initial step is to locate data in the texture properly, so that intrinsic properties of the GPU are exploited optimally. Therefore, after reading the I & Q data from A/D buffers, two samples of data from channel I and two samples of data from channel Q are located alternatively in each pixel memory of the texture, which includes 4 elements of RGBA. Figure 4 illustrates I & Q data location in the pixel memory.

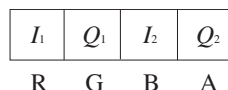


Figure 4: I & Q data location in pixel memory.

Data packet will be located in whole pixel memories of the texture. So, vector operation on 4-element data is done faster in this way.

After data loading to the texture, processing on the data begins. Processing steps respectively include Pulse Compression, Down Sampling, Delay Line Canceller, Filter Bank and CFAR. Each step is investigated as follows:

Pulse Compression: In this step, each output sample corresponding to a number of input samples (equal to Barker Code length) is calculated by adding all results from multiplying each input sample to the related element of Barker Code array. This function is expressed as a kernel to input streams in GPU programming. Since vector operations are executed faster on GPUs, the function is implemented using inner product of Barker Code array and the mentioned numbers of input stream.

Down Sampling: In this step, every n samples obtained from previous step are averaged and the result is sent to the output. In fact, number of samples decrease by $1/n$. Function of averaging is applied in the form a kernel to the input stream to this step.

Delay Line Cancellers: Samples of two consecutive cycles of the input stream are subtracted from each other in this step. Like previous mentioned functions, the function of subtraction is employed as a kernel to GPU.

Filter Banks: In this step, FFT is applied on corresponding samples of 16 consecutive cycles of input stream that the result for each set of samples is the frequency response for those samples. These samples are all echoes from one specific point in radar's scope. FFT function on each set of samples is applied on the stream of data as a kernel.

CFAR: In this step, in order to detect desirable moving targets, it is necessary to find an adaptive threshold for each sample, if the threshold value is greater than sample value the output is equal to zero otherwise the output is identical to sample value. This threshold value is obtained by weighted averaging over a window in spatial-frequency space. This function is likewise applied on data as a kernel. We implemented the given processing method on the GPU using C++, OpenGL library and shader programming [3]. In following section, a conclusive discussion is presented.

5. DISCUSSION AND CONCLUSION

To evaluate GPU's performance as the processor of MTI radars, we should estimate the amount of required operations executed in time unit for appropriate results with desirable speed. Then by comparing results of implementation on GPU and CPU in similar condition, their ability as MTI processor is evaluable. For this purpose, the features in Table 1 were considered in both processors.

According to the Table 1, amount of operations in each step and operations in the whole procedure obtained that is shown in Table 2. The first column in the table is the function executed in each step. The second column is the number of operation on each sample; the third column represents number of samples under computation in unit time. The last column shows total operations done in time unit.

Table 1: Considered features value in analysis.

Feature	Value
Barker Code Length	13 Elements
Down Sampling Ratio	1/5
CFAR Window	8×8 Spatial Frequency Window

Table 2: Operation Volume in processing steps.

Step of Processing	Number of operation on each sample	Number of samples affected in time unit	Total Operation
Barker Code	28	20 M	560 M
Down Sampling	5	20 M	100 M
D-L Cancellor	2	4 M	8 M
Filter Bank	256	4 M	1024 M
CFAR	64	4 M	256 M
Total Procedure	- - - -		1948 M

A/D buffers of I/Q channels deliver approximately 20 M samples in unit time to the processor. In addition, some other operations must be employed to communicate between functions and also display results in final step which aggregately number of operations exceed 2000 M. Although more than this amount is executable by CPUs, this goal realizes when the whole data can exist and locate consecutively in main memory of CPU. Moreover jumps in different data locations to access consecutive cycles of signal, decrease efficiency of using CPU in MTI processing, while 2D structure of GPU's memory omits this problem by appropriately arrangement of data.

Implementation applied to GPU "GeForce8800 GTS" and CPU "Core Duo 3GHz". GPU executed operations in less than **0.5 sec** whereas CPU took **2 sec** to perform operations. Therefore, implementation on GPU is restricted by amount of data received from A/D buffers, while CPU itself limits processing speed.

It can be concluded that GPUs are proper apparatus as radar's processor. Compatibility of radar algorithms and GPU structure has caused using these apparatuses in many radar applications such as radar algorithms evaluation. Besides, GPUs price is about 5% of DSPs and implementation and debugging of algorithms are much easier using GPUs.

REFERENCES

1. Skolnic, M. I., *Introduction to RADAR Systems*, 3rd Edition, McGraw Hill, 2000.
2. GPGPU: General-purpose Computation Using Graphics Hardware, <http://www.gpgpu.org/>.
3. ATI Technologies Inc., "Image processing with pixel shader in OpenGL".
4. Ino, F., J. Gomita, Y. Kawasaki, and K. Hagihara, *A GPGPU Approach for Accelerating 2-D/3-D Rigid Registration of Medical Images*, Springer Berlin, 2006.

Can We Build an Adaptive Fractal Radio System?

A. A. Potapov

Institute of Radio Engineering and Electronics of Russian Academy of Sciences
Building 11, Mokhovaya Street, Moscow 125009, Russia

Abstract— Main results of theoretical and experimental investigations since eighties of XX that led to formation and developing of new fundamental science discipline: “Fractal Radio Physics and Fractal Radio Electronics: Fractal Radio Systems Designing” are briefly classified in the paper.

1. INTRODUCTION

For a long time stationary behaviors and periodical motions were assumed to be the only possible conditions. However the discoveries of the latter part of XX century principally changed our idea of dynamic processes behavior. Now we realize that our world is not only non-linear but also is fractal. At present the lack of conventional physical models is obviously felt. In other words the full description of signals and fields up-to-date processing is impossible via classical mathematics formulas.

It is absolutely evident for the author that the application of scale invariance (“scaling”) conceptions and of modern functional analysis, which are related with set theory, theory of fractional dimension, general topology, geometrical measure theory and dynamic systems theory, to modern informational technologies reveals great potential opportunities and new prospects in multidimensional signals processing and in the related scientific and technical areas.

Aim of the work — sufficiently thorough and at the same time compact presentation of “fractal computing technique” and “fractal language” for a quantity of modern physical and applied problems.

2. THE MAIN COURSES OF “FRACTAL” INVESTIGATIONS

In the Figure 1, there are main lines of researches that are performing in IREE RAS and also information about the moment of its intensive growth; for the details see references [1–4]. The author and his subordinate research group perform all the investigations exceptionally in the framework of the new fundamental interdisciplinary project in IRE RAS which is briefly called as “*Fractal radio physics and fractal radio electronics: Fractal radio systems designing*”. The main principles of this course are investigated by the author in IRE RAS as noted earlier *since the eighties of XX century*. In the beginning this work concerned the super-poor radio signals and images filtering for the non-Gaussian interference.

Then it became clear that such a “fractal” approach was useful for other problems. It is natural for such “fractal” approach to focus attention on description and processing of radio physics signals (fields) exceptionally in fractional measuring space using hypothesis of scaling and distributions with “heavy tails” (stable distributions). Note that scale transformations and scaling effects are widespread in present physics when relationships between different thermodynamics values in renormgroup phase transition theory are established.

Fractals belong to sets which have extremely branched and irregular structure. In December of 2005 in USA B. Mandelbrot approved [3] of fractal classification that was developed by author and that is presented in the Figure 2, where fractal features are characterized so long as space where the fractal structure with a fractal dimension D is considered has topological dimension D_0 .

Physic mathematical problems of the fractals theory and fractional measuring are represented in monographs [1–3] in detail.

Here the main results of fractal approaches of information processing are presented and most perspective fields of application of fractal theory, scaling conception and deterministic chaos in radio physics and radio location are considered. More detailed results are presented in [1–21].

While the concept of an FDI (Figure 2) operator was known as early as the end of the 17th century, wide application of fractional calculus in science and technology started in the late 1980s–early 1990s. A fractional integral is the generalization of an n -dimensional integral, and fractal functions that are not differentiable everywhere in the standard sense can be differentiable in the Rie-mann-Liouville sense [1, 2].

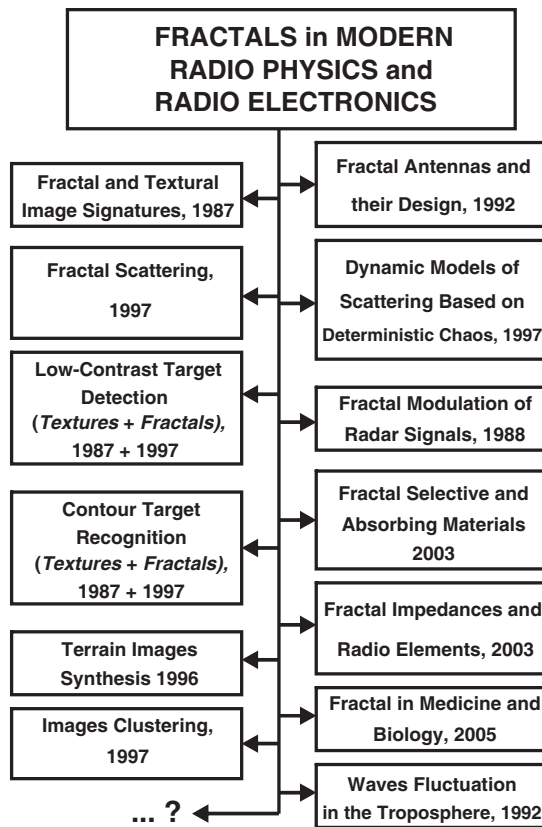


Figure 1: Sketch of a new information technologies development in IREE RAS.

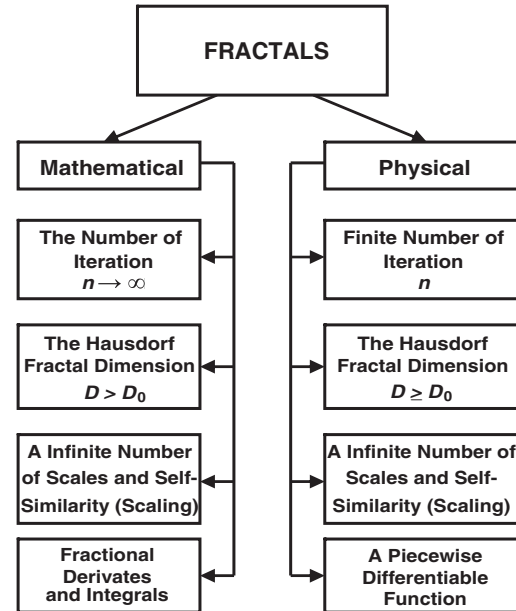


Figure 2: Fractal sets and fractal signatures classification and morphology.

3. FRACTAL PROCESSING OF ONE DIMENSIONAL AND MULTI DIMENSIONAL SIGNALS FOR THE LOW-TO-NOISE RATIIONS

We start with works that for the first time revealed one of fundamental application of fractal theory — processing of one-dimensional and multi-dimensional signals for low ratios of signal-to-noise q_0^2 (Figure 3).

Full description of the signals and fields up-to-date processing processes is impossible using classical mathematics formulas [1–4].

Fractal numerical methods that are being worked up allow us to overcome partly a priori uncertainty in radar problems using information about geometry (topology) of sampling — one-dimensional or multi-dimensional [1–4].

At that topological features of individual sampling take on special significance rather than averaged realizations that often have absolutely different behavior.

Characteristics of classical and original measuring methods for fractal dimension D , fractal signatures and respective fractal cepstrums of one-dimensional and multi-dimensional, which are being used in IREE RAS and which are experimentally examined, are presented in [1–7].

4. THE AUTHORS CONCEPTION OF FRACTAL RADIO ELEMENTS AND FRACTAL RADIO SYSTEMS

Creation of the first target classes fractal characteristics etalon dictionary and permanent improvement of algorithmic supply are the main steps at development of *the world first fractal non-parametric radio signals detector* as specially designed processor [3, 8].

Basing on the results obtained one can say directly about design of *fractal radio systems* but not only of fractal elements (devices) [1–5, 8, 13–15]. Such fractal radio systems (Figure 4) that structurally include (starting with entry) fractal antennas and digital fractal detectors are based on the information processing fractal methods and can use radio signals modulation and demodulation fractal methods [1–4].

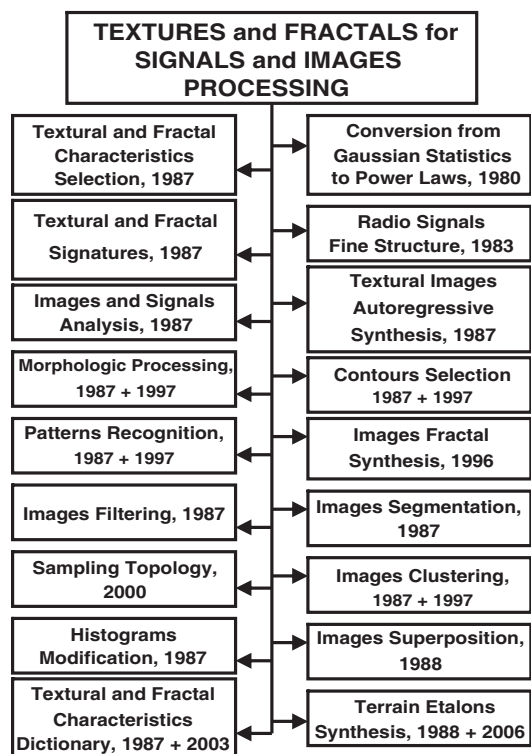


Figure 3: Textural and fractal methods of processing of low-contrast images and poop signals in non-Gaussian interferences.

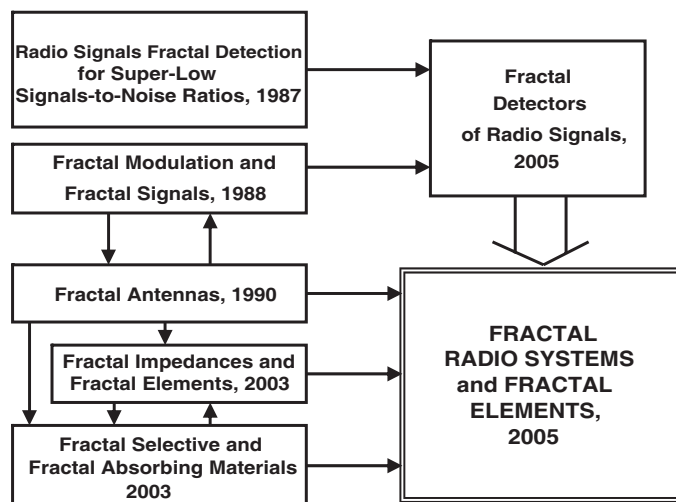


Figure 4: The author conception of fractal radio systems.

5. FRACTAL ANTENNAS AND FRACTAL RADIO ABSORPTION MATERIALS AND SURFACES \equiv FRACTAL FREQUENCY SELECTIVE SURFACES AND FRACTAL IMPEDANCE = “CLEVER” MATERIALS

Antenna devices and frequency selective surfaces (FSS) are essential part of the radio system. Experience of analysis and synthesis of the fractal antennas prove wideband and multiband properties [1–3, 5, 6, 10, 15]. Therefore such fractal antennas are highly effective in development of two-frequency and multi-frequency radar-location and telecommunication systems.

Fractal antenna works because of wire-geometry, but doesn't due to accumulation of different components or elements (as for classical antennas), that increase complexity and potential destruction points. The fractal antennas also allow to create multiband version, reduced scale, and optimal or “smart” antenna technology. A merit of fractal antennas (monopole and dipole) are that they have a lesser resonance frequencies then classical (Euclid) antennas of the same size. Native wide-band merit of fractal antennas are ideal for intellectual applications and protection.

In contrast to traditional methods, when smooth antenna directional diagrams are synthesized, in the base of fractal synthesis theory is a idea of realization radiation characteristics with periodic structure on arbitrary scale. This gives us possibility to create new regimes in *fractal electrodynamics*, and to obtain principle new features. In particular, placing fractal antennas on the object corps can significantly distort signature or radio location image of current object.

Application fields of the fractal antennas: modern telecommunications, noise radio location, non linear radio location, retrieval systems, localization and mobile object tracing, direction-finding in complex city conditions, detection of location of a unauthorized radio sources in struggle against terrorists, modern physical experiments and other.

Under the direction of author on the base of algorithms of a numerical solution of hyper-singular integral equations analysis was performed of electro dynamical properties of different *fractal antennas* (monopole and dipole with the help of classical Serpinsky curve and Keily tree of different iteration orders) analysis was performed for fractal antennas with variable apical angle. Input impedances of fractal antennas $Z = \text{Re}Z + i\text{Im}Z$ were calculated in the range 0.1–10.0 GHz and determined all resonance frequency of considered fractal antennas (fractal FSS). First calculation of electromagnetic fields structure in the near-field region was calculated of concerned fractal antenna.

Broad measurement results in anechoic room confirmed numerical results.

Practically sum of random values doesn't converged to the Gaussian distribution, but a stable or "Levi-Pareto" distributions with heavy tails (i.e., fractal distributions — paretians). Their distribution function is a "broad". This leads to some frequency moments of this distribution are formally infinite. Modeling of Levi-Pareto distribution of random values leads to anomaly diffusion processes, which described by fractal space or/and time derivative. As a matter of fact, the equations with fractal derivative are describe non-Markov process with memory (*heredity*).

Physical modeling of fractal integration and differentiation operators allows on the base of nanotechnology create radio elements on the passive elements, which modeling fractal impedance with frequency scaling

$$Z(\omega) \equiv A(j\omega)^{-\eta}, \quad (1)$$

where $0 \leq \eta \leq 1$, A — *const*, ω — radial frequency.

For that independently of [1–3] an impedance $Z(\omega)$ model was designed like (infinite) chain fraction. In case of final stage of creation of the equivalent electric circuit for RC -chains, where we use n -th appropriate fraction to the infinite fraction, it's possible to handle bandwidth, where powered dependence like $\omega^{-\eta}$ is presented.

Thus we first realize non-linear "fractal condenser" in practice of analog and digital view [1, 2, 18, 19], which was interested by the private meeting B. Mandelbrot. It worth to add to this direction a number of modeling problems of the microelectronic fractal impedance for the fractal radio elements of low- and high-frequency range of wave length.

6. CONCLUSION

As result of lecturing on the fractal technologies developed by author in IREE RAS and reports on ISTC project in USA (Washington, New-York, Huntsville, Atlanta, Franklin) in 2000 and 2005, American specialists wrote in official letter for Director of IREE RAS academician Yu. V. Gulyaev in December of 2005. "... *Dr. A. Potapov has successfully presented several seminars in the Center for Space Plasma and Aeronomic Research (CSPAR) at the University of Alabama in Hunstville. The seminars were of essential interests and confirmed high scientific credentials of Dr. A. Potapov. RADAR technologies presented by Dr. Potapov are novel and based on the fractal theory. Their importance for the international community of specialists and scientists is undeniable*". At the same time (December of 2005) scientific meeting of author and fractal geometry founder B. Mandelbrot [3].

Fundamental steps consisted in transfer of integer measuring signals received by radio system into fractional measuring space using scaling relations; allow to introduce absolutely new conceptions and approaches in conventional fields of the classical radio physics and radio electronics and to obtain sufficiently unexpected for practice but physically validated results on the basis of these conceptions.

New challenging information technologies development and introduction on the basis of fractal radio physics and fractal radio electronics principles relates with training of specialists for these scientific fields. First of all, in a number of universities there is a need to organize courses on the *simultaneous study* of fractal theory foundation, determined chaos theory, fractional operators theory and its physical-technical application.

Methodological base (see for example monographs [1–4]) for these purposes has already been studied sufficiently. For the same purpose author established scientific-technical journal "*Nelineiniy mir*" ("*Nonlinear world*") in 2003 that represents fundamental investigation lines of physics, mathematics and other natural and humanitarian sciences from interdisciplinary positions of synergetics and non-linear dynamics (it was included in HCC list in 2006, index in All-Russian catalogue 82651) [11].

ACKNOWLEDGMENT

This work was financially supported by Russian Foundation for Basic Research (projects No. 05-07-90349-v, No. 07-07-07005-d, No. 07-07-12054 and No. 07-08-00637-a).

REFERENCES

1. Potapov, A. A., *Fractals in Radio Physics and Radar*, Logos, Moscow, 2002.
2. Potapov, A. A., *Fractals in Radio Physics and Radar: Topology of Sample*, University Library, Moscow, 2005.

3. Potapov, A. A. and R. M. Crownover, *Introduction to Fractals and Chaos*, 374–479, Tekhnosfera, Moscow, 2006.
4. Potapov, A. A., Y. V. Gulyayev, S. A. Nikitov, A. A. Pakhomov, and V. A. German, *Newest Images Processing Methods*, Edited by A. A. Potapov, FIZMATLIT, Moscow, 2008.
5. Potapov, A. A., “Innovation in radio engineering information — Telecommunication technologies,” *Proc. Jubilee Sci.-Tech. Conf. Dedicated to the 60th Birthday of OAO Radiotekhnicheskii Inst. im. A.L. Mintsa and Faculty of Aircraft Electronics, Moscow Aviation Inst.*, Part. 1, 66–84, Moscow, Oct. 24–26. 2006.
6. Potapov, A. A., “Workshop on space antenna systems and technologies,” *Proc. 28th ESA Antenna*, Part 2, 1047–1050, ESTEC, Noordwijk, Netherlands, May 31–June 3, 2005.
7. Potapov, A. A., *Synergetic*, Vol. 8, 163–179, Moscow, 2006.
8. Potapov, A. A. and V. A. German, “Optoelectronics, instrumentation and data processing,” Vol. 42, No. 5, 3–25, 2006.
9. Gulyaev, Yu. V., S. A. Nikitov, A. A. Potapov, and V. A. German, “Concepts of scaling and fractal dimension in the design of a fractal detector of radio signals,” *Journal of Communications Technology and Electronics*, Vol. 51, 909–915, 2006.
10. Potapov, A. A., *Journal of Communications Technology and Electronics*, Vol. 52, 245–292, 2007.
11. Potapov, A. A., *Nonlinear World*, Vol. 1, 3, 2003.
12. Potapov, A. A., *Application and Industry Mathematics Review*, Vol. 14, 742–744, 2007.
13. Potapov, A. A., *Nonlinear World*, Vol. 5, 415–444, 2007.
14. Potapov, A. A., *Nonlinear Radar*, edited by A. A. Gorbachyov, A. P. Koldanov, A. A. Potapov, and E. P. Chigin, Vol. 3, 5–34, (“Nonlinear World Journal Library: Scientific Series “Fractals. Chaos. Probability”), 2007.
15. Potapov, A. A., E. N. Matveev, V. A. Potapov, and A. V. Laktyunkin, *Proc. of the Second European Conference on Antennas and Propagation EuCAP 2007*, ThPA.031. pdf. 6 pp., Edinburgh, UK, November 11–16, 2007,
16. Potapov, A. A. and A. V. Laktyunkin, *Proc. of the Second European Conference on Antennas and Propagation EuCAP 2007*, MoPP.016. pdf. 6 pp., Edinburgh, UK, November 11–16, 2007,
17. Laktyunkin, A. V. and A. A. Potapov, “Waves scattering dependence on the statistical parameters of classical and fractal rough surfaces,” *Proc. XXIX URSI General Assembly*, BP16.1 (228). pdf., Chicago, Illinois, USA, August 7–16, 2008, <http://ursi.org/Chicago08/Index%20GA08.htm>.
18. Potapov, A. A., A. A. Potapov, (Jr.), and V. A. Potapov, *Nonlinear World*, Vol. 4, 172–187, 2006.
19. Potapov, A. A., “Fractional operators and fractals for non-linear radio physics problems,” *Abstracts 3rd IFAC Workshop on Fraction Differentiation and its Applications FDA’08*, 55, pdf. 5 pp., Ankara, Turkey, November 5–7, 2008.
20. Potapov, A. A., “The fractal methods of investigations of the signals fluctuations and the dynamic systems in the fractional dimension space,” *Fluctuations and Background in Complex Systems of the Organic and Inorganic Nature*, Ministry of Education and Science of Tatarstan Republic, Kazan, 257–310, 2008.
21. Potapov, A. A., A. Kh. Gil’mutdinov, and P. A. Ushakov, *Fractal Elements and Radio Systems: Physical Aspects*, Edited by A. A. Potapov, Radiotekhnika (Series Fractal. Chaos. Probability. Editor A. A. Potapov), Moscow, 2009.

Eddy Current Modeling in Composite Materials

M. Cacciola, S. Calcagno, G. Megali,
D. Pellicanó, M. Versaci, and F. C. Morabito
University “Mediterranea” of Reggio Calabria, DIMET
Via Graziella Feo di Vito, Reggio Calabria I-89100, Italy

Abstract— The production of carbon fiber reinforced polymers, which are widely used both in civil and military applications, is an elaborate process un-free from faults and problems. Problems during the manufacturing, such as plies’ overlapping, can cause flaws in the resulting material, this way compromising its integrity. Compared with metallic materials, carbon epoxy composites show a number of advantages: Higher tensile strength, lower density and coefficient of thermal expansion, absence of fatigue state related phenomena, possible manufacturing of large layered structures. Within this framework, this work aims to propose a design of ferrite core probe for eddy current non destructive evaluation, in order to investigate the presence of defects in carbon fiber epoxy composite materials. The effect of the ferrite core is analyzed in order to focus magnetic flux density on the investigated specimen. Eddy currents generated by high speed ferrite core probe movement were investigated by using numerical simulation. Particularly, a Finite Element Approach has been exploited in order to characterize the transducer to specially emphasize the presence of defects in a multi-layer carbon fiber epoxy structure.

1. INTRODUCTION

Given their specific characteristic, the Carbon Fiber Reinforced Polymers Epoxy (CFRP/E) composites are used in different application, from aerospace industry to civil applications. Nowadays, air companies exploit airplanes of their fleets as much as possible in order to amortize purchase and maintenance costs, in a sort of trade-o with the high safety requirements. Moreover, it is easy to understand how mechanic solicitations and atmospheric agents are responsible for a relatively rapid degradation of airplanes’ structures. Therefore, they must be produced in an almost perfect state, in order to not introduce other dangerous risk factors. But the manufacture process of CFRPs can induce a number of characteristic flaws, e.g., delaminations, inclusions, porosities. Therefore, it is absolutely necessary to carry out cheap tests of conformity and integrity. Thus, Non-Destructive Testings (NDTs) and in particular ferrite core Eddy Current (EC) probes are useful for our aims. In fact, it is possible to easily analyze even highly thick metallic as well as nonmetallic materials, with a good resolution and a remarkable operative versatility [1]. This technique, based on the investigation of magnetic flux of coils placed close to the specimen under analysis, is used to detect and characterize possible flaws or anomalies in workpieces. Typical testing configurations may consist of ferrite core coil probes, placed above a planar (or at least locally planar) conductive specimen and operating in the time-harmonic domain, at frequency depending on the problem (typically between a few [Hz] to a few [MHz]) [2]. The aim of ferrite core is to focus the magnetic fields into the specimen, in order to increase the probe sensitivity to the defect. For each application, the coil model as well as the operating frequencies are set according to the task. This work proposes an integrated approach starting from the design and implementation of a novel probe in order to optimize the sensor effect and the drop-in suppression, the operating parameters of the frequency and field strength. For our purposes, a Finite Element Analysis (FEA) code will be exploited for geometrical and physical modeling. Problems are so related to the possibility of classifying the flaw starting from the eddy current measurements. Various solutions are known in scientific literature to solve this kind of inverse problem [3]. In particular, an essential approach is due to advances of computational intelligence techniques. The paper is structured as follows. Section 2 briefly describes the electrical properties of carbon fiber. Section 3 presents the FEA approach. Subsequently, results about crack detection are shown. Finally, Section 4 draws up our conclusions.

2. CARBON FIBER ELECTRICAL PROPERTIES

In this section, a characterization of electromagnetic properties of CFRP materials is proposed. Knibbs and Morris [4] demonstrated that there is a linear relationship between the electrical resistivity and $\sin^2(\theta)$, where θ is the angle between the nominal lay of fibers with respect to the x -axis (see Figure 1). Carbon fibers have an intrinsic electrical conductivity; therefore, one might expect that the composite material made from these fibers would be electrically conductive in the

direction of the fibers. However, considerable transverse electrical conductivity is also observed. This transverse conductivity is a result of significant fiber-to-fiber contact. As might be expected, the longitudinal conductivity increases linearly with the fiber volume fraction. The transverse conductivity increases with the fiber volume fraction in a more complicated scaling relationship. The electrical anisotropy depends on the volume fraction of the material; hence, the longitudinal conductivity varies between 5×10^3 and 5×10^4 [S/m] while the transverse conductivity between 10 and 100 [S/m]. When the unidirectional layers are composed in a cross-ply forming a composite plate, there is the presence of a cross-ply [4], equal to 7633 [S/m]. Another peculiarity of these materials concerns the trend of the induced currents: They have an elliptical pattern caused by the anisotropy (see Figure 5).

3. FEA APPROACH

In this section of the paper, we want to show how simulate the behavior of a ferrite cored EC in order to detect delamination defects in CFRP materials. The simulations exploit the Finite Element Method (FEM) and require geometrical and physical definition of the same coil, its ferrite core and the CFRP plate. The exciting current, i.e., I_{eff} , and the frequency, i.e., f_{exc} , have been chosen according to the skin-effect phenomenon. For our purpose, we verified the distortion of EC's flux lines (A/m^2) caused by the presence of defect and the magnetic field's density (T) while the probe moves right over the surface defect. In our FEAs we use the $\mathbf{A} - \psi$ formulation [5]. In a general subdomain Ω , the magnetic potential \mathbf{A} is obtained by:

$$-\nabla \cdot (j\omega\sigma - \omega^2\epsilon_0\epsilon_r) \mathbf{A} - \sigma \mathbf{v} \times (\nabla \times \mathbf{A}) + (\sigma + \omega\epsilon_0\epsilon_r) \nabla V - \mathbf{J}^e = 0 \quad (1)$$

$$(j\omega\sigma - \omega^2\epsilon_0\epsilon_r) \mathbf{A} + \nabla (\mu_0^{-1}\mu_r^{-1}\nabla \times \mathbf{A}) - \sigma \mathbf{v} \times (\nabla \times \mathbf{A}) + (\sigma + \omega\epsilon_0\epsilon_r) \nabla V = \mathbf{J}^e \quad (2)$$

where σ is the conductivity; ω is the angular pulsation; μ_0 and μ_r are the void's magnetic constant and the material's permeability respectively; ϵ_0 and ϵ_r are the void's and the material's dielectric constants, respectively; \mathbf{v} is the instantaneous velocity of the object derived from the expression of the Lorentz force and \mathbf{J}^e is the external current density on exciting coil. \mathbf{v} has been varied, and set to 5, 10 and 15 m/s. In order to set point-by-point \mathbf{J}^e , we used the direction cosine trigonometric formulation [6]. The ferrite core probe has been modeled according Figure 2 and Table 1. In our FEA code, we set the boundary conditions as follows. Magnetic insulation ($\mathbf{n} \times \mathbf{A} = 0$ derived from

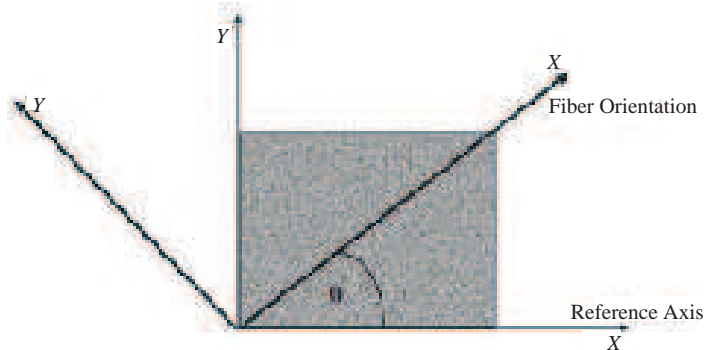


Figure 1: Relation between the principal axes, reference axes, and fiber orientation.

Table 1: Coil and E-shaped ferrite-cored dimensions.

Coil (mm)	E-shaped core (mm)
External diameter: 6	F: 4
Internal diameter: 4	E: 8
Height: 2	A: 11
Number of turns: 18	B: 5.25
Lift-off: 0.005	D: 3.5
	D': 1.5
	H: 2

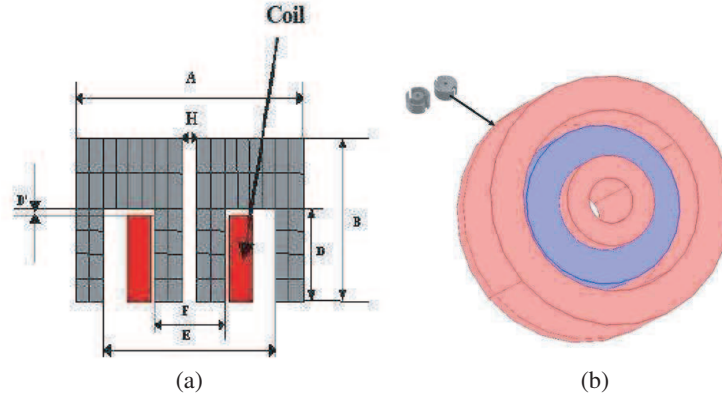


Figure 2: Design of the probe and the ferrite core, implemented in numerical simulations. (a) Probe constituted by a coil placed inside an E-profiled core (slice view), (b) 3D representation of the ferrite-core EC probe (the exciting coil, in blue, and ferrite core, in pink).

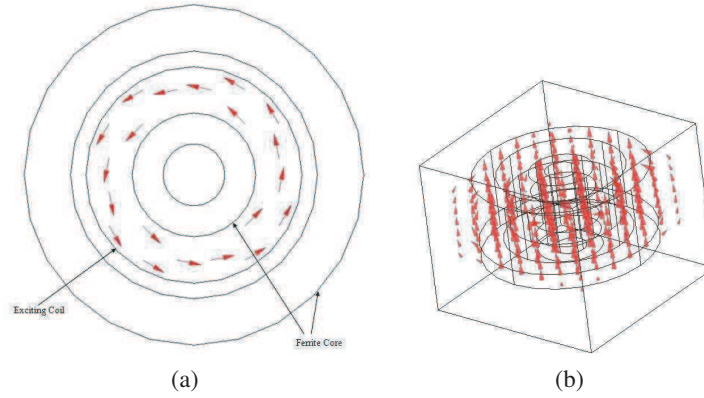


Figure 3: Exciting coil. (a) Current, (b) magnetic flux.

$\mathbf{B} \cdot \mathbf{n} = 0$), for fictitious subdomain (representation of an infinite volume) [8]. Regarding boundaries of plate, the continuity is insured by $\mathbf{n} \times (\mathbf{H}_1 - \mathbf{H}_2) = 0$ [8]. Our studies have been based on a discrete domain [9] having number of elements equal to 17287. Mesh has been generated with tetrahedral elements and a geometric dimension of 0.5 (mm) for the CFRP plate, the exciting coil and its ferrite core. The composite plate $[90^\circ, 0^\circ, 90^\circ]$ with dimensions 7 [cm] \times 4 [cm] \times 3 [mm] has been modeled with three parallelepipeds representing three different layers. The conductivity of the CFRP plate is given by the following expression:

$$[\sigma] = [R]^{-1} \cdot [\sigma'] \cdot [R] \quad (3)$$

where $[R]$ is a rotation matrix which relates the components in the primed coordinate system to the unprimed coordinate system (see Figure 1). Respectively, $[R]$ and $[\sigma']$ are equal to:

$$[R] = \begin{bmatrix} \cos \theta & -\sin \theta & 0 \\ \sin \theta & \cos \theta & 0 \\ 0 & 0 & 1 \end{bmatrix} \quad (4)$$

$$[\sigma'] = \begin{bmatrix} \sigma_l & 0 & 0 \\ 0 & \sigma_t & 0 \\ 0 & 0 & \sigma_{\text{cross}} \end{bmatrix} \quad (5)$$

where σ_l is the conductivity along the fibers, σ_t is the conductivity transverse to the fiber and σ_{cross} is the conductivity with overlapping of unidirectional layers [7]. These reference axes, along which the conductivity matrix is diagonal, are called the principal axes. When the fibers are oriented at some arbitrary angle θ (as shown in Figure 1) with respect to the x -axis, the conductivity matrix is no longer diagonal and there is cross coupling of the components. Figure 4 illustrates the eddy currents distribution for various fiber orientation. During our computer simulations, frequency f_{exc} ,

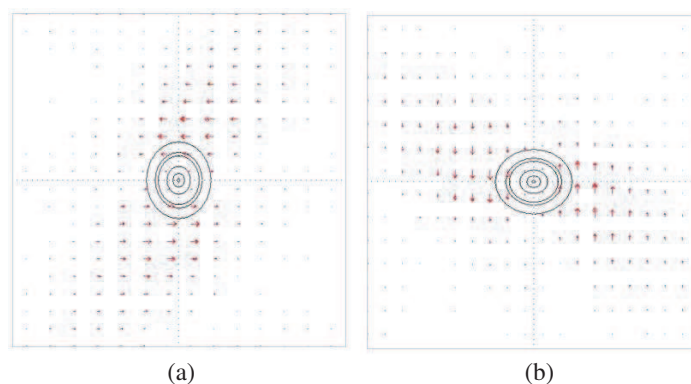


Figure 4: XY plane: Eddy current distribution for various fiber orientations. (a) Fiber orientation: 0 Degrees, (b) fiber orientation: 90 Degrees.

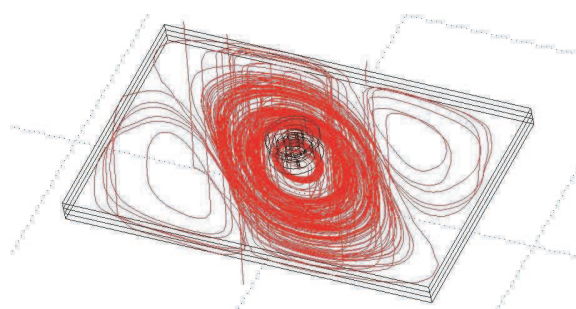


Figure 5: Elliptical pattern for induced currents.

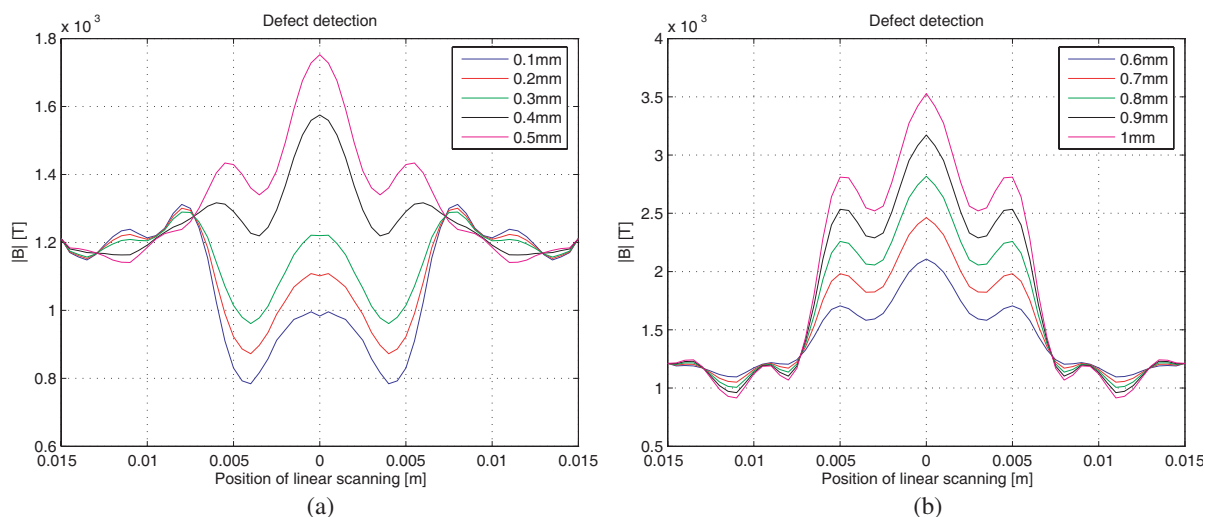


Figure 6: Variation of magnetic flux with respect on linear scanning direction with variation of the dimension of the crack.

current I_{exc} and the size of the defect have been varied. Figure 6 depicts results of the analysis for different size of defect in CFRP, with a $f_{exc} = 1$ [MHz] and a $I_{exc} = 100$ [mA]. Figure 6 shows results of numerical simulations for a cylindrical defect's with a basis' diameter from 0.1 [mm] to 1 [mm]. It is possible to note a clear magnetic field's variation for $x = 0$ [mm]. Figure 6 shows that an increasing of defect's dimension corresponds to an increasing of magnitude of magnetic flux density, from $1.2 \cdot 10^{-3}$ [T] to $3.5 \cdot 10^{-3}$ [T]. We expect such kind of increment also in real applications, but other experimental conditions (e.g., absence of perfect geometry) may affect the increment itself. Figure 7 describes how the magnetic field in high-speed case is asymmetric. In general, the magnetic field strength decreases when the probe speed is increased. Therefore, eddy currents due to probe movement not only distort the prole of magnetic field but also decrease the

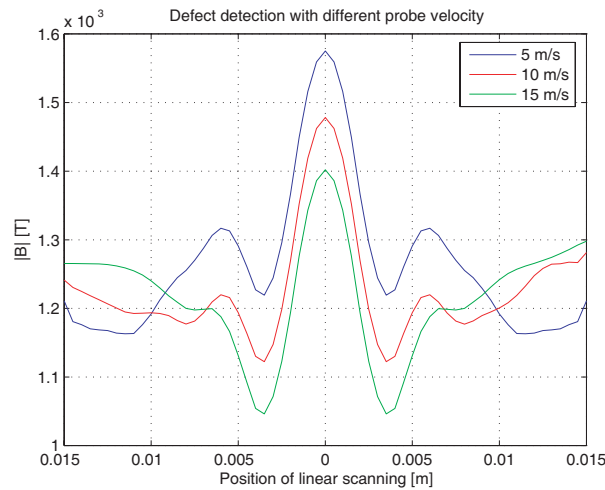


Figure 7: Magnitude of B vs. position of linear scanning against probe velocity.

intensity of the magnetic field during the inspection.

4. CONCLUSION

In this paper, an implementation of high speed ferrite cored EC probe for detection of defect in composite materials is presented. Based on numerical simulations carried out with a FEM based approach, eddy currents and magnetic flux's density variations during the inspection have been investigated. For the implementation of ferrite core EC probe, a time-harmonic FEA code with 3-D geometries has been studied to evaluate the progressive increase of the investigation size of the defect for the variation of magnetic flux density (in modulus). The proposed method provides a good overall accuracy in detecting defect's presence, as our simulations demonstrate. At the same time, the procedure should be validate for defect with different shape of for different ferrite core probe profiles. The presented results can be considered as preliminary results; further work suggests the possibility to focus on the development of the proposed high speed inspection system, which involves: Probe design and optimization based on 3-D numerical simulations; feature extraction from FEA signals; defect characterization using signal processing techniques and Artificial Neural Networks for inversion algorithms at high speed measurements. The authors are actually engaged in this direction.

REFERENCES

1. Yamada, S. M., "Eddy-current testing," *IEEE Trans. Magn.*, Vol. 31, No. 6, 3185–3187, 1995.
2. Theodoulidis, T. P., "Model of ferrite-cored probes for eddy-current nondestructive evaluation," *J. Appl. Phys.*, Vol. 93, 3071–3078, 2003.
3. Doyum, A. and M. Duerer, "Defect characterization of composite honeycomb panels by non-destructive inspection methods," *Proceedings DGZfP Conference*, Weimar, Germany, 2002.
4. Knibbs, R. H. and J. B. Morris, "The effects of bre orientation on the physical properties of composite," *Composites*, Vol. 5, No. 5, 209–218, 1974.
5. Roger, D., P. J. Leonard, and H. C. Lai, "Interfacing the general 3D A- ψ method with a thin sheet conductor model," *IEEE Trans. Magn.*, Vol. 28, No. 2, 1115–1117, 1992.
6. Cacciola, M., S. Calcagno, G. Megali, F. C. Morabito, D. Pellicano, and M. Versaci, "FEA design and misfit minimization for in-depth flaw characterization in metallic plates with eddy current nondestructive testing," *IEEE Trans. Magn.*, Vol. 45, No. 3, 1506–1509, 2009.
7. Pratap, B. and W. F. Weldon, "Eddy currents in anisotropic composites applied to pulsed machinery," *IEEE Trans. Magn.*, Vol. 32, No. 2, 437–444, 1996.
8. Tsuboi, H. and T. Misaki, "Three dimensional analysis of eddy current distribution by the boundary element method using vector variables," *IEEE Trans. Magn.*, Vol. 26, No. 2, 454–457, 1990.
9. Weissenburger, D. W. and U. R. Christensen, "A network mesh method to calculate eddy current on conducting surfaces," *IEEE Trans. Magn.*, Vol. 18, No. 2, 422–425, 1982.

The Use of Thin Layer Conditions for the Reconstruction of Objects Buried in a Layered Medium

Ö. Özdemir¹, H. Haddar², and A. Yaka¹

¹Istanbul Technical University, Turkey

²INRIA Saclay Ile de France & CMAP, France

Abstract— Higher order thin layer conditions for three layered media are derived and applied for the imaging of objects located in such a medium. These boundary conditions connects the field values at the boundaries of the middle layer, which allows one to obtain the field values at the lower boundary from the measured on the upper boundary. Then Reciprocity Gap-Linear Sampling Method (RG-LSM) is applied to image buried objects. Numerical simulations show that thin layer conditions gives quite satisfactory results.

1. INTRODUCTION

Equivalent boundary conditions are widely used for mathematical modeling in the solution of scattering problems [1, 2]. Here the main idea is to replace the complex scattering problem with simple one having new boundary conditions which can be solved in a more easier way than the original one. In electromagnetics, equivalent boundary conditions are especially used to model geometrical and physical properties of the actual structure in scattering, propagation and antenna problems. Equivalent Boundary conditions are called as Thin Layer Conditions when they are used to model thin layers [3]. These conditions are very important for practical application in which layered medium is involved, such as geophysics, underground imaging, etc. On the other hand, reconstruction of objects buried in layered medium has been very popular subject in many areas and constitutes an inverse scattering problem. They have very important practical applications such as mine detection, tumor cells recognition, etc. Several techniques have been developed to image buried objects. Among these methods, Reciprocity Gap Sampling Method (RG-LSM) [4] seems more attractive since it does not require the knowledge of Green's function of background medium.

To be able to use RG-LSM, we need to know the field values and its normal derivative on the boundary of the medium which the object is located. However, for three layered medium, it is not possible to obtain these data from real experiment. In this paper, thin layer conditions which gives relation between fields at the upper and lower boundary of layer are proposed to obtain the required data. Afterwards, RGLSM method is applied by using these data for the imaging of object.

In Section 2, thin layer conditions are derived for three layered medium having planar boundaries. Reciprocity Gap Sampling Method is then explained for two layered medium in Section 3. Finally, numerical results are presented to show the applicability of the proposed method in Section 4.

2. THIN LAYER CONDITIONS

Let us consider a thin layer Ω_δ of thickness δ with medium index n_δ , see Figure 1. Then total electric field in Ω_δ is given by $E = (0, 0, u_\delta)$ and satisfies

$$\Delta u_\delta + k_0^2 n_\delta^2 u_\delta = 0 \quad \text{in } \Omega_\delta \quad (1)$$

where k_0 denotes the wavenumber of the air and where n_δ denotes the medium index which might be complex. We shall set $k_\delta = k_0 \sqrt{n_\delta}$ where the square root is the one non-negative imaginary part.

Let $\partial\Omega_+^\delta$ and $\partial\Omega_-^\delta$ be the upper and lower boundary of the thin layer Ω_δ , respectively. u_δ^+ and $\frac{\partial u_\delta^+}{\partial n}$ show the field and its normal derivative at the $\partial\Omega_+^\delta$. In a same manner, u_δ^- and $\frac{\partial u_\delta^-}{\partial n}$ show the field and its normal derivative at the $\partial\Omega_-^\delta$. We would like to derive thin layer conditions that links $(u_\delta^+, \frac{\partial u_\delta^+}{\partial n})$ to $(u_\delta^-, \frac{\partial u_\delta^-}{\partial n})$ without solving (1). Derivation of these conditions is based on Taylor expansion of the fields.

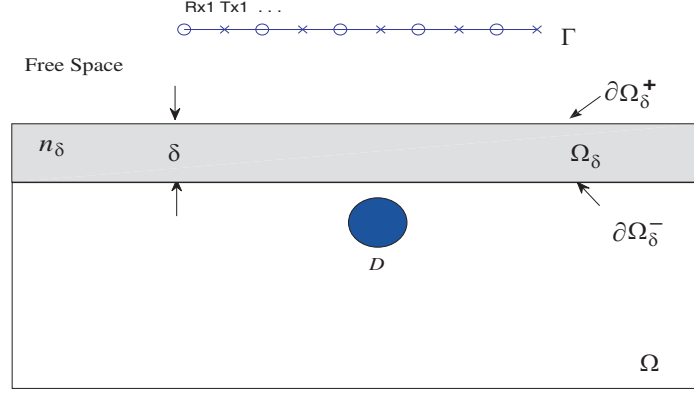


Figure 1: Geometry of three-layered medium.

Using Taylor expansion to get approximation of u_δ^+ in terms of u_δ^- and u_δ^- in terms of u_δ^+ ,

$$\begin{aligned} u_\delta^+ &= u_\delta^- + \delta \frac{\partial u_\delta^-}{\partial n} + \mathcal{O}(\delta^2) \\ u_\delta^- &= u_\delta^+ - \delta \frac{\partial u_\delta^+}{\partial n} + \mathcal{O}(\delta^2) \end{aligned} \quad (2)$$

If same procedure is applied to normal derivatives as follows,

$$\begin{aligned} \frac{\partial u_\delta^+}{\partial n} &= \frac{\partial u_\delta^-}{\partial n} + \delta \frac{\partial^2 u_\delta^-}{\partial^2 n} + \mathcal{O}(\delta^2) \\ \frac{\partial u_\delta^-}{\partial n} &= \frac{\partial u_\delta^+}{\partial n} - \delta \frac{\partial^2 u_\delta^+}{\partial^2 n} + \mathcal{O}(\delta^2) \end{aligned} \quad (3)$$

Before proceed further, let us precise some notation that will be adopted in the following. Let V be standing for u_δ or $\frac{\partial u_\delta}{\partial n}$. Then we set, $[V] = V^+ - V^-$ and $\langle V \rangle = \frac{1}{2}(V^+ + V^-)$. Since u_δ^- and u_δ^+ satisfy the Helmholtz Equation (1), we can replace their normal second derivatives with tangential second derivatives. By rearranging (3) and (4) the following second order thin layer conditions are obtained,

$$\begin{aligned} [u_\delta] &= \delta \left\langle \frac{\partial u_\delta}{\partial n} \right\rangle + \mathcal{O}(\delta^2) \\ \left[\frac{\partial u_\delta}{\partial n} \right] &= -\delta \left(k_\delta^2 + \frac{\partial^2}{\partial s^2} \right) \langle u_\delta \rangle + \mathcal{O}(\delta^2) \end{aligned} \quad (4)$$

where $\frac{\partial}{\partial s}$ shows the tangential derivative and k_δ shows the wavenumber of thin layer.

Notice that these conditions are called second order thin layer conditions since δ^2 and higher order terms are omitted in the Taylor expansion. If we want to derive $(k + 1)$ th order conditions, we have to include δ^k order terms in Taylor expansion.

3. RECIPROCITY GAP SAMPLING METHOD

For the sake of simplicity, in this section, we assume the background is two layered medium (without thin layer, only upper medium and the one object is buried). Let v be a field satisfying the Helmholtz equation in Ω with downward propagating condition. We define the *Reciprocity Gap* between $u(\cdot; x_0)$ and v by

$$\mathcal{R}(u(\cdot; x_0), v) := \int_{\partial\Omega} \left(u(x, x_0) \frac{\partial v}{\partial \nu_x}(x) - v(x) \frac{\partial u}{\partial \nu_x}(x, x_0) \right) ds(x). \quad (5)$$

where $u(\cdot; x_0)$ is the total field due to point source is located at x_0 . Notice that if there are no obstacles ($D = \emptyset$), then $\mathcal{R}(u(\cdot; x_0), v) = 0$. We now introduce a sufficiently rich parametrization of

the set of admissible functions v by choosing v to be a *single layer potential* defined by

$$v = s_g := \int_{\Lambda} g(y) \Phi(x, y) ds(y) \quad (6)$$

where g is an unknown potential and where

$$\Phi(x, y) = \frac{i}{4} H_0^{(1)}(k_1 |x - y|)$$

$H_0^{(1)}$ is the Hankel function of the first kind with the order zero and Λ is a straight horizontal line in the upper medium.

The RG-LSM amounts to find an approximate solution $g_z \in L^2(\Lambda)$ to the (integral) equation

$$\mathcal{R}(u(\cdot; x_0), s_{g_z}) \simeq \mathcal{R}(u(\cdot; x_0), \Phi(\cdot, z)) \quad \text{for all } x_0 \in \Gamma, \quad (7)$$

where z is a parameter, so-called sampling point, lying in the search domain Ω . In other words, for a given sampling point $z \in D$ one would like to test whether there exists a *regular solution* to the Helmholtz equation in Ω , namely s_{g_z} , whose reciprocity gap with $u(\cdot; x_0)$ coincides with reciprocity gap of a singular solution, namely $\Phi(\cdot, z)$, with the same fields and for all sources x_0 . Helmholtz equation outside D while $\Phi(\cdot, z)$ satisfies the equation with $-\delta_z$ source term. The method then stipulates that given an approximate solution to (7) the norm of $\|g_z\|$ would be much larger for z outside D than for z inside D .

From the practical point of view (7) can be written in the form

$$\mathcal{A}g_z \simeq \phi(\cdot, z) \quad (8)$$

where $\mathcal{A} : L^2(\Lambda) \rightarrow L^2(\Gamma)$ is the integral operator with kernel,

$$A(x_0, y) = \mathcal{R}(u(\cdot, x_0), \Phi(x, y)) \quad x_0 \in \Gamma, y \in \Lambda, \quad (9)$$

and where with

$$\phi(x_0, z) = \mathcal{R}(u(\cdot, x_0), \Phi(\cdot, z)) \quad x_0 \in \Gamma, z \in \Omega. \quad (10)$$

To construct an approximate solution to the ill-posed Equation (8), one can use the Tikhonov regularization by solving

$$(\alpha + A^* A)g_{z,\alpha} = A^* \phi(\cdot, z) \quad (11)$$

where α is the regularization parameter and A^* is the adjoint of A .

The numerical procedure to locate the target object is then the following: Uniform sampling points $\{z_i\}_{i=1, \dots, N}$ of the probed region are considered and then for each point z_i ,

$$\mathcal{G}(z_i) = \|\phi(\cdot, z_i)\|_{L^2(\Gamma)} / \|g_{z_i,\alpha}\|_{L^2(\Lambda)} \quad (12)$$

is computed. Then the contours of the function $z_i \rightarrow \mathcal{G}(z_i)$ are visualized. As explained above, the values of \mathcal{G} are expected to be much smaller where z_i does not belong the scatterers.

4. NUMERICAL RESULTS

In this section, we presented some numerical results to verify the proposed thin layer condition. We analyzed how thin layer condition approximates the field values and how it affects the RG-LSM results.

In all examples the frequency of the exciting sources are chosen as $f = 300$ MHz which corresponds $k_0 = 2\pi$. Measurement field are obtained synthetically by solving the forward scattering problem using an integral equation method.

As a first example, thin layer is placed between free space and homogeneous medium with index $n = 2.5 + 0.2i$. Thickness of the thin layer is chosen as $\delta = 0.1\lambda_0$ and index as $n_\delta = 1.2 + 0.2i$. Perfectly conducting rectangle-shaped object with dimensions $\lambda_0 \times \lambda_0/2$ is buried in a lower homogeneous medium. The field and its normal derivative on lower boundary of the layer are approximated by thin layer condition and compared with the exact data, Figure 2. It is clear from Figure 2 that second order thin layer condition gives quite good approximation of the fields. Then we compared the reconstructions of the object made by using exact and approximated data,

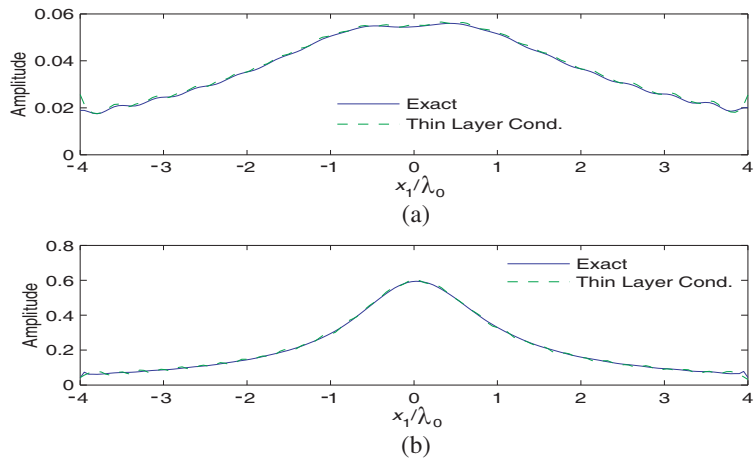


Figure 2: Comparison of the amplitude of (a) total field on the lower boundary of layer, (b) normal derivative of the field on the lower boundary of layer for layer thickness $\delta = 0.1\lambda_0$.

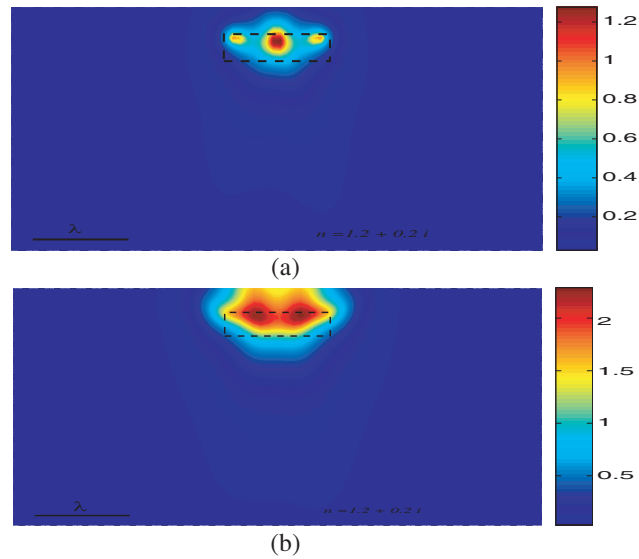


Figure 3: (a) Reconstruction associated with exact data for layer thickness $\delta = 0.1\lambda_0$, (b) reconstruction associated with thin layer condition. Dashed line: Exact boundary of the object.

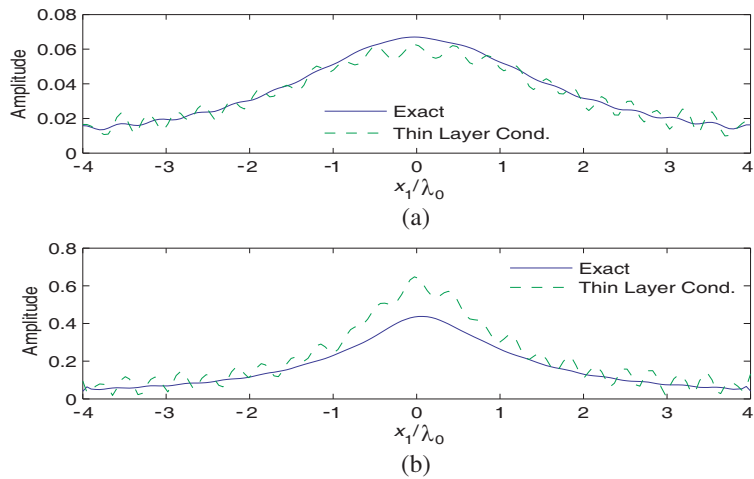


Figure 4: Comparison of the amplitude of (a) total field on the lower boundary of layer, (b) normal derivative of the field on the lower boundary of layer for layer thickness $\delta = 0.2\lambda_0$.

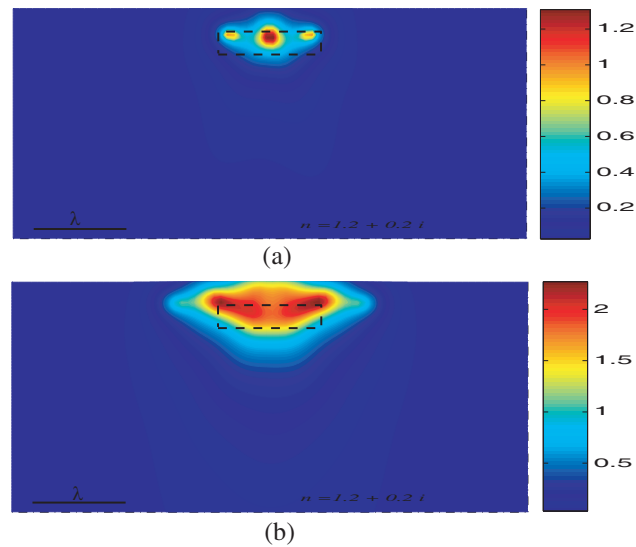


Figure 5: (a) Reconstruction associated with exact data for layer thickness $\delta = 0.2\lambda_0$, (b) Reconstruction associated with thin layer condition. Dashed line: Exact boundary of the object.

Figure 3. Even though the reconstruction made by using approximated data is not same as the one by exact data, it is still gives acceptable result.

To see the effect of thickness, in this example we increase the thickness to a $\delta = 0.2\lambda_0$. The other parameters are same as in first example. Comparison of the field values are presented in Figure 4. As it can be noticed, the approximation is getting worse when the thickness is getting bigger. We can also see this from the reconstruction of the object, Figure 5. It is clear that we need higher order thin layer condition for bigger thickness.

5. CONCLUSION

Second Order Thin Layer conditions are developed for three layered medium having planar boundaries. With these conditions, the field distributions on the lower interface of the thin layer determined from the measurement data on the upper boundary of the layer. Then RG-LSM method is carried out to image the object. Numerical simulations show that thin layer conditions gives quite satisfactory results to determine the field values. Imaging of the object can be accomplished with these data by using RG-LSM. However, when the thickness is getting larger or the permittivity is higher, second order conditions are not enough for modeling, higher order terms are needed.

ACKNOWLEDGMENT

This work was supported by the Turkish Scientific and Technological Research Council under Grant 108E173.

REFERENCES

1. Senior, T. B. A. and J. L. Volakis, *Approximate Boundary Conditions in Electromagnetics*, IEE Electromagnetic Waves Series, Institution of Engineering and Technology, 1995.
2. Rojas, R. G. and Z. A. Hekail, "Generalized impedance/resistive boundary conditions for EM scattering problems," *Rad. Sci.*, Vol. 12, No. 1, 1989.
3. Engquist, B. and J. C. Nedelec, "Effective boundary conditions for acoustic and electromagnetic scattering in thin layers," *Ecole Polytechnique-CMAP*, 278, France, 1993.
4. Colton, D., H. Haddar, and M. Piana, "An application of the reciprocity gap functional to inverse scattering theory," *Inverse Problems*, Vol. 21, 2005.

Fractal Characteristics of Radio Thermal Radiation of a Different Layer of Atmosphere in a Range of Millimeter Waves

V. A. German, A. A. Potapov, and E. V. Sukhonin

Institute of Radio Engineering and Electronics of Russian Academy of Sciences, RAS
Mokhovaya Street, 11, Building 7, Moscow 125009, Russia

Abstract— In the report, new results of measurement of characteristics of radio of thermal radiation of troposphere in a range of millimeter waves (8 mm) are presented. Measurements are spent in natural conditions at various weather conditions: — Overcast; — Rains of various intensity. For an estimation fractal, parameters the original software developed by authors has been used. Use of this, software has allowed to increase accuracy and to reduce time of calculations.

1. INTRODUCTION

Radio thermal radiation of the troposphere is a particular case of thermal (temperature) emission. The last one represent electromagnetic radiation emitted a mater and occurred due to its internal energy. The thermal radiation spectrum is limited by frequencies occupied by radio waves, i.e., by the frequencies from 3 kHz up to 6000 GHz. Special attention is paid to the frequency range of millimeter waves (MMW) 30–300 GHz. The reason is that the MMW actively interact with atmospheric gases especially with oxygen and water vapour as well with hydrometeor formations such as rainfalls, clouds, snowfalls etc. As a result, the MMW are strongly absorbed and scattered in the troposphere [1]. In this work, for the first time, there are the fractal characteristics of natural process of radio thermal radiation at wavelength 8.2 mm.

2. RADIO THERMAL RADIATION TRANSFER PROCESS IN THE TROPOSPHERE

In the prince of emission, absorption and scattering processes of MMW in the troposphere one may study the radiation transfer processes i.e., study MMW propagation. In some cases, solving the radiation transfer equation (RTE) allows to find the connection between radio brightness troposphere temperature T_b and values characterizing MMW propagation in the troposphere. Practical application of the obtained results may include noise estimation and radio wave attenuation statistic on satellite communication lines [2].

The RTE is differential equation in particular derivates relatively intensity as a function of coordinates, time and direction. In the general, this equation is not analytical solved. However in some assumptions solving RTE is possible. For example, if to assume that in homogeneous troposphere scattering is absent and only molecular absorption takes place then one can obtain the expression for T_I which is called “radiometric formula”:

$$T_I = T (1 - e^{-\Gamma}), \quad (1)$$

where T — Physical temperature of homogenous troposphere and $\Gamma = k_0 s \sec \theta$ — Total absorption homogenous troposphere layer with absorption coefficient k_0 and zenith angle [2].

In formation of hydrometeor radio thermal radiation in the troposphere, the multiple scattering effect play highly essential role. Therefore one should take these effects into condition in calculations and measurements of intensity of own thermal radiation of rainfall other hydrometeors scattering radiation. With purpose of determining attenuation atmospheric noise level or with the purpose of remote sensing of scattering medium parameters. If follow from RTE analysis that taking the multiple scattering effects into condition depends on the value of single scattering albedo ω determined as the ratio of scattering coefficient k_p to attenuation coefficient k_0 . The values ω for different wavelengths λ and rainfall rate R are given in the Table 1.

Note, that albedo ω almost does not depend on distribution of rain drops by fazes because radiation attenuation and scattering equally depend on rainfall microstructure. It follows from the tables that value ω in the MMW range is considerably larger then in centimeter wave range independently on. The results show that in the short-wave part of MMW range multiple scattering should be accounted already in case of weak rainfall.

The RTE is usually solved in the MMW range by numeric methods [1] due to difficulty of solving RTE in analytical method with account for multiple radio wave scattering. It is not practically

Table 1: The values ω for different wavelengths λ and rainfall rate R .

λ , mm \diagdown R , mm/h	0.25	1	5	10	25	50	100
30	0.02	0.03	0.05	0.06	0.08	0.10	0.15
8.6	0.16	0.27	0.35	0.40	0.44	0.47	0.49
4.2	0.32	0.37	0.44	0.47	0.48	0.49	0.50
3.0	0.39	0.44	0.46	0.48	0.48	0.49	0.50
1.0	0.46	0.48	0.49	0.49	0.50	0.50	0.50

convenient in analysis influence parameters of radio waves, hydrometeors and covering surface on layer value T_I .

There are works when the solution was obtained in the analytical form [3]. However, the layer scattering indicatrix enters the obtained expressing that is not exactly known. Therefore the expressions may be used only in rough estimations of scattering effects.

A new iterative method was suggested and developed in [4] for solving RTE in analytical form in a hydrometeor layer with account for multiple scattering. The method allows one to estimate layer scattering indicatrix and scattering radiation contribution to T_I .

According to [4] radiobrightness temperature T_I of hydrometeors with scattering is described by the expression:

$$T_I = T (1 - e^{-\Gamma}) T - \Delta T, \quad (2)$$

where in difference from (1) the value Γ is total attenuation but not total absorption in a homogeneous hydrometeor layer, ΔT — Contribution scattered radiation to T_I .

3. EXPERIMENT DESCRIPTION

Radio thermal troposphere radiation intensity characterized as radiobrightness temperature T_I was measured by radiometrical method at wavelength $\lambda = 8.2$ mm. The radiometer was made using the modulation scheme with superheterodine receiver at input had sensitivity 0.5 K and provided noise signal measurement in the frequency band $\Delta f = 400$ MHz by main and mirror channels at intermediate frequency 250 MHz.

Signal modulation with frequency 1000 Hz was carried out using ferrite switch. The horn with directivity pattern $9^\circ \times 1^\circ$ was used as antenna. The internal calibration derive at receiver input included a waveguide switch, matched loadings at temperature of environment and liquid nitrogen, a switch electromechanical drive and its position sensors. The switch observation angle was equal to 90° .

4. METHODS OF MEASUREMENT AND DATA PROCESSING

We measured mainly the vertical absorption value Γ^B using method of absolute measurements T_I and (1) where T is replaced by T_{cp} . The mean troposphere temperature is calculated in [5] for inhomogeneous troposphere in which T and molecular concentration of O_2 and H_2O decrease with height.

In absolute T_I measurements, one should take into consideration the influence of antenna directivity, i.e., the contribution brought by side and back antenna beams to T_I , and in small $\Gamma < 0.1$ dB — Background space radiation with $T \approx 3$ K. There is a technique of absolute measurements T_I when T_I is compared with brightness temperature of the reference disks T_1 and T_2 placed into the antenna Fraunhofer zone whose radiation is known [6].

A technique for T_I measurements is suggested in [7] that allows to take experimentally into consideration of the antenna side and back beams to measured antenna temperature. It was shown in [8] that all considered methods may be applied in measuring vertical attenuation clouds Γ_{reg}^B accounting for that cloudness can be broken when clouds are separated one from others by clear sky intervals.

Rainfalls and some other hydrometeor are extremely inhomogeneous that is why measurements of their T_I can be carried out only with the help of the absolute measurements method. Therefore, the measurement is universal one and may be used for troposphere monitoring on the constant basis.

5. MEASUREMENT RESULT

The fragments of obtained measurements results of radio thermal radiation at $\lambda = 8.2$ mm are given on Figure 1. There were analyzed 5 series of records produced under different meteoconditions.

The obtained data were used for phase portrait reconstructed for every series and constructed autocorrelation function of the studied series. An example of the reconstructed phase portrait (for series No. 1) and autocorrelation function $R(\tau)$ for the same series are shown accordingly on Figure 2 and Figure 3.

Signal values in relative units are marked along abscissa and ordinate on Figure 2. On Figure 3, the reading numbers are marked along abscissa axis and the signal values are marked along ordinate axis in relative units. Diagrams for different series are very similar.

6. STATISTICAL CHARACTERISTICS OF RADIO THERMAL RADIATION

The empirical probability distributions of radio thermal radiation values constructed at different series of experimental data differ weakly between them. Statistical characteristics analysis of radio thermal radiation was carried out with help of the Pearson diagram [9–11]. The Pearson diagram is shown on Figure 4 with the points corresponding to measurements series considered. On the diagram, the division boundary is shown higher of which the distributions may not exist. One

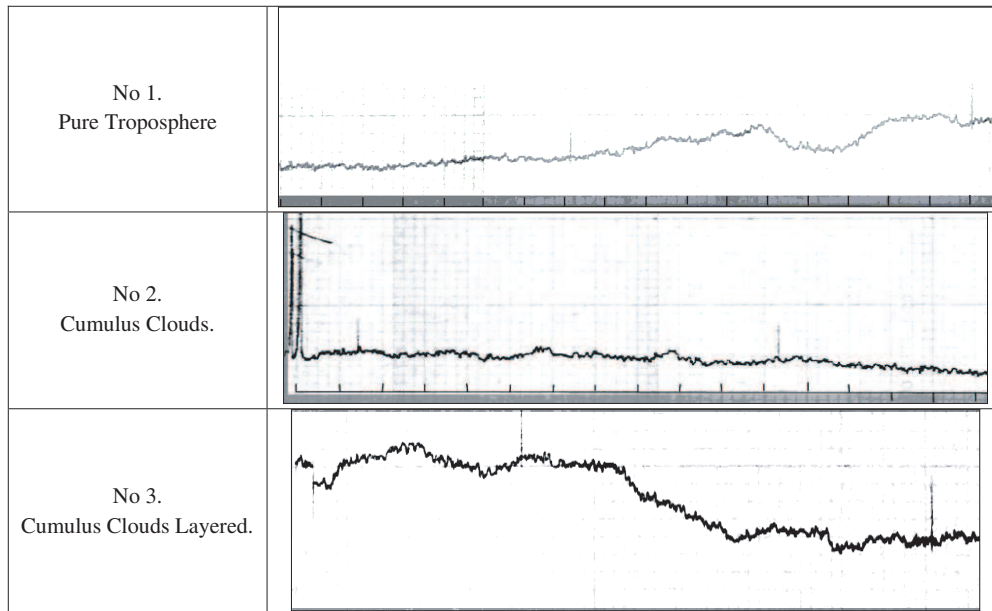


Figure 1: Results of measurements of radio thermal radiation on $\lambda = 8.2$ mm.

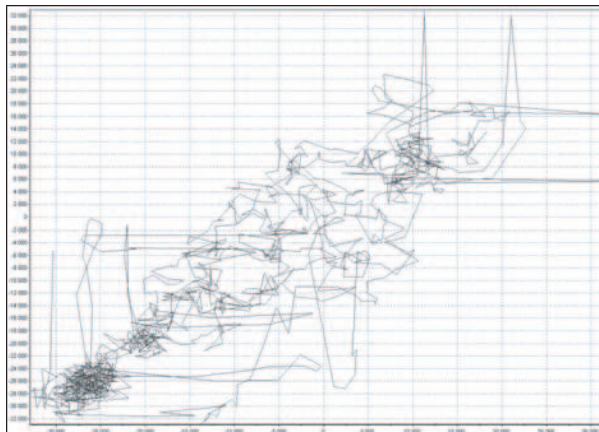


Figure 2: The phase portrait for series No. 1.

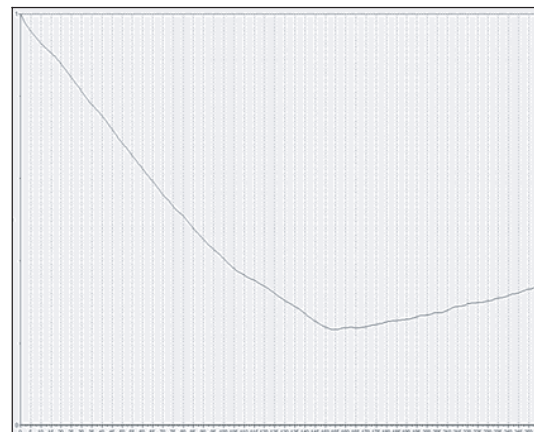


Figure 3: Autocorrelation function $R(\tau)$ for series No. 1.

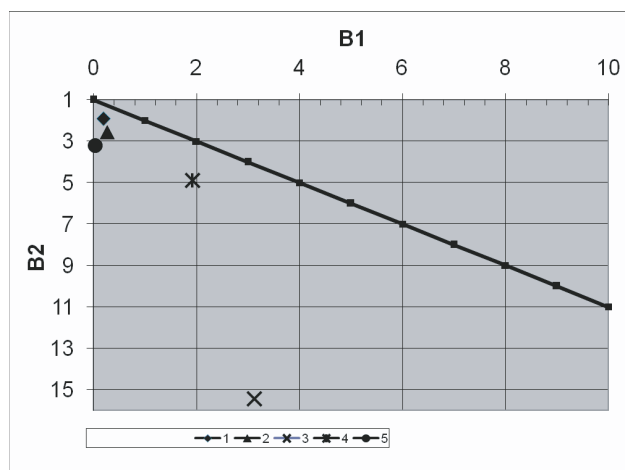


Figure 4: The Pearson diagram for series of radio thermal measurements.

can see that statistical characteristics of the series No. 1 and No. 2 are grouped in the region of distribution law close to the Gaussian one. From the other side, the series Nos. 3–5 are in the field of power law with heavy tails. It follows from this fact that it is just expedient the fractal processing.

7. FRACTAL PROCESSING OF RESULTS

The fractal dimension and Hirst index were measured [9–11]. Analysis was made using the graphs $D_C = f(M)$ and $\log \frac{R}{S} = f[\log(t)]$ where D_C — Correlation dimension, M — Enclosure dimension, R/S — Ratio of swing to dispersion, t — “Time” (record number at time axis). Estimated of correlation dimension D_C and Hirst index are given in [9].

Hirst index characterizes persistence $1/2 < H < 1$ or antipersistence ($0 < H < 1/2$) of current sampling depending on its value $H = 1/2$. In the first case, when $1/2 < H < 1$, we observe a process saving trend of growth or decrease of instant amplitudes. In second case $0 < H < 1/2$, when in the “past” means decrease in the “future”, and vice versa i.e., process growth more subjected to changes which is often meant as “return to average”.

The measured value of Hirst index H shows that the radio thermal radiation process has high fractal for all measurement series.

8. CONCLUSION

In this work for the first time, the fractal characteristics of radio thermal troposphere radiation in the MMW range were measured. The positions given in the work will be widened in the future. It is obvious that estimate of parameter H current value can be lightly introduced now into theory and practice of classical processing of radar data on noise background. Considerable changes of acting radio system schemes are not required.

REFERENCES

1. Sukhonin, E. V. and V. A. Korotkov, “Micrometer wave scattering in atmosphere with hydrometeors,” Survey, *Radioengineering*, Vol. 41, 68–91, VINITI, Moscow, 1990.
2. Sukhonin, E. V., “Prediction of millimeter waves attenuation in the atmosphere,” Survey, *Radioengineering*, Vol. 41, 3–68, VINITI, Moscow, 1990.
3. Ishimaru, A., *Propagation and Scattering of Waves in Random, Inhomogeneous Media*, Vol. 1, Mir, Moscow, 1981.
4. Korotkov, V. A. and E. V. Sukhonin, “Solving the radiation transfer equation in analytical form for calculation of rainfall radio brightness temperature with account for multiple scattering effects,” *J. Commun. Technol. Electron.*, Vol. 33, No. 8, 1569–1573, 1988.
5. Kisliakov, A. G., “Effective path length and mean atmosphere temperature,” *Radiophysics*, Vol. 9, No. 3, 451–461, 1966.
6. Krotikov, V. D., A. G. Porfir’ev, and V. S. Troitskiy, “Method development for field intensity precision measurement and referencing of Moon radiation at wavelength 3.2 cm,” *Radiophysics*, Vol. 4, No. 6, 1004–1012, 1961.

7. Babkin, Y. S., A. G. Kisliakov, and E. V. Sukhonin, “To a technique of measurement of millimeter wave attenuation in rain using its own radiation,” *J. Commun. Technol. Electron.*, Vol. 31, No. 6, 1105–1109, 1986.
8. Zabolotniy, V. F., I. I. Zinchenko, Iskhakov, et al., “Experimental study of millimeter waves in cloudy atmosphere,” *Radiophysics*, Vol. 23, No. 9, 1020–1025, 1980.
9. Potapov, A. A., *Fractals in Radio Physics and Radar: Topology of Sample*, 2nd Edition and Correction, University Library, Moscow, 2005.
10. Potapov, A. A., Y. V. Gulyayev, S. A. Nikitov, A. A. Pakhomov, and V. A. German, *Newest Images Processing Methods*, A. A. Potapov Ed., Fizmatlit, Moscow, 2008.
11. Potapov, A. A. and V. A. German, “Detection of artificial objects with fractal signatures,” *Pattern Recognition and Image Analysis*, Vol. 8, No. 2, 226–229, 1998.

The Effects of Self Steepening and Intrapulse Raman Scattering on Frequency Spectrum of Dark Soliton Switching

F. Kargar¹, M. Hatami², and P. Elahi³

¹Physics Department, Pyam-Noor University, Shiraz, Iran

²Atomic and Molecular Group, Faculty of Physics, Yazd University, Yazd, Iran

³Department of Physics, Faculty of Science, Shiraz University of Technology
P.O. Box 71555-313, Shiraz, Iran

Abstract— In this paper, the nonlinear Schrödinger equation (NLS) is developed for nonlinear directional coupler switches (NLDS) by taking into account the self steepening and intrapulse Raman scattering effects. By numeric simulation of propagation of dark soliton in the nonlinear directional coupler switch we study of those effects. The result of simulation shows in high power input intensity the spectrum of pulse is a little change with respect to bright soliton switching. This result prove the stability of dark soliton for optical switching as we expected.

1. INTRODUCTION

The switching performance increase by increasing the nonlinear refractive index and decreasing the absorption coefficient [1], also the switching energy and the length of switch is decreased. Solitons are formed in nonlinear optical Kerr medium that have second order dispersion. Dark solitons are produce in normal dispersion but Bright solitons are formed in the anomalous dispersion medium [2].

Bright soliton have no any background but in some time interval the pulse exist on the other hand the dark solitons have a constant background but in some time interval the pulse goes to zero. Dark solitons are more stable in the presence of noise and spread more slowly in the presence of fiber loss compared with bright solitons [3].

One of the most important effects in the short pulse propagation in nonlinear medium is the self steepening and the intrapulse Raman scattering. Self steepening creates an optical shock on the trailing edge of the pulse in the absent of the GVD effects. This phenomenon is due to the intensity dependence of the group velocity that results in the peak of the pulse moving slower than the wings. The GVD dissipates the shock and smoothes the trailing edge considerably. However, self steepening would still manifest through a shift of the pulse center.

The effect of intrapulse Raman scattering on higher-order solitons is similar to the case of self steepening. Intrapulse Raman scattering has no effect in the amplitude of the solitons but changes the frequency spectrum. When the order of soliton is increased the coefficient of intrapulse Raman scattering is decreased.

2. EQUATIONS

The equation of pulse propagation in the nonlinear Kerr medium (NLSE) has the following form:

$$i \frac{\partial A}{\partial Z} + i \frac{\alpha}{2} A - \frac{\beta_2}{2} \frac{\partial^2 A}{\partial T^2} + \gamma |A|^2 = 0 \quad (1)$$

For optical pulses with small width ($T_0 < 1PS$) it is necessary to take the effect of time derivative of nonlinear terms:

$$\frac{\partial A}{\partial Z} + \frac{\alpha}{2} A + i \frac{\beta_2}{2} \frac{\partial^2 A}{\partial T^2} - \frac{\beta_3}{6} \frac{\partial^3 A}{\partial T^3} = i \gamma \left(|A|^2 A + \frac{i}{\omega_0} \frac{\partial}{\partial T} (|A|^2 A) - \tau_{RA} \frac{\partial |A|^2}{\partial T} \right) \quad (2)$$

By using the normalize U :

$$A(Z, \tau) = \sqrt{P_0} \exp \left(-\alpha \frac{Z}{2} \right) U(Z, \tau) \quad (3)$$

Then Equation (2) is then governed by:

$$\frac{\partial U}{\partial Z} + i \frac{\text{sgn}(\beta_2)}{2L_D} \frac{\partial^2 U}{\partial \tau^2} = \frac{\text{sgn}(\beta_3)}{6L'_D} \frac{\partial^3 U}{\partial \tau^3} + i \frac{e^{-\alpha Z}}{L_{NL}} \left(|U|^2 U + i s \frac{\partial}{\partial \tau} (|U|^2 U) - \tau_R U \frac{\partial |U|^2}{\partial \tau} \right) \quad (4)$$

Here we have three normalized quantities that normalized to scale of length defined by

$$L_D = \frac{T_0^2}{|\beta_2|} \quad L'_D = \frac{T_0^3}{|\beta_3|} \quad L_{NL} = \frac{1}{\gamma P_0} \quad (5)$$

The parameters s and τ_R are self steepening and intrapulse Raman scattering respectively and are defined as

$$s = \frac{1}{\omega_0 T_0} \quad \tau_R = \frac{T_R}{T_0} \quad (6)$$

T_0 is the initial width pulse.

By taking the normalized distance ($Z = z/L_{NL}$), neglecting the fiber loss ($\alpha = 0$), and $\text{sgn}(\beta_2) = 1$ for dark soliton the Equation (4) reaches the following form:

$$\frac{\partial U}{\partial Z} = -\frac{i}{2} \frac{\partial^2 U}{\partial \tau^2} + i|U|^2 U - s \frac{\partial}{\partial \tau} (|U|^2 U) - i\tau_R U \frac{\partial |U|^2}{\partial \tau} \quad (7)$$

The Nonlinear Directional Coupler (NLDC) consist of two wave guide or fiber that placed near each other such that each evanescent field of one fiber can propagate to other fiber such that the energy exchange is placed in the length of coupler. The equation of two waveguide of coupler is related to each other by the linear coupling coefficient (κ), thus the coupling equations of two fiber of coupler are governed by:

$$\frac{\partial U_1}{\partial Z} = -\frac{i}{2} \frac{\partial^2 U_1}{\partial \tau^2} + i|U_1|^2 U_1 - s \frac{\partial}{\partial \tau} (|U_1|^2 U_1) - i\tau_R U_1 \frac{\partial |U_1|^2}{\partial \tau} - i\frac{\pi}{2} \kappa U_2 \quad (8)$$

$$\frac{\partial U_2}{\partial Z} = -\frac{i}{2} \frac{\partial^2 U_2}{\partial \tau^2} + i|U_2|^2 U_2 - s \frac{\partial}{\partial \tau} (|U_2|^2 U_2) - i\tau_R U_2 \frac{\partial |U_2|^2}{\partial \tau} - i\frac{\pi}{2} \kappa U_1 \quad (9)$$

The U_1 and U_2 are the wave amplitude in each waveguide of the coupler.

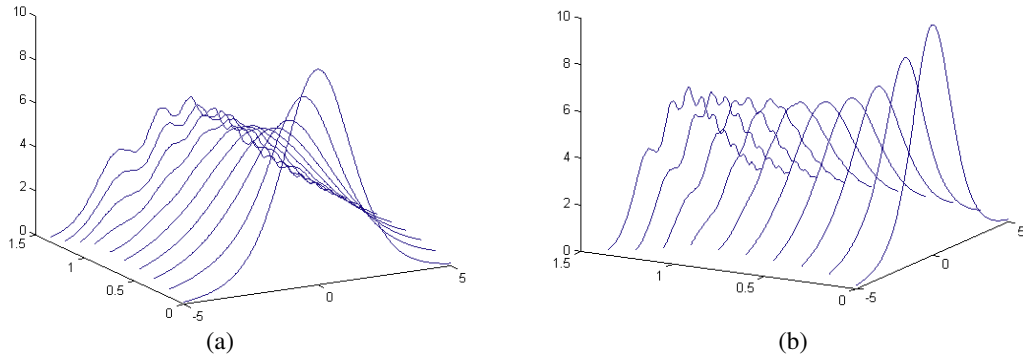


Figure 1: (a) Spectrum of bright fiber without any effect (b) spectrum of bright fiber with effect of self steepening ($s = 0.01$) and intrapulse Raman scattering ($\tau_R = 0.01$) $A = 2.7$.

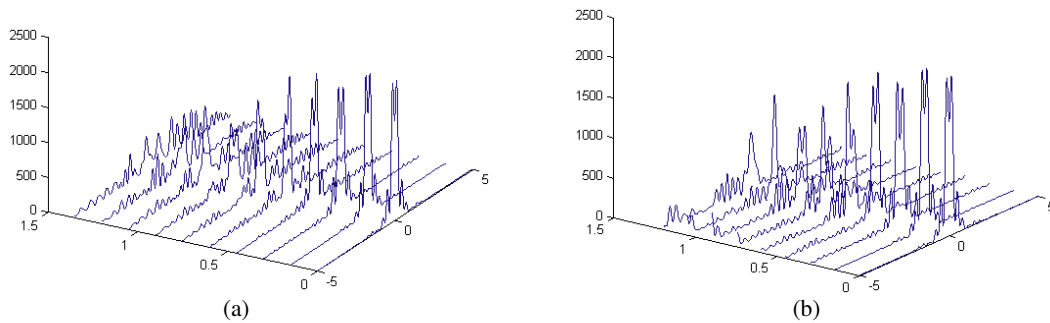


Figure 2: (a) Spectrum of dark fiber without any effect (b) spectrum of dark fiber with effect of self steepening ($s = 0.01$) and intrapulse Raman scattering ($\tau_R = 0.01$) $A = 2.7$.

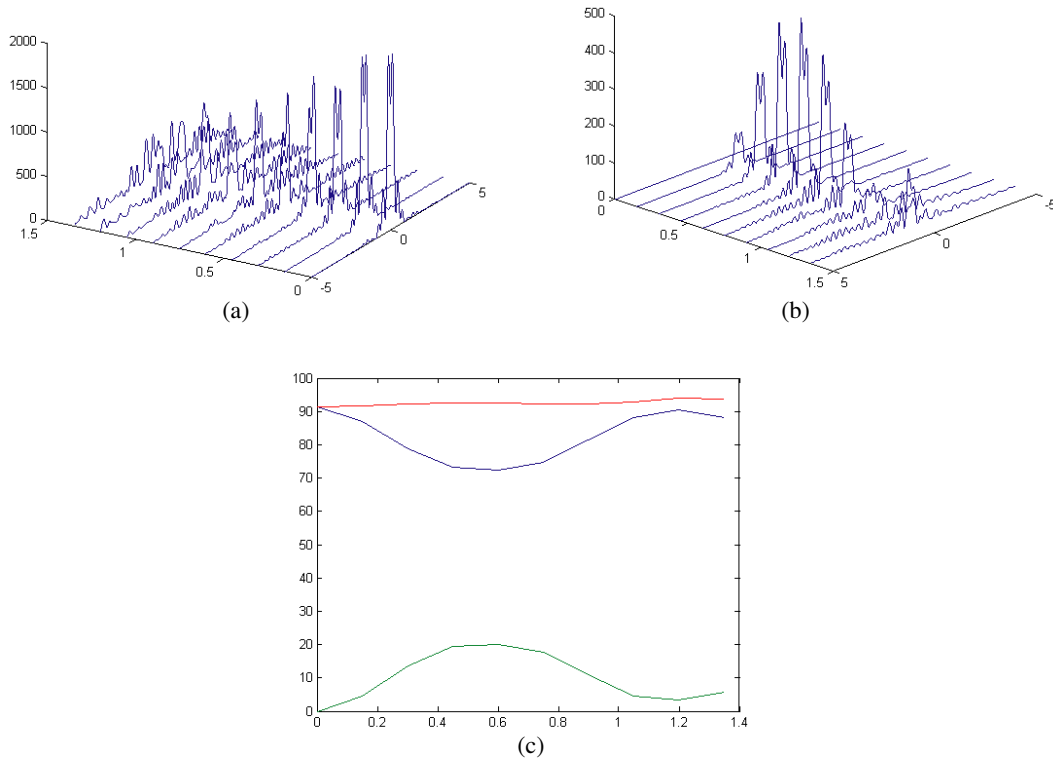


Figure 3: (a) Spectrum of upper waveguide (b) spectrum of lower waveguide (c) switching energy with coupling coefficient ($\kappa = 1$) and without effect of self steepening and intrapulse Raman scattering in dark soliton amplitude $A = 2.7$.

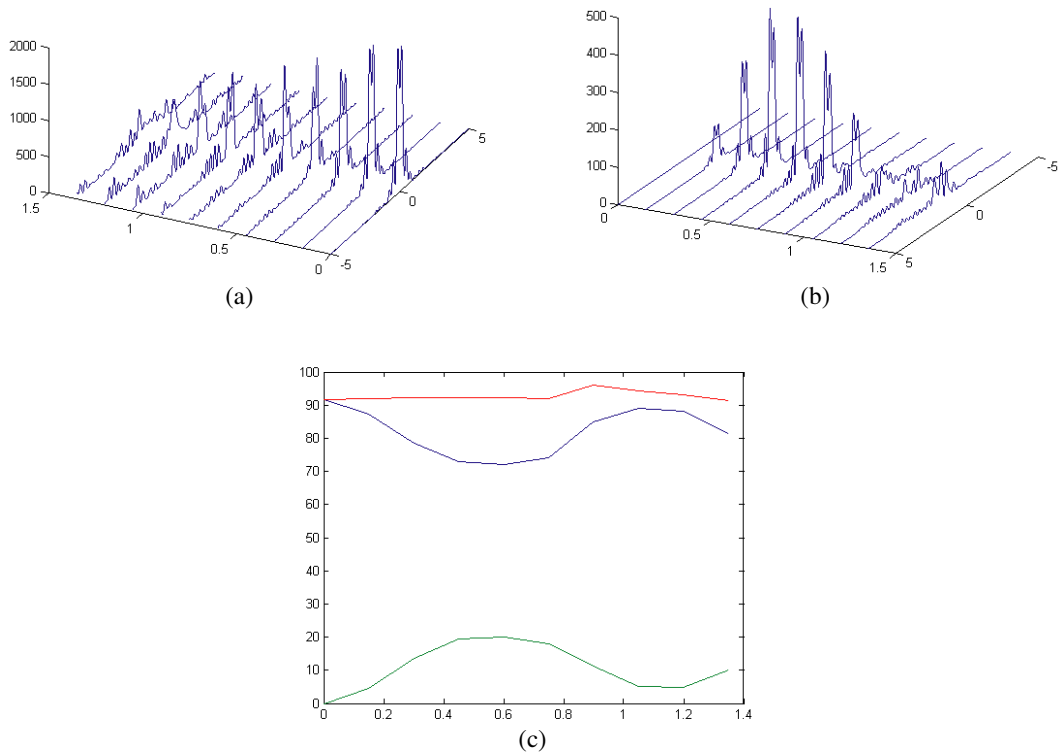


Figure 4: (a) Spectrum of upper waveguide (b) spectrum of lower waveguide (c) switching energy with coupling coefficient ($\kappa = 1$) and with effect of self steepening ($s = 0.01$) and intrapulse Raman scattering ($\tau_R = 0.01$) in dark soliton amplitude $A = 2.7$.

3. NUMERICAL RESULTS

By numeric simulation [2, 4] of propagation of dark soliton in the nonlinear directional coupler switch we study of those effects and solved coupling Equations (8) and (9) with combination of method Crank Nicolson and finance difference. We take the input pulse as following:

$$U(0, \tau) = A \tanh(\tau) \quad (10)$$

Figure 1(a) shows spectrum of bright fiber without any effect and 1(b) shows spectrum of bright fiber by effect of self steepening and intrapulse Raman scattering.

Figure 2(a) shows spectrum of dark fiber without any effect and Figure 2(b) shows spectrum of dark fiber by effect of self steepening and intrapulse Raman scattering. In this figure, it's seen that the spectrum of dark fiber sharper than bright fiber.

Hear for namely simulation of propagation of dark soliton with effect of coupling without any effect shows in Figure 3 and Figure 4 shows dark soliton by effect of self steepening and intrapulse Raman scattering.

Because of stability of dark soliton rather than bright soliton we observed in dark soliton this effect is small relative to bright soliton and only make a little distortion in pulse.

We have simulated the pulse propagation by taking into account the amplitude of input pulse a critical value 2.7 that switching is observed.

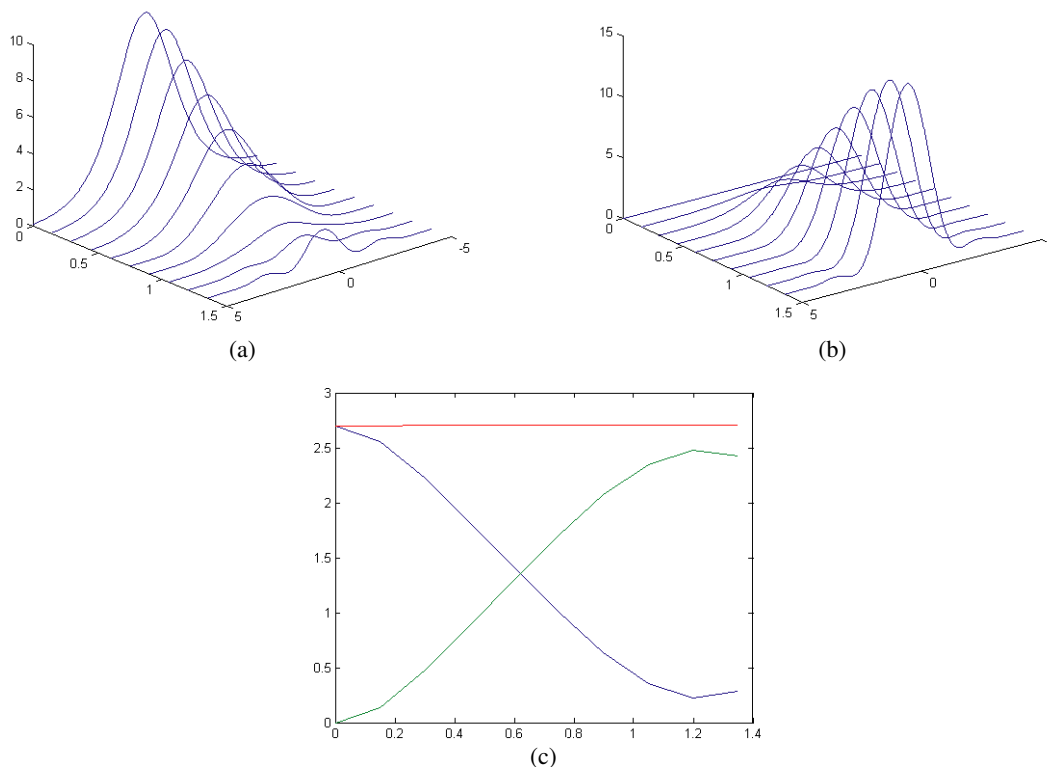


Figure 5: (a) Spectrum of upper waveguide (b) spectrum of lower waveguide (c) switching energy with coupling coefficient ($\kappa = 1$) and with effect of self steepening ($s = 0.01$) and intrapulse Raman scattering ($\tau_R = 0.01$) in bright soliton amplitude $A = 2.7$.

4. CONCLUSION

For pulse widths ~ 1 ps or shorter, the spectral width of the pulse is large enough that the Raman gain can amplify the low frequency (red) spectral components of the pulse, with high-frequency (blue) components of the same pulse acting as a pump. The process continues along the fiber, and the energy from blue components is continuously transferred to red components. Such an energy transfer appears as a red shift of the soliton spectrum, with shift increasing with distance.

The production of dark soliton rather than bright soliton need a higher energy for transfer but it has higher stability and transferred information with high speed than bright soliton. The self

steepening and intrapulse Raman scattering effect author change in switching energy in bright soliton and decrease switching and increase path of exit for input amplitude low and high but has not important effect on switching energy and the shape of the output pulse.

REFERENCES

1. Zakeri, A. and M. Hatami, “Nonlinear optical properties of pulsed laser-deposited GeAsSe films and simulation of a nonlinear directional coupler switch,” *J. of Opt. Society of Am. B*, Vol. 22, 591, 2005.
2. Zakeri, A. and M. Hatami, “Design of an ultra-fast all optical dark soliton switch in a nonlinear directional coupler (NLDC) made in chalcogenide glasses,” *Applied Physicd D*, Vol. 12, 591, 2006.
3. Kivshar, Y. S. and G. P. Agrawal, *Optical Solitons*, Academic Press, 2003.
4. Hatami, M., H. Ghafouri-Shiraz, and A. Zakery, “Analysis of gained nonlinear directional coupler pulse switch,” *Optical and Quantum Electronics*, Vol. 38, 1259–1268, 2007.

Simulation of Soliton Propagation in Photovoltaic Photorefractive Two-photon Materials and Study the Switching Behavior

Alireza Keshavarz¹, Leila SadralSadati², and Mohsen Hatami²

¹Department of Physics, Faculty of Science, Shiraz University of Technology
P.O. Box 71555-313, Shiraz, Iran

²Atomic and Molecular Group, Faculty of Physics, University of Yazd, Yazd, Iran

Abstract— The nonlinear dynamics of photovoltaic soliton pair in two-photon photorefractive material have been investigated. In the steady-state regime, these coupled soliton can propagate in bright-bright, dark-dark, and bright-dark forms. Also we studied numerically bright-bright soliton interaction in the (LiNbO₃) crystal under open circuit conditions. The result show there is some critical input peak power that make it as an all optical self-routing switching that can be used in communication system.

1. INTRODUCTION

Today's, photorefractive (PR) spatial solitons (PRSS) are obvious in various branches of physics and engineering. Self-trapped PRSS are potentially useful for various applications such as all optical switching and routing interconnectors. Since it is possible to create optical solitons at very low optical power in order of microwatts in PR crystals [1]. Also these crystals are the wavelength dependence so one can generate solitons with low power and use the waveguides induced by these solitons to guide high power beam in different wavelength [6]. Till now several types of steady-state PR solitons have been predicted. The first is the screening soliton (SS) [2], which generated when an external bias voltage is applied to a non photovoltaic PR crystal. The second kind is the photovoltaic soliton (PS) [2], which requires an unbiased PR crystal that exhibits the photovoltaic effect, generation under dc current in a medium illuminated by a light beam and the third kind of PR soliton is screening photovoltaic soliton (SPS) [3] generated when the bias field be much stronger than the photovoltaic field, then the SPS are just like SS and on the other hand, if the applied field is absent, then are like photovoltaic solitons in the closed circuit condition. Recently, a new model was introduced by Castro-Camus and Magana [4], which involves two-photon PR instead of single-photon PR effect. This model includes a valance band (VB), a conduction band (CB) and an intermediate allowed level (IL). A gating beam is used to maintain a fixed quantity of excited electrons from the VB, which are then excited to the CB by signal beam. The signal beam induces a charge distribution to its intensity distribution, which in turn gives rise to a nonlinear change of refractive index through space charge field. Our goal in this paper is to simulation of propagation two-component photovoltaic soliton in photorefractive two-photon material and study the switching behavior under open circuit conditions.

2. PHYSICAL MODEL

We consider a pair of optical beams which are propagating along the z -direction in a PR material with two-photon PR effect. The crystal here is taken to be Fe-doped LiNbO₃ [5] with its optical c axis oriented along the x coordinate. These optical beams are allowed to diffract only along the x direction, and the PR material is assumed to be loss-less. The two optical beams can be obtained by splitting a laser beam using a polarizing beam splitter. Making their optical path difference greatly exceed than the coherence length of the laser and can make these two beams with same frequency but mutually incoherent at the input of the crystal. Notice the crystal is illuminated by separate gating beam. The optical fields of beams are expressed in the form $\vec{E}_1 = \hat{x}\Phi(x, z) \exp(ikz)$ and $\vec{E}_2 = \hat{x}\Psi(x, z) \exp(ikz)$ where $k = k_0 n_e = (2\pi/\lambda_0) n_e$, n_e is the unperturbed extraordinary index of refraction and λ_0 is the free-space wavelength; Φ and Ψ are slowly varying envelopes of two optical fields, respectively satisfy in the following form of the basic equations [6]:

$$i \frac{\partial \Phi}{\partial z} + \frac{1}{2k} \frac{\partial^2 \Phi}{\partial x^2} - \frac{k_0 n_e^3 r_{33} E_{sc}}{2} \Phi(x, z) = 0 \quad (1)$$

$$i \frac{\partial \Psi}{\partial z} + \frac{1}{2k} \frac{\partial^2 \Psi}{\partial x^2} - \frac{k_0 n_e^3 r_{33} E_{sc}}{2} \Psi(x, z) = 0 \quad (2)$$

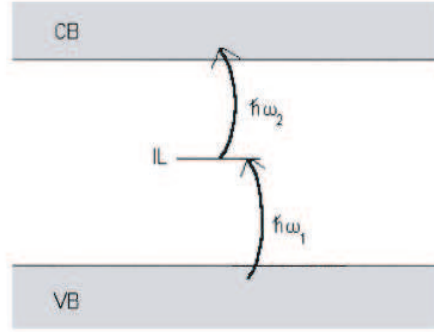


Figure 1: Transition scheme corresponding to the two-photon photorefractive effect.

where r_{33} is the electro-optic coefficient, and E_{sc} is the space charge field which perturbs the refractive index through the Pockel's effect. The expression for space charge field is given by [7]:

$$E_{sc} = -E_p \frac{s_2 I_2 (I_2 + I_d + ((\gamma_1 N_A)/s_2))}{(s_1 I_1 + \beta_1) (I_2 + I_d)} \quad (3)$$

where $E_p = \kappa \gamma N_A / e \mu$ is photovoltaic field, κ is the photovoltaic constant [5, 8]. $I_d = \beta_2 / s_2$ so called the dark irradiance, N_A is the acceptor or trap density, γ and γ_1 are the recombination factors of the CB-VB, IL-VB transitions, respectively; β_1 and β_2 are the thermo ionization probability constants for transitions VB-IL and IL-CB, respectively. I_1 is intensity of the gating beam ($\hbar\omega_1$) in Fig. 1, which is kept constant; and $I_2 = (n_e / 2\eta_0) (|\Phi|^2 + |\Psi|^2)$ is the intensity of the two mutually incoherent beams, $\eta_0 = \sqrt{\mu_0 / \epsilon_0}$. Substituting expression for E_{sc} into Eqs. (1) and (2), we drive the following dimensionless dynamical equation for the incident pulses [9]:

$$i \frac{\partial U}{\partial \zeta} + \frac{1}{2} \frac{\partial^2 U}{\partial s^2} + \frac{\alpha \eta (1 + \sigma + |U|^2 + |V|^2) (|U|^2 + |V|^2) U}{(1 + |U|^2 + |V|^2)} = 0 \quad (4)$$

$$i \frac{\partial V}{\partial \zeta} + \frac{1}{2} \frac{\partial^2 V}{\partial s^2} + \frac{\alpha \eta (1 + \sigma + |U|^2 + |V|^2) (|U|^2 + |V|^2) V}{(1 + |U|^2 + |V|^2)} = 0 \quad (5)$$

where $U = \sqrt{n_e / 2\eta_0 I_d} \Phi$, $V = \sqrt{n_e / 2\eta_0 I_d} \Psi$, $\zeta = z / k_0 n_e x_0^2$, $s = x / x_0$, $\alpha = (k_0 x_0)^2 (n_e^4 r_{33} / 2) E_p$, $\sigma = \gamma_1 N_A / \beta_2$, $\eta = \beta_2 / s_1 I_1 + \beta_1$ and x_0 is an arbitrary spatial width taken for scaling [1]. Depending upon the value of different system parameters, the above set of two equations is suitable for two-component bright-bright, dark-dark and bright-dark solitons. Eqs. (4) and (5) are the coupled modified nonlinear Schrödinger equations, which are non integrable in nature. These Eqs. may be solved by approximation methods for example: Vlasov's moment methods [1].

An alternative approach is to solve these equations numerically that we will do it by modified the Crank-Nicolson method, which is explained in Part 3.

3. SIMULATION OF PULSE PROPAGATION AND RESULTS

We now investigate the two-component bright-bright solitons. In this case input pulses are assumed in the form $U = A \operatorname{sech}(s - s_0)$, $V = A \operatorname{sech}(s + s_0)$, respectively and A amplitude of two input pulses. Intensities of both beams are expected to vanish at infinity ($x \rightarrow \pm\infty$). Let us consider a LiNbO₃: Fe crystal with the parameters $n_e = 2.2$ and $r_{33} = 3 \times 10^{-11} \text{ mV}^{-1}$ at a wavelength $\lambda_0 = 0.5 \mu\text{m}$, and other parameters are taken to be $E_p = 4 \times 10^6 \text{ Vm}^{-1}$, $s_1 = 3 \times 10^{-4} \text{ m}^2 \text{W}^{-1} \text{ s}^{-1}$, $s_2 = 3 \times 10^{-4} \text{ m}^2 \text{W}^{-1} \text{ s}^{-1}$, $\gamma_1 = 3.3 \times 10^{-17} \text{ m}^3 \text{ s}^{-1}$, $N_A = 10^{22} \text{ m}^{-3}$, $\beta_1 = 0.05 \text{ s}^{-1}$, $\beta_2 = 0.05 \text{ s}^{-1}$ [7]. The gating beam intensity I_1 is taken to be 10^6 Wm^{-2} and the scaling parameter $x_0 = 0.5 \mu\text{m}$. Therefore $\alpha \approx 22.2$, $\eta = 1.67 \times 10^{-4}$. The value of σ can be controlled by modulating the dark irradiance artificially using incoherent illumination, and for the present investigation $s_0 = 1$, $\sigma = 10^5$. Now we investigate propagation pulses by controlling amplitude of input pulses. The results of simulation of propagation bright-bright solitons for two different amplitudes show in Fig. 2, Fig. 3 and Fig. 4.

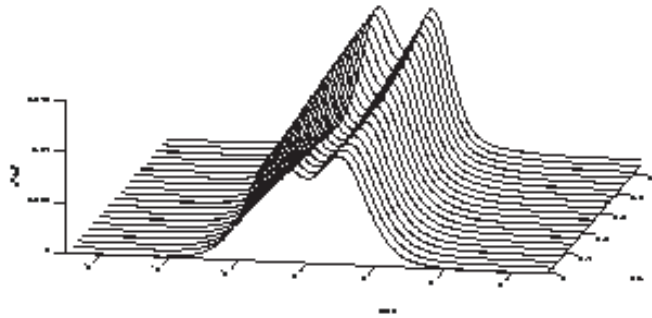


Figure 2: Pulse propagation without nonlinear effect at $A = 0.1$.

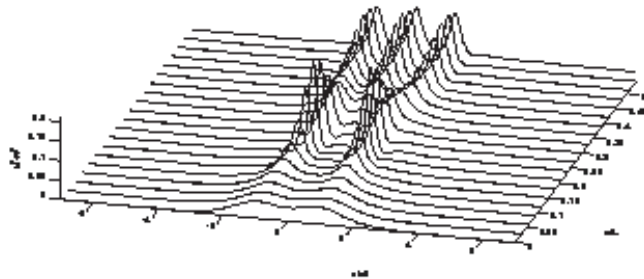


Figure 3: Pulse propagation by considering nonlinear effect at $A = 0.2$. As It's seen the pulse divided into three same solitons.

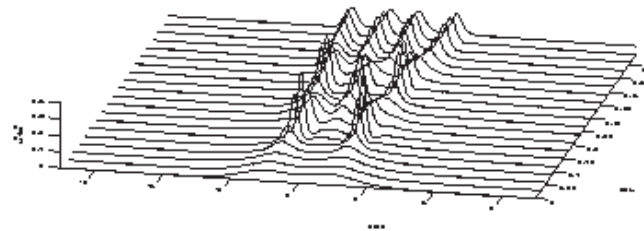


Figure 4: By increasing the input peak pulse ($A = 0.25$) the pulse divided into four same solitons in outputs.

Figure 2 shows the pulse propagation without nonlinear effect at $A = 0.1$. The result indicates that the two pulses propagate separately in low intensity, and only pulse broadening take place as we expected. If we increase input pulse intensity the nonlinear effect appeared as it's seen in Fig. 3. In this figure, the pulse is broken into three same solitons that means the filamentation is taken place. By further increasing of input pulse intensity, the number of filaments is increased. The Fig. 4 shows this effect with generation of four same solitons in the output.

In this paper, we have studied the simulation of soliton propagation in photovoltaic photorefractive two-photon materials and the switching behavior. The results show that the number of pulse is strongly depended on the input pulse intensity. We find two critical input pulse amplitude that produced three and four same solitons in output corresponding in normalized coordinate as $A = 0.2$ and $A = 0.25$ respectively in different places, which can be used in as all optical self routing switches.

REFERENCES

1. Zhang, Y., C. F. Hou, and X. D. Sun, "Grey photovoltaic solitons in two-photon photorefractive materials under open-circuit case," *J. Opt. A: Pure Appl. Opt.*, Vol. 10, 025101, 2008.
2. Valley, G. C., M. Segev, B. Crosignani, A. Yariv, M. M. Fejer, and M. C. Bashaw, "Dark and bright photovoltaic spatial solitons," *Phys. Rev. A*, Vol. 50, R4457, 1994.
3. Hou, C., Y. Li, X. Zhang, B. Yuan, and X. Sun, "Grey screening-photovoltaic spatial solitons in biased photovoltaic photorefractive crystals," *Opt. Commun.*, Vol. 181, 141, 2000.

4. Castro-Camus, E. and L. F. Magana, "Prediction of the physical response for the two-photon photorefractive effect," *Opt. Lett.*, Vol. 28, 1129, 2003.
5. Anastassiou, C., M. F. Shih, M. Mitchell, Z. Chen, and M. Segev, "Optically induced photovoltaic self-defocusing-to-self-focusing transition," *Opt. Lett.*, Vol. 23, 6–924, 1998.
6. Zakery, A. and A. Keshavarz, "Simulation of the incoherent interaction between two bright spatial photorefractive screening solitons in one and two dimensions," *J. Phys. D: Appl. Phys.*, Vol. 37, 3409–3418, 2004.
7. Hou, C., Y. Zhang, Y. Jiang, and Y. Pei, "Photovoltaic soliton in two-photon photorefractive materials under open-circuit conditions," *Opt. Commun.*, Vol. 273, 8–544, 2007.
8. Zhang, M., K. Lu, G. Cheng, et al., "One-dimensional steady-state bright photovoltaic solitons in LiNbO_3 : Fe crystal with background illumination," *J. Light and Electron Optics*, Vol. 9, 20, 2009.
9. Srivastava, S. and S. Koar, "Two-component coupled photovoltaic soliton pair in two photon photorefractive materials under open circuit conditions," *Opt. Laser Technol.*, Vol. 08, 005, 2008.

Design of an All Optical Routing Self Switch by Using the Collision of the Spatial Solitons in a Non-Kerr Nonlinearity

Mohsen Hatami¹, Alireza Keshavars², Najmeh Dehkordi Balali³, and Fatemeh Kargar³

¹Atomic and Molecular Group, Faculty of Physics, Yazd University, Yazd, Iran

²Department of Physics, Shiraz University of Technology, Shiraz, Iran

³Physics Department, Payam-Noor University, Shiraz, Iran

Abstract— In this paper we have developed the equation of the collision of spatial solitons by taking in to account the effects of two-photon absorption. Although the effects of two-photon absorption is reduced the interaction of two solitons and dissipates the energy, but we use this effect and design an all optical routing self switch that can be used as an ultra fast all optical switch.

1. INTRODUCTION

In the context of nonlinear optics, solitons are classified as being either temporal or spatial, depending on whether the confinement of light occurs in time or space during wave propagation. Temporal solitons represent optical pulses that maintain their shape, whereas spatial solitons represent self-guided beams that remain confined in the transverse directions orthogonal to the direction of propagation. Both types of solitons evolve from a nonlinear change in the refractive index of an optical material induced by the light intensity—a phenomenon known as the optical Kerr effect in the field of nonlinear optics. The intensity dependence of the refractive index leads to spatial self-focusing (or self-defocusing) and temporal self-phase modulation (SPM), the two effects that are responsible for the formation of optical solitons. A spatial soliton is formed when the self-focusing of an optical beam balances its natural diffraction-induced spreading. In contrast, the SPM contracts the natural dispersion-induced broadening the optical pulse and lead to the formation of temporal soliton. Here we have considered the effect of two-photon absorptions and higher nonlinear absorption that affect the soliton collisions. The main equation governing the evolution of optical fields in a nonlinear medium is known as the nonlinear Schrödinger (NLS) equation. The Maxwell equations can be used to obtain the following optical wave propagation equation for polarized wave [1].

$$\nabla^2 E - \frac{1}{c^2} \left(\frac{\partial^2 E}{\partial t^2} \right) = \frac{1}{\varepsilon_0 c^2} \left(\frac{\partial^2 P}{\partial t^2} \right) \quad (1)$$

A general soliton of Equation (1) can be written in the form $\vec{E}(r, t) = A(\vec{r}) \exp(j\beta_0 z - i\omega t)$ where $\beta_0 = k_0 n_0 \equiv 2\pi n_0 / \lambda$ is propagation constant. By taking into account the slowly varying amplitude approximation it can be written Equation (1) as follow:

$$2i\beta_0(\partial A / \partial Z) + (\partial^2 A / \partial X^2 + \partial^2 A / \partial Y^2) + 2\beta_0 k_0 n_{nl}(I)A = 0 \quad (2)$$

In the case of Kerr nonlinearity $n_{nl} = n_2 I$ where n_2 is the nonlinear Kerr coefficient. By replacing the variables $x = X/w_0$, $y = Y/w_0$, $z = Z/L_D$, $u = (k_0 |n_2| L_D)^{1/2} A$ the Equation (2) can be written as follow:

$$i\partial u / \partial z + 1/2(\partial^2 u / \partial x^2 + \partial^2 u / \partial y^2) \pm |u|^2 u = 0 \quad (3)$$

Equation (3) is named as standard (2+1)-dimensional NLS equation.

Where w_0 is a transverse scaling parameter that related to the input beam width and $L_D = \beta_0 w_0^2$ is the diffraction length. Where the choice of the sign in Equation (3) depends on the sign of the nonlinear parameter n_2 ; the minus sign is chosen in the self-defocusing case ($n_2 < 0$) and plus sign is chosen in the self-focusing ($n_2 > 0$). The (2+1)-dimensional NLS equation means 2 corresponds to the number of the transverse dimensions in the NLS equation and +1 indicates the propagation direction. When a nonlinear medium is in the form of a planar waveguide, the optical field is confined in one of the transverse directions (y axis) therefore Equation (3) obtained as follow

$$i\partial u / \partial z + 1/2(\partial^2 u / \partial x^2) \pm |u|^2 u = 0 \quad (4)$$

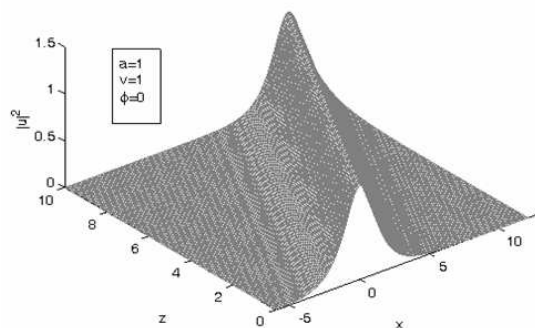


Figure 1: Collisions of two spatial solitons in the Kerr nonlinear media for three different phases $\phi = 0$, $\phi = \pi/2$, $\phi = \pi$.

The bright and dark spatial solitons corresponding to the choice of + and – signs respectively. For the case of another form of nonlinearity $n_{nl} = n_2 F(I)$. With $n_2 > 0$, focusing on the waveguide geometry, the (1 + 1)-dimensional NLS equation takes the form

$$i\partial u/\partial z + 1/2(\partial^2 u/\partial x^2) + F(I) = 0 \quad (5)$$

where in the special case of the Kerr nonlinearity $F(I) = I$ Equation (5) results in soliton solutions using the inverse scattering transform method. The one-soliton solution of the NLS equation has the following most general form:

$$u(x, z) = a \operatorname{sech}[a(x - vz)] \exp[ivx + i(v^2 - a^2)z/2 + i\phi] \quad (6)$$

where ϕ is an arbitrary phase. For a spatial soliton, the parameters a , v are related to the amplitude and transverse velocity of the soliton. When $v \neq 0$, the soliton propagates at an angle to the z axis, v provides a measure of the transverse displacement of the soliton beam. Pulse propagation at angle to the z axis is shown in Figure 1.

In this paper we have developed the Equation (4) with same parameters by considering the effects of second-order and fourth-order nonlinear absorption. Therefore the NLS equation can be written as the following form:

$$i\partial u/\partial z + 1/2(\partial^2 u/\partial x^2) + |u|^2 u = i\alpha |u|^2 u + i\beta |u|^4 u \quad (7)$$

where α is related to the two-photon absorption coefficient and β is related to the fourth-order nonlinear absorption coefficient.

2. RESULTS AND CALCULATIONS

We have simulated the propagation of solitons and their collisions by numerical solution of Equation (7), with and without considering the effects of absorption. In Figure 2 the simulation of propagation of two solitons are shown. Figure 2(a) shows that two solitons are attracted each other when they are in the same phase ($\phi = 0$) and finally combine and made one pulse. In the intermediate case, shown in part (b), two solitons interaction is accompanied by strong energy exchange, so that two solitons repel each other in phase ($\phi = \pi/2$). To out-of-phase solitons ($\phi = \pi$) they repel each other as shown in part (c).

Here, we have simulated the propagation of pairs of solitons, under the effects of two-order and four-order two-photon absorption. If the effect of absorption is not considered, the two spatial solitons attract each other in phase $\phi = 0$ and are fused together, so that output pulse amplitude is increased. In Figure 3(a) two spatial solitons attract each other in phase $\phi = 0$ under the effects of second-order absorption $\alpha = -0.1$, also the width and amplitude of pulse intensity is decreased. When the fiber length is increased, the two pulse combined and change to one pulse. The pulse energy of two solitons is shown in Figure 3(b) is decrease. If absorption index α increase, two spatial solitons in phase $\phi = 0$ disappears under the effect of absorption $\alpha = -0.5$. In Figure 4, two pulses are fused together under the effects of fourth-order absorption, after collision. If absorption coefficient β increase, output intensity is decreased. If we consider both absorption effects, i.e., second and fourth order absorption we observed in Figure 6 that one of the solitons disappears.

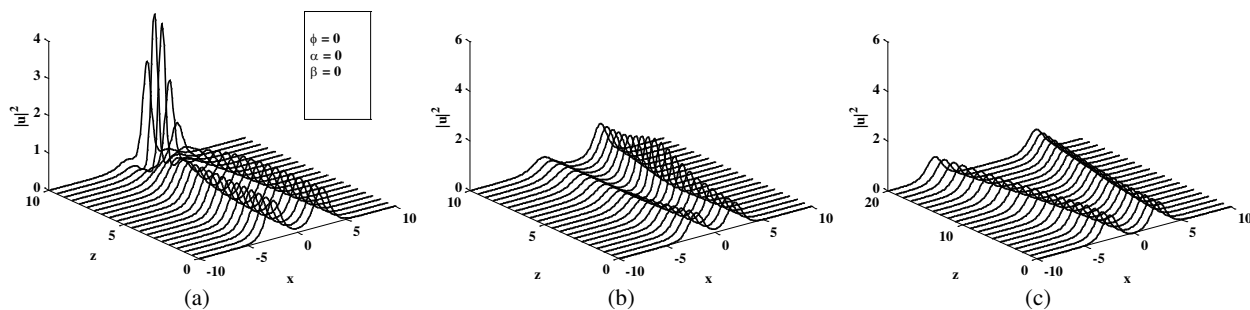


Figure 2: Collisions of two spatial solitons in the Kerr nonlinear media for three different phases $\phi = 0$, $\phi = \pi/2$, $\phi = \pi$.

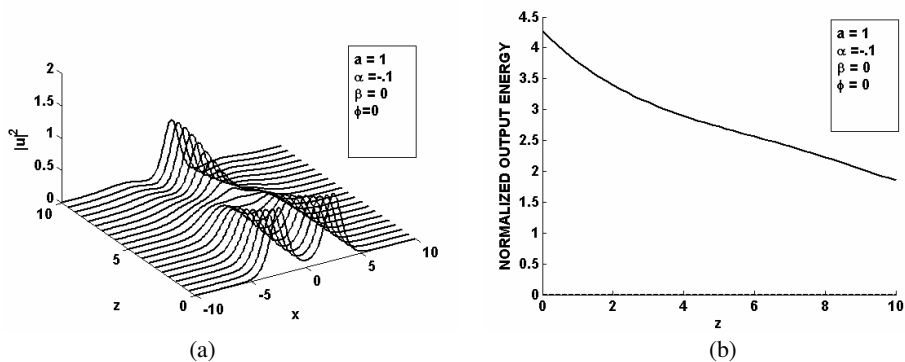


Figure 3: (a) Two spatial solitons interaction intensity in the non Kerr nonlinear media. (b) Energy related to two spatial solitons interaction in the non Kerr nonlinear media. $\alpha = -0.1$, $\beta = 0$, $\phi = 0$.

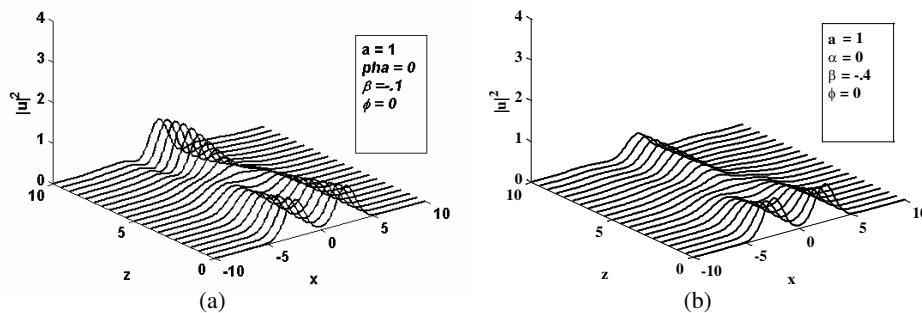


Figure 4: Two spatial solitons interaction intensity in the non Kerr nonlinear media. (a) $\alpha = 0$, $\beta = -0.1$, $\phi = 0$. (b) $\beta = -0.4$.

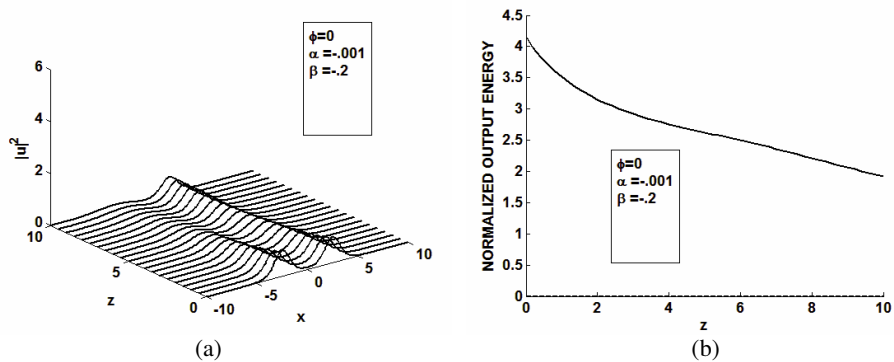


Figure 5: (a) Two spatial solitons interaction intensity in the non Kerr nonlinear media. (b) Energy related to two spatial solitons interaction in the nonKerr nonlinear media. $\alpha = -0.001$, $\beta = -0.2$, $\phi = 0$.

If we change the input pulse amplitude to $a = 1.4$ we observe that the input intensity and shape of pulse is the same as output pulse by taking $\phi = 0$, $\alpha = -0.2$ and $\beta = 0$ that make different behavior relative to previous that we had only one output pulse as it has been shown in Figure 7.

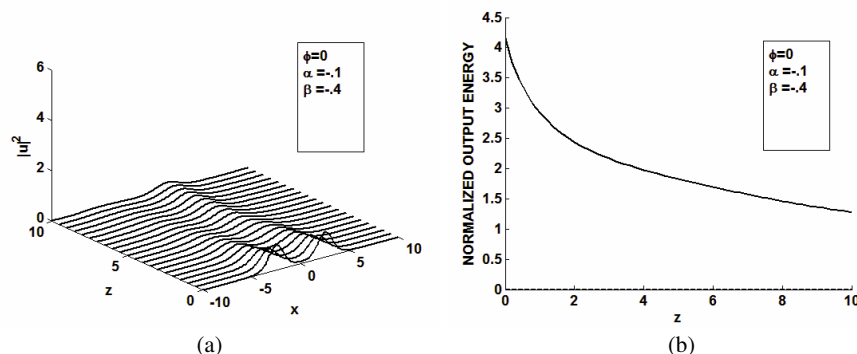


Figure 6: (a) Two spatial solitons interaction intensity in the non Kerr nonlinear media. (b) Energy related to two spatial solitons interaction in the nonKerr nonlinear media. $\alpha = -0.1$, $\beta = -0.4$, $\phi = 0$.

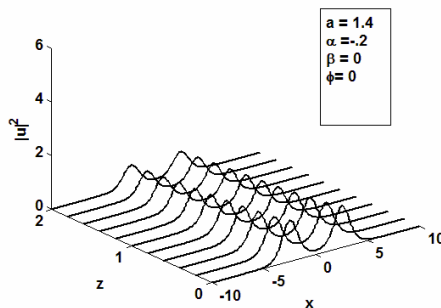


Figure 7: Two spatial solitons interaction intensity in the non Kerr nonlinear media. $\alpha = -0.2$, $\beta = 0$, $\phi = 0$, $a = 1.4$.

3. CONCLUSIONS

In this paper, we have studied collision of spatial solutions based on Schrödinger nonlinear equation by considering the effects of two-photon absorption. We have simulated collision between spatial solitons affected with the effect of second-order and fourth-order absorption in phase $\phi = 0$ by Fourier Series Analysis Technique (FSAT) [2]. The results show two solitons attract each other without considering the effects of two-photon absorption and also the output amplitude of wave is increased and the width is decreased. By further study and simulation with different values of absorption parameter and pulse amplitude of the input pulse, we have reached to conditions that there is one output rather than two outputs due to variation of the input amplitude. It means that output pulses can be controlled based on the variations of input amplitude which means that it can be used as an all optical self-controlling routing switch in optical [3].

REFERENCES

1. Agrawar, G. P., *Optical Solitons*, Academic Press, San Diego, 2003.
2. Hatami, M., H. Ghafouri-Shiraz, and A. Zakery, "Analysis of a gained nonlinear directional coupler pulse switch," *Optical and Quantum Electronics*, Vol. 38, 1259–1268, 2007.
3. Zakeri, A. and M. Hatami, "Nonlinear optical properties of pulsed-laser-deposited GeAsSe films and simulation of a nonlinear directional coupler switch," *J. of Opt. Society of Am. B*, Vol. 22, 591–597, 2005.

Performance Enhancement of Circularly Polarized Microstrip Antenna Using Electromagnetic Band Gap Structures

Muhammad Mahfuzul Alam, Md. Mustafizur Rahman Sonchoy, and Md. Osman Goni

Department of Electronics and Communication Engineering
Khulna University of Engineering and Technology, Bangladesh

Abstract— In this paper, design and simulation of two circularly polarized microstrip antennas and their performance improvements using Electromagnetic Band Gap (EBG) structure are given. Square shape EBGs are used in a planar structure for these cases. Sharp resonances are found with no harmonics and improvement of axial ratio for both of these antennas. Return loss of these antennas is below -40 dB or more lower. The effectiveness of the use of EBG structure is also discussed. The operating frequencies of these antennas are 2.45 GHz and 2.50 GHz.

1. INTRODUCTION

Microstrip patch is one of the most widely used radiators for circular polarization generators. Various shapes for microstrip antennas capable of circular polarization operation have been reported in literature such as square, circular, pentagonal, equilateral triangular, ring, elliptical shapes etc. However, square and circular patches are widely utilized in practice [1]. Circular polarization provides nearly constant receiving power levels in such application [1]. Circular polarization can be achieved if two orthogonal modes are excited with a 90° time-phase difference between them. This can be accomplished by adjusting the physical dimensions of the patch and using either single, or two or more feeds. For square patch element, the easiest way to excite ideally circular polarization is to feed the element at two adjacent edges. The quadrature phase difference is obtained by feeding the element with a 90° power divider or 90° hybrid [2]. We discuss two circularly polarized antennas and their performance enhancement using EBG. In recent years, there has been growing interest in utilizing electromagnetic band-gap structures in electromagnetic and antenna community [3]. The electromagnetic band gap structures are defined as artificial periodic (or sometimes non-periodic) objects that prevent/assist the propagation of electromagnetic waves in a specified band of frequency for all incident angles and all polarization states. EBG structures are usually realized by periodic arrangement of dielectric materials and metallic conductors [4]. Electromagnetic band gap materials offer pass-band and stop-band (band-gap) to electromagnetic waves in the same way as the semiconductor does in electronics. Another important characteristic of these materials is the ability to open localized electromagnetic modes inside the forbidden frequency band-gap by introducing defects into the periodic structures [4]. EBG structures have been used in several applications, such as suppressing surface waves [3], directive antennas [5], harmonic control [6], etc. Here we design a simple EBG based antenna with better return losses and axial ratio.

2. CIRCULARLY POLARIZED ANTENNA USING POWER DIVIDER

Circular polarization can be obtained using a square patch, driven at adjacent sides through a power divider. Operating frequency of the simulated antenna is 2.45 GHz and substrate permittivity is $\epsilon_r = 2.2$ (RT/duroid 5880). A $\lambda/4$ length transmission line is used for 90° phase difference. Return loss is -15.0 dB at 2.45 GHz, but better return loss (-17.91 dB) is found at 2.43 GHz, which is somewhat shifted. The simulated gain and directivity of the antenna are 5.61975 dBi and 6.34837 dBi respectively when right circularly polarized (RCP). Axial ratio is 9.5 dB, which is undesired for circular polarization.

Improvement of antenna performance can be achieved using Electromagnetic band gap structure. Two dimensional mushrooms like EBG surfaces are one of the choices. Operation mechanism of this EBG structure can be explained using an effective medium model with equivalent lumped LC elements as shown in Figure 3 [3]. Patch width W , gap width, substrate thickness h , dielectric constant ϵ_r . The capacitor results from the gap between the patches and the inductor results from the current along adjacent patches. The impedance of the parallel resonance LC circuit is given by [3, 4]

$$Z = j\omega L / (1 - \omega^2 LC) \quad (1)$$

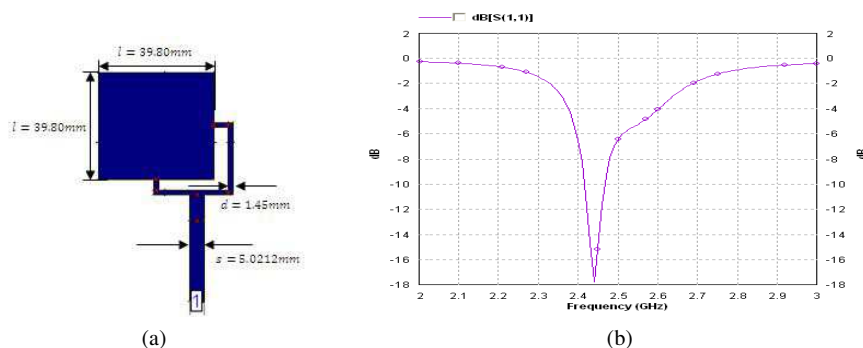


Figure 1: (a) Circular polarized square patch antenna and (b) return loss.

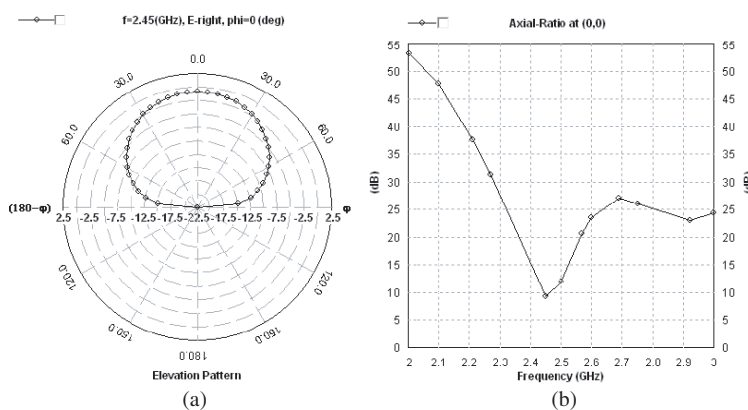


Figure 2: (a) Simulated Radiation pattern of the antenna, (b) axial ratio.

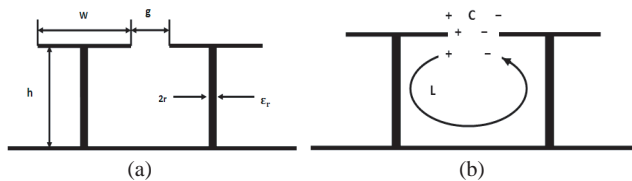


Figure 3: LC model of the EBG.

The resonance frequency of the circuit can be calculated using the following formula,

$$\omega_0 = 1/\sqrt{LC} \tag{2}$$

Edge capacitance for the narrow gap condition and inductance which depends only on the thickness of the structure and permeability are calculated using the following formulas.

$$C = \frac{W\epsilon_0(1 + \epsilon_r)}{\pi} \cosh^{-1} \left(\frac{W + g}{g} \right) \tag{3}$$

$$L = \mu_0 h \tag{4}$$

$$BW = \frac{1}{\eta} \sqrt{\frac{L}{C}} \tag{5}$$

where μ_0 the free space permeability and η is the free space impedance that is 120π . Two things are concerned in this EBG design if we increase the width of the patch the capacitance is increased and the resonance frequency decreases and band width becomes narrow. On the other hand, if we increase the gap between patches then capacitance decreases and both resonance frequency and bandwidth increases.

The above formulas are simple and not consider via's radius. Using the theory of transmission

line and periodic circuits a more accurate formula for inductor L can be found [4].

$$L = 2 \times 10^{-7} h \left[\ln \left(\frac{2h}{r} \right) + 0.5 \left(\frac{2r}{h} \right) - 0.75 \right] \quad (6)$$

where r is the vias radius.

In our simulation EBG gap is 0.2275 mm, between two 3×1 EBG array the antenna is inserted (Figure 4(a)). EBGs are arranged in this way to achieve better return loss. Dimension of the antenna and EBG is $143 \times 136 \text{ mm}^2$. Simulated Return loss is -40.68 dB and axial ratio is 2.6 dB at 2.45 GHz. So an improvement in return loss and axial ratio is found. We consider via's radius $r = 0.025 \text{ mm}$ and use Transmission theory for EBG structure. Figure 4(b) shows this layout, now EBG gap is 0.16 mm. Return loss improvement is not as high as in previous cases because of via's radius consideration. Consideration of via's radius is more realistic and practical. In this case return loss and axial ratio is -31.2 dB and 2.8 dB respectively. Dimension is $167 \times 166 \text{ mm}^2$ for antenna and EBG. From Figure 6, we see some backward radiation in radiation pattern of the antenna, these is due to the presence of EBG structure. This simulated antenna can be a suitable one for 2.4 GHz band WLAN system.

3. CIRCULAR POLARIZED ANTENNA USING BRANCH-LINE COUPLER

Circular polarized antenna can be designed using quadrature hybrids. Quadrature hybrids are directional couplers with a 90° phase difference in the outputs of the through and coupled arms. This type of hybrids is often made in microstrip or stripline and is also known as branch-line hybrid. Figure 8(a) gives the layout of the simulated antenna. It's operating frequency is 2.50 GHz and substrate permittivity is $\epsilon_r = 2.2$ (RT/duroid 5880). Simulated return loss is -18.75 dB (Figure 8(b)) at the 2.50 GHz but better return loss is found at 2.513 GHz so operating frequency is shifted. The gain and directivity of the antenna are 5.74519 dBi and 6.38042 dBi respectively when right circularly polarized (RCP). Axial ratio of the antenna is 7.2 dB, which is unacceptable for

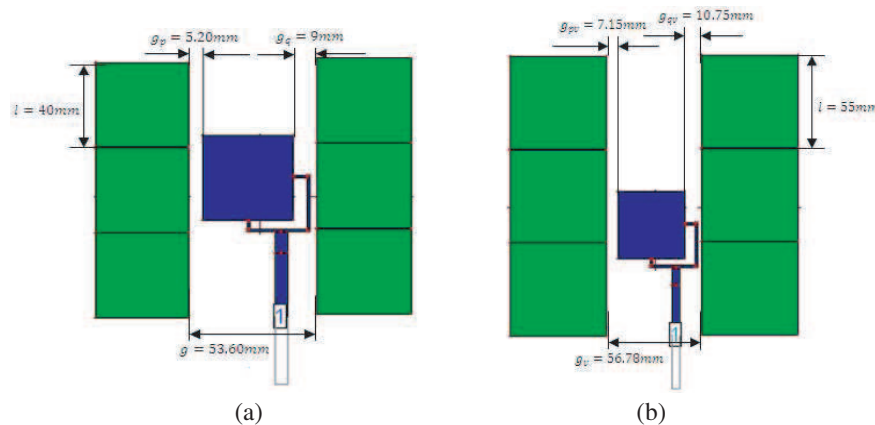


Figure 4: (a) Antenna with EBG structure not considering via's radius, (b) considering via's radius.

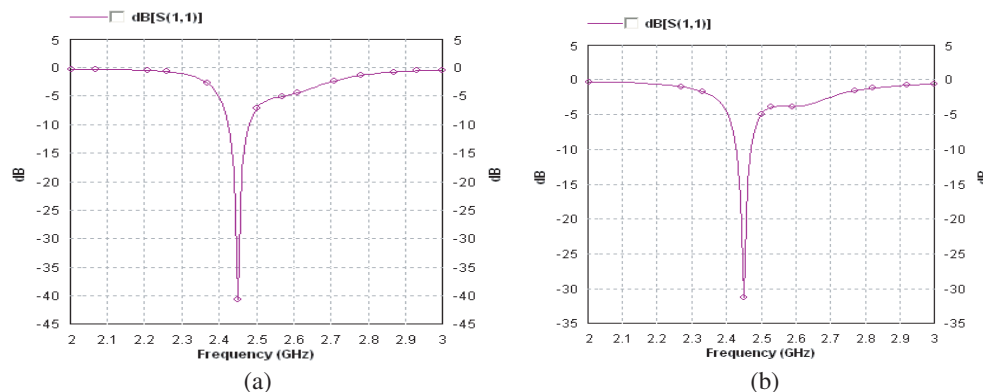


Figure 5: (a) Improved Return loss using EBG not considering via's radius and (b) with via's radius.

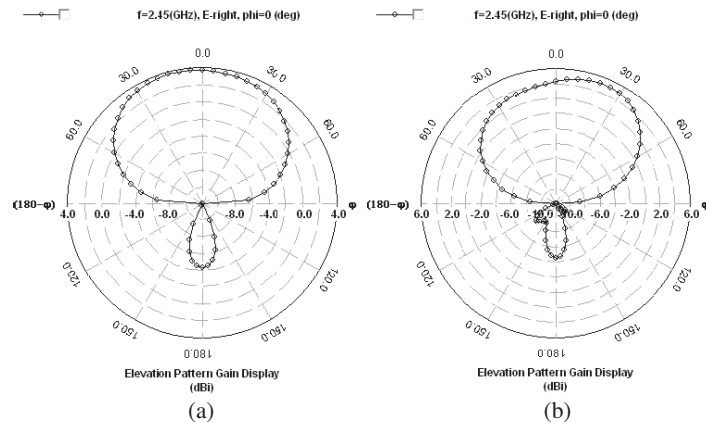


Figure 6: (a) Radiation pattern with out via's radius and (b) with via's radius.

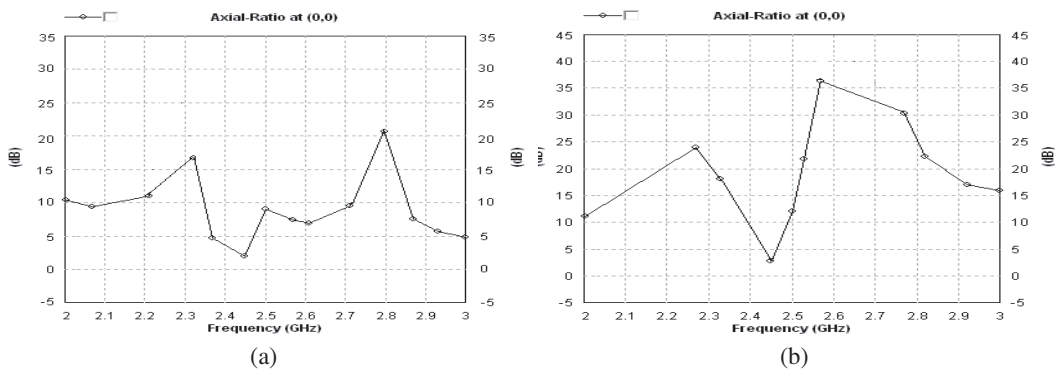


Figure 7: (a) Axial ratio without considering via's radius and (b) considering via's radius.

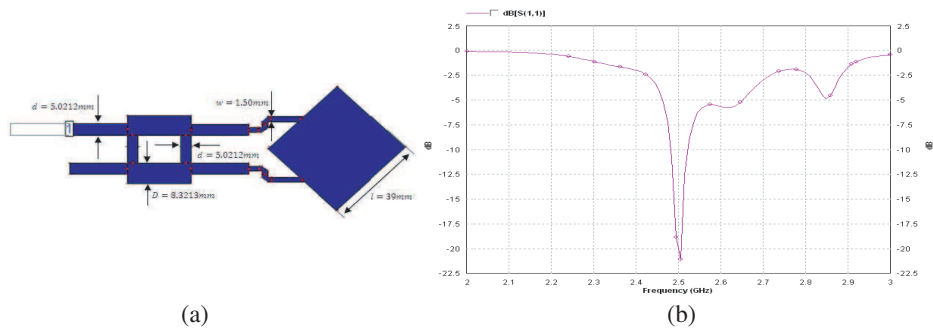


Figure 8: (a) Circularly polarized antenna layout and (b) return loss at 2.5 GHz.

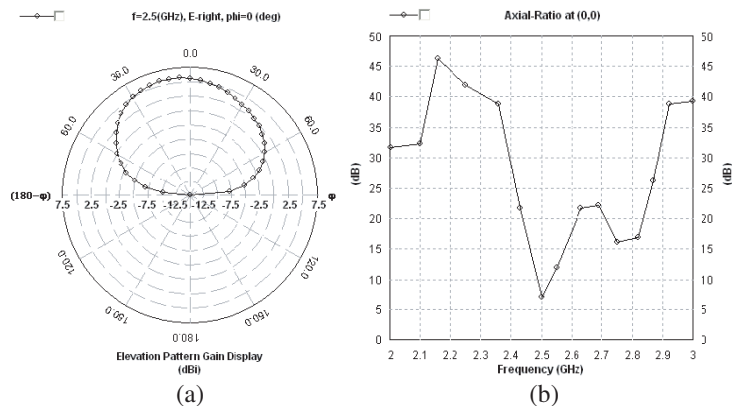


Figure 9: (a) Simulated radiation pattern of the antenna and (b) improved axial ratio.

circular polarization. Performance improvement of this antenna is possible using EBG as we use in previous antenna.

EBG patches are separated 0.60 mm apart, between two 3×1 arrays EBG the antenna is inserted (Figure 10(a)). This configuration gives better return loss and axial ratio. Dimension of the antenna and EBG is $137 \times 159 \text{ mm}^2$. Simulated return loss and axial ratio of the antenna is -41.75 dB and 2.3 dB respectively. Then considering the vias radius we calculate the EBG dimensions, gap between the EBG is 0.21 mm and via's radius is 0.025 mm. Layout of the structure is shown in Figure 10(b), simulated return loss and axial ratio is -37.6 dB and 2.3 dB respectively at resonance frequency. Total dimension of this antenna is $166 \times 175 \text{ mm}^2$. In Figure 12(b) there is no backward radiation, this implies changing the size and spacing of EBG we can remove backward radiation. Simulated antenna can be a good candidate for satellite radio services such as GlobalStar (2.5 GHz).

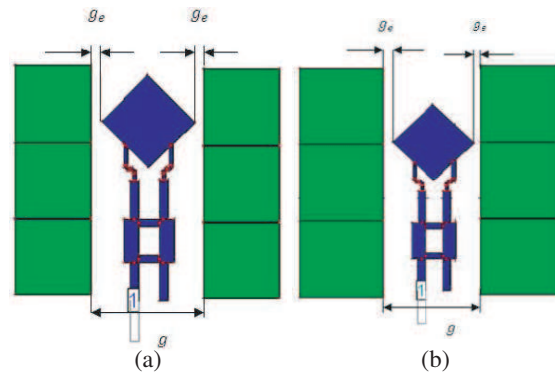


Figure 10: (a) Antenna structure using EBG without vias and (b) with vias radius.

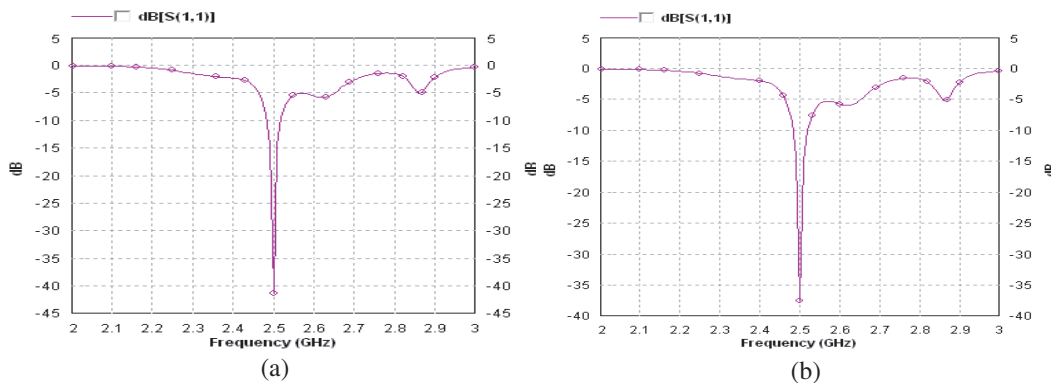


Figure 11: (a) Return loss of the antenna without vias radius and (b) with vias radius.

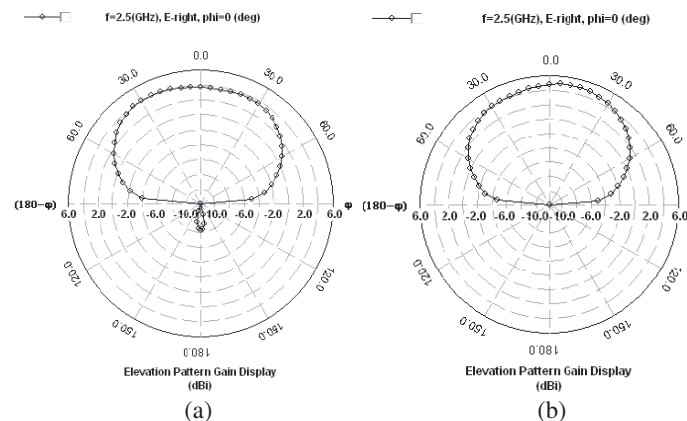


Figure 12: (a) Radiation pattern without vias radius, (b) with vias radius.

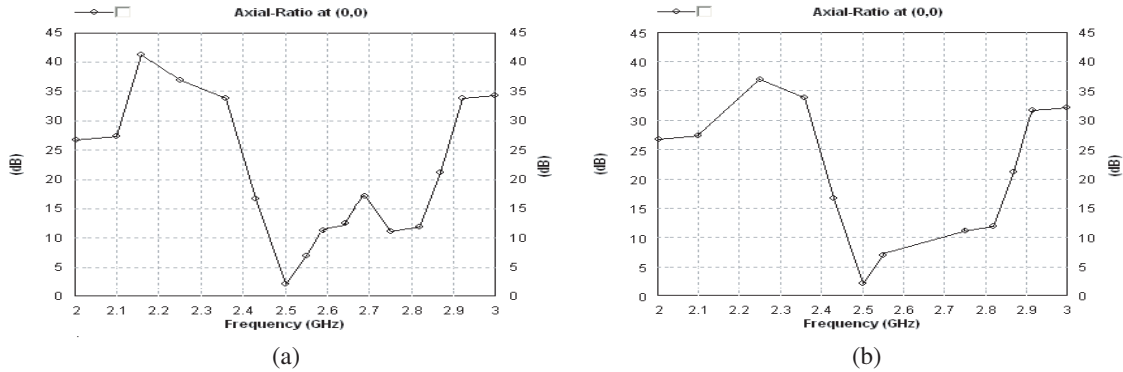


Figure 13: (a) Axial ratio without considering via's radius, (b) considering via's radius.

4. CONCLUSION

We discuss about circularly polarized microstrip antenna and there performance using EBGs. Use of EBG total dimension of the structure is increased but performance of the antenna is also increased. For simulation we consider LC modeling of EBG with and without vias radius. Without vias radius consideration of EBG the output result is relatively higher but for more practical point of view one should consider vias radius for simulation. In our simulation we show that changing the size and spacing of EBG backward radiation can be removed. Simulations have done using Zeland IE3D software.

REFERENCES

1. Garg, R., P. Bhartia, I. Bahl, and A. Ittipiboon, *Microstrip Antenna Design Handbook*, Artech House, Inc, 2001.
2. Balanis, C. A., *Antenna Engineering*, 2nd Edition, Wiley.
3. Yang, F. and Y. Rahmat-Samii, "Microstrip antenna integrated with Electromagnetic Band-Gap (EBG) structures: A low mutual coupling design for array application," *IEEE Trans. Antenna Propagation*, Vol. 51, 2936–2946, Oct. 2003.
4. Yang, F. and Y. Rahmat-Samii, *Electromagnetic Bandgap Structures in Antenna Engineering*, Cambridge University Press, 2009.
5. Boutayed, H., T. A. Denidni, A. R. Sebak, and L. Talbi, "Design of elliptical electromagnetic bandgap structures for directive antennas," *IEEE Antennas and Wireless Propagation Letters*, 93–96, 2005.
6. Horii, Y. and M. Tsutsumi, "Harmonic control by photonic bandgap on microstrip patch antenna," *IEEE Microwave and Guided Wave Letters*, Vol. 90, No. 1, Jan. 1999.

Design and Performance Analysis of Microstrip Array Antenna

Muhammad Mahfuzul Alam, Md. Mustafizur Rahman Sonchoy, and Md. Osman Goni

Department of Electronics and Communication Engineering
Khulna University of Engineering and Technology, Bangladesh

Abstract— This paper describes the design of different microstrip array antennas. Series-feed, corporate-feed and their combination that makes series-corporate feed and full-corporate feed antennas are analyzed and simulated. These antennas are designed on a thin substrate for the application of conformal microstrip array antenna. In all cases we get return losses below than -15 dB at resonance frequency. The gain of these antennas are simulated and found adequate results also sidelobe level is maintained 11.0 dB or lower than main lobe. One of these simulated antennas is implemented for performance tests. Operating frequency of these antennas are 2.45 GHz, 1.88 GHz, so these antennas are suitable for L-band and S-band application.

1. INTRODUCTION

Microwave equipments require low profile and light-weight to assure reliability, an antenna with these characteristics is essentially required and a microstrip antenna satisfies such requirement. The key features of a microstrip antenna are relative ease of construction, light weight, low cost and either conformability to the mounting surface or, at least, an extremely thin protrusion from the surface. Microstrip arrays are limited in that they tend to radiate efficiently only over a narrow band of frequencies and they can not operate at the high power levels of waveguide, coaxial line, or even stripline [1]. In various communications and radar systems microstrip antenna is greatly desired. Microstrip antennas are very versatile and are used, among other things, to synthesize a required pattern that cannot be achieved with a single element. In addition, they are used to scan the beam of an antenna system, increase the directivity, and perform various other functions which would be difficult with any one single element. The elements can be fed by a single line or by multiple lines in a feed network arrangement. The first is referred to as a *series-feed network* while the second is referred to as a *corporate-feed network* [2]. This paper presents the characteristic of microstrip array antennas, series-feed, corporate feed and their combination. There performance comparisons are also given for better understanding. Substrate selection and element spacing for grating lobe minimization are also given. For microstrip antennas, the dielectric constants are usually in the range of $2.2 \leq \epsilon_r \leq 12$. Dielectric constants in the lower end of the range can give us better efficiency, large bandwidth, loosely bound electric field for radiation into space, but at the expense of large element size. In microwave circuit that requires tightly bound fields to minimize undesired radiation and coupling, and lead to smaller element size. In some application we need small size antennas, substrate with high dielectric constant is a better choice in this application. High dielectric constants have greater losses so they are less efficient and have relatively small bandwidth [2]. In our design, we consider all these things. Simulated antennas can be easily fabricated on FR-4 ($\epsilon_r = 4.4$), RT/duroid 5880 ($\epsilon_r = 2.2$) or high dielectric constant of ($\epsilon_r = 10.2$, R03010) substrate. Recessed microstrip line feeding techniques is used as this gives a good impedance matching at inputs of the radiating elements.

2. MICROSTRIP SERIES-FEED ARRAY ANTENNA

If we reduce the width of the patch, the radiation conductance is insufficient to match the input. We can use the microstrip patch as a transmission line and connect a line opposite the feed to lead to other patches. If we space the patches by half wavelengths, the impedances of the patches will add in phase at the input, because it rotates once around the Smith chart in $\lambda/2$. The Characteristic impedance of the connecting lines has no effect at center frequency. The junction of transmission-line feeder and the patch introduces extra phase shift [3]. The difference in phase between two adjacent elements in series-fed array as given in [4] as

$$\phi = 2\pi fl/v = 2\pi l/\lambda \quad (1)$$

where f = frequency of the electromagnetic signal, l = length of line connecting adjacent elements, v = velocity of propagation, and λ = signal wavelength. The main limitation in series-fed arrays is the large variation of the impedance and beam-pointing direction over a band of frequencies.

The main limitation in series-fed arrays is the large variation of the impedance and beam-pointing direction over a band of frequencies. The main beam direction and the scan sensitivity can be calculated from the following equations [5].

$$d \sin \theta + \sqrt{\epsilon} l = \lambda = \frac{c}{f} \tag{2}$$

$$\frac{\partial \theta}{\partial f} = -\frac{c}{df^2 \cos \theta} \tag{3}$$

where d is the element spacing, l is the length of transmission line joining the successive elements, c is the velocity of light, f is the operating frequency, and θ is the beam-pointing angle measured from the broadside direction. Such a configuration can be used as a frequency scanned array. For the low side lobe design, the radiation resistance offered by each patch is chosen according to the required amplitude distribution. This can be achieved by varying the nonresonant width of the rectangular patch element [5]. For series feed linear array, we consider all excitation amplitude are same. The radiated fields of the E -plane for a single element patch and array factor can be expressed using the following formulas [2, 6].

$$E = +jk_0 W V_0 e^{-jk_0 r} / \pi r \left\{ \sin \left(\frac{k_0 h}{2} \cos \phi \right) / \frac{k_0 h}{2} \cos \phi \right\} \cos \left(\frac{k_0 L_e}{2} \sin \phi \right) \tag{4}$$

Here W is the width of the patch antenna, L_e is the extended length, $V_0 = hE_0$ is the voltage across radiating slot. h is the substrate height, $K_0 = 2\pi/\lambda$ and r is the far field distance from the antenna.

$$FA = \sin(N\pi d_x(u - u_0)) / \sin(\pi d_x(u - u_0)) \tag{5}$$

Here $u = \sin \theta$, $u_0 = \sin \theta_0$, d_x is the element spacing. N is the number of elements. Combining array factor and element voltage radiation pattern we get the total element normalized power radiation pattern that is $20 \log(|E|FA)$ [8]. Gain is the most important performance parameter of an antenna. The general formula for approximating gain is given by Warren Stutzman [7].

$$G = 26000 / HP_{E^0} HP_{H^0} \tag{6}$$

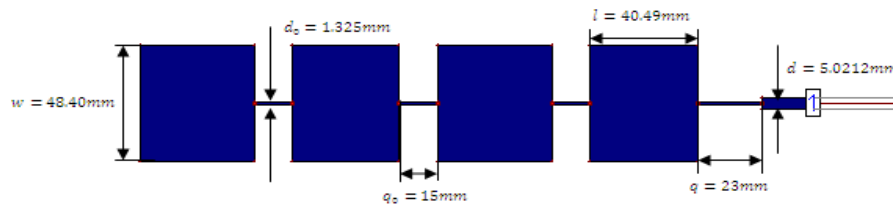


Figure 1: Series-fed array (4-element), $f = 2.45$ GHz.

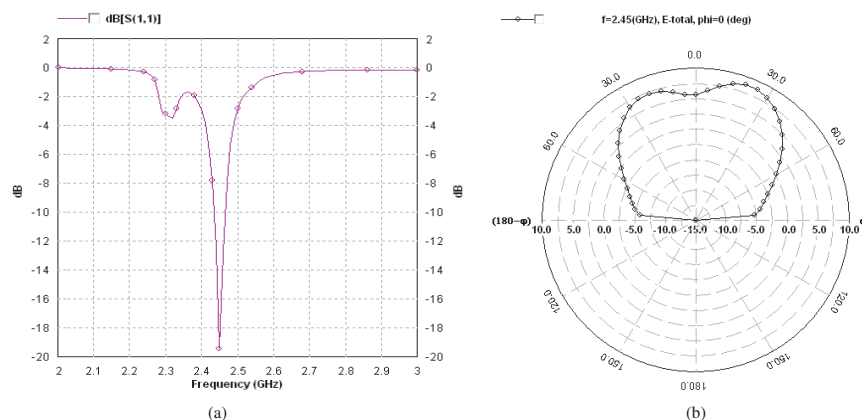


Figure 2: (a) Return loss (−19.38 dB) for 2.45 GHz and (b) radiation pattern at 2.45 GHz.

where HP_{E^0} and HP_{H^0} are the principal-plane beamwidths in degrees. 26000 is the directivity-beamwidth product in deg^2 . Substrate permittivity of the antenna is $\epsilon_r = 2.2$ (RT/duroid 5880), height is 1.58 mm and resonance frequency of the antenna is 2.45 GHz. There is 44.10° phase difference between adjacent elements. After simulation we found that, return loss is -19.38 dB. The simulated gain and directivity of the antenna after simulation are found 8.67563 dBi and 9.15724 dBi respectively. This techniques is limited to arrays with a fixed beam or those which are scanned by varying frequency, also it can be applied to linear and planar arrays. This antenna has poor side lobe level and return loss -10 dB or lower from 2.432 GHz to 2.467 GHz, so it can be used in 2.4 GHz band WLAN system.

3. MICROSTRIP CORPORATED-FEED ARRAY ANTENNA

The corporate-feed network is used to provide power splits of 2^n (i.e., $n = 2, 4, 8, 16, 32$, etc.). This is accomplished by using either tapered lines or using quarter wavelength impedance transformers. Corporate-fed arrays are general and versatile. With this method the designer has more control of the feed of each element (amplitude and phase) and it is ideal for scanning phased arrays, multibeam arrays, or shaped-beam arrays [2]. The radiated field formula that is given in Equation (4) is same for this array and array factor as given in [4, 8] as

$$FA = \sin^2(N\pi(d_x/\lambda)\sin\theta) / N^2 \sin^2(\pi(d_x/\lambda)\sin\theta) \quad (7)$$

Combining the element radiation pattern and array factor we get the normalized power radiation pattern. The substrate permittivity of the antenna is $\epsilon_r = 4.4$, height is 1.58 mm and resonance frequency of the antenna is 2.45 GHz. Simulated return loss of the antenna is -22.0 dB. Gain and directivity of the antenna are 11.3139 dBi and 12.5309 dBi respectively. Sidelobe level is 11.0 dB lower than main lobe. Antenna return loss is -10 dB or lower from 2.437 GHz to 2.462 GHz, so this can be used in 2.4 GHz band WLAN system. We implement this antenna for performance evaluation. Measured radiation pattern is not satisfactory; sidelobe level is -7.5 dB lower than main lobe. This is because of fabrication and measuring equipment limitation.

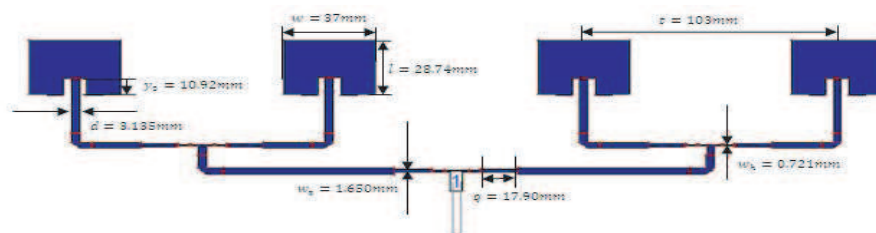


Figure 3: Corporate-fed array (4-element) $f = 2.45$ GHz.

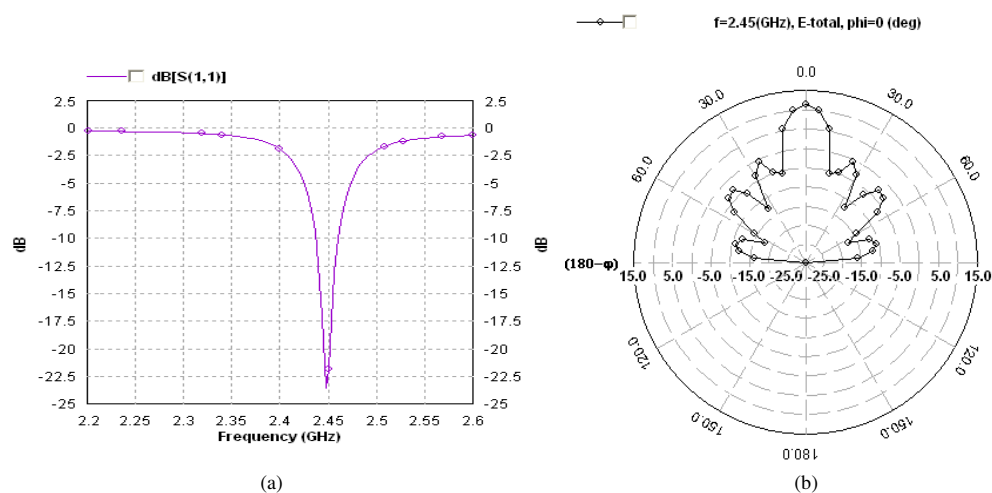


Figure 4: (a) Return-loss (-22.0 dB) at $f = 2.45$ GHz and (b) radiation pattern.

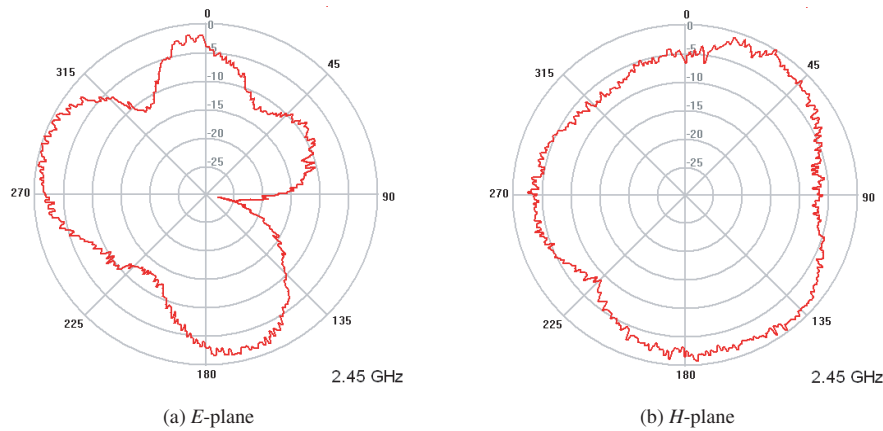


Figure 5: Measured radiation pattern (a) E -field and (b) H -field of this antenna.

4. COMBINATION OF SERIES AND CORPORATE FEED MICROSTRIP ANTENNAS

The combination of series feed and corporate feed can be used for array antenna. A 16-element array antenna can be constructed using this method. It's a two dimensional, rectangular planar array whose aperture illumination can be separated into two orthogonal planes such as the horizontal and vertical planes, the radiation pattern may then be written as the product the radiation patterns in these two planes. The array factor of this antenna with element spacing in the x and y direction are d_x and d_y respectively as given in [4, 8] as

$$FA = \left(\frac{\sin^2(N\pi(d_x/\lambda)\sin\theta_a)}{N^2 \sin^2(\pi(d_x/\lambda)\sin\theta_a)} \right) \cdot \left(\frac{\sin^2(M\pi(d_y/\lambda)\sin\theta_e)}{M^2 \sin^2(\pi(d_y/\lambda)\sin\theta_e)} \right) \quad (8)$$

Here N = number of vertical elements of array that gives rise to the azimuth angle θ_a and M = number of horizontal elements of array that gives rise to the elevation angle θ_e . Multiplying the above equation with element radiated field gives normalized power radiation pattern. Substrate permittivity of the antenna is $\epsilon_r = 2.2$ (RT/duroid 5880) and height is 1.58 mm. Simulated return loss is -17.60 dB at $f = 2.45$ GHz. Gain and directivity of the antenna are 15.1504 dBi and 15.7942 dBi respectively. Antenna return loss is -10 dB or lower from 2.437 GHz to 2.475 GHz. This antenna have high gain and sidelobe level is 13 dB lower than main lobe so it can be used for 2.4 GHz band WLAN base station system or sub-array antenna for radar system.

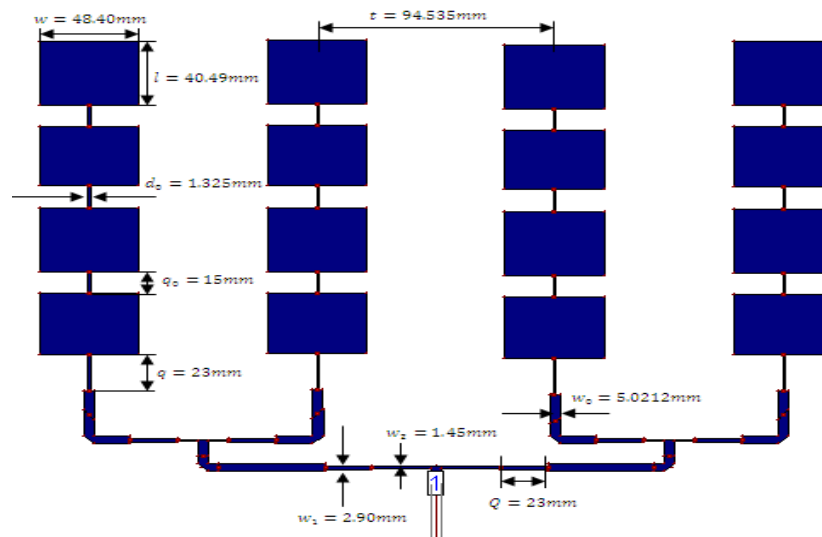


Figure 6: 16-element array antenna, combination of series and corporate feed.

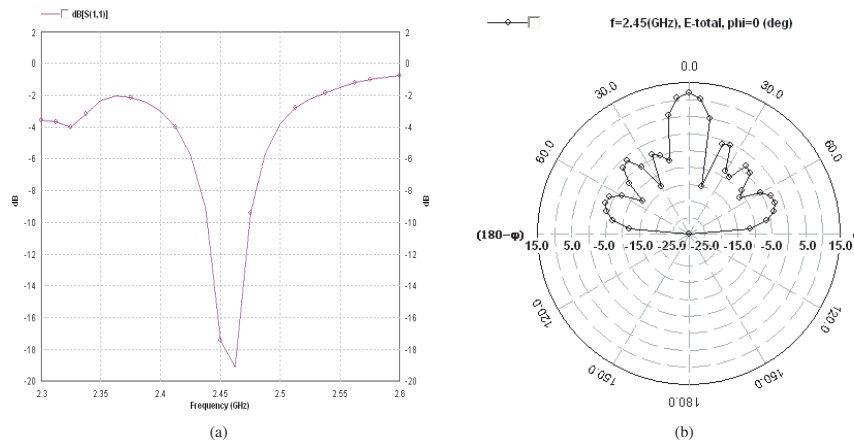


Figure 7: (a) Return loss (-17.42 dB) at $f = 2.45$ GHz and (b) radiation pattern.

5. COMBINATION OF CORPORATE AND CORPORATE FEED MICROSTRIP ANTENNAS

A fully corporate feed encompasses both branch and main feeds. This type of feed is often used with microstrip patch arrays. We design and simulate an 2×8 array antenna that is 16 element full-corporate configurations. The elements spacing are little bit more than half of wavelength, so no grating lobe is created because the element pattern will suppress it. The array factor equation of this antenna is same as given in Equation (8). The substrate dielectric constant is considered $\epsilon_r = 10.2$ (high dielectric constant is used for size reduction), height is 1.58 mm and antenna operating frequency is 1.88 GHz. The return loss of the antenna is -18 dB at 1.88 GHz but better return loss -33.03 dB is found at 1.882 GHz, which is somewhat shifted. Simulated antenna has return loss -10 dB or lower from 1.860 GHz to 1.887 GHz. The simulated gain and directivity of the antenna are 16.4071 dBi and 17.8751 dBi respectively and sidelobe level is 12.0 dB lower than main lobe. It's a high gain antenna and is a good candidate for different wireless communication system.

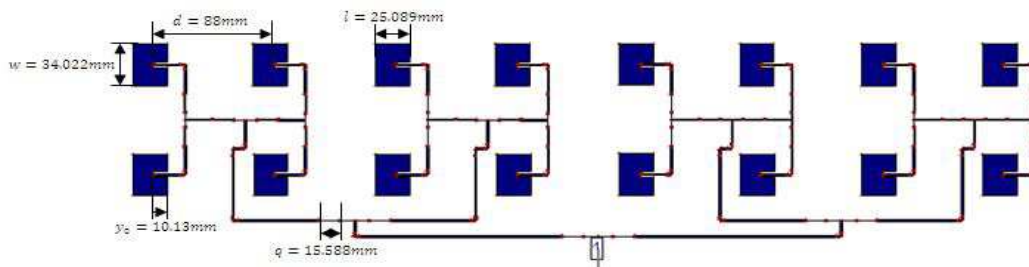


Figure 8: 16-element full-corporate antenna array (layout).

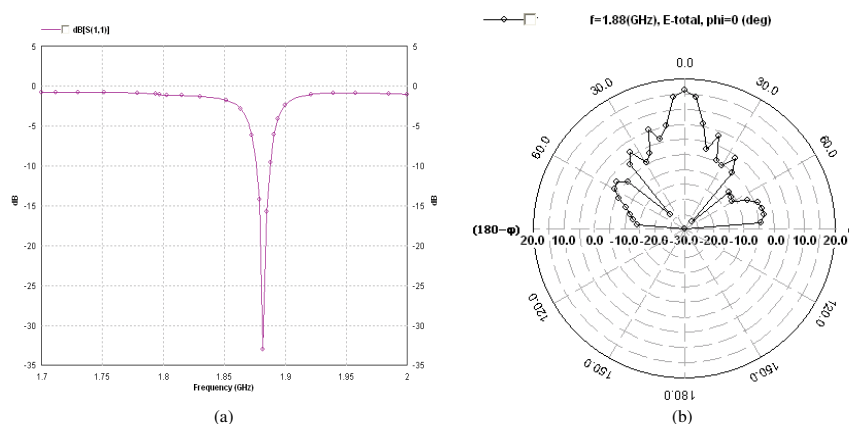


Figure 9: (a) Return loss of the antenna at 1.88 GHz (-18.0 dB) and (b) simulated Radiation pattern.

6. CONCLUSION

The characteristic of these antennas are investigated using IE3D simulator. We see that changing the geometry of antenna and array element spacing gives us different result. These things should be consider in array antenna designing system. First and second simulated antennas are linear arrays so this type of antenna only controls the pattern in one plane; it depends on the element pattern to control the beam in the other plane. Third and forth simulated antennas are planar array, so these antennas can control the beam shape in both planes and form pencil beams. This implies that planar array have their advantages over linear array antenna.

REFERENCES

1. Mailloux, R. J., J. F. Mclvenna, and N. P. Kernweis, "Microstrip array technology," *IEEE Trans. Antenna Propag.*, Vol. 29, No. 1, 25–27, January 1981.
2. Balanis, C. A., *Antenna Engineering*, 2nd Edition, Willey.
3. Milligan, T. A., *Modern Antenna Design*, 2nd Edition, IEEE Press, John Wiley & Sons inc, Publication.
4. Skolnik, M. I., *Introduction to RADAR System*, 3rd Edition, McGraw Hill Higher Education, 2000.
5. Garg, R., P. Bhartia, I. Bahl, and A. Ittipiboon, *Microstrip Antenna Design Handbook*, Artech House, INC., 2001.
6. Mailloux, R. J., *Electronically Scanned Arrays*, Morgan & Claypool, 2007
7. Stutzman, W. L., "Estamating directivity and gain of antennas," *IEEE Antennas and Propagation Magazine*, Vol. 40, No. 4, 7–11, August 1998.
8. Visser, H. J., *Array and Phased Array Antenna Basics*, John Wiley & Sons Ltd., 2005.

A Special Use of Wavelet Transform for Detecting the Live after Earthquake with Radar Waves

N. Uzunoglu¹ and S. J. Javadi²

¹School of Electrical and Computer Engineering, National Technical University of Athens, Greece

²Department of Electrical Engineering, University of Zabol, Iran

Abstract— In this paper, New algorithm for Detecting the Live after Earthquake is presented. Here the application of the Radar waves with frequency 2.45 GHz in a portable system for detecting the live below a mass of concrete or trash is introduced. The characters of radar hardware are shown too. The software which is used for computer process is Lab-View, that some part of it is presented. Output of the Radar system which is analog convert to digital signal and enters into PC then for using of continues filtering by a section of the program digital signal is converted to an analog signal again. Now a software band-pass filter with variable pass band is applied, which change the quantity of the system. For the mathematic analyze a special wavelet transform (in-place kind) is applied that its algorithm and its mathematic debate are existed.

1. INTRODUCTION

As we know an earthquake is the result of a sudden release of energy in the Earth's crust that creates seismic waves. Earthquakes are recorded with a seismometer, also known as a seismograph. The moment magnitude of an earthquake is conventionally reported. The unit of earthquake is Richter Earthquakes With magnitude 3 or lower mostly are imperceptible and Earthquakes With magnitude 7 causing serious damage over large areas. There are some injury people below the damage of earthquake that if detect on time will save.

In present system, it has been used from Radar wave with special separating techniques for raise quality of detecting the live after earthquake. For sensitivity improvement, wavelet transform have been used.

2. BASE OF THE SOFTWARE

The program of the system has been written with Lab-View software. The program prepares a one dimension array that timely save digital data from Analog/Digital convertor that is output of Radar system Then in program this digital data convert into Sinuses wave again (a kind of software Digital to Analog Converted-D/A C). In the program, the last 6 digital inputs are used as data for wavelet transformer that have explained in the next part. If the wavelet shows the variation it mine that there is a movement or even birthing in front of the Radar system. If this variation is further than of an amount, that is regulative by user, the software will broadcast a sound accord the movement.

In Fig. 4, a part of program's algorithm without the details have been seen. At the first the received data of A/D convertor enter into a one dimension array. Then wavelet transform operate on the $4, 8 \dots 2^n$ samples of the last samples, of course n is variable by user as a sensitive changer, increase of n cause increase of sensitive however it cause decrease of the speed of the system. After testing some kinds of wavelet transfer, we found that the system is working better by In-Place wavelet transform. In the next part, the details and algorithm of this kind of wavelet transform have been explained.

For the "Is there any variation" Block of the Fig. 4, mid element of the wavelet transfer, that show difference between all elements of wavelet transform block, is separated and compare with a factor. This is another variable part by operator of program for changing the sensitive of the system. If the mid element of wavelet transform is further than this factor, it is seeing that there are movements and in next block the system will broadcast an alarm. This process is continuing until the operator of system push stop bottom.

As it has been explained before, we have used a radar sender unit and a radar receiver unit that work with a frequency 2.45 MHz. Out put of the hardware is the difference between waves of these two units. This deference changes when there are a movement or even birthing in front of system. Therefore this system is useable for other targets such measurement of liquid, exist the water flow under the earth surface and

Then difference between two waves that is an analog signal, is converted into a digital signal by an Analog to Digital convertor (ADC-42) and transfer into PC. Now this digital signal is processed by lab-view software.

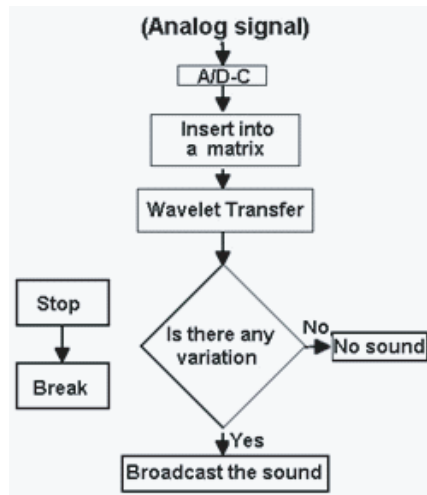


Figure 1: Block diagram of using the software for detect the live after earthquake system.

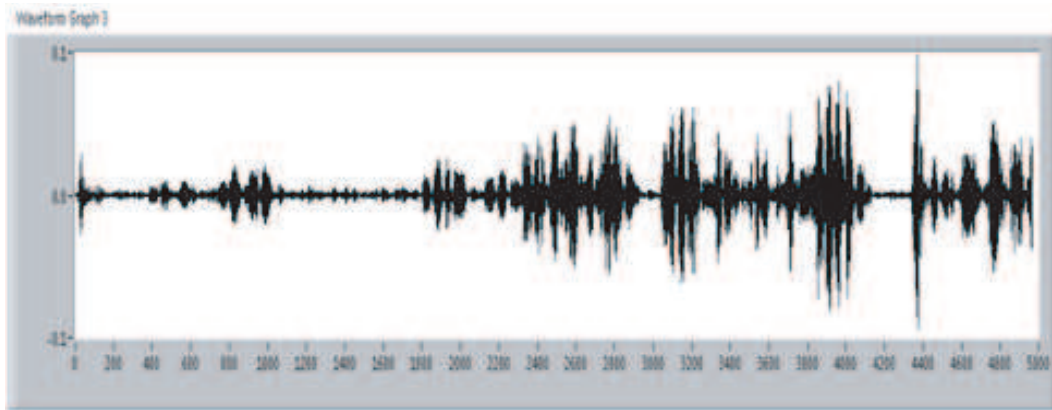


Figure 2: A real sample of radar system output the changes in amplitude is made by moving or birthing a live below the concrete.

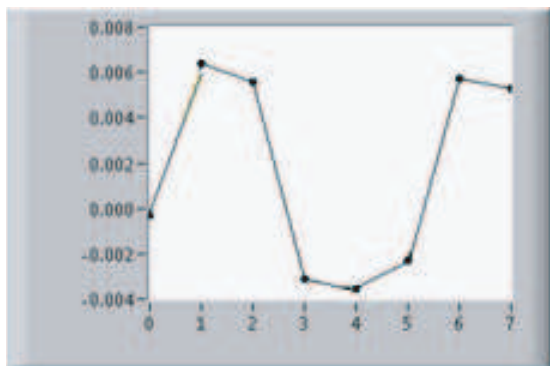


Figure 3: A sample of last 8 point of Radar output.

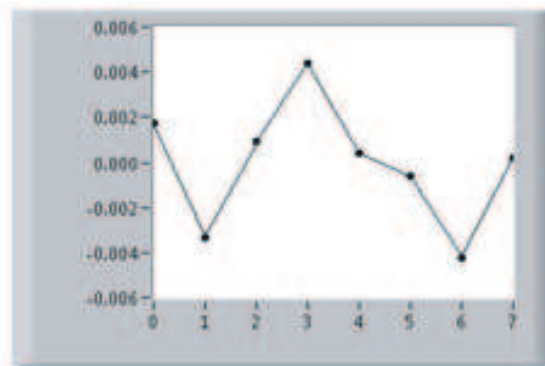


Figure 4: The wavelet transform of signal of Fig. 6.

3. THEORETICAL ANALYSIS

3.1. The Ordered Fast Wavelet Transform

The preceding section has demonstrated how a first sweep of the basic transform applies to all the consecutive pairs (S_{2k}, S_{2k+1}) of the initial array of sample values $\vec{a}^{(n)} = \vec{s}$.

In general, the λ th sweep of the basic transform begins with an array of $2^{n-(\lambda-1)}$ values.

$$\vec{a}^{(n-[\lambda-1])} = \left(a_0^{(n-[\lambda-1])}, \dots, a_{2^{n-[\lambda-1]}-1}^{(n-[\lambda-1])} \right)$$

And applies the basic transform to each pair $(a_{2k}^{(n-[\lambda-1])}, a_{2k+1}^{(n-[\lambda-1])})$ which gives two new wavelet coefficients

$$\begin{aligned} a_k^{(n-\lambda)} &:= \frac{a_{2k}^{(n-[\lambda-1])} + a_{2k+1}^{(n-[\lambda-1])}}{2} \\ c_k^{(n-\lambda)} &:= \frac{a_{2k}^{(n-[\lambda-1])} - a_{2k+1}^{(n-[\lambda-1])}}{2} \end{aligned}$$

These $2^{(n-\lambda)}$ pairs of new coefficients represent the result of the λ th sweep, a result that can also be reassembled into two arrays:

$$\begin{aligned} \vec{a}^{(n-\lambda)} &:= \left(a_0^{(n-\lambda)}, a_1^{(n-\lambda)}, \dots, a_k^{(n-\lambda)}, \dots, a_{2^{n-\lambda}-1}^{(n-\lambda)} \right) \\ \vec{c}^{(n-\lambda)} &:= \left(c_0^{(n-\lambda)}, c_1^{(n-\lambda)}, \dots, c_k^{(n-\lambda)}, \dots, c_{2^{n-\lambda}-1}^{(n-\lambda)} \right) \end{aligned}$$

The arrays related to the λ th sweep have the following significance.

$\vec{a}^{(n-[\lambda-1])}$: The beginning array,

$$\vec{a}^{(n-[\lambda-1])} = \left(a_0^{(n-[\lambda-1])}, \dots, a_{2^{n-[\lambda-1]}-1}^{(n-[\lambda-1])} \right)$$

Lists the values $\vec{a}^{(n-[\lambda-1])}$ of a simple step function $\tilde{f}^{(n-[\lambda-1])}$ that approximates the initial function f with $2^{n-(\lambda-1)}$ steps of narrower width $2^{(\lambda-1)-n}$.

$$\tilde{f}^{(n-[\lambda-1])} = \sum_{j=0}^{2^{n-[\lambda-1]}-1} a_j^{(n-[\lambda-1])} \varphi_j^{(n-[\lambda-1])}$$

$\vec{a}^{(n-\lambda)}$: The first array produced by the λ th sweep,

$$\vec{a}^{(n-\lambda)} = \left(a_0^{(n-\lambda)}, \dots, a_{2^{n-\lambda}-1}^{(n-\lambda)} \right)$$

Lists the values $a_k^{(n-\lambda)}$ of a simple step function $\tilde{f}^{(n-\lambda)}$ that approximates the initial function f with $2^{n-\lambda}$ steps of wider width $2^{\lambda-n}$,

$$\tilde{f}^{(n-\lambda)} = \sum_{j=0}^{2^{n-\lambda}-1} a_j^{(n-\lambda)} \varphi_j^{(n-\lambda)}$$

$\vec{c}^{(n-\lambda)}$: The second array produced by the λ th sweep,

$$\vec{c}^{(n-\lambda)} = \left(c_0^{(n-\lambda)}, \dots, c_{2^{n-\lambda}-1}^{(n-\lambda)} \right)$$

Lists the coefficients $c_k^{(n-\lambda)}$ of simple wavelets $\psi_j^{(n-\lambda)}$ also of wider width $2^{\lambda-n}$,

$$\tilde{f}^{(n-\lambda)} = \sum_{j=0}^{2^{n-\lambda}-1} c_j^{(n-\lambda)} \psi_j^{(n-\lambda)}$$

The wavelets given by the second new array $\tilde{c}^{(n-\lambda)}$ represent the difference between the finer steps of the initial approximation $\tilde{f}^{(n-[\lambda-1])}$ and the coarser steps of $\tilde{f}^{(n-\lambda)}$. Thus, each sweep of basic transforms expresses the previous finer approximation as the sum of a new, coarser approximation and a new, lower-frequency, and set of wavelets. Nevertheless, because the basic step of wavelet transform does not alter the sampled function but merely expresses it with different wavelets, it follows that the initial approximation $\tilde{f}^{(n-[\lambda-1])}$ still equals the sum of the two new approximations, $\tilde{f}^{(n-\lambda)}$ and $\tilde{f}^{(n-\lambda)}$:

$$\tilde{f}^{(n-[\lambda-1])} = \tilde{f}^{(n-\lambda)} + \tilde{f}^{(n-\lambda)}.$$

3.2. The In-place Fast Haar Wavelet Transform

Whereas the presentation in the preceding section conveniently lays out all the steps of the Fast Wavelet Transform, it requires additional arrays at each sweep, and it assumes that the whole sample is known at the start of the algorithm. In contrast, some applications require real-time processing as the signal proceeds, which precludes any knowledge of the whole sample, and some applications involve arrays so large that they do not allow sufficient space for additional arrays at each sweep. The two problems just described, lack of time or space, have a common solution in the In-Place Fast Wavelet Transform presented here, which differs from the preceding algorithm only in its indexing scheme.

For each pair $(a_{2k}^{(n-[\lambda-1])}, a_{2k+1}^{(n-[\lambda-1])})$ instead of placing its results in two additional arrays, the λ th sweep of the in-place transform merely *replaces* the pair $(a_{2k}^{(n-[\lambda-1])}, a_{2k+1}^{(n-[\lambda-1])})$ by the new entries $(a_k^{(n-\lambda)}, c_k^{(n-\lambda)})$.

When

$$a_k^{(n-\lambda)} := \frac{a_{2k}^{(n-[\lambda-1])} + a_{2k+1}^{(n-[\lambda-1])}}{2}$$

$$c_k^{(n-\lambda)} := \frac{a_{2k}^{(n-[\lambda-1])} - a_{2k+1}^{(n-[\lambda-1])}}{2}$$

Replace the initial pair $(a_{2k}^{(n-[\lambda-1])}, a_{2k+1}^{(n-[\lambda-1])})$ by the transformed pair $(a_k^{(n-\lambda)}, c_k^{(n-\lambda)})$.

4. CONCLUSION

Basic uses of in-place wavelet transform in this paper:

In the Fig. 5, a sample with 5000 point of Radar that is an input for lab-view program is shown. In the figure is seen the variation in the amplitude which create with difference between transmitter and receiver signals that come from moving or birthing in front of the Radar system.

Here we used $c_0^{(n-n)}$ for comparison. We take in-place wavelet transform of final 8 or 16 or 2^k (depend to needed sensitivity) of discrete last input point that come from RADAR system online and after that we subtract last input volume of input from $c_0^{(n-n)}$ of this wavelet transform. We named this volume obtain after subtract d and it is a base for diagnostic variation in input signal that show existence of a live below the concrete which is our target. Now we comparison this d with a volume which is manually variable, we named it h , (depend to application of resolution) and finally if d is further from h the sound system will be active and we recognize existing the live.

As an example in Fig. 6 came a sample of 8 point of Radar output, it mean that we chose $n = 8$.

In Fig. 6 you can see the wavelet transform of sample that came in Fig. 5.

Here c^0 is amount of the forth term and it is about 0.001 that is very small. With experience we found $d = 0.015$. Therefore in this sample, we won't have sound and it means not existing of live or movement.

REFERENCES

1. Spence, W., S. A. Sipkin, and G. L. Choy, "Measuring the size of an earthquake," *United States Geological Survey*, 1989, Retrieved on November 3, 2006.
2. Jonsson, A., "The discreet wavelet transform," May 2002.
3. Nievergelt, Y., *Wavelets Made Easy*, Birkhauser Boston, 1999.
4. Hagelberg, C. and J. Helland, "Thin-line detection in meteorological radar images using wavelet transforms," *Journal of Atmospheric and Oceanic Technology*, Vol. 12, No. 3, 633–642, June 1995.

5. Liò, P., “Wavelets in bioinformatics and computational biology: State of art and perspectives,” *Bioinformatics*, Vol. 19, No. 1, 2–9, 2003.
6. Torrence, C. and G. P. Compo, “A practical guide to wavelet analysis,” *Bulletin of the American Meteorological Society*, Vol. 79, No. 1, January 1998.
7. Gollmer, S. M., Harshvardhan, R. F. Cahalan, and J. B. Snider, “Windowed and wavelet analysis of marine stratocumulus cloud inhomogeneity,” *Journal of the Atmospheric Sciences*, August 1995.
8. Lau, K.-M. and H. Weng, “Climate signal detection using wavelet transform: How to make a time series sing,” *Bulletin of the American Meteorological Society*, Vol. 76, No. 12, December 1995.
9. Hagelberg, C. and J. Helland, “Thin-line detection in meteorological radar images using wavelet transforms,” *Journal of Atmospheric and Oceanic Technology*, Vol. 12, June 1995.
10. Shen, Z., W. Wang, and L. Mei, “Fine structure of wind waves analyzed with wavelet transform,” *American Meteorological Society*, Vol. 24, May 1994.
11. Ekstrom, P. A. and J. M. Hales, “A wavelet-based approach for atmospheric pollution modeling: Algorithm development,” *American Meteorological Society*, Vol. 128, September 2000.
12. Liu, P. C. and G. S. Miller, “Wavelet transforms and ocean current data analysis,” *Journal of Atmospheric and Oceanic Technology*, Vol. 13, 1996.
13. Al-Thahab, O. Q. J., W. A. Mahmoad, and M. S. Abdul-Wahab, “Design and simulation of radon-multiwavelet based OFDM system,” *Journal of Applide Electromagnetism*, Vol. 9, 1109–1606, 2007.
14. Kestin, T. S., D. J. Karoly, and J.-I. Yano, “Time-frequency variability of ENSO and stochastic simulations,” *American Meteorological Society*, 1998.
15. Willemsen, J. E., “Analysis of swade discus N wind speed and wave height time series. Part I: Discrete wavelet packet representations,” *Journal of Atmospheric and Oceanic Technology*, Vol. 12, 1995.
16. Grotjahn, R., D. Hodyss, and C. Castello, “Do frontal cyclones change size? Observed widths of north pacific lows,” *Monthly Weather Review*, Vol. 127, June 1999.
17. Gollmer, S. M., Harshvardhan, R. F. Cahalan, and J. B. Snider, “Windowed and wavelet analysis of marine stratocumulus cloud inhomogeneity,” *American Meteorological Society*, Vol. 52, No. 16, August 1995.
18. Lee, S. H., J. N. Lee, J. K. Park, and H. S. Kim, “Desing of the compact UWB antenna with PI-shaped matching stub,” *Journal of Electromagnetic Waves and Applications*, Vol. 22, No. 10, 1440–1449, 2008.
19. “Getting started with LabVIEW,” National Instruments, Part No. 323427A-01, 2003.
20. “LabVIEW user manual,” National Instruments, Part No. 320999E-01, 2003.
21. “LabVIEW performance and memory management,” National Instruments, Part No. 342078A-01, 2003.
22. “Introduction to labview six-hour course,” National Instruments, Part No. 323669B-01, 2003.
23. Bishop, R. H., *Learning With Labview 7 Express*, Prentice Hall, 2003.

Effects of the Air-Hole Positions on Transmission Spectrum of a Silicon Micro-Cavity Photonic Crystal Filter

F. Emami, A. R. Kashavarz, and H. Sarikhani-Khorami

Optoelectronic Research Centre, Shiraz University of Technology, Shiraz, Iran

Abstract— We impose two dimensional finite difference time domain (2-D FDTD) method on an air-hole waveguide microcavity photonic crystal filter fabricated on a ridge silicon waveguide. Inserting cavity between the sets of holes can cause a filter-like behavior in the frequency response of the structure. We found that for higher hole radii there is a shift toward the lower part of the wavelength, whereas for smaller hole radii the transmission peak and bandwidth would be increased. By using a nonuniform hole radius structure, we could increase the full width at half maximum of such filters. We introduce an engineering designation on the defect dimension to have a peak frequency at the desired wavelength of 1550 nm.

1. INTRODUCTION

There are many researches on the photonic crystals (PCs) and their applications in optical communication. In these structures a wide range of a frequency stop band exists, so there is not any light propagation through this stop band [1]. Based on this property, PCs are used in many different and interesting applications such as low threshold lasers and low loss micro-bends [2–5]. Application of some defects into the PC structure generates one or more possible light frequencies which can propagate through the stop band with a determined bandwidth. This effect is used to design a resonator or a high-Q filter [6, 7]. In a simple method of creating a defect, it is easy to remove one hole from total number of periodic and regular holes, fabricated on a (usually silicon-based) ridge waveguide. This can produce a photonic crystal mirror in both sides of this hole vacancy [7]. It is clear that the filter response of such structure depends on the hole shapes (symmetric or maybe non-symmetric), their relative hole distances and the dimensions of the vacated space. This concept is used to other periodic structures too. One of the most important of them is phase-shifted Bragg gratings.

2. STRUCTURE, MATHEMATICAL BACKGROUND AND FORMULATION

To simulate photonic crystal structures and find the transfer function of them, we must determine the field components in the waveguide. To do this, we should use a numerical procedure such as finite element or finite difference method. In this paper we use finite difference time domain (FDTD) method and solve the Maxwell equations in the medium. But, at first the shape of the used PC is described.

2.1. Structure Description

A typical two dimensional simulated PC with two defect regions is shown in Fig. 1. As seen, the material characteristics in x - and y -directions are varied and we assumed that it is infinite in z -direction. With this idea, two modes, TE and TM, are existed separately. We considered TE modes only and using the shown axes in Fig. 1, so the field components which should be studied are: E_x , E_y and H_z .

One of the most important problems for computer simulation of this structure is the outer region of the PC waveguide. There is an infinite space at the outside and hence truncating the numerical calculations of the decomposed equations is a serious problem. Also the guide is open at both ends and we did not consider any reflection at the waveguide ends. These restrictions are removed by using uniaxial perfectly matched layers (UPMLs) [8] with the main advantage of: There is no any reflection from the waveguide-outer space interfaces.

2.2. Mathematical Formulation

As said, the medium transfer function is found by using two dimensional FDTD [9–11]. In this method, the Maxwell equations are solved in the PC structure and different components of the

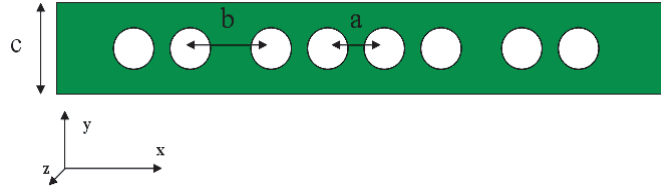


Figure 1: Schematic of a photonic crystal waveguide filter made by two defects (with separation b).

electric and magnetic fields are found. Hence, starting with these equations in a source-free region:

$$\begin{aligned}\nabla \times \vec{E}(x, y, t) &= -\mu \frac{\partial \vec{H}(x, y, t)}{\partial t} \\ \nabla \times \vec{H}(x, y, t) &= \varepsilon \frac{\partial \vec{E}(x, y, t)}{\partial t}\end{aligned}\quad (1)$$

and for TE modes, we have:

$$\begin{cases} \frac{\partial E_x}{\partial t} = \frac{1}{\varepsilon(x, y)} \frac{\partial H_z}{\partial y} \\ \frac{\partial E_y}{\partial t} = -\frac{1}{\varepsilon(x, y)} \frac{\partial H_z}{\partial x} \\ \frac{\partial H_z}{\partial t} = -\frac{1}{\mu(x, y)} \left(\frac{\partial E_y}{\partial x} - \frac{\partial E_x}{\partial y} \right) \end{cases}\quad (2)$$

Utilizing the idea in FDTD method, we decompose the guide surface to finite lengths Δx and Δy , in x - and y -directions respectively. Then we can convert the partial differential equations to finite difference equations in both time and space domains. In the outer region, where an UPML media are used, we have the phasor representation of Maxwell equations as:

$$\begin{aligned}\nabla \times \vec{E} &= -j\omega \bar{\mu} \vec{H} \\ \nabla \times \vec{H} &= -j\omega \bar{\varepsilon} \vec{E}\end{aligned}\quad (3)$$

The tensors $\bar{\varepsilon}$ and $\bar{\mu}$ in (3) are:

$$\bar{\mu} = \mu_0 \begin{bmatrix} s_y & 0 & 0 \\ s_x & s_x & 0 \\ 0 & s_y & s_x s_y \end{bmatrix} = \mu_0 \bar{s} \quad \& \quad \bar{\varepsilon} = \varepsilon_0 \begin{bmatrix} s_y & 0 & 0 \\ s_x & s_x & 0 \\ 0 & s_y & s_x s_y \end{bmatrix} = \varepsilon_0 \bar{s}, \quad s_v = k + \frac{\sigma_v(v)}{j\omega \varepsilon_0}, \quad v = x, y \quad (4)$$

k is the propagation constant and all of the entries are complex.

Considering a piecewise smooth variations for σ , we can derive filed descriptions in the simulated medium [12].

3. SIMULATION RESULTS

Due to nature of FDTD method, we inject an exciting wave into the simulated medium. Let to excite the micro-cavity by a wave with a relative wide frequency spectrum to study the filtering response of the structure. The input wave frequency spectrum is shown in Fig. 2. We can find the filter transfer function using the ratio of the z -component of the magnetic field at the output to the input. It is seen in Fig. 3. As shown, there is not any defect in the hole set made on a ridge waveguide and a stop band exists in the transfer function.

By inserting two defects with length b into the hole set, such as shown in Fig. 4 (seen also in Fig. 1), a peak can be created in this stop band. In other words, in the stop band of this PC there are some frequencies of the input light which can transmit from the structure; this is an optical

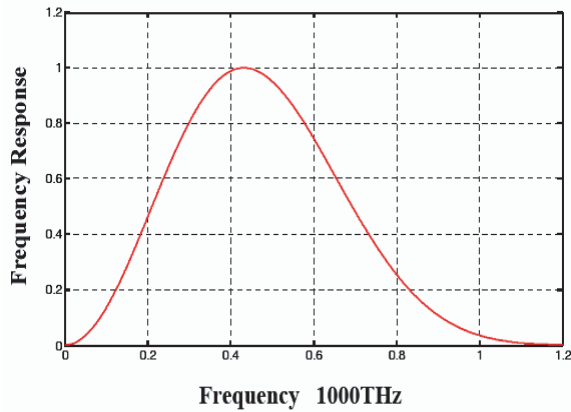


Figure 2: Frequency spectrum of a typical input.

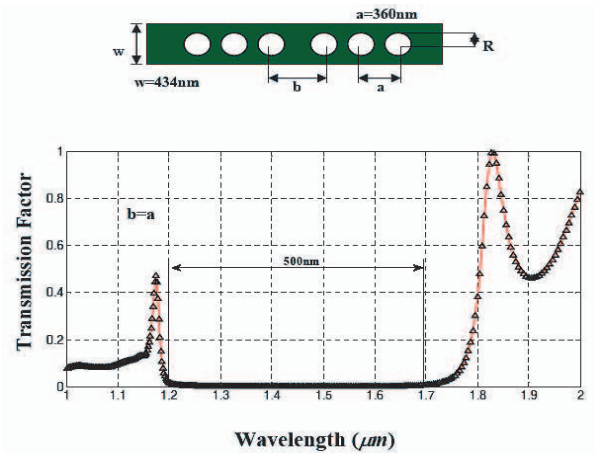


Figure 3: Transfer function of a uniform PC ($b = a$ and $R = 131$ nm).

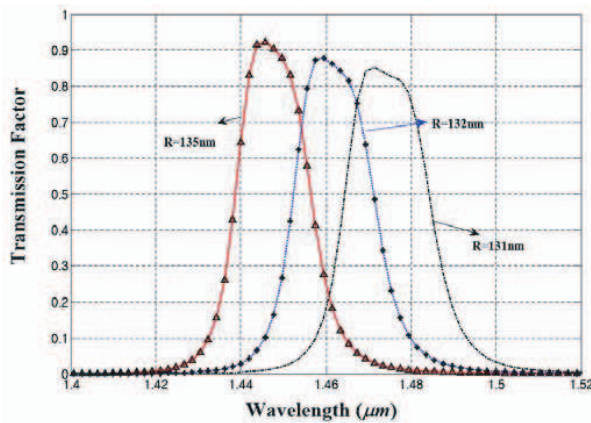


Figure 4: Transmission spectrum of a typical two-holes PC.

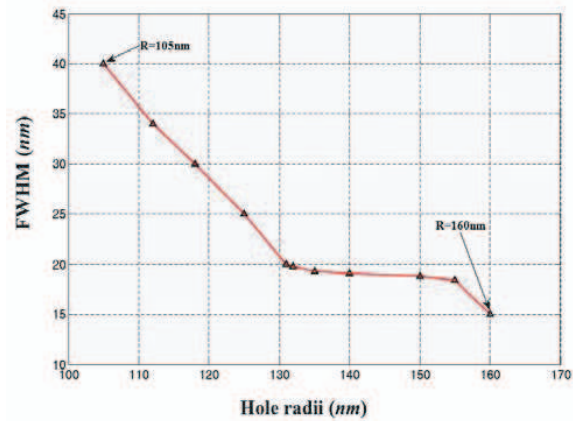


Figure 5: FWHM versus hole radii.

filter. For a fixed hole separation a and constant defect lengths b (Fig. 1), increasing the hole radius raises the peak of the resonance frequency (or decreases the peak of the resonance wavelength) of the structure. At the same time, the filter bandwidth diminished with hole radius increments. This is shown in Fig. 5. Indeed, the full width at half maximum (FWHM) of this filter would be wider with lower hole radii.

As a final result, we studied the effects of nonuniform hole radii in this filter structure. For a uniform hole arrangement with $a = 215$ nm, $b = w = 260$ nm, and $R_1 = R_2 = R_3 = 131$ nm, we can have a peak at 820 nm (improper wavelength) with FWHM = 11.6 nm [12]. Hence, we can change the various parameters to have peak at the wavelength of ≈ 1550 nm using different hole radii with variable b parameter as seen in Fig. 6.

Simulation of the tapered structure of Fig. 6 shows increments in the peak wavelength toward 980 nm (relative to 820 nm). The results are plotted in Fig. 7. As shown, we can have a transmission

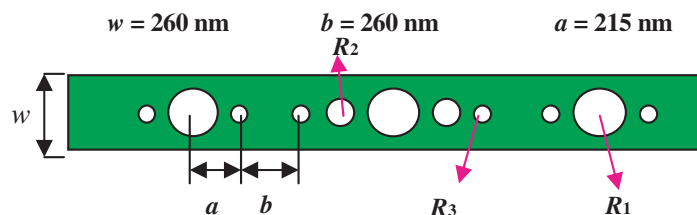


Figure 6: Schematic of a two micro-cavities PC filter with nonuniform hole radii.

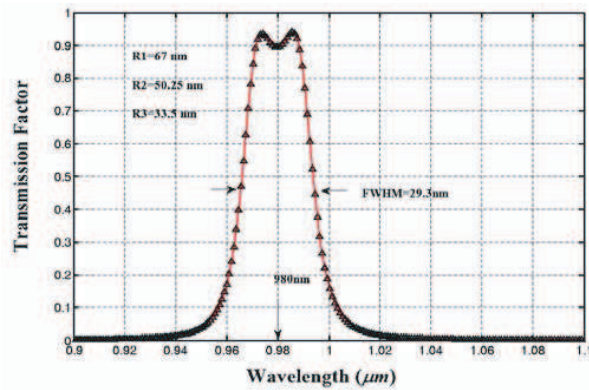


Figure 7: Transfer function of nonuniform filter.

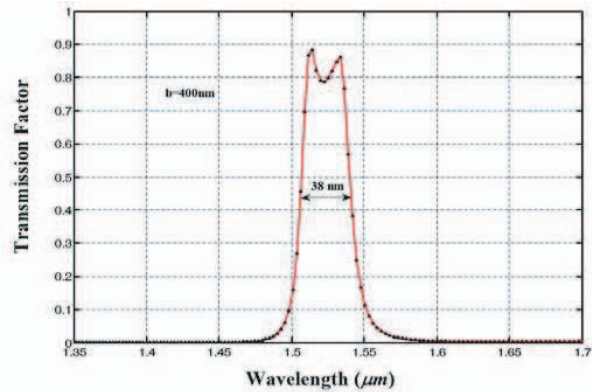


Figure 8: Desired transfer function of a nonuniform filter.

of about 0.94 with $\text{FWHM} \approx 29.3$ nm. Utilizing an optimization method we found a transmission of ≈ 0.89 at the wavelength of ≈ 1520 nm. It can be seen in Fig. 8. This transmission is obtained for $R_1 = 131$ nm, $R_2 = 98.25$ nm, $R_3 = 65.5$ nm and $b = 400$ nm. We found a FWHM of about 38 nm, as shown.

4. CONCLUSION

In this work, we simulated a micro-cavity photonic crystal filter using FDTD method. Application of any defect in the hole region of such structures can generate a filter. In this filter, variations of the parameters change the peak frequency and bandwidth of the filter. If the air-hole radius increased the transmitted peak wavelength and FWHM decreased. For nonuniform configuration with different hole radii, we can control the transmitted peak of the input waves around 1550 nm with a proper FWHM.

REFERENCES

1. Haus, J. W., "A brief review of theoretical results for photonic band structures," *J. Modern Opt.*, Vol. 41, No. 2, 195–207, 1994.
2. Meade, R. D., A. Annopoulos, O. L. Alherhand, D. A. Smith, and K. Kash, "Novel applications of photonic band gap materials: Low loss bends and high-Q cavities," *J. Appl. Phys.*, Vol. 75, No. 9, 4753–4755, 1994.
3. Krauss, T. F. and R. M. de la Rue, "Photonic crystals in optical regime past, present and future," *Progress Quantum Electron.*, Vol. 23, No. 2, 51–96, 1999.
4. Bogaerts, W., D. Taillaert, B. Luyssaert, P. Dumon, J. Van Compenhout, P. Bientman, D. Van Dourhout, R. Baets, V. Wiaux, and S. Beckx, "Basic structures for photonic integrated circuits in silicon-on-insulators," *Opt. Express*, Vol. 12, No. 8, 1583–1591, 2004.
5. Boutami, S., B. B. Bakir, J. L. Leclercq, X. Letartre, C. Seassal, P. Rojo-Romeo, P. Regreny, M. Carrigues, and P. Viktorovitch, "Photonic crystal-based MOEMS devices," *IEEE J. Select. Top. in Quantum Elect.*, Vol. 13, No. 2, 244–252, 2007.
6. Jugessure, A. S., P. Pottier, and R. M. de la Rue, "One-dimensional periodic photonic crystal microcavity filters with transition mode-matching features, embedded in ridge waveguides," *Electron. Lett.*, Vol. 39, No. 4, 367–369, 2003.
7. Jugessure, A. S., R. M. de la Rue, P. Pottier, and P. Viktorovitch, "One-dimensional photonic crystal microcavity with enhanced transmission," *Integrated Photonics Research (IPR)*, Paper IFD2, Vancouver, 2002.
8. Gendey, S. D., "An isotropic perfectly matched layer absorbing media for the truncation of FDTD lattices," *IEEE Trans. on Antenna and Propagation*, Vol. 44, 1630–1639, 1996.
9. Taflove, A. and S. C. Hagness, *Computational Electromagnetics*, Artech-House, 2nd Edition, 2000.
10. Tarso-Neves, Jr., P. and A. P. Pohl, "Bandwidth analysis of silicon PhC filters for CWDM systems using FDTD-2D method," *Journal of Comm. and Inform. Sys.*, Vol. 20, No. 3, 96–104, 2005.

11. Johnson, S. G. and J. D. Joannopoulos, *Photonic Crystals: The Road from Theory to Practice*, Springer-Verlag New York, LLC, Kluwer, Boston, 2001.
12. Sarikhani-Khorrami, H., “An investigation of waveguide parameter variations on the photonic bandgap micro-cavities with flat-top response,” M.S. Thesis, Shiraz University of Technology, Shiraz, Iran, Oct. 2008.

Detection of Three Dimensional Objects Buried in a Half-space by the Use of Surface Impedance

Egemen Bilgin and Ali Yapar

Electrical and Electronics Eng. Faculty, Istanbul Technical University, Istanbul, Turkey

Abstract— A method to determine the locations of three dimensional objects buried in a half space medium is presented. The method is based on the reconstruction of a surface impedance function defined by the co-polarized tangential components of electric and magnetic fields via remote field measurements of scattered field. In the presence of 3-D objects, surface impedance becomes a two dimensional function of location and the locations of the peaks of this function indicates the position of buried objects. The scattered field distribution and its derivative on the half space boundary which are required for determination of surface impedance function are obtained through a continuation method of the measured data to the interface. Numerical simulations show that unless the objects are very close, the surface impedance is highly effective in locating the buried objects and also carries information about relative depth, size or material properties of the objects.

1. INTRODUCTION

The objective of this study is to detect three dimensional objects buried in a lossy half space medium observing a predefined surface impedance function. The method applied in this work is an extension of the one presented in [1] to the three dimensional case which is based on the reconstruction of the equivalent surface impedance of the planar interface via the remote field measurements of scattered field. For 3-D problems the equivalent surface impedance is in general composed of a 2×2 dyadic and requires to calculate 4 different elements which is a more complicated problem. On the other hand since the co-polarized components of the scattered field are more significant one can define an impedance type scalar function which carries enough information about the buried objects for detection aimed applications. The calculation of the impedance function requires the tangential components of the total electric and magnetic fields on the planar interface separating the two half-spaces. For this purpose the half space is illuminated by a plane wave and resulting scattered field is assumed to be measured on a surface above the interface. The measured scattered field data is then represented as a spectral integral by two dimensional Fourier transformation. This spectral representation immediately allows us to write the required field values on the interface separating the two half-spaces. It is shown that it is possible to detect the locations of the buried objects by observing the variation of the surface impedance which will be a two dimensional function in the case of 3-D burials. Numerical simulations show that illumination by a plane wave with single frequency and incident angle results in enough information to detect dielectric and/or conducting objects of different size and depth. It is also observed that unless the objects are very close to each other, the surface impedance is highly effective in locating buried physical objects and also carries information about relative depth, size or material properties of the objects.

2. FORMULATION OF THE PROBLEM

Consider the geometry given in Figure 1. Here N disjoint three dimensional objects are buried in the lower half space which is illuminated by a time harmonic plane wave with an incident angle ϕ_0 and electric field vector $\vec{E}^i(0, u^i(x_1, x_2, x_3), 0)$ parallel to x_2 axis where $u^i(x_1, x_2, x_3) = e^{-ik_0(x_1 \cos \phi_0 + x_3 \sin \phi_0)}$.

The problem is to detect the location of 3-D objects via scattered field measured on a surface $x_3 = \ell, \ell > 0$. For this purpose we first define an impedance function

$$Z_g(x_1, x_2) = -i\omega\mu_0 \frac{E_t(x_1, x_2, x_3 = +0)}{\frac{\partial E_t(x_1, x_2, x_3 = +0)}{\partial x_3}} \quad (1)$$

where E_t denote the tangential component of total electric field vector \vec{E} . Here $Z_g(x_1, x_2)$ can be considered as a special part of surface impedance of the interface which characterize the lower half space with buried inhomogeneties.

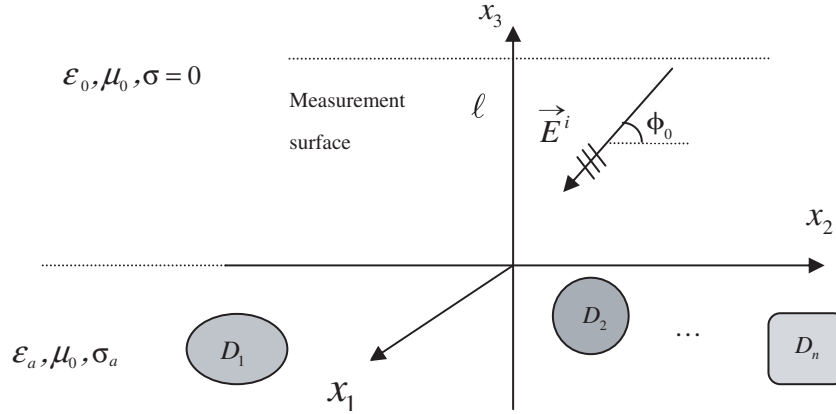


Figure 1: Geometry of the problem.

In the absence of objects the geometry becomes homogeneous along x_1 and x_2 axis, so the surface impedance becomes a constant complex number which depends on characteristics of half spaces and incident angle. In this case the total electric field is also a scalar function. On the other hand in the presence of the 3-D buried objects the scattered field is vectorial. However for the impedance function given in (1) we need the tangential component of scattered field. Therefore we will denote the scalar component of the scattered field along x_2 axis, by u_s and define a scalar impedance function as

$$Z(x_1, x_2) = i\omega\mu_0 \frac{(u_0 + u_s)}{\frac{\partial(u_0 + u_s)}{\partial x_3}} \quad (2)$$

Here u_0 is the total scalar electric field in the absence of the buried objects and the surface impedance $Z(x_1, x_2)$ characterizes the lower half space carrying information about the locations of the burials. In order to extract the effect of half space we define the difference

$$Z_d(x_1, x_2) = Z(x_1, x_2) - Z_s. \quad (3)$$

Here Z_s is surface impedance in the absence of burials [1]. To determine u_s and its derivative on the boundary from measurements on the surface $x_3 = \ell$, a continuation method is used. This method is based on the technique explained in [2] and involves a two dimensional Fourier transform of measured data. The values of u_s and $\partial u_s / \partial x_3$ are obtained as

$$u_s(x_1, x_2, 0) = \frac{1}{(2\pi)^2} \int_{-\infty}^{\infty} \int_{-\infty}^{\infty} e^{\gamma \ell} \hat{u}_s(v, \mu, \ell) e^{ivx_1 + i\mu x_2} dv d\mu \quad (4)$$

$$\frac{\partial u_s(x_1, x_2, 0)}{\partial x_3} = \frac{1}{(2\pi)^2} \int_{-\infty}^{\infty} \int_{-\infty}^{\infty} -\gamma e^{\gamma \ell} \hat{u}_s(v, \mu, \ell) e^{ivx_1 + i\mu x_2} dv d\mu \quad (5)$$

with

$$\gamma = \sqrt{v^2 + \mu^2 - k_0^2} \quad (6)$$

In (4) and (5) $\hat{u}_s(v, \mu, \ell)$ denotes the two dimensional Fourier transform of the scattered field measured on the surface $x_3 = \ell$. The integration region in the above integrals is restricted to the interval $(-k_0/\sqrt{2}, k_0/\sqrt{2})$. Note that this restriction corresponds to take only the propagating waves into account.

3. NUMERICAL SIMULATIONS

In this section, the results of some numerical simulations are presented to show the validity of the method. The scattered field which will be used to determine the surface impedance is obtained via method of moments [3]. In all examples the scattered field is measured on a surface with an area

of $4\text{ m} \times 4\text{ m}$, 1 m . above the interface. The plane wave has the frequency of 300 MHz and it is normally incident from upper space. The lower half space has a dielectric constant of $\epsilon_r = 3 + i0.1$. Different examples demonstrate the effects of depth, size and material properties of buried objects.

In the first example two identical dielectric cubes having $\epsilon_r = 2.9 + i0.05$ and volume of 0.008 m^3 are buried in a depth of 0.1 m and 0.2 m respectively under surface. In Figure 2, the amplitude of normalized surface impedance function clearly shows the location of both objects. The object which is closer to surface has more contribution to the impedance function than the one that buried in deeper depth, i.e., 0.2 m . This example also shows that the surface impedance is very sensitive to depth of buried objects. Different simulations demonstrate that the contribution of any buried object to surface impedance rapidly diminishes as its depth increases. Effect of the same object used in previous example halves when it is buried 1 m below the surface and it does not make any significant contribution when it is buried deeper than 3 m . This is shown in Figure 3.

The objects of different sizes also have different contributions to surface impedance. An example of this situation is shown in Figure 4. Here two objects of same material are buried in equal depth. The object having larger contribution has a volume of 0.012 m^3 ($0.2\text{ m} \times 0.2\text{ m} \times 0.3\text{ m}$) while the other object is a cube of 0.008 m^3 . Another important factor determining the surface impedance is material properties. In Figure 5 two objects of equal sizes with different dielectric constants are buried in same depth. The object with $\epsilon_r = 4 + i0.07$ has clearly larger effect than the object with

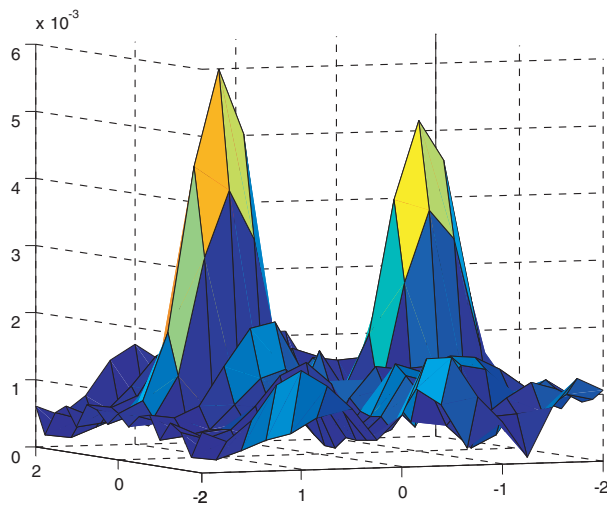


Figure 2: Two cubes buried in different depths.

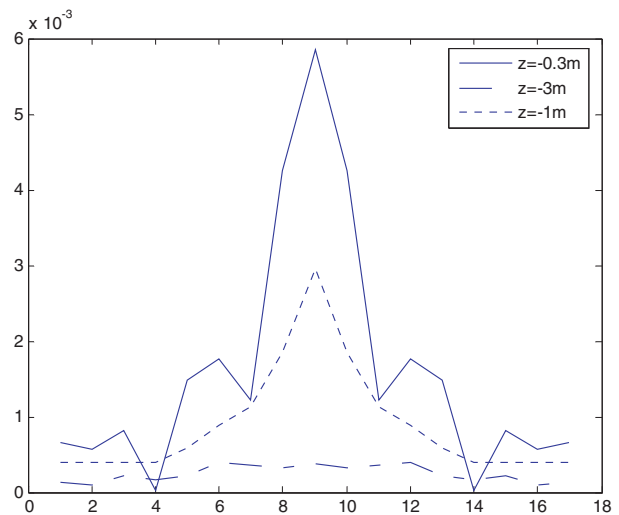


Figure 3: Amplitudes of impedance function for objects of different depths.

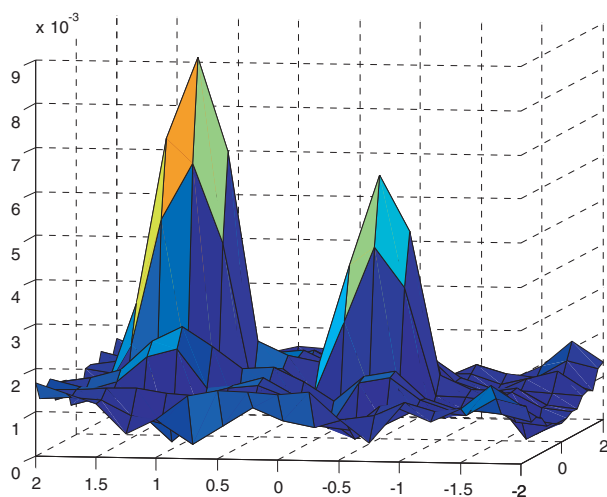


Figure 4: Two buried objects with different sizes.

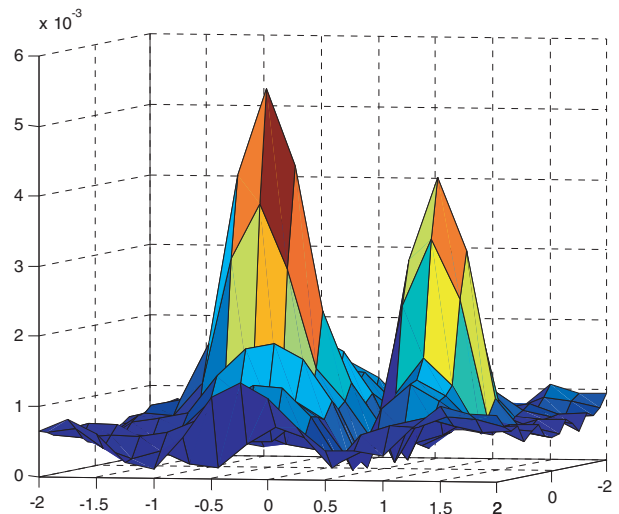


Figure 5: Two dielectric objects with different dielectric constant.

$\varepsilon_r = 2.9 + i0.05$. Those examples demonstrate that surface impedance carries valuable information about relative size, depth and material properties of buried dielectric objects.

The comparison of impedance function and direct observation of scattered electrical field in the case of multiple buried objects is presented in Figures 7 and 8. In this example four objects are buried: two objects with volume of 0.004 m^3 and two objects with volume of 0.006 m^3 . One object of each couple is buried 0.2 m below surface and the other is buried 0.1 m below surface. Figure 6 shows the observed scattered field while Figure 7 demonstrates related surface impedance function. Comparison of two figures demonstrates that surface impedance is more reliable for detecting buried objects. Also it carries relative information about sizes and depth of objects. For example it is hard to detect the difference of depth between larger objects from scattered field whereas surface impedance clearly shows the difference between each object.

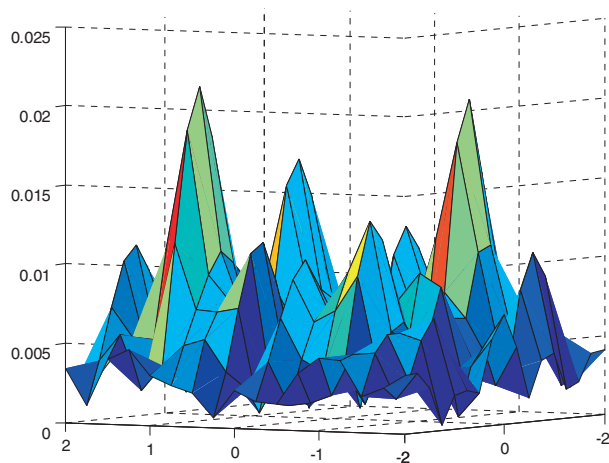


Figure 6: x_2 component of scattered field from 4 objects.

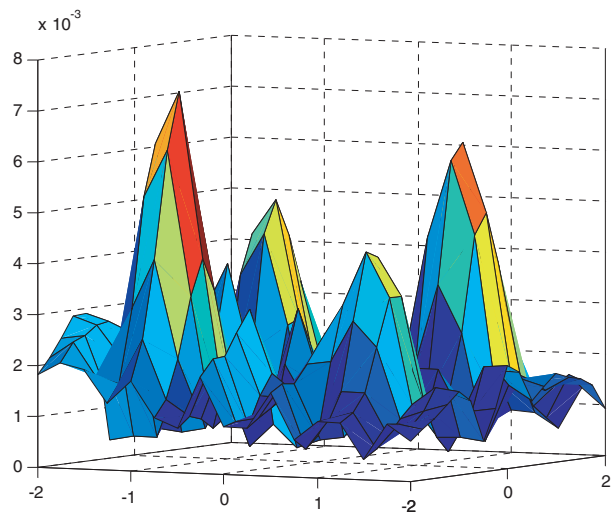


Figure 7: Amplitude of impedance function for 4 objects.

4. CONCLUSION

A method to locate buried 3D objects in a half space is presented. The method is based on calculation of an impedance function to characterize lower half space. Different examples demonstrate the effects of the properties of burials to the impedance function. To sum up if the burials are not very close to each other or buried too deeply below the boundary, the surface impedance can be used effectively to locate buried objects and to receive information about their positions and sizes.

REFERENCES

1. Altuncu, Y., I. Akduman, and A. Yapar, "Detecting and locating dielectric objects buried under a rough interface," *IEEE Geoscience and Remote Sensing Letters*, Vol. 4, No. 2, 251–255, 2007.
2. Akduman, I. and A. Yapar, "Surface impedance determination of a planar boundary by the use of scattering data," *IEEE Trans. on Antennas and Propagat.*, Vol. 46, No. 3, 429–436, 2000.
3. Jun Hui, T., W. Wiesbeck, and A. Herschlein, "Electromagnetic scattering by multiple three dimensional scatterers buried under multilayered media," *IEEE Trans. on Geoscience and Remote Sensing*, Vol. 36, No. 2, March 1998.

Design of High Symmetry Microwave Frequency Selective Surfaces with Trapped-mode Resonance

M. N. Kawakatsu¹, V. A. Dmitriev¹, and S. L. Prosvirnin²

¹Federal University of Para, Brasil

²Institute of Radio Astronomy, Ukraine

Abstract— The trapped-mode response in frequency selective surfaces which are periodic multi-element arrays is analyzed in this work. Two new array configurations, which support the trapped-mode regime with polarization insensitivity are suggested. Numerical results for different values of their design parameters are presented and discussed.

1. INTRODUCTION

High quality factor (Q-factor) resonances of planar frequency selective surfaces (FSSs) are essential for various applications. Generally speaking, a high Q-factor and small thickness of the layer are conflicting requirements. Actually, a thin open structure can not have inner resonating volumes and, on the other hand, resonating inclusions are usually coupled strongly with free space and this reduces the Q-factor. Nevertheless, there is a way to produce very thin structures with high Q-factor resonances in planar FSSs by using an array of two resonant elements and the regime of the so-called trapped-modes [1, 2].

A characteristic feature of the previously suggested FSSs with excitation of trapped-modes is their polarization sensitivity. For some applications, however, it is necessary to use FSS which operates with any polarization of incident waves. The development of this type of FSSs gave rise to novel photonic applications such as described in [3, 4]. In [5], an attempt was made to realize a polarization insensitive structure with elements having a four-fold symmetry. However, the quality factor of resonances for the suggested structure is not so high as it was observed earlier in polarization sensitive cases [1, 2].

The main objective of our work is the development of new array configurations which possess high Q-factor resonance and polarization insensitivity. The known structure has two concentric rings per array cell (Fig. 1(a)) [5, 6]. In this paper, we present results of our study of reflection and transmission characteristics of two new arrays with unit cells consisting of two or three resonant elements. One of them is the FSS which each element is a combination of a simple ring and a corrugated ring placed inside the simple ring, as illustrated in Fig. 1(b). The second FSS consists of three concentric rings (Fig. 1(c)). The geometric parameters of the corrugated ring, which is a bent sinusoidal strip, are the number of periods n and the amplitude $B = (r_o - r_i)/2$. The metal particles placed on a thin dielectric substrate from one side possess an n -fold rotational symmetry in the case of the two element arrays (Fig. 1(b)) and ∞ -fold symmetry in the case of the three element array (Fig. 1(c)).

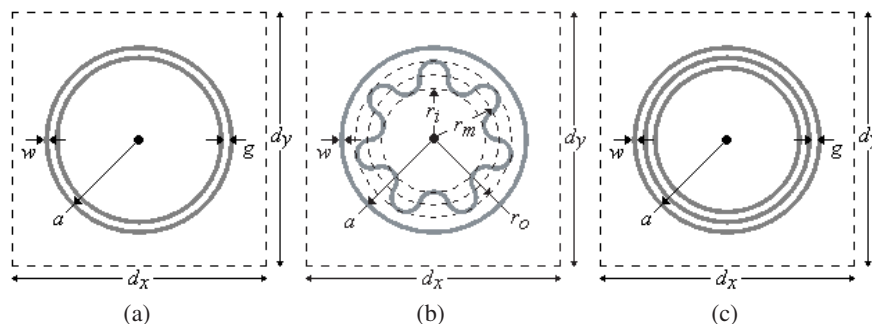


Figure 1: Unit cells of the array of two concentric rings (a), array with inner corrugated ring (b) and array of three concentric rings (c). The planar arrays are supported by a dielectric substrate.

2. ARRAY WITH TWO CONCENTRIC RINGS

Below, we present a study of the array consisting of two concentric rings in the unit cell with trapped-mode response. The numerical calculations are fulfilled varying geometrical and physical parameters of the rings and the substrate. All the numerical simulations were performed using the spectral domain moment method (SDMM) for the problem of scattering from the FSS excited by a normally incident plane wave.

The unit cell of the array of two concentric rings is described by the parameters indicated in Fig. 1(a), with $d_x = d_y = 15$ mm and $a = 5.45$ mm. The other parameters g and w were varied. The array is supported by a dielectric substrate with thickness $h = 1.6$ mm and relative complex permittivity $\epsilon = \epsilon' - i\epsilon''$. The chosen thickness of the copper strips is 35 μm , and the conductivity of the copper is $5.8 \cdot 10^7$ mhos/m.

In Table 1, the resonance frequency (f_r), maximum transmission coefficient ($|T_{\max}|$) and Q-factor (Q_f) of trapped-mode are given for $w = 0.2$ mm and three different values of g , and in Table 2, for $g = 0.2$ mm and three different values of w . These results were calculated for the rings made of copper and a lossless substrate with $\epsilon' = 4.5$. In the definition of the Q-factor, the full width of -3 dB from the maximum of transmission was considered.

Table 1: Resonance frequency (f_r), maximum transmission coefficient ($|T_{\max}|$) and Q-factor (Q_f) of the array with two concentric rings for $w = 0.2$ mm and three values of g .

g (mm)	0.2	0.3	0.4
f_r (GHz)	9.43	9.55	9.68
$ T_{\max} $ (dB)	-0.60	-0.40	-0.27
Q_f	21.81	18.51	15.68

Table 2: Resonance frequency (f_r), maximum transmission coefficient ($|T_{\max}|$) and Q-factor (Q_f) of the array with two concentric rings for $g = 0.2$ mm and three values of w .

w (mm)	0.3	0.4	0.5
f_r (GHz)	5.83	5.85	5.92
$ T_{\max} $ (dB)	-0.88	-0.60	-0.43
Q_f	19.50	16.19	14.10

We see in Tables 1 and 2 that the higher Q-factor is obtained for smaller g and w , i.e., for smaller difference in the resonance frequencies of the inner and outer rings, as it is in the case of double-split ring FSS [1, 2].

For the dimensions $g = 0.2$ mm and $w = 0.2$ mm, giving the highest Q-factor, we calculated resonance frequency (f_r), maximum transmission coefficient ($|T_{\max}|$) and Q-factor (Q_f) for different values of ϵ'' fixing the value of $\epsilon' = 4.5$. As it was expected, increasing the substrate loss reduces the maximum of the transmission coefficient and also the Q-factor.

Table 3: Resonance frequency (f_r), maximum transmission coefficient ($|T_{\max}|$) and Q-factor (Q_f) of the array of two concentric rings for $g = 0.2$ mm, $w = 0.2$ mm and three values of ϵ'' .

ϵ''	0.01	0.05	0.10
f_r (GHz)	5.67	5.70	5.73
$ T_{\max} $ (dB)	-1.90	-3.01	-3.84
Q_f	16.68	12.13	10.05

In Fig. 2(a), the reflection ($|\Gamma|$) and transmission ($|T|$) coefficients and the normalized power absorption ($A = 1 - |\Gamma|^2 - |T|^2$) are shown for $g = 0.2$ mm, $w = 0.2$ mm and lossless substrate, and in Fig. 2(b), for $\epsilon'' = 0.05$.

As it can be seen in Fig. 2, in this type of array pattern, the trapped-mode results in a sharp transmission resonance between the two reflection resonances, which corresponds to individual rings resonances. The maximum of power absorption achieves near the resonance frequency of the trapped-mode due to a high current amplitudes in the elements. In the case of lossless substrate,

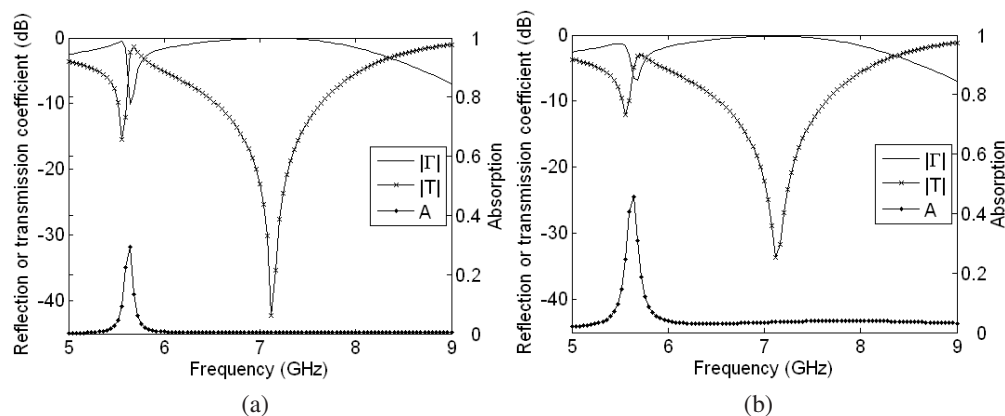


Figure 2: Reflection ($|\Gamma|$) and transmission ($|T|$) coefficients and normalized power absorption (A) for $g = 0.2$ mm, $w = 0.2$ mm and lossless substrate $\epsilon'' = 0$ (a), and for $\epsilon'' = 0.05$ (b).

the absorption is caused only by the conduction losses in the metal (which we do not take into account) and in the case of lossy substrate, is caused by both conduction and dielectric losses.

3. ARRAY WITH INNER CORRUGATED RING

In the case of two concentric rings, a higher Q-factor was achieved for smaller difference in the resonance frequencies of the rings. Based on that, the inner ring was replaced by a corrugated ring in order to approximate the resonance frequencies of the inner and the outer elements.

The following approach was applied for the array with the inner corrugated ring combined with simple external ring. Firstly, the resonance frequencies of the arrays with the isolated elements were calculated, i.e., the array of simple ring and the arrays of corrugated ring for different values of the number of periods n and the amplitude B of the sinusoidal strip. Then the conditions for the highest Q-factor of the array with the two combined elements were searched.

The unit cell of the array with only corrugated ring is described by the parameters indicated in Fig. 1b, with $d_x = d_y = 15$ mm, $w = 0.2$ mm, $a = 5.45$ mm and $r_m = 3.85$ mm. The other two parameters n and B were varied. This array is supported by a dielectric substrate with thickness $h = 1.6$ mm and the relative complex permittivity $\epsilon = \epsilon' - i\epsilon''$.

In Fig. 3(a), the resonance frequency of the arrays with the isolated corrugated rings for $B = 0.8$ mm is plotted as a function of n , and in Fig. 3(b), as a function of B with $n = 7$. These results were calculated for a lossless substrate with $\epsilon' = 4.5$. As expected, when n or B increases, the total length of the strip is increases, hence, the resonance frequency becomes lower.

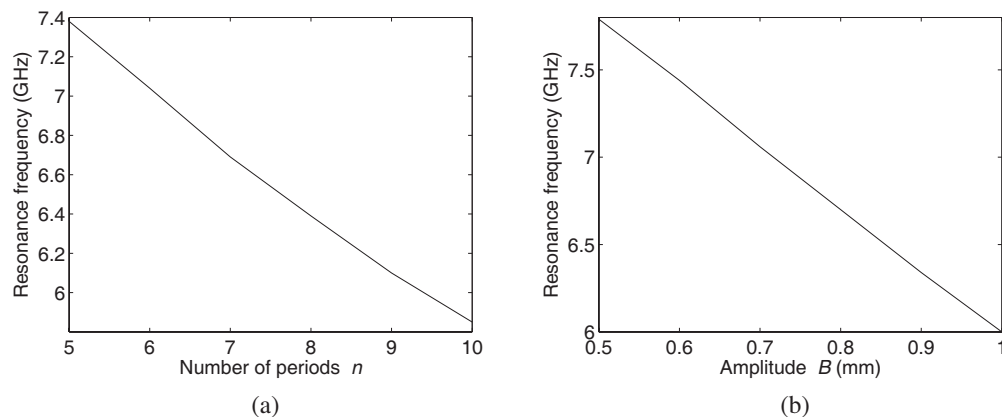


Figure 3: Resonance frequency of the arrays with isolated corrugated rings as a function of the number of periods n (a) and as a function of the amplitude B (b).

The resonance frequency of the array composed of the simple rings with the radius $a = 5.45$ mm is around 6.4 GHz, which is approximately equal to that of the corrugated ring with $n = 8$ and the average radius $r_m = 3.85$ mm.

In Table 4, the resonance frequency (f_r), maximum transmission coefficient ($|T_{\max}|$) and Q-factor (Q_f) are given for $B = 0.8$ mm and five different values of n , and in Table 5, for $n = 7$ and five different values of B . These results were calculated considering a lossless substrate with $\epsilon' = 4.5$. The results remain unaltered for any polarization of the incident plane wave for the array patterns having four-fold symmetry.

Table 4: Resonance frequency (f_r), maximum transmission coefficient ($|T_{\max}|$) and Q-factor (Q_f) of the array with inner corrugated ring for $B = 0.8$ mm and different values of n .

n	5	6	7	8	9
f_r (GHz)	5.82	5.66	5.42	5.27	5.04
$ T_{\max} $ (dB)	-0.35	-0.49	-0.76	-1.27	-2.08
Q_f	10.03	12.58	13.55	12.85	7.87

Table 5: Resonance frequency (f_r), maximum transmission coefficient ($|T_{\max}|$) and Q-factor (Q_f) of the array with inner corrugated ring for $n = 7$ and different values of B .

B	0.6	0.7	0.8	0.9	1.0
f_r (GHz)	5.88	5.65	5.42	5.16	4.89
$ T_{\max} $ (dB)	-0.30	-0.45	-0.76	-1.30	-2.28
Q_f	9.97	12.02	13.55	11.22	6.35

For the case with the highest Q-factor obtained previously with $n = 7$ and $B = 0.8$ mm, we calculated the characteristics of the arrays for three different values of ϵ'' with the fixed $\epsilon' = 4.5$ (Table 6).

Table 6: Resonance frequency (f_r), maximum transmission coefficient ($|T_{\max}|$) and Q-factor (Q_f) of the array with inner corrugated ring for $n = 7$, $B = 0.8$ mm and different values of ϵ'' .

ϵ''	0.01	0.05	0.10
f_r (GHz)	5.43	5.45	5.50
$ T_{\max} $ (dB)	-1.16	-2.21	-2.87
Q_f	11.55	8.26	7.05

In Fig. 4(a), the reflection ($|\Gamma|$) and transmission ($|T|$) coefficients and the normalized power absorption (A) are shown for $n = 7$, $B = 0.8$ mm and the lossless substrate, and in Fig. 4(b), for $\epsilon'' = 0.05$.

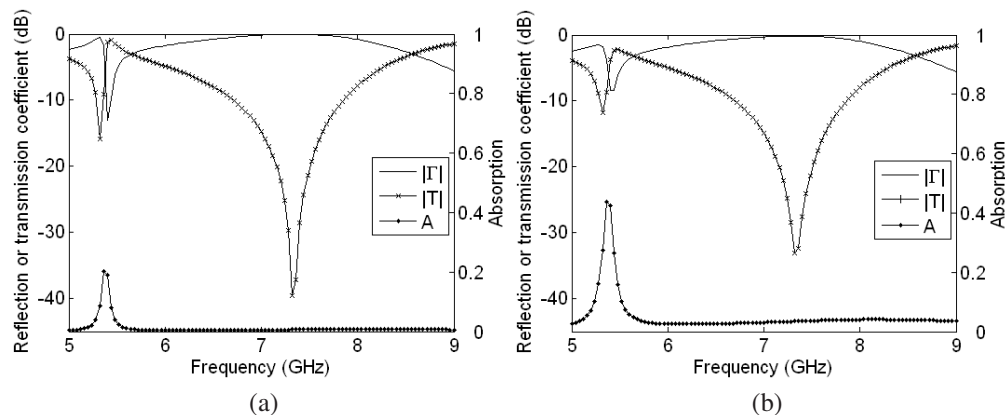


Figure 4: Reflection ($|\Gamma|$) and transmission ($|T|$) coefficients and normalized power absorption (A) of the array with inner corrugated ring for $n = 7$, $B = 0.8$ mm and lossless substrate $\epsilon'' = 0$ (a) and for $\epsilon'' = 0.05$ (b).

It is important to note that the resonance frequency of the array of simple ring is around 6.4 GHz, but in the combined array its resonance frequency is reduced by more than 1 GHz, it becomes 5.3 GHz, while the resonance frequency of the corrugated ring is increased by more than 0.6 GHz.

The array with inner corrugated ring has presented a lower Q-factor of the trapped-mode as compared with the array of two concentric rings. This is probably caused by the influence of the coupling between the two elements, because the inner corrugated ring causes a larger shift in the resonance frequencies of the inner and outer elements.

4. ARRAY WITH THREE CONCENTRIC RINGS

In the case of two element array, the resonance frequency of the outer element is shifted toward a lower frequency in the presence of the inner element. Based on this fact, a three element array was considered in order to approximate the second reflection resonance to the first, thus obtaining a higher Q-factor trapped-mode.

The resonance frequency of the middle ring (second reflection resonance) is shifted toward the resonance frequency of the outer ring (the first reflection resonance) creating the narrower transmission band in comparison with the two array configurations presented before. From the results obtained for different values of g , there is a compromise between Q-factor and deepness of the resonance, since increasing the gap between the rings the Q-factor reduces but, on other hand, the maximum of the transmission increases. The maximum transmittivity in the three-element array is lower than in the case of two-element array due to a larger field concentration in the array pattern which increases the losses.

When a fourth ring is put inside the smaller ring, the first transmission-band is practically unaltered.

5. CONCLUSION

The trapped-mode response of arrays consisting of two and three resonant elements in a cell was analyzed in this work in order to design a FSS with high Q-factor transmission resonance and polarization insensitivity. The three array configurations, two concentric rings, inner corrugated ring combined with ideal ring and three concentric rings posses high Q-factor resonance, namely, $Q = 21.7$, $Q = 13.5$ and $Q = 28.2$, respectively, for the cases with lossless substrate.

ACKNOWLEDGMENT

We would like to acknowledge the financial support provided by the Foundation for the Support of Research of the State of Pará (FAPESPA), the Brazilian agency CNPQ and National Academy of Sciences of Ukraine (Grant No. 1-02-a).

REFERENCES

1. Prosvirnin, S. L. and S. Zouhdi, "Resonances of closed modes in thin arrays of complex particles," *Advances in Electromagnetics of Complex Media and Metamaterials*, 281–290, S. Zouhdi, et al. (eds.), Kluwer Academic Publishers, 2003.
2. Fedotov V. A., M. Rose, S. L. Prosvirnin, N. Papasimakis, and N. I. Zheludev, "Sharp trapped-mode resonances in planar metamaterials with a broken structural symmetry," *Phys. Rev. Lett.*, Vol. 99, No. 14, 147401(4), 2007.
3. Zheludev, N. I., S. L. Prosvirnin, N. Papasimakis, and V. A. Fedotov, "Lasing spaser," *Nature Photonics*, Vol. 2, No. 6, 351–354, 2008.
4. Debus, C. and P. H. Bolivar, "Frequency selective surfaces for high sensitivity terahertz sensing," *Appl. Phys. Lett.*, Vol. 91, No. 18, 184102(3), 2007.
5. Prosvirnin, S., N. Papasimakis, V. Fedotov, S. Zouhdi, and N. Zheludev, "Trapped-mode resonances in planar metamaterials with high structural symmetry," *Metamaterials and Plasmonics: Fundamentals, Modelling, Applications*, 201–208, S. Zouhdi, et al. (eds.), Springer, 2009.
6. Misran, N., R. Cahill, and V. F. Fusco, "Design optimization of ring elements for broadband reflectarray antenna," *IEE Proc.-Microw. Antennas Propag.*, Vol. 150, No. 6, 440–444, 2003.

Electric Field Measurement from Tremendously Low Frequency to DC Based on Electro-optic Integrated Sensors

Huan Li, Rong Zeng, and Bo Wang

High Voltage Lab, the Department of Electrical Engineering, Tsinghua University, China

Abstract— The previous efforts on the measurement of DC electric field are concisely summarized and a novel method of electric field measurement from tremendously low frequency to DC based on electro-optic integrated sensors is proposed. In this new method the electric field waveform being measured is deduced from the distorted output of the sensor and the sensor frequency response. The experiments have preliminarily verified the feasibility of this method.

1. INTRODUCTION

Several methods of DC electric field measurement have been proposed before, which are classified into two categories and concisely summarized as follows.

1.1. The Conventional Electrical Methods

In 1983, D. Train and R. Dube developed a technique for measuring the DC voltage distribution on suspension insulator strings [1]. The technique involves the application of specialized electrostatic volt meters made of metal and might probably disturb the electric field being measured.

1.2. The Methods Utilizing Electro-optic Devices

In 1982, Kunihiro Hidaka and Hiroyuki Fujita measured the electric field distribution in a needle-to-plane gap of 10 cm with a positive DC corona discharge, using the Pockels effect of a bulk Lithium Niobate crystal, which was rotated to eliminate field disturbances caused by surface charges accumulated on it [2]. Although the Pockels device hardly disturbs the measured electric field and does not require a power source in it, the sophistication of the whole set of apparatus makes it difficult or in some cases almost impossible to use this method.

In sum, the conventional electrical methods inevitably involve the probability of severely distorting the measured electric field; while the methods utilizing electro-optic devices without integrated optical techniques inevitably involve sophisticated apparatus.

2. ELECTRO-OPTIC INTEGRATED ELECTRIC FIELD SENSORS

In order to reduce the complexity of the application of electro-optic devices, integrated optical techniques have been used to implement such electric field sensors [3–5]. Fig. 1 shows the typical packaging of the sensors described in this paper.

The schematic diagram of the sensing system is demonstrated in Fig. 2. The laser at a constant power generated by the laser diode is transmitted into the sensor by an input optical fiber and modulated in the sensor by the measured electric field. Subsequently, the laser with modulated power is transmitted into an Optic/Electrical (O/E) converter by an output optical fiber and converted linearly to electrical signals which could be observed and recorded by a digital oscilloscope.

According to the theoretical analysis in [3–5], under certain assumptions, the sensing system could be regarded as a linear time-invariant system, whose excitation and response signal are the electric field to be measured and the output voltage of the O/E converter, respectively. In this paper, the response of the sensing system and the response of the sensor alone are not rigorously differentiated.

Experiment results have shown that the sensor's response waveforms in time domain are completely identical to the line frequency and lightning pulse excitation waveforms, with a constant scale factor [3–5].

However, under the frequency range from tremendously low frequency to DC, the response and the excitation waveforms in time domain are not identical, and the measurement could not be carried out directly, which shall be showed as follows.

3. SENSOR RESPONSE UNDER TREMENDOUSLY LOW FREQUENCY TO DC

The sensor is placed in a plane-to-plane gap of 4 cm; and high voltage of different waveforms is applied on the gap, generating in the gap uniform electric field of corresponding waveforms.



Figure 1: Typical packaging of the electro-optic integrated electric field sensors described in this paper.

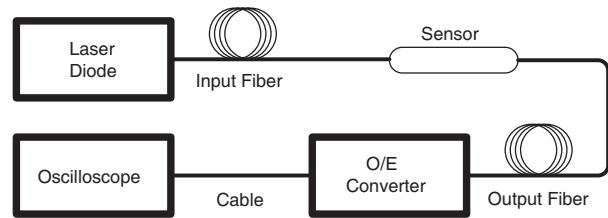


Figure 2: Schematic diagram of the sensing system.

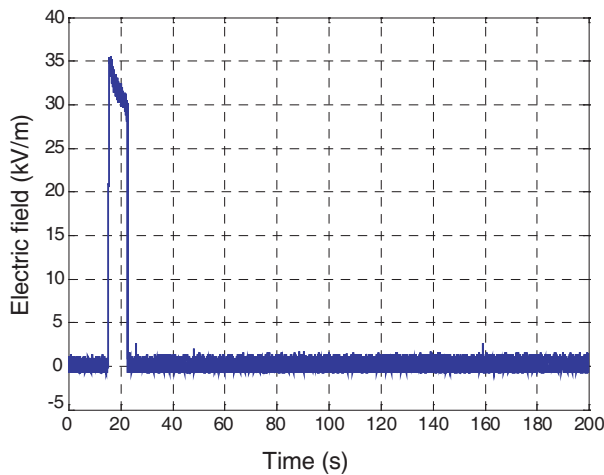


Figure 3: Typical approximate rectangular pulse excitation electric field.

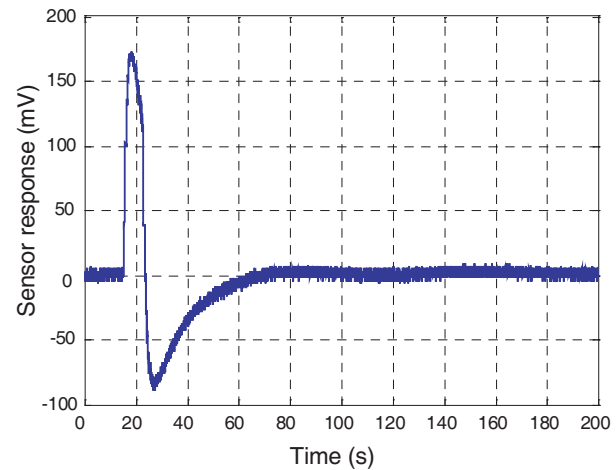


Figure 4: Typical sensor response to the electric field shown in Fig. 3 (DC bias subtracted).

If the theoretical analysis mentioned above is correct, the sensor could be regarded as a linear time-invariant system under certain assumptions, and its characteristics could be fully represented by its frequency response.

In order to investigate the frequency response, an approximate rectangular pulse excitation electric field, which is rich in frequency components, is applied in the gap, as shown in Fig. 3, and the sensor response is recorded, as shown in Fig. 4.

Fast Fourier Transform (FFT) analysis is performed on the waveforms shown in Fig. 3 and Fig. 4, the amplitude spectrum densities are shown in Fig. 5 and Fig. 6, respectively. It could be observed that the major frequency components are lower than 1 Hz.

By dividing the FFT result of the response by that of the excitation, the sensor frequency response is deduced, as shown in Fig. 7 and Fig. 8.

It could be observed in Fig. 7 and Fig. 8 that near several frequencies such as 0.14 Hz, 0.28 Hz, 0.42 Hz, etc., the frequency response curves are not smooth, due to the low signal noise ratio near these particular frequencies. In order to obtain smooth curves, it is necessary to use the vector fitting method [6].

A vector fitting with three poles and three zeros is performed, and the fitting results are demonstrated in Fig. 9 and Fig. 10. The numberS of the poles and zeros are determined by the analysis of an equivalent RC network proposed particularly for the sensor used in this paper, which is not going to be described in more detail here due to lack of space.

4. DEDUCING THE ELECTRIC FIELD WAVEFORM MEASURED FROM THE SENSOR RESPONSE

Another excitation of a waveform slightly different from the one shown in Fig. 3 is applied on the sensor; and the recorded response is shown in Fig. 11.

FFT analysis is performed on the waveform in Fig. 11; and the frequency components higher

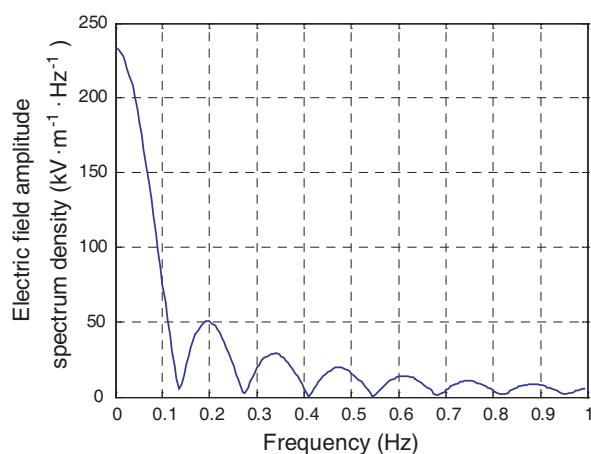


Figure 5: Amplitude spectrum density of the electric field waveform in Fig. 3.

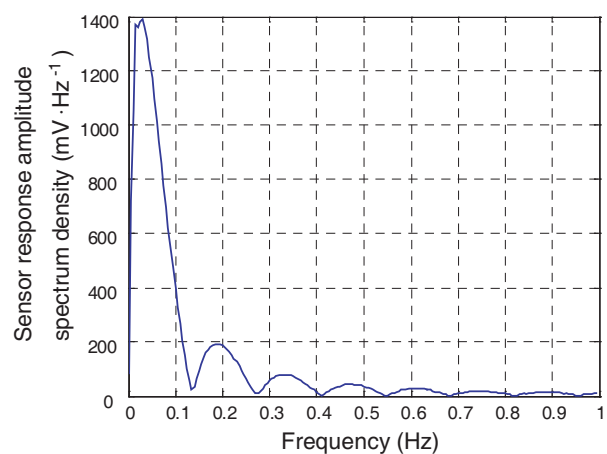


Figure 6: Amplitude spectrum density of the sensor response waveform in Fig. 4.

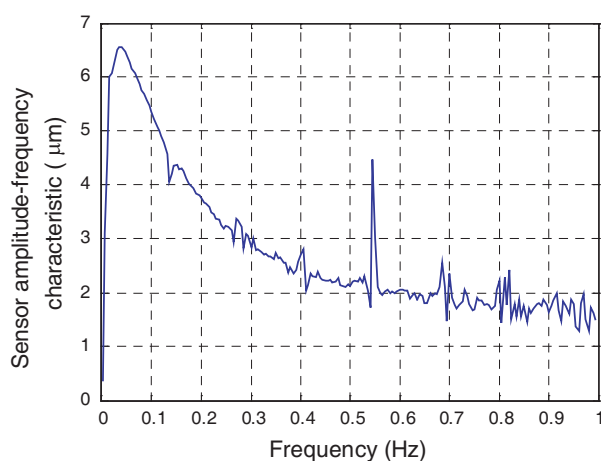


Figure 7: Typical sensor amplitude-frequency characteristic deduced from the experiment data in Fig. 3 and Fig. 4.

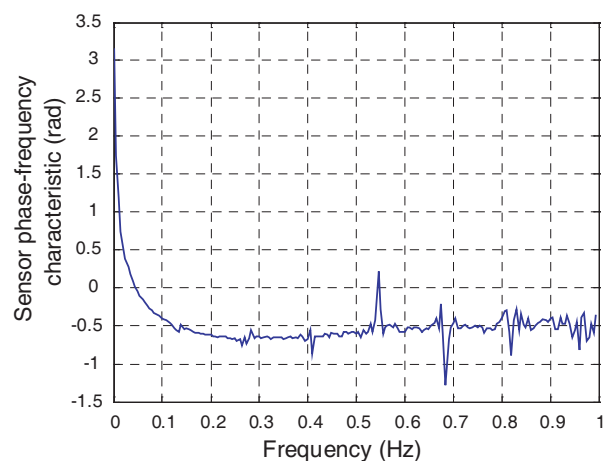


Figure 8: Typical sensor phase-frequency characteristic deduced from the experiment data in Fig. 3 and Fig. 4.

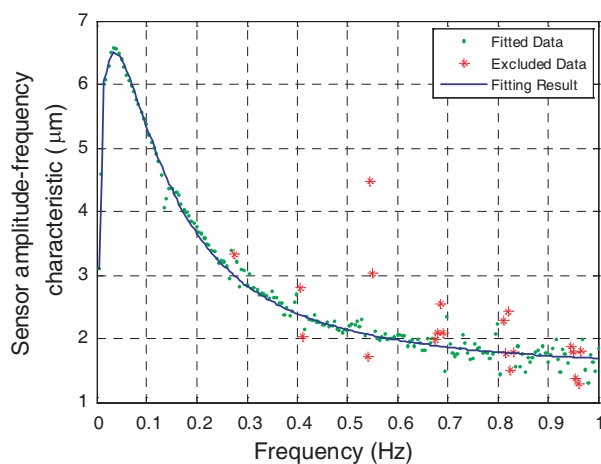


Figure 9: Vector fitting result of the sensor amplitude-frequency characteristic in Fig. 7.

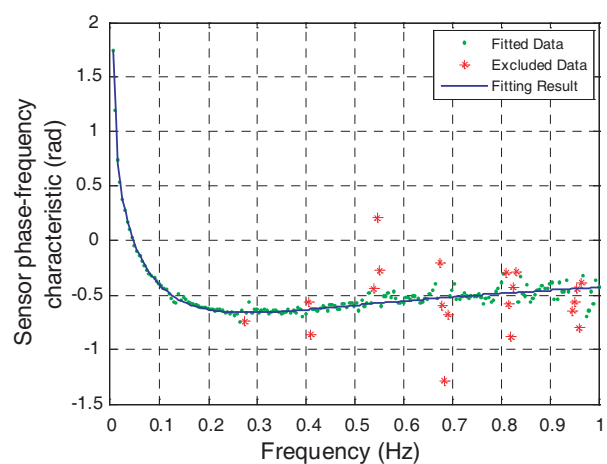


Figure 10: Vector fitting result of the sensor phase-frequency characteristic in Fig. 8.

than 1 Hz were neglected. The excitation waveform deduced from the FFT result of the sensor response waveform in Fig. 11 and the fitting result of the sensor frequency response is shown in Fig. 12, together with the original excitation waveform. It could be observed that the two waveforms are almost identical. To be more specific: in this particular case, the frequency components lower than 1 Hz in the original waveform are restored from the sensor response with a moderately high accuracy. The details from 4 s to 20 s are demonstrated in Fig. 13.

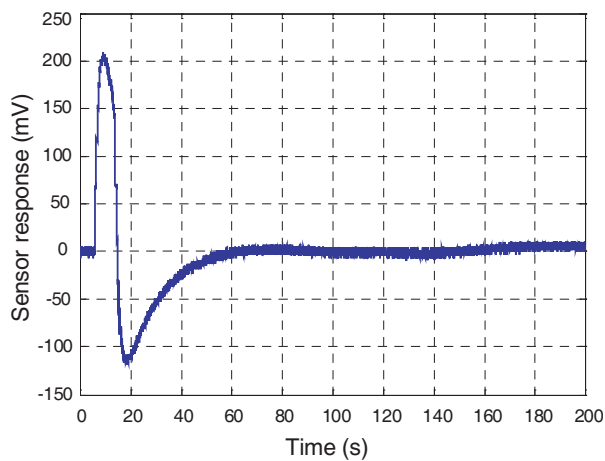


Figure 11: Sensor response to a certain excitation electric field (DC bias subtracted).

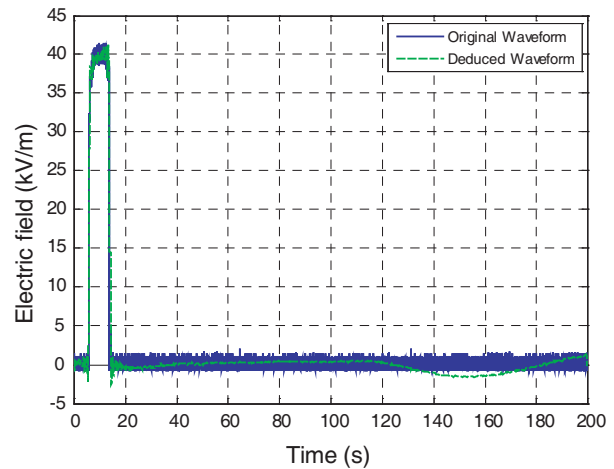


Figure 12: Original and deduced excitation electric field waveforms.

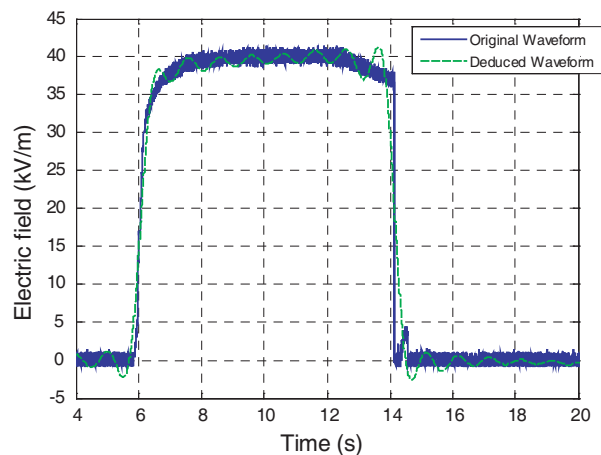


Figure 13: Original and deduced excitation electric field waveforms from 4 s to 20 s.

5. CONCLUSION

The frequency response of the electro-optic integrated electric field sensor from tremendously low frequency to DC is investigated by experiments and fitted with the Vector Fitting method. The frequency response is further used for restoring the original excitation electric field waveform whose major frequency components are in the same band. The restored waveform is almost identical to the original one.

The method proposed in this paper might be a feasible solution for electric field measurement from tremendously low frequency to DC.

The feasibility of this measurement method has to be further verified by more experiments; and its potential applications in various research fields (e.g., measuring the electric field distribution along the High Voltage DC insulator strings) are to be investigated.

ACKNOWLEDGMENT

The authors wish to acknowledge Prof. Jinliang He and Prof. Wei Zhao for valuable and interesting discussions.

REFERENCES

1. Train, D. and R. Dube, "Measurements of voltage distribution on suspension insulators for HVDC transmission lines," *IEEE T. Power Ap. Syst.*, Vol. 102, No. 8, 2461–2475, 1983.
2. Hidaka, K. and H. Fujita, "A new method of electric field measurements in corona discharge using Pockels device," *J. Appl. Phys.*, Vol. 53, No. 9, 5999–6003, 1982.
3. Chen, W., "Research on optoelectronic integrated sensor for intensive electric field measurement," Ph.D. Eng. thesis, Tsinghua University, Beijing, P. R. China, 2006.
4. Niu, B., "Research on integrated electro-optic time domain electric field sensor for intensive electric field," Ph.D. Eng. thesis, Tsinghua University, Beijing, P. R. China, 2008.
5. Li, H., "Research on characteristics of single arm shielded integrated optical intensive electric field sensor," B. Eng. thesis, Tsinghua University, Beijing, P. R. China, 2007.
6. Gustavsen, B. and A. Semlyen, "Rational approximation of frequency domain responses by vector fitting," *IEEE T. Power Deliver.*, Vol. 14, No. 3, 1052–1061, 1999.

Bistability of Nonlinear Photonic Crystal Microring Resonators

T. Ahmadi Tameh, B. Memarzadeh Isfahani, N. Granpayeh, and A. R. Maleki Javan
Faculty of Electrical Engineering, K. N. Toosi University of Technology
Tehran, Iran

Abstract— In this paper, two structures of nonlinear photonic crystal microring resonator have been analyzed by the finite-difference time-domain method and their optical bistability curves have been derived. In a modified structure, by increasing the interaction of the lightwave and material, the optical bistability threshold is decreased to one third of that of first structure.

1. INTRODUCTION

Since the early days of nonlinear optics, optical resonators have been considered as an attractive way to enhance nonlinear optical phenomena, such as optical bistability (OB) [1]. Optical bistability has been studied in many different fields, including optical computing, logic gates, optical limiting, pulse reshaping, and optical switching [2]. According to the low nonlinear coefficient of available materials, proper structures are required to enhance the nonlinearity and to decrease the dimensions [3]. A smaller dielectric ring resonator leads to higher radiation loss; this means that small dielectric microring resonators are inapplicable for all optical integrated circuits [4]. However, in photonic crystal microring resonators (PC-MRRs) according to the waveguiding mechanism, small PC-MRRs have negligible radiation loss, which makes them suitable for all-optical integrated circuits. Small ring resonators have high quality factor which leads to high nonlinear effects. Therefore, PC-MRRs are appropriate structures for enhancing nonlinear effects and having optical bistability [5, 6].

In this paper, two structures of PC-MRRs are proposed and their optical bistability curves are derived. In the second structure, the nonlinear effects are enhanced and the optical bistability threshold is decreased.

2. PHOTONIC CRYSTAL MICRORING RESONATORS

Photonic crystals are the periodic structures of dielectric rods in air, or air holes in dielectric with square or hexagonal lattices. In this paper, dielectric rods in air with square lattice have been employed. The dielectric is supposed to be Chalcogenide glass with refractive index of 3.1 and nonlinear coefficient of $n_2 = 9.0 \times 10^{-17} \frac{m^2}{W}$ at 1550 nm wavelength, the third window of optical communication systems [7].

By creating a ring shape defect in two-dimensional (2D) photonic crystal structure, one can obtain a PCMR, as depicted in Fig. 1. When microring resonator is situated between two waveguides, it can show switching behavior. These two waveguides should be single moded in the whole band gap of the structure. In addition, the ring resonator should have two degenerate modes which are symmetric [8].

For increasing the interaction of wave and material, four rods with radius of $0.1a$, where a is the lattice constant of PC structure, are added in the ring resonator which results enhancing nonlinear effects. In the corners of PC-MRRs, four rods with the same radius and material are added prevent the back reflection of the lightwave at the corners [9].

To have the maximum band gap, the radii of the rods are assumed to be $0.185a$. The complete band gap of this structure has been derived by plane wave expansion (PWE) method to be from $a/\lambda = 0.3455$ to $a/\lambda = 0.4692$.

When the input power is low, the Kerr effect can be neglected and the structure can be assumed as a linear structure. The transmission spectrum of this structure can easily be derived for the linear case by obtaining the ratio between the Fourier transforms of the outputs and input pulses. The structure is excited by a wide band Gaussian source from port A. The Gaussian pulse contains the whole frequency range of the structure band gap. The transmission spectra of this structure are shown in Fig. 2.

The structure resonant frequency is $f_r = 0.4129c/a$ in the linear case where c is the speed of light in vacuum. In this frequency, the input energy couples to the ring and then decouples to port D.

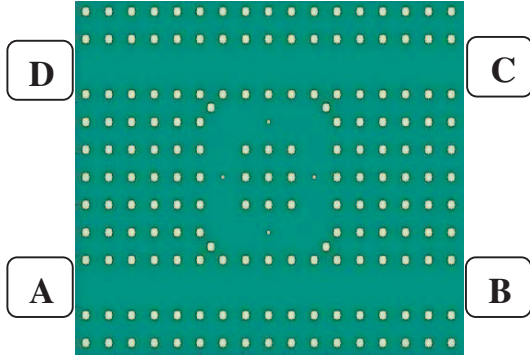


Figure 1: The e structure of a 5×5 photonic crystal microring resonator, inserted between two parallel waveguides.

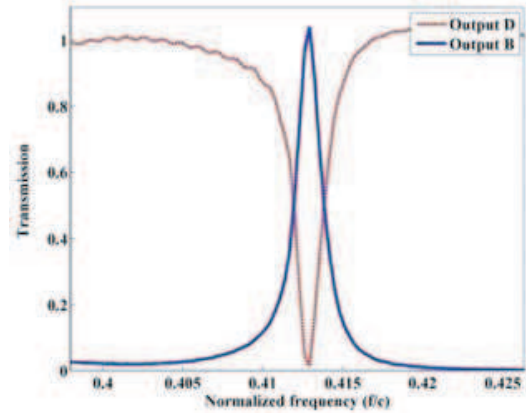


Figure 2: The transmission spectra of the structure shown in Fig. 1.

When the structure is excited from port A by a high power sinusoidal signal with the frequency derived above (f_r), the Kerr nonlinear effect will be enhanced, the effective refractive index of the rods will increase, and the resonant frequency of the structure will be shifted toward lower frequencies. Hence, the signal will not couple to the ring and will propagate towards port B.

To have low threshold optical bistability, the structure should have high transmission, narrow full width at half maximum power (FWHM) or high quality factor, and large frequency shifting by nonlinear effect [10].

For achieving optical bistability curve, the structure should be excited with triangular amplitude modulated with the sinusoidal signal, given by:

$$E_z(t) = E_0 \Lambda(t) \exp(j\omega_{in} t)$$

where $\Lambda(t)$ is given by,

$$\Lambda(t) = \begin{cases} 1 - \left| \frac{2t}{\tau_0} - 1 \right| & 0 \leq t \leq \tau_0 \\ 0 & \text{otherwise} \end{cases}$$

where E_0 is the maximum amplitude, τ_0 is the pulse width of triangular source, and $\omega_{in}(2\pi f_{in})$ is the input lightwave angular frequency which is selected to be lower than f_r . To derive the bistability curve, E_0 should be selected large enough to excite the nonlinear effects and τ_0 should be large enough, thus running the simulation program needs numerous time steps.

The bistability curve is plotted as the output power vs. input power. Fig. 3 illustrates the input signal, output signals of ports B and D, and bistable loop of the transmitted output intensities vs. input intensity.

At the front edge of the triangular source which the amplitude is low, the resonant frequency of the structure is f_r , while f_{in} is lower than f_r , thus the lightwave does not couple to the ring and transmits to output B. By increasing the intensity of lightwave, the effective refractive index of the rods will increase. Therefore, the resonant frequency of the structure shifts toward lower frequencies. If E_0 , high input intensity, is large enough, the resonant frequency shifts significantly and for some steps of the time coincides the input frequency of PC-MRR structure of Fig. 1, f_{in} , hence energy couples to port D.

3. STRUCTURE WITH LOWER OPTICAL BISTABILITY THRESHOLD

In a modified structure the waveguides are made by reducing the radii of rods to $0.1a$ instead of removing them. The waveguide is single moded in whole band gap. Also quality factor should stay almost fix and the interaction of wave and material should increase, thus the ring resonator is stretched vertically, as shown in Fig. 4. If the ring resonator stretches more, the interaction of wave and material increases but the quality factor decreases which leads to decreasing the nonlinear effects.

The transmission spectrum of the structure of Fig. 4 is shown in Fig. 5. It can be observed that in this structure, the resonant spectrum will be narrower, but the maximum transmission will decrease. The resonant frequency is $f_r = 0.3854c/a$.

Figure 6 demonstrates the input and output field intensities of ports B and D of the proposed structure of Fig. 4 and their bistable loops.

By comparison of Figs. 3 and 6, it is obvious that the bistability threshold of PC-MRR of the second structure is one third of that of the first structure.

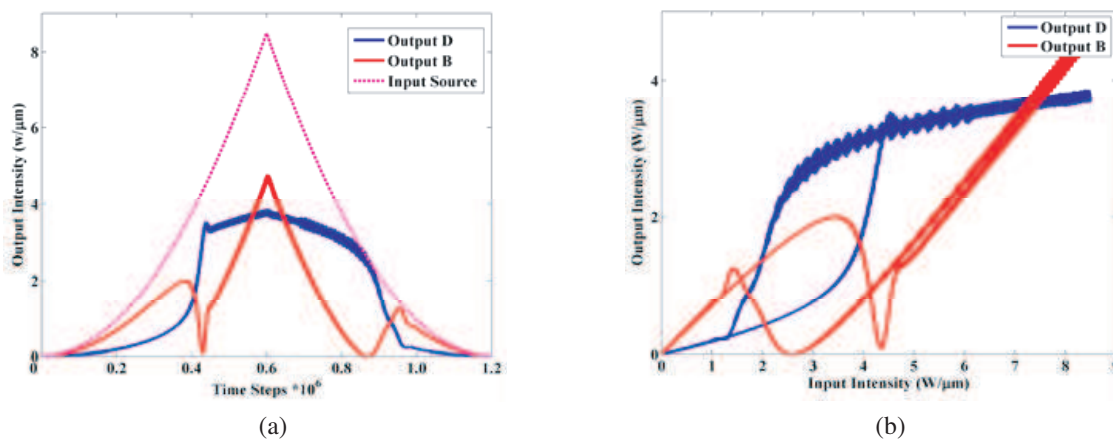


Figure 3: (a) The input and output intensities of ports B and D of Fig. 1 vs. time steps, (b) bistable loop of the ports B and D.

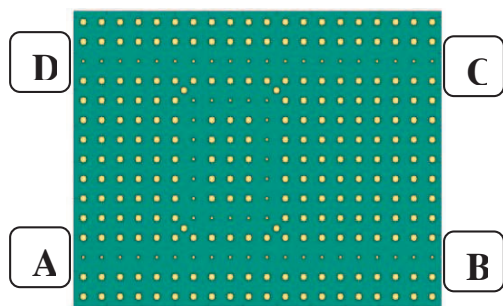


Figure 4: Proposed structure with lower optical bistability threshold.

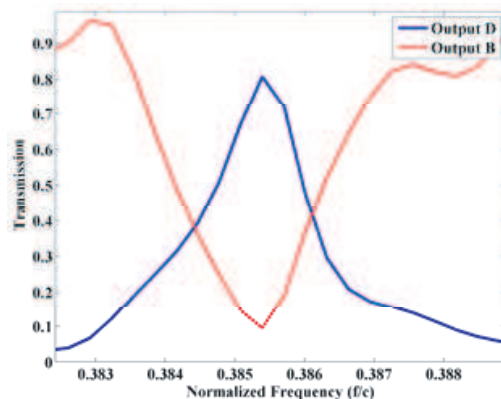


Figure 5: The transmission spectra of the Fig. 4.

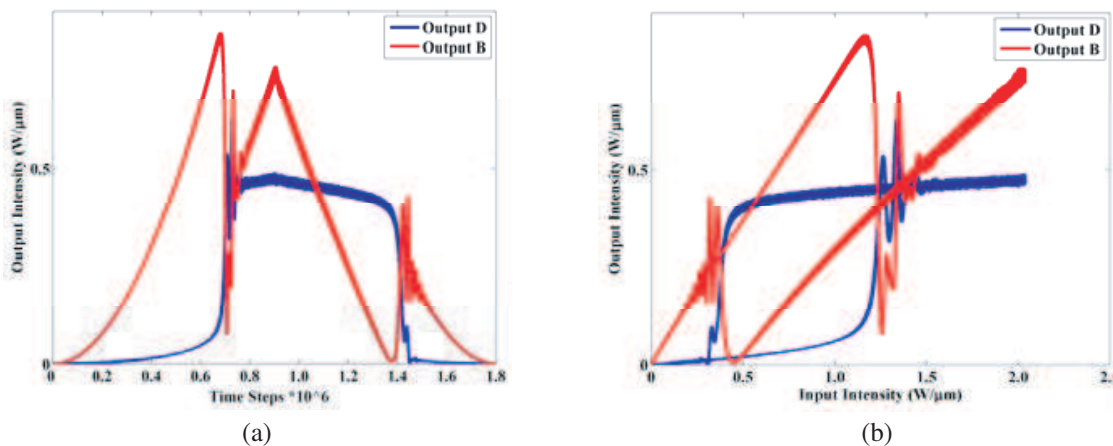


Figure 6: The output intensities of ports B and D of Fig. 4 vs. time steps, (b) bistable loop of the ports B and D.

4. CONCLUSION

In this paper, nonlinear PC-MRRs are proposed and it is shown that they demonstrate optical bistability. It is shown adding four rods in the ring increases the interaction of wave and material and enhances the nonlinear effects. In the second structure, all waveguides are made by reducing the radii of the rods and the ring is stretched vertically. In this situation, the threshold of optical bistability of the second structure is decreased to one third of that of the first structure.

ACKNOWLEDGMENT

Authors would like to thank Iran Telecommunication of Research center for the financial support of this project.

REFERENCES

1. Bravo-Abad, J., A. Rodriguez, P. Bermel, S. G. Johnson, J. D. Joannopoulos, and M. Soljacic, "Enhanced nonlinear optics in photonic-crystal microcavities," *Opt. Exp.*, Vol. 15, 16161–16176, 2007.
2. Noberga, K. Z. and H. E. Hernandez-Figueroa, "Optical bistability in nonlinear waveguides with photonic crystals," *Micro. And Opt. Technol. Lett.*, Vol. 41, 40–43, 2004.
3. Glud, S., A. Jebali, and N. Moll, "Optimization of ultrafast all-optical resonator switching," *Opt. Exp.*, Vol. 13, 9502–9515, 2005.
4. Xu, Q. and M. Lipson, "All-optical logic based on silicon micro-ring resonators," *Opt. Exp.*, Vol. 15, 924–929, 2007.
5. Joannopoulos, J. D., R. D. Meade, and J. N. Winn, *Photonic Crystals: Modling the Flow of Light*, Princeton University Press, 1995.
6. Qiang, Z., W. Zhou, and R. Soref, "Optical add-drop filters based on photonic crystal ring resonators," *Opt. Exp.*, Vol. 15, 1823–1831, 2007.
7. Ogaust, K., J. Yamasaki, S. Maeda, M. Kitao, and M. Minakata, "Linear and nonlinear optical properties of Ag-As-Se chalcogenide glasses for all-optical switches," *Opt. Lett.*, Vol. 29, 265–269, 2004.
8. Ahmadi Tameh, T., B. Memarzade Isfahani, N. Granpayeh, and A. R. Maleki Javan, "Enhancement of nonlinearity in nonlinear photonic crystal ring resonator for all-optical switching," *IEEE/LEOS Winter Topical Meetings*, 26–27, 2009.
9. Memarzade Isfahani, B., T. Ahmadi Tameh, N. Granpayeh, and A. R. Maleki Javan, "All-optical NOR gate based on nonlinear photonic crystal microring resonator," *Journal of the Optical Society of America B*, to be published, 2009.
10. Chen, L.-X. and D. Kim, "A bistable switching of two-dimensional photonic crystal with kerr point defect," *Opt. Commun.*, Vol. 218, 19–26, 2003.

Time-domain Experimental Investigation of One-dimension Photonic Crystal Based on Microstrip

Shougang Liu, Ziyang Li, and Yewen Zhang

Pohl Institute of Solid State Physics, Tongji University, 1239 Siping Road, Shanghai 200092, China

Abstract— In recent years, photonic crystal (PC) has aroused the attention of people as a new type of material that can be used to control electromagnetic waves. Our researches are based on the transmission properties on the photonic crystal transmission line (PC TL) within the second pass band of our PC TL by time-domain method. Different experimental models are designed to study the properties of PC TL, especially in the aspect of dispersion.

1. INTRODUCTION

The photonic crystal is multidimensional periodic structure comprising combination of two or more media different in refractive index. In these structures, the electromagnetic wave propagation is inhibited in certain frequency ranges, which is called a photonic band gap, analogous to electronic band gap in semiconductors [1]. These years, PC has been found many applications in microwave and optical systems. Some PC applications based on microwave technology are proposed such as microwave filters, antennas, couplers, etc. [2, 3]. Concretely, people become more and more interested in the dispersion of PC, some conclusions of the previous studies even showed an abnormal dispersion with negative group velocities [4]. But some scholars do not agree with them, they concluded the dispersion of photonic crystal is normal [5].

Our team is one of those who believe the dispersion of photonic crystal is normal. We focus on one-dimensional PC TL [6] in order to know its dispersion properties, especially in the second pass band. In this paper, a time-domain measurement is presented, which shows directly that the phase velocity is toward the source and consequently parallel to the group velocity. It presents measurements on the position and time behavior of a Gaussian modulated wave form in the PC TL. We have also carried out the time-domain experiments by using 4 different couplers: PC-CRLH (composite right-left handed) [6–9], RH-CRLH, PC-RH and RH-RH. It enhanced our cognition on the second pass band of PC TL: It possesses normal dispersion.

2. TIME-DOMAIN EXPERIMENTAL RESULTS

2.1. Experiment in One-dimensional Array PC TL

The initial simulations and experiments (time-domain) were carried out with a one-dimensional array PC TL (photonic crystal transmission line), as it is shown in the Figure 1. (The simplest metamaterial realization of magnetoinductive waves is in the form of a one-dimensional array of identical resonant elements in which each element is coupled magnetically to all the other elements.)

The permittivity of the substrate is 4.75 and the thickness is 1.6 mm. Dimensions of our PC TL unit are as follows: length $a = 15$ cm, $b = 35$ mm; width $a = 2.945$ mm, $b = 0.8$ mm. We prepared the PC TL with the technique of PCB (printed circuit board).

We have demonstrated both by simulations and time-domain experiments by using the montage as in Figure 2 that: the first pass band of PC TL stops at 1.2 GHz, the second pass band of this PC TL is from 2.0 GHz to 3.0 GHz. Then we have carried out some time-domain experiments in order to know the properties of the wave propagation in this transmission line.

We chose the wave 2.5 GHz as the first group of our time-domain experiment, and obtained the results as in Figure 3.

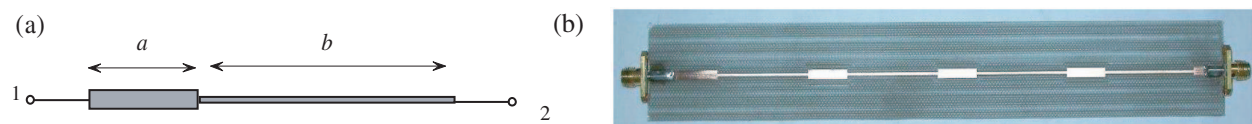


Figure 1: PCTL, image (a) is the elements of each PC unit; image (b) is the PC TL on a substrate.

Visually, we can predict that the wave propagation in our one-dimensional array PC TL has a positive group velocity and a positive phase velocity. We have also continued the same experiment

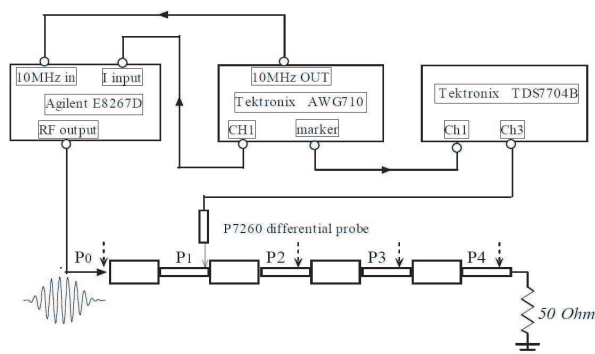


Figure 2: Experimental montage.

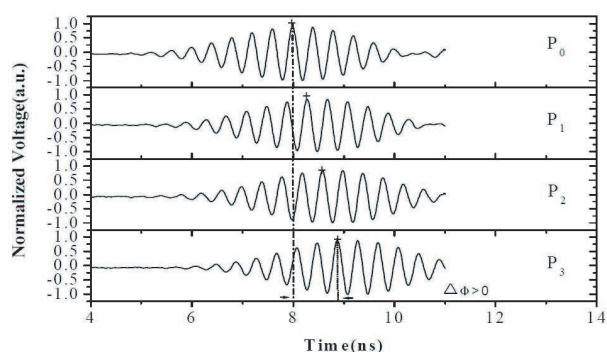


Figure 3: Measurements at 2.5 GHz.

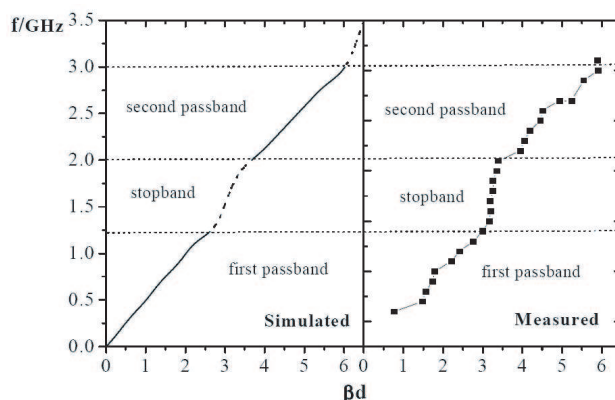


Figure 4: Simulated and experimental dispersion curve of the individual PC TL.

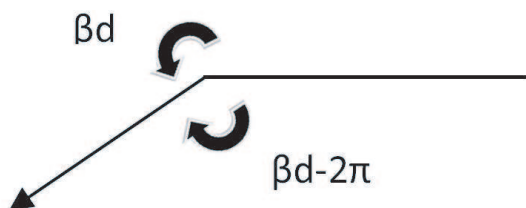


Figure 5: Uncertainty of phase shift.

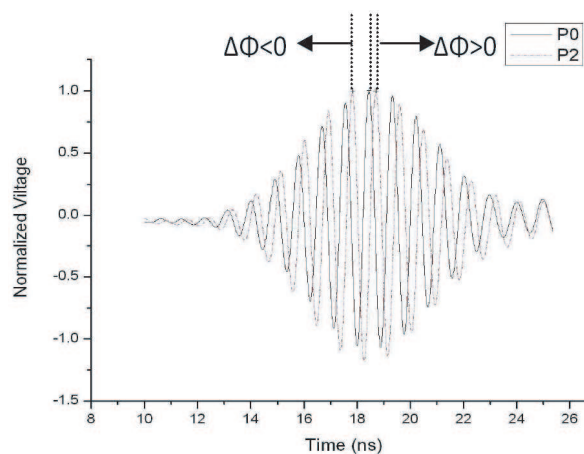


Figure 6: Uncertain results of phase shift.

in other frequencies (0.8 GHz, 1.0 GHz, and 2.3 GHz), all these results gave us the same conclusions about the electromagnetic wave propagation in our PC TL: positive group velocity and positive phase velocity.

All our judgments are visually based on the figures of the results (by choosing the peak of the incident wave as the reference, and comparing the following peaks with it), so here we are having some difficulties to differ the phase shift. As we have seen in the Figure 4 that, in the second pass band of our PC TL (when the wave frequency is above 2.0 GHz), the phase shift βd is going to exceed π . In a common dispersion curve, the axis of phase shift starts from $-\pi$ and ends at π . So here in our experiments, we can say the phase shift is βd , it does go exceeding π , or else, we may possibly think this phase shift has a negative value that equals $\beta d - 2\pi$. (Figure 5).

The Figure 6 is from one of our results, we can't decide for sure which the phase shift we are looking for is, due to the uncertainty that is previously described. In this article, we consider the phase shift positive, and obtained the dispersion curve as Figure 4.

2.2. Experiment in Couplers

In order to avoid the possible faults by the uncertain phase shift, and also to enhance our cognition of one dimensional array PC TL, we have proposed some experiments by using the method of coupling. Especially, we focused our research on the vortex-like interface mode existing at the interface of a PC-CRLH (composite right-/left-handed transmission line) coupler.

Dimensions of our PC-CRLH unit are as follows: $l = 11.8\text{ mm}$, $h = 12.5\text{ mm}$, $d = 3\text{ mm}$, $c = 1\text{ pF}$, $L = 1.8\text{ nH}$, $s = 0.2\text{ mm}$. We measured the group delay at each unit both by simulation and time-domain experiments, and obtained the results as Figure 8.

We see from the figures that the group delay of wave propagation in this coupler is about 1 ns. In our previous research, we've found that the group delay of wave propagation in a RH CRLH coupler is also about 1ns as it is shown in Figure 9.

And also, we have carried out the experiments by using PC-RH coupler and RH-RH coupler, the results are shown as below in Figures 10 and 11.

The group delays in these 2 couplers are of the same level. In combining all the four couplers, it clear shows that the average group delay of the PC-CRLH coupler is approximately ten times longer than that of the microstrip coupler, which indicates that vortex mode leads to slow propagation. In the aspect of group delay, PC-CRLH coupler has the same propriety comparing with RH-CRLH coupler which has been demonstrated both by simulation and experiment, and so does the comparison between PC-RH coupler and RH-RH coupler.

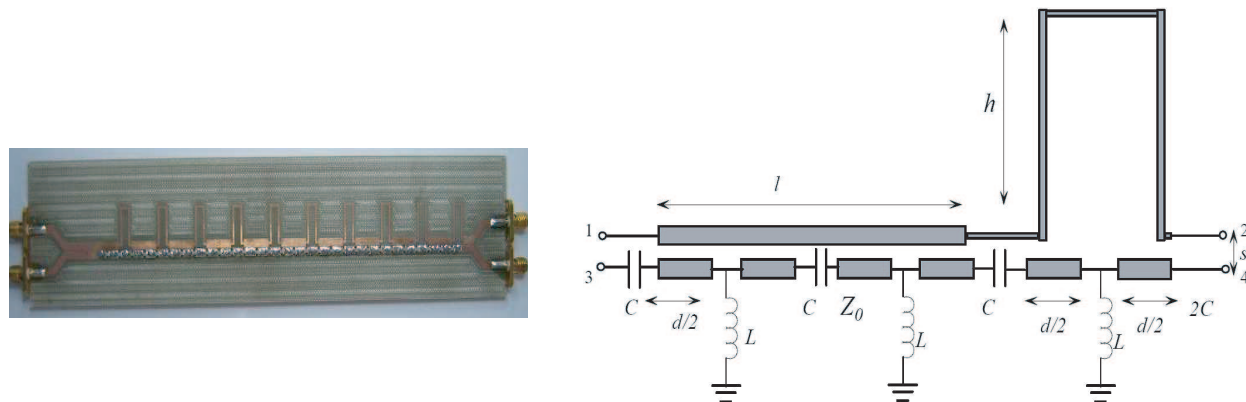


Figure 7: PC-CRLH coupler.

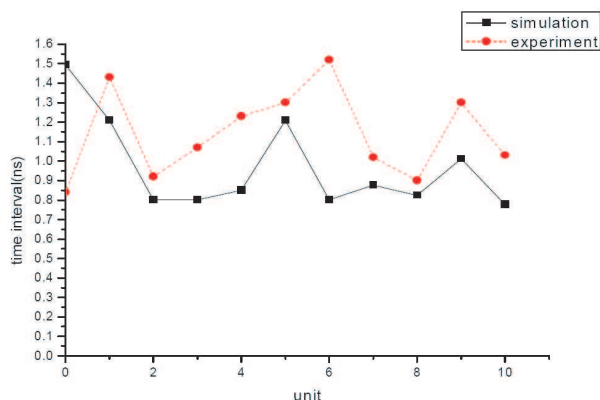


Figure 8: PC-CRLH coupler group delay.

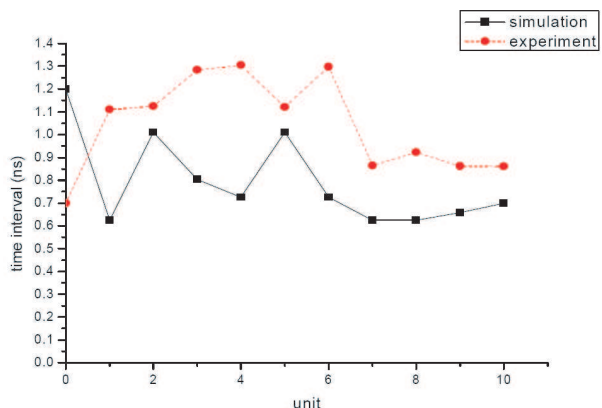


Figure 9: RH-CRLH coupler group delay.

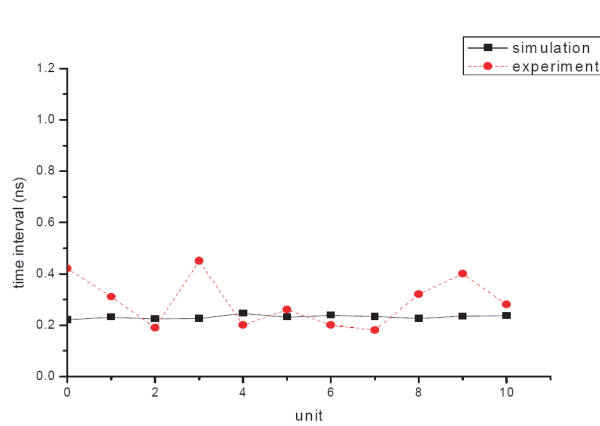


Figure 10: PC-RH coupler group delay.

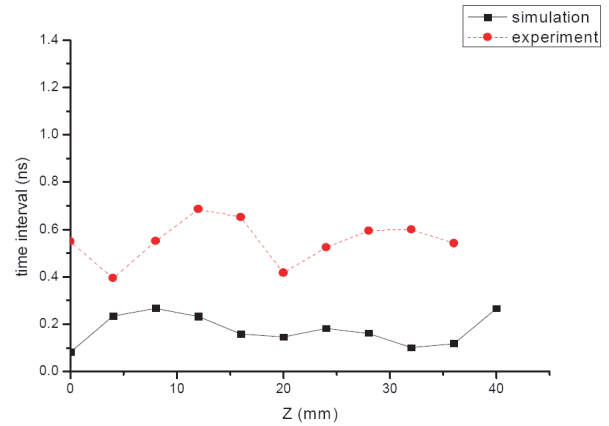


Figure 11: RH-RH coupler group delay.

3. CONCLUSION

These coupling experiments agree well with the simulation and theoretical results. This is another way to prove that PC TL is such as RH TL, whose dispersion is normal. However, when we studied on a one-dimensional array PC TL without the coupling proprieties, we can't be sure about the value of the phase shift; does it equal βd or $\beta d - 2\pi$.

ACKNOWLEDGMENT

This project is supported by the 973 project (Grant No. 2006CB0L0901), and by Shanghai Committee of Science and Technology (contract No. 07DZ22302).

REFERENCES

1. Joannopoulos, J. D., R. D. Meade, and J. N. Winn, *Photonic Crystals: Molding the Flow of the Light*, Princeton Univ. Press, Princeton, NJ, 1995.
2. Karmakar, N. C. and M. N. Mollah, "Investigations into nonuniform photonic-bandgap microstripline low-pass filters," *IEEE Transactions on Microwave Theory and Techniques*, Vol. 51, 564–572, 2003.
3. Weily, A. R., L. Horvath, K. P. Esselle, B. C. Sanders, and T. S. Bird, "A planar resonator antenna based on a woodpile EBG material," *IEEE Transactions on Antennas and Propagation*, Vol. 53, 216–223, Jan. 2005.
4. Parimi, P. V., W. T. Lu, P. Vodo, J. Sokoloff, J. S. Derov, and S. Sridhar, "Negative refraction and left-handed electromagnetism in microwave photonic crystals," *Physical Review Letters*, Vol. 92, No. 12, March 26, 2004.
5. Fen, L. J., H. T. Jiang, H. Q. Li, Y. W. Zhang, and H. Chen, "Dispersion characteristics of Photonic crystal waveguide coupled-cavity," *Acta Physica Sinica*, Vol. 54, 2102–2105, May 2005.
6. Shelby, R. A., D. R. Smith, and S. Schultz, "Experimental verification of a negative index of refraction," *Science*, Vol. 292, 77–79, 2001.
7. Caloz, C. and T. Itoh, "Application of the transmission line theory of left-handed (LH) materials to the realization of a microstrip LH transmission line," *IEEE AP-S Int. Symp. Dig.*, Vol. 2, 412–415, June 2002.
8. Oliner, A. A., "A periodic-structure negative-refractive-index medium without resonant elements," *IEEE AP-S/URSI Int. Sym Dig.*, 41, San Antonio, TX, June 2002.
9. Iyer, A. K. and G. V. Eleftheriades, "Negative refractive index metamaterials supporting 2-D waves," *IEEE MTT-S Int. Microwave Symp., Dig.*, Seattle, WA, 1067–1070, June 2002.

Effect of FWM Output Power Induced by Phase Modulation in Optical Fiber Communication

Li Wang, Wenzheng Ban, Yang Song, Jiangbo Chen, and Xinping Zhang
College of Applied Sciences, Beijing University of Technology, Beijing 100124, China

Abstract— The Four wave mixing (FWM) power with pump light parameters in standard single-mode fiber, dispersion-shifted fiber, non-zero dispersion fiber and two kinds of dispersion compensating fibers have been compared through numerical simulated calculations. The effect of pump wavelength deduced to the phase-mismatching factor, pump wavelength, pump power and propagation distance to parametric gain and power of FWM have been analyzed in a self-phase modulation and cross-phase modulation. The effect of the pump power, propagation distance and fiber effective core area to FWM have been obtained. It is useful to select the category of fiber and pump, signal wavelength in communication system devices.

1. INTRODUCTION

Because of the development of Internet, E-commerce, multimedia, IP and data operation, the demand of communications rises exponentially. In order to meet the needs of improving information quantity, wavelength division multiplexing (WDM) has become the main research area in optical fiber communication for 21th century [1, 2]. With the increase of optical power, channel amount, transmission rate and distance, and the construction of all-optical network (AON), the influence of four-wave mixing (FWM) has become the main factor which limits the capability of communication system [3, 4]. Therefore, the research on FWM is significant for the keeping information quantity and transmission rate in communication system [5, 6]. The origin and phase matching condition of FWM have been studied in detail. The FWM in standard single-mode fiber, dispersion-shifted fiber, non-zero dispersion fiber and two kinds of dispersion compensating fibers have been compared using numerical simulated calculations. It has been analyzed that the influence of pump wavelength to phase-matching factor and the relation between FWM and the two preceding factors. The numerical simulated calculations of influence of pump wavelength, pump power and propagation distance to parametric gain have been studied. The influence of self-phase modulation and cross-phase modulation has been discussed. The influence of pump power, propagation distance and fiber effective core area to FWM have been used to study. It is useful in the aspects of selecting the category of fiber and pump, signal wavelength in communication system devices.

2. THEORETICAL ANALYSIS AND SIMULATION

The output power of FWM in the optical fiber communication is affected by the factors of the phase mismatching, optical length, optical decay coefficient and phase modulation, therefore the phase mismatching will be affected as the difference of the pump and signal wavelength, the pump light and the optical fiber non-dispersion wavelength. Then the FWM efficiency with the different factors is hardly any affection in the phase matched, but there are prominent influences of FWM output power with the various factors in phase mismatching.

2.1. FWM with Channel Power

When the self-phase and cross-phase modulation is not considered in FWM, the FWM power can be described by [7, 8],

$$P_1(L) = \frac{\eta}{9} D^2 \gamma^2 P_2 P_3 P_4 \exp(-\alpha L) \left\{ \frac{[1 - \exp(-\alpha L)]^2}{\alpha^2} \right\} \quad (1)$$

where η is FWM efficiency, D is germination factor and $D = 3$ with a germination FWM, α is optical decay coefficient, L is optical length. $\gamma = \frac{n_2 \omega_0}{c A_{eff}}$ is a nonlinear coefficient, n_2 is optical refractive index, $A_{eff} = \pi \omega^2$ is optical fiber core area. FWM efficiency as the power P_1 , P_2 and P_3 of pump light are incident into the fiber can be written by,

$$\eta = \frac{\alpha^2}{\alpha^2 + \Delta k^2} \left\{ 1 + \frac{4 \exp(-\alpha L) \sin^2(\Delta k L / 2)}{[1 - \exp(-\alpha L)]^2} \right\} \quad (2)$$

where the linear phase mismatches Δk is not related with light intensity in Equation (1), and it has been given by

$$\Delta k = \frac{2\pi\lambda^2}{c} \Delta f_{23} \Delta f_{24} \left[D_c + \frac{\lambda^2}{2c} (\Delta f_{23} + \Delta f_{24}) \frac{dD_c}{d\lambda} \right] \quad (3)$$

where Δf_{23} and Δf_{24} is the channel spacing, $dD_c/d\lambda$ is the fiber dispersion slope.

The FWM power and conversion efficiency with phase mismatching factor has obtained as the self-phase and cross-phase modulation are consideration as follows,

$$P_1'(L) = \frac{\eta'}{9} D^2 \gamma^2 P_2 P_3 P_4 \exp(-\alpha L) \left\{ \frac{[1 - \exp(-\alpha L)]^2}{\alpha^2} \right\} \quad (4)$$

$$\eta' = \frac{\alpha^2}{\alpha^2 + (\Delta k')^2} \left\{ 1 + \frac{4 \exp(-\alpha L) \sin^2(\Delta k' L/2)}{[1 - \exp(-\alpha L)]^2} \right\} \quad (5)$$

where $\Delta k'$ is the phase mismatching with intensity and can be expressed as

$$\Delta k' = \Delta k - \gamma (P_2 + P_3 - P_4) \left\{ \frac{1 - \exp(-\alpha L_{eff})}{\alpha L_{eff}} \right\} \quad (6)$$

where the effective interaction length L_{eff} can be written by

$$L_{eff} = \frac{1 - \exp(-\alpha L)}{\alpha} \quad (7)$$

Because the fiber is long enough in the optical fiber communication system, the effective interaction length can be simple given as follows

$$L_{eff} = \frac{1}{\alpha} \quad (8)$$

According to the analysis above, in the case of considering the self-phase and cross-phase modulation respectively, we studied the effect of FWM for the optical fiber.

We choose a fiber with of length $L = 20$ km, two pump lights wavelengths of 1558 nm and 1558.8 nm, and the channel spacing of 0.8 nm, respectively. For the standard single mode fiber of G.652, we adopted the optical fiber decay coefficient of $\alpha = 0.35$ dB/km, effective core area of $A_{eff} = 55 \mu\text{m}^2$, dispersion parameter of $D_c = 17$ ps/(nm·km), dispersion slope of $dD_c/d\lambda =$

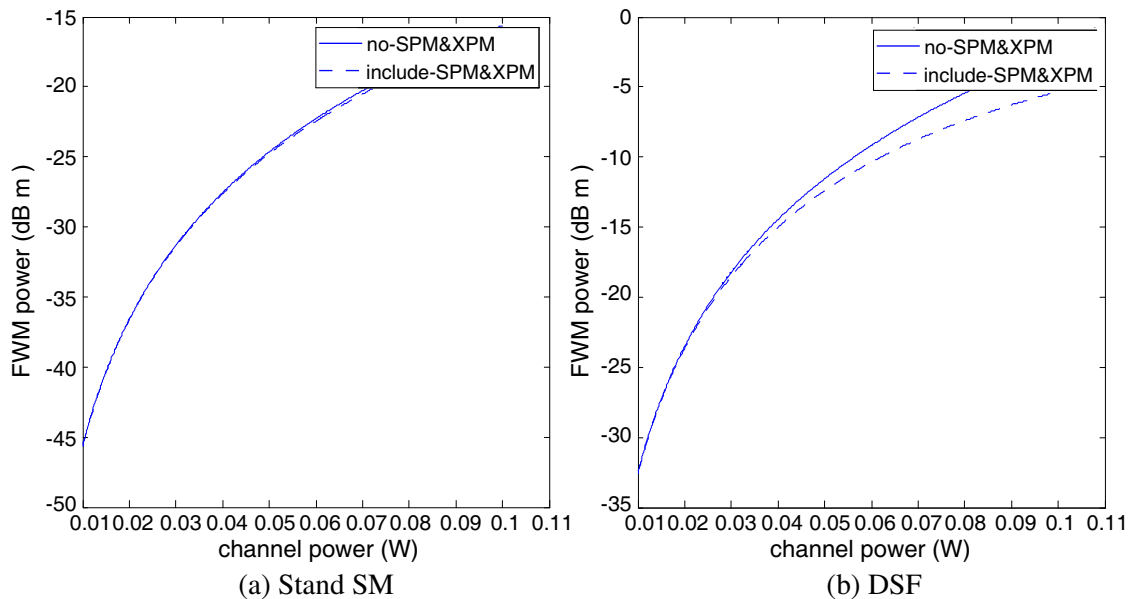


Figure 1: Curves of FWM power and pump power.

0.09 ps/(nm²·km), and nonlinear refractive index of $n_2 = 2.2 \times 10^{-20}$ m²/W in theoretical simulation. We supposed the pump power range of 10 mW \sim 1 W, and deduced from Equation (1) and (2) the variation of FWM power is shown in Fig. 1(a).

For the dispersion compensating fiber (DCF) in the density wavelength division multiplexing (WDM) communication system, we choose the optical fiber decay coefficient of $\alpha = 0.3$ dB/km, effective core area of $A_{eff} = 19 \mu\text{m}^2$, dispersion parameter of $D_c = -87$ ps/(nm·km), dispersion slope of $dD_c/d\lambda = -0.71$ ps/(nm²·km), and nonlinear index of $n_2 = 2.32 \times 10^{-20}$ m²/W, then the fiber length and the condition of pump light are the same as in the Fig. 1(a), and we can get the curve of FWM power of DCF, as shown in Fig. 1(b). In the Fig. 1, the solid line was obtained results for a linear phase mismatching and the influence of self-phase and cross-phase modulation was not considered using numerical analysis. The dotted line was obtained results when the phase mismatches related with intensity, and self-phase and cross-phase modulation was considered. By comparing the two curves we can find that when the increase of pump power, the FWM power also increases. Fig. 1(a) can see clearly that the curves almost coincidence in a standard single-mode fiber, Fig. 1(a) shows that the influence of self-phase and cross-phase modulation can be ignored in the effect of FWM. But for the dispersion compensating fiber, Fig. 1(b) shows that the two curves almost coincidence, and the self-phase and cross-phase modulation have a little influence on the effect of FWM and can be ignored when the pump power less than 25 mW, but if the increase of pump power, the influence of self-phase and cross-phase modulation becomes very strong. The errors without the consideration of self-phase and cross-phase modulation will be about 5 dB when the power of pump light is 100 mW. The FWM power of the linear phase mismatches has a gradually large error, so the influence of self-phase and cross-phase modulation can not be ignored. A choice for a fiber length L is 20 km, the pump lights with their wavelengths is 1558 nm and 1558.8 nm, respectively, with the channel spacing will be 0.8 nm. In the case of considering the self-phase and cross-phase modulation, by comparing the effects of FWM of five common kinds of fibers, such as a standard single-mode fiber, dispersion-shifted fiber (DSF), non-zero dispersion fiber (NZ-DSF) and dispersion compensating fibers of A (DCF-A) and B (DCF-B) category, then we can get the relation curves of FWM power of all kinds of fibers by numerical calculation, as shown in the Fig. 2. The FWM powers of different kinds of fibers at communication window of 1550 nm have shown in Fig. 2, from Fig. 2, we can see clearly that the powers increase of FWM pump power for different kinds of fibers, and the order of FWM power will become from high to low that is DSF fiber, NZ-DSF, DCF-A, standard single-mode fiber and DCF-B. When pump power less than 35 mW, the FWM powers generated in NZ-DSF and DCF-A are almost equal.

2.2. Propagation Distance and FWM

In the case of considering self-phase and cross-phase modulation, keeping the pump power of 40 mW, two pump wavelengths of 1558 nm and 1558.8 nm, and choosing five different kinds of fibers in Fig. 2, then we can get the relation curves of FWM power and propagation distance of different kinds of fibers from formula (1) to (8) using the simulated calculation, as shown in Fig. 3. From

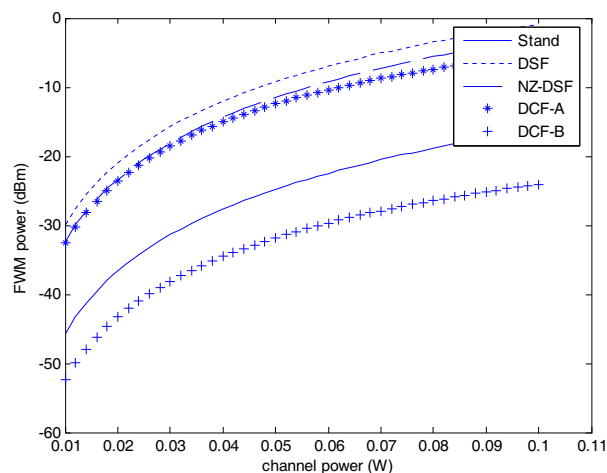


Figure 2: Relation curves of FWM power and pump power.

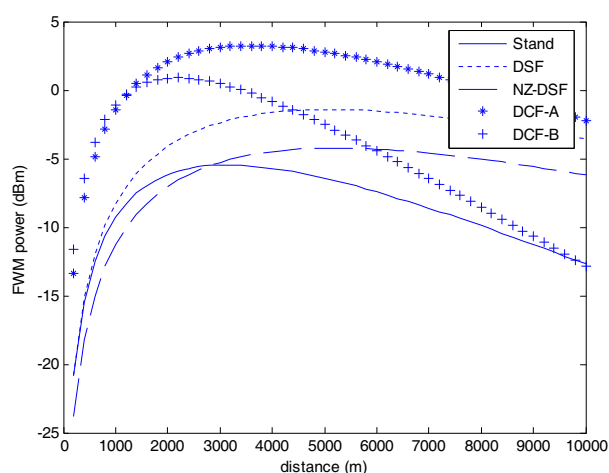


Figure 3: Relation curves of FWM power and distance.

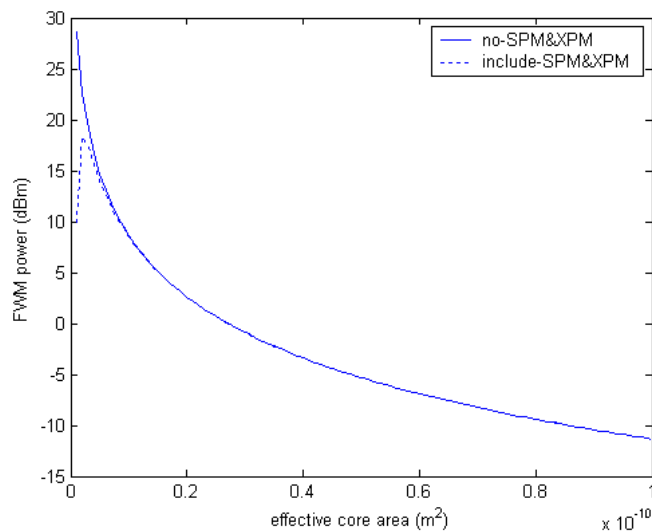


Figure 4: FWM power and effective core area.

Fig. 3, with the increase of propagation distance, FWM power first increases rapidly, then decreases slowly. The reason is the increase of propagation distance causes fiber loss increases so that pump power decreases. For the standard single-mode fiber and dispersion compensating fiber, when the propagation distance is large than 2 km, FWM power begins to decrease significantly. But for the dispersion-shifted fiber and non-zero dispersion fiber, when the propagation distance is large than 4 km, FWM power begins to decrease, but its amplitude is slow and changes to be steady. From the above, when needing obvious FWM effect, we should control fiber length according to the different kinds of fibers.

2.3. Effective Core Area and FWM Power

Choosing the propagation distance of 2 km, channel power of 40 mW, channel spacing of 0.8 nm, fiber effective core area of $0 \sim 100 \mu\text{m}^2$, standard single-mode fiber of G.652, optical fiber decay coefficient of $\alpha = 0.35 \text{ dB/km}$, effective core area of $A_{eff} = 55 \mu\text{m}^2$, dispersion parameter of $D_c = 17 \text{ ps}/(\text{nm}\cdot\text{km})$, dispersion slope of $dD_c/d\lambda = 0.09 \text{ ps}/(\text{nm}^2\cdot\text{km})$, and nonlinear index of $n_2 = 2.2 \times 10^{-20} \text{ m}^2/\text{W}$, we can get the relation curves of FWM power and fiber effective core area by simulated calculation that is shown in Fig. 4.

In Fig. 4, the solid line was obtained by numerical analysis using linear phase mismatches in Equation (1) to (4), and the influence of self-phase and cross-phase modulation was not considered, the dotted line was obtained using phase mismatches related with intensity, and the influence of self-phase and cross-phase modulation was considered. By comparing the two curves we can find that when the fiber effective core area is large than $5 \mu\text{m}^2$, the two curves coincide, and with the increase of fiber effective core area, the FWM power decreases rapidly. When the fiber effective core area is small than $5 \mu\text{m}^2$, with the increase of fiber effective core area, the FWM power without consideration of self-phase and cross-phase modulation decreases, but the FWM power with increasing, as the former, there will be a larger error of FWM power. In view of the case that the effective core area is bigger more $15 \mu\text{m}^2$ in the fiber parameter now, so when we discuss the influence of effective core area to FWM, we can ignore the influence of self-phase and cross-phase modulation. For the optical fiber communication system, we can decrease FWM by choosing the fiber of bigger effective core area, while when needing FWM to get wavelength conversion, we should reduce the fiber effective core area as possible.

3. CONCLUSION

We described the generation mechanism of FWM in the fiber. By the analysis of phase matching condition in detail, and got the relations of pump light wavelength and phase mismatches. According to the coupled wave equation of FWM, we have got FWM efficiency, FWM power and the expression of parametric gain by numerical analysis. By numerical calculation, we have discussed the influence of some parameters, such as a phase mismatches, pump wavelength, pump power,

optical fiber decay coefficient, fiber dispersion characteristics, fiber effective core area, propagation distance, self-phase and cross-phase modulation and so on in the process of FWM of fiber. Also by simulated calculation, we have compared and analyzed the processes of FWM of common standard single-mode fiber, dispersion-shifted fiber, non-zero dispersion fiber and dispersion compensating fiber in the optical fiber communication system. Some theoretical results will take the guidance meaning to the choice of fiber.

ACKNOWLEDGMENT

We would like to thank the Specialized Research Fund for the Doctoral Program of Higher Education under Grant No. 200800050013.

REFERENCES

1. Hansryd, J., H. Sunnerud, P. A. Andrekson, et al., "Impact of PMD on four-wave-mixing-induced crosstalk in WDM systems," *IEEE Photonics Technology Letters*, Vol. 12, No. 9, 1261–1263, 2000.
2. Spalter, S., H. Y. Hwang, J. Zimmermann, G. Lenz, T. Katsufuji, S. W. Cheong, and R. E. Slusher, "Strong selfphase modulation in planar chalcogenide glass waveguides," *Opt. Lett.*, Vol. 27, 363–365, 2002.
3. Wong, K. Y., M. E. Marhic, K. Uesaka, and L. G. Kazovsky, "Polarization-independent one-pump fiber-optical parametric amplifier," *IEEE Photonics Technology Letters*, Vol. 14, 1506–1508, 2002.
4. Gauchard, S., "Theoretical and experimental investigation of the impact of four wave mixing on DWDM," *IEEE Photonics Technology Letters*, Vol. 5, No. 2, 460–463, 2004.
5. Yamamoto, T. and M. Nakazawa, "Highly efficient four-wave mixing in an optical fiber with intensity dependent phase matching," *IEEE Photonics Technology Letters*, Vol. 9, 327–329, 1997.
6. Marhic, M. E., Y. Park, F. S. Yang, et al., "Widely tunable spectrum translation and wavelength exchange by four-wave mixing in optical fibers," *Opt. Lett.*, Vol. 21, No. 23, 1906–1908, 1996.
7. Shinji, Y., "Efficiency improvement of optical fiber wavelength converter without spectral spread using synchronous phase/frequency modulations," *Journal of Lightwave Technology*, Vol. 21, No. 4, 1039–1044, 2003.
8. Guan, Y. L. and S. S. Jian, "Effect of FWM and dispersion in optical fiber," *Optical Communication Technology*, No. 4, 279–283, 1998.

Magnetic Particles (Magnetons) — Structural Components of Atoms and Substance, Immediate Sources of Magnetic Fields

Robert Sizov

Individual researcher, Moscow, Russia

Abstract— Theory and experiments as a result of more than 30 years of experimental and theoretical investigations, the author discovered and presented to the attention of scientific community (in 2001, in his first book [1]) the magnetic fundamental particle (magnetic charge, pole), which the author referred to as *magneton*. Magneton, which is a structural element of atoms and substance, was not discovered before, because the conditions of its bond with substance or the conditions of its confinement are other than those of electron. One has to recognize as another important reason, which served a barrier in the path toward detection and legalization of magnetons for 135 years, the fallacious Maxwell “virus” referred to in this book, i.e., the erroneous concept, according to which moving or rotating electric charges, for example, electrons, were taken to be immediate sources of all magnetic fields and magnetic manifestations. The basic physical parameters of magneton are as follows.

1. **Charge.** Magneton has a magnetic charge g , whose value is equal to that of electron charge ($g = e$).
2. **Sign of charge.** Like electron, magneton is negatively charged (g^-).
3. **Mass.** Similar to electron, magneton is a massless material particle exhibiting the property of inertia. The measure of inertia of magneton (designated as m_g^i) is equal to that of electron (condition: $m_g^i = m_e^i$).
4. **Class of elementary particles** — lepton.
5. **Statistical properties** — fermion.

Following are several possible terms involving the suggested name of magnetic particle:

- magneton current — the current of magnetic charges in a conductor;
- conduction magnetons — magnetic charges which define magnetic conduction.

In a number of cases, terms may be used which involve only the root of the name of magnetic particle:

- magnetostatic voltage — magnetic analog of electrostatic voltage;
- magnetic conduction — conductivity of magnetic charges.

It is to be reminded that the word *magneton* in the effective physical terminology defines the unit magnetic moment of electron. However, as was repeatedly mentioned above, electron does not have a magnetic moment (and never had), i.e., the electron is absolutely “bare” from the magnetic standpoint. It was dressed in magnetic “clothes” thanks to Maxwell; in 135 years that have passed, the magnetic “equipment” of electron was perfected in any possible way.

Of course, the electrons, which move in a conductor and “spin up” eddies of magnetic charges, turn out to be indirectly involved in the generation of magnetic field $\text{rot } \mathbf{H}^\circ$ but this is an entirely different “story”. Note that electrons bear no relation, even indirectly, to the generation of, for example, magnetostatic field by a fixed magnetic pole. Therefore, the name of magneton must, in essence and by right, belong only to the true source of magnetic field, namely, to the magnetic fundamental particle suggested by the author.

Magnetons (magnetic poles) are natural and only sources of almost all universally known magnetic fields and manifestations, including magnetic components of EM fields and emissions. In order to explain magnetic manifestations in atoms, the so-called magnetic moment was ascribed to electrons in the existing physical theories; since the real magnetic charges were ignored, this magnetic moment bore their unquestionable pole “load”.

The results of investigations of the present author and of other researchers enable one to state with assurance that atomic shells are electromagnetic rather than electronic, as is now customary to assume. In the case of EM shell made up of electrons and magnetons, the use of the concept of magnetic moment of electron ceases to make any sense and becomes useless, similar to a prosthesis which becomes useless after it has served its function.

Proceeding from his own theoretical assumptions, he performed experiments, the results of which provided evidence in favor of real existence of magnetic fundamental particles (magnetic charges)

which, along with electric fundamental particles, enter as structural elements into the composition of physical mass (nucleons, atoms, substance).

Effective Experiments:

1. **Magnetic Neutron Scattering**
2. **Experiments in Charging Test Bodies with Magnetic Charges of Unlike Signs. Magnetostatic Interaction of Charged Bodies**
3. **Experiments in Creating Primary Magnetomotive Force (MMF) and Direct Current of Magnetic Charges in a Static Superconductor**

1. FALLACIOUS MAXWELL “VIRUS” (FMV) AND DIRAC MONOPOLE

The focusing of attention on this erroneous concept of Maxwell is nothing like the present author’s whim. The scale of its negative impact on physics and, to a significant extent, on engineering is too large. To mention but one missed opportunity such as engineering gravitation leads one to understand what are the potentialities which could be opened to humanity if Maxwell, who was laying down the theoretical fundamentals of electromagnetism 135 years ago, would not have overlooked real magnetic charges (poles) and would not have declared moving electrons to be immediate sources of magnetic fields.

Of course, it is the experimentally obtained fact that a magnetic field is generated around a conductor with electric current (Oersted experiment). However, it is not a fact that this field is directly produced by moving electrons. It is simply assumed that there is nothing but electrons that can move in the conductor under the effect of electrical voltage. And if this is so, then. . . .

However, one can as “successfully” make, for example, an inference that it is the electric current flowing from electric network to a hair drier that pushes the air out from the drier nozzle, provided that one is not aware of the existence of a fan and electric motor in the housing of the hair drier and does not feel their noise and vibrations. There is no doubt that if the eddies of magnetic charges, “organized” in the conductor under the effect of moving electrons, would generate noise and vibration, Maxwell would have arrived at an entirely different conclusion concerning the true source of magnetic field.

We can safely state at present that none of the researchers, which were active in physics after Maxwell, avoided being “infected” with FMV. The most striking fact is that the ideologist of magnetic monopolism P. Dirac himself did not doubt the truth of Maxwell’s doctrine. The stand he took as regards problems associated with magnetic particles appears to be strange at the least. On the one hand, Dirac was exclaiming that it would be surprising if nature would not have utilized this possibility, i.e., that of realizing magnetic poles in structures of substance, and even demonstrated that the quantum EM theory quite allows them existence. On the other hand, however, he “powered” his monopole of magnetic field by means of filaments-solenoids which, in his opinion, “operated” in full accord with the Maxwell theory, i.e., “without any participation of magnetic poles.

Figuratively speaking, the Dirac monopole is a perforated envelope into which a magnetic field is “pumped in” along ultrafine filaments-solenoids as if along hoses; after that, the magnetic field flows out into ambient space via holes in the envelope. One cannot but see that this monopole is an exotic phantom which bears no relation whatsoever to our terrestrial conditions. Dirac himself does not relate it in any way to magnetic fields and manifestations which surround man, because he is guided by FMV and it never even crossed his mind that his monopole or something like it may bear any relation to these fields and manifestations. All this does not quite sink in. How can one suggest the magnetic pole as natural source of magnetic field and rule out the possibility of its manifestation in this capacity in human environment?

Therefore, the estimates of the contribution made by Dirac to the resolution of the problem of magnetic particles (magnetic charges) do not appear to be unambiguous. Naturally, Dirac paid attention to this interesting problem from the height of his authority, and this gave rise to a wave of relevant investigations. On the other hand, because of his being influenced by FMV, Dirac obtained a very abstract result which bears hardly any relation to real practice. This is the case usually referred to as “all this is very interesting but bears no relation to the matter at hand”. Note that dozens of theoretical and experimental studies were “spinning” around just the Dirac monopole with its exotic parameters and incomprehensible attitude to reality. And the author of this magnetic abstraction P. Dirac himself appears to be the second (after Maxwell) “switchman” who, once again, 58 years later, drove the problem of real magnetic poles (charges) to faraway “siding”.

2. SOME OF REFINED PHYSICAL TERMS

Charge of both material and physical-vacuum (PV) fundamental particles consists in their capacity for transformations of the initial PV fields into excited states (electric or magnetic fields), as well as for utilization (transformation) of excited PV fields into initial (unexcited) fields. In the former case, it is exclusively material fundamental parts, such as electrons and magnetons, that are involved in the transformation processes; in the latter case, it is physical-vacuum fundamental particles that “perform” the utilization of excited PV fields. Note that the physical-vacuum fundamental particles are realized exclusively in the compositions of physical mass as antispinor particles with respect to spinor electrons and magnetons. It is the pattern or directionality of the process of transformation of PV fields by both material and physical-vacuum particles that defines the characteristic of particles such as the sign of their charge. If a fundamental particle such as electron causes the transformation of initial PV fields into excited, i.e., electric, fields, the charge of particles with the minus sign corresponds to such process. If the inverse process of transformations is realized, in which the excited states of PV fields are transformed by PV particles into unexcited states, the charges of PV particles utilizing excited fields exhibit the plus sign. An example of PV particles which always define the positive charge is provided by PV antielectrons and antimagnetons, which may be further referred to as charge vacancies or “holes”. In view of the fact that protons have a positive electric charge, it follows that this charge is formed by electric PV particles which, in accordance with the logic of definitions adopted in this book, may be defined as PV minielectrons.

Therefore, the material fundamental particles such as electron and magneton have a charge with the minus sign, and the PV fundamental particles are always charged positively.

For example, the positron is not a fundamental particle, because its positive charge may be formed exclusively by PV particles in its composition. The positron is a compound particle, which is a variety of mass, because PV particles are produced and exist in compositions of PM. Therefore, the positron may in no way be regarded as a true antiparticle with respect to fundamental electron.

Electron is an electrically charged material fundamental particle, which has a primary spin of $1/2$ and exhibits inertial properties. The fundamentality of electron shows up in its capacity for interaction with initial PV fields with the production of excited electric fields. The capacity for transformation of initial PV fields into electric fields defines the property of electron such as its charge, and the direction of the process of transformation from initial PV fields to excited fields always corresponds to negative charge of particles in general and of electron in particular. The electron spin defines both the geometric direction of the process of transformation of PV fields (spin vector) and the rate of the process of transformation of fields and, in the final analysis, the rate of propagation of electric field intensity and the velocity of light (modulus of spin vector). Electron is a purely material particle which is not a variety of mass. Therefore, electron *per se* cannot produce an intrinsic gravitational field and, consequently, cannot have a weight. Therefore, electron is a massless particle. In view of this, it makes absolutely no sense physically to ascribe any mass, including the inert one, to electron. Electron as a purely material particle exhibits the property of inertness; however, this property may in no way relate it to mass. Electrons may be both spinor, i.e., bound with PV particles in the compositions of physical mass, and extraspinor, i.e., devoid of PV “companions”. In the former case, electrons produce bispinor fields in combination with electric PV particles; in the latter case, electrostatic extraspinor fields are produced, which make up “dark energy” in the environment. In the combined dynamic EM process in the compositions of s-gravitons, spinor electrons and magnetons produce gravitational fields. Outside of mass, electrons enter into the compositions of the so-called “dark matter”. Electron is a purely electric particle without any “admixture” of magnetism. The so-called “magnetic moment” of electron is a theoretical prosthesis “attached” to electron for somehow explaining the diverse magnetic manifestations under conditions of disregard of real magnetic particles (magnetic poles).

Magnetic Field is a physical field developed by magnetic material fundamental particles (magnetic poles, charges) as a result of the process of transformation of initial PV fields by these particles. Therefore, the magnetic field is a special magnetic form of excited PV fields. The magnetic field may be both bispinor, i.e., existing within a bispinor form, and extraspinor. In the latter case, the magnetic field is developed by a magnetic fundamental particle such as magneton which is not spinor. Depending on the state of motion of magnetic poles, magnetic fields may be both static and dynamic. An example of dynamic spinor magnetic field is provided by the field developed around a conductor with electric current. It is known that the intensity of such field is defined by the axial vector $\text{rot } H^\circ$. The magnetic field enters as the mandatory component into the composition of gravitational field, as well as into the composition of intensities of photons.

Magneton is a magnetic material fundamental particle (magnetic charge, magnetic pole). It is a direct source of magnetic field. Magneton is a magnetic analog of electron by all of its physical parameters, including the sign of charge. Similar to electron, magneton is a lepton and a fermion (spin is equal to $1/2$). In compositions of physical mass (atoms, substance), magnetons are spinor particles which form spinor pairs and spinor fields with magnetic PV particles. Magnetons enter, along, with electrons as constituent elements into the shells of atoms, which are electromagnetic rather than electronic, as was always believed. It is in the EM shells of atoms, in the compositions of s-gravitons, and in close “cooperation” with electrons and PV particles that magnetons take part in the generation of gravitational field. Magnetons are not mass, because they form the mass in combination with electrons and PV particles. Magnetons have no weight, i.e., they are not attracted to the Earth, because they cannot *per se* produce gravitational field. This is indicative of the obvious violation of the equivalence principle. At the same time, magnetons as purely material particles exhibit the property of inertia.

The following can be said about the sign of charge of magneton. If we proceed from the fact that the negative charge of electron corresponds to the process of transformation of initial PV fields into electric fields, then, by analogy, magneton is to be defined as a negatively charged particle, because its interaction with initial PV fields results in their excitation with the production of magnetic field. Note that previously the author had erroneously ascribed the positive charge to magneton.

By virtue of their confinement in substance and atoms, magnetons apparently cannot be forced out of substance and made to individually fly in space (vacuum) like electrons do. However, it is technically possible to develop a magnetomotive force MMF which is a magnetic analog of EMF, and organize the current of magnetic charges in a conductor. One must note here that the significant conductivity of magnetic charges and generation of their currents under the effect of MMF is possible only under conditions of superconductivity.

REFERENCES

1. Sizov, R. A., *New Presentation the Nature of Magnetism, Gravitation and Nuclear Bonding Forces*, Moscow, 2001.
2. Sizov, R. A., *Electric, and Magnetic Spinor Particle — Structure-forming Component Mass and Electromagnetic Source of Gravitation*, Moscow, 2008.

Electrodynamic Analysis of Nonlinear Propagation of Electromagnetic Waves in Gyromagnetic Nanostructured Media at Microwave Frequencies

G. S. Makeeva¹, M. Pardavi-Horvath², and O. A. Golovanov¹

¹Penza State University, Russia

²The George Washington University, USA

Abstract— A rigorous mathematical model of nonlinear propagation of electromagnetic waves (EMWs) in 3D periodic arrays of arbitrary shaped magnetic nanoelements for microwave and magnetophotonic applications is developed by solving the full nonlinear Maxwell's equations with electrodynamic boundary conditions, complemented by the Landau-Lifshitz equation of motion of the magnetization vector, taking into account the exchange interaction.

1. RIGOROUS MATHEMATICAL MODEL OF NONLINEAR MAGNETIC NANOSTRUCTURES TAKING INTO ACCOUNT THE EXCHANGE FIELD

A rigorous mathematical model of nonlinear propagation of electromagnetic waves in gyromagnetic nanostructured media is based on the solution of the full nonlinear Maxwell's equations

$$\operatorname{curl} H(t) = \varepsilon_0 \varepsilon \frac{\partial \vec{E}(t)}{\partial t} + \sigma \vec{E}(t); \quad (1)$$

$$\operatorname{curl} E(t) = -\frac{\partial \vec{B}(t)}{\partial t}; \quad (2)$$

$$\vec{B}(t) = \vec{M}(t) + \mu_0 \vec{H}(t),$$

with electrodynamic boundary conditions, complemented by the Landau-Lifshitz equation with the exchange term [1],

$$\frac{d\vec{M}(t)}{dt} = -\gamma \vec{M}(t) \times (\vec{H}(t) + \vec{H}_q(t)) + \omega_r (\chi_0 \vec{H}(t) - \vec{M}(t)) \quad (3)$$

$$\vec{H}_q(t) = q \nabla^2 \vec{M}(t), \quad (4)$$

where $\vec{E}(t)$ and $\vec{H}(t)$ are the electric and magnetic field intensity vectors, $\vec{M}(t)$ is the magnetization vector, \vec{B} is the magnetic induction vector, \vec{H} is the external magnetic field, \vec{H}_q is the exchange field, σ is the electrical conductivity, ε is the relative dielectric constant, ε_0 , μ_0 are the electric and magnetic constants of the vacuum, γ is the gyromagnetic ratio, ω_r is the relaxation frequency, χ_0 is the static magnetic susceptibility, $q = 2A/\mu_0 M_s$, A is the exchange constant of the magnetic material.

Using the formulas of vector analysis, we represent Eq. (4) in the form:

$$\vec{H}_q(t) = q \left(\operatorname{grad} \operatorname{div} \vec{M}(t) - \operatorname{curl} \operatorname{curl} \vec{M}(t) \right). \quad (5)$$

Taking into account that $\operatorname{div} \vec{M}(t) = 0$, introduce the new vector function

$$\vec{F}(t) = \operatorname{curl} \vec{M}(t), \quad (6)$$

and write Eq. (5) as

$$\vec{H}_q(t) = -q \operatorname{curl} \vec{F}(t). \quad (7)$$

Assuming that the monochromatic waves having frequencies $\omega_1, \omega_2, \dots, \omega_n$ propagate in nanostructured gyromagnetic media and excite nonlinear magnetization waves at combination frequencies ω_m , we represent the vector functions $\vec{E}(t)$, $\vec{H}(t)$, $\vec{M}(t)$, $\vec{F}(t)$, \vec{H}_q in the form of series in terms of the combination frequencies ω_m . Substituting these series into Eqs. (1), (2), (6), and (7), we

reduce the nonstationary nonlinear equations to nonlinear stationary equations in terms of the combination frequencies.

$$\begin{aligned} \text{curl} \vec{H}(\omega_m) &= i\omega_m \varepsilon_0 \dot{\varepsilon}(\omega_m) \vec{E}(\omega_m), \\ \text{curl} \vec{E}(\omega_m) &= -i\omega_m \vec{M}(\omega_m) - i\omega_m \mu_0 \vec{H}(\omega_m), \end{aligned}$$

$$\begin{aligned} \gamma \sum_{i=-\infty}^{\infty} \sum_{j=-\infty}^{\infty} \gamma_{ij} \left(\vec{M}(\omega_i) \times \left(\vec{H}(\omega_j) + \vec{H}_q(\omega_j) \right) \right) &= -(\omega_r + i\omega_m) \vec{M}(\omega_m) + \omega_r \chi_0 \vec{H}(t) - \gamma \vec{M}_0 \times \vec{H}(\omega_m) \\ &\quad - \gamma \vec{M}_0 \times \vec{H}_q(\omega_m) - \gamma \vec{M}(\omega_m) \times \vec{H}_0; \end{aligned}$$

$$\begin{aligned} \text{curl} \vec{M}(\omega_m) &= \vec{F}(\omega_m), \\ \text{curl} \vec{F}(\omega_m) &= -q^{-1} \vec{H}_q(\omega_m); \quad m = \pm 1, \pm 2, \dots, \end{aligned} \quad (8)$$

where ω_m are combination frequencies ($\omega_m > 0, \omega_{-m} = -\omega_m, \omega_0 = 0$); $\vec{H}_0 = \vec{H}(\omega_0)$; $\vec{M}_0 = \vec{M}(\omega_0)$, $\dot{\varepsilon}(\omega_m) = \varepsilon(\omega_m) - i \frac{\sigma(\omega_m)}{\varepsilon_0 \omega_m}$; $\gamma_{ij} = \begin{cases} 0, & \text{if } \omega_i + \omega_j \neq \omega_m \\ 0, & \text{if } \omega_i + \omega_j = \omega_m \end{cases}$.

2. THE CHARACTERISTIC EQUATION FOR THE PROPAGATION CONSTANTS OF ELECTROMAGNETIC WAVES IN 3D PERIODIC ARRAYS OF NONLINEAR MAGNETIC NANOELEMENTS

The model of the gyromagnetic nanostructured media is a 3D periodic nanoarray, as shown in Fig. 1. The electromagnetic waves (fields \vec{E}, \vec{H} ; frequency ω) propagating in the array are considered as a superposition of inhomogeneous plane EMWs having propagation constants [2]:

$$\Gamma_n = \nu + \frac{2\pi n}{\Lambda}, \quad n = 0, \pm 1, \pm 2, \dots, \pm \infty, \quad (9)$$

where $\Gamma_0 = \nu$ is the unknown propagation constant of the fundamental wave ($n = 0$); and Λ is the length of the array cell along the direction of the EMW propagation.

The approach to mathematical modeling of nonlinear propagation of EMWs in 3D periodic magnetic nanoarray of Fig. 1(b) was developed using the decomposition algorithm by autonomous blocks with virtual Floquet channels, partially filled by the nonlinear gyromagnetic medium (MFAB) [3]. We consider an array cell (Fig. 1(c)) as an MFAB and use a descriptor of nonlinear MFAB as a MFAB scattering matrix at each combination frequency ω_m [4].

It follows from Floquet's theorem, applied to the fields \vec{E}, \vec{H} in the periodic nanoarray, that the magnitudes of the incident $C_{l(p)}^+(\omega_m)$ and reflected $C_{l(p)}^-(\omega_m)$ modes at each combination frequency

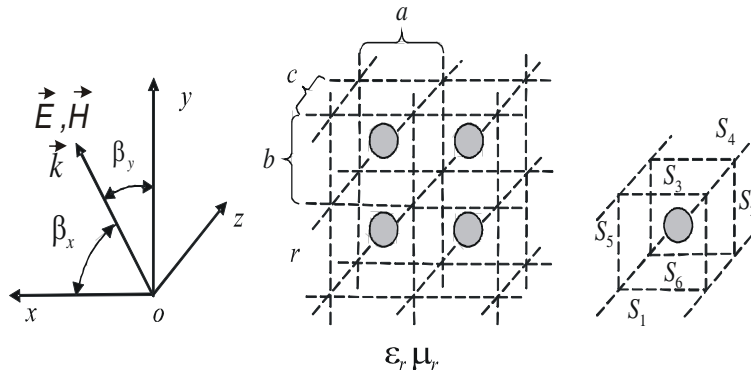


Figure 1: Model of EMW propagation in the nanostructured gyromagnetic media: (a) direction of the propagation of the EMW of wave vector \mathbf{k} ; (b) 3D array of nonlinear magnetic nanospheres, radius r ; periodicity a ; (c) model of the cell of the array using MFAB with input cross-sections $S_p, p = 1, 2, 3, \dots, 6$.

ω_m are coupled on the input cross-sections S_p of MFAB according to [2]:

$$C_{l(p)}^\pm(\omega_m) = C_{l(p)}^\pm(\omega_m) \exp(-i\varphi_i) \quad (10)$$

where p is the index of MFAB cross-sections $p = 1, 2, \dots, 6$; l is the index of eigenwaves of the Floquet channels $l = 1, 2, \dots$; ω_m are combination frequencies, $m = \pm 1, \pm 2, \dots$, and $\varphi_i = \Gamma_n a \cos \beta_i$, for $i = (x, y, z)$.

Let's substitute Eq. (11) into the relationship for \mathbf{R} the MFAB scattering matrix [2]

$$\mathbf{R} = \begin{bmatrix} R_{AA} & R_{AB} \\ R_{BA} & R_{BB} \end{bmatrix}$$

here $R_{AA}, R_{AB}, R_{BA}, R_{BB}$ are the blocks of \mathbf{R} , the indices A are for $p = 1, 2, 3$; and B for $p = 4, 5, 6$

$$\mathbf{c}^- = \mathbf{R} \cdot \mathbf{c}^+, \quad (11)$$

where $\mathbf{c}^-, \mathbf{c}^+$ are vectors, having components $C_{l(p)}^-(\omega_m), C_{l(p)}^+(\omega_m)$.

Based on Floquet's theorem, we obtain the characteristic equation for propagation constants of EMWs in 3D periodic nanoarrays in the following form:

$$\Delta(\Gamma_n) = |R_{AA} - Q^{-1} \cdot R_{BA} + R_{AB} \cdot Q - Q^{-1} \cdot R_{BA} \cdot Q|, \quad (12)$$

where $\Delta(\Gamma_n)$ is the determinant of matrix; Q is a diagonal matrix having diagonal elements $q_{i(l_j)} = -i\delta_{ij}\Gamma_n a \cos \beta_i$, for $i = (x, y, z)$.

The characteristic Eq. (12) includes the blocks $R_{AA}, R_{AB}, R_{BA}, R_{BB}$ of the MFAB scattering matrix \mathbf{R} at combination frequencies ω_m , taking into account electrodynamic boundary conditions [3]. That's why the electrodynamic analysis of nonlinear propagation of EMWs in 3D periodic arrays of arbitrary shaped magnetic nanoelements, is possible, using the computational algorithm for calculating the MFAB scattering matrix \mathbf{R} at combination frequencies. The MFAB scattering matrix \mathbf{R} is determined by solving the nonlinear 3D diffraction boundary problem for Maxwell's equations Eqs. (1), (2) with electrodynamic boundary conditions, complemented by the Landau-Lifshitz equation Eq. (3), taking into account the exchange field Eq. (4). The computational algorithm for determining of the MFAB scattering matrix \mathbf{R} at combination frequencies was developed to solve the stationary nonlinear Eq. (8) with non-asymptotic radiation boundary conditions [5], using the Galerkin's projection method [6].

3. RESULTS OF ELECTRODYNAMIC ANALYSIS OF ELECTROMAGNETIC WAVES IN 3D PERIODIC ARRAYS OF FERROMAGNETIC METAL NANOPARTICLES

From the characteristic Eq. (12), using the above described computational algorithm for calculating of the MFAB scattering matrix \mathbf{R} , the electrodynamic analysis of propagating EMWs at microwave frequencies in 3D periodic array (Fig. 1) of ferromagnetic metal (iron) nanospheres in a nonmagnetic matrix for longitudinal and transverse orientations of the bias magnetic field \vec{H}_0 was performed. The values of parameters, used in the calculations, were for a ferromagnetic metal (iron), i.e., $4\pi M_0 = 21,580 \text{ G}$, $A = 2.2 \cdot 10^{-9} \text{ Oecm}^2$, the Gilbert damping constant $\alpha = \frac{\omega_r}{\omega_H}$, where $\omega_H = \gamma H_0$ [1], $\alpha = 0.0023$ [4], $H_0 = 1000 \text{ Oe}$ at a frequency $f = 30 \text{ GHz}$.

The results of electrodynamic analysis for the propagation constants ν of the fundamental modes of clockwise and counterclockwise polarized EMWs ($\vec{H}_0 = H_0 \vec{z}$), and the ordinary and extraordinary EMWs ($\vec{H}_0 = H_0 \vec{x}$), depending on the ratio r/a of the period of the array a and the radius of the nanospheres $r = 150 \text{ nm}$ in a dielectric matrix $\epsilon_r = 2.25$, $\mu_r = 1$, are shown in Fig. 2.

As follows from the results of mathematical modeling due to the change of the character of the propagation of EMWs the propagation constants change significantly with decreasing separation r/a on the interval $0.1 < r/a < 0.35$. The propagation constants of counterclockwise polarized and extraordinary modes become imaginary for $r/a > 0.25$ and, consequently, these are not propagating waves. Upon reducing the separation of nanospheres $r/a > 0.25$ (transition to the range of exchange length), the exchange interaction in the system of strongly coupled magnetic nanoparticles plays a dominant role [7] and the magnetic nanoarray starts to behave like a quasi-bulk continuum. As for the case of ferromagnetic metals, from the 4 normal modes [8] there are two, counterclockwise polarized and ordinary, modes with real propagation constants, having a large phase velocity, propagating in the gyromagnetic nanostructured media as the separation r/a of magnetic nanoparticles $0.25 < r/a < 0.35$ approaches the exchange length.

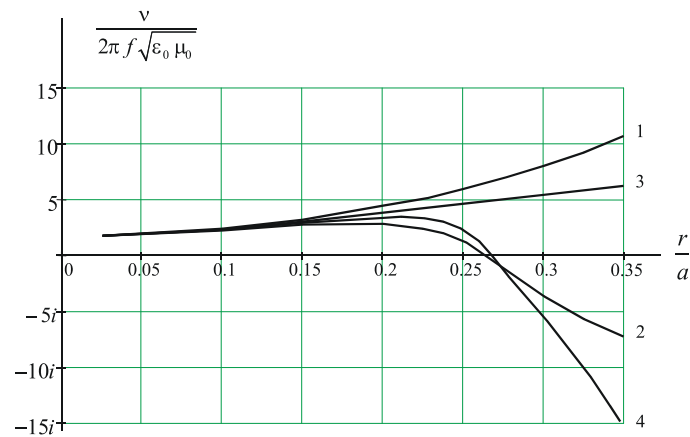


Figure 2: Propagation constants ν of EMWs in 3D magnetic nanoarray depending on r/a , the ratio of the ferromagnetic (iron) nanosphere radius $r = 150$ nm to the periodicity a : 1, 2 — clockwise and counterclockwise polarized EMWs, $\vec{H}_0 = H_0 \vec{z}$; curves 3, 4 — ordinary and extraordinary EMWs $\vec{H}_0 = H_0 \vec{x}$; $H_0 = 1000$ Oe; $f = 30$ GHz.

ACKNOWLEDGMENT

The research of M. Pardavi-Horvath is partially supported by NSF Award ECS0601547.

REFERENCES

1. Gurevich, G. and G. A. Melkov, *Magnetization Oscillations and Waves*, CRC Press, 1996.
2. Nikol'skii, V. V., *Electrodynamics and Propagation of Radiowaves*, Nauka, Moscow, 1978 (in Russian).
3. Makeeva, G. S. and O. A. Golovanov, "The computational algorithm for determining of descriptors of autonomous blocks with virtual Floquet channels loaded with magnetic nanoinsertions," *Transaction of the Volga Region Universities. Izvestiya Vysshikh Uchebnykh Zavedenii. Physico-matematicheskoye Nauki*, No. 2, 72–85, 2009 (in Russian).
4. Golovanov, O. A. and G. S. Makeeva, "Mathematical modeling of nonlinear microwave devices by using autonomous blocks with Floquet channels," *Physics of Wave Processes and Radiotechnical Systems*, Vol. 10, No. 4, 63–70, 2007.
5. Golovanov, O. A., "Numerical algorithm for solving the problems of diffraction for microwave waveguides with nonlinear media," *Radiotekhnika i Elektronika*, Vol. 35, 1853–1863, 1990.
6. Bahvalov, N. S., *Numerical Methods*, M. Nauka, 1975 (in Russian).
7. Pardavi-Horvath, M., G. S. Makeeva, and O. A. Golovanov, "Nonlinear phenomena in magnetic nanoparticle systems at microwave frequencies," *IEEE Trans. Magnetics*, Vol. 44, 3067–3070, 2008.
8. Patton, C. E., *Czech. J. Phys.*, Vol. B26, No. 8, 925, 1976.

Size and Shape Effects in the Diffraction of Electromagnetic Waves on Magnetic Nanowire Arrays at Photonic Frequencies

G. S. Makeeva¹, M. Pardavi-Horvath², and O. A. Golovanov¹

¹Penza State University, Russia

²The George Washington University, USA

Abstract— Rigorous mathematical modeling of the diffraction of electromagnetic waves on magnetic nanoarrays was performed by solving the 3D diffraction boundary problem for Maxwell's equations with electrodynamic boundary conditions, complemented by the Landau-Lifshitz equation with the exchange term, taking into account constrained geometries. The modulus of transmission $|R_{21}|$ of iron nanowire arrays, depending on the bias magnetic field, for various nanowires diameter and array periodicity were obtained at $f = 30$ THz. The mathematical modeling shows that the scattering parameters of magnetic nanowire arrays strongly depend on the value of the bias magnetic field for different wire diameter/periodicity ratios.

1. THE RIGOROUS MATHEMATICAL MODEL BASED ON THE SOLUTION OF THE 3-D DIFFRACTION BOUNDARY PROBLEM

The mathematical modeling of diffraction of electromagnetic waves on arrays of magnetic nanowires, shown in Fig. 1, is based on the solution of the 3D diffraction boundary problem for Maxwell's equations with electrodynamic boundary conditions, complemented by the Landau-Lifshitz equation of motion of the magnetization vector including the exchange term [1].

To solve the 3D diffraction boundary problem at the electrodynamic accuracy level the decomposition approach by autonomous blocks with virtual Floquet channels, partially filled by the nonlinear gyromagnetic medium (MFABs) was developed [2]. We consider an array cell (Fig. 1(c)) as the MFAB. The cell is described by its MFAB scattering matrix \mathbf{R} , taking into account electrodynamic boundary conditions, the geometry of the array, and the shape of nanowire.

The computational algorithm for determining of MFAB scattering matrix \mathbf{R} by solving the 3-D nonlinear diffraction boundary problem for MFAB was developed using Galerkin's projection method [3]. We use the eigenwaves of the rectangular cavity (Fig. 1(c)) as the basis functions $\{\vec{E}_n(\omega_m)\}$, $\{\vec{H}_n(\omega_m)\}$, where n are the indices of basis functions and m are the indices of combination frequencies. We determine the eigenfrequencies ω_k and the eigenwaves $\{\vec{E}_n(\omega_m)\}$, $\{\vec{H}_n(\omega_m)\}$ by solving the homogenous Maxwell's equations with periodic boundary conditions on the walls of the rectangular cavity (the MFAB bounds).

The solution of the diffraction problem for the stationary nonlinear Maxwell's equations with non-asymptotic radiation boundary conditions [5] were found in the form of Fourier's series using

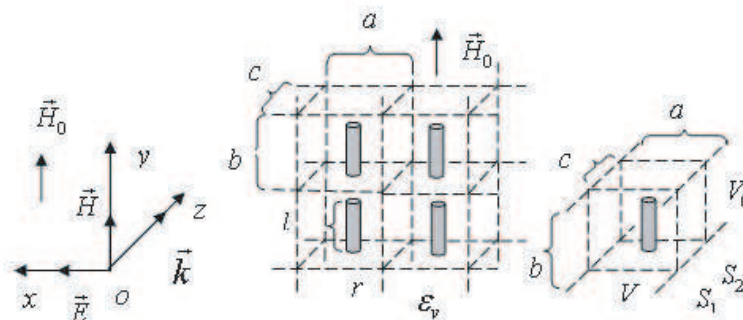


Figure 1: Geometry of the magnetic nanowire array for the diffraction problem: (a) direction of incident plane EMW of wave vector \mathbf{k} ; (b) 2D-array of nanowires, periodicity a, b, c ; $2r$ — wire diameter, l — wire length; the bias magnetic field \mathbf{H}_0 is normal to the propagation of EMW; (c) model of the cell of the array using the autonomous blocks with Floquet channels partially filled by the nonlinear gyromagnetic medium (MFAB) with the input cross-sections S_β , where $\beta = 1, 2$.

the eigenwaves $\{\vec{E}_n(\omega_m)\}$, $\{\vec{H}_n(\omega_m)\}$ of the rectangular cavity inside the MFAB region V_0 , or the eigenwaves $\{\vec{e}_{l(\beta)}(\omega_m)\}$, $\{\vec{h}_{l(\beta)}(\omega_m)\}$ of the Floquet channels on the MFAB input cross-sections S_β . The tangential electromagnetic field on each MFAB input cross-section S_β is represented as a superposition of eigenwaves of the Floquet channels [4]:

$$\begin{aligned}\vec{E}_\beta(\omega_m) &= \sum_{l=1}^{\infty} \left(c_{l(\beta)}^+(\omega_m) + c_{l(\beta)}^-(\omega_m) \right) \vec{e}_{l(\beta)}(\omega_m); \\ \vec{H}_\beta(\omega_m) &= \sum_{l=1'}^{\infty} \left(c_{l(\beta)}^+(\omega_m) - c_{l(\beta)}^-(\omega_m) \right) \vec{h}_{l(\beta)}(\omega_m).\end{aligned}$$

where $C_{l(\beta)}^+(\omega_m)$, $C_{l(\beta)}^-(\omega_m)$ are the magnitudes of the incident and reflected modes, β are the indices of MFAB cross-sections, l are the indices of the eigenwaves. We find the unknown magnitudes $C_{l(\beta)}^-(\omega_m)$ of the reflected modes, when the magnitudes $C_{l(\beta)}^+(\omega_m)$ of the modes, incident on the MFAB input cross-sections, are known.

Substituting the Fourier's series into the stationary nonlinear Maxwell's equations, which are represented in the projecting integral form [6], we obtain the system of nonlinear algebraic equations. These equations were solved by using the iterative method [3] or the alternative Newton's method [3].

2. RESULTS OF ELECTRODYNAMIC CALCULATION OF THE SCATTERING PARAMETERS OF 2-D MAGNETIC NANOWIRE ARRAYS

A monochromatic homogeneous plane EMW (TEM-wave, fields $\mathbf{E} = E\mathbf{x}_0$, $\mathbf{H} = Hy_0$, wave vector \mathbf{k} ; frequency ω is incident on the input cross-section S_1 of a 2D periodic array of metallic magnetic nanowires, shown in Fig. 1 (a, b, c — periodicity along axes x, y, z ; $2r$ — nanowire diameter, l — nanowire length), embedded in a nonmagnetic, dielectric matrix, having relative permittivity $\varepsilon_r = 5$ and relative magnetic permeability $\mu_r = 1$. A bias magnetic field $\mathbf{H}_0 = H_0\mathbf{y}_0$ is applied normal to the propagation direction z (Fig. 1(a)) along the axis of nanowires (Fig. 1(b)). The periodicity of the array is $a = 3.5r$, $b = 1.25l$, $c = 2r$.

The scattering parameters of the multimode, multi-channel \mathbf{S} matrix of arrays of 2D periodic array of metallic magnetic nanowires, embedded in a dielectric matrix, were calculated by the numerical method of MFABs [2]. The following parameters of iron, as the magnetic component, were used in the calculations: exchange constant $A = 2.2 \times 10^{-9}$ Oe cm^2 , saturation magnetization $M_s = 21,580\text{G}$, and Gilbert damping parameter $\alpha = 0.0023$ [1].

The results of computing the modulus of the transmission coefficient $|R_{21}|$ of 2D magnetic nanoarrays, depending on the bias magnetic field \mathbf{H}_0 , for various diameters $2r$ of nanowires are illustrated in Fig. 2. As it follows from the results of mathematical modeling, the scattering parameters of magnetic nanowire arrays strongly depend on the value of the bias magnetic field \mathbf{H}_0 . The transmission coefficient $|S_{21}|$ curves show two maxima (curves $a-d$ in Fig. 2). Upon

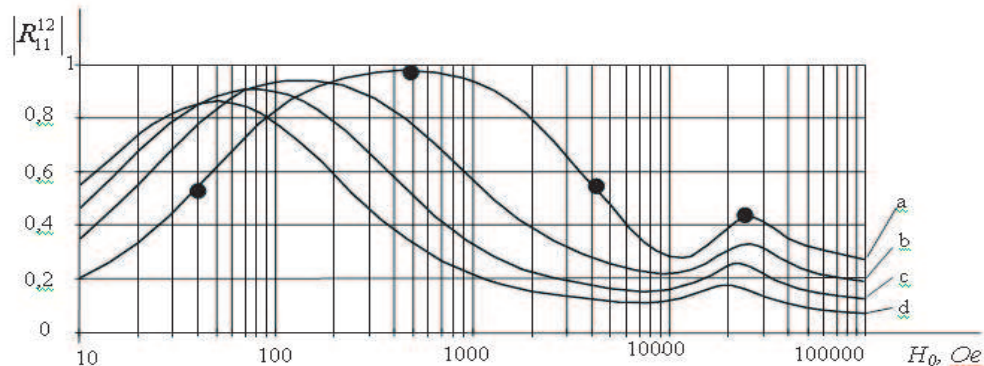


Figure 2: Bias field H_0 dependence of the transmission coefficient $|R_{21}|$ of 2-D magnetic nanowire arrays for different wire diameters $2r$: (a) 10 nm; (b) 15 nm; (c) 20 nm; (d) 25 nm, $l = 300$ nm. The periodicity of the array is $a = 3.5r$; $b = 1.25l$, $c = 2r$. $\mathbf{H}_0 = H_0\mathbf{y}_0$; $f = 30$ THz.

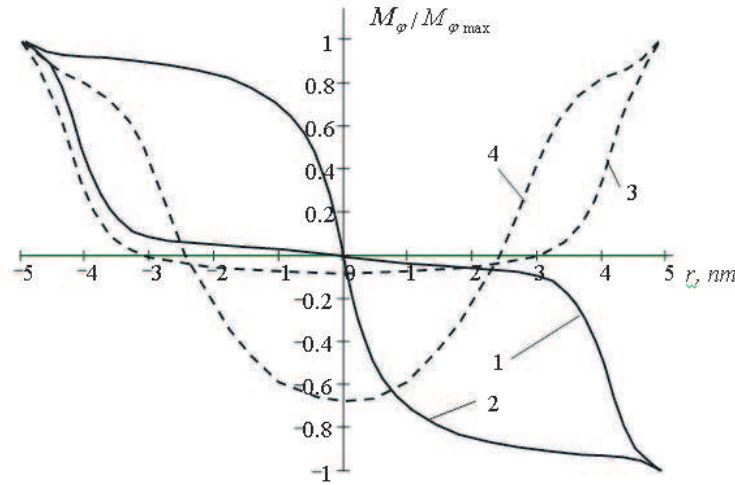


Figure 3: The rf magnetization profiles of two exchange spin-wave modes in a $2r = 10$ nm iron nanowire of a 2D magnetic nanoarray, depending on the position r across the nanowire, for different value of bias field H_0 in points 1–4 in Fig. 2. Curves 1,2 — surface spin-wave modes $n = 2$; curves 3, 4 — $n = 1$. The periodicity of the array is $a = 3.5r$; $b = 1.25l$, $c = 2r$; $l = 300$ nm; $\mathbf{H}_0 = H_0\mathbf{y}_0$; $f = 30$ THz.

increasing the wire diameter the maxima of the transmission coefficient are moving to lower fields and the transmission at the maxima is decreasing.

The spectrum of excited exchange spin-wave-modes in the iron nanowires (diameter $2r = 10$ nm) of 2D arrays was analyzed at the electrodynamic accuracy level by the MFAB method [2], without simplifying Maxwell's equations and the boundary conditions. The rf magnetization profiles of these modes are numerically simulated taking into account the depth of penetration of electromagnetic field in a ferromagnetic metal at photonic frequencies. The distributions of the rf magnetization component M_φ depending on the coordinate r across the nanowire for low order exchange spin-wave-modes are shown in Fig. 3 for different values of bias field H_0 corresponding to points 1–4 in Fig. 2.

The results of the rigorous mathematical modeling show that upon increasing the value of the bias magnetic field H_0 the exchange spin-wave-mode of second order $n = 2$ (curves 1, 2 in Fig. 3) and after then the spin-wave-mode of low order $n = 1$ (curves 3, 4 in Fig. 3) are excited in the ferromagnetic metal (iron) nanowire array at a frequency $f = 30$ THz. There are surface spin-wave-modes with complex waves numbers [1], having a hyperbolic distribution of the rf magnetic field (curves 1–4 in Fig. 3), satisfying the boundary conditions on the surfaces of the ferromagnetic metallic nanowire, and depending on the value of the bias magnetic field H_0 .

3. SPIN-WAVE RESONANCE AND ANTIRESONANCE IN MAGNETIC NANOWIRE ARRAYS AT PHOTONIC FREQUENCIES

The electromagnetic waves, while being transmitted through an “effective ferromagnetic metallic medium”, are damped with an attenuation coefficient k'' , given as [1]:

$$k'' = k_0 \sqrt{\frac{2\pi\sigma}{\omega}} (|\mu_{eff}| + \mu''_{eff})^{1/2} = \sqrt{\mu_{effR}}/\delta = 1/\delta_1, \quad (1)$$

where k_0 is the wave number of electromagnetic wave in free space; $\mu_{eff} = \mu'_{eff} - i\mu''_{eff}$ is the effective scalar permeability [1]; and $\mu_{effR} = |\mu_{eff}| + \mu''_{eff}$, and δ_1 is the skin-depth in the ferromagnetic metallic medium.

In accordance with Eq. (1) the minimum of the absorption of electromagnetic waves is determined by the maximum of the skin-depth $\delta_1 = \delta(\mu_{effR})^{-1/2}$. This maximum is realized when the effective permeability μ_{effR} has a minimum (i.e., the real part of the effective permeability $\mu'_{eff} = 0$ and the imaginary part of the effective permeability $\mu''_{eff} \rightarrow 0$), i.e., in the *antiresonance* point [1]. The frequency of the antiresonance in an unbounded ferromagnetic metallic medium is [1]

$$\omega_{ares} = \omega_H + \omega_M, \quad (2)$$

where ω_{ares} is the frequency of antiresonance; $\omega_H = \gamma H_0$ and $\omega_M = 4\pi M_s$.

Applying the condition for antiresonance in Eq. (2) for a finite size ferromagnetic ellipsoid, the resonance condition becomes

$$\omega_{ares} = \omega_0 + \omega_M \quad (3)$$

where ω_0 is the eigenfrequency of the ferromagnetic resonance (FMR) of the magnetized ellipsoid, determined by the internal magnetic field H_{0int} [1]

$$\vec{H}_{0int} = \vec{H}_0 - \vec{N}\vec{M}_0,$$

where \vec{N} is the demagnetizing tensor.

When a standing wave spin-wave resonance in magnetic nanoarrays is allowed for the thin nanowires the frequencies of the partial antiresonance become [1].

$$\omega_{aresn} = \omega_{0n} + \omega_M, \quad (4)$$

where ω_{0n} are the eigenfrequencies of the standing spin-wave resonance of exchange spin-wave modes number n in thin ferromagnetic nanowire [7], determined by the internal magnetic field H_{0int} .

As it follows from the bias field dependence of the modulus of the transmission $|R_{21}|$ of the 2D magnetic nanoarrays, shown in Fig. 3, the maxima of the transmission coefficients $|S_{21}|$ are located in the points as given by Eq. (4). When the skin-depth $\delta_1 = \delta(\mu_{effR})^{-1/2}$ of penetration of the electromagnetic field in a ferromagnetic metal near the antiresonance frequency increases, it results the increase of the transmitted electromagnetic waves through the magnetic nanoarray. The maxima of the transmission coefficient $|R_{21}|$ curves in Fig. 3 correspond to the exchange spin-wave-modes of eigenfrequencies ω_{0n} of the standing spin-wave resonances in the ferromagnetic nanowire of the 2-D magnetic nanoarrays, given by Eq. (4), and those are determined by the internal magnetic field H_{0int} . The first maximum (curves 1 in Fig. 2) is at a lower field H_0 due to the second order mode of standing spin-wave resonance of at the eigenfrequencies ω_{aresn} for $n = 2$, the others are due to the standing spin-wave resonance of the $n = 1$ mode at the eigenfrequencies ω_{aresn} . Near the antiresonance, when the skin-depth $\delta_1 = \delta(\mu_{effR})^{-1/2}$ in a ferromagnetic metal increases, the distribution of the *rf* magnetic fields at the maxima of the transmission coefficient $|S_{21}|$ (curves 2, 4 in Fig. 3) is modified from hyperbolic to a mainly cosinusoidal or sinusoidal function [7].

The effective permeability depends on the geometry of the magnetic array, thus it can be influenced by array geometry. According to the results of numerical simulation, shown in Fig. 2, the maxima can be tuned by the bias magnetic field \mathbf{H}_0 for different wire diameter/periodicity ratios. When the separation of the magnetic nanowires, having diameter $2r = 25$ nm, is large, as for $a > 100$ nm, then the model for the non-interacting nanowires is a thin long cylinder in a longitudinal external magnetic field H_0 , and the demagnetizing factors are $N_x = N_y = 2\pi$, $N_z = 0$ [8]. In this case the eigenfrequency of the FMR is

$$\omega_0 = \gamma(H_0 + 2\pi M_0). \quad (5)$$

Upon further reducing the diameter and the separation of magnetic nanowires (i.e., transition to the exchange length range), the system becomes strongly coupled, and the exchange interaction plays the dominant role. For the diameter of the nanowires $2r = 10$ nm and separation $a = 17.5$ nm the array behaves as an effective quasi-continuum, i.e., a thin magnetic film with demagnetizing factors $N_x = 0$, $N_y = 4\pi$, $N_z = 0$ [8], and the eigenfrequency of the FMR for high density arrays becomes

$$(\omega_0/\gamma)^2 = H_0(H_0 + 4\pi M_0). \quad (6)$$

From Eqs. (5) and (6) it is clear that for high density arrays (curve *a* in Fig. 2) a higher external bias field \mathbf{H}_0 is necessary to reach the antiresonance point (Eq. (3)) than for lower density arrays (curve *b* in Fig. 2).

To our best knowledge the antiresonance phenomena, predicted here, are yet to be observed.

ACKNOWLEDGMENT

The research of M. Pardavi-Horvath is partially supported by NSF Award ECS0601547.

REFERENCES

1. Gurevich, G. and G. A. Melkov, *Magnetization Oscillations and Waves*, CRC Press, 1996.
2. Makeeva, G. S. and O. A. Golovanov, “The computational algorithm for determining of descriptors of autonomous blocks with virtual Floquet channels loaded with magnetic nanoinsertions,” *Transaction of the Volga Region Universities. Izvestiya Vysshikh Uchebnykh Zavedenii. Physico-mathematicheskoye Nauki*, Vol. 12, No. 2, 72–85, 2009 (in Russian).
3. Bahvalov, N. S., *Numerical Methods*, Nauka, Moscow, 1975 (in Russian).
4. Makeeva, G. S. and O. A. Golovanov, “Electrodynamic analysis of microwave devices and systems using autonomous blocks with floquet channels,” *Physics of Wave Processes and Radiotechnical Systems*, Vol. 8, No. 4, 10, 2005.
5. Golovanov, O. A., “Numerical algorithm for solving the problems of diffraction for microwave waveguides with nonlinear media,” *Radiotekhnika i Elektronika*, Vol. 35, 1853–1863, 1990.
6. Nikol’skiy, V. V., *Variational Methods for Internal Problems of Electromagnetics*, Nauka, Moscow, 1975 (in Russian).
7. Arias, R. and D. L. Mills, “Theory of spin excitations and the microwave response of cylindrical ferromagnetic nanowires,” *Physical Review B*, Vol. 63, 134439, 2001.
8. Pardavi-Horvath, M., P. E. Si, M. Vazquez, W. O. Rosa, and G. Badini, “Interaction effects in permalloy nanowire systems,” *J. Appl. Phys.*, Vol. 103, 07D517, 2008.

Investigation of the Nonlinearity Thresholds of Magnetic Nanostructures by Computing the Bifurcation Points at Microwave Frequencies

G. S. Makeeva¹, M. Pardavi-Horvath², and O. A. Golovanov¹

¹Penza State University, Krasnaya, 40, Penza 440026, Russia

²Department of Electrical and Computer Engineering, The George Washington University
Washington, D.C. 20052, USA

Abstract— The bifurcation analysis of the threshold for collective behavior, due to the instabilities (the parametric excitation) of magnetostatic waves (MSW) and dipole-exchange spin-waves (SW) in 3D magnetic nanostructures, is developed. The numerical method is applied to determine the bifurcation points of the nonlinear Maxwell operator (the nonlinear Maxwell equations with electrodynamic boundary conditions complemented by the Landau-Lifshitz equation including the exchange term). The original computational algorithm is improved by combining it with a qualitative method of analysis, based on Lyapunov stability theory. The threshold magnitudes of the pumping electromagnetic waves (EMWs) in the magnetic particle arrays are determined by computing the bifurcation point for different size nanoparticles and for various separations. This technique, based on the bifurcation theory, is a pioneering approach in nano-electrodynamics, taking into account the constrained geometries.

1. INTRODUCTION

Magnetic nanocomposites of nanometer size magnetic particles embedded in a non-magnetic, insulating matrix provide a novel solution for low loss microwave materials up to mm wave frequencies. The electromagnetic properties of magnetic materials change drastically upon reducing the dimensions into the nano-range, including the early onset of nonlinear effects, important for high power applications and non-linear signal processing. To investigate this effect, the instability of parametric excitation process of *magnetostatic waves* MSW and *dipole-exchange spin-waves* SW in 3D magnetic nanostructures should be simulated, taking into account the constrained geometries.

In contrast to the bifurcation analysis of the instability of parametric excitation of electromagnetic oscillations in resonator structures with nonlinear planar ferrite inserts [1] and the parametric instability of MSW in thin film ferrite structures [2], in this work the parametric excitation of dipole-exchange SW in the arrays of magnetic nanoparticles is analyzed. For the analysis of nonlinear phenomena (i.e., the parametric instability of SW) in magnetic nanoparticle systems the numerical method, developed by us earlier [3], is modified here to determine the bifurcation points of the nonlinear Maxwell's operator including the Landau-Lifshitz equation with the exchange term.

2. NUMERICAL TECHNIQUE OF BIFURCATION ANALYSIS OF INSTABILITIES IN 3D MAGNETIC NANOSTRUCTURES

The numerical technique to investigate the nonlinear effects involves finding the bifurcation points of the nonlinear Maxwell operator, i.e., the full Maxwell's equations

$$\operatorname{curl} \bar{H} = \varepsilon_0 \varepsilon \frac{\partial \bar{E}}{\partial t}, \quad \operatorname{curl} \bar{E} = -\frac{\partial \bar{B}(\bar{H})}{\partial t} \quad (1)$$

with electrodynamic boundary conditions, including the Landau-Lifshitz equation of motion of magnetization vector in ferromagnet with the exchange term [4]:

$$\partial \vec{M} / \partial t = -\gamma \left[\vec{M}, \vec{H}_{\text{eff}} \right] - (\alpha / M) \left[\vec{M}, \partial \vec{M} / \partial t \right], \quad (2)$$

where \vec{M} is the magnetization vector, γ is the gyromagnetic ratio, α is the damping constant, $\vec{H}_{\text{eff}} = \vec{H} + \vec{H}_{\text{ex}}$ is the effective field, \vec{H} is the external magnetic field, $\vec{H}_{\text{ex}} = (2A/\mu_0 M_s) \Delta \vec{M}$ is the exchange field, A is the exchange constant, M_s is the saturation magnetization, and μ_0 is the vacuum permeability.

To solve the 3D nonlinear diffraction boundary problem for 3D magnetic nanostructures at the electrodynamic accuracy level a computational algorithm was developed based on the decomposition approach by autonomous blocks with virtual Floquet channels, partially filled by the nonlinear gyromagnetic medium (MFABs) [5]. However, in general, it is not easy to see the physical meaning of numerical solutions. That's why for the analysis of nonlinear phenomena, related to the parametric instability, the numerical method to determine and analyze the bifurcation points of nonlinear Maxwell's operator including the Landau-Lifshitz equation with the exchange term is developed.

The branching points of the nonlinear Maxwell operator are analyzed under the assumption that one solution \tilde{y} in the neighborhood of a singularity point is known [1]. The decomposition MFABs algorithm [5] can be used to find this solution \tilde{y} of Maxwell's equations (1) with electrodynamic boundary conditions complemented by the Landau-Lifshitz equation with the exchange term given in Equation (2). However, there is a possible situation when a second solution \tilde{y} exists in the neighborhood of a branching point and it is very close to first solution. When the nonlinear boundary problem for the Equations (1), (2) is solved with the use of traditional computational algorithms, such branching points may be missed. Therefore, the decomposition computational algorithm should be improved via its combination with a qualitative method of analysis of branching points [3].

According to the linearization principle [6] the detection of the bifurcation points of the nonlinear Maxwell's operator is reduced to determining the eigenvalues of the linearized Maxwell's operator. The linearization procedure results a system of linear ordinary differential equations, written in a matrix form as in [2]:

$$\mathbf{A}(z)\vec{x} = \frac{d\vec{x}}{dz}, \quad (3)$$

where $\mathbf{A}(z)$ is the resulting matrix; z is a coordinate; the vector-function $\vec{x} = \vec{y} - \tilde{y}$ is the difference between the unknown solution \vec{y} , appearing at the bifurcation point, and the known solution \tilde{y} .

To obtain the solution \tilde{y} the 3D nonlinear diffraction boundary problem is solved by using the decomposition algorithm on MFABs [5]. To analyze the second new solution \vec{y} , describing the onset of instabilities, our original computational algorithm to determine the bifurcation points of nonlinear Maxwell's operator, including the Landau-Lifshitz equation with the exchange term, is applied.

The partial solutions of the system of linear ordinary differential Equation (3) are the exponential functions:

$$x_m = \alpha_m \cdot e^{\lambda_m \cdot z}, \quad (4)$$

Substituting (2) into (1), we obtain the following matrix equation:

$$\mathbf{A} \cdot \vec{\alpha} = \lambda \cdot \vec{\alpha}, \quad (5)$$

where $\vec{\alpha}$ is a vector having components $\alpha_1, \alpha_2, \dots, \alpha_m$; λ_m and $\vec{\alpha}$ are the eigenvalues and eigenvectors of matrix \mathbf{A} . Using numerical methods (e.g., QR-algorithm) to solve the matrix Equation (5) the eigenvalues λ_m and eigenvectors $\vec{\alpha}$ of matrix \mathbf{A} are determined.

Our original computational algorithm to determine the bifurcation points of nonlinear Maxwell's operator, including the Landau-Lifshitz equation with the exchange term, was improved by combining it with a qualitative method of analysis, based on Lyapunov stability theory [7, 8].

According to the Lyapunov method [7, 8] if at least one of the real parts of the eigenvalues λ_m is positive, then the solution of Equation (3) is unstable. The change of the sign of the real part of λ_m occurs in the bifurcation points. The qualitative analysis of the stability of the numerical solution was made by using the eigenvalues λ_m of matrix \mathbf{A} in Equation (5). The real parts of complex eigenvalues λ_m are positive in the regions of the solution instability, and the real parts of λ_m are negative in the regions of the solution stability.

3. RESULTS OF CALCULATION OF NONLINEARITY THRESHOLDS BY COMPUTING BIFURCATION POINTS OF NONLINEAR MAXWELL'S OPERATOR INCLUDING THE LANDAU-LIFSHITZ EQUATION

The accurate electromagnetic modeling of EMW diffraction and their nonlinear interactions with MSW and SW in periodic arrays of magnetic nanoparticles was performed by solving the 3D

diffraction problem for Maxwell's equations (1) the with electrodynamic boundary conditions complemented by the Landau-Lifshitz Equation (2). The model for the analysis is a 3D array of ferrite nanospheres, shown in Fig. 1.

A monochromatic plane EMW (TEM-wave, $C_{1(1)}^+(\omega_H)$ magnitude, frequency ω) incident on the input cross-section S_1 of 2D array of ferrite spheres (the period of the array $a = b = c$, r is the radius of the nanospheres) in a nonmagnetic matrix with ε_r and μ_r (Fig. 1). A bias magnetic field $\mathbf{H}_0 = H_0 \mathbf{y}_0$ is applied normal to the direction of the propagating plane EMW. The values of the ferrite parameters used in the calculations were: $M_s = 0.016$ T, $A = 3.1 \times 10^{-9}$ Oecm², $\alpha = 0.025$ [3], $H_0 = 3330$ Oe at a frequency of $f = 9.375$ GHz.

The instability regions of parametric generation of MSW and SW in the nonlinear ferrite nanosphere array, depending on the magnitude $C_{1(1)}^+(\omega_H)$ of the incident pumping wave at frequency ω_H , are simulated for the case, when the radius r of nanospheres and the separations h of nanoparticles in the arrays are reduced to the order of the exchange length. Upon reducing the size and the separation of magnetic nanoparticles (transition to the range of exchange length), the exchange interaction in the strongly coupled system and the "short" dipole-exchange SW spectrum plays the dominant role. The instability regions for the parametric excitation of MSW and SW are obtained at microwave frequencies for different size particles in the *nm* range, and for various separations, taking into account constrained geometries. The results for the first order processes of the parametric excitation in case of transverse pumping are shown in Fig. 2.

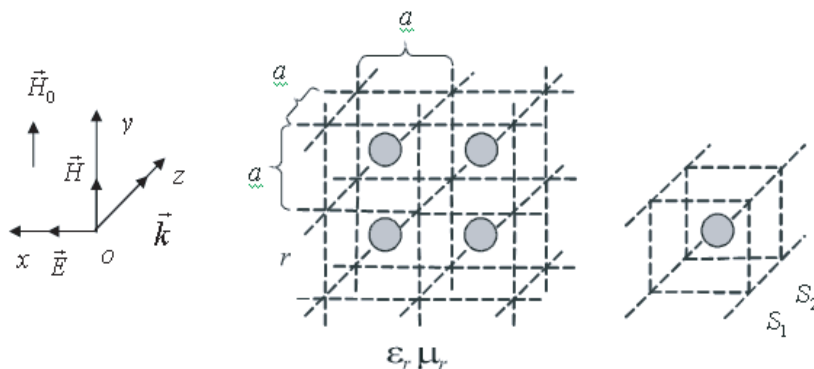


Figure 1: Geometry of the 3D periodic array of magnetic nanoparticles for the diffraction problem: (a) direction of incident plane EMW of wave vector \mathbf{k} ; (b) 2D array of ferrite nanospheres, radius r ; periodicity a ; (c) model of the cell of the array using MFAB with the input cross-section S_1 .

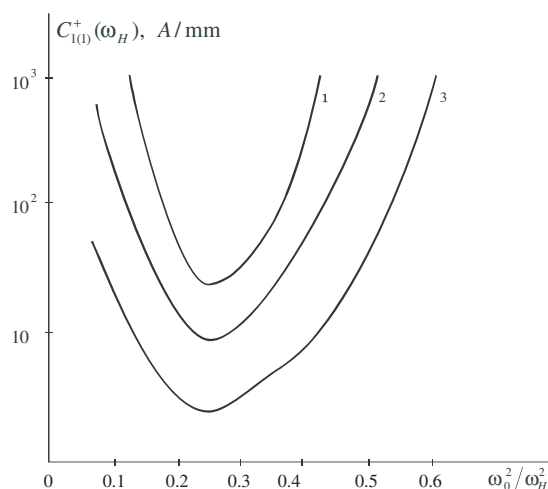


Figure 2: Parametric instability thresholds of MSW and SW in the array of ferrite nanospheres ($r = 250$ nm) depending on the separation h of nanoparticles: 1 — $h = 3000$ nm; 2 — $h = 750$ nm; 3 — $h = 600$ nm; $H_0 = 3330$ Oe, $\omega_0 = 2\pi f_0$ — frequency of the signal wave, $f_0 = 9.330$ GHz, ω_H — frequency of the pumping wave; $C_{1(1)}^+(\omega_H)$ — magnitude of the incident pumping wave.

The threshold magnitudes of the pumping EMW $C_{1(1)}^+(\omega)$, where the nonlinear processes and the parametric instability excitation of MSW and SW occur, are determined by computing the bifurcation points of nonlinear Maxwell's operator including the Landau-Lifshitz equation with the exchange term (2). According to the Lyapunov stability theory [7, 8] the qualitative analysis of the stability of the numerical solution was made by using the eigenvalues λ_m of matrix \mathbf{A} in Equation (5). According to the Lyapunov method [7, 8] the curves in Fig. 2 divide the instability regions for the parametric generation of MSW and SW from the stable regions.

The real parts of complex eigenvalues λ_m are positive in the regions of the solution instability (above the curves Fig. 2), and the real parts of λ_m are negative in the regions of the solution stability (below the curves).

The threshold magnitudes of parametric instability in the array of ferrite nanospheres (Fig. 2) depend on the MSW and SW spectrum of the collective modes in the magnetic nanoparticle array, influenced by the frequency, the bias magnetic field, the magnetization and the shape of particles.

Using this technique, reliable engineering methods for the CAD for the numerical computation of nonlinear electromagnetic properties of magnetic nanocomposite materials, applied in the modern high technology, and 3D nanodevices may be developed.

ACKNOWLEDGMENT

The research of M. Pardavi-Horvath is partially supported by NSF Award ECS0601547.

REFERENCES

1. Makeeva, G. S., O. A. Golovanov, and M. Pardavi-Horvath, "Mathematical modeling of nonlinear waves and oscillations in gyromagnetic structures by means of bifurcation theory methods," *Journal of Electromagnetic Waves and Applications*, Vol. 20, No. 11, 1503–1510, 2006.
2. Makeeva, G. S., O. A. Golovanov, and M. Pardavi-Horvath, "Bifurcation analysis of parametric interaction of magnetostatic and electromagnetic waves in nonlinear 3D ferrite film structures," *IEEE Transaction on Magnetics*, Vol. 43, No. 6, 2633–2635, 2007.
3. Makeeva, G. S., O. A. Golovanov, and M. Pardavi-Horvath, "Numerical analysis of electromagnetic wave instability in nonlinear ferrite structures using bifurcation points of the nonlinear Maxwell's operator," *IEEE Transaction on Magnetics*, Vol. 42, No. 10, 3350–3352, 2006.
4. Gurevich, A. G. and G. A. Melkov, *Magnetic Oscillations and Waves*, Nauka, Moscow, 1994.
5. Makeeva, G. S. and O. A. Golovanov, "The computational algorithm for determining of descriptors of autonomous blocks with virtual Floquet channels loaded with magnetic nanoinsertions," *Transaction of the Volga Region Universities. Izvestiya Vysshikh Uchebnykh Zavedenii. Physico-matematicheskoye Nauki*, Vol. 12, No. 2, 72–85, 2009 (in Russian).
6. Krasnoselskiy, M. A., *Functional Analysis*, Nauka, Moscow, 1964.
7. Lyapunov, A. M., *The General Problem of the Stability of Motion*, Gostehizdat, Moscow, 1950 (reprint of original thesis, 1892).
8. Lyapunov, A. M., *Stability of Motion*, Academic Press, New York, 1966.

Tensor and Toeplitz Structures Applied to Direct and Inverse 3D Electromagnetic Problems

S. A. Goreinov, D. V. Savostyanov, and E. E. Tyrtshnikov

Institute of Numerical Mathematics, Russian Academy of Sciences, Gubkina 8, Moscow 119333, Russia

Abstract— We discuss the matrices of special structure: multilevel matrices with Toeplitz and Hankel structure on different levels and tensor product matrices. They appear as discretisations of volume integral equations in a cube. Generally, solving such an equation, we have to deal with n^3 -size vectors and n^6 -size dense matrix (n is the number grid elements along each side). This puts severe restrictions on the value of n , even if we use a multiprocessor system. Using the structure of data we can reduce the computational costs to a value of $n^3 \log n$ or even to $n \log n$.

We consider a 3D scattering problem for a bounded scatterer in a homogeneous halfspace bounded by a perfectly conducting plane. Applying the Galerkin discretisation on uniform Cartesian grids to the corresponding volume integral equation, we obtain a linear system with a three-level block matrix, with levels of Toeplitz or Hankel structure. This allows us to perform a multiplication with $n^3 \log n$ operations, where n^3 is a number of unknowns.

On nonuniform (but still Cartesian) grids, the multiplication cost and the memory requirements for the matrix grow as n^6 , that limits us to a very small values of n . To remove this restriction, we approximate the matrix by a sum of tensor products which need only $\mathcal{O}(n)$ memory and likewise cut down the CPU time. To construct this tensor approximation, we use the 3D-Cross algorithm which requires the computation of a small fraction of matrix elements, resulting in complexity of the order $n \log n$. The results of solving the inverse problem with the use of Born approximation show a high accuracy of the method proposed.

1. TOEPLITZ AND TENSOR STRUCTURES IN DIRECT 3D ELECTROMAGNETIC SCATTERING PROBLEM

Procedures of inversion of multitransmitter electromagnetic data can be based on different approximations of the following integral equations [1]

$$\begin{aligned} \mathbf{H}^s(x) &= -i\omega\varepsilon^0 \text{rot} \int_V G(x, y) \gamma(y) (\mathbf{E}^0(y) + \mathbf{E}^s(y)) dy, & x \notin V; \\ \mathbf{E}^s(x) &= ((\kappa^0)^2 + \text{graddiv}) \int_V G(x, y) \gamma(y) (\mathbf{E}^0(y) + \mathbf{E}^s(y)) dy, & x \in V, \end{aligned} \quad (1)$$

where \mathbf{E}^0 , \mathbf{H}^0 are background fields, ε^0 , κ^0 are parameters of background medium, \mathbf{E}^s , \mathbf{H}^s are anomalous (or scattered) fields, $\gamma(y) = \varepsilon(y)/\varepsilon^0 - 1$ is the (relative) anomalous permittivity supported in the scatterer domain V . The fields are time harmonic as $e^{-i\omega t}$.

Our formulation is motivated by a horizontal logging problem, where one has metallic cylinder with several coils (logging tool) moving horizontally in a borehole and the problem is to determine the resistivities of the formation layers in the vicinity of current tool position using one coil as a transmitter and other coils as receivers (see left part of Fig. 1).

Due to local sensitivity character of logging tools, some simplification of the problem geometry is possible as a first step. Instead of cylinder, we consider Cartesian geometry (see central and right part of Fig. 1), with the plane $y = 0$ as a surface of the perfect conductor ‘tool’, the halfspace $y > 0$ being uniform medium save the inclusion in the form of parallelepiped, and the source is magnetic dipole at $(0, y_{\text{obs}}, 0)$ oriented along y axis.

The direct 3D scattering problem can be posed in the form of *volume integral equation* [2]

$$\gamma^{-1} \mathbf{J}(x) - (k_0^2 + \text{graddiv}) \int_V G(x, y) \mathbf{J}(y) dy = \mathbf{E}^0, \quad x \in V. \quad (2)$$

with respect to the unknown $\mathbf{J} = \gamma(\mathbf{E}^0 + \mathbf{E}^s)$.

Green function for uniform media with perfect conducting plane $y = 0$ reads $G = \text{diag}(g_1, g_2, g_3)$

$$g_1(x, y) = g_3(x, y) = \frac{e^{ik_0 \|x-y\|}}{4\pi \|x-y\|} - \frac{e^{ik_0 \|x-y^*\|}}{4\pi \|x-y^*\|}, \quad g_2(x, y) = \frac{e^{ik_0 \|x-y\|}}{4\pi \|x-y\|} + \frac{e^{ik_0 \|x-y^*\|}}{4\pi \|x-y^*\|},$$

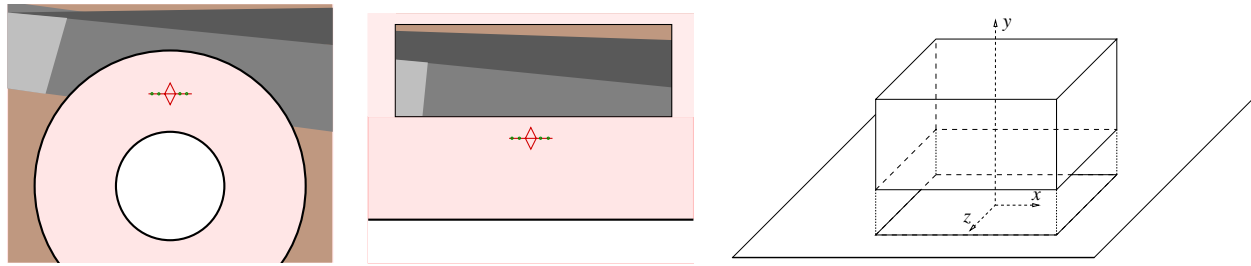


Figure 1: Initial (left) and simplified (center, right) geometry of the problem.

where point $y^* = (y_1, y_2, y_3)^* = (y_1, -y_2, y_3)$ is the reflection of y in the perfect conductor plane.

Since the Green function has special structure $G(x, y) = G^{(1)}(|x - y|) + G^{(2)}(|x - y^*|)$, the discretisation of (2) on uniform tensor $n \times n \times n$ grid leads to linear system $Au = f$ with 3×3 block matrix $A = [A_{kl}]$, and each block inherits the special ‘TTT + THT’ structure, where ‘T’ stands for Toeplitz and ‘H’ for Hankel (cf. [2, 5, 6])

$$(A_{kl})_{i_1 i_2 i_3, j_1 j_2 j_3} = A_{kl}^{(1)}(i_1 - j_1, i_2 - j_2, i_3 - j_3) + A_{kl}^{(2)}(i_1 - j_1, i_2 + j_2, i_3 - j_3). \quad (3)$$

Due to this special structure, A requires only $\mathcal{O}(n^3)$ memory cells for storage and $\mathcal{O}(n^3 \log n)$ flops for matrix-vector multiplication. But even then the straightforward solution of direct scattering problem takes enormous CPU time and memory, see Table 1.

Hence the interest to approximations of A by tensor product matrices in *Tucker format* [7]

$$A \approx \sum_{a=1}^{r_1} \sum_{b=1}^{r_2} \sum_{c=1}^{r_3} g_{abc} U_a \otimes V_b \otimes W_c, \quad \text{or} \quad a_{i_1 i_2 i_3, j_1 j_2 j_3} \approx \sum_{a=1}^{r_1} \sum_{b=1}^{r_2} \sum_{c=1}^{r_3} g_{abc} u_{i_1 j_1, a} v_{i_2 j_2, b} w_{i_3 j_3, c}, \quad (4)$$

where coefficient tensor $\mathcal{G} = [g_{abc}]$ is referred to as *core* and matrices U, V , and W as *mode factors*.

This format requires $n^2(r_1 + r_2 + r_3) + r_1 r_2 r_3$ memory cells in general case and $2n(r_1 + r_2 + r_3) + r_1 r_2 r_3$ for matrices with multilevel Toeplitz or Hankel structure, because Tucker factors U_a, V_b and W_c are also Toeplitz or Hankel matrices. Therefore, this format provides *sublinear* compression of data. Unlike the widely used *canonical decomposition* (PARAFAC/CANDECOMP model) [8] $A \approx \sum_{a=1}^R U_a \otimes V_a \otimes W_a$, compression in Tucker format can be performed by reliable SVD-based algorithm [9], which computes (4) with almost optimal values of mode ranks r_1, r_2, r_3 , that often turn to be considerably smaller than possible tensor rank R of canonical approximation. However, SVD-based method is very expensive for large-scale tensors, because SVD of $n \times n^2$ matrix requires $\mathcal{O}(n^4)$ operations. To perform the approximation, we apply methods with linear in n complexity proposed in [10] (see further development of these ideas in [11, 12]). The resulting values of mode ranks are given in Table 2.

Table 1: Storage requirements for TTT+THT matrix on $n \times n \times n$ grid.

n	16	32	64	128	256
vector	64 kB	512 kB	4 MB	32 MB	256 MB
matrix	9 MB	72 MB	576 MB	4.6 GB	37 GB

Table 2: Storage requirements for Tucker approximation matrix on $n \times n \times n$ grid.

n		16	32	64	128	256
$\Re A^{11}$	mem	60 kB	280 kB	1.2 MB	6.2 MB	13 MB
	(r_1, r_2, r_3)	(11, 11, 8)	(13, 11, 11)	(15, 13, 13)	(18, 16, 14)	(20, 18, 16)
$\Im A^{11}$	mem	60 kB	250 kB	1.0 MB	4.4 MB	9 MB
	(r_1, r_2, r_3)	(10, 10, 8)	(11, 11, 9)	(12, 10, 9)	(13, 11, 10)	(14, 12, 11)

2. INVERSE SCATTERING PROBLEM

The *Born approximation* is based on the assumption that anomalous electric fields inside scatterers are negligible compared to background electric fields [3],

$$y \in V \Rightarrow |\mathbf{E}^s(y)| \ll |\mathbf{E}^0(y)|.$$

Hence \mathbf{E}^s may be deleted from the right-hand side of (1), and we obtain explicit formulas for \mathbf{E}^s , \mathbf{H}^s as linear functions of $\gamma(x)$.

Quasi-linear approximation [4] is based on the assumption

$$y \in V \Rightarrow \mathbf{E}^s(y) = \lambda(y)\mathbf{E}^0(y),$$

where $\lambda(y)$ is assumed to be rather smooth, i.e., well approximated on a coarse mesh. In general case, $\lambda(y)$ may be tensor-valued, however we restrict ourselves to isotropic case and scalar $\lambda(y)$, since in our model geometry y -component of background field is generically zero (and therefore λ_2 is deleted from governing equations).

Rewrite (1) in a more compact form:

$$\begin{aligned} \mathbf{H}^s(x) &= G_H(\gamma(\mathbf{E}^0 + \mathbf{E}^s)), & x \notin V; \\ \mathbf{E}^s(x) &= G_E(\gamma(\mathbf{E}^0 + \mathbf{E}^s)), & x \in V. \end{aligned} \quad (5)$$

In quasi-linear approximation, function λ is the solution to the following formula,

$$\min_{\lambda} \|\lambda\mathbf{E}^0 - G_E(\gamma(\lambda + 1)\mathbf{E}^0)\|_V, \quad (6)$$

where $\|\cdot\|_V$ -norm is computed numerically on a mesh which is finer than the one used to discretize λ , and therefore (6) leads to a regular least squares problem.

Localized quasi-linear approximation [4] is a variant of quasi-linear approximation in which the functional (6) is substituted by the following one,

$$\min_{\lambda} \sum_{k=1}^3 \|\lambda e_k - G_E(\gamma(\lambda + 1)e_k)\|_V^2. \quad (7)$$

Here e_1, e_2, e_3 are unit vectors of the Cartesian coordinate system. Solution of (7) gives the so-called localized reflectivity function λ , which is obviously source-independent.

Approximation of Gao, Fang, Torres-Verdin [3] is based on the assumption

$$y \in V \Rightarrow \mathbf{E}^s(y) + \mathbf{E}^0(y) = e(y)|\mathbf{E}^0(y)|,$$

where the new unknown field $e(y)$ is assumed to be much smoother than $\mathbf{E}(y)$, i.e., well approximated on a coarse mesh.

Fields $e(y), \gamma(y)$ are discretized on a coarse mesh, while $|\mathbf{E}^0(y)|, G(x, y)$ and the integral operator are discretized on a finer mesh. Equation (6) with $\mathbf{E}^s(x)$ substituted in both places by $e(x)|\mathbf{E}^0(x)| - \mathbf{E}^0(x)$, leads to a least squares problem.

3. INVERSION SCHEMES BASED ON APPROXIMATIONS

Generally adopted inversion scheme consists in defining the so-called modified material property tensor $m(x)$ by solving, in the least squares sense, the linear equations

$$\begin{aligned} \mathbf{H}^s(x) &= G_H(m\mathbf{E}^0), & x \notin V; \\ \mathbf{E}^s(x) &= G_E(m\mathbf{E}^0), & x \in V. \end{aligned} \quad (8)$$

Here $\mathbf{H}^s(x)$ or $\mathbf{E}^s(x)$ are given in some observation points, \mathbf{E}^0 is known background field and m is sought. Of course, the number of observation points should be larger than the number of degrees of freedom used in discretizing m .

Now, the chosen approximation method should be modified since $\gamma(x)$ is not available. To this end, $\gamma(x)$ should be somehow substituted by $m(x)$.

Born approximation: nothing is required, the least-squares solution $m(x)$, if the tensor is assumed to be scalar, is the same as $\gamma(x)$.

(Localized) quasi-linear approximation: in (7) and (8), $\gamma(\lambda + 1)$ should be substituted by the (already known) function m . Solving (7), (8) is the second step. The third step is the cell-wise inversion of the equation $m(x) = \gamma(x)(\lambda(x) + 1)$, $x \in V$, for the single probing frequency case; otherwise, it can be solved in the least squares sense for a set of given frequencies ω .

Approximation of Gao, Fang, Torres-Verdin: the equation $e(x)|\mathbf{E}^0(x)| - \mathbf{E}^0(x) = G_E(m\mathbf{E}^0)$ is solved for $e(x)$ with known m (coarse grid), \mathbf{E}^0 (finer grid) in the least-squares sense.

Other schemes. An evident and probably sound approach consists in using successive iterations in γ using (6).

Consider the sequence $\gamma^0(x), \gamma^1(x), \dots$ defined on a coarse mesh, and the sequence $\mathbf{E}^{s0}(x), \mathbf{E}^{s1}, \dots$ defined on a finer mesh, by the following algorithm:

(1) $\mathbf{E}^{s0}(x) := 0, \gamma^0(x) := m(x)$, the Born approximation;

(2) for $k = 0, 1, \dots$,

(2a) compute $\mathbf{E}^{s,k+1}(x) := G_E(\gamma^k(\mathbf{E}^0 + \mathbf{E}^{s,k}))$, $x \in V$;

(2b) solve $\mathbf{H}^s(x) = G_H(\gamma^{k+1}(\mathbf{E}^0 + \mathbf{E}^{s,k+1}))$ in the least squares sense, with given observation data \mathbf{H}^s , known $\mathbf{E}^{s,k+1}$ and unknown γ^{k+1} .

4. IMPLEMENTATION OF THE BORN APPROXIMATION

The inclusion parallelepiped V consists of layers “modelling” borehole and geophysical layer(s). The resistivity inside V is defined to be constant in every cell of a regular 3D mesh (Cartesian product of uniform 1D meshes), which will be called the reference mesh. The Born solver mesh is obtained by dividing each cell of the reference mesh in a constant number of subcells.

The logging data is defined to be (imaginary parts of) y -components of magnetic field measured on a dipole transmitters/receivers array. The latter is a 1D grid of magnetic dipoles oriented along the y axis. The grid slides in the positive x direction; a set of logging data is defined as magnetic field values on that grid for several fixed positions of the grid. We have used the transmitter grids with odd number of dipoles in one dimension; the central dipole was the only source.

The structure of the matrix of the least-squares problem may be represented by the following formula:

$$\min_{\gamma} \left\| \begin{pmatrix} G_H(\text{obs}_1, V)\mathbf{E}^0(V, \text{src}_1) \\ G_H(\text{obs}_2, V)\mathbf{E}^0(V, \text{src}_2) \\ \vdots \\ G_H(\text{obs}_n, V)\mathbf{E}^0(V, \text{src}_n) \end{pmatrix} \gamma(V) - \begin{pmatrix} (\mathbf{H} - \mathbf{H}^0)(\text{obs}_1) \\ (\mathbf{H} - \mathbf{H}^0)(\text{obs}_2) \\ \vdots \\ (\mathbf{H} - \mathbf{H}^0)(\text{obs}_n) \end{pmatrix} \right\|_2.$$

Here n is the number of fixed positions of the transmitter grid, dense matrix $G_H(\text{obs}_k, V)$ is the discrete analog of the integral operator G_H on the mesh in V and observation points of fixed position number k of the transmitter grid, diagonal matrix $\mathbf{E}^0(V, \text{src}_k)$ contains the values of background field \mathbf{E}^0 on the mesh in V for source dipole corresponding to fixed position number k of the transmitter

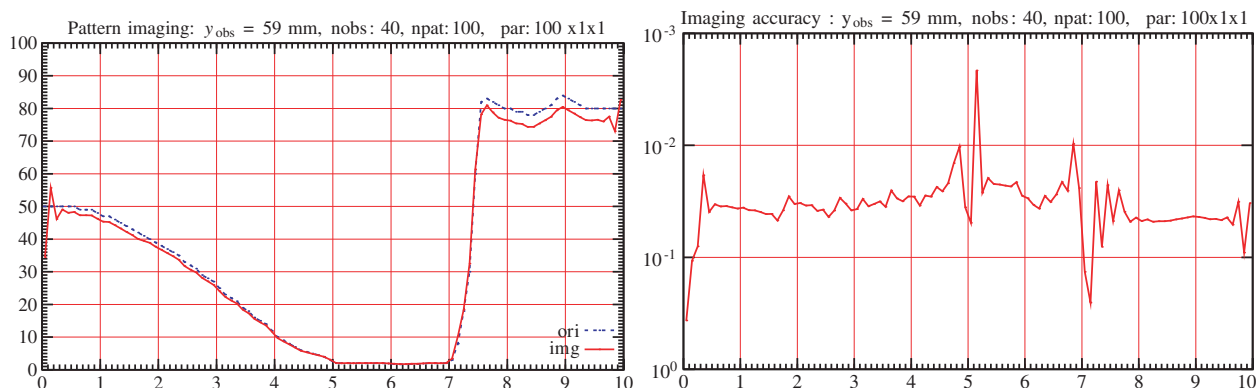


Figure 2: Results of horizontal logging: original and restored pattern (left), relative error (right).

grid, $\gamma(V)$ is the (unknown) relative permittivity in V , $(\mathbf{H} - \mathbf{H}^0)(\text{obs}_k)$ is the logging data for fixed position number k of the transmitter grid.

For our problem, a special parametrization of the Tikhonov regularization $\min_x \|Ax - f\|_2^2 + \alpha\|x\|_2^2$ was successful: instead of α , we have used $\|\Delta f\|_2$, corresponding to the so-called misfit condition [13].

Suppose that we are given the “noise” level $\|\Delta f\|_2$ (or relative “noise” level $\|\Delta f\|_2/\|f\|_2$). The misfit condition requires that α should be chosen so that the equality $\|Ax - f\|_2 = \|\Delta f\|_2$ is valid. If $\|\Delta f\|_2 > \|f - UU^*f\|_2$, where U is any orthonormal matrix with columns spanning the image space of A , this is always possible; if only $\frac{1}{2}\|f\|_2 > \|\Delta f\|_2$, one can show that $0 \leq \alpha \leq \|A\|_2^2$. In practice, any univariate zero-finding algorithm can be used.

ACKNOWLEDGMENT

This work was partially supported by RFBR grant 08-01-00115 and Priority Research Grant of Department of Mathematical Sciences of the Russian Academy of Sciences.

REFERENCES

1. Ilyinskiy, A. S., V. V. Kravtsov, and A. G. Sveshnikov, *Mathematical Models in Electrodynamics*, Vishaja Shkola, Moscow, 1991 (in Russian).
2. Smirnov, Y. G. and A. A. Tsupack, “Volume singular integral equations for solving diffraction problem of electromagnetic waves in microwave oven,” *Proc. of European Symp. on Numer. Meth. in Electromagnetics*, 172–176, 2002.
3. Gao, G., S. Fang, and C. Torres-Verdin, “A new approximation for 3D electromagnetic scattering in the presence of anisotropic conductive media,” *3DEMIII Workshop*, Adelaide, 2003.
4. Zhdanov, M. S. and E. Tartaras, “Three-dimensional inversion of multitransmitter electromagnetic data based on the localized quasi-linear approximation,” *Geophys. J. Int.*, Vol. 148, 506–519, 2002.
5. Ivakhnenko, V. I., A. V. Kukk, and E. E. Tyrtysnikov, “Application of 3D volume integral equations to solution of electromagnetic wave scattering problems,” *Elegant Mathematics*, Research Report EM-RR 22/95, 1995.
6. Ivakhnenko, V. I. and E. E. Tyrtysnikov, “Block-Toeplitz-Structure-based solution strategies for CEM problems,” *11th Annual Review of Progress in Applied Comp. Electromagnetics, Conf. Proceedings*, 181–188, Monterey, CA, 1995.
7. Tucker, L. R., “Some mathematical notes on three-mode factor analysis,” *Psychometrika*, Vol. 31, 279–311, 1966.
8. Harshman, R. A., “Foundations of the Parafac procedure: Models and conditions for an explanatory multimodal factor analysis,” *UCLA Working Papers in Phonetics*, Vol. 16, 1–84, 1970.
9. De Lathauwer, L., B. de Moor, and J. Vandewalle, “A multilinear singular value decomposition,” *SIAM J. Matrix Anal. Appl.*, Vol. 21, 1253–1278, 2000.
10. Oseledets, I. V., D. V. Savostyanov, and E. E. Tyrtysnikov, “Tucker dimensionality reduction of three-dimensional arrays in linear time,” *SIAM J. Matrix Anal. Appl.*, Vol. 30, No. 3, 939–956, 2008.
11. Flad, H.-J., B. N. Khoromskij, D. V. Savostyanov, and E. E. Tyrtysnikov, “Verification of the cross 3D algorithm on quantum chemistry data,” *Rus. J. Numer. Anal. Math. Model.*, Vol. 23, No. 4, 210–220, 2008.
12. Goreinov, S. A., “On cross approximation of multi-index array,” *Doklady Math.*, Vol. 420, No. 4, 1–3, 2008.
13. Tikhonov, A. N. and V. Y. Arsenin, *Methods of Solution of Ill-conditioned Problems*, Moscow, Nauka, 1986 (in Russian).

Application of Mosaic-Skeleton Approximations for Solving EFIE

S. L. Stavtsev and E. E. Tyrtshnikov
INM RAS, Russian Federation

Abstract— To solve EFIE on the surfaces of arbitrary shape, RWG functions are traditionally used. In spite of their effectiveness when solving diffraction problems on complex surfaces, on multiple objects as well as the problems with high frequencies, the necessity arises to calculate dense matrices of high dimensionality ($n > 10^4$) and also to solve correspondent linear systems.

We suggest using nonlinear matrix approximations to work with large matrices. We can calculate $O(n \log(n))$ elements of matrix (instead of $O(n^2)$), where n is a number of variables in system of linear equations. The multiplication of matrix and vector we can execute also for $O(n \log(n))$ operations. The nonlinear matrix approximations allow to operate with matrixes $n \cdot 10^5 - 10^6$. System of linear equation with matrixes of such order is solved by iterative method (GMRES). To reduce of number of iterations we are used precondition which is based on mosaic-skeleton approximations.

1. INTRODUCTION

Scattering solution of arbitrarily shaped tree-dimensional conducting bodies have always been of interest in computational electromagnetics. Often, it is important to have the full knowledge of the scatterer's spectral properties. It is known solvers that calculates the scattering solutions, but these solutions demand more memory and CPU time as the solution frequency increase.

A common approach for solving arbitrarily shaped 3-D bodies is using method of moments. In order to solve for the scattered field when the target body is illuminated with a plane wave, we first need to discretize the surface using small triangle. A matrix is filled with the electromagnetic interaction values of these triangular elements. The solution of the ensuring matrix equation is the coefficients of the surface currents induced on the scatterer. In order to solve accurately enough, dimensions of each triangle should not be larger than $\lambda/10$, where λ corresponds to the wavelength. It can be seen that, when the solution frequency increases, the size of the interaction matrix also increases, hence the solution of that system becomes difficult.

To increase the solution efficiency of the matrix system in the paper we applied mosaic-skeleton method for approximation large matrices. We expect what this method improvement to method of moments is quite effective in increase the maximum solvable frequency limit.

To calculate the scattering field at any point in space we have to not only approximate matrix but solve system of linear equation with one. For solving system we will use some iteration algorithm, for example GMRES algorithm. From numerical experiments it is known, when the solution frequency increases, the number of iteration also increases, i.e., demand more memory and CPU time increase. In the paper we describe method construction precondition. The precondition will be used mosaic-skeleton structure matrix, what will increase its effectiveness.

2. METHOD OF MOMENTS

Let S denote the surface of a closed perfectly conducting scatterer with unit normal \bar{n} and D is domain out surface S . An electric field \bar{E}_0 is induced surface currents \bar{J} on S .

The scattered electric field \bar{E} can be computed from the surface current by

$$\bar{E}(M) = -i\omega\bar{A}(M) - \nabla_M\Phi(M), \quad M \in D, \quad (1)$$

where

$$\bar{A}(M) = \frac{\mu}{4\pi} \int_S \bar{J}(N) \frac{e^{-ik|M-N|}}{|M-N|} dS_N, \quad \Phi(M) = \frac{1}{4\pi\epsilon} \int_S \sigma(N) \frac{e^{-ik|M-N|}}{|M-N|} dS_N. \quad (2)$$

In (1) $k = \omega\sqrt{\mu\epsilon} = 2\pi/\lambda$, where λ is the wavelength, μ and ϵ are respectively the permeability and permittivity of the surrounding medium.

The surface charge density σ is related to the surface divergence of \bar{J} through the equation of continuity

$$\nabla_S \cdot \bar{J} = -i\omega\sigma. \quad (3)$$

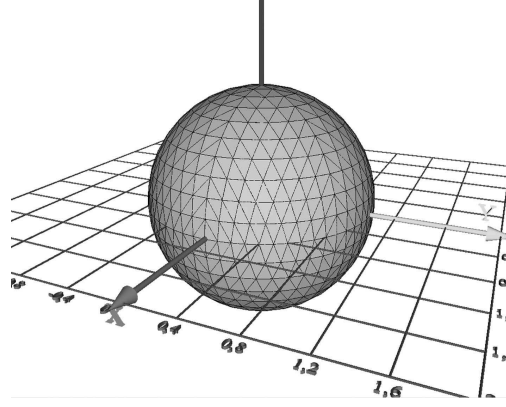


Figure 1: The sphere discretization.

For total electrical field on surface S perform the boundary condition

$$\bar{n} \times \left(\bar{E}_0(M) + \bar{E}(M) \right) = \bar{0}. \quad (4)$$

From (1)–(4) we derive electric field integrodifferential equation (EFIE) $\bar{E}_{0\tau}(M) = \left(i\omega\bar{A}(M) + \nabla\Phi(M) \right)_\tau$, $M \in S$ or

$$\frac{1}{4\pi} \nabla_\tau \int_S \nabla_N \cdot \bar{J}(N) \frac{e^{-ik|M-N|}}{|M-N|} dS_N + \frac{k^2}{4\pi} \int_S \bar{J}(N) \frac{e^{-ik|M-N|}}{|M-N|} dS_N = \frac{ik}{\mu} \bar{E}_{0\tau}(M), \quad M \in S. \quad (5)$$

We discretize the surface using small triangle (for example, discretization sphere illustrated in Fig. 1).

In the method of moments we will use follows basis functions [1]

$$\bar{f}_n(M) = \begin{cases} -\frac{l_n}{2A_n^-} \bar{\rho}_n^-, & M \in T_n^-, \\ \frac{l_n}{2A_n^+} \bar{\rho}_n^+, & M \in T_n^+, \\ 0 & \text{otherwise,} \end{cases} \quad (6)$$

where A_n^\pm are squares of triangles T_n^\pm and parameters l_n , $\bar{\rho}_n^\pm$ are illustrated in Fig. 2. The basis functions associate with the n th edge and are represent the normal component of surface current.

The current on S will be approximated in terms of the \bar{f}_n as

$$\bar{J}(M) \approx \sum_{n=1}^N J_n \bar{f}_n(M). \quad (7)$$

The next step in the method of moments is to choose a testing functions, for example $f_n(M)$, and to define scalar product as

$$(\bar{f}, \bar{g}) = \int_S \bar{f}(N) \cdot \bar{g}(N) dS_N. \quad (8)$$

Scalar multiplication left and right-hand (5) with $f_m(M)$ and substitution of the current expansion (7) into (5) yields a system of N equations which is written in matrix form as

$$AJ = b, \quad A = (a_{ij})_{N \times N}, \quad J = (J_n), \quad b = (b_n). \quad (9)$$

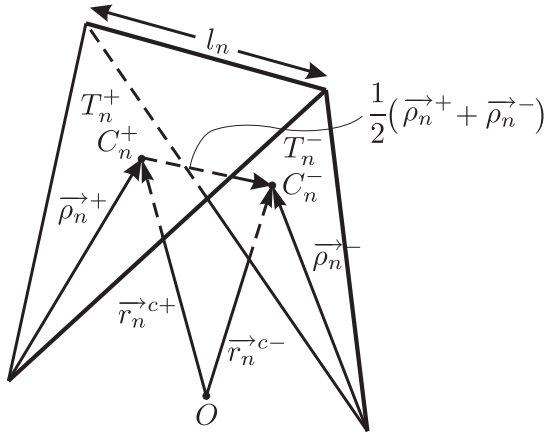


Figure 2: The basis elements of MOM.

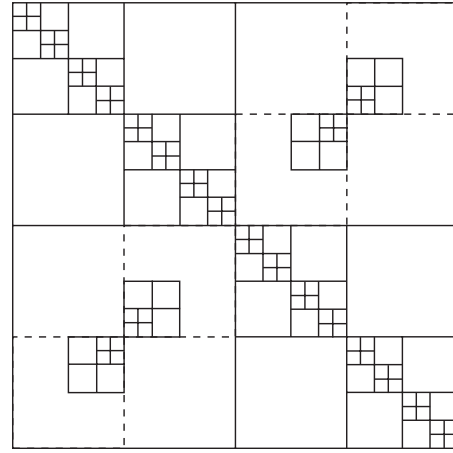


Figure 3: The blocks of mosaic-skeleton approximation.

Elements a_{ij} , $i, j = 1, \dots, N$ are given by (see Fig. 2, C_n^\pm — the points of crossing of medians T_n^\pm)

$$a_{ij} = l_m \left(\frac{k^2}{2} \bar{A}_{ij}^+ \cdot \bar{\rho}_i^+ + \frac{k^2}{2} \bar{A}_{ij}^- \cdot \bar{\rho}_i^- + \Phi_{ij}^- - \Phi_{ij}^+ \right), \tag{10}$$

where

$$\bar{A}_{ij}^\pm = \frac{1}{4\pi} \int_S \bar{f}_j \frac{e^{-ik|C_i^\pm - N|}}{|C_i^\pm - N|}, \quad \Phi_{ij}^\pm = \frac{1}{4\pi} \int_S \nabla_N \cdot \bar{f}_j \frac{e^{-ik|C_i^\pm - N|}}{|C_i^\pm - N|}. \tag{11}$$

In (9) elements b_i , $i = 1, \dots, N$ are given by (see Fig. 2)

$$b_i = \frac{l_m}{2} \left(\bar{E}_0(C_i^+) \cdot \bar{\rho}_i^+ + \bar{E}_0(C_i^-) \cdot \bar{\rho}_i^- \right). \tag{12}$$

3. MOSAIC-SKELETON METHOD

The cross approximation in mosaic-skeleton method is in detail described in works [2–4]. The mosaic-skeleton method was bred in a simple observation that rather large blocks in very large matrices coming from integral formulations can be approximated by a sum of just few rank-one matrices (skeletons). These blocks might correspond to a region where the kernel is smooth enough, and anyway it can be a region where the kernel is approximated by a short sum of separable functions.

On the first stage, the method builds up an appropriate mosaic partitioning using the concept of a tree of clusters and extra information rather than the matrix entries (the centers of edges). On the second stage, it approximates every (allowed) block by skeletons using the entries of some rather small cross which is chosen by an adaptive procedure. The constructed blocks without crossings cover all matrix (Fig. 3).

As the result for each block A_{lm} of matrix A in (9) we find matrixes C and R , satisfying to a condition

$$\|A_{lm} - C_{lm}R_{lm}^T\| \leq \varepsilon, \quad C_{lm}R_{lm}^T = \sum_{j=1}^K c_j r_j^T, \tag{13}$$

where the range of matrix $C_{lm}R_{lm}^T$ is equal $K \ll \dim(A_{lm})$, ε is a accuracy of approximation. We receive the approached matrix $\tilde{A}(C_{lm}R_{lm}^T)$.

4. PRECONDITION USED MOSAIC-SKELETON METHOD

The approach we are going to pursue is to use an approximative LU decomposition

$$\tilde{A} = LU, \tag{14}$$

of the coefficient matrix A , where the two triangular factors L and U are stored in sparse format. The arising equations with coefficient matrix \tilde{A} can then be solved by forward substitution with the same complexity as the mosaic-skeleton-matrix — vector multiplication. We expect what the setup of the factors L and U can be done with complexity $O(n \log n)$.

5. NUMERICAL RESULTS

We had been investigate the scattering plane wave from a PEC sphere with radius of 1 (see Fig. 1). The wavenumber is $k = 1$. The error of approximation $\varepsilon = 10^{-6}$. Calculation time is resulted in Table 1.

In Table 1, N is the size of matrix, T_{st} — time of direct calculation of matrix; T_{ms} — time of mosaic-skeleton approximation; I_{re} — impact factor of real part matrix; I_{im} — impact factor of image part matrix;

Table 1: Time approximation.

N	1800	2592	4608	7200	8712
T_{st}	2 min. 42c.	10 min. 17c.	33 min. 06c.	46 min. 13c.	1 h. 08 min. 13c.
T_{ms}	3 min. 14c.	5 min. 15c.	11 min. 55c.	19 min. 24c.	23 min. 40 c.
I_{re}	0.875	0.702	0.494	0.342	0.300
I_{im}	0.640	0.466	0.287	0.195	0.165
N	10368	22050	36450	54450	88200
T_{st}	1 h. 31 min. 46c.	21h. 21 min. 40c.	-	-	-
T_{ms}	29 min. 59 c.	1 h. 21 min. 29c.	2 h. 10 min. 24c.	3 h. 23 min. 27c.	6 h. 18 min.01c.
I_{re}	0.263	0.144	0.096	0.068	0.046
I_{im}	0.143	0.073	0.046	0.032	0.021

ACKNOWLEDGMENT

The work was supported by the Russian Fond of Basic Research (grants 08-01-00115-a, 09-01-00565-a).

REFERENCES

1. Rao, S. M., D. R. Wilton, and A. W. Glisson, "Electromagnetic scattering by surfaces of arbitrary shape," *IEEE Transactions on Antennas and Propagation*, Vol. 30, No. 3, 409–418, 1982.
2. Tyrtysnikov, E. E., "Incomplete cross approximation in the mosaic-skeleton method," *Computing*, Vol. 64, No. 4, 367–380, 2000.
3. Tyrtysnikov, E. E., "Mosaic-skeleton approximations," *Calcolo*, Vol. 33, No. 1–2, 47–57, 1996.
4. Goreinov, S. A., E. E. Tyrtysnikov, and N. L. Zamarashkin, "A theory of pseudo-skeleton approximations," *Linear Algebra Appl.*, Vol. 261, No. 4, 1–21, 1997.

Numerical Analysis of Scattering and Absorption Problems of Electromagnetic Waves of a Mobile Communication Range on Non-uniform Biological Structures

Sergey P. Kulikov and Natalya Y. Voronina

Moscow Institute of Radio Engineering, Electronics and Automation, Russia

Abstract— The problem of the numerical analysis of interaction of electromagnetic waves of a mobile communication range and other microwaves sources with non-uniform biological bodies and structures is put in the strong formulation on the basis of the volume integral equation and further in the mathematical plan is reduced to the numerical solution of large complex systems of the linear algebraic equations (SLAE) with symmetric non-hermit matrix. For the solution, such SLAE application of a method of optimum simple iteration (MOSI) proves. Successful application of this method is based on knowledge of spectral properties of the integral transition operator and on the developed algorithms of optimum parameter MOSI definition. The principle of optimum parameter stability is used at transition from a problem with a rare computing grid to some with a dense one. Some absorption problems of electromagnetic waves of a mobile communication range on models of human bodies are numerically solved.

1. INTRODUCTION

The rapid development of mobile communication technics puts a problem of modeling of radiation interaction from a mobile source of frequencies 400 MHz–3 GHz with the human bodies and also calculation of specific absorption rate on biological body with the purpose of prevention of excess of admissible sanitary norms [1]. Opportunities of computer facilities and progress of numerical methods allow the numerical evaluation of heating of human head due to Magnetic Resonance Imaging [2]. Last decade extended computer methods of the harmless and not destroying control and diagnostics of bodies and fabrics such, how the method of Magnetic Resonance Imaging [3, 4] using a variable magnetic field of a radio-frequency range (40–300 MHz). All these technical achievements lean on an opportunity of effective modeling of interaction of electromagnetic radiation with non-uniform biological bodies and structures.

2. SECTION 1

Numerical modeling of stationary harmonious electromagnetic scattering and absorption on locally non-uniform dielectric non-magnetic body is based on the volume integral equation concerning amplitude of an electric field [5]

$$\begin{aligned} \vec{E}(p) = & \vec{E}^0(p) + \nu(\varepsilon(p) - 1)\vec{E}(p) + v.p. \int_Q (\varepsilon(q) - 1)\vec{E}(q)k_0^2 G(r)dQ \\ & + \int_Q \left((\varepsilon(q) - 1)\vec{E}(q), \text{grad} \right) \text{grad} G(r)dQ \end{aligned} \quad (1)$$

Here $v.p.$ is a singular integral in sense of a principal value, the factor in an outintegral member matters $\nu = \frac{1}{3}$ in a three-dimensional vector case and $\nu = \frac{1}{2}$ in a two-dimensional vector case, Green's function in a three-dimensional case is $G(r) = \frac{\exp(-ik_0 r)}{4\pi r}$, and in two-dimensional — $G(r) = -\frac{i}{4}H_0^{(2)}(r)$, where $r = |p - q|$ — Distance between a point of a source $q = (x', y')$ and a point of supervision $p = (x, y)$, x, y — The system of the coordinates connected with area borrowed by dielectric. The specific absorption rate (SAR) of a harmonious electromagnetic field in local area of a body with the coordinates set radius-vector \vec{r} , is calculated as

$$\text{SAR}(\vec{r}) = \frac{\sigma(\vec{r}) \left| \vec{E}(\vec{r}) \right|^2}{2\rho(\vec{r})} \quad (2)$$

where $\sigma(\vec{r})$ — Tissue conductivity, $\rho(\vec{r})$ — Tissue density, $\vec{E}(\vec{r})$ — Total electric field in a voxel of tissue.

For calculation of an electric field through a dielectric body by means of the volume integral Equation (1) the knowledge of distribution of dielectric permeability $\varepsilon(\vec{r}) = \varepsilon_1(\vec{r}) - j\varepsilon_2(\vec{r}) = \varepsilon_1(\vec{r}) - j\frac{\sigma(\vec{r})}{\omega\varepsilon_0}$ is necessary. Here ε_0 — Permeability of free space. In works [2–4, 6], values dielectric permeability human bodies and head in various frequency radiatoranges, in particular in range UHF 300 MHz–3 GHz, including a range of mobile communication and microwave-heating are resulted.

3. SECTION 2

Modeling is based on the numerical solution of the volume integral equation of scattering (1). That or a different way the integrated operator of a problem is discretized (for example, by means of a method of the final sums and formulas of rectangulars) also is reduced to system of the linear algebraic equations (SLAE). In a considered resonant range of frequencies, when the length of a wave is commensurable with the sizes of area of heterogeneity, SLAE size is great enough, $N > 1000$, where N is a number of complex unknowns. For biological objects both real, and imaginary values of dielectric permeability are great (see Figs. 1 and 3). Accordingly the length of a wave in the environment considerably decreases, and SLAE size still increases, as for good physical approximation of a problem it is necessary to adhere to 8–10 units of a grid for length of a medium wavelength. Received SLAE is complex symmetric non-hermith. In view of its big size application of direct methods for the solution SLAE is rather inconvenient. Usually iterative methods of numerical solution on a regular computational grid in conjunction with Fast Fourier transform (FFT) are used for fast matrix-vector multiplication. In our opinion, among the iterative solutions the stationary method of optimum simple iteration (MOSI) is one of the most effective methods. Its effectiveness is based on the properties of the spectral set of the transition operator (matrix) to determine the optimum complex parameter of convergence, and also on the in principal of relative invariability

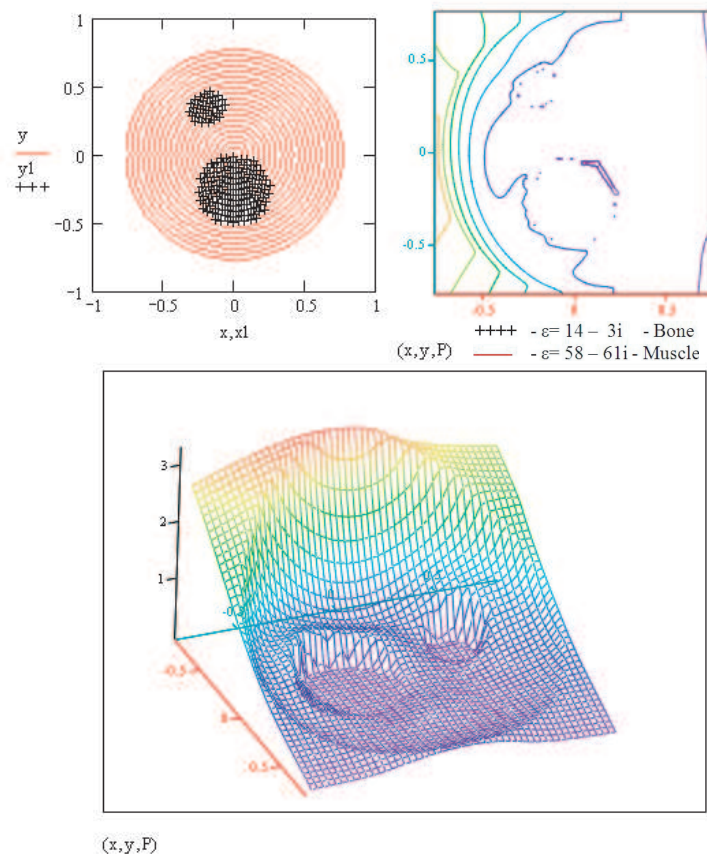


Figure 1: $F = 900$ MHz, $d = 0.085$ m. . . , $\alpha = 0^\circ$ — A corner a wave vector with an axis x , $K = 25$ — Number of units of a grid on radius, $N = 1875$ — The general number of units of a grid, $m = 94$ — Number of iterations for achievement of accuracy of the solution 10^{-3} on a field in the area of heterogeneity.

of the spectral picture of the transition operator and, consequently, the optimum parameter of convergence, with the improvement of the approximation of problem with a weak approximation with 2–3 nodes on a medium wavelength to a good approximation with 8–10 nodes and more [7]. A spectral set of an integral transition operator at (1) in the three-dimensional and two-dimensional vector cases has two components: continuous and discrete. Continuous component depends on the values of medium permittivity ε and includes uninterrupted continuum of spectral values from 0 to ε . Discrete component has the points of accumulation at the continuous spectrum. In a scalar case of E -polarization only a discrete component of the spectrum with the only accumulation point 0 is. In all cases a discrete spectrum depends only on the sizes and the geometry of the scattering region and in Rayleigh case its departure from the accumulation points is vanishing.

The most simple for calculations is the case of Rayleigh scattering and near resonant scattering (40–400 MHz), when the wavelength is more or much more the region of heterogeneity. Especially rapid convergence of MOSI has occurred in a scalar case. μ_1 is supposed the largest in magnitude complex eigenvalue of discrete spectrum in a scalar case. Then for Rayleigh scattering $|\mu_1| \ll 1$, the optimum parameter for the convergence of MOSI is $\kappa = \frac{\mu_1}{2}$, and the denominator of convergence is $q = |\frac{\kappa}{\kappa-1}| \ll 1$. In case of near resonant scalar scattering (as well as in a case when one coordinate of the region of heterogeneity is Rayleigh and the other is resonant) the formula for an optimum parameter value remains, and the denominator of convergence $q < 1$. For vector cases convergence of MOSI depends essentially on the values of a permittivity medium. Let the values of permittivity medium are piecewise constant and there are M different values $\varepsilon_i, i = 1, \dots, M$. The continuous spectrum consists of M segments from 0 to $\varepsilon_i, i = 1, \dots, M$. Only continuous spectrum is significant in Rayleigh scattering. As an optimum parameter of convergence of MOSI it should be taken the center of circle covering polygon $0, \varepsilon_1, \varepsilon_2, \dots, \varepsilon_M$ and “visible” from the point 1 of the complex plane on a minimum corner. The algorithms for finding the center of this circle and the optimum parameter of MOSI are developed [7].

Impact of a discrete spectrum on convergence of MOSI has become essential in a resonant scattering of biological bodies and human tissues (900 MHz–3 GHz). In a scalar case it is possible to move farthest in a resonant range. The points of a discrete spectrum are suited closely to the point 1 in the complex plane. It significantly impairs convergence of iterations. Matrix SLAE is approaching a singular, conditionality is getting worse. The research shows that well-known unsteady methods (method of minimal residuals, method of conjugate gradients) are losing convergence in these circumstances. Nevertheless, using of MOSI succeeds to find an optimum parameter of convergence and to solve SLAE.

On Fig. 1, the numerical solution of a scalar absorption problem of a flat E -polarization wave

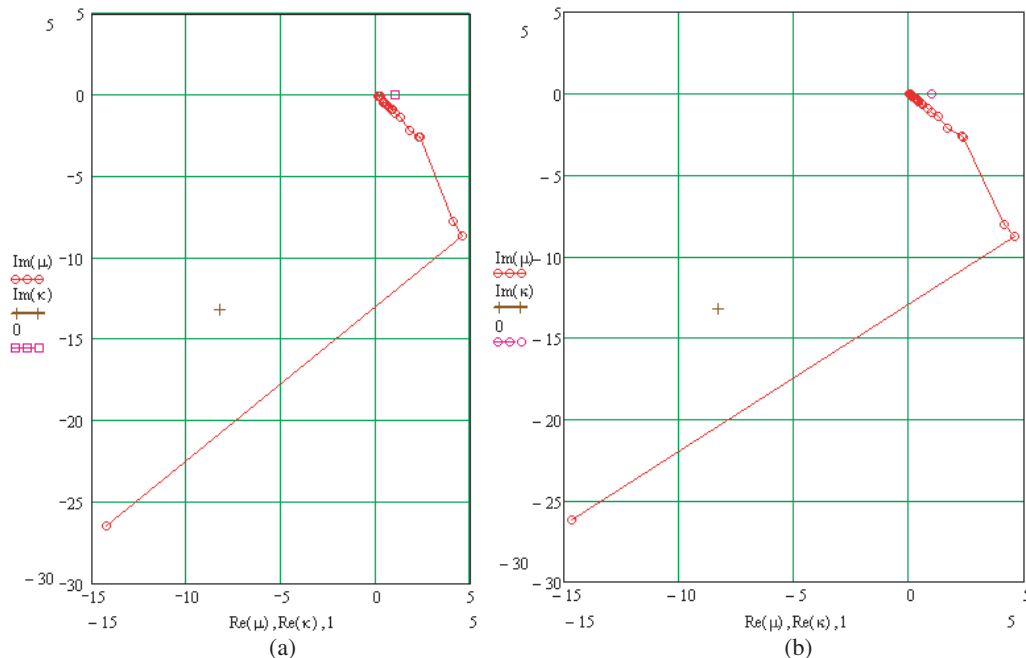


Figure 2: (a) 3 units of a grid for length of a wave, (b) 19 units of a grid for length of a wave.

on the muscular cylinder with diameter $d = 0.085$ meters and with two bone inclusions is presented. The asymmetrical geometry of a problem, line of a level of SAR (2) and a surface picture of SAR are presented. In this problem it was enough to choose the value $K = 10$ for sufficient approximation of wave phenomena in a medium (8 grid nodes on medium wavelength). However, it was chosen $K = 25$ for sufficient approximation of complex geometry. The electric sizes of the cylinder are rather insignificant — 0.25 lengths of a wave in free space and 2 lengths of a wave in a muscular tissue. Therefore, the wave attenuation in cylinder is smooth, diffraction effects on bone inclusions are noticeable.

On Fig. 2 the spectral picture of a transition operator in this problem is presented. The optimum parameter of convergence κ close to the Rayleigh value $\kappa = \mu_1/2$ was found for a rare grid with $N = 27$ (Fig. 2(a)), and then was used in a problem with $N = 1200$ (Fig. 2(b)) and $N = 1875$. A spectral picture and κ are practically with no change, but a field in scattering region and SAR are undergone with significant changes.

On Fig. 3, the geometry and SAR of a flat wave of E -polarization on cylindrical model of a human head is presented.

On Fig. 4, the spectral picture of the transition operator for the previous problem is presented. The case of resonant scattering takes place, the optimum parameter $\kappa = -27 + 80i$ is defined by special algorithms on a rare grid. The spectrum is near to a singular point of the problem operator that causes low speed of convergence. Nevertheless, the significant gain in comparison with direct and variational methods of the such task solution takes place.

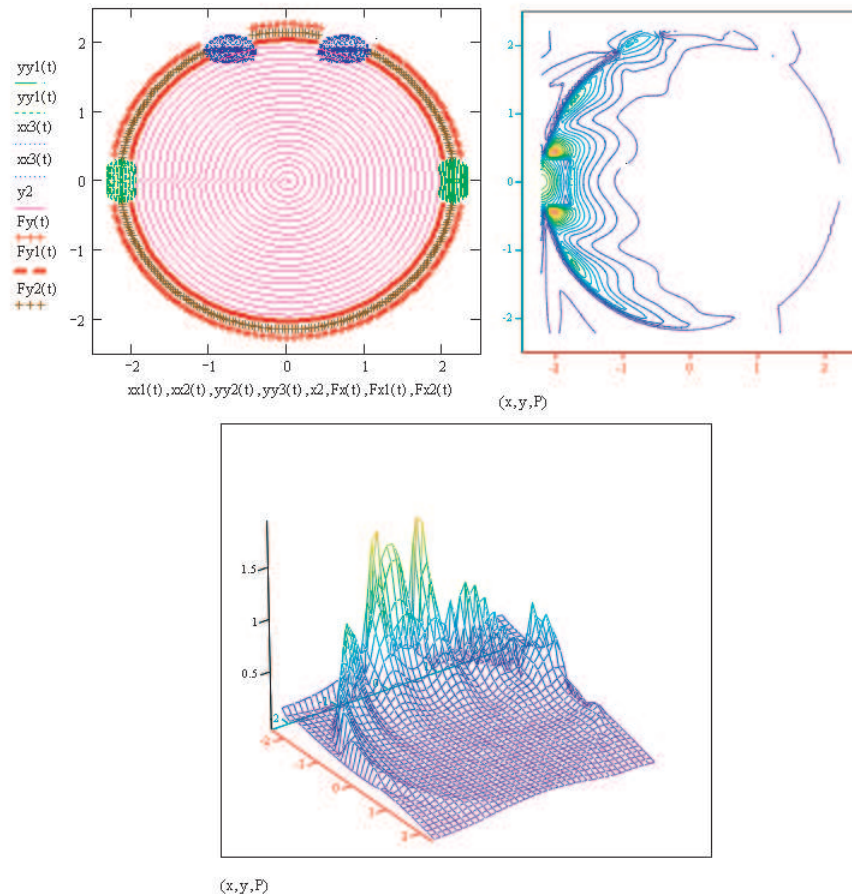


Figure 3: $F = 1200$ MHz, $d = 0.18$ meters, 1. $\varepsilon = 8-1.8i$ — Bone, 2. $\varepsilon = 64.8-24.7i$ — CSF, 3. $\varepsilon = 53.8-21.7i$ — Brain, 4. $\varepsilon = 60-27i$ — Eye, 5. $\varepsilon = 30.6-7.9i$ — Cartilage. $\alpha = 0^\circ$ — A corner a wave vector with an axis x , $K = 25$ — Number of units of a grid on radius, $N = 1875$ — The general number of units of a grid, $m = 750$ — Number of iterations for achievement of accuracy of the solution 10^{-3} on a field in the area of heterogeneity.

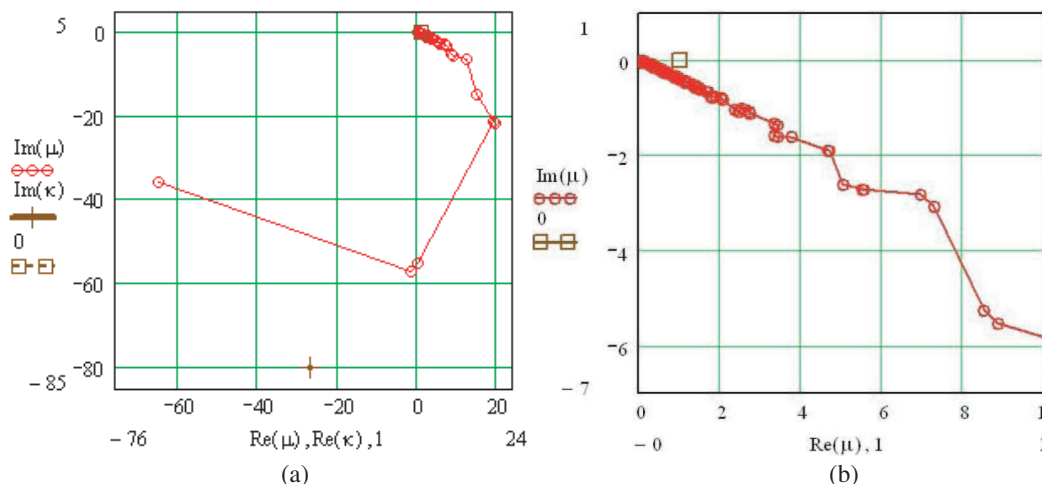


Figure 4: (a) Spectrum and optimal parameter κ , (b) spectrum near to a point of accumulation 0 and point of singularity 1.

4. CONCLUSION

The opportunity of the numerical solution of practical scattering and absorption electromagnetic problems of a microwave range and range of mobile communication on non-uniform biological bodies and structures by means of a method of optimum simple iteration and the volume integral equation of scattering is shown. The solution of specific targets of a resonant range is presented.

REFERENCES

1. "American National Standard safety levels with respect to human exposure to radio frequency electromagnetic fields, 300 kHz to 100 GHz," *IEEE*, NY, 1991.
2. Nguyen, U. D., J. S. Brown, I. A. Chang, J. Krycia, and M. S. Mirotznik, "Numerical evaluation of heating of the human head due to magnetic resonance imaging," *IEEE Trans. Biomed. Eng.*, Vol. 51, No. 8, 2004.
3. Jin, J. M., "Electromagnetics in magnetic resonance imaging," *IEEE Antennas and Propagation Magazine*, Vol. 40, No. 6, 1998.
4. Van Uitert, R., C. Johnson, and L. Zhukov, "Influence of head tissue conductivity in forward and inverse magnetoencephalographic simulations using realistic head models," *IEEE Trans. on Biomed. Eng.*, Vol. 51, No. 12, 2004.
5. Samokhin, A. B., *Integral Equations and Iterative Methods in Electromagnetic Scattering*, 160, Radio I Svyaz, Moscow, 1998.
6. Foster, K. R., H. P. Schwan, and M. A. Stuchly, "Dielectric properties of tissues and biological materials: A critical review," *Crit. Rev. Biomed. Eng.*, Vol. 17, 25–104, 1989.
7. Kulikov, S. P. and A. B. Samokhin, *Mathematical Substantiations of Library Programs for Solution SLAE by a Method of Optimum Simple Iteration*, Vol. 1, No. 2, 71–80, Nauchny vestnik MIREA, Moscow, 2007.

On Singular Integral Equations in the Class of Distributions and Their Appli-ance to Antennas Theory Issues

A. V. Setuha and A. S. Nenashev
Air Force Academy, Moscow, Russia

Abstract— The present article is focused on the theory and methods of numerical calculations for singular and hypersingular integral equations in the class of distributions.

The present paper introduces the definition of “continuation for integral operators with the special integrals”, meaning Cauchy’s principal value and Hadamard’s final value on the distributions. In this concern the approaches based on spectral decomposition as well as on linear functionals extending by their continuity are employed. Formulas of Cauchy and Hilbert integrals inversion are extended to the distributions. The equations of considered types arise at the solution of boundary value problems for Laplas equation in a class of the functions having singularity on border of definition area.

Distributions are entered as continuous linear functionals over some special space of the test functions. It is shown, that considered problem is reduced to the boundary integral equation with singularity in integrals in a class of distributions.

The attained theoretical results are applied for the development of mathematical models of antenna excitation sources and methods of their entrance resistance defining.

1. INTRODUCTION

At present the theory of integral equations is widely used in the solution of various electrodynamic problems. First of all, popularity of the given approach is caused by small computing complexity of turning out numerical schemes in comparison to net methods of the Maxwell equations solution. In the given work development of singular integral equations theory towards continuation of functional space of solutions is offered. As it will be shown later, necessity of such continuation caused by creation of new mathematical models of antenna’s excitation source. Two approaches to introduction of distributions are presented in the solution of integral equations.

2. TEST FUNCTIONS AND DISTRIBUTIONS. CONTINUATION OF OPERATOR

Let Ψ is some space of test functions. In space Ψ the concept of functions sequence $\{\varphi_k\}$, $k \in N$, convergence to function φ is set, which we will name convergence in sense of Ψ and designate as

$$\{\varphi_k\} \xrightarrow{\Psi} \varphi.$$

Let’s consider linear space Ψ' of continuous functionals over Ψ . If $f \in \Psi'$ and $\varphi \in \Psi$ then action f on φ we will designate as $\langle f, \varphi \rangle$. A continuity of functional f we will understand in the following sense

$$\{\varphi_k\} \xrightarrow{\Psi} \varphi \Rightarrow \{\langle f, \varphi_k \rangle\} \rightarrow \langle f, \varphi \rangle.$$

Space of continuous linear functionals Ψ' we will call space of distributions. In space Ψ' it is also possible to define concept of convergence which we will call convergence in sense of Ψ'

$$\{f_k\} \xrightarrow{\Psi'} f \Leftrightarrow \forall \varphi \in \Psi : \{\langle f_k, \varphi \rangle\} \rightarrow \langle f, \varphi \rangle.$$

Let now consider some operator A defined in subspace $\Psi'_1 \subset \Psi'$ which everywhere dense in space Ψ' . We will construct continuation of space operator A in all space Ψ' . We will say that the operator \tilde{A} is continuation of A if

$$\forall \varphi \in \Psi, \forall \{f_k\} \subset \Psi'_1 : \{f_k\} \xrightarrow{\Psi'} f \Rightarrow \langle Af_k, \varphi \rangle \rightarrow \langle \tilde{A}f, \varphi \rangle.$$

Further we will consider concrete examples of integral operators’ continuation construction and their appli-ance to the solution of integral equations.

3. DISTRIBUTIONS OVER THE SPACE OF FINITE FUNCTIONS AND INTEGRAL OPERATORS

Let's consider the space of distributions over the space of finite functions. Let $\Omega \subset R^N$ is some domain. We will say that function φ belongs to space of finite functions $D(\Omega)$ if $\varphi \in C^\infty(\bar{\Omega})$ and there is $\text{supp}\varphi \subset \Omega$ a compact set. We will define convergence of finite functions sequence $\{\varphi_k\}$ to function φ in sense of $D(\Omega)$ as follows

- 1) $\{D^n\varphi_k\} \Rightarrow D^n\varphi$ on set $\bar{\Omega}$ for all derivatives, $D^n = \frac{\partial^{(n)}}{\partial x_{i_1} \dots \partial x_{i_n}}$, $n = 0, 1, \dots$
- 2) There is a compact set $B \subset \Omega$ that $\text{supp}\varphi_k \subset B$, $k = 1, 2, \dots$

Let's notice, that any function $f \in L_1(\Omega)$ can be considered as regular linear functional operating under the formula

$$\langle f, \varphi \rangle = \int_{\Omega} f(x) \varphi(x) dx, \varphi \in D(\Omega).$$

Let's consider space of the distributions $D'(\Omega)$ which we will understand as continuous linear functionals over the space $D(\Omega)$. We will also introduce the space $D^0(\Omega) \subset D'(\Omega)$ defined as

$$D^0(\Omega) = \{f \in D'(\Omega) | \text{supp}f \subset \Omega\}.$$

Let's notice, that it is possible to continue functional $f \in D^0(\Omega)$ in space $C^\infty(\Omega)$ using the formula:

$$\langle f, \varphi \rangle = \langle f, \vartheta\varphi \rangle,$$

where $\varphi \in C^\infty(\Omega)$, ϑ — is a function where $\vartheta \in D(\Omega)$ and $\vartheta \equiv 1$ on $\text{supp}f$.

Let now Ω is the interval on a real axis (a, b) . We will construct continuation of Cauchy's integral operator S in space $D^0(a, b)$ which acts under the following formula

$$(S\varphi)(x_0) = \frac{1}{2\pi} \int_a^b \frac{\varphi(x) dx}{x_0 - x}.$$

At first let $f \in C^1[a, b]$. Then

$$\int_a^b f(x_0) \frac{1}{2\pi} \left(\int_a^b \frac{\varphi(x) dx}{x_0 - x} \right) dx_0 = - \int_a^b \varphi(x) \frac{1}{2\pi} \left(\int_a^b \frac{f(x_0) dx}{x - x_0} \right) dx.$$

Last formula can be written in abbreviated form

$$\langle Sf, \varphi \rangle = - \langle f, S\varphi \rangle. \quad (1)$$

If now f is a linear functional from space $D^0(a, b)$ then (1) allows us to define continuation of S in the space of distributions

$$\langle \tilde{S}f, \varphi \rangle \stackrel{\text{def}}{=} - \langle f, S\varphi \rangle,$$

$f \in D^0(a, b)$, $\varphi \in D(a, b)$.

Let's now consider a solution of integral equation with Cauchy's kernel

$$\frac{1}{2\pi} \int_a^b \frac{g(x) dx}{x_0 - x} = f(x_0). \quad (2)$$

In the classical theory of singular integral equations [1] the equation is considered under condition $f \in H^\mu(a, b)$, $\mu \in (0, 1]$ where $H^\mu(a, b)$ - space of Hölder functions. The continuation of the integral operator defined above allows to solve the equation if $f \in D^0(a, b)$ [2].

Theorem 1. *Let there is $f \in D^*(a, b)$ a function representable in a kind $f = f_1 + f_2$ where $f_1 \in H^\mu(a, b)$, $f_2 \in D^0(a, b)$. Then*

a) *Function*

$$g = -4R^{-1}S[Rf] \quad (3)$$

is a solution of Equation (2) in class of functions $g \in D^*$ satisfying a condition $(g, e) = 0$ where $e \in C^\infty[a, b]$ — a function defined by equality $e(x) \equiv 1$ at $x \in [a, b]$.

Common solution of the Equation (2) in class of functions $g \in D^*$ looks like

$$g = -4R^{-1}S[Rf] + CR^{-1},$$

where C is some undefined constant.

b) Function

$$g = -4R_0^{-1}S[R_0f]$$

is a solution of Equation (2) in class of functions $g \in D^*$ limited in a point $x = b$ and function

$$g = -4R_0S[R_0^{-1}f]$$

is a solution of Equation (2) in class of functions $g \in D^*$ limited in a point $x = a$. Given solution is unique in considered class of functions.

c) The solution of Equation (2) in class of limited functions $g \in D^*$ in points $x = a$ and $x = b$ exists if and only if the following condition is satisfied

$$(f, R^{-1}) = 0,$$

and this solution is defined by the formula

$$g = -4RS[R^{-1}f].$$

Given solution is unique in considered class of functions.

In this theorem:

$$R(x) = \sqrt{(b-x)(x-a)}, \quad R_0(x) = \sqrt{\frac{x-a}{b-x}}.$$

Let's now consider hypersingular integral operator G :

$$(G\varphi)(x_0) = \frac{1}{\pi} \int_{-1}^1 \frac{\varphi(x) dx}{(x-x_0)^2}.$$

We will construct continuation of the given operator on a space of distributions.

Let's consider the given operator in a space of test functions $D(-1, 1)$. If function f such, that $f' \in H^\mu(-1, 1)$, $f(\pm 1) = 0$, we hold

$$(Gf)(x_0) = \frac{1}{2\pi} \int_{-1}^1 \frac{f(x) dx}{(x-x_0)^2} = \frac{1}{2\pi} \int_{-1}^1 \frac{f'(x) dx}{x_0-x} = (Sf')(x_0).$$

Then

$$\langle Gf, \varphi \rangle = \langle Sf', \varphi \rangle = -\langle f', S\varphi \rangle = \langle f, (S\varphi)' \rangle = \langle f, S\varphi' \rangle = \langle f, G\varphi \rangle.$$

Thus, continuation of hypersingular operator in space of distributions is defined as follows

$$\langle \tilde{G}f, \varphi \rangle \stackrel{def}{=} \langle f, G\varphi \rangle.$$

Accordingly, it is possible to consider the equation solution

$$\frac{1}{2\pi} \int_{-1}^1 \frac{g(x) dx}{(x-x_0)^2} = f(x_0). \quad (4)$$

In a case when $f \in D^0(-1, 1)$ the solution of this equation will be functional g operating under the formula:

$$\langle g, \varphi \rangle = \langle \gamma, \psi \rangle,$$

where $\gamma = -4R^{-1}S[Rf]$ (solution of (2) in form (3)), $\psi(x) = \int_{-1}^x \tilde{\varphi}(y) dy$, $\tilde{\varphi}(x) = \varphi(x) - \int_{-1}^1 \varphi(y) dy$.

The offered approach is generalised on hypersingular and singular integral operators in spaces of any dimension.

4. DISTRIBUTIONS OVER THE HILBERT SPACE AND INTEGRAL OPERATORS

Let's now consider the alternative approach to construction of space of distributions used at the solution of the integral equations. Let H is a real Hilbert space (for complex space following constructions remain fair with respective alterations). Operation of dot product of vectors $f, g \in H$ we will write as (f, g) . Let the system of vectors $\{\psi_1, \psi_2, \dots, \psi_n, \dots\}$ is orthonormal basis in space H , i.e., satisfies conditions $(\psi_i, \psi_j) = \delta_{i,j}$. Then any vector f from H is represented as

$$f = \sum_{k=1}^{\infty} a_k \psi_k, \quad \sum_{k=1}^{\infty} a_k^2 < \infty.$$

Let's now define the set of test vectors S in space H .

Definition 1. The vector $f \in H$ belongs to the set of test vectors S if its decomposition on basis has only final number of nonzero coefficients. Let's notice, that the set $S = S(H)$ is linear and everywhere dense in space H but is not closed in H . Therefore we will define in set S other concept of vectors' convergence.

Definition 2. We will say, that the sequence of vectors $f^{(1)}, f^{(2)}, \dots, f^{(n)}, \dots$ from set S converges to a vector f if there is a general number K , that $a_k^{(n)} = 0, k > K, n = 1, 2, \dots$ and for any $n = 1, 2, \dots$ the condition $\lim_{n \rightarrow \infty} |a_k^{(n)} - a_k| = 0$ is satisfied.

The space of test functions together with the defined convergence in it generates space of the distributions as it is described in Section 2. We will consider now the appendix of such construction of the distributions' space to the solution of integral equations.

Let's write spectral parities for singular and hypersingular operators, considered in Section 3.

$$\frac{1}{2\pi} \int_{-1}^1 \frac{1}{\sqrt{1-x^2}} \frac{T_n(x) dx}{x_0 - x} = -\frac{1}{2} U_{n-1}(x_0), \quad x_0 \in (-1, 1), \quad n = 0, 1, 2, \dots \quad (5)$$

$$\frac{1}{2\pi} \int_{-1}^1 \sqrt{1-x^2} \frac{U_n(x) dx}{(x_0 - x)^2} = -\frac{(n+1)}{2} U_n(x_0), \quad x_0 \in (-1, 1), \quad n = 0, 1, 2, \dots \quad (6)$$

where $T_n(x) = \cos(n \arccos x)$, $U_n(x) = \sin((n+1) \arccos x) / \sin(\arccos x)$. Let the function f appeared in the right part of the Equations (2) and (4) is understood as the distribution over Hilbert space, i.e., it is represented in the form

$$f(x_0) = \sum_{k=0}^{\infty} f_k U_k(x_0),$$

then on the basis of spectral parities (5) and (6) the solution of the Equations (2) and (4) can be written as

$$g_S(x) = -\frac{2}{\sqrt{1-x^2}} \sum_{k=1}^{\infty} f_{k-1} T_k(x) + \frac{C}{\sqrt{1-x^2}},$$

$$g_G(x) = -2\sqrt{1-x^2} \sum_{k=0}^{\infty} \frac{f_k}{k+1} U_k(x),$$

where C — some constant, and the numbers standing in the right parts, are understood as distributions over corresponding Hilbert spaces.

5. MATHEMATICAL MODELS OF DIPOLE ANTENNA'S EXCITATION SOURCES

Let's consider a classical problem of dipole antenna radiation as an example [3]. Mathematical model of the dipole antenna excitation by an external field which is described by hypersingular integral equation looks like [4]:

$$\frac{1}{i\omega\epsilon} \int_a^b I(z) \left(\frac{\partial^2}{\partial z_0 \partial z} - k^2 \right) K(z - z_0) dl = E_z^0(z_0), \quad z_0 \in [a, b],$$

where $I(z)$ — the full current induced at the surface of a conductor, $E_z^0(z_0)$ — a longitudinal component of an exciting field, ρ — radius of the dipole antenna,

$$K(z - z_0) = \frac{1}{2\pi} \int_0^{2\pi} \frac{e^{-ik\sqrt{(z-z_0)^2 + 2\rho^2(1-\cos\varphi)}}}{\sqrt{(z-z_0)^2 + 2\rho^2(1-\cos\varphi)}} d\varphi.$$

In work [4] following features of behaviour of function $K(z - z_0)$ are shown when $z \rightarrow z_0$:

$$K(z - z_0) = -\frac{2}{\pi} \frac{\ln \frac{|z-z_0|}{2\rho}}{\sqrt{(z-z_0)^2 + 4\rho^2}} + F_0(z - z_0), \quad (7)$$

$$\frac{\partial}{\partial z} K(z - z_0) = \frac{1 + \omega_1(z - z_0)}{\pi\rho(z_0 - z)} + F_1(z - z_0), \quad (8)$$

$$\frac{\partial^2}{\partial z^2} K(z - z_0) = \frac{1 + \omega_2(z - z_0)}{\pi\rho(z - z_0)^2} + \frac{k^2}{\pi} \frac{\ln \frac{|z-z_0|}{2\rho}}{\sqrt{(z-z_0)^2 + 4\rho^2}} + F_2(z - z_0), \quad (9)$$

where $F_n(x) \in C_{(-\infty, \infty)}^0$, $\omega'_n(x) \in H_{(-\infty, \infty)}^{1-\alpha}$, $0 < \alpha < 1$, $\omega_n(0) = 0$, $n = 1, 2, \dots$

Special interest is represented by a problem of calculation of dipole antenna entrance resistance, as this parameter plays the important role at the coordination of a feeding line and the antenna.

For calculation of the given parameter it is necessary to simulate a field created by feeding line. It is possible to consider a classical model of dipole antenna excitation by the source of EPS described, for example, in work [3]. Its mathematical description looks as follows:

$$E_z(z_0) = \begin{cases} \frac{U}{d}, & z_0 \in \left[-\frac{d}{2}, \frac{d}{2}\right], \\ 0, & z_0 \notin \left[-\frac{d}{2}, \frac{d}{2}\right], \end{cases}$$

where U — source voltage, and d — width of the field concentrated at a surface of a conductor. If limit d to zero then we will receive model so-called as δ — generator:

$$E_z(z_0) = U\delta(z_0).$$

In works [3] and [4] the lack of such mathematical model of antenna's excitation is shown. Namely, the current which is turning out at the solution of the integrated equation has logarithmic feature in a excitation point. Such behaviour of a current mismatches a physical model of the phenomenon. That is why in work [4] the alternative mathematical model of the excitation by the current source has been offered:

$$E_z^0(z_0) = \frac{I}{i\omega\varepsilon} \left(\frac{\partial}{\partial z_0} K\left(z_0 + \frac{d}{2}\right) - \frac{\partial}{\partial z_0} K\left(z_0 - \frac{d}{2}\right) + k^2 \int_{-d/2}^{d/2} K(z - z_0) dz \right).$$

Let's notice, that in this case the surface of the dipole antenna has rupture on a piece $[-d/2, d/2]$. From properties (7)–(9) follows, that the corresponding integral equation will have feature of a kind $(z_0 - q)^{-1}$ in the right part.

Both mathematical models of dipole antenna's excitation lead us to consideration the solution of the integral equation in class of distributions. That is why researches presented in Sections 3 and 4 are actual.

REFERENCES

1. Muskhelishvili, N. I., *Singular Integral Equations*, Nauka, Moscow, 1968 (in Russian).
2. Setuha, A. V., "The singular integral equations with Cauchy's kernel in distributions," *Differential Equations*, Vol. 40, No. 9, 1208–1218, 2004 (in Russian).
3. Vainshtein, L. A., "Symmetric electric fluctuations of ideally spending hollow cylinder of final length," *Journal of Technical Physics*, Vol. 37, No. 7, 1181–1195, 1967 (in Russian).
4. Lifanov, I. K. and A. S. Nenashev, "Hypersingular integral equations and the theory of wire antennas," *Differential Equations*, Vol. 41, No. 1, 121–137, 2005 (in Russian).

Integral Equations Approach to TM-Electromagnetic Waves Guided by a (Linear/Nonlinear) Dielectric Film with a Spatially Varying Permittivity

V. S. Serov¹, K. A. Yuskaeva², and H. W. Schürmann²

¹Department of Mathematical Sciences, University of Oulu, P. O. Box 3000, FIN-90014, Finland

²Department of Physics, University of Osnabrueck, D-49069 Osnabrueck, Germany

Abstract— A method is proposed for obtaining solutions of Maxwell's equations describing guided TM-waves in a three-layer structure consisting of a nonlinear dielectric film situated between two linear semi-infinite media. All media are assumed to be lossless and nonmagnetic. The linear part of the permittivity is modelled by a continuously differentiable real valued function of the transverse coordinate. The problem is reduced to a system of two integral equations. On the basis of the Banach fixed-point theorem, it is shown that the solution exists in form of a uniformly convergent sequence of iterations. The dispersion relation is presented. Some results are evaluated numerically.

1. INTRODUCTION

The exact analytical solution of Maxwell's equations for a plane three-layer structure consisting of a central film between two half-spaces with a permittivity of the film depending on the (transverse) coordinate as well as on the field intensity is not known in the literature (to our knowledge). In particular, solutions representing guided waves are unknown. Compared with the TE-case the TM-case is more complicated leading to a system of two (nonlinear) differential equations that cannot be reduced to an exact differential equation if the permittivity of the film is a function of the coordinate. — Thus, it seems reasonable to consider an integral equation approach [1] to this problem.

2. STATEMENT OF THE PROBLEM

We consider electromagnetic waves guided by a homogeneous, anisotropic, nonmagnetic layer filled with a Kerr-type nonlinear dielectric medium situated between two linear semi-infinite half-spaces $x < 0$ and $x > h$ consisting of isotropic, nonmagnetic media without sources and having constant permittivities ε_1 and ε_3 , respectively. Fig. 1 shows the geometry of the problem.

The (real) electrical field

$$E(x, y, z, t) = E_+(x, y, z) \cos \omega t + E_-(x, y, z) \sin \omega t \quad (1)$$

satisfies Maxwell's equations

$$\operatorname{rot} \mathbf{H} = -i\omega \varepsilon \mathbf{E} \quad (2)$$

$$\operatorname{rot} \mathbf{E} = i\omega \mu \mathbf{H}, \quad (3)$$

where

$$\mathbf{E}(x, y, z) = E_+(x, y, z) + iE_-(x, y, z) \quad (4)$$

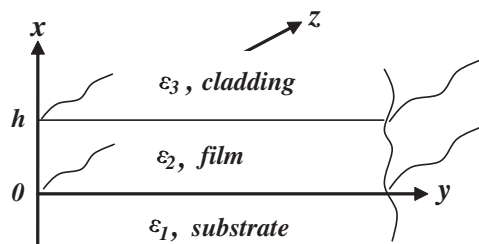


Figure 1: Geometry of the problem.

is a complex amplitude. The permittivity inside the film is described by the Kerr law

$$\varepsilon_2 = \begin{pmatrix} \varepsilon_{21} + f(x) + a|E_x|^2 + b|E_z|^2 & 0 \\ 0 & 0 \\ 0 & \varepsilon_{22} + f(x) + b|E_x|^2 + a|E_z|^2 \end{pmatrix}, \quad (5)$$

where ε_{21} , ε_{22} , a , b are (real) constants and $f(x)$ is a continuously differentiable real-valued function. It can be shown [2] that Maxwell's equations can be reduced to the system

$$\begin{cases} -\frac{d^2 Z}{dx^2} + \gamma \frac{dX}{dx} = \varepsilon_z Z \\ -\frac{dZ}{dx} + \gamma X = \frac{\varepsilon_x}{\gamma} X. \end{cases} \quad (6)$$

Here, the components of the electric field, E_x , E_z , are written as $E_x = -iX(x)e^{i\gamma z}$, $E_z = Z(x)e^{i\gamma z}$ and x , γ , ε have been normalized appropriately [2].

The problem is to find real solutions to (6) X , Z in whole space with real γ and

$$\varepsilon_x = \begin{cases} \varepsilon_1, & x < 0 \\ \varepsilon_{21} + f(x) + aX^2 + bZ^2, & 0 < x < h \\ \varepsilon_3, & x > h \end{cases} \quad (7)$$

$$\varepsilon_z = \begin{cases} \varepsilon_1, & x < 0 \\ \varepsilon_{22} + f(x) + bX^2 + aZ^2, & 0 < x < h \\ \varepsilon_3, & x > h. \end{cases}$$

3. INTEGRAL EQUATIONS AND ITERATIONS

Separating the constant part ε_{21} , ε_{22} in (7) system (6) can be rewritten as

$$\begin{cases} \frac{d^2 Z(x)}{dx^2} + \varepsilon_{22} Z(x) = \gamma \frac{dX(x)}{dx} \tilde{\varepsilon}_z Z(x) \\ \frac{dX(x)}{dx} = \frac{\gamma \frac{d^2 Z(x)}{dx^2} + \frac{d}{dx} (\tilde{\varepsilon}_x X(x))}{\gamma^2 - \varepsilon_{21}} \end{cases}, \quad (8)$$

where

$$\begin{cases} \tilde{\varepsilon}_x = f(x) + aX^2 + bZ^2 \\ \tilde{\varepsilon}_z = f(x) + bX^2 + aZ^2 \end{cases}, \quad (9)$$

and $0 < x < h$.

Combination of (6) and (8) yields

$$\frac{d^2 Z(x)}{dx^2} + \frac{\varepsilon_{22} (\varepsilon_{21} - \gamma^2)}{\varepsilon_{21}} = \frac{\gamma^2 - \varepsilon_{21}}{\varepsilon_{21}} \tilde{\varepsilon}_z Z(x) - \frac{\gamma}{\varepsilon_{21}} \frac{d}{dx} (\tilde{\varepsilon}_x X(x)). \quad (10)$$

For further considerations we assume that $\gamma^2 < \varepsilon_{21}$. Equation (10) can be transformed to the integral equation applying the second Green's formula

$$Z(x) = Z_0(x) - \frac{\varepsilon_{22} (\varepsilon_{21} - \gamma^2)}{\varepsilon_{21}} \int_0^h G(x, y) \tilde{\varepsilon}_z(y) Z(y) dy + \frac{\gamma}{\varepsilon_{21}} \int_0^h G(x, y) \tilde{\varepsilon}_x(y) X(y) dy. \quad (11)$$

$Z_0(x)$ is given by

$$Z_0(x) = E_z^{(0)} \cos \kappa x + \frac{E_z^{(h)} - Z(0) \cos \kappa h}{\sin \kappa h} \sin \kappa x. \quad (12)$$

Here $E_z^{(0)} = Z(0)$ is prescribed and κ is given by $\kappa = \sqrt{\frac{\varepsilon_{22}(\varepsilon_{21} - \gamma^2)}{\varepsilon_{21}}}$. $E_z^{(h)} = Z(h)$ must be determined.

The Green's function $G(x, y)$, corresponding to (10) is defined by [3]

$$G(x, y) = \begin{cases} \frac{\sin \kappa x \sin \kappa(y-h)}{\kappa \sin \kappa h}, & x \leq y \\ \frac{\sin \kappa y \sin \kappa(x-h)}{\kappa \sin \kappa h}, & y \leq x \end{cases}, \quad (13)$$

where $\kappa h \neq \pi l$, $l = 1, 2, \dots$

Integration by parts in (11) yields

$$Z(x) = Z_0(x) - \frac{\varepsilon_{21} - \gamma^2}{\varepsilon_{21}} \int_0^h G(x, y) \tilde{\varepsilon}_z(y) Z(y) dy + \frac{\gamma}{\varepsilon_{21}} \int_0^h \frac{\partial G(x, y)}{\partial y} \tilde{\varepsilon}_x(y) X(y) dy. \quad (14)$$

Using the second equation in (6) and (14) leads to the integral equation for the x -component of the electric field

$$X(x) = \frac{\gamma \varepsilon_{21}}{\varepsilon_x (\gamma^2 - \varepsilon_{21})} \frac{dZ_0(x)}{dx} + \frac{\gamma}{\varepsilon_x} \int_0^h \frac{\partial G(x, y)}{\partial x} \tilde{\varepsilon}_z(y) Z(y) dy + \frac{\gamma^2}{\varepsilon_x (\gamma^2 - \varepsilon_{21})} \int_0^h \frac{\partial^2 G(x, y)}{\partial y \partial x} \tilde{\varepsilon}_x(y) X(y) dy. \quad (15)$$

The system (14) and (15) can be written in matrix form as follows

$$\vec{v}(x) = \vec{v}_0(x) + \int_0^h M(\vec{v})(y) \vec{v}(y) dy + L(\vec{v})(x), \quad (16)$$

where

$$\vec{v}_0 = \begin{pmatrix} Z_0(x) \\ 0 \end{pmatrix}, \quad \vec{v}(x) = \begin{pmatrix} Z(x) \\ X(x) \end{pmatrix}, \quad L(\vec{v})(x) = \begin{pmatrix} 0 \\ \frac{\gamma \varepsilon_{21}}{\varepsilon_x (\gamma^2 - \varepsilon_{21})} \frac{dZ_0(x)}{dx} \end{pmatrix} \quad (17)$$

and matrix M is given by

$$M = \begin{pmatrix} -\frac{\varepsilon_{21} - \gamma^2}{\varepsilon_{21}} G(x, y) \tilde{\varepsilon}_z(y) & \frac{\gamma}{\varepsilon_{21}} \frac{\partial G(x, y)}{\partial y} \tilde{\varepsilon}_x(y) \\ \frac{\gamma}{\varepsilon_x(x)} \frac{\partial G(x, y)}{\partial x} \tilde{\varepsilon}_z(y) & \frac{\gamma^2}{\varepsilon_x(x) (\gamma^2 - \varepsilon_{21})} \frac{\partial^2 G(x, y)}{\partial y \partial x} \tilde{\varepsilon}_x(y) \end{pmatrix}. \quad (18)$$

We consider Equation (16) in the Banach vector space $(C[0, h])$ of continuous complex-valued functions on the segment $[0, h]$ and solve it by iterations using the Banach fixed-point theorem. The iteration sequence

$$\vec{v}_j(x) = \vec{v}_0(x) + \int_0^h M(\vec{v}_{j-1})(y) \vec{v}_{j-1}(y) dy + L(\vec{v}_{j-1})(x), \quad j = 1, 2, \dots \quad (19)$$

yields the exact solution \vec{v} (as the limit of \vec{v}_j) of the Equation (16) if the conditions of the Banach fixed-point theorem are satisfied, namely

$$I_0^2 \leq \frac{4(1 - f_0 b_0)^3}{27 a_0 b_0}, \quad 1 - f_0 b_0 > 0, \quad (20)$$

$$0 < R_{\min} \leq R \leq R_{\max}, \quad (21)$$

where R_{\min} , R_{\max} are two positive roots of the polynomial $a_0 b_0 R^3 - (1 - f_0 b_0) R + I_0 = 0$, and

$$0 < q < 1, \quad (22)$$

where

$$q = 3 a_0 b_0 R^2 + \frac{\kappa h^2 |\gamma| |a^2 - b^2| R^4}{|\sin \kappa h| (\varepsilon_{21} - f_0)^2} + \left(b_0 + \frac{2 a_0 R^2 |\gamma| \kappa h^2}{|\sin \kappa h| (\varepsilon_{21} - f_0)^2} \right) f_0 + \frac{2 |\gamma| \varepsilon_{21} a_0 R}{|\varepsilon_{21} - \gamma^2| (\varepsilon_{21} - f_0)^2} \left\| \frac{dZ_0(x)}{dx} \right\|, \quad (23)$$

$$f_0 = \max |f(x)|, \quad (24)$$

$$a_0 = \max(a; b), \quad (25)$$

$$b_0 = \frac{\kappa h}{2 |\sin \kappa h|} \max \left\{ \frac{h^2 |\varepsilon_{21} - \gamma^2|}{4 \varepsilon_{21}} + \frac{h |\gamma|}{\varepsilon_{21} - f_0}; \frac{h |\gamma|}{\varepsilon_{21}} + \frac{\gamma^2}{|\varepsilon_{21} - \gamma^2| (\varepsilon_{21} - f_0)} \right\}, \quad (26)$$

and

$$I_0 = \|Z_0(x)\| + \frac{|\gamma|\varepsilon_{21}}{|\varepsilon_{21} - \gamma^2|(\varepsilon_{21} - f_0)} \left\| \frac{dZ_0(x)}{dx} \right\|. \quad (27)$$

The a priori error estimate [4] for \vec{v} reads

$$\|\vec{v} - \vec{v}_j\| \leq \frac{q^j}{1 - q} \|\vec{v}_1 - \vec{v}_0\|. \quad (28)$$

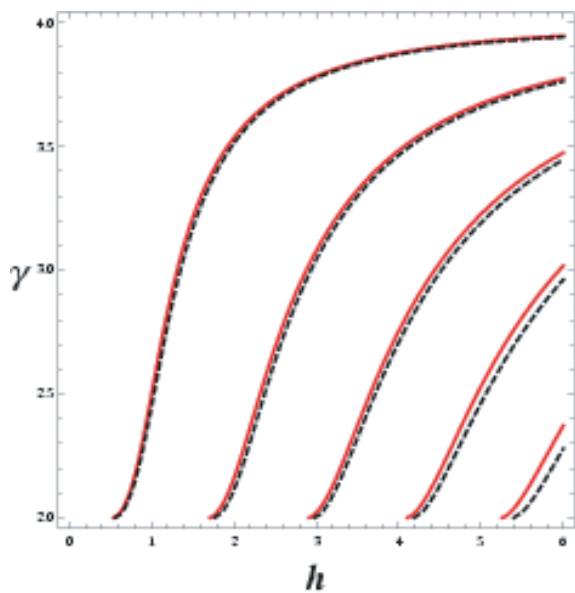


Figure 2: Plot of the dispersion relation for $a = 0$, $b = 0$, $Z(0) = 1$, $m = 0.9$, $n = 0.6$ (solid curves) compared with the linear case (dashed curves), $Z(0) = 1$.

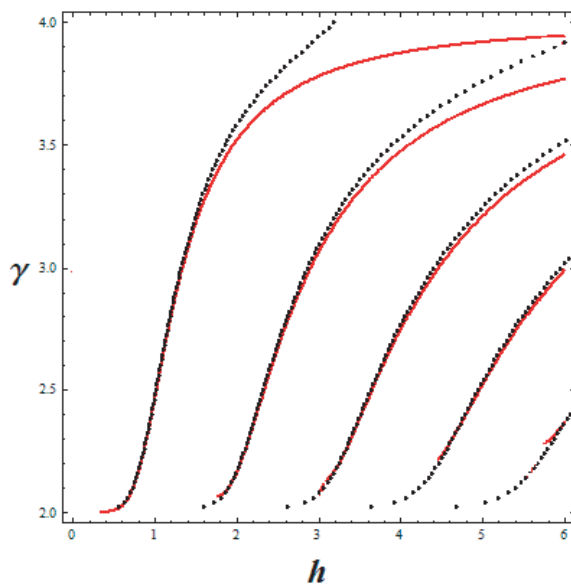


Figure 3: Plot of the dispersion relation for the pure Kerr-case (solid curves) compared with the exact (dashed) curves; $a = 0.3$, $b = 0.2$, $m = 0$, $Z(0) = 1$.

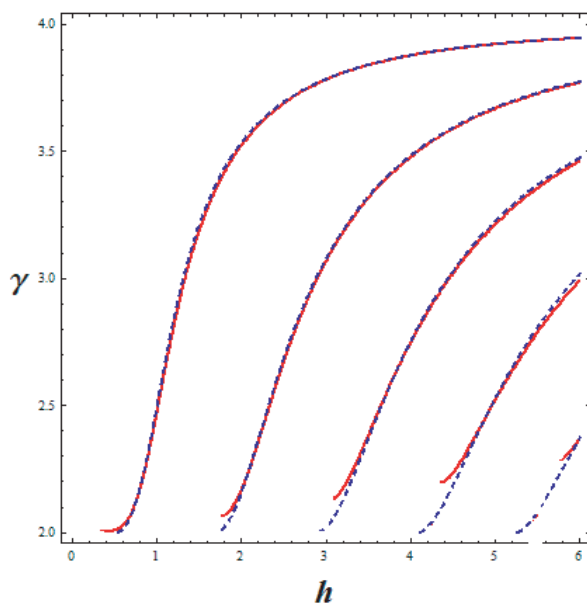


Figure 4: Plot of the dispersion relation for $a = 0.3$, $b = 0.2$, $m = 0.9$, $n = 0.6$, $Z(0) = 1$ (solid curves) compared with the one for $a = 0$, $b = 0$, $m = 0.9$, $n = 0.6$, $Z(0) = 1$ (dashed curves).

4. DISPERSION RELATION

The dispersion relation can be obtained by combining (14), (15) with the boundary conditions. $Z(x)$ and $\gamma X(x) - \frac{dZ(x)}{dx}$ must be continuous at the boundaries $x = 0$ and $x = h$ leading to

$$\varepsilon_x (X(0+0, \gamma, Z(0)), Z(0)) X(0+0, \gamma, Z(0)) = Z(0) \frac{\gamma \varepsilon_1}{\sqrt{\gamma^2 - \varepsilon_1}}, \quad (29)$$

$$\varepsilon_x (X(h-0, \gamma, Z(0)), Z(h, \gamma, Z(0))) X(h-0, \gamma, Z(0)) = -Z(h, \gamma, Z(0)) \frac{\gamma \varepsilon_3}{\sqrt{\gamma^2 - \varepsilon_3}}. \quad (30)$$

Rewriting the left-hand side of (29) by using (15) one obtains,

$$Z(h, Z, X) = Z_{\text{lin}}(h) + \frac{\varepsilon_{21} - \gamma^2}{\varepsilon_{21} \kappa} \int_0^h \sin \kappa(y-h) \tilde{\varepsilon}_z(y) Z(y) dy - \frac{\gamma}{\varepsilon_{21}} \int_0^h \cos \kappa(y-h) \tilde{\varepsilon}_x(y) X(y) dy, \quad (31)$$

where $Z_{\text{lin}}(h) = Z(0)(\cos \kappa h + \beta \sin \kappa h)$ is the solution of the problem in the linear case ($f(x) = 0$, $a = b = 0$) with $\beta = -\varepsilon_1 \sqrt{\frac{\varepsilon_{21} - \gamma^2}{\varepsilon_{21} \varepsilon_{22} (\gamma^2 - \varepsilon_1)}}$. Equations (14), (15), (29), (30) are a representation of dispersion relation. It relates h , γ , $Z(0)$ to the parameters a , b , ε_1 , ε_{21} , ε_{22} , ε_3 and function $f(x)$. Evaluation of the first iteration in (19) yields results shown in Figs. 2–4. The parameters are $\varepsilon_1 = 4$ (in substrate), $\varepsilon_3 = 1$ (in cladding), $\varepsilon_{21} = 16$, $\varepsilon_{22} = 9$ (in the film). We assume $f(x) = m \cos^2 nx$.

5. CONCLUSION

For the TM-case an iterative approach is presented to solve Maxwell's equations for a three layer structure with a permittivity given by (7). The solution $Z(x)$, $X(x)$ has been expressed as a uniformly convergent sequence of iterations of the corresponding vector integral equation (subject to the conditions of the Banach fixed-point theorem). For the problem in question, the Banach conditions are derived and used to estimate the quality of the approximation. The exact dispersion relation is presented and evaluated numerically in first approximation. The approach seems applicable to permittivities more general as (7).

ACKNOWLEDGMENT

One of us (K. A. Y.) gratefully acknowledges the support by the German Science Foundation (DFG) (Graduate College 695).

REFERENCES

1. Serov, V. S., H. W. Schürmann, and E. Svetogorova, "Integral equation approach to reflection and transmission of a plane TE-wave at a (linear/nonlinear) dielectric film with spatially varying permittivity," *Journal of Physics A: Mathematical and General*, Vol. 37, No. 10, 3489–3500, 2004.
2. Yuskaeva, K. A., V. S. Serov, and H. W. Schürmann, "TM-electromagnetic guided waves in a (Kerr-) nonlinear three-layer structure," *Progress In Electromagnetics Research Symposium*, Moscow, Russia, August 18–21, 2009.
3. Stakgold, I., *Green's Functions and Boundary Value Problems*, 2nd Edition, 464–465, Springer-Verlag, New York, 1998.
4. Zeidler, E., *Applied Functional Analysis [Part1]: Applications to Mathematical Physics*, 18–26, Springer-Verlag, New York, 1995.

3G Base Station Optimal Positioning for Heterogenous Network with Fixed Sector and Adaptive Antennas

Lajos Nagy, Andrea Farkasvölgyi, and Róbert Dady

Department of Broadband Infocommunications and Electromagnetic Theory
Budapest University of Technology and Economics
H-1111 Budapest, Goldmann György tér 3, Hungary

Abstract— During the planning of an UMTS radio network, there is a natural need for a base station positioning procedure. Good coverage at an acceptable level of network installation and maintaining costs, low interference and uniform interface load are the main requirements. In this paper, we present an approach based on simulated annealing for optimization of heterogenous radio network with fixed sector antennas and with adaptive antennas.

1. INTRODUCTION

In our paper, we concentrate on the maximal reachable service level at a pre-defined level of cost. It is known that in 3G in order to optimize the radio subsystem there are different aspects to be dealt with than in older systems. This is a consequence of the WCDMA technology and the coherent demodulation. The interference-limited behaviour of an UMTS WCDMA radio network and the technology used causes that the positioning problem which interests us is NP-complete. We are considering several different approaches, the goal of which is the evaluation and the comparison of algorithms that solve this problem. One of the possible solutions relies on the heuristic algorithm known as simulated annealing. We implemented this algorithm, using as inputs user distributions generated by stochastic geometrical processes and a user distribution generated along the main roads of Budapest. We present the interference-model built in the program, describe the used annealing parameters and present the simulation results. Two networks are investigated, the homogenous sectorized base station configuration and the heterogenous with sectorized base station antennas and adaptive antennas. The optimum coverage percentage and the optimal base station positions are compared for the two radio networks.

2. THE PROBLEM

A rectangular area on the plane is given. We know the possible base station positions, which are points of that given area, provided in a realistic case based on regulatory and residential considerations. Typically, the installation of all members of the base station vector would cause too high costs, hence at a complete level of service. We are assuming known the positions of the mobile stations to be served. We define to all subsets of the base station vector a cost function, the values of which are non-negative rational numbers. The task now is to find an algorithm, which identifies a subset with a minimal cost. Heuristic methods can be used to solve this NP-complete combinatorial optimization problem [1], however, the solution might not be optimal. The model in [1] is rather restricted — the two major drawbacks are the two-dimensional representation and the stationary mobile station distribution (in fact, it considers demand node instead of individual mobiles), adopted in this paper too — but it can be still efficiently used for the network layout planning, because the stationary mobile pattern can be evolved through different realizations of the stationary process, thus simulating the dynamic behaviour of the users.

3. SIMULATED ANNEALING

Simulated annealing is a heuristic procedure of optimization, which is based on some results of statistical physics. Today, there are several annealing methods that differ in their complexity and effectiveness. A good survey of the variations can be found in [3]. There also interesting theoretical results in the field of simulated annealing used for discrete combinatorial optimization purposes [4].

In the first case, the simulated annealing is a series of homogenous Markov-chains, this is also called homogenous annealing. Neighbours are searched at a given temperature until stationarity of the chain is reached. Cooling is applied afterwards. The main concern in this case is the chain length. With the properties of Markov-chains, presuming a priori Gaussian distribution and evaluating the chain length until the stationary state of the chain is reached using this assumption,

it can be proven, that at several different cooling schedules the algorithm finds an optimal solution in the discrete solution-space in infinite time with a probability of 1. If we terminate the algorithm in finite time, approximations for the deviation from the minimum can be made in some cases [3].

In the second case, we used as comparison the classical Boltzmann annealing, which is one of the so-called inhomogenous simulated annealing algorithms. After each successful neighbour selection (Metropolis criterion satisfied) follows a cooling and then a new neighbour search. One must be careful here with the choice of the cooling schedule, once the probability density function used to find neighbours in the state space is defined. This is necessary in order to satisfy the condition of finding the minimum with probability 1, achieved if each point in the state space is sampled “infinitely often in annealing time” (IOT) [3]. If not satisfied, we are dealing with the so-called simulated squenching (SQ) case [3] which does not guarantee the finding of the minimum but does not necessarily produce bad results and hence it itself is largely used with success in several areas. The simple neighbourhood probability density paper used in this paper itself represents a Boltzmann squenching rather than annealing, according to [3].

3.1. Neighborhood Structure and Cost Function

We have defined a simple neighbourhood structure, in which given a vector v of BS of cardinality b (the number of BSs that can be simultaneously installed), considers neighbour every vector v' in which one BS differs from v . In other words, the neighbourhood exploration probability density function may be written as:

$$g(\Delta x) = \begin{cases} 1, & \Delta x \leq 1 \\ 0, & \Delta x > 1 \end{cases} \quad (1)$$

which can be shown to be a probability density function. In the first case (homogenous annealing), the cooling schedule has been:

$$T_h(k) = m \cdot T_h(k - 1) \quad (2)$$

where k represents the discretized time. For the case of Boltzmann squenching, the cooling schedule is the well known one:

$$T_B(k) = \frac{T_0}{\ln k} \quad (3)$$

The cost function to be minimized is the number of mobile stations on the plane that are not served, or the sum of the requested downlink bit-rates of these users (we supposed, that the requested downlink bit-rates are not necessarily equal to the uplink ones, due to some 3G services having strongly asymmetric character). In the literature, generally more sophisticated cost functions are used, but these need access to base station cost information in run-time. So the two cost functions in our simulations are:

$$C_1 = \#\{\text{MS}_i \mid \text{MS}_i \text{ not served}\} \quad (4)$$

$$C_2 = \sum_{i, \text{MS}_i \text{ not served}} B_i \quad (5)$$

Evaluating the cost function in itself is not a trivial task. For example, if evaluating first the cost of serving all the mobiles it turns out, that we have reached the soft interference limit or the aggregate bitrate limit, then it is not obvious, which user has to be dropped in order to have an optimal cost function. In a realistic scenario, the inverse is true, namely the system gets more and more loaded until new incomers are refused. The order in which the users switch on determines the exact limit, when the resources are exhausted, therefore different successions will lead to different costs. Clearly some heuristic is necessary. We have followed two different heuristic strategies, according to the cost we are evaluating. In the case of C_1 , we always drop the users for which the following drop cost, is minimal:

$$C_d = c_B \cdot \frac{B}{B_{\max}} + c_I \cdot \frac{d_{\text{MS-BS}}}{d_{\max}} \quad (6)$$

where c_B is a coefficient that reflects our knowledge about low bit-rate mobiles generating less interference as high ones and mobiles at a greater distance from the serving base station generate more interference as mobiles at smaller distances. The choice of coefficients c_B and c_I cannot be made in a simple manner, or at least we do not have the knowledge how to do it. In this work, we

present the case in which we have chosen the value of 0.5 for each. As for C_2 , the drop profit is defined as:

$$P_d = c_B \cdot \frac{B}{B_{\max}} + c_I \cdot \frac{d_{\max}}{d_{\text{MS-BS}}} \quad (7)$$

is maximal.

In order to lower the computational complexity, the droppings are made adaptively: At first, a given percentage of users is dropped. If saturation still holds, we double the percentage of dropped users. If not, we try to reconnect the half of the previously dropped percentage of users and so on. In this paper only simulations using C_1 are considered.

4. UTRAN PHYSICAL LAYER (FMA1 MODE)

According to [5], in a WCDMA UMTS, as a result of the interferences in the two frequency bands, which are alone dedicated for the uplink and respectively the downlink, the link budgets for the uplink and the downlink are presented in the following.

Our model fits only an outdoor environment of microcell type, in which semiempirical models have been established and widely used, see [6] for details. The downlink equations are the following:

$$\left(\frac{E_b}{N_0}\right)_{i, \text{downlink}} \cdot v_{i, \text{downlink}} \cdot G_{i, \text{downlink}} = \frac{(P_{\text{BS}_i}/a_i) \cdot \eta_i}{\sum_{\substack{\text{cell no } j \\ j \neq i}} P_{\text{BS}_j}/a_{ji} + N_{0i} + P_{\text{BS}_i} \cdot (1 - \eta_i)} \quad (8)$$

where $(E_b/N_0)_{i, \text{downlink}}$ is the bit-energy-to-noise ratio of the i th mobile in the downlink direction, $v_{i, \text{downlink}}$ is the activity factor of the user data stream in the downlink, $G_{i, \text{downlink}}$, is the code gain of the i th MS in the downlink, P_{BS_i} is the power of the serving BS, a_i is the propagation attenuation from the serving BS to the i th MS, η_i is the orthogonality factor in the downlink in the neighbourhood of i th MS (between 0 and 1, usual values are from 0.4 to 0.9), P_{BS_j} are the powers of the interfering BS-s (every BS except the serving one), a_{ji} are the propagation attenuations between interfering BS-s and i th MS, N_{0i} being the values of thermal noise in the neighbourhood of the i th MS.

The BS adaptive antenna directional patterns ($F(\varphi)$) are taken into account in a_i and a_{ji} .

$$a_i^{\text{adaptive}} = a_i \cdot F(\varphi_i)$$

$$a_{ji}^{\text{adaptive}} = a_{ji} \cdot F(\varphi_{ji})$$

Figure 1 presents a simple scenario in which these influences are illustrated.

For the downlink the following relationship holds:

$$\left(\frac{E_b}{N_0}\right)_{i, \text{uplink}} \cdot v_{i, \text{uplink}} \cdot G_{i, \text{uplink}} = \frac{P_{\text{MS}_i}/a_i}{\sum_{\substack{\text{cell no } j \\ j \neq i}} P_{\text{MS}_j}/a_{ji} + N_{0i}} \quad (9)$$

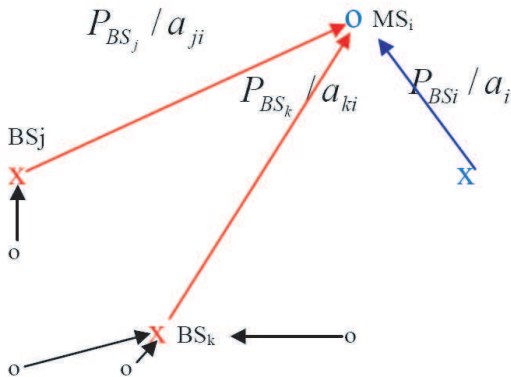


Figure 1: Downlink interference.

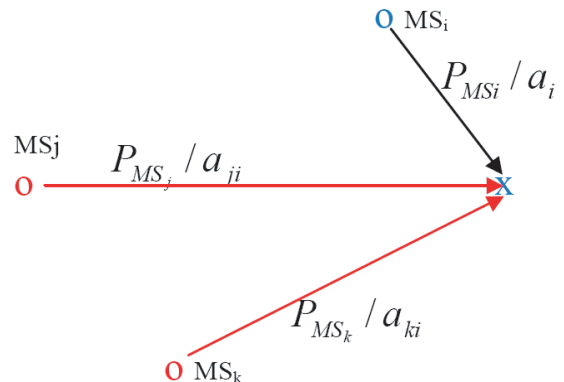


Figure 2: Uplink influences.

where $(E_b/N_0)_{i,\text{uplink}}$, represents the bit-energy-to-noise ratio for the i th MS in the uplink, $v_{i,\text{uplink}}$ is the activity factor of the i th MS in the uplink, $G_{i,\text{uplink}}$, is the code gains for the data flow of i th MS, $P_{\text{MS}i}$, is the uplink power of i th MS, a_i is the attenuation between i th MS and the serving BS, a_{ji} is the propagation attenuation between j th MS and the serving BS of i th MS and N_{0i} is the noise of the serving BS of i th MS. Fig. 2 presents a simple scenario in which these influences are briefly presented. The adaptive antenna pattern effect is taken into account as in downlink direction.

The two linear equation systems are solved in each step of the procedure before calculating cost, in order to verify the correctness of a mobile station — Base station link structure.

In our model, there is a one to one mapping between the link structure and one subset2 of the possible BS positions — Which is one solution of the combinatorial optimization problem [4]. The unequivocal character of the cost is a consequence of that property.

The following assumptions are made in the physical layer:

- 1) Power control is ideal, in other words, every communicating item transmits at a level that assures the prescribed bit-energy-to-noise ratio,
- 2) Each MS is supposed to generate only one type of traffic. This assumption does not reduce generality. For example, a 3G terminal generating voice and video traffic can be viewed as two different terminals, one generating voice traffic and the second one generating a video stream, being closely positioned in the 2D plane.

At this point, soft and hard handover are not taken into account.

- 3) First simple empirical wave propagation modeling has been selected (Hata and Okumura) [5], for the sake of simplicity. Results within this article are based on the COST231 Walfisch-Ikegami model. A more realistic simulation needs a more precise model, appropriate for the radio environment specific for microcells.
- 4) At this moment, only one layer of cells is taken into account. In other words, parallel coverage of locations by indoor and microcell base stations is not considered yet.
- 5) In this work, the user and BS locations are based on a tool considering the traffic on the main roads of Budapest.

5. SIMULATION RESULTS

First simulation results using the homogenous annealing are presented. A total number of 369 MS-s have been considered, main parameters: Orthogonality 1, bitrates 12.2 and 64 kbps, activity 1, max. power 125 mW, E_b/N_0 4.2 and 3.9 dB. As for the BS-s, 75 possible locations have been offered, from which we have elected a budget of 5, 10, 15, 20 and 25. Their main parameters: 2 Mbps max. bitrate capacity, 20 W max. transmitted power (common and shared channels are neglected). Fig. 4 present the evolution of the cost function in the first of the 5 presented cases.

One can observe that for BS = 15, a minimal cost of 0 exists, but for BS = 5, this minimum is not reached, in other words, we have MS-s that are not served.

The initial value for the control parameter has been 24 and the multiplier factor α as been 0.9. The length of each independent homogenous Markov chain was the 1/4-th of the cardinality of the

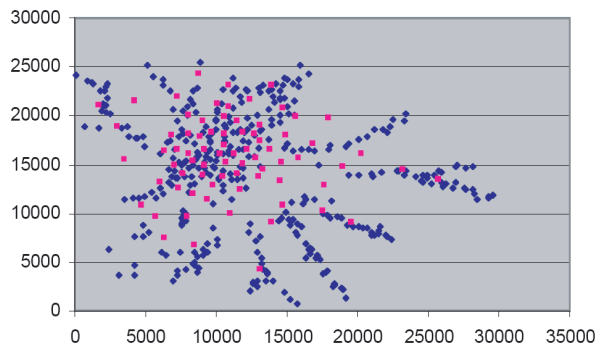


Figure 3: BS and MS along the main roads of Budapest.



Figure 4: Cost function, BS = 5, homogenous, thr = 20.

neighborhood of a solution. Note that every solution has the same number of neighbours for which case the theorems stated in [3] are valid.

In order to avoid infinite loops in the case of trapping in local minima, we have defined a threshold (thr in Fig. 4) for unsuccessful Metropolis trials, which has been 20 in this first set of simulations. One can remark the convergence of the algorithm towards smaller values of the cost function in the cases of too low budgets and towards 0 in the case of appropriately high budgets Fig. 5 presents the obtained layout for the presented case:

In the second set of simulations, we have analyzed how the length of the Markov chains affects the convergence of the algorithm and the finding of the minimum. We have chosen a BS budget of 10 which has been found undersized during the first set of simulations. The Metropolis threshold has been the same, 20. Surprisingly, we have found that for relatively low chain sizes (20, 40 and 60) the algorithm finds an optimum, but for bigger chains, it doesn't find one. Fig. 6 presents the convergence in the case of chain size 20:

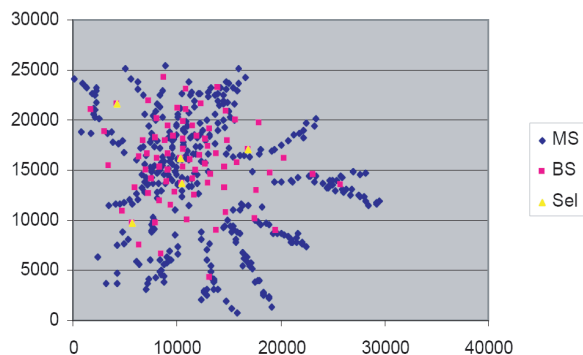


Figure 5: Layout for BS budget = 5.

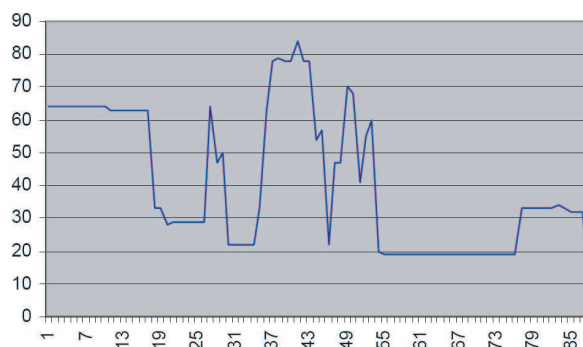


Figure 6: Convergence for chain size 20, BS budget 10.

Finally, in the third set of simulations, the Boltzmann squenching has been analyzed for the case of BS budget of 10 and for different initial temperatures. We have found that no matter how high the initial temperature was, the squenching did not find the minimal cost, which obviously existed, as already seen in the case of homogenous annealing with relatively small chain sizes. Increasing the Metropolis threshold with an order of magnitude (from 20 to 200) did not significantly change the outcome, meaning that indeed the simulation has been trapped in a local minimum and the cooling was too fast, in fact rather a squenching.

6. CONCLUSIONS AND OUTLOOK

Different homogenous and inhomogenous simulated annealing and squenching algorithms have been tested from the viewpoint of fitness to solve the BS selection problem for WCDMA multiple access. We have found that homogenous annealing is more appropriate than Boltzmann squenching and medium sized Markov chains behave better than chains having bigger size. On the other hand, using squenching instead of annealing for the homogenous case is not appropriate in this case.

In order to be able to draw more general conclusions, several inhomogenous annealing and squenching algorithms have to be tested against each other. For the homogenous case, a method for the evaluation of the appropriate chain size has to be provided.

Instead of the simple cost function presented herein more complex ones have to be tested as well and the performance of the method will be compared with other heuristics: Simple genetic algorithms and tabu search.

ACKNOWLEDGMENT

This work was carried out in the framework of Mobile Innovation Center, Hungary (Mobil Innovációs Központ) supported by the National Office for Research and Technology (NKTH) Asbóth Oszkár Programme.

REFERENCES

1. Tran-Gia, P. and N. Gerlich, "Impact of customer clustering on mobile network performance," Report, No. 143, Institute of Computer Science, University of Würzburg, 1996.

2. Galota, M., C. Glasser, S. Reith., and H. Vollmer, “A polynomial approximation scheme for base station positioning in UMTS networks,” *Proc. Discrete Algorithms and Methods for Mobile Computing and Communications*, 2001 (Electronic Version).
3. Ingberg, L., “Simulated annealing: Practice versus theory,” *Mathl. Comput. Modeling*, Vol. 18, No. 11, 29–57, 1993.
4. Aarts, E. and J. Korst, *Simulated Annealing and Boltzmann Machines: A Stochastic Approach to Combinatorial Optimization and Neural Computing*, Wiley, 1989.
5. Harri, H., and A. Toskala, *WCDMA for UMTS*, 155–170, Wiley, 2000.
6. COST 231 Final Report.
7. Nagy, L., Z. Sándor, Z. Szabó, B. Pelhős, and I. Laki, “Deterministic urban wave propagation models,” *Proceedings of the Microcoll*, 253–256, Budapest, Hungary, 2000.
8. Farkas, L., C. Orosz, and L. Nagy, “UTRAN resource planning based on a PTAS using a complex profit function,” *URSI General Assembly*, Maastricht, the Netherlands, 2002.

Tuning Microstrip Patch Antennas on Ferrite Substrate Using Simple Ground Plane Structures

M. A. Alsunaidi

King Fahd University of Petroleum & Minerals, Saudi Arabia

Abstract— An additional tuning strategy for microstrip patch antennas on magnetized ferrite substrates is presented. It is shown that by introducing simple ground plane structures, the response of the patch antenna can be improved considerably. The analysis method is based on a 3D FDTD algorithm. The FDTD model utilizes the auxiliary differential equation approach to represent the frequency dependent permeability tensor in the time domain equations. The resulting 3D full-wave numerical model is tested and verified against experimental data showing very good agreement.

1. INTRODUCTION

Microstrip patch antennas on ferrite substrates offer a number of advantages over normal dielectric material. Due to their fairly high dielectric constant, miniaturization is possible. Further, because of the property of frequency tuning by external biasing fields, the radar cross section of such antennas can be reduced [1–6]. Also, changing the beam width and direction is possible in ferrite-based antenna arrays [7]. However, the analysis of ferrite-based problems is often complex due to the inherent anisotropy and nonlinearity in the material. Analytical solutions are generally inaccurate because they are based on simplifying assumptions [8]. Therefore, the development of accurate numerical techniques is essential. Several numerical techniques have been used to study the response of ferrite-based microstrip patch antennas including the finite-element method (FEM) [9], the transmission line method (TLM) [10] and using Green's functions [11]. Schuster and Luebbers [12] reported the application of the FDTD method coupled with the recursive convolution method to model the frequency dependent response of ferrite materials. In their algorithm, four convolutions in the update equations required the storage of four complex numbers per cell. Because the FDTD method solves for the basic field quantities, it offers a great amount of information usually from one simulation run. This property makes the method very attractive and very popular in the computational electromagnetics society [13]. The FDTD algorithm presented in this paper is a straightforward full-wave algorithm based on the auxiliary differential equation (ADE) technique [14] to model the frequency dependent permeability tensor of ferrite materials. The resulting scheme retains the fully explicit nature of the original FDTD method and enjoys the same features of flexibility and simplicity. It is used in this paper to investigate the tuning capability of simple ground plane structures on the response of a microstrip patch antenna printed on a magnetized ferrite substrate. The simulation results are compared to published experimental data.

2. FORMULATIONS

For a ferrite material with magnetizing DC field in the z -direction, the frequency-dependent permeability tensor is given by

$$\mu = \begin{bmatrix} \mu_r & jk & 0 \\ -jk & \mu_r & 0 \\ 0 & 0 & \mu_o \end{bmatrix} \quad (1)$$

The non-zero elements in Equation (1) are given by

$$\mu_r = \mu_o \left[1 + \frac{\omega_m(\omega_o + j\alpha\omega)}{(\omega_o + j\alpha\omega)^2 - \omega^2} \right] = \mu_o + \frac{\mu_o\omega_m\omega_o + (j\omega)\alpha\mu_o\omega_m}{\omega_o^2 + (j\omega)2\alpha\omega_o + (j\omega)^2(1 + \alpha^2)} \quad (2)$$

and

$$jk = \frac{j\mu_o\omega_m\omega}{(\omega_o + j\alpha\omega)^2 - \omega^2} = \frac{(j\omega)\mu_o\omega_m}{\omega_o^2 + (j\omega)2\alpha\omega_o + (j\omega)^2(1 + \alpha^2)} \quad (3)$$

where, $\omega_m = 2\pi\gamma M_s$ is the magnetization frequency, $\omega_o = 2\pi\gamma(H_{DC} - N_z M_s)$ is the resonance frequency, γ is the gyromagnetic ratio, M_s is the saturation magnetization, H_{DC} is the applied

DC magnetic field, N_z is the demagnetization, α is the damping factor and μ_o is the free space permeability. The magnetic flux density, B , is given by

$$\begin{pmatrix} B_x \\ B_y \\ B_z \end{pmatrix} = \begin{bmatrix} \mu_r & jk & 0 \\ -jk & \mu_r & 0 \\ 0 & 0 & \mu_o \end{bmatrix} \begin{pmatrix} H_x \\ H_y \\ H_z \end{pmatrix} \quad (4)$$

Employing the ADE approach, the components of B in Equation (4) can be written in the time domain as

$$\begin{aligned} \omega_o^2 B_x + 2\alpha\omega_o \frac{\partial B_x}{\partial t} + (1 + \alpha^2) \frac{\partial^2 B_x}{\partial t^2} &= \mu_o\omega_o(\omega_o + \omega_m)H_x + \mu_o\alpha(2\omega_o + \omega_m) \frac{\partial H_x}{\partial t} \\ &+ \mu_o(1 + \alpha^2) \frac{\partial^2 H_x}{\partial t^2} + \mu_o\omega_m \frac{\partial H_y}{\partial t} \end{aligned} \quad (5)$$

$$\begin{aligned} \omega_o^2 B_y + 2\alpha\omega_o \frac{\partial B_y}{\partial t} + (1 + \alpha^2) \frac{\partial^2 B_y}{\partial t^2} &= \mu_o\omega_o(\omega_o + \omega_m)H_y + \mu_o\alpha(2\omega_o + \omega_m) \frac{\partial H_y}{\partial t} \\ &+ \mu_o(1 + \alpha^2) \frac{\partial^2 H_y}{\partial t^2} - \mu_o\omega_m \frac{\partial H_x}{\partial t} \end{aligned} \quad (6)$$

and,

$$B_z = \mu_o H_z \quad (7)$$

The resulting fully-explicit algorithm [14] starts by first finding all B^{n+1} components using the usual Yee's algorithm. Next, H_x^{n+1} , H_y^{n+1} and H_z^{n+1} are computed in the given order using Equations (5)–(7). Finally, the electric field components are computed using the standard Yee's algorithm.

3. SOLUTION METHOD AND NUMERICAL RESULTS

To test the application of the proposed numerical scheme to microstrip patch antennas, the response of a typical patch antenna is considered. The structure is shown in Figure 1 with the following dimensions: $x_1 = 9$ mm, $x_2 = 5$ mm, $x_3 = 2.5$ mm, $y_1 = 3.1$ mm, $y_2 = 0.7$ mm, $y_3 = 0.3$ mm and $y_4 = 0.9$ mm. The antenna is printed on a ferrite substrate with thickness of 1 mm, dielectric constant of 13.69, loss tangent of 0.0002 and saturation magnetization of 27.85 kA/m. The gyromagnetic ratio is taken as 35.173 kHz m/A. A DC biasing magnetic field of 234 kA/m is applied in the z -direction. Figure 2 shows the simulated return loss parameter (S_{11}) for the patch antenna under investigation. The simulation results are compared to published experimental data for the same antenna [10]. The simulated response shows three distinct resonances that can be identified at 6.6075 GHz, 7.1775 GHz and 8.1375 GHz. In general, the agreement between the measured and simulated responses is very good. To examine the effectiveness of device tuning using ground plane

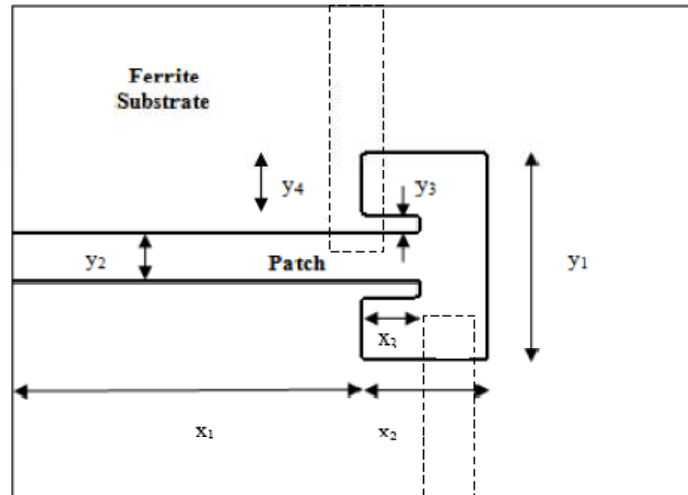


Figure 1: The ferrite-based patch antenna used in the analysis.

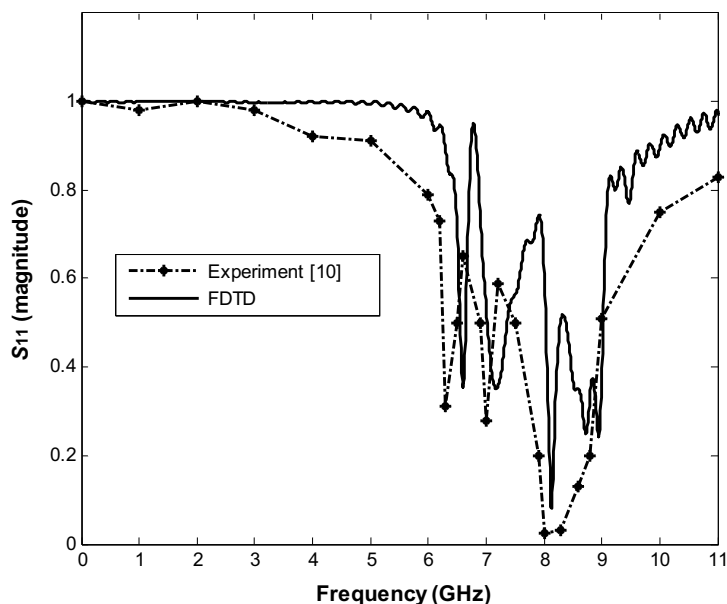


Figure 2: Return loss parameter S_{11} for the patch antenna as obtained using the FDTD calculations compared to experimental data [10].

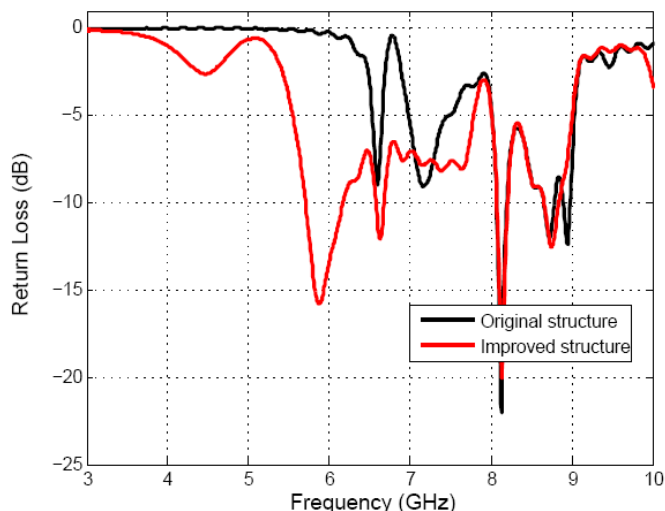


Figure 3: Return loss parameter for the patch antenna as obtained using the FDTD calculations with ground plane features of Figure 1 introduced.

structures, the features shown in Figure 1 (dashed lines) are introduced in the ground plane. Figure 3 shows the simulated return loss parameter for the original patch antenna under investigation with complete ground plane (black line) and the antenna response with ground plane features introduced (red line). The simulated response shows that the response is improved and can be tuned to the desired frequency and bandwidth. Future analysis will focus on the possibilities of tuning the device further by changing the dimensions and orientation of the ground plane features.

4. CONCLUSIONS

The response of microstrip patch antennas on magnetized ferrite substrates has been investigated using a 3D full-wave FDTD algorithm. To incorporate the frequency-dependent nature of the permeability tensor of the ferrite material in the time domain equations, the auxiliary differential equation approach has been utilized. Additionally, tuning of the device response using simple ground plane structures has been demonstrated. This method can introduce improvements to device bandwidth as well.

ACKNOWLEDGMENT

The author would like to acknowledge the support of King Fahd University of Petroleum & Minerals.

REFERENCES

1. Baden-Fuller, A. J., *Ferrite at Microwave Frequencies*, IEE Publishing, 21–28, 1987.
2. Pozar, D. M. and V. Sanchez, “Magnetic tuning of a microstrip antenna on a ferrite substrate,” *Electronics Letters*, Vol. 24, 729–731, 1988.
3. Pozar, D. M., “Radar cross-section of microstrip antenna on normally biased ferrite substrate,” *Electronics Letters*, Vol. 25, 1079–1080, 1989.
4. Pozar, D. M., “Radiation and scattering characteristics of microstrip antenna on normally biased ferrite substrates,” *IEEE Trans. Antennas Propag.*, Vol. 40, 1084–1092, 1992.
5. Mishra, R. K., S. S. Pattnaik, and N. Das, “Tuning of microstrip antenna on ferrite substrate,” *IEEE Trans. Antennas Propag.*, Vol. 41, 230–233, 1993.
6. Tsang, K. K. and R. J. Langley, “Design of circular patch antennas on ferrite substrates,” *IEE Proc. — Microwave Antennas Propag.*, Vol. 145, 49–55, 1998.
7. Batchelor, J. C. and R. J. Langley, “Microstrip ring antenna operating at higher order modes for mobile communications,” *IEE Proc. — Microwave Antennas Propag.*, Vol. 142, 151–155, 1995.
8. Kyriacou, G. A., A. A. Mavridis, and J. N. Sahalos, “Approximate resonant frequencies of certain antennas printed on magnetized ferrites,” *URSI Int. Symp. on Electromagnetic Theory*, Vol. 97, 13–21, 1999.
9. Brown, A. D., J. L. Volakis, L. C. Kempel, and Y. Botros, “Patch antennas on ferromagnetic substrates,” *IEEE Trans. Antennas Propag.*, Vol. 47, 26–32, 1999.
10. Sobhy, M. I., M. W. Ng, R. J. Langley, and J. C. Batchelor, “TLM analysis of microstrip patch antenna on ferrite substrate,” *IEEE MTT-S Digest*, 1297–1300, 1999.
11. Losada, V., R. R. Boix, and M. Horno, “Resonant modes of circular microstrip patches over ground planes with circular apertures in multilayered substrates containing anisotropic and ferrite materials,” *IEEE Trans. Microwave Theory Tech.*, Vol. 48, 1756–1762, 2000.
12. Schuster, J. and R. Luebbers, “FDTD for three-dimensional propagation in a magnetized ferrite,” *IEEE Antenna and Propag. Society International Symposium*, 1648–1651, 1996.
13. Taflove, A., *Computational Electrodynamics: The Finite-Difference Time-Domain Method*, Artech House, Norwood, MA, 1995.
14. Alsunaidi, M. A., “FDTD analysis of microstrip patch antenna on ferrite substrate,” *Microwave and Opt. Tech. Lett.*, 1848–1851, 2008.

Regularization of Boundary Integral Equations in a Easy-to-Implement and Efficient Method

E. Korkmaz

Department of Electrical and Electronics Engineering, Fatih University, Turkey

Abstract— In this paper, a simple and easy to implement regularization technique has been introduced for both EFIE and MFIE. The singularity of Green's function is coped by taking the spherical mean over only the singular part of Green's function which is little different than spherical mean of Green's function as a whole. After regularization of integral equations the solutions are obtained by means of conjugate gradient method.

1. INTRODUCTION

The calculation of electromagnetic scattering from arbitrarily shaped perfectly electrical conducting materials find broad applications in RCS calculations. Since analytical solutions are available only for limited geometries numerical techniques has to be used. Usually the scattering from PEC objects are formulated by boundary integral equation formulations. This formulation is based on the calculation of unknown surface current induced on the surface of the scatterer when it is irradiated by an incident wave. This formulation leads to two types of integro-differential equations for the surface current, the electric field integral equation (EFIE) and the magnetic field integral equation (MFIE). From the theoretical point of view both equations are expected to give a solution for an arbitrary scatterer. In MFIE formulation the extra cross product with the unit vector can cause numerical instabilities when it is used for thin bodies or bodies with edges and corners. On the other hand EFIE does not suffer the same limitations and is expected to be capable to solve both for closed and open surfaces [1]. However for arbitrarily shaped objects the regularization of EFIE is more difficult from the presence of derivatives appearing in conjunction with its singular kernel in the integral equation.

The regularization of these integral equations starts with the proper choice of basic functions to represent the induced unknown current on the surface. In the literature Rao-Wilton-Glisson (RWG) functions are the mostly used basis and testing functions [2]. Further, solving the EFIE and MFIE in frequency domain involves the integration of Green's function kernel and its derivatives which possesses singularity when the point of interest coincides with the point of integration. Several techniques have been introduced to cope with the singularity problem. E.g., spherical mean of Green's function [3] and the singularity extraction technique [4, 5]. The singularity extraction method is the most popular one and it is well established for RWG basis function, however, in the application suffers accuracy problems and complexity of the implementation.

In this paper, a simple and easy to implement regularization technique has been introduced for both EFIE and MFIE. For the basis and testing functions the barycentric coordinate system is used which is easy to evaluate. The singularity of Green's function is coped by taking the spherical mean over only the singular part of Green's function which is little different than spherical mean of Green's function as a whole. After regularization of integral equations the solutions are obtained by means of conjugate gradient method.

2. BOUNDARY INTEGRAL EQUATIONS

The induced unknown current density \mathbf{J} is a solution of an integral equation which can be calculated from the following boundary integral equations

$$[\mathbf{n} \times \mathbf{E}^i](\mathbf{x}_p) = \frac{1}{i\omega\epsilon_0} \mathbf{n}_p \times [k_0^2 + \nabla_p \nabla_p] \oint_S G(R) \mathbf{J}(\mathbf{x}) dS, \quad (1)$$

$$[\mathbf{n} \times \mathbf{H}^i](\mathbf{x}_p) = \frac{1}{2} \mathbf{J}(\mathbf{x}_p) - \mathbf{n}_p \times \left[\nabla_p \times \oint_S G(R) \mathbf{J}(x) dS \right], \quad (2)$$

where (1) is the electric field integral equation and (2) is the magnetic field integral equation. In the equations \mathbf{n} and \mathbf{n}_p are the unit vectors along the normal to the scatterer surface S at position \mathbf{x} and \mathbf{x}_p , while \mathbf{E}^i and \mathbf{H}^i are the incident electric and magnetic fields, k_0 is the free space wave

number, and $R = |\mathbf{x} - \mathbf{x}_p|$. The ∇_p and $\nabla_p \nabla_p \cdot$ operators represent the spatial differentiations with respect to \mathbf{x}_p , while the integrations are with respect to \mathbf{x} . The free space Green's function is given by

$$G(\mathbf{x} - \mathbf{x}_p) = \frac{e^{ik_0 R}}{4\pi R}. \quad (3)$$

The kernel of integral Equations in (1) and (2) are singular when $\mathbf{x} = \mathbf{x}_p$. To avoid the singularity we replace the kernel in a discretized form by its spherical mean to obtain a weak formulation. The radius of the spherical domain is taken equal to the average discretization size Δ of the object under consideration. In this work, we do not take the spherical mean of the whole Green's function but we restrict it to the singular part only, $1/4\pi R$ [6]. The weak formulation of Green's function is

$$G^w(R) = \begin{cases} \frac{3e^{ik_0 R}}{4\pi \Delta^3} \left(\frac{1}{2} \Delta^2 - \frac{1}{6} R^2 \right), & \text{when } 0 \leq R < \Delta \\ \frac{e^{ik_0 R}}{4\pi R}, & \text{when } \Delta \leq R < \infty \end{cases} \quad (4)$$

for the MFIE we need also the gradient of Green's function

$$\nabla_p G^w(R) = -(\mathbf{x} - \mathbf{x}_p) \begin{cases} [ik_0 R - 1] \frac{e^{ik_0 R}}{4\pi \Delta^3}, & \text{when } 0 \leq R < \Delta \\ [ik_0 R - 1] \frac{e^{ik_0 R}}{4\pi R^3}, & \text{when } \Delta \leq R < \infty \end{cases} \quad (5)$$

further, for the EFIE we need the gradient divergence of Green's function

$$\nabla_p \nabla_p G^w(R) \cdot \mathbf{J} = \begin{cases} \frac{\exp(ik_0 R)}{4\pi \Delta^3} [k_0^2 (\mathbf{x} - \mathbf{x}_p)(\mathbf{x} - \mathbf{x}_p) \cdot \mathbf{J} + (ik_0 R - 1) \mathbf{J}], & \text{when } 0 \leq R < \Delta \\ \frac{\exp(ik_0 R)}{4\pi R} \left[\frac{3\Theta_p \Theta_p \cdot \mathbf{J} - \mathbf{J}}{R^2} + \frac{ik_0 (\mathbf{J} - 3\Theta_p \Theta_p \cdot \mathbf{J})}{R} - k_0^2 \Theta_p \Theta_p \cdot \mathbf{J} \right], & \text{when } \Delta \leq R < \infty \end{cases} \quad (6)$$

where $\Theta_p = \nabla_p |x - x_p| = -(x - x_p)/|x - x_p|$ is the unit vector.

3. NUMERICAL EVALUATION OF INTEGRAL EQUATIONS

Typically the boundary surface S is discretized into N planar triangular surface elements S_n . The position vectors of the vertices on a triangular patch S_n are denoted as $\mathbf{x}_{n,i}$, $\{i = 1, 2, 3\}$. The barycentric linear interpolation function has been used to express any quantity defined on S_n , so that the integral over the object surface S of the surface current $\mathbf{J}(x)$ is replaced by

$$\oint_S \mathbf{J}(\mathbf{x}) dS = \sum_{n=1}^N \sum_{i=1}^3 \frac{A_n}{3} \mathbf{J}(\mathbf{x}_{n,i}). \quad (7)$$

Since the weak formulation of Green's function is now continuous and bounded everywhere, we are able to discretize the integral equations of (1) and (2) straightforwardly, using a linear interpolation of the integrand as described in [7]. We consider a finite set of equations by requiring consistency in each node j of each triangle patch m with normal vector \mathbf{n}_m . After interchanging the order of differentiation and integration, we obtain

$$[\mathbf{n} \times \mathbf{E}^i](\mathbf{x}_{m,j}) = \frac{1}{i\omega\epsilon_0} \mathbf{n}_m \times \sum_{n=1}^N \sum_{i=1}^3 \frac{A_n}{3} [k_0^2 + \nabla_{m,j} \nabla_{m,j} \cdot] G^w(\mathbf{x}_{n,i} - \mathbf{x}_{m,j}) \mathbf{J}(\mathbf{x}_{n,i}), \quad (8)$$

$$[\mathbf{n} \times \mathbf{H}^i](\mathbf{x}_{m,j}) = \frac{1}{2} \mathbf{J}(\mathbf{x}_{m,j}) - \mathbf{n}_m \times \left[\sum_{n=1}^N \sum_{i=1}^3 \frac{A_n}{3} \nabla_{m,j} G^w(\mathbf{x}_{n,i} - \mathbf{x}_{m,j}) \times \mathbf{J}(\mathbf{x}_{n,i}) \right]. \quad (9)$$

For the solution of these integral equations the conjugate gradient scheme has been used. The error criterion is based on the normalized error norm

$$\text{ERR}_{EFIE} = \frac{\|\mathbf{n} \times \mathbf{E}^i - \mathbf{LJ}\|_S^2}{\|\mathbf{n} \times \mathbf{E}^i\|_S^2} \quad (10)$$

$$\text{ERR}_{MFIE} = \frac{\|\mathbf{n} \times \mathbf{H}^i - \mathbf{KJ}\|_S^2}{\|\mathbf{n} \times \mathbf{H}^i\|_S^2}, \quad (11)$$

where \mathbf{LJ} is the right hand side of Equation (8) and \mathbf{KJ} is the right hand side of Equation (9). The norm of a vector \mathbf{F} on S is defined as

$$\|\mathbf{F}\|_S^2 = \langle \mathbf{F}, \mathbf{F} \rangle_S = \sum_{m=1}^N \sum_{j=1}^3 \frac{A_m}{3} \mathbf{F}(\mathbf{x}_{m,j}) \cdot \overline{\mathbf{F}}(\mathbf{x}_{m,j}), \quad (12)$$

where the overline denotes the complex conjugate. The adjoint operators are

$$\begin{aligned} L^*[\mathbf{n} \times \mathbf{J}] &= \mathbf{n}_m \times \mathbf{n}_m \\ &\times \frac{i}{\omega \varepsilon_0} \sum_{n=1}^N \sum_{i=1}^3 \frac{A_n}{3} [k_0^2 \overline{G^w}(\mathbf{x}_{n,i} - \mathbf{x}_{m,j}) + \nabla_{n,i} \nabla_{n,i} \overline{G^w}(\mathbf{x}_{m,j} - \mathbf{x}_{n,i})] [\mathbf{n} \times \mathbf{J}](\mathbf{x}_{n,i}) \end{aligned} \quad (13)$$

$$\mathbf{K}^*[\mathbf{n} \times \mathbf{J}] = \frac{1}{2} [\mathbf{n} \times \mathbf{J}](\mathbf{x}_{n,i}) + \mathbf{n}_m \times \sum_{n=1}^N \sum_{i=1}^3 \frac{A_n}{3} \nabla_{n,i} \overline{G^w}(\mathbf{x}_{n,i} - \mathbf{x}_{m,j}) \times [\mathbf{n} \times \mathbf{J}](\mathbf{x}_{n,i}). \quad (14)$$

In fact, the conjugate gradient scheme solves iteratively the symmetrized integral equations on S

$$\begin{aligned} \mathbf{LL}^*[\mathbf{J}] &= \mathbf{L}[\mathbf{n} \times \mathbf{E}^i], \\ \mathbf{KK}^*[\mathbf{J}] &= \mathbf{K}[\mathbf{n} \times \mathbf{H}^i]. \end{aligned} \quad (15)$$

REFERENCES

1. Wilton, D. R., "Review of current status and trends in the use of integral equations in computational electromagnetics," *Electromagnetics*, Vol. 12, 287–341, 1992.
2. Rao, M. S., D. R. Wilton, and A. W. Glisson, "Electromagnetic scattering by surfaces of arbitrary shape," *IEEE Transactions on Antennas and Propagation*, Vol. 30, No. 3, May 1982.
3. Zwamborn, A. P. M. and P. M. van den Berg, "The three-dimensional weak form of the conjugate gradient FFT method for solving scattering problems," *IEEE Transactions on Microwave Theory Technik*, Vol. 40, 1757–1766, 1992.
4. Graglia, R. D., "On the numerical integration of the linear shape functions times the 3-D Green's function or its gradient on a plane triangle," *IEEE Transactions Antennas Propagation*, Vol. 41, No. 10, 1448–1455, 1993.
5. Gürel, L. and Ö. Ergül, "Singularity of the magnetic-field integral equation and its extraction," *IEEE Antennas and Wireless Propagation Letters*, Vol. 4, 229–232, 2005.
6. Korkmaz, E., "A different approach to the singularity problem of boundary integral equations," *Proceedings 12th International Conference on Mathematical Methods in Electromagnetic Theory*, 331–333, Odesa, Ukraine, July 2008.
7. Korkmaz, E., "Electromagnetic interaction modeling on radio proximity fuzes for incoming targets," Ph.D. dissertation, ISBN 90-9016148-1, Delft University of Technology, The Netherlands, 2002.

Computational Modeling of New Kinds of Fractal Antennas and Fractal Frequency-selective Structures Based on Them

E. N. Matveev and A. A. Potapov

Institute of Radio Engineering and Electronics by V. A. Kotelnikov, RAS, Russia

Abstract— Authors’ realized modeling of two kinds of fractal antennas with similar structure, but different algorithms of development. The first antenna geometry is a figure “Life Flower” and the second one is series of crossed circles nested to each other. The obtained results were analyzed and conclusion of the practical applicability for these antennas was made. The obtained theoretical results allow us to conclude that synthesized fractal antennas have multiband and wide-band features. Besides the direct usage, such fractal structures performed on micron-level may reveal an application in a wide class of new fractal frequency-selective materials and surfaces. The applicability sphere of fractal antennas in modern technologies was shown: cellular communication, wireless information transmission and reception, and radar location devices. Also application filed was described for fractal antennas in modern technology: cellular communications, wireless receiving and transmitting information devices, and radar.

1. INTRODUCTION

The word “Fractal” means that the selected geometry has a fractional dimension. In the radio physics it means, that a given radio-element has a specific geometry which has a fractional dimension [1], like fractional geometry of antenna [2]. This feature makes such fractal antennas a wide- and multi-band high effective in modern microwave devices, cell phones [3]. Author’s explored two kinds of fractal geometry in application to antennas. The geometry one of the antennas is a figure of “Life Flower”, which presents a series of circles crossed in certain order. The geometry of the other one is also a series of crossed circles, according to the authors’ algorithm. Both models have a coaxial feeder and modeled over the range of 0.1 GHz to 20 GHz. Moreover, the comparison of both antennas and there features are described in the article. It is notable, that the figure of “Life Flower” is well-known all over the world, but no information about its application as a geometrical aperture was found by the authors.

2. FRACTAL ANTENNA CIRCULAR MONOPOLE

The circle monopole presents an a series of circles nested to each other. Radius of the outer circle $R = 11$ mm, and the radius of inner circles 3 times smaller than the outer $R_1 = R/3$. All seven inner circles allocated inside of outer circle so that each inner circle gets in touch with neighbor inner circles and outer circle too. Each iteration of this fractal structure presents new seven circles of three times smaller radius allocated inside the circle of previous iteration. So the radius of each iteration $R_{i+1} = R_i/3$. In the Figure 1. presents the circle monopole of first iteration and in

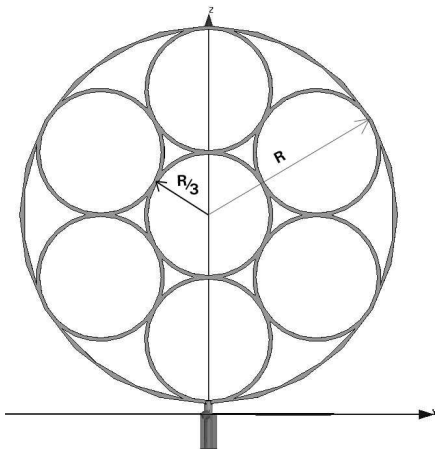


Figure 1: Fractal circle monopole of first order.

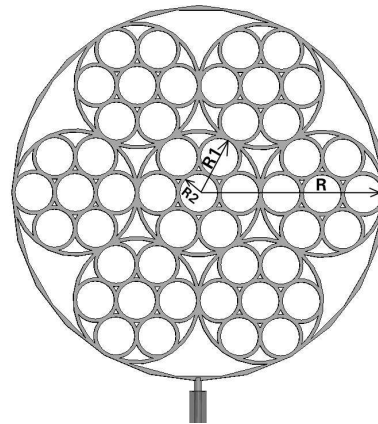


Figure 2: Fractal circle monopole of second order.

the Figure 2. presents the second iteration of the same fractal geometry. Both antennas have a monopole feeder. The constructed antennas was computational modeled in the AntSoft HFSS™ v10 and impedance, SWR frequency depending, radiation pattern were resulted.

The computational modeling [4] was made over the frequency range of 0.1 GHz–20 GHz. The obtained frequency depending of transition-loss matrix (S_{11}) show in the Figure 3. On the figure present three wideband which has given fractal antenna. Also the frequency depending of SWR and impedance was obtained an shown in the Figure 4 and Figure 5.

In Figure 4, several resonant frequency presents: 2.8 GHz, 3.9 GHz, 7.5 GHz which coincides with widebands of S_{11} dependence. There is a good confirmation of SWR occurs at the resonant frequency (2.8 GHz, 3.9 GHz, 7.5 GHz) of the given fractal circle monopole.

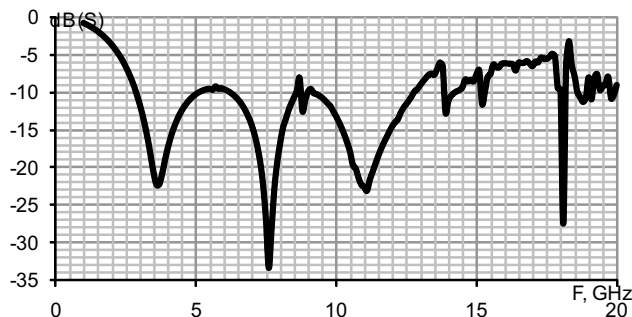


Figure 3: Frequency depending of S_{11} (transition) of the first order fractal circle monopole.

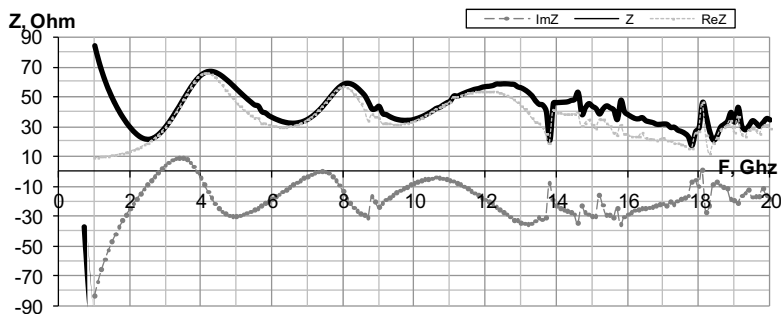


Figure 4: Frequency dependence of impedance of the first iteration.

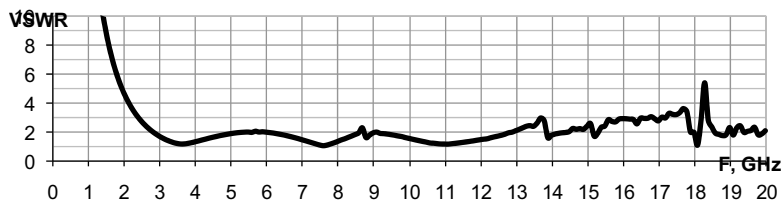


Figure 5: Frequency dependence of SWR of the first iteration.

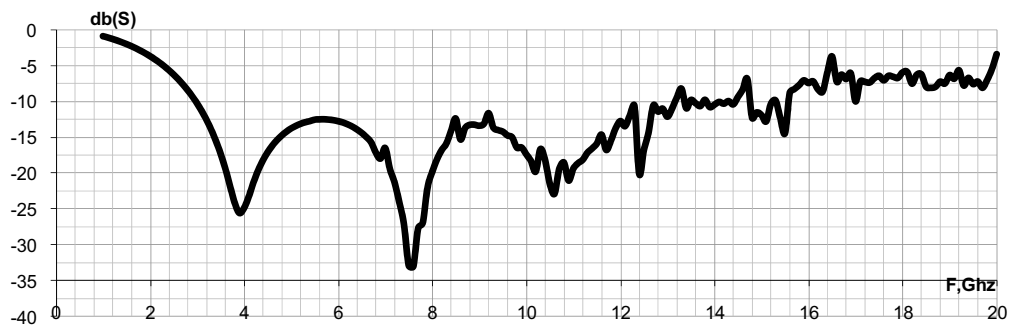


Figure 6: Frequency dependence of impedance of the second iteration.

So we can say that this fractal antenna has a good multi wide band features. The same frequency dependencies for the second iteration of circle fractal monopole are was modelled and analyzed.

The corresponding to resonance frequency radiation patterns of first order circular monopole are present on the Figure 7.

And the Figure 8 displays the radiation patterns for the second order of circular monopole.

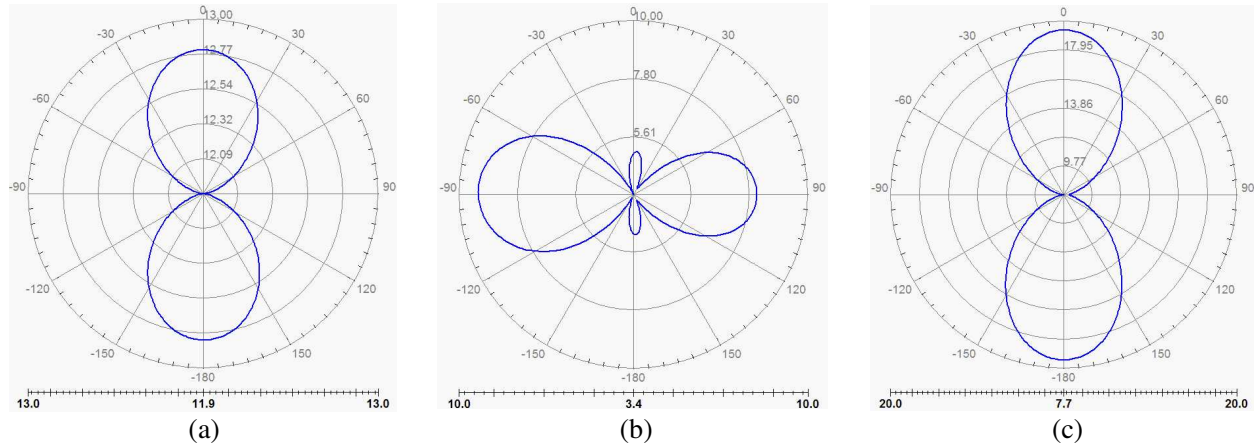


Figure 7: Radiation pattern for the resonant frequency of first order circular monopole: (a) 2.8 GHz, (b) 7.5 GHz, (c) 11.1 GHz.

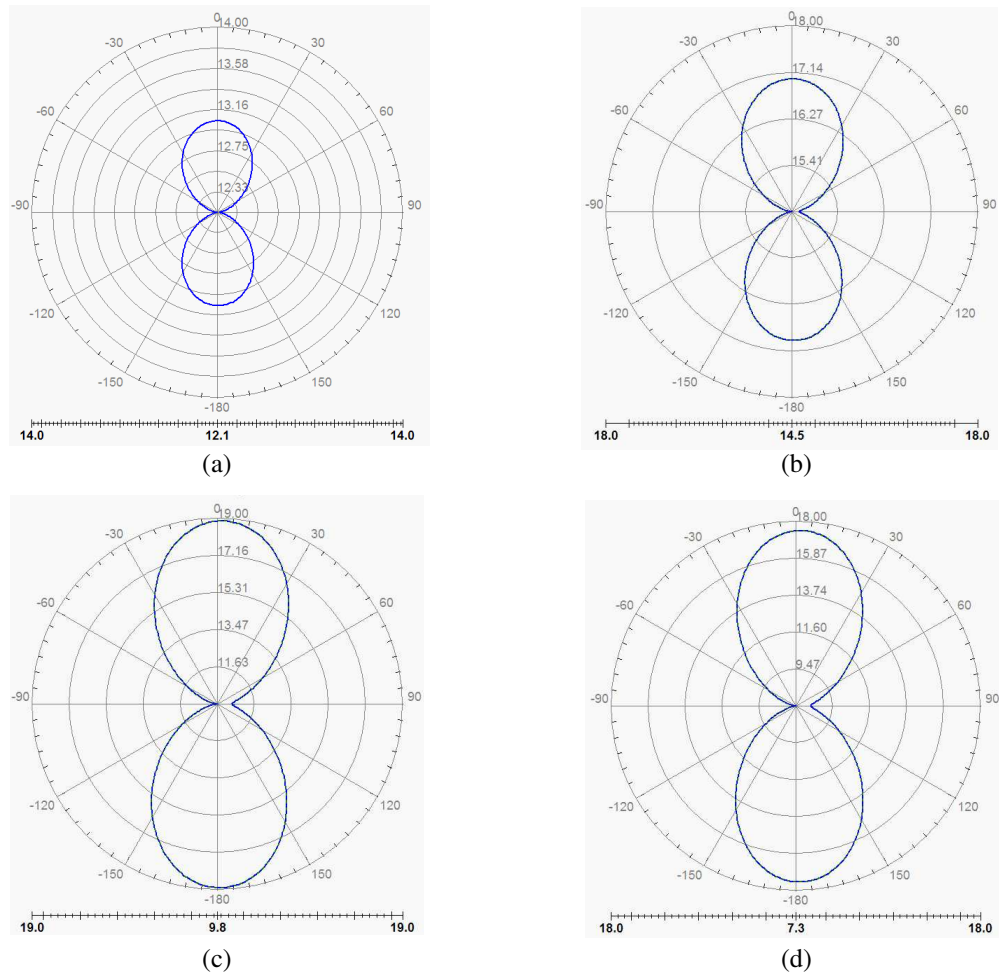


Figure 8: Radiation pattern for the second order circular monopole: (a) 2.9 GHz, (b) 4.1 GHz, (c) 7.1 GHz, (d) 7.7 GHz.

3. FRACTAL ANTENNA “LIFE FLOWER”

The second kind of fractal antenna geometry is Life-Flower, which presents a series of circles nested to each other in differ order then first antenna. The outer circle has a radius 11 mm. All other circles inside the outer ones have a radius three times less. More carefully you can introduce to the geometry of this antenna in the Figure 9. this antenna feeded at the center of the outer circle. Due to each circle gets in touch to the next circles the current is distributed over the hole antenna circles.

Computational modelling gives us the interesting results. Life-Flower antenna has a several resonant frequency with wide bands over the range 0.1–20 GHz.

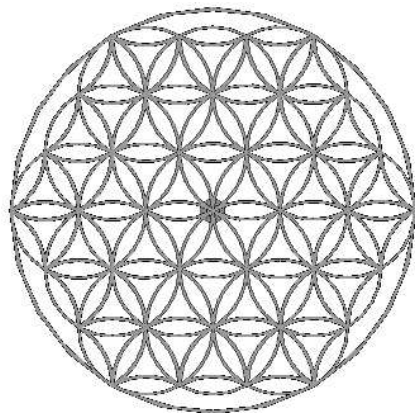


Figure 9: The Life-Flower geometry antenna.

4. CONCLUSIONS

In this paper we examined the two new kinds of fractal antennas with circle monopole geometry and Life-Flower geometry. The computational modelling allows us to verify in specific features of fractal antennas: multi- and wide-band. These properties makes fractal antennas high effective and applicable in cellular communications and microwave transit-receive devices.

REFERENCES

1. Potapov, A. A., *Fractals in Radio Physics and Radar*, Logos, oscow, 2002.
2. Potapov, A. A., *Fractals in Radio Physics and Radar: Topology of Sample*, 2th Issue Edition and Correct, University Library, oscow, 2005.
3. Potapov, A. A., E. N. Matveev, and V. A. Potapov, “The practical application of fractal antennas in modern mobil telephones,” *Proc. XLVIII Sci. Conf.*, “Modern problems of fundamental and applied science,” *Quantum and Physical Electronic*, Pt. V, 112–113, MIPT (SU), Moscow, Dolgoprudny, Russian, November 2005 (Russia).
4. Potapov, A. A., E. N. Matveev, V. A. Potapov, and A. V. Laktyunkin, “Mathematical and physics modelling of fractal antennas and fractal frequency selective surfaces and volumes for the fractal radio systems”, *Proceedings EuCAP 2007*, ThPA. 031. pdf. 6, Edinburgh, UK, November 2007, (<http://www.eucap2007.org/programme1.htm>).

Photons Production and Communications in Biological Systems

S. N. Mayburov and Ilya Volodyaev

Lebedev Institute of Physics, Russia

Abstract— The possible mechanisms of communications between distant bio-systems by means of optical and UV photons are studied. It is shown that for experimentally observed photon rates it can be similar to the binary data exchange in computers net via optical channels in photocounting regime.

1. INTRODUCTION

Currently, the term ‘biophoton’ is attributed to the optical and UV photons emitted by bio-systems in the processes which are different from standard bioluminescence. The significant bio-photon production (BP) in optical and close UV range is established for a variety of bio-systems [1, 2]. Its energy spectrum is nearly constant within optical and close UV frequency range, so it is essentially different from the spectra expected for the system with the temperature about 300°K, which in this range should fall on 15 orders of magnitude [2, 3]. The related phenomena is the delayed luminescence (DL) which is the secondary photon emission, stipulated by the irradiation of the biological sample by the short pulse of visible light. BP rate demonstrates the nonlinear dependence on some bio-systems parameters, such as the density of living cells in the culture, etc. [3]. The observed DL time dependence is strikingly different from the exponential one, expected for the independent emission of photons. The experiments evidence that BP rate is proportional to the rate of cell mitosis in particular bio-system [1, 3]. Other novel feature of bio-photons is that they seemingly perform the communications between distant bio-systems. In particular, being radiated by the developing bio-system, they can rise the rate of cell mitosis in another bio-system of the same or similar specie up to 50%, this phenomenon called mitogenetic effect (ME) [1, 2]. The communications of some other types were reported also, for example, for the bio-systems in the states of abrupt stress [1].

Until now, BP and DL properties, as well as ME, can’t be described within the standard premises of cellular biology [2, 3]. To explain them, Popp proposed that the electromagnetic ($e-m$) field of bio-system is in coherent quantum state, analogously to laser [3]. Such field can produce the nonlinear patterns in some situations, but only for a very short time. However, the observed range of DL lifetimes, up to several minutes, are hardly compatible with the quantum coherence (QC), because such field inevitably suffers the fast loss of coherence from its interaction with the molecules of bio-system and its environment. For typical bio-systems the field coherence should be destroyed during several picoseconds, the experiments confirm this predictions for optical excitations in bacteria [4]. This and other objections put the serious doubts on the hypothesis of coherent BP.

Alternatively, in this paper we propose that BP nonlinearities and ME are explained by the well-known properties of living organisms, in particular, their complex dynamics which can result in the nonlinear reactions on the external perturbations and signals. Such back-reaction can induce the emission of response radiation which in its turn can influence the behaviour of initial radiation source and result in the complicated nonlinear correlations between the source and receiver, i.e., the back-reaction loop. The exchange of information between the bio-systems and also between the distant parts of the same bio-system is analyzed in the framework of information theory. From that the simple scheme of information exchange between the bio-systems by means of noncoherent photons is constructed, which is similar to the communications between computers by the binary encoded messages. Under simple assumptions, this model explains also the influence of external nonbiological irradiation on BP rate and ME.

2. INFORMATION EXCHANGE BETWEEN BIO-SYSTEMS

Before considering the photon exchange between the bio-systems, it’s worth to consider how the similar communications can be realized between the distant parts of the same bio-system.

The optical and UV excitations in the dense media can exist and spread as the quasiparticles called excitons e with mass m which can spread freely through the whole media volume [5]. They are strongly coupled with $e-m$ field, so they can be produced during the photons absorption by the media with high efficiency, the inverse process results in the photons emission from the system

volume. It's established experimentally now that the excitons play the important role in the energy transfer inside the bio-systems, in particular, during the photosynthesis in plants and bacteria [6]. BP induced by the nonlinear excitons spreading along the protein molecules was considered in [7]. In distinction, in our model the excitations of biological media as the whole play the main role in biophotons generation and absorption.

Usually, BP rates are quite low, about 10 photons/cm²sec from the surface of large, dense bio-system. It was argued also that such e - m field can't be coherent, hence it described as the stochastic ensemble of photons. Then at its best the absorption of single photon or narrow bunch of photons can be detected by the bio-system as the single independent 'click' or one bit of information, analogously to standard photodetector devices. This is the photocounting regime of e - m field detection well-known in Quantum Optics [8]. We assume that the same approach is applicable also for the excitons radiated and absorbed in the different regions of the same bio-system. Let us suppose that on the average, the mitosis rate $R_M(r)$ in a given bio-system's region r grows proportionally to the number of excitons $N_e(r)$ absorbed in it. Each exciton absorbed by the particular cell, supposedly identified by it as the single short-time 'click'. It supposes that the cell acts also as the exciton 'repeater', because, for the typical ME conditions in each cell cycle one absorbed bio-photon corresponds to $10^{3\div 4}$ cells in which it supposedly induces or accelerates mitosis [1]. Of the similar order should be this ratio for the excitons, hence the absorption of exciton by the individual cell can be too crude approximation of the real mitogenetic mechanism. Probably, it is more similar to the simultaneous interaction of exciton with many cells of the same region r , i.e., the cells cluster with diameter about 0.1 mm [6]. However, for the simplicity we shall discuss our model in terms of exciton interaction with individual cell, since it doesn't influence the results for photonic communications.

It's natural to expect that the evolution of living species made the information exchange by means of excitons radiation and absorption practically optimal for given bio-systems. Then the simple scheme of communications between the cell clusters can be formulated. It turns out that it's quite similar to the exchange of messages between two computers C_1 and C_2 , encoded by the binary code. This scheme can be deduced from the first principles of information theory, but its the formal derivation is rather tedious, meanwhile, it can be obtained from the simple common sense reasoning. First of all, for such low exciton rate it's quite important to suppress the exciton background induced by all possible sources, like the violations of cell metabolism, the cosmic rays and soil radioisotopes, etc. In this case, as the criteria, characterizing the efficiency of information exchange, the signal to noise ratio K_O can be used, i.e., the ratio of registered 'clicks' induced by bio-system signals and the background. If the typical information channel characterized by the high rate of noise, then the simplest method to reduce it, is the preliminary agreement between computers C_1 and C_2 , connected by this channel, on the time moments when the messages are sent, i.e., the signals synchronization. To perform it inside bio-system, the cell or the cells cluster not only should registrate the absorption of single exciton as the single 'click', but also records the time of this event with the accuracy about 10^{-1} sec. The existence of 'biological clocks' inside the living organisms is well established now. The additional noise reduction can be achieved, if any message send by C_1 to C_2 , partly depends on the content of messages received by C_1 from C_2 previously. Hence such exchange constitutes the nonlinear back-reaction loop, entangling the previous messages of both computers, however, here such complicated scheme isn't used.

For communications inside the same bio-system, because its background is supposedly constant in time, the simplest method to suppress it considerably, is to synchronize the exciton radiation all over its volume. It means that the excitons should be produced inside the cell media only at some regular moments t_j as the short regular bursts of width τ_e interspersed by long periods of cells 'silence' $T - \tau_e$. During this part of cycle the mitosis mechanism is supposedly insensitive to any irradiation and cells themselves don't emit excitons, whereas during the short intervals τ_e , the 'detection' of such exciton signals would induce or accelerate the mitosis inside the cells or cells cluster in which they were absorbed. For such time dependence of cells sensitivity to the impact excitons, if the mitosis is initiated by the registration of single burst, then the background will be suppressed by a factor $\frac{\tau_e}{T}$ and K_O enhanced respectively. Furthermore, in this framework it is sensible to assume that the mitosis in the cells is initiated not by the single burst but the detection of signal S_N constituted by the sequence of N periodic bursts with the intensity larger than some J_b and period T , the reasonable estimate is that N can be of the order $10^{1\div 2}$. Plainly, such 'time encoding' of exciton bursts would permit to suppress the background rate by the additional large factor $(\frac{\tau_e}{T})^N$. Correspondently, the biophoton emission from the bio-system, related to exciton

production, should have the same structure of periodic short-time bursts which width is of the order of τ_e .

If in addition to this ‘main’ cell cycle with period T there are also other longer cell cycles, they wouldn’t interfere with each other if the corresponding excitation periods T_j are related to the shortest period T as $T_L = LT$, where L are arbitrary natural numbers, i.e., this cells are sensitive to the excitations at the same t_j , but with larger interval T_L . This additional harmonics, in principle, can contain the additional information which regulates more fine features of bio-system development. The recent results for BP in fish eggs and fibroblast cell cultures agree well with such exciton and, correspondently, BP time structure [1]. For fibroblast cells beside the constant background, the short periodic photon bursts were registered, they correspond mainly to the periods $T \approx 10, 40, 100$ and 400 sec. For loach eggs the most pronounced harmonics of time spectra are 7 and 70 sec. For both species the relative intensity of harmonics can vary depending on the development stages and external interventions into their development, like the compression or injection of drugs, stimulating the development. However, the presence of periodic bursts, which periods are related by the natural numbers is the invariable feature of all obtained spectra. There are multiple evidences that for many bio-systems, for example yeast, such exciton communications are beneficial for their germination [2]. In particular, such long-distance communications inside the bio-system, can, probably, explain also the morphogenesis of developing bio-systems.

It’s sensible to expect that if the cell mitosis is stipulated by the synchronized regular bursts of excitons, than the bio-system should contain the auxiliary mechanism which permit to vary slightly the time of exciton emission by the individual cells to conserve their synchronization. Really, the external perturbations and internal bio-system fluctuations would tend always to destroy this synchronization in the long run, so the cells should have the ability to tune their own burst time, so that it would coincide with their irradiation maxima. From this reasoning we shall assume also that the bio-system as the whole, as well as its parts, can also vary T value for some small ΔT with each new burst, it is enough that it can be of the order $10^{-2}T$. As was supposed above, despite that the mitosis initiation is sensitive to the excitons or external irradiation only inside τ_e time gaps, the cells are sensitive to their presence and ‘measure’ the exciton rate $R_e(t)$ all through T period. Because of this sensitivity and assumed tendency to the synchronization with irradiation peaks, under the external irradiation the burst moments t_j of organism each time supposedly can be shifted in the direction of larger radiation intensity. For example, if this irradiation is periodical with the same period T and its maxima lays at:

$$t_j^M = t_j + aT \quad (1)$$

where $a < 0.5$, then $\Delta T > 0$ and the moment of cell burst would shift in the direction of the irradiation maximum so that:

$$t_{j+1} = t_j + T + \Delta T \quad (2)$$

until the external and internal radiation maximum would coincide in time.

Now let us consider in this approach the exchange of information between two distant bio-systems A, B of the same sort and age. Naturally, for both A, B the period of exciton bursts has the same T value, but by itself without temporary electromagnetic contact their burst moments will be independent: $t_i^B \neq t_j^A$ for arbitrary i, j . Hence in the considered model, due to this time difference t_d between A, B bursts, the photons radiated from A surface would not induce the mitosis in B and vice versa. Let’s suppose that from some moment A, B are located nearby and can irradiate effectively each other. Then, under our assumptions this B bursts, which is the external irradiation for A would shift its moments t_j^A of bursts for ΔT in each cycle in the direction of B bursts and vice versa. This variations of A, B periods will continue until both A, B bursts will be completely synchronized, which will take approximately:

$$t' \approx \frac{t_d T}{\Delta T} + T \quad (3)$$

After that the normal T value will be gradually restored for both A and B without violation of this synchronization. Altogether, this A, B communications and resulting evolution present the simple example of back-reaction correlations. In this set-up the photons radiated by A can be absorbed by B cells and produce the excitons in B during its burst period only. Hence, in principle, they can accelerate the cell mitosis in B and vice versa, i.e., A, B constitute the joint mitotic system with high K_O . The experiments with the swarms of *Dinoflagellates* confirmed such effect and permitted

also to study how such synchronization of flickering moments occur [3], the transition time for its establishment is less than 30 sec. Similar results are obtained for the bursts synchronization between two fibroblast cell cultures and two sets of fish eggs [1].

3. BIOPHOTON DUMPING BY NONBIOLOGICAL RADIATION

DL experiments show that the typical bio-system possesses the large density $W(E)$ of metastable optical and UV levels, which only slightly depends on energy E . For the bio-systems in the darkness, considered until now, its optical levels are excited by some chemical reactions which on the average occur during cells mitosis with constant rate. The consequent photon emission in the form of periodic bursts with intensity C is controlled by some collective mechanism of unobvious nature, however, it is sensible to expect that it is independent of the levels excitation mechanism. Therefore, if the same bio-system is exposed to the constant white light flow J , then this levels would be additionally excited with higher rate [8]. Hence one can suppose that under this conditions the bio-system will emit the photon bursts which intensity is proportional to $C + kJ$ over constant background J . For the regarded photocounting regime, the background noise has poissonian distribution and at large J its rate would be proportional to \sqrt{J} . Hence such irradiation is favourable for ME since K_O would grow as \sqrt{J} as well, and results in noise suppression with simultaneous gain of signal amplitude. As J would grow further, the levels saturation can become important, resulting in K_O reduction and, probably, ME rate as well.

The experiments show that ME for most of studied bio-systems is more pronounced when they are irradiated by the external visible light, than in case of complete darkness [9]. The optimal J corresponds to about 10^{-1} of full day light intensity, for higher J ME rate gradually declines. Some experiments [9] evidence that ME is induced mainly by UV photons in the range from 200 to 300 nm. Given it's correct, then in addition to the regarded 'direct' level dumping, the mechanism similar to photon up-conversion can become important. For example, if the monochromatic J with energy E_1 in optical range will dump the corresponding levels E_1 of detector bio-system, and one of them would absorb the biophoton E_2 emitted by other bio-system, then the resulting excitation with energy $E_1 + E_2$ can belong to UV range and initiate the mitosis. Note that at high J in UV range, the cells start to degrade and their mitotic mechanism can be spoiled as well.

4. CONCLUSIONS

In this paper it was shown that the exciton's exchange supposedly constitutes the effective system of signalling and regulation of the bio-system development. It seems that such signalling to the large extent regulates the homogeneity of bio-system growth, preventing from the large fluctuations of its global form, i.e., defines its morphogenesis. In our approach, each cell or cells cluster is the analogue of computer, which reaction is defined by the signals dispatched by the absorbed excitons. Basing on it, the simple scheme of information exchange inside the bio-system was proposed, from that the similar scheme of photons communications between the distant bio-systems was derived. It turns out to be similar to the standard procedure of information exchange between the distant computers by means of photonic signals transferred by the light-guides or optical fibres. It's important to notice that the obtained scheme of photon communications is practically independent of particular BP mechanism. The calculations of BP time variations are in a reasonable agreement with the experimental results for BP in fish eggs [1]. Exploiting the rules of quantum optics, this model explains also the influence of external nonbiological irradiation on BP rate and ME.

Note that the similar cell's control and regulation features are well studied for inter- and extracellular biochemical reactions [6]. Concerning the extracellular chemical signalling in the tissues, its efficiency and precision is principally restricted by the molecular diffusion effects inside the media. In addition, it can be smeared by the reactions fluctuations, occurring in the chain of intermediate molecule-messengers transferring the signal to the cell nucleus. Note also that the exciton signalling inside organism can be much faster, than the corresponding chemical one. Hence it can be efficient in case of stress, or the abrupt change of external conditions. Experimental results show that under the different stress conditions the photon rates from bio-system can rise in short time significantly, probably, as the consequence of intensive internal signalling, it was shown also that this signals can perturb the evolution of nearby bio-systems [1, 2].

ACKNOWLEDGMENT

This work was partly performed in collaboration with C. Nicolini and V. Sivojelezov from NWI, Universita di Genova. Author thanks for the useful discussions of related problems L. Belousov, I. Volodiaev and I. Volovich.

REFERENCES

1. Belousov, L. V., “Ultraweak photon emission in cells,” *Biophotonics and Coherent Systems in Biology*, 139–159, Springer, Berlin, 2007.
2. Van Wijk, R., “Biophotons and biocommunications,” *J. Sci. Explor.*, Vol. 15, 183–209, 2001.
3. Chang, J. J. and F. A. Popp, “Mechanism of interaction between electromagnetic field and living organisms,” *Science in China*, Vol. 43, 507–522, 2000.
4. Engel, G. S., et al., “Evidence for wavelike energy transfer in photosynthetic systems,” *Nature*, Vol. 446, 782–787, 2008.
5. Davidov, A., *Solitons in Molecular Physics*, Kluwer, Dordrecht, 1991.
6. Shubin, A. F., *Biophysics*, Moscow, Nauka, 1999.
7. Brizhik, L., “Delayed luminescence of biological systems,” *Phys. Rev. E*, Vol. 64, 031902–031917, 2003.
8. Glauber, R. J., *Quantum Optics*, Academic Press, N-Y, 1969.
9. Gurwitsch, A. A., *Problems of Mitogenetic Radiation*, Medicina, Leningrad, 1968.

Computer Simulation of Electromagnetic Force Effect on Melting Pool in Layer-laminated Deposition Process

Haiou Zhang¹, Chao Wang¹, and Guilan Wang²

¹School of Mechanical Engineering, Huazhong University of Science and Technology
Wuhan, China

²School of Materials Science and Engineering, Huazhong University of Science and Technology
Wuhan, China

Abstract— A new computer simulation was carried out for investigating the electromagnetic force effect on melting pool in layer-laminated deposition process. Because of the gravity and the fluid motion of molten metal in melting pool during the layer-laminated deposition process without supporting, it will difficult to form complex shape parts. So a new scheme which using the magnetic field to restrict the melting metal flow was proposed. The method designed a restricted equipment of magnetic field in order to prevent and reduce the fluid flow and collapse of the melting pool. Compared with traditional method, as the height of the deposition shape increased, the process restricted with electromagnetic force can make the shape of parts more complex and more accurate. The changes of the electromagnetic force field were simulated with the finite element analysis, while the effects of electromagnetic force on forming process were discussed. Simulation and experimental results show that the control system is feasible and practicable. The electromagnetic force will decrease the post-treatment procedure and could contribute to the process of layer-laminated deposition shaping.

1. INTRODUCTION

Electromagnetic Forming Technology was founded in the late 50's. In the age of 60 to 70, it has been rapid development. In the 80's in the United States, the former Soviet Union the technology has been systematized and standardized. The technique Using the electromagnetic force which generated by alternating electromagnetic field to constraint the forming of melting metal has been widely used in smelting and forming of aluminum and many chemical active metal. However, the current electromagnetic forming technology only available on forming of simple shape parts. So this paper discuss the research of electromagnetic force on melting pool in layer-laminated deposition process, this method can make complex parts more easier [1–4].

2. PRINCIPLES OF ELECTROMAGNETIC FORMING TECHNOLOGY

Figure 1 is the schematic drawing that illustrates the produce process. A high frequency alternating current loads on the coil which is fixed on the welding torch. Alternating current will generate alternating electromagnetic field, it will generate induced current in the closed-loop melt. Because of the skin effect, the induced current mainly concentrated in the surface of molten metal, as its direction in each moment will opposed to the current direction in the coil, it also will cause magnetic field ($\pm B_z$) in the internal of molten metal to z axis [5].

Set the surface of molten metal as the x - z plane and the direction of y axis is perpendicular to the surface to the outside, as shown in Fig. 2 [5].

The induced current can be represented by

$$\vec{J} = V \times \vec{H} \quad (1)$$

$$V = \frac{1}{\mu_0} \quad (2)$$

Based on Ampere circuital theorem

$$\oint_{(L)} B \cdot dr = \mu_0 \iint_{(s)} j \cdot dS \quad (3)$$

And Stokes theorem

$$\oint_L B \cdot dr = \iint_{(s)} \nabla \times B \cdot dS \quad (4)$$

In the rectangular coordinate system

$$\nabla \times B = \left(\frac{\partial B_z}{\partial y} - \frac{\partial B_y}{\partial z} \right) i + \left(\frac{\partial B_x}{\partial z} - \frac{\partial B_z}{\partial x} \right) j + \left(\frac{\partial B_y}{\partial x} - \frac{\partial B_x}{\partial y} \right) k \tag{5}$$

Eq. (4) substituted in Eq. (3)

$$\nabla \times B = \mu_0 j$$

So

$$J_x = \frac{1}{\mu_0} \frac{\partial (\pm B_z)}{\partial y}$$

$$J_y = \frac{1}{\mu_0} \frac{\partial (\pm B_z)}{\partial x}$$

The magnetic force that load on the metal

$$\vec{F} = \mu_0 \vec{J} \times \vec{H}$$

$$F_y = -J_x \cdot (\pm B_z) = -\frac{1}{\mu_0} \cdot \frac{\partial (\pm B_z)}{\partial y} (\pm B_z) = -\frac{1}{\mu_0} \frac{\partial B_z}{\partial y} B_z$$

$$F_x = -\frac{1}{\mu_0} \frac{\partial B_z}{\partial x} B_z$$

where \vec{H} is the magnetic density, B is the magnetic flux density, μ_0 is material permeability, \vec{J} is the ampere density, \vec{F} is the magnetic force. B_z is proportional to y , so \vec{F} is always negative, the molten metal will receive compressive force.

To ensure the weld don't flow, the maxwell force must greater than or equal to the static pressure on molten metal [6].

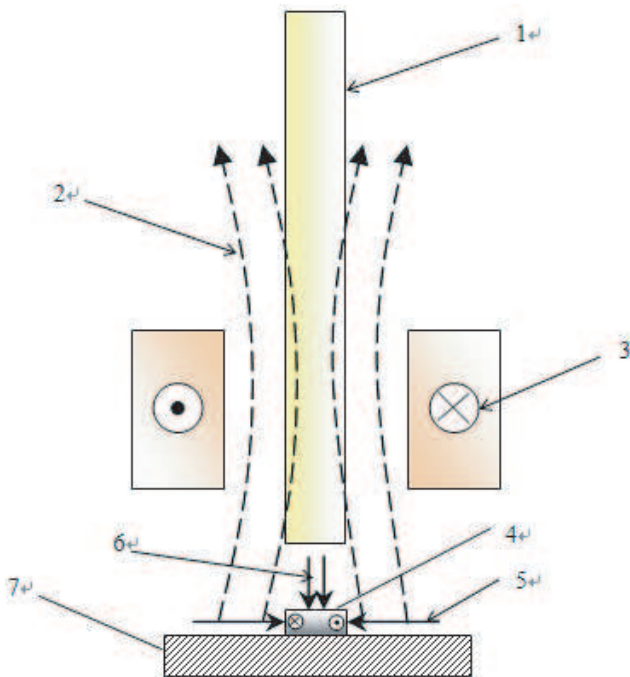


Figure 1: Schematic drawing of electric-magnetic forming on layer laminated deposition process. 1. Welding torch, 2. magnetic line of force, 3. alternating current, 4. molten metal, 5. maxwell force of x -axis, 6. maxwell force of y -axis, 7. placode.

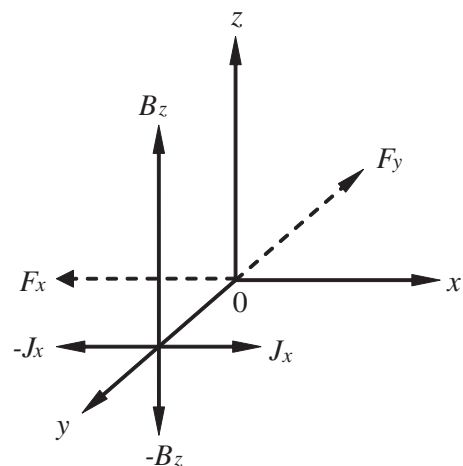


Figure 2: Schematic diagram of magnetic force.

3. COMPUTER SIMULATION AND ANALYSIS

There are two dominate method in the assays of magnetic force: Analysis method, finite element method.

Analysis method: Maxwell equations describe all the basic laws of electromagnetic phenomena. Solving the equations all the analytic solution of electromagnetic parameters can be obtained, including magnetic force. Magnetic field force can be solved by using the equations under similar conditions and carried out integrations. But the solution process is complex.

Finite element method: This method uses mesh, gives appropriate boundary conditions, computers laplace field, solves the magnetic flux density between the coil and the metal. According to the Maxwell equations, it can calculate the magnetic force applied to the metal. Compare to others, the results will be agree better with the experimental results [7].

The model of experiment equipment in ANSYS is show in Fig. 3, as show A4 is infinite element. A1 is welding torch, A2 is coil, A3 is molten metal, A5 is air element.

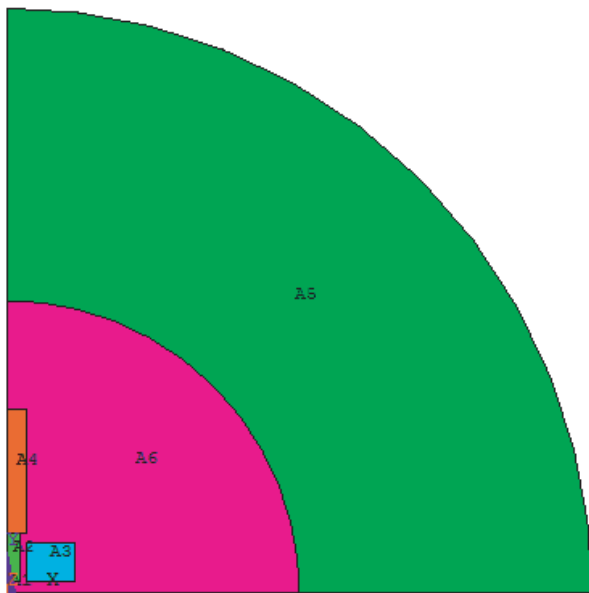


Figure 3: The model of experiment equipment.

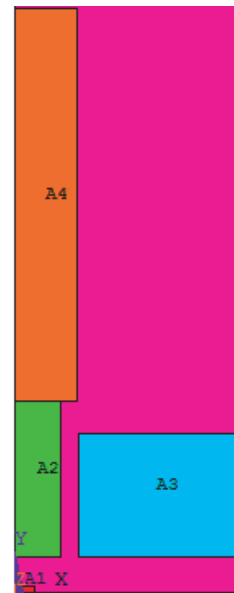


Figure 4: Partial enlarged drawing.

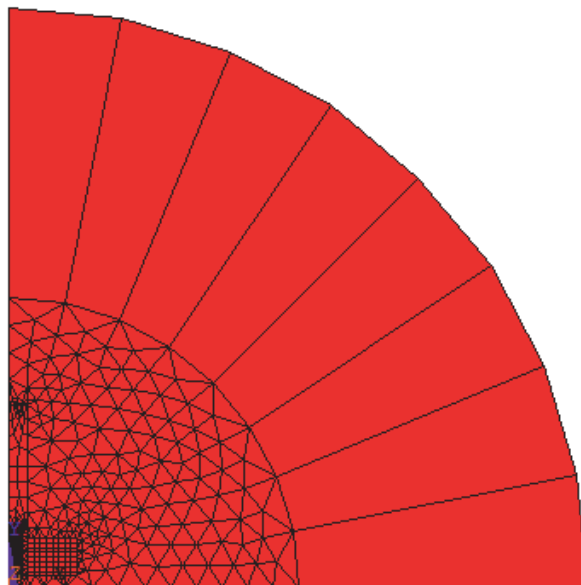


Figure 5: The result of meshing process.

The result of meshing process is show in Fig. 5.

Table 1: The parameter of electromagnetic coil.

Frequency of current (kHz)	Current (A)	Electromagnetic coil turns	Cross section (mm ²)	Ampere density (A/m ²)	Coil fill factor
$F = 35$	$I = 100$	$N = 20$	$S = 630$	$J = 1.984 \times 10^6$	0.95

The model of experiment equipment in ANSYS is show in Fig. 3, as show A5 is infinite element, A2 and A4 is welding torch, A3 is coil, A1 is molten metal, A6 is air element. Fig. 4 is the partial enlarged drawing of the model.

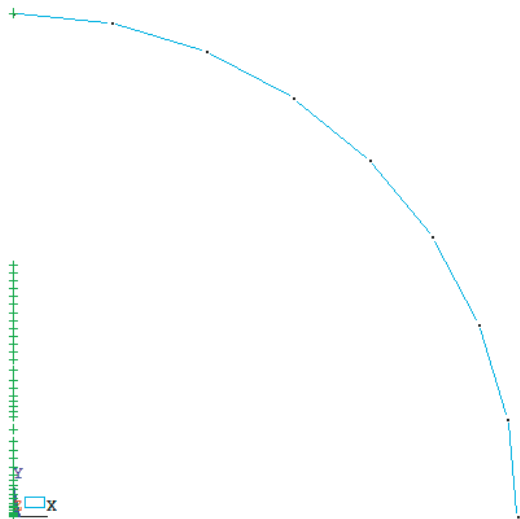


Figure 6: The constraints to the model.

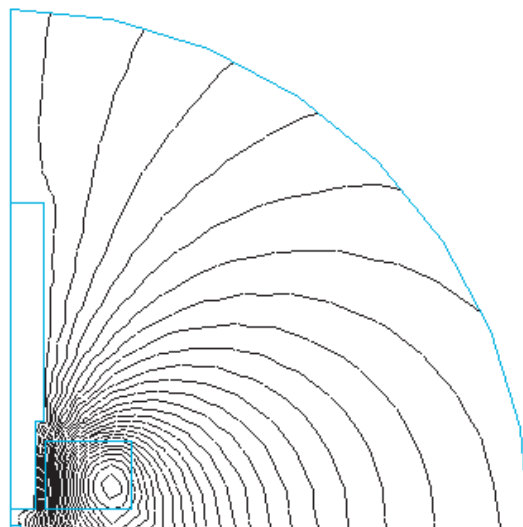


Figure 7: The magnetic lines of flux.

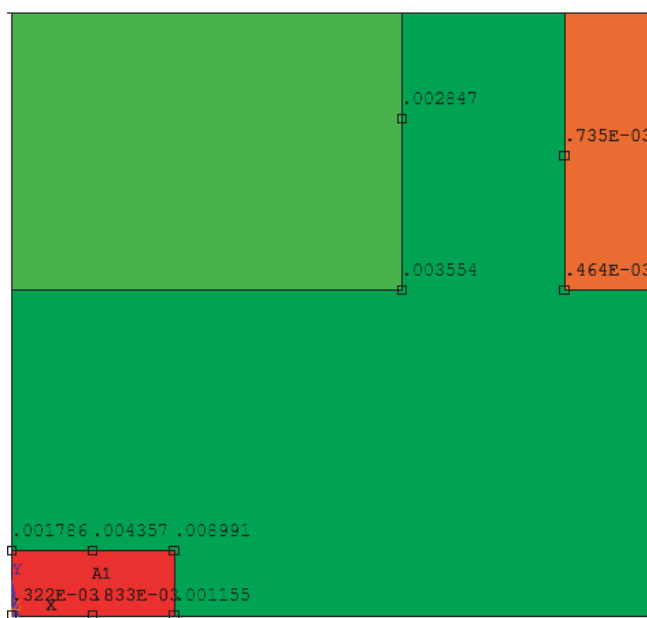


Figure 8: The magnetic induction density near the molten metal and coil.

According to the vector magnetic potential, when the distance from the excitation source is 5 ~ 10 times than the size of excitation source. The magnetic potential is already close to zero. In addition, in problems of axial symmetry, the equipotential which magnetic is zero is coincide to the axes.

Define the constraints to the model including magnetic line of force parallel to y axis and add magnetic flag on node of infinite boundary. Loading high frequency alternating current to the coil, adopting harmonic analysis method, It is show in Fig. 6.

The magnetic lines of flux is plot in Fig. 7. As show, the magnetic flux density is most strongest near the coil and molten metal.

The magnetic induction density of the coil and the welding torch including the space around is show in Fig. 8 [8]

When welding, the side pressure on the molten metal is

$$\begin{aligned}
 Ph &= \rho \times g \times h \times S \\
 &= 8.0 \times 10^3 \text{ kg/m}^3 \times 9.8 \text{ N/kg} \times 0.003 \text{ m} \times 0.005 \text{ m} \times 0.003 \text{ m} \\
 &= 0.003528 \text{ N}
 \end{aligned}$$

where Ph is the side pressure, h is the height of the coil, ρ is the density of material, g is the acceleration of gravity.

As the maxwell force should greater than the side pressure Ph to ensure the molten metal don't flow.

The simulation results is show in Fig. 9:

SUMMARY OF FORCES BY VIRTUAL WORK		
Load Step Number:	1.	
Substep Number:	1.	
Time:	0.3500E+05	
Units of Force:	(N/m)	
Component	Force-X	Force-Y
WELD	-0.10968E+01	0.64561E+00

SUMMARY OF FORCES BY MAXWELL STRESS TENSOR		
Units of Force:	(N/m)	
Component	Force-X	Force-Y
WELD	-0.10568E+01	-0.29488E+00

Note: Maxwell forces are in the Global Cartesian coordinate system.
 Virtual work forces are in the element ESYS coordinate system.
 The following element table items are available for printing and plotting of the forces obtained by Virtual Work and the Maxwell Stress Tensor methods.

Element Item Name	Method	Direction
FVW_X	Virtual Work	X
FMX_X	Maxwell Stress	X
FVW_Y	Virtual Work	Y
FMX_Y	Maxwell Stress	Y

Figure 9: The magnetic force load on the molten metal.

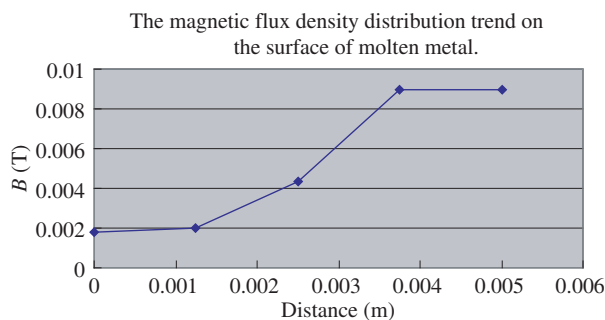


Figure 10: The magnetic flux density distribution trend on the surface of molten metal.

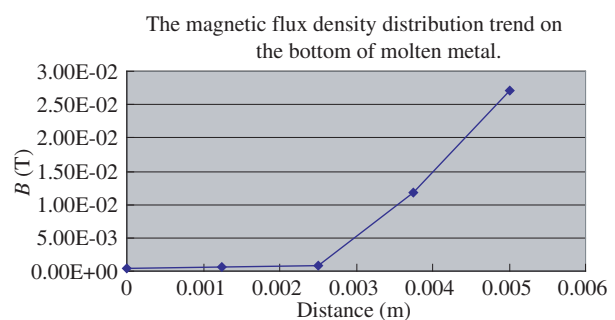


Figure 11: The magnetic flux density distribution trend on the bottom of molten metal.

From the Fig. 9, the molten metal accept maxwell force in x -axis is about:

$|Fx| = 1.0568 \times 0.005 = 0.005284 > 0.003528 \text{ N}$, so the result of computer simulation can demonstrate adding electromagnetic force effect on melting pool to constraint the welding process is feasible.

It also can be seen from Figs. 10 and 11 that the magnetic flux density gradually becomes stronger towards the part's outer regions near the magnetic coil. It is both happened on the surface and bottom of the molten metal, and the magnetic lines of flux almost concentrate on the surface of the weld bead.

Table 2: The magnetic flux density distribution trend on the surface of molten metal.

The distance to the symmetry axis on the surface of molten metal (m)	0	0.00125	0.0025	0.00375	0.005
The magnetic flux density (T)	0.001786	0.002006	0.004357	0.008941	0.008991

Table 3: The magnetic flux density distribution trend on the bottom of molten metal.

The distance to the symmetry axis on the bottom of molten metal (m)	0	0.00125	0.0025	0.00375	0.005
The magnetic flux density (T)	0.322E-3	0.620E-3	0.833E-3	0.011707	0.02707

4. CONCLUSION

The computer simulation of the electromagnetic force effect on melting pool in layer-laminated deposition process verified the feasibility of this method, using the electromagnetic field to constraint the molten metal achieve the goal of preventing metallic solution flow.

As the simulation results show, in the harmonic analysis, the magnetic field generated by high frequency electromagnetic coil can balance the side pressure on the molten metal, it can reduce the fluid flow and collapse of the melting pool and contribute to the forming of deposition material. The magnetic flux density almost concentrate on the surface of the molten metal and becomes stronger towards the part's outer regions near the magnetic coil, compare to the traditional welding process, the magnetic effect make it easier to shape complex parts.

At present, in the analysis, the current intensity, the coil turns and the height between the coil and plancode is only assumed value. The value should adjust during the experiment to ensure the magnetic can generate best effect. The effect of torch material and workpiece material to the high frequency magnetic field should also be considered. Transient analysis can solve the problem it should be taken based on the known material characteristic.

ACKNOWLEDGMENT

Authors gratefully acknowledge the contribution of the National Nature Science Foundation of China (Grant No. 50474053 and No. 50875096). In particular, thanks are given to School of Mechanical Engineering, Huazhong University of Science and Technology.

REFERENCES

1. Li, C., *High-efficiency Forming Technique*, National Defence Industry Press, Beijing, 2001.
2. Jin, J., *Finite Element Method of Electromagnetic Field*, Xidian University Press, Xian, 1998.
3. Fu, H. and J. Zhang, *Electromagnetic Hydromechanics and Material Engineering [A], the Fore-front of Science and Technology of China (Edition of Chinese Academy of Engineering) [C]*, 187–224, China Higher Education Press, Beijing, 1998.
4. Li, S., J. Li, Q. Hao, et al., "Electromagnetic shaping of molten metal for near net shape," *China Mechanical Engineering*, Vol. 11, No. 1–2, 73–76, 2000.
5. Zhou, T., Y. Qu, and Z. Han, "Electromagnetic casting for steel," *Iron and Steel*, Vol. 29, No. 12, 71–74, 1994.
6. Lavers, J. D., "Computational methods for the analysis of molten metal electromagnetic confinement systems," *ISIJ International*, Vol. 29, No. 12, 993, 1989.
7. Jiang, H., C. Li, et al., "Current research situation of electromagnetic forming technique," *Material Science & Technology*, Vol. 12, No. 3, 327–330, 2004.
8. Sun, M. and R. Hu, *Guide and Examples of Finite Element Analysis of Electromagnetics in ANSYS 10.0*, China Machine Press, Beijing, 2007.

Modeling of Heat Transfer, Fluid Flow and Solute Diffusion in the Plasma Deposition Manufacturing Functionally Gradient Materials

Fanrong Kong^{1,2}, Haiou Zhang¹, and Guilan Wang³

¹College of Mechanical Science and Engineering, Huazhong University of Science and Technology
Wuhan 430074, China

²Research Center for Advanced Manufacturing, Southern Methodist University
3101 Dyer Street, Dallas, Texas 75205, USA

³College of Material Science and Engineering, Huazhong University of Science and Technology
Wuhan 430074, China

Abstract— A solid-liquid-gas unified model is developed based on finite volume method (FVM) to acquire the thermo-physical data in the plasma deposition manufacturing (PDM) of functionally graded materials (FGMs). An enthalpy porosity model combined with level-set method are applied to deal with the melting and solidification at the solid/liquid interface and evolution of the free surface of the molten pool (liquid/gas interface), respectively. In this study, a numerical experiment of nickel base alloy powder and mild steel powder with gradual mass ratio deposited on the mild steel substrate by PDM is implemented, in which concentration gradient of the deposited materials, temperature field of the deposited layer, and fluid flow in the molten pool are studied in detail. Numerical results show that the geometry of the molten pool and the fluid flow inside directly influence gradient distribution of solute concentration along the thickness of deposited layers and to further decide the forming quality of FGMs.

1. INTRODUCTION

Functionally graded materials (FGMs) belong to composite materials consisting of two or more constituent phases with a continuously variable composition. FGMs have a number of advantages that make them attractive in potential applications, including a potential reduction of in-plane and transverse through-the-thickness stresses, enhanced thermal properties, an improved residual stress distribution, higher fracture toughness, and reduced stress intensity factors [1]. Plasma deposition manufacturing (PDM) [2], as one kind of rapid manufacturing techniques, has been developed to directly fabricate the metal part with gradual material composition. So far, most studies on the directly forming FGMs are based on the experimental work. Pei et al. [3] applied one-step laser cladding to produce AlSi40 FGMs. Wu et al. [4] developed an in situ method to produce a Ni alloy composite coating reinforced by in situ reacted TiC particles with a gradient distribution, using one-step laser cladding with a pre-placed powder mixture on a 5CrMnMo steel substrate. Abboud et al. [5] investigated the laser surface cladding of Ti-Al/TiB₂ composites as a means of producing a FGM on a commercially pure Ti substrate. Lin et al. [6] applied laser rapid forming technique to fabricate a functionally graded Ti-Rene88DT alloy wall and to experimentally check the microstructure and element distribution in the FGM wall. In fact, some difficulties still exist in experimentally studying FGM forming process obtained by PDM and laser cladding techniques, which limits the further understanding of the physical mechanisms in the FGM forming process. For instance, it is difficult to detect the fluid flow in the molten pool and quantify the optimal processing parameters. In order to investigate the mechanism of rapid solidification of the molten pool and its effect on fabricating quality, the numerical simulation technologies are prior to the experiment researches on studying the heat and mass transfer during the PDM or laser cladding of FGM. The purpose of this paper is based on previous modeling [7] to further predict the temperature distribution, flow velocity of liquid phase and solute concentration of multi-component materials in the deposition layer and substrate during PDM of FGM process. In addition, a novel method called level set method is adopted to trace the surface profile of the molten pool and deposition layer changing with processing time.

2. MATHEMATICAL MODELING

2.1. Physical Modeling

The experimental setup for PDM of FGM material components can be schematically shown in Fig. 1. Powders of variably proportional composition controlled by FGM powder feeding system

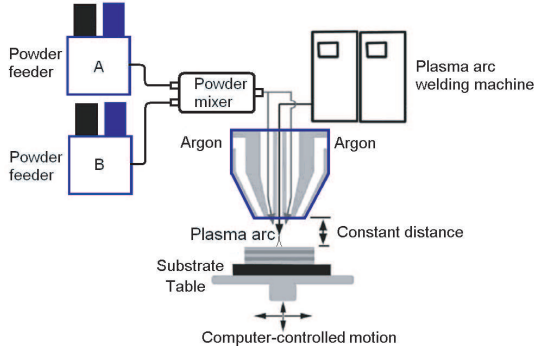


Figure 1: Schematic of PDM of FGM.

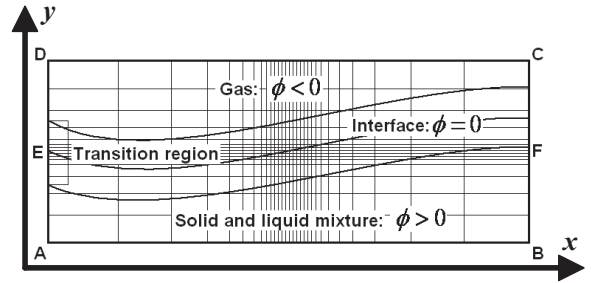


Figure 2: Schematic of level-set approach.

are delivered onto the substrate concentrically with the plasma arc burning. A small area of the surface of substrate and/or the present deposited layer under the plasma arc burning gets heated and melted, and a molten pool forms. A metal part with designed shape and composition is formed with the multi-layer scanning of plasma arc torch controlled by CNC machine tool and continuous powder addition with a variable mass ratio of bi-material composition.

To establish the mathematical model describing the whole deposition process, some fundamental assumptions are presented as follows: (1) Gas flow is assumed to be incompressible, and liquid flow is assumed to be incompressible and laminar flow; (2) regarding the mixture region of solid phase and liquid phase as mushy region; and (3) the chemical composition redistribution in the clad layer is due to the existence of convection of liquid phase in the molten pool.

2.2. Mathematical Modeling

The calculation domain is illustrated in Fig. 2, which includes the substrate and deposited layer (solid phase), the molten pool (liquid phase), and part of the surrounding air (gas phase). The continuum model, which introduces the Darcian damping term, governs the conservations of mass, momentum, and energy for the mushy zone, liquid region, and solid region, and governs the conservations of solute diffusion in the liquid region, and it may be described as follows:

Mass conservation equation:

$$\frac{\partial \rho}{\partial t} + \frac{\partial(\rho u)}{\partial x} + \frac{\partial(\rho v)}{\partial y} = 0 \quad (1)$$

Solute diffusion equation:

$$\frac{\partial}{\partial t}(\rho C_i) + \frac{\partial(\rho C_i u)}{\partial x} + \frac{\partial(\rho C_i v)}{\partial y} = \frac{\partial^2(\rho f_l D C_i)}{\partial x^2} + \frac{\partial^2(\rho f_l D C_i)}{\partial y^2} \quad (2)$$

Momentum conservation equations:

$$\begin{aligned} \frac{\partial(\rho u)}{\partial t} + \frac{\partial(\rho u u)}{\partial x} + \frac{\partial(\rho v u)}{\partial y} &= \mu \left(\frac{\partial^2 u}{\partial x^2} + \frac{\partial^2 u}{\partial y^2} \right) - \frac{\partial p}{\partial x} - \left[\frac{E(1-f_l)^2}{f_l^3 + b} \right] (u - V_S) \\ &+ e_x \cdot \left(-\tau \kappa(\phi) \nabla \phi + \nabla_s T \frac{d\tau}{dT} \right) \cdot \delta(\phi) \end{aligned} \quad (3)$$

$$\begin{aligned} \frac{\partial(\rho v)}{\partial t} + \frac{\partial(\rho u v)}{\partial x} + \frac{\partial(\rho v v)}{\partial y} &= \mu \left(\frac{\partial^2 v}{\partial x^2} + \frac{\partial^2 v}{\partial y^2} \right) - \frac{\partial p}{\partial y} - \left[\frac{E(1-f_l)^2}{f_l^3 + b} \right] v \\ &+ e_y \cdot \left(-\tau \kappa(\phi) \nabla \phi + \nabla_s T \frac{d\tau}{dT} \right) \cdot \delta(\phi) + \rho g \beta (T - T_m) \end{aligned} \quad (4)$$

Energy conservation equation:

$$\rho c \frac{\partial T}{\partial t} + \rho c \left(\frac{\partial T}{\partial x} u + \frac{\partial T}{\partial y} v \right) = k \left(\frac{\partial^2 T}{\partial x^2} + \frac{\partial^2 T}{\partial y^2} \right) + [q_{\text{plasma}} - \sigma \varepsilon (T^4 - T_\infty^4) - h_c (T - T_\infty)] \cdot \delta(\phi) \quad (5)$$

In the aforementioned equations, ρ is mean density, t is time, C_i is mass fraction of solute i , u , and v are components of velocity along x and y coordinates, respectively. D is solute diffusion

coefficient, f_l is the mass fraction of liquid phase in a certain control volume, p is pressure, μ is dynamical viscosity of liquid phase, and b is small positive constant to avoid the denominator to be zero. V_s is scanning speed of plasma welding torch relative to substrate, T is temperature, T_m is the melting point of deposited material, E is the permeability coefficient dependent on the material microstructure, g is the gravity acceleration, β is thermal expansion coefficient, k is heat conductivity, and q_{plasma} is heat input from plasma arc, σ is the Stefan-Boltzmann constant, ϵ is the emissivity, h_c is the forced convection coefficient, T_∞ is the room temperature, $\delta(\phi)$ is position control and expressed as follows:

$$\delta(\phi) \equiv \begin{cases} 1 & \text{if } \phi = 0, \\ 0 & \text{otherwise} \end{cases} \quad (6)$$

The intensity profile of the plasma arc acting on the top surface of the molten pool is also assumed to obey Gaussian distribution:

$$q_{\text{plasma}} = \frac{2\eta P_{\text{plasma}}}{\pi R^2} \exp\left(-\frac{2r^2}{R^2}\right) \quad (7)$$

where, P_{plasma} is the plasma arc power, R is the efficient beam spot radius, r is the distance from the calculation cell to the arc center, and η is absorptivity. As aforementioned, the physical phenomena occurring at the solid/liquid interface and liquid/gas interface are implicitly implemented as the parts of the source terms of energy and momentum conservation equations correspondingly. In this study, it is assumed that there exist convection and radiation heat transfer between solid phase boundaries, AB, AE, BF and the ambient boundary, and gas phase boundaries, DC, DE and CF, are thermal insulated boundaries (see Fig. 2). Due to the solid phase and liquid phase simultaneously exist of one cell in the porous region, a mixture properties are used for density, specific heat, conductivity, enthalpy, and velocity vector, the more detailed description can reference to Ref. [7]. In the case of PDM process, the fluid flow in the molten pool is mainly driven by surface tension, thermocapillary force, and electromagnetic force of the plasma arc acting on the molten pool surface. In order to track the evolution of the molten pool surface, a level-set approach [8] is introduced to deal with complex physical phenomena occurring on the free surface of the molten pool, as shown in Fig. 2. In order to veritably reflect the physical process of PDM, a level-set function can be simplified and shown as follows [7–9]:

$$\phi_t + F_e |\nabla\phi| + U(x, y, t) \cdot \nabla\phi = 0 \quad (8)$$

Here, $U(x, y, t)$ is a convection velocity function, and F_e is a velocity function dependent on the motion of L/G interface based on the powders deposition. In the present paper, F_e is assumed to comply with Gaussian distribution as below:

$$F_e = \begin{cases} \frac{\eta' \dot{m}}{\pi R'^2} \exp\left(-\frac{r'^2}{R'^2}\right) / (\rho_l V_s) & r' \leq R' \\ 0 & r' > R' \end{cases} \quad (9)$$

where r' is the distance from the center of top surface of the molten pool, R' is the efficient radius of the powder feeding flow. \dot{m} is the mass of the powders feeding in unit interval, η' is an efficient utilization ratio, ρ_l is the density of powders in the liquid phase, V_s is the scanning speed of the plasma arc torch.

3. NUMERICAL SIMULATION APPROACH AND CASE ANALYSIS

In this study, material of substrate is mild steel AISI 1045 and feeding powder materials used are Nickel base alloy K163 and AISI 1045. Physical parameters of K163 and AISI 1045 refer to Ref. [7] The dimensions of substrate are 60 mm×15 mm, the dimension of simulation region is 60 mm×30 mm. In this case, arc currents are set to 35 A, 70 A and 105 A, respectively. electric voltage is kept constant as 34 V, the effective diameter of the plasma arc is 6 mm, the effective diameter of powder flow beam is 5 mm, absorptivity of plasma arc power is 0.3, powder feed rate is 0.25 g/s, and scanning speed is 6 mm/s. Four-layered PDM process is simulated, in which surface tension and buoyancy are considered as driving forces of flow field in molten pool. The numerical implementation of the transport equations is based on the semi-implicit finite-difference approximation method [10], and a staggered grid is employed for convergence and stability. The

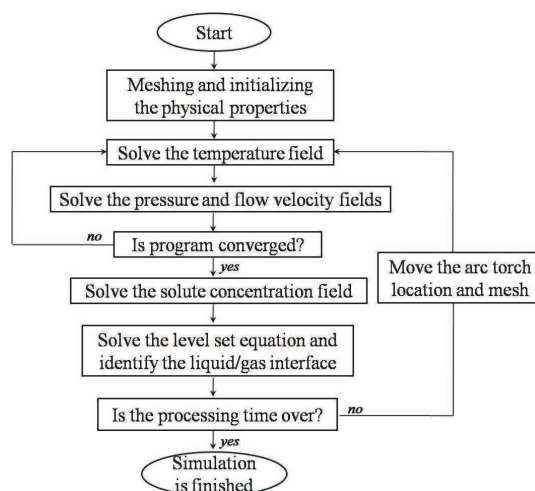


Figure 3: Flowchart of the numerical procedure.

detailed procedure can be depicted in Fig. 3. In addition, a self-adaptive asymmetric grid has been applied in this study, i.e., finer meshes distribute near and inside the melt pool in order to require the precise simulation, and much sparser meshes distribute far from the molten pool so as to reduce the whole computational cost.

4. RESULTS ANALYSIS AND DISCUSSION

The transient temperature distribution in the PDM of FGM is shown in Fig. 4(a). A higher temperature gradient locates in the molten pool zone due to the plasma arc heating. Fig. 4(b) shows the transient fluid velocity distribution during PDM of FGM. The numerical results of fluid flow in the molten pool further show that the dimension of the molten pool shape tends to increase with the scanning of the plasma arc torch, and the depth of molten pool increases as well. At the second, third and fourth layer deposition processes, the plasma arc heat source also makes the previous deposited layer even with substrate remelting locally, which further drives the diffusion of the solute of deposited material into substrate and simultaneously forms solute gradient distribution along the deposited layer thickness, which is shown in Fig. 4(c).

Figure 5(a) shows that concentration distribution of FGMs manufactured by PDM technique along the deposited layer thickness at $x = 30$ mm with three cases of different variations of powder compositions mass ratios. These three cases are described as below: (1) Case A: The mass fractions of Nickel alloy in mixed deposited powder at first, second, third, and the fourth deposited layers are 40%, 70%, 90% and 100%, respectively; (2) Case B: The mass fractions of Nickel alloy in mixed deposited powder at first, second, third, and the fourth deposited layers are 25%, 50%, 75% and 100%, respectively; and (3) Case C: The mass fractions of Nickel alloy in mixed deposited powder at first, second, third, and the fourth deposited layers are 10%, 30%, 60% and 100%, respectively. It clearly indicates that powder compositions mass ratios directly influence the final material composition gradient distribution. Fig. 5(b) shows that solute concentration distribution of substrate material along the thickness of the deposited layer obtained by different plasma arc

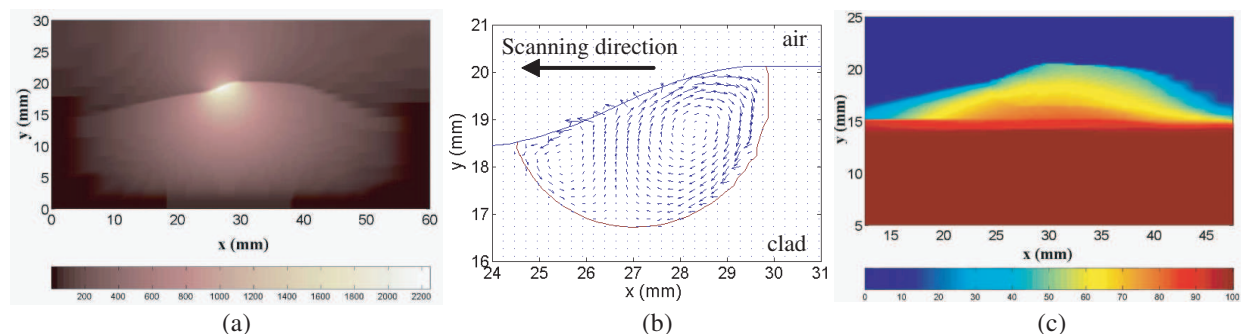


Figure 4: Transient temperature distribution. (a) Flow velocity distribution of liquid phase, (b) and transient concentration distribution of substrate solute, (c) in the fourth layer deposition ($t = 18$ s) during PDM of FGMs.

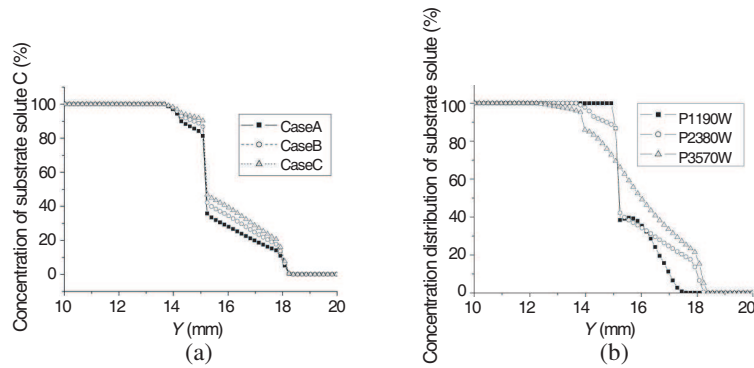


Figure 5: (a) Concentration distribution of substrate material in FGMs along the deposited layer thickness ($x = 30$ mm) in three cases of different variations of powder compositions mass ratios, (b) concentration distribution of FGMs manufactured by PDM technique ($x = 30$ mm) at different powers of plasma arc.

powers. The results describe that the composition gradient transverse to the deposited layers of FGM parts becomes more uniform with an increase in plasma arc power.

5. SUMMARY AND FUTURE WORK

In this study, a transient solid-liquid-gas unified model is developed to investigate the influence of the temperature distribution and fluid flow of the liquid phase inside the molten pool on the composition gradient formation during PDM of FGMs. The model shows that convection plays a significant role in the heat dissipation, solute diffusion and deciding the melt pool shape; moreover, compared with previous assumption of a flat free surface, tracking the surface profile of the deposition layer by level-set approach may cause an apparent improvement towards the real situation. Furthermore, the results of this study will give some insight into the practical applications of rapid manufacturing FGM by other high energy beam techniques. Due to the challenges existing in the experimentally realization of rapid manufacturing FGMs, it is critical and necessary for further developing the numerical modeling of plasma deposition manufacturing FGMs to combine with reliable experimental implementation, and a three-dimensional numerical investigation will make a deeper understand of heat and mass transfer process available in the high energy beam forming FGMs.

REFERENCES

1. Birman, V. and L. W. Byrd, "Modeling and analysis of functionally graded materials and structures," *ASME Applied Mechanics Reviews*, Vol. 60, No. 5, 195–225, 2007.
2. Zhang, H., J. Xu, and G. Wang, "Fundamental study on plasma deposition manufacturing," *Surface and Coating Technology*, Vol. 171, Nos. 1–3, 112–118, 2003.
3. Pei, Y. T. and J. Th. M. De Hosson, "Functionally graded materials produced by laser cladding," *Acta Materialia*, Vol. 48, No. 10, 2617–2624, 2000.
4. Wu, X., "In situ formation by laser cladding of a TiC composite coating with a gradient distribution," *Surface and Coating Technology*, Vol. 115, Nos. 2–3, 111–115, 1999.
5. Abboud, J. H., D. R. F. West, and R. D. Rawlings, "Functionally gradient titanium-aluminide composite produced by laser cladding," *Journal of Materials Science*, Vol. 29, No. 13, 3393–3398, 1994.
6. Lin, X., T. M. Yue, H. O. Yang, W. D. Huang, "Microstructure and phase evolution in laser rapid forming of a functionally graded Ti-Rene88DT alloy," *Acta Materialia*, Vol. 54, No. 7, 1901–1915, 2006.
7. Kong, F., H. Zhang, and G. Wang, "Numerical simulation of the transient multiphase transient field during plasma deposition manufacturing composite materials," *Science in China Series G: Physics, Mechanics and Astronomy*, Vol. 52, No. 4, 508–517, 2009.
8. Chen, S., B. Merriman, S. Osher, et al., "A simple level set method for solving Stefan problems," *Journal of Computational Physics*, Vol. 135, No. 1, 8–29, 1997.
9. Han, L., F. W. Liou, and K. M. Phatak, "Modeling of laser cladding with powder injection," *Metallurgical and Materials Transactions B*, Vol. 35, No. 6, 1139–1150, 2004.
10. Patankar, S. V., *Heat Transfer and Fluid Flow*, Hemisphere, New York, 1980.

Rapid Manufacturing of FGM Components by Using Electromagnetic Compressed Plasma Deposition

Haiping Zou, Haiou Zhang, Guilan Wang, and Jian Li

Huazhong University of Science and Technology, Wuhan 430074, China

Abstract— Layered Manufacturing (LM) is emerging as a new technology in recent years that enables the fabrication of three-dimensional heterogeneous objects, especially Functionally Graded Materials (FGM) whose composition or the microstructure is locally varied to alter the material properties. This paper presents a new fabrication method for fabricating FGM component by using electromagnetic compressed Plasma Deposition Manufacturing (PDM) process. Ni-base alloy/ Al_2O_3 -ceramic FGM test component with continuous gradient transition composition were fabricated in the PDM process and the specimens' cross-sections were analyzed using optical metallography and Micro-hardness test. No defects were noticed on the cross-sections and the micro-hardness of the FGM component was increasing gradually while Al_2O_3 -ceramic ingredient ratio increased. With the quantity of Al_2O_3 -ceramic granule joined in the molten bath increasing, the Ni-base alloy's organization proportion reduced significantly according predefined materials gradients.

1. INTRODUCTION

Functionally graded materials (FGM) are a new generation of engineering materials with continuous changes of microstructures and properties across the material [1]. The unique characteristics in structure distribution make FGM offer great promising characteristics such as low residual and thermal stresses and improved bonding strength between dissimilar materials. Generally the manufacturing processes that can fabricate FGM objects are Laser Engineered Net-Shaping (LENS) [2], Directed Light Fabrication (DLF) [3], Electron Beam Freeform Fabrication (EBF) [4], which are termed as rapid prototyping (RP) or layered manufacturing (LM). Electromagnetism compressed Plasma deposition manufacturing (PDM) [5], as a newly developed direct metal fabrication process, belongs to 3D welding. This technique is characterized by supplying head delivering a well-defined flow rate of material powder, which is deposited in molten pool formed by controlled plasma heating. Thereby full strength parts with the single or multifarious materials can be built up layer by layer, by melting and rapid solidifying the feed material into the desired shape. Those fabrication techniques involve deposition of material to create objects, unlike conventional methods, in which material is removed to obtain the final object [6]. The deposition of material can be explicitly controlled thereby providing unique opportunities to selectively deposit material. In other words, the material deposited can be varied continuously to yield a functionally graded material object with varying material distribution.

2. EXPERIMENTAL PROCEDURES

The functionally gradient materials (FGM) component was fabricated by using electromagnetic compress plasma deposition system that consists of plasma transferred arc and non-transfer arc generating unit and its cooling unit, magnetic field generator, a five-axis numerical control working table, and a set of flexible control 3-units synchronous powder feeder unit with a coaxial powder feed nozzle. A schematic diagram of the system is given in Fig. 1.

The plasma torch was mounted on a support structure of the deposition system. When fabricating the component through plasma deposition process, the plasma non-transfer arc and transferred arc beam were directed onto the substrate to create a molten pool into which the material powders were injected through the powder feed nozzle. The metal powders were melted and subsequently resolidified to form the deposition layer.

During the plasma deposition process, the feasibility, characteristic and quality of plasma deposition were influenced by many parameters such as transferred arc current, powder flow rate and the moving speed of workpiece. We adjusted the workpiece's moving speed primarily and synchronously controlled plasma arc power's match to guarantee the molten bath surface temperature's basic consistent in the entire forming process. Based on previous experiments, parameters of the optimal transferred arc current, powder flow rate and workpiece's moving speed scope used in our deposition processing were listed in Table 1.

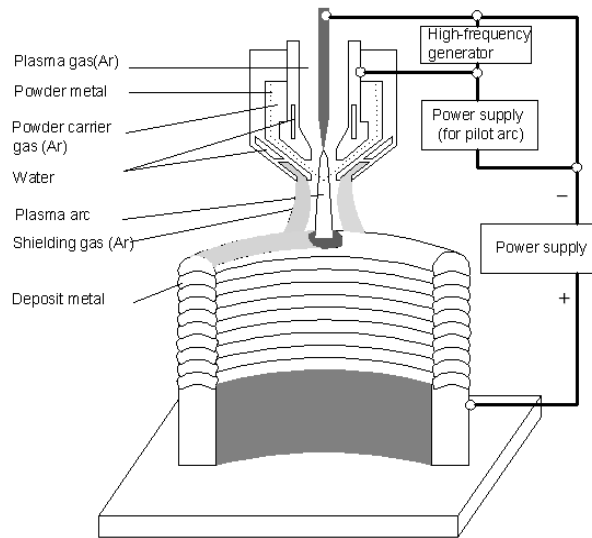


Figure 1: Schematic diagram of electromagnetic compressed plasma deposition.

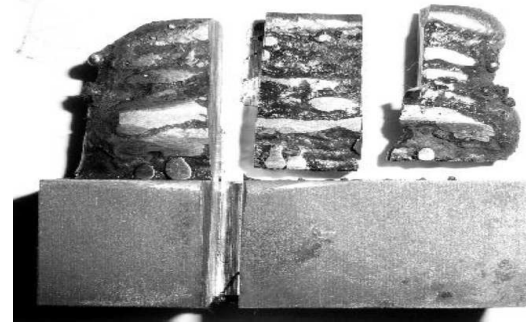


Figure 2: The solid form of the Ni-base alloy / Al₂O₃ functionally graded material.

Table 1: Plasma deposition processing parameters.

Transferred arc current (A)	Powder flow rate (g/min)	Workpiece's speed (mm/min)	Argon flow rate (l/min)		
			Pilot gas	Shielding gas	Carrier gas
48	8	200–300	0.15	0.3	0.36

The magnetic field used to compress the plasma arc during FGM component deposition process was generated by the magnet exciting coil which mounted on the carriage near plasma powder feed nozzle and in the position of being coaxial with the plasma torch. The magnetic field strength and the magnetic field frequency could be adjusted manually and the produced magnetic field was a longitudinal field or coaxial magnetic fields (magnetic lines of force directions were in parallel with plasma arc axial line, and formed axis-symmetrical distribution.)

A FGM component with a rectangular profile (Fig. 2) was fabricated, with its first 4 layers (Approximately 2 mm from the substrate) composed of 100% Ni-base alloy. The composition of the deposition was then changed from 0 to 57% Al₂O₃ over the next 28 layers. The variation in composition along the height of the solid structure was achieved by using our new developed flexible control 3-units synchronous powder feeder to deliver proper proportion of each powder according predetermined materials powder ratio of the graded structure, and then the delivered powders out of the powder feeder were well-mixed in the powder feed tube and coaxial powder feed nozzle before sending into the molten bath the powder to realize the desired ingredient gradient distribution of the component during the whole electromagnetic compress PDM fabricating process. The PDM deposition processing parameters used in the experiment were presented in Table 1. The substrate material used for the experiment was 45# medium carbon steel sheet. The surface of the substrate was cleaned by sandblasting prior to plasma deposition. In order to eliminate any water that was trapped in the powders, the powders were dried in an oven more than 4 h. Argon gas was also used to deliver the metal powders to prevent the melt pool from oxidizing and from oxide contamination occurring during processing.

3. EXPERIMENTAL RESULTS

The fabricated FGM component was sliced into several cross-section specimens to measure the micro-hardness and examine the microstructure along gradient direction.

3.1. Micro-hardness of the FGM Component

In our study, we used the HXD-1000 micro-hardness tester to survey micro-hardness of the deposition component. The micro-hardness measurements (load 1/4 1.961N) were carried out on the pol-

ished longitudinal cross-sections of the deposited FGM component. Fig. 3 presents micro-hardness profiles along specimens' height direction (material gradient direction) cross-section. Obviously, the FGM component fabricated by electromagnetic compressed plasma deposition processing change its micro-hardness from 450 HV at the bottom of the specimen with compositions of 100% Ni-base alloy (1 mm from the substrate) to 1050 HV at the top of the specimen with compositions of 43% Ni-base alloy and 57% Al_2O_3 (15 mm from the substrate).

The results revealed largely that gradual change of micro-hardness values was the result of Al_2O_3 -ceramic ingredient gradient distribution as expected.

3.2. Microstructure

Figure 4 shows the microstructures taken in cross-section parallel to the gradient direction and at various distance away from the substrate along the compositional gradient (height direction). These photos show that no defects were noticed on the whole cross-sections, good metallurgy union was formed between various gradients layers, and no obvious contact surface slit was observed between various gradients level organization. The Ni-base alloy's organization proportion reduced significantly while the quantity of Al_2O_3 -ceramic granule join in the molten bath increasing when

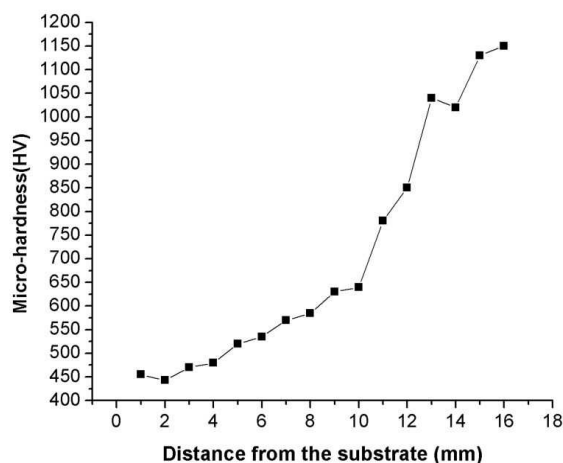


Figure 3: Longitudinal micro-hardness profiles along material gradient direction.

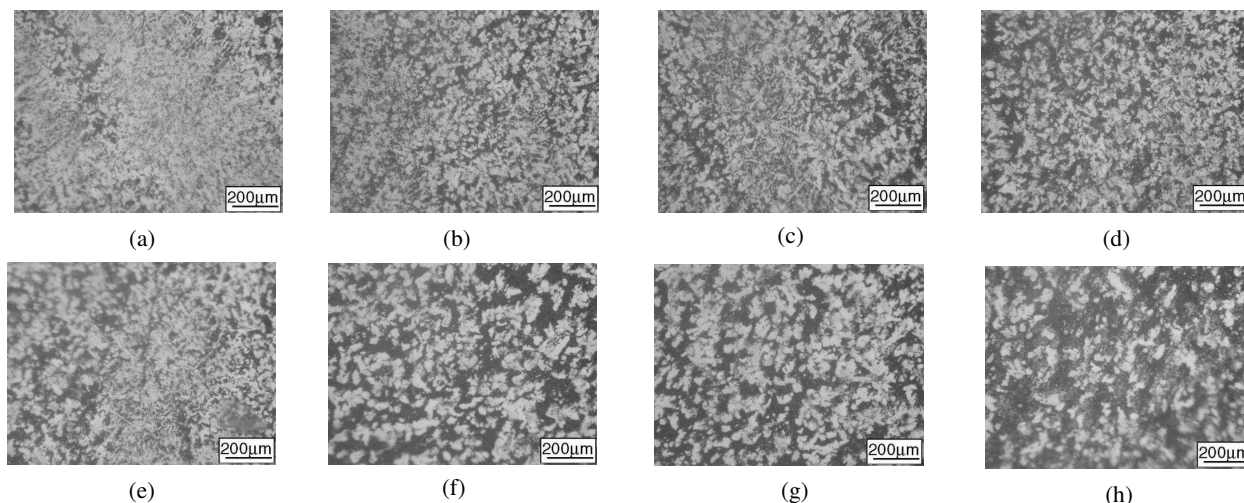


Figure 4: The microstructure of the graded material with different compositions. (a) Ni-base alloy (1 mm from the substrate); (b) 86% Ni-base alloy + 14% Al_2O_3 (3 mm); (c) 79% Ni-base alloy + 21% Al_2O_3 (5 mm); (d) 72% Ni-base alloy + 28% Al_2O_3 (7 mm); (e) 65% Ni-base alloy + 35% Al_2O_3 (9 mm); (f) 58% Ni-base alloy + 42% Al_2O_3 (11 mm); (g) 50% Ni-base alloy + 50% Al_2O_3 (13 mm); (h) 43% Ni-base alloy + 57% Al_2O_3 (15 mm).

formed the Al₂O₃-ceramic ingredient gradient distribution solidification layers.

The photo showed graded materials distributions were realized with smooth multilayered gradients. Transition zone thickness between each two layers was almost indistinguishable. During the plasma deposition process, an appropriate change in process parameters is required to keep growth rate and geometrical parameters stable to build up a gradient between the materials for Ni-base alloy and Al₂O₃ powders having different material characters. In the deposition process the more Ni-base alloy proportion in the mixed powder, the more plasma arc power dense is required to keep the growth rate constant. We adjusted the workpiece's moving speed from 200 mm/min to 300 mm/min assuming a linear relation between values related to material when materials change from compositions of 100% Ni-base alloy to compositions of 43% Ni-base alloy and 57% Al₂O₃ to guarantee the molten bath surface temperature's basic consistent in the entire forming process.

4. CONCLUSIONS

The functionally gradient materials component of Ni-base alloy / Al₂O₃-ceramic was fabricated by using electromagnetic compress plasma deposition system. A linear compositional gradient, from 100% Ni-base alloy to 57% Al₂O₃-ceramic, was achieved within a height of about 16 mm. The micro-hardness and microstructure along the composition gradient were investigated. The results show that, within the processing parameters of the study, the micro-hardness of the deposition component increased gradually from 450 HV at the bottom of specimen cross-section to 1050 HV at the top of specimen cross-section when the Ni-base alloy ingredient ratio changed from 100% to 43% while the Al₂O₃-ceramic ingredient ratio changed from 0 to 57%. Microstructure of longitudinal section showed multi-layered construction of the component and no defects were noticed on the cross-sections. While the quantity of Al₂O₃-ceramic granule joined in the molten bath increased, the Ni-base alloy's organization proportion reduced significantly according predefined materials gradients.

ACKNOWLEDGMENT

The research described in this paper was supported by the National Nature Science Foundation of China under project No. 50475134 and the State High-technology Development Program of China under project No. 2007AA04Z142.

REFERENCES

1. Banks, L., R. Eliahi, and Y. Berlin, "Modeling of functionally graded materials in dynamic analyses," *J. Composites Part B: Engineering*, Vol. 33, 7–15, 2002.
2. Griffith, M., D. M. Keicher, and C. L. Atwood, "Freeform fabrication of metallic components using laser engineered net shaping (LENS)," *Proceedings of the Solid Freeform Fabrication Symposium*, 125–131, University of Texas at Austin, 1996.
3. Lewis, G., J. Milewski, and D. Thoma, "Properties of near-net shape metallic components made by the direct light fabrication process," *Proceedings of the Solid Freeform Fabrication Symposium*, 513–520, University of Texas at Austin, 1997.
4. Karen, M. B and R. Taminger, "A electron beam freeform fabrication a rapid metal deposition process: A rapid metal deposition process," *Proceedings of the 3rd Annual Automotive Composites Conference*, 9–10, 2003.
5. Zhang, H., J. Xu, and G. Wang, "Fundamental study on plasma deposition manufacturing," *Surf. Coat.*, Vol. 171, 112–118, 2003.
6. Karapatis, N. P., J. P. Griethuysen, and R. Glardon, "Direct rapid tooling: A review of current research," *Rap. Proto. J.*, Vol. 4, 77–89, 1998.

Research on Brushless Doubly-fed Machine with a New Wound Rotor and Its Generating System

Zhongchao Wei, Xuefan Wang, Xia Chen, and Chaohao Kan

Department of Electrical Machines and Drives, Huazhong University of Science and Technology, China

Abstract— The Brushless Doubly-Fed Machine (BDFM) is a new-type of special electrical device. This kind of machine solve the structural problems of brushless, combining with the favorable characteristic of the asynchronous motor and synchronous generator. This paper presents the principle, structure and operation mode of BDFM. Based on the BDFM with the conventional rotor structure, a novel BDFM with a special rotor structure is proposed according to the tooth harmonic theory. The design of the rotor coil and the basic theory are discussed in detail. Furthermore, aiming to the simulation and practical test research, the prototype is developed and be tested, which proves its application prospect.

1. INTRODUCTION

The conventional brushless doubly-fed machine employs the special rotor or reluctance motor, in which the special rotor is the best choice for the large capacity machine. However, the disadvantages can't be avoided, such as much harmonic, the low utilization of the conductor [1]. This paper proposed a new rotor structure, which adopts the wound type instead of the cage type. With a smaller size and high efficiency, it can reduce the harmonic component considerably. Aimed to the requirement of the generator for the ship, a prototype of a 50 kW brushless doubly-fed machine was developed and the principle was discussed combined with the practical application. Due to reducing the capacity of the frequency converter, the active power and reactive power can be regulated conveniently without the reactive power compensation device and filter [2]. According to the design parameters and the test results, it was validated that this type of machine presents favorable performance.

2. THE PRINCIPLE AND THE MATHEMATICA MODEL

The principle of the brushless doubly-fed machine working in the mode of generation is illustrated as Fig. 1. The stator has two sets of windings. One is connected with the frequency converter; the other (the assistant winding) is used as the control winding. Both of the windings are corresponding to different pole pair number [3]. Whenever the two sets of windings connected at the same time or respectively, the stator winding will produce two different rotating magnetic filed. It is not desired that the two rotating magnetic fields interfered each other, so it's required that the main control winding will produce the induced potential in the stator winding and no potential difference between the three output terminals. Moreover, when the control winding is supplied, the additional current will not arose at the power supply port. Due to the wound rotor, the two sets of windings can be deemed as the reversal cascade. There is no coupling between the magnetic fields produced by the two sets of windings. The energy is transferred through the rotor field instead that of the stator.

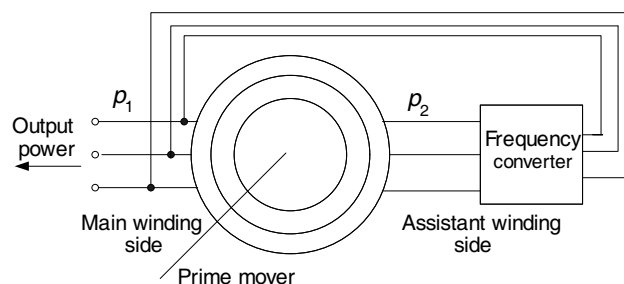


Figure 1: The operation principle of brushless double-fed machine.

The prime mover drives the generator at the speed of n_r , and the assistant winding is supplied by the frequency converter, the frequency of the output voltage is

$$f_1 = \frac{(p_1 + p_2)}{60} n_r \pm f_2 \quad (1)$$

In which, p_1 and p_2 are the pole pair number of the main winding and assistant winding respectively.

Variable speed constant frequency operation can be realized by changing the output voltage and frequency of the frequency converter.

On the assumption that the Permeability of iron core is infinite, ignoring the magnetic voltage drop; regardless of the tooth and slot effects and considering the air gap distributing equally; the main winding and assistant winding are symmetrical in the space structure, only flowing the fundamental wave current and the initial phase angle of the current of A phase winding is zero [4].

Based on the electrical machine theory, the main winding adopts the generator rule and the assistant winding adopts the motor rule. The voltage equation of the brushless doubly-fed machine in d - q coordinate system is as following [5]:

$$\begin{aligned} \begin{bmatrix} u_{dq1} \\ u_{dq2} \\ u_{dqr} \end{bmatrix} &= \begin{bmatrix} R_1 & 0 & 0 \\ 0 & R_2 & 0 \\ 0 & 0 & R_r \end{bmatrix} \begin{bmatrix} i_{dq1} \\ i_{dq2} \\ i_{dqr} \end{bmatrix} + \begin{bmatrix} p_1 \omega_r \Gamma & & \\ & p_2 \omega_r \Gamma & \\ & & 0 \end{bmatrix} \begin{bmatrix} \psi_{dq1} \\ \psi_{dq2} \\ \psi_{dqr} \end{bmatrix} + p \begin{bmatrix} \psi_{dq1} \\ \psi_{dq2} \\ \psi_{dqr} \end{bmatrix} \\ &= \left(\begin{bmatrix} R_1 & 0 & 0 \\ 0 & R_2 & 0 \\ 0 & 0 & R_r \end{bmatrix} + \begin{bmatrix} p_1 \omega_r \Gamma & & \\ & p_2 \omega_r \Gamma & \\ & & 0 \end{bmatrix} \begin{bmatrix} L_{dq1} \\ L_{dq2} \\ L_{dqr} \end{bmatrix} \right) \begin{bmatrix} i_{dq1} \\ i_{dq2} \\ i_{dqr} \end{bmatrix} + p \begin{bmatrix} \psi_{dq1} \\ \psi_{dq2} \\ \psi_{dqr} \end{bmatrix} \end{aligned}$$

That is:

$$u_{dq} = R_{dq} i_{dq} + L_{dq} \frac{d}{dt} i_{dq} \quad (2)$$

In which:

$$\Gamma = \begin{bmatrix} 0 & -1 & 0 \\ 1 & 0 & 0 \\ 0 & 0 & 0 \end{bmatrix} R = \begin{bmatrix} R_1 & 0 & 0 \\ 0 & R_2 & 0 \\ 0 & 0 & R_r \end{bmatrix} + \begin{bmatrix} p_1 \omega_r \Gamma & & \\ & p_2 \omega_r \Gamma & \\ & & 0 \end{bmatrix} \begin{bmatrix} L_{dq1} \\ L_{dq2} \\ L_{dqr} \end{bmatrix}$$

The torque equation is

$$T_e = i_{dq1}^t H_{sr1} i_{dqr} + i_{dq2}^t H_{sr2} i_{dqr} = i_{dq}^t M i_{dq} \quad (3)$$

In which:

$$\begin{aligned} i_{dq}^t &= [i_{dq1}^t \ i_{dq2}^t \ i_{dqr}^t], \\ M &= \begin{bmatrix} 0 & 0 & H_{sr1} \\ 0 & 0 & H_{sr1} \\ H_{sr1}^t & H_{sr1}^t & 0 \end{bmatrix}, \\ H_{sr1} &= \frac{3}{2} p_1 L_{m1} \begin{bmatrix} 0 & -1 & 0 \\ 1 & 0 & 0 \\ 0 & 0 & 0 \end{bmatrix} \\ H_{sr2} &= \frac{3}{2} p_2 L_{m2} \begin{bmatrix} 0 & 1 & 0 \\ 1 & 0 & 0 \\ 0 & 0 & 0 \end{bmatrix} \end{aligned}$$

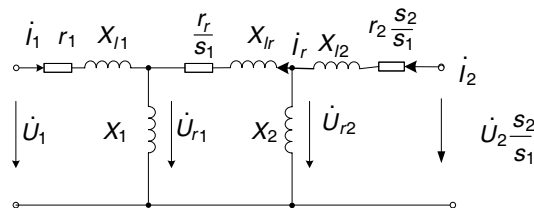


Figure 2: The equivalent circuit of the double fed machine.

Simplified expression:

$$T_e = \frac{3}{2}p_1L_{m1}(i_{q1}i_{dr} - i_{d1}i_{qr}) + \frac{3}{2}p_2L_{m2}(i_{q2}i_{dr} + i_{d2}i_{qr}) \quad (4)$$

According to the expression above, the equivalent circuit of the double fed machine is as follows [6].

In which: $r_r = k_1^2R_r$, $r_2 = k_2^2R_2$, $L_{lr} = k_1^2L_{lr}$, $L_{l2} = k_2^2L_{l2}$, $X_{l1} = \omega_1L_{l1}$, $X_{l2} = \omega_1L_{l2}$, $X_{lr} = \omega_1L_{lr}$, $X_1 = \frac{3}{2}\omega_1L_{m1} = \frac{3}{2}\omega_1k_1L_{sr1}$, $X_2 = \frac{3}{2}\omega_1k_2^2L_{m2} = \frac{3}{2}\omega_1kk_1L_{sr2}$, $s_1 = \frac{p_2f_1 - p_1f_2}{f_1(p_1 + p_2)}$, $s_2 = \frac{p_1f_2 - p_2f_1}{f_2(p_1 + p_2)}$ are the slip ratio of the main winding and assistant winding respectively.

3. THE DESIGN OF THE WINDING

The coupling of the stator fields between different pole pairs number is achieved by the modulating of rotor [4]. Therefore, the machine with different pole pairs number of stator winding such as P_1, P_2 as much as possible, the design of such machine should strengthen the p_1 th, p_2 th harmonic and eliminate other order harmonic [7]. The paper proposed a wound rotor structure based on the tooth harmonic principle. As for the AC winding, the number of the slot is Z and the pole pair number of the fundamental wave is p .

All v th harmonic ($v = nZ \pm p, n = 1, 2, 3 \dots$) in the AC winding with fundamental wave pole pair number p , whose short distance factor and distribution factor are the same as that of fundamental wave. Such harmonic is the so-called tooth harmonic. This harmonic is featured as the equal winding coefficient between the magnetomotive force of the tooth harmonic and fundamental wave emerging as the pair.

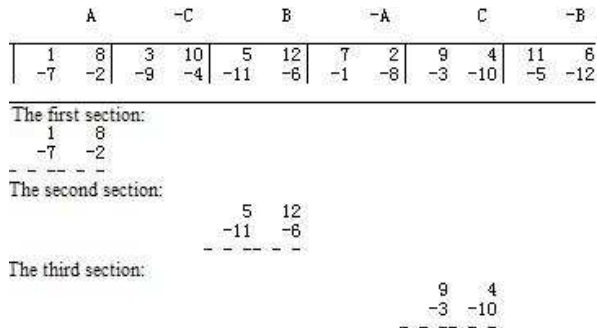


Figure 3: 12 slot/14 pole.

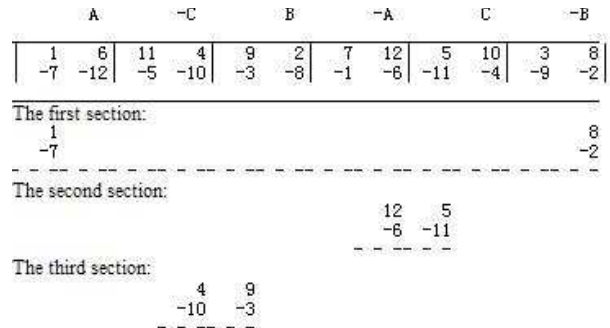


Figure 4: 12 slot/10 pole.

Table 1: The rotor harmonic analysis with the method of tooth harmonic.

Pole number	Short distance coefficient	Winding coefficient	Natural rotating Magnetic potential of the (%)	Reverse rotating Magnetic potential (%)
2	0.2588	0.0670	50.2577	0
10	0.9659	0.9330	0	140.0
14	0.9659	0.9330	100.0	0
22	0.2588	0.0670	0	4.5689
26	-0.2588	0.0670	3.8660	0
34	-0.9659	0.9330	0	41.1765
38	-0.9659	0.9330	36.8421	0
46	-0.2588	0.0670	0	2.1851
50	-0.2588	0.0670	2.0103	0

The operation principle of the brushless double-fed machine requires the rotor winding to produce rotating magnetomotive force of the pole pair number P_1 and P_2 . The rotating direction of the two kinds of magnetomotive force is just opposite. So the first task is to determine the required pole pair number P_1 of the main winding and P_2 of the assistant winding. Choose the slot number Z_2 as the relationship $Z_2 = p_1 + p_2$ on the Premise of symmetrical rotor winding.

The slot number phase maps are given in the case of the rotor 12 slot/14 pole and 12 slot/10 pole in Fig. 3 and Fig. 4, and Table 1 shows the corresponding harmonic analysis.

Aiming to the generation requirement for the use of the ship, the design of the new type brushless double-fed machine with wound rotor is completed. The rated speed of the machine is $n_r = 600\text{rpm}$, the output power 60 kW, the output phase voltage 220 V/50 Hz, the power factor of the inductive load 0.8. Table 2 has listed the design parameters.

4. THE ANALYSIS OF THE TEST AND RESULT

The prototype shown as Fig. 5 was tested and the principle diagram of the test is shown as Fig. 6.

The three-phase asynchronous motor was employed as the prime mover. The prototype was connected with the grid and the assistant winding is connected to the output terminal of the three-phase frequency converter. The DC bus of the frequency converter is connected with the active energy feedback device. The results in the case of the no-load and load can be seen from Fig. 7 and Fig. 8.

It can be observed from the test curves that the new type brushless double-fed machine with wound rotor can achieve the constant frequency generation as the speed of the prime mover changing. The output voltage keep stable, the regulating range of the speed wide, which validate the correctness of the theory analysis and has the prospect of the practical application.

Table 2: The design parameter of the prototype.

Output power of the main winding(kW)	50
Output power of assistant winding(kW)	10
Rated output voltage/frequency V/Hz	380/50
Rated rotating speed rpm	600
Slot number	72
Rotor number	54
Pole number of main winding	8
Pole number of assistant winding	4



Figure 5: The prototype of brushless double-fed machine with wound rotor.

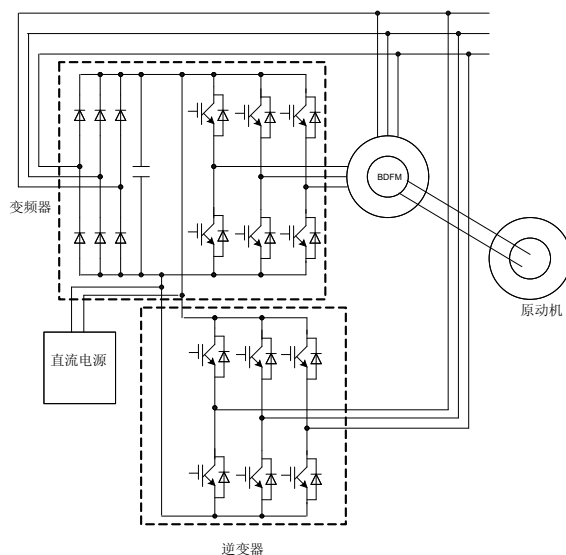


Figure 6: The test principle of the machine.

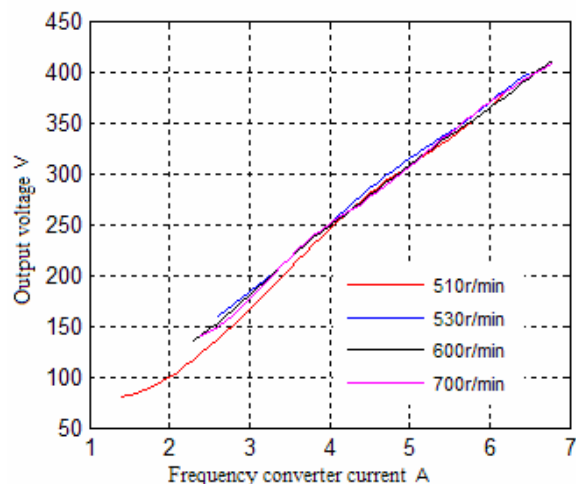


Figure 7: No load test curves of brushless doubly-fed generator.

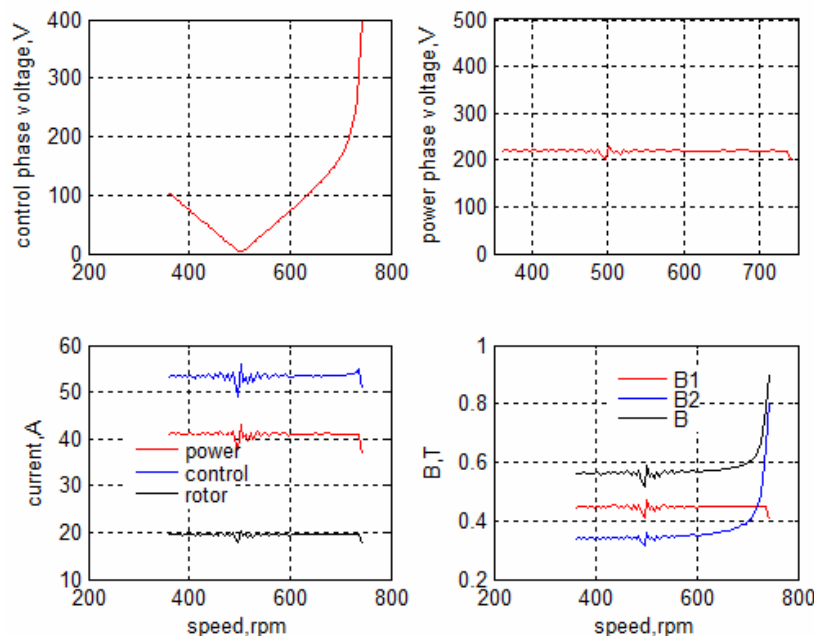


Figure 8: Load test curves of brushless doubly-fed generator.

REFERENCES

- Wallace, A. K., R. Spee, and H. K. Lauw, "Dynamic modeling of brushless doubly-fed machines," *IEEE Industrial Applications Social Annual Meeting*, 329–334, San Diego, 1989.
- Boger, M., A. K. Wallace, and R. Spee, "Investigation of appropriate pole number combinations for brushless doubly fed machines as applied to pump drives," *IEEE Trans. Ind. Appl.*, Vol. 31, No. 5, 1022–1028, 1996.
- Brune, C. S., R. Spee, and A. K. Wallace, "Experimental evaluation of a variable-speed, doubly-fed wind-power generation system," *IEEE Trans. Ind. Appl.*, Vol. 30, No. 2, 648–655, 1994.
- Williamson, S., A. C. Ferreira, and A. K. Wallace, "Generalized theory of the brushless doubly-fed machine. Part I: Analysis," *IEE Proc., Electra. Power Appl.*, Vol. 144, 111–122, 1997.
- Roberts, P. C. and R. A. McMahon, "Performance of BDFM as generator and motor," *IEE Proc., Electra. Power Appl.*, Vol. 153, No. 2, 289–299, 2006.
- Williamson, S., A. C. Ferreira, and A. K. Wallace, "Generalized theory of the brushless doubly-fed machine. Part 2: Model verification and performance," *IEE Proc., Electra. Power Appl.*, Vol. 144, No. 2, 123–129, 1997.
- Wallace, A. K., P. Rochelle, and R. Splee, "Rotor modeling and development for brushless doubly-fed machines," *Conf. Record of the Int. Conf. on Electrical Machines*, Vol. 1, Cambridge, 1990.

Study on Offsetting Path Planning for Electromagnetic-compressed Plasma Deposition Manufacturing in Rapid Metal Tooling

Jiang Jiang¹, Haiou Zhang², Guilan Wang², and Jian Li¹

¹State Key Laboratory of Materials Processing and Die & Mould Technology
Huazhong University of Science and Technology, Wuhan 430074, China

²State Key Laboratory of Digital Manufacturing and Equipment Technology
Huazhong University of Science and Technology, Wuhan 430074, China

Abstract— Direct metal shaping has been received more and more eyes in rapid manufacturing and Plasma Deposition Manufacturing has provided an effective way in fabricating metal parts directly from their digital models. In this paper, the electromagnetic-compressed plasma deposition manufacturing is presented which employs the electromagnetic-compressed plasma arc as the thermal source which is provided with the characteristics of low-cost and high efficiency. The influence of torch path to the performance of metal parts is researched and the algorithms of offsetting path planning are studied including the self-intersection algorithm and across-intersection algorithm between complicated two dimension rings. According to the algorithm, the valid rings are extracted and the redundant ring is eliminated successfully and efficiently in the torch path. The algorithm is verified on path planning of sheet metal stamping mould of wheel fender. The result shows that the crystal grain was greatly refined with the help of electromagnetic and the complicated contour of sheet stamping mould can be fully filled with the help of developed algorithms which suggest an efficient way for virtual manufacturing of rapid metal tooling.

1. INTRODUCTION

For more than a decade, layered manufacturing technology, also known as rapid prototyping (RP) has given industry an approach to achieve the goal of providing products in a shorter time and at a lower cost. Most of the current RP systems are built on a 2.5-D platform. Among them, the high density beam deposition process is a potential technique that can produce fully functional parts/mould directly from a CAD system and eliminate the need for intermediate steps [1–3]. Electromagnetic-compressed Plasma Deposition Manufacturing (EPDM) being developed in the HUST combined plasma deposition manufacturing and machining processes together to develop a hybrid process to build functional metal parts/moulds [4, 5]. In this process, path planning with offsetting style is the key point and many researchers have studied on offsetting style in path planning [6, 7].

2. PATH PLANNING WITH OFFSETTING STYLE

Path planning with offsetting style is an important style in 2D contour path planning and interference is the key problem. the Interference maybe appears when a two dimensional concave ring is offsetted and there are some self-intersections between two segments which are not adjacent to each other in a interfered ring. In this paper, the measurement of treating with interfered ring is grouped into 4 steps:

(1) Calculating all the intersections between two segments which are not adjacent to each other.

Self-intersection is the key reason of interference in offsetting, so the first step is to find all the intersections between all the segments which are not adjacent to each other. All the self-intersections are stored in the form of ((point coordinate value), the index of the start point of the intersected segment).

(2) Sequence all the intersections and delete all the repeated intersections.

The storage of self-intersected points is disorderly and unsystematic after first step. For example, some intersections are located in the middle of the segment some are on the endpoint. Some segments have only one intersected point, some have two or more. So it is necessary and important to sequence all the intersections in order to keep all the segments with one self-intersected point at most which will simplify the computation for the next step.

(3) Reconstruct new rings from the interfered ring.

Reconstruction is the key step of the whole process of treating with interfered ring. Reconstruction is to obtain several new rings by reorganizing the vertex of the interfered ring. The process is described as follows:

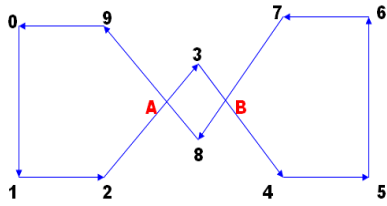


Figure 1: Interfered ring before treatment.

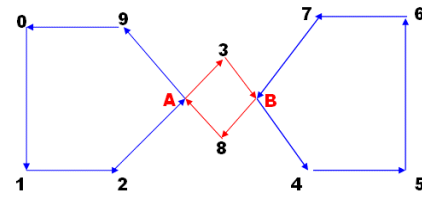


Figure 2: Constructed rings after treatment.

- (a) The first vertex of the first constructed ring is started at the index of zero in interfered ring. The storage sequence is the same with the interfere ring (0->1-> ...) until the self-intersected point is met. Store the self-intersected point and alternate the storage sequence. For example, in Fig. 1, the original sequence is (1->2->3->4), however, there is an intersection in the segment (2->3), so store the intersection (A), and transfer the storage sequence from (1->2->A->3->4) to (1->2->A->9) until the next self-intersected points is met or the endpoint of the interfered ring is met. When the endpoint of the interfered ring (9) is met. The new constructed ring is obtained.
- (b) The remained rings are started at the intersect-point and the same way is followed until all the remained new rings are constructed. For example, in Fig. 1, the interfered ring is transferred into three new rings: (1) 0->1->2->A->9, (2) A->8->B->3, (3) B->4->5->6->7.
- (4) Recognize the effective rings.

The effective ring is stored in the style of counter-clockwise (CCW). So the red ring No. 2 in Fig. 2 is deleted in this step. Two blue rings (ring No. 1 and ring No. 3) with clockwise (CW) are



Figure 3: The 3D model of stamping mould of vehicle fender.

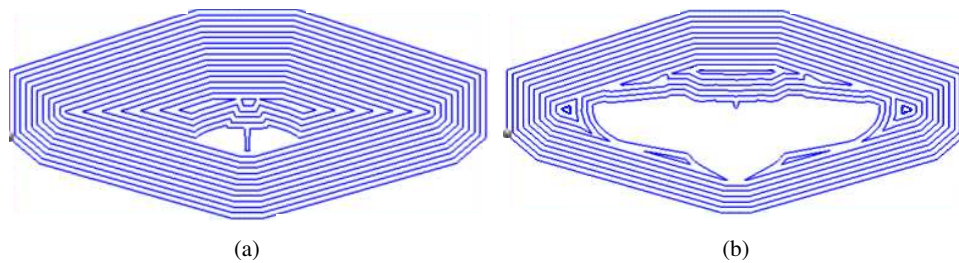


Figure 4: The offsetting path of two certain layers.

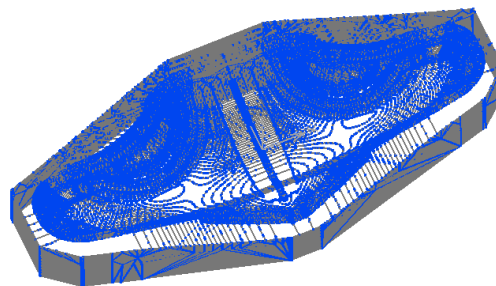


Figure 5: The overall path of stamping mould of vehicle fender.

reserved and these two rings will be continued to be offsetted to the end.

3. VERIFICATION

The algorithm is verified by stamping mould of vehicle fender Fig. 3 is the 3D model of stamping mould of vehicle fender. Fig. 4 is the offsetting path of two certain layers. Fig. 5 is the overall path of stamping mould of vehicle fender. The result shows that the algorithm is quite satisfied.

4. CONCLUSION

Interference is the key problem in path planning of offsetting style. A novel way of treating with interfered ring is represented whose approach includes calculating the self-intersection, sequence the intersection, reconstruct new rings, judging the effectiveness of the newrings. The algorithm is verified by the complex stamping mould of vehicle fender. The result shows that the algorithm is quite satisfied and it also provide a software support for EPDM.

REFERENCES

1. Zhang, J. and F. Liou, "Adaptive slicing for a multi-axis laser aided manufacturing process," *Journal of Mechanical Design*, Vol. 126, 254–261, March 2004.
2. Ruan, J., K. Eiamsa-ard, and F. Liou, "Automatic multi-axis slicing based on centroidal axis computation," *Proceedings of IDETC/CIE 2005 ASME 2005 International Design Engineering Technical Conferences & Computers and Information in Engineering Conferences*, 383–393, 2005.
3. Ruan, J., T. E. Sparks, A. Panackal, et al., "Automated slicing for a multiaxis metal deposition system," *Journal of Manufacturing Science and Engineering*, Vol. 129, 303–310, April 2007.
4. Zhang, H., X. Xiong, G. Wang, et al., "Direct manufacturing technology of metal parts by hybrid plasma deposition shaping and milling finishing," *China Mechanical Engineering*, Vol. 16, No. 20, 1863–1866, 2005.
5. Zhang, H., X. Xiong, and G. Wang, "Directly manufacturing of superalloy double integrated impeller by hybrid plasma deposition & milling," *China Mechanical Engineering*, Vol. 18, No. 14, 1723–1726, 2007.
6. Maekawa, T., "An overview of offset curves and surfaces," *Computer Aided Design*, Vol. 31, No. 3, 165–173, 1999.
7. Tiller, W. and E. G. Hanson, "Offsets of two-dimensional profiles," *Proceedings of International Symposium on Medical Images and Icons*, 36–46, July 1984.

Fabrication of Solid Oxide Fuel Cells with Powder/Suspension Plasma Spraying

Haiou Zhang, Daoman Rui, Kankan Zhang, and Guilan Wang
Huazhong University of Science and Technology, Wuhan 430074, China

Abstract— Solid oxide fuel cells (SOFC) is electrochemical energy conversion device, its high efficiency, pollution-free, all-solid-state structure and a wide range of fuel gas adaptability, and so on, make the SOFC research become a rising hotspot. At present, the reliability and cost competitiveness of the SOFC system are recognized as the key technical barriers that hinder the entry of SOFCs into commercial market. Thermal spray, especially atmospheric plasma spraying (APS) seems to be an economically attractive and effective technique for industrial production of SOFC due to its advantages such as low cost, easy operation, high deposition efficiency, wide selection of materials, etc. In this paper, the current progress and key manufacturing techniques of Positive-Electrolyte-Negative (PEN) and sub-assemblies of SOFC fabricated by plasma spray were over viewed. The work in this paper also focuses on PEN with porous metal-supported of planar SOFC fabricated by powder/suspension plasma spraying. The influence of the plasma spraying parameters on electrolyte defects and density, electrode porosity and substrate deformation was studied. The process of atmospheric plasma spraying and suspension plasma spraying is discussed.

1. INTRODUCTION

Solid oxide fuel cells (SOFCs) are electrochemical energy conversion device, its high efficiency, pollution-free, all-solid-state structure and a wide range of fuel gas adaptability, and so on, make the SOFCs research become a rising hotspot. They can be used for electrical power and heat generation with low environmental pollution and greenhouse gas emissions [1]. The application of SOFCs technology for Auxiliary Power Unit (APU) particularly passenger cars, buses, different truck types, boats and ships, different kinds of trains and aircraft also have been considered [2]. Though the technology has significant application potential, at present, the insufficient reliability and durability of the stack, cost competitiveness and manufacturing techniques for mass production are recognized as the key technical barriers that hinder the entry of SOFCs into commercial market.

Conventionally, SOFC components and entire cells have been made by processes which can be called wet ceramic processing techniques such as extrusion, tape casting, screen-printing, and spin coating. A general demand on the production process is the ability to generate the desired product quality together with the availability of the materials for the product in appropriate quality (size and purity). The process should show a high yield and productivity. Also, it should be suited for automation and for mass production allowing for reproducible manufacturing [3]. However, the wet ceramic processing techniques generally require multiple fabrication steps for each of the cell layers (anode, cathode, electrolyte, and interconnects), interspersed by high temperature sintering or co sintering steps [4]. In recent years an increasing number of research and development efforts have been devoted to manufacturing solid oxide fuel cells (SOFCs) by plasma spraying. The use of plasma spraying for SOFC manufacturing presents many advantages over wet ceramic processing with regards to both performance and cost. One obvious advantage is the speed of processing that results from elimination of the sintering steps, so that the cell layers can be processed in rapid succession [5]. In addition, the plasma spraying process is easily automated, thus making the process particularly well suited for mass production. Plasma spraying can also potentially be used to achieve greater control over the spatial variation of the microstructure and composition of the cell layers and for the creation of functionally graded cell coatings [6]. In the last few years, different teams have published results on the fabrication of SOFC using plasma spraying technologies. A. A. Syed, Z. Ilhan et al. examined the influences of feedstock powder and plasma gases on deposition efficiency, gas tightness, and the electrochemical behavior of vacuum plasma-sprayed (VPS) yttria-stabilized zirconia for solid oxide fuel cell electrolytes. The electrolyte they produced by VPS with optimized parameters exhibited lower porosity, > 50% lower leak rates, and 11% higher ionic conductivity at 800°C compared with the reference 9.5 mol% YSZ electrolyte [7]. P. Fauchais and his colleagues have been actively working on the fabrication of SOFC components with Suspension direct current plasma spraying [8]. R. Vaßen, D. Hathiramani et al. evaluated the manufacture

of planar solid oxide fuel cells by atmospheric plasma spraying, they pointed atmospheric plasma spraying could be successfully applied. For the deposition of anode and electrolyte, Dense and rather thin ($< 40 \mu\text{m}$) electrolyte layers produced by them via APS gave high OCV values above 1 V [9]. Though VPS and APS have many distinct advantages in terms of short fabrication time and simple automation, the quality of cell layers, especially that of electrolytes, needs significant improvement. The plasma-sprayed coatings are generally of lamellar structure. Pores, vertical cracks and non-bonded interfaces were always presented in the obtained coatings [10].

In the present work, PEN with porous metal-supported of planar SOFC fabricated by powder/suspension plasma spraying was investigated. The influence of the plasma spraying parameters included standoff distance, parameters of suspension injection and substrate temperature on electrolyte defects and density, electrode porosity and substrate deformation was studied.

2. EXPERIMENTAL

2.1. Material Preparation

Commercial 8YSZ (8 mol% yttria-stabilized zirconia oxide, WIENER Corp., China) and Ni (WIENER Corp., China) (45 vol.%) powders were mixed for the anode material. The powder mixture after ball milling for 24 h was dried at 80°C in a baking oven and then crushed. The powder mixed with polyvinyl alcohol was screened and heated at 160°C in an insulated box for 3 h to make it suitable for APS. Then the particle dimension distribution was sieved to the range of $90 \mu\text{m}$ to $120 \mu\text{m}$ for good flowability. 8YSZ powder with sizes ranging from $37 \mu\text{m}$ to $53 \mu\text{m}$ was used as the electrolyte material. Ethanol YSZ suspensions with a solid loading of 10 wt% were prepared using absolute ethanol. Polyvinyl alcohol was used to enhance the particle dispersion in the suspensions. $\text{La}_{0.8}\text{Sr}_{0.2}\text{Co}_{0.5}\text{Fe}_{0.5}\text{O}_3$ powder was prepared for the cathode, the particle dimension distribution was adjusted to in the range of $90 \mu\text{m}$ to $120 \mu\text{m}$.

2.2. Plasma Spraying Process

The GP-80 equipment is used in experiments and the plasma torch is mounted on the end arm of six-axis MOTOMAN-UP20 robot (Shougang Motoman Robot Co., Ltd., Beijing, China). For the powder/suspension plasma spraying process a home-made powder and suspension feeding system was used. Figure 1 shows the sketch of external injection of powders and suspensions. The suspension carrier gas flow rate and injector's position including angle α axial distance D and radial distance d could be adjusted to ensure that most of the atomized suspension injected into the core of the plasma jet.

Commercially available Ni super alloy was used as metallic support the alloy's physical property was in Table 1. Before depositing the metallic support was pressed to approximate 1 mm in thickness to get higher area density. The pressed porous metallic substrate was annealed at 300°C in a baking oven to release the stress, then porous substrate was cut to $8 \text{ cm} \times 8 \text{ cm}$ in dimension and fixed on the top of a ceramic substrate.

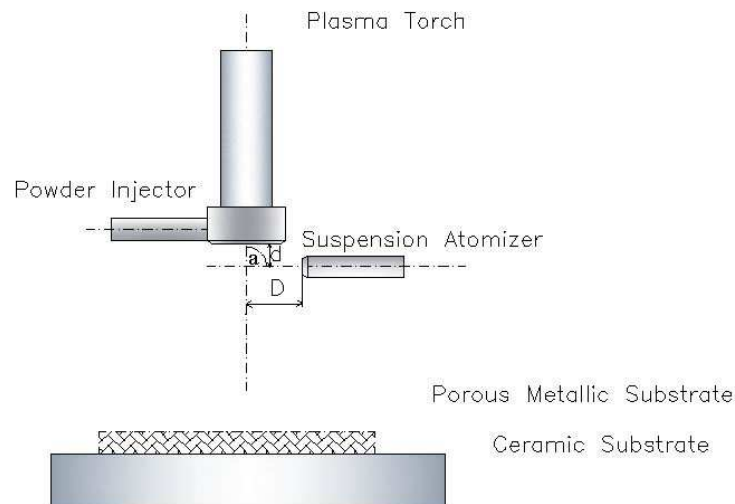


Figure 1: Sketch of external injection of powders and suspensions.

Table 1: Physical property of the Ni super alloy.

Density, g/m ²	Porosity per inch	Thickness, mm	Tensile strength, N/mm ²		Elongation, percent		Flexibility	
			L	T	L	T	L	T
400±30	80–110	1.1–2.5	≥ 1.25	≥ 1.0	≥ 5	≥ 12	180° bending, no break.	
1200 ± 30	> 200	1.4–2.0	≥ 2.0	≥ 1.5	≥ 5	≥ 8	180° bending, no break.	

L was the longitudinal measured values

T was the transversal measured values

To investigate the influence of standoff distance, spray angle and parameters of suspension injection on the PEN's formability, two porous Ni felt substrate with different area density were prepared. Group A (GA) porous Ni substrate's density was 400 g/m² while Group B (GB) was 1200 g/m². GA and GB's PEN was fabricated by the following process. Firstly, the fixed porous Ni substrate was preheated to 400° in a baking oven and then Ni/8YSZ anode layer was deposited on the prepared substrates by APS. For GA's anode all the 180 passes were sprayed at the angle of 90 degrees, while GB's anode was deposited at three kinds of angle and the spray sequence was 90°, 75°, 60°. Then 8YSZ electrolyte layer was deposited by SPS, different standoff distance was used in the GA and GB for the electrolyte's deposition. Finally, LSCF cathode layer was made by APS, all the 60 passes in GA were sprayed at the angle of 90°, GB's first 30 passes was sprayed at the angle of 90° and then the angle was adjusted to 75° for the following 30 passes. More detail deposition parameters were listed in Table 2.

Table 2: Plasma spraying parameters.

Feedstock	Power, kw	Plasma gas flow rate, L/h		Standoff distance, mm	Spray angle, degrees	Number of passes
Ni+YSZ	30	1000	300	120	90 ^a /60 ^b	60
					90 ^a /75 ^b	60
					90 ^a /90 ^b	60
YSZ	36	1000	300	80 ^a /100 ^b	90	80
LSCF	35	1000	300	120	90	60

N₂'s flow rate was measured at 0.7 Mpa while Ar's flow rate was measured at 0.5 Mpa

^aValue was GA's spray parameters

^bValue was GB's spray parameters

3. RESULTS AND DISCUSSION

3.1. Influence of Spraying Distance

Using the electron probe microanalyzer (Sirion 200, FEI Corp., Netherlands), the material elements and microstructure of the PEN were analyzed qualitatively and quantitatively. Figure 2 illustrates the surface line-scan photograph of the GA and GB PEN coatings, respectively. GA's electrolyte was deposited by SPS with a distance of 80 mm while GB's spraying distance was 100 mm. The injector's position was adjusted, angle $\alpha = 90^\circ$, distance $D = 25.1$ mm and radial distance $d = 6.7$ mm. These optimized parameters ensured that most of the atomized suspension could be injected into the core of the plasma jet. Figure 2(a) shows the surface element line-scan photograph of the GA, the cathode elements (La, Sr, Fe, Co) and the anode elements (Ni, Zr) superposed each other, so the electrolyte layer was not observed for GA. One possible reason was that the distance of 80 mm was too short to melt the particles, the un-molten particles were bounded off the surface after impacting on the substrate. The electrolyte layer's thickness was about 60 μm . The layer was composed of a porosity of 4.33% which was measured by image analysis method.

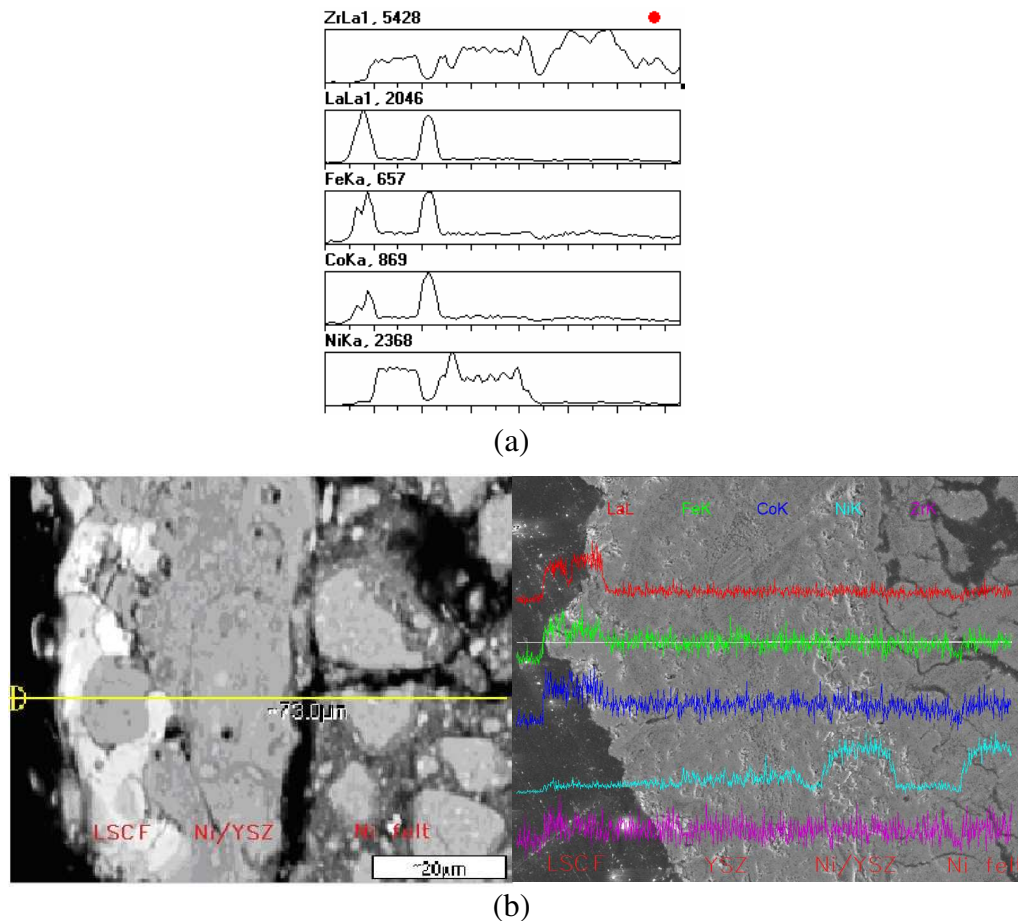


Figure 2: Photographs of surface linear scan of the GA's PEN (a) and the GB's PEN (b).

3.2. Effect of Spraying Angle

GA's anode were sprayed at the angle of 90 degrees for all the 180 passes, the thickness of GA's anode layer was about $20\ \mu\text{m}$, the porosity of the layer was 15.16% which was measured by image analysis method. For GB's anode layer, 180 passes was deposited at a changed angle which was measured between the axis of spray gun and the substrate. The GB anode layer's thickness was about $25\ \mu\text{m}$ and the layer's porosity reached 30.21%. As shown in Figure 3, many through pores were observed from the microstructure, these pores could provide sufficient fuel during the reaction. GB anode layer's porosity was much higher than GA's, so the spray angles severely influence the porosity of the electrodes. Generally, the porosity increased with the decreasing of the spray angle. It was corresponded with our previously research [11].

3.3. Study on Porous Metallic Support Deformation

Porous metallic support's deformation was observed in the experiment, it was unfavorable for PEN to contact with metal bipolar plate and the charge transfer rate would decrease. Figure 4 showed the photo of sprayed porous Ni felt supported PEN which fixed on ceramic substrate. GA's metallic support was obviously deforming and warping while GB's metallic support deformation was tiny.

The deformation mainly result from the high stress. As the Reference [12] shown, the particles impacted on the substrate and cooled rapidly, the cooling rate lied in the rang of $10^6\ \text{K/s}$ to $10^7\ \text{K/s}$, similar to the rates achieved in liquid quenching, obviously, much high stress would produce during the spraying process. Some factors had to be controlled to decrease the metallic support's deformation including the metallic support temperature's fluctuation during a spraying cycle, metallic support's strength and the way of the support's fixation. The metallic support temperature had important influence, in the experiment the fixed porous Ni substrate was preheated to 400° and the temperature was assured above 300° during a spraying cycle. In addition, the ceramic substrate was used to decrease temperature fluctuation during a spraying cycle. Comparing the sprayed metallic support of GA and GB, the strength of the metallic play significant roles in decreasing support deformation and the fixation of the support should be beneficial to stress release.

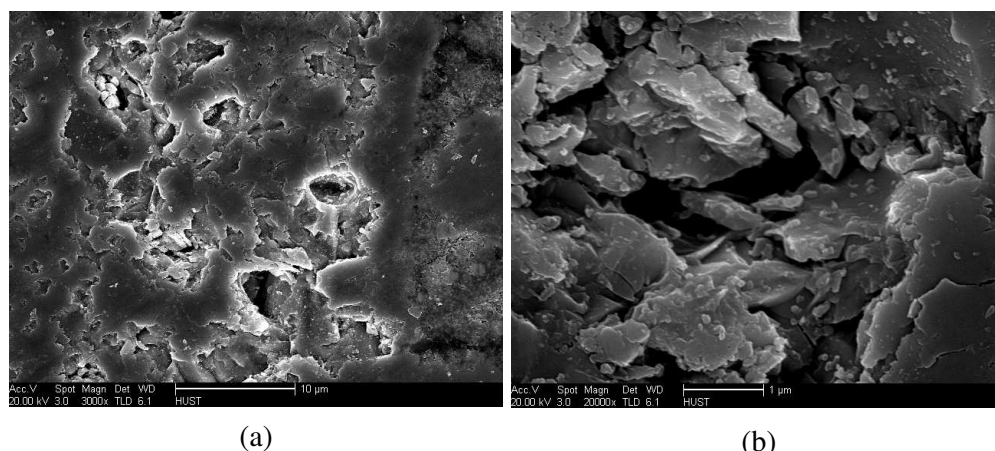


Figure 3: Microstructure of APS GB's anode (a) and a pore's structure (b).

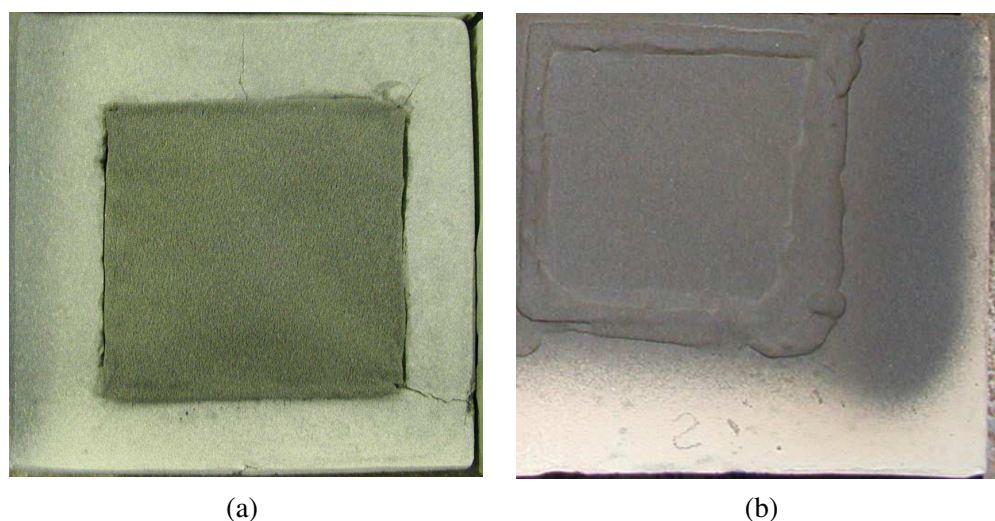


Figure 4: Photo of sprayed porous Ni felt supported PEN, GA's PEN (a) and GB's PEN (b).

4. CONCLUSION

Optimized microstructure porous Ni felt supported SOFC's PEN was fabricated by APS and SPS process. The influence of plasma spraying parameters including standoff distance, spraying angle and porous Ni felt deformation was investigated. Too high or low standoff distance was not useful for the particles deposition and the solidified droplet would be observed in the as-sprayed coating. Dense electrolyte layer was deposited by SPS at a distance of 100 mm, and this standoff distance's deposition efficiency was much higher than the distance of 80 mm. GB's anode layer deposited with a changed spraying angle had a porosity of 30.21%, it was much higher than GA's, so the spray angle severely influenced the porosity of the electrodes. Generally, the porosity increased with the decreasing of the spray angle. Ni felt's deformation was studied, it was mainly related with the metallic support temperature's fluctuation during a spraying cycle, metallic support's strength and the way of the support's fixation.

ACKNOWLEDGMENT

Authors gratefully acknowledge the contribution of the National Nature Science Foundation of China (Grant No. 50474053 and No. 50875096). In particular, thanks are given to School of Mechanical Engineering, Huazhong, University of Science and Technology.

REFERENCES

1. Gorte, R. J., J. M. Vohs, and S. McIntosh, "Recent developments on anodes for direct fuel utilization in SOFC," *Solid State Ionics*, Vol. 175, No. 1–4, 1–6, 2004.
2. Lamp, P., J. Tachtler, O. Finkenwirth, S. Mukerjee, and S. Shaffer, "Development of an

- auxiliary power unit with solid oxide fuel cells for automotive applications,” *Fuel Cells*, Vol. 3, No. 3, 146–152, Wiley-VCH, 2003.
3. Henne, R., “Solid oxide fuel cells: A challenge for plasma deposition processes,” *Journal of Thermal Spray Technology*, Vol. 16, No. 3, 381–403, 2007.
 4. White, B. D., O. Kesler, and L. Rose, “Air plasma spray processing and electrochemical characterization of SOFC,” *Journal of Power Sources*, Vol. 178, 334–343, 2008.
 5. Tang, Z., I. Yaroslavsky, A. Burgess, O. Kesler, B. White, and N. Ben-Oved, “Manufacturing solid oxide fuel cells with an axial-injection plasma spray system,” *International Scientific Journal for Alternative Energy and Ecology ISJAE*, No. 4, 48, 2007.
 6. Hui, R., Z. Wang, O. Kesler, L. Rose, J. Jankovic, S. Yick, R. Maric, and D. Ghosh, *J. Power Sources*, Vol. 170, No. 2, 308–323, 2007.
 7. Syed, A. A., Z. Ilhan, J. Arnold, G. Schiller, and H. Weckmann, “Improving plasma-sprayed yttria-stabilized zirconia coatings for solid oxide fuel cell electrolytes,” *Proceedings of the International Thermal Spray Conference*, 617–622, 2006.
 8. Fauchais, P., V. Rat, J.-F. Coudert, R. Etchart-Salas, and G. Montavon, “Operating parameters for suspension and solution plasma sprayed coatings,” *Surface & Coatings Technology*, Vol. 202, 4309–4317, 2008.
 9. Vaßen, R., D. Hathiramani, J. Mertens, V. A. C. Haanappel, and I. C. Vinke, “Manufacturing of high performance solid oxide fuel cells (SOFCs) with atmospheric plasma spraying (APS),” *Surface & Coatings Technology*, Vol. 202, 499–508, 2007.
 10. Li, C.-J. and A. Ohmori, “Relationships between the microstructure and properties of thermally sprayed deposits,” *Journal of Thermal Spray Technology*, Vol. 11, No. 3, 365–374, 2002.
 11. Yang, Y. Z., H. O. Zhang, and W. S. Xia, “Fabrication of functionally graded SOFC by APS,” *Journal of Thermal Spray Technology*, Vol. 16, No. 5–6, 768–775, December 2007.
 12. Cedelle, J., M. Vardelle, and P. Fauchais, “Influence of stainless steel substrate preheating on surface topography and on millimeter- and micrometer-sized splat formation,” *Surface & Coatings Technology*, Vol. 201, 1373–1382, 2006.

The Digital Simulation System Development for the Electrical Machine

Zhongchao Wei¹, Xia Chen¹, Shuo Liu², and Jian Li¹

¹Department of Electrical Machines and Drives, Huazhong University of Science and Technology, China

²Dongfang Electric Company, Sichuan, China

Abstract— The conventional electromagnetic computing software for electrical machine is usually restricted to programming and can't associate with the simulation function. While some simulation software such as Matlab/Simulink only can simulate the conventional electrical machine due to the models are not available for public. As for the machine with special structure, a new model has to be established by cumbersome work. To optimize the design of the electrical machine and obtain exact simulating result of its performance, a new model method combining the electromagnetic computing and dynamic characteristic simulation of the machine is put forward in this paper based on the software of Modelica/Mworks, which enables convenient and efficient modeling and simulation of complex, multi-domain physical systems described by differential, algebraic and discrete equation and supports non-causal modeling. The simulation results validated the feasibility of integrating the machine design with the characteristic simulation to obtain the optimal design parameters.

1. INTRODUCTION

Dynamic simulation is a very important tool in the characteristic analysis of electrical machine. However, some conventional modeling tools, such as Simulink, in which each model must have definite input and output signals, therefore, the users have to transform component's differential equations and algebraic equations into blocks with input and output and establish the component model according to the input and output relations, which make the dynamic characteristic simulation of electrical machine constrained to cumbersome and complex calculation.

Modelica is today the most promising modeling and simulation language in that it provides the non-causal modeling which means the component models can be directly described by differential algebraic equations and frees the users from the task of pre-processing the equations and rewriting them to fit the modeling environment. It is an object-oriented general-purpose modeling language that is under development in an international effort to define a unified language for modeling of physical system. Moreover, object-oriented modeling is a fast-growing area of modeling and simulation that provides a structured, computer-supported way of dealing with mathematical and equation-based modeling [1].

Mworks which is developed by CAD center of Huazhong University of Science and Technology is a special modeling and simulation platform for complex multi-domain physical systems. The current version based on Modelica 2.1 supports visual modeling, automatically translating and solving, as well as convenient postprocessor.

Mworks has features as follows [2]:

With modern integrated development environment styles, it provides friendly user interfaces such as syntax high-lighting, code assistance;

Based on object-oriented compiler framework, it perfectly supports almost all the syntax and semantics of modelica;

Using self-adapting solving strategies, it can agilely solve differential equation, algebraic equations and discrete equations.

2. MATHEMATICAL MODEL OF INDUCTION MACHINE

As a mature technology the induction machine enjoys uses in many established applications and is frequently the first machine considered for emerging application. The machine is comprised of a stator and a rotor. The windings of the stator and the rotor are assumed to be sinusoidally distributed in space to simplify the analysis of the machine [3].

The three-phase machine model is established on the following assumptions. Due to space phase theory, the fundamental wave of air gap field is considered only, higher harmonic effects are not taken into account. The parameters (resistance and inductances) of the machine are constant,

therefore, saturation effects are not considered. Skin effects, eddy currents, iron losses, and friction losses are not taken into account [4].

In a three-phase machine, each phase couples with others. To obtain a much simpler induction machine model, based on power invariant transformation principle [4], we adopt abc to $\alpha\beta$ stationary coordinate transformation to convert a three-phase machine into an equivalent two-phase machine, the windings of which is not existing a coupling relationship because $\alpha\beta$ axes are orthogonal. The matrix is used for converting abc quantities to $C_{3/2}$ quantities.

$$C_{3/2} = \sqrt{\frac{2}{3}} \begin{bmatrix} 1 & -\frac{1}{2} & -\frac{1}{2} \\ 0 & \frac{\sqrt{3}}{2} & -\frac{\sqrt{3}}{2} \end{bmatrix} \quad (1)$$

Under $\alpha\beta$ stationary coordinate axis, the voltage equation can be written as

$$\begin{bmatrix} u_{s\alpha} \\ u_{s\beta} \\ 0 \\ 0 \end{bmatrix} = \begin{bmatrix} R_s + L_s\rho & 0 & L_m\rho & 0 \\ 0 & R_s + L_s\rho & 0 & L_m\rho \\ L_m\rho & \omega_r L_m & R_r + L_r\rho & \omega_r L_r \\ -\omega_r L_m & L_m\rho & -\omega_r L_r & R_r + L_r\rho \end{bmatrix} \times \begin{bmatrix} i_{s\alpha} \\ i_{s\beta} \\ i_{r\alpha} \\ i_{r\beta} \end{bmatrix} \quad (2)$$

where the subscript $s\alpha$, $s\beta$ are components in α -axis and β -axis of the windings of stator respectively, the subscript $r\alpha$, $r\beta$ are components in α -axis and β -axis of the windings of rotor respectively, u is the voltage component, i is the current, ω_r is rotor speed, R_s , R_r are stator and rotor resistance respectively, L_s , L_r is the stator and rotor self-inductance, L_m is the mutual inductance, ρ is the differential operator d/dt .

Expressing the flux linkage with current in the two-phase stationary frame

$$\begin{cases} \psi_{s\alpha} = L_s i_{s\alpha} + L_m i_{r\alpha} \\ \psi_{s\beta} = L_s i_{s\beta} + L_m i_{r\beta} \\ \psi_{r\alpha} = L_r i_{r\alpha} + L_m i_{s\alpha} \\ \psi_{r\beta} = L_r i_{r\beta} + L_m i_{s\beta} \end{cases} \quad (3)$$

where ψ represents the flux linkage.

The equation for the electromagnetic torque is as follows

$$T_e = p L_m (i_{s\beta} i_{r\alpha} - i_{s\alpha} i_{r\beta}) \quad (4)$$

The motion equation is

$$T_e - T_L = \frac{J}{p} \frac{d\omega_r}{dt} \quad (5)$$

In which: p represents the number of pole pairs, J is the moment of inertia assumed to include the inertia of the induction machine, and T_L is the load torque.

3. MODELING OF INDUCTION MACHINE ON MWORKS/MODELICA

For some physical domains Modelica Standard Library provides a comprehensive collection of physical models. The object oriented structure of the library allows the organization of models in such way that the developed partial models and model code can be reused. This is a challenging task, since model interfaces and parameters have to be selected carefully to enable a perfect interaction of the models. Thus, the connections between partial model components will be very important. Modelica supports equation-based non-causal connections, which means that connections are realized as equations. Two types of coupling can be established by connections depending on whether the variables in connected connectors are declared as laws below [5]:

- Equality coupling, for non-flow variables, according to Kirchhoff's first law.
- Sum-to-zero coupling, for flow variables, according to Kirchhoff's second law.

A connection statement connect (pin1, pin2), with pin1 and pin2 of connector class Pin, and connects the two pins so that they form one node. This produces two equations, namely:

$$\text{Pin1.v} = \text{Pin2.v} \quad (6)$$

$$\text{Pin1.i} + \text{Pin2.i} = 0 \quad (7)$$

Equation (6) says that the voltages of the connected wire ends are the same. Equation (7) corresponds to Kirchoff's second law meaning that the currents sum to zero at a node. Similar laws apply to force and torque in mechanical systems, for example, as for the Flange Connector used for connecting with the mechanical module, the torque is considered as non-flow variable and the angular velocity as the flow variable. Hence, the electrical part and the mechanical part of the motor are associated through this connector. Meanwhile, these two physical variables may be observed from the Flange Connector.

Due to the magnetic field analysis of the asynchronous machine is a tough problem; it's difficult to adopt the components from Modelica Standard Library to describe the motor. Therefore, in the process of modeling, the method of directly translating formulas into Modelica language is employed. According to the rule described above, we can establish the electrical machine library as the structure in Fig. 1:

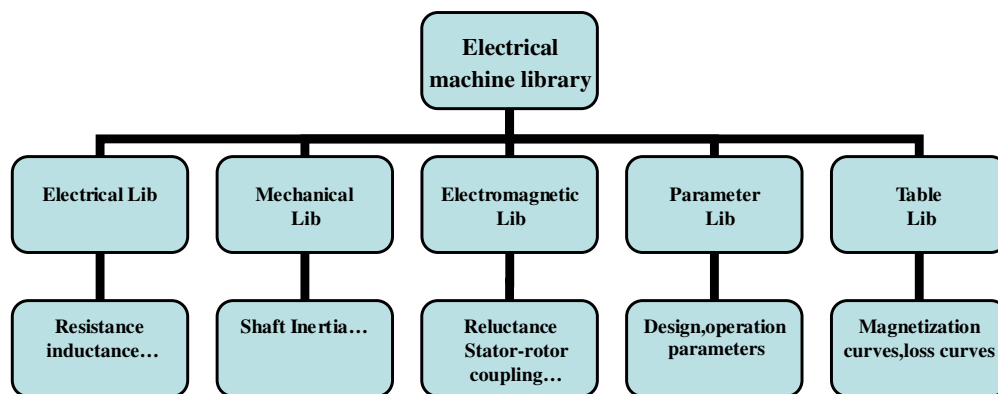


Figure 1: The model library structure of electrical machine.

(1) Electrical Lib

The electrical component library includes the basic elements, the resistance, inductance, and capacitor and so on, which can be used to describe the phase resistor and reactance of the stator and the rotor. The component such as sensor can function as the ammeter and voltmeter. The source consisting of the AC and DC supply can provide the machine with all kinds of power supply

(2) Mechanical Lib

The mechanical library can support the machine with the mechanical drive force such as the rotating shaft, the moment of inertia. The torque can be observed from the Flang. The component Torque can be used as the load of the machine and be driven by the machine.

(3) Electromagnetic Lib

The components in the electromagnetic library are used to establish the coupling relation between the electric circuit and the magnetic circuit, combining with some components from the electricity library and mechanical library, which could establish a simulation model of the asynchronous machine.

(4) Parameter Lib

The basic design data such as the power value, pole pair number, diameter, slot number, width are saved in the package `asynchronism_motor input_data`. They will be displayed on the simulation interface in which they can be modified conveniently. From the simulation results, the start-up current and start-up torque of the electrical machine influenced by the variable design parameter can be observed. Besides, the other data involved in the electromagnetic calculation are all saved in this package.

(5) Table Lib

The curves and diagrams such as magnetization curves, saturation curves, possessing the relation of one-dimensional functions, could be dealt with using lagrangian unitary three points interpolation method. All of these are programmed as a data file loaded in the package `e_motor_table` which will be opened automatically from the data interface of Modelica if the program needs calling these curves.

4. SIMULATION AND VALIDATION ON MWORKS

For the sake of proving accuracy of the model, the asynchronous machine is connected with source component. Some related parameter is given: $P_N = 200$, $U_N = 690$, $f_N = 33.3$,

The motor is starting with no-load and the simulating intervals are 3s. After 3s, the rated torque is added. Meanwhile, by modifying some critical parameters of the asynchronous machine such as the stator's resistor and the rotor's inductance, we can obtain different simulating results and analyze the influence of these coefficients on the performance of the motor. The simulation results are shown as follows.

As shown in Fig. 2, the rotor speed undergoes a short overshoot, and then stabilizes at a constant speed about 1000 rpm and the time of the whole starting process is about 0.6s. Due to the no-load starting, the torque finally comes to zero as the Fig. 4 shown. At the time of 3s, the torque becomes the rated torque. During the initial starting period, Fig. 4 and Fig. 5 show that the currents on both the stator and rotor sides fluctuate between the maximum and minimum values due to the sinusoidal power supply, the stator current is gradually becoming stable and the rotor current is close to zero. After the rated torque is loaded, the current of the stator and the rotor reach the proper value. According to the analysis above, we can conclude that the output waveforms accord running characteristic of the motor.

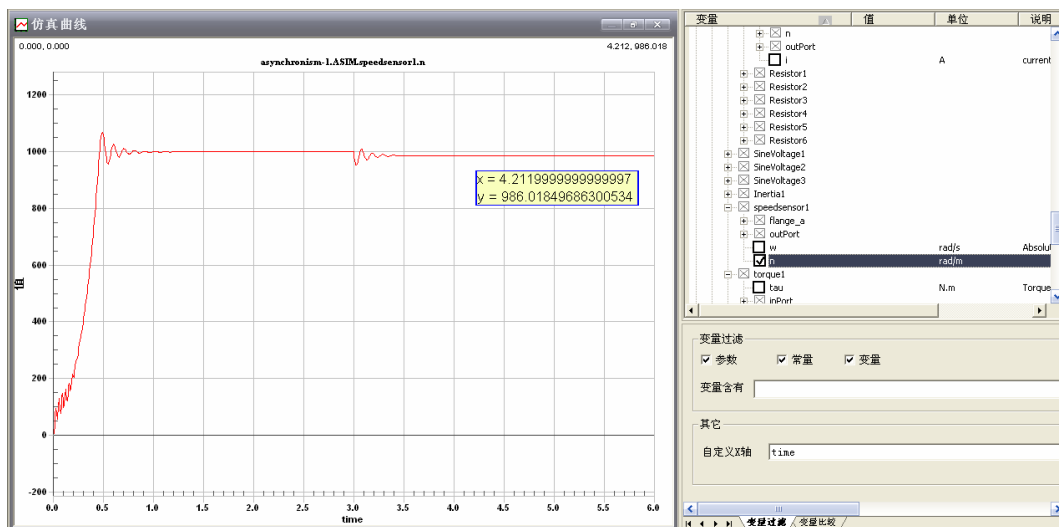


Figure 2: The angular velocity of motor viewed from the speedsensor.

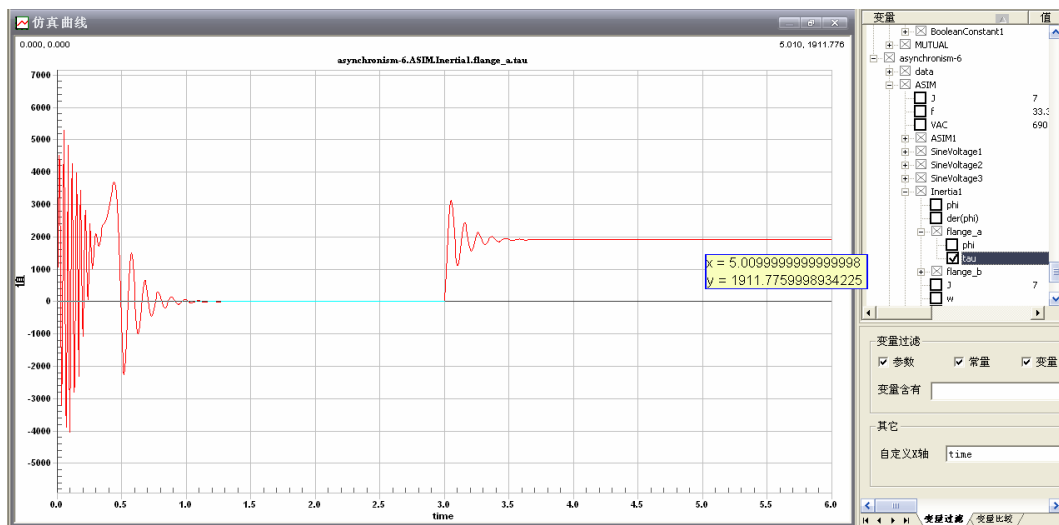


Figure 3: The output torque waveform.

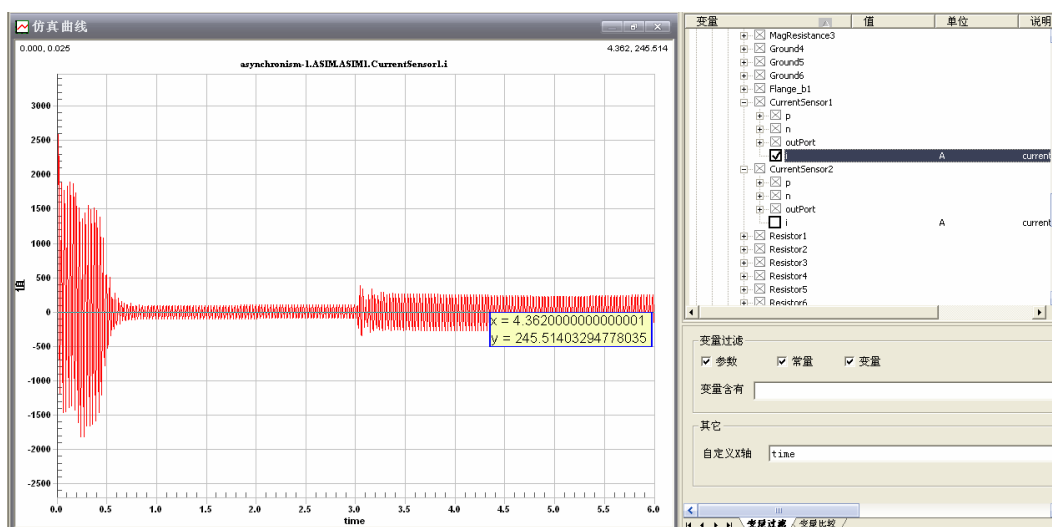


Figure 4: Stator current.

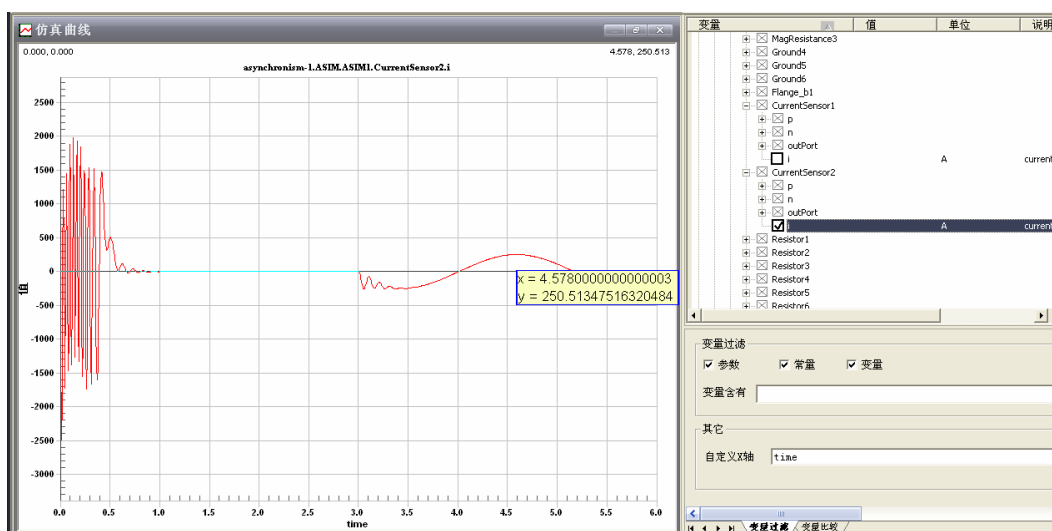


Figure 5: Rotor current.

So through this example, we can see that the modeling of asynchronous motor shows a good example of the multi-domain modeling capability of Modelica. The model of the electrical machine can be applied in a large-scale control system.

REFERENCES

1. Modelica Association. <http://www.Modelica.org>.
2. Mworks User's Manual.
3. Lee, R. J., D. Pillay, and R. G. Harley, "Reference frame for the simulation of induction motor," *Electric Power Systems Research*, Vol. 8, 233–240, 1984.
4. Fitzgerald, A. E., C. Kingsley, Jr., and S. D. Umans, *Electric Machinery*, 5th Edition, McGraw-Hill, 1990.
5. Fritzson, P., *Principles of Object-Oriented Modeling and Simulation with Modelica 2.1*, IEEE Press, Piscataway, NJ, 2004.

Modeling and Design of Switched Reluctance Starter/Generator System

Jianbo Sun, Zhongchao Wei, Shuanghong Wang, Qionghua Zhan, and Zhiyuan Ma
School of Electrical and Electronics Engineering
Huazhong University of Science and Technology, China

Abstract— Switched Reluctance Motors (SRMs) show great advantages of structural simplicity and high reliability applying to aerial starter/generator. This paper proposes a modeling method of switched reluctance starter/generator system, including switched reluctance machine, power circuit and filter circuit. The simulation model is constructed based on magnetic finite element analysis and electromechanical dynamic equations, which considers magnetic saturation and electromechanical coupling. Through simulations, the performance of the system is evaluated. The control parameters of the controller and component parameters of filter circuit are designed to satisfy the specification performance of the system. The simulation results validate the design of the system.

1. INTRODUCTION

Switched Reluctance Machines (SRMs) have been extensively researched for mission critical high performance applications due to their high reliability, performance, fault tolerance and high power densities. Compared to other machine types, SRM offers an excellent balance between reliability, power density, function of both starter and high speed capability. It not only realizes generator easily, but also has good starting and speed regulating characteristics used as SRM and fine electric power quality, high power density and unique fault tolerance used as generator. SRMs are ideal to operate as starters to start the main engines/turbines and then act as generators and provide power to the electrical systems.

The SRM S/G is compatible with demanding applications. To date, applications include sourcing aerospace power systems [1–3], starter/alternators for hybrid vehicles [4–8], and wind turbine applications [9, 10]. The aerospace and automotive applications are generally characterized by high-speed operation. The absence of windings and permanent magnets on the rotor support both high rotational speeds and high-temperature operation. Further, the absence of windings on the rotor helps to keep the majority of the losses within the stator, making the SRG relatively easy to cool. The switched nature of the SRG makes it compatible with any application that requires variable-speed operation.

This paper is devoted to theoretical modeling and design on a SRM S/G system for aerospace applications. The paper is organized as follows. Section 2 focuses on the mathematic model of the SRM S/G system. Section 3 focuses on the simulation results of the SRM S/G system. Section 4 will describe the design of the component parameters of the filter circuit based on the simulation results. Finally, the conclusions are drawn in Section 5.

2. MATHEMATIC MODEL

The SRM S/G system discussed in this paper consists of three main parts: a three-phase 12/8 poles switched reluctance machine, Power circuit and filter circuit. The power circuit of the system is shown in Fig. 1. The three-phase windings of phase A, phase B and phase C are connected to a asymmetric half-bridge circuit. The battery (U_e) is the power source during the starting process. Avoiding the electric power flowing from the battery to the load (R_L) directly, the DC bus is separated into two bus: the exciting bus and the generating bus. Two bus are connected by a diode (R_{D2}). The battery doesn't permit being charged. So a diode (R_{D1}) is employed to connect the battery with the exciting bus. To smoothen the output voltage, the voltage of the generating bus should be filtered by a filter circuit, which consists of two capacities (C_2 and C_3) and one inductance (L).

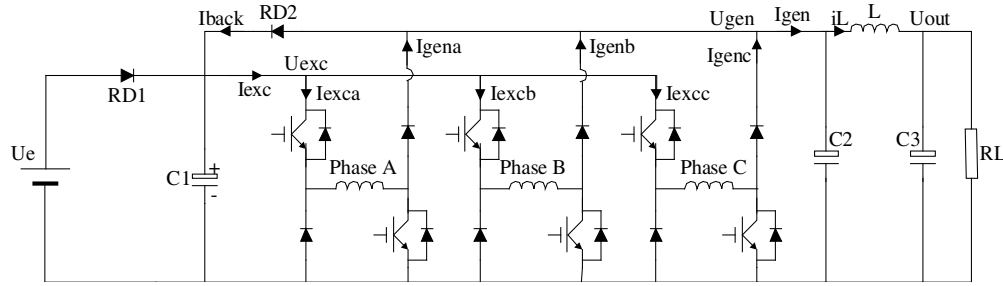


Figure 1: Power circuit of SRM S/G system.

The mathematic model of SRM is expressed as Equation (1).

$$\begin{cases} \frac{d\psi_k}{dt} = U_{pk} - i_k R_p \\ \frac{d\omega}{dt} = (T_e - T_L)/J \\ \frac{d\theta}{dt} = \omega \end{cases} \quad (1)$$

$$\text{where, } U_{pk} = \begin{cases} U_{exc} & S_k = 1 \\ 0 & S_k = 0 \\ -U_{gen} & S_k = -1 \end{cases} \quad (k = 1, 2, 3).$$

U_{pk} is the terminal voltage of the phase windings. S_k is the switching function. U_{exc} is the exciting bus voltage. U_{gen} is the generating bus voltage. i_k is the phase currents. R_p is the resistance of phase winding. ψ_k is the flux linkage of phase winding. ω is electric angular speed. T_e is the electromagnetic torque. T_L is the mechanical torque. J is the inertia of machine rotor. θ is the electric angle of machine rotor.

The mathematic model of power circuit and filter circuit can be summarized as follows.

$$\begin{cases} \frac{dU_{exc}}{dt} = \frac{U_e - U_{exc}}{C_1 \cdot R_{D1}} + \frac{I_{back} - I_{exc}}{C_1} \\ \frac{dU_{gen}}{dt} = \frac{I_{gen} - i_L}{C_2} \\ \frac{dU_{out}}{dt} = (i_L - \frac{U_{out}}{R_L})/C_3 \\ \frac{di_L}{dt} = \frac{U_{gen} - U_{out}}{L} \end{cases} \quad (2)$$

$$i_{exc} = i_{exca} + i_{excb} + i_{excc} \quad (3)$$

$$\text{where, } i_{exck} = \begin{cases} i_k & S_k = 1 \\ 0 & S_k = 0 \\ 0 & S_k = -1 \end{cases}$$

$$i_{gen} = i_{gena} + i_{genb} + i_{genc} - i_{back} \quad (4)$$

$$\text{where, } i_{genk} = \begin{cases} 0 & S_k = 1 \\ 0 & S_k = 0 \\ i_k & S_k = -1 \end{cases}$$

$$i_{back} = \frac{U_{gen} - U_{exc}}{R_{D2}} \quad (5)$$

where,

$$R_{D1} = \begin{cases} 0.01 & U_{exc} \leq U_e \\ \inf & U_{exc} > U_e \end{cases}$$

$$R_{D2} = \begin{cases} 0.01 & U_{gen} \geq U_{exc} \\ \inf & U_{gen} < U_{exc} \end{cases}$$

U_e is the battery voltage. I_{exc} is the current of the exciting bus. I_{gen} is the current of the generating bus. I_{back} is the current flowing from the generating bus to the exciting bus. U_{out} is the output voltage of the system. C_1 is the capacity of the exciting bus. C_2 and C_3 are the capacities of the filter circuit. R_D is the equivalent resistance of diode. i_L is inductance current of the filter circuit.

3. SIMULATION RESULTS

The parameters of the three-phase 12/8 poles SRM are listed in the appendix. The flux linkage per phase is a nonlinear function of that phase current and the position angle of rotor, as shown in Fig. 2. The flux linkage characteristics of SRM are stored as a table. The interpolation of this table can provide us the conversion from the flux linkage and the rotor angle to the current flowing into the phase winding.

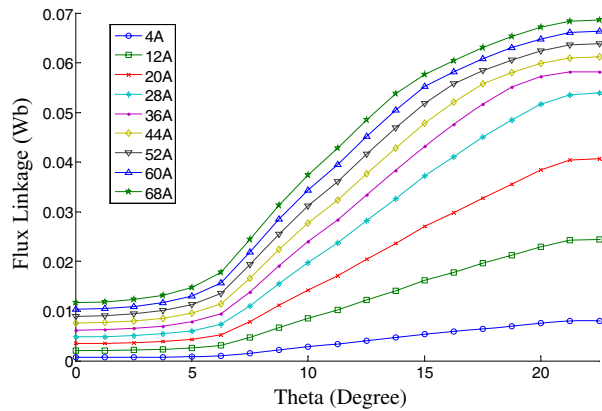


Figure 2: Flux linkage characteristics of SRM.

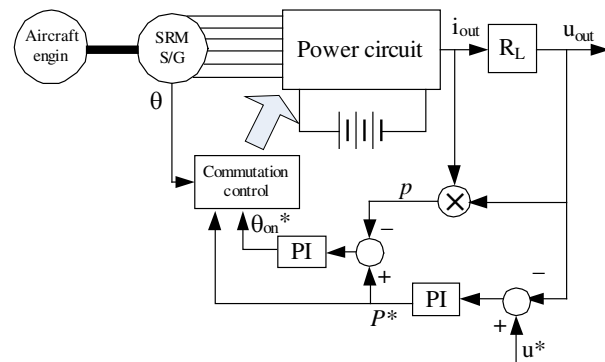


Figure 3: Control scheme of SRM S/G system.

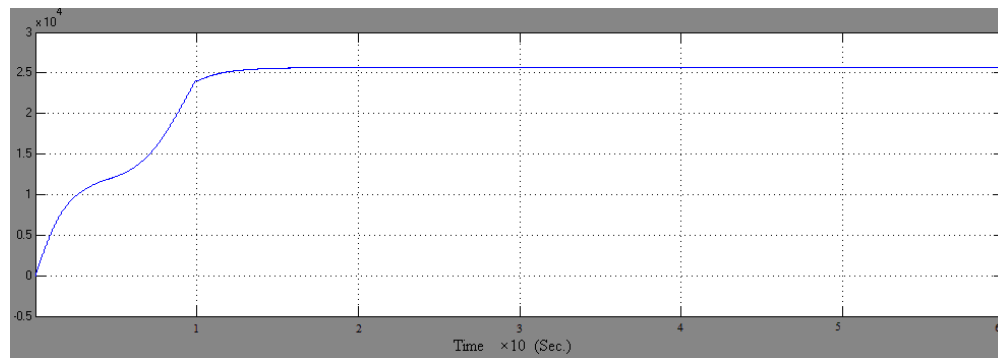


Figure 4: Speed response of the system at starting process.

The control scheme of the system is plotted in Fig. 3. There are two loops in this control scheme. During the starting process, the outer loop is opened. The inner loop is used to control the phase current. The current reference is given as the maximum of phase winding to start the aircraft engine as soon as possible. During the generating process, the outer loop is used to regulate the output voltage. The inner loop is used to regulate the output power. Combining the rotor angle, the output of the power loop and the output of the voltage loop, the optimal switching signals are obtained to drive the power circuit.

Firstly, the machine operates as a motor to start the aircraft engine from the still status to the speed of 25,000 r/min. The speed response of the system is seen in Fig. 4. The starting process costs about 15 seconds.

Secondly, when the SRM operates as generator at the speed of 25,000 r/min, phase winding currents are shown in Fig. 5. The maximum current of 60 A occurs after the phase winding being turned off.

The Voltage of exciting bus, generating bus, output bus, and current of filter inductance are shown in Fig. 6. The output voltage ripple is much lower than the generating bus voltage ripple

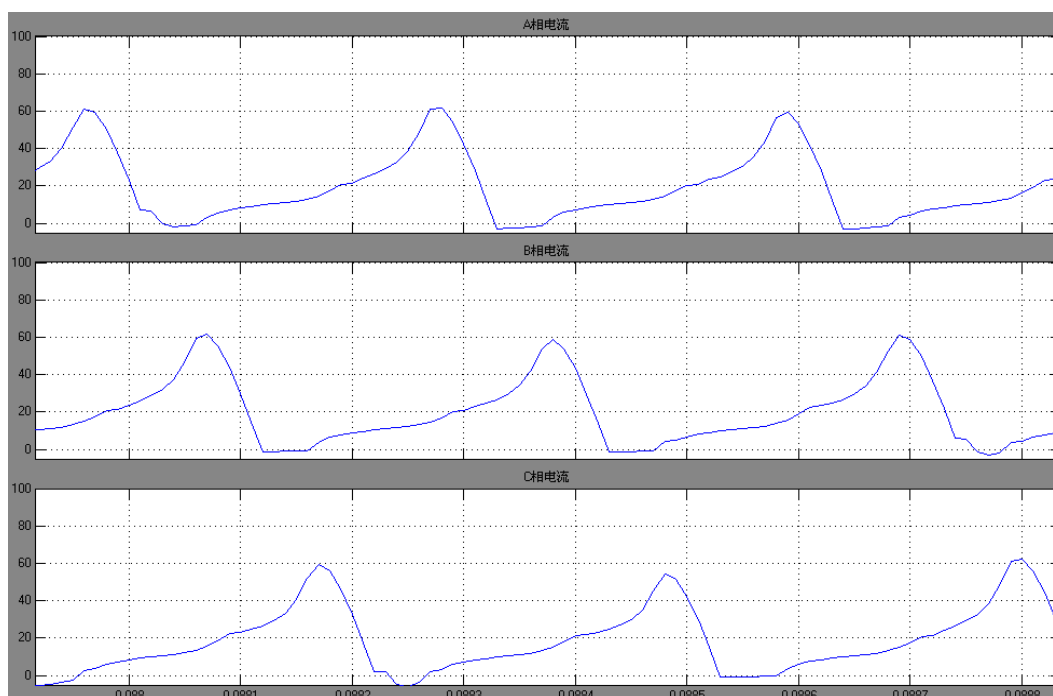


Figure 5: Phase winding current of SRM at static operation.

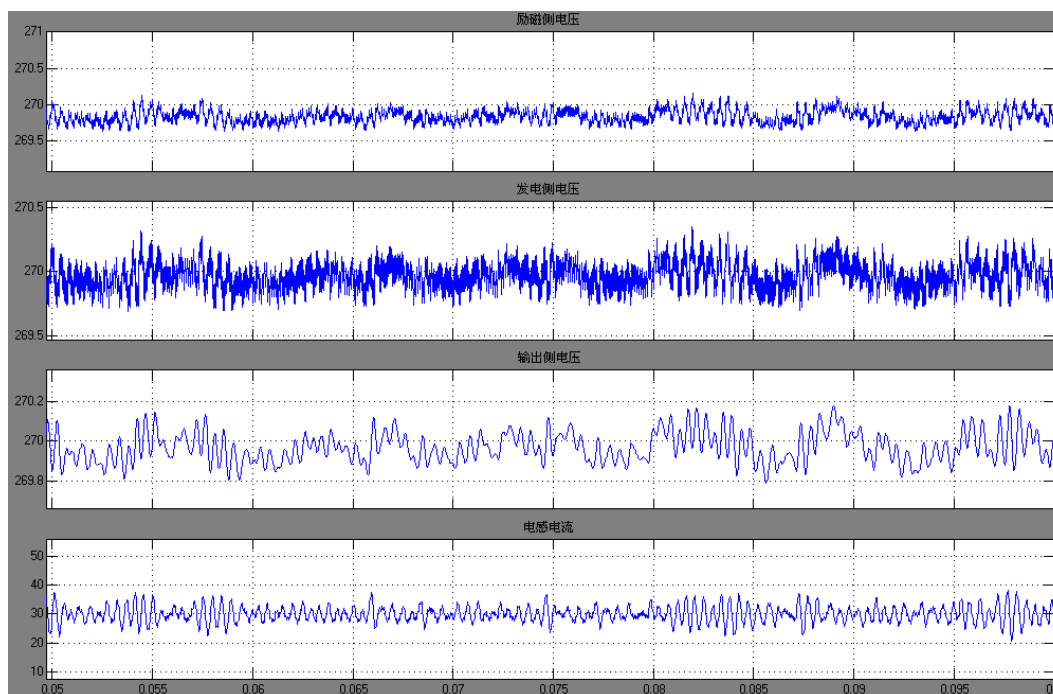


Figure 6: Voltage of exciting bus, generating bus, output bus, and current of filter inductance at static operation.

due to the existence of filter circuit. The output voltage ripple is maintained within 270 ± 0.2 V. Thus, the static performance of system is acceptable.

The Current of exciting bus, generating bus, and current flowing from generating bus to exciting bus are shown in Fig. 7. When the current flowing from the generating bus to the exciting bus occurs, the exciting bus voltage is forced to be about 270 V, which is larger than the battery voltage (200 V). So the battery is off-line during the generating process.

At the static status of speed is 25,000 r/min, the analysis of electromagnetic torque ripple is

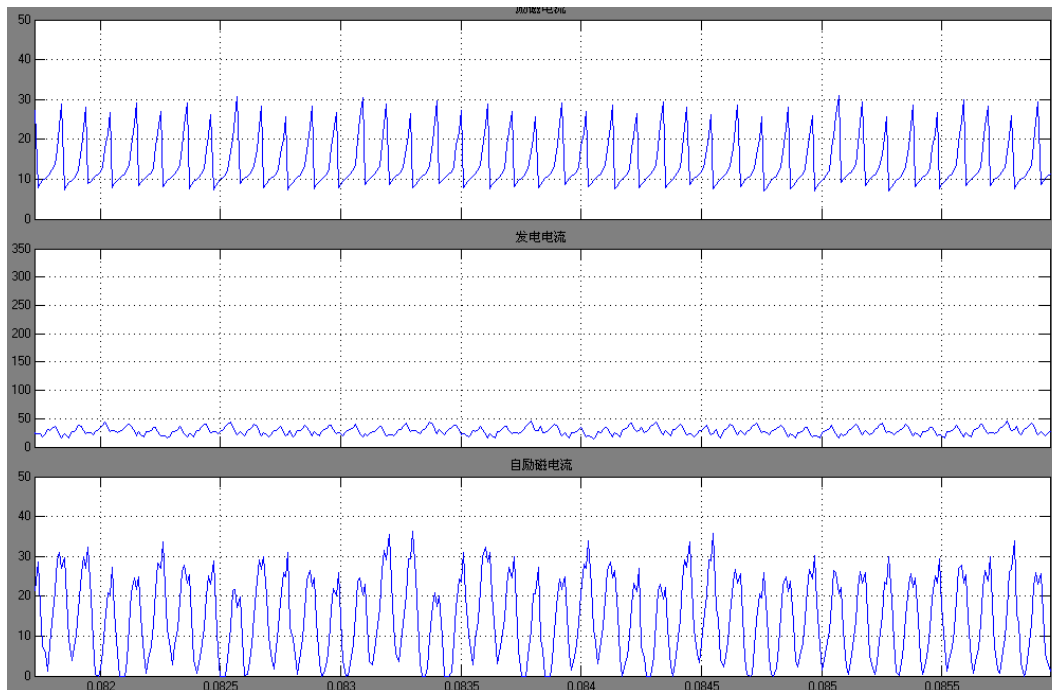


Figure 7: Current of exciting bus, generating bus, and current flowing from generating bus to exciting bus at static operation.

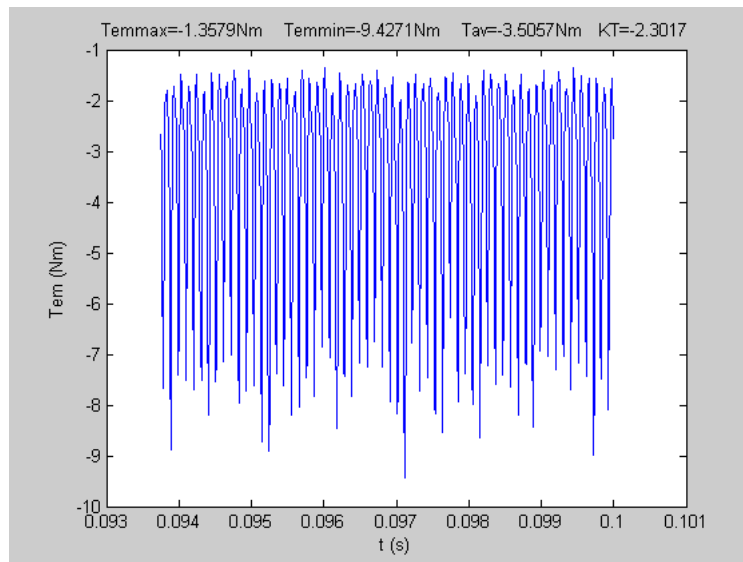


Figure 8: Analysis of electromagnetic torque ripple at static operation.

carried on, as seen in Fig. 8. Too large torque ripple will be harmful for the mechanical system. Thus, the electromagnetic torque ripple should be evaluated. The ratio of torque ripple of this system is 2.3017.

Thirdly, the dynamic performance is essential for an aircraft power source. Load's sudden change influenced on voltage quality is simulated and analyzed, as seen in Fig. 9. Under the condition of the speed is 25,000 r/min, from $t = 0$ s to $t = 0.04$ s, the electric load is 8 kW; from $t = 0.04$ s to $t = 0.08$ s, the electric load is 9.2 kW; from $t = 0.08$ s to $t = 0.1$ s, the electric load is 4 kW.

From Fig. 9, we can see that the output voltage is controlled to be within 270 ± 1 V, though the electric load changes from the rated power to 1.15 times and half of rated power. The system offers good dynamic performances.

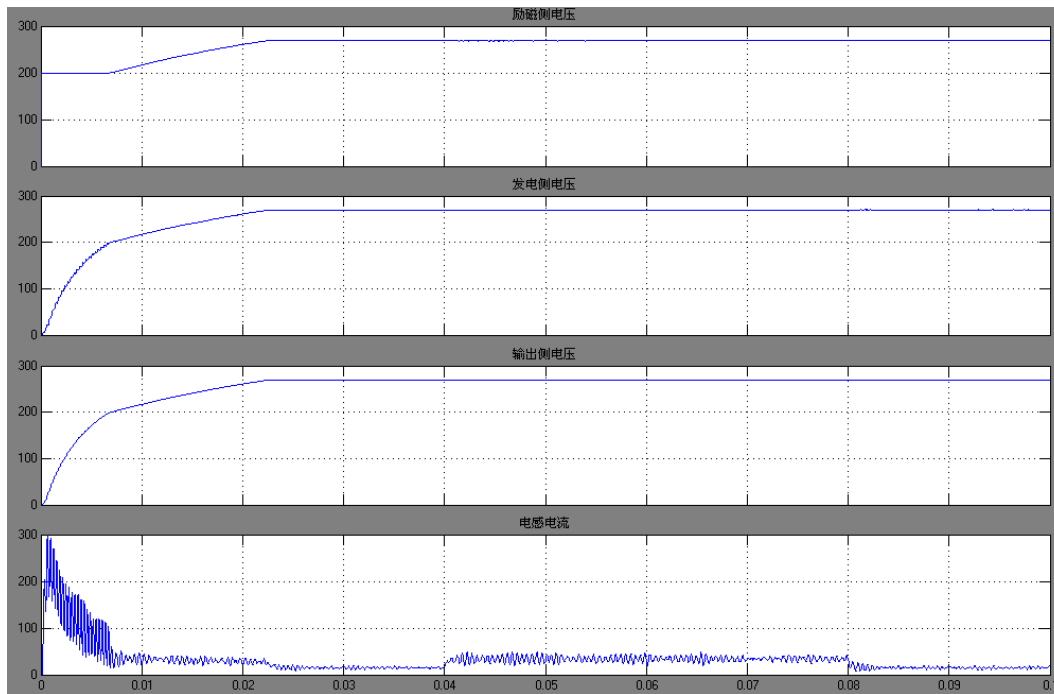


Figure 9: Voltage of exciting bus, generating bus, output bus, and current of filter inductance at load's sudden change.

4. DESIGN OF FILTER CIRCUIT

The harmonics of output voltage should be impressed according to the requirement by designing the components of the filter circuit, as seen in Fig. 10. The capacities of C_1 , C_2 , C_3 can smoothen the voltage of the exciting bus, the generating bus and the output bus, respectively. The inductance L is used to adjust the frequencies of the harmonic voltages. When the values of C_1 , C_2 , C_3 and L are chosen as 2200 μF , 1000 μF , 4000 μF and 0.003 mH, respectively, the harmonics of output voltage are impressed to meet the standard, as seen in Fig. 11.

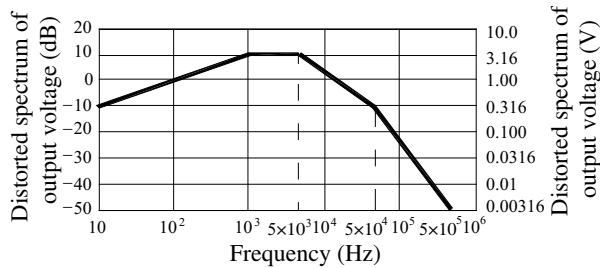


Figure 10: Spectrum requirement of output voltage.

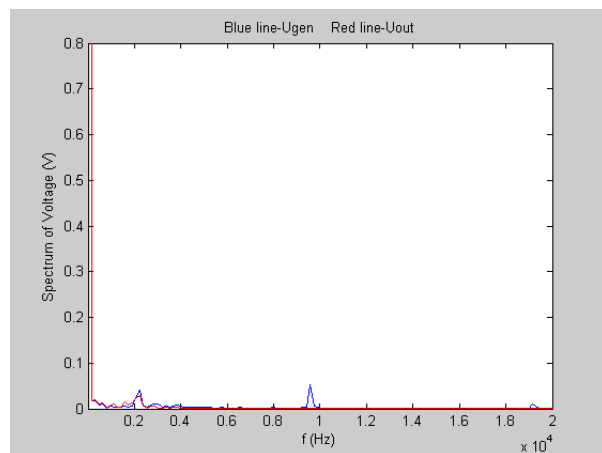


Figure 11: Spectrum analysis of output voltage.

5. CONCLUSION

The machine, circuit and controller are designed to make the static and dynamic performances of the output voltage of system meet the requirements, such as the power quality standard MIL-STD-704E. The simulation results validate the design of the system.

Appendix

The specifications of the prototype motor are: Outer stator diameter = 0.14 m; Inner stator diameter = 0.09 m; Shaft diameter = 0.04 m, Number of stator poles = 12; Number of rotor poles = 8; Arc of stator pole = 14.5°; Arc of rotor pole = 17.5°; Turns of per-phase winding = 38; Length of air gap = 0.0003 m; Length of stack = 0.3 m; Height of stator yoke = 0.0125 m; Height of rotor yoke = 0.014 m.

ACKNOWLEDGMENT

The assistance of Mr. Zhe Kuang in preparing some of the figures and simulation data is gratefully acknowledged.

REFERENCES

1. MacMinn, S. R. and J. W. Sember, "Control of a switched-reluctance aircraft starter-generator over a very wide speed range," *Proc. Intersociety Energy Conversion Engineering Conf.*, 631–638, 1989.
2. Radun, A., "Generating with the switched-reluctance motor," *Proc. IEEE APEC'94*, 41–47, 1994.
3. Cameron, D. E. and J. H. Lang, "The control of high-speed variable-reluctance generators in electric power systems," *IEEE Trans. Ind. Applicat.*, Vol. 29, 1106–1109, Nov./Dec. 1993.
4. Kokernak, J. M., D. A. Torrey, and M. Kaplan, "A switched reluctance starter/alternator for hybrid electric vehicles," *Proc. PCIM'99*, 74–80, 1999; *IEEE Transactions on Industrial Electronics*, Vol. 49, No. 1, February 2002.
5. Mese, E., Y. Sozer, J. M. Kokernak, and D. A. Torrey, "Optimal excitation of a high speed switched reluctance generator," *Proc. IEEE APEC 2000*, 362–368, 2000.
6. Besbes, M., M. Gabsi, E. Hoang, M. Lecrivain, B. Grioni, and C. Plasse, "SRM design for starter-alternator system," *Proc. ICEM 2000*, 1931–1935, 2000.
7. Kioskeridis, I. and C. Mademlis, "Optimal efficiency control of switched reluctance generators," *IEEE Transactions on Power Electronics*, Vol. 21, No. 4, 1062–1072, July 2006.
8. Torrey, D. A., "Switched reluctance generators and their control," *IEEE Trans. Ind. Electron.*, Vol. 49, No. 1, 3–14, February 2002.
9. Torrey, D. A., "Variable-reluctance generators in wind-energy systems," *Proc. IEEE PESC'93*, 561–567, 1993.
10. Cardenas, R., W. F. Ray, and G. M. Asher, "Switched reluctance generators for wind energy applications," *Proc. IEEE PESC'95*, 559–564, 1995.

On the Reflection Function Calculation Method in the Problem of Radiowave Propagation

I. I. Orlov, V. I. Kurkin, and A. V. Oinats
Institute of Solar-Terrestrial Physics SB RAS, Russia

Abstract— In our report, we consider a task of the reflection function calculation, which arises in the problem of wave propagation in a stratified inhomogeneous medium. We present a method of the reflection function calculation based on combined ordinary differential equations of the first-order that is strictly equivalent to the initial wave equation. The example of the reflection function calculation is presented for the case of radiowave propagation in the ionosphere plasma. However the domain of applicability of the presented method can be wide.

1. INTRODUCTION

There are many studies devoted to the problem of the reflection function calculation for the case of wave propagation in a stratified inhomogeneous medium [1, 3, 5]. However, many undecided questions still remain concerned with elaboration of the calculation methods that can be applicable without any restrictions on the propagation properties. In our report we present a method of solution based on the reduction of the initial wave equation to strictly equivalent combined ordinary differential equations of the first-order [7, 8]. The combined equations can be presented in a compact matrix form and can be easily numerically solved using a simple difference scheme. Examples of the reflection function calculation are also presented in the paper. In present study we consider a task of the radiowave propagation in the stratified inhomogeneous ionosphere. Nevertheless our approach can be easily used in the other cases of wave propagation in stratified medium.

2. BASIC EQUATIONS

Let wavenumber equals to $k = \omega/c_0$ and permittivity of the medium is given by function $\varepsilon'(x, k)$. It is known that the problem of the wave radiation is equivalent to finding corresponding Green function. For the case of layered ionosphere Green function can be constructed from linearly independent solutions of the ordinary differential equation [1]

$$\frac{d^2 u(x, k)}{dx^2} + k^2 \varepsilon'(x, k) u(x, k) = 0, \quad \varepsilon'(x, k) = 1 - \frac{\omega_k^2 q(x)}{\omega(\omega + i\nu)}, \quad (1)$$

where ω_k is a layer cutoff frequency, ν is an effective collision frequency, and function $q(x)$ normalized in its maximum specifies a shape of the layer.

Let find the solution of the Equation (1) in the framework of the scheme based on the analogy of the radiowave propagation in the homogeneous medium. Introduce two functions (in the form of JWKB approximation [2]) normalized at infinity

$$f_{\pm}(x, k) = \frac{1}{\sqrt{n(x)}} \exp \left(\pm ikx \mp ik \int_x^{\infty} [n(y) - 1] dy \right), \quad (2)$$

where $n(x)$ is a refractive index of the medium $\varepsilon'(x, k) = n^2(x)$.

Transform ordinary Equation (1) to formally non-ordinary equation

$$\frac{d^2 u(x, k)}{dx^2} + \left\{ k^2 n^2(x) - S \left(\sqrt{n(x)} \right) \right\} u(x, k) = -S \left(\sqrt{n(x)} \right) u(x, k), \quad (3)$$

where $S(f(x)) = f(x)(f(x)^{-1})''$ is the Schwarzian derivative. As is easy to see functions (2) are solutions of the ordinary equation with operator from the left-hand side of the Equation (3). Therefore we can formally strictly reduce the initial task (1) to non-ordinary differential Equation (3) with Green function constructed from (2) by standard way. The transformation used here is not based on asymptotical assumptions and does not require any “smoothness” of the equation coefficients.

Using constructed Green function, we can transform Equation (3) to Volterra integral equation with corresponding boundary conditions at infinity

$$u_+(x) = f_+(x) + \frac{1}{2ik} \int_x^\infty S(\sqrt{n(x)}) [f_+(x)f_-(y) - f_-(x)f_+(y)] u_+(y) dy. \quad (4)$$

The sign “+” means that the solution $u_+(x)$ tends to $f_+(x)$ in the limit $x \rightarrow \infty$. A similar integral equation can be found also for a second linearly independent solution $u_-(x)$ of Equation (3). Let break solution (4) to two parts $u_+(x) = u_+^+(x) + u_+^-(x)$ and introduce designations

$$\begin{cases} u_+^+(x, k) = f_+(x, k) \left\{ 1 + \frac{1}{2ik} \int_x^\infty S(\sqrt{n(x)}) f_-(y, k) u_+(y) dy \right\}, \\ u_+^-(x, k) = -f_-(x, k) \frac{1}{2ik} \int_x^\infty S(\sqrt{n(x)}) f_+(y, k) u_+(y) dy. \end{cases} \quad (5)$$

Differentiating (5) and similar combined equations for the second linearly independent solution and forming from the parts $u_\pm^\pm(x)$ a square matrix $Z(x, k)$, we can present the Equation (4) in the compact matrix form

$$\frac{dZ(x, k)}{dx} = ikn(x)I_3Z(x, k) - \frac{S(\sqrt{n(x)})}{ikn(x)} I_+Z(x, k), \quad \text{where } Z(x, k) = \sqrt{n(x)} \begin{pmatrix} u_+^+(x) & u_+^-(x) \\ u_+^-(x) & u_+^+(x) \end{pmatrix} \quad (6)$$

and I_α are the Pauli matrices, $I_+ = (I_3 + iI_2)/2$.

Thus initial wave Equation (1) is reduced to strictly equivalent combined ordinary differential equations of the first-order. It is interesting that formal integration of (6) leads to a solution similar to the second-order JWKB approximation [2]. At the same time if we discard the second term in the right-hand side of (6) then formal integration of (6) will lead to a solution similar to the first-order JWKB approximation.

Let introduce function $R_+(x, k) = u_+^-(x, k)/u_+^+(x, k)$ which is equal to the ratio of the components of the first column of the matrix $Z(x, k)$. In that case we can find the differential Riccati-type equation from (6)

$$\frac{dR_+(x, k)}{dx} = -2ikn(x)R_+(x, k) + \frac{S(\sqrt{n(x)})}{2ikn(x)} [1 + R_+(x, k)]^2. \quad (7)$$

The structure of the Equation (7) is similar to equations found for the reflection function in the context of the wave propagation theory in layered media [3]. Somewhat different equations for the reflection function were found in the case of the radiowave propagation in the ionosphere by the authors of [4, 5]. Noted similarity allows us to suppose that introduced “ R -function” has the properties of the reflection function. Strict consideration of this question is outside of the scope of the present study.

3. PROPERTIES OF THE MATRIX EQUATION COEFFICIENTS

It is interesting to examine the properties of the coefficients of the Equation (6). Let choose a symmetrical layer to our detailed analysis [1]

$$q(x) = \frac{4 \exp(\alpha x)}{(1 + \exp(\alpha x))^2}, \quad (8)$$

where $\alpha = 4\pi/\Delta$ is a parameter determined by semi thickness of the layer Δ .

It is obvious that the coefficient of the first term of (6) has no singularity. Behavior of its real and imaginary parts is defined by the shape of the layer. Its imaginary part is equal to zero beyond the layer but its real part is equal to zero inside the layer.

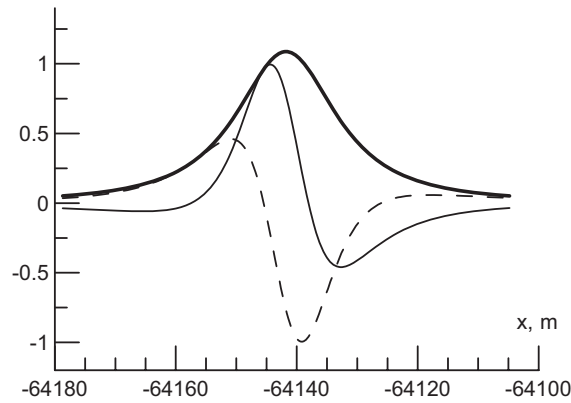


Figure 1: Real (thin line) part, imaginary (dotted line) parts and absolute value of the second term coefficient about the left turning point.

The real and imaginary parts of the second term coefficient have a different behavior. The absolute value of the second term coefficient is equal nearly zero everywhere excepting geometrical turning points but it become significant about the turning points. Figure 1 shows the behavior of the real part, imaginary part and absolute value of the second term coefficient about the left turning point. The figure corresponds to following layer parameters: $\Delta = 300$ km, $\nu = 10^4$, $\omega_k = 2\pi \cdot 10$ MHz and $\omega = 2\pi \cdot 7$ MHz. The thickness of the absolute value peak is equal about wave-length of the incident wave λ on the level 20%. The thickness become smaller with losses decrease and it tends to zero in the limit $\nu \rightarrow 0$.

The thickness of the peak is comparable with the wave-length in the case of typical ionosphere losses values (for ionosphere E layer $\nu = 10^4 \div 10^5$ and for F layer $\nu = 10^3 \div 10^4$) everywhere excepting the cutoff frequency region. In other words the second term of the Equation (6) makes sufficient contribution to the solution in the region that is comparable with the wave-length of the incident wave. Thus this conclusion confirms well-known statement of the geometrical optics [6] that the solution of Equation (1) can be presented in the form of JWKB approximation everywhere beyond the neighborhood of the turning points. Using found properties of the coefficients and some general understanding the authors [8] derived also an analytical expression for the reflection function.

4. NUMERICAL CALCULATION SCHEME AND SIMULATION

It is not convenient to solve numerically the nonlinear Equation (7). It is better to carry out the numerical calculation of the R -function from the matrix Equation (6). The matrix Equation (6) is ordinary differential equation of the first-order therefore we can use a standard difference scheme to solve it.

Let consider the propagation media as homogeneous media in the bounds of small interval h everywhere along the coordinate x . Let $A(x)$ is a designation for the matrix coefficient in the right-hand side of the Equation (6) at given value of the wavenumber k . According to the difference scheme the value of the function at the next interval $Z(x+h)$ is determined by recurrence relation

$$Z(x+h) = \{h \cdot A(x) + I_0\} Z(x), \text{ where } A(x) = ikn(x) \left\{ I_3 + \frac{S(\sqrt{n(x)})}{k^2 n^2(x)} I_+ \right\}. \quad (9)$$

The full solution is a priori known only at infinity therefore the calculation should be carried out from the right to the left. Taking into account the relation (9) we obtain the following expression

$$Z(x) = \tilde{A}^{-1}(x) Z(x+h), \quad (10)$$

where $\tilde{A}^{-1}(x)$ is an inverse matrix to $\tilde{A}(x) = h \cdot A(x) + I_0$. The accuracy of the calculations by the expression (10) depends on the step of iteration h and it is improved with the step decrease. However the step of iteration must be smaller than a typical scale of the matrix $A(x)$ changes. Taking into account the properties of the matrix coefficients described in Section 3 a variable step of iteration is used to reach an acceptable speed of the calculation scheme.

It is also necessary to take into consideration that the components of the matrix $Z(x)$ can increase exponentially during the calculations inside the layer. An operation of $Z(x)$ matrix renormalization is used to avoid the losses of calculation accuracy inside the ionosphere layer. The renormalization consists in the multiplication of the $Z(x)$ matrix by another diagonal matrix so that the components of the matrix $Z(x)$ remain limited but the reflection function doesn't change.

Figure 2(a) shows the result of the R -function calculation for the following parameters: $\Delta = 200$ km, $\omega_k = 2\pi \cdot 10$ MHz, $\omega = 2\pi \cdot 7$ MHz and $\nu = 10^4$. Figures 2(b) and 2(c) illustrate in detail a behavior of the R -function about the left and the right turning points accordingly. As we can see there are two maxima about the neighborhood of the turning points. The value of the R -function is close to 1 at the left turning point. This feature is in agreement with the properties of the matrix equation coefficients and allows finding an analytical expression for the R -function [8].

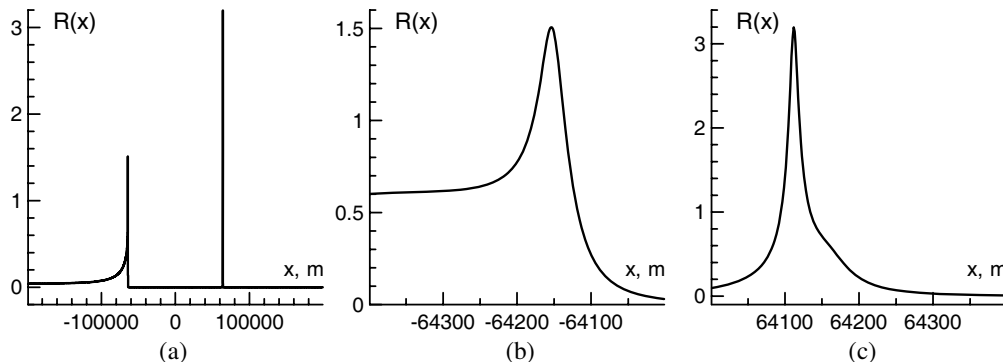


Figure 2: R -function calculated for $\nu = 10^4$.

5. CONCLUSIONS

The new method of the wave equation solution in the case of stratified propagation medium is presented based on the strict reduction of the initial wave equation to the combined ordinary differential equations of the first-order. The properties of the found combined equations and the numerical scheme for the R -function calculation based on the presented method are described. The example of the R -function calculation is also presented for the case of radiowave propagation in the ionosphere plasma. Nevertheless the presented approach can be used in other cases of the wave propagation in the stratified medium.

ACKNOWLEDGMENT

The present work was done under support of the Russian fund of basic research (grant No. 08-05-00658-a).

REFERENCES

1. Ginzburg, V. L., *Propagation of Electromagnetic Waves in Plasma*, Izd. Nauka, Moscow, 1967 (in Russian).
2. Fröman, N. and P. O. Fröman, *JWKB Approximation: Contributions to the Theory*, Izd. Mir, Moscow, 1967 (in Russian).
3. Brekhovskikh, L. M., *Waves in Layered Media*, Izd. Nauka, Moscow, 1973 (in Russian).
4. Orlov, I. I., "On electromagnetic energy transfer in stratified inhomogeneous media," *Research on Geomagnetism, Aeronomy and Solar Physics*, Vol. 103, 142–149, 1995.
5. Kunitsyn, V. E., I. A. Nesterov, and A. D. Stefanchuk, "Numerical modeling of the radio wave propagation in layered plasma," *Journal of Communications Technology and Electronics*, Vol. 44, No. 12, 1331–1337, 1999.
6. Kravtsov, Y. A. and Y. I. Orlov, *Geometrical Optics of Inhomogeneous Media*, Izd. Nauka, Moscow, 1980 (in Russian).
7. Orlov, I. I., V. I. Kurkin, and A. V. Oinats, "Wave propagation and geometrical optics," *Optics of Atmosphere and Ocean*, Vol. 19, No. 12, 1016–1020, 2006.
8. Orlov, I. I., V. I. Kurkin, and A. V. Oinats, "On the reflection function calculation in the problem of wave propagation in stratified medium," *Proceedings of XXII All-Russian Scientific Conference "Radiowave Propagation"*, Vol. 2, 65–68, Rostov-na-Dony, Russia, September 2008.

About Strict and Asymptotic Solutions for Focusing of Cylindrical Wave by Veselago Lens with Finite Size and Losses in $kD \gg 1$ Region

A. P. Anyutin

Russian New University, Russia

Abstract— A modification of the method of discrete sources (MMDS) and geometric optic approximation are applied for solving a 2D scattering and focusing problems by single ideal Veselago lens with finite size and losses or lenses from LHM material. The field structure in the region of focus and limits of the focusing effects were considered.

1. INTRODUCTION

In recent years one can see that such problem as focusing field by ideal Veselago lens (plane lens with negative refractive index $n_r = -1$) or lens with negative refractive index $n_r < 0$ (or LHM material, or metamaterial) is widely discussed both theoretical and experimental points of view [1–6]. In 1968 V. Veselago had pointed that flat layer of dielectric with negative refractive index $n = -1$ would focus the field of cylindrical incident wave after the layer [1]. Later in 2000 D. Smith and J. Pendry had made the experimental demonstration of focusing effect in metamaterial (medium with negative refractive index $n_r < 0$) [2]. Within this time a lot of publications were made (see [3, 4] and the references therein). It is important to emphasize that in many publication the focusing effect (or cloaking effect) were considered by using an asymptotic methods: geometrical optic, some its modifications, Kirchhoff's approximation or a strict integral presentation of the scattering field by flat layer. Recently in (see [4, 6, 7] and reference in it) some strict numerical results for this problem were obtained but for a case when the size of the lens is about few wave lengths.

This paper presents a strict numerical solution for the field in focusing regions when 2D ideal Veselago lens ($n_r \approx -1$) with finite size or flat lens from metamaterial ($n_r < 0$) with losses has its maximum size (kD , k -wave number for free space) much more then wave lengths ($kD \gg 1$). The influence of geometrical sizes of the lens, losses and value of the refractive index $|n_r|$ of metamaterial on focusing effect inside or outside of the lens were explored. Besides, the geometric optic (GO) approximation was applied to explain the results of numerical calculations.

2. 2D SCATTERING PROBLEM BY DIELECTRIC SLAB WITH FINITE SIZE AND NEGATIVE REFRACTIVE INDEX

Let us consider the 2D problem of scattering of cylindrical wave $u_0(r, \varphi)$:

$$u_0(r, \varphi) = H_0^{(2)}(k|\vec{r} - \vec{r}_0|)$$

by dielectric cylinder in the cylindrical coordinate system (r, φ, z) . We suppose that the z -axis is the axis of the cylinder. In (1) k — the wave number for free space; $\vec{r} = \{r, \varphi\}$ — cylindrical coordinates for point of view; $\vec{r}_0 = \{R_0, \varphi_0\}$. The medium of the cylinder is characterized by negative refractive index $-n_r - i\nu$ (where $n_r = \sqrt{|\varepsilon_r||\mu_r|}$, ε_r — relative dielectric permittivity, μ_r — relative magnetic permeability, ν — losses of medium, accordingly). Let the cylinder's (slab's) cross-section have the equation in the polar coordinates:

$$\rho(\varphi) = \frac{1}{\sqrt[n]{(\cos(\varphi)/a)^n + (\sin(\varphi)/b)^n}}, \quad n \geq 20, \quad (1)$$

numeral where $\rho(\varphi)$ is analytical function and its shape is very close to rectangular one if parameter $n \geq 20$. At Fig. 1, one can see the geometry of the problem, the geometry of contour $\rho(\varphi)$ and GO-ray trace for $n = 20$.

It is well known that diffracted field $u^1(\vec{r})$ outside of $\rho(\varphi)$ and refracted field $u_2(\vec{r})$ inside of $\rho(\varphi)$ have to satisfy to Helmholtz equation, two boundary conditions on contour $\rho(\varphi)$ and principal of limiting absorption.

We had applied the modification to the method discrete sources (MMDS) [5] for obtaining a strict numerical solution of this value boundary scattering problem [5]. As this method was well

described in [5], we do not present and discuss the details of MMDS in our case. We only underline that the error of the numerical solution estimates as the residual $\Delta = \Delta_{1,2}$ of both boundary conditions on contour $\rho(\varphi)$: $\Delta_1 = |u_0 + u^1 - u_2|_S$ and $\Delta_2 = |\partial u_0/\partial n + \partial u^1/\partial n - (1/\mu_r)\partial u_2/\partial n|_S$ when $m = 1, 2, \dots, M$. In all results which were presented below the residual Δ less than 10^{-4} . A typical example of distribution the residual Δ as function of the points m along the contour $\rho(\varphi)$ is shown at Fig. 2 (for parameters of the lens: $M = 1200$; $ka = 45$; $kb = 15$). So, it is clear that we have a numerical solution of the problem with high accuracy and it is increasing with increasing parameter M [5].

The traces for GO-rays family passing through Veselago lens (when we do not take into account the rays which can reflect by boundaries of the lens) were calculated and depicted at Figs. 3, 5, and 7. The parameters of the lenses were: $n_r = -0.5$, $ka = 45$, $kb = 15$; $n_r = -1$, $ka = 30$, $kb = 15$; $n_r = -2.0$, $ka = 45$, $kb = 20$ accordingly. It is seen that point of ideal focusing exists for $n_r \approx -1$ only and for cases $|n_r| < 1$ or $|n_r| > 1$ the point of focusing transforms into a caustics with one cusp and limited branches. Also one can see that the space location of the caustic's cusp depends on value of refractive index n_r .

The distribution of the field in near zone of the lens with refractive index $n_r = -0.5 - i0.001$, $n_r = -1.0001 - i0.001$ and $n_r = -2 - i0.001$ ($2ka = 90$; $2kb = 30$ or $2kb = 40$) are illustrated by Figs. 4, 6, and 8. It is seen that structure of the field in focusing regions and field distribution near boundaries of the lens depends strongly on value of $|n_r|$. It was detected too that the distribution of the field near boundaries of the lens depends on the way of forming $|n_r| = 1$.

The resolution for lenses kD with fixed width $2kb$ (curves: 1 — $n_r = -0.5$; 2 — $n_r \approx -1$; 3 — $n_r = -2$ accordingly) is presented by Fig. 9. This result shows that an ideal focusing for flat lenses

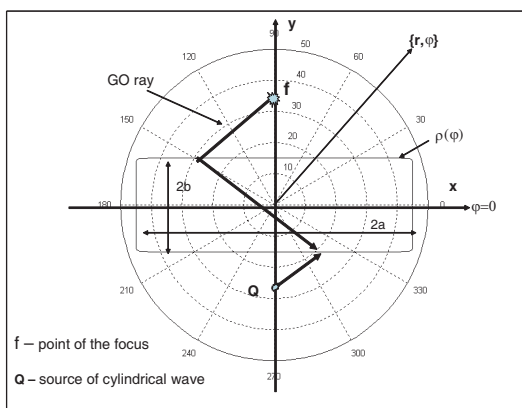


Figure 1: The geometry of the problem.

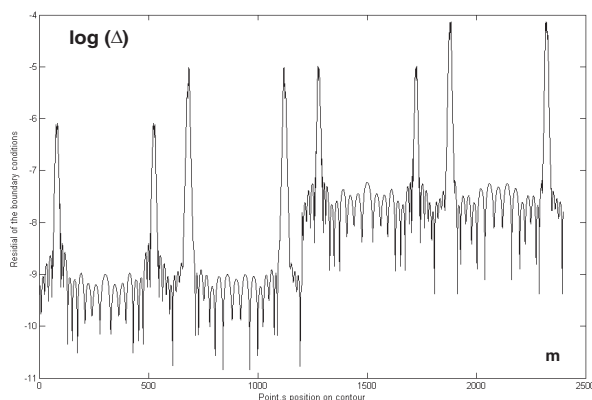


Figure 2: The residual of boundary condition.

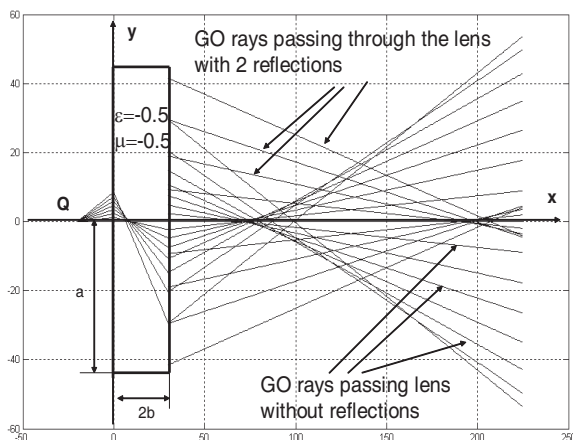


Figure 3: GO ray family for $n_r = -0.5$.

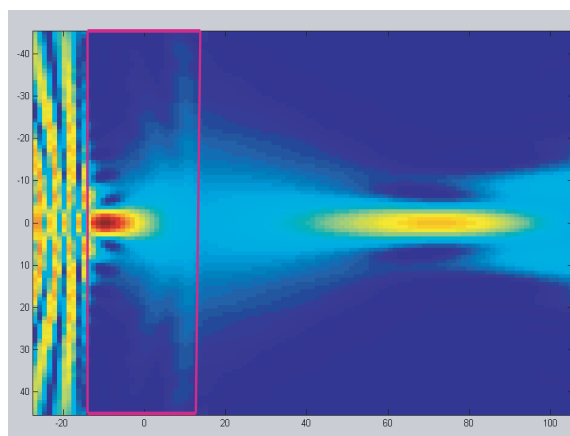


Figure 4: The near field distribution for lens ($n_r = -0.5$).

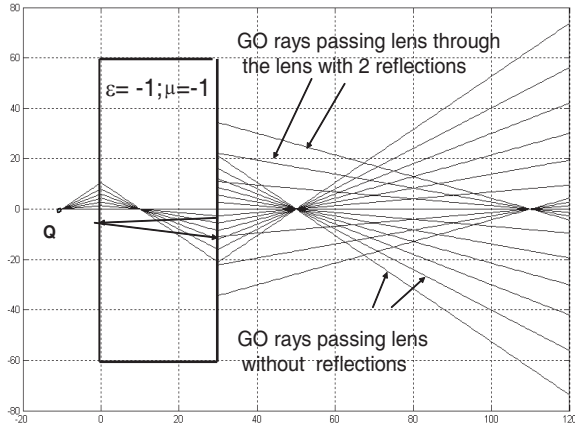


Figure 5: GO ray family for $n_r \approx -1$.

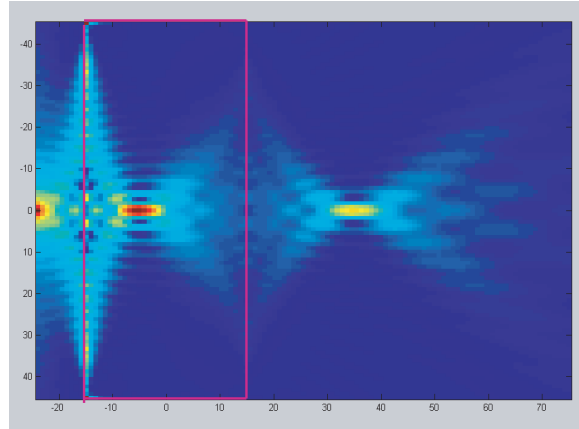


Figure 6: The near field distribution for ideal lens.

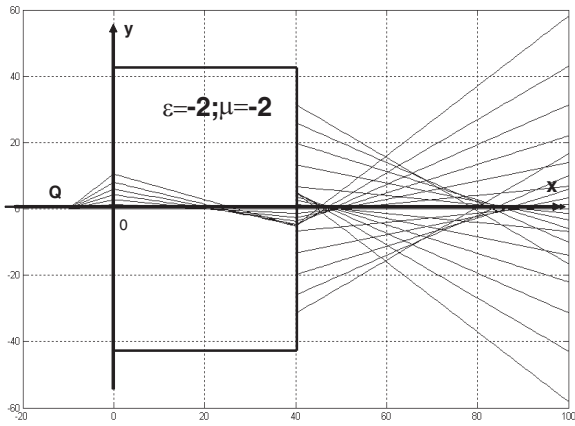


Figure 7: GO ray family for $n_r = -2$.

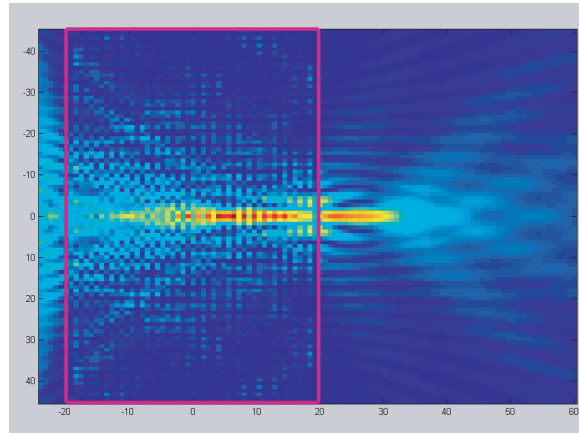


Figure 8: The near field distribution for lens ($n_r = -2$).

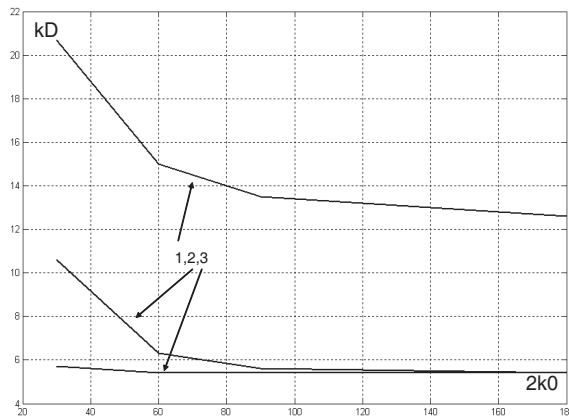


Figure 9: The near field distribution for lens ($n_r = -2$).

is impossible.

The cross-section distribution of the field $|U(kx)|$ behind the ideal Veselago lens with parameters: $n_r = -1.0001 - i0.001$, $2ka1 = 90$, $2kb1 = 40$; $kR_0 = 30$, $\varphi_0 = -\pi/2$ (curves: 1 — $ky = 20$, 2 — $ky = 40$, 3 — $ky = 50$, 4 — $ky = 60$, 5 — $ky = 80$) are depicted at Fig. 10.

The influence of source's coordinates kR_0 (curves: 1 — $kR_0 = 25$; 2 — $kR_0 = 30$; 3 — $kR_0 = 35$,

accordantly) on longitudinal ($kx = 0$) distribution of the field $|U(kx = 0, ky)| \equiv |U(ky)|$ inside and behind the ideal Veselago lens ($n_r = -1.0001 - i0.001$) are illustrated by Fig. 11. Parameters of the lenses is presented at Figs. 11, 12. It is seen that amplitude of the field in focusing points and amplitude of the field on the boundaries of the lens depends on value of source's coordinate R_0 .

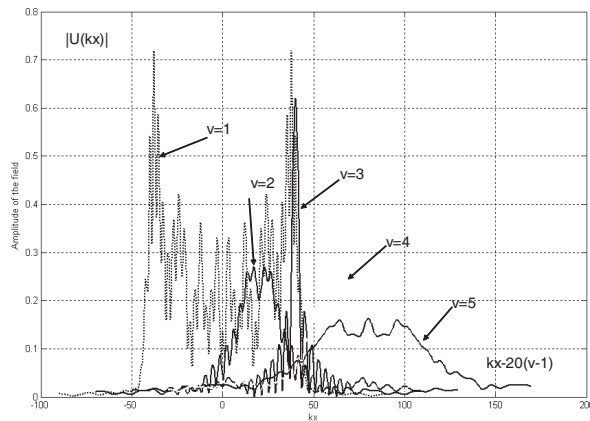


Figure 10: The cross-section distribution of the field for ideal for ideal Veselago lens.

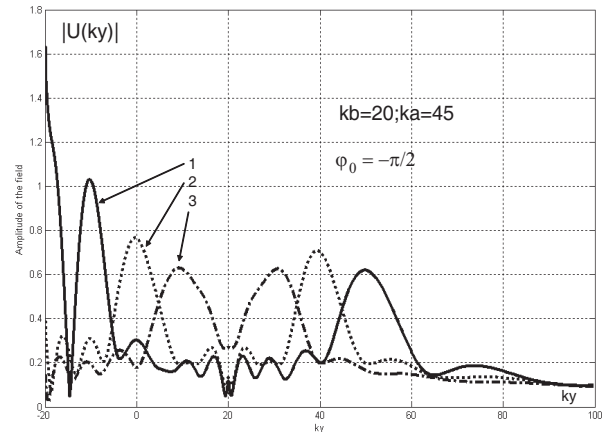


Figure 11: The longitudinal distribution of the field for ideal Veselago lens.

ACKNOWLEDGMENT

This work was supported by the Russian Foundation for Basic Research, project No. 09-02-00126 and Russian New University.

REFERENCES

1. Veselago, V. G., "The electrodynamics of substances with simultaneously negative values of ϵ and μ ," *Sov. Phys. Usp.*, Vol. 10610, 509, 1968.
2. Pendry, J. B., "Negative refraction makes a perfect lens," *Phys. Rev. Lett.*, Vol. 85, 3966, 2000.
3. Pendry, J. B. and D. R. Smith, "Reversing light with negative refraction," *Physics Today*, 37, 2004.
4. Veselago, V. G, L. Braginsky, V. Shklover, and C. J. Hafner, *Comput. and Theoret. Nanoscience*, Vol. 2, 1, 2006.
5. Anioutine, A. P, A. G. Kyurkchan, and S. A. Minaev, "About a universal modification to the method of discrete sources and its application," *JQSRT*, Vol. 79–80, 509, 2003.
6. Anyutin, A. P., "Features of the field of cylindrical wave scattered and focused by an isolated perfect Veselago lens with finite dimensions or by a system of tree lenses," *Journal of Communication Technology and Electronics*, Vol. 53, No. 11, 1323, 2008.
7. Anyutin, A. P., "About focusing and scattering of cylindrical wave by Veselago lens with finite size," *Radiotechnica and Electronica*, Vol. 53, No. 4, 431, 2008.

About 2D Multiple Scattering Problem by Lattice and Its Application for Constructing Metamaterial

A. P. Anyutin

Russian New University, Russia

Abstract— The modification of the method of discrete sources (MMDS) was applied for making solution of the scattering E or H polarized cylindrical incident waves from finite 2D lattice structure (finite 2D crystal). It is shown that there is a diffracted maximum of passing field behind the lattice only and it is not a ray focusing process. So we had shown that this type of structure can not be use for constructing metamaterials with negative refraction index.

1. INTRODUCTION

A multiple scattering by 2D cylindrical lattice infinitive structures is the classical problem of the diffraction theory and its field in fare zone has been under discussing since the middle of 20th century [1–6]. The near field of these structures was not practically investigated. In recent years, the problem deal with calculation of near field for lattice has arisen again due to attempts of constructing metamaterial with negative refractive index (for example see [7] and reference in it).

2. DIFFRACTION OF H POLARISED CYLINDRICAL WAVE BY LATTICE

In this paper we has developed 2D modification of the method of discrete sources (MMDS) for scattering E or H polarized cylindrical incident waves from finite 2D lattice structure (finite 2D crystal). The crystal was constructed by array of perfect conducting circular cylinders. Each cylinder has an “electrical” diameter ka (k — wave number for free space). The distance between cylinders was fixed and formed a hexagonal structure with lattice constant kh . The total numbers layers were seven (or nine). The number of cylinders in each layer was 12 (or 9). The example of this structure ($khx = 2\pi/1.54$; $khy = (\sqrt{3}/2)khx$; $ka = 1.697$) illustrates by Fig. 1.

We consider that a source of H polarized cylindrical wave Q is located near lattice Fig. 1. The field $u_0(\vec{r})$ of the source is given by following expression:

$$u_0(\vec{r}) = H_0^{(2)} \left(k \sqrt{r^2 + R_0^2 - 2rR_0 \cos(\varphi - \varphi_0)} \right), \quad (1)$$

where $\{r, \varphi\}$ — cylindrical coordinates for point of view, $\{R_0, \varphi_0\}$ — coordinates of the source of cylindrical wave Q .

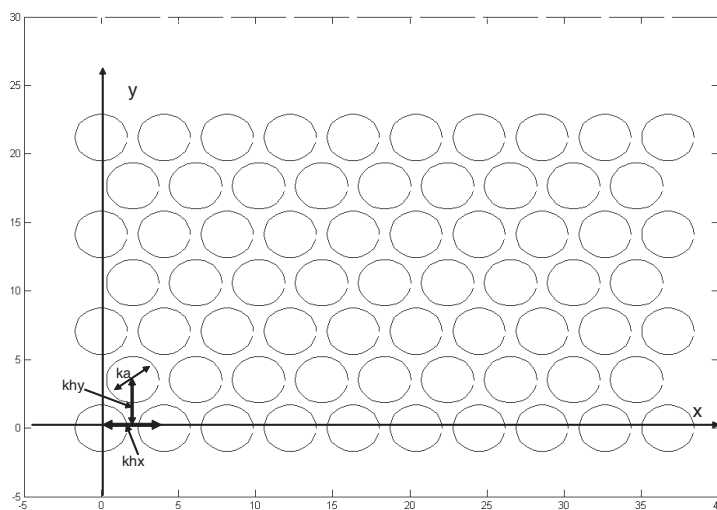


Figure 1: Geometry of the lattice.

Let consider the 2D multiple scattering problem of H polarized wave $u_0(\vec{r})$ (1) by M perfect conducting cylinders which were arranged in free space as lattice (finite 2D crystal) described above. The total diffracted field $u^1(\vec{r})$ outside of the finite 2D crystal could be presented as follows:

$$u^1(\vec{r}) = \sum_{j=1}^M u_j^1, \quad (2)$$

Diffracted field $u_j^1(\vec{r})$ of the each cylinder S_j is a solution to Helmholtz equation:

$$\Delta u_j^1 + k^2 u_j^1 = 0, \quad (3)$$

outside of cylinder S_j and satisfies to boundary condition:

$$\frac{\partial}{\partial n} [u_0(\vec{r}) + u^1(\vec{r})] |_{S_j} = 0, \quad j = 1, 2, \dots, M, \quad (4)$$

and Sommerfeld radiation condition:

$$\frac{\partial u_j^1(\vec{r})}{\partial r} + iku_j^1(\vec{r}) = o(r^{-1/2}), \quad |r| \rightarrow \infty. \quad (5)$$

In accordance with the method MMDS, we could present each fields $u_j^1(\vec{r})$:

$$u_j^1(r, \varphi) = \sum_{m=1}^M A_{mj} H_0^{(2)}(k|\vec{r} - \vec{r}_{mj}|); \quad (6)$$

and unknown coefficients A_{mj} have to be found by making solution of linear equations which one can obtain by satisfaction to boundary condition (4).

The coefficients A_{mj} having been found, the scattering field $u^1(\vec{r})$ could be calculated as follows

$$u^1(\vec{r}) = \sum_{j=1}^M \sum_{m=1}^M A_{mj} H_0^{(2)}(k|\vec{r} - \vec{r}_{mj}|). \quad (7)$$

The accuracy of the solving problems we estimate as the residual Δ of the boundary conditions.

The example of calculated near field distribution for structure Fig. 1 presented at Fig. 2 (the parameters of the lattice were taken from [7]). The result presented at Fig. 2 shows that we have a diffracted maximum for passing field behind the lattice only and it is not a ray focusing process.

For example, at Figs. 3 and 4, the calculated structure of the ray family and structure of the field in focusing region for a plate of metamaterial (flat lens) with negative refractive index $n_r = -0.7$ are presented.

Comparison this results with results of [7] shows that we can not use such type of structure for constructing metamaterials with negative refraction index $n_r = -0.7$ or other values.

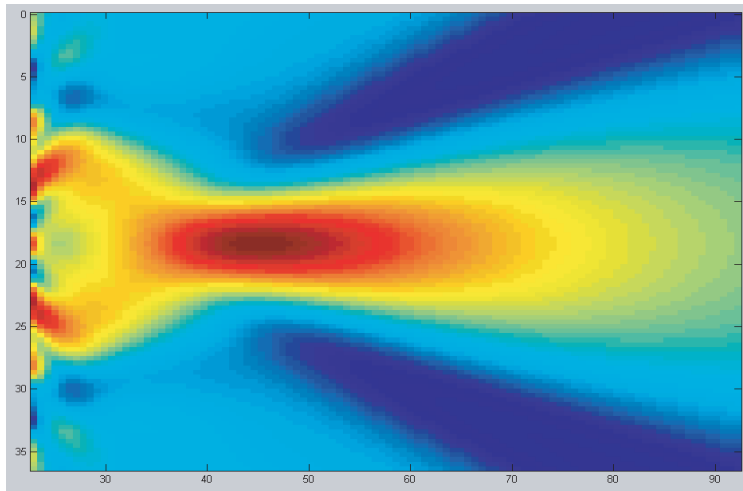


Figure 2: Field's structure behind the lattice.

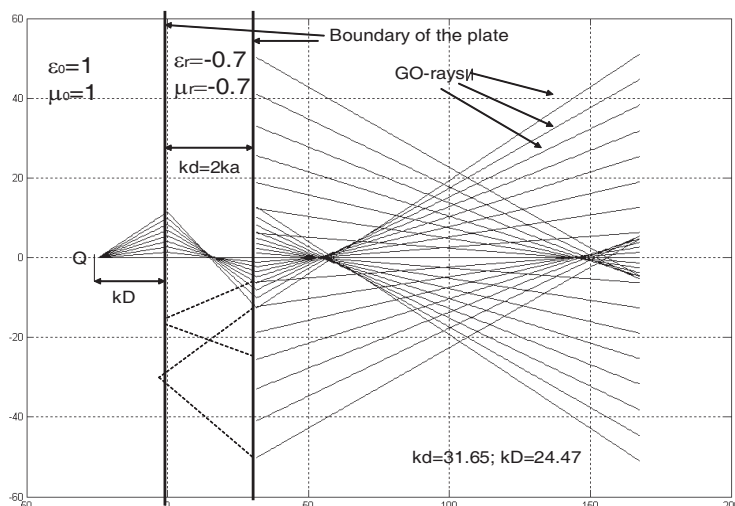
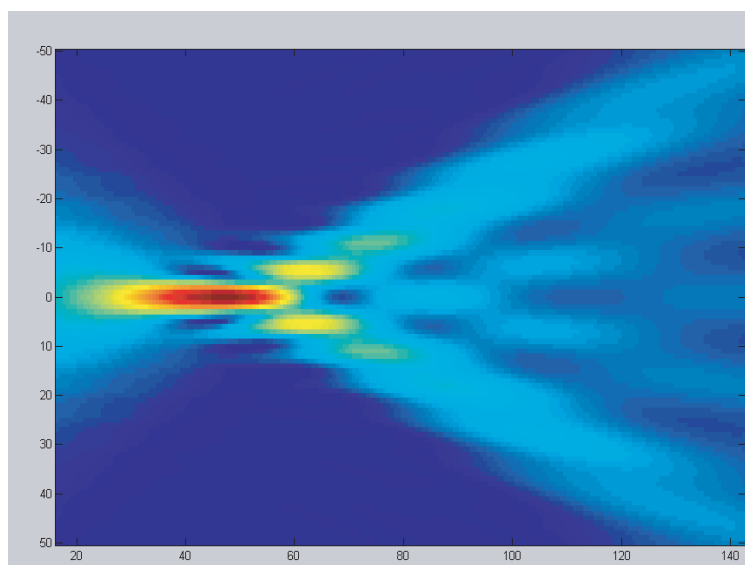


Figure 3: Ray family.

Figure 4: Field in focusing region for flat lens with $n_r = -0.7$.

3. CONCLUSION

It was shown that lattice can not be use for constructing metamaterial with negative refraction index ($n_r = -0.7$ or other values) and the field's maximum is not subjected to Veselago low.

ACKNOWLEDGMENT

This work was supported by the Russian Foundation for Basic Research, project No. 09-02-00126 and Russian New University.

REFERENCES

1. Tversky, V., "Multiple scattering by arbitrary configurations in three dimensions," *J. of Math. Phys.*, Vol. 3, No. 1, 83–91, 1962.
2. Feld, Y. N., *Radiotekhnika and Elektronika*, Vol. 31, No. 7, 1265–1275, 1986.
3. Kyurkchan, A. G., "Application of the method of pattern equation for solving a scattering problem by system of bodies," *Radiotekhnika and Elektronika*, Vol. 41, No. 1, 40–45, 1996.
4. Harrington, R. F., *Field Computation by Moment Methods*, Macmillan, New York, 1968.
5. Sveshnikov, A. G and A. S. Ilinsky, *Four Lectures on Numerical Method in Diffraction Theory*, Leningrad State University, Leningrad, 1972.

6. Shestopalov, V. P., *The Method of the Riemann-Hilbert Problem in the Theory of Electromagnetic Wave Diffraction and Propagation*, Harkov University, Harkov, 1971.
7. Qin, C., X. Zhang, and Z. Liu, "Far-field imaging of acoustic waves by a two-dimensional sonic crystal," *Physical Review B*, Vol. 71, 054302, 2005.

About Scattering and 2D Coating Problems by Multilayer Metamaterial Structures

A. P. Anyutin

Department of Science and Information Technology, Russian New University
P. O. 105007, h. 22, Radio Street, Moscow, Russia

Abstract— In this presentation we will tell about strict solution of diffraction problem by 2D multilayer metamaterial structure. The field in near and far zones of such structure was calculated and presented. It is detected the effect of coating (but not invisible) for some structures.

1. INTRODUCTION

It is known that scattering from 2D multilayer dielectrically structures could be reduced to multiple scattering problems. The last problem is a classical problem of the diffraction theory, which has been under wide discussing since the middle of 20th century. During a few recent years, an artificial medium (metamaterial or medium with negative index refraction) have been attracting much attention both theoretical and experimental points of view. At present time the problem of electromagnetic wave interaction with metamaterial structures is discussed in many publication (see [1–4] and reference in it). However we would like to emphasize that up to now there is no a satisfactory solution of this problem for compact scatterer in high frequency region.

This paper is concerning to a strict numerical solution of multiple scattering problem by 2D compact metamaterial structures. Some of them are illustrated by Figs. 1–2. We also had considered following cases of the structures: plate with negative refractive index $n_r \approx -1$ with circular insertion from vacuum or metal; single plate or single cylinder with $n_r \approx -1$ and losses; single shell with $n_r < 0$ or shell with $n_r \approx -1$ and circular insertion from metal; plate with $n_r \approx -1$ with circular insertion from air and outer metamaterial cylinder with $n_r \approx -1$. We had obtained the field distribution in near zone of all types of the structures and the scattering pattern in far zone of its (examples of the field distribution in near zone see at Figs. 3–10).

2. 2D DIFFRACTION PROBLEM BY MULTILAYER METAMATERIAL STRUCTURES

Let consider the 2D scattering of cylindrical wave $u_0(r, \varphi)$:

$$u_0(r, \varphi) = H_0^{(2)}(k|\vec{r} - \vec{r}_0|), \quad (1)$$

by metamaterial cylindrical structure with surface S_1 inside of which there are placed one (\sim or two) other cylindrical structures with surfaces S_2 (S_3). The medium of the first structure S_1 is

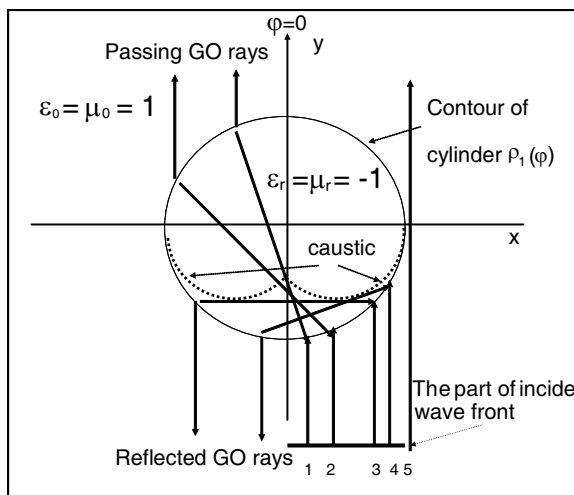


Figure 1: Ray family for cylinder with $n_r \approx -1$.

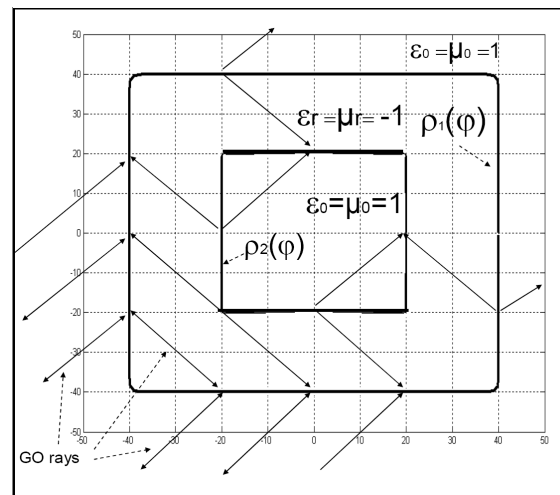


Figure 2: Ray family for structure with $n_r \approx -1$.

characterized by negative refractive index $-n_r - i\nu$ (where $n_r = \sqrt{|\varepsilon_r||\mu_r|}$, ε_r — relative dielectric permittivity, μ_r — relative magnetic permeability, ν — losses of medium accordingly). In cylindrical system of coordinates (z, r, φ) the surfaces S_l ($l = 1, 2, 3$) have a cross section contours $\rho_l(\varphi)$:

$$\rho_l(\varphi) = \frac{1}{\sqrt[n]{(\cos(\varphi)/a_l)^n + (\sin(\varphi)/b_l)^n}}, \quad n \geq 20, \quad (2)$$

Evidently that the shape of contours $\rho_l(\varphi)$ (2) could be easily changed by varying of n or a_l and b_l (for example, if $a = b$; $n \geq 20$ the shape of $\rho_l(\varphi)$ is very close to rectangular one, if $a = b$; $n = 2$ — is a circular). The center of contour $\rho_2(\varphi)$ ($\rho_3(\varphi)$) can have some displacement $\{h_x, h_y\}$ with regard to the center of $\rho_1(\varphi)$ ($\rho_2(\varphi)$). The medium inside of $\rho_2(\varphi)$ (\sim or ($\rho_3(\varphi)$) can be vacuum (\sim or perfect conducting metal) and $\vec{r}_0 = \{r_0, \varphi_0\}$ in (1) — coordinates of the source of cylindrical wave.

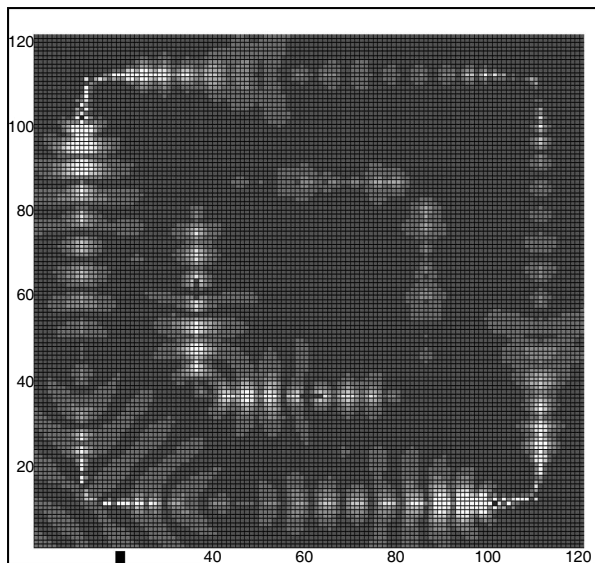


Figure 3: Near field for structure Fig. 2 (inside in vacuum) ($kR_0 = 600$; $\varphi_0 = 1.25\pi$; $n_r = -1.0001 - i0.001$).

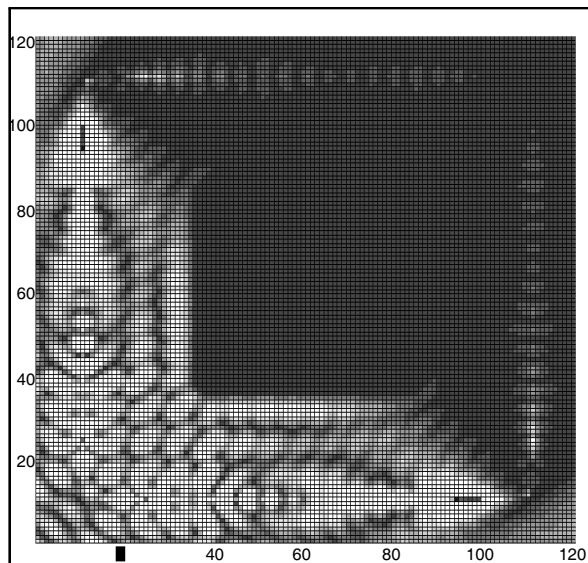


Figure 4: Near field for structure Fig. 2 (inside square is metal) ($kR_0 = 600$; $\varphi_0 = 1.25\pi$; $n_r = -1.0001 - i0.001$).

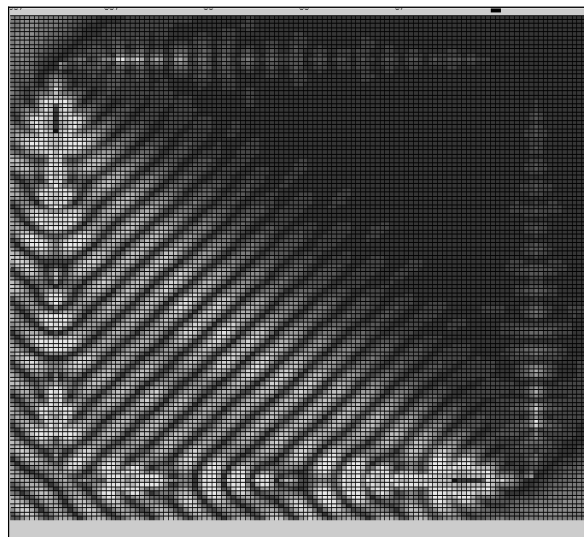


Figure 5: Near field for single plate with $n_r \approx -1$ and plane incident wave with $\varphi_0 = 1.25\pi$ ($kR_0 = 600$; $\varphi_0 = 1.25\pi$; $n_r = -1.0001 - i0.001$).

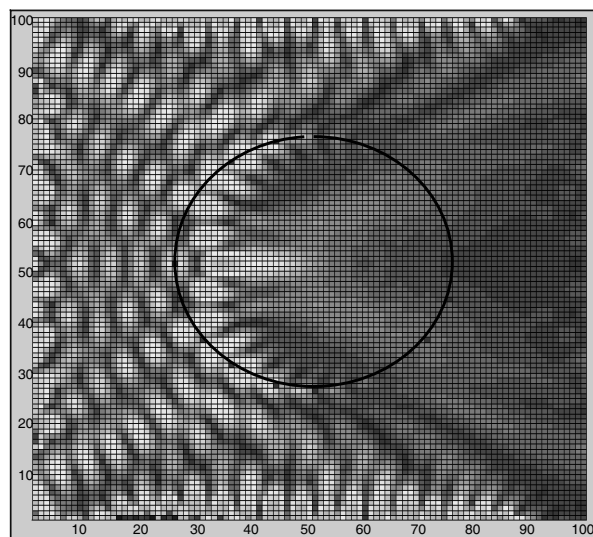


Figure 6: Near field for plate with $n_r \approx -1$ and circular insertion from vacuum (plane incident wave $\varphi_0 = \pi$).

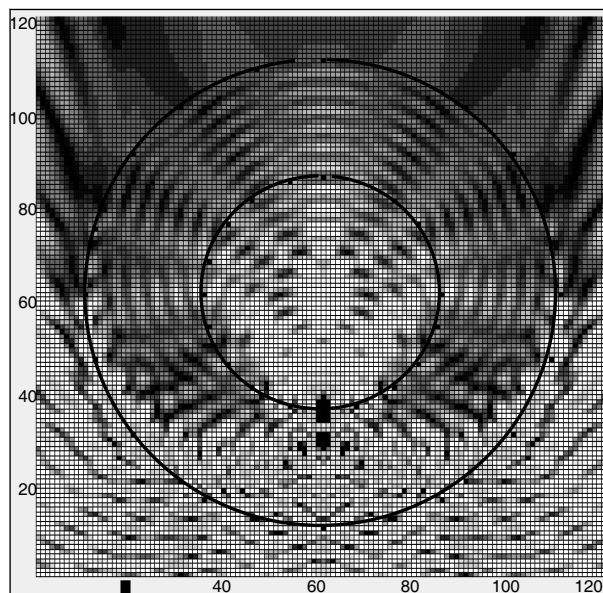


Figure 7: Near field for single shell with circular insertion from vacuum; $kR_0 = 800$; $\varphi_0 = -\pi/2$; $ka_1 = 40$; $ka_2 = 20$.

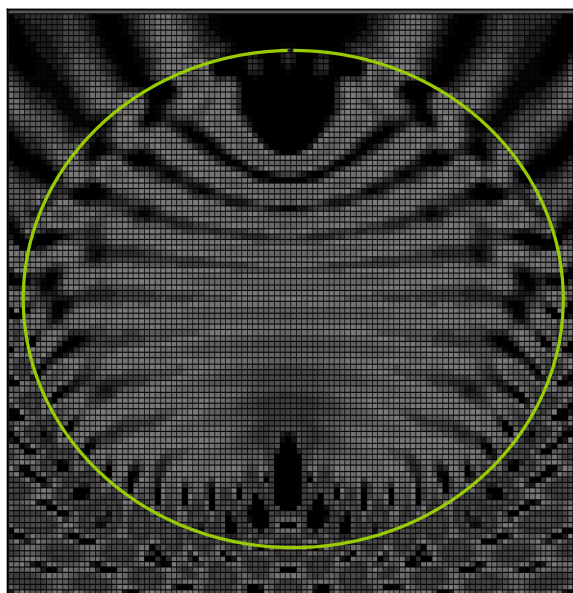


Figure 8: Near field for metamaterial cylinder; inside cylinder is metal; $kR_0 = 800$; $\varphi_0 = -\pi/2$; $ka_1 = 40$; $ka_2 = 3$; $h_y = 30$.

A strict solution of diffraction problem by structure (2) was obtained by applying the modification of the method discrete sources (MMDS) [5, 6]. The error of the solution we estimate as the residual Δ of the boundary conditions on contours $\rho_l(\varphi)$ and it was less than 10^{-4} for all obtained results.

At Fig. 1, Fig. 2 a correct geometrical optic ray families for contours $\rho_{1,2}(\varphi)$ and $\rho_1(\varphi)$ are presented. These pictures help us to explain and understand the results which are shown below.

Figures 3–8 illustrate calculated field distribution in near zone for some metamaterial structures mentioned above. For example, at Fig. 3 or Fig. 5 one can find a region in which a negative refraction is seen clearly. At Fig. 6 we can see a field distribution which is typical for ray family and caustic presented by Fig. 1. At Fig. 8 we see a reflection waves inside and outside of the structure.

These results show that reflection field and diffraction effects are taking place for metamaterial with $n_r \approx -1$. It was detected that there is a coating effect for structures like Fig. 8 in its far zone only.

ACKNOWLEDGMENT

This work was supported by the Russian Foundation for Basic Research, project No. 06-02-16804, No. 06-02-16483.

REFERENCES

1. Veselago, V. G., "The electrodynamics of substances with simultaneously negative values of ε and μ ," *Sov. Phys. Usp.*, Vol. 10, 509, 1968.
2. Pendry, J. B., "Negative refraction makes a perfect lens," *Phys. Rev. Lett.*, Vol. 85, 3966, 2000.
3. Pendry, J. B. and D. R. Smith, "Reversing light with negative refraction," *Physics Today*, 37, 2004.
4. Veselago, V., L. Braginsky, V. Shklover, and C. J. Hafner, *Comput. and Theoret. Nanoscience*, Vol. 2, 1, 2006.
5. Anioutine, A. P., A. G. Kyurkchan, and S. A. Minaev, "About a universal modification to the method of discrete sources and its application," *JQSRT*, Vol. 79–80, 509–520, 2003.
6. Anioutine, A. P. and V. I. Stasevich, "Scattering of E and H polarized waves from covered cylindrical structures," *JQSRT*, Vol. 100, 15–25, 2006.

Caustic Singularities Arising at Propagation of Short Radiowaves in Anisotropic Ionospheric Plasma

A. S. Kryukovsky, D. S. Lukin, and D. V. Rastyagaev
 Dept. of Phys. & Math Problems of Wave, Processes, MIPT
 Institutsky per., 9, Dolgoprudny, Moscow Reg. 141700, Russia

Abstract— The bi-characteristic method for description of propagation of electromagnetic waves in non-uniform ionosphere in view of influence of a magnetic field of the Earth investigates. The propagation features of ordinary and non-ordinary parts of an electromagnetic field both with the account, and without the account of radial symmetry of a task on one-reflecting and multi-reflecting) traces are considered. One-layer and double-layer models, and also model with a horizontal gradients leading to occurrence of the wave channel at working frequencies as higher, and below critical frequency are considered.

1. INTRODUCTION

The modeling of electromagnetic wave propagation in non-uniform ionosphere in view of influence of a magnetic field of the Earth by the bi-characteristic method (1) has been executed. The Hamiltonian bi-characteristic system of the equations is possible to write down as [1]

$$\frac{d\vec{k}}{dt} = \frac{\partial \omega^2 \varepsilon}{\partial \vec{r}} \bigg/ \frac{\partial \omega^2 \varepsilon}{\partial \omega}, \quad \frac{d\vec{r}}{dt} = \left(2c^2 \vec{k} - \frac{\partial \omega^2 \varepsilon}{\partial \vec{k}} \right) \bigg/ \frac{\partial \omega^2 \varepsilon}{\partial \omega} \quad (1)$$

where $\vec{k} = (k_x, k_y, k_z)$ — a wave vector, $\vec{r} = (x, y, z)$ — coordinates of a view point, ω — circular frequency of radiation, $c = 2,997925 \cdot 10^{10}$ cm/c — light speed, t — parameter along a ray trace, $\varepsilon \equiv \varepsilon(\vec{r}, \vec{k}, \omega)$ — effective permittivity of propagation medium.

For magnetic medium the effective permittivity can be submitted as [2]:

$$\varepsilon_{\pm} = 1 - \frac{2v(1-v)}{2(1-v) - u \sin^2 \alpha \pm \sqrt{u^2 \sin^2 \alpha + 4u(1-v)^2 \cos^2 \alpha}} \quad (2)$$

where

$$v = \frac{\omega_p^2}{\omega^2} = \frac{4\pi e^2 N}{m_e \omega^2}, \quad u = \frac{\omega_H^2}{\omega^2} = \frac{e^2 H_0^2}{m_e^2 c^2 \omega^2}, \quad (3)$$

$e = 4,8029 \cdot 10^{-10}$ C.G.S.E. — electronic charge, $m_e = 9,108 \cdot 10^{-28}$ gm. — electron mass, H_0 — a magnitude of a magnetic field intensity of the Earth, N — structure of electronic concentration. Angle α is an angle between a vector of the magnetic field intensity of the Earth $\vec{H}_0 = (H_{0x}, H_{0y}, H_{0z})$ and a wave vector. That is why

$$\cos^2 \alpha = \frac{H_{0x} k_x + H_{0y} k_y + H_{0z} k_z}{H_0^2 |\vec{k}|}. \quad (4)$$

The sign “+” corresponds to an ordinary wave, and the sign “−” — an non-ordinary wave.

It is supposed, that the point source of radiation is located in the beginning of coordinates ($\vec{r}(0) = 0$), and the initial wave vector depends on corners of a ray in an output point:

$$k_x(0) = \frac{\omega}{c} \cos \zeta \cos \eta, \quad k_y(0) = \frac{\omega}{c} \sin \zeta \cos \eta, \quad k_z(0) = \frac{\omega}{c} \sin \eta. \quad (5)$$

The propagation singularities of ordinary (Figs. 1, 3) and non-ordinary (Fig. 2) waves of electromagnetic fields both with (Fig. 3) the account, and without (Figs. 1, 2) the account of radial symmetry of a problem on one-reflecting and multi-reflecting (Fig. 1) traces are considered.

One-layer and double-layer models (Fig. 4), and also model with a horizontal gradients (Fig. 5) leading to occurrence of the wave channel at working frequencies as higher, and below critical (plasma) frequency are considered.

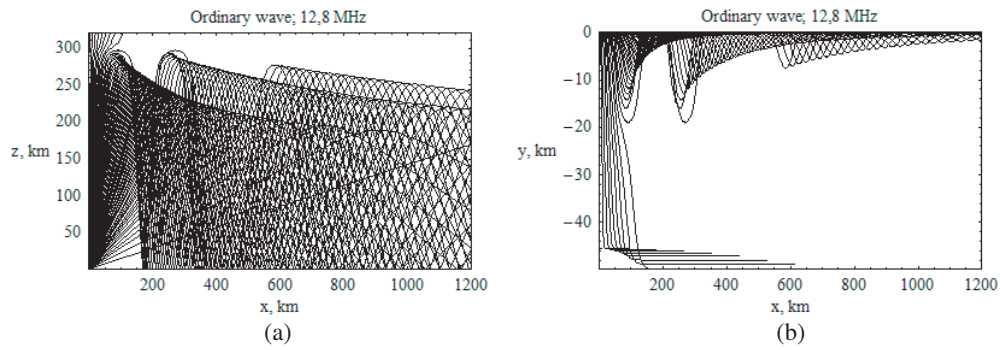


Figure 1.

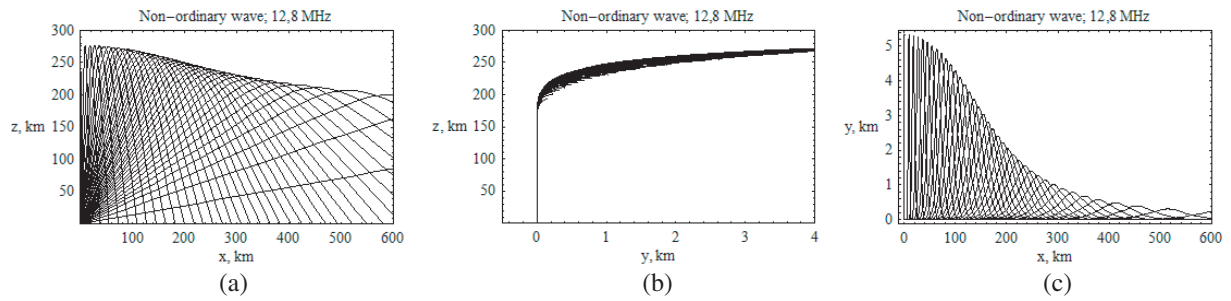


Figure 2.

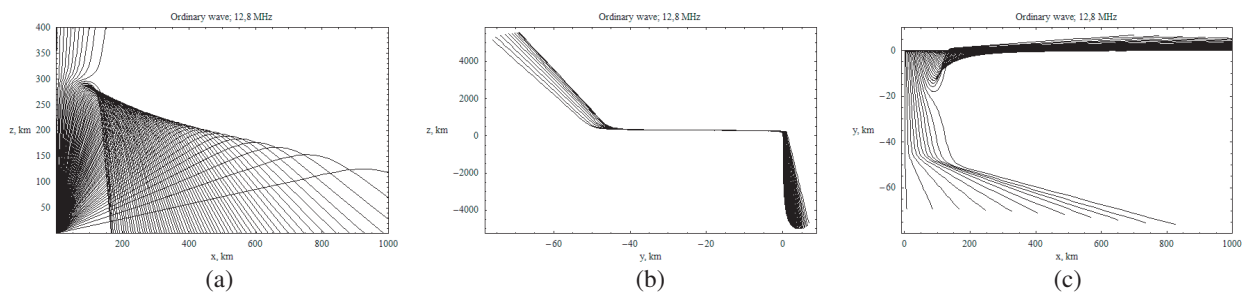


Figure 3.

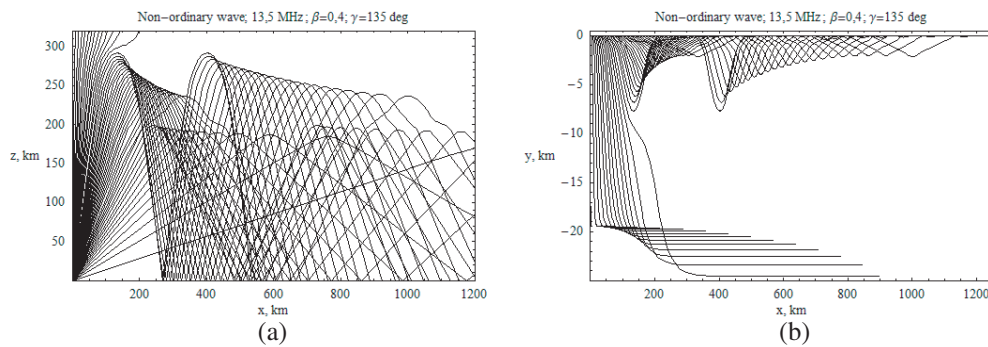


Figure 4.

Caustic singularities of ray structures arising in the basic vertical section, in lateral sections and projection of ray trajectories to a horizontal plane are investigated. The important effect describing anisotropic media, is the ray exit from a propagation plane (Fig. 6) with formation caustic singularities, elementary of which are a smooth caustic and a cusp. Ray and caustic of

structure in various cases are considered in detail. In particular, the propagation of an ordinary wave in an ionospheric plasma layer F (with various orientations of a magnetic field) is considered.

As the plasma frequency of a layer is chosen a little bit below by worker, part of rays at angels of fall close to vertical, pass an ionospheric layer, and others come back to the Earth and form the cusp. The less initial angle of a deviation of a ray from a vertical, the grater it deviates concerning an initial plane of propagation, and then comes back. The rays which are propagating through an ionospheric layer, deviating on certain distance, do not come back more in an initial plane, as it is done by rays reflected from the ionosphere, and, the more initial angle between a ray and vertical, the deviation is more. For a non-ordinary wave the excess of working frequency above plasma for any angles of falls.

The radio wave propagation in cases, when height of a maximum of an ionospheric layer has periodically varying size is considered. In a Fig. 7 (“a” — non-ordinary wave, “b” — ordinary wave) the case is shown, when height begins to grow with growth of coordinate x , and in a Fig. 8 on the contrary decreases. The formation complex caustic of structures in researched planes is visible.

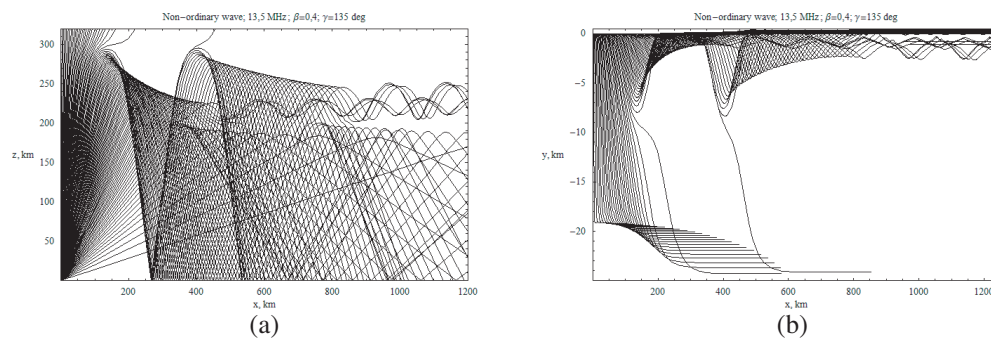


Figure 5.

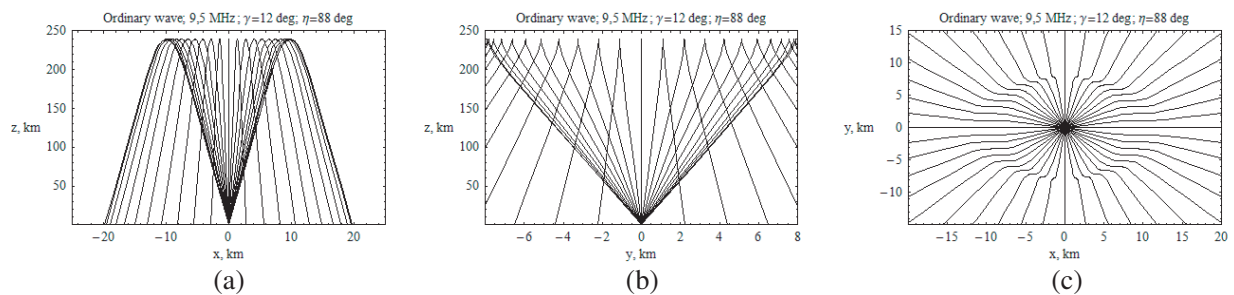


Figure 6.

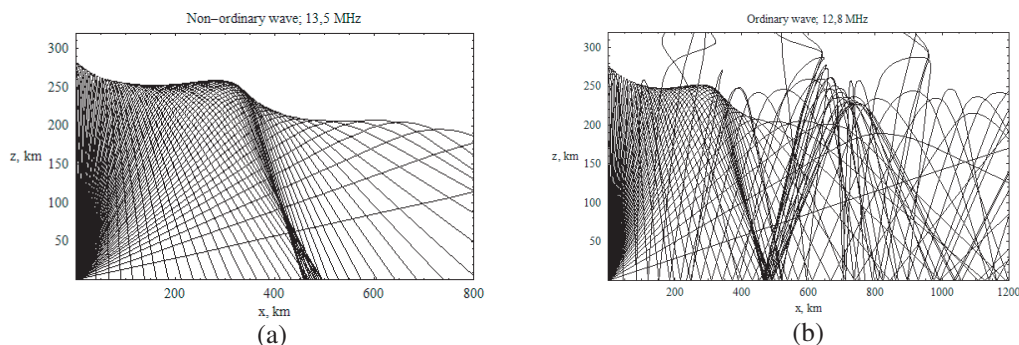


Figure 7.

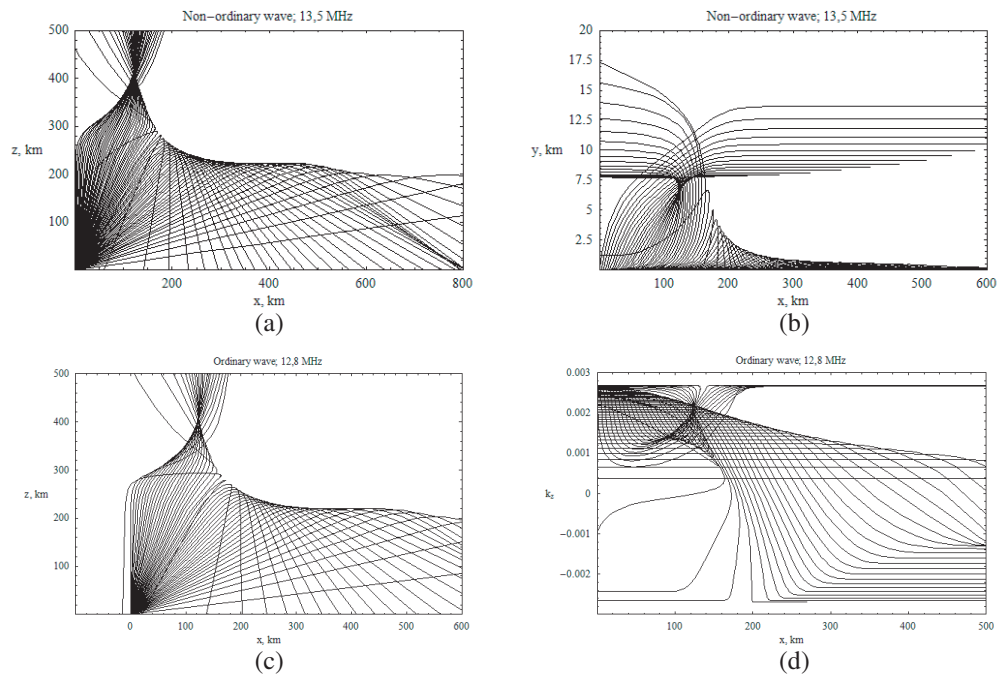


Figure 8.

ACKNOWLEDGMENT

The work was supported by RFFI (grant # 07-02-00663).

REFERENCES

1. Lukin, D. S. and Y. G. Spiridonov, "Application of a method of the characteristics for the numerical decision of problems of radio wave propagation in non-uniform and nonlinear medium," *Journal of Communication Technology and Electronics*, Radio Technology and Electronics, Vol. 14, No. 9, 1673–1677, 1969, in Russian.
2. Lukin, D. S. and E. A. Palkin, "Numerical canonical method in problems of a diffraction and propagation of electromagnetic waves in non-uniform media," *M. MIPT*, 159, 1982, in Russian.
3. Davies, K., *Ionospheric Radio Waves*, A Division of Ginn and Company Waltham, Blaisdell Publishing Company, Massachusetts, Toronto, London, 1969.

Applying the Wave Catastrophe Theory to Solve of Problems of EM Waves Propagation, Diffraction and Focusing in Non-uniform Media

A. S. Kryukovsky, D. S. Lukin, and D. V. Rastyagaev

Dept. of Phys & Math Problems of Wave, Processes, MIPT
Institutsky per., 9, Dolgoprudny, Moscow Reg. 141700, Russia

Abstract— The review of results of mathematical and numerical modeling for processes of propagation, diffraction, and focusing of electromagnetic waves in non-uniform and dispersive media is resulted on the basis of applying of the wave catastrophe theory. The mathematical means of the solving of problems is developed by methods of the theory of the main, edge and corner catastrophes. As against traditional asymptotical methods (such as, a method of geometrical optics, the geometrical theory of diffraction, physical optics, the physical theory of diffraction, method of the parabolic equation, Gaussian beams summation, etc) the wave catastrophe theory allows to analyze singularities of complex focal and diffraction structures of wave fields. Such structures are not described by traditional asymptotical methods, or their description is extremely complicated or in general it is impossible because of formation of the complex focal areas. The wave catastrophe theory operates in terms of singularities of smooth mapping or catastrophe which physically correspond to steady focusings of wave fields. In essence, the type of wave catastrophe determines the diffraction structure of a field in general. In this work is considered the application of the given approach to the solving of applied problems in which singularities of caustic types such as the main, edge and corner catastrophe take place.

The general rules of the wave catastrophe theory, including classification, indexes and types of focusings, and also methods of uniform asymptotic construction, used for the description of structure of wave fields in such areas, the analysis of amplitude and phase structure of a field are considered. Classes of applied problems in which application of wave catastrophe appeared productive are submitted. The general description of classes of the special functions used for construction uniform asymptotic solving for wave fields, properties of these functions and methods of calculation of one-dimensional, two-dimensional, three-dimensional (space-time) focusings of wave fields is given.

1. INTRODUCTION

The review of results of mathematical and numerical modeling for processes of propagation, diffraction, and focusing of electromagnetic waves in non-uniform and dispersive media is resulted on the basis of applying of the wave catastrophe theory [1–6]. The mathematical means solving the problems is developed by methods of the main, edge and corner catastrophes [5, 6]. In the work, the basic concepts of the wave catastrophe theory and its application to processes of propagation, diffraction and scattering of electromagnetic waves are stated. The most widespread asymptotical methods are well-known various ray approaches, such as approximation of geometrical optics (GO), a method of geometrical acoustics, etc. The ray approach takes a special place among others asymptotical methods for some reasons, one of them, and not last, consists in its exclusive simplicity and an opportunity of reception of the analytical decision for a wide range of the problems which are not giving in to research exact or another asymptotical methods.

There are traditional methods researching and modeling of processes of propagation, diffraction and scattering of electromagnetic waves based on ray approach. In short-wave approximation there are various asymptotical methods: A method of geometrical optics [7], the geometrical theory of diffraction [8], physical optics, the physical theory of diffraction, methods of the parabolic equation, Gaussian beams summation, etc. As against the traditional asymptotical methods, the wave catastrophe theory allows to analyze singularities of complex focal and diffraction structures of wave fields. Such structures are not described by traditional asymptotical methods, or their description extremely complicated, or in general, it is impossible because of the formation of the complex focal regions.

The wave catastrophe operates in terms of the singularities of differentiable maps (or catastrophe) which physically correspond to steady focusings of wave fields (steady in relation to small indignations connected to them beam congruence). In essence, the type of the catastrophe determines the diffraction structure of a field in general.

2. STATEMENT OF WAVE CATASTROPHE THEORY

Applying of the theory of singularities of differential mapping (catastrophe theory) for construction uniform asymptotical (on parameter $\Lambda \gg 1$) solutions of the linear differential equations of wave type with determined boundary and initial conditions is considered:

$$\hat{L} \left(x, -\frac{i}{\Lambda} \frac{\partial}{\partial x_k}, -\frac{1}{\Lambda^2} \frac{\partial^2}{\partial x_k \partial x_j} \right) U(\Lambda, x) = 0 \quad (1)$$

The most widely spread asymptotic methods of constructing solutions of wave-type equations are diverse ray methods, including the approximation of geometric optics, WKB method, method of geometric acoustics, etc. According to ray methods, a solution of Equation (1) is constructed in the form of a product of a rapidly oscillating exponential of the phase function and an asymptotic series in negative powers of the large parameter of the problem,

$$U(\Lambda, x) \approx \exp(i\Lambda\Theta(x)) \times \sum_{j=0}^{+\infty} \frac{1}{(i\Lambda)^j} b_j(x) \quad (2)$$

or in the form of a finite sum of series of this kind,

$$U(\Lambda, x) \approx \sum_{k=1}^{N_g} \exp(i\Lambda\Theta_k(x)) \times \sum_{j=0}^{+\infty} \frac{1}{(i\Lambda)^j} b_{jk}(x). \quad (3)$$

Substituting (2) into Equation (1), we obtain a chain of recurrent relations (first-order differential equations) first of which is a Hamilton-Jacobi-type equation and defines the phase function $\Theta(x)$ and the other are transport equations which define the amplitude functions $b_0(x)$, $b_1(x)$, ... in succession (see, e.g., [7]). The solution of this recursive system of equations is found by using the bicharacteristics constructed by using the symbol of the operator \hat{L} of the Equation (1), which is reduced to evaluation of the functions $\Theta(x)$, $b_0(x)$, $b_1(x)$, ... along the ray trajectories which are the projections of the bicharacteristics from the phase space to the configuration one [9].

However, ray methods cannot be applied in a neighborhood of envelopes of ray families, i.e., in neighborhoods of caustics and their singularities. When approaching these objects, already the first amplitude coefficient $b_0(x)$ tends to infinity because it is inversely proportional to the quantity $\sqrt{|J|}$, where $J = \frac{\partial x}{\partial(\alpha, \tau)}$ stands for the divergence Jacobian that vanishes on the caustic and α and τ are the ray coordinates. Moreover, when passing through the caustic, the type of the solution is changed (i.e., the number of summands (rays of geometric optics) N_g in the sum (3)).

There are diverse integral methods which enable one to obtain uniform asymptotic solutions of the form

$$U(\Lambda; x) \cong \Lambda^{\delta/2} \int_G f(\Lambda; \eta, x) \cdot \exp(i\Lambda\Phi(\eta, x)) d\eta, \quad \delta = \dim \eta, \quad (4)$$

which can be applied both on the caustic surfaces and in their neighborhoods.

The most general tool is the Maslov canonical operator [9, 10]. Without going into details of constructing the solutions of type (4), note that the amplitude of the integrand has the form of an asymptotically convergent series

$$f(\Lambda; \eta, x) = \sum_{j=0}^{+\infty} \frac{1}{(i\Lambda)^j} f^{(j)}(\eta, x), \quad (5)$$

and for functions $\Phi(\eta, x)$ and $f^{(j)}(\eta, x)$, $j = 1, 2, \dots$, as in the case of ray solutions as well, one can obtain a recursive chain of first-order differential equations. As a rule, when using integral methods, the amplitude of the integrand is defined on a compact support, which enables one to treat the integrals (4) as convergent ones, although $G = \mathbf{R}^\delta$.

As a rule, the integral form of an asymptotic solution of a problem is not final because. First, it is difficult to evaluate multiple rapidly oscillating integrals, and, second, the subsequent analysis is possible, together with a passage to reference uniform asymptotic solutions related to singularities of caustic surfaces. The singularities of caustic surfaces correspond to singularities of differentiable maps and are classified in detail [11].

According to the catastrophe theory in a vicinity $\Omega \subset R^\kappa \times R^d$ saddle points (η^c, x^c) it is possible to replace function $\Phi(\eta, x)$ by its universal unfolding F_Σ [11]:

$$\Lambda\Phi(\eta, x) = \Lambda\Theta(x) + F_{\Sigma}(\xi, a(\Lambda, x), \lambda(\Lambda, x)), \quad (6)$$

using non-degenerate transformation:

$$\eta = \eta(\Lambda, \xi, x). \quad (7)$$

The unfolding looks like:

$$F_{\Sigma}(\xi, a, \lambda) = \varphi_0^{\Sigma}(a, \xi_1, \dots, \xi_{\bar{\kappa}}) + \sum_{j=1}^L \lambda_j \varphi_j^{\Sigma}(\xi_1, \dots, \xi_{\bar{\kappa}}) + \sum_{j=1+\bar{\kappa}}^{\kappa} \pm \xi_j^2, \quad (8)$$

For example, for catastrophe $\Sigma = D_N$, (for $N = 4$ it is describe focal regions of the elliptical or hyperbolical ombilicus types):

$$F_{D_N}(\xi, \lambda) = \xi_1^{N-1} \pm \xi_1 \xi_2^2 + \lambda_1 \xi_2 + \lambda_2 \xi_1 + \lambda_3 \xi_1^2 + \dots + \lambda_{N-1} \xi_1^{N-2}. \quad (9)$$

Using this classification, one can represent a uniform asymptotic solution of Equation (1) in the form of an expansion in a finite family of special functions of wave catastrophes (SWC) and their first derivatives with the coefficients in the form of asymptotically convergent series, and the form of the “principal” SWC (the main SWC) depends on the type of the singularity. The type of the degeneration of the generalized eikonal $\Phi(\eta, x)$ corresponds to a certain type of the caustic singularity; in turn, this singularity corresponds to a certain type of the diffraction structure of the wave field. For this reason, the field in a neighborhood of a caustic singularity turns out to be “proportional” to a special function of wave catastrophe (SWC) of the form

$$I^{\Sigma}(\lambda, a) = \int_{-\infty}^{+\infty} \exp(i F_{\Sigma}(\xi, a, \lambda)) d\xi. \quad (10)$$

To describe the diffraction of electromagnetic waves on conducting bodies, Keller suggested a geometric diffraction theory, which was further developed by Borovikov and Kinber (see [8]). In geometric diffraction theory, to the initial ray fields of geometric optics one adds the secondary ray fields excited by primary fields on the boundaries of the bodies. These fields can be described by ray families, namely, boundary and corner rays excited on edges of bodies, sliding rays occurring in the diffraction on convex surfaces, ray families corresponding to whispering gallery waves, and also to lateral and surface waves.

The special domains of a solution of problem (1) are still caustics of families of geometric optics rays; however, caustics of boundary rays and also boundaries of the form “light-shadow” of families of geometric optics rays are to be added to these domains.

In the case of a boundary value problem, the uniform asymptotic integral solutions can also be represented as sums of type (4) (see [3–6]). However, the domain of investigation G has now boundaries which are related to the fact that, in the case of boundary value problems, the variety on which the bicharacteristics are constructed is a Lagrangian manifold with boundary. Using an appropriate change of variables, one can represent the domain of integration (for a broad class of problems) in the form

$$G = R_{+}^{\nu} \times R^{\delta-\nu} = [\eta_1^*, +\infty) \times [\eta_2^*, +\infty) \times \dots \times [\eta_{\nu}^*, +\infty) \times R^{\delta-\nu}. \quad (11)$$

Thus, the problem to construct uniform asymptotics of rapidly oscillating integrals of type (4) with the domain of integration of the form (11) with catastrophe-type singularities in the phase of the integrand arises.

The formulas (6)–(10) is fair in the case of edge ($\nu = 1$), corner ($\nu = 2$) and generalized edge ($\nu > 2$) catastrophe [3–6].

Problems for which integrals of this kind occur include problems on the propagation and diffraction of electromagnetic and acoustic waves in non-homogeneous non-stationary (anisotropic) dispersive media (for instance, ionospheric plasma).

All stated is fair both for stationary, and for non-stationary problems above. On time can depend both the characteristic of the medium of signal propagation, and parameters of a source of radiation. The geometrical optics in non-stationary problems with dispersive media refers to space-time GO (STGO) and has the specificity connected first of all with existence of a space-time cone. By analogy with GTD, for the description of pulses propagation in dispersive media the space-time geometrical theory of diffraction (STGTD) is constructed. In this theory besides usual edge waves “time” edge waves are entered in consideration, radiated by the beginning or the end of a radio pulse and extending in media by laws of usual geometrical optics. It is obvious, that edge rays also can have caustics and diffract on obstacles, and STGO borders of ray families coincide with the space-time cone lines which are taking place through the beginning or the end of a pulse.

3. UNIFORM ASYMPTOTICS

Let's consider uniform asymptotics, constructed by methods of the wave catastrophe theory. All of them without dependence from type of singularities have one common property: The solution is under construction as the sum of some special functions with the coefficients which are looking like asymptotically converging series on parameter Λ . Such uniform asymptotics can be received or heuristically (from comparison with real caustic structures of a problem with the reference caustic structure arising in a vicinity of catastrophe of this or that type), or from the analysis integrated asymptotical solutions of the systems of (pseudo) the differential equations in partial derivatives.

According to the wave catastrophe theory [1–6] uniform asymptotics of a field in a vicinity of the catastrophe of main type Σ looks like:

$$U(\Lambda, x) \cong \exp [i\Lambda\Theta(x)] \times \left[l_1 I^\Sigma (S(\Lambda, x)) + \sum_{j=2}^N l_j \frac{\partial I^\Sigma (S)}{\partial S_{j-1}} \right], \quad (12)$$

where

$$l_j = \sum_{n=0}^{+\infty} l_j^{(n)}(\Lambda, x) = \Lambda^{\sigma_j} \sum_{n=0}^{+\infty} \frac{1}{\Lambda^n} \tilde{l}_j^{(n)}(x) \quad (13)$$

— coefficients of asymptotical expansion,

$$S = (\lambda, a) \quad (14)$$

and

$$I^\Sigma (\lambda, a) = \int_{-\infty}^{+\infty} \dots \int_{-\infty}^{+\infty} \exp [i F_\Sigma (\xi, a, \lambda)] d\xi \quad (15)$$

— special function of wave catastrophe — main SWC.

The chains of recursive relations to define the coefficients of the asymptotic expansion in terms of the amplitude and phase of the integrand are of the following form [6]:

$$\begin{aligned} \Lambda^{\frac{\delta}{2}} f |\Delta| &= \left(l_1^{(0)} \right)_g + i \sum_{j=2}^{N_g} \frac{\partial F_\Sigma}{\partial S_{j-1}^g} \left(l_j^{(0)} \right)_g + \sum_{j=1}^{\delta} \frac{\partial F_\Sigma}{\partial \xi_j} \left(H_j^{(0)} \right)_g \\ i \sum_{j=1}^{\delta} \frac{\partial \left(H_j^{n-1} \right)_g}{\partial \xi_j} &= \left(l_1^{(n)} \right)_g + i \sum_{j=2}^{N_g} \frac{\partial F_\Sigma}{\partial S_{j-1}^g} \left(l_j^{(n)} \right)_g + \sum_{j=1}^{\delta} \frac{\partial F_\Sigma}{\partial \xi_j} \left(H_j^{(n)} \right)_g \quad (n = 1, 2, \dots). \end{aligned} \quad (16)$$

In common place the special function of the generalized edge catastrophe of type Σ has a form:

$$I^\Sigma (\lambda, a) = \int_0^{+\infty} \dots \int_0^{+\infty} d\xi_1 \dots d\xi_\nu \int_{-\infty}^{+\infty} \dots \int_{-\infty}^{+\infty} d\xi_{\nu+1} \dots d\xi_\kappa \times \exp \{ i F_\Sigma (\xi, a, \lambda) \}. \quad (17)$$

And generalized formula have the structure like (12), see [1, 2, 5]:

$$U(\Lambda, x) \cong \exp (i\Lambda\Theta(x)) \{ [g] + [E_i] + [E_i E_j] + [E_i E_j E_k] + \dots + [E_1 \dots E_\nu] \}, \quad (18)$$

This expansion consists of 2^ν summands. The first of them gives the leading term, and the other terms are corrections [1, 2, 6]. In (18), every square bracket is an asymptotic expansion likes (12):

$$[Q] = (l_1)_Q \cdot I^{\tilde{\Sigma}_Q} (S^Q) + \sum_{\tau=2}^{N_Q} (l_\tau)_Q \cdot \frac{\partial I^{\tilde{\Sigma}_Q}}{\partial S_{\tau-1}^Q}, \quad (19)$$

with respect to the special functions and their first derivatives. The coefficients of the asymptotic expansions have the form of asymptotically convergent series like (13). The difference concerns the restriction of Q type of the unfolding F_Σ to the boundary; $\tilde{\Sigma}_Q$ — stands for the type of the

generalized boundary catastrophe that corresponds to the restriction of type Q . To define the coefficients there are the recurrent relations like (16).

The special functions of the main, edge, and corner catastrophes (SWC) and their derivatives are of the form of multiple rapidly oscillating integrals. Due to special form of the universal deformation, SWC have a series of properties which enable one to develop efficient algorithms for the computation of these functions. It can be shown that the SWC's defined by (17) satisfy systems of second-order or first-order canonical differential equations [8, 10, 17] of the form

$$\tilde{M}_k I^\Sigma(\lambda, a) = \begin{cases} iI^{\Sigma_k}, & k = 1, \dots, \nu \\ 0, & k = \nu + 1, \dots, \bar{\delta} \end{cases}, \quad (20)$$

$$\tilde{S}_k I^\Sigma(\lambda, a) = \left(i \frac{\partial}{\partial S_k} - \frac{\partial^2}{\partial \lambda_{h_k^1} \partial \lambda_{h_k^2}} \right) I^\Sigma(\lambda, a) = 0, \quad k = 1, \dots, L + \dim a - \bar{\delta}. \quad (21)$$

Using the systems of differential canonical equations, in [5], a method of ordinary differential equations (ODE) was developed for the computation of SWC; this method enables one to avoid the immediate calculation of multiple SWC (17). The problem is reduced to solving a linear system of first-order ordinary differential equations with respect to an SWC and its first derivatives entering the uniform asymptotics.

The full statement of methods of the coefficients and SWC's computation is submitted in works [1–6].

ACKNOWLEDGMENT

This work was supported by the Russian Foundation for Basic Research (under grants No. 07-02-00663 and 09-07-00189).

REFERENCES

1. Kryukovskii [Kryukovsky], A. S., D. S. Lukin, and D. V. Rastyagaev, "Construction of uniform asymptotic solutions of wave-type differential equations by methods of catastrophe theory," *Russian Journal of Mathematical Physics*, Vol. 16, No. 2, 232–245, 2009.
2. Kryukovsky, A. S., D. S. Lukin, E. A. Palkin, and D. V. Rastyagaev, "Wave catastrophes: Types of focusing in diffraction and propagation of electromagnetic waves," *Radiotekhnika i Elektronika*, Vol. 51, No. 10, 1155–1192, 2006.
3. Kryukovsky, A. S., D. S. Lukin, and E. A. Palkin, "Uniform asymptotics for evaluating oscillatory edge integrals by methods of catastrophe theory," *Soviet J. Numer. Anal. Math. Modelling*, Vol. 2, No. 4, 279–312, 1987.
4. Kryukovsky, A. S., D. S. Lukin, and E. A. Palkin, "Uniform asymptotics of integrals with rapidly oscillating functions with degenerate saddle points," *Inst. Electrical Engrg., Akad. Nauk SSSR*, No. 41, 413, Moscow, 1984.
5. Kryukovsky, A. S., D. S. Lukin, and E. A. Palkin, "Edge and angular catastrophes in problems of wave diffraction and propagation," Kazan Aviation Institute, Kazan, 1988.
6. Kryukovsky A. S. and D. S. Lukin, "Geometric diffraction theory created by the methods of edge and angle catastrophes," *Radiotekhnika i Elektronika*, Vol. 43, No. 9, 1–16, 1998.
7. Babich, V. M. and V. S. Buldyrev, *Short-wavelength Diffraction Theory, Asymptotic Methods*, Nauka, Moscow, 1972; Springer, Berlin, 1991.
8. Borovikov, V. A. and B. Y. Kinber, "Geometrical theory of diffraction," Svyaz, Moscow, 1978; Institution of Electrical Engineers (IEE), London, 1994.
9. Maslov, V. P. and M. V. Fedoruk, *Semi-classical Approximation in Quantum Mechanics*, Nauka, Moscow, 1976; Reidel, Dordrecht, 1981.
10. Maslov, V. P., *Perturbation Theory and Asymptotic Methods*, Izdat. Moskov. Gos. Univ., Moscow, 1965; Dunod, Paris, 1972.
11. Arnold, V. I., S. M. Gusein-Zade, and A. N. Varchenko, *Singularities of Differentiable Maps.*, Vol. I, The Classification of Critical Points, Caustics and Wave Fronts, Nauka, Moscow, 1982; Birkhauser, Boston, 1985.